جامعة بجاية
Tasdawit n Bgayet
Université de Béjaïa

Proceeding

Electrical Engineering International Conference

University of Bejaia
December 04-05, 2019

Université Abderrahmane MIRA Bejaia
LGEB
Laboratoire de Genie Electrique Bejaia

LMER
Laboratoire de Maitrise des Energies Renouvelables

Electrical Engineering International Conference (EEIC'19)

Supported by:

Electrical Engineering International Conference (*EEIC'2019*)

Editor: Electrical Engineering Department

Address: University A. Mira of Bejaia, Road of Targa Ouzemmour, 06000, Bejaia, Algeria

Tel/Fax : +213 34 81 37 13

Mail : dept.ge@tech.univ-bejaia.dz

BASIC CONFERENCE INFORMATIONS

Title	The Electrical Engineering International Conference (EEIC'19)
Date	December 04 – 05, 2019
Location	Bejaia, Algeria
Venue	University of Bejaia
Official Language	English

COMMITTEES

Honorary chairs:

- Pr. Boualem SAIDANI (Rector of Bejaia University, Algeria)
- Pr. Amar BOUKERROU (Dean of Technology Faculty)

Conference General Chair:

- Pr. Kassa IDJDARENE

Conference Co-Chair:

- Dr. Nabil TAIB

SCIENTIFIC COMMITTEE

Abdelli R. (U. Bejaia, Algeria)

Abdessemed R. (U. Batna, Algeria)

Abid H. (U. SBA, Algeria)

Achour A. (U. Bejaia, Algeria)

Alkama R. (U. Bejaia, Algeria)

Amimeur H. (U. Bejaia, Algeria)

Aouzellag D. (U. Bejaia, Algeria)

Aouzellag N. (U. Bejaia, Algeria)

Attari M. (USTHB, Algeria)

Azni M. (U. Bejaia, Algeria)

Bacha S. (U. Grenoble, France)

Bachari NE. (USTHB, Algeria)

Bahi T. (U. Annaba, Algeria)

Belaid S. (U. Bejaia, Algeria)

Benamrouche N. (U. Tizi Ouzou, Algeria)

Bendahmane B. (U. Bejaia, Algeria)

Benkhoris MF. (U. Nantes, France)

Benyahia N. (U. Tizi Ouzou, Algeria)

Berkouk EM. (ENP, Algeria)

Boudries Z. (U. Bejaia, Algeria)

Boukortt A. (U. Mostaghanem, Algeria)

Bouzidi A. (U. Bejaia, Algeria)

Chabour F. (U. Lehavre, France)

Chaiba A. (U. Khenchela, Algeria)

Chibani Y. (USTHB, Algeria)

Dascalescu L. (U. Poitiers, France)

Djebbar AB. (U. SBA, Algeria)

Djennoune S. (U. Tizi Ouzou, Algeria)

Fergani B. (USTHB, Algeria)

Ghedamsi K. (U. Bejaia, Algeria)

Guéguen H. (SUPELEC, France)

Berrah S. (U. Bejaia, Algeria)

Boubakeur A. (ENP, Algeria)

Boudissa R. (U. Bejaia, Algeria)

Guenounou O. (U. Bejaia, Algeria)

Haddad S. (U. Tizi Ouzou, Algeria)

Bellahsene H (U. Bejaia, Algeria)

Hamoudi F. (U. Bejaia, Algeria)

Haraoubia B. (USTHB, Algeria)

Hassam A. (U. Setif, Algeria)

Idjdarene K. (U. Bejaia, Algeria)

Idoughi D. (U. Bejaia, Algeria)

Kasdi A. (U. Bejaia, Algeria)

Kasmi R. (U. Bouira, Algeria)

Khenfer N. (U. Setif, Algeria)

Khireddine A. (U. Bejaia, Algeria)

Krim F. (U. Setif, Algeria)

Labiod S. (U. Jijel, Algeria)

Lamamra K. (U. O El Bouaghi, Algeria)

Lefebvre D. (U. Le Havre, France)

Medjdoub A. (U. Bejaia, Algeria)

Mahtout S. (U. Bejaia, Algeria)

Maouche B. (U. Bejaia, Algeria)

Mekhaldi A. (ENP, Algeria)

Mekhilef S. (U. Malaya, Malaysia)

Mendil B. (U. Bejaia, Algeria)

Mokrani K. (U. Bejaia, Algeria)

Nabti H. (U. Bejaia, Algeria)

Nichita C.(U. Le Havre, France)

Ouari K. (U. Bejaia, Algeria)

Ouhrouche M. (U. Chicoutimi, Canada)

Rekioua D. (U. Bejaia, Algeria)

Rekioua T. (U. Bejaia, Algeria)

Remram Y. (USTHB, Algeria)

Rouha N. (U. Bejaia, Algeria)

Saou R. (U. Bejaia, Algeria)

Tafinine F. (U. Bejaia, Algeria)

Taib N. (U. Bejaia, Algeria)

Taibi S. (U. Batna, Algeria)

Takorabet N. (U. Nancy, France)

Teguar M. (ENP, Algeria)

Tounzi A. (U. Lille, France)

Zaim M. (U. Nantes, France)

Zebboudj Y. (U. Bejaia, Algeria)

ORGANIZING COMMITTEE

- **F. Hamoudi**
- **A. Laifaoui**
- **O. Guenounou**
- **R. Abdelli**
- **S. Tamalouzt**
- **H. Lehouche**
- **A. Medjdoub**
- **S. Idjdarene**
- **S. Belaid**
- **L. Achour**
- **F. Tazerart**
- **H. Ouatah**
- **S. Atroune**
- **S. Chekkal**
- **A. Kasdi**
- **A. Mekhmoukh**
- **A. Bouzidi**
- **A. Azib**
- **F. Tafinine**
- **A. Alliche**
- **N. Benamirouche**
- **S. Hadji**
- **N. Mezai**
- **D. Ziane**

TOPICS

- **T1: EMD (Electrical Machines and Drives)**
- **T2: PS (Power Systems)**
- **T3: RES (Renewable Energy Systems)**
- **T4: PEA (Power Electronics and Applications)**
- **T5: ICS (Identification and Control Systems)**
- **T6: TSN (Telecommunication Systems and Networks)**
- **T7: SIP (Signal and Image Processing)**
- **T8: EEF (Electric and Electromagnetic Field)**
- **T9: EHV (Electrical High Voltage)**

PREFACE

This volume contains the proceedings of the first Electrical Engineering International Conference (EEIC'19) which was held in Bejaia from December 4 to 5, 2019. This conference is an opportunity to bring together researchers, doctoral students as well as industrialists in order to present the results of their latest research work for some and to express their needs and proposals for others. It is in this perspective that this conference included in its topics the majority of disciplines covering the broad field of electrical engineering.

The holding of this first edition of the conference is not an end in itself, because the organizers aim to register it in the long term by organizing it every two years. This will undoubtedly create a discussion forum between the various actors of the scientific community to exchange their ideas and define new research perspectives.

This conference will also be a godsend for industrialists and the socio-economic sector in order to submit their issues and develop partnerships with universities and research laboratories.

The scientific program of EEIC'19 contains the presentation of 100 selected communications (52 in oral form and 48 in poster) as well as two plenary conferences led by eminent researchers.

1- **Pr. Noreddine TAKORABET,** University of Nancy (France), **"On the hybridization of 3D Finite Element Models and Reluctance Networks for shape optimization of magnetic devices".**

2- **Pr. Aissa CHOUDER,** University of M'Sila (Algeria), **"Monitoring, fault detection and diagnosis of PV grid connected systems".**

Program of the Electrical Engineering International Conference

EEIC'19

Bejaia - Algeria,

December 04-05, 2019

Wednesday 4th December 2019, Morning

8h00 - 9h00	Registration							
9h00 - 9h30	Opening Ceremony							
9h30 - 10h30	Plenary Session							
10h30 - 11h00	Coffee-Break							
11h00 - 11h15	Oral Sessions 1	PS-55	Room 3	ICS-34	Room 2	EEF-30	Room 1	
11h15 - 11h30		PS-120		ICS-57		EEF-56		
11h30 - 11h45		PS-129		ICS-63		EEF-165		
11h45 - 12h00		PS-156		ICS-125		EEF-185		

Wednesday 4th December 2019, Afternoon

12h00 - 14h00	Lunch							
14h00 - 14h15	Oral Sessions 2	EHV-16	Room 3	PEA-93	Room 2	SIP-87	Room 1	
14h15 - 14h30		EHV-90		PEA-122		SIP-162		
14h30 - 14h45		EHV-116		PEA-164		SIP-186		
14h45 - 15h00		EHV-132		PEA-210		SIP-244		
15h00 - 16h30	Coffee-Break & Poster Session 1	ICS	91 - 131 - 163 - 189 - 229 - 232 - 234					
		EEF	26 - 32 - 67 - 175					
		RES	2-36-49-84-100-113-135-138-184-216					
		EMD	88 - 89 - 96 - 117					
		EHV	66 - 110 - 124 - 171					
16h30 - 16h45	Oral Sessions 3	TSN-9	Room 3	RES-14	Room 2	EMD-42	Room 1	
16h45 - 17h00		TSN-121		RES-37		EMD-59		
17h00 - 17h15		TSN-174		RES-94		EMD-71		
17h15 - 17h30		TSN-241		RES-104		EMD-72		

Thursday 5th December 2019, Morning

8h30 - 9h30	Plenary Session							
9h30 - 9h45	Oral Sessions 4	RES-127	Room 1	EHV-141	Room 2			
9h45 - 10h00		RES-205		EHV-142				
10h00 - 10h15		RES-221		EHV-151				
10h15 - 10h30		RES-240		EHV-191				
10h30 - 11h30	Coffee-Break & Poster Session 2	PEA	17 - 64 - 130 - 158					
		SIP	1-80-99-134-173-176-224					
		TSN	85-105-148-152-212-228					
		EMD	137 - 172 - 187 - 188					
11h30 - 11h45	Oral Sessions 5	ICS-149	Room 1	EMD-98	Room 2			
11h45 - 12h00		ICS-180		EMD-106				
12h00 - 12h15		ICS-214		EMD-147				
12h15 - 12h30		ICS-233		EMD-177				
12h30 - 13h00	Closing Ceremony							
13h00 - 14h30	Lunch							

Program of the Electrical Engineering International Conference

EEIC'19

Bejaia - Algeria,

December 04-05, 2019

Wednesday 4th December 2019, Morning

Room 1

8h00 - 9h00	**Registration**		
9h00 - 9h30	**Opening Ceremony**		
9h30 - 10h30	**Plenary Session Chairman: Pr REKIOUA Toufik**	**Presented by : Pr TAKORABET Noureddine**	**Title : On the hybridization of 3D Finite Element Models and Reluctance Networks for shape optimization of magnetic devices**
10h30 - 11h00	**Coffee-Break**		
11h00 - 11h15	**Oral Session Chairman Pr. Zebboudj Y.**	EEF-30	Electromagnetical modeling a planar inductance for integration in a buck DC- DC
11h15 - 11h30		EEF-56	Design of Tri_band Pass Filter using Complementary Split Ring Resonators Defected Ground Structure (CSRRs-DGS)
11h30 - 11h45		EEF-165	Investigation On EM Radiation of Carbon Nanotubes Interconnects
11h45 - 12h00	**Pr. Mahtout S.**	EEF-185	Study of a novel optical mirror with biisotropic slabs

Wednesday 4th December 2019, Afternoon

12h00 - 14h00	**Lunch**		
14h00 - 14h15	**Oral Session Chairman Pr. Mokrani K.**	SIP-87	Colors Skin Lesions Detection for Melanoma Discrimination
14h15 - 14h30		SIP-162	A Novel Approach for Breast Mass Segmentation by Cooperation Fuzzy Possibilistic and Deformable Model
14h30 - 14h45		SIP-186	Hyperspectral Feature Selection using Improved F-Score Technique
14h45 - 15h00	**Dr. Kasmi R.**	SIP-244	New aproach in vibration monitoring of bearing faults in induction motor using CSA
15h00 - 16h30	**Coffee-Break & Poster Session 1**	**ICS** (Chairman : Achour A.Y. & Ouari K.) - **EEF** (Chairman : Mahtout S.) - **RES** (Chairman : Rekioua Dj. & Chaiba A.) - **EHV** (Chairman : Boudissa R. & Medjdoub A.) - **EMD** (Chairman : Boudries Z. & Amimeur H.)	
16h30 - 16h45	**Oral Session Chairman Pr. Tounzi A.**	EMD-42	Sliding mode control of double star induction motor using SVM technique
16h45 - 17h00		EMD-59	Direct Torque Control Using Self-Tuning Speed Controller of the Induction Motor Drive
17h00 - 17h15		EMD-71	Fault Tolerant Control of Brushless DC Motor based on Backstepping control
17h15 - 17h30	**Pr. Aouzellag D.**	EMD-72	Early diagnosis of the electrical insulation degradation based on transient inter-turn voltage distribution in windings fed from inverter pulses

Thursday 5th December 2019, Morning

8h30 - 9h30	**Plenary Session Chairman: Pr GHEDAMSI K.**	**Présented by : Pr CHOUDER Aissa**	**Title : Monitoring, fault detection and diagnosis of PV grid connected systems**
9h30 - 9h45	**Oral Session Chairman Pr. Krim F.**	RES-127	A new signal filtering strategy for photovoltaic controller improvement
9h45 - 10h00		RES-205	Design and comparison of two intelligent controllers for global maximum power point tracking of PV system under partial shading conditions
10h00 - 10h15		RES-221	Reactive Power Control for Power Improvement in Wind Farms Unsing STATCOM
10h15 - 10h30	**Pr. Alkama R.**	RES-240	Direct Torque Control based on Fuzzy Switching Table of IM for PV Pumping System
10h30 - 11h30	**Coffee-Break & Poster Session 2**	**PEA** (Chairman : Boudries Z.) - **SIP** (Chairman : Chelbi S. & Alliche A.) - **TSN** (Chairman : Azni M. & Bellahsene H.) - **EMD** (Chairman : Ouari K.)	
11h30 - 11h45	**Oral Session Chairman Dr. Lamamra K.**	ICS-149	Neural Network for Abnomalities Detection in Raditherapy Service
11h45 - 12h00		ICS-180	The slotine-Li controller for a manipulator robot has two degree of freedom
12h00 - 12h15		ICS-214	Fractional Order Adaptive Model Predictive Control
12h15 - 12h30	**Dr. Guenounou O.**	ICS-233	Fault Diagnosis and Fault Tolerant Control for Mobile Robot Based on Multi-sensors Data Fusion
12h30 - 13h00	**Closing Ceremony**		
13h00 - 14h30	**Lunch**		

Program of the Electrical Engineering International Conference

EEIC'19

Bejaia - Algeria,

December 04-05, 2019

Wednesday 4th December 2019, Morning

Room 2

8h00 - 9h00	**Registration**		
9h00 - 9h30	**Opening Ceremony**		
9h30 - 10h30	**Plenary Session**		
10h30 - 11h00	**Coffee-Break**		
11h00 - 11h15	**Oral Session**	ICS-34	Effect of tasks reallocation on the performances of a multi robot system in goods transportation
11h15 - 11h30	**Chairman**	ICS-57	Job Shop and parallel machine scheduling problems: minimization of Makspan
11h30 - 11h45	**Pr. Mendil**	ICS-63	Predictive Functional Control of Building HVAC Systems
11h45 - 12h00	**Dr. Lamamra K.**	ICS-125	Design and voltage control of an automatic voltage regulator using partcile swarm optimization

Wednesday 4th December 2019, Afternoon

12h00 - 14h00	**Lunch**		
14h00 - 14h15	**Oral Session**	PEA-93	Thermal Modeling of an Integrated Circular Inductor Using Separation of Variables Method
14h15 - 14h30	**Chairman**	PEA-122	Modeling of Octagonal Planar Microtransformer for Integrated RF Systems
14h30 - 14h45	**Pr. Rekioua T.**	PEA-164	A Three Phase Input-Six phase Output Indirect Matrix Converter and Space Vector Modulation.
14h45 - 15h00	**Pr. Ghedamsi K.**	PEA-210	Design and Implementation of Shunt Active Power Filter using STM32F4 Board
15h00 - 16h30	**Coffee-Break & Poster Session 1**	**ICS** (Chairman : Achour A.Y. & Ouari K.) - **EEF** (Chairman : Mahtout S.) - **RES** (Chairman : Rekioua Dj. & Chaiba A.) - **EHV** (Chairman : Boudissa R. & Medjdoub A.) - **EMD** (Chairman : Boudries Z. & Amimeur H.)	
16h30 - 16h45	**Oral Session**	RES-14	Study and control of the hybrid renewable generation system supplying standalone load
16h45 - 17h00	**Chairman**	RES-37	A new power management technique for a standalone wind energy conversion system based on the SCIG with storage battery
17h00 - 17h15	**Pr. Rekioua Dj.**	RES-94	Organic Solar Cells Structures and Performance
17h15 - 17h30	**Pr. Chouder A.**	RES-104	Power Management Strategy Based on Utilisation Cost of Stand-Alone Hybrid (PV/Battery/Hydrogen) System

Thursday 5th December 2019, Morning

8h30 - 9h30	**Plenary Session**		
9h30 - 9h45	**Oral Session**	EHV-141	Characterisation of a two-wire corona electrode
9h45 - 10h00	**Chairman**	EHV-142	Optimization of the inter electrode spacing to improve the efficiency of a Multi-wires-to-plates type electrostatic precipitator
10h00 - 10h15	**Pr. Boudissa R.**	EHV-151	FTIR and DSC Study of XLPE Exposed to Thermal and Electrical Constraints
10h15 - 10h30	**Dr. Rouha N.**	EHV-191	Effect of natural rain on the electrical performance of inclined silicone insulation putting out of voltage
10h30 - 11h30	**Coffee-Break & Poster Session 2**	**PEA** (Chairman : Boudries Z.) - **SIP** (Chairman : Chelbi S. & Alliche A.) - **TSN** (Chairman : Azni M. & Bellahsene H.) - **EMD** (Chairman : Ouari K.)	
11h30 - 11h45	**Oral Session**	EMD-98	Simulation study of the dual star permanent magnet synchronous machine using different modeling approaches with an open circuit fault
11h45 - 12h00	**Chairman**	EMD-106	Influence of geometric and physical parameters on the thrust force of a linear induction motors
12h00 - 12h15	**Pr. Takorabet N.**	EMD-147	2D Finite Element Thermal Modeling of Induction Motor under Healthy and Faulty Operations
12h15 - 12h30	**Pr. TAIBI S.**	EMD-177	Use of the Fuzzy Logic Technique in the Diagnosis of the Sotorical Faults of the Squirrel Cage Asynchronous Machine
12h30 - 13h00	**Closing Ceremony**		
13h00 - 14h30	**Lunch**		

Program of the Electrical Engineering International Conference

EEIC'19

Bejaia - Algeria,

December 04-05, 2019

Wednesday 4th December 2019, Morning

Room 3

8h00 - 9h00	**Registration**		
9h00 - 9h30	**Opening Ceremony**		
9h30 - 10h30	**Plenary Session**		
10h30 - 11h00	**Coffee-Break**		
11h00 - 11h15	**Oral Session**	**PS-55**	Upgrading and Improvement of the A.M.B. program
11h15 - 11h30	**Chairman**	**PS-120**	A Dynamic Neural Network Model for Solving Combined Economic and Emission Dispatch with Real-Time Applications
11h30 - 11h45	**Dr. Lahaçani N.**	**PS-129**	Environmental/Economic Dispatch Problem Solution Based on Discontinuous Recurrent Neural Network
11h45 - 12h00	**Dr. Bouzidi A.**	**PS-156**	Superconducting Magnetic Energy Storage for power system transient stability enhancement in presence of wind generation

Wednesday 4th December 2019, Afternoon

12h00 - 14h00	**Lunch**		
14h00 - 14h15	**Oral Session**	EHV-16	Numerical Simulation of Streamer Propagation in Point-Plane Air Gaps Computed With Finite Element Method
14h15 - 14h30	**Chairman**	EHV-90	Experimental study of the active and controlled neutralization of polypropylene nonwoven media
14h30 - 14h45	**Pr. Zebboudj Y.**	EHV-116	Corona Charging and Charge Decay on Polyethylene Terephthalate Films (PET)
14h45 - 15h00	**Dr. Bendahmane B.**	EHV-132	Optimization of a superhydrophobic insulation's performance by ejection of any deposit of water drops covering it using an alternating electrical field
15h00 - 16h30	**Coffee-Break & Poster Session 1**	**ICS** (Chairman : Achour A.Y. & Ouari K.) - **EEF** (Chairman : Mahtout S.) - **RES** (Chairman : Rekioua Dj. & Chaiba A.) - **EHV** (Chairman : Boudissa R. & Medjdoub A.) - **EMD** (Chairman : Boudries Z. & Amimeur H.)	
16h30 - 16h45	**Oral Session**	TSN-9	Performance Comparison of APD and PIN Photodiodes using RZ and NRZ
16h45 - 17h00	**Chairman**	TSN-121	Plasmonic nano-sensor and band-pass filter based on metal-insulator-metal waveguide with a hexagonal ring based cavity
17h00 - 17h15	**Pr. Khireddine A.**	TSN-174	The impact of jitter on the HEVC video streaming with Multiple Coding
17h15 - 17h30	**Pr. Berrah**	TSN-241	Enhanced Performances of SAC-OCDMA System Operating with Different Codes

Contents

Sliding mode control of double star induction motor using SVM technique

Farid BELOUAHCHI/ Materials physics laboratory, radiation and nanostructure
Electrical engineering department
University of Bourdj Bou Arreridj
Bourdj Bou Arreridj, Algeria
farid.belouahchi@univ-bba.dz

Elkhier MERABET/ Materials physics laboratory, radiation and nanostructure
Electrical engineering department
University of Bourdj Bou Arreridj
Bourdj Bou Arreridj, Algeria
elkheir34@gmail.com

Abstract— The present paper is focused on sliding mode control (SMC) of double star induction motor (DSIM) fed by two-level six-phases inverter. The inverter switches control is based on space vector modulation technique (SVM), the use of this technique has a lot of advantages compared with PWM, among of this advantages is minimization of harmonic distortions in output voltages and alternating currents generated. The (SMC) is a robust nonlinear optimal controller. In order to reduce a torque ripple, we tested the performance of the system under different operating conditions, and by using MatLab/Simulink the simulation results are presented and analyzed.

Keywords: Double star induction motor (DSIM), sliding mode control (SMC), space vector modulation (SVM), pulse width modulation (PWM).

I. INTRODUCTION

In modern industrialized drives, the use of thripahses machine is degraded in front of the multiphase machine for the high reliability of this last [1, 2]. DSIM is one of the machines multiphases. It has been used in different fields of industry that need high power such as electric hybrid vehicles, locomotive traction and ship propulsion and other applications which requires safeness conditions such as aerospace and offshore wind energy systems. DSIM guarantees a decrease of rotor harmonics currents and lower torque ripple and also has many other advantages such as: reliability, power segmentation and higher efficiency, it has a greater fault tolerance; it can continue to operating even with open-phase faults thanks to the important number of phases it owns [3, 4].

The sliding mode control theory was proposed by Utkin in 1977[5]. Thereafter, the applications of its theoretical works were developed. The sliding mode control (SMC) is a non linear control, it has a fast dynamic response where the system stability is guaranteed by reducing transient state error, it ensures robustness against parameter variation and external disturbance when the system reaches and remains in the sliding surface. This last is the best advantage of a sliding mode control, for this reason it has been widely employed to control nonlinear systems that have model uncertainty and external disturbance [6]. In other hand the only disadvantage of the SMC is the chattering phenomenon., this unwanted phenomenon is appeared under high frequency ripples form caused by the switching control law [7, 8], for eliminate this phenomene can be used the saturation function 'sat' or hyperbolic tangent instead of the utilization of the sign function in a thin boundary layer near the sliding surface. SMC has recently been applied on doubly fed induction generator where it has proved its robustness against parameters variation and disturbances in front of the both proportional-Integral and backstepping control [9, 10].

There are several control techniques using pulse width modulation, such as sinusoidal modulation, hysteresis modulation, [11], DTC [12, 13, 14] and space vector modulation [15, 16]. Space vector modulation introduced by [17] is the most efficient and the most used technique.

The main objective of this work is to improve the quality of the output voltage and current waveform and prove the robustness of the SMC.

This paper is organized as follows: The DSIM model will be presented in the next section. The control method by SMC will be discussed in section three. Moreover, in the fourth section the explanation of SVM technique and in fifth section the simulation results are discussed on Matlab/Simulink for the proposed control schemes. Finally, a general conclusion summarizes this work.

II. *SLIDING MODE CONTROL (SMC) of DSIM*

The DSIM dynamic equations in the reference d-q are established in [18.]

A.SLIDING MODE THEORY [19]

The sliding mode control is based on the convergence of system state trajectory to a sliding surface. The state vector is kept around this surface by the switching control effort in order that the trajectory slides to the origin through the sliding surface. The design of SMC can be reach in two successive steps:

First step: definition of sliding surfaces. The following equation is the most used surface S(x) in the literature:

$$s(t) = (\lambda + \frac{d}{dt})^{r-1}(x_{ref} - x) \quad (1)$$

Where x is the state vector, x_{ref} is the reference state vector, r is the degree of the sliding mode and λ is the weighting factor.

Second step: Control law design

The sliding mode control has two command components and can be written as follows:

$$s(t) = u_{eq}(t) + u_N(t) \quad (2)$$

The component u_{eq} called the equivalent control (decoupling control) is obtained by putting surface derivate equals zero $s(t)^{\bullet} = 0$, its role is holding the system on the sliding surface which is definite by $s(t) = 0$. The other constituent u_N is the discontinuous control (switching control) it ensures the convergence of system state trajectory toward sliding surface. The reaching condition is based on Lyapunov theory stability and must verify $s^{\bullet} \cdot s < 0$

B.APPLICATION OF SMC ON DSIM

The SMC algorithm for DSIM has been presented in [20, 21]. In order to eliminate or decrease the chattering phenomena in steady state, a saturation function sat(t) is used instead the signum function sgn (t) for the switching control [22]. The sat (t) function is defined as [23]:

$$sat(t) = \frac{s}{|s| + m} \quad (3)$$

Where m is a small positive gain and $|s| \succ m$.

Therefore, the SMC for DSIM can be designed as follows:

Speed and flux SMC:

$$\begin{cases} s(\omega_r) = \omega^* - \omega \\ s(\phi_r) = \phi^* - \phi \end{cases} \quad (4)$$

The time derivative of equation (4) gives:

$$\begin{cases} s^{\bullet}(\omega_r) = \omega^{\bullet *} - \omega^{\bullet} \\ s^{\bullet}(\phi_r) = \phi^{\bullet *} - \phi^{\bullet} \end{cases} \quad (5)$$

By substituting equations of speed and of rotor flux in [18] into (5) we get:

$$\begin{cases} s^{\bullet}(\omega_r) = \omega^{\bullet *} - \frac{P^2}{J}\frac{L_m}{L_m + L_r}\phi^*\left(i_{qs1} + i_{qs2}\right) + \frac{P}{J}T_L + \frac{K_f}{J}\omega_r \\ s^{\bullet}(\phi_r) = \phi^{\bullet *} + \frac{R_r}{L_m + L_r}\phi_r - \frac{L_m R_r}{L_m + L_r}\left(i_{ds1} + i_{ds2}\right) \end{cases} \quad (6)$$

Assuming that:

$$\begin{cases} i_{ds1} + i_{ds2} = i_{ds} \\ i_{qs1} + i_{qs2} = i_{qs} \\ i_{ds1} = i_{ds2} \\ i_{qs1} = i_{qs2} \end{cases} \quad (7)$$

And putting:

$$\begin{cases} i_{ds} = i^*{}_{ds} = i_{dseq} + i_{dsn} \\ i_{qs} = i^*{}_{qs} = i_{qseq} + i_{qsn} \end{cases} \quad (8)$$

Using equations (6), (7) and (8) we obtain:

$$\begin{cases} s^{\bullet}(\omega_r) = \omega^{\bullet *} - \frac{P^2}{J}\frac{L_m}{L_m + L_r}\phi^* i_{qseq} - \frac{P^2}{J}\frac{L_m}{L_m + L_r}\phi^* i_{qsn} + \frac{P}{J}T_L \\ s^{\bullet}(\phi_r) = \phi^{\bullet *} + \frac{R_r}{L_m + L_r}\phi_r - \frac{L_m R_r}{L_m + L_r} i_{dseq} - \frac{L_m R_r}{L_m + L_r} i_{dsn} \end{cases} \quad (9)$$

By applying the SMC theory, we find the d-q axis components of currents control:

$$\begin{cases} i_{dseq} = \frac{L_m + L_r}{R_r L_m}\left[\phi_r{}^{\bullet *} + \frac{R_r}{L_m + L_r}\phi_r\right] \\ i_{qseq} = \frac{J}{P^2}\frac{L_m + L_r}{L_m}\phi_r{}^*\left[\omega_r{}^{\bullet *} + \frac{K_f}{J}\omega_r + \frac{P}{J}T_L\right] \\ i_{dsn} = K_{\phi_r}\frac{S(\phi_r)}{|S(\phi_r)| + m_{\phi_r}} \\ i_{qsn} = K_{\omega_r}\frac{S(\omega_r)}{|S(\omega_r)| + m_{\omega_r}} \end{cases} \quad (10)$$

Where $K_{\Phi r}$ et $K_{\omega r}$ are positive constants.

Currents SMC:

$$\begin{cases} S(i_{ds1}) = i^*{}_{ds1} - i_{ds1} \\ S(i_{qs1}) = i^*{}_{qs1} - i_{qs1} \\ S(i_{ds2}) = i^*{}_{ds2} - i_{ds2} \\ S(i_{qs2}) = i^*{}_{qs2} - i_{qs2} \end{cases} \quad (11)$$

The derivative of equation (11) according the time gives:

$$\begin{cases} S^{\bullet}(i_{ds1}) = \dfrac{d}{dt}i^{*}_{ds1} - \dfrac{d}{dt}i_{ds1} \\ S^{\bullet}(i_{qs1}) = \dfrac{d}{dt}i^{*}_{qs1} - \dfrac{d}{dt}i_{qs1} \\ S^{\bullet}(i_{ds2}) = \dfrac{d}{dt}i^{*}_{ds2} - \dfrac{d}{dt}i_{ds2} \\ S^{\bullet}(i_{qs2}) = \dfrac{d}{dt}i^{*}_{qs2} - \dfrac{d}{dt}i_{qs2} \end{cases} \quad (12)$$

By using equations of tension in [18] the system of equations (12) became:

$$\begin{cases} S^{\bullet}(i_{ds1}) = i^{\bullet *}_{ds1} - \dfrac{1}{L_{s1}}\left(v_{ds1} - R_{s1}i_{ds1}\right) - \dfrac{1}{L_{s1}}\left[\omega_s\left(L_{s1}i_{qs1} + T_r\phi^{*}\omega_{gl}\right)\right] \\ S^{\bullet}(i_{qs1}) = i^{\bullet *}_{qs1} - \dfrac{1}{L_{s1}}\left(v_{qs1} - R_{s1}i_{qs1}\right) + \dfrac{1}{L_{s1}}\left[\omega_s\left(L_{s1}i_{ds1} + \phi^{*}\right)\right] \\ S^{\bullet}(i_{ds2}) = i^{\bullet *}_{ds2} - \dfrac{1}{L_{s2}}\left(v_{ds2} - R_{s2}i_{ds2}\right) - \dfrac{1}{L_{s2}}\left[\omega_s\left(L_{s2}i_{qs2} + T_r\phi^{*}\omega_{gl}\right)\right] \\ S^{\bullet}(i_{qs2}) = i^{\bullet *}_{qs2} - \dfrac{1}{L_{s2}}\left(v_{qs2} - R_{s2}i_{qs2}\right) + \dfrac{1}{L_{s2}}\left[\omega_s\left(L_{s2}i_{ds2} + \phi^{*}\right)\right] \end{cases} \quad (13)$$

Putting:

$$\begin{cases} v_{ds1} = v^{*}_{ds1} = v_{ds1eq} + v_{ds1n} \\ v_{qs1} = v^{*}_{qs1} = v_{qs1eq} + v_{qs1n} \\ v_{ds2} = v^{*}_{ds2} = v_{ds2eq} + v_{ds2n} \\ v_{qs2} = v^{*}_{qs2} = v_{qs2eq} + v_{qs2n} \end{cases} \quad (14)$$

Finally, by following the same method used with the currents sliding mode control, we get the decoupling control voltages:

$$\begin{cases} v_{ds1eq} = L_{s1}\dfrac{d}{dt}i^{*}_{ds1} + R_{s1}i_{ds1} + \omega_s\left(L_{s1}i_{qs1} + T_r\phi^{*}r\omega^{*}gl\right) \\ v_{qs1eq} = L_{s1}\dfrac{d}{dt}i^{*}_{qs1} + R_{s1}i_{qs1} - \omega_s\left(L_{s1}i_{ds1} + \phi^{*}r\right) \\ v_{ds2eq} = L_{s2}\dfrac{d}{dt}i^{*}_{ds2} + R_{s2}i_{ds2} + \omega_s\left(L_{s2}i_{qs2} + T_r\phi^{*}r\omega^{*}gl\right) \\ v_{qs2eq} = L_{s2}\dfrac{d}{dt}i^{*}_{qs2} + R_{s2}i_{qs2} - \omega_s\left(L_{s2}i_{ds2} + \phi^{*}r\right) \end{cases} \quad (15)$$

And also the switching control voltages:

$$\begin{cases} v_{ds1n} = K_{ds1}\dfrac{S(i_{ds1})}{\left|S(i_{ds1})\right| + m_{ds1}} \\ v_{qs1n} = K_{qs1}\dfrac{S(i_{qs1})}{\left|S(i_{qs1})\right| + m_{qs1}} \\ v_{ds2n} = K_{ds2}\dfrac{S(i_{ds2})}{\left|S(i_{ds2})\right| + m_{ds2}} \\ v_{qs2n} = K_{qs2}\dfrac{S(i_{qs2})}{\left|S(i_{qs2})\right| + m_{qs2}} \end{cases} \quad (16)$$

Fig.1 illustrates the synoptic diagram of the SMC-SVM of DSIM.

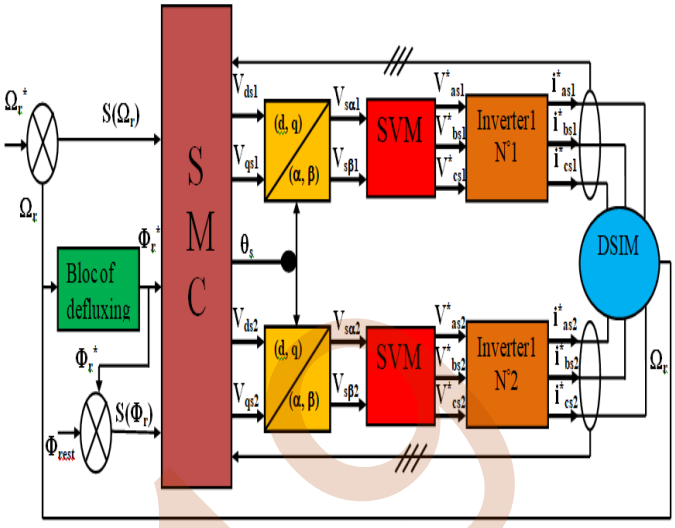

Fig.1. Block diagram of SMC-SVM of DSIM

III. Space Vector Modulation Technique

The SVM is an algorithm for the control of pulse width modulation (PWM), it is one of the methods to reduce losses and decrease the distortions of the alternating current generated from DC compared to standard PWM. For the stator 1, the figure2 in the plan (α, β) illustrates the vectors (v_1-v_6) divide the design into six sectors, each sector is moved 60 degrees. The reference voltage (v_{ref}) is generated using two adjacent vectors (v_1-v_6) and a null vector (v_0 or v_7) [24].

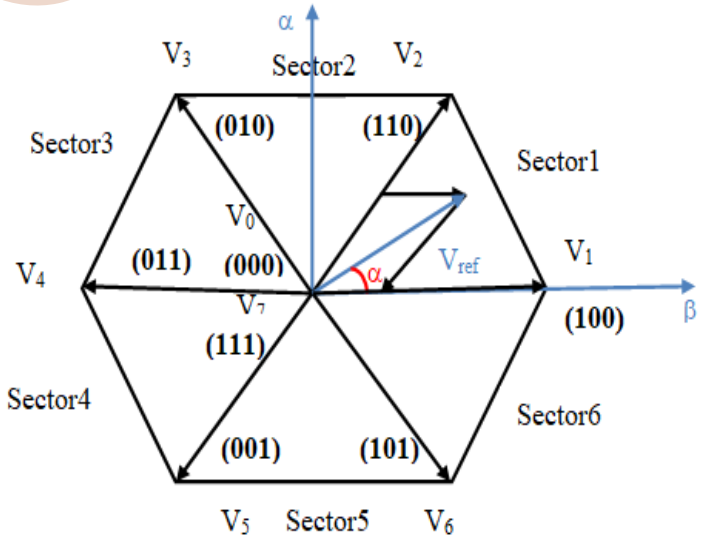

Fig.2. Voltages space vector

Therefore, space vector PWM can be implemented by the following steps:

- Step 1. Determine Vd, Vq, Vref, and angle (α)
- Step 2. Determine time duration T1, T2, T0
- Step 3. Determine the switching time of each transistor (S1 to S6).

IV. Simulation results and discussion

The control of the drive system has been tested by simulation under SMC scheme using SVM technique; the results are performed in this paper by using MATLAB/SIMULINK. The used double star induction motor has the following parameters, the nominal power P_n is 4.5kw, Nominal voltage V_n is 220V, stator resistances R_{s1} and R_{s2} are 3.72 Ohm, rotor resistance R_r is 2.12 Ohm, Mutual inductance L_m is 0.3672H, Rotor inductance L_r is 0.006H, moment of inertia J is 0.0662kg.m^2, and friction coefficient K_f is 0.001.All simulation results have been obtained for two tests conditions.

The first test is the no load start then under load with load torque is T_r= 14 N.m and reference speed is w_{ref}=100rd/sec.

The second test is the no load start with inversion of reference speed from 100rd/sec to -100rd/sec.

Table I (Appendix) summarize the main THD values of stator current with SVM and with PWM.

Fig.3, 4, 5 and 6 respectively presents different responses of electromagnetic torque, speed and stator current with SVM and PWM for the first test and the second test.

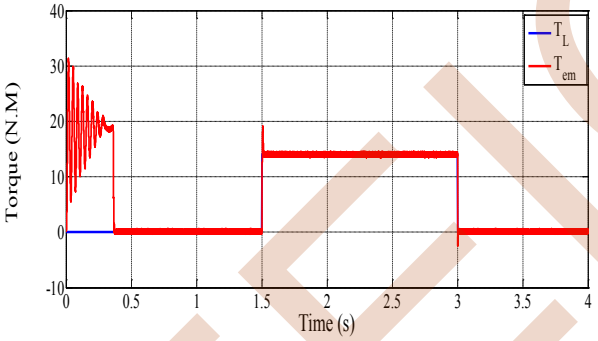

(a)

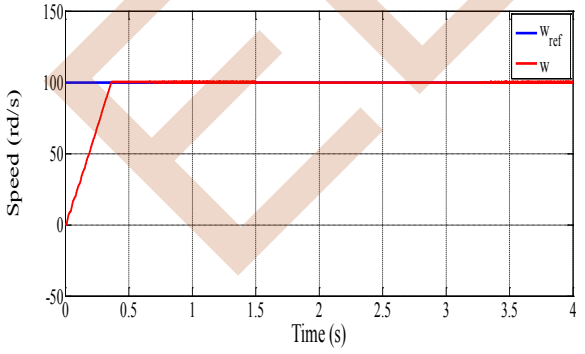

(b)

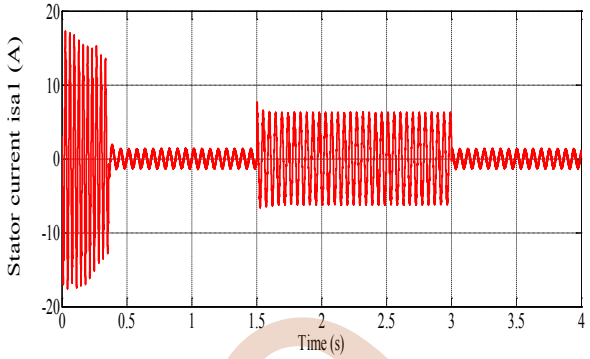

(c)

Figure 3. Torque, speed and stator current responses with SVM technique for the first test

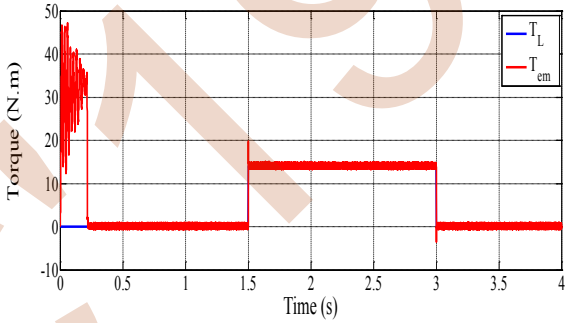

(a)

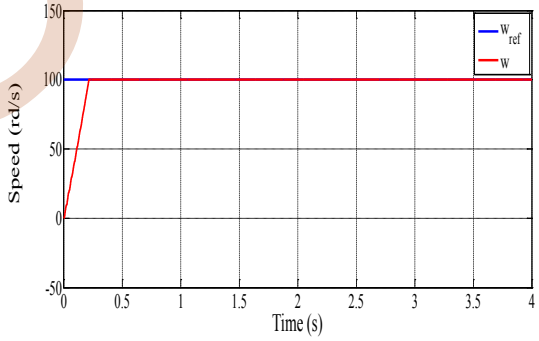

(b)

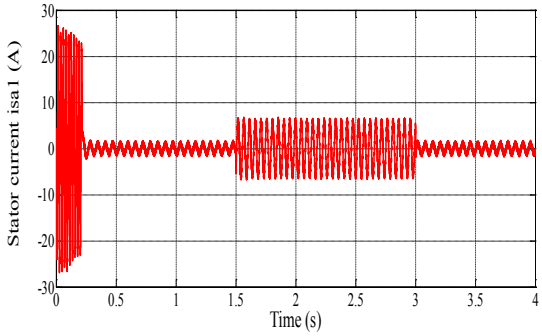

(c)

Figure 4. Torque, speed and stator current responses with PWM technique for the first test.

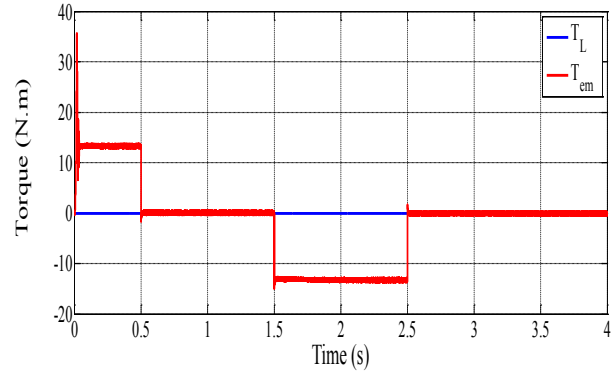

(a)

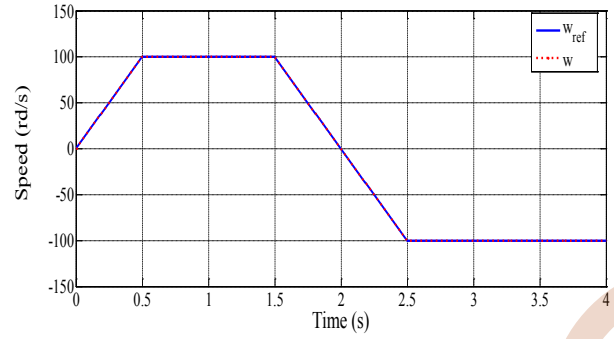

(b)

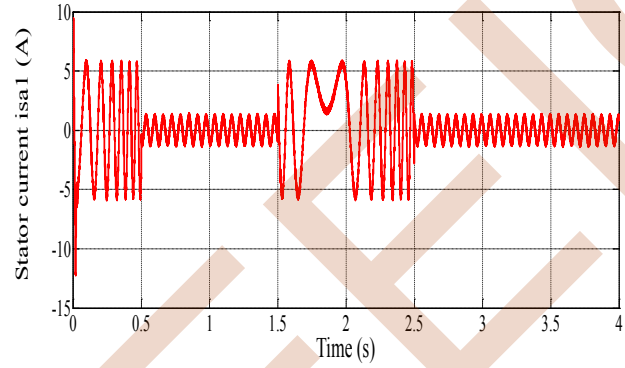

(c)

Figure 5. Torque, speed and stator current responses with SVM technique for the second test.

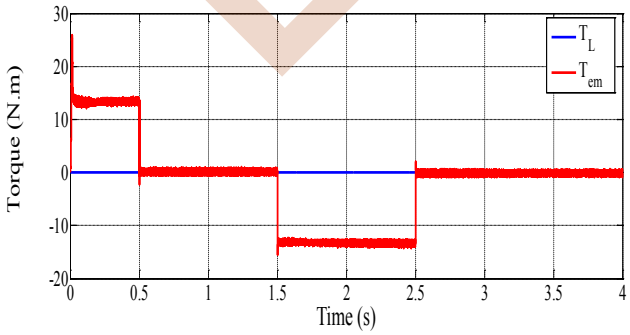

(a)

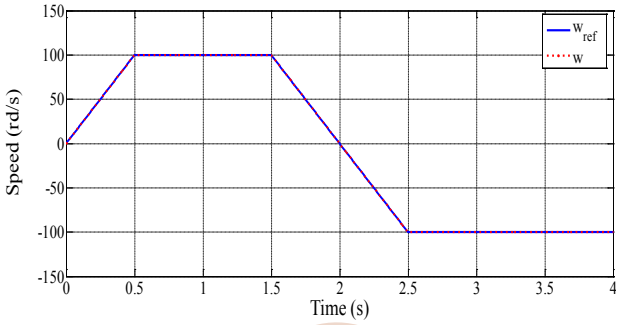

(b)

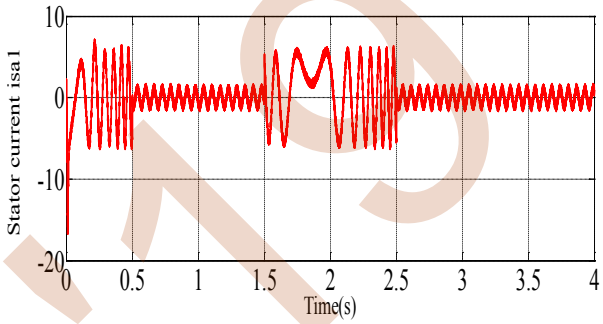

(c)

Figure 6. Torque, speed and stator current responses with PWM technique for the second test.

Figures 3, 4 illustrated the simulation results with SVM and PWM of the first test, the electromagnetic torque has the same form of the load torque wich shows that it compensates the load torque and the friction in the established regime fig 3(a), 4(a), the speed reaches the reference speed and follows it perfectly, it also noticed that the speed controller rejects the load disturbance quickly fig 3(b), 4(b) the stator current has a peak value at the start up of 18A with SVM fig and 28A with PWM, in the presence of load its peak value is 7A and 1.5A in the absence of theme (no load) fig 3(c), 4(c).

Figures 5, 6 represented the simulation results with SVM and PWM of the second test, the speed follows its reference and reverses such as it reaches the value -100rd/s at t=2.5s fig 5(a), 6(a) the reversal of direction of rotation leads to a negative electromagnetic torque of about -14N.m, when reversing the direction of rotation from t=1.5s to t=2.5s fig 5(b), 6(b), the stator current amplitude is similar to that the starting current fig 5(c), 6(c). It also noticed that in the two tests the THD of current with SVM is lower than the current with PWM.

V.CONCLUSION

In this paper the double star induction motor has been controlled by the sliding mode control (SMC) using space vector modulation (SVM) technique, for improve the quality of the output voltage and current waveform and prove the robustness of the SMC two test has been performed via Matlab/Simlink, as can be seen from the simulation results of

the system under different conditions with SMC-SVM, the robustness in terms of stability and performance is reached. An excellent stability and disturbances rejection with high performance are offered and the phase current THD decreases when using the SVM technique compared with PWM.

APPENDIX

TABLE I. SVM AND PWM CORRESPONDING PHASE CURRENT THD

Parameters	Tests	
	Test1	*Test2*
Current THD with SVM	14.72	13.55
Current THD with PWM	27.73	27.76

REFERENCES

[1] M. AnkaRao, M. Vijayakumar, N. Premanath Kumar« Speed Control of Parallel Connected DSIM Fed by Six Phase Inverter with IFOC Strategy Using ANFIS,». International Journal of Research and Engineering, 2017, vol. 4, no 9, p. 244-250.

[2] Zheng Wang, Xueqing Wang, Jiawei Cao, Ming Cheng and Yihua Hu, « Direct torque control of T-NPC inverters-fed double-stator-winding PMSM drives with SVM, » IEEE Transactions on Power Electronics, 2018, vol. 33, no 2, p. 1541-1553.

[3] I. Kortas, A. Sakly and M. F. Mimouni, "Optimal Vector Control to a Double star Induction Motor", Energy, vol.131, pp.279-288, 2017.

[4] Z. Tir, Y. Soufi, M. N. Hashemnia, O.P. Malik and K. Marouani, "Fuzzy Logic Field Oriented Control of Double Star Induction Motor Drive", Electrical Engineering, vol.99, No.2, pp.495-503, 2017.

[5] Utkin VI. Variable structure systems with sliding modes—a survey. IEEE Trans Automat Control 1977;AC-22(2):212–22.

[6] Amimeur H, Abdessemed R, Aouzellag D, Merabet E, Hamoudi F. A sliding mode control associated to the field-oriented control of dual-stator induction motor drives. J Electr Eng 2010;10(3) [Art. 2].

[7] S. Abderazak and N. Farid, "Comparative study between Sliding mode controller and Fuzzy Sliding mode controller in a speed control for doubly fed induction motor", Proceedings of the 4th International Conference on Control Engineering & Information Technology, Hammamet, Tunisia, pp.1-6, 2016.

[8] A. Fatima, T. Almas, M. A. K. A. Biabani and M. Imran, "Sliding mode control of induction motor used in traction", Proceedings of the International Conference on Electrical, Electronics and Optimization Techniques, Chennai, India, pp.3336-3343, 2016.

[9] M. El Azzaoui, H. Mahmoudi, C. Ed-dahmani and K. Boudaraia, "Comparing performance of PI and Sliding Mode in control of grid connected doubly fed induction generator", Proceedings of the International Renewable and Sustainable Energy Conference, Marrakech, Morroco, pp.769-774, 2016.

[10] M. El Azzaoui, H. Mahmoudi, B. Bossoufi and M. El Ghamrasni, "Comparative study of the sliding mode and backstepping control in power control of a doubly fed induction generator", Proceedings of the International Symposium on Fundamentals of Electrical Engineering, Bucharest, Romania, pp.1-5, 2016.

[11] B. Singh, N. Mittal, D. Verma, D. Singh, S. Singh, R. Dixit, M. Singh, A. Baranwal, "Multi-Level Inverter: a Literature Survey on Topologies and Control Strategies", International Journal of Reviews in Computing, Vol. 10, No. 1, 2012, pp. 1-16.

[12] A. Khedher, M. Mimouni "Sensorless-adaptive DTC of double star induction motor", Energy Conversion and Management, Vol. 51, No. 12, 2010, pp. 2878–2892.

[13] Y. Gao, J. Wang, X. Qiu, "The Improvement of DTC System Performance on Fuzzy Control", Procedia Environmental Sciences, Vol. 10, 2011, pp. 589-594.

[14] H. Kouki, M. Ben Fredj ; H. Rehaoulia, "SVPWM control strategy to minimize circulation harmonic currents for VSI fed double star induction machine", Systems, Signals & Devices (SSD), 2015 12th International Multi-Conference on, 16-19 March 2015, pp. 1-7.

[15] E. Benyoussef, A. Meroufel, S. Barkat, "Three-Level Direct Torque Control Based on Artificial Neural Network of Double Star Synchronous Machine", Leonardo Journal of Sciences, Vol. 13, No. 24, 2014, pp. 15-27.

[16] A. Bennassar, A. Abbou, M. Akherraz, M. Barara," Fuzzy logic based adaptation mechanism for adaptive luenberger observer sensorless direct torque control of induction motor", Journal of Engineering Science and Technology, Vol. 11, No. 1, 2016, pp. 46-59.

[17] H. Vanderbroeck, H. Skudelny, G. Stanke, "Analysis and realization of a pulse width modulator based on voltage space vectors," IEEE Transactions on Industrial Applications, Vol. 24, No. 1, 1988, pp. 142-150.

[18] L, Noureddine, Z, Samir, B, Fouad, et al. Comparative Study between Sliding Mode Control and Backstepping Control for Double Star Induction Machine (DSIM) under Current Sensor Faults, International Journal of Information Technology and Electrical Engineering, Vol 6, Issue 6 Dec 2017.

[19] H. Amimeur, D. Aouzellag, R. Abdessemed and K.Ghedamsi, "Sliding mode control of a dual-stator induction generator for wind energy conversion systems", International Journal of Electrical Power & Energy Systems, vol.42, No.1, pp.60-70, 2012.

[20] H. Amimeur, R. Abdessemed, D. Aouzellag, K. Ghedamsi, F. Hamoudi and S. Chekkal, "A sliding mode control for dual-stator induction motor drives fed by matrix converters", J Eletric Eng, vol.11, No.2, pp.136-143, 2011.

[21] H. Amimeur, R. Abdessemed, D. Aouzellag, E. Merabet and F. Hamoudi, "A sliding mode control associated to the field-oriented control of dual-stator induction motor drives", J Electr Eng, vol.10, No.3, pp.7-12, 2010.

[22] S. Lekhchine, T. Bahi, I. Abadlia and H. Bouzeria, "PV-battery energy storage system operating of asynchronous motor driven by using fuzzy sliding mode control", International Journal of Hydrogen Energy, vol.42, No.13, pp.8756-8764, 2017.

[23] E. E. M. Mohamed, M. A. Sayed, T. A. Ahmed and M. M. Hamada, "Position control of linear induction motor using cascaded sliding mode controller", Proceedings of the Eighteenth International Middle East Power Systems conference, Cairo, Egypt, pp.617-624, 2016.

[24] Saber M. E. Fadul, Ishak Aris, Norhisam Misron, Izhal A Halin, A.K.M. Parvez Iqbal, « Modelling and simulation of electric drive vehicle based on Space Vector Modulation technique and Field Oriented Control strategy, » In : Communication, Control, Computing and Electronics Engineering (ICCCCEE), 2017 International Conference on. IEEE, 2017. p. 1-7.

Direct Torque Control Using Self-Tuning Speed Controller of the Induction Motor Drive

TAZERART Farid, KERROUCHE Farid, RAMTANI Farah, OUBRAHAM Amina
Faculté de technologie, Département de génie électrique de l'université de Bejaia
Laboratoire de Technologie Industrielle et de l'Information (LTII).
Bejaia, Algérie.
farid.tazerart@gmail.com

***Abstract* — Direct Torque Control - or DTC - is the most advanced AC drive technology developed by any manufacturer in the world. DTC describes the way in which the control of torque and speed are directly based on the electromagnetic state of the motor. Because torque and flux are motor parameters that are being directly controlled, there is no need for a modulator, as used in PWM drives, to control the frequency and voltage. However, some disadvantages are to be deplored. The variable switching frequency, although may result in less irritating noise emissions, produces a wide band of harmonic spectra and is thus more likely to induce mechanical resonance. This, in turn, may result in higher noise emission. At low speed, the positive torque slope is large, which can cause torque overshoot, hence increasing the torque ripple. In this paper, we propose a simple but robust model independent in which the production of the reference torque value is achieved by using a self-tuning scheme for fuzzy logic controllers (FLC's). The response of the fuzzy PI is compared to the response of a classic PI speed controller. Results, shows that the fuzzy PI speed controller has a better response in a wide range area of motor speed.**

Keywords: Induction Motor (IM), Direct torque control (DTC), Proportional-Integral-Derivative (PID), Fuzzy Logic (FL)

I. INTRODUCTION

Direct torque control (DTC) is one method used in variable frequency drives to control the torque (and thus finally the speed) of three-phase AC electric motors [1,2]. This involves calculating an estimate of the motor's magnetic flux and torque based on the measured voltage and current of the motor. The input currents are measured; flux, torque are estimated. In this paper we propose an approach to improve the direct torque control (DTC) of an induction motor (IM). The proposed DTC is based on fuzzy logic technique switching table, is described compared with conventional direct torque control (DTC). The reference speed which is the input of the motor controller and the production of the reference torque value is achieved by using a self-tuning scheme for fuzzy logic controllers (FLC's).

The present paper focuses about the artificial intelligence technique particularly fuzzy logic in the speed control of induction motor. Fuzzy logic is a technique to embody human-like thinking into a control system [3,4].

The previously explained DTC limitations involve plenty of nonlinear functions [5]. Therefore, artificial intelligence is suggested to overcome the DTC limitations. Hence, a fuzzy logic DTC controller, which is bad on the classical DTC but includes a fuzzy logic controller, is fully described [7,8].

The paper is organised in five sections. Section 2 describes direct torque control strategy. In section 3 the proposed self tuning fuzzy controller is presented. In section 4, the proposed technique fuzzy logic for the speed control of induction motor is deduced, and section 5 presents simulations results with system performances.

II. FUZZY LOGIC DIRECT TORQUE CONTROL

The generic Direct Torque Control scheme for an inverter fed induction motor drive is as shown in figure 1. The DTC scheme comprises of flux and torque estimator, hysteresis controllers for torque and flux and a switching table.

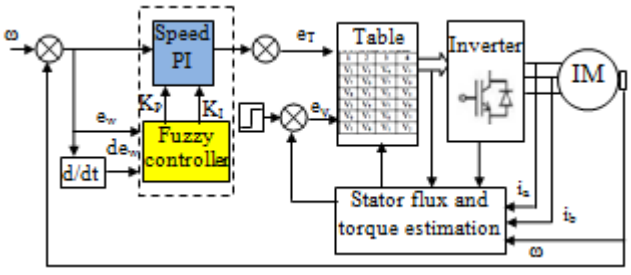

Figure 1. Fuzzy DTC system with self-adaptive speed PI.

III. DIRECT TORQUE CONTROL STRATEGY

DTC method uses a simple switching table to identify the most suitable inverter state to achieve a desired output torque. The algorithm, based on the flux and torque hysteresis controllers, determines the voltage needed to drive the flux and torque to the desired values. These hysteresis controllers maintain the flux and torque within an allowed upper and lower limit.

A. Basic direct torque control for IM

From the model of the machine expressed in a reference frame linked to the stator, the stator flux vector is estimated from the following relationship:

$$\vec{\phi}_s(t) = \int_0^t (\vec{V}_s(t) - R_s \vec{i}_s(t))dt \qquad (1)$$

The stator flux components $\phi_{s\alpha}$ and $\phi_{s\beta}$ can be estimated by:

$$\begin{cases} \phi_{s\alpha}(t) = \int (V_{s\alpha}(t) - R_s.i_{s\alpha}(t))dt \\ \phi_{s\beta}(t) = \int (V_{s\beta}(t) - R_s.i_{s\beta}(t))dt \end{cases} \qquad (2)$$

Where: $V_{s\alpha}$, $V_{s\beta}$, $i_{s\alpha}$ and $i_{s\beta}$ are stator voltages and currents along $\alpha$and β stator axes respectively.
The magnitude of the stator flux can then be estimated by:

$$\phi_s = \sqrt{\phi_{s\alpha}{}^2 + \phi_{s\beta}{}^2} \qquad (3)$$

The phase angle of the stator *flux* can be calculated by:

$$\theta_s = \tan^{-1}\frac{\phi_{s\beta}}{\phi_{s\alpha}} \qquad (4)$$

And the electromagnetic torque can be estimated by:

$$T_e = \frac{3}{2}.p.(\phi_{s\alpha} i_{s\beta} - \phi_{s\beta} i_{s\alpha}) \qquad (5)$$

The full block diagram of the IM drive system controlled by the DTC is shown in figure 1. The proportional integral (PI) controller is used to transfer the speed feedback in to the torque reference value.

So, the process is able to perform speed control. Thus not only the torque, but also the speed can be controlled.

B. Stator flux control

Figure.2 shows the voltage vectors which are usually used in DTC scheme with, as example, the stator flux located in sector 1, the stator flux vector is varied in the same direction as the applied stator voltage vector thus in each sector four of the six non zero voltage vectors along with zero vectors may be used.

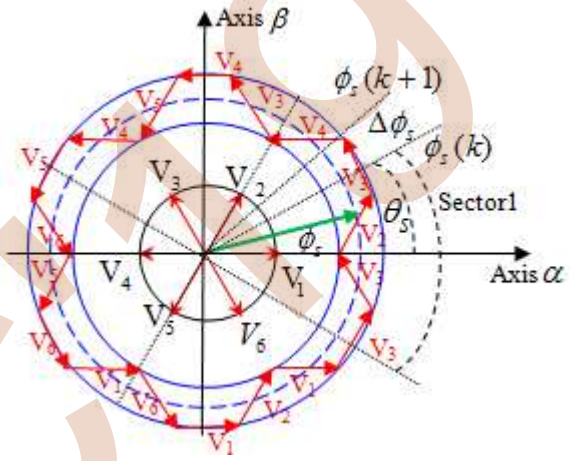

Figure 2. Forming of the stator flux trajectory by appropriate voltage vector selection.

C. Switching table for controlling flux and torque

According to the signal generated by the hysteresis controller of stator flux and electromagnetic torque, just one voltage vector can be selected to adjust the torque and flux. The choice of this vector depends on the outputs of the torque and flux controller and the position of the stator flux vector, as shown in Table 1 [8].

TABLE I. SWITCHING TABLE

H_ϕ	H_{Te}	S(1)	S(2)	S(3)	S(4)	S(5)	S(6)
1	1	V_2	V_3	V_4	V_5	V_6	V_1
	0	V_0	V_7	V_0	V_7	V_0	V_7
	-1	V_6	V_1	V_2	V_3	V_4	V_5
-1	1	V_3	V_4	V_5	V_6	V_1	V_2
	0	V_7	V_0	V_7	V_0	V_7	V_0
	-1	V_5	V_6	V_1	V_2	V_3	V_4

IV. THE PROPOSED SELF TUNING FUZZY CONTROLLER

In order to highlight the performances of the proposed approach, a simulation work is carried out. A simplified block diagram of the proposed DTC strategy, based on the fuzzy logic strategy, is shown in Fig. 3.

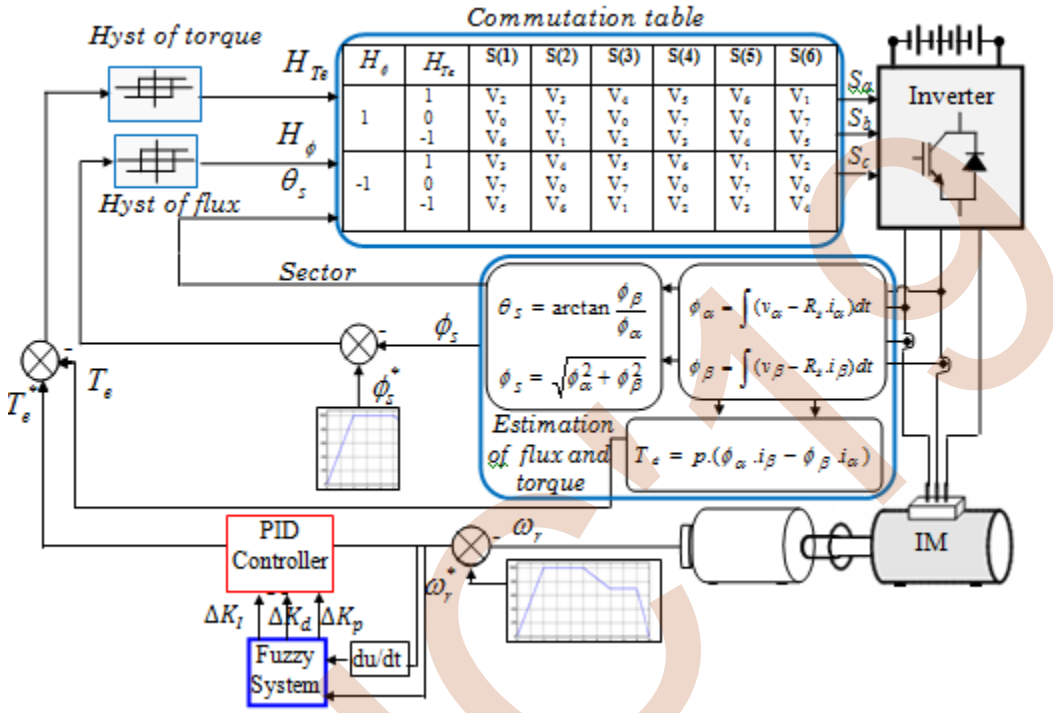

Figure 3. Direct torque control using self-tuning speed controller

V. FUZZY LOGIC DTC CONTROLLER

The fuzzy control has with the same objective of regulation as control realized in classical automatic. However, it is possible to happen of an explicit model of the controlled process. Using linguistic variables in place of numerical variables, that approach represents a substantive departure from the conventional quantitative techniques of system analysis and control. The basic configuration of a FLC (fuzzy logic controller) with three linguistic variables (two inputs and one output) is shown in figure 4.

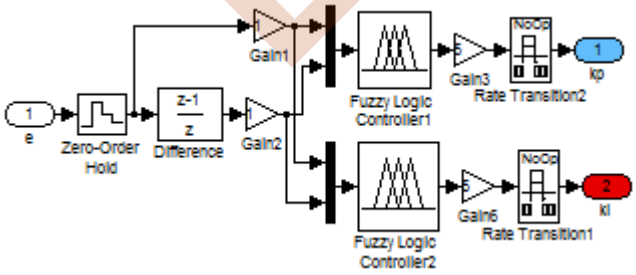

Figure 4. Simulink diagram of controller base system

TABLE II. KP FUZZY CONTROLRULETABLE

kp	*De*		
e		***NB***	***Z***	***PB***
	NB	*Z*	*PB*	*Z*
	Z	*Z*	*PS*	*PM*
	PB	*Z*	*PB*	*Z*

Corresponding linguistic values are characterized by the symbols likewise:
NB : Negative big
NS : Negative small
Z : Zero
PS : Positive small
PB: Positive big.

TABLE III. KI FUZZY CONTROLRULETABLE

ki	***de***			
e		***NB***	***Z***	***PB***
	NB	*P*	*Z*	*P*
	Z	*P*	*P*	*P*
	PB	*P*	*Z*	*P*

VI. SIMULATION RESULTS

In this section, the computer simulation results for a 1.5 kW cage rotor induction machine, using the fuzzy controller described in section V is compared to a conventional controller. The simulation results are effectuated with the output gain of the speed fuzzy regulator G3 = 0.725.

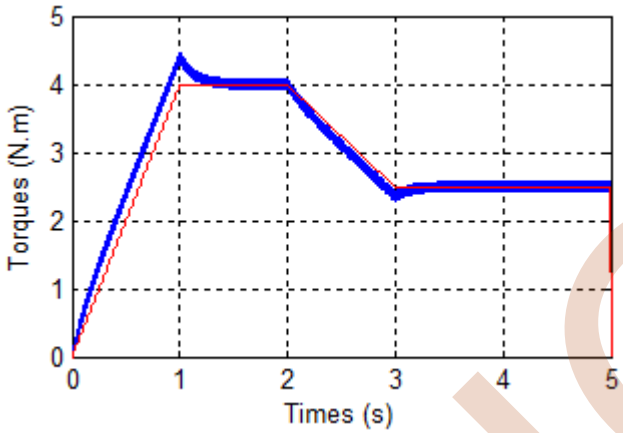

Figure 5. Torque curves

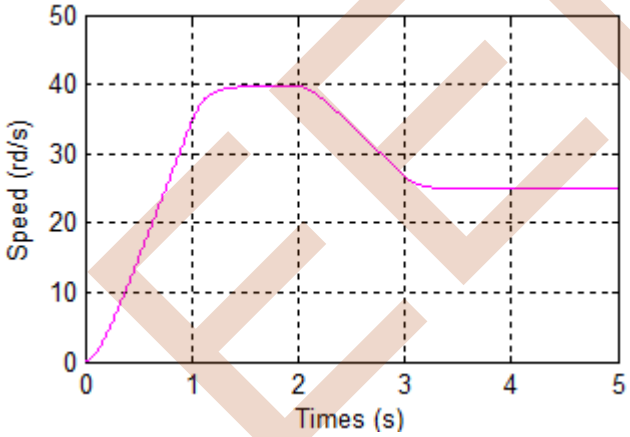

Figure 6. Speed curves

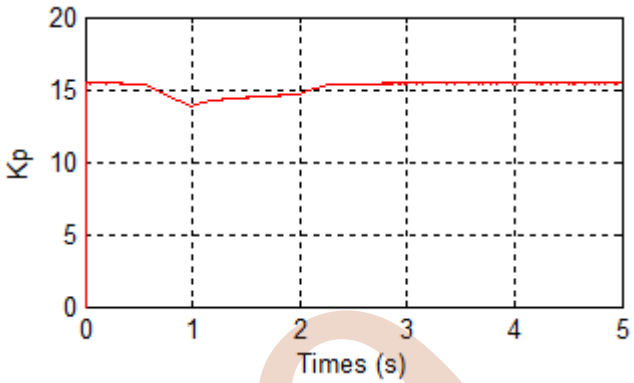

Figure 7. Kp with self-adaptive.

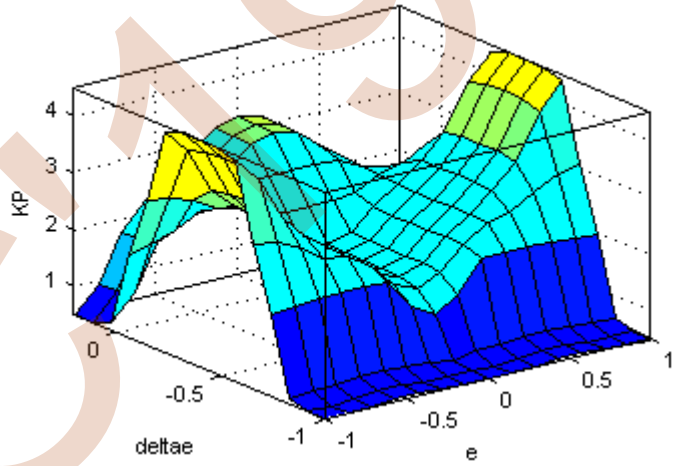

Figure 8. Surface view of fuzzy controller output for KP

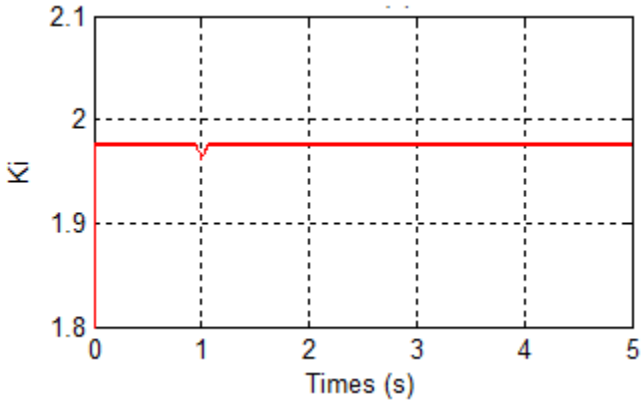

Figure 9. Ki with self-adaptive.

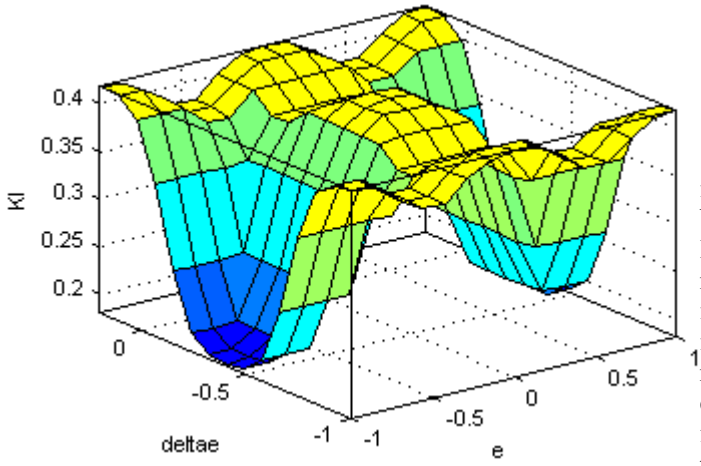

Figure 10. Surface view of fuzzy controller for KI

Figures 5 and 6 show that, the torque and speed reaches its references values, the electromagnetic torque compensates the resistant torque and presents at starting a value equal to 4 N.m. Fig. 7 and 9 shows that the system using Fuzzy logic and PI control under no load have good performance in terms of settling time.

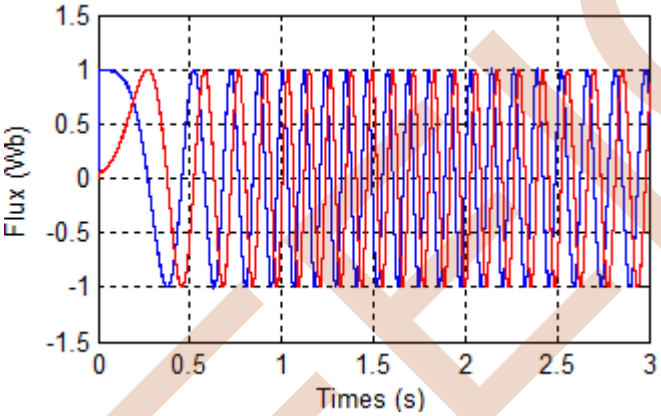

Figure 11. Stator flux components with classical DTC method

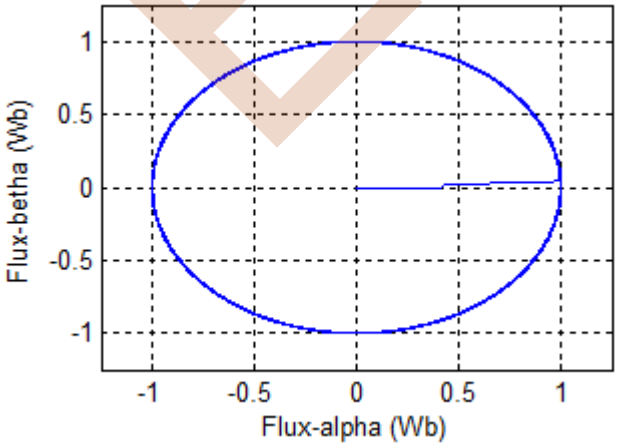

Figure 12. Circular trajectory of stator flux with classical DTC method.

CONCLUSION

In order to realize high performance control of induction motor, a combined controller, which combines both DTC technique and artificial intelligence technique. In this paper, the direct torque control of an induction machine using self-tuning speed controller is achieved, this is performed by incorporating a self adjusting regulator block into a classical direct torque control system. The fuzzy regulator has a very interesting dynamic performances compared with the conventional PI-regulator. In fact, the fuzzy regulator synthesis is realized without take in account the machine model. Simulations and theoretical results show the effectiveness of the proposed method DTC and self-tuning speed controller.

References

[1] I Takahashi, T Noguchi. A new quick-response and high-efficiency control strategy of an induction motor. IEEE Transactions on Industry Applications. 1986; IA-22(5): 820-827.

[2] M Depenbrock. Direct self-control of inverter-fed induction machine. IEEE Transactions on Power Electronics. 1988; 3(4): 420-429.

[3] A. Kalantri, M. Mirsalim and H. Rastegar, "Adjustable speed drive based on fuzzy logic for a dual three-phase induction machine," Electrics Drives II, Electrimacs. August 18–21, 2002.

[4] M. P. Veeraiah and S. M. Chitralekha Mahanta, "Fuzzy proportional Integral–proportional derivative (PI-PD) controller," Proceeding of the 2004 American control conferences, pp. 4028–4033, Boston Massachusetts June 30 – July 2, 2004.

[5] F. Tazerart, Z. Mokrani, D. Rekioua, T. Rekioua, "Direct torque control implementation with losses minimization of induction motor for electric vehicle applications with high operating life of the battery", International Journal of Hdyrogen Energy, Vol. 40, No. 39, pp. 13827-13838, 2015.

[6] F. Tazerart, T. Rekioua, M. Adli, A. Betka, " Fuzzy Logic Control for a Speed Control of Induction Motor Fed by a Nine Switch Matrix Converter " (ICEEA'1), 02-03 November 2010, , Béjaia, Algeria.

[7] F. Tazerart, N. Taïb, T. Rekioua, D. Rekioua, Abdelmounaïm Tounzi " Direct Torque Control Optimization with Loss Minimization of Induction Motor" Conférence Internationale en Sciences Technologies Electriques au Maghreb-CISTEM , 3-6 novembre 2014, Tunis.

[8] F. Tazerart, Nabil taïb, t. Rekioua, d. Rekioua, abdelmounaïm tounzi" Direct Torque Control Optimization with Loss Minimization of Induction Motor " Conférence Internationale en Sciences Technologies Electriques au Maghreb-CISTEM, 3-6 novembre 2014, Tunis. DOI: 10.1109/CISTEM.2014.7077002 Publisher: IEEE.

Fault Tolerant Control of Brushless DC Motor based on Backstepping control

Izzeddine Dilmi
LGE Research Laboratory
Department of Electrical Engineering, Faculty of Technology, University of Msila, BP 166 Ichbilia 28000, Algeria
izzeddine.dilmi @univ-msila.dz

Abderrahmen Bouguerra
LGE Research Laboratory
Department of Electrical Engineering, Faculty of Technology, University of Msila, BP 166 Ichbilia 28000, Algeria
abderrahmen.bouguerra@univ-msila.dz

Ali Djrioui
LGE Research Laboratory
Department of Electrical Engineering, Faculty of Technology, University of Msila, BP 166 Ichbilia 28000, Algeria
ali.djerioui@univ-msila.dz

Larbi Chrifi-Alaoui
Laboratory of Innovative Technology
University of Picardie Jules Verne, 02880 Cuffies, France
larbi.alaoui@u-picardie.fr

***Abstract*— This paper addresses the Fault Tolerant Control (FTC) passive of BLDC Machine based on Backstepping control. The main idea of the proposed method is to modify a conventional BLDC controller by superposing an appropriate compensation signal to offset the effect of a fault , to facilitate the procedures for setting and controlling the current . we establish a dynamic model for direct current. We introduced a faults to test the robustness of the control laws. A theoretical analysis is presented, and both simulation is presented in order to validate the proposed compensation . The proposed FTC-Backstepping control can achieve favorable tracking performance.**

I. INTRODUCTION

The necessity of more powerful actuators in small sizes in industrial application. The BLDC motors were gradually replacing DC motors and to solve the problem associated with contacts and gives improved reliability and enhances life, we need to Elimination of brushes and commutators. The BLDC motor has the low inertia, high efficiently, high power factor, high torque, lower maintenance and low noise [1] [2].

In general, the BLDC machine is powered through a three-phase inverter transistor that acts as the electronic switch of the phase current, The torque control is then reached at the current control [3]. the directly control of the current is easier than the control of the phase currents required since the reconstitution of these currents .In most cases, a current-controlled voltage inverter is used. As the motor torque is proportional to the DC input of the switch, the interest is the influencing to the current forme in order to optimize the torque and minimize the current [4].

The backstepping design recursively selects some appropriate functions of state variables as pseudo control inputs for lower dimension subsystems of the overall system [8]. The most appealing point of it is to use the virtual control variable to make the original high order system to be simple enough thus the final control outputs can be derived step by step through suitable Lyapunov functions. A nonlinear velocity controller for an induction motor was designed based on adaptive backstepping approach, in which over parameterization may occur[9].

On the other hand, in the control design and fault tolerance domains, the reappears to very little new theoretical development based backstepping approach. Starting from those works [12] [13]. In general, the FTC approaches can be classified into two types: the active approach and the passive approach as presented in this paper. The survey book [14] reviews the concepts and the state of the art in the field of FTCs, comparative study between these two approaches and the recent advances have been reported in [15] [16].

The reminder of this paper is presented as follows. A description of the studied system is presented in section I. The Section II develops the dynamic model. The section III is devoted to the FTC passive control based on Backstepping approach. Finally, the simulation results to demonstrate the robustness of the proposed approach is presented in Section IV.

II. MODELING AND ANALYSIS OF BLDC MACHINE

A. Equations of Electrical and Mechanical of bldc Machine

The model simplified of the BLDC Machine is shown in Fig. 1:

For a symmetrical winding and a balanced system (Fig. 1), the vector of voltages across the three phases of the BLDC motor is given by:

$$\begin{bmatrix} v_a \\ v_b \\ v_c \end{bmatrix} = \begin{bmatrix} R & 0 & 0 \\ 0 & R & 0 \\ 0 & 0 & R \end{bmatrix} \begin{bmatrix} i_a \\ i_b \\ i_c \end{bmatrix} + \frac{d}{dt} \begin{bmatrix} L_0 & M & M \\ M & L_0 & M \\ M & M & L_0 \end{bmatrix} \begin{bmatrix} i_a \\ i_b \\ i_c \end{bmatrix} + \begin{bmatrix} e_a \\ e_b \\ e_c \end{bmatrix} \quad (1)$$

where

$$Mi_a + Mi_b = -Mi_c \quad (2)$$

Substituting Equation (2) into (1), the voltage equation of the BLDC motor can be simplified as follows:

$$\begin{bmatrix} v_a \\ v_b \\ v_c \end{bmatrix} = \begin{bmatrix} R & 0 & 0 \\ 0 & R & 0 \\ 0 & 0 & R \end{bmatrix} \begin{bmatrix} i_a \\ i_b \\ i_c \end{bmatrix} + \frac{d}{dt} \begin{bmatrix} L & 0 & 0 \\ 0 & L & 0 \\ 0 & 0 & L \end{bmatrix} \begin{bmatrix} i_a \\ i_b \\ i_c \end{bmatrix} + \begin{bmatrix} e_a \\ e_b \\ e_c \end{bmatrix} \quad (3)$$

Where v_a, v_a and v_c are the phases voltages of the BLDC Machine ; i_a, i_a and i_c are the phases currents; R is the resistance and L is the inductance of the machine which $L=L_0-M$; e_a, e_a and e_c are the electromotive forces of the phases.

The electric torque is given by:

$$C_e = \frac{\left(e_a i_a + e_b i_b + e_c i_c\right)}{\omega_r} \quad (4)$$

Where C_e is the electromagnetic torque and ω_r is the angular velocity.

The law of meshes is applied to obtain the equations of currents in the three phases [5].

• Sub-interval 1: the main current i_d flows in the two excited phases through the two transistors turned on, a circular current flow in the third phase through a of the two transistors and the diode of the freewheel.

• Sub-interval 2: the current i_d flows in the two excited phases, the diode is blocked, and the current vanishes in the third phase.

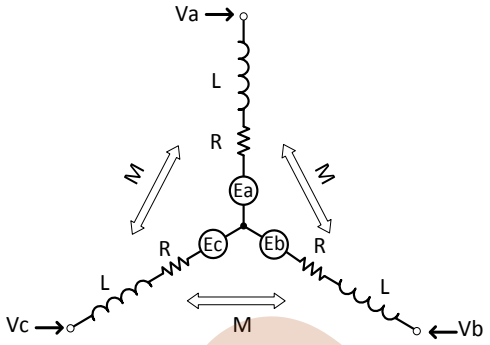

Fig1.The model simplified of the BLDC

B. *Modeling of the BLDC Machine*

Fig.2 show the schematic diagram for controlling the BLDC Machine.

We will make the following assumptions:

- The six transistors *T1, T2, T3, T1', T2'* and *T3'* have identical characteristics. In the state "OFF" and in the state "ON" are respectively represented by an infinite impedance and threshold voltage v_T in series with a dynamic resistance r_T.
- Similarly, it is assumed that the diodes *D1, D2, D3, D1', D2'* and *D3'* has an infinite impedance in the state OFF and in the state ON are threshold voltage v_D in series with a dynamic resistance r_D.
- The model of the machine is generally established in a landmark three-phase (*a, b, c*) related to the stator due to the trapezoidal shape of the FCEM. For a symmetrical machine winding connected in star and whose permanent magnets are mounted on the surface [16].

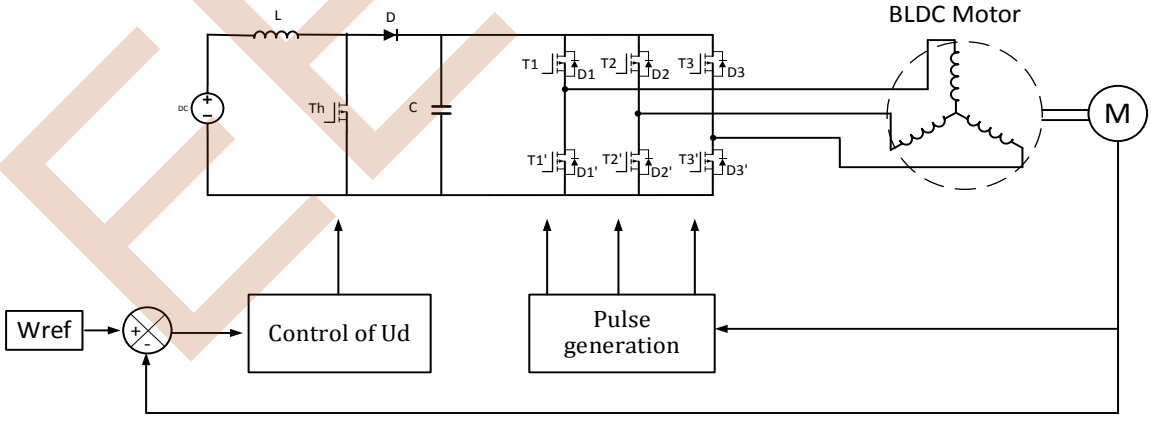

Fig.2 : Block diagram for controlling the BLDC motor

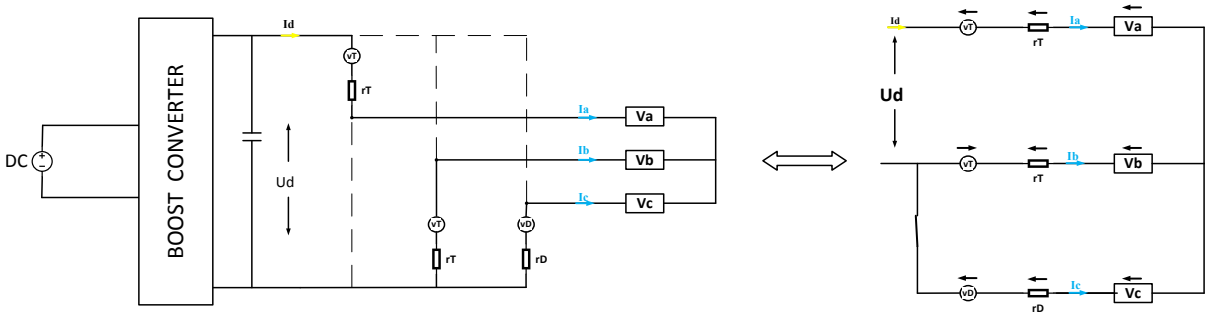

Fig. 3: Equivalent diagram of the motor-switch assembly.

This model can be written as follows:

$$\begin{cases} V_a = Ri_a + L_c \dfrac{di_a}{dt} + e_a & (5.a) \\ V_b = Ri_b + L_c \dfrac{di_b}{dt} + e_b & (5.b) \\ V_c = Ri_c + L_c \dfrac{di_c}{dt} + e_c & (5.c) \end{cases}$$

Depending on the position of the inductor, the current i_d is switched in phase at the time the trapezoidal FCEM in this phase Fig. 3.

- The model of the machine is generally established in a landmark three-phase (*a, b, c*) related to the stator due to the trapezoidal shape of the FCEM. For a symmetrical machine winding connected in star and whose permanent magnets are mounted on the surface [16].

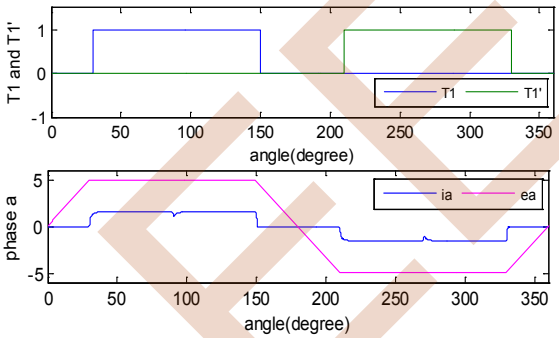

b. Current ib and FCEM eb and pulses T2 and T2'

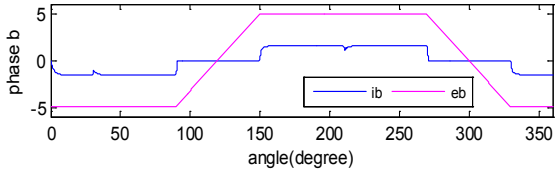

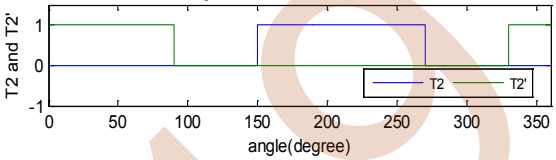

a. Current ia and FCEM ea and pulses T1 and T1'

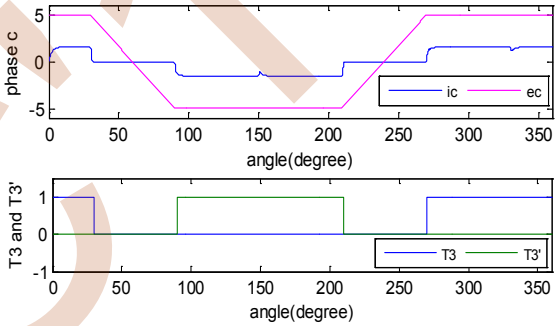

c. Current ic and FCEM ec and pulses T3 and T3'

Fig. 4: Control pulses of transistors for the direct sense.

From the signals of the Hall sensors, the sequence is generated by choosing a sequence of notice pulses of transistors well defined Fig. 5, there are 6 distinct intervals noted *IT*. The opening of the 2 transistors of an arm of the electronic switch produces the conduction of a diode D_p and D_n. This corresponds to setting a series of phase with the remaining 2 in parallel in these intervals are denoted *ID* and *ID'*.

C. Continuous Model of BLDC Motor

Is characterized by two distinct modes:

1) DC1 Mode

DC1 mode corresponds to the two phases in series "Fig.6":

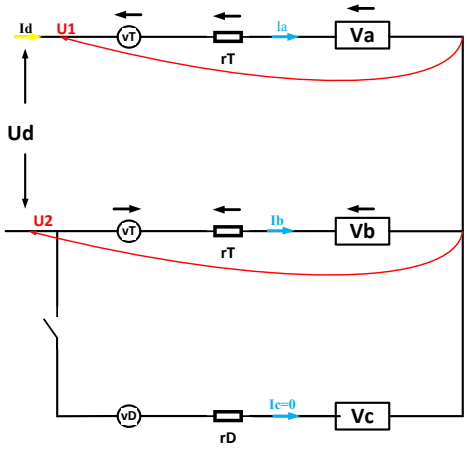

Fig.5 : Structure of the BLDC motor when two phases are supplied

in this mode dynamics DC1 current id is expressed by:

$$2L_c \frac{di_d}{dt} = u_d - 2(R+r)i_d - 2E - 2v_T \qquad (6)$$

2) DC2 Mode

In this mode, a phase in series with the other two phases in parallel "Fig.7":

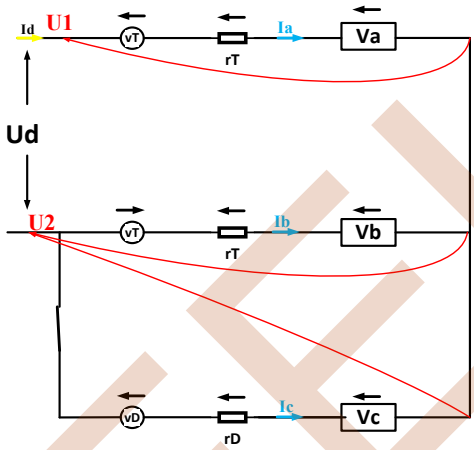

Fig.6: Structure of the BLDC motor when three phases are supplied

In this case the dynamics of the current i_d check in DC2 mode: are given by:

$$3L_c \frac{di_d}{dt} = 2u_d - 3(R+r)i_d - 2E - 3v_T + v_D \qquad (7)$$

III. BACKSTEPPING CONTROL OF THE BLDC MOTOR

Recently, A backstepping control is developed control method for nonlinear system. The backstepping technique is featured by the final controller as well as the laws can be derived systematically step by step. which is shown in the following procedures[17].

A. Control objective

The control objective is to design a asymptotically stable speed controller for the BLDC motor to make the mechanical speed follow the reference signals satisfactorily [18].

B. Nonlinear backstepping controller design

in this work we design systematically a nonlinear backstepping speed controller based on suitable Lyapunov function and adaptation laws .

The compact form of the system can be written as follows:

$$\dot{x} = f \times x + g \times U$$

where

$$x = \begin{bmatrix} \omega & i_d \end{bmatrix}$$

$$\text{et } f = \begin{bmatrix} \frac{1}{j}(-f_d\omega - C_r + k_v i_d \\ \frac{1}{j}(2v_t - E'R'i_d) \end{bmatrix}$$

$$g = \begin{bmatrix} 0 \\ 1 \end{bmatrix} \quad , \quad U = u_d$$

we define the new variable as follows:

$$z_1 = \omega$$

$$z_2 = i_d$$

The state-space equations of system can be written as:

$$\begin{bmatrix} \dot{z}_1 \\ \dot{z}_2 \end{bmatrix} = \begin{bmatrix} \frac{1}{j}(-f_d z_1 - C_r + k_v z_2 \\ \frac{1}{L'}(2v_t - E'R'z_2) \end{bmatrix} + \begin{bmatrix} 0 \\ 1 \end{bmatrix} \times U$$

Step 1 :

Stabilization of $\mathbf{z}_1$ to z_{1d}

so $e = z_1 - z_{1d}$

$$\dot{e} = \dot{z}_1 - \dot{z}_{1d}$$

$$V(e) = \frac{1}{2}e^2 \qquad \dot{V}(e) = e\dot{e}$$

$$\dot{V}(e) = e\underbrace{\left(\frac{1}{j}(-f_d z_1 - C_r + k_v z_2) - \dot{z}_{1d}\right)}_{-\alpha_1 e}$$

$$\frac{1}{j}(-f_d z_1 - C_r + k_v z_2) - \dot{z}_{1d} = -\alpha_1 e$$

and we put $\frac{1}{j}\left(-C_r + k_v z_2\right)$ as a virtual control

so we have $\frac{1}{j}\left(-C_r + k_v z_2\right) = \frac{1}{j} f_d z_1 + \dot{z}_{1\mathbf{d}} - \alpha_1 e$

and

$$e_1 = \frac{1}{j}\left(-f_d z_1 - C_r + k_v z_2\right) - \dot{z}_{1\mathbf{d}} + \alpha_1 e$$

Step 2 :

$$V\left(e, e_1\right) = \frac{1}{2}e^2 + \frac{1}{2}e_1^2 \qquad \dot{V}\left(e, e_1\right) = e\dot{e} + e_1\dot{e}_1$$

$$U = \frac{j}{\alpha_1}\left(\left(\alpha_1 - \frac{f_d}{j}\right)\dot{z}_1 + \frac{k_v}{j}\dot{z}_2 + \alpha_2 e_1 - \ddot{z}_{1\mathbf{d}}\right) + 2v_t - E'R'z_2$$

C. *Results and discussion*

In this section, simulations results are presented to illustrate the performance and robustness of proposed control law when applied to the BLDC MACHINE . The parameters values of the motor as shown in Tab. 1.

Table 1: BLDC Motor Parameters

Item	Symbol	Data
resistance of phase	R	4Ω
phase inductance	Lc	0.002H
inertia constant	J	4.65e-6kg.m2
Back-EMF Constant	ke	26.1e-3V/rd.s-1
coefficient of friction	kf	1.5e-006N.m/rd.s-1
supply voltage	un	48(V)
rated current	In	2(A)

Fig. 8 show the results of the controller

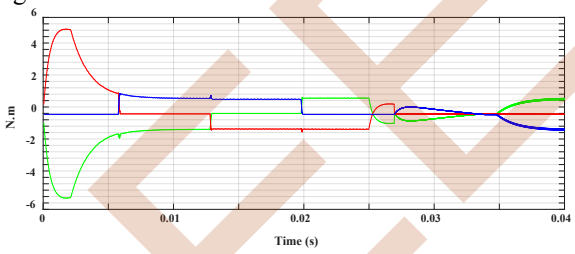

a) The 3 phase currents

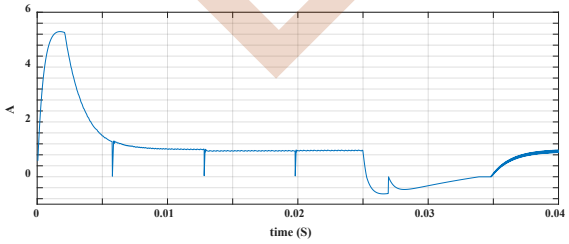

b) Form of continuous current id

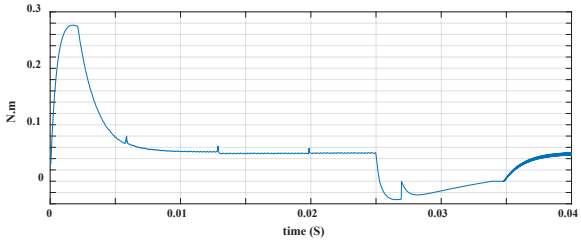

d) The engine torque Ce

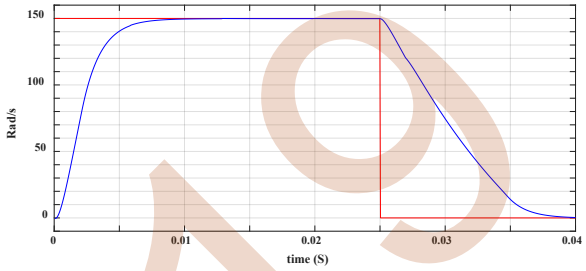

d) Form of speed

Fig. 6: Response of the motor using Backstepping controller

1) *A robustness test :*

Test 1 :

At time t = 0.015 s a robustness test is carried out where an external additive defect represented by a perturbation which is a 20% increase in the resistance phase, a 30% reduction in the cyclic inductance, 10% of the excitation flux and The nominal load torque 0.055 N.m The results are shown in Fig. 7.

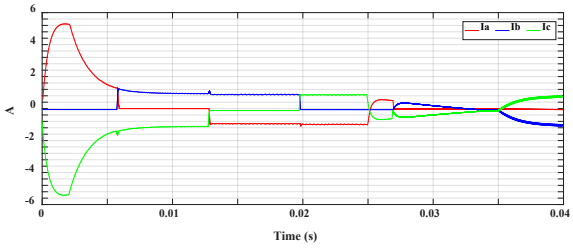

a) The 3 phase currents

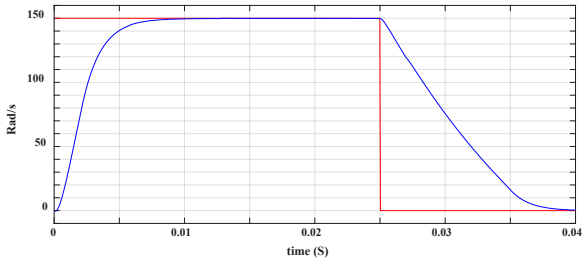

b) Form of speed

Fig.7: Response of the motor using Backstepping controller under the parametric variation

Test 2 :
the second test represented by a 40% increase in the resistance phase, a 40% reduction in the cyclic inductance, 20% of the excitation flux and The nominal load torque 0.065during the time interval [0.015s, 0.04s].The results are shown in Fig. 8.

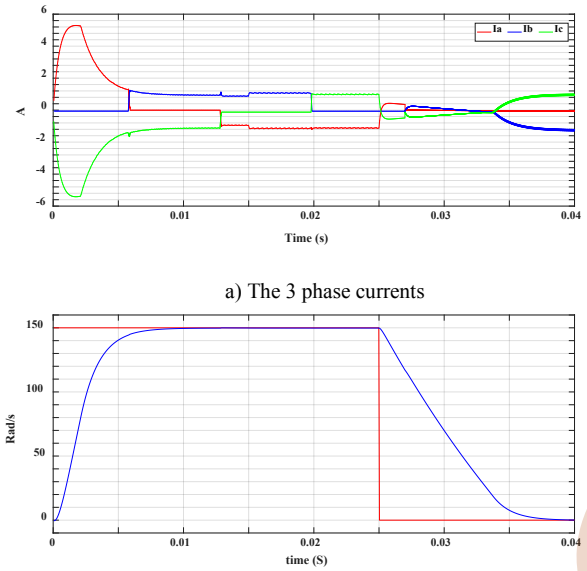

a) The 3 phase currents

b) Form of speed

Fig.8: Response of the motor using Backstepping controller under the parametric variation

2) Result discussion

- After the test, the speed remains practically insensitive to the perturbation .
- BLDC motor speed control testing shows that Backstepping control provides good performance even in the presence of an external fault .

IV. CONCLUSION

This paper presents a method of Backstepping based fault tolerant control scheme for BLDC motor systems with parameter variations faults. To achieve our goal a continuous mathematical model of BLDC motor was presented. Based on this model, we synthesized the Backstepping control of the BLDC MACHINE . The obtained simulation results illustrate the good performance of the proposed method in the case of the fault (parameter variations) for tow scenario. This work allowed us to conclude that the Backstepping method can tolerate some important faults such as: variation of parameter and the variation of reference.

REFERENCES

[1] T. J. E Miller, "Brushless Permanent-Magnet and Reluctance Motor Drives", Clarendon Press, Oxford 1989.
[2] K. Ohishi, M. Nakao, K. Ohnishi and K. Miyachi, "Microprocessor-Controlled DC Motor for Load-Insensitive Position Servo System", IEEE Trans. Ind. Electron., Vol. 34, No. 1, 1987, pp. 44-49.
[3] Y. Dal, Ohm and J. H. Park, "About commutation and current control Methods for brushless motors", 29th annual IMCSD symposium, San Jose 1999.
[4] K. Ang, G. Chong, and Y. Li, "PID control system analysis, design, and technology", IEEE Trans. Control System Technology, Vol. 13, No. 4, July 2005, pp. 559-576.
[5] K. D. Young, V. I. Utkin, and Ü. Özgüner, "A control engineer's guide to sliding mode control", IEEE Trans. Control Sys. Tech., Vol. 7, No. 3, 1999, pp. 328-342.
[6] S. V. Drakunov and V. I. Utkin, "Sliding mode control in dynamic systems", Int. J. Control, Vol. 55, No. 4, 1992, pp. 1029-1037.
[7] F. Barrero, A. Gonzalez, A. Torralba, E. Galvan and L. G. Franquelo, "Speed control of induction motors using a novel fuzzy sliding-mode structure", IEEE Trans. on Fuzzy Systems, Vol. 10, No. 3, 2002, pp. 375-383.
[8] Krstic, M., Kanellakopoulos, I., & Kokotovic, P. (1995).Nonlinear and adaptive control design. New York: Wiley.
[9] Shieh, H. J., & Shyu, K. K. (1999). Nonlinear sliding-mode torque control with adaptive backstepping approach for induction motor drive.IEEE Transactions on Industrial Electronics, 46(2), 380–389.
[10] O. Barambones, A. J. Garrido, F. J. Maseda and P. Alkorta, "An adaptive sliding mode control law for induction motors using field oriented control theory", IEEE Conference on Computer Aided Control System Design, Munich, Germany, 4-6 Oct. 2006, pp. 1008-1013.
[11] A. Tahour, H. Abid, A. G. Aissaoui, "Speed Control of Switched Reluctance Motor Using Fuzzy Sliding Mode", Advances in Electrical and Computer Engineering, 2008, Vol. 8 (15), No. 1 (29), pp. 21-25.
[12] ZHANG, Duo, LIU, Guohai, ZHOU, Huawei, et al. Adaptive sliding mode fault-tolerant coordination control for four-wheel independently driven electric vehicles. IEEE Transactions on Industrial Electronics, 2018, vol. 65, no 11, p. 9090-9100.
[13] BA, Dang Xuan, YEOM, Hoyeon, KIM, Jihoon, et al. Gain-adaptive robust backstepping position control of a BLDC motor system. IEEE/ASME Transactions on Mechatronics, 2018, vol. 23, no 5, p. 2470-2481.
[14] M. Prashant, L. Jinfeng and D. C. Panagiotis, "Fault-tolerant process control methods and applications", London: Springer-Verlag; 2013.
[15] Y. M. Zhang, J. Jiang, "Bibliographic review on reconfigurable fault-tolerant control systems", Annu. Rev. Control, Vol. 32, No. 2, 2008, pp. 229-52.
[16] H. Mekki, O. Benzineb, D. Boukhetala, M. Tadjine and M. Benbouzid, "Sliding mode based fault detection, reconstruction and fault tolerant control scheme for motor systems", ISA Transactions, Vol. 57, July 2015, pp. 340-351.
[17] ZHOU, Jianguo et WANG, Youyi. Real-time nonlinear adaptive backstepping speed control for a PM synchronous motor. Control Engineering Practice, 2005, vol. 13, no 10, p. 1259-1269.
[18] Krause, P. C. (1995).Analysis of electric machinery(2nd ed.). NewYork: McGraw-Hill.

Early diagnosis of the electrical insulation degradation based on transient inter-turn voltage distribution in windings fed from inverter pulses

N. Radja, M. Rachek and S. Nait Larbi
Department of Electrical Engineering, Mouloud Mammeri University, BP 15000 Tizi-Ouzou, Algeria
e-mail: n_radja@yahoo.fr, rachek_mhemed@yahoo.fr, soraya_naitlarbi@yahoo.fr

***Abstract*—This paper proposes a numerical simulation method dedicated to assess the integrity of windings Electrical Insulation Systems (EIS) fed from voltage source inverters based on the Transient Voltage Signature prediction in correlation with the Insulation Capacitance changes. A Finite Element Method is used to estimate the high frequency distributed-circuit parameters such as resistances (R), capacitances (C), self and mutual inductances (LM) of the insulation-winding system according to the skin and proximity effects. The (R) and (LM) matrix parameters are calculated by the use of the magnetic vector potential magnetodynamic harmonic formulation. In addition, the calculation of the capacitance (C), the electric scalar potential electrostatic formulation is applied. An equivalent (RLMC) circuit under high frequency is then used to simulate the voltage stress distribution among the turns of the stator winding in the cases of healthy and degraded insulation. The spectral analysis using the Fast Fourier Transformation (FFT) leads to establish the insulation defect signatures.**

I. INTRODUCTION

During operation environmental conditions and mechanical stress, especially vibrations may lead to the electrical insulation degradation. The application of pulse width modulation (PWM) in induction motor speed control is very popular nowadays. These pulses are responsible for high overvoltage at motor input terminals and for an irregular voltage distribution along the windings [1], [3]. These over-voltages are especially dangerous for the insulation-winding system. In such a case, the effect of these voltage transients can result in undesirable electrical and thermal stresses in the stator windings, which can lead to the premature failure of the insulating material between the coils and, definitely, to the failure of the whole component.

The voltage distribution prediction has some important diagnosis purpose concerning the maintenance and the winding construction. The voltage level can strongly affect the partial discharge activity inside the winding and so the reliability of the electrical machine [2], [4]. The variations of geometrical parameters and physical properties can be adopted for testing the degradation of the insulation system.

The insulation testing and monitoring methods can generally be divided into two different categories. The first one is the offline-testing, which requires the electrical equipment to be removed from service, whereas the second one is on-line monitoring, which can be performed under operation. The popular, reliable, and very frequently used on-line methods to assess the turn-to-turn insulation system of medium- and high-voltage electrical equipment are the Voltage Surge test and the Partial Discharge (PD) test that also can be applied off-line. Common off-line tests methods used to test the phase-to-ground insulation are the Insulation Resistance (IR), Dielectric Dissipation Factor (DDF) and the Polarization Index (PI). Other new techniques such as Return Voltage Method (RVM), Time/Frequency Domain Spectroscopy (T/F-DS) measurements, Fourier Transform Infrared (FTI), Power Factor (PF) as function of frequency, etc… are still being explored. All of these experimental classical methods are complementary but incomplete and complicated with heavy experimental process since they require the installation of costly additional equipment. In addition, they can present serious limits for in situ monitoring when the measurements are done in a noisy environment [5], [6], [7]. Since the measurement of such parameters is oftentimes not feasible due to the practical difficulties in high-frequency range, they require high-cost equipment and still do not describe the internal phenomena such as the voltage distribution across the conductor, inductive/capacitive coupling between conductors, and the skin and proximity effects [8], [9]. Therefore, the possibility of their determination from computational or analytical/empirical methods is highly desirable. The Finite Element method (FEM) Electromagnetic (EM) analysis and electric circuits methodologies are able to model even complex geometries such as the multi-conductor insulation structures [10].

A Diagnostic Indicator (DI) built with the turn-to-turn or turn-to-ground capacitance estimated values can be used for evaluating the health state of the insulation [11]. Indeed, it has been shown that the value of these capacitances increases with aging [12], [13]. So, the premature supervision of the insulation ageing or degradation (oxidation) requires to follow the evolution of these capacitances during operation according to the dielectric and geometrical characteristics. The originality of this work is that it provides effective models based on the spectral analysis of the inter-turn transient voltage signatures which can be used to monitor the health-status of the electrical insulation.

In this paper, an equivalent circuit model is used to predict inter-turns voltage distribution in the multi-conductor-insulation system. The equivalent circuit consists in the turn resistances (R), the turn self and mutual inductances (L), the turn-to-turn and turn-to-ground capacitances (C). The high frequency (RLMC) parameters are obtained using Finite Element Method (FEM). The (R,L) parameters are obtained from the coupled model of the magnetic field equation, expressed in terms of Magnetic Vector Potential (A) and the total current (I) equation. The capacitances parameters are obtained after solving the electrostatic equation, using floating potential approach.

II. Insulated-Multiconductor Distributed Lumped Electric Circuit

Based on the transmission line approach [14], the insulated-winding is formed by N_c turns modeled by the distributed lumped electric (RLMC)-circuits depicted by Fig.1. The occurrence of the insulation degradation is introduced by the addition of the inter-turn capacitance (defect capacitance) in series with the inter-turn capacitance in healthy state. In order to take into account the skin and proximity effect, numerical methods are used to calculate RLMC parameters of the multiconductor-insulation system.

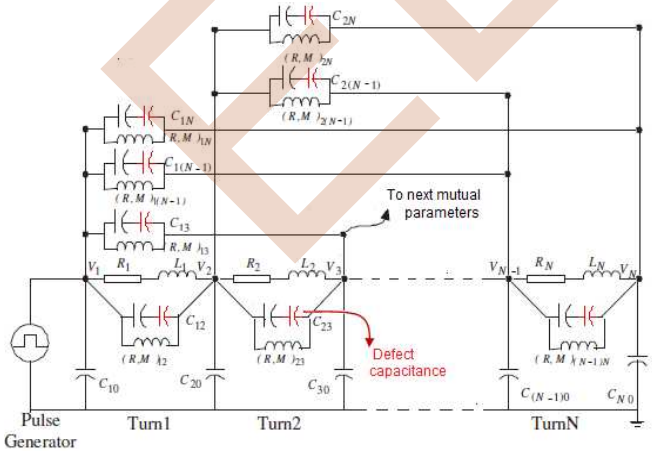

Figure 1. Lumped parameters equivalent circuit of the Turns in a Slot

III. Electromagnetics Models

The problem becomes two dimensional in the (x, y) plane. The source current density $\vec{J}_s$ and the magnetic vector potential $\vec{A}$ have only the component in z-direction. The coupled magnetic-eddy current density (A-I) model is described by the following equations:

$$\left(\frac{\partial}{\partial x}\cdot\frac{1}{\mu}\frac{\partial A_z}{\partial x}+\frac{\partial}{\partial y}\cdot\frac{1}{\mu}\frac{\partial A_z}{\partial y}\right)-j\omega(\sigma+j\omega\varepsilon)A_z+J_{sz}=0 \quad (1)$$

$$\iint_{\Omega_c^k} j\omega(\sigma+j\omega\varepsilon)A_z(x,y)d\Omega_c^k+\iint_{\Omega_c^k} j\omega\sigma\left(J_{sz}/j\omega\sigma\right)d\Omega_c^k = \iint_{\Omega_e^k} J_k^t d\Omega_c^k = I_k^t \quad (2)$$

Where ω is the pulsation, μ the magnetic permeability and σ is the electric conductivity. The symmetric formulation of coupled equations (1) and (2) is obtained after using the variable substitution $J_{sz}=(j\omega\sigma)G_{sz}$, where G_{sz} is the modified electric scalar potential. To ensure the solution's uniqueness, appropriate boundary conditions are required.

The finite element (FE) formulation of the $(A-I)$ model equations (1) and (2) is based on the first order triangular discretization mesh elements in which the weighted residual method and the approximation function of the magnetic vector potential A_z and the modified electric field G_{sz} are expressed for each conductor into the discrete form as follows:

$$\begin{cases} \sum_{j=1}^{N_{nodes}} \iint_{\Omega}\left[\frac{1}{\mu}\left(\frac{\partial N_i}{\partial x}\frac{\partial N_j}{\partial x}+\frac{\partial N_i}{\partial y}\frac{\partial N_j}{\partial y}\right)+j\omega(\sigma+j\omega\varepsilon)N_iN_j\right] \\ \quad .A_z dxdy-\sum_{j=1}^{N_{nodes}}\iint_{\Omega} j\omega\sigma N_i G_{sz}dxdy=0 \\ \sum_{k=1}^{N_c}\iint_{\Omega_c}\sum_{j=1}^{N_{nodes}}\left(j\omega(\sigma+j\omega\varepsilon)N_iA_z+j\omega\sigma G_{sz}\right)dxdy=I \end{cases} \quad (3)$$

After having expressed equations (3) for the N_{nodes} nodes and for the N_c conductors, the algebraic equations system to be solved is given by the algebraic equation system (4) as follows:

$$\left[\begin{pmatrix}[K] & -[Q0]\\ -[Q0]^{tr} & [W0]\end{pmatrix}+j\omega\sigma\begin{pmatrix}[T] & -[Q]\\ -[Q]^{tr} & [W]\end{pmatrix}+ j\omega(j\omega\varepsilon)\begin{pmatrix}[K] & -[Q0]\\ -[Q]^{tr} & [W0]\end{pmatrix}\right]\begin{pmatrix}A_z\\ G_{sz}\end{pmatrix}=\begin{pmatrix}0\\ I\end{pmatrix} \quad (4)$$

The zero matrices are related to the $Q0(1,N_c)$ and $W0(N_c,N_c)$ matrices. The usual FE stiffness and mass matrices are, respectively, $K(N_{nodes}, N_{nodes})$ and $T(N_{nodes}, N_{nodes})$. The current density matrices of the N_c conductors are as follows:

$$[Q]=\left[\sum_{j=1}^{N_{nodes}1}\iint_{\Omega_{c1}}(\sigma N_i\,dxdy)_1 \quad \sum_{j=1}^{N_{nodes}2}\iint_{\Omega_{c2}}(\sigma N_i\,dxdy)_2 \quad \cdots\cdots \quad \sum_{j=1}^{N_{nodes}N_c}\iint_{\Omega_{cN_c}}(\sigma N_i\,dxdy)_{N_c}\right] \quad (5)$$

$$[G]=\begin{pmatrix}G_1 & G_2 & \dots & G_k & \dots & G_{N_c}\end{pmatrix} \quad (6)$$

$$W=\sum_{j=1}^{N_{nodes}1}\sigma\begin{bmatrix}\int_{\Omega_{c1}}(dxdy)_1 & 0 & \cdots & 0\\ 0 & \int_{\Omega_{c2}}(dxdy)_2 & \cdots & 0\\ \vdots & \vdots & \ddots & \vdots\\ 0 & 0 & \cdots & \int_{\Omega_{cN_c}}(dxdy)_{N_c}\end{bmatrix} \quad (7)$$

$$K_{ij}=\iint_{\Omega}\frac{1}{\mu}\left(\frac{\partial N_i}{\partial x}\frac{\partial N_j}{\partial x}+\frac{\partial N_i}{\partial y}\frac{\partial N_j}{\partial y}\right)dxdy \quad (8)$$

$$T_{ij}=\iint_{\Omega}(N_iN_j)dxdy \quad (9)$$

A 2D electrostatic model expressed in term of electric scalar potential (V) is used to calculate the capacitances according to the insulated-multi-conductor geometry and dielectric properties. It is given as follows:

$$\left(\frac{\partial}{\partial x}\left(\varepsilon\frac{\partial V}{\partial x}\right)+\frac{\partial}{\partial y}\left(\varepsilon\frac{\partial V}{\partial y}\right)\right)=0 \quad (10)$$

$$V(x,y)|_{\Gamma_d}=\begin{cases}V_0 & \text{for excited conductors}\\ 0 & \text{for ground or unexcited conductor}\end{cases} \quad (11)$$

Where ε is the electric permittivity, V_0 is the applied voltage on the Γ_d boundaries.

The first-order triangular finite element is used to mesh the slot box containing the insulated-multiconductor system. Using the weighted residual method with the approximation function of the electric scalar potential (V), the FE formulation of (10) with boundary condition (11) is written for each mesh node into the discrete form as follows:

$$\sum_{j=1}^{N_{nodes}}\iint_{\Omega}\varepsilon\left(\frac{\partial N_i}{\partial x}\frac{\partial(N_jV_j)}{\partial x}+\frac{\partial N_i}{\partial y}\frac{\partial(N_jV_j)}{\partial y}\right)dxdy= \int_{\Gamma_e}\varepsilon N_i\frac{\partial V(x,y)}{\partial n}\cdot\vec{n}d\Gamma_e \quad (12)$$

where N_{nodes} is the total number of nodes, N_i is the Galerkine shape function of the node $i=1,\dots,N_{nodes}$, N_j is the approximation function of the electric scalar potential V_j at the node j. For each node of the meshed domain, equation (12), leads to the following algebraic equations system:

$$[K].\{V\}=\{F\}_{\Gamma_e}+\{F\}_{\Gamma_d} \quad (13)$$

where $[K]$ is the stiffness matrix, $\{F\}_{\Gamma_e}$ and $\{F\}_{\Gamma_d}$ are respectively the source terms related to the Dirichlet or Neumann boundary conditions.

IV. RLMC Parameters Computation

Based on the Finite Element (FE) formulation of magnetodynamic-total current coupled model (*A-I*), the analysis is performed to calculate the frequency dependent (R,L) parameters of the insulation multi-conductor system. The sequential Supply Electric Total Current process (SETC) approach is based on N_c supply sequence such as $(I_t,0,0,...,0),(0,I_t,0,...,0),(0,0,I_t,0,...,0)$, until $(0,0,...,I_t)$ in where I_t is an arbitrary total current. While each sequence of forced electric total current process is considered for the (FE) formulation of the coupled magnetic-eddy current $(A-I)$ model, the related algebraic equation system (4) is solved to get the unknown magnetic vector potential values and the modified electric scalar potential of each conductor mesh nodes. After each solution, the resistance, self and mutual inductance are calculated using the impedance formula:

$$R_{ik}+j\omega L_{ik}=\frac{[V_{ik}]}{[I_k]}=\left(\frac{[J_{sz}]_{ik}}{\frac{\sigma}{[I_k]}}\right)_{(i,k)=1,2,\dots,N_c} \quad (14)$$

The indices $i=k$ are related to the (R_{ii}) resistance and (L_{ii}) self inductance. The indices $i \neq k$ are related to (R_{ik}) and (M_{ik}) mutual resistances and inductances respectively.

The capacitances between turns are calculated using the stored electrostatic energy of the i^{th} and j^{th} conductors under the voltage potentials V_i and V_j respectively. The turn-to-ground and the self-capacitance of the i^{th} conductor are obtained by considering that its applied electrical potential is V_i while the potential of other conductors is zero, such that:

$$W_e = \frac{1}{2}\int_{\Omega}\left(\varepsilon E^2\right)d\Omega = \frac{1}{2}C_{ii}V_i^2 + \frac{1}{2}C_{jj}V_j^2 - C_{ij}V_iV_j \qquad (15)$$

$$C_{ii} = \frac{W_e}{V_i^2} \qquad (16)$$

$$C_{i0} = C_{ii} - \sum_{j=1, j\neq i}^{N} C_{ij} \qquad (17)$$

Where C_{ii}, C_{i0} and C_{ij} are respectively the i^{th} turn capacitance, the i^{th} turn-to-ground capacitances and between i^{th} and j^{th} turn-to-turn capacitances.

V. Application and Discussions

The studied multi-conductor system presented in Fig. 2 consists in six isolated conductors of $1.25mm$ diameter and $0.04mm$ insulation thickness (the insulation thickness is made of two identical insulation layers). The conductors made of copper are surrounded by an insulation material of electric permittivity $\varepsilon_r = 3.4$. The frequency is set to $f = 10\ MHz$.

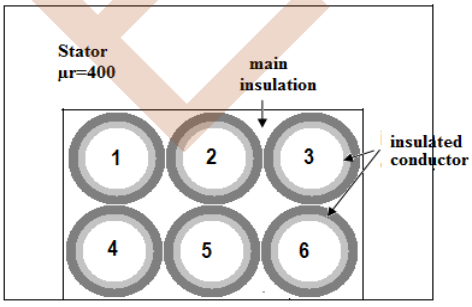

Figure 2. Electrical machines geometrical slot-multiconductor system.

The calculated (RLC) parameters in the case of healthy and degraded insulation, such as oxidation of intern insulation layer of the first turn and all turns are given in Table I. The emulated ageing/degradation (oxidation) of the winding electrical insulation system concerns the sensitive changes of the insulation dielectric properties relating to single turn (1st) and complete turns (All turns). From the comparison we note that only capacitances are affected by the degradation of the insulation.

TABLE I. (RLC) Parameters for Healthy and Degraded Insulation

Parameters	(FE) Models			Analytical Method [15]
	Healthy	*Oxidation insulation*		
		1st turn	*All turns*	
Turn resistance [Ω]	0.42785	0.42785	0.42785	-
Turn inductance [μH]	0.0705	0.0705	0.0705	-
Turn to turn capacitance [pF]	46.382	43.312	40.477	53.8047
Turn to ground capacitance[pF]	26.607	23.752	20.105	21.5759

The comparison between simulated and measured transient inter-turn voltage is shown in Fig.3 when the step voltage is applied to the coil. The results are obtained in % of 300V voltage level.

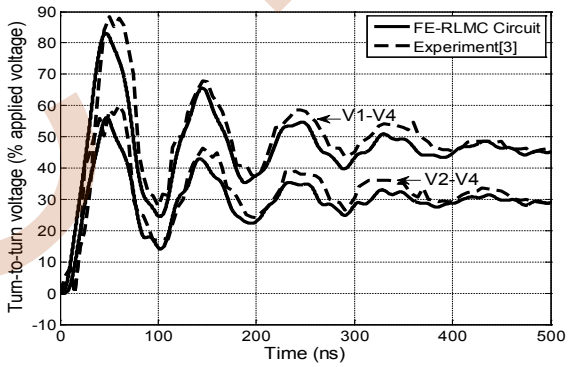

Figure 3. Comparison between simulated and measured inter-turn voltage

In order to find more fault indicators, we present the spectral analysis of the inter-turn transient voltage for healthy and degraded insulation system for the second, third, fourth, fifth, sixth, seventh, eighth and ninth harmonics are depicted in Fig.4-11.

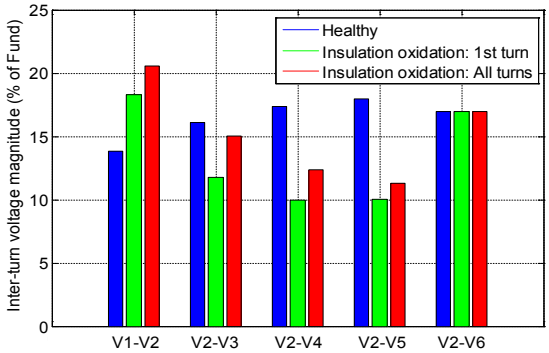

Figure 4. Spectral analysis (FFT) of inter-turn voltage for healthy and degraded insulation for the second harmonic rank

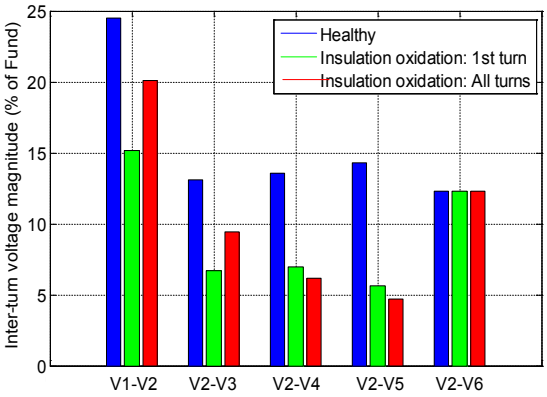

Figure 5. Spectral analysis (FFT) of inter-turn voltage for healthy and degraded insulation for the third harmonic rank

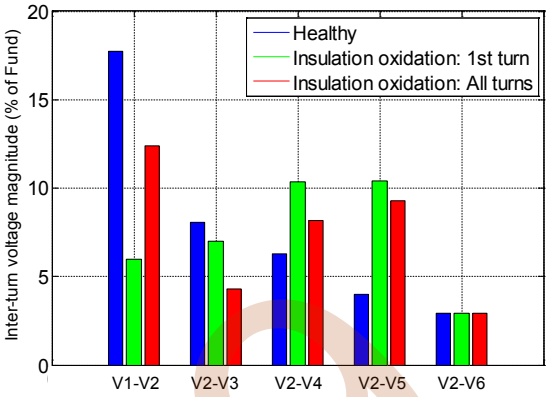

Figure 8. Spectral analysis (FFT) of inter-turn voltage for healthy and degraded insulation for the sixth harmonic rank

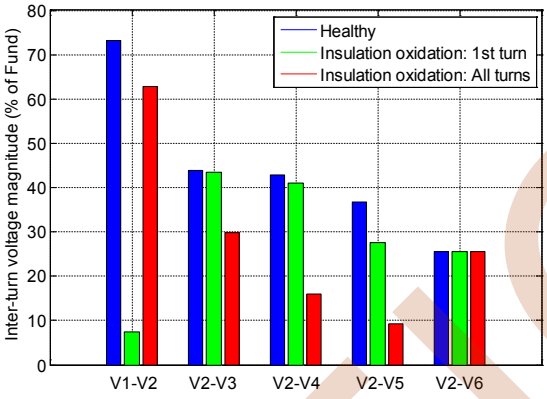

Figure 6. Spectral analysis (FFT) of inter-turn voltage for healthy and degraded insulation for the fourth harmonic rank

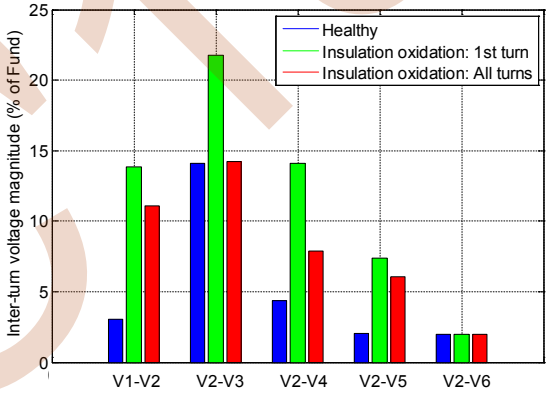

Figure 9. Spectral analysis (FFT) of inter-turn voltage for healthy and degraded insulation for the seventh harmonic rank

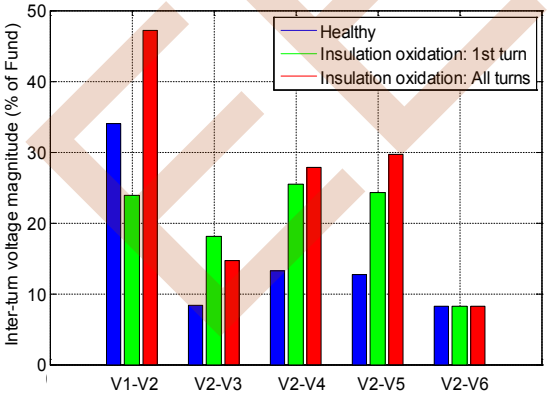

Figure 7. Spectral analysis (FFT) of inter-turn voltage for healthy and degraded insulation for the fifth harmonic rank

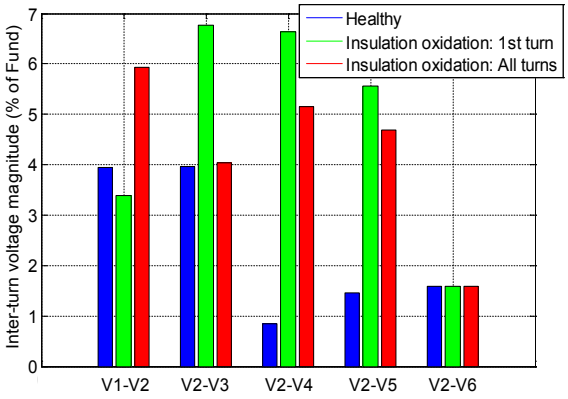

Figure 10. Spectral analysis (FFT) of inter-turn voltage for healthy and degraded insulation for the eighth harmonic rank

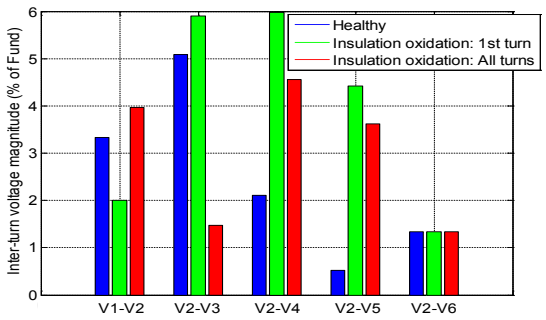

Figure 11. Spectral analysis (FFT) of inter-turn voltage for healthy and degraded insulation for the ninth harmonic rank

The simulation results are in concordance with experimental measurements (Fig. 3). From the data given in Table I, the variation of the relative permittivity due to the degradation or oxidation of the insulation causes directly a decrease of the turn-to-turn capacitance compared with the healthy value. In addition, moderate capacitance changes lead to initiate the degradation of the insulation, whereas for significant capacitance decrease according to deterioration or oxidation, the insulation quality is considerably affected, and consequently the initiated inter-turn short circuits.

The key of interpretation is the trend, which allows through the spectrum analysis (FFT) to make appear increased magnitude of the inter-turn voltages corresponding to the harmonics rank, particularly for the harmonics number five to nine. In the cases of locally inhomogeneous insulation degradation of the 1st turn, significant changes are detected in magnitude of the inter-turn voltage harmonics. This is observed only for the incriminated adjacent turns.The spectral analysis establishes that the inter-turn voltage magnitude increase from fifth harmonics rank.

We found that every harmonic rank contains enough information that permit to evaluate the spectral analysis magnitude of the inter-turn voltage. The evaluation of the inter-turn voltage magnitude according to the localization of the insulation degradation (first turn and all turn) comparing with healthy state according to the harmonic rank are shown in Table II.

TABLE II. EVALUATION OF THE SPECTRAL ANALYSIS MAGNITUDE OF INTER-TURN VOLTAGE ACCORDING TO THE HARMONIC RANK

Degradation Insulation	**Harmonic rank**				
	3	***5***	***7***	***8***	***9***
First turn	Decrease	Increase^{+}	Increase^{++}	Increase^{++}	Increase^{++}
All turn	Decrease	increase^{++}	Increase^{+}	Increase^{+}	Increase^{+}

VI. CONCLUSION

In this paper an indicator of insulation degradation has been investigated. The considered insulation degradation concerns a single turn, and all turn oxidation insulation. The decrease in turn-to-turn capacitances is observed. The spectral analysis obtained from the RLMC-circuit simulation for healthy and insulation degradation, such as oxidation of the winding electrical insulation system show increase of the magnitude of the inter-turn voltage harmonic components is observed for the incriminated adjacent turns. In the case of locally inhomogeneous insulation degradation of the first turn, a significant increase in magnitude inter-turn voltage harmonic is observed beyond the fifth harmonic number.

REFERENCES

[1] H. Kim, T. Kong, S. B. Lee, T. Kang, N. Oh, Y. Kim, S. Park, C. Lim, and G. C. Stone, "Experience with Stator Insulation Testing and Turn/Phase Insulation Failures in the Power Generation Industry," IEEE Tran. Ind. Appl. , Vol. 54, No. 3, pp. 2225- 2236, 2018.

[2] A. Cavallini, D. Fabiani,and G.C. Montanari, "A novel method to diagnose PWM-fed induction motors," Dielectrics and Electrical Insulation, IEEE Trans. Dielectrics and Electrical Insulation Vol. 15, No. 5, pp.1313-1321, 2008

[3] V. Mihaila,"New Design of Stator Windings of AC Machines for Reducing the Negative Effects of dV/dt. Ph.D. Thesis, University Lille Nord: Lille, France, 2011

[4] M. Tozzi, G. C. Montanari, D. Fabiani, A. Cavallini , and G. Gao, "Off-Line and On-Line PD Measurements on Induction Motors Fed by Power Electronic Impulses," 2009 IEEE Electrical Insulation Conference, Montreal, QC, Canada, 31 May- 3 June 2009

[5] R. M. Tallam, S. B. Lee, G. C. Stone, G. B. Kliman, J. Yoo, T. G. Habetler, "A survey methods for detection of stator-related faults in induction machines," IEEE Transaction on Industry Application, Vol. 43, No.4, pp. 920-933, 2007.

[6] S. Grubic, J. M. Aller, B. Lu, and T. G. Habetler, "A Survey on Testing and Monitoring Methods for Stator Insulation Systems of Low-Voltage Induction Machines Focusing on Turn Insulation Problems," IEEE Transactions on Industrial Electronics, Vol. 55, No. 12, pp. 4127-4136 , 2008

[7] A. Cavalini, G.C. Montanari, F. Puletti, A. Contin, "A New Methodology for the Identification of PD in Electrical Apparatus: Properties and Applications," IEEE Transactions on Dielectrics and electrical Insulation, Vol. 12, No. 2, pp. 203-215, 2005 .

[8] A. Boglietti, A. Cavagnino, M. Lazzari, "Experimental High-Frequency Parameter Identification of AC Electrical Motors,"IEEE Trans. on Ind. Appl., Vol. 43, No. 1, pp.23-29, 2007.

[9] L. Wang, C. N.-M. Ho, F. Canales, and J. Jatskevich, "High-Frequency Modeling of the Long-Cable-Fed Induction Motor Drive System Using TLM Approach for Predicting Overvoltage Transients," IEEE Trans. Power Electronics., Vol. 25, No. 10, pp. 2653–2664, 2010. .

[10] O. A. Mohammed, S. Ganu, N. Abed, S. Liu, and Z. Liu, "High Frequency PM Synchronous Motor Model Determined by FE Analysis," IEEE Trans. Mag, Vol. 42, no. 4, pp. 1291–1294, 2006

[11] E. Ferdjallah-kherkhachi, E. Schaeffer, L. Loron, et M. Benbouzid, « Online Monitoring of Marine Turbine Insulation Condition Based on High Frequency Models », in IECON 2014 - 40th Annual Conference on IEEE Industrial Electronics Society, 2014.

[12] S. Savin, S. Ait-Amar, et D. Roger, "Turn-to-turn capacitance variations correlated to PDIV for AC motors monitoring," IEEE Trans. Dielectr. Electr. Insul., Vol. 20, No 1, pp. 34-41, 2013.

[13] P. Werynski, R. Corton, D. Roger, et J. F. Brundy,"On-line monitoring of Insulation Aging in AC Motors Fed by PWM Inverters," in 2005 IEEE International Conference on Electric Machines and Drives, pp. 1942-1948, 2005.

[14] M. Toudji, G. Parent, S. Duchesne, and P. Dular, "Determination of Winding Lumped Parameter Equivalent Circuit by Means of Finite Element Method," IEEE Trans. Magn., Vol. 53, No. 6,pp. 9401904-9401904 , June 2017.

[15] N. Djukic, L. Encica and J. J. H. Paulides, "Overview of Capacitive Couplings in Windings,"Tenth International Conference on Ecological Vehicles and Renewable Energies (EVER), 2015.

Simulation study of the dual star permanent magnet synchronous machine using different modeling approaches with an open circuit fault

Amirouche Elyazid, Ghedamsi Kaci, Aouzellag Djamal
Laboratoire de Maitrise des Energies Renouvelables
Faculté de Technologie, Université de Bejaia 06000, Algerie
Emails: elyazid.amirouche@hotmail.com, kghedamsi@yahoo.fr, aouzellag@hotmail.com

***Abstract*— Three mathematical models of a dual star permanent magnet synchronous machine (DSPMSM) are presented, one in the natural reference frame, and two others in a synchronously rotating d-q reference frame. In order to simplify the machine analysis, a proper transformation is needed to transform the time varying quantities of the machine into constant variables, many transformations are reported in the literature. In this paper, two transformations are selected and applied to a DSPMSM. The models are implemented and simulated using Matlab/Simulink environment, the simulation results are discussed, finally, the models behavior under an open circuit fault is analyzed and discussed.**

Keywords- dual star permanent magnet synchronous machine, machine modeling, different modeling methods, rotating dq reference frame, open circuit fault.

I. INTRODUCTION

Nowadays, power electronic converters are used to supply alternative current machines, consequently, the machines are decoupled from the grid, so the number of the machine's phases is not limited to three anymore, making possible the exploitation of multiphase machines in domains requiring some specific advantages, such as lower torque ripples [1] and fault tolerance [2]. The voltage source inverter fed double star machine is one of the widely discussed topics in the literature [3], [4].

Because the machine's variables are not constant in time in steady state, the use of an adequate transformation in order to obtain constant variables presents many advantages, constant variables are easier to analyze, and the rotor position dependency of inductances that characterizes salient pole machines is eliminated, simplifying the model as well as the control of the machine.

Many modeling technics are proposed in the literature, the double winding approach represents the machine with two pairs of d-q windings with a mutual coupling between each other [5], so this model is an extension of the conventional three phase machine model. With the aim of simplifying this model, [6] proposes a transformation where the stator circuits are completely decoupled called extended 0dq transformation.

This paper focuses on the double star permanent magnet synchronous machine modeling, many modeling approaches will be presented, simulated and compared, the behavior of these models under single phase open circuit fault will also be simulated and analyzed.

II. DOUBLE STAR ELECTRICAL MACHINES

Multiple star machines are a particular case of multiphase machines, where the phases are divided into multiple three phase sets, with isolated neutral points.

In a double star machine, the angle between the sets can have any value from 0° to 60°, the study of [1] shows that the torque characteristics of a double star with a displacement angle of 30° between the sets is better than any other value, the torque ripple is greatly reduced, also the predominant frequency has been shifted 12 times the supply frequency [1].

The use of multiphase machines instead of their conventional three phase counterparts presents multiple advantages, in addition to the torque ripple reduction, as stated above, the machine's power is divided among more inverter legs, so the power electronics rating is reduced, also, the reliability of the machine is increased in case of loss of one or more machine phases [7].

Because of the fault tolerant behavior of multiphase machines, they are intensively used in applications requiring continuous service even with partial power, for example, in ship propulsion systems, aerospace applications, electrical vehicles, and in renewable energy conversion systems [7].

III. NATURAL FRAME MODEL (ABC) OF THE DSPMSM

Before doing any transformation, the natural frame model of the machine must be developed, figure 1 shows the coils configuration of a dual star synchronous motor.

In order to simplify the modeling of the machine, the following assumptions are made: all the sets are identical, and the windings are sinusoidally distributed around the air gap, mutual leakage inductances, saturation and eddy current are not considered.

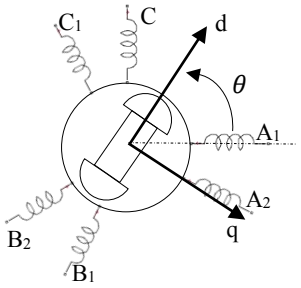

Figure 1 : Dual star synchronous machine

A. Electric model

Starting from the natural reference frame, the electric equation of the system can be written:

$$v_{abc} = r\, i_{abc} + \frac{d\,\varphi_{abc}}{dt} \qquad (1)$$

where

$$v_{abc} = \left[v_{a_1} v_{b_1} v_{c_1} v_{a_2} v_{b_2} v_{c_2}\right]^t$$

$$i_{abc} = \left[i_{a_1} i_{b_1} i_{c_1} i_{a_2} i_{b_2} i_{c_2}\right]^t$$

$$\varphi_{abc} = \left[\varphi_{a_1} \varphi_{b_1} \varphi_{c_1} \varphi_{a_2} \varphi_{b_2} \varphi_{c_2}\right]^t$$

$$r = \begin{bmatrix} r_s & \cdots & 0 \\ \vdots & \ddots & \vdots \\ 0 & \cdots & r_s \end{bmatrix}$$

φ_{abc} is the resultant air gap flux, r a 6x6 matrix with r_s the armature resistance.

The resultant air gap flux can be written according to the inductance matrix and permanent magnet flux vector as follow:

$$\varphi_{abc} = \begin{bmatrix} [L_1] & [M_{12}] \\ [M_{12}]^t & [L_2] \end{bmatrix} i_{abc} + \varphi_{PM_{abc}} \qquad (2)$$

where $[L_i]$ the inductance matrix of the same three phase set windings, $[M_{12}]$ the mutual inductance matrix between the different sets, and $\varphi_{PM_{abc}}$ the flux produced by the permanent magnets given by (3).

$$\varphi_{PM_{abc}} = \Psi_{pm} \begin{bmatrix} \cos(\theta) \\ \cos(\theta - \frac{2\pi}{3}) \\ \cos(\theta + \frac{2\pi}{3}) \\ \cos(\theta - \alpha) \\ \cos(\theta - \frac{2\pi}{3} - \alpha) \\ \cos(\theta + \frac{2\pi}{3} - \alpha) \end{bmatrix} \qquad (3)$$

With α the electric displacement angle between the sets, and Ψ_{pm} the amplitude of the permanent magnet flux.

B. Inductance matrix

Considering the rotor position dependency of the inductances, the self and mutual inductances are generally expressed by Fourier expansions [7]. Taking into account higher order harmonics, the self inductance of winding i is written as follow:

$$L_i(\theta) = L_{s_0} + \sum_{n=1}^{\infty} L_{s_{2n}} \cos\left(2n(\theta + \theta_i) + \varphi_{i_n}\right) \qquad (4)$$

where L_{s_0} is a constant average value, $L_{s_{2n}}$ is the coefficient of inductance harmonics (2^{nd}, 4^{th},…), θ_i is the electric displacement angle of the ith winding magnetic axis from the reference axis (chosen to be the magnetic axis of coil A_1 as shown in figure 1), while φ_{i_n} is the displacement angle of the corresponding harmonic component.

The constant term L_{s_0} can be expressed as the sum of the stator leakage inductance L_{s_l} and the stator magnetizing inductance m [8].

$$L_{s_0} = L_{s_l} + m \qquad (5)$$

Similarly, the mutual inductance between the phases can be expressed as:

$$M_{ij}(\theta) = m\cos(\theta_i - \theta_j) + \sum_{n=1}^{\infty} M_{s_{2n}} \cos\left(n(2\theta + \theta_i + \theta_j) + \varphi_{i_n}\right) \qquad (6)$$

Considering only the first inductance harmonic ($n = 1$), the self and mutual inductance equations become:

$$L_i(\theta) = L_{s_0} + L_{s_2}\cos(2\theta_i) \qquad (7)$$

$$M_{ij}(\theta) = m\cos(\theta_i - \theta_j) + M_{s_2}\cos\left(2\theta + \theta_i + \theta_j\right) \qquad (8)$$

Comparing to the general equation given by [6], the coefficients L_{s_2} and M_{s_2} are equal.

The full inductance matrix of the windings can be constructed as shown in (9).

$$L_s(\theta) = \begin{bmatrix} L_{a_1} & M_{a_1b_1} & M_{a_1c_1} & M_{a_1a_2} & M_{a_1b_2} & M_{a_1c_2} \\ M_{a_1b_1} & L_{b_1} & M_{b_1c_1} & M_{a_2b_1} & M_{b_1b_2} & M_{b_1c_2} \\ M_{a_1c_1} & M_{b_1c_1} & L_{c_1} & M_{a_2c_1} & M_{c_1b_2} & M_{c_1c_2} \\ M_{a_1a_2} & M_{a_2b_1} & M_{a_2c_1} & L_{a_2} & M_{a_2b_2} & M_{a_2c_2} \\ M_{a_1b_2} & M_{b_1b_2} & M_{c_1b_2} & M_{a_2b_2} & L_{b_2} & M_{b_2c_2} \\ M_{a_1c_2} & M_{b_1c_2} & M_{c_1c_2} & M_{a_2c_2} & M_{b_2c_2} & L_{c_2} \end{bmatrix} \qquad (9)$$

The four matrices presented earlier in (2) can be recognised in this matrix.

Note that every single term of this matrix is θ dependent, as a consequence, the inverse of this matrix must be calculated at every time step, making this model very complex, time consuming, and requires a high processing power.

C. Electromagnetic torque

The expression of the electromagnetic torque can be written as the derivative of the electromagnetic energy stored in the machine with respect to the geometric angle of the rotor:

$$T_e = \frac{P}{2}\frac{\partial W_c}{\partial \theta_m} \quad (10)$$

Where θ_m is the geometric angle of the rotor, and W_c is expressed by

$$W_c = \frac{1}{2} i_{abc}^t L_s i_{abc} + i_{abc}^t \varphi_{PM_{abc}} \quad (11)$$

IV. DOUBLE D-Q WINDING MODEL

In this model, the park transformation is applied to the natural frame system, leading to a couple of d-q windings with a mutual coupling between theme [9].

The standard park transformation matrix for a three phase system is defined as:

$$T(\theta) = \sqrt{\frac{2}{3}}\begin{bmatrix} \cos(\theta) & \cos(\theta - \frac{2\pi}{3}) & \cos(\theta + \frac{2\pi}{3}) \\ -\sin(\theta) & -\sin(\theta - \frac{2\pi}{3}) & -\sin(\theta + \frac{2\pi}{3}) \\ \frac{1}{\sqrt{2}} & \frac{1}{\sqrt{2}} & \frac{1}{\sqrt{2}} \end{bmatrix} \quad (12)$$

Starting from this, the transformation matrix T_1 for a dual star system can be deduced [9].

$$T_1 = \begin{bmatrix} T(\theta) & 0_{3,3} \\ 0_{3,3} & T(\theta - \alpha) \end{bmatrix} \quad (13)$$

With $0_{3,3}$ a 3x3 null matrix.

The transformation is given by (14).

$$X_{dq} = T_1 X_{abc} \quad (14)$$

Where X can be any phase variable vector (current, voltage or flux).

Applying (14) to the stator flux (15) will result in (16)

$$\varphi_{abc} = L_s i_{abc} + \varphi_{PM_{abc}} \quad (15)$$

$$\varphi_{dq} = (T_1 L_s T_1^t) i_{dq} + \varphi_{PM_{dq}} \quad (16)$$

with

$$\varphi_{PM_{dq}} = \begin{bmatrix} \frac{\sqrt{6}}{2}\Psi_{pm} & 0 & 0 & \frac{\sqrt{6}}{2}\Psi_{pm} & 0 & 0 \end{bmatrix}^t \quad (17)$$

After several lines of trigonometric simplifications, the transformed inductance matrix can be obtained.

$$L_{T1} = T_1 L_s T_1^t = \begin{bmatrix} L_{d_1} & 0 & 0 & M_{d_1} & 0 & 0 \\ 0 & L_{q_1} & 0 & 0 & M_{q_1} & 0 \\ 0 & 0 & L_{0_1} & 0 & 0 & 0 \\ M_{d_2} & 0 & 0 & L_{d_2} & 0 & 0 \\ 0 & M_{q_2} & 0 & 0 & L_{q_2} & 0 \\ 0 & 0 & 0 & 0 & 0 & L_{0_2} \end{bmatrix} \quad (18)$$

In this matrix, we can see four square sub-matrices, related to two couples of orthogonal windings dq_1 and dq_2, with a mutual coupling between theme.

$$L_{d_1} = L_{d_2} = L_{s_0} + \frac{m}{2} + \frac{3}{2}L_{s_2}$$

$$L_{q_1} = L_{q_2} = L_{s_0} + \frac{m}{2} - \frac{3}{2}L_{s_2}$$

$$L_{0_1} = L_{0_2} = L_{s_0} - m$$

$$M_{d_1} = M_{d_2} = \frac{3}{2}m + \frac{3}{2}L_{s_2}$$

$$M_{q_1} = M_{q_2} = \frac{3}{2}m - \frac{3}{2}L_{s_2}$$

As can be seen, the resultant matrix inductance is not diagonal, adding some complexity to the model simulation and analysis.

A. The current model in the coupled d-q reference frame

The machine electric model can now be obtained by applying the transformation matrix to the electric equation (1) and combining the equations aforementioned, leading to the electric equation in the dq reference frame (19).

$$v_{dq} = r\, i_{dq} + \frac{d\,\varphi_{dq}}{dt} + \omega\, j\, \varphi_{dq} \quad (19)$$

The current model of the machine (20) is obtained by developing (19).

$$\frac{di_{dq}}{dt} = L_{T1}^{-1}\left(v_{dq} - \omega j \varphi_{PM_{dq}} - \frac{d\varphi_{PM_{dq}}}{dt} - (r + \omega j L_{T_1}) i_{dq}\right) \quad (20)$$

Where

$$j = \frac{1}{\omega}\left(T_1 \frac{dT_1^{-1}}{dt}\right) = \begin{bmatrix} 0 & -1 & 0 & 0 & 0 & 0 \\ 1 & 0 & 0 & 0 & 0 & 0 \\ 0 & 0 & 0 & 0 & 0 & 0 \\ 0 & 0 & 0 & 0 & -1 & 0 \\ 0 & 0 & 0 & 1 & 0 & 0 \\ 0 & 0 & 0 & 0 & 0 & 0 \end{bmatrix}$$

$$\varphi_{dq} = L_{T_1} i_{dq} + \varphi_{PM_{dq}} \quad (21)$$

B. Electromagnetic torque

Starting from the instantaneous output power, the electromagnetic power as well as torque can be derived.

$$P_{out} = v_{d_1} i_{d_1} + v_{q_1} i_{q_1} + v_{d_2} i_{d_2} + v_{q_2} i_{q_2} \quad (22)$$

By replacing the voltage by it's equation given by (19), and eliminating the terms giving the joule losses and the rate of change in magnetic energy, and dividing the resultant equation by the mechanical angular speed, the expression of the developed electromechanical torque shown in (23) is then deduced.

$$t_e = P\left(\varphi_{d_1} i_{q_1} - \varphi_{q_1} i_{d_1} + \varphi_{d_2} i_{q_2} - \varphi_{q_2} i_{d_2}\right) \quad (23)$$

V. EXTENDED D-Q MODEL

Starting from the following three phase park transformation matrix $T(\theta)$, the full transformation matrix $T_p(\theta)$ for the dual star system can be constructed according to [6].

$$T(\theta) = \sqrt{\frac{2}{3}} \begin{bmatrix} \frac{1}{\sqrt{2}} & \cos(\theta) & -\sin(\theta) \\ \frac{1}{\sqrt{2}} & \cos(\theta - \frac{2\pi}{3}) & -\sin(\theta - \frac{2\pi}{3}) \\ \frac{1}{\sqrt{2}} & \cos(\theta + \frac{2\pi}{3}) & -\sin(\theta + \frac{2\pi}{3}) \end{bmatrix} \quad (24)$$

$$T_p(\theta) = \frac{1}{\sqrt{2}} \begin{bmatrix} T(\theta) & T(\theta) \\ T(\theta - \alpha) & -T(\theta - \alpha) \end{bmatrix} \quad (25)$$

Note the introduction of a coefficient $\frac{1}{\sqrt{2}}$ to get an invariant power.

The application of this transformation to the inductance matrix $L_s(\theta)$ will result in the following matrix:

$$L_T = T_p^t \, L_s \, T_p = \begin{bmatrix} L_{n_0} & 0 & 0 & 0 & 0 & 0 \\ 0 & L_{n_d} & 0 & 0 & 0 & 0 \\ 0 & 0 & L_{n_q} & 0 & 0 & 0 \\ 0 & 0 & 0 & L_{a_0} & 0 & 0 \\ 0 & 0 & 0 & 0 & L_{a_d} & 0 \\ 0 & 0 & 0 & 0 & 0 & L_{a_q} \end{bmatrix} \quad (26)$$

Where

$$L_{n_0} = L_{a_0} = L_{a_d} = L_{a_q} = L_{s_0} - m$$
$$L_{n_d} = L_{s_0} + 3L_{s_2} + 2m$$
$$L_{n_q} = L_{s_0} - 3L_{s_2} + 2m$$

This transformation splits the machine into two decoupled systems, one called normal system, and the other is called anti system, in the normal system, the current support each other, creating a normal rotational field in the air gap, and in the anti system, the currents oppose each other leaving only leakage fluxes in the stator [6].

A. The current model in the extended 0dq reference frame

As done in section IV.A, the current model of the machine in the extended 0dq reference frame is given by:

$$\frac{di_{0dq}}{dt} = L_T^{-1}\left(v_{0dq} - \omega j \varphi_{PM_{0dq}} - \frac{d\varphi_{PM_{0dq}}}{dt} - (r + \omega j L_T) i_{0dq}\right) \quad (27)$$

with

$$j = \frac{1}{\omega}\left(T_p^t \frac{dT_p^{t^{-1}}}{dt}\right) = \begin{bmatrix} 0 & 0 & 0 & 0 & 0 & 0 \\ 0 & 0 & -1 & 0 & 0 & 0 \\ 0 & 1 & 0 & 0 & 0 & 0 \\ 0 & 0 & 0 & 0 & 0 & 0 \\ 0 & 0 & 0 & 0 & 0 & -1 \\ 0 & 0 & 0 & 0 & 1 & 0 \end{bmatrix}$$

$$\varphi_{PM_{0dq}} = T_p \, \varphi_{PM_{abc}} = \begin{bmatrix} 0 & \sqrt{3}\Psi_{pm} & 0 & 0 & 0 & 0 \end{bmatrix}^t$$

B. Electromagnetic torque

Similar to what done in section IV.B, the electromagnetic torque is given by (28).

$$t_e = P\left(\varphi_{nd} i_{nq} - \varphi_{nq} i_{nd} + \varphi_{ad} i_{aq} - \varphi_{aq} i_{ad}\right) \quad (28)$$

VI. SIMULATION RESULTS

All the three models have been simulated using Matlab/Simulink environment, the machine is simulated as a generator driven with constant speed, and feeding a resistive load. The simulation results are presented and discussed below. The parameters of the considered machine are shown in table 1.

The open circuit fault it created by adding a high value resistance in series with the load in the considered phase.

A. Safe mode operation

The figures 2-3 present the currents in the transformed reference frames. Since the extended model splits the machine into two distinct sub-machines, and the excitation is only present in the normal machine, only the latter is responsible for the entire machine torque generation, the second system describes the losses inside the machine, unlike the coupled d-q model, which splits the machine into two similar sub-machines, and the excitation is present in both systems, the two sub-machines contribute to the torque generation.

After applying the inverse transformation, the currents in the natural frame are obtained, the currents of the transformed models (figure 4 and 5) are identical to the natural frame model (figure 6), the only difference is that the currents of the second star of the coupled d-q model are inversed in respect to other models.

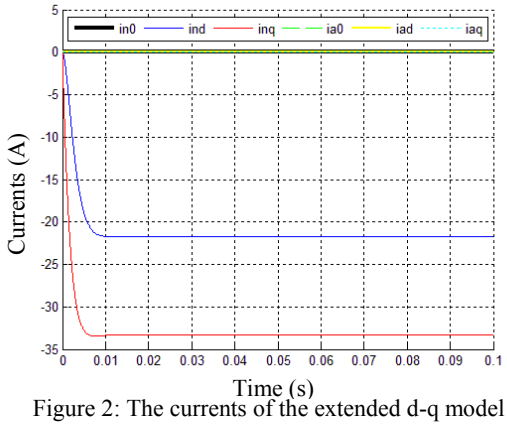

Figure 2: The currents of the extended d-q model

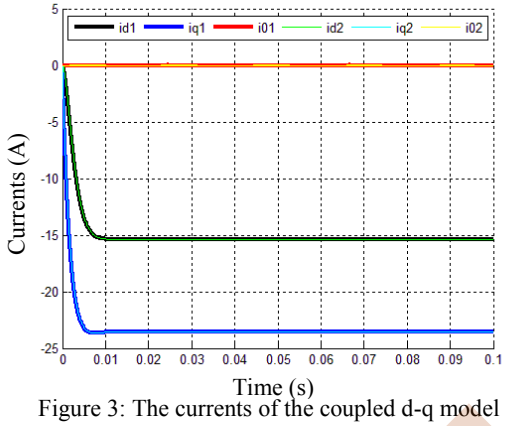

Figure 3: The currents of the coupled d-q model

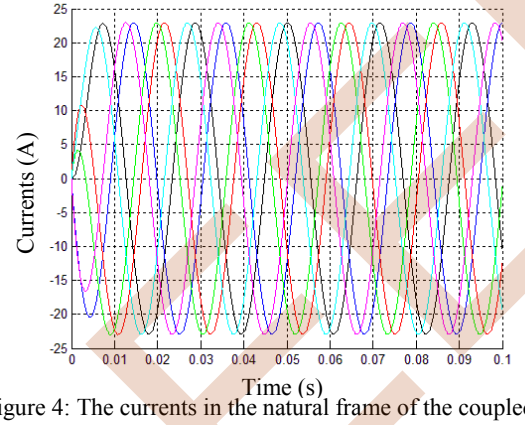

Figure 4: The currents in the natural frame of the coupled d-q model

The torque is shown in figure 7, a zoom into the plot shows an error of about 0.0063% of the transformed models compared to natural frame model in the steady sate, this error is negligible and do not influence the accuracy of the transformed models.

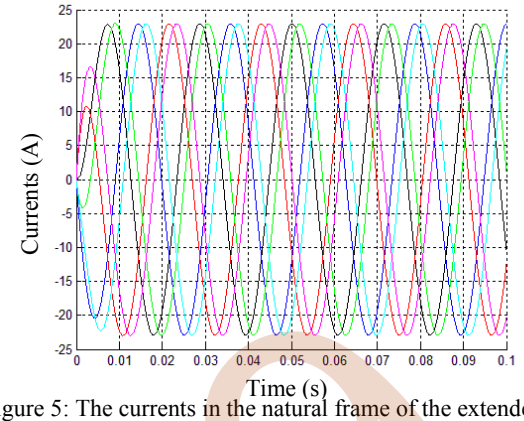

Figure 5: The currents in the natural frame of the extended d-q model

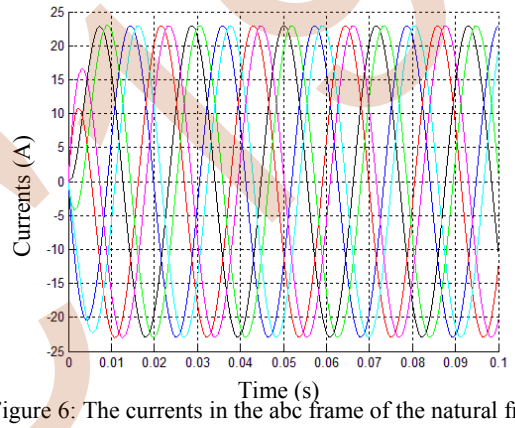

Figure 6: The currents in the abc frame of the natural frame model

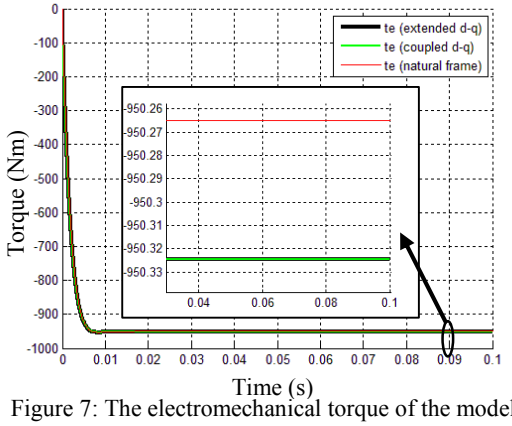

Figure 7: The electromechanical torque of the models

B. Open Circuit Fault operation

Figure 8-10 show the simulation results of an open circuit fault occurring at phase A_1.

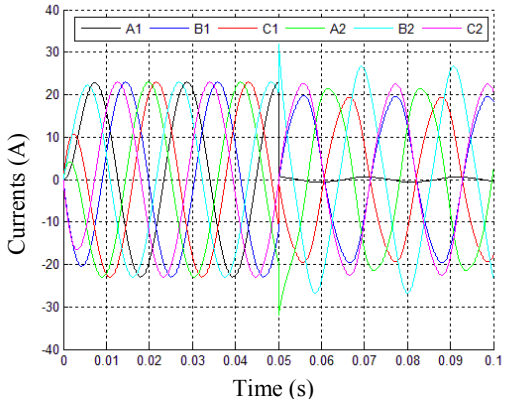

Figure 8: The currents in the natural frame of the coupled d-q model pre and post-fault occurrence

The current of the two phases of the same set (B_1 and C_1) decreases by about 15% compared to the pre-fault state. To verify the Kirchhoff law, the two currents have a displacement angle of 180°. The winding orthogonal to A_1, i.e. C_2, have not been affected. The closest winding to the faulty one (A_2) see its current decreases by about 6.9%, and the current of B_2 increases by 16.5%.

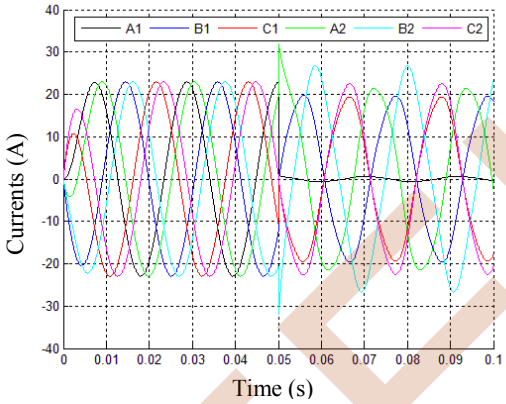

Figure 9: The currents in the natural frame of the extended d-q model pre and post-fault occurrence

Concerning the torque (presented in figure 11), a high ripples appear with a frequency of about 93 Hz, which represents two times the electric frequency of the stator current. The oscillation amplitude reaches a value of 465.6 Nm. This comportment is identical to the three models, confirming, once again the validity of the models.

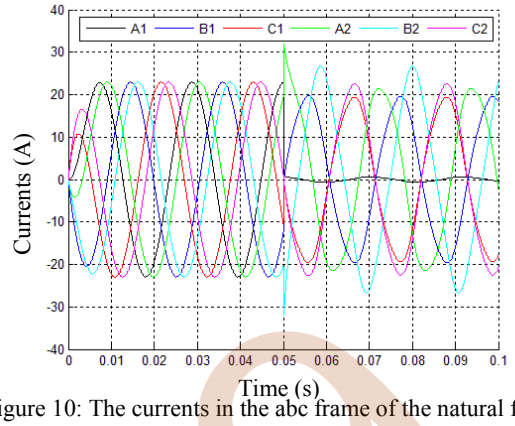

Figure 10: The currents in the abc frame of the natural frame model pre and post-fault occurrence

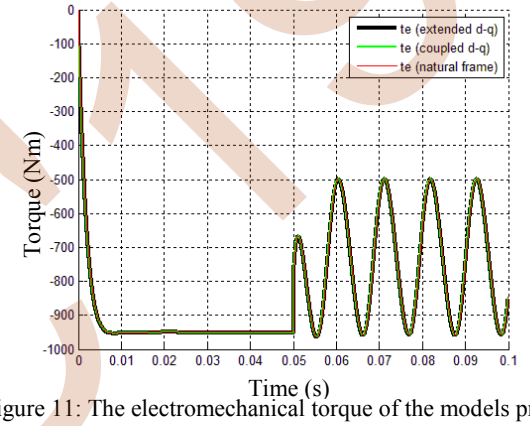

Figure 11: The electromechanical torque of the models pre and post-fault occurrence

Table 1 : Machine parameters [10]

Description	Value
Stator resistance	0.53 Ω
Average self inductance L_{s_0}	18.93 mH
Second harmonic coefficient L_{s_2}	-3.03 mH
Mutual inductance m	10.53 mH
Permanent magnet flux	1.8328 Wb
Number of pole pairs	8
Rotational speed	350 rpm

VII. CONCLUSION

To simplify the analysis and control of double star machine, an adequate mathematical model must be constructed, for this purpose, many models are reported in the literature.

The natural frame model gives more details about the machine since it can include all the voltage harmonics, and can take into account saturation effect and other phenomena, but it's very complex to solve and requires a high computational power. Simplified models have been proposed, the double winding model is very simple to compute, but the mutual coupling

between the two winding couples makes it require some more processing time. Also, in this model, all the current components are active, so the analysis of the machine behaviour becomes more complex comparing to the other simplified model.

To solve the problems encountered with the double winding model, an other transformation is proposed which fully decouple the windings, this new approach is called extended d-q transform, it deals with a diagonalized inductance matrix which make it requiring less processing power.

The three models have been simulated, the results show an error of only 0.0063% of the transformed models compared to the natural frame model. Also a simulation under a single phase open circuit fault have been realized, the comportment of the three models is quite similar, confirming the validity of the transformed models despite of their differences. The main difference between all these models is the complexity and the difficulty of implementation.

REFERENCES

[1] R. H. Nelson and P. C. Krause, "Induction machine analysis for arbitrary displacement between multiple winding sets," *IEEE Trans. Power Appar. Syst.*, vol. PAS-93, no. 3, pp. 841–848, 1974.

[2] E. Levi, R. Bojoi, F. Profumo, H. A. Toliyat, and S. Williamson, "Multiphase induction motor drives - A technology status review," *IET Electr. Power Appl.*, vol. 1, no. 4, pp. 489–516, 2007.

[3] D. Star, P. Magnet, S. Machine, S. Order, and S. Mode, "Direct Torque Control Using Second Order Sliding Mode of a Double Star Permanent," vol. 80, no. December, 2018.

[4] R. Zaimeddine and E. M. Berkouk, "A novel DTC scheme of double-star induction motors using three-level voltage source inverter," 2012.

[5] F. Barrero, M. R. Arahal, R. Gregor, S. Toral, and M. J. Durán, "A proof of concept study of predictive current control for VSI-driven asymmetrical dual three-phase AC machines," *IEEE Trans. Ind. Electron.*, vol. 56, no. 6, pp. 1937–1954, 2009.

[6] H. Knudsen, "Extended Park's Transformation for 2x3-phase Synchronous Machine and Converter Phasor Model with Representation of AC Harmonics," *IEEE Trans. Energy Convers.*, vol. 10, no. 1, pp. 126–132, Mar. 1995.

[7] I. Industriale, "Double Star Pm Machine : Analysis and Simulations," Politecnico di Milano, 2016.

[8] H. Knudsen, "Extended Park's Transformation for 2x3-phase Synchronous Machine and Converter Phasor Model with Representation of AC Harmonics," *IEEE Trans. Energy Convers.*, vol. 10, no. 1, pp. 126–132, Mar. 1995.

[9] E. F. Fuchs and L. T. Rosenberg, "Anai ysis of an alternator with two displaced stator windings," *IEEE Trans. Power Appar. Syst.*, vol. PAS-93, no. 6, pp. 1776–1786, Nov. 1974.

[10] J. Karttunen, P. Peltoniemi, S. Kallio, P. Silventoinen, and O. Pyrhönen, "Determination of the inductance parameters for the decoupled d–q model of double-star permanent-magnet synchronous machines," *IET Electr. Power Appl.*, vol. 8, no. 2, pp. 39–49, Feb. 2014.

Influence of Geometric and Physical Parameters on the Thrust Force of a Linear Induction Motors

BENSEHILA Aissa[1], BOUZIDI Athmane[1], HAMOUDI Yanis[1], BENHAMOUCHE Slimane[1]
[1]Laboratoire de Génie Electrique de Bejaia (LGEB), Faculté Technologie, université A. Mira Bejaia, Bejaia 06000,Algérie
aissabensehila@gmail.com

TAKORABET Noureddine [2]
[2] Groupe de Recherche en Energie Electrique de Nancy (GREEN), Université de Lorraine Nancy, France
noureddine.takorabet@univ-lorraine.fr

***Abstract*—This article presents the geometric and physical parameters influence on the thrust force of a linear three-phase single-sided face induction motor by the finite element method under Matlab. In fact, mathematical models were formulated to solve partial differential equations that govern the electromagnetic phenomenon. The objective of this work is mainly based on the evaluation of the thrust force generated by the motor according to the different geometric and physical parameters such as thickness, conductivity and relative magnetic permeability. Through this study we show the effect of these parameters on the machine operation allowing an efficient choice of the parameters to optimize. The used method fixes the geometric and physical parameters which generate the optimal forces to obtain optimal geometries. This study makes it possible to set the parameters.**

I. INTRODUCTION

Linear motors have been used in rail transport and in many industrial applications. Compared to other types, the single-sided linear induction motor are widely used because of its simplicity and low construction cost [1, 2], they are widespread and meet the industry's requirements [1, 3,4]. It is therefore not at all surprising that it is still the subject of much research aimed to improve its modeling and optimizing its design [5, 6, 7, 8, 9]. Despite its simplicity of manufacture and implementation, the modeling and calculation of different quantities of the linear induction motor are not easy tasks. This is mainly due to the complex geometry of linear machines, and the non-linear character of materials. The requirement for precision, within the design process requires the use of accurate numerical models [10].The finite element method is widely adopted compared to other methods and is the most suitable to complex geometries, which has also been the subject of several research projects [11].

In the design of a linear three-phase induction motor, we are generally confronted to the choice issue of the physical and geometrical parameters. It is therefore essential to go through electromagnetic modeling, using field theory to develop equations that govern the linear induction motor [12, 11, 9]. In this work, the study is mainly based on the influence of different geometrical and physical parameters on the electromagnetic force generated by the linear induction motor. The force computation is obtained under Matlab using the 2D finite element method.

II. DEVICE STUDIED

For complex structures, numerical calculation is very useful; it allows to define the physical quantities at different points of the studied system.

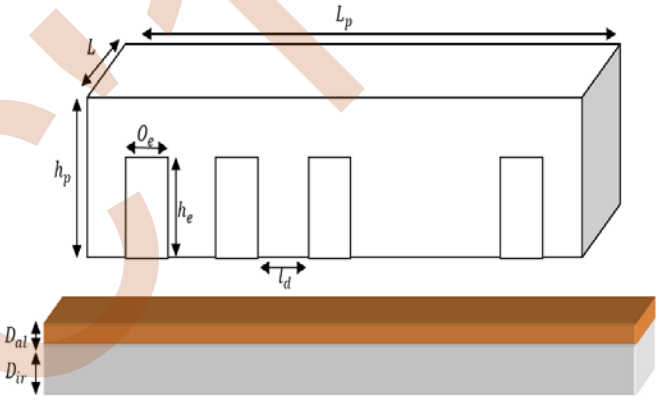

Figure 1. Linear motor geometric model

The single-sided three-phase linear induction motor is shown in Fig.1. The inductor consists of a high permeability magnetic core with 12 notches and a three-phase winding with two return plates an aluminum conductive plate and a steel plate.

III. MATHEMATICAL MODEL

From the Maxwell-Ampere equation combined with the Maxwell-flux equation (Div B=0), the magnetic induction B derived from a potential magnetic vector A, hence the equation governing the electromagnetic is given as follows:

The equation governing the studied system is given by the following form

$$\overrightarrow{Rot}\left(\frac{1}{\mu}\overrightarrow{Rot}\left(\overrightarrow{A}\right)\right)=\overrightarrow{J}_s-\sigma\left[\frac{\partial\overrightarrow{A}}{\partial t}-\left(\overrightarrow{V_x}\wedge\left(\overrightarrow{Rot}\left(\overrightarrow{A}\right)\right)\right)\right] \quad (1)$$

The induced current by the potential vector A in the conducting medium with conductivity σ and speed V_x, is given by formula (2):

$$\vec{J}_{induit} = \sigma\left[\frac{\partial \vec{A}}{\partial t} - \left(\vec{V}_x \wedge \left(Rot\left(\vec{A}\right)\right)\right)\right] \quad (2)$$

$\vec{J}_{induit}$: Eddy current in the secondary

The two-dimensional formulation with magnetic vector potential A (strong form) is given as follows

$$\frac{\partial}{\partial x}\left(\frac{1}{\mu}\frac{\partial A_Z}{\partial x}\right)+\frac{\partial}{\partial y}\left(\frac{1}{\mu}\frac{\partial A_Z}{\partial y}\right)=-J_S+\sigma\left(\frac{\partial A_Z}{\partial t}+V_x\frac{\partial A_Z}{\partial x}\right) \quad (3)$$

This model provides the evolution of electromagnetic fields in time and space. The space discretization particularly in complex geometries case, as well as the discretization and the time presence of the saturation requires significant computational times [13].

On the other hand, the use of the harmonic model (also called complex magneto-dynamic model) allows overcoming the time constraint. Suppose that the power supply currents are purely sinusoidal and the electromagnetic fields are also sinusoidal varying. In these conditions, the representation of the Fresnel model is cited in [14, 15, 16, 17].

The current density is illustrated by $\vec{J} = J_S e^{j(wt+\varphi)}$

The temporal derivative of vector potential A is then written as follows:

$$\frac{\partial \vec{A}}{\partial t} = jg\omega\vec{A} \quad (4)$$

g: is the relative slippage of the velocity relative to the slippery field.

IV. 2D FINITE ELEMENT MODEL

A direct 2D linear finite element calculation model of the induction machine is performed with Matlab program.

For the finite element modeling the equations which govern the electromagnetic phenomenon, we have used the two-dimensional formulation of the magnetic vector potential obtained from the Maxwell equations and simplifying assumptions.

Then a 2D finite element resolution is applied to the integral form (weak form) of the magnetic vector potential formulation. After calculating the elementary matrices of the system and their assembly, we obtained the matrix system that we solved using a direct method. Farther more, we introduce the data of each region for both, geometric (Dimensions) and physic (Permeability, Conductivity) parameters in the studied system. Once the magnetic vector potential A is computed, the derived quantities such as, magnetic induction B, magnetic induction field H, force field dF, global force F, induced currents J, etc., will be calculated.

In fact, in 2D the triangular elements fit to any geometric configuration which allows a simple discretization of the resolution. The approximate interpolation function of the unknown (A) to be approximated (the magnetic potential vector in this case) is given by the following form:

$$A(x,y)=\alpha_1+\alpha_2 x+\alpha_3 y \quad (5)$$

This vector potential is perfectly defined, in every point of a triangular element, by assuming that,

$$A(x,y)=\sum_{i=1}^{3}F_i(x,y)A_i \quad (6)$$

With Fi (i=1,3) are the shape functions, or area coordinates due to their geometric properties.

A_i or (A_1, A_2 and A_3) express the values of the vector potentials in the three vertices of the triangle element.

$$F_i(x,y)=a_i+b_i x+c_i y$$

Where a_i, b_i and c_i are constants which depend on the triangle vertice coordinates.

Then, the equation (3) can be written as follow:

$$\frac{\partial}{\partial x}\left(\frac{1}{\mu}\frac{\partial A_Z}{\partial x}\right)+\frac{\partial}{\partial y}\left(\frac{1}{\mu}\frac{\partial A_Z}{\partial y}\right)=-J_s+\sigma\left(jg\omega A_Z+V_X\frac{\partial A_Z}{\partial x}\right) \quad (7)$$

The second term of equation (7) is equal to Js in the source, and is equal to 0 in the air and magnetic core. Hence, it takes the following expression in the rail:

$$\sigma\left(jg\omega A_Z+V_X\frac{\partial A_Z}{\partial x}\right)$$

Integral formulations:

$$\frac{1}{\mu}\iint_S\left(\frac{\partial[F]}{\partial x}\frac{\partial[F]^t}{\partial x}+\frac{\partial[F]}{\partial y}\frac{\partial[F]^t}{\partial y}\right)[A]dx\,dy\cdots$$
$$+\sigma\iint_S[F][F]^t\frac{\partial[A]}{\partial t}dxdy-\sigma V_x\iint_S[F][F]^t dx\,dy\cdots$$
$$+J_S\iint_S[F]dx\,dy-\frac{1}{\mu}\oint_c[F]\frac{\partial A}{\partial n}dc=0 \quad (8)$$

Where c is the contour of the element, and $\frac{\partial A}{\partial n}$ is the projection gradient of A over the normal at the elemental contour dc. We assume that the, $\frac{1}{\mu}\oint_c[F]\frac{\partial A}{\partial n}dc$ term depends on boundary and interface conditions. After simplifying the integrals of (8), we obtain the following elementary system:

$$[LL]^{(e)}[A]^{(e)} + [ZZ]^{(e)}\frac{\partial[A]^{(e)}}{\partial t} - [VV]^{(e)}[A]^{(e)} = [f]^{(e)}$$

The basic matrices are given as follows:

$$[LL]^{(e)} = -\frac{S}{\mu}\begin{bmatrix} b_i^2+c_i^2 & b_ib_j+c_ic_j & b_ib_k+c_ic_k \\ b_jb_i+c_jc_i & b_j^2+c_j^2 & b_ib_k+c_ic_k \\ b_kb_i+c_kc_i & b_kb_j+c_kc_j & b_k^2+c_k^2 \end{bmatrix}$$

$$[ZZ]^{(e)} = \frac{\sigma.S}{12}\begin{bmatrix} 2 & 1 & 1 \\ 1 & 2 & 1 \\ 1 & 1 & 2 \end{bmatrix}$$

$$[VV]^{(e)} = \frac{\sigma.V_xS}{3}\begin{bmatrix} b_i & b_j & b_k \\ b_i & b_j & b_k \\ b_i & b_j & b_k \end{bmatrix}$$

$$[f]^{(e)} = J_S\frac{S}{3}\begin{bmatrix} 1 \\ 1 \\ 1 \end{bmatrix}$$

S: is the surface of an element

$[LL]^{(e)}$: Elementary rigidity matrix

$[ZZ]^{(e)}$: Elementary Mass Matrix

$[VV]^{(e)}$: Elemental displacement matrix

$[f]^{(e)}$: Primary source vector.

A. Assembly and application of boundary conditions

All the elementary matrices (mass, rigidity and displacement) must be assembled in order to form the global algebraic system for the nodal values of the physical variables.

The overall matrix system obtained after assembly is given as follow: $[LL][A] + [ZZ]\frac{\partial[A]}{\partial t} - [VV][A] = [f]$ (9)

Using the complex representation (harmonic mode), the following matrix system is obtained and given by:

$$[LL][A] + j\omega g([ZZ] - [VV])[A] = [f] \quad (10)$$

System resolution (9) or (10) occurs after introducing the Dirichlet and Neumann boundary conditions.

$$A = A_0 \quad (11)$$

$$\frac{\partial A}{\partial n} = 0 \quad (12)$$

B. Global system Resolution

First, the parameters σ, μ, ε are considered linear, the system of equations (10) can be solved by a direct method.

Depending on the medium where the finite element model is applied, equation 10 takes different forms. In the case of the inductor winding for a current source, only the rigidity matrix [LL] and the source term Js remain, the others disappear. We suppose that the current is set and that its value is not performed by induced currents.

Whether in the air or in the magnetic core, only the matrix stiffness remains, with a relative magnetic permeability equal to 1 in the first and takes important values in the second. In the induced medium all the terms are imposed except the source term Js which is null. If one induces with several layers the conductivity and magnetic permeability takes different values.

C. Thrust force calculation

The magnetic induction divergence is zero, implying that it derives from a magnetic potential vector.

$$\vec{B} = \vec{Rot}\ \vec{A} \quad (13)$$

In the two-dimensional hypothesis, the magnetic potential vector (A) has a single component oriented along the transverse axis (OZ), and its value depends only on the x and y coordinates, which gives,

$$\vec{B} = \frac{\partial A}{\partial y}\vec{i} - \frac{\partial A}{\partial x}\vec{j} \quad (14)$$

The tangential component of magnetic induction creates normal forces in the linear induction motor whereas, the normal component generates the motor thrust [7]. Hence, Lorentz's formula in its general form which expresses the primary force is given in [18]:

- The force field is formulated:

$$\vec{f} = \vec{J}_{induit} \Lambda \vec{B} \quad (15)$$

- The global generated force is written as follows:

$$F = \iint_s (J_{induit}.B)ds \quad (16)$$

$$F_x = \Re\left(J_{induit}.Conj(B_y)\right) \quad (17)$$

$$F_y = \Re\left(-J_{induit}.Conj(B_x)\right) \quad (18)$$

V. APPLICATION AND GEOMETRY

The primary or inductor of the motor of length Lp (207. 8 mm) and cross width L (100 mm) and of a height hp (45.2 mm), the teeth have a length ld of 8.6 mm and a height he of 35.2 mm, the notch opening is of Oe (8 mm) and its height is 35.2 mm with a pole pitch of 50 mm. The inductive winding powered by a three-phase sine current of 7 A with a frequency of 50 Hz which contains 12 notches each consists

of 490 coils with a 2 mm gap. The armature is 150mm long, it contains two plates, the first is in aluminum of a thickness of 4.7 mm and of an electrical conductivity of 32.3 *106 Ωm-1, the second is in steel of a thickness of 9.5 mm with a permeability of 4416 H/m.

A. *MLI mesh size*

The mesh generated by the finite elements program uses linear triangular elements, it is refined on the notches and the part of the rail close to them is more and more wide while moving away from these and very broad with the external border as shown in Figure 2, the mesh consists of 43885 triangular elements and 87360 nodes.

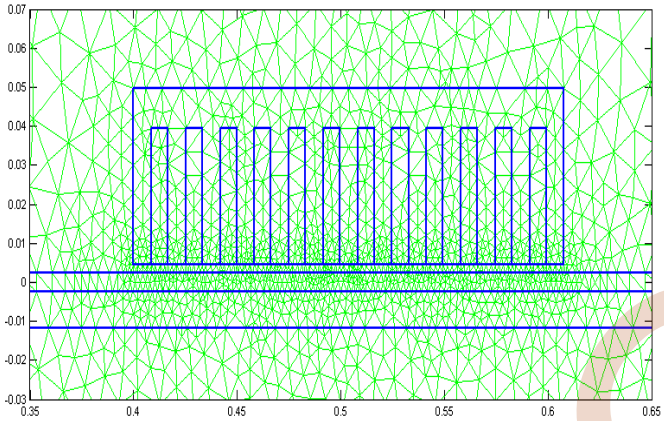

Figure 2. Linear induction motor two-dimensional mesh (12 notches)

B. *Magnetic potential vector and its derived quantities calculation*

Figure 3 represents the magnetic field vectors derived from the calculated magnetic potential vector A (Eq.14) at each node of the field of study space. We notice that the magnetic circuit allowed channeling the field liners, and the 4 motor poles are well defined by the direction of the vectors orientation.

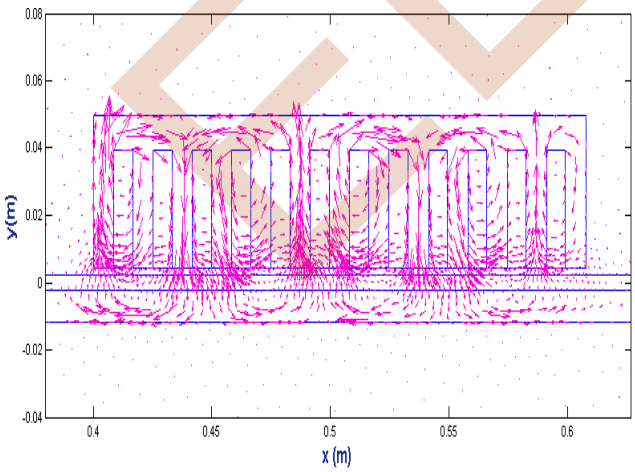

Figure 3. Distribution of magnetic induction field

The equipotential lines in Figure 4 show a satisfactory agreement between the two equipotential maps drawn on a longitudinal section of the studied linear motor, powered by current Js=7 A.

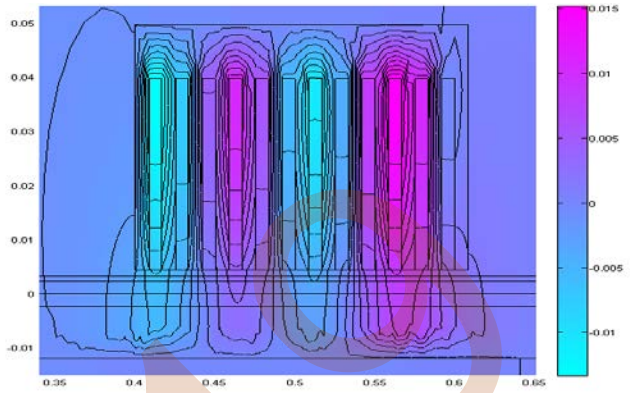

Figure 4. Equipotential lines in a longitudinal section of a linear motor

C. *Effect of physical and geometric parameters on the thrust force*

We will study the influence on the thrust force of some parameters such as the presence of the steel back plate the rail electrical conductivity and the plate thickness. To see the return magnetic circuit influence, we calculated the thrust force as a function of the displacement speed with and without return steel in order to qualify the difference.

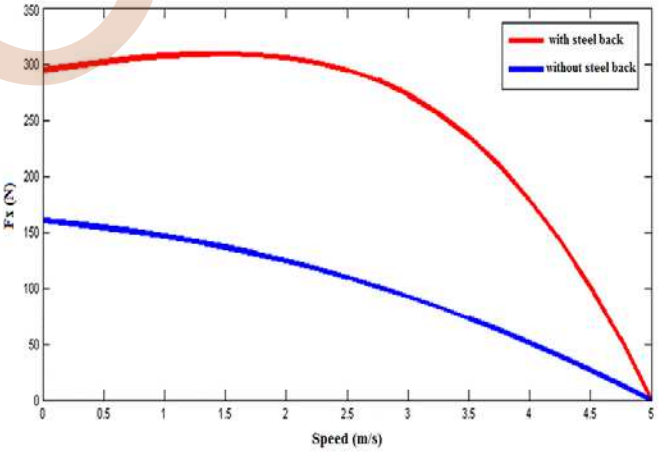

Figure 5. Thrust force as a function of the different conductivity values of the conductive plate

Figure 5 shows a considerable increase in the thrust force in the presence of the ferromagnetic return plate, because this one channels the field, which passes through the conductive plate. The electrical conductivity of the armature conductive plate influences the magnetic thrust force. The result of the variations of the thrust force as a function of different values of the electrical conductivity with a displacement speed of 1.5 m / s is shown in figure 6.

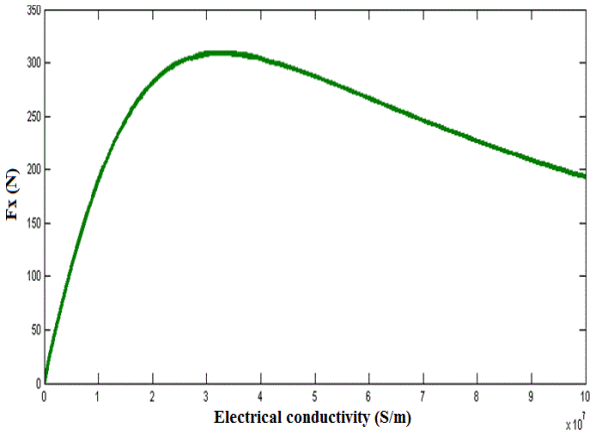

Figure 6. Thrust force as a function of the different conductivity values of the conductive plate

The thrust force increases to a maximum value of 300 N corresponding to electrical conductivity of $3*10^7$ s/m and then decreases.

The aluminum conductivity of approximately 30ms/m seems to be the most appropriate in this case for the plate to generate maximum thrust force.

The thickness of the conductive plate of the armature also influences the magnetic force. By varying the thickness of the armature from 0.1 mm to 10 mm, keeping the other parameters constant at a speed of 1.5 m/s, the value of the force generated is calculated for each thickness. We obtained the result shown in Figure 7.

Figure 7.Thrust force value acording of the plate thicknesses

The thrust force increases with the thickness of the plate to reach the maximum value of 380 N for 2 mm thickness and then it decreases to reach 50% of the maximum value at 10 mm thickness.

Figure 8 shows the influence of the magnetic permeability of the motor's magnetic circuit on the thrust force at a speed of 1.5 m/s, the force increases gradually to reach the value of 310 N and stabilizes at this value. The relative magnetic permeability is used to channel the magnetic field lines and the force is evaluated only in the conductive plate.

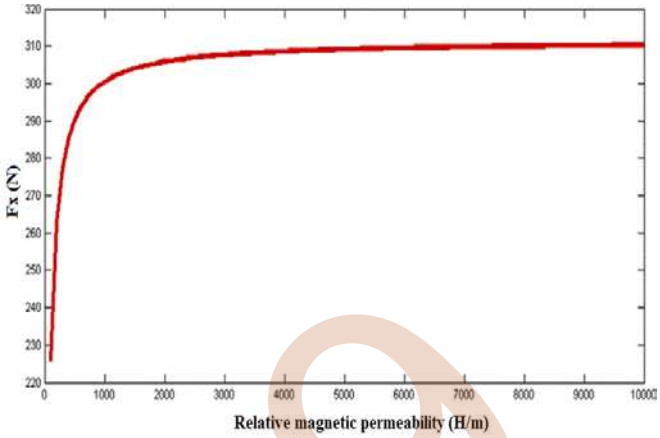

Figure 8. Thrust force as a function of the relative magnetic permeability of the magnetic circuit

The influence of the armature thickness and conductivity besides the steel back plate presence on the electromagnetic force generated by the motor shows that for each parameter, a maximum value of the thrust force. For the choice of these, an optimal calculation is necessary. For the permeability of the magnetic circuit, the results show that it must be close to 180 H/ m, the values above 180 H/ m allow the machine to saturate.

VI. CONCLUSION

After validating the MATLAB code calculation, this work is mainly devoted to the evaluation of the force generated by the linear induction motor as well as to the study of the influence of several geometric and physical parameters (the thickness, the conductivity of the armature, the steel return plate and the relativity magnetic permeability).This study allows us a better choice of the parameters for an efficient force optimization.

A prototyping software for the design of a linear motor can be realized based on this program allowing a simulation of this type of machines by the industrial machine manufacturer in order to gain on the of realizations cost, machines performances and the accuracy.

REFERENCES

[1] ZARE-BAZGHALEH, Amir, FALLAH-CHULABI, Esmaeil, et SHAHALAMI, Seyed Hamid. Force calculation with complete modeling of end-effect in single-sided linear induction motors. In : 2016 7th Power Electronics and Drive Systems Technologies Conference (PEDSTC). IEEE, 2016. p. 19-23.

[2] ISFAHANI, A. Hassanpour, EBRAHIMI, B. M., et LESANI, H. Design optimization of a low-speed single-sided linear induction motor for improved efficiency and power factor. IEEE transactions on magnetics, 2008, vol. 44, no 2, p. 266-272.

[3] J.GONG. Pascal BROCHET « Modélisation et Conception Optimale d'un Moteur Linéaire à Induction Pour Système de Traction Ferroviaire », Lille, France, tel-00663812, version 1 - 27 Jan 2012

[4] GONG, Jinlin, GILLON, Frédéric, et BROCHET, Pascal. Magnetic and thermal 3D finite element model of a linear induction motor. In : 2010 IEEE Vehicle Power and Propulsion Conference. IEEE, 2010. p. 1-6.

[5] GONG, J., GILLON, F., et ZHONG, H. Optimal Design of a Linear Induction Motor for Traction Application. In : Proceedings of the 5th

International Conference on Electrical Engineering and Automatic Control. Springer, Berlin, Heidelberg, 2016. p. 251-258.

[6] LEE, Sung Gu, LEE, Hyung-Woo, HAM, Sang-Hwan, et al. Influence of the construction of secondary reaction plate on the transverse edge effect in linear induction motor. IEEE Transactions on Magnetics, 2009, vol. 45, no 6, p. 2815-2818

[7] QASEER, Layth et MARZOUK, Razzak. Hybrid finite-element–boundary element analysis of a single-sided sheet rotor linear induction motor. IEEE Transactions on Energy Conversion, 2014, vol. 29, no 1, p. 188-195..

[8] TAKORABET, Noureddine. Computation of force density inside the channel of an electromagnetic pump by Hermite projection. IEEE Transactions on magnetics, 2006, vol. 42, no 3, p. 430-433.

[9] RAVANJI, Mohammad Hasan et NASIRI-GHEIDARI, Zahra. Design optimization of a ladder secondary single-sided linear induction motor for improved performance. IEEE Transactions on Energy Conversion, 2015, vol. 30, no 4, p. 1595-1603..

[10] C. M. Neto, G. M. Jacinto, and C. B. Cabrita, "Optimised design aided by computer of single-sided, three-phase, linear induction actuators," in MELECON '98. 9th Mediterranean Electrotechnical Conf. Proc., Tel-Aviv, Israel, 1998, vol. 2, pp. 1157–1160.

[11] LEE, Sung Gu, LEE, Hyung-Woo, HAM, Sang-Hwan, et al. Influence of the construction of secondary reaction plate on the transverse edge effect in linear induction motor. IEEE Transactions on Magnetics, 2009, vol. 45, no 6, p. 2815-2818.

[12] LEE, Byung-Jun, KOO, Dae-Hyun, et CHO, Yun-Hyun. Investigation of linear induction motor according to secondary conductor structure. IEEE Transactions on Magnetics, 2009, vol. 45, no 6, p. 2839-2842.

[13] Mokrani, lakhdar. contribution a la cao optimsee des machines electriques, application au moteur lineaire a induction. diss. université de batna 2, 2005.

[14] SMOLYANOV, Ivan A. et SARAPULOV, Fedor N. Influences on performance of the linear induction motor for the mining systems with different parameters of the power source. In : 2018 IEEE Conference of Russian Young Researchers in Electrical and Electronic Engineering (EIConRus). IEEE, 2018. p. 789-792

[15] A.T.BRAHIMI, "Contribution à la Modélisation de la Machine Asynchrone à Cage par Logiciels d'Eléments Finis 2D et 3D", Thèse de Docteur de l'INPG, Grenoble, France, Juin 1992.

[16] G.W. MCLEAN, 'Review of Recent Progress in Linear Motors,' IEE Proceedings, Vol. 135, Pt.B, No.6, pp. 380-421, November 1988.

[17] SMOLYANOV, Ivan, TARCHUTKIN, Nikolay, et GASHEVA, Daria. Influence of Magnetic Field Attenuation on Linear Induction Motor Performance. In : 2019 International Ural Conference on Electrical Power Engineering (UralCon). IEEE, 2019. p. 290-294.

[18] SMOLYANOV, Ivan A. Study of Electrodynamic Levitation Force in a Traction Linear Induction Motor. In : 2019 IEEE Conference of Russian Young Researchers in Electrical and Electronic Engineering (EIConRus). IEEE, 2019. p. 1083-1087.

2D Finite Element Thermal Modeling of Induction Motor under Healthy and Faulty Operations

Mustapha ZAOUIA
LATAGE Laboratory, Mouloud Mammeri University, B.P17
RP, Tizi-Ouzou, 15000, Algeria
zbmust@yahoo.fr

Arezki DICHE
Department of Electrotechnics, Mouloud Mammeri University, Tizi-Ouzou 15000, Algeria.
ardiche@yahoo.fr

Meziane Hamel
Faculty of Engineering Science, M'Hamed Bougara University, Boumerdes 35000, Algeria.
h_meziane@hotmail.com

***Abstract*— The aim of this paper is to present a 2D finite element thermal modeling of Three-phase squirrel cage induction motor taken into account faults conditions. The model is based on the resolution of the stationary electromagnetic equation, in term of magnetic vector magnetic (MVP) coupled to the thermal one using finite elements method (FEM). The coupled electromagnetic phenomenon and the thermal one is assured by the power density. The considered faults are principally the fault due to the open-circuit and the fault due to the broken rotor bars. We will study the influence of the different considered faults on the magnetic flux density and the temperature in several regions of the motor.**

I. INTRODUCTION

Due to their robustness, induction motors have known an accelerated growth in the last decades. Indeed, they are frequently used in industrial domain and also in domestic application, particularly the squirrel cage induction motors. However, they can be exposed to hostile environment or subject to manufacturing defects leading to failures which can generate stops and, as a consequence, high economic losses. To avoid this, the industrial maintenance systems almost integrate on-line condition monitoring of induction motors.

The faults may be internal such as short circuits of motor leads, inter-turn short circuits, ground faults, bearing and gearbox failures, broken rotor bar and cracked rotor end-rings, or external like phase failure, asymmetry of main supply and mechanical overload.

Recent years have seen many works in this area devoted to the fault diagnosis in an early stage in order to prevent such disagreements. To build such systems, researchers have exploited different physical signals such vibrations, stator current, thermal images, acoustic signals, rotor currents, etc. Various models-based diagnostic systems exploiting different methods such as finite element method [1], analytical methods or magnetic coupled circuits method [2], have been established. The most accurate motor model is based on finite element method since it can take into account the actual geometry and the material non-linearity.

In the present paper, a 2D finite element model exploiting the temperature repartition is introduced in order to detect the faulty operating in two cases: stator phase open-circuit and broken rotor bars.

II. MAGNETO-THERMAL MODELISATION

A. Electromagnetic problem formulation

The governing magnetic field equation in terms of magnetic vector potential is given as follows in the 2D cylindrical coordinates:

$$\frac{\partial}{\partial x}\left(\upsilon\frac{\partial A}{\partial x}\right)+\frac{\partial}{\partial y}\left(\upsilon\frac{\partial A}{\partial y}\right)-\sigma\, j\omega A=-J_s \tag{1}$$

$$\vec{J}_s=\left(kf.\frac{N_c}{S_c}I\right)\cdot\vec{n} \tag{2}$$

Where υ is the magnetic reluctivity of the material and A the magnetic vector potential. J_s is the exciting current density, N_c and S_c are respectively the number of coil turns and the cross-sectional area of the coil, $\vec{n}$ is the unit vector along the direction of the exciting current. K_f is the volume occupation space coefficient and ω is the pulsation.

The currents feeding of three phases current are given by the following system:

$$\begin{cases} J_{s1} = J_{s\,max}\ \cos\omega t \\ J_{s2} = J_{s\,max}\ \cos\omega t - \dfrac{2\pi}{3} \\ J_{s3} = J_{s\,max}\ \cos\omega t + \dfrac{2\pi}{3} \end{cases} \quad (3)$$

Using the Galerkin finite element method, the expression (1) is written in space as follow:

$$\iint_{\Omega} \upsilon\left(\frac{\partial\alpha_i}{\partial x}\frac{\partial A}{\partial x}+\frac{\partial\alpha_i}{\partial y}\frac{\partial A}{\partial y}\right)dx\,dy+\iint_{\Omega}(\alpha_i\sigma\, j\omega A)\,dx\,dy - \int_{\Gamma}\left[\frac{\alpha_i}{r}\left(\frac{\partial A}{\partial n}\right)\right]d\Gamma = \iint_{\Omega_S}(\alpha_i J_s)dx\,dy \quad (4)$$

Γ is the boundary surrounding the meshed regions area Ω, and Ω_s is conductors region. α_i represents the weighted function.

The introduction of the approximation functions of the magnetic vector potential (4) for each node, leads to the following algebraic equation system:

$$([M]+ j\omega[K])\{A\}=\{F\} \quad (5)$$

Where M is the stiffness matrix, K is the mass matrix and F represents the source term.

B. Thermal problem formulation

For thermal equation in the considered regions, considering Fourier's Law by applying the first thermodynamics principal in elementary volume (Ω), the equation of the conduction may be given in its general shape:

$$\rho_m C_p \frac{\partial T}{\partial t} = div(\lambda\, grad(T)) + q(T) \quad (6)$$

$$\left[-\lambda\frac{\partial T}{\partial n}\right]_{\Gamma h} = h_c[T - T_a] \quad (7)$$

Where ρ_m is the mass density, C_p is the specific heat, λ the thermal conductivity, q is the power density, T is the searched temperature located in (x, y) at time t and the ambient temperature is T_a.

In the same way of the electromagnetic modelling in axisymmetric case, the equation (6) is given, in cylindrical coordinates as follow:

$$\frac{\partial}{\partial x}\left(\lambda\frac{\partial T}{\partial x}\right)+\frac{\partial}{\partial x}\left(\lambda\frac{\partial T}{\partial x}\right)-\rho_m C_p\frac{\partial T}{\partial t}=-q(T) \quad (8)$$

Using the Galerkin's procedure, and after shape function projection at each element nodes of the finite element mesh, the resulting discrete form of expressions (7) and (8) is obtained as follow:

$$\sum_{j=1}^{nn}\iint_{\Omega}\lambda\left(\frac{\partial\alpha_i}{\partial x}\frac{\partial\alpha_j}{\partial x}+\frac{\partial\alpha_i}{\partial y}\frac{\partial\alpha_j}{\partial y}\right)r\,dr\,dz\,\{T_i\}+\sum_{j=1}^{nn}\int_{\Gamma h}h_c(\alpha_i\alpha_j)r\,d\Gamma_h\,\{T_i\} + \sum_{j=1}^{nn}\iint_{\Omega}\rho_m C_p\alpha_i\frac{\partial(\alpha_j T_i)}{\partial t}rdrdz-\sum_{j=1}^{nn}\int_{\Gamma h}h_c(\alpha_i\alpha_j)rd\Gamma_h\{T_i\} = \sum_{j=1}^{nn}\iint_{\Omega}q(T)\alpha_i\,rdrdz \quad (9)$$

The time derivative is replaced by a finite difference scheme.

The power density generated by the Joule's effect in the studied regions is given as follow [3]:

$$q(T)=\frac{J^2}{\sigma_{eq}(T)} \quad (10)$$

σ_{eq} is given by $\sigma_{eq}=\sigma.k_f$.

Finally, one gets:

$$\sigma_{eq}(T)=\frac{\sigma_{eq\,0}}{1+\alpha(T-T_a)} \quad (11)$$

Where $\sigma_{eq\,0}$ is the material equivalent electrical conductivity at ambient temperature. α is the temperature coefficient of this material.

The winding of the machine is a heterogeneous element of complex structure: it consists of enameled copper wires impregnated with resin that dissipate heat by the Joule effect. This components requires careful modeling since it is the hottest point of the machine, thus its thermal behavior must be reproduced as precisely as possible.

Like most authors, we have then compared the winding to an equivalent homogeneous medium with the average thermal conductivity of $\lambda_{eq,copper}$ [4], and we focus on determining the values of the equivalent thermal conductivity and heat capacity. Several studies provide data on the equivalent conductivity of the winding. These data come from experimentation [5], from numerical integration carried out on an element area section of a slot [6], from an analytical approach [7], or from finite element modeling of an elementary pattern [8].

The slot with copper and insulation is transformed to one equivalent homogeneous medium with the average thermal conductivity of $\lambda_{eq,copper}$. The steps of the transformation are illustrated in Fig.3. which gives the actual slot with wires and the equivalent slot with the equivalent wire presenting equivalent electrical conductivity and an equivalent thermal conductivity.

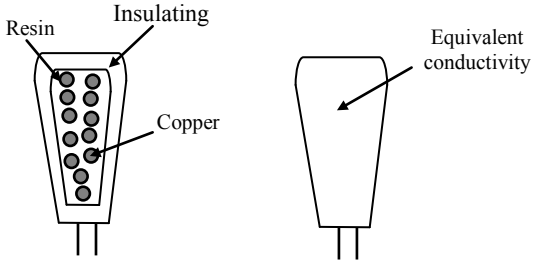

Fig.1. Transformation of the stator slot for average thermal conductivity calculations, (a) Original slot area, (b) Equivalent conductivity

$$\lambda_{eq,copper} = \lambda_r \frac{\left(1-\sqrt{K_f}\right)\cdot\lambda_{copper} + \sqrt{K_f}\cdot\lambda_{copper}}{\lambda_r + \left(1-\sqrt{K_f}\right)\cdot\sqrt{K_f}\cdot\lambda_{copper}} \quad (9)$$

$$\lambda_{eq,copper} = \frac{\lambda_r}{1-\sqrt{K_f}} \quad (10)$$

By taking λ_r equal to 0.2 [$Wm^{-1}c^{-1}$], the thermal conductivity of slot region is calculated as:

$$\lambda_{eq,copper} = \frac{\lambda_r}{1-\sqrt{K_f}} = \frac{0.2}{1-\sqrt{0.45}} = 0.6\ [Wm^{-1}c^{-1}] \quad (11)$$

The equivalent specific heat when considering two materials A and B which present respectively k_f and $(1-k_f)$ fractional ponderation volume is given by [3]:

$$\rho_m C_p eq = k_f\left(\rho_{mA} C_{pA}\right) + \left(1-k_f\right)\left(\rho_{mB} C_{pB}\right) \quad (12)$$

Where the volumic mass density and the heat capacity of the materials A and B are respectively ρ_{mA}, ρ_{mB} and C_{pA}, C_{pB}.

III. RESULTS IN HEALTH AND FAULT OPERATING

The geometrical of the studied induction motor is shows by Fig.2. It depicts also the considered nodes where one withdraws temperatures in order to see the influence of the defect on its evolution. The geometrical and electrical characteristics are given by the Table.I. While Table II and Table III give respectively the electrical and thermal characteristics of the considered motor.

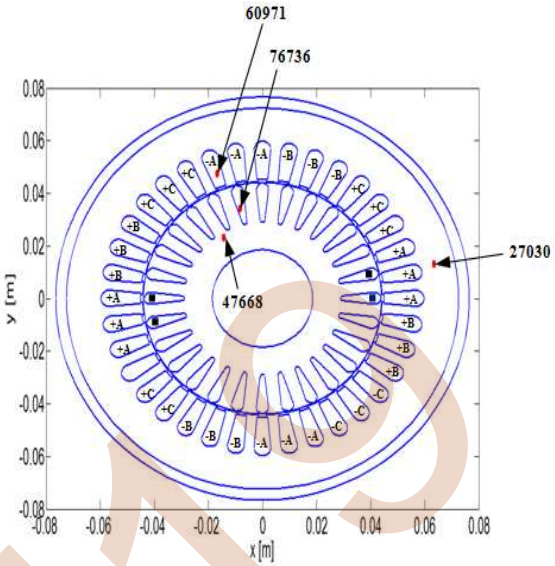

C: first fault : Phase C open
Second fault: Four bars broken
Nodes temperatures evaluation

Fig.2. Geometrical and studied domain of induction motor and different considered faults in the induction motor

TABLE.I. GEOMETRICAL CHARACTERISTIQUE OF INDUCTION MOTOR

Components	values
stator outside diameter	145mm
Stator internal diameter	88.5mm
Number of stator slot	36
Rotor outside diameter	88mm
Rotor internal diameter	57.75
Rotor internal diameter	37
Number of rotor slot	28

TABLE.II. ELECTRICAL CHARACTERISTICS OF INDUCTION MOTOR

Components	Values
Electrical power	2.2Kw
Number of phase	3
Frequency	50Hz
Voltage	380 V
Current	5.2 A
Rotating velocity	1500 tr/mn

TABLE.III. THERMAL CHARACTERISTICS OF INDUCTION MOTOR

Components	Thermal Conductivity (W/m .°C)	Heat Capacity (J/kg. K)	Mass density (Kg/m^3)
Stator	71	444	7860
Moving armature (Rotor)	51	460	7750
Copper	386	383	8954
Conductors insulator	0.2	1700	1350
Air	0.025	1600	1.2
Aluminum	204	896	2707

A. Healthy operating

Fig. 3 shows the flux lines distribution for healthy operating of induction motor. The lines form four poles. Fig.4 and Fig.5 give the magnetic vector potential, and the normal flux density waveforms in the air gap.

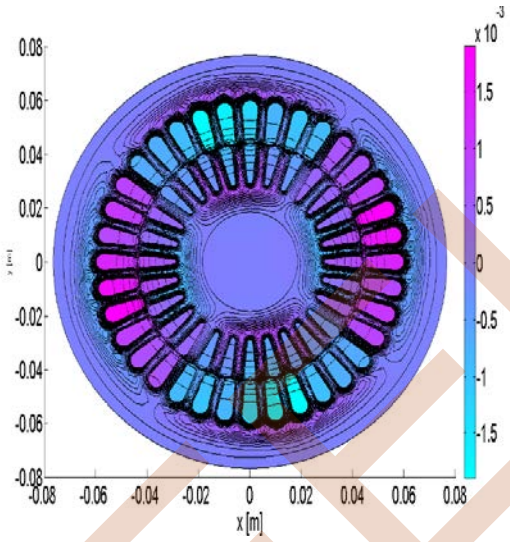

Fig.3. Flux lines distribution in induction motor in healthy operating

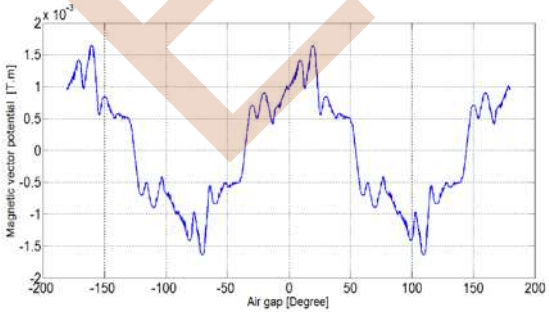

Fig.4. Wave form of air gap magnetic potential vector in healthy operating

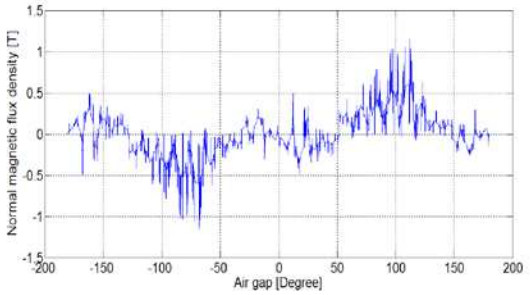

Fig.5. wave form of air gap magnetic flux density in healthy operating

Fig.6 depicts the distribution of the temperature in the induction motor for the case of healthy operation. Fig.7 gives the temperatures versus time at node (60971), node (76736), node (27030) and node (47668) representing different regions of the motor as shows in Fig.1.

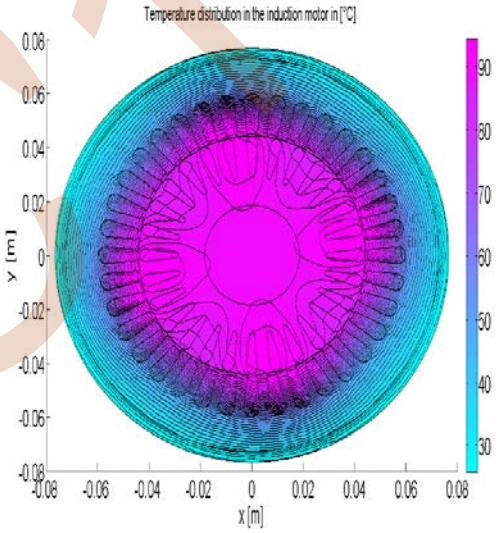

Fig.6. Isotherms in induction motor in healthy operating

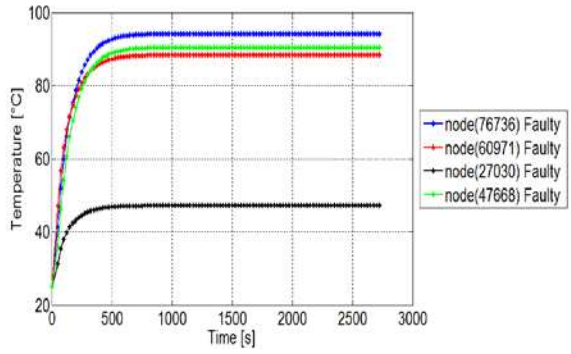

Fig.7. Temperature versus time computed at nodes representing different regions of the induction motor in healthy operating

B. *Fault operating with phase C open*

In this section we present the results in the case of the fault operating of the induction motor. The first considered fault is only open circuit faults. In our work, the phase C is open.

When the phase C is open, several simulations have been carried out to evaluate the effect of this fault type on the potential magnetic potential, flux magnetic density and the temperature.
Fig.8 and Fig.9 show respectively the superposition of wave form of air gap magnetic potential vector in and the wave form of air gap magnetic flux density in faulty (Phase C open) and healthy operating.

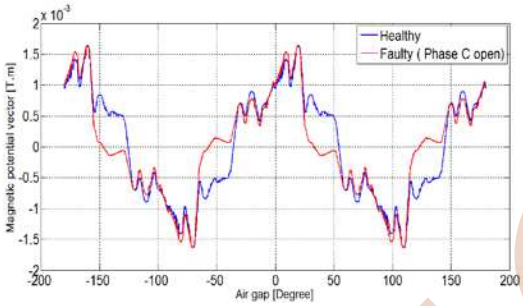

Fig.8. Wave form of air gap magnetic potential vector in faulty (Phase C open) and healthy operating

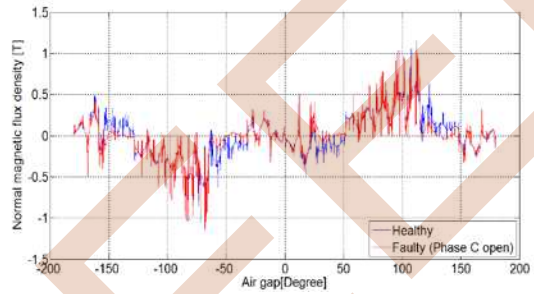

Fig.9. Wave form of air gap magnetic flux density in faulty (Phase C open) and healthy operating.

Fig.10 gives the superposition of the temperature versus time at node (60971), node (76736), node (27030) and node (47668) in healthy and faulty operating when the phase C is open. As seen from the Fig.10, we notice that the temperatures in case of healthy operating are more important compared to those of faulty operating.

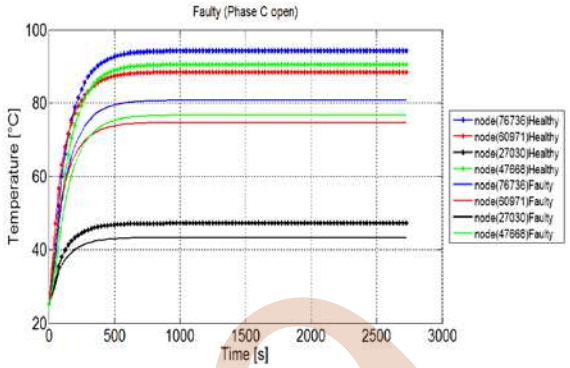

Fig.10. Temperature versus time computed at nodes representing different regions of the motor faulty (Phase C open) and healthy operating

C. *Fault operating with four broken rotor bars*

The second considered faults is only broken rotor bars. We consider in this case of health, four broken rotor bars as shown in Fig.1. The Fig.11 and Fig.12 show respectively the superposition of wave form of air gap magnetic potential vector and the wave form of air gap magnetic flux density in faulty operating with four broken rotor bars and healthy operating.

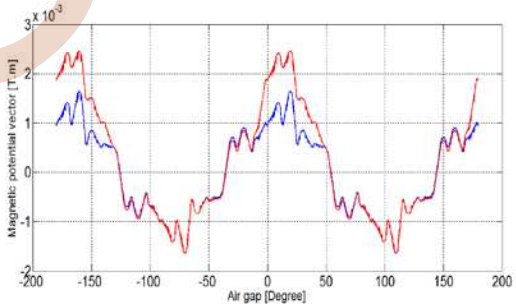

Fig.11. Wave form of air gap magnetic potential vector in faulty (Four broken rotor bars) and healthy operating

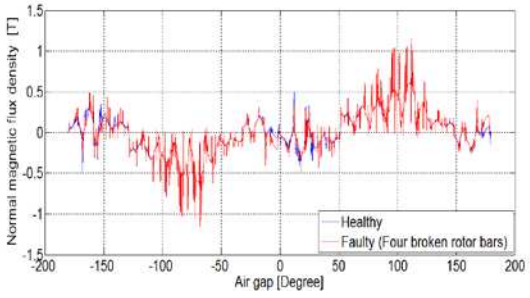

Fig.12. Wave form of air gap magnetic flux density in faulty (Four broken rotor bars) and healthy operating.

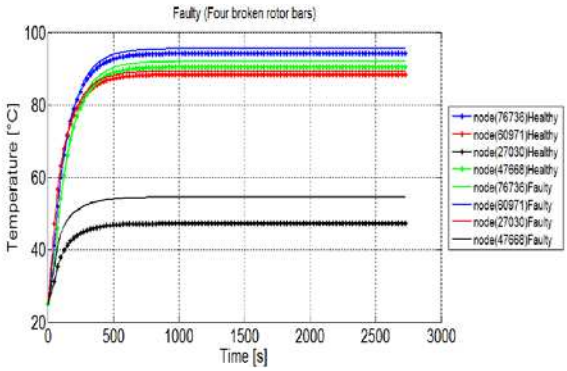

Fig.13. Temperature versus time at nodes representing different regions in case of four broken rotor bars and healthy operating.

TABLE.IV. TEMPERATURES IN HEALTHY AND FAULTY OPERATING

Node	Healthy	Faulty(Phase C open)	Faulty (four broken rotor bars)
76736	94.205 °C	80.683 °C	95.586 °C
60971	88.397 °C	74.727 °C	89.402 °C
27030	47.219 °C	43.238 °C	54.485 °C
47668	90.508 °C	76.585 °C	92.029 °C

One can see from the results above that in case of broken rotor bars, a temperature increasing is registered. Table IV gives a recapitulation of the temperatures at steady state in the different considered points. The temperature decreases in case of stator phase open circuit, however in case of broken rotor bar, the last increase. This shows that temperature may constitute an indication of the defect presence in the motor. Furthermore, the flux density waveform presents perturbations in the defect zone.

IV. CONCLUSION

In the present work, a 2D finite element thermal modeling of three-phase squirrel cage induction motor under healthy and faulty operating is presented. In this goal, a weak coupled electromagnetic-thermal model was solved. The coupling parameter between the two models is the Joule power density.

Two cases of faulty operating were investigated: they consist first on a stator phase open circuit, namely the phase C, and a broken rotor bars (4 bars). Temperature was withdrawn in several points representing the different regions of the studied motor. From the obtained results, one can affirm that temperature repartition may give precious information about the presence of defects in the motor.

REFERENCES

[1] Panagiotou, P. ; Arvanitakis, I. ; Lophitis ,N.; Antonino-Daviu, J.A.; Gyftakis, K.N., FEM approach for diagnosis of induction machines' non-adjacent broken rotor bars by short-time Fourier transform spectrogram, 9th International Conference on Power Electronics, Machines and Drives (PEMD) 2018, pp.4566-4570.

[2] Aroui, T. ; Koubaa, Y. ; Toumi, A. ,Magnetic Coupled Circuit Modeling of induction Machines oriented to diagnosis, Leonardo Journal of Sciences, 2018, pp.103-121.

[3] E. Chauveau, Contribution au Calcul Electromagnétique et Thermique des Machines Electriques Application à l'Etude de l'Influence des Harmoniques sur l'Echauffement des Moteurs Asynchrones, PHD Thesis, Nantes, France 2001.

[4] Kremers, M.F.J. ; Motoasca, T.E. ; Paulides, J.J.H. ,Transient thermal analysis of flux switching PM machines, 8th International Conference and Exhibition on Ecological Vehicles and Renewable Energies (EVER) 2013, pp.1-7.

[5] General Electric Company, Heat transfer and fluid flow, Data book, Vol.1 section 502. 2, New York, USA: Genrum, 1984.

[6] M. Broussely, Réduction de modèles thermiques par la théorie des réseaux, application à la surveillance d'une machine asynchrone par couplage d'un modèle thermique réduit avec un schéma équivalent électrique, PHD Thesis, University of Poitiers (France), december 2000.

[7] G. S. Springer and S. W. Tsai,Thermal *Conductivity of* Unidirectional Materials, Journal of Composte Materials, Vol. 1, No. 2, 1967, pp. 166-173.

[8] D.T. Lussier, S.J. Ormiston, R.M. Marko, Theoretical determination of anisotropic effective thermal conductivity in transformer windings, International Communications in Heat and Mass Transfer, Vol.30, N°3, April 2003, pp.311-322.

Prediction of the Flashover Voltage of F160D-146DC High Voltage Insulator by Fuzzy Logic.

H. Bourenane
Department of Electrical Engineering
Ibn Khldoun University
Electrotechnical Research Laboratory
Tiaret, Algeria
Haiat.bourenane @univ-tiaret.dz

A.Mekhaldi,
Department of Electrical Engineering
National Polytechnic School
Electrotechnical Research Laboratory
Algiers
Algeriaabdelouahab.mekhaldi@g.enp.edu.dz

M. Teguar
Department of Electrical Engineering
National Polytechnic School
Research Laboratory Electrical
Algiers Algeria
madjid.teguar@g.enp.edu.dz

***Abstract*—The objective of our study is to predict the flashover voltage of the polluted High Voltage F160D-146DC insulator subjected to the influence of applied voltage amplitude, clean bandwidth and conductivity using an artificial intelligence technique based on fuzzy logic. Experiments were conducted on this isolator to collect a database used in the implementation of the Fuzzy logic concept.**

I. INTRODUCTION

The transport of electrical energy requires, for technical and economic reasons, the use of high voltages (HV and THT lines). This requires the design and production of products, devices and systems capable of generating and supporting intense electric fields: their dimensioning must therefore be scrupulously studied.

The development of high voltage lines, the use of which reduces energy losses and transportation costs. But in return, the high voltage lines are subject to damage that can put them out of service; among these damages, we can mention the flashover chains insulators. In the vicinity of industrial, agricultural and coastal regions, pollution is the main cause of the circumvention phenomenon. To examine this phenomenon, many theoretical [1-5] and experimental [6-8] works have been developed.

In this study, we are interested in the prediction of F160D-146DC insulator flashover voltage that is non-uniformly polluted under AC voltage using fuzzy logic.

II. EXPERIMENTAL SETUP

The experimental setup is described in Fig.1.

The test object is the Plan model simulates the F160D-146DC insulator that is frequently used by the Algerian SONALGAZ gas and electricity company for 400 kV high-voltage lines between Bechar and Naama.

The model consists of a glass plate 50cmX50cm and 5 mm thick on which are laid two electrodes one of earth and the ~~other of~~ high voltage, these electrodes are made with aluminum foil. the dimensions of the electrodes and the inter-electrode distance L (37.5 cm) are kept constant during all the tests.

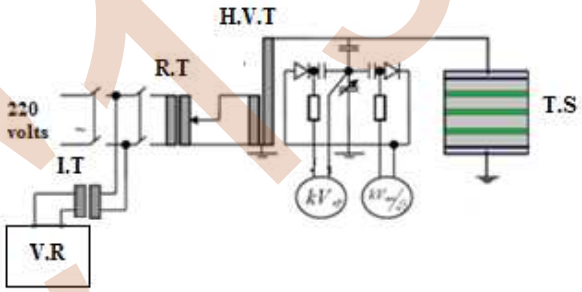

H.V.T: High voltage transformer; R.T: Regulating transformer
I.T: insulating transformer; V.R; Voltage Regulator
T.S: Test sample

Fig.1. Experimental setup.

The plane model is the J.Danis model [9], which takes into account the discontinuity of the pollution layer and its distribution along its creepage (Fig 2).

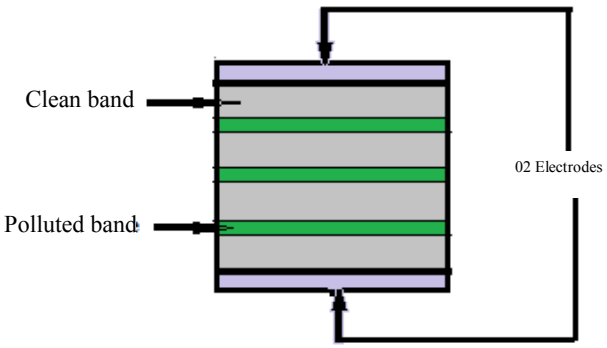

Fig.2. Object of test

Two configurations were considered:

- the first configuration contains three clean bands each of which is 1 cm and then 3 cm wide and finally 5 cm, the other strips are sprayed with a pollutant solution of 1 mS / cm based on sodium chloride (NaCl) and distilled water.
- the second configuration contains three clean bands each of which is 1 cm wide. The pollution of the other bands is carried out by the raised sand of the ground of Ain Safra close to the zone where our model of real insulator "F 160 D_146 DC" is installed, the sand of the ground is uniformly distributed on the plane model with a 10g amount in each polluted strip then spraying is performed with distilled water. The same procedure is repeated with the sand dunes coming from the same region then the sand of the dunes is replaced by the sea sand of Bordj Elkifane (Algiers).

After each test, the test object is cleaned with tap water and then dried with paper towels to remove the maximum amount of impurities deposited; a second cleaning is done using a cotton soaked in surgical alcohol to ensure almost total cleanliness.

III. APPLICATION OF FUZZY LOGIC

Fuzzy logic is one of the techniques of artificial intelligences that are used in general where mathematical modeling is difficult or where experimental studies are complex and expensive [10]. The fuzzy inference system (SIF) used is the Mamdani system because it is intuitive and well suited to human participation its architecture is given in fig. 3

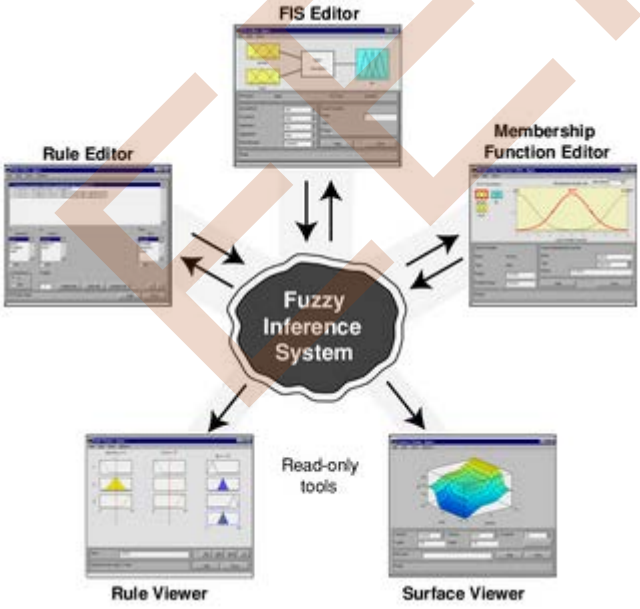

Fig.3 Mamdani Fuzzy Inference System [11].

A. *Linguistic variables and input and output intervals*

- *The first configuration*

The variables of the width of the bands (lbp) and the applied voltage (Uapp) are used as inputs of our SIF. The output is the percentage of flashover.

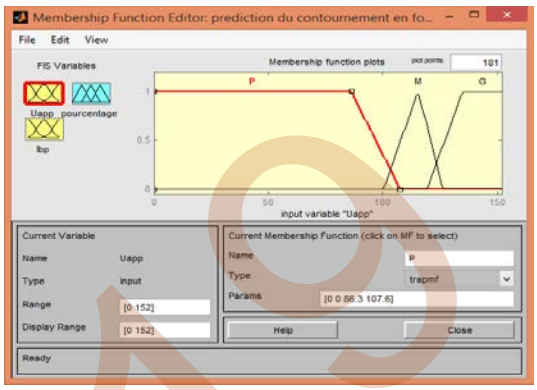

Membership function of the applied voltage (Uapp).

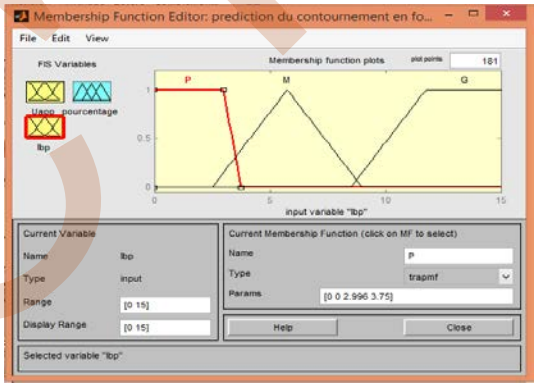

Membership functions of the width of the clean bands (lbp).

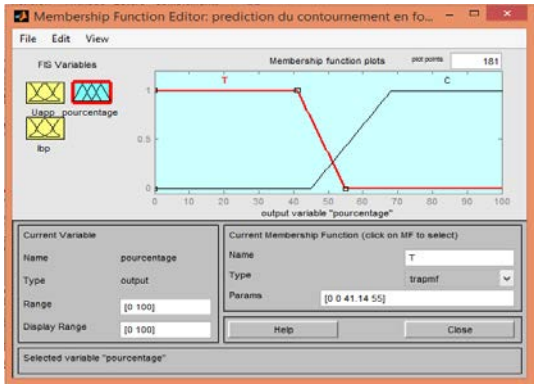

Percentage membership function of flashover.

Fig. 4. Fuzzification of the inputs and defuzzification of the 1st configuration output.

The trapezoidal and triangular membership functions of the inputs and the trapezoidal membership functions of the output are shown in fig.4.

Laboratory tests help us to provide fuzzy intervals for each input and output.

- *The second configuration*

The conductivity variables σ of the pollution and the applied voltage are used as SIF inputs.

The membership functions of the inputs and the output are defined by fig. 5.

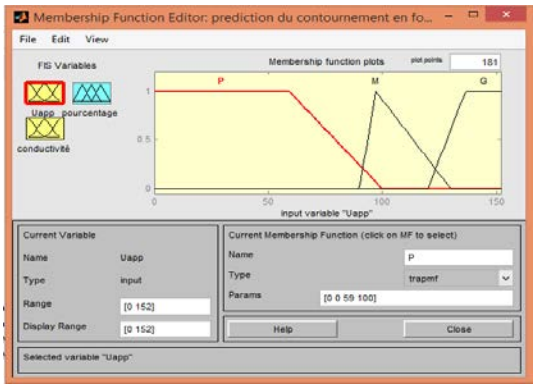

Membership function of the applied voltage (Uapp).

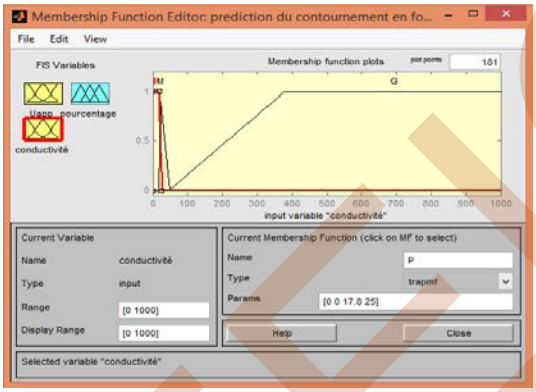

Membership function of the conductivity (σ).

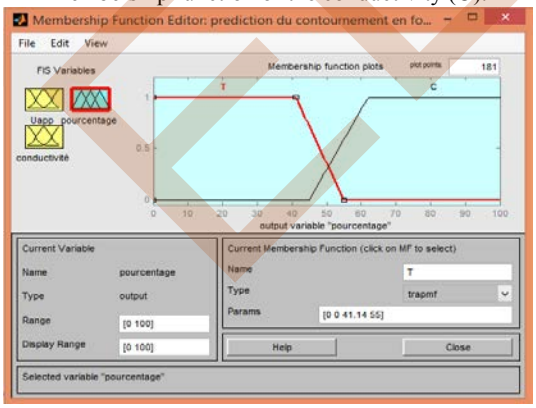

Percentage membership function of flashover.

Fig. 5. Fuzzification of the inputs and defuzzification of the 2nd configuration output

B. *Fuzzy Rules Foundation (Language Rules)*

Fuzzy inference system rules are based on human expertise. The linguistic variables and fuzzy rules proposed in our work are given in Table 1 and 2.

The abbreviations of the tables are defined as follows: S is small, A is average, G is great, NF is no flashover and F is flashover..

Fuzzy rules can be expressed in the following form:

If lbp is A and Uapp is S then output is NF or
If lbp is G and Uapp is A then output is F or
If σ is G and Uapp is A then output is F or
If.....

TABLE 1. Fuzzy rules of the first configuration.

Uapp (kV)	**lbp(cm)**		
	S	***A***	***G***
S	NF	NF	NF
A	F	NF	F
G	F	F	F

Table 2. Fuzzy rules of the second configuration.

Uapp (kV)	**σ(μS/cm)**		
	S	***A***	***G***
S	NF	NF	NF
A	F	NF	F
G	F	F	F

C. *Results Obtained*

After implementing our SIF using the "fuzzylogictoolbox" graphical interface under MATLAB, we predicted the F160D-146DC insulator flashover for different values of clean bandwidth (lbp), conductivity and applied voltage.

Figure 6 shows an example of our SIF application for the width of the clean bands lbp = 5cm x 3 and an applied voltage of Uapp = 112.7 kV for a percentage exit after defuzzification of 77.2% which belongs to the flashover interval obvious isolator is: [68.12-100].

According to Table 3, the results given by our SIF are in perfect agreement with the practical results. Which means that the fuzzy system is valid for predicting the HV insulator flashover voltage.

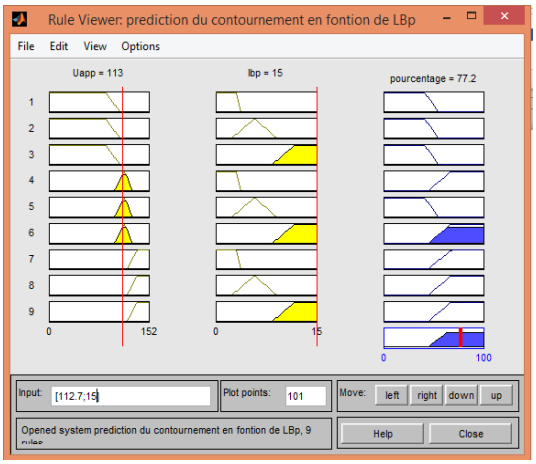

Fig. 6. Editor of fuzzy rules.

Table 7. Comparison between the experimental results and those found by SIF.

	Uapp (kV)	Practical Results	Results by SIF
lbp =1 cmx3	115.33	Flashover	Flashover
lbp=3 cmx3	128	Flashover	Flashover
lbp=5 cm x3	112.66	Flashover	Flashover

IV. CONCLUSION

This work shows that fuzzy logic has great aptitude and efficiency in the flashover prediction of the high voltage insulator studied. The right choice of membership functions, and linguistic variables and input intervals leads to good results.

REFERENCES

[1] E. Asenjo S ,N. Morales O, "Low Frequency Complex Fields in Polluted Insulators", IEEE Transactions on Electrical Insulation, Vol. EI-17 No. 3, pp. 262-268, June 1982

[2] S. Chakravorti, P. K Mukherjee, "Power Frequency and Impulse Field Calculation around HV Insulator with Uniform or Nonuniform Surface Pollution", IEEE Transactions on Electrical Insulation Vol. 2B, No. 1, pp. 43-53, February 1993.

[3] N. Dhahbi-Megriche, "Modélisation Dynamique des Décharges sur les Surfaces d'Isolateurs Pollués sous Différentes Formes de Tension: Elaboration d'un Critère Analytique de Propagation", thèse de Doctorat, L'Ecole Centrale de LYON.1998.

[4] B. M'hamdi, M. Teguar, A. Mekhaldi, "Potentiel and Electrical Field Distribution Distribution on HV Insulators String used in 400 kV Novel Transmission Line in Algeria" , IEEE International Conference on Solid Dielectrics, Bologna, Italy, June 30-July4, 2013.

[5] F. Aouabed, A. Bayadi, A. Rahmani, R. Boudissa, "Finite Element Modelling of Electric Field and Voltage Distribution on a Silicone Insulating Surface Covered With Water Droplets", IEEE Transaction on Dielectrics and Electrical Insulation Vol. 25, No. 2, pp. 413-420, April 2018.

[6] S. Farokhi, M. Farzaneh, I. Fofana, "Experimental Investigation ofthe Process of Arc Propagation over an Ice Surface", IEEE Transactions on Dielectrics and Electrical Insulation Vol. 17, No. 2, pp. 458-464, April 2010.

[7] B.Moula, A. Mekhaldi, M Teguar, A. Haddad, "Characterization of Discharges on non-Uniformly Polluted Glass Surfaces Using a Wavelet Transform Approch", IEEE Transactions on Dielectrics and Electrical Insulation Vol. 20, No. 4, pp. 1457-1466, August 2013.

[8] M.Bouhmama, S.Flazi, F.Miloua, Y.Bellebna, A.Tilmatine "Experimental modeling of the flashover of polluted insulator with the presence of ametal plate using rsm technique", Journal of Electrical Engineering Vol.17 N°2, pp. 446-455, 2017.

[9] J. Danis « A stochastic pollution flashover model », International Symposium on High Voltage Engineering, Rapport 46 - 12, Septembre 5 –9, Athènes, Grèce, 1983.

[10] V.T. Kontargyry, A.A. Gialketsi, G.J. Tsekouras, I.F. Gonos, I.A Stathopulos"Design of an artificial neural network for the estimation of the flashover voltage on insulators", Electr. Power Syst. Res. 77, 1532 (2007).

[11] J.S. Roger Jang, N. Gulley, MATLAB Fuzzy Logic Toolbox_User's Guide Fuzzy Logic. Version 1 (Copyright, Math Works, 1984–1997)

Comparative Study Between Input-Output Linearization Control and Vector Control Of an Asynchronous Machine

BENALI Tarek
Laboratoire de Génie Électrique
Faculté de Technologie
Université de Bejaia, ALGERIE
tarekbenali.fett@gmail.com

BEKHOUCHE Lemnouar
Laboratoire de Génie Électrique Département de Génie Électrique
Faculté des Sciences et Technologies, Université de Djelfa, Algérie
blemnouer@gmail.com

SAOU Rachid
Laboratoire de Génie Électrique
Département de Génie Électrique
Université de Bejaia, ALGÉRIE
r_saou@yahoo.fr

OUKAOUR Amrane
Laboratoire des Sciences Appliquées de Cherbourg (LUSAC)
Université de Caen Normandie
FRANCE
amrane.oukaour@unicaen.fr

***Abstract*— Advances in power electronics in digital electronics are now making it possible to study variable speed control in low power applications. In parallel with these technological advances, the scientific community has developed different approaches to control the flow and torque of electrical machines in real time. In this paper, we discuss two types of control, vector control and linearization control and their comparison. Both command types will be tested for different modes of operation.**

***Keywords*: MAS, MAS modeling, NL control, input-output linearization control, observers.**

I. INTRODUCTION

The nonlinear control by linearization is another alternative to decouple the control of the asynchronous machine while ensuring a perfect linearization irrespective of the profiles of the trajectories imposed on the system.

The techniques of nonlinear control are based on the theory of differential geometry [12]. Among these techniques, the linearization technique in the sense of the input-state and input-output are the most important [2], [5], [6], [7], [8], [9], [10], [11], [12].

The purpose of this article is the application of the input-output linearization control to the asynchronous motor and shows the advantages of this command developed over that of conventional vector control. This technique generalizes the vector-type commands while ensuring the decoupling and linearization of the input-output relationships of the system. Ease of Use

II. MODELIZATION

In order to establish simple relations between the supply voltages of the motor and its currents, it is necessary to rely on a certain number of hypotheses:

- Perfect symmetry of construction;
- Assimilation of the cage to a short-circuit winding of the same number of phases as the stator winding;
- Sinusoidal distribution, along the air gap, of the magnetic fields of each winding.
- Lack of saturation in the magnetic circuit.

The two most used repositories in the control of the asynchronous machine are [4]:

- Axis reference *(α, β)* fixed with respect to the stator: two-phase system with orthogonal axes ($\theta = 0$)
- Repository rotating axes *(d, q)* rotating at the speed of the stator field: two-phase system with orthogonal axes.

Model of the asynchronous machine

The equations of the stator and rotor voltages and fluxes of the vector model of the machine in a reference frame (d, q) rotating at a speed relative to the stator are:

$$\begin{cases} \vec{u}_s = R_s \vec{i}_s + \dfrac{d\vec{\phi}_s}{dt} + j\omega_s \vec{\phi}_s \\ \vec{u}_r = 0 = R_r \vec{i}_r + \dfrac{d\vec{\phi}_r}{dt} - j\omega_r \vec{\phi}_r \end{cases} \quad (1)$$

$$\begin{cases} \vec{\phi}_s = L_s \vec{i}_s + M \ \vec{i}_r \\ \vec{\phi}_r = L_r \vec{i}_r + M \ \vec{i}_s \end{cases} \quad (2)$$

The vector model of the machine in this repository (d, q) is shown schematically in *FIG. 1*

By projecting the equations of the vector model in this rotating repository, it obtains:

For the tensions:

$$\begin{cases} u_{rd} = 0 = R_r i_{rd} + \dfrac{d\phi_{rd}}{dt} - (\omega_s - \omega)\phi_{rq} \\ u_{rq} = 0 = R_r i_{rq} + \dfrac{d\phi_{rq}}{dt} + (\omega_s - \omega)\phi_{rd} \end{cases} \quad (3)$$

$$\begin{cases} u_{sd} = R_s i_{sd} + \dfrac{d\phi_{sd}}{dt} - \omega_s \phi_{sq} \\ u_{sq} = R_s i_{sq} + \dfrac{d\phi_{sq}}{dt} + \omega_s \phi_{sd} \end{cases} \quad (4)$$

For magnetic flux

$$\begin{cases} \phi_{sd} = L_s i_{sd} + M\ i_{rd} \\ \phi_{sq} = L_s \vec{i}_{sq} + M\ i_{rq} \end{cases} \quad (5)$$

$$\begin{cases} \phi_{rd} = L_r i_{rd} + M\ i_{sd} \\ \phi_{rq} = L_r \vec{i}_{rq} + M\ i_{sq} \end{cases} \quad (6)$$

The equations of the stator and rotor voltages and fluxes of the vector model of the machine in a fixed reference frame linked to the stator are:

$$\begin{cases} \vec{u}_s = R_s \vec{i}_s + \dfrac{d\vec{\phi}_s}{dt} \\ \vec{u}_r = 0 = R_r \vec{i}_r + \dfrac{d\vec{\phi}_r}{dt} - j\omega_r \vec{\phi}_r \end{cases} \quad (7)$$

$$\begin{cases} \vec{\varphi}_s = L_s \vec{i}_s + M\ \vec{i}_r \\ \vec{\varphi}_r = L_r \vec{i}_r + M\ \vec{i}_s \end{cases} \quad (8)$$

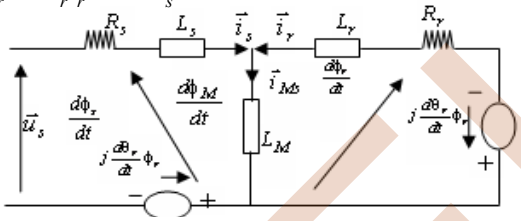

***Figure 1**: Dynamic equivalent schema in a rotating repository*

The vector model of the machine in this reference system is shown schematically in *FIG. 2*

By projecting the equations of the vector model in this rotating repository, it obtains:

For the tensions

$$\begin{cases} u_{s\alpha} = R_s i_{s\alpha} + \dfrac{d\phi_{s\alpha}}{dt} \\ u_{s\beta} = R_s i_{s\beta} + \dfrac{d\phi_{s\beta}}{dt} \end{cases} \quad (9)$$

$$\begin{cases} u_{r\alpha} = 0 = R_r i_{r\alpha} + \dfrac{d\phi_{r\alpha}}{dt} + \omega\phi_{r\beta} \\ u_{r\beta} = 0 = R_r i_{r\beta} + \dfrac{d\phi_{r\beta}}{dt} - \omega\phi_{r\alpha} \end{cases} \quad (10)$$

For magnetic flux

$$\begin{cases} \phi_{s\alpha} = L_s i_{s\alpha} + M\ i_{r\alpha} \\ \phi_{s\beta} = L_s i_{s\beta} + M\ i_{r\beta} \end{cases} \quad (11)$$

$$\begin{cases} \phi_{r\alpha} = L_r i_{r\alpha} + M\ i_{s\alpha} \\ \phi_{r\beta} = L_r i_{r\beta} + M\ i_{s\beta} \end{cases} \quad (12)$$

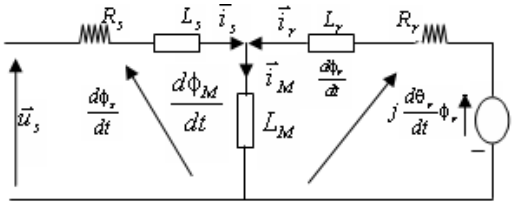

***Figure 2:** Dynamic equivalent schema in a fixed repository*

III. VECTOR COMMAND

Description of the command: this technique consists of rewriting the dynamic model of the asynchronous machine in a reference system rotating with the rotor flow. By this non-linear transformation, it suffices to maintain the flow of the rotor constant to ensure the decoupling between the speed and the flow of the machine.

In [3] three methods proposed to decouple the control in the case of stator flow regulation, rotor flow and asynchronous motor air gap flow.

PI type regulators are used to control flow, speed and torque. The parameters of the machine allow us to calculate the values of the different coefficients of the regulators used.

The block diagram of the direct vector control by rotor flux orientation powered by a voltage inverter is shown in *FIG. 3*

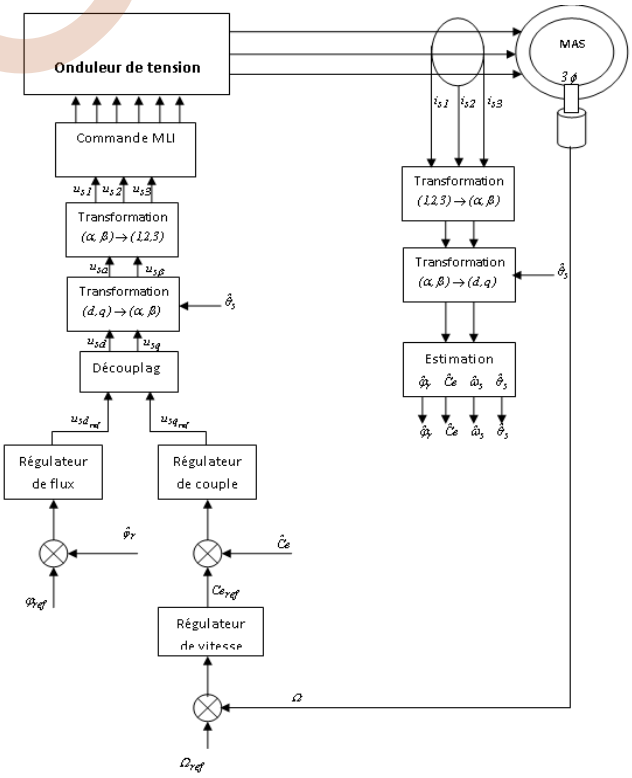

***Figure 3:** Command-Inverter-MAS Simulation Scheme*

IV. INPUT / OUTPUT LINEARISATION CONTROL

This method generalizes vector-type commands by decoupling and linearizing the relations between inputs and outputs. This technique assumes that the totality of the state vector is measurable by direct measurement of the quantities; it is thus possible to design nonlinear state feedback, which ensures the stability of the looped system. Several studies have shown that this nonlinear control technique has shown interesting properties with respect to torque / flux decoupling, torque response time, and parametric robustness. This control structure thus appears as an interesting alternative to the control by flow orientation.

The state model of the asynchronous machine, in a fixed reference frame linked to the stator(α,β), is a non-linear representation of the shape:

$$x = F(x) + gu(t) \qquad (13)$$

Where:

$$x = [is_\alpha \quad is_\beta \quad \phi r_\alpha \quad \phi r_\beta \quad \Omega]$$

Le vecteur d'état X appartient à l'ensemble :

$$\Omega = \{x \in \Re 5 : \phi r2\alpha + \phi r2\beta \neq 0\}$$

$$F(x) = \begin{bmatrix} -\gamma i_{s\alpha} + \frac{K}{T_r}\phi_{r\alpha} + pK\omega\phi_{r\beta} \\ -\gamma i_{s\beta} + \frac{K}{T_r}\phi_{r\beta} - pK\omega\phi_{r\alpha} \\ \frac{M}{T_r} i_{s\alpha} - \frac{1}{T_r}\phi_{r\alpha} - p\omega\phi_{r\beta} \\ \frac{M}{T_r} i_{s\beta} - \frac{1}{T_r}\phi_{r\beta} + p\omega\phi_{r\alpha} \\ \frac{pM}{jL_r}\left(\phi_{r\alpha} i_{s\beta} - \phi_{r\beta} i_{s\alpha}\right) - \frac{1}{j}\left(f_r\omega + T_L\right) \end{bmatrix}$$

$$g = [g_1 \quad g_2] = \begin{bmatrix} \frac{1}{\delta L_s} & 0 & 0 & 0 & 0 \\ 0 & \frac{1}{\delta L_s} & 0 & 0 & 0 \end{bmatrix}$$

The system to be controlled must be of the square type. The variables to be controlled in this work are torque and the rotor squared flux standard.

The choice of the squared standard is due to the fact that this shape simplifies the differential calculation.

So…:

$$Y(x) = \begin{bmatrix} Y_1(x) \\ Y_2(x) \end{bmatrix} = \begin{bmatrix} h_1(x) \\ h_2(x) \end{bmatrix} = \begin{bmatrix} Ce \\ \phi_{r\alpha}{}^2 + \phi_{r\beta}{}^2 = \phi \end{bmatrix} \qquad (14)$$

The linearization condition for checking whether a non-linear system allows an input/output linearization is the relative degree order of the system [13].

The *FIG.* 4 gives its simulation block

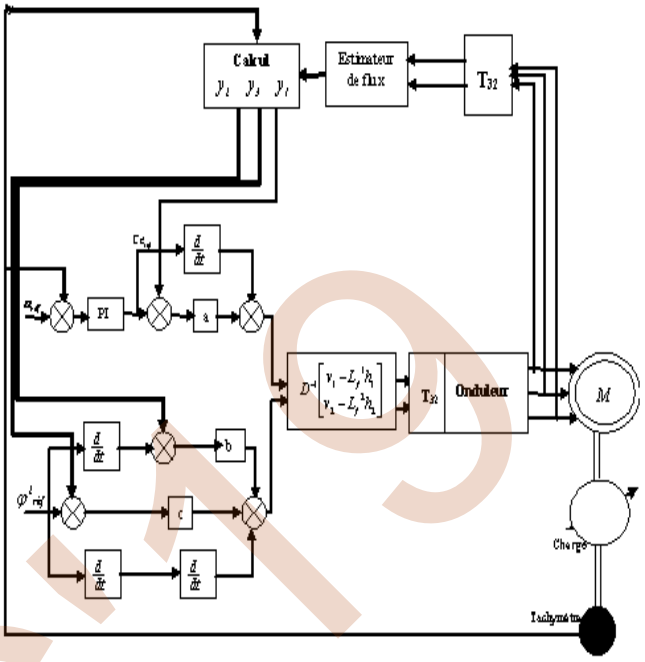

Figure 4: *Block Diagram of the Linearization Control*

V. COMPARATIVE STUDY

The two control methods described above (vector control and linearization control) have very interesting performances despite the disadvantages. To show the difference, we simulate the two non-inverter commands for the following operating modes:

- Startup load up to t = 0.5s, constant flux equals 0.9Web.
- Constant speed and flux, of t = [0.5s, 1s], the speed equal to 100rad / s corresponds to the low speed operation.
- Speed in acceleration mode from 100rad / s to its nominal speed 157rad / s in t = [1s, 2.25s], then it remains constant without load torque and at constant flux of t = [2.25, 2.5s].
- Speed in acceleration mode from 157rad / s until stabilized at 210 rad / s (operation in over speed mode), variable flux 0.9web decreases to 0.7web (defluxing), without load torque.
- From t = 3.5s introduction of a load torque of 7.5Nm, and at t = 3.75 the speed decreases in deceleration mode up to the nominal speed, at the moment when the flux resumes its initial value 0.9Web, the rotor resistance increases at t = 4s from 6.3Ohm to 9.45 Ohm the variation of the resistance is given by the figure (3. 7). The profiles of the imposed trajectories and the results of simulations are presented in *FIG.3*

The results obtained show that the speed and flow performance performances are satisfactory for the two types of control, but those obtained by the input-output linearization control are better, as is shown in the *TAB.1*. High desired performance is obtained at low speed and over speed for the linearization control.

Type de commande	Commande Vectorielle	Commande par Linéarisation
Contrôle en régime transitoire	Oui	Oui
Contrôle en régime permanant	Oui	Oui
Sensibilité aux variations des paramètres	**Très Sensible**	**Sensible**
Comportement à basse vitesse	Bon	Bon
Adaptation aux vitesses élevées	**Médiocre**	**Bonne**

***Table (1)**: Criteria for comparison between, Vector Control, and I/O Linearization Control*

The profiles of the imposed trajectories and the results of simulations are presented in *FIG. 5*

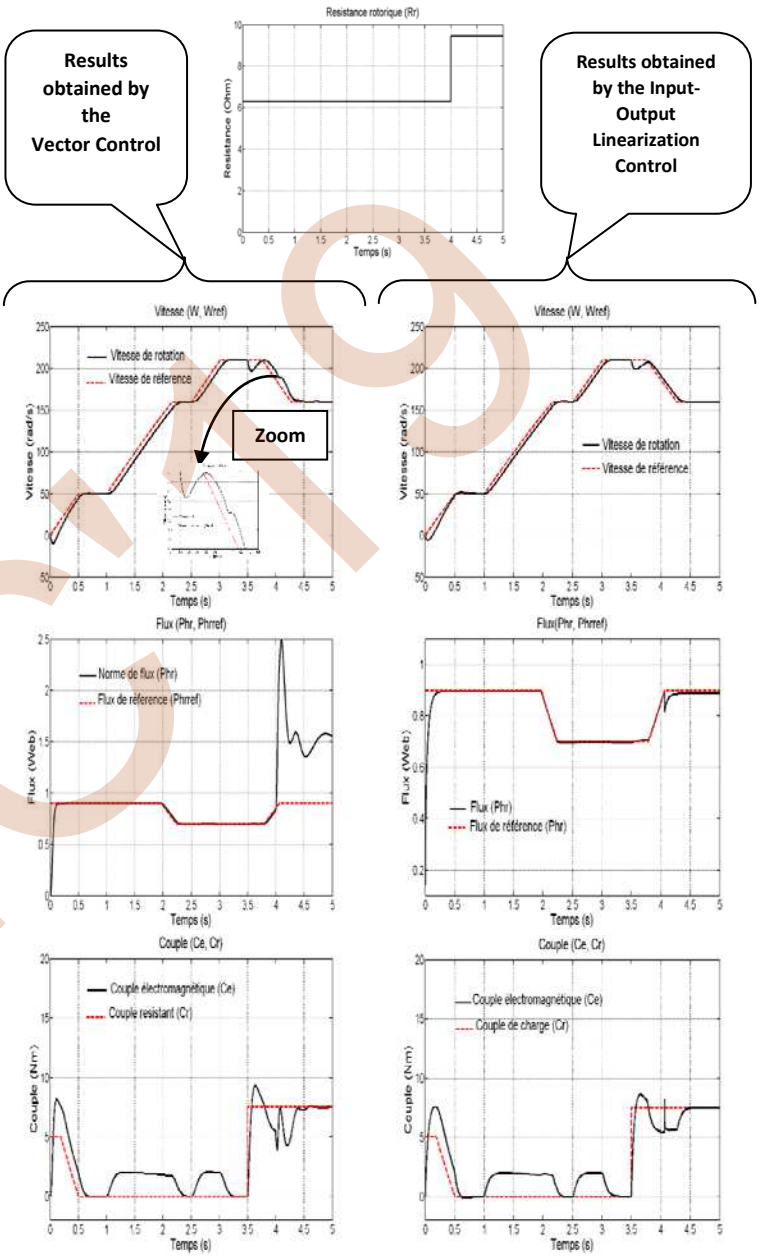

***Figure 5:** Comparison between Input-Output Linearization Control and Vector Control*

VI. CONCLUSIONS

The comparative study of the two techniques makes it possible to draw the following conclusions:

- Interesting performance in nominal operation in both commands.
- Choice of parameters and design are very simple in the Linearization Control
- *Mode of operation (Over speed, Defluxing)*
  - Degradation of performance (decoupling) of the vector control,
  - Maintain the performance of the control by Linearization INPUTS-OUTPUTS
- *Variation paramètres*
  - High sensitivity of the vector control
  - Less sensitivity of the Control by Linearization
- A common disadvantage between the two commands is the assumption of the availability of the entire state vector. However, only currents and stator voltages that are measurable.

REFERENCES

[1] Adel M." Commande non linéaire à modèle prédictif pour une machine asynchrone", thèse doctorat, université du Québec, Mai 2007.
[2] Brockett R. W."Feedback Invariants for Nonlinear Systems", IFAC congress, Helsinki, 1978, pp. 11-15.
[3] Canudas C. de Wit, "Commande des moteurs asynchrones 1– Modélisation contrôle vectoriel et DTC", Hermès Science Publication, France, 2000.
[4] Chiasson J."Nonlinear Controllers for an Induction Motor", Control Engineering. Practice, vol. 4, no.7, pp 977-990, 1996.
[5] Conte G., Claude H. M. et Anna M. P. "Algebraic methods for nonlinear control systems", 2nd edition, May 2006.
[6] Hedrick J. K. and A. Girard, "Feedback Linearization". Control of Nonlinear Dynamic Systems: Theory and Applications, 2005.
[7] Hischorn R. M., 'Inevitability of multivariable nonlinear svstems', IEEE Trans. on AC, AC-24, 1979, pp. 855.
[8] Hunt R. L., R. Su et G. Meyer, 'Design for Multi-input Systems', Differential Geometric Control Theory, edited by R. Brockett et al, Boston, vol. 27, 1983, pp. 268.
[9] Isidori A., "Nonlinear control systems: communication and control", Engineering Serie, Berlin, Springer Verlag, 2 edition, 1989.
[10] Kemer A. J., "On the equivalence of Control Systems and the Lineanzation of Nonlinear Systems", SIAM J. Control, pp. 670, 1973.
[11] Krause P. C., O. Wasynczuk et S. D. Sudhoff, "Analysis of electric machinery"' IEEE press, 1994.
[12] Lévine J., "Analyse et Commande des Systèmes Non Linéaires", Centre Automatique et Systèmes, école des Mines de Paris, Mars 2004.
[13] Meroufel, B. Belabbes, M. K. Fellah, A. Benaissa "Commande linéarisante d"un moteur synchrone à aimants permanents avec limitation du courant par poursuite d"une trajectoire de vitesse a accélération constante" Université Djillali Liabes Sidi Bel –Abbes, Algérie.

Performance Analysis of Dual Star Induction Generator Under Open Phase Fault

Lyes KHALDI, Samira CHEKKAL, Kaci GHEDAMSI, Djamal AOUZELLAG
Laboratoire de maitrise des énergies renouvelables,
Faculté de technologie,
Université de Bejaia 06000, Algérie
*Corresponding author. Tel: +213-541-338-993; Fax: +0-000-000-000
E-mail address: khaldii_lyes@yahoo.com

Abstract—The objective of this paper is a performance analysis of multiphase generation systems (GS) based on dual star induction generator (DSIG) with indirect field oriented control (IFOC) under open phase fault (OPF) with two cases of OPF such as, one open phase (D_1) and two open phase (D_2). The DSIG has been modeled in natural frame, in the aspiration to validate the results compared to the model of DSIG in dq frame with IFOC in one hand, or in other hand to exploit the advantages offered using the model in natural frame namely, several faults can be simulated simultaneously and its very efficient for the analysis of faults. To reach the goal of this proposed work a deep analysis to determine exact the effect of OPF on the torque ripples, electrical losses, mechanical speed and current ripples of this machine has been investigated.

Keywords- Dual star induction machine; indirect field oriented control; Open Phase Fault; Torque Ripples; Current Quality;

I. INTRODUCTION

The issue of sustainable development is now becoming a major element in some large-scale politico-economic decision, and the focus on the transition to renewable energy is beginning to bear fruit, and leading to a new way of thinking. The new challenges today are therefore to propose increasingly clean solutions, which make it possible to keep a maximum of the benefits acquired, but with a clear vision of the risks represented by a misuse of natural resources. An energy conversion chain exploiting renewable primary energies consists mainly of three parts. The first part is the primary energy source and the turbines. The second part corresponds to the (machine – converter) set. Finally the last is the connection to either a power network (operation connect to the power grid) or an isolated or autonomous load.

The most well-known architecture in power generation applications is the combination of a three-phase AC machine with a conventional three-phase inverter. With this classical architecture, the occurrence of a fault in its environment can have a bad impact on the continuity of service and the supply of energy. One of solution to increase reliability of GS and ensure power generation in normal and degraded mode is the use of multi-phase machine. The dual star machine whatever in a motor or generator operation is among and the most studied machines in the literature. A lot of research has been carried out to the development of this machine namely, behavior [1-2], modeling [3-5], and control [6-7]. The search is to look at the case of continuity of operation during a fault where several works have been started in this direction that is, open phase fault [8-10], and short circuit fault [11]. The absence of a feeding phase is less noticeable when their number increases. In this sense shows that according to the acceptable tolerance on the torque ripple, the loss of one of the phases can be admitted without any modification of the command, the system can operate with reduced capacity, which is called degraded mode [12].

The aim of this work is to study a performance analysis of DSIG with indirect field oriented control (IFOC) under open phase fault, where it is indented to provide information about the impact of OPF on the torque ripples, copper losses, efficiency and mechanical speed, and that will be useful and help researchers who are interested on the control to minimize or eliminate this effect.

II. MODEL OF THE DSIG IN THE NATURAL FRAME

The stator of DSIG is composed of two three-phase windings shifted between them by an electrical angle $\alpha = \pi/6$ (fig.1), and in order to simplify the study, the modeling approach is bases on the following assumptions:

• Magnetic saturation, hysteresis, eddy current, the temperature effect and the effect of skin are neglected;

• The magneto-motive forces created by each phase of the two plates are sinusoidal distribution, the inductances are constant and that the windings are sinusoidal functions of the angle between their magnetic axes;
• The machine is balanced constitution.

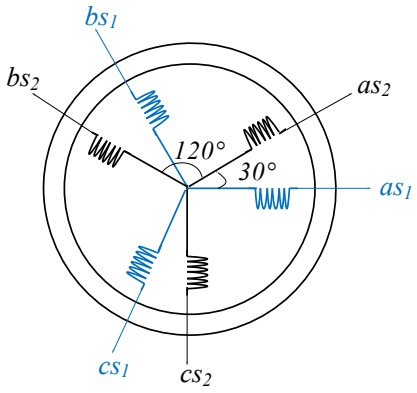

Figure 1. Stator winding Shame of DSIG

This approach consists of modeling the machine in the natural base in a healthy diet. Then introduce a high resistance in series with the phase in default, which cancels the current which crosses it. With this approach several faults can be simulated simultaneously.

The dynamic behavior of the DSIG is described by the equations mentioned here after ware; the voltage equations of the DSIG are expressed as follow:

$$\begin{cases} [v_{s1}] = [r_{s1}][i_{s1}] + \frac{d}{dt}[\psi_{s1}] \\ [v_{s2}] = [r_{s2}][i_{s2}] + \frac{d}{dt}[\psi_{s2}] \\ [v_r] = [r_r][i_r] + \frac{d}{dt}[\psi_r] \end{cases} \quad (1)$$

The flux equations of stator and rotor can be written as:

$$\begin{bmatrix} [\psi_{s1}] \\ [\psi_{s2}] \\ [\psi_r] \end{bmatrix} = \begin{bmatrix} [L_{1,1}] & [L_{1,2}] & [L_{1,r}] \\ [L_{2,1}] & [L_{2,2}] & [L_{2,r}] \\ [L_{r,1}] & [L_{r,2}] & [L_{r,r}] \end{bmatrix} \begin{bmatrix} i_{s1} \\ i_{s2} \\ i_r \end{bmatrix} \quad (2)$$

The stator inductance matrix of the first and second star is given as follows:

$$[L_{1,1}] = [L_{2,2}] \begin{bmatrix} L_s & L_m \cos\left(\frac{2\pi}{3}\right) & L_m \cos\left(\frac{4\pi}{3}\right) \\ L_m \cos\left(\frac{4\pi}{3}\right) & L_s & L_m \cos\left(\frac{2\pi}{3}\right) \\ L_m \cos\left(\frac{2\pi}{3}\right) & L_m \cos\left(\frac{4\pi}{3}\right) & L_s \end{bmatrix} \quad (3)$$

The mutual matrix inductance between the first and second star given as follows:

$$[L_{1,2}] = L_m \begin{bmatrix} \cos(\alpha) & \cos\left(\alpha + \frac{2\pi}{3}\right) & \cos\left(\alpha + \frac{4\pi}{3}\right) \\ \cos\left(\alpha - \frac{2\pi}{3}\right) & \cos(\alpha) & \cos\left(\alpha + \frac{2\pi}{3}\right) \\ \cos\left(\alpha - \frac{4\pi}{3}\right) & \cos\left(\alpha - \frac{2\pi}{3}\right) & \cos(\alpha) \end{bmatrix} \quad (4)$$

The mutual matrix inductance between the first star and rotor is given as follows:

$$[L_{1,r}] = L_m \begin{bmatrix} \cos(\theta_r) & \cos\left(\theta_r + \frac{2\pi}{3}\right) & \cos\left(\theta_r + \frac{4\pi}{3}\right) \\ \cos\left(\theta_r - \frac{2\pi}{3}\right) & \cos(\theta_r) & \cos\left(\theta_r + \frac{2\pi}{3}\right) \\ \cos\left(\theta_r - \frac{4\pi}{3}\right) & \cos\left(\theta_r - \frac{2\pi}{3}\right) & \cos(\theta_r) \end{bmatrix} \quad (5)$$

The mutual matrix inductance between the second star and rotor is given as follows:

$$[L_{2,r}] = L_m \begin{bmatrix} \cos(\theta_r - \alpha) & \cos\left(\theta_r - \alpha + \frac{2\pi}{3}\right) & \cos\left(\theta_r - \alpha + \frac{4\pi}{3}\right) \\ \cos\left(\theta_r - \alpha - \frac{2\pi}{3}\right) & \cos(\theta_r - \alpha) & \cos\left(\theta_r - \alpha + \frac{2\pi}{3}\right) \\ \cos\left(\theta_r - \alpha - \frac{4\pi}{3}\right) & \cos\left(\theta_r - \alpha - \frac{2\pi}{3}\right) & \cos(\theta_r - \alpha) \end{bmatrix} \quad (6)$$

With: $[L_{2,1}] = [L_{1,2}]^t$, $[L_{r,1}] = [L_{1,r}]^t$ and $[L_{r,2}] = [L_{2,r}]^t$

And the electrical angle (θ_r) is given by:

$$\theta_r = \int \omega_r \, dt$$

Substituting (2) - (6) into (1) we obtain:

$$\begin{cases} [v_{s1}] = [r_{s1}][i_{s1}] + \frac{d}{dt}\left([L_{1,1}][i_{s1}] + [L_{1,2}][i_{s2}] + [L_{1,r}][i_r]\right) \\ [v_{s2}] = [r_{s2}][i_{s2}] + \frac{d}{dt}\left([L_{2,2}][i_{s2}] + [L_{2,1}][i_{s1}] + [L_{2,r}][i_r]\right) \\ [v_r] = [r_r][i_r] + \frac{d}{dt}\left([L_r][i_r] + [L_{r,1}][i_{s1}] + [L_{r,2}][i_{s2}]\right) \end{cases} \quad (7)$$

In order to design the complete model, it is necessary to integrate the mechanical equation characterizing the machine, or the mechanical system is expressed as follow:

$$\Gamma_{em} - \Gamma_r = J\frac{d\Omega_r}{dt} + f\Omega_r \quad (8)$$

With the electromagnetic torque is:

$$\Gamma_{em} = P\left\{[i_{s1}]^t \frac{d}{d\theta_r}[L_{1,r}][i_r] + [i_{s2}]^t \frac{d}{d\theta_r}[L_{2,r}][i_r]\right\} \quad (9)$$

As the stator and rotor inductances matrices do not depend on time, and the mutual matrices depend of the electrical angle(θ_r),a variables change has been established to develop the equation (7), finally we obtain a system of state which :

$$\begin{cases} \frac{d}{dt}([i_{s1}]) = [L_{1,1}]^{-1}\begin{pmatrix} [v_{s1}]-[r_{s1}][i_{s1}]-[L_{1,2}]\frac{d}{dt}([i_{s2}]) \\ -[L_{1,r}]\frac{d}{dt}([i_r])-\omega_r\frac{d}{d\theta_r}([L_{1,r}])\,[i_r] \end{pmatrix} \\ \frac{d}{dt}([i_{s2}]) = [L_{2,2}]^{-1}\begin{pmatrix} [v_{s2}]-[r_{s2}][i_{s2}]-[L_{2,1}]\frac{d}{dt}([i_{s1}]) \\ -[L_{2,r}]\frac{d}{dt}([i_r])-\omega_r\frac{d}{d\theta_r}([L_{2,r}])[i_r] \end{pmatrix} \\ \frac{d}{dt}([i_r]) = [L_r]^{-1}\begin{pmatrix} [r_r][i_r]-[L_{1r}]\frac{d}{dt}([i_{s1}]) \\ -\omega_r\frac{d}{d\theta_r}([L_{1,r}])[i_{s1}]-\omega_r\frac{d}{d\theta_r}([l_{2,r}])[i_{s2}] \end{pmatrix} \end{cases}$$

III. INDIRECT FIELD ORIENTED CONTROL OF A DSIG

The main objective of the vector control of induction machines is, as in DC machines, to independently control the torque and the flux. In this order, one proposes to study the IFOC of the DSIM. The control strategy used consists to maintain the quadrate component of the flux null ($\varphi_{qr} = 0$) and the direct flux equals to the reference [13]:

$$\varphi_{dr} = \varphi_r^* \tag{10}$$

And the quadrate components of flux equal to zero:

$$\varphi_{qr} = 0 \tag{11}$$

$$\frac{d\varphi_r^*}{dt} = 0 \tag{12}$$

After application of the park transformation to the equation system (1) we obtain :

$$\begin{cases} v_{d1} = r_1 i_{d1} + \frac{d\varphi_{d1}}{dt} - \omega_s\varphi_{q1} \\ v_{q1} = r_1 i_{q1} + \frac{d\varphi_{q1}}{dt} + \omega_s\varphi_{d1} \\ v_{d2} = r_2 i_{d2} + \frac{d\varphi_{d2}}{dt} - \omega_s\varphi_{q2} \\ v_{q2} = r_2 i_{q2} + \frac{d\varphi_{q2}}{dt} + \omega_s\varphi_{d2} \\ v_{dr} = r_r i_{dr} + \frac{d\varphi_{dr}}{dt} - \omega_{sl}\varphi_{qr} = 0 \\ v_{qr} = r_r i_{qr} + \frac{d\varphi_{qr}}{dt} + \omega_{sl}\varphi_{dr} = 0 \end{cases} \tag{13}$$

Substituting (10)-(12), into (13) yields

$$r_r . i_{dr} = 0 \Rightarrow i_{dr} = 0 \tag{14}$$

$$r_r . i_{qr} + \omega_{sl}^* . \varphi^*{}_r = 0 \Rightarrow i_{qr} = -\frac{\omega_{sl}^* . \varphi^*{}_r}{r_r} \tag{15}$$

With $\omega_{sl}^* = \omega_s^* - \omega_r$ (ω_{sl}^* is the slip speed)

The rotor currents in terms of the stator currents are divided from (13) as:

$$i_{dr} = \frac{\varphi^*{}_r}{L_m + L_r} - \frac{L_m}{L_m + L_r}(i_{ds1} + i_{ds2}) \tag{16}$$

$$i_{qr} = -\frac{L_m}{L_m + L_r}(i_{qs1} + i_{qs2}) \tag{17}$$

With taking into the rotor field orientation, the stator voltage equations can be rewritten as:

$$\begin{cases} V^*{}_{ds1} = r_{s1} i_{ds1} + L_1\frac{d}{dt} i_{ds1} - \omega_s^*\begin{pmatrix} L_1 i_{qs1} \\ +\tau_r \cdot \varphi_r^* \cdot \omega_{sl}^* \end{pmatrix} \\ V^*{}_{qs1} = r_{s1} i_{qs1} + L_1\frac{d}{dt} i_{qs1} + \omega_s^*(L_1 i_{ds1} + \phi_r^*) \\ V^*{}_{ds2} = r_{s2} i_{ds2} + L_2\frac{d}{dt} i_{ds2} - \omega_s^*\begin{pmatrix} L_2 i_{qs2} \\ +\tau_r \cdot \varphi_r^* \cdot \omega_{sl}^* \end{pmatrix} \\ V^*{}_{qs2} = r i_{qs2} + L_2\frac{d}{dt} i_{qs2} + \omega_s^*(L_2 i_{ds2} + \varphi_r^*) \end{cases} \tag{18}$$

With $\tau_r = \frac{L_r}{R_r}$

The final expression of electromagnetic torque is:

$$\Gamma_{em}^* = P\frac{L_m}{(L_m + L_r)}(i_{qs1} + i_{qs2})\varphi_r^* \tag{19}$$

Consequently, the electrical and mechanical equations for the system after these transformations in the space control may be written as follows:

$$\begin{cases} \frac{d}{dt} i_{ds1} = \frac{1}{L_s}\left\{V_{ds1}^* - r_{s1} i_{ds1} + \omega_s^*\begin{pmatrix} L_s i_{qs1} \\ +\tau_r \cdot \varphi_r^* \cdot \omega_{sl}^* \end{pmatrix}\right\} \\ \frac{d}{dt} i_{qs1} = \frac{1}{L_s}\{V_{qs1}^* - r_{s1} i_{qs1} + \omega_s^*(L_s i_{ds1} + \varphi_r^*)\} \\ \frac{d}{dt} i_{ds2} = \frac{1}{L_s}\left\{V_{ds2}^* - r_{s2} i_{ds2} + \omega_s^*\begin{pmatrix} L_s i_{qs2} \\ +\tau_r \cdot \varphi_r^* \cdot \omega_{sl}^* \end{pmatrix}\right\} \\ \frac{d}{dt} i_{qs2} = \frac{1}{L_s}\{V_{qs2}^* - r_{s2} i_{qs2} + \omega_s^*(L_s i_{ds2} + \varphi_r^*)\} \\ \frac{d}{dt}\Omega_r = \frac{1}{J}\left\{\frac{P\,L_m(i_{qs1}+i_{qs2})\varphi_r^*}{(L_m + L_r)} - \Gamma_r - f\Omega_r\right\} \end{cases} \tag{20}$$

IV. INTERPRETATION AND SIMULATION RESULTS

The proposed control shame of (GS) based on dual star induction generator with indirect field oriented control is showed in fig.2

In order to verify the validity of this proposed work, a series of simulation of the behavior of DSIG fed by two VSI with 2 kHz switching frequency under IFOC has been obtained using MATLAB/Simulink. The proposed IFOC of DSIG modeled in natural frame was given the desired results compared to the works done before, where the DSIG

is modeled in d-q frame as [13], [14]. The obtained results represent the evolution of the characteristics of the DSIG with IFOC by imposing the reference flow $\emptyset_r^* = 0.7(\text{Wb})$ and a mechanical speed in the form of slots

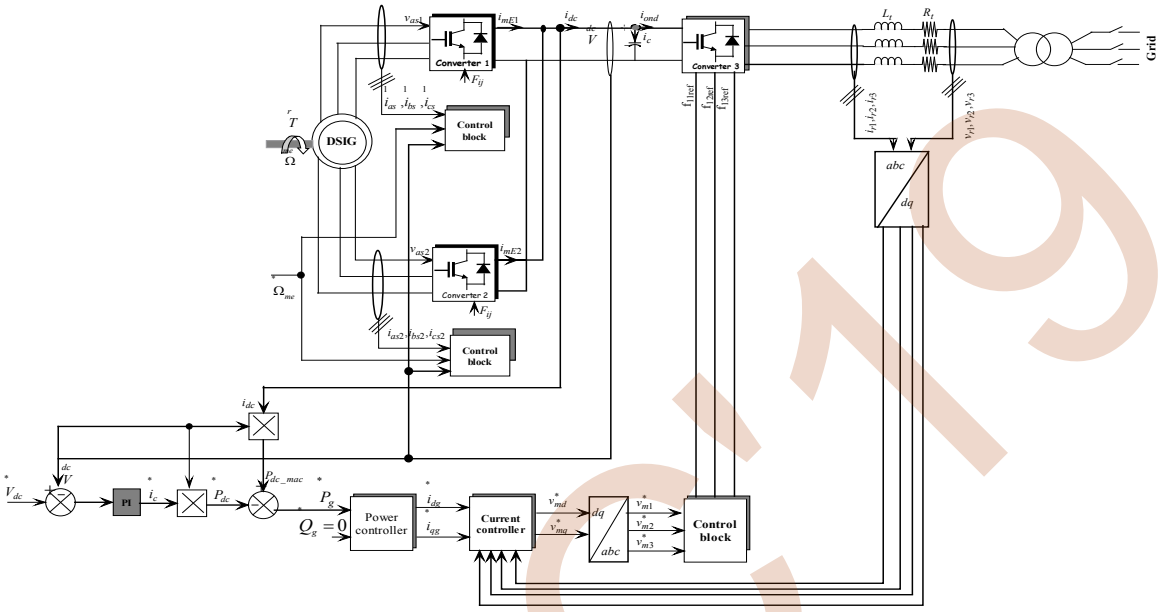

Figure 2. Bloc diagram of control system

$\omega_r^* = [301, 258, 153, 203](\text{rad/s})$ following the time intervals t = [0, 1.2 , 2, 2.7, 4] (s).The fig.3 show the wave form of the generator torque, where he faithfully follows the variation of the speed. The stator currents are presented in Fig.4 and fig.7 illustrate the currents of the two stars and their representation in zoom. The construction of the GASDE imposes that there is a shift of an electric angle (α = 30 °) between the first star ahead of the second. The voltage and current are in phase opposition, this justifies that the power flow is always towards the grid as showed in fig.8. The fig.9 represents the speed of the mechanical speed and we note that the speed of rotation perfectly follows its set point, which is variable according to the speed reference.

To show the interest of using the model in natural frame an OPF was occurred at *t=3s*. The OFP of DSIG has caused a degradation of the performance of the GS and has always as results, the unbalanced stator currents projecting on the electromagnetic torque, the mechanical speed and the efficiency which are illustrated on (fig 3-9). In the case of opening of two phases the performance of the GS has further decreased compared to the operation of the machine with one phase open, where the stator currents of the healthy phases have considerably increased compared to the opening of the one phase, this increase leads to additional copper losses that adversely affect the efficiency of FPIM and followed by high electromagnetic torque ripples and a decrease of mechanical speed as presented in table 1 and Fig.10 the continuity of service is ensured by DSIG but with degrade performances.

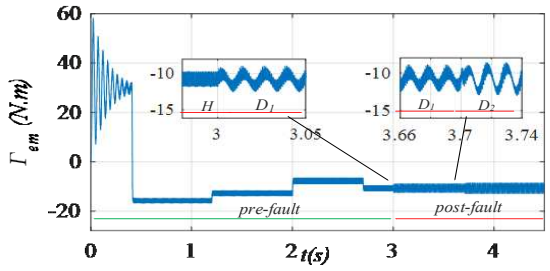

Figure 3. Generator electromagnetic torque

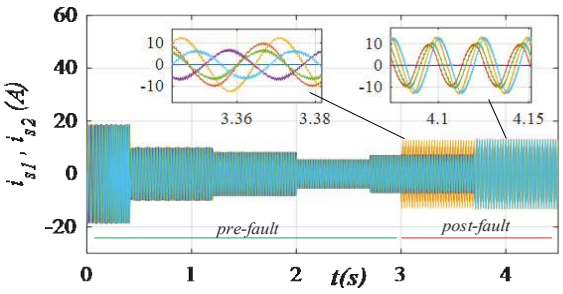

Figure 4. Stator currents of DSIG

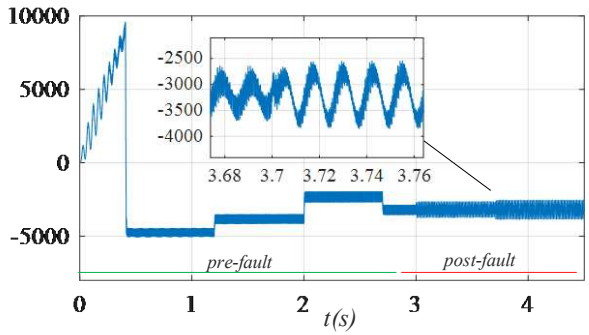

Figure 5. Stator power of DSIG

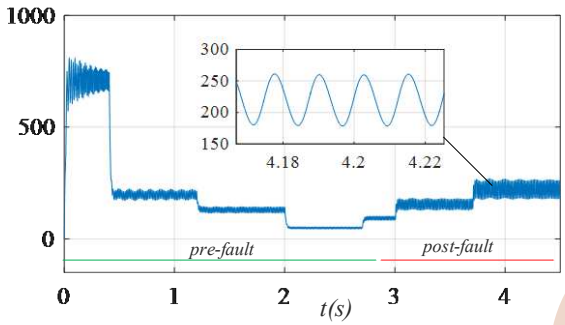

Figure 6. Stator copper losses of DSIG

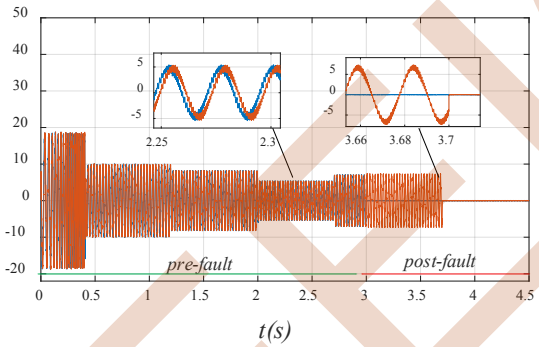

Figure 7. Two first current of each stator

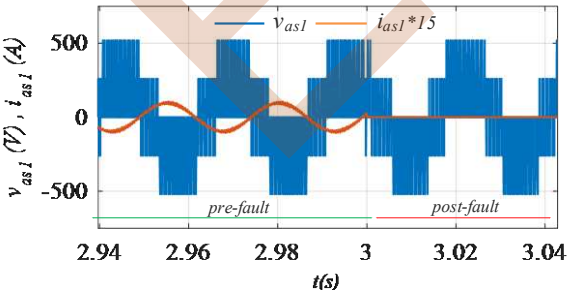

Figure 8. Zoom of stator current and voltage

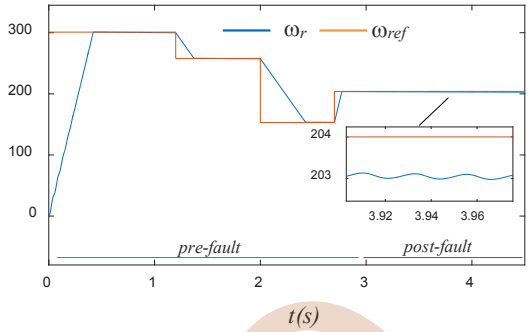

Figure 9. Electrical speed of DSIG

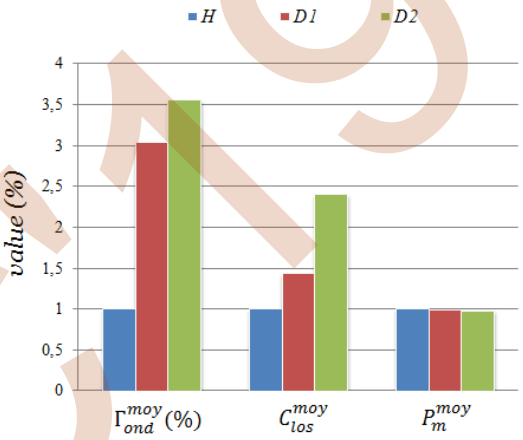

Figure 10. Comparison between the variables of the DSIG under OPF

TABLE I. FAILURE OF DSIG UNDER OFP

Default type	$\Gamma_{em}^{moy}(N.m)$	ω_r^{rip} (%)	$P_m^{moy}(W)$	Γ_{em}^{rip} (%)	$C_{loss}^{moy}(W)$
Healthy	-10.84	0.2	-3206.90	7.58	92.76
D_1	-10.71	1.02	-3186.80	23.81	134.18
D_2	-10.69	1.12	-3148.12	27.04	222.85

V. CONCLUSION

In this paper the performance analysis of a generation systems based on dual star induction generator with indirect field oriented control under open phase fault has been presented. A simulation results for the both healthy and OFP of DSIG show in first hand, the validity of the model in the natural frame with IFOC and in the second hand, the possibility of simulating a different OPF. the effect of OPF on the torque ripples, mechanical speed, copper losses and efficiency has been investigated, and has always as results, a high torque ripples, increase copper losses and a decrease in mechanical speed.

The continuity of service in this proposed work has been demonstrated by simulation and successfully implemented in a generation system based on DSIG.

REFERENCES

[1] M. Mengoni, L. Zarri, A. Tani, Y. Gritli, G. Serra, and F. Filippetti, "Behavior of Multiphase Induction Machines With Unbalanced Stator Resistances", 15th International Power Electronics and Motion Control Conference,2012, Novi Sad, Serbia

[2] K. Iffouzar, S. Taraft, H. Aouzellag, K. Ghedamsi, D. Aouzellag, "behavior of six phase Inductionmotor fed by multilevel inverter," International conference of Electrical Engineering, ICEE15, pp 1-7, Algeria , 2015.

[3] M. Duran and F. Barrero, "Recent advances in the design, modeling and control of multiphase machines—Part II," IEEE Trans. Ind. Electron., vol. 63, no. 1, pp. 459–468, Jan. 2016.

[4] E.K. Appiah ,G. M'boungui, A.A. Jimoh , J.L. Munda , and A.S. Ogunjuyigbe , "Symmetrical Analysis of a Six Phase Induction Machine Under Fault Conditions", International Journal of Electrical and Computer Engineering ,vol:7,No:3,2013.

[5] D. Star, P. Magnet, S. Machine, S. Order, and S. Mode, "Direct Torque Control Using Second Order Sliding Mode of a Double Star Permanent," vol. 80, no. December, 2018.

[6] F. Barrero, M. R. Arahal, R. Gregor, S. Toral, and M. J. Durán, "A proof of concept study of predictive current control for VSI-driven asymmetrical dual three-phase AC machines," IEEE Trans. Ind. Electron., vol. 56, no. 6, pp. 1937–1954, 2009.

[7] E. Levi.: Advances in converter control and innovative exploitation of additional degrees of freedom for multiphase machines," IEEE Trans. Ind. Electron., on, vol.63, no.1, pp.433-448, Jan. 2016

[8] A. Mohammad and L. Parsa, "Global fault-tolerant control technique for multiphase permanent-magnet machines," IEEE Trans. Ind. Appl., vol. 51 , no. 1, pp. 178-186, Jan. 2015

[9] Hisham M. Eldeeb, Ayman S. Abdel-Khalik, Senior Member, IEEE, Christoph M. Hackl, Senior Member, IEEE,"Post-Fault Full Torque-Speed Exploitation of Dual Three-Phase IPMSM Drives", IEEE TRANSACTIONS ON INDUSTRIAL ELECTRONICS; DOI 10.1109/TIE.2018.2880698.

[10] W. Munim, M. Duran, H. S. Che, M. Bermudez, I. Gonzalez-Prieto, and N. Abd Rahim "A unifiedanalysis of the faultt olerance capability in six-phase induction motor drive," IEEE Trans. Power Electron., vol. 32, no. 10, pp. 7824-7836, Oct. 2017.

[11] L. Khaldi, K. Iffouzar, K. Ghedamsi, D. Aouzellag, "Performance analyis of five phase Induction motor under unbalanced parametres" In conf., IC3E18, Bouira, Algeria , 2018.

[12] Ayman S. Abdel-Khalik, Mohamed A. Elgenedy, Ahmed M. Massoud, "An Improved Fault-Tolerant Five-Phase Induction Machine Using A Combined Star/Pentagon Single Layer Stator Winding Connection" IEEE transactions on industrial electronics,DOI 10.1109/TIE.2015.2426672.

[13] S. Chekkal, N. Aouzellag Lahaçani, D. Aouzellag, K. Ghedamsi, "Fuzzy logic control strategy of wind generator based on the dual-stator induction generator ", Electrical Power and Energy Systems,vol 59, pp 166–175,2014.

[14] H. Amimeur, D. Aouzellag, R. Abdessemed, K. Ghedamsi "Sliding mode control of a dual star induction generator for wind energy conversion systems" Electrical power and energy systems, vol.42, pp 60-70 , 2012.

Tidal power systems: A review

Amirouche Elyazid, Ghedamsi Kaci, Aouzellag Djamal
Laboratoire de Maitrise des Energies Renouvelables
Faculté de Technologie, Université de Bejaia 06000, Algerie
Emails: elyazid.amirouche@hotmail.com, kghedamsi@yahoo.fr, aouzellag@hotmail.com

***Abstract*—The marine tidal energy is a promising renewable energy source as it presents many advantages compared to other renewables, such as long-term predictability and high power potential. Thanks to its advantages, numerous projects have started all around the world in order to exploit this source, but only few projects have reached the stage of grid connection because of the harsh marine environment characteristics. On the subject of this new emerging area of research, this paper reviews the marine tidal power extraction systems fundamentals starting from the energy resource to the power electronic devices used for grid connection, and reports some main projects in the world and recent works in this scope. Also, the problems related to the marine environment have been highlighted.**

Keywords— marine energy, tidal power, tidal power extraction system, marine current turbine, electric generator, power converter.

I. INTRODUCTION

Extracting energy from the flowing sea water is a new form of renewable energy which seems to be promising. The general aspect of tidal currents is similar to wind, with the advantage of being 800 times denser, meaning that for a same power, the size of a marine turbine is lower than that of a wind turbine, also, marine currents doesn't reach extreme velocities in the most available sites, thus, no expensive structure reinforcement is needed. The main big advantage of tidal currents is the long term predictability [1], so the identification of production dip periods is easy, and an emergency plan can be planned early and neatly.

Many projects have started all around the world to extract power from tidal currents. SeaGen was the world's first large scale grid connected tidal power generator, installed by SIMEC Atlantis Energy Limited in UK in 2008 and successfully decommissioned in 2019, it has a power of 1.2 MW, it exported over 11.6 GWh of power during its service. The lessons learned from this project will help the evolution of current and future projects [2]. MeyGen is another promising project in the UK, it's currently the largest planned tidal stream project, and the first commercial multi-turbine array, it's always under construction. The construction is split into three phases, and aims to reach 398 MW [3]. OpenHydro was an Irish company who designed the 250 kW Open Center Turbine, the first tidal turbine to be grid connected in Scotland, installed in 2006, this project hasn't gone beyond the test stage, and the company was liquidated by its parent company Naval Energies in July 2018 [4]. In France, the company Sabella launched Sabella D10, a 10 meters' diameter turbine with a power of 1 MW, the first grid connected turbine in France since 2015 [5].

Many other projects stayed in prototype phase and have not been connected to the grid, like the Enermar Project, located along Sicilian coast, Italy, it was a 50 kW vertical axis turbine prototype mounted on a floating platform, installed in January 2001. The project ended in January 2005 [6].

To extract the power from tides, a system must be constructed, principally composed of a marine current turbine, an electric generator, and a power converter. All these elements will be discussed in the present paper starting from the tidal current characteristics. Some recent works concerning tidal power systems development will also be evoked.

II. OCEAN ENERGY

Over last years, in a scope of searching a non-polluting renewable energy, ocean energy got a particular interest. Effectively, it's a big source of several renewable energy forms, such as wave energy, tidal energy, offshore wind energy and thermal energy. The latter consists on the exploitation of the thermal gradient available between the warm surface sea water and the cold deep water to operate a heat engine to produce mechanical work [7]. At present, no firm estimate can be given about the potential of this energy source [8].

The wave energy is induced by wind, thus, it's only a small proportion of the world's wind power potential, which is in turn, a small proportion of global solar power, making the wave energy more concentrated with an average power intensity of 2–3 kW/m^2 [9], [10]. The global power potential of waves that hits worldwide coasts has been estimated to be in order of 1 TW, and the global wave power in the open ocean was expected to be larger than 10 TW [10]. A system absorbing wave energy consists of a damped oscillator which interacts with the wave such as to reduce the amount of energy present in it [11].

The exploitable global tidal energy potential has been estimated to be larger than 100 GW [12], but only a small fraction of this potential can be harnessed. The technology used to extract such energy is similar to the one used in wind energy extraction systems due to the fact that the two sources are quite similar, since it's about a moving fluid.

III. TIDAL ENERGY

Tidal energy is mainly induced by gravitational interactions between the sun, the earth and the moon. Since the comportment of the sun and the moon is periodic and can be forecasted for decades, the tidal currents are also periodic and highly predictable with an accuracy up to 98% [1]. Some weather conditions can influence tidal currents, such as wind and swell.

According to their behaviour, the tidal currents are of two types, diurnal and semi diurnal. Semi diurnal tides have a period of 12h25mn, the amplitude of the tides being maximal at new and full moon, called spring tides, and the minimum occurs at the first and third quarter of the moon, and are called neap tides, thus the semi diurnal tides are dominated by lunar behaviour, while the diurnal tides depend on the declination of the moon in respect to the equator, the maximum tide currents occurs when the declination is at its maximum, this type of tides has a period of 24h50mn. Some sites can display a combination of diurnal and semi diurnal tides, creating a thirst type called mixed tides, like those observed in the Mediterranean sea [13]. Figure 1 shows an example of a shape of a semi diurnal tide.

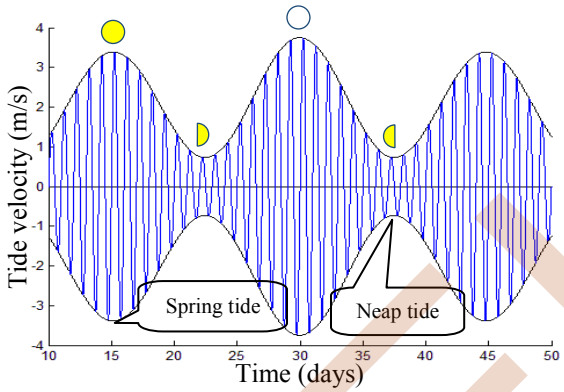

Figure 1 : Monthly cycle of semi diurnal tides.

A mathematical model describing the evolution of the tide velocity can be easily deduced, a first order model neglecting the effect of swell and wind is reported by [14].

IV. TIDAL ENERGY EXTRACTION SYSTEM

Despite of the differences between tidal currents and wind, extracting energy from these two sources follows the same philosophy, a turbine must be placed such to cross the current and connected to a generator which converts the kinetic motion into electricity which is in turn injected to the grid. Figure 2 shows a global scheme of this system.

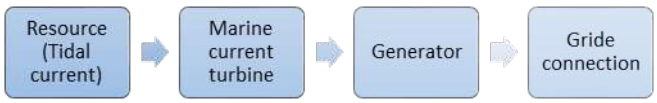

Figure 2 : Global schem of tidal energy extraction system

A. *Marine current turbine*

A marine current turbine (MCT) must be used to extract energy from tides, many topologies exist, but in final, they all have the same role, convert the kinetic motion of the current into a mechanical torque on a generator shaft.

The horizontal axis turbine (figure 3) is the most common turbine concept used in marine energy and wind energy conversion systems, the axis of the turbine is parallel to the current flow and uses the aerodynamic lift effect to operate, since it permits a higher efficiency (also called power coefficient) than devices using aerodynamic drag effect [15]. This type of turbines can either have a pitch variation system or not, omitting this mechanism will grant more reliability to the system minimizing the high cost maintenance needs, but will need the use of complex control systems for the electric generator and a yaw control mechanism to rotate the turbine in order to face the ebb and flood tides, but the turbines with pitch variation systems can be adjusted to harness power from both ebb and flood tides without changing the turbine direction.

Figure 3 : SeaGen horizontal axis turbine with pitch variation system

Unlike the horizontal axis turbine, the vertical axis turbine uses the aerodynamic drag effect to operate, the rotation axis is perpendicular to the current flow (figure 4), it has the advantage of being omnidirectional [16], meaning that the turbine can harvest tidal power regardless of current direction, so no rotation system is needed.

Figure 4: KOBOLD vertical axis turbine with floating platform

If the turbine is employed with a floating platform, the generator can be installed in the platform above sea level in an easily accessible place [16]. But this type of turbine suffers from a low efficiency compared to the horizontal axis turbine, since it works using the drag effect of the current like stated earlier.

The power coefficient of these two turbines can be improved by using a diffuser, it`s a concept taking advantage of the Venturi effect, which consists on accelerating the fluid in the neighborhood of the turbine, so more power can be extracted using the same turbine since the extracted power is proportional to the cube of the current velocity [17], [18]. A free flow horizontal axis turbine can reach a maximum power coefficient of 0.59 known as Betz limit, a duct design was developed by [19] that allows an horizontal axis turbine to overcome this limit and reach a maximum power coefficient of 0.75. Figure 5 shows a ducted horizontal and vertical axis turbines.

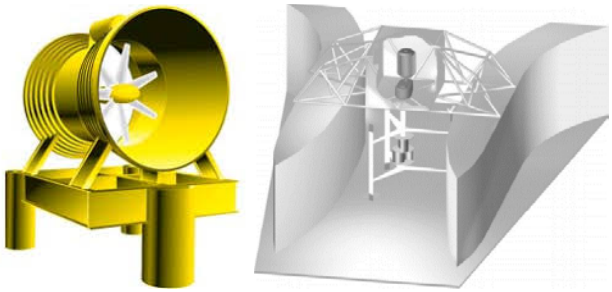

Figure 5 : Horizontal and vertical axis ducted turbines

The Stingray concept, illustrated by figure 6, is a non conventional turbine developed by Engineering Business, it consists of a hydroplane with a variable angle of attack, this variation is created by a mechanism. Using the hydrodynamic lift of the current causes the supporting arm to oscillate creating a linear motion, which is used to act a cylinder containing a high pressure oil which in turn drives a generator. Ref [20] reports a detailed analysis of an oscillating hydrofoil.

Figure 6 : The Stingray turbine

B. Electric generator

Many technologies suggested for tidal current energy extraction are based on that used for wind energy systems because of the similarities between the two domains [21]. The most used generator for wind turbines is the doubly fed induction generator (DFIG) since it offers a big advantage, the machine generated power is directly connected to the grid and only a small scale power converter is connected to the rotor circuit for the control purpose, thus, the high cost power converter which is used in other topologies to connect the machine to the grid is eliminated. But the speed range of this generator is limited to ±30% of its nominal speed, hence a gearbox must be used to connect the turbine to the generator. The gearbox ratio must be set to match the middle value of the turbine speed range with the machine nominal speed. Also the access to the machine rotor is allowed by using slip rings. All these mechanical items decrease the reliability of the system and increase the maintenance need, which is considered to be a key feature for marine turbine development [22], making the use of this generator in tidal energy systems long-term expensive. Many works are focusing on the DFIG for tidal power systems, ref [23] proposed a tidal power extraction system using a DFIG with a maximum power point tracking strategy, and [24] designed a nonlinear speed controller for DFIG to increase the generated power, therefore the efficiency of such system. Figure 7 shows a schematic of a marine energy extraction system topology using DFIG.

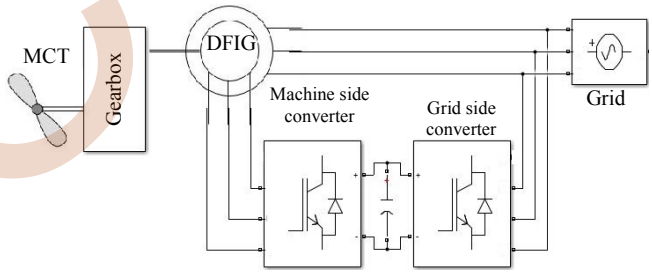

Figure 7 : Tidal power conversion system topology using a DFIG

Another technology used in renewable energy conversion systems is the permanent magnet synchronous generator (PMSG), the excitation is generated using permanent magnets so no rotor access is needed, and in case of use of a multipole machine, the gear box can be eliminated. It also offers a full range speed control. This machine is characterized by low maintenance level and high power density. But it also has its own disadvantages, in order to control the machine, a full scale power converter must be used to connect the stator to the grid, which may be expensive, and the use of permanent magnets grows up the cost of the machine. Figure 8 shows a schematic of a marine energy conversion system topology using a PMSG.

Most of works concerning tidal energy conversion are focusing on the use of PMSG, [25] designed and constructed a prototype of a PMSG which is tested with three different fixed

pitch horizontal axis turbines, and [26] designed and tested a 600 kW horizontal axis turbine coupled to a PMSG through a low transmission ratio gearbox. Also [27] realised a comparative study of sensor fault tolerant strategies performance for marine current turbines, this may increase the reliability of the system, therefore decrease system maintenance cost.

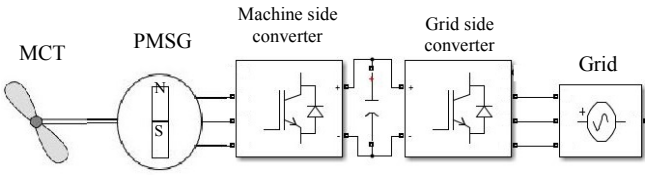

Figure 8 : Tidal power conversion system topology using a PMSG

In [28] a tidal current turbine driving either a DFIG or a PMSG was described, the stability tests shows the advantages of using a PMSG over the DFIG.

The rim tidal turbine is a non conventional generator structure proposed to extract tidal current energy. The turbine and the permanent magnet synchronous generator are combined into one structure. The permanent magnet rotor forms a ring around the tips of the turbine blades, and the stator is integrated into the turbine ducting [29]. This design can improve the system reliability and minimize the maintenance requirement. Figure 9 shows the Open Centre Turbine, a turbine constructed by the company OpenHydro which adopts the mentioned design.

Figure 9 : The Open Center Turbine

Adopting fault tolerant structures and strategies in tidal energy conversion systems is a key to push such technology ahead, since it permits the reduction of maintenance cost. The multiphase machines are one of these strategies, this machine can offer a continuous service even in case of loss of one or more phases but with a reduced power, thus reducing the maintenance need, or at least, postpone the maintenance operation in case of harsh weather conditions and give more time for a good intervention planning.

Ref [30] compared a three phase and a five phase PMSG fault tolerance performance in a marine current turbine, and concluded that the multiphase generator is a candidate of choice for marine energy applications even in healthy conditions compared to his three phase counterpart. In [31] the impact of a multi-star winding design of a permanent magnet synchronous generator on the reliability of a marine current turbine is studied, the results show that as the star number is increased, the reliability of the system is improved, and the three-star configuration seems to be a trade-off. A fault tolerant control strategy is proposed by [32] aiming to ensure a continuous and safe operation with minimum torque ripple under open circuit condition.

C. Power converter

Many converter topologies can be used in marine current turbines to control the power flow from the generator to the grid. The simplest topology is the two-level inverter (figure 10), it uses a minimum number of power switches (two per phase). The maximum power that can be converted is limited by the switches technology, thus, the converter cost grows up when the maximum supported power must be high.

The term "two-level" means that the output line voltage can only have two levels, +Vdc and –Vdc, where Vdc is the DC input voltage.

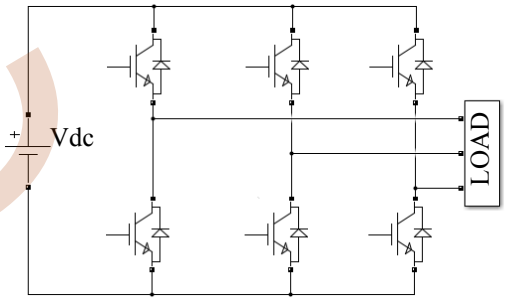

Figure 10 : Two level inverter

In case of a DC voltage exceeding the maximum voltage rating of the switches, this structure becomes useless, because of using multiple switches in series in order to get a higher total voltage rate, will result in unequal stress between the switches. The solution to this problem is the use of multilevel converter topologies [33].

In order to obtain a better power quality, reduced switches dimensions, and for high voltage applications, multi-level inverters are the key. In this kind of converters, each leg can generate at least three different output voltage levels. Principally, two multi-level topologies can be used in wind and tidal power conversion systems, neutral point clamped (NPC) and the flying capacitor (FC) structures.

The NPC structure, first developed by [34], consists on the use of multiple series connected capacitors in parallel to the DC source in order to subdivide the DC bus voltage into

required voltage levels [35], and multiple combined two-level converters interconnected with diodes with minor adjustments [36]. The number of required diodes is $(n-1)(n-2)$ (where n the number of output voltage levels) if the diodes voltage rating is the same as the power switches. This scheme allows obtaining more levels at the output voltage. Figure 11 represents a three level NPC inverter.

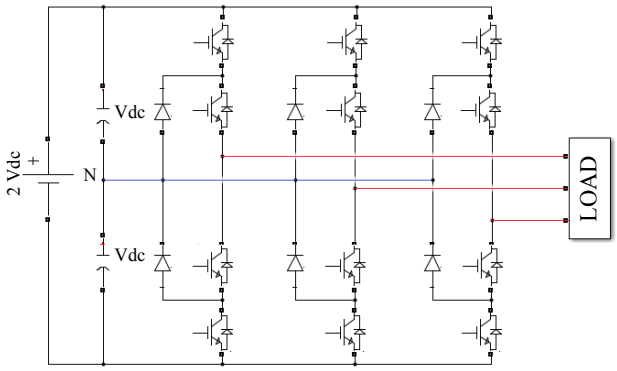

Figure 11 : Three-level NPC inverter

In [37], the two and three level inverter performances are compared, the inverters are used in a DTC scheme feeding an induction machine, the results show the superiority of the three level inverter in term of torque and current ripples.

Many recent works are focusing in the fault tolerant capability of the NPC structure. Effectively, the NPC structure combined with a proper control strategy can acquire a fault tolerant behaviour. Such control strategies were proposed by many researchers like [38] and [39].

Also, the integration of this type of converters in wind energy systems and other renewable energy sources has been studied, like done in [40] and [41].

The FC topology is similar to the NPC, since the diodes are replaced by capacitors, it was first developed by [42]. Figure 12 shows a three level FC inverter.

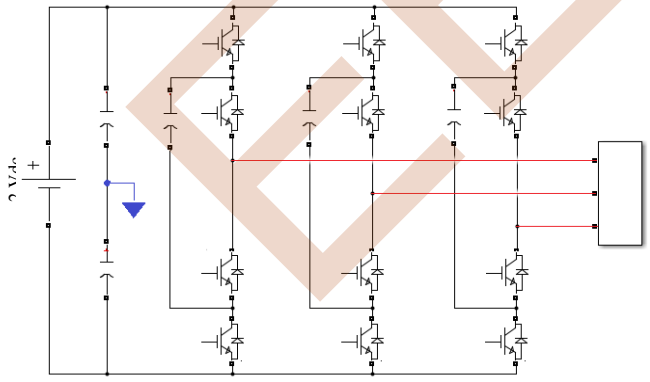

Figure 12 : Three-level FC inverter

According to [43], the NPC and FC structures presents the same characteristics in term of output voltage harmonic content. Another comparison reported by [44] shows that the FC converter suffers from high commutation losses compared to NPC, but the current across power switches is lesser. The main advantage of the FC topology compared to NPC is that the number of capacitors per phase in the FC structure is half the number of diodes per phase in the NPC structure.

Same as for the NPC topology, the FC structure can be used in a fault tolerant system as done by [45].

V. SUMMARY

This paper has reviewed a general state of art of marine tidal power extraction systems, every element in the conversion chain has been described and discussed, with a focus on different used technologies, and some recent works have been reported. Also, attempts have been made to highlight the major barriers for the development of this area, and some worldwide used solutions have been reported.

REFERENCES

[1] P. Meisen and T. Hammons, "Harnessing the untapped energy potential of the oceans: tidal, wave, currents and OTEC," in *IEEE Power Engineering Society General Meeting, 2005*, 2005, pp. 1853–1854.

[2] SIMEC Atlantis Energy, "Atlantis Successfully Decommissions 1.2 MW SeaGen Tidal System in Industry First," 2019. [Online]. Available: https://simecatlantis.com/2019/07/26/meygen-operational-update-3-2/. [Accessed: 24-Sep-2019].

[3] SIMEC Atlantis Energy, "MeyGen," 2016. [Online]. Available: https://simecatlantis.com/projects/meygen/. [Accessed: 24-Sep-2019].

[4] EMEC The European Marine Energy Center LTD, "OPEN HYDRO," 2019. [Online]. Available: http://www.emec.org.uk/about-us/our-tidal-clients/open-hydro/. [Accessed: 24-Sep-2019].

[5] Sabella, "SABELLA D10 - France," 2018. [Online]. Available: https://www.sabella.bzh/fr/les-projets/d10. [Accessed: 24-Sep-2019].

[6] Tethys, "Enermar Project," 2017. [Online]. Available: https://tethys.pnnl.gov/annex-iv-sites/enermar-project. [Accessed: 25-Sep-2019].

[7] M. Ravindran and Raju Abraham, "The Indian 1 MW demonstration OTEC plant and the development activities," in *Oceans '02 MTS/IEEE*, 2002, vol. 3, pp. 1622–1628.

[8] A. Hossain, A. Azhim, A. B. Jaafar, M. N. Musa, S. A. Zaki, and D. N. Fazreen, "Ocean thermal energy conversion: The promise of a clean future," in *2013 IEEE Conference on Clean Energy and Technology (CEAT)*, 2013, pp. 23–26.

[9] M. T. Pontes, L. Cavaleri, and D. Mollison, "Ocean Waves: Energy Resource Assessment," *Mar. Technol. Soc. J.*, vol. 36, no. 4, pp. 42–51, Dec. 2002.

[10] J. Falnes, "A review of wave-energy extraction," *Mar. Struct.*, vol. 20, no. 4, pp. 185–201, Oct. 2007.

[11] K. BUDAR and J. FALNES, "A resonant point absorber of ocean-wave power," *Nature*, vol. 256, no. 5517, pp. 478–479, Aug. 1975.

[12] M. Benbouzid *et al.*, "Concepts, Modélisation et Commandes des Hydroliennes. Energies Marines Renouvelables, Hermes Science Publications, pp.265-328, 2011. <hal-01090515>."

[13] T. J. Hammons, "Tidal power," *Proc. IEEE*, vol. 81, no. 3, pp. 419–433, Mar. 1993.

[14] S. E. Ben Elghali, R. Balme, K. Le Saux, M. El Hachemi Benbouzid, J. F. Charpentier, and F. Hauville, "A simulation model for the evaluation of the electrical power potential harnessed by a marine current turbine," *IEEE J. Ocean. Eng.*, vol. 32, no. 4, pp. 786–797, 2007.

[15] E. Hau, *Wind Turbines*, vol. 9783642271. Berlin, Heidelberg: Springer Berlin Heidelberg, 2013.

[16] S. Zanforlin, "Advantages of vertical axis tidal turbines set in close proximity: A comparative CFD investigation in the English Channel," *Ocean Eng.*, vol. 156, no. August 2017, pp. 358–372, May 2018.

[17] A. H. Elbatran, O. Yaakob, Y. Ahmed, and F. Abdallah, "Augmented Diffuser for Horizontal Axis Marine Current Turbine," *Int. J. Power Electron. Drive Syst.*, vol. 7, no. 1, p. 235, Mar. 2016.

[18] F. L. Ponta and P. M. Jacovkis, "Marine-current power generation by diffuser-augmented floating hydro-turbines," *Renew. Energy*, vol. 33, no. 4, pp. 665–673, Apr. 2008.

[19] R. Luquet, D. Bellevre, D. Fréchou, P. Perdon, and P. Guinard, "Design and model testing of an optimized ducted marine current turbine," *Int. J. Mar. Energy*, vol. 2, pp. 61–80, Jun. 2013.

[20] T. Kinsey and G. Dumas, "Testing and Analysis of an Oscillating Hydrofoils Turbine Concept," in *ASME 2010 3rd Joint US-European Fluids Engineering Summer Meeting: Volume 1, Symposia – Parts A, B, and C*, 2010, vol. 1, no. PARTS A, B AND C, pp. 9–22.

[21] S. E. Ben Elghali, M. E. H. Benbouzid, and J. F. Charpentier, "Marine Tidal Current Electric Power Generation Technology: State of the Art and Current Status," in *2007 IEEE International Electric Machines & Drives Conference*, 2007, vol. 2, pp. 1407–1412.

[22] A. . Bahaj and L. . Myers, "Fundamentals applicable to the utilisation of marine current turbines for energy production," *Renew. Energy*, vol. 28, no. 14, pp. 2205–2211, Nov. 2003.

[23] S. E. Ben Elghali, M. E. H. Benbouzid, and J.-F. Charpentier, "Modelling and control of a marine current turbine-driven doubly fed induction generator," *IET Renew. Power Gener.*, vol. 4, no. 1, p. 1, 2010.

[24] S. E. Ben Elghali, M. El Hachemi Benbouzid, T. Ahmed-Ali, and J. F. Charpentier, "High-Order Sliding Mode Control of a Marine Current Turbine Driven Doubly-Fed Induction Generator," *IEEE J. Ocean. Eng.*, vol. 35, no. 2, pp. 402–411, Apr. 2010.

[25] K. Yuen *et al.*, "Matching a Permanent Magnet Synchronous Generator to a Fixed Pitch Vertical Axis Turbine for Marine Current Energy Conversion," *IEEE J. Ocean. Eng.*, vol. 34, no. 1, pp. 24–31, Jan. 2009.

[26] Y. Li, H. Liu, Y. Lin, W. Li, and Y. Gu, "Design and test of a 600-kW horizontal-axis tidal current turbine," *Energy*, vol. 182, pp. 177–186, Sep. 2019.

[27] H.-T. Pham, J.-M. Bourgeot, and M. E. H. Benbouzid, "Comparative Investigations of Sensor Fault-Tolerant Control Strategies Performance for Marine Current Turbine Applications," *IEEE J. Ocean. Eng.*, vol. 43, no. 4, pp. 1024–1036, Oct. 2018.

[28] H. H. H. Aly, "Dynamic modeling and control of the tidal current turbine using DFIG and DDPMSG for power system stability analysis," *Int. J. Electr. Power Energy Syst.*, vol. 83, pp. 525–540, Dec. 2016.

[29] S. M. A. Sharkh, M. D, T. S.R, M. L, and B. A.S, "Performance of an integrated water turbine PM generator," in *International Conference on Power Electronics Machines and Drives*, 2002, vol. 2002, no. 487, pp. 486–491.

[30] F. Mekri, S. Ben Elghali, and M. E. H. Benbouzid, "Fault-Tolerant Control Performance Comparison of Three- and Five-Phase PMSG for Marine Current Turbine Applications," *IEEE Trans. Sustain. Energy*, vol. 4, no. 2, pp. 425–433, Apr. 2013.

[31] C. Olmi, F. Sculiller, and J.-F. Charpentier, "Impact of a multi-star winding on the reliability of a permanent magnet generator for marine current turbine," *Int. J. Mar. Energy*, vol. 19, pp. 319–331, Sep. 2017.

[32] H.-T. Pham, J.-M. Bourgeot, and M. Benbouzid, "Fault-tolerant model predictive control of 5-phase PMSG under an open-circuit phase fault condition for marine current applications," in *IECON 2016 - 42nd Annual Conference of the IEEE Industrial Electronics Society*, 2016, pp. 5760–5765.

[33] G. Séguier, F. Labrique, and P. Delarue, *Électronique de puissance: Structures, commandes, applications 10e édition*, Dunod. Paris, 2015.

[34] A. Nabae, I. Takahashi, and H. Akagi, "A New Neutral-Point-Clamped PWM Inverter," *IEEE Trans. Ind. Appl.*, vol. IA-17, no. 5, pp. 518–523, Sep. 1981.

[35] B. P. McGrath, D. G. Holmes, M. Manjrekar, and T. A. Lipo, "An improved modulation strategy for a hybrid multilevel inverter," in *Conference Record of the 2000 IEEE Industry Applications Conference. Thirty-Fifth IAS Annual Meeting and World Conference on Industrial Applications of Electrical Energy (Cat. No.00CH37129)*, 2000, vol. 4, pp. 2086–2093.

[36] J. Rodriguez *et al.*, "Multilevel Converters: An Enabling Technology for High-Power Applications," *Proc. IEEE*, vol. 97, no. 11, pp. 1786–1817, Nov. 2009.

[37] E. P. Sarika and R. S. P. Raj, "Performance comparison of direct torque control of two level and three level neutral point clamped inverter fed three phase induction motor," in *2014 International Conference on Advances in Green Energy (ICAGE)*, 2014, no. December, pp. 179–183.

[38] H. Ben Abdelghani and A. B. Ben Abdelghani, "Fault tolerant SVM strategy for 3-level NPC inverter," in *Eighth International Multi-Conference on Systems, Signals & Devices*, 2011, no. 1, pp. 1–6.

[39] A. Joseph, Y. Bak, S. S. Lee, and K. Lee, "Fault-Tolerant and Reconfiguration Control for Boost Multi-level NPC Converter Fed Doubly Fed Induction Machines," in *2019 10th International Conference on Power Electronics and ECCE Asia (ICPE 2019 - ECCE Asia)*, 2019, pp. 2466–2472.

[40] R. Kumar, S. Kumar, N. Singh, and V. Agrawal, "SEPIC converter with 3-level NPC multi-level inverter for wind energy system (WES)," in *2017 4th International Conference on Power, Control & Embedded Systems (ICPCES)*, 2017, vol. 2017-Janua, pp. 1–6.

[41] R. L. Mathew and K. S. Jiji, "A three level neutral point clamped Inverter with buck-boost capability for renewable energy sources," in *International Conference on Sustainable Energy and Intelligent Systems (SEISCON 2011)*, 2011, vol. 2011, no. 583 CP, pp. 201–206.

[42] T. A. Meynard and H. Foch, "Multi-level conversion: high voltage choppers and voltage-source inverters," in *PESC `92 Record. 23rd Annual IEEE Power Electronics Specialists Conference*, 1992, pp. 397–403.

[43] A. Prayag and S. Bodkhe, "A comparative analysis of classical three phase multilevel (five level) inverter topologies," in *2016 IEEE 1st International Conference on Power Electronics, Intelligent Control and Energy Systems (ICPEICES)*, 2016, pp. 1–5.

[44] R. TROUDI, S. MOREAU, G. CHAMPENOIS, M. BOUZID, and K. JELASSI, "A Comparative Study of Three Classic Five-Level Inverters Connected to the Power Grid," in *2019 10th International Renewable Energy Congress (IREC)*, 2019, pp. 1–6.

[45] H. Wang, H. Li, C. Yan, and D. Xu, "A Short-Circuit Fault-Tolerant Strategy for Three-Phase Four-Wire Flying Capacitor Three-Level Inverters," in *2019 IEEE 10th International Symposium on Power Electronics for Distributed Generation Systems (PEDG)*, 2019, no. 51777189, pp. 781–786.

Finite Element Analysis of Induction Motor under open Phase Fault

Bouheraoua Mustapha
Department of Electrical Ingineering Advanced Technology Laboratory (LATAGE)
University Mouloud Mammeri
Tizi-ouzou,Algeria
bouheraoua@hotmail.com

Atig Mahdi
Department of Electrical Ingineering Advanced Technology Laboratory (LATAGE)
University Mouloud Mammeri
Tizi-ouzou,Algeria
Mahdiatig36@yahoo.fr

***Abstract*— The open phase fault is much specified in three–phase squirrel cage induction motors. However, this defect develops an unsymmetrical magnetism generates noise and vibration in the motor. Finite Element Method (FEM) is the most accurate technique to analyze the induction motor, because it can include all actual characteristics of both healthy and faulty conditions. In this paper, an FEM to analyze a 2.2 kW three–phase squirrel cage induction motor with the open phase fault is proposed. An experimental investigation to display the stator current waveforms with healthy and faulty conditions are obtained and compared under different load operations. The currents obtained are introduced into FEM analysis, which is used for magnetic field calculation and the magnetic flux density in the air-gap, stator teeth and in the stator yoke for both healthy and faulty operations.**

I. INTRODUCTION

Induction machines are widely used in the industry, thanks to their low cost, reasonable size and low maintenance. But, these machines are subject to a variety of defects such as the open phase fault which leads to asymmetry of the machine. Indeed, the open phase faults disturb motor operation and shorten its lifetime. But, diagnosis and detection of this fault can preserve good motor performance and lifetime [1]. Therefore, a proper modeling of the induction motor with open phase fault is the first step in the development of fault diagnosis and fault tolerant machine design. For that, during the last years, several investigations of induction motor defect have been presented in the literature. The fault study of electrical machines can be operated either by experimental tests, or computer-based analysis.

Obviously, studying faults in induction machines by numerical models enables correct evaluation of data produced by diagnostic techniques [2]. However, the most used method to model electrical machines, especially under fault conditions is the Finite Element Method (FEM). FEMs are based on the magnetic field distribution, which gives more precise information about the motor; indeed both consider the complicated non-linear behavior of the motor, and the spatial harmonic effects [3-4]. For example, research [5-6], presented the application of an FEM to predict the performance of induction motors having electric and magnetic asymmetry of the rotor cage due to some broken rotor bars. However, propagation of broken rotor bar defects and their influence on the magnetic flux density distribution of the machine cage were observed. In addition, the study reported in papers [7,8], investigated different improved methods for broken rotor bar detection in a squirrel-cage induction motor. Moreover, the works presented in research [9,10], focused on the application of an FEM to predict the performance of an induction motor with broken rotor bar and an inter-turn short circuit in the stator winding. In reference [11], a time-stepping FEM that identifies mixed eccentricity by analysis, without direct access to the motor, has been proposed. This method simulates the spectrum of the line current of a production-line motor and compares it to the spectrum of a known healthy motor, to detect eccentricity. On the other hand and out of these defects, the open phase fault is much noted in induction motors. For example, L. Alberti and N. Bianchi [12], proposed a set of experimental tests of a dual three-phase induction motor. In this paper, different winding configurations have been studied and compared in cases of both open-circuit and short-circuit faults. Moreover, in references [13,14], the authors have dealt with the modeling of a three-phase induction motor under open-phase fault using the Matlab/Simulink implementation.The aim of our research is to develop a thermal model of the 2.2 kW three–phase squirrel cage induction motor, with an open phase fault, to validate the experimental results obtained in paper [15]. But, before proposing the heat study, it is important to provide and investigate the electromagnetic performance of the machine. However, in this paper, an FEM analysis of the motor is established to simulate the flux density distribution of the induction motor for healthy and faulty operations.

II. MAXWELL'S EQUATION

In order to study the electromagnetic behaviour of the induction motor, the FEMM (Finite Element Method Magnetics) package software is used, which addresses some limited cases of Maxwell's equations [16]. However, these equations describe the relationships between the electric field intensity E [V/m], the field intensity H [A/m], the electric flux density D [C/m2] and flux density B [T].

$$\nabla \times E = -\frac{\partial B}{\partial t} \quad (1)$$

$$\nabla \times H = J \quad (2)$$

$$\nabla \cdot D = \rho \quad (3)$$

$$\nabla \cdot B = 0 \quad (4)$$

Where J [A/m2] and ρ [C/m3] represent source current density and charge density respectively. Moreover, Maxwell equations have to be subject to a constitutive relationship between B and H for each material.

$$B = \mu H \quad (5)$$

On the other hand, electric flux density and electric field intensity are related to one another via the constitutive relationship.

$$D = \varepsilon E \quad (6)$$

Where μ [H/m] and ε [F/m] are the permeability and the permittivity of the materials.

The flux density is computed by means of the magnetic vector potential, A [Tm], which, is written in terms of the vector potential, A, as:

$$B = \nabla \times A \quad (7)$$

Finally, this definition of B always satisfies equation (4). Equation (2) can be rewritten for magneto-static problems in which the fields are time-invariant, as:

$$\nabla \times \left(\frac{1}{\mu(B)} \nabla \times A \right) = J \quad (8)$$

If the magnetic field is time-varying, eddy currents can be induced in materials with the presence of electric conductivity σ. In this case, other Maxwell equations related to the electric field distribution must be accommodated. The relation between the electric field intensity E and the current density is as follow.

$$J = \sigma E \quad (9)$$

III. INDUCTION MOTOR MODEL

Fig. 1 shows the machine studied in this paper with the dimensions and characteristics given in Table I [17].

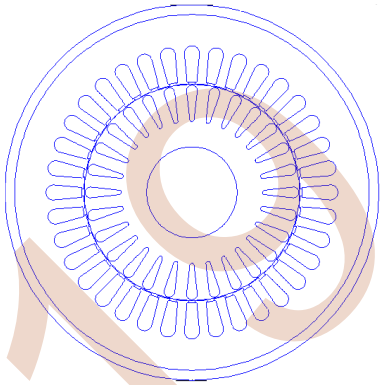

Figure 1. 2D simulation model of induction motor

Table I. Dimensions and Motor characteristics

parameters	Value
Stator outer diameter [mm]	145
Stator inner diameter [mm]	88.5
Axial Length [mm]	110
Rotor outer diameter	88
Air-gap length [mm]	0.25
Power [kW]	2.2
Voltage [V]	380
Current [A]	5.2
Speed [/min]	1420
Frequency [Hz]	50
Insulation Class	F
Connection	Delta

IV. ELECTROMAGNETIC FIELD ANALYSIS

To simulate the electromagnetic performance of the induction motor with and without defect, a test bench has been realized as shown in Figure 2. The aim of this test is to display the new stator currents waveforms which are recorded by using an oscilloscope of the coils I1, I2 and I3, for both healthy and faulty operations under different loads, then the currents obtained are introduced in the FEM analysis. The experimental test rig is composed of a 2.2 kW three phase induction motor. The machine is mechanically coupled to a separately excited DC machine for loading processes. Moreover, the temperatures are controlled using thermocouples. Indeed, the thermal experimental results obtained under open phase fault are reported in paper [15].

Figure 2. Motor during the experimental tests.

A. *load of 5.4 Nm*

To avoid exceeding the rated values of the motor with an open-phase fault, we will gradually increase the load on the machine. Initially, we will impose a load of 5.4 Nm. The current waveforms of the phases I1, I2 and I3 obtained under open-phase fault are shown in Figure 3. However, if a balanced induction motor is fed from a balanced three-phase power system, peak value of the motor current is approximately 2.9 A. On the other hand, the presence of the defect creates a remarkable imbalance in the machine. It is found that peak stator currents I1, I2 and I3 become respectively 2.6 A, 4.7 A and 2.6 A. So, we can note that the results obtained from the test are as expected because in our motor the windings are coupled in delta configuration and in the presence of the open-phase fault, thus we will have two coils with equal currents, in parallel with the third coil. The insertion of the new instantaneous stator currents into the numerical model, gives a new distribution of flux density in the induction motor. However, Figures 4 and 5 show the 2D FEM of flux density distribution for both healthy and faulty operations. In addition, Figure 6 shows the magnetic flux density in the air-gap, the stator teeth and the stator yoke respectively with and without the open phase fault.

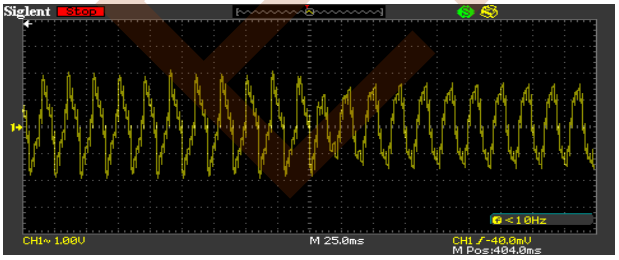

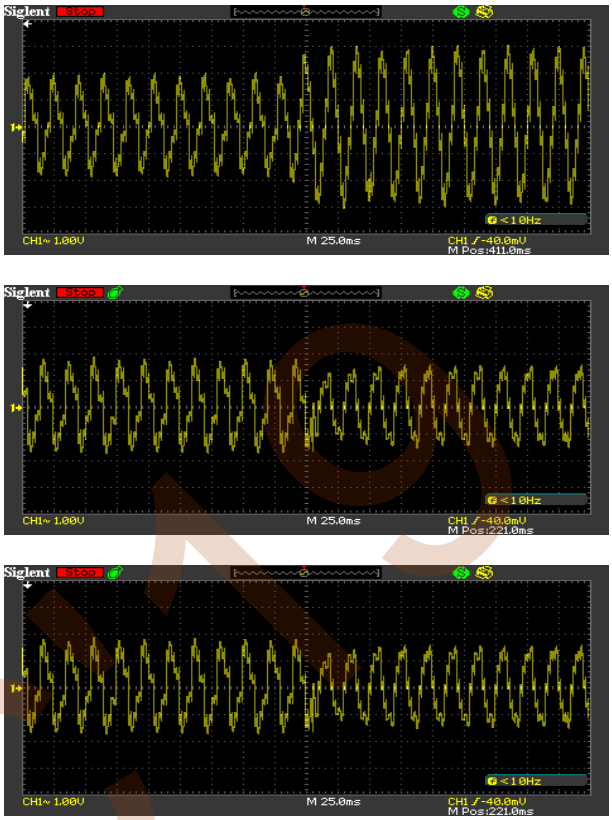

Figure 3. The currents I1, I2 and I3 waveforms with a load of 5.4 Nm for healthy and faulty operating conditions

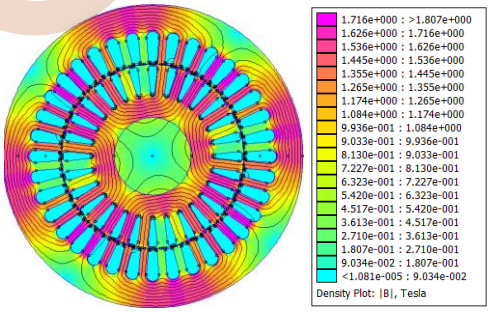

Figure 4. Flux density distribution of the motor with a load of 5.4 Nm for healthy operation

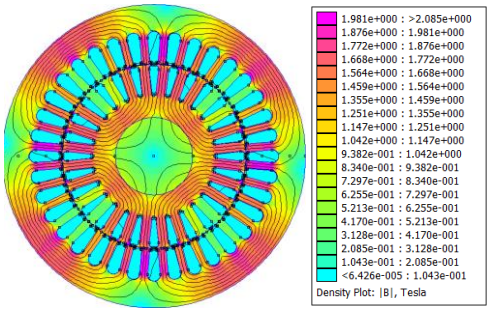

Figure 5. Flux density distribution of the motor with a load of 5.4 Nm for faulty operation

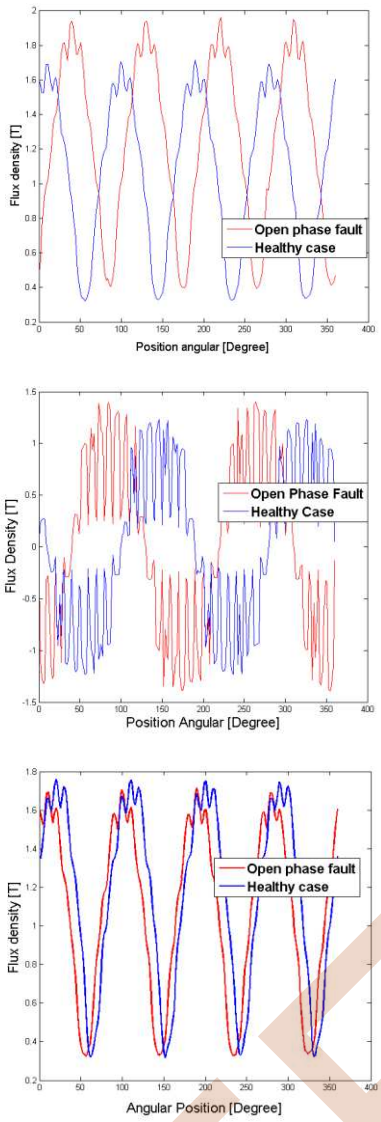

Figure 6.. Flux density distribution with a load of 5.4 Nm under healthy and faulty operations, a) stator teeth, b) Air_gap, c) stator yoke

B. load of 9.1 Nm

In this part, the test undertaken is the same as that of 5.4 Nm. Indeed, the current waveforms of coils I1, I2 and I3 obtained with and without the defect, are shown in Figure 7. However, for healthy operation the peak current measured before the apparition of the fault is about 3.2 A. On another side the open-phase fault causes current imbalance in a similar manner with the above test giving 3.1 A, 6 A and 3.1 A approximately. Furthermore, the new distributions of flux density in the induction motor and of magnetic flux density in the air-gap, the stator teeth and the stator yoke with and without the open phase fault are shown in Figures 8, 9 and 10 respectively.

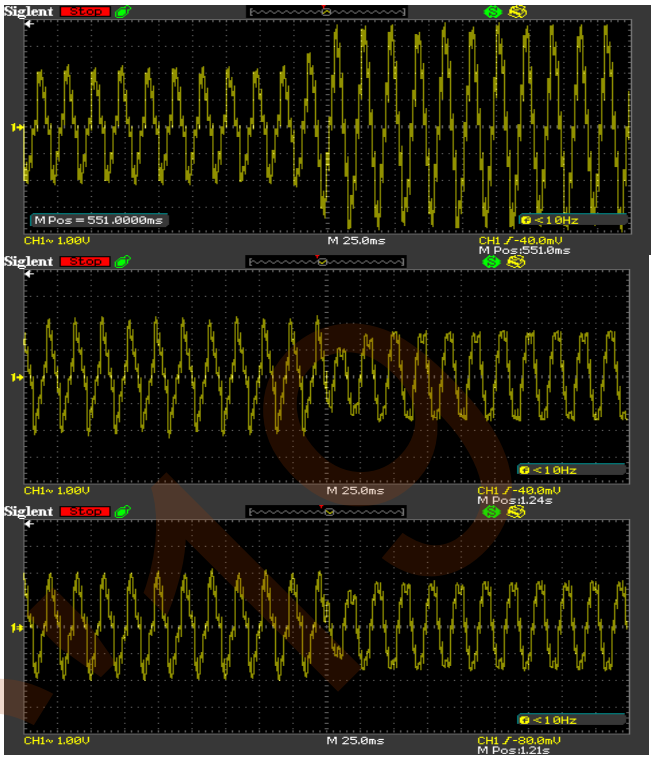

Figure 7. The currents I1, I2 and I3 waveforms with a load of 9.1 Nm for healthy and faulty operating conditions

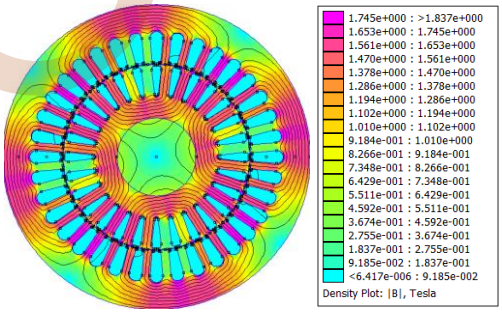

Figure 8. Flux density distribution of the motor with a load of 9.1 Nm for healthy operation

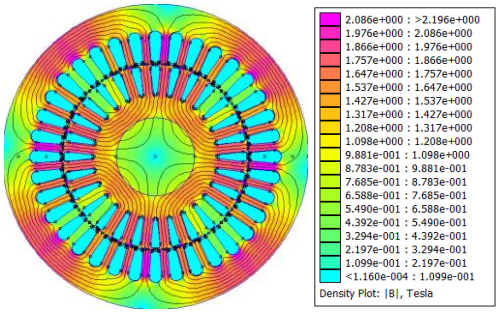

Figure 9. Flux density distribution of the motor with a load of 9.1 Nm for faulty operation.

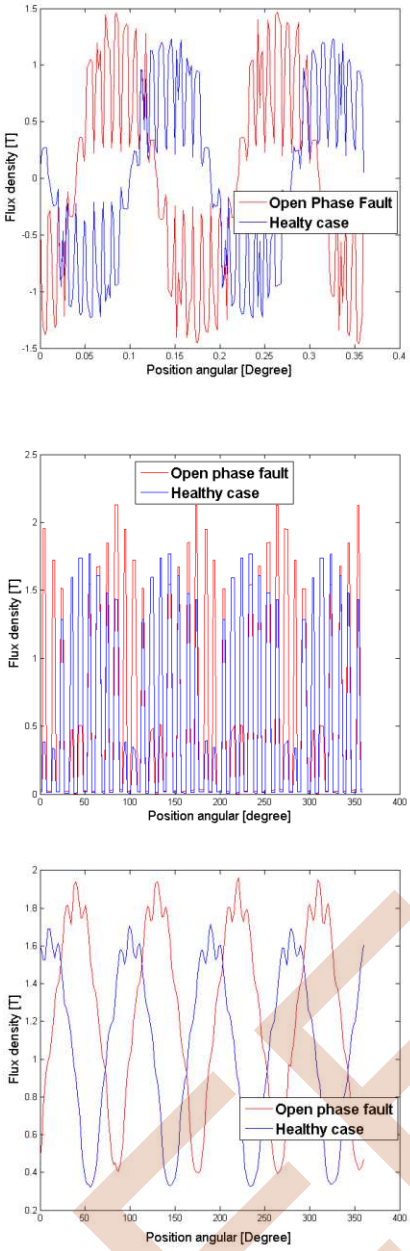

Figure 10. Flux density distribution with a load of 9.1 Nm under healthy and faulty operations, a) air gap, b) stator teeth, c) stator yoke

V. DISCUSSION

The results obtained in this investigation, present the influence of the open-phase fault in induction motor behaviour. However, from the tests presented with a load of 5.4 Nm and 9.1 Nm, the new current waveforms obtained indicated that the power input is more significant, which consequently causes a redistribution of the rises in the temperatures of the motor [15]. In addition, the simulation results obtained by FEM indicated that maximum values of the motor flux density distribution with a load of 5.4 Nm are about 1.807 T and 2.085 T, for healthy and faulty operations respectively, therefore increase of 15%. On the other hand, the results obtained with a load of 9.1 Nm, indicated that the flux density becomes 1.837 T, before the apparition of the fault and 2.196 T when one phase is opened. Consequently, the increase in flux density distribution is about 19 % on this test. Moreover, if we compare the results obtained from the test with a load of 9.1 Nm on a test at full load, we note an increase by 13 % of the maximum flux density values. Since the rated load of the machine is about 15 Nm, it is clear that the open-phase fault at full load becomes impossible, because the temperatures will exceed the rated values of the motor. In addition, the air-gap magnetic flux density is a straightforward indicator of the induction motor magnetic performance where all the changes are directly reflected. Figures 6 and 10 illustrate the comparisons of flux density distribution in the air-gap, stator teeth and stator yoke for healthy and faulty operations. From the results obtained, we find that the flux density waveforms are delayed by $\pi/3$. Moreover, the maximum flux density comparison between healthy and faulty conditions under different loads is presented in Table II.

Table II. Flux density comparison [Tesla]

		Air gap	teeth	Stator yoke
A load of 15 Nm	Healthy operation	1.35	1.88	1.82
	Faulty operation	-	-	-
	Difference %	-	-	-
A load of 9.1 Nm	Healthy operation	1.28	1.79	1.73
	Faulty operation	1.47	2.13	1.98
	Difference %	14	18	14
A load of 5.4 Nm	Healthy operation	1.46	1.76	1.69
	Faulty operation	1.40	2.02	1.83
	Difference %	11	14	8

VI. CONCLUSION

This paper, established a test bench of a delta connected induction motor, in order to display the stator current waveforms with and without the open-phase fault, then the current obtained is introduced into the FEM. However, to not exceed the rated values of the induction motor, a test bench with a full load has been presented. Then, the influence of the open-phase defect on motor behaviour is shown, for two load conditions. Indeed, the results show that the electromagnetic analysis is capable of providing an understanding of failure mechanisms of induction motors and also providing a guide to develop monitoring technologies for detecting induction motor faults. In addition, from the simulation results, we can deduce losses to introduce in the thermal model, and the heat study can be carried out.

REFERENCES

[1] J. Faiz, B. M. Ebrahimi & M. B. B. Sharifian, Time stepping finite element analysis of broken bars fault in a three-phase squirrel-cage induction motor, *Progress In Electromagnetics Research*, Vol. 68, pp. 53-70,2007.

[2] B. Vaseghi, N. Takorabet & F. Meibody-Tabar, Transient finite element analysis of induction machines with stator winding turn fault, *Progress In Electromagnetics Research*, Vol. 95, pp. 1-18, 2009.

[3] J. F. Watson & D. G. Dorrell, The use of finite element methods to improve techniques for the early detection of faults in 3-phase induction motors, *IEEE Transactions on Energy Conversion*, Vol. 14, No. 3, pp. 655-660, 1999.

[4] T. H.,P. F. Wendling, S. J. Salon & H. Acikgoz, Transient finite element analysis for an induction motor with external circuit connections and electromechanical coupling, *IEEE Transactions on EnergyConversion*, Vol. 14, No, 4, pp. 1407-1412, 1999

[5] K. Boughrara, N. Takorabet, R. Ibtiouen, O. Touhami & F. Dubas, Analytical analysis of cage rotor induction motors in healthy, defective, and broken bars conditions, *IEEE Transactions on Magnetics*, Vol. 51, No. 2, pp. 1-17, 2015.

[6] D. G. Jerkan, D. D. Reljic & D. Marcetic. Broken rotor bar fault detection of IM based on the countercurrent braking method, *IEEE Transactions on Energy Conversion*, Vol. 32, No. 4, pp. 1356-1366, 2017.

[7] N. Halem, S. E. Zouzou, K. Srairi & K. N. Gyftakis, FEM analysis for comparative investigation of the stator circuit connexion impact on the induction motor broken bar fault higher order signatures, *International Journal on Electrical Engineering and Informatics*, Vol. 8, No. 4, pp. 739-752, 2016.

[8] T. Vaimann, A. Belahcen & A. Kallaste, Changing of magnetic flux density distribution in a squirrel-cage induction motor with broken rotor bars, *Elektronika ir Elektrotechnika*, Vol. 20, No. 7, pp. 11-14, 2014.

[9] W. Zaabi, Y. Bensalem & H. Trabelsi, Fault analysis of induction machine using finite element method (FEM), *Sciences and Techniques of Automatic Control and Computer Engineering (STA), 2014 15th International Conference on. IEEE*, pp. 388-393, 2014.

[10] M. F. Far, A. Arkkio & J. Roivainen, Electrical fault diagnosis for an induction motor using an electromechanical FE model, *Electrical Machines (ICEM), 2014 International Conference on. IEEE*, pp. 1881-1887, 2014.

[11] J. Faiz, B. M. Ebrahimi, B. Akin & H. A. Toliyat, Finite-element transient analysis of induction motors under mixed eccentricity fault, *IEEE transactions on magnetics*, Vol. 44, No. 1, pp. 66-74, 2008.

[12] L. Alberti & N. Bianchi, Experimental tests of dual three-phase induction motor under faulty operating condition, *IEEE Transactions on Industrial Electronics*, Vol. 59, No. 5, pp. 2041-2048, 2012.

[13] M. Jannati & T. Sutikno, Modelling of a 3-phase induction motor under open-phase fault using Matlab/Simulink, *International Journal of Power Electronics and Drive Systems (IJPEDS)*, Vol. 7, No. 4, pp. 1146-1152, 2016.

[14] M. Jannati, T. Sutikno, N. R. N. Idris & M. J. Abdul Aziz, Modeling of balanced and unbalanced threephase induction motor under balanced and unbalanced supply based on winding function method, *International Journal of Electrical and Computer Engineering (IJECE)*, Vol. 5, No. 4, pp. 644-655, 2015

[15] M. Atig, M. Bouheraoua & A. Fekik, An experimental investigation of heating in induction motor under open phase fault, *International Journal of Electrical and Computer Engineering (IJECE)*, Vol. 8, No3, 2018.

[16] D. Meeker, Finite Element Method Magnetics, *User's Manual Version 4.2*, 2015.

[17] ELECTRO-INDUSTRIES,'' Company specialized in manufacturing and marketing motors'', Azazga,Algeria.

New Analytical model for PMSM Analysis Considiring Finite Soft-Magnetic Material Permeability

B. Ladghem Chikouche
Département de Génie Electrique, Faculté de Technologie, Université Md Boudiaf, BP 166 Ichbelia, M'sila, Algeria
brahim.Lch@univ-msila.dz

***Abstract*—This paper deals with the influence of magnetic finite permeability of iron core on machine's parameters of a surface mounted permanent magnet synchronous machine. On the open circuit, two-dimensional field distributions produced by permanent magnets synchronous machine (PMSM) are obtained in analytical approach forms by taking into account the relative permeability value of a ferromagnetic rotor and stator core. The analytical solution is derived by solving the field governing equations in each subdomain and with applying the boundary and interfaces conditions. Analytical results are validated by the finite-element analysis(FEA).**

1. INTRODUCTION

New features proposed in various systems of electromechanical engineering made those electrical machines cannot satisfy the increasing requests of electrical energy. Many industrial applications require high performance electrical drive systems. Among three-phase ac machines, permanent magnet synchronous machines (PMSMs) are very popular. Along the past several years, most of works have been based on the standard model where the magnetic characteristic is described by a linear relation. Numerous researches have been carried out in order to investigate the influence of the magnetic saturation on permanent magnet synchronous machine parameters, such as PM flux-linkage, armature flux, inductance, back-EMF, cogging torque and torque ripples. Electromagnetic vibration and noise are one of the problems of the PMSM. It is associated with parasitic effects due to higher space and time harmonics, eccentricity, phase unbalance, slot openings, magnetic saturation, and magnetostrictive expansion of the core laminations. Generally, the generated electrical torque and EMF of the permanent magnet synchronous machine are nonlinear functions. Many different methods have been developed for the design and analysis of electric machines, but assumptions were done in all the cases [1-2]. Magnetic equivalent circuit (MEC) and lumped parameter models are one of the design methods of PMSM and it is generally used for characteristics analysis [3-8]. Generally, accurate modeling of electric machines requires the use of finiteelement analysis, it is one of the most suitable methods for numerically solving magnetic saturation problem; however, the disadvantage of this method is the associated long computation time especially when attempting to get high accuracy results. The analytical calculation of the machines which present complex geometries is a very difficult task because of its inhomogeneous regions leading to a high number of boundary conditions. The stator slotting effect should be considered accurately to predict the magnetic field distribution in the air-gap region of permanent-magnet (PM) motors. A high number of regions can increase the number of equations to be solved and, consequently, the computing times become very long even by using powerful software packages. In all circumstances, the analytical method is the favorite one for the electrical machines design optimization.

In this research, it is attempted to develop an approach to determine the finite permeability effect of iron core on the parameters of permanent magnet synchronous machine. This approach is based on the analytical method by the subdomain method [9-10]. An investigation is done in order to represent the finite permeability effect on the component of flux density in the middle of airgap. Analytical results are validated by finite-element analysis (FEA).

2. ANALYTICAL SOLUTION OF MAGNETIC FIELD IN THE DIFFERENT SUBDOMAINS

In this paper, an analytical solution approach of magnetic field distribution based on subdomain method in Surface-Mounted PM motors is presented. The subdomain method consists in solving directly Maxwell's equations in different subdomains, i.e., air-gap, stator slots and magnets by employing the method of variables separation. The magnetic field distribution is obtained in each region by using boundary and interface conditions.

Some assumptions are made in the paper to simplify the problem as follows:

1. Permeability of stator/rotor iron is different to infinity;
2. The stator and rotor slots have radial sides;
3. End effects are negligible;

4. Magnet material is nonconductive;
5. Magnetization is radial;
6. Demagnetization characteristics of magnet are linear.

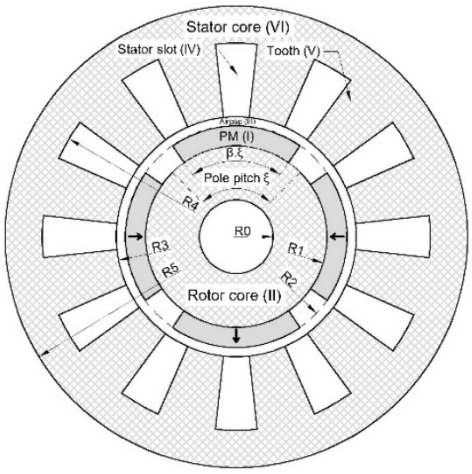

Figure 1. Surface-mounted PM machine.

3. CALCULATION OF MAGNETIC VECTOR USING SUBDOMAIN METHOD

The machine is constituted by six regions Fig.1. The first one contains the permanent magnets, which results in the resolution of Poisson's equation in polar coordinates. The machine will be studied in no-load operating conditions. For this, the calculation of the field distribution in other regions such as the air-gap, rotor core and stator core will be achieved by solving Laplace's equations.

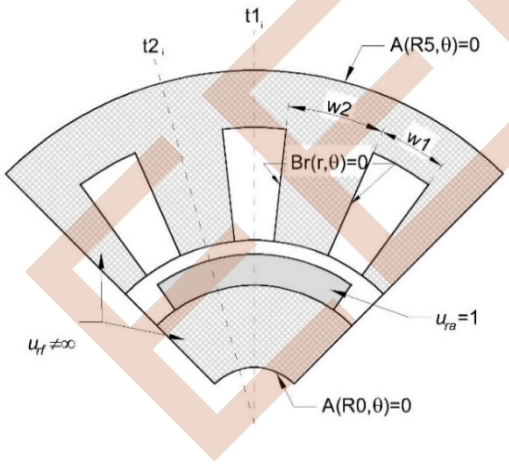

Figure. 2. Representation of different condition boundary.

The general expressions of the vector potential distribution in polar coordinates can be expressed by:

3.1. Magnetic Field in Region I

The Poisson's equation in subdomain region I where the relative recoil permeability is equal to 1 is given by:

$$\frac{\partial^2 A^I(r,\theta)}{\partial r^2}+\frac{1}{r}\frac{\partial A^I(r,\theta)}{\partial r}+\frac{1}{r^2}\frac{\partial^2 A^I(r,\theta)}{\partial \theta^2}=-\frac{\mu_0}{r}\left(M_\theta(\theta)-\frac{\partial M_r(\theta)}{\partial \theta}\right) \quad (1)$$

μ_0 is the permeability of vacuum. The relative permeability of permanent magnet μ_{ra} is equal to unity.
The radial and circumferential magnetization in region I is given according to Fourier series expansion as:

$$M_\theta(\theta)=0 \quad (2)$$

$$M_r(\theta)=\sum_{n=1}^{nh}\left(Mrs_n cos(np\theta)+Mrc_n sin(np\theta)\right) \quad (3)$$

where

$$Mrs_n=-\frac{4B_{rm}}{n\pi}\sin\left(\frac{n\pi}{2}\right)sin\left(\frac{n\pi\beta}{2}\right)sin\left(\frac{n\tau}{2}\right) \quad (4)$$

$$Mrc_n=-\frac{4B_{rm}}{n\pi}\sin\left(\frac{n\pi}{2}\right)sin\left(\frac{n\pi\beta}{2}\right)cos\left(\frac{n\tau}{2}\right) \quad (5)$$

B_{rm}, τ, β are respectively magnet remanence, the relative angular position between the PM and the origin of axis and magnet arc to pole pitch ratio. Mrs_n and Mrc_n are the nth element of the radial component Mr of magnet.
The radial and circumferential flux densities in all regions are deduced from the magnetic vector potential by

$$B_r(r,\theta)=\frac{1}{r}\frac{\partial A(r,\theta)}{\partial \theta} \quad (6)$$

$$B_\theta(r,\theta)=-\frac{\partial A(r,\theta)}{\partial r} \quad (7)$$

3.2. Magnetic Field in the Regions II, III, IV,V and VI

The machine will be studied in no-load operating condition. For this, the calculation of the field distribution in other regions such as the air-gap or stator slots will be achieved by solving Laplace's equations:

$$\frac{\partial^2 A^{II..VI}(r,\theta)}{\partial r^2}+\frac{1}{r}\frac{\partial A^{II..VI}(r,\theta)}{\partial r}+\frac{1}{r^2}\frac{\partial^2 A^{II..VI}(r,\theta)}{\partial \theta^2}=0 \quad (8)$$

Solving Laplace equation is usually achieved by exploiting the principle of Euler-Cauchy and Sturm-Liouville, while solving Poisson equation is solved by the method of Green [11]. The solution of magnetic vector potential in the region I can be written as in expression (9).

$$A^I(r,\theta)=\sum_{n=1}^{nh}\left(C_{3n}^I r^{np}+C_{4n}^I r^{-np}+\Gamma_s(r)\right)sin(np\theta)+\sum_{n=1}^{nh}\left(C_{5n}^I r^{np}+C_{6n}^I r^{-np}+\Gamma_c(r)\right)cos(np\theta) \quad (9)$$

where

$$\Gamma_s(r)=\begin{cases}+\dfrac{np.Mrs_n}{(np)^2-1} & if\ np\neq 1\\ +\dfrac{Mrs_1}{2}r.ln(r) & if\ np=1\end{cases} \quad (10)$$

$$\Gamma_c(r) = \begin{cases} -\dfrac{np.Mrc_n}{(np)^2-1} & if\ np \neq 1 \\ -\dfrac{Mrc_1}{2} r.ln(r) & if\ np = 1 \end{cases} \quad (11)$$

The solution of magnetic vector magnetic potential in the region II, III, and VI taking into account the periodicity condition at 2π/p is given by:

$$A^{II,III,VI}(r,\theta) = \sum_{n=1}^{nh} \left(C_{3n}^{II,III,VI} r^{np} + C_{4n}^{II,III,VI} r^{-np}\right) sin(np\theta) + \sum_{n=1}^{nh} \left(C_{5n}^{II,III,VI} r^{np} + C_{6n}^{II,III,VI} r^{-np}\right) cos(np\theta) \quad (12)$$

Most studies done on the permanent magnet synchronous machine suppose that the permeability of rotor and stator iron core is assumed to be equal to infinity The radial flux density in the sides of each slot must be equal to zero. Fig. 2 shows the conditions of the radial flux density in the positions $\theta = t1_i \pm w1/2$. In this present work, we are going to keep this assumption whatever the value of the permeability of iron core. This assumption is justified by the distance between two adjacent slots where should be acceptable.

In the region IV and V, the solution of magnetic vector potential taking into account the assumption (13) and (15) can be written as in expression (14) and (16):

$$B_{ri}^{IV}(r,\theta) = 0|^{t1_i \pm w1/2} \quad (13)$$

$$A^{IV}(r,\theta) = C_{i1}^{IV} \ln(r) + C_{i2}^{IV} + \sum_{n=1}^{nh} \left(C_{i3n}^{IV} r^{\frac{m\pi}{w1}} + C_{i4n}^{IV} r^{-\frac{m\pi}{w1}}\right) cos\left(\frac{m\pi}{w1}(\theta - t1_i + w1/2)\right) \quad (14)$$

$$B_{ri}^{V}(r,\theta) = 0|^{t2_i \pm w2/2} \quad (15)$$

$$A^{V}(r,\theta) = C_{i1}^{V} \ln(r) + C_{i2}^{V} + \sum_{n=1}^{nh} \left(C_{i3n}^{V} r^{\frac{m\pi}{w2}} + C_{i4n}^{V} r^{-\frac{m\pi}{w2}}\right) cos\left(\frac{m\pi}{w2}(\theta - t2_i + w2/2)\right) \quad (16)$$

In order to give the final solution of the different Equations (9), (12), (14) and (16), the constants $C^{I..IV}$ should be determined by applying interface conditions (these interface conditions must satisfy the continuity of the radial component of the flux density and the continuity of the circumferential component of the magnetic field). Fig. 2 show different boundary conditions between the slots regions and teethes region. At the radii R0 and R5, the boundary condition showed where the vector magnetic potential $\overrightarrow{A}$ is equal to zero.

4. Analytical Results and Validation With FEA

The main dimensions and parameters of the studied machine are given in Table I.

At no-load, flux lines distribution in the machine for different relative permeability value of stator and rotor core is given in Fig. 3. The effect of the permeability value μ_{rf} on the regions having narrow zone is clear. We can observe that the flux lines are concentrated in three teeth per pole. Fig. 4 and 5 respectively presents the distribution of the radial and circumferential flux densities in the middle of the air-gap for different relative permeability value of stator and rotor iron calculated analytically. The results of analytical calculationswere in a very good agreement with the results of the finite-element method [12].

It can be seen that the distribution of air gap flux density in permanent magnet synchronous machine, with no-load condition, has a distorted waveform caused by the finite permeability effect on the rotor and stator iron. The RMS value is decreased by decreasing the value of permeability of iron core.

Table I.
Parameters Of Studied Permanent-Magnet Motors

Parameter	Symbol	Value and unite
Max of magnet remanence	B_{rm}	1.28 T
Magnetic circuit relative permeability	μ_{rf}	Variable
Number of pole pairs	p	2
Magnet arc to pole pitch ratio	β	82%
Magnetization direction	-	Radial
Number of stator slots	Qs	12
Inner rotor radius	R_0	30.00 mm
Outer rotor radius	R_1	57.50 mm
Outer magnet radius	R_2	64.00 mm
Stator bore radius	R_3	64.65 mm
Outer stator slot radius	R_4	84.65 mm
Outer stator radius	R_5	110.0 mm
Rotor magnet thickness	Ea	06.50 mm
Air-gap length	e	00.65 mm
Slot opening	w_1	12 deg
Harmonics number	nh	99

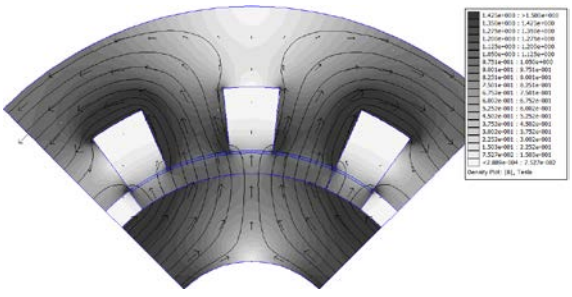

$\mu_{rf} = 1000$

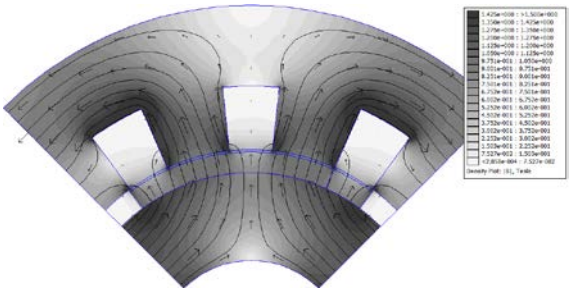

$\mu_{rf} = 100$

Figure. 3. Machine Teeth Saturated.

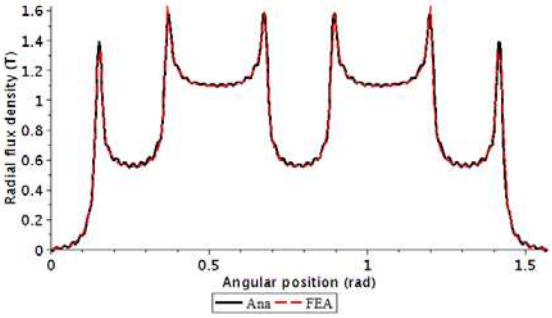

$\mu_{rf} = 1000$

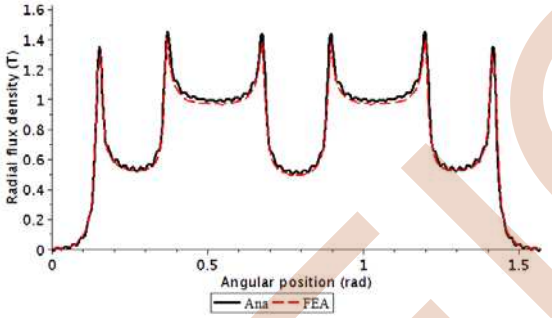

$\mu_{rf} = 100$

Figure. 4. Radial components of flux density in the middle of the airgap for $\beta = 81\%$ considering$\mu_{rf} = 1000$ and $\mu_{rf} = 100$ respectively.

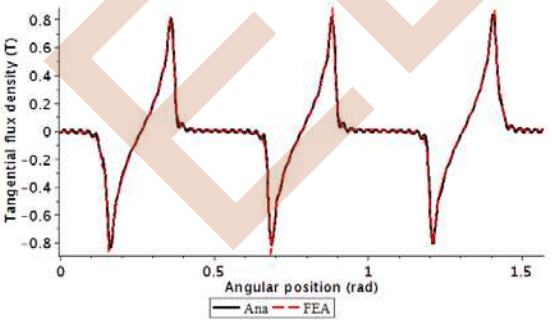

$\mu_{rf} = 1000$

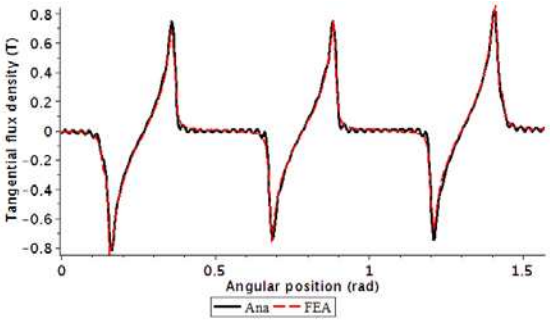

$\mu_{rf} = 100$

Figure. 5. Circumferential components of flux density in the middle of the airgap for $\beta = 81\%$ considering$\mu_{rf} = 1000$ and $\mu_{rf} = 100$ respectively.

In this paper, we will focus our analysis only on the flux density in the middle of air-gap. Fig. 5 compares the finite element analysis and analytically predicted air-gap radial flux density distributions considering the permeability value of stator and rotor iron core. A good agreement is achieved. The accuracy in FEA depends on the mesh generation. A relatively dense mesh is chosen, such that a sufficiently accurate FEA solution is obtained. The accuracy in the analytical method depends on the number of harmonics. To reduce the computation time, analytical calculation of magnetic field can be done for one pole pair, the numbers of harmonics is chosen to be equal to 99 and that to get good results and avoid solution to diverge. Finite element analysis which uses a meshed geometry has a limited accuracy related to the density of the mesh. The computational time requirements for magnetic field calculation with subdomain model and FEA are shown in Table II.

Table II

Computational Time Comparison Between Subdomain Model and FEA

Subdomain model (s)	FEA (s)	Mesh (nodes, elements)
1.5s	31s	67415, 134565
	54s	136087, 271909

Figure 7 shown the influence of permeability value of iron core on the RMS radial flux density in the middle of the airgap calculated by analytical method. Figures 8 and 9 show the RMS-error between the analytical and finite element analysis. A large RMS-error in order to 1% can be observed if the slot opening exceeds 2/3 of the tooth pitch. The same remark can be observed if the permeability value of iron core is too small $\mu_{rf} < 30$. The main challenge of RMS-errors value is returned to the approach which is based on the assumption cited in the expression (13) and (15).

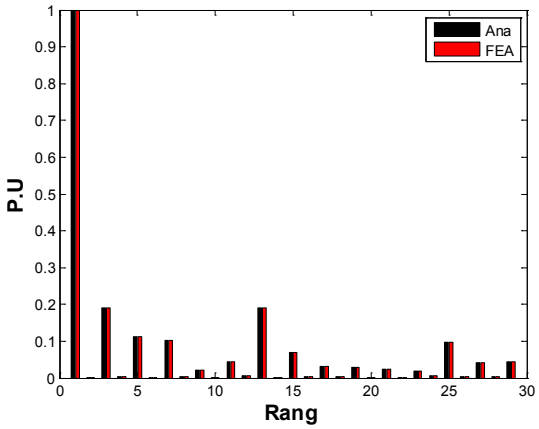

$\mu_{rf} = 1000$

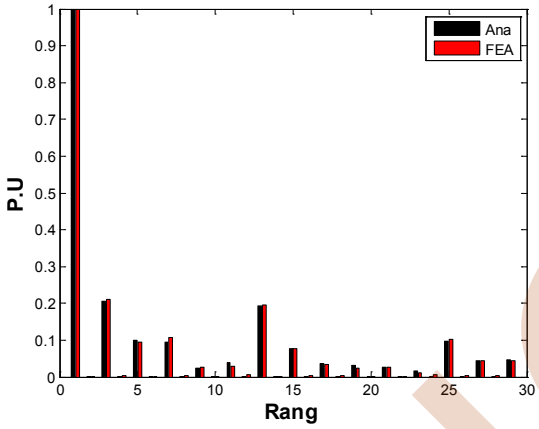

$\mu_{rf} = 100$

Figure. 6. Harmonic spectrum analysis for radial components of flux density in the middle of the airgap considering $\mu_{rf} = 1000$ and $\mu_{rf} = 100$ respectively.

$$RMS_{error} = \left| \frac{B_{r\_eff}^{Ana} - B_{r\_eff}^{FEA}}{B_{r\_eff}^{Ana}} \right| 100\% \quad (17)$$

where

$$B_{r\_eff}^{Ana}{}^{2} = \frac{1}{2r^2} \sum_{n=1}^{nh} np^2 (C_{3n}^{III} r^{np} + C_{4n}^{III} r^{-np})^2 + \frac{1}{2r^2} \sum_{n=1}^{nh} np^2 (C_{5n}^{III} r^{np} + C_{6n}^{III} r^{-np})^2 \quad (18)$$

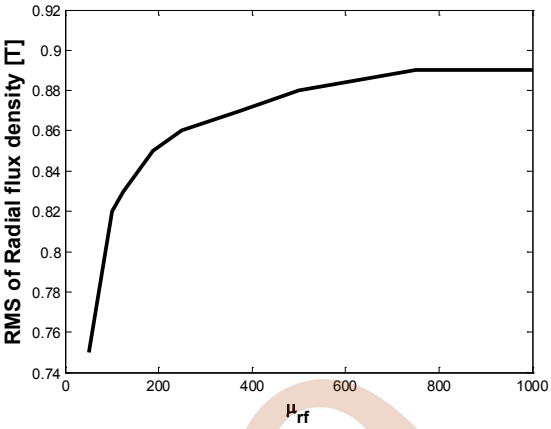

Figure. 7. Influence of permeability value of iron core on the RMS radial flux density in the middle of the airgap calculated by analytical method.

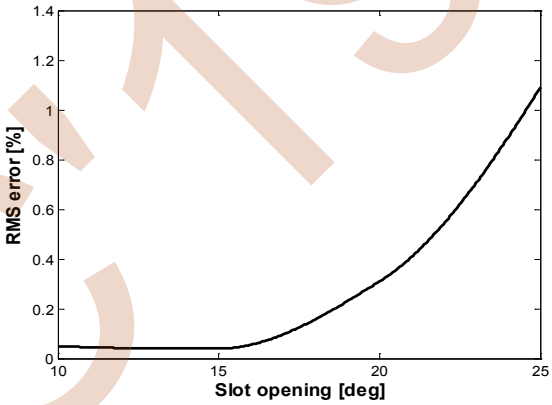

Figure. 8. Influence of slot opening on the RMS-error of radial components of flux density in the middle of the airgap.

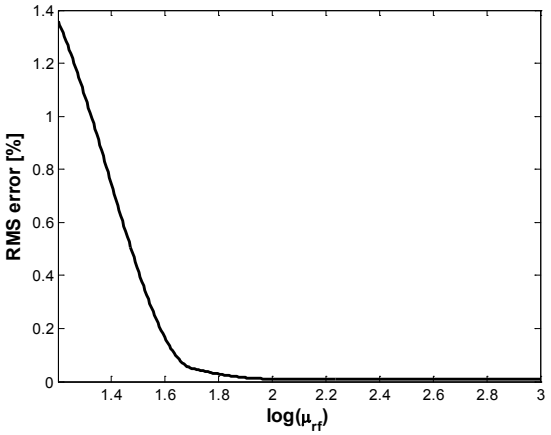

Figure. 9. Influence of permeability value of iron core on the RMS-error of radial components of flux density in the middle of the airgap.

5. CONCLUSION

Many of analytic technique are required for characteristic analysis of PMSM. In this paper, a new approach based on the analytical method has been presented to calculate the effect of permeability value of stator and rotor core on

the component of flux density on the airgap of PMSM taken into account the stator slotting effect. It is based on polar coordinate 2-D analysis, and involves the solution of Laplace's and Poisson's equation in the different regions by using the Fourier's series and the method of separating variables. One of the largest advantages of the discussed approach is its ability to account for the finite permeability and dimensions of magnetic core. This new approach takes significantly less computing time than the FEA; it is eminently suitable for design and optimization of PMSM. The use of B(H) curve can be used by means of an iterative algorithm. These curves are usually found by finite element analysis FEA or experimentally. The analytical results obtained have giving good results compared with finite element analysis.

REFERENCES

[1] P. Kumar and P. Bauer, "Improved Analytical Model of a Permanent-Magnet Brushless DC Motor," IEEE Transactions on Magnetics, vol. 44, no. 10, pp. 2299-2309, October 2008.

[2] Ahmed Chebak, Philippe Viarouge, and Jérôme Cros, "Improved Analytical Model for Predicting the Magnetic Field Distribution in High-Speed Slotless Permanent-Magnet Machines," IEEE Transactions on Magnetics, vol.51, no. 3, paper 8102904, March 2015.

[3] R. L. J. Sprangers, J. J. H. Paulides, B. L. J. Gysen, and E. A. Lomonova," Magnetic Saturation in Semi-Analytical Harmonic Modeling for Electric Machine Analysis", IEEE Trans on Mag, Vol. 52, No. 2, Feb 2016, paper # 8100410.

[4] J. W Jung, J. J Lee, S. O. Kwon, J. P Hong, K. N Kim, "Equivalent Circuit Analysis of Interior Permanent Magnet Synchronous Motor Considering Magnetic saturation", World Electric Vehicle Journal Vol. 3, pp.114-118, May. 2009.

[5] P. L. Alger, Induction Machines: Their Behavior and Uses, 2nd ed. Gordon and Breach, Science Publishers, Inc., 1970.

[6] J. Pyrhonen, T. Jokinen, and V. Hrabovcova, Design of Rotating Electrical Machines. John Wiley & Sons, Ltd, 2008.

[7] I. Boldea and S. A. Nasar, The Induction Machines Design Handbook. CRC Press, Taylor and Francis Group, 2010.

[8] V. Ostovic, Dynamics of Saturated Electric Machines. New York: Springer-Verlag, 1989.

[9] B. Ladghem Chikouche, K. Boughrara and R. Ibtiouen, "Cogging Torque Minimization of Surface-Mounted Permanent Magnet Synchronous Machines Using Hybrid Magnet Shapes". Progress in Electromagnetics Research B, Vol. 62, p49-61, 2015.

[10] K. Boughrara , R. Ibtiouen , and T. Lubin, "Analytical Prediction of Magnetic Field in Parallel Double Excitation and Spoke-Type Permanent-Magnet Machines Accounting for Tooth-Tips and Shape of Polar Pieces", IEEE Trans on Mag, Vol. 48, no. 7, pp. 2121-2137, July 2012.

[11] Jeffrey, A., "Advanced Engineering Mathematics", University of Newcastle-upon-Tyne, Harcourt/Academic Press, 2002.

[12] Meeker, D. C., Finite Element Method Magnetics, Version 4.2, Apr. 2009 Build, http://www.femm.info.

EEIC'2019 University of Bejaia

Analysis of double Star Induction Motor with Stator Winding Fault using ANSYS MAXWEL

H.hammache, D. Aouzellag

Laboratory of Renewable Energy Mastery
Abderhamne Mira University Bejaia,
Algeria
hammache.hakim@gmail.com

Abstract— **Basic concepts of six-phase ac motor drives have been in existence for a number of years and were considered extensively in the eighties for safety-critical and/or high power applications. There has been an upsurge in the interest in these drives in recent times, initiated by various application areas, such as 'more-electric' aircraft, electric ship propulsion and EV/HVs. In our study, an ac drive with dual stator windings fed by dual six step converters is proposed. Two sets of electrically isolated windings are placed in the stator slots, and one set is shifted from the other by 30° in space. Two converters are used to fed the dual windings, and the phase voltages from the two converters are also shifted 30° from each other in time.**

Based on finite element models, this paper studies the influence of the stator winding fault on the DSIM behavior under various conditions and severity. The comparison of the results obtained by simulation tests allowed verifying the precision of the proposed FEM model. The presented fault model is used to study of the DSIM under fault conditions and seems to be well adapted for DSIM health monitoring and short-circuit fault diagnosis.

Index Terms— dual-stator induction machine, finite elements method, winding opened-circuit fault.

I. INTRODUCTION

Three-phase induction machines are today a standard for industrial electrical drives. Cost, reliability, robustness, and maintenance-free operation are among the reasons these machines are replacing dc drive systems. The development of power electronics and signal processing systems has eliminated one of the greatest disadvantages of such ac systems, that is, the issue of control. With modern techniques of field-oriented vector control, the task of variable-speed control of induction machines is no longer a disadvantage.

The need to increase system performance, particularly when facing limits on the power ratings of power supplies and semiconductors, motivates the use of phase number other than three, and encourages new pulse width modulation (PWM) techniques, new machine design criteria, and the use of harmonic current and flux components.

In a multiphase system, here assumed to be a system that comprises more than the conventional three phases, the machine output power can be divided into two or more solid-state inverters that could each be kept within prescribed power limits. Also, having additional phases to control means additional degrees of freedom available for further improvements in the drive system.

With split-phase induction machines, and appropriate drive system, the sixth harmonic torque pulsation, typical in a six-step three-phase drive, can be eliminated [1], [2]. Also, air-gap flux created by fifth and seventh harmonic currents in a high-power six-step converter-fed system is dramatically reduced with the penalty of increased converter harmonic currents [3].

A particular case of split-phase or dual-stator machine, the six-phase machine can be built by splitting a three-phase winding into two groups. Usually these three-phase groups are displaced by 30 electrical degrees from each other. This arrangement composes an asymmetrical six-phase machine since the angular distance between adjacent phases is not all the same . The analysis of an induction machine for multiple phases and arbitrary displacement between them is presented in where the six-phase induction machine is used as an example and an equivalent circuit has been derived. The model for a six-phase machine was developed in [4].

Reliability is one of the advantages in using six-phase systems. In the case of failure of one of the phases, either in the machine or in the power converter, the system can still operate at a lower power rating since each three-phase group can be made independent from each other. In the case of losing one phase, the six-phase machine can continue to be operated as a five-phase machine as described in [5].

Inter turn fault cause a large circulating fault current in the shorted turn, leading to localized thermal overloading. This one can cause open-circuit failures (melting of conductors), short circuit faults (insulation damage) in the electrical circuit, and electrical fire.

In this paper, the transient analysis was done using 2D finite element electromagnetic field analysis. The designed metric dimension is modeled in the FE using Ansys-Maxwell 19.

In this context, FEM can be successfully used, because it takes into account the non-linearity of the magnetic material being suitable for a detailed study of the DSIM behavior with faults, and in this case of the broken rotor bar fault type.

The use of simulation tools helps the researchers to emphasis the effects caused by faults in an electrical machine and to develop efficient fault detection methods. Using FEM analysis, the changes in electric, magnetic and mechanic behavior of the machine due to any fault can be easily observed without the need of opening the machine, or experimenting in laboratories. The main idea is to understand the electric, magnetic and mechanical behavior of the machine in its healthy state and under fault conditions.

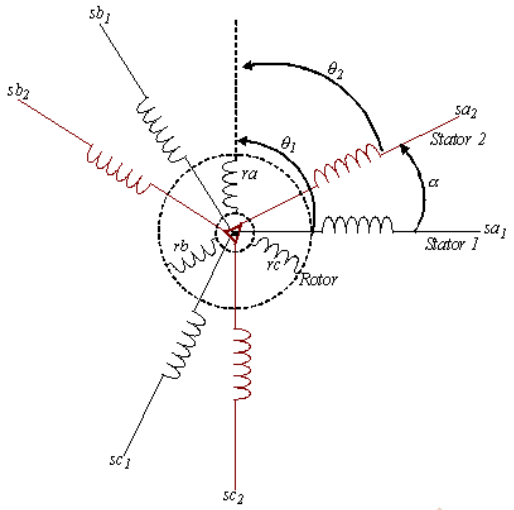

Fig. 1. Windings of the Double-star induction machine (DSIM).

II. Motor Design

Standard squirrel cage induction motors, rated at 4 kW, was used to investigate the new drive configurations. the motor was wound in a 2-pole concentric arrangement with four slots per-phase per-pole in a twenty-four slot stator.

One can build electric machines using Maxwell in different ways. However, the process is simplified by letting the RMxprt do the most of the job. RMxprt is a machine model whereby a software user can insert machine design parameters and related information. In the process of imputing the design data in the RMxprt, a user has to specify the dimensions of the stator and rotor of the machine and related parameters such as machine type, number of poles of the machine and control type.

Furthermore, a user has to specify the rated parameters such as speed and voltage. A user has also to specify other parameters such as winding, slot, wire, conductors, insulation and some other related parameters [6].

III. Digital Test Platform Structure

2D FEM field calculations are performed using Maxwell 2D. This program is suitable for this kind of applications. It offers a lot of useful features like especially partial automatic mesh generation, sliding air gap band for calculations in rotation, or external coupled circuits. Due to the fact that a 2D FEM calculation is used, it is necessary to take into account the end-winding leakages through an adequate definition of the external coupled circuits, as defined in Figure 4. The mesh generation in Figure 4 is also a cardinal point of the whole procedure; it has to be carefully performed. The post-processing stage contains the analysis of the FEM calculations results; it leads to the characteristic quantities and to the equivalent circuits of the machine.

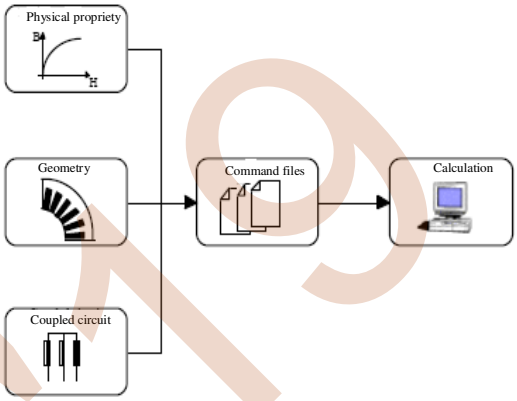

Fig. 2. Pre-processing steps.

IV. Field Calculation

In the following, the results concerning two kinds of six-phase asynchronous machines are presented, it depend of the angle between winding. The rated values of these machines are summarized in Table I.

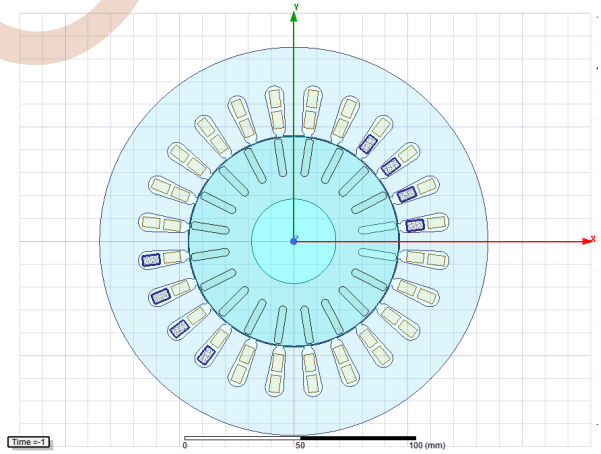

Fig. 3. Motor cross section.

TABLE I
MACHINES CHARACTERISTICS

Rated power Sn (kVA)	4.54
Rated voltage Un (V)	380
Power factor cosϕ	0.88
Pole number	2
Rated frequency f_n (Hz)	50
phase number	6
Stator slot number	24
rotor slots number	20

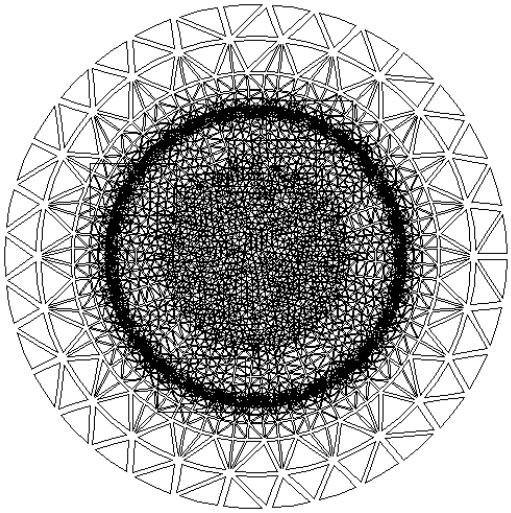

Fig. 4. Finite-element mesh.

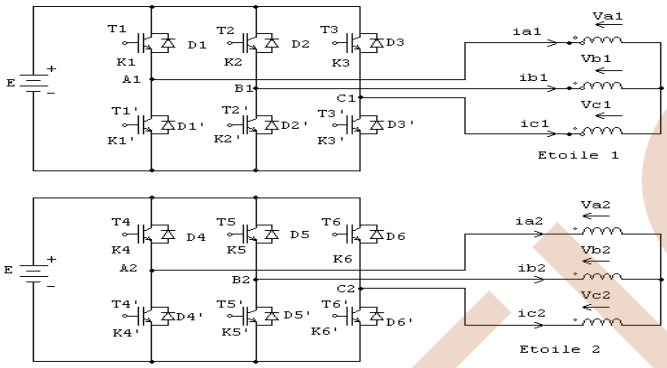

Finite-element analysis is conducted in the six-phase machine to calculate the air gap flux distribution and to demonstrate the influence of different harmonics like harmonic 5, 7, 11 and 13; other harmonics are not studied because, for symmetrical structure and balanced feeding, they don't exist.

An asymmetric six-phase induction motor was designed using a conventional three-phase motor as baseline. The new winding distribution accommodates in the same frame size as the baseline three-phase motor. For the baseline machine, from the nameplate and geometrical data, the air-gap flux is calculated. The stator phase voltage of the machine is calculated as

$$V_{sf} = \omega_e k_1 N_s \Phi_p \quad (1)$$

Where

$$\Phi_p = \frac{2 D_{is} l_s}{P} B_{g1} \quad (2)$$

Where Dis is the stator inner diameter, ls the stator length, P the number of poles, and Bg1 the peak fundamental air-gap flux.

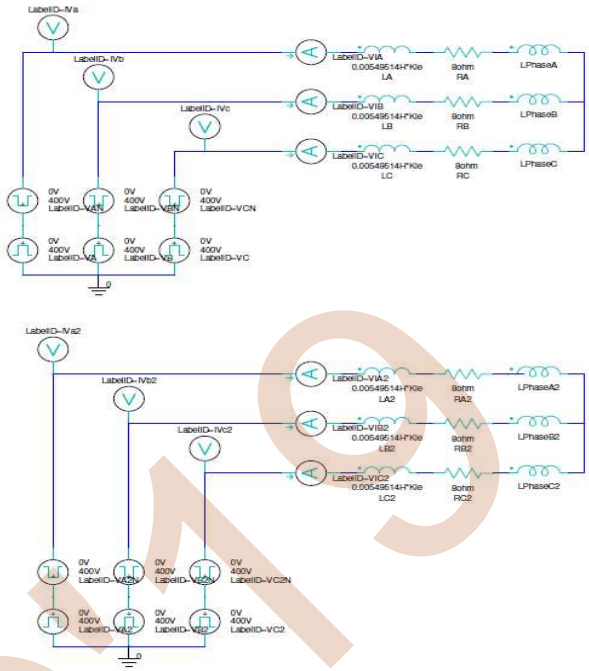

Fig. 5. Coupled circuits

One of the most common faults in the electrical motors is the opened phase circuit in the one of stator coils. The fault is mostly caused by mechanical stress, moisture and partial discharge, which is accelerated for electrical machines supplied by inverters.

Most of dynamic fault models, presented in different works, are based on healthy machine circuit model with an additional fault circuit. However, when a fault occurs the current and flux density distribution is more or less modified as a function of fault severity. Therefore, it is necessary to verify these dynamic models precision. The behavior study of electrical machines in steady state, transient and fault conditions require accurate knowledge of the equivalent circuit parameters. Some authors have validated their proposed model experimentally by measuring the machine external variables (stator voltages and currents) [6]. However, experimental tests for parameter identification can be replaced by digital simulation using finite element method (FEM).

The validated finite element model is used to simulate the DSIM with stator opened phase fault. In this paper, Co-simulation of DSIM fed by the full wave inverter with different degrees of stator fault circuit using Ansoft Maxwell and Simplorer.

In order to analyse the characteristic on stator faults, different levels of this fault are tested in which one and two opened phase of the stator windings are investigated. Simulation results for healthy and faulty machine are given in Fig. 6, 7 and 8.

IV SIMULATION RESULTS

A. Healthy machine

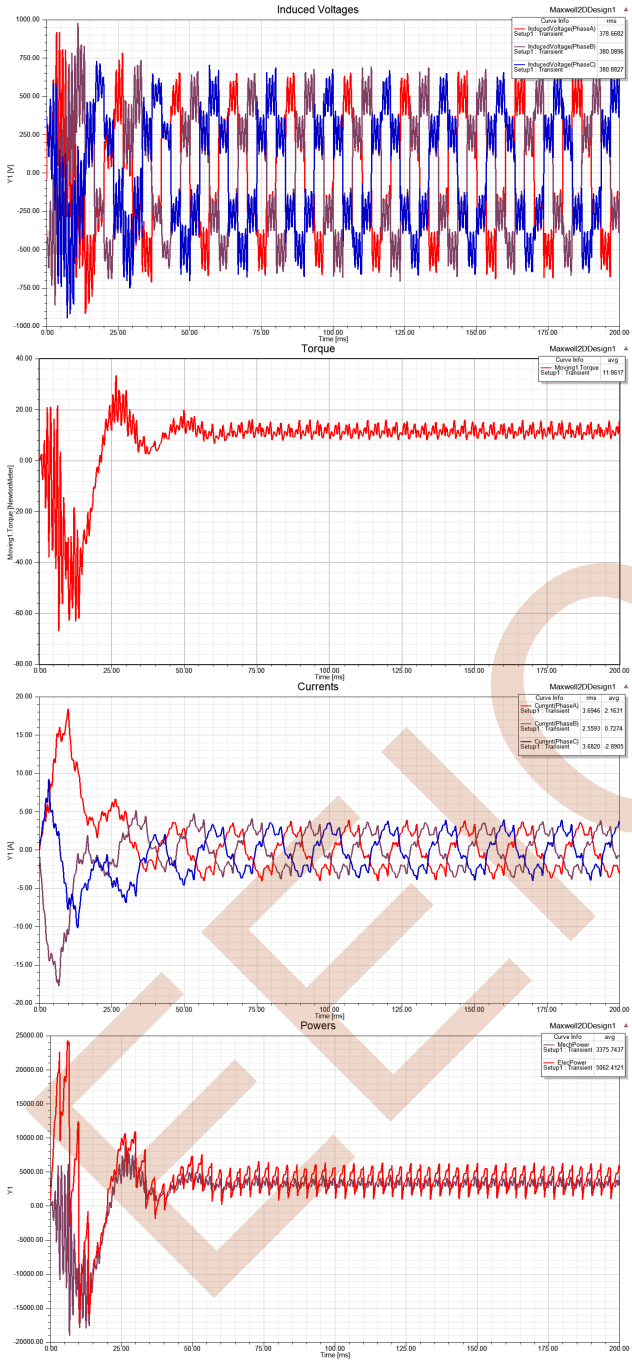

Fig. 6. Results obtained by Simplorer for healthy machine (a) phases Induced voltage (b) electromagnetic torque (c) phases current (d) power

B. Faulty machine: Opening of a single phase

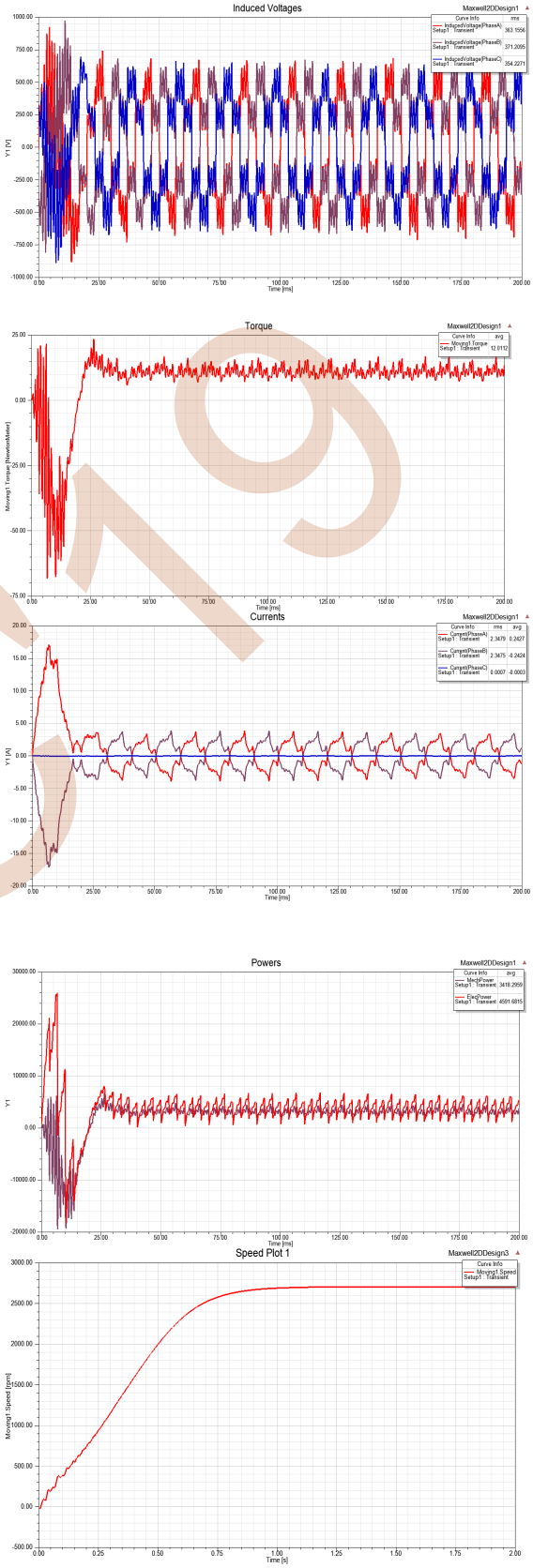

Fig. 7. Results obtained by Simplorer for healthy machine (a) phases Induced voltage (b) electromagnetic torque (c) phases current (d) power

C. Faulty machine: Opening of two non-adjacent phases

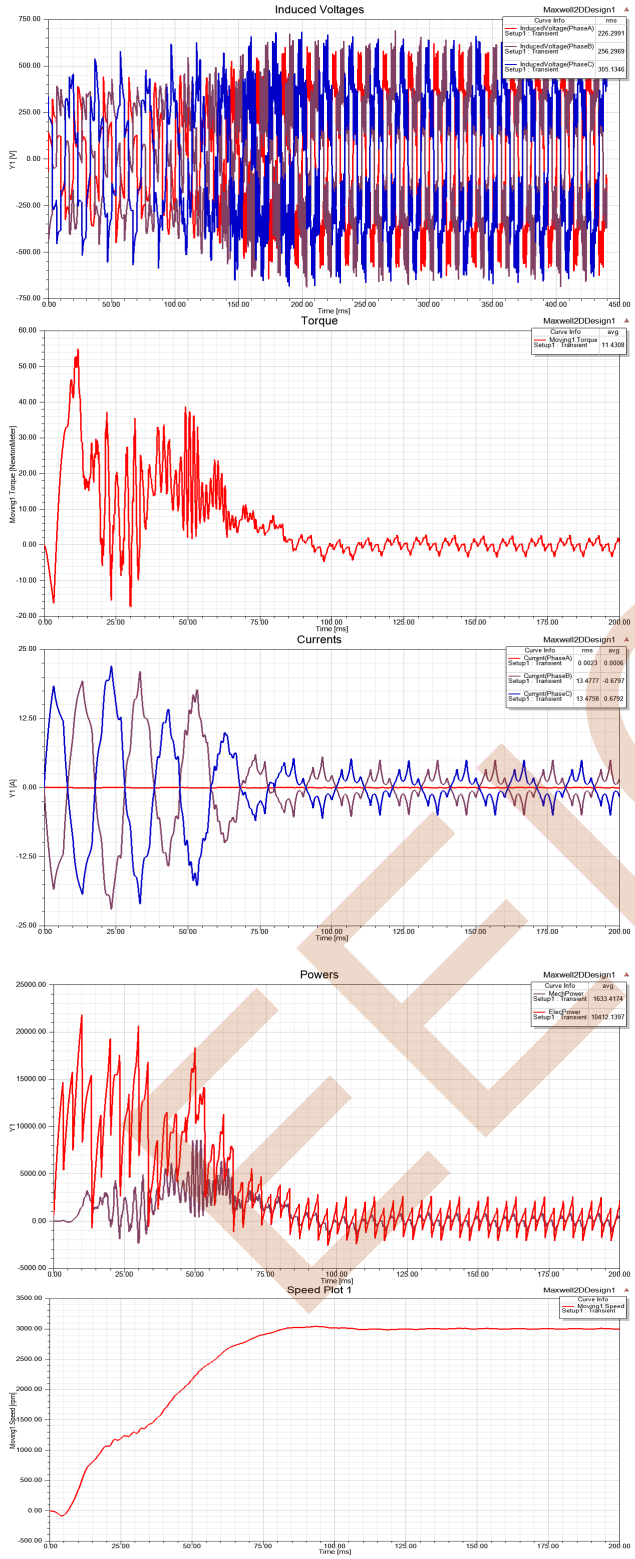

Fig. 8. Results obtained by Simplorer for faulty machine (a) phases Induced voltage (b) electromagnetic torque (c) phases current (d) power

V. CONCLUSION

When for any reason the operation is impaired at the machine or its power supply, the operation of the system is no longer satisfactory. This mode of operation is known as "degraded mode" or "faulty mode" which is only an exceptional operation where one or more elements of the drive system are malfunctioning.

This mode can occur at the machine during its natural operation either by opening or a short circuit at a phase or several phases, it allows us to study and monitor the evolution of different currents, the couple electromagnetic and speed of the machine.

In what we have limited our study in the cases of the following defects:

- Opening of a single phase.
- Opening of two phases of the same star.
- Opening of two adjacent phases.
- Opening of two non-adjacent phases.
- Elimination of a complete star.

In this work, a dynamic model coupling 2D finite element method in Maxwell and equivalent circuit simulation in Simplorer is proposed to compute the performances of an DSIM fed by inverter. The nonlinear magnetization characteristics have been considered and calculated by FEM.

The circuits of the inverter are built by using the circuit components in Simplorer. The magnetic fields, the winding characteristics and the torque of the DSIM are presented. All results of different simulation are compared for revealing the effect of faulty mode.

REFERENCES

[1] A. R. Bakhshai, G. Joos, and H. Jin, "Space vector PWM control of split-phase induction machine using the vector classification technique," in Proc. IEEE APEC'98, vol. 2, Feb. 1998, pp. 802–808.

[2] R. H. Nelson and P. C. Krause, "Induction machine analysis for arbitrary displacement between multiple windings," IEEE Trans. Power App. Syst., vol. PAS-93, pp. 841–848, May 1974.

[3] L. Xu and L. Ye, "Analysis of a novel stator winding structure minimizing harmonic current and torque ripple for dual six-step converter-fed high power ac machines," IEEE Trans. Ind. Applicat., vol. 31, pp. 84–90, Jan./Feb. 1995.

[4] A. R. Munoz and T. A. Lipo, "Dual stator winding induction machine drive," IEEE Trans. Ind. Applicat., vol. 36, pp. 1369–1379, Sept./Oct. 2000.

[5] O. Ojo and I. E. Davidson, "PWM-VSI inverter-assisted stand-alone dual stator winding induction generator," IEEE Trans. Ind. Applicat., vol. 36, pp. 1604–1611, Nov./Dec. 2000.

[6] G. Oriti, L. Julian, and T. A. Lipo, "An inverter/motor drive with common mode voltage elimination," in Conf. Rec. IEEE-IAS Annu. Meeting, vol. 1, Oct. 1997, pp. 587–592.

[7] T. A. Lipo, "A d–q model for six phase induction machines," in Proc. ICEM'80, Athens, Greece, Sept. 1980, pp. 860–867.

Direct power control of dual star permanent magnet synchronous generator dedicated to standalone wind energy systems

Mohamed Amine Bettouche[1,2], Djamal Aouzellag[2], Mohamed Fouad Benkhoris[1], Mourad Ait Ahmed[1], Jean-Claude Le Claire[1], Kaci Ghedamsi[2]

[1]IREENA - Laboratory, University of Nantes 44602, Saint-Nazaire, France
[2]LMER - Laboratory, University of Bejaia06000- Bejaia – Algeria

mohamed-amine.bettouche@etu.univ-nantes.fr,aouzellag@hotmail.com, mohamed-fouad.benkhoris@univ-nantes.fr, ait-ahmed-m@univ-nantes.fr, jean-claude.le-claire@univ-nantes.fr, kghedamsi@yahoo.fr

***Abstract*—In this paper, a strategy for controlling the DC bus voltage is proposed for wind energy conversion systems. The architecture study consists of a dual star permanent magnet synchronous generator (2S-PMSG) combined to a PWM rectifier. The study concerns the direct power control (DPC) method, which allows the adjustment of active and reactive power. The purpose of this study is to obtain bidirectional power flow, reduce harmonic distortions in the line current and regulate the input power factor to unity. The simulation results under Matlab/ Simulink/ SimPowerSystems have been obtained, which show the efficiency of the DPC control.**

***Keywords*-2S-PMSG, PWM rectifier, Wind turbine, Direct Power Control.**

I. INTRODUCTION

Multiphase machines continue to receive an increasing interest both in research and industrial fields aimed to renewable energy applications, such as ship propulsion, and wind parks [1]. Some papers propose multiphase PMSG as useful solution in wind applications [2-3]. Multiple stars arrangement, as the 2S-PMSG [4-5], are relatively new in this field, which have been attracting much attention in recent years since they could be convenient to achieve lower torque pulsation, a good choice of the angle of phase shift between the two stars of the stator, in this case an electric angle of 30 degrees, reduces these pulsations even more [6-7], Also their uses is interesting in the case of fault tolerance [8-9]. It exists different control techniques based on the PMSG, such as ordering by the field guides (FPC), and direct torque control (DTC). In this paper the operating principle of the direct power control (DPC) is presented. The latter is based on the error between the active and reactive powers estimates and references [10], and the power limitation for high wind speed values is achieved by varying the blade angle (Pitch control) which corresponds to decreasing power coefficient [11]. The active and reactive powers is used as the pulse width modulated (PWM). The advantage of the direct control of power is that it doesn't need the internal regulation loops or blocks current PWM modulation. Indeed, the converter switching states are selected from a switching table.

II. MODELING OF DIFFERENT PARTS OF THE SYSTEM

A. *Wind turbine modeling*

The aerodynamic power converted by the wind turbine is depending on the power coefficientCp , such as:

$$P_m = \frac{1}{2}\rho\, Cp(\lambda,\ \beta)\, \pi\, R^2 V_W^3 \qquad (1)$$

Where: ρ: The density of air (ρ = 1.225 kg / m^3), R: The blade length, and V_W: The wind speed.

The power coefficient is depending on the pitch angle β and the tip speed ratio λ given by:

$$\lambda = \frac{R\,\Omega}{V_W} \qquad (2)$$

Where Ω : The rotational speed of the wind turbine and generator.

The power coefficient is given by the expression [12]:

$$Cp(\lambda,\beta) = 0.5(116\frac{1}{\delta} - 0.4\beta - 5)e^{-21\frac{1}{\delta}} \quad (3)$$

With: $\frac{1}{\delta} = \frac{1}{\lambda+0.08\beta} - \frac{0.035}{1+\beta^3}$

B. Modeling of the 2S-PMSG

The equations of the DS-PMSG are written in the natural base. The expression of stator voltages is given by the following relationship:

$$[V_{s1}] = [R_{s1}].[i_{s1}] + \frac{d[\emptyset_{s1}]}{dt} \quad (4)$$

$$[V_{s2}] = [R_{s2}].[i_{s2}] + \frac{d[\emptyset_{s2}]}{dt} \quad (5)$$

Where:

$[i_{s1}] = [i_{a1}\ \ i_{b1}\ \ i_{c1}]^T$; $[i_{s2}] = [i_{a2}\ \ i_{b2}\ \ i_{c2}]^T$

$[R_{s1}] = diag[R_{a1}\ R_{b1}\ R_{c1}]$; $[R_{s2}] = diag[R_{a2}\ R_{b2}\ R_{c2}]$

$[\phi_{s1}] = [\phi_{as1}\ \ \phi_{bs1}\ \ \phi_{cs1}]^T$; $[\phi_{s2}] = [\phi_{as2}\ \ \phi_{bs2}\ \ \phi_{cs2}]^T$

The expression of magnetic flux is given by:

$$\begin{bmatrix}[\emptyset_{s1}]\\ [\emptyset_{s2}]\end{bmatrix} = \begin{bmatrix}[M_{1,1}] & [M_{1,2}]\\ [M_{2,1}] & [M_{2,2}]\end{bmatrix}.\begin{bmatrix}[i_{s1}]\\ [i_{s2}]\end{bmatrix} + \Psi.\begin{bmatrix}[E_{s1}]\\ [E_{s2}]\end{bmatrix} \quad (6)$$

$$[M_{1,1}] = \begin{bmatrix} (l_{fs}+M_s) & M_s.\cos(\frac{2.\pi}{3}) & M_s.\cos(-\frac{2.\pi}{3}) \\ M_s.\cos(-\frac{2.\pi}{3}) & (l_{fs}+M_s) & M_s.\cos(\frac{2.\pi}{3}) \\ M_s.\cos(\frac{2.\pi}{3}) & M_s.\cos(-\frac{2.\pi}{3}) & (l_{fs}+M_s)\end{bmatrix} \quad (7)$$

$$[M_{1,2}] = \begin{bmatrix} M_s.\cos(\alpha) & M_s.\cos(\alpha+\frac{2.\pi}{3}) & M_s.\cos(\alpha-\frac{2.\pi}{3}) \\ M_s.\cos(\alpha-\frac{2.\pi}{3}) & M_s.\cos(\alpha) & M_s.\cos(\alpha+\frac{2.\pi}{3}) \\ M_s.\cos(\alpha+\frac{2.\pi}{3}) & M_s.\cos(\alpha-\frac{2.\pi}{3}) & M_s.\cos(\alpha)\end{bmatrix} \quad (8)$$

With: $[M_{2,2}] = [M_{1,1}]$; $[M_{2,1}] = [M_{1,2}]^T$

Where: Ψ: The flux of permanent magnets, M_s: The mutual inductance and l_{fs}: The leakage inductance.

$$[E_{s1}] = \begin{bmatrix}\cos(P\theta)\\ \cos(P\theta-\frac{2.\pi}{3})\\ \cos(P\theta+\frac{2.\pi}{3})\end{bmatrix} ; [E_{s2}] = \begin{bmatrix}\cos(P\theta-\alpha)\\ \cos(P\theta-\frac{2.\pi}{3}-\alpha)\\ \cos(P\theta+\frac{2.\pi}{3}-\alpha)\end{bmatrix}$$

Where: P: The number of pole pairs, θ : The mechanical angle.

The electrical equations of the PMSG in the natural base, are written in matrix form:

$$\begin{bmatrix}[V_{abc,s1}]\\ [V_{abc,s2}]\end{bmatrix} = \begin{bmatrix}[R_{s1}] & 0\\ 0 & [R_{s2}]\end{bmatrix}.\begin{bmatrix}[I_{s1}]\\ [I_{s2}]\end{bmatrix} + \begin{bmatrix}[M_{1,1}] & [M_{1,2}]\\ [M_{2,1}] & [M_{2,2}]\end{bmatrix}.\begin{bmatrix}\frac{d}{dt}[I_{s1}]\\ \frac{d}{dt}[I_{s2}]\end{bmatrix} + \Psi.\begin{bmatrix}\frac{d}{dt}[E_{s1}]\\ \frac{d}{dt}[E_{s2}]\end{bmatrix} \quad (9)$$

III. METHOD OF DIRECT POWER CONTROL

The principle of DPC for one star is illustrated in (Fig 1).

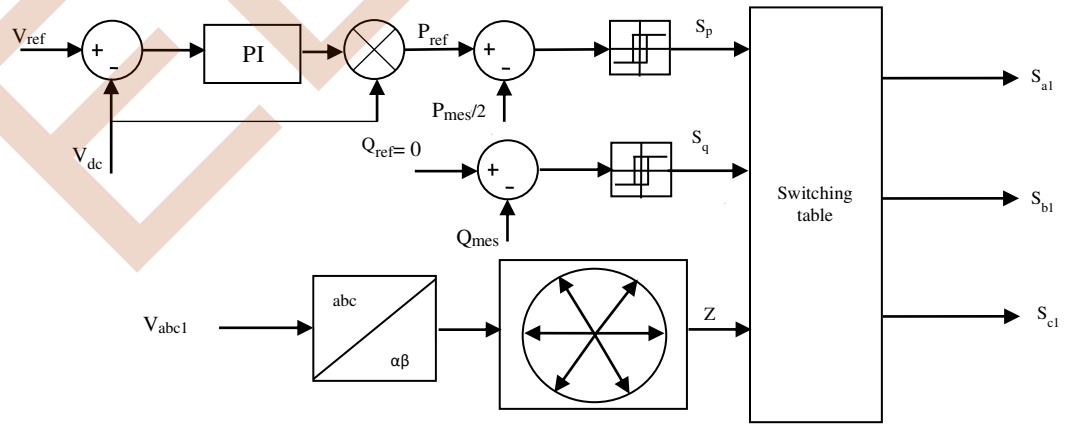

Fig 1. Diagram of the DPC command

DPC is a control strategy based on instantaneous active and reactive powers control loops. In this method there are no current control loops and PWM modulator block, because the switching states of the converter are selected by a switch table based on instantaneous errors between the commanded value and the estimated value of active and reactive powers.

IV. DIRECT POWER CONTROL OF 2S-PMSG

The overall system studied consists of a dual star permanent magnets synchronous generator which is considered as two three-phase machines sharing the same rotor, and an equivalent load brought back from the continuous side. The control is restricted to that of the output voltage of the DC bus using a PI (Proportional Integral) controller, the reference active power is calculated from the output of the DC bus voltage regulator and the reference of the reactive power is set zero to ensure a unit power factor. The voltage reference ($V_{dc\text{-}ref}$)is calculated with the following equation:

$$V_{dc-réf} = \sqrt{P_m \frac{V_{dc}^2}{P_n}} \quad (10)$$

Where*:* P_n:The nominal power.

The studied system is represented in (Fig 2).

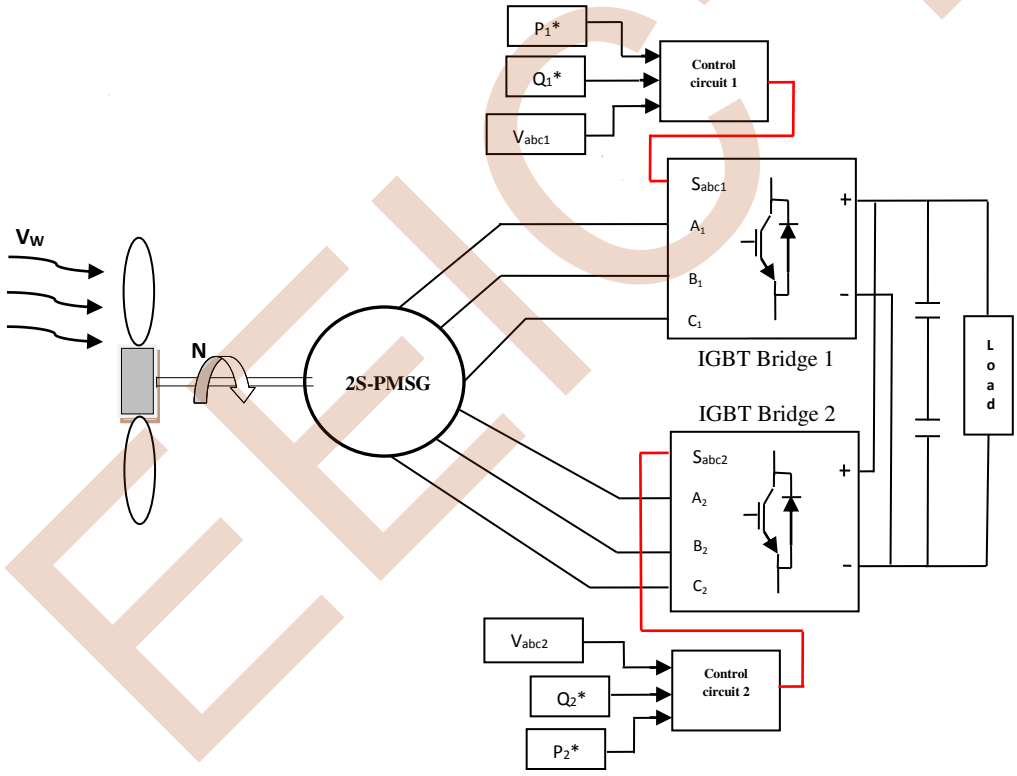

Fig 2. Diagram of the wind turbine principle with DPC control

A. CALCULATIONS OF THE INSTANTANEOUS POWERS

The instantaneous power theory is used to calculate the instantaneous values of active and reactive powers. The instantaneous values of the three-phase voltages and currents for star one are respectively: V_{a1}, V_{b1}, V_{c1}et i_{a1}, i_{b1}, i_{c1}.The active and reactive powers are given by the following equations:

$$\boldsymbol{P_1 = Re\{V.i*\} = V_{a1}i_{a1} + V_{b1}i_{b1} + V_{c1}i_{c1}} \quad (11)$$

$$\boldsymbol{Q_1 = Im\{E.(i*)\} = \frac{1}{\sqrt{3}}(V_{b1c1}i_{a1} + V_{c1a1}i_{b1} + V_{a1b1}i_{c1})} \quad (12)$$

Where:

P_1 and Q_1 are instant active and reactive powers respectively for the first star.
V: voltage vector.
i: current vector and the symbol (*) denotes the conjugate.

This method works in ($\alpha\beta$) coordinates. Thus, the instantaneous powers are calculated as follows:

$$\boldsymbol{P_1 = V_\alpha i_\alpha + V_\beta i_\beta} \quad (13)$$

$$\boldsymbol{Q_1 = V_\beta i_\alpha - V_\alpha i_\beta} \quad (14)$$

Another factor intervenes in the calculation of instantaneous power, which is the flux. Thus, the integration of the voltage of the generator generates a flux vector in the coordinates ($\alpha\beta$). V_α and V_β are the transforms in the reference ($\alpha\beta$) of the voltages V_{a1}, V_{b1}, V_{c1}, such that:

$$\begin{bmatrix} V_\alpha \\ V_\beta \end{bmatrix} = \frac{2}{3}\begin{bmatrix} 1 & \frac{-1}{2} & \frac{-1}{2} \\ 0 & \frac{-\sqrt{3}}{2} & \frac{\sqrt{3}}{2} \end{bmatrix}\begin{bmatrix} V_{a1} \\ V_{b1} \\ V_{c1} \end{bmatrix} \quad (15)$$

V. SIMULATION RESULTS

The simulations were performed using Matlab/Simulink/SimPowerSystems software.

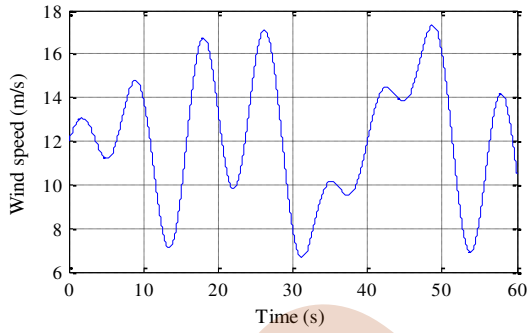

Fig 3. Wind speed

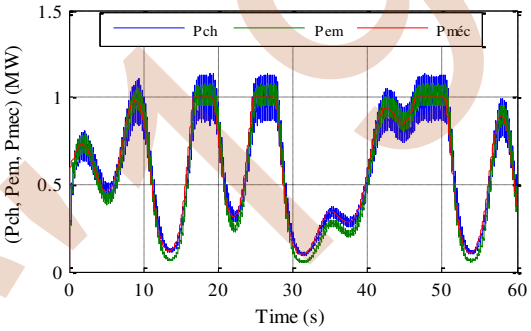

Fig 4. Power (load, electromagnetic, mechanical)

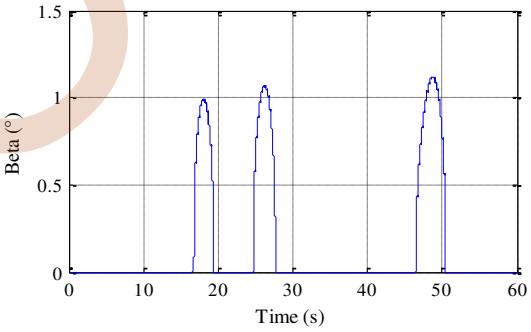

Fig 5. Pitch angle

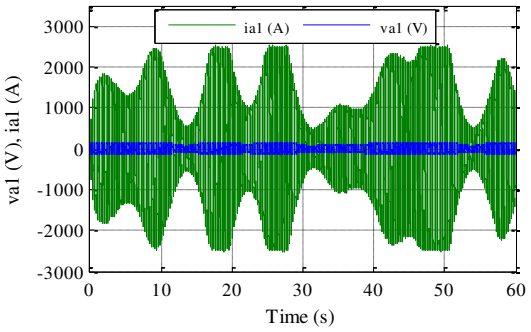

Fig 6. Voltage and current phase

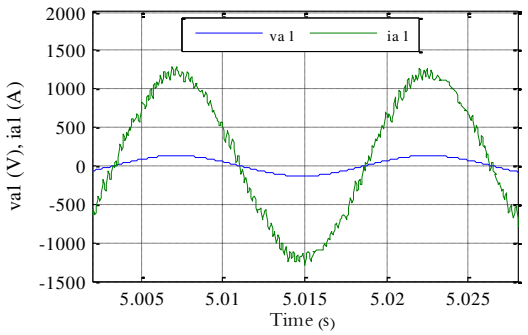

Fig 7. Zoom voltage and current phase

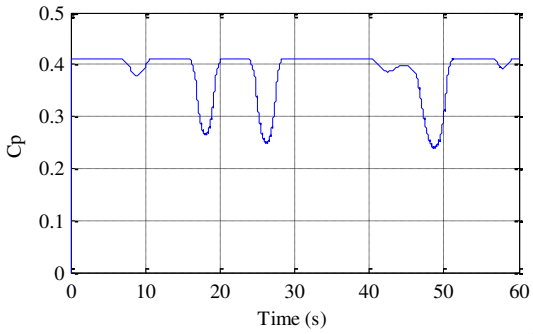

Fig 8. Power coefficient

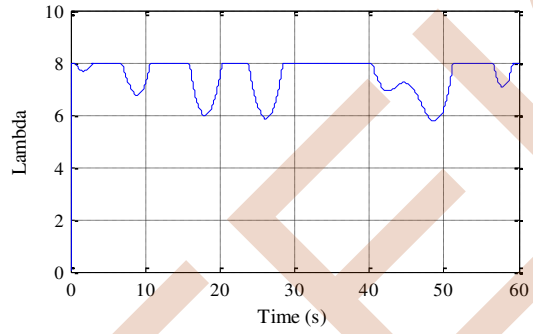

Fig 9. Tip speed ratio

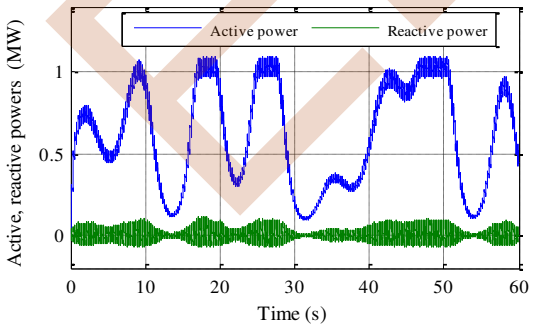

Fig 10. Active, reactive powers

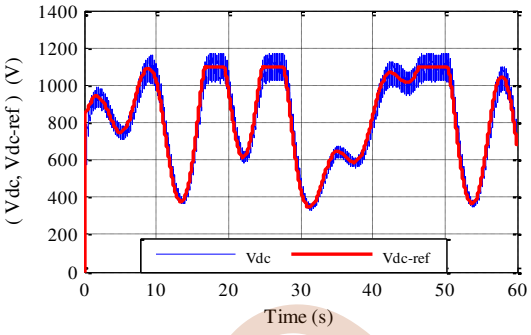

Fig 11. DC bus voltage and its reference

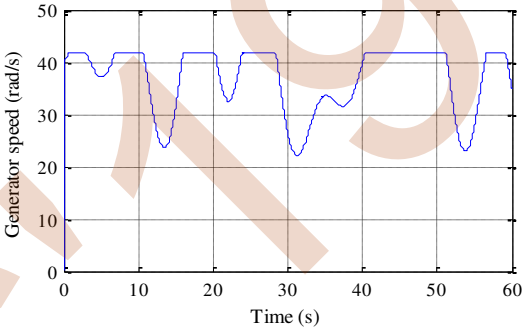

Fig 12. Generator speed

Figure 3 represents the wind speed and figure 4 is power of load, mechanical and electromagnetic power, the load power is given by the equation:$P_{dc} = \frac{V_{dc}^2}{R_r}$. We note that the powers vary according to the variation of the wind speed, and the power reaches its maximum of 1 (MW) which is the nominal power of the machine and the limitation of the power for the values of high wind speed is obtained by varying the blade angle (Pitch control) (Fig 5).The voltage and current phase are illustrated in figure 6 whose the current vary with the variation of the wind, and which is in phase with the phase voltage (Fig 7). Figures 8 and Fig 9 shows respectively the power coefficient and the trip speed ratio. The active and reactive powers are presented in figure 10, where we can see that the reactive power is zero.

Figure 11 represents reference voltage and the voltage of dc bus, the voltage follows its reference which shows the performance of the DPC. Figure 12 is the generator speed who reaches its maximum at nominal power.

PARAMETERS OF THE MACHINE

TABLE I. Machine parameters

Nominal speed	N (tr/min)	400
Nominal power	P_{nom} (MW)	1
Number of pole pairs	p	11
Offset angle	α (degree)	30
Resistance of a phase	R_s (m ohm)	0.63060
Leakage inductance	L_f (μH)	30.918
Mutual inductance	M_s (µH)	22.848
DC bus voltage	V_{dc} (V)	1100
Capacitor	C_1=C_2 (mF)	2.2
Maximum flow	Ψ_{max} (Wb)	0.3244
Load	R_r (Ω)	1.21

VI. CONCLUSION

In this article, we presented a control strategy for a DS-PMSG connected to a PWM rectifier. It concerns the use of direct power control based on the PI controller. The two hysteresis controllers that allow adjustment of active and reactive powers. This DPC control technique has a variable switching frequency. The results of the simulation obtained showed that the DPC technique improves the performance of the system. These affect the performance of the system response to DC bus voltage, power factor correction, sinusoidal current, and improved machine performance.

REFERENCES

[1] F. Blaabjerg, M. Liserre, and K. Ma, "Power electronics converters for wind turbine systems," *IEEE Transactions on Industry Applications*, vol. 48, no. 2, pp. 708–719, 2012.

[2] M. J. Duran, S. Kouro, W. Bin, E. Levi, F. Barrero, and S. Alepuz, "Sixphase PMSG wind energy conversion system based on medium-voltage multilevel converter," *Proceedings of the 14th European Conference onPower Electronics and Applications (EPE 2011)*, pp. 1–10, 2011.

[3] D. Vizireanu, X. Kestelyn, S. Brisset, and P. Brochet, "Polyphased modular direct-drive wind turbine generator," *European Conference onPower Electronics and Applications (EPE 2005)*, pp. 1–9, 2005.

[4] M. S. Carmeli, F. Castelli-dezza, G. Marchegiani, M. Mauri, and D. Rosati, "Design and Analysis of a Medium Voltage DC Wind Farm with a Transformer-less Wind Turbine Generator," in *XIX InternationalConference on Electrical Machines - ICEM*, Rome, 2010, pp. 1–6.

[5] M. Andriollo, G. Bettanini, G. Martinelli, A. Morini, and A. Tortella, "Analysis of double-star permanent-magnet synchronous generators by a general decoupled d-q model," *IEEE Transactions on Industry Applications*, vol. 45, no. 4, pp. 1416–1424, 2009.

[6] E. B. Sedrine, "Machines à commutation de flux à grand nombre de phases : Modèles comportementaux en mode dégradé et élaboration d'une stratégie de commande en vue de l'amélioration de la tolérance aux pannes," *PhD thesis*, Ecole Normale Superieure of Cachan, 2014.

[7] N. K. N. O. Fall, J. F. Charpentier, "Comparaison de performances de différentes structures de machines synchrones à aimants permanents polyphasées en mode normal et en mode dégradé en vitesse variable avec défluxage pour des applications hydroliennes," in *Symposium de Genie Electrique*, 2016 Grenoble France.

[8] A.Dieng, "Modélisation dynamique et Commande d'un ensemble génératrice synchrone pentaphasée à FEM non sinusoïdale – convertisseur AC/DC tolérant aux défauts", *PhD thesis* of university of Nantes, October, 2014.

[9] F.Locment, "Conception et modélisation d'une machine synchrone à 7 phases à aimants permanents et à flux axial : commande vectorielle en mode normal et dégradé", *PhD thesis* of university of Lille, décember 2006.

[10] F. Bouchafaa, I. Hamzaoui, S. Hadjamar, "Direct Power Control of AC / DC converter-phase Associating a DFTG, "*International Conference on Energy and Sustainable Development*, Adrar, Aigeria, 29-30, November 2011.

[11] C. Jauch, S. M. Islam, P. Sørensen, and B.B. Jensen, "Design of a Wind Turbine Pitch Angle Controller for Power System Stabilization", *Science Direct, Renewable Energy Journal,* Vol. 32, pp. 2334–2349.

[12] A. Remli, D. Aouzellag, and K. Ghedamsi, "Study and Control of Wind Energy Conversion System based Permanent Magnet Synchronous Generator connected to the Grid", *International Journal of Research and Reviews in Computing Engineering,* Vol. 1, No. 1, March 2011.

Updating and Improvement of the A.M.B. program

Fatiha Latri
LGEB laboratory of Bejaia, Faculty of technology
University Abderahmane MIRA,
Bejaia, Algeria
e-mail: samia_latri@yahoo.fr

Abstract—**A.M.B. (Arc Model Blockset) program was a MATLAB/Simulink Power Systems Blockset extension that contains several black box arc models. It has been developed by Delft University of Technology at 2001 in order to make arc-circuit interaction studies during the interruption process of high-voltage circuit breakers. At present, this useful tool only works in MATLAB 6 and cannot be activated in recent versions of MATLAB due to important changes in MATLAB/Simulink Power Systems libraries. To update the A.M.B. program we have re-created it again in MATLAB/Simulink Power Systems, by using a method simpler than that used in the old A.M.B. program. We have also ameliorate the menu of the program, the result is a flexible tool, easier to use than the old A.M.B. program. In this paper, the different conception phases of the new A.M.B. program are described and then followed by an example of numerical computations by using the modified Mayr arc model.**

I. INTRODUCTION

High voltage circuit breakers play an important role in transmission and distribution systems. In the closed position, the circuit breaker conducts the current with negligible voltage drop across its contacts. When a fault occurs and contacts are being separated, the current flows through the arc channel that has been formed by the plasma between the breaker contacts, it is the arc current. Because of arc channel resistance, a voltage drop is produced, it is the arc voltage. A very small current called post-arc current continues to flow in the first few microseconds after the arc current has been interrupted and the transient recovery voltage (T.R.V.) builds up, because after the extinction of the arc, the steel hot gas does not change to a cold gas instantaneously [1].

Black box arc models are mathematical descriptions of the arc conductance very nonlinear behavior in the high voltage circuit breaker during the interruption process; they are used to study arc-circuit interaction.

MATLAB is a well-known and popular program; it contains several ODE solvers with both fixed and variable step size. With the introduction of the Simulink Power Systems Blockset, the MATLAB program becomes a suitable tool for the electrical transient's computations [2]. A.M.B. program was a MATLAB/Simulink/Power System Blockset extension, developed in order to make arc-circuit interaction studies during the interruption process of high-voltage circuit breakers [3]. It contained the black box arc models of Cassie, Mayr, modified Mayr, Habedank, KEMA, Schavemaker and Schwarz [4]. At present, the A.M.B. program does not work in recent versions of MATLAB because of important changes in MATLAB/Simulink Power Systems libraries. The objective of this work is to update and improve this program. The paper is organized as follows: Section II lists the arc models incorporated in the A.M.B. program. Section III gives some changes in recent versions of MATLAB compared to the old versions. Sections IV presents the conception phases of the new A.M.B. program. Section V presents an example of numerical computations. Finally, Section VI presents the advantages of the new A.M.B. program compared with the old one. Finally, section VII presents the conclusion.

II. BLACK BOX ARC MODELS

Basic descriptions of the arc conductance behaviour were first given by Cassie arc model and Mayr arc model [5], after that, a great number of modifications of these arc models have been proposed. In this section are presented the most used black box arc models.

A. Cassie arc model

Cassie arc model is described by the equation:

$$\frac{1}{g}\cdot\frac{dg}{dt}=\frac{1}{\tau}\left(\frac{u^2}{U_0^2}-1\right) \quad (1)$$

u arc voltage
g arc conductance
τ arc time constant

U_0 constant arc voltage.

This arc model is valid in the high currents area; and has two constant parameters to be determined τ and U_0.

B. Mayr arc model

Mayr Arc Model is described by the following equation:

$$\frac{1}{g}\cdot\frac{dg}{dt}=\frac{1}{\tau}\left(\frac{ui}{P}-1\right) \quad (2)$$

i arc current
P cooling power considered constant

This arc model is valid in the low currents area and has two constant parameters to be determined τ and P.

C. Modified Mayr arc model

Modified Mayr Arc Model is a Mayr-type arc model, which considers the parameter τ constant and the cooling power function of the arc current: $P=p(P_0+U_0|i|)$

This arc model is described by the following equation [6]:

$$\frac{1}{g}\cdot\frac{dg}{dt}=\frac{1}{\tau}\left(\frac{ui}{p(P_0+U_0|i|)}-1\right) \quad (3)$$

P_0 cooling power constant
p fill pressure of the circuit breaker.

The free parameters of this arc model are τ, P_0, and U_0

D. Schwarz arc model

Schwarz arc model [7] is a Mayr-type arc model, with the time constant τ and the cooling power P are function of the arc conductance:

$$\tau=\tau_0 g^{\alpha} \qquad P=P_0 g^{\beta}$$

The following equation describes the arc model:

$$\frac{1}{g}\cdot\frac{dg}{dt}=\frac{d\ln g}{dt}=\frac{1}{\tau_0 g^{\alpha}}\left(\frac{ui}{P_0 g^{\beta}}-1\right) \quad (4)$$

τ_0 time constant
P_0 cooling power constant
α parameter that influences the conductance dependency of τ
β parameter that influences the conductance dependency of *P*

E. Schavemaker arc model

Schavemaker arc model [8] is a Mayr-type arc model, which considers the parameter τ constant and the cooling power function of the electric arc power: $P=P_0+P_1 ui$

The following equation describes the arc model:

$$\frac{1}{g}\cdot\frac{dg}{dt}=\frac{d\ln g}{dt}=\frac{1}{\tau}\left(\frac{ui}{P_0+P_1 ui}-1\right) \quad (5)$$

P_0 cooling power constant (originating from the design of circuit breaker) in Watt.
P_1 cooling power constant (regulates the influence of the electrical power input on the cooling power),

This arc model has three free parameters to be determined; τ, P_0 and P_1.

F. Habedank arc model

Habedank arc model [9] is a series connection of Cassie and Mayr arc models. It is described by the following equations:

$$\frac{dg_c}{dt}=\frac{1}{\tau_c}\left(\frac{u^2 g^2}{U_0^2 g_c}-g_c\right) \quad (6)$$

$$\frac{dg_m}{dt}=\frac{1}{\tau_m}\left(\frac{u^2 g^2}{P_0}-g_m\right) \quad (7)$$

$$\frac{1}{g}=\frac{1}{g_c}+\frac{1}{g_m} \quad (8)$$

g: total arc conductance of the arc
u voltage across the arc
i current through the arc
g_c arc conductance described by Cassie equation
g_m arc conductance described by Mayr equation
τ_m Mayr time constant
τ_c Cassie time constant

This arc model has four free parameters to be determined τ_c, τ_m, U_o and P_0

G. KEMA arc model

KEMA arc model [10] is a series connection of three modified Mayr arc models:

$$\frac{dg_1}{dt}=\frac{1}{P_1\tau_1}\cdot g_1^{\lambda_1}u_1^2-\frac{1}{\tau_1}\cdot g_1 \quad (9)$$

$$\frac{dg_2}{dt} = \frac{1}{P_2 \tau_2} \cdot g_2^{\lambda_2} u_2^2 - \frac{1}{\tau_2} \cdot g_2 \qquad (10)$$

$$\frac{dg_3}{dt} = \frac{1}{P_3 \tau_3} \cdot g_3^{\lambda_3} u_3^2 - \frac{1}{\tau_3} \cdot g_3 \qquad (11)$$

$$\frac{1}{g} = \frac{1}{g_1} + \frac{1}{g_2} + \frac{1}{g_3} \qquad (12)$$

$$u = u_1 + u_2 + u_3 \qquad (13)$$

$$i = gu = \frac{g_1 g_2 g_3}{g_1 g_2 + g_1 g_3 + g_2 g_3} \qquad (14)$$

$$\tau_2 = \frac{\tau_1}{k_1} \qquad \tau_3 = \frac{\tau_2}{k_2} \qquad P_3 = \frac{P_2}{k_3}$$

$$\lambda_1 = 1.4 \quad \lambda_2 = 1.9 \quad \lambda_3 = 2$$

g: total arc conductance of the arc
g_n conductance of the n-th arc.
u voltage across the arc
u_n voltage across the n-th arc
i current through the arc
P_n cooling constant of the the n-th arc
τ_n time constant of the n-th arc
λ_n Cassie-Mayr control of the n-th arc; λ=1results in a Cassie arc and λ=2 results in a Mayr arc.
k_n constants representing the breaker design.

The free parameters of KEMA arc model are τ_1, P_1 and P_2.

III. A.M.B. Program in Recent Versions of MATLAB

The A.M.B. program cannot be activated in recent versions of MATLAB, because of changes in MATLAB/Simulink power systems libraries. The differential equations of the arc models constituting the A.M.B. program have been incorporated by means of the DEE (Differential Equation Editor) block (Fig.1) [3, 4]; this block not exists in the Simulink libraries in recent versions of MATLAB. Furthermore many blocks constituting the test circuit of the A.M.B. program (Fig. 2) cannot be activated in recent versions of MATLAB, consequently, the A.M.B. program must be re-created again in MATLAB/Simulink.

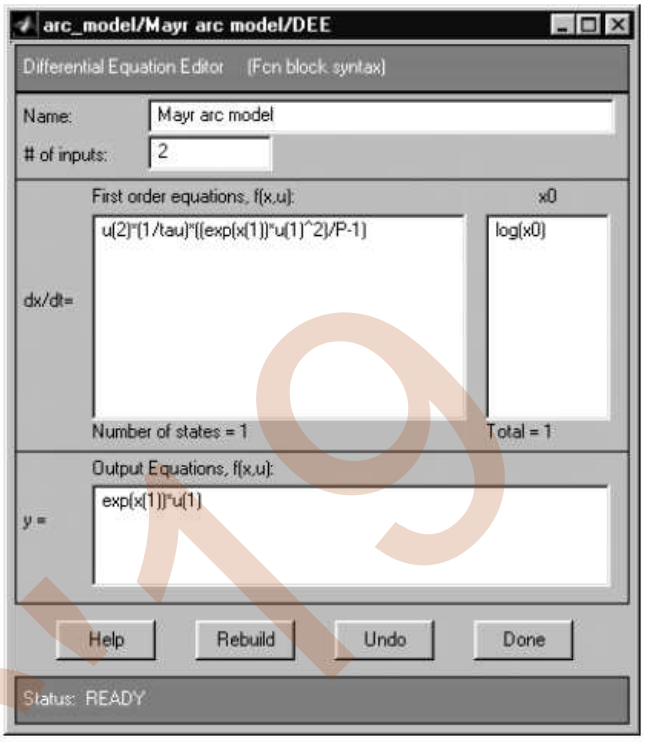

Fig. 1. Equations of Mayr arc model incorporated by means of Simulink DEE block. Reproduced from [3]

IV. Creation of The New A.M.B. Program

The creation of the new A.M.B. program, in MATLAB/Simulink Power Systems, is made in three phases. In the first phase, the seven arc models cited above are created in MATLAB/Simulink. In the second phase, the test circuit in which the arc models will be inserted is realized and finally the menu which allows users to choose an arc model among the existing arc models is prepared.

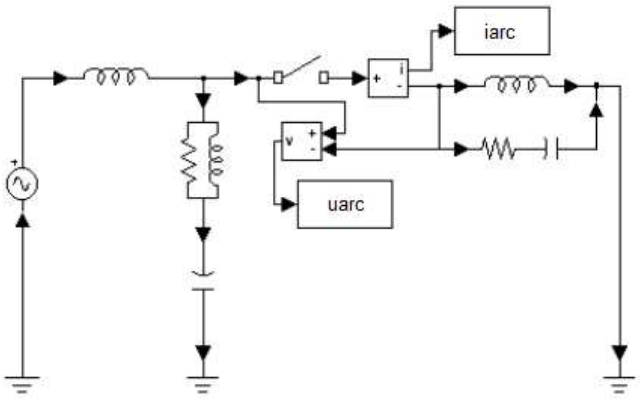

Fig. 2. the test circuit containing an arc model. Reproduced from [4]

A. *Creation of arc models*

Arc models of the new A.M.B. program are created in MATLAB/Simulink Power Systems, with a method simpler than this used in the old A.M.B. To explain this method, the creation of the modified Mayr arc model is described. The procedure is the same for the creation of the others arc models.

The equation (3) of modified Mayr arc model is rearranged as:

$$\frac{dg}{dt} = \frac{1}{\tau}\left(\frac{uig}{p(P_0 + U_0|i|)} - g \right) \tag{15}$$

To incorporate the modified Mayr arc model in MATLAB/Simulink, the following system of equations must be solved:

$$\frac{dg}{dt} = \frac{1}{\tau}\left(\frac{u^2 g^2}{p(P_0 + U_0|gu|)} - g \right) \tag{16}$$

$$i = gu \tag{17}$$

The above system of equations can be written in MATLAB/Simulink Power Systems (Fig. 3), as:

$$x_1 = \frac{dU(3)}{dt} = \frac{U(2)}{\tau}\left(\frac{U(1)^2 U(3)^2}{p(P_0 + U_0|U(3)U(1)|)} - U(3) \right) \tag{18}$$

$$y_1 = U(3)U(1) \tag{19}$$

U(1) is the first input of the arc model, it is equal to the arc voltage u.
U(2) is the second input, it represents contact separation of the circuit breaker:
U(2)=0 when contacts are closed
U(2)=1 when contacts are being opened
y_1 is the output of the arc model , it is equal to arc current i.
U(3) is the state variable of the differential equation of the arc model, it is equal to arc conductance g, instead to natural logarithm of the arc conductance ln(g) in the old A.M.B.
x_0 is the initial value of the state variable, it represents the initial value of the arc conductance g(0) at the moment of the contacts separation.

After creating a subsystem, the following Simulink blocks are added (Fig. 4):

- Voltage Measurement block to measure the arc voltage
- Controlled Current Source block to convert the Simulink input signal into an equivalent current source.
- Hit crossing block to detect when current crosses the zero value.

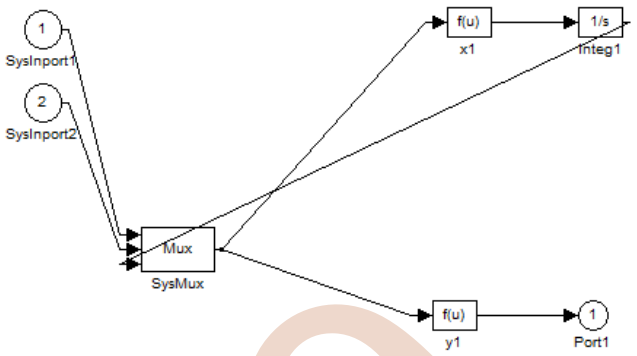

Fig. 3. Modified Mayr arc equations set in MATLAB/Simulink.

- Step block to control the contacts separation of the circuit breaker.

After that, a subsystem is created, it represents the arc model.

B. *Creation of the test circuit*

For numerical computations, a test circuit in which an arc model can be inserted, is realized (Fig. 5).

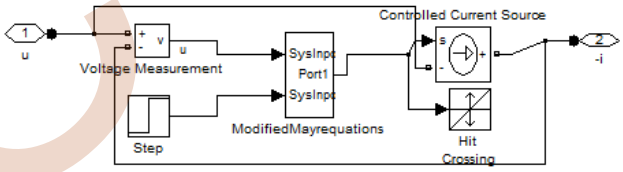

Fig. 4. Modified Mayr arc model built in MATLAB/Simulink Power System.

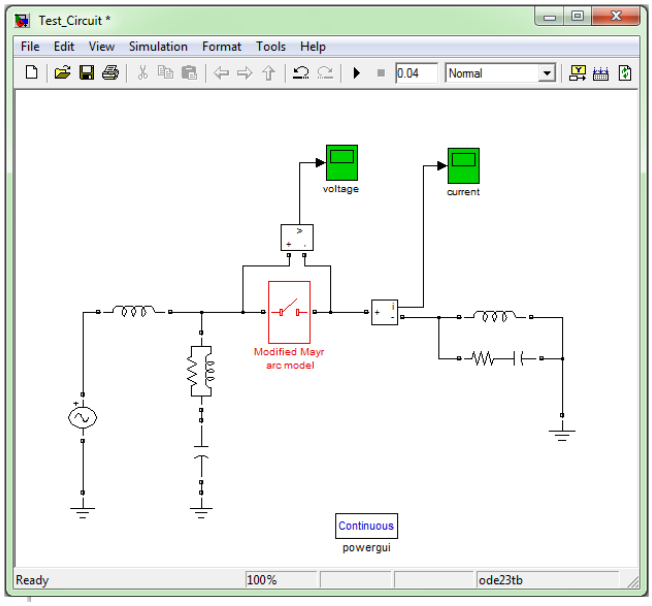

Fig. 5. Modified Mayr arc model inserted in the test circuit.

C. *Menu of the new A.M.B. program*

The menu of the new A.M.B. program is simpler than this used in the old A.M.B. program because rather than using two tests circuits one test circuit is used. The arc models of Cassie, Mayr, modified Mayr, Habedank, KEMA, Schavemaker and Schwarz are incorporated in the new A.M.B. program (Fig. 6). The user can choose an arc model and insert it in the test circuit of figure 5. He will introduce the free parameters of the chosen arc model as well as the parameters of the test circuit to do numerical computations

The new A.M.B. program is a flexible tool because the user can easily incorporate to this program any other arc model.

V. NUMERICAL COMPUTATIONS WITH THE NEW A.M.B. PROGRAM

As an example of numerical computations with the new A.M.B. program, modified Mayr arc model is used. The arc model parameters needed were extracted from measured arc voltage and arc current traces (Fig. 7) during a test performed on an SF6 circuit breaker 72kV for a successful interruption of 21. 2 kA_{RMS}. An expansion around current zero of the arc current shows the measured post-arc current (Fig. 8) [5].

Modified Mayr arc model parameters extracted from measured curves are given in the table I. They are set by means of the dialogue box of the modified Mayr arc model. The initial conductance of the arc g(0) and the time at which contact separation of the circuit breaker takes place must be specified too.

The computational results are shown in Fig.9 to 12. Modified Mayr arc model has predicted a successful interruption, like in the real test, because current is null after current zero (Fig. 9) and the T.R.V. is amortized (Fig. 10).

TABLE I. FREE PARAMETERS OF MODIFIED MAYR ARC MODEL [6]

U0 (V/bar)	*P0 (W/bar)*	*τ (µs)*
248	15000	0.6

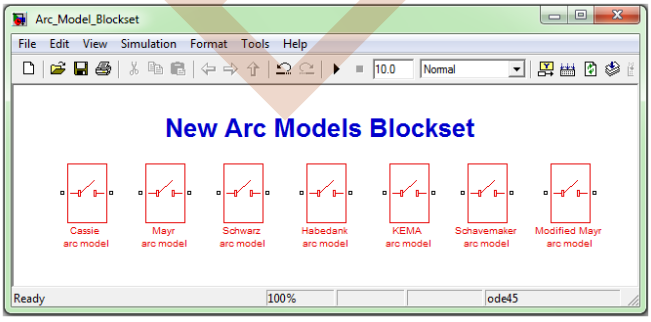

Fig. 6. The arc models incorporated in the new A.M.B. program.

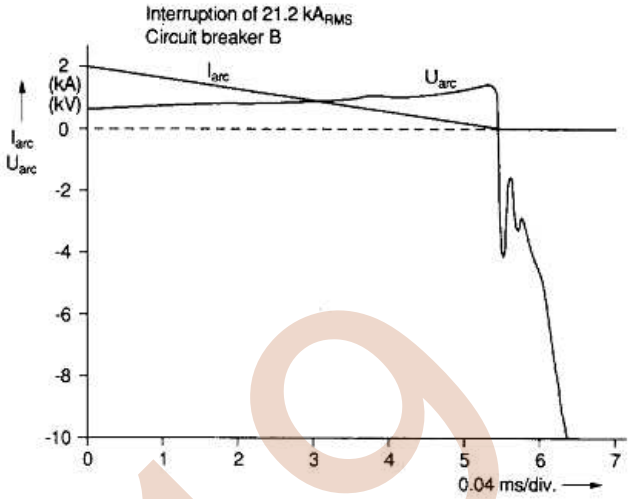

Fig. 7. Measured arc voltage and arc current traces. Reproduced from [6].

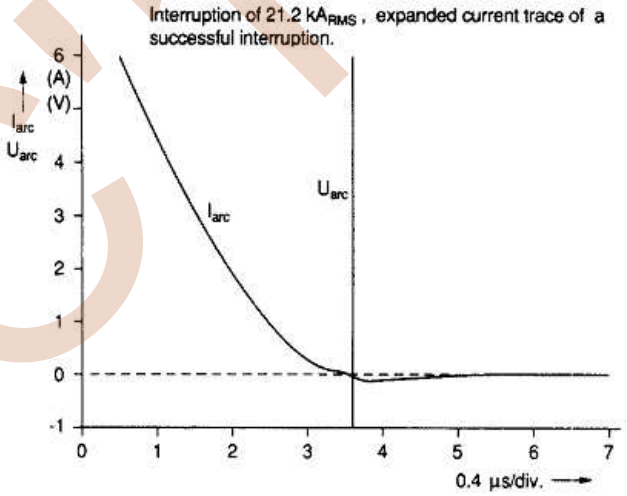

Fig. 8. Measured post-arc current. Reproduced from [6].

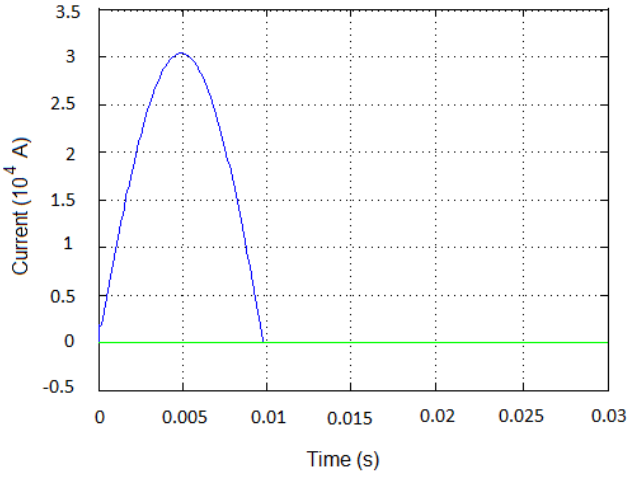

Fig. 9 Computed Current trace by using modified Mayr arc model.

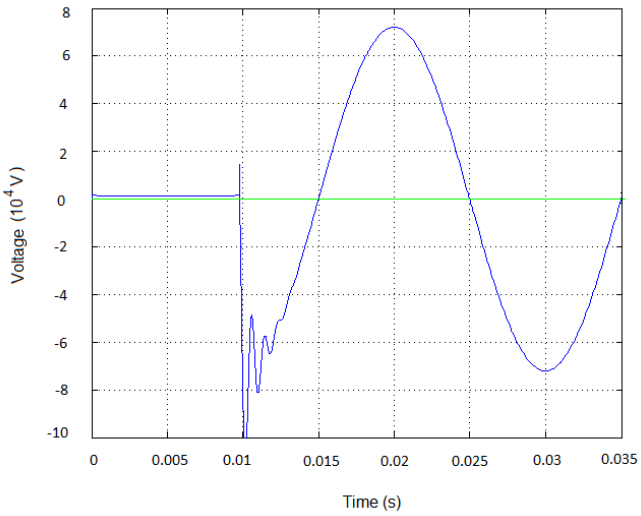

Fig. 10. Computed T.R.V. by using modified Mayr arc model

An expansion around current zero of the arc current trace shows the computed post-arc current (Fig. 11) and the computed extinction pick (fig. 12).

VI. ADVANTAGES OF THE NEW A.M.B.PROGRAM

Compared with the old A.M.B. program, the new A.M.B. program presents the following advantages:

- It works in recent versions of MATLAB
- Its integration to MATLAB/Simulink is easier due to Simulink upgrade.
- The incorporation method of the arc models in MATLAB/Simulink Power Systems is more simple.
- The menu is more simple.
- The computation time is shorter due to the high performance of actual PC.
- User can add any other arc model to the new A.M.B.

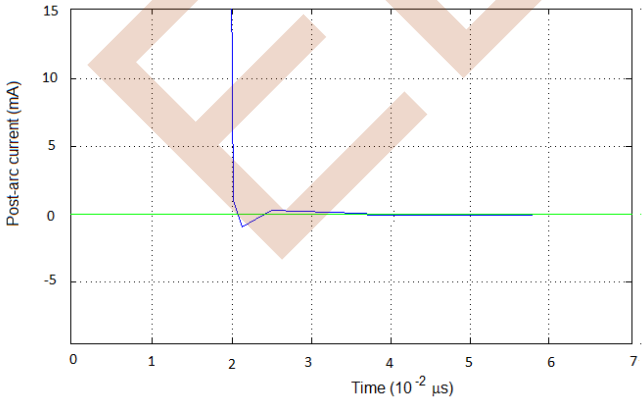

Fig. 11. Computed post-arc current trace by using modified Mayr arc model.

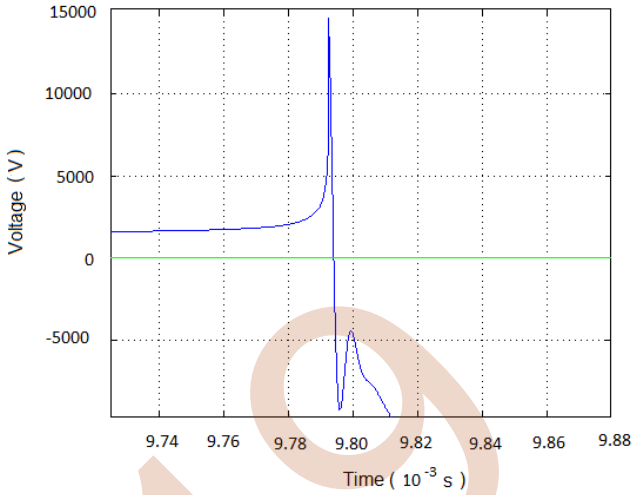

Fig. 12. Computed extinction pick by using modified Mayr arc model

VII. CONCLUSION

Through this work, the A.M.B. program is updated and improved, the result is a new A.M.B. program more simple than the old A.M.B., it can work in the recent versions of MATLAB quite easy for use and it is a flexible tool at which, any other arc model can be added.

REFERENCES

[1] P. H Schavemaker, and L. van der Sluis, A. Pharmatrisanti, " Post-arc current reconstruction based on actual circuit breaker measurements ", IEE Proc. Sei. Meas. Technol, Vol. 149 no.1, pp. 17-20, Jan. 2002.

[2] P. H Schavemaker, A.J.P de Lange and L. van der Sluis," A Comparison between Three Tools for Electrical Transient computations ", in Proc. IPST 99 – International conference on Power Systems Transients, Budapest, Hungary, June 20-24, 1999, pp. 13-18

[3] P. H Schavemaker, and L. van der Sluis," The Arc Model Blockset ", Proceedings of the Second IASTED International Conference POWER AND ENERGY SYSTEMS (EuroPES), Crete, Greece, June 25-28, 2002, pp. 644-648 .

[4] P. H Schavemaker, "Arc Model Blockset for use with MATLAB Simulink and Power System Blockset", Delft University of Technology, User's Guide, Version 2, 2001.

[5] Juan A. Martinez-Velasco, Modeling of Circuit Breakers Using the Type-94 Component, EEUG News February 1997, 55-97

[6] L. Van der Sluis, W.R. Rutgers, "The Comparison of Test Circuits with Arc Models", IEEE Transaction on Power Delivery, vol. 10, no. 1, pp. 280-285, Jan. 1995.

[7] L.R Orama, Numerical arc model Parameters Extracion for SF6 Circuit Breaker simulations, International Conference on Power Systems transients, IPST 2003 New Orleans, USA, 1-5

[8] P.H. Schavemaker, L.Van der Sluis, "An improved Mayr-type arc model based on current-zero measurement", IEEE Transaction on Power Delivery, Vol. 15 No. 2, April 2000, 580-584

[9] U. Habedank and A.G Siemens, "Application of a New Arc Model for the Evaluation Short-circuit breaking Tests", IEEE Transactions on Power Delivery, Vol. 8, N° 4, October 1993, pp: 1921-1925

[10] R.P.P. Smeets and V.Kertesz, "Evaluation of high-voltage circuit breaker performance with a validated arc model", IEE Proc. Gener. Transm. Distrib., Vol. 147, N° 2, March 2000, 121-125

A Dynamic Neural Network Model for Solving Combined Economic and Emission Dispatch with Real-Time Applications

Smail Boudab
LGEA Laboratory Electrical Engineering Department,
Larbi Ben M'hidi University, 04000 Oum El-Bouaghi,
Algeria.
Email: smail_ln@yahoo.fr.

Noureddine Goléa
LGEA Laboratory Electrical Engineering Department,
Larbi Ben M'hidi University, 04000 Oum El-Bouaghi,
Algeria.
Email: nour_golea@yahoo.fr.

***Abstract*— In this paper, a Dynamic Neural Network Model (DNN) has been proposed to find the optimal solution for Combined Economic and Emission Dispatch problems (CEED) with Real-Time applications. It is aimed, in the CEED problem, that scheduling of generators should operate with both minimum fuel costs and emission levels, simultaneously, while satisfying the load demand and operational constraints. In this paper, the CEED problem is formulated as a multi-objective problem by considering the fuel cost and emission objective of generating units. The bi-objective optimization problem is converted into a single objective function using a price penalty factor in order to solve it with (RT-DNN). The new algorithm is applied and tested to an example from the literature (IEEE 30-bus system of six thermal units) and the solution is then compared with that obtained by some other techniques to prove the superiority and effectiveness of the proposed algorithm.**

Keywords- Economic load dispatch (ELD), Combined Economic and Emission Dispatch (CEED), environmental dispatching*, *Dynamic Neural Network (DNN), Optimization.

I. INTRODUCTION

Economic load dispatch (ELD) problem is a computational process to determine the generation contribution of each unit at minimum fuel cost while satisfying the total load demand and all operational constraints [2,3]. The electricity generation from fossil fuels is exacerbating the atmospheric pollution which has become one of the most important concerns in recent years. So, besides moving toward generating electricity from clean and renewable energies [4], pollutant emissions released by traditional generation units should also be considered in the generation scheduling of the system. Emission constrained dispatch (ECD) is similar to ELD, except that its goal is minimizing emissions instead of fuel cost. However, due to the fact that fuel cost and emission are in conflict with each other (minimizing one increases the other), system operation with either minimum fuel cost or minimum emissions will be unworkable. To deal with this problem, a load dispatching technique to simultaneously minimize both fuel cost and emissions, called combined economic emission dispatch (CEED), has been developed. It is clear that the determination of a single optimal solution for the bi-objective CEED problem requires that the weight of both objective functions be specified [5].

The combined economic emission dispatch (CEED) problem is one of the most important issues in optimizing the operation of electric power systems. In practice, the CEED problem is a highdimensional non-convex optimization problem with several equality and inequality constraints, and it is one of the most complicated optimization problems in electrical power engineering [6]. Generally, there are three main approaches to solve the CEED problems:

The first approach is to convert the bi-objective CEED problem into a single-objective optimization task by defining a price penalty factor (h) or normalizing the fuel cost and emissions. This approach has been practiced in several previous research works using different methods such as particle swarm optimization algorithm (PSO), gravitational search algorithm (GSA) and gravitational acceleration enhanced PSO algorithm (GAEPSO) [7], moth swarm algorithm (MSA) [8], real coded chemical reaction algorithm (RCCRO) [9], spiral optimization algorithm (SOA) [10], opposition-based harmony search algorithm [11], biogeography based optimization algorithm (BBO) [12], and hybrid PSO and GSA (PSOGSA) [13].

The second method involves simultaneous minimization of fuel cost and emissions as a bi-objective optimization problem. This approach has been practiced in several previous papers using different methods such as multi-objective particle swarm optimization (MOPSO) [14], multi-objective differential evolution (MODE) [15], multi-objective harmony search (MOHS) [16], tribe-modified differential evolution (Tribe-MDE) [17], non-dominated sorting bacterial foraging (NSBF) and fuzzy dominance sorting bacterial foraging (FSBF) [18], and elitist non-dominated sorting genetic algorithm (NSGA-II) [19]. However, these methods are computationally involved and time-consuming and might produce only sub-optimal solutions.

The third approach is to consider the emission as a constant within the permitted limits, in which the problem can be solved through a single-objective optimization task. However, this approach is unable to provide any information regarding tradeoffs between fuel cost and emissions. For instance,

Davidon- Fletcher-Powell's method of optimization has been used in [20] for solving the CEED problem while the emission amount has been considered as a constant in the allowed limits.

Neural networks have been extensively studied over the past few decades and have found applications in variety of areas such as associative memory, moving object speed detection, image and signal processing, and pattern recognition. In many applications, real-time solutions are usually imperative [1,32,33]. These applications strongly depend on the dynamic behavior of the networks. In this paper, we propose a one-layer neural network developed by [34] for solving nonlinear optimization problems with general linear constraints CEED. In particular, since simple structure and global stability are the most desirable dynamic properties of the neural networks,

In this paper, we present a dynamic neural network model (DNN) for the solution of CEED. The bi-objective CEED problem is converted into a single objective optimization task by defining a modified price penalty factor. The performance of the proposed method has been demonstrated under simulated conditions on IEEE- 30-Bus system with 6-Generation units. The system was solved excluding/including the losses as two separate cases. In addition to solving the CEED problem, the ELD and ECD problem also have been solved, and the obtained results are compared with a large number of other existing algorithms.

II. EED FORMULATION

The typical EED problem can be formulated as a bi-criteria optimization model. The two conflicting objectives, i.e, fuel cost and pollutants emission, should be minimized simultaneously while fulfilling certain system constraints. This problem is formulated as follows.

A. *Minimization of fuel cost*

The total fuel cost $C_T(P_{ig})$ can be represented as follows:

$$C_T(P_{ig}) = \sum_{i=1}^{n} (a_i + b_i P_{ig} + g_i P_{ig}^2) \quad (1)$$

where a_i, b_i, g_i are fuel cost coefficients of i-th generator; P_{ig} is the real power output of the i-th generator.

B. *Minimization of pollutants emission*

The most important emissions considered in the power generation industry due to their effects on the environment are sulfur dioxide (SO_2) and nitrogen oxides (NO_x). These emissions can be modeled through a combination of polynomial and exponential terms [21]:

$$E_T(P_{ig}) = \sum_{i=1}^{n} d_i + s_i P_{ig} + r_i (P_{ig})^2 + c_i exp(J_i P_{ig}) \quad (2)$$

where d_i, s_i, r_i, c_i, and J_i are coefficients of the i-th generator emission characteristics.

C. *Problem Constraints*

There are two constraints considered in the problem, i.e., the generation capacity of each generator and the power balance of the entire power system.

• Constraint 1: Generation capacity constraint

For normal system operations, real power output of each generator is restricted by lower and upper bounds as follows:

$$P_{ig}^{\min} \le P_{ig} \le P_{ig}^{\min} \quad , \; i = 1,2,....,n \quad (3)$$

where $P_{ig}^{\min}$ and $P_{ig}^{\min}$ are the minimum and maximum power generated by generator *i*, respectively.

• Constraint 2: Power balance constraint

The total power generation must cover the total demand P_D and the real power loss in transmission lines P_L. This relation can be expressed as:

$$\sum_{i}^{n} P_{ig} = P_D + P_L \quad (4)$$

Here a reduction is applied to model transmission losses as a function of the generators output through Kron's loss coefficients. The Kron's loss formula can be expressed as follows:

$$P_L = \sum_{i=1}^{n}\sum_{j=1}^{n} P_{ig} B_{ij} P_{jg} + \sum_{j=1}^{n} B_{0j} P_{jg} + B_{00} \quad (5)$$

where B_{ij} is the transmission loss coefficient ($i = 1,2,....,n$; $j = 1,2,....,n$), B_{0j} is the i-th element of the loss coefficient vector. B_{00} is the loss coefficient constant.

III. CEED FORMULATION

The CEED problem can be formulated by combining two independent objectives, which are emission and fuel cost using a price penalty factor. In this way, the bi-objective CEED problem is expressed in a single-objective form. To solve the CEED problem, this form is intended to minimize while satisfying the constraints expressed above. The single-bjective CEED problem is formulated as follows:

$$Minimize \; F_T(P_{ig}) = C_T(P_{ig}) + h_i E_T(P_{ig}) \quad (6)$$

$$F_T(P_{ig}) = \sum_{i=1}^{n} (a_i + b_i P_{ig} + g_i P_{ig}^2) + h_i \sum_{i=1}^{n} d_i + s_i P_{ig} + r_i (P_{ig})^2 + c_i exp(J_i P_{ig}) \quad (7)$$

where h_i [22] is the price penalty factor in \$/h. It is the ratio between maximum fuel cost and maximum emission, and is described as follows:

$$h_i = \frac{C(P_i^{\max})}{E(P_i^{\max})} = \frac{a_i + b_i P_i^{\max} + g_i (P_i^{\max})^2}{d_i + s_i P_i^{\max} + r_i (P_i^{\max})^2 + c_i exp(J_i P_i^{\max})} \quad (8)$$

The following steps are used to find the price penalty factor for a particular load demand [23]:

a. Find the ratio between maximum fuel cost and maximum emission of each generator.

b. Arrange the values of price penalty factor in ascending order.

c. Add the maximum capacity of each unit ($P_i^{\max}$) one at a time, starting from the smallest h_i , until $\sum P_i^{\max} \geq P_D$.

d. At this point, h_i which associated with the last unit in this process is the approximate price penalty factor value (h) for the given load.

Hence, a modified price penalty factor (h) is used to give the exact value for the particular load demand by interpolating the values of (h), corresponding to their load demand values. So, the optimization formulation of the CEED multi-objective problem under equality and inequality constraints has become as follows:

$$\begin{cases} Min \quad F(P_{ig}) = \sum_{i=1}^{n} (a_i + b_i P_{ig} + g_i P_{ig}^2) + h_i \sum_{i=1}^{n} d_i + s_i P_{ig} + r_i (P_{ig})^2 + c_i exp(J_i P_{ig}) \\ subject\ to\ P_{P_{ig}}^{\min} \leq P_{P_{ig}} \leq P_{P_{ig}}^{\max}, \quad i = 1,..,n \\ \sum_{i=1}^{ng} P_{ig} = PL + P_D \end{cases} \quad (9)$$

IV. OPTIMIZATION OF THE CEED PROBLEM BASED ON RT-DNN

In this part, we propose a single-layer neural network to solve the nonlinear problem of combined economic environmental dispatching (9) with its linear constraints.

In particular, the simple structure and overall stability are the most desirable dynamic properties of neural networks; our motivation for this study is mainly focused on the development of a neural network with these properties suitable for solving optimization problems nonlinear in real time.

Another objective of this study is to be concerned with the real-time application of the proposed DNN model in solving the problem of optimal power distribution. The main idea here is to convert the problem of convex programming into a problem of variational inequality. The inequality constraint in (9) can be rewritten as $E^T P \geq X_{\min}$. So the problem CEED (9) became as follows:

$$\begin{cases} \min & F(P) \\ \text{sujet à} & JP \geq X_{\min} \\ & EP = D \end{cases} \quad (10)$$

where :

$$J = \begin{bmatrix} J_1 \\ J_2 \end{bmatrix} \text{ with } J_1 = \begin{bmatrix} 1 & 0 & 0 & .... & 0 \\ 0 & 1 & 0 & .... & 0 \\ M & M & M & M & M \\ 0 & 0 & 0 & .... & 1 \end{bmatrix}, \quad J_2 = \begin{bmatrix} -1 & 0 & 0 & .... & 0 \\ 0 & -1 & 0 & .... & 0 \\ M & M & M & M & M \\ 0 & 0 & 0 & .... & -1 \end{bmatrix},$$

$$X_{\min} = \begin{bmatrix} P_{\max} & -P_{\min} \end{bmatrix}^T, E^T = \begin{bmatrix} 1 & ... & 1 \end{bmatrix} \text{ and } D = P_L + P_D$$

The solution of the problem CEED (10) requires the formulation of the Lagrangian function also called the function of increased cost given by [24]:

$$\begin{aligned} L &= F(P) + l\,(E^T P - D) + k^T (P - X_{\min}) \\ &= \sum_{i=1}^{ng} (a_i + b_i P_{ig} + g_i P_{ig}^2) + h_i \sum_{i=1}^{ng} d_i + s_i P_{ig} + r_i (P_{ig})^2 + c_i exp(J_i P_{ig}) + \\ &\quad l\,(E^T P - D) + k^T (P - X_{\min}) \end{aligned} \quad (11)$$

where l and k are also known as dual decision variables. $l \in R$ is the Lagrange multiplier associated with the equality constraint and $k \in R^n$ is the Lagrange multiplier associated with the inequality constraint.

The necessary conditions for the optimal solution of (11) are found by setting the partial derivatives of L to zero with respect to P, l and k respectively:

$$\begin{aligned} \nabla_P L &= \nabla_P F(P) + l\,E + k = 0 \\ \nabla_k L &= JP - X_{\min} = 0 \\ \nabla_l L &= E^T P - D = 0 \end{aligned} \quad (12)$$

where $\nabla F(P) = (\partial F(P)/\partial P_1, \partial F(P)/\partial P_2, ..., \partial F(P)/\partial P_{ng})^T$ is the gradient vector of the function $F(P)$.

By applying the Kuhn-Tucker conditions for convex optimization [90], the optimal decision variables P^* and (l^*, k^*) must satisfy:

$$\begin{aligned} &\nabla_P F + l\,E + Jk = 0 \\ &JP - X_{\min} = 0 \\ &E^T P - D = 0 \end{aligned} \quad (13)$$

According to the Karush-Kuhn-Tucker (KKT) conditions (13) and the well-known projection theorem [25], we see that P^* is the optimal solution for the problem (11) if and only if there exists $y^* \in R$ and $z^* \in R^{ng}$ such that $(P^{*T}, y^{*T}, z^{*T})^T$ satisfies the following conditions:

$$\begin{cases} P = y_1(P - a(\nabla F(P) + J^T y - Ez) \\ y = y_2(y + a(JP - X_{\min})) \\ z = E^T P - D \end{cases} \quad (14)$$

where a is positive constant $y_2(y) = [y_2(y_1), y_2(y_2), ..., y_2(y_{ng})]^T$ in which $y_2(y_i) = \max\{0, y_i\}$ and $y_1(P) = [y_1(P_1), y_1(P_2), ..., y_1(P_{ng})]^T$ where for $i = 1,...,n$

$$y_1(P) = \begin{cases} P_i^{\min} & si\ P_i \leq P_i^{\min} \\ P_i & si\ P_i^{\min} \leq P_i \leq P_i^{\max} \\ P_i^{\max} & si\ P_i \geq P_i^{\max} \end{cases} \quad (15)$$

The equation (14) can be equivalently written as

$$\begin{bmatrix} P \\ y \\ z \end{bmatrix} = \begin{bmatrix} y_1(P - a(\nabla F(P) + J^T y - Ez)) \\ y_2(y + a(JP - X_{\min})) \\ z - a(E^T P - D) \end{bmatrix} \quad (16)$$

Based on (16), we propose a dynamic neural network for solving problem (11), with the following dynamical equation:

$$\frac{dz}{dt} = \frac{d}{dt}\begin{pmatrix} P \\ y \\ z \end{pmatrix} = q\begin{pmatrix} P + y_1(P - a(\tilde{N}F(P) + J^T y - Ez)) \\ -y + y_2(y + a(JP - X_{\min})) \\ a(E^T P - D) \end{pmatrix} \quad (17)$$

where $q > 0$ is a positive constant and , $(P^T, y^T, z^T)^T$ is a state vector.

The simplified architecture of the dynamic neural network (17) is shown in Fig.1.

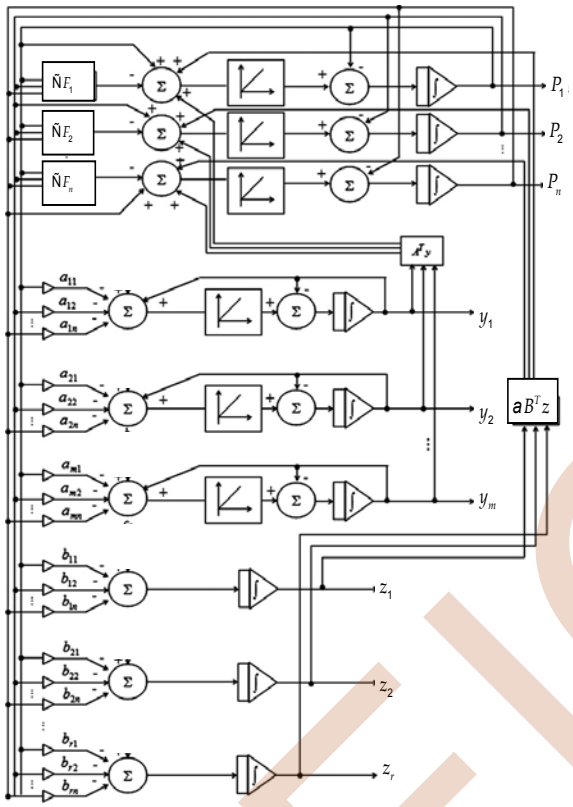

Figure 1. A simplified architecture of the DNN (4)

The dynamic system (17) can be easily realized in a dynamic neural network with a hidden layer structure. In Fig.1, a block diagram of this neural network is presented where P, y and z are the outputs of the network. The other parameters are $\tilde{N}F(P) = (\tilde{N}F_1(P), \tilde{N}F_1(P), \ldots \tilde{N}F_n(P))^T$, $J = (a_{ij})_{m \times n}$ and $E = (b_{pj})_{r \times n}$.

V. Simulation Results and Discussions

In order to verify the feasibility of the proposed method RT-DNN, comprehensive simulation studies are performed. The results are compared with previously published ones. The proposed approach RT-DNN is tested on the standard IEEE 30-bus six generator test system with load demand 2.834 pu on 100 MVA base value. Fuel cost and total emission function coefficients along with each generator capacity limits are given in Tables 1 and 2 respectively [31]. RT-DNN based simulations are developed in Matlab language R2013a and it executed on a Intel(R) Core(TM) Duo 2.2 GHz personal computer with 4.00 Go RAM. The given test system has been further subdivided into 3 cases as given below.

TABLE 1. Fuel cost coefficients and capacity limits.

No	$P_i^{\min}$	$P_i^{\max}$	a_i	b_i	g_i
1	0.05	1.5	10	200	100
2	0.05	0.6	10	150	120
3	0.05	1	20	180	40
4	0.05	1.2	10	100	60
5	0.05	1	20	180	40
6	0.05	0.6	10	150	100

TABLE 2. Emission coefficients of thermal generating units.

$r_i(10^{-3})$	s_i	d_i	c_i	J_i
4.091	-5.554	6.490	2.0×10^{-4}	2.857
2.543	-6.047	5.638	5.0×10^{-4}	3.333
4.258	-5.094	4.586	1.0×10^{-5}	8.000
5.326	-3.550	3.380	2.0×10^{-3}	2.000
4.258	-5.094	4.586	1.0×10^{-6}	8.000
6.131	-5.555	5.151	1.0×10^{-5}	6.667

Case 1: The proposed method is applied to the mentioned test system and system loss is neglected. In this case the respective fuel cost and emission objective functions have been optimized separately as given by Equations (1) and (2). Figures 2 and 3 illustrate the convergence characteristics of cost and emission functions, respectively. The minimum fuel cost that has been obtained by RT-DNN algorithm is 600.1114 $/h, and minimum emission was 0.1862 ton/h. Further, to prove the robustness of the proposed technique RT-DNN, the results of the various optimization algorithms such as heuristic modified group search optimization (MGSO) algorithm proposed in [26] A multiobjective fuzzy dominance based bacterial foraging algorithm (FSBF) proposed in [27], multiobjective q-particle swarm optimization (q -PSO) in [28], Strength Pareto evolutionary algorithm (SPEA) [29] and modified bacterial foraging algorithm (MBFA) presented in [30] have been compared and presented in Tables 4 and 5 for fuel cost and emission level, respectively.

TABLE 3. Numerical results for case 1 (without losses).

	Cost Dispatch	**Emission Dispatch**
P_1 (pu)	0.1097	0.3907
P_2 (pu)	0.2998	0.4928
P_3 (pu)	0.5244	0.5029
P_4 (pu)	1.0160	0.4525
P_5 (pu)	0.5244	0.502 9
P_6 (pu)	0.3597	0.4923
Cost ($/h)	**600.1114**	633.3390
Emission (T/hr)	0.2051	**0.1862**

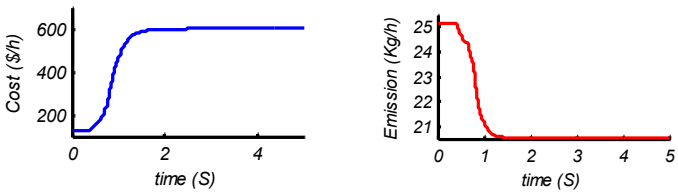

Fig.2. Convergence characteristic of minimizing fuel cost (case 1)

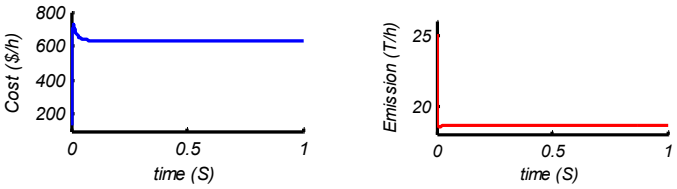

Figure 3. Convergence characteristic of minimizing emission (case 1)

TABLE 4. Comparative results for pure economic power dispatch of case 1

	MGSO[26]	FSBF [27]	q-PSO [28]	SPEA [29]	MBFA [30]	**RT-DNN**
P_1 (pu)	0.1091	0.1077	0.1097	0.1062	0.1133	**0.1097**
P_2 (pu)	0.2990	0.3011	0.2997	0.2897	0.3005	**0.2998**
P_3 (pu)	0.5232	0.5249	0.5242	0.5289	0.5202	**0.5244**
P_4 (pu)	1.0183	1.0143	1.0161	1.0025	0.9882	**1.0160**
P_5 (pu)	0.5242	0.5223	0.5242	0.5402	0.5409	**0.5244**
P_6 (pu)	0.3602	0.3638	0.3597	0.3664	0.3709	**0.3597**
Cost ($/hr)	600.1119	600.114	601.126	600.15	600.17	**600.1114**
Em (T/h)	0.2222	0.2222	0.222	0.2215	0.22	**0.2051**

TABLE 5. Comparative results for pure emission dispatch of case 1.

	MGSO[26]	FSBF [27]	q-PSO [28]	SPEA [29]	MBFA [30]	**RT-DNN**
P_1 (pu)	0.4043	0.4057	0.4060	0.4116	0.3943	**0.3907**
P_2 (pu)	0.4592	0.4635	0.4590	0.4532	0.4627	**0.4928**
P_3 (pu)	0.5376	0.5315	0.5379	0.5329	0.5423	**0.5029**
P_4 (pu)	0.3841	0.3849	0.3829	0.3832	0.3946	**0.4525**
P_5 (pu)	0.5384	0.538	0.5379	0.5383	0.5346	**0.502 9**
P_6 (pu)	0.5103	0.5105	0.5100	0.5148	0.5056	**0.4923**
Cost ($/h	638.073	638.283	638.273	638.51	636.73	**633.339**
Em (T/h)	0.1942	0.1942	0.19420	0.1942	0.1942	**0.1862**

Case 2: In this case, the transmission line losses have been considered, which were calculated using Kron's relation given by equation (5). The *B*-loss coefficients of this system have been taken from Yong Zhang and al [31]. Initially, the respective fuel cost and emission objective functions have been optimized separately. The results obtained for this case are given in Table 6. Figures 4 and 5 illustrate the convergence characteristics of cost and emission functions, respectively.

According to Tables 7 and 8, system total cost and level emission using the proposed method has impressive difference in comparison with methods published by [26-30].

TABLE 6. Numerical results for case 2 (with losses).

	Cost Dispatch	**Emission Dispatch**
P_1 (pu)	0.1104	0.3914
P_2 (pu)	0.3003	0.4937
P_3 (pu)	0.5260	0.5040
P_4 (pu)	1.0171	0.4540
P_5 (pu)	0.5260	0.5040
P_6 (pu)	0.3604	0.4933
Cost ($/h)	**601.4988**	634.7528
Emission (T/hr)	0.2051	**0.1862**

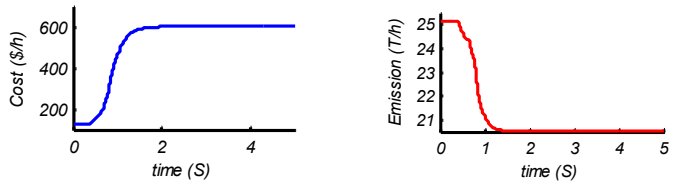

Figure 4. Convergence characteristic of minimizing fuel cost (case 2)

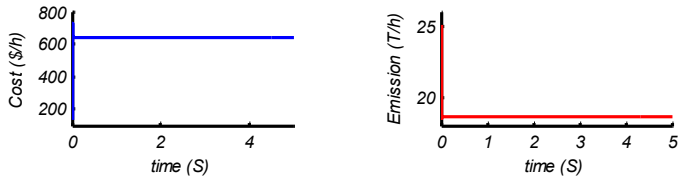

Figure 5. Convergence characteristic of minimizing emission (case 2)

TABLE 7. Comparative results for pure economic power dispatch of case 2

	MGSO[26]	FSBF [27]	q-PSO [28]	SPEA [29]	MBFA [30]	**RT-DNN**
P_1 (pu)	0.1182	0.1173	0.1209	0.1086	0.1141	**0.1104**
P_2 (pu)	0.3017	0.3049	0.2863	0.3056	0.3108	**0.3003**
P_3 (pu)	0.5302	0.5983	0.5835	0.5818	0.5994	**0.5260**
P_4 (pu)	1.017	0.978	0.9928	0.9846	0.9816	**1.0171**
P_5 (pu)	0.5263	0.5129	0.5239	0.5288	0.5048	**0.5260**
P_6 (pu)	0.3628	0.3545	0.3518	0.3584	0.3559	**0.3604**
Cost ($/hr)	604.422	607.508	605.99	607.81	607.67	**601.498**
Em (T/h)	0.222	0.2196	0.222	0.2201	0.2198	**0.2051**

TABLE 8. Comparative results for pure emission dispatch of case 2.

	MGSO[26	FSBF [27	q-PSO [28	SPEA [29	MBFA [30	**RT-DNN**
P_1 (pu)	0.4105	0.4135	0.4109	0.4043	0.4055	**0.3914**
P_2 (pu)	0.462	0.4652	0.4636	0.4525	0.4609	**0.4937**
P_3 (pu)	0.5424	0.539	0.5444	0.5525	0.5444	**0.5040**
P_4 (pu)	0.388	0.3894	0.3903	0.4079	0.3986	**0.4540**
P_5 (pu)	0.5403	0.5398	0.5444	0.5468	0.544	**0.5040**
P_6 (pu)	0.5102	0.5174	0.5154	0.5005	0.5134	**0.4933**
Cost ($/h	644.67	645.3981	649.207	642.6	644.43	**634.753**
Em (T/h)	0.1942	0.1942	0.1941	0.19422	0.1942	**0.1862**

Case 3: The proposed approach has been implemented to optimize cost and emission objectives simultaneously considering the two cases stated above (without and with losses). According to Section III, in order to handle the problem, a penalty factor is used. As it was mentioned, (8) presents the maximum amount of penalty factor and here price is assumed to be 0.98. The results obtained for this case are given in Table 9. Table 10 presents the comparative results for this case. Methods such as FSBF [27], MBFA [30], MGSO [26] and SPEA [29] are found around 615.7 and 617.5 ($/h); however, the proposed method is found 615 ($/h).

TABLE 9. Numerical results for case 3 (CEED without and with losses).

	Without losses	**With losses**
P_1 (MW)	0.2516	0.2367
P_2 (MW)	0.3770	0.3616
P_3 (MW)	0.5283	0.5887
P_4 (MW)	0.7124	0.7041
P_5 (MW)	0.5566	0.5635
P_6 (MW)	0.4081	0.4087
Cost ($/h)	**608.65**	**615.00**
Emission ($/hr)	**0.2007**	**0.2001**

TABLE 10. Comparative results for CEED (case 3).

	without losses		**with losses**	
	Cost ($/hr)	**Em (T/h)**	**Cost ($/h**	**Em (T/h)**
MGSO[26]	610.5587	0.2007	615.7835	0.2003
FSBF [27]	610.1841	0.2006	616.1627	0.2005
SPEA [29]	610.300	0.2004	617.57	0.2001
MBFA [30]	610.906	0.2000	616.496	0.2002
RT-DNN	**608.650**	**0.2007**	**615.00**	**0.2001**

Comparing the results of the proposed algorithm given in Table 4-10, it can be seen that the proposed RT-DNN technique is superior to all reported techniques and gives better results in terms of the fuel cost saving achieved and the

emission pollution. It can also be concluded that the proposed algorithm is capable of exploring more efficient solutions. This demonstrates the potential and effectiveness of the proposed technique to solve CEED problem.

VI. CONCLUSION

In this paper, a Dynamic Neural Network algorithm was proposed and successfully implemented to solve the multi-objective environmental economic dispatch problem. The proposed method has been applied to IEEE 30-bus test system. The mentioned problem is solved with and without considering system losses at pure power dispatch, pure emission dispatch and combined economic power and emission dispatch conditions. The solutions found by RT-DNN were compared with the results reported in several other research works. The numerical and statistical results clearly demonstrated the high efficiency of RT-DNN and its superiority compared to other existing optimization techniques in solving CEED problems.

VII. REFERENCES

[1] N. Kalouptisidis, "Signal Processing Systems, Theory and design". Wiley, New York (1997)

[2] Z. W Geem, "Economic dispatch using parameter-setting-free harmony search", Journal of Applied Mathematics, 2013.

[3] J. Kim, C. S. Kim and Z. W Geem, "A memetic approach for improving minimum cost of economic load dispatch problems", Mathematical Problems in Engineering, 2014.

[4] H. Rezaie, S. Moosavy, M. Chashmi, M. Mirsalim and H. Rastegar, "Enhancing LVRT capability and smoothing power fluctuations of a DFIG-based wind farm in a DC microgrid", Electric Power Components and Systems, 45(10) , 2017, pp 1080–1090.

[5] A. Chatterjee, S. P. Ghoshal and V. Mukherjee, "Solution of combined economic and emission dispatch problems of power systems by an opposition based harmony search algorithm", International Journal of Electrical Power & Energy Systems, 39(1) , 2012, pp 9–20.

[6] H. Rezaie, M. H. Kazemi-Rahbar , B. Vahidi and H. Rastegar, "Solution of combined economic and emission dispatch problem using a novel chaotic improved harmony search algorithm", Journal of Computational Design and Engineering, 6, 2019, pp 447–467.

[7] S. Jiang, Z. Ji and Y. Wang, "A novel gravitational acceleration enhanced particle swarm optimization algorithm for wind–thermal economic emission dispatch problem considering wind power availability", International Journal of Electrical Power & Energy Systems, 73, 2015, pp 1035–1050.

[8] M. Jevtic, N. Jovanovic, J. Radosavljevic and D. Klimenta, "Moth swarm algorithm for solving combined economic and emission dispatch problem", Elektronika ir Elektrotechnika, 23(5), 2017, pp 21–28.

[9] K. Bhattacharjee, A. Bhattacharya, and S. H. nee Dey, "Oppositional real coded chemical reaction optimization for different economic dispatch problems", International Journal of Electrical Power & Energy Systems, 55, 2014, pp 378–391.

[10] L. Benasla, A. Belmadani and M. Rahli, "Spiral optimization algorithm for solving combined economic and emission dispatch", International Journal of Electrical Power & Energy Systems, 62, 2014, pp 163–174.

[11] A. Chatterjee, S. P. Ghoshal and V. Mukherjee, "Solution of combined economic and emission dispatch problems of power systems by an opposition based harmony search algorithm", International Journal of Electrical Power & Energy Systems, 39(1), 2012, pp 9–20.

[12] S. Rajasomashekar and P. Aravindhababu, "Biogeography based optimization technique for best compromise solution of economic emission dispatch", Swarm and Evolutionary Computation, 7, 2012, pp 47–57.

[13] J. Radosavljevic, "A solution to the combined economic and emission dispatch using hybrid PSOGSA algorithm", Applied Artificial Intelligence, 30(5), 2016, pp 445–474.

[14] M. A. Abido, "Multiobjective particle swarm optimization for environmental/ economic dispatch problem", Electric Power Systems Research, 79(7), 2009, pp 1105–1113.

[15] M. A. Abido, "Multiobjective evolutionary algorithms for electric power dispatch problem", IEEE Transactions on Evolutionary Computation, 10(3), 2006, pp 315–329.

[16] S. Sivasubramani and K. S. Swarup, "Environmental/economic dispatch using multi-objective harmony search algorithm", Electric Power Systems Research, 81 (9), 2011, pp 1778–1785.

[17] T. Niknam, H. D. Mojarrad and B. B. Firouzi, "A new optimization algorithm for multi-objective economic/emission dispatch", International Journal of Electrical Power & Energy Systems, 46, 2013, pp 283–293.

[18] B. K. Panigrahi, V. R. Pandi, S. Das and S. Das, "Multiobjective fuzzy dominance based bacterial foraging algorithm to solve economic emission dispatch problem", Energy, 35(12), 2010, pp 4761–4770.

[19] R. T. A. King, H. C. Rughooputh and K. Deb, "Evolutionary multiobjective environmental/economic dispatch: Stochastic versus deterministic approaches", In International conference on evolutionary multi-criterion optimization, March 2005, pp 677–691, Berlin, Heidelberg: Springer.

[20] L. D. Arya, S. C. Choube and D. P. Kothari, "Emission constrained secure economic dispatch", International Journal of Electrical Power & Energy Systems, 19 (5), 1997, pp 279–285.

[21] A. Farag, S. Al-Baiyat, T. C. Cheng, "Economic load dispatch multiobjective optimization procedures using linear programming techniques", IEEE Trans Power Syst. 10 (2) , 1995, pp 731-738.

[22] R. Bharathi, M. J. Kumar, D. Sunitha and S. Premalatha, "Optimization of combined economic and emission dispatch problem—a comparative study", Proceedings of the Power Engineering Conference, Singapore, pp 134–139.

[23] A. Y. Abdelaziz, E. S. Ali and S. M. Abd Elazim, "Flower pollination algorithm to solve combined economic and emission dispatch problems", Engineering Science and Technology, an International Journal 19, 2016, pp 980–990.

[24] D. P. Bertsekas, Constrained Optimization and Lagrange Multiplier Methods Academic Press, New York, 1982.

[25] Y. Xia and G. Feng, "A modified neural network for quadratic programming with real-time applications", Neural Inf. Process, 3(3), 2004, pp 69–76.

[26] N. Daryani and K. Zare, "Multiobjective power and emission dispatch using modified group search optimization method", Ain Shams Engineering Journal 9, 2018, pp 319–3283.

[27] B. K. Panigrahi, V. Ravikumar Pandi, Das Sanjoy and Das Swagatam, "Multi objective fuzzy dominance based bacterial foraging algorithm to solve economic emission dispatch problem", Energy; 4761, 2010 , pp 35–70.

[28] T. Niknam and H. Doagou-Mojarrad, "Multi-objective economic/ emission dispatch by multiobjective h-particle swarm optimization", IET Gener Transm Distrib, 6(5), 2012, pp 363–77.

[29] M. A. Abido, "Environmental/economic power dispatch using multiobjective evolutionary algorithm", IEEE Trans Power Syst, 18(4), 2003, pp 1529.

[30] P. K. Hota, A. K. Barisal and R. Chakraborty, "Economic emission load dispatch through fuzzy based bacterial foraging algorithm", Electr Power Energy Syst, 2010, pp 32–37, 794–803.

[31] Y. Zhang, D. W. Gong and Z. Ding. "A bare-bones multi-objective particle swarm optimization algorithm for environmental/economic dispatch", Information Sciences 192 , 2012, pp 213–227.

[32] T. Youshikawa, "Foundations of Robotics. Analysis and Control". MIT Press, Cambridge (1990)

[33] A. Cichocki, and R. Unbehauen, "Neural Networks for Optimization and Signal Processing". Wiley, England (1993)

[34] A. Malek and M. Yashtini, " A Neural Network Model for Solving Nonlinear Optimization Problems with Real-Time Applications" International Symposium on Neural Networks ISNN 2009 , pp 98-108.

Environmental/Economic Dispatch Problem Solution Based on Discontinuous Recurrent Neural Network

Smail Boudab
LGEA Laboratory Electrical Engineering Department,
Larbi Ben M'hidi University, 04000 Oum El-Bouaghi,
Algeria.
Email: smail_ln@yahoo.fr.

Noureddine Goléa
LGEA Laboratory Electrical Engineering Department,
Larbi Ben M'hidi University, 04000 Oum El-Bouaghi,
Algeria.
Email: nour_golea@yahoo.fr.

Neural Network (DRNN) algorithm for solving environmental economic load dispatch problem (EED). This problem is formulated as a multi-objective one with two competing functions, namely economic cost and emission functions, subject to different constraints. The inequality constraints considered are maximum and minimum limits of power generation while the equality constraint is demand-generation balance. The results are obtained for a simple power 3-generator system. The solution is then compared with that obtained by some other techniques to prove the superiority and effectiveness of the proposed algorithm.

***Keywords— Environmental/Economic Dispatch EDD, Emission, Recurrent Neural Network, Optimization*.**

I. INTRODUCTION

The main objective of economic load dispatch (ED) is to minimize fuel cost of thermal units while satisfying both equality and inequality constraints including load balance constraint, upper and lower generation limit on thermal units. Nowadays, emission control is an important objective to consider along with fuel cost and utility planners are trying to improve their operating strategies to reduce pollution [1]. In fact, apart from heat, thermal units produce particulates and gaseous emissions. A number of substances such as carbon di-oxide CO_2, sulphur oxides SO_2, nitrogen oxides NO_x, dust particles etc. are emitted during the operation of thermal units. Society demands adequate and secure electricity not only at the cheapest possible price, but also at minimum level of pollutant's emission [2]. Therefore, the objective of the EED problem is to minimize both fuel cost and the gaseous emission.

In the past two decades, recurrent neural networks for optimization and their engineering applications have been widely investigated. Tank and Hopfield applied the Hopfield network for solving linear programming problems [14], which motivated the development of neural networks for optimization [15]-[21]. Kennedy and Chua presented a neural network with a finite penalty parameter for nonlinear programming [15], which can converge to approximate optimal solutions. To avoid using the penalty parameter, many other methods have been introduced to develop various neural networks. Based on the Lagrangian method, Zhang and Constantinides proposed a two-layer network structure [16]. Wang developed the deterministic annealing network for linear and convex programming [17], [18]. Xia proposed a primal-dual neural network for solving some convex quadratic programming problems [19]. The projection neural network was proposed for solving general convex programming problems [20], which is globally convergent to exact optimal solutions.

In order to reduce the architecture complexity, the dual neural networks were introduced for solving convex quadratic programming problems [3], [11], [13]. Forti et al. proposed a generalized neural network for solving nonsmooth nonlinear programming problems based on the gradient method [12]. Recently, a simplified dual neural network [13] and a delayed projection neural network [14] were proposed for solving convex quadratic programming problems.

This paper focuses on SO_2 and NO_x because their control is important at global level. It uses a one layer recurrent neural network [21] to solve the problem of combined economic and emission dispatch. Penalty factors are defined which blend the emission costs with the fuel costs. The familiar quadratic form of objective functions are used which gives the optimal dispatch directly. The power capacity limits of plants are treated as the operating constraints and the total generation which is a function of load plus transmission losses is considered as the demand constraint. The computation results are compared with the results of the Tabu Search (TS) [11] and an elitist multi-objective evolutionary algorithm based on the Non-dominated Sorting Genetic Algorithm (NSGA-II) [13].

II. EVIRONEMENTAL/ECONOMIC DISPATCH

The environmental/economic dispatch involves the simultaneous optimization of fuel cost and emission objectives which are conflicting ones. The problem is formulated as described below.

A. Economic Dispatch

The classical economic dispatch problem of finding the optimal combination of power generation which minimizes the total fuel cost while satisfying the total required demand can be mathematically stated as follows [3]:

$$F = \sum_{i=1}^{n} (a_i P_i^2 + b_i P_i + c_i) \quad (1)$$

where F is the total fuel cost (\$/hr), approximated as a quadratic function of the active power output from the generating units; a_i, b_i, c_i are fuel cost coefficients of the i^{th} generating unit; P_i (MW) is the power output of the i^{th} generator; n is the number of thermal units.

Subject to the following constraints:

B. Demand constraint:

$$P_D + P_L - \sum_{i}^{n} P_i = 0 \quad (2)$$

C. Generating capacity limits:

$$P_{i\min} \le P_i \le P_{i\max} \quad (3)$$

where P_L is the total real power losses; P_D is the total real power demand; $P_{i\min}$, $P_{i\max}$ are, respectively, minimum and maximum values of real power generation at bus *i*.

D. Emission Dispatch:

The SO_2 and NO_x emission objectives can be modeled using second order polynomial functions [4]:

$$E_S = \sum_{i=1}^{n} (d_i P_i^2 + e_i P_i + f_i) \quad (4)$$

$$E_N = \sum_{i=1}^{n} (g_i P_i^2 + h_i P_i + k_i) \quad (5)$$

where E_S and E_N are total SO_2 and NO_x emissions releases (Kg/hr), respectively; d_i, e_i, f_i and g_i, h_i, k_i are the i^{th} generating unit fuel emission coefficients for SO_2 and NO_x, respectively.

E. Economic/Emission Dispatch:

The emission/economic dispatch is a contradictory problem, as the economic dispatch reduces the total fuel cost (operating cost) of the system at an increased rate of emissions. On the other hand, emission dispatch reduces the total emission from the system by an increase in the system operating cost. The combined economic and emission dispatch problem seeks an optimal balance between cost and emission [5]. The EED can be formulated as:

$$\begin{aligned} &Min && C(F, E_S, E_N) \\ &\text{Subject to:} && P_D + P_L - \sum_{i}^{n} P_i = 0 \\ & && P_{i\min} \le P_i \le P_{i\max} \end{aligned} \quad (6)$$

The above multi-objective optimization problem can be converted to a single objective optimization problem by introducing emission weights as follows [6]:

$$Min \quad C = F + w_S E_S + w_N E_N) \quad (\$/hr) \quad (7)$$

where w_S and w_N are price penalty factors for SO_2 and NO_x, respectively, blending the emission costs with the normal fuel cost. The total operating cost of the system due to the price penalty factors for SO_2 and NO_x emissions is the cost of fuel plus the implied cost of emission. The procedure to find out penalty factors for is as follows [7]:

1. The fuel cost of each generator is evaluated at its maximum output.
$$F_i = a_i P_{i\max}^2 + b_i P_{i\max} + c_i \quad (8)$$
2. The emission release of each generator for NO_x is evaluated at its maximum output.
$$E_N^i = g_i P_{i\max}^2 + h_i P_{i\max} + k_i \quad (9)$$
3. Penalty factor for each generating unit is calculated.
$$w_N^i = F_i / E_N^i \quad (10)$$
4. $w_N^i (i = 1, 2, .., n)$ are arranged in ascending order.
5. The maximum capacity of each unit $P_{i\max}$ is added one at a time, starting from the smallest w_N^i unit until $\sum_{i=1}^{n} P_{imax} \ge P_D$.
6. At this stage w_N^i, associated with the last unit in the process, is the price penalty factor w_N (\$/Kg) for the given load demand P_D. The price penalty factor for SO_2 w_S is calculated similarly.

Once the values of w_N and w_S are known, by minimizing the equation (7) subjected to the constraint equations (2) and (3), the optimal generation schedule can be obtained.

III. PROPOSED APPROACH

The EED minimization problem can be formulated as a time-varying quadratic program subject to linear equality and bound constraints as follows:

$$\begin{aligned} &Min && F(p) = \frac{1}{2} P^T Q P + C^T P + D \\ &\text{Subject to:} && EP = b \\ & && P_{\min} \le P \le P_{\max} \end{aligned} \quad (11)$$

where $P^T = \begin{bmatrix} P_1 & P_2 & \dots & P_n \end{bmatrix}$

$$Q = \begin{bmatrix} a_1 + w_S d_1 + w_N g_1 & \cdots & 0 \\ \vdots & \ddots & \vdots \\ 0 & \cdots & a_n + w_S d_n + w_N g_n \end{bmatrix}, \quad E^T = \begin{bmatrix} e_1 & \cdots & e_n \\ f_1 & \cdots & f_n \\ k_1 & \cdots & k_n \end{bmatrix}$$

$$C = \begin{bmatrix} b_1 + w_S e_1 + w_N h_1 \\ b_2 + w_S e_2 + w_N h_2 \\ \vdots \\ b_n + w_S e_n + w_N h_n \end{bmatrix}, P_{\min} = \begin{bmatrix} P_{1\min} \\ P_{2\min} \\ \vdots \\ P_{n\min} \end{bmatrix}, P_{\max} = \begin{bmatrix} P_{1\max} \\ P_{2\max} \\ \vdots \\ P_{n\max} \end{bmatrix}$$

$D = \sum_{i=1}^{n} (c_i + w_S f_i + w_N k_i)$ and $b = P_L + P_D$.

Several recurrent neural networks based on the KKT conditions have been developed for solving quadratic programming problems with convex objective functions, e.g., [9], [10], [15]-[21]. In the following, the recurrent neural network developed in [21] is adopted for solving problem (11).

According to the Karush-Kuhn-Tucker (KKT) conditions [8], if P^* is a solution of (11), then there exist $y^* \in R^m$ and $z^* \in R^n$ such that $(P^*, y^*, z^*)^T$ satisfies the following optimality conditions:

$$QP + C + E^T y + z = 0 \tag{12}$$

$$EP = b \tag{13}$$

$$\begin{cases} P_i = P_{i\min} & \text{if } z_i < 0 \\ P_i = P_{i\max} & \text{if } z_i > 0 \\ P_{i\min} < P_i < P_{i\max} & \text{if } z_i = 0 \end{cases} \tag{14}$$

Since (11) is a convex programming problem, then the KKT conditions (12)-(14) are both necessary and sufficient. From (12), we have

$$P = (I - Q)P - C - E^T y - z \tag{15}$$

where I is an identity matrix. Substituting (14) into (13), we have

$$E(I - Q)P - EC - EE^T y - Ez = b \tag{16}$$

Because E is full row-rank, EE^T is invertible, then:

$$y = (EE^T)^{-1}(E(I - Q)P - Ez - EC - b) \tag{17}$$

Substituting (17) into (12), we have

$$QP + C + E^T (EE^T)^{-1} (E(I - Q)P - Ez - EC - b) + z = 0 \tag{18}$$

Let $S = -C + xC + E^T (EE^T)^{-1} b$, then, (18) is written as

$$(I - x)z + [(I - x)Q + x]P - S = 0 \tag{19}$$

The projection matrix x has the properties shown in the following lemma.

Lemma [21]:

1) x is symmetric, $x^2 = x$ and $(I - x)^2 = I - x$

2) For any $z > -1$, $I + zx$ is invertible and

$$(I + zx)(I + x) = I - x$$

Proof [21]:

1) $x^T = (E^T (EE^T)^{-1} E)^T = E^T (EE^T)^{-T} E = E^T (EE^T)^{-1} E = x$, thus x is symmetric.

$$x^2 = E^T (EE^T)^{-1} EE^T (EE^T)^{-1} E = E^T (EE^T)^{-1} E = x$$

$$(I - x)^2 = I - 2x + x^2 = I - x$$

2) Since $x^2 = x$, the eigenvalues of x are 0 and 1 and the eigenvalues of $I - zx$ are 1 and $1 + z$. Since $z > -1$, $I + zx$ is invertible. Moreover, $(I + zx)(I + x) = I - x$ from 1).

By multiplying $I + zx$ in both sides of (19), (19) is equivalent to the following:

$$(I - x)z + [(I - x)Q + ax]P - q = 0 \tag{20}$$

where $a = 1 + z > 0$ is a parameter and

$$q = (I - zx)S = -C + xC + aE^T (EE^T)^{-1} b$$

According to (14), the following hard-limiting activation function $g_i(z_i)$ is defined as shown in figure 1:

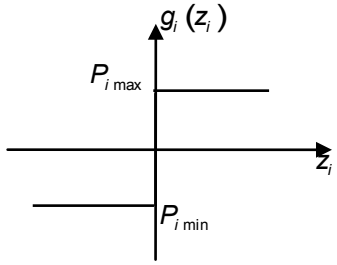

Figure.1. Discontinuous hard-limiting activation function $g_i(z_i)$.

$$g_i(z_i) = \begin{cases} = P_{i\max} & \text{if } z_i > 0 \\ \in [P_{i\min}, P_{i\max}] & \text{if } z_i = 0 \\ = P_{i\min} & \text{if } z_i < 0 \end{cases} \tag{21}$$

If $P_{i\min} < P_{i\max}$ then g_i is discontinuous. when $z_i = 0$, $g_i = (z_i)$ can take any values between $P_{i\min}$ and $P_{i\max}$.

Based on (20) and (21), the recurrent neural network model is described as follows:

• State equation:

$$\frac{dz}{dt} = b\{-(I - x)z - [(I - x)Q + ax]g(z) + q\} \quad (22)$$

• Output equation

$$P = ((I - x)Q + ax)^{-1}(-(I - x)z + q) \quad (23)$$

where b is a positive scaling constant. Here, we assume there exists $a > 0$ such that $(I - x)Q + ax$ is invertible. When the objective function in (11) is strictly convex on a set defined by the equality constraints.

For any, $z \in R^n$ the output vector of the neural network satisfies (20). Since (18)–(20) are equivalent, (18) also holds. Let $y = (EE^T)^{-1}(E(I - Q)P - Ez - EC - b$ and substitute it into (18), then (13) holds. From (13) we have $z = -QP - E^T y - C$ and substitute it into $y = (EE^T)^{-1}(E(I - Q)P - Ez - EC - b$. Then, we have $EP = b$. That is to say, for any $z \in R^n$, the output vector P of the neural network always satisfies the equality constraints.

Let $R = I - x$, $U = -(RQ + ax)^{-1}R$ $W = -(RQ + ax)$, and $v = W^{-1}q$.

Then, equations (21)-(22) can be written as

$$\begin{cases} \frac{dz}{dt} = b[-Rz + Wg(z) + q] \\ P = Uz + v \end{cases} \quad (24)$$

The architecture of the neural network described in (24) is depicted in figure. 2.

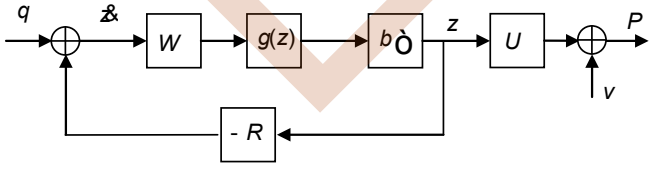

Figure 2. The Discontinuous recurrent neural network architecture.

IV. SIMULATION RESULTS

The recurrent neural network (24) is validated on the solution of environmentally constrained economic dispatch problem. The method is implemented with Matlab on an Intel (R) Core (TM) 2 Duo 2.2 GHz CPU with 4 Mb RAM. The test system is a 3-unit power system with 850 MW demand and with transmission losses. The cost and emission functions coefficients are given in Tables 1-3 [11].

TABLE 1. Cost coefficients and generation limits.

n	a_i	b_i	c_i	P_{min} (MW)	P_{max} (MW)
1	0.00165	7.92	561	150	600
2	0.00194	7.85	310	100	400
3	0.00482	7.97	78	50	200

TABLE 2. SO_2 Emission coefficients.

n	d_i	e_i	f_i
1	1.6103e-6	0.00816466	0.5783298
2	2.1999e-6	0.00891174	0.3515338
3	5.4658e-6	0.00903782	0.0884504

TABLE 3. NO_x Emission coefficients.

n	g_i	h_i	k_i
1	1.4721848e-7	-9.4868099e-5	0.04373254
2	3.0207577e-7	-9.7252878e-5	0.055821713
3	1.9338531e-6	-3.5373734e-4	0.027731524

Firstly, the algorithm is used to optimize the power dispatch for the three objective problems: fuel cost, SO_2 emission and NO_x emission. To illustrate the convergence advantages of DRNN, the cost and emission objectives over number of generations for a total load demand equal to 850 MW are plotted in figures 3, 4 and 5. The active powers of the 3 generators as shown in the table 4 are all in their allowable limits.

TABLE 4. Minimum values of individual objectives (DRNN).

	Best Fuel Cost	Best SO_2 emission	Best NO_x emission
P_1 (MW)	442.463	432.041	461.052
P_2 (MW)	273.414	276.884	278.791
P_3 (MW)	149.002	150.444	113.209
Cost ($/hr)	**8344.596**	8697.234	8235.426
Emission SO_2 (ton/hr)	9.01518	**8.9659**	8.8736
Emission NOx ton/hr)	0.10035	0.1005	**0.09594**
Losses P_L MW)	15.265	15.215	14.910

TABLE 5. Best fuel cost (minimum Cost)

Methods	T S [11]	NSGA-II [13]	DRNN
P_1 *(MW)*	435.69	436.366	**442.463**
P_2 *(MW)*	298.828	298.187	**273.414**
P_3 *(MW)*	131.28	131.228	**149.002**
Cost *($/hr)*	**8344.598**	**8344.606**	**8344.596**
Emission SO_2 (ton/hr)	9.02146	9.02083	9.01518
Emission NOx(ton/hr)	0.0987	0.09866	0.10035
Losses P_L (MW)	15.798	15.781	15.265

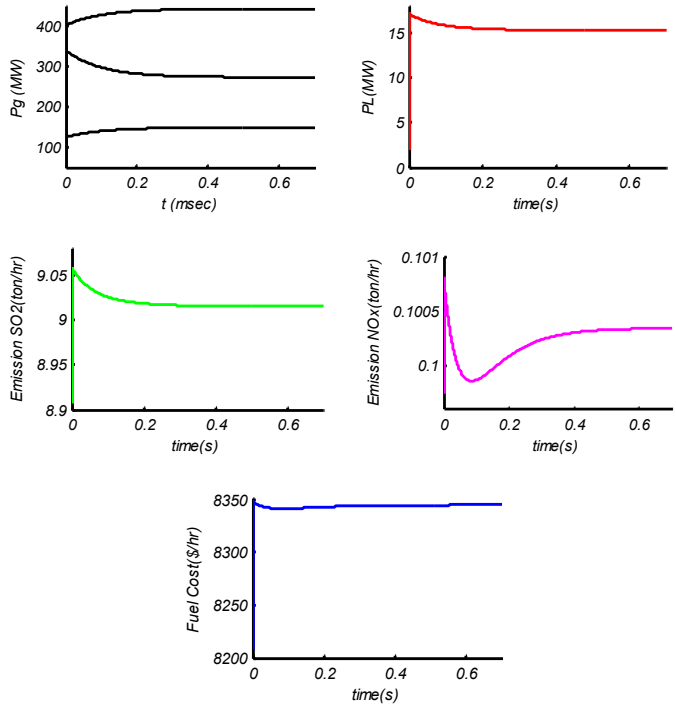

Figure 3. Convergence plot of cost objective (for 850 MW).

TABLE 6. Best NO_x emission (minimum NO_x)

Methods	T S [11]	NSGA-II [13]	**DRNN**
P_1 (MW)	502.914	505.810	**461.052**
P_2 (MW)	254.294	252.951	**278.791**
P_3 (MW)	108.592	106.023	**113.209**
Cost *($/hr)*	8371.143	8363.627	**8235.426**
Emission SO_2 (ton/hr)	8.986	8.9747	**8.8736**
Emission NOx(ton/hr)	**0.0958**	**0.0959**	**0.09594**
Losses P_L (MW)	15.8	14.784	14.910

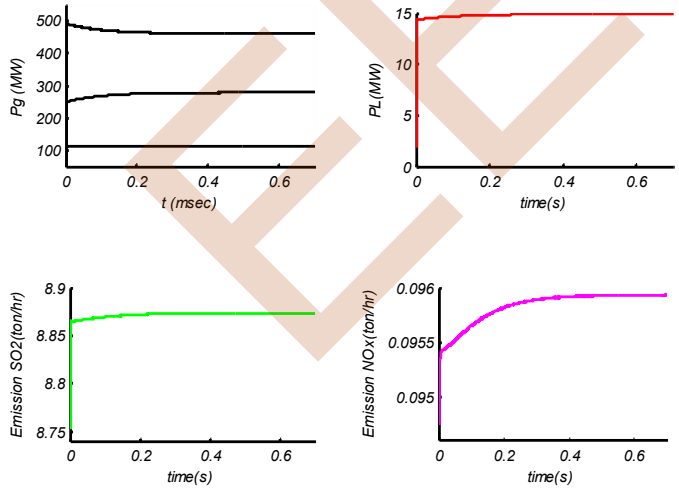

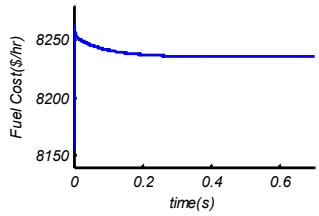

Figure 4. Convergence plot of NO_x emission objective (Best NO_x Emission).

TABLE 7. Best SO_2 emission (minimum SO_2)

Methods	T S [11]	NSGA-II[13]	DRNN
P_1 (MW)	549.247	541.308	**432.041**
P_2 (MW)	234.582	223.249	**276.884**
P_3 (MW)	81.893	99.919	**150.444**
Cost *($/hr)*	8403.485	8387.518	**8309.368**
Emission SO_2 (ton/hr)	**8.974**	**8.9665**	**8.9659**
Emission NOx(ton/hr)	0.0976	0.0964	0.1005
Losses P_L (MW)	15.722	14.476	15.215

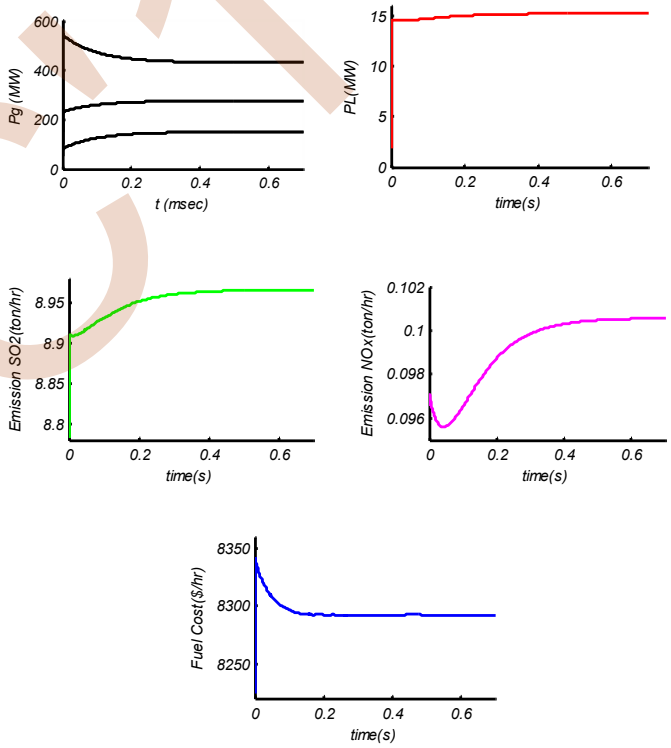

Figure 5. Convergence plot of SO_2 emission objective (Best SO_2 Emission).

In tables 5, 6 and 7 the computation results of the (RNN) approach for the classical economic dispatch, minimum SO_2 and minimum NO_x are compared with the results of the Tabu search (TS) [11], an elitist multi-objective evolutionary algorithm based on the Non-dominated Sorting Genetic Algorithm (NSGA-II) [13].

Table 5 gives the simulation results for best fuel cost as compared to the Tabu search and NSGA-II. It is observed that the RNN approach achieves the same best fuel cost than the

other approaches. From the tables 6 and 7, it is clear that. In the SO_2 emission dispatch, SO_2 emission is minimum and the production cost is better than those of the classical economic dispatch ED. In the NO_x emission dispatch, NO_x emission is minimum and the production cost is better than those of the SO_2 emission dispatch.

Through the comparison of simulations results of table 5-6 and 7, it can be seen that the proposed method has the best solution quality in terms generation cost, NO_x emission dispatch, SO_2 emission dispatch, and losses power, compared to the other methods. The active powers of the 3 generators as shown in this table are all in their allowable limits.

V. CONCLUSION

A Discontinuous Recurrent Neural Network algorithm (DRNN) has been used for solving the Environmental/ Economic Dispatch problem. Firstly, a bi-objective optimization problem is considered where simulations results on a 3-generator test system considering fuel cost and SO_2 emission and then fuel cost and NO_x emission have been presented. Finally, a three objective optimization problem considering fuel cost, SO_2 emission and NO_x emission simultaneously has been considered. The obtained minimum values of fuel cost and emissions are comparable to those obtained using Tabu search (single objective optimization) and elitist multi-objective evolutionary algorithm based on the Non-dominated Sorting Genetic Algorithm (NSGA-II). Simulation results reveal that the algorithm can identify the Pareto-optimal front with a good diversity for the environmental/economic dispatch problem.

VI. REFERENCES

[1] J. S. Dhillon and D. P. Kothari, "Multiobjective fixed head hydrothermal scheduling using integrated predator-prey optimization and Powell search method", Nitin Narang Energy, vol. 47, (2012), pp. 237-252.

[2] N. Trung Thang, "Economic emission load dispatch with multiple fuel options using Hopfiled Lagrange Network", International Journal of Advanced Science and Technology, vol. 57, (2013), pp. 9-24.

[3] A. J. Wood and B. F. Wollenberg, Power Generation, Operation, and Control, John Wiley & Sons, Inc., 1984

[4] J. H. Talaq, F. El-Hawary and M. E. El-Hawary, .A Summary of Environmental/Economic Dispatch Algorithms., IEEE Transactions on Power Systems, Vol. 9, No. 3, pp. 1508-1516, August 1994.

[5] M Sudhakaran and S M Slochanal, "Application of Refined Genetic Algorithm to Combined Economic and Emission Dispatch", Vol 85, September 2004

[6] S.P. Baskar, P. Subbaraj and M.V.C. Rao, "Hybrid Genetic Algorithm Solution to Emission and Economic Dispatch Problem", Journal of the Indian Institute of Engineers (India), Vol.82,pp243-249, March 2002.

[7] K. Srikrishna and C. Palanichamy," Economic Thermal Power Dispatch With Emission Constraint", Journal of the Indian Institute of Engineers(India),Vol. 72, pl1, April 1991.

[8] M. S. Bazaraa, H. D. Sherali, and C. M. Shetty, *Nonlinear Programming: Theory and Algorithms*, 2nd ed. New York: Wiley, 1993.

[9] Y. Xia and J. Wang, "A recurrent neural network for solving nonlinear convex programs subjected to linear constraints," *IEEE Trans. NeuralNetw.*, vol. 16, no. 2, pp. 379–386, Mar. 2005.

[10] S. Liu and J. Wang, "A simplified dual neural network for quadratic programming with its KWTA application," *IEEE Trans. Neural Netw.*, vol. 17, no. 6, pp. 1500–1510, Nov. 2006.

[11] R. Sepulveda and al., ". Environmental Economic Dispatch via hopfield neural network and Tabu search" ,UPEC' 96 Universities Power Engeneering Conference , Greece, 18-20 Septembrs,1996, PP . 1001-1004.

[12] T. Yalcinoz and M.J. Short, " large –scale economic dispach using an improved hopfield neural network" IEE Proc Gener . Transm. Distrib., Vol. 144, No. 2, March 1997, pp.181-185.

[13] R. Ah King and H. Rughooputh "Elitist Multiobjective Evolutionary Algorithm for Environmental/Economic Dispatch " IEEE International Conference on Industrial Technology, 2003, pp 48 – 53, Vol. 1.

[14] D. W. Tank and J. J. Hopfield, "Simple neural optimization networks: An A/D converter, signal decision circuit, and a linear programming circuit," *IEEE Trans. Circuits Syst.*, vol. CAS-33, no. 5, pp. 533–541, May 1986.

[15] M. P. Kennedy and L. O. Chua, "Neural networks for nonlinear programming," *IEEE Trans. Circuits Syst.*, vol. CAS-35, no. 5, pp. 554-562, May 1988.

[16] S. Zhang and A. G. Constantinides, "Lagrange programming neural networks," *IEEE Trans. Circuits Syst.*, vol. 39, no. 7, pp. 441–452, Jul. 1992.

[17] J. Wang, "Analysis and design of a recurrent neural network for linear programming," *IEEE Trans. Circuits Syst. I, Fundam. Theory Appl.*, vol. 40, no. 9, pp. 613–618, Sep. 1993.

[18] J. Wang, "A deterministic annealing neural network for convex programming," *Neural Netw.*, vol. 7, pp. 629–641, 1994.

[19] Y. Xia, "A new neural network for solving linear and quadratic programming problems," *IEEE Trans. Neural Netw.*, vol. 7, no. 6, pp. 1544–1547, Nov. 1996.

[20] Y. Xia, H. Leung, and J. Wang, "A projection neural network and its application to constrained optimization problems," *IEEE Trans. Circuits Syst. I, Fundam. Theory Appl.*, vol. 49, no. 4, pp. 447–458, Apr.2002.

[21] Q. Liu, *Student Member, IEEE*, and Jun Wang "A One-Layer Recurrent Neural Network With a Discontinuous Hard-Limiting Activation Function for Quadratic Programming "IEEE *Trans.* On neural networks, vol . 19, no. 4, April 2008.

Superconducting Magnetic Energy Storage for power system transient stability enhancement in presence of wind generation

A.Zebar
Department of Electrical Engineering
Setif1 University
Setif, Algeria
zebarkarim@yahoo.fr

***Abstract*— The increase of environmental pollution and the decreasing of the energy is extremely related to social progress. The renewable energy based wind energy system is one of better solutions to reduce the environment pollution. Wind energy offers power supply for locations that are remotely located and also allows economical way of producing power. The impact of a wind farm on the power system transient stability will be negligible, however, when the penetration of wind farm increases, its impact is no longer restricted to the distribution network but starts to influence the whole system, including the transmission system transient stability. The integration and penetration of these energy sources in power system have become a challenge for network managers, especially, with wind turbines that do not offer control of reactive power. This type of wind turbines requires the addition of capacitor banks to reduce reactive power absorbed in the network and to keep them connected in case of fault. However these capacitor banks present several disadvantages, this requires the use of superconducting magnetic Energy Storage (SMES). The effectiveness of the proposed model is tested on the IEEE11-bus test system applied to the case of three-phase short circuit fault in one transmission line. A simulation results are presented in this document.**

I. INTRODUCTION

Recently, the wind power generation included in the standard grid showed a further increase, in a significant way so, the electric utilities grid codes are forced to be revised, thus the reliability in systems with high wind energy diffusion will be guaranteed [1]. In power system stability studies the term transient stability usually refers to the ability of the synchronous machines to remain in synchronism during the brief period following large disturbances, such as severe lightning strikes, loss of heavily loaded transmission lines, loss of generation stations, or short circuits on buses [2]. To enhance the transient stability, a Superconducting Magnetic Energy Storage (SMES) which is able to swiftly exchange active and reactive powers with the power systems, can be used [3], [4]. However, to attain the high stabilizing effect, the large capacity of converter and energy storage of SMES are required. Besides, the SMES cannot absorb enough energy during severe faults since the bus voltage where the SMES is installed, falls substantially. One of the requirements of transient stability analysis is to compute a transient stability index (TSI) for the contingencies, which is used to assess the stability of single contingency and furthermore rank the severity of different contingencies [5]. The Critical Clearance Time (CCT) of a fault is generally considered as the best measurement of severity of a contingency and thus widely used for ranking contingencies in accordance with their severity [6]. In this paper Critical Clearing Time (CCT) is employed as a transient stability index to evaluate test system. The Critical Clearing Time is defined as "the maximum time between the fault initiation and its clearing such that the power system is transiently stable".

Many methods for transient stability analysis and assessment have been proposed and improved over the years, such as equal area criteria, numerical integration and Lyapunove method, in this study the numerical integration method is required in order to get the exact CCTs. The numerical integration method is the most reliable and accurate method for transient stability assessment [7].

proposed work is aimed to investigate the potential influence of the Superconducting Magnetic Energy Storage (SMES) for improving both transient stability and voltage regulation of the power system containing a distributed wind generation (DWG) based on conventional fixed speed induction generator. Moreover, the optimal location of the proposed controller (SMES) is also analyzed. The

effectiveness of the proposed model is tested on the IEEE 11-bus test system applied to the case of three-phase short circuit fault in one transmission line. The toolbox Sim Power Systems of MATLAB/SIMULINK software is used to carry out simulations studies (in the mode " phasor simulation"). Computer simulation results for system under study are presented and discussed.

II. Mathematical Model

This section gives a mathematical model for the power system network which includes modelling of synchronous generator, DWGs and SMESs.

A. Synchronous Generator

With few characteristic assumptions, the synchronous generator can be modelled by the subsequent group of nonlinear equations [8, 9]:

$$d\delta/dt = \omega - \omega_0 \quad (1)$$

$$2H\, d\omega/dt = P_m - P_e - D\omega \quad (2)$$

$$dE_q^{'}/dt = (E_{fd} - E_q^{'} - (x_d - x_d^{'})i_d)/T_{do}^{'} \quad (3)$$

$$dE_d^{'}/dt = (-E_d^{'} - (x_q - x_q^{'})i_q)\ /T_{qo}^{'} \quad (4)$$

Where

δ : Rotor angle of the generator.

ω : Angular speed of the generator.

ω_0 : Rated generator rotor angle speed.

H : Inertia time constant.

P_m : Mechanical power.

$P_e = T_e.\omega_0$: Electrical power.

D : Damping coefficient.

x_d : d-axis synchronous reactance.

x_q : q-axis synchronous reactance.

$x_d^{'}$: d-axis transient reactance.

$x_q^{'}$: q-axis transient reactance.

$E_d^{'}$: d-axis transient voltage.

$E_q^{'}$: q-axis transient voltage.

The electrical torque T_e as:

$$T_e = E_q^{'} i_q + E_d^{'} i_d + (x_q^{'} - x_d^{'}) i_d i_q \quad (5)$$

The equation of the stator are given by:

$$v_d = -r_s i_d + x_q^{'} i_q + E_d^{'} \quad (6)$$

$$v_q = -r_s i_q - x_d^{'} i_d + E_q^{'} \quad (7)$$

$$V_t^2 = v_d^2 + v_q^2 \quad (8)$$

Where

v_d, v_q : Direct and quadrature axis stator terminal voltage components.

V_t : generator terminal voltage.

i_d, i_q : Direct and quadrature axis stator current components.

B. DWG

DWGs contain many wind turbines and their detailed modelling may be unaffordable due to computational burden. In order to reduce the dimensionality, aggregation techniques are used to obtain equivalent models. A proper equivalent model can be easily obtained for fixed-speed wind turbines where a one-to-one correspondence between wind speed and active power output exists. In this case, aggregation is performed by adding the mechanical power of each wind turbine and by using an equivalent squirrel cage induction generator (SCIG) which receives the total mechanical power [10], [11].

A simplified transient model of a SCIG can be described by the following algebraic-differential equations [12]:

$$dE'_{qr} = \left(E'_{qr} + (x - x')I_{ds} + S\omega_s T_0' E'_{dr}\right)/T_0' \quad (9)$$

$$dE'_{dr} = \left(E'_{dr} + (x - x')I_{qs} + S\omega_s T_0' E'_{qr}\right)/T_0' \quad (10)$$

$$dS = \left(T_m - T_e\right)/2H_g \quad (11)$$

$$\left(V_{ds} + jV_{qs}\right) = \left(R_S + jx'\right)\left(I_{ds} + jI_{qs}\right) + \left(E'_{qr} - E'_{dr}\right) \quad (12)$$

Here, x' = (xs + xm xr) / (xm + xr) is the transient reactance, Rs is the stator resistance which is assumed to be zero, xr is the rotor reactance, xm is the magnetizing reactance, x = (xs + xm) is the rotor open circuit reactance, T0' is transient open circuit time constant, Tm is the mechanical torque, S is the slip, Te = (Edr' Ids – Eqr' Iqs) is the electrical torque, Edr' and Eqr' are the direct and quadrature axis transient voltages respectively, Ids and Iqs are the direct and quadrature axis currents respectively, and ωs is the synchronous speed.

The DWG penetration level in the system is defined as [13]:

$$\%\,DWG = P_{DWG} * 100/(P_{DWG} + P_{CG}) \quad (13)$$

Where PDWG and PCG are the amount of total active power generated by DWG and Centralized generation respectively.

C. SMES

Figure 1, shows the basic configuration of a thyristor-based SMES unit, which consists of a Y- Delta transformer, an ac/dc thyristor controlled bridge converter, and a superconducting coil or inductor [14]. The converter impresses positive or negative voltage on the superconducting coil. Charge and discharge are easily controlled by simply changing the delay angle that controls the sequential firing of the thyristors.

- If α is less than 90, the converter operates in the rectifier mode (charging)
- If α is greater than 90, the converter operates in the inverter mode (discharging)

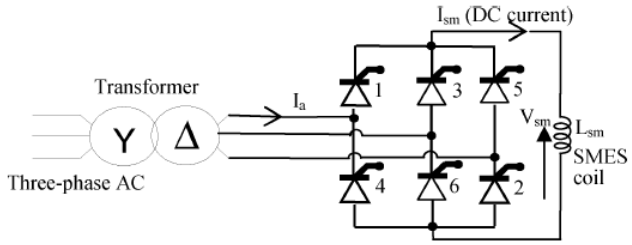

Figure 1. SMES model

As a result, power can be absorbed from or released to the power system according to requirement. At the steady state, SMES should not consume any real or reactive power. The voltage V_{sm} of the dc side of the converter is expressed by,

$$V_{sm} = V_{sm0} \cos\alpha \quad (14)$$

Where, V_{sm0} is the ideal no-load maximum dc voltage of the bridge. The current and voltage of superconducting inductor are related as,

$$I_{sm} = \frac{1}{L_{sm}} \int_{t_0}^{t} V_{sm} dt + I_{sm0} \quad (15)$$

Where, I_{sm0} is the initial current of the inductor.

The real power, P_{sm} absorbed or delivered by the SMES can be given by,

$$P_{sm} = V_{sm} I_{sm} \quad (16)$$

The energy stored in the superconducting inductor is

$$W_{sm} = W_{sm0} + \int_{t_0}^{t} P_{sm} dt \quad (17)$$

where, $W_{sm} = 1/2\ L_{sm} {I_{sm0}}^2$ is the initial energy in the inductor. This is applicable for the twelve pulse converter also [14]. Since the bridge current I_{sm} is not reversible, the bridge output power P_{sm} is uniquely a function of, which can be positive or negative depending on V_{sm}. If V_{sm} is positive, power is transferred from the power system to the SMES unit. While if $V_{sm}$is negative, power is released from the SMES unit.

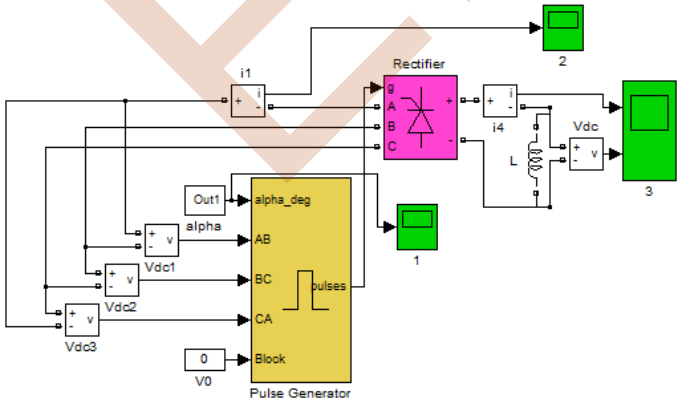

Figure 2. Circuit of SMES

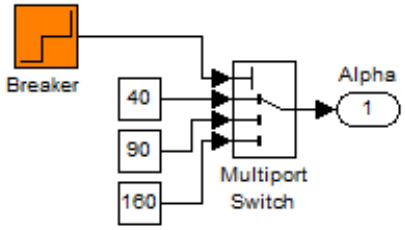

Figure 3. Alpha angle circuit

III. Simulation Results

To investigate the efficiency and the robustness of the proposed controller based SMES on the power system transient stability enhancement in presence of distributed wind generation; the model is integrated in the IEEE benchmark four-machine two-area eleven bus test system in the case of three phase short circuit fault in the transmission line. DWG is connected to each of the load buses. The one line configuration is shown in Figure. 4. Technical data such as machine, voltage regulator, governor turbine, buses and branches information are taken from [15]. The transient stability is assessed by the criterion of relative rotor angles, using the time domain simulation method. The toolbox Sim Power Systems of MATLAB/SIMULINK software is used to carry out simulations studies.

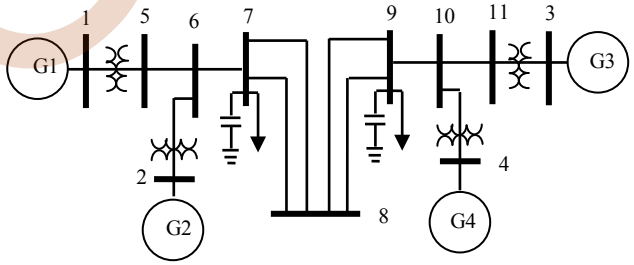

Figure 4. On-line diagram of the Electrical Power System.

IV. Optimal Location Of SMES

Optimal location and control of multi FACTS devices is a vital and complex research area. In the literature many modern techniques and indices proposed for optimal location and control of multi FACTS devices. For secure operation of power systems, it is required to maintain an adequate voltage stability margin, not only under normal conditions, but, also, in contingency cases. In this study the voltage stability index using continuation power flow proposed for optimal location of SMES.

From the continuation power flow results which are shown in the Figure. 5, the buses 5, 6, 7, 8, 9, 10 and 11 are the critical buses. Among these buses, bus 8 has the weakest voltage profile. Figure. 6 shows PV curves for IEEE four-

machine two-area test system without considering SMES.

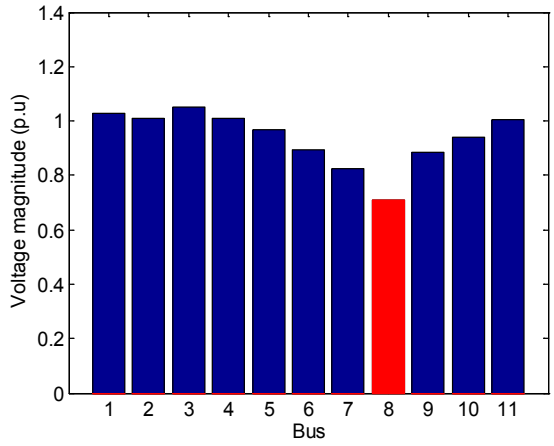

Figure 5. PV curves for the IEEE four-machine two-area test system

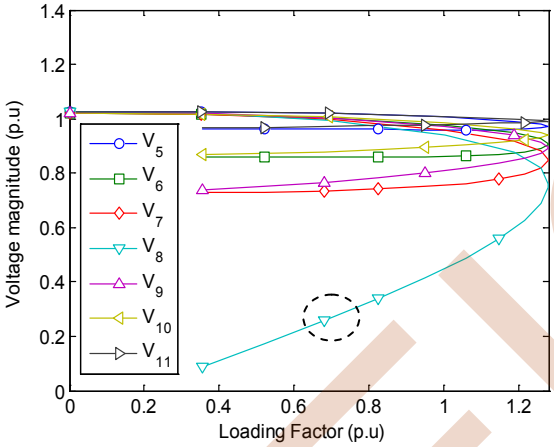

Figure 6. Critical buses based on continuation power flow.

First, buses are classified based on two procedures:
Procedure1: all buses are classified based on voltage stability index, the weak buses are identified based on voltage stability index, in this study, the bus 8 is considered as a candidate bus, the main role of the SMES is to control voltage at this bus by exchanging reactive (capacitive or inductive) power with the network.
Procedure 2: Buses are classified based on the reactive power compensation witch consume by the DWG, the DWG will generate an active power, equal to the amount consumed by the load. However, in order to generate this necessary active power, the DWG need to consume reactive power from the network, the bus 9 is considered as the point of common coupling (PCC) where the WG is connected, the main role of the SMES is to compensate for this reactive power.

V. Impacts Of SMES Controller On Power System Transient Stability Enhancement

We have three logic Cases: Base case, which indicates the original system where there is no SMES, in the system. Second case, with SMES at the weak bus (low voltage stability index). Third case, with SMES at the PCC.
Figure. 7, shows the location of the SMES controller and the WG.

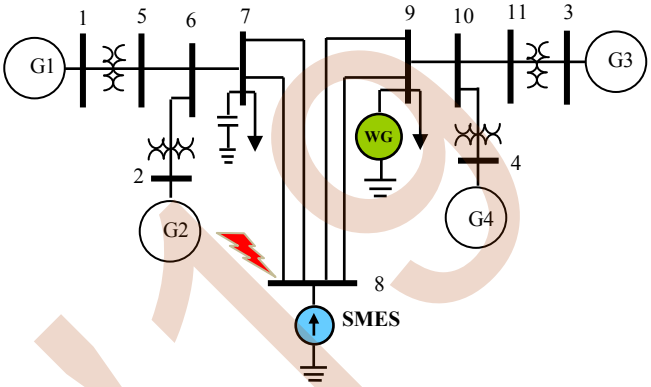

Figure 7. Modified electrical test system considering SMES controller: and DWG.

A. Case 1

A 3-phase fault is occurs at t = 1 second on line 7–8 near the bus 8 and it is cleared by opening the line at both ends. we consider a DWG at bus 9 with a penetration level of 20 %. Generator 2 is the nearest generator to the fault location and therefore it has the most rotor speed deviation for this fault. The fault clearing time (FCT = 0.266 s) at first then (FCT = 0.300 s). Simulation results on the rotor angle differences and rotor speed deviation of four generators without considering SMES Controller are shown in Figures. 8–9 respectively.

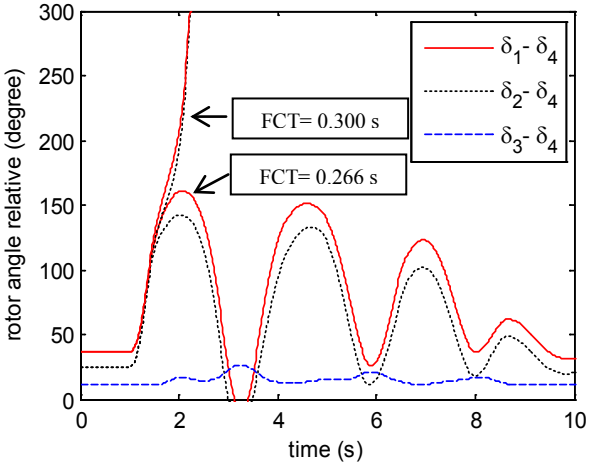

Figure 8. Relative rotor angles without SMES.

It can be seen that the relative rotor angles are damped and consequently the system maintains its stability, but when the fault clearing time increased to 0.300 s, the relative angles (δ14, δ24 and δ34) increase indefinitely, so at this critical situation the system loses its stability. Figure .10 shows the distribution of voltage magnitudes at all buses.

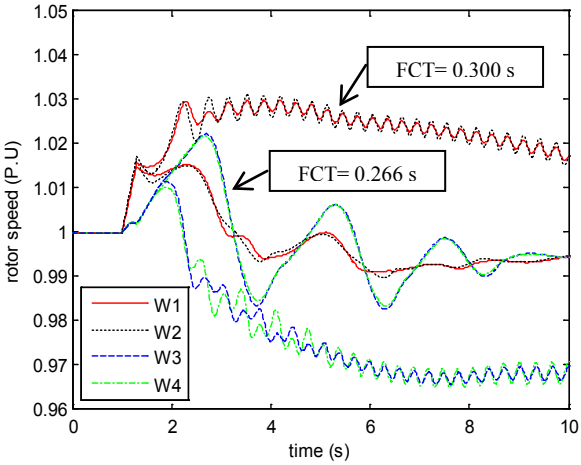

Figure 9. Rotor speed deviation without SMES.

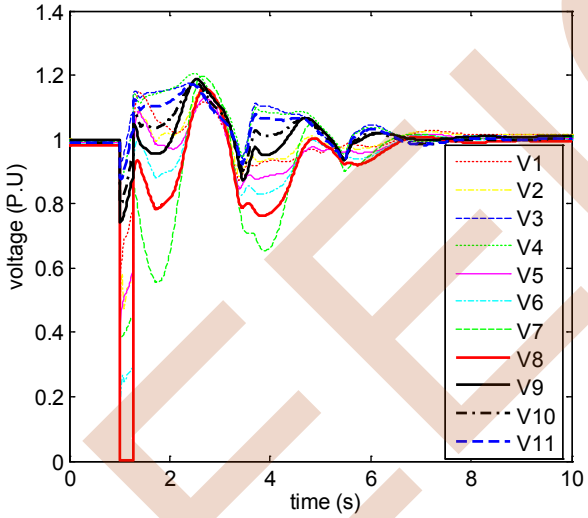

Figure 10. Voltage magnitudes without SMES.

B. *Case 2*

In order to maximize voltage stability index and to improve power system transient stability, SMES located at the weak bus (low voltage stability index). The SMES will try to support the voltage by injecting reactive power on the line when the voltage is lower than the reference voltage. The first mentioned fault in the previous sub-section is applied again.

Time domain simulation performed at the cleared time 0.333 s, we can see from Figure. 11 the maximum relative rotor angles are (δ14 = 97°, δ24 = 91° and δ34 = 10°), the relative rotor angles (δ14, δ24 and δ34) are damped and therefore the system becomes stable compared to the first case (system unstable).

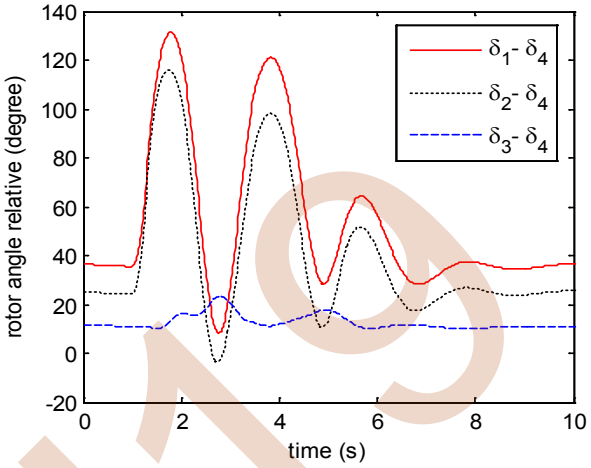

Figure 11. Relative rotor angles with SME located at the weak bus (low voltage stability index).

C. *Case 3*

In case 2 the SMES is placed at the weak bus (low voltage stability index) however in this case the SMES is placed at the PCC. The purpose maximize dynamically voltage stability index, in this case the SMES compensate the reactive power consumed by the DWG during fault, and alternatively the required size of SMES will be reduced (economic aspect). As a result, the reactive powers delivered by generating units reduce. Compared to the two others cases, the critical clearing time is improved. The SMES is placed at the weak bus. The first mentioned fault in the sub-section (case 1) is applied again. The fault is cleared after 0.427 s.

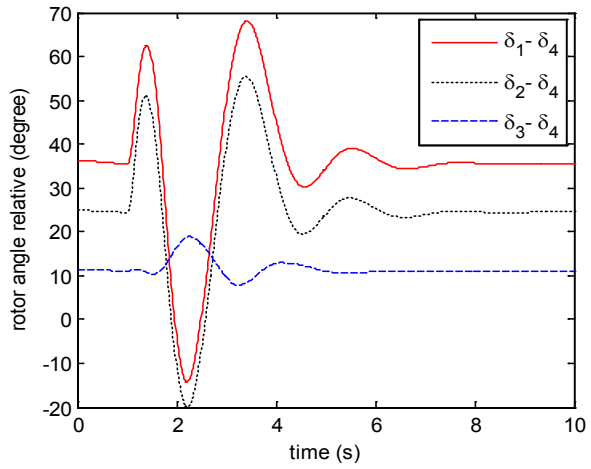

Figure 12. Relative rotor angles considering SMES at the PCC.

In Figure. 13, It can be seen that the maximum relative rotor angles are (δ12 = 15°, δ13 = 31° δ14 = 26°, δ15 = 48° and δ16 = 58°), the relative rotor angles (δ12, δ13, δ14, δ15 and δ16) are damped and therefore the system becomes stable compared to the first and second cases (system unstable). It can be also seen that the system response with the SMES at the PCC is better than that with the SMES at the weak bus in the sense of the settling time is reduced. The critical clearing time is enhanced to a new value (0.461 s). It is important to conclude that integration of SMES in suitable location may help the system to improve the transient stability. Table 1 shows the values of margin stability (CCT) obtained corresponding to different cases.

TABLE I. MARGIN STABILITY (CCT) FOR DIFFERENT CASES

	Controller	Margin stability (CCT) 's'
Case 1	Without SMES	0.262
Case 2	With SMES at the weak bus (High voltage stability index)	0.345
Case 3	With SMES at the PCC	0.461

VI. CONCLUSION

Modern electric power systems' operation, control andstability have been heavily affected by The rising penetration of energy sources renewal, increasing demands, restricted resources, and deregulated electricity markets power systems. In this study, the multi-machine power system transient stability improvement contains a large DWG via superconducting superconducting magnetic Energy Storage (SMES) when applied through coordinated application was discussed and investigated. Simulation results performed on the IEEE benchmarked four-machine two-area test system in presence of distributed wind generation considering three phase short circuit clearly indicate that proposed controller placed at suitable locations can be used as an effective mean capable to enhance the margin stability and extend the critical clearing time in a multi-machine power system. Future research will focus on investigation the effect of combined application of superconducting fault current limiter and SMES devices in the presence of the distributed generation by considering the optimal value of SFCL and location of this hybrid Controller.

REFERENCES

[1] M. F. Farias, M. G. Cendoya, P. E. Battaiotto, Wind Farms in Weak Grids Enhancement of Ride-Through Capability Using Custom Power Systems, IEEE/PES Transmission and Distribution Conference and Exposition Latin America, pp. 1-5, 2008.

[2] A. Karami and S.Z. Esmaili, "Transient stability assessment of power systems described with detailed models using neural networks", International Journal of Electrical Power and Energy Systems 45 (2013) 279–292

[3] A. Karami and S.Z. Esmaili, "Transient stability assessment of power systems described with detailed models using neural networks", International Journal of Electrical Power and Energy Systems 45 (2013) 279–292

[4] N. Mithulananthan, C.A. Canizares, J. Reeve, G.J. Rogers, "Comparison of PSS, SVC, and STATCOM controllers for damping power system oscillations", IEEE Trans. PWRS 18 (No. 2) (1993) 786–792.

[5] K. Phorang, M. Leelajindakraireak, and Y. Mizutani, "Damping improvement of oscillation in power system by fuzzy logic based SVC stabilizer" Asia Pacific. IEEE/PES Transmission and Distribution Conference and Exhibition 2002, Vol.3, Oct. 2002, pp.1542–1547

[6] R. Ebrahimpour, E. K. Abharian, S. Moussavi, Z. & A. A Motie Birjandi, "Transient stability assessment of a power system by mixture of experts" International Journal of Engineering (IJE) Volume (4): Issue (1). pp. 93–104

[7] P. Kundur, "Definition and classification of power system stability IEEE/CIGRE joint task force on stability terms and definitions" IEEE Transactions on Power Systems, vol. 19, no. 2, p. 1387-1401, May 2004

[8] N. ABU-TABAK, "Stabilité dynamique des systèmes électriques multi-machines: modélisation, commande, observation et simulation", Doctoral Thesis, University of Lyon, 2008.

[9] A. Mourad, G.. Keltoum, " Terminal sliding mode control based power system stabilizer" Rev. Roum. Sci. Techn.– Électrotechn. et Énerg. Vol. 62, 1, pp. 98–102, Bucarest, 2017

[10] H. Arnaldo, Wind farm model for power system stability analysis, Doctoral Thesis, University of Illinois at Urbana-Champaign, 2010.

[11] A.Zebar, A. Hamouda and K. Zehar, "Impact of the location of fuzzy controlled static var compensator on the power system transient stability improvement in presence of distributed wind generation", Rev. Roum. Sci. Techn. – Électrotechn. et Énerg., 60, 4, p. 426–436, Bucarest, 2015.

[12] Roy, Naruttam Kumar, M. J. Hossain, and H. R. Pota, Voltage profile improvement for distributed wind generation using D-STATCOM, IEEE Power and Energy Society General Meeting, 2011.

[13] M. Reza, PH. Schavemaker, JG. Slootweg, WL. Kling, L. Van Der Sluis, Impacts of distributed generation penetration levels on power systems transient stability, IEEE Power Engineering Society General Meeting, 2004.

[14] M. Sjostrom, R.Cherkaoui and B.Dutoit, "Enhancement of power system transient stability using superconducting fault current limiters", IEEE Trans. Applied Superconductivity, vol.9, no.2, pp.1328-1330, 1999.

[15] M. Klein, G. Rogers, Moorty and P. Kundur: "Analytical investigation of factors influencing PSS performance" , IEEE Trans. on Energy Conversion, vol. 7, no 3, pp. 382-390, September 1992

Study and control of the hybrid renewable generation system supplying standalone load

Amina CHENNA
Laboratoire de Maitrise des Energies Renouvelables, Faculté de Technologie, Université de Bejaia
06000, Algérie
a.chenna@hotmail.fr

Djamel AOUZELLAG,
Laboratoire de Maitrise des Energies Renouvelables, Faculté de Technologie, Université de Bejaia
06000, Algérie
aouzellag@hotmail.com

Kaci GHEDAMSI
Laboratoire de Maitrise des Energies Renouvelables, Faculté de Technologie, Université de Bejaia
06000, Algérie
kghedamsi@yahoo.fr

***Abstract*— The hybrid Renewable Energy Source (RES) power generation appears to be an attractive solution for isolated, autonomous electric grids in order to increase the RES energy penetration and cost-effectiveness. In this paper, a pumped-storage hydropower energy system (PHES) combined to the renewable energy source (RES) is investigated. PHES based a reversible pump-turbine, a servo-machine, a permanent magnet synchronous machine (PMSM), and PWM (pulse width modulation) power converter. Also investigated is a control method of the PHES system, which consists of the reversible pump-turbine unit entrained by the PMSM, supplied off the variable power renewable energy source (RES) through a power electronic converter. Simulation results obtained on the basis of the dynamic models of the pump-turbine are given, for different operating points, to validate the performance of the proposed system.**

***Keywords:* Pumped-storage hydropower; renewable energy; permanent magnet synchronous machine; power control**

I. INTRODUCTION

Nowadays, the increase of energy demand and the depletion of fossil fuel have necessitated the large-scale utilization of renewable energy (RE). More and more REs, like wind and solar powers have access to the power grid [1]. The global newly installed capacity of renewable energy sets a new record in 2016, with an increase of nearly 9% over 2015 [2]. Solar power and wind power play key roles in the generation mix of renewable energy, accounting for 47% and 34% of total installed renewable capacity respectively [3]. Though, an important feature of the renewable energies is the fluctuation of the power produced over time. However, the stability of the network is based on the balance between the energy produced and the energy consummate. Hybrid generation systems are being considered as a prospective solution to mitigate fluctuations of RES generation [4]. When hybrid systems operated effectively, they increase the overall efficiency of the system and become a more reliable energy supply. For this, a storage system is required to adapt with the mismatch between the renewable energy (RE) production and the time distribution of load demands [5]. The PHES is a well-established and commercially acceptable technology for utility-scale electricity storage and has been used since as early as the 1890s [6]. Hydropower is not only a renewable and sustainable energy source, but its flexibility and storage capacity also makes it possible to improve grid stability and to support the deployment of other intermittent renewable energy sources such as wind and solar [7, 8]. Pumped storage hydro-plants are commonly used for load balancing in power systems [9]. The PHES is the dominating grid-connected energy storage capacity in the world [10]. Variable-speed PSH technology has been used in recent years and can provide fast power regulation capability in both modes: pumping mode and as well as in generation mode [11].

The present study aims at the hybrid generation systems combined the RES with the PHES, which is considered as a promising technology for RES. The system described is shown schematically in figure 1. PHES stores energy in the form of potential energy of water that is pumped from a lower reservoir to a higher level reservoir. The hydraulic machine is a reversible pump-turbine with 520kW. This the latter is fed by a penstock connected to the two upstream and downstream reservoirs. When operating in generation mode, the main objective is the extraction of the maximum power for the compensation of power fluctuations on the load. The modeling details of the scheme studied in figure 1 are described in detail in the following sections.

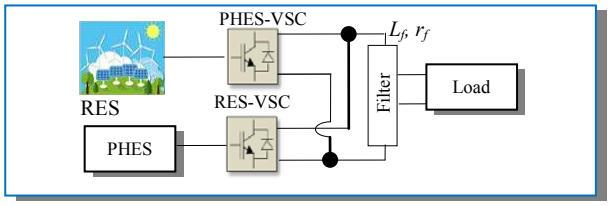

Figure 1. Global scheme of the studied system

II. MODELING OF CONTROL SYSTEM

A. Renewable energy ressource modeling

Figure 2 illustrates the RES random power profile. In this proposed hybrid system, the electrical load is mainly supplied by the RES whit fixed power. The excess of energy from the RES is used to pump the water from the lower reservoir to store it in an upper reservoir. During periods of high electrical demand, the stored water is released from the upper reservoir to the lower reservoir through turbines to produce electric power.

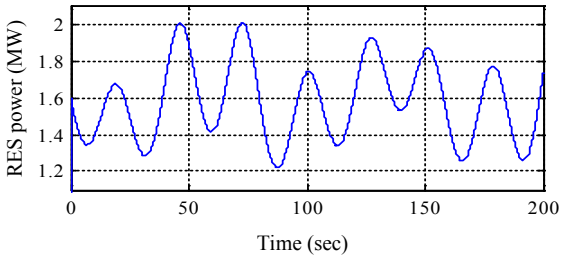

Figure 2. RES random power profile

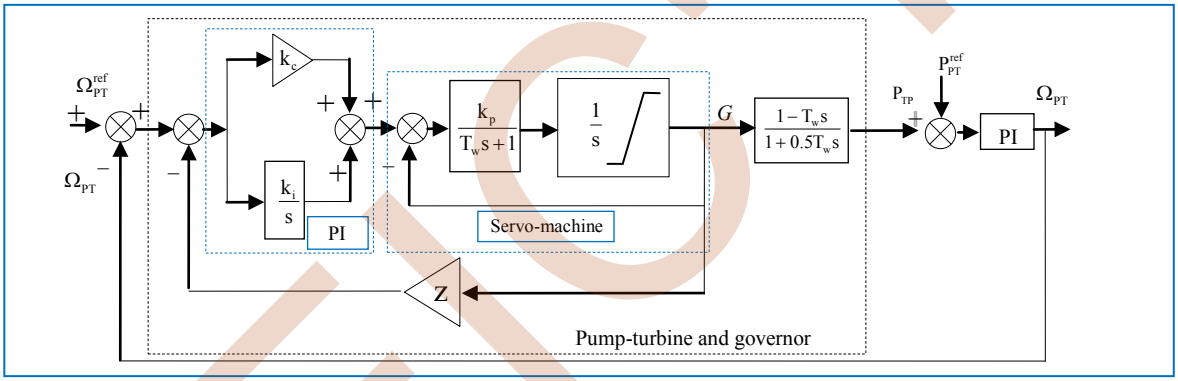

Figure 3. Structure of the servomechanism and PI controller

of water turbine. It is made up by the major servomotor and auxiliary servomotor. The maximum displacement speed of the servomotor is restricted by a rate limiter.

The power set point is imposed by the load conditions and the speed set point is calculated by a speed optimizer in order to maximize the turbine efficiency [14].

The servomechanism is the actuator of the speed governor. It is used to amplify the control signal and provide power to operate the guide vane of a pump-turbine unit. The structure of the servomechanism and PI controller are shown as figure 3.

The transfer function of the PI regulator is given by:

$$G_{PI}(s)=\frac{1}{z}\frac{\frac{1+k_c}{k_i}}{1+\left(\frac{1}{z.k_i}+\frac{k_c}{k_i}\right).s} \quad (2)$$

3) Mathematical model of PMSG: In the synchronous *dq* frame, the PMSG can be modelled as follows [15]:

B. PHES modeling

The PHES under study includes three parts: reversible pump-turbine unit, governor system and PMSM, which are modelled and described in the following subsections.

1) Reversible pump-turbine unit: The mathematical model of the pump-turbine describes the relationship between the output mechanical power of the pump-turbine and the guide vane opening. In this paper, the ideal pump-turbine model is used without losses [12, 14]. The transfer function can be written as follows:

$$P_{PT}=\frac{1-T_w s}{1+0.5T_w s}G \quad (1)$$

Where: P_{PT}: The pump-turbine mechanical output power; G : The guide vane opening; T_w : The water starting time.

2) Control strateg of speed pump-turbine: the control strategy of speed pump-turbine generator is presented in figure 3, consists of a PI regulator with droop coefficient and servomechanism. The servomechanism is the actuator

$$\begin{cases} v_d = L_d\frac{di_d}{dt}+R_s i_d-\omega_e L_q i_q \\ v_q = L_q\frac{di_q}{dt}+R_s i_q+\omega_e\left(L_d i_d+\psi_f\right) \end{cases} \quad (3)$$

Where: R_s is the stator winding resistance; ψ_f is the permanent magnet flux vector, Ω_e is the electrical rotational speed, i_d and i_q are, respectively, the direct and quadratic currents.

The direct and quadratic magnetic fluxes are given by (the excitation flux ψ_f is constant):

$$\begin{cases} \psi_d = L_d i_d+\psi_f \\ \psi_q = L_q i_q \end{cases} \quad (4)$$

The electromagnetic torque is also expressed as fellow:

$$T_e = p\left(\psi_d i_q-\psi_q i_d\right) \quad (5)$$

p is the pair pole number of the synchronous generator

The active and reactive powers are given according to:

$$\begin{cases} P = v_d i_d + v_q i_q \\ Q = v_q i_d - v_d i_q \end{cases} \quad (6)$$

4) PMSM currents regulation: PMSM currents are regulated by hysteresis controllers, which allow keeping the current wave into range defined around the reference value. When current wave reached the band limits, the hysteresis controller generate a logic signal (0 or 1) (Figure 5). So, for (j=1, 2, 3) we have:

$$\begin{cases} F_j = 1 \text{ if } i_{mj}^{ref} - i_{mj} \geq \Delta i \\ F_j = 0 \text{ if } i_{mj}^{ref} - i_{mj} \leq \Delta i \end{cases} \quad (7)$$

With Δi is the hysteresis band defined in the controller.

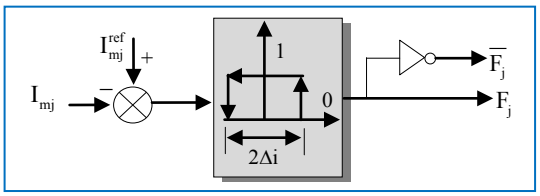

Figure 4. Hysteresis current controller

C. Converter modeling

A switching function T_{ij}, of the PWM rectifier (Figure 5), is defined for each power switch. It represents the ideal commutation and takes the value 1 if the switch is close, 0 when he is open (off):

$$T_{ij} = \begin{cases} 1 \; T_{ij} \text{ is close} \\ 0 \; T_{ij} \text{ is open} \end{cases} \quad (8)$$

$i \in \{1,2,3\}$ number of the arm

$j \in \{1,2\}$ number of the switch in the arm

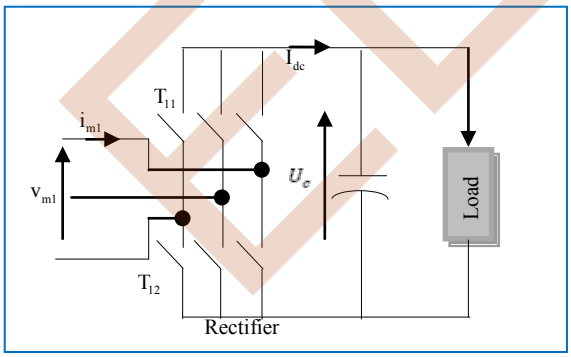

Figure 5. PWM rectifier

III. CONTROL STRATEGY OF HYBRID SYSTEM

A. PHES operation modes

The typical operation of PHES could be described as follows. When the electrical energy needs to be stored, the water is pumped from the bottom tank to the top. When the system needs electrical energy, the water is released from the top tank to the bottom in order to generate power.

B. Control of optimal combined operation system

1) Pumping mode: When the DC voltage is less than the DC voltage reference the control mode I work. The PHES will adjust the speed of the reversible pump-turbine, meantime modifying the scheduled pumping capacity in this hour period.

2) Generation mode: When the DC voltage is higher than the DC voltage reference the control mode II works. The PHES will convert its present operation mode immediately, and then adjust the speed of the reversible pump-turbine to the maximum in order to reduce the large fluctuation.

$$P_{Load} = P_{RES} \pm P_{TP}^{ref} \quad (9)$$

Due to the PHES operating mode change, Dc-voltage control is recommended to keep the DC-voltage constant, equal to the U_{dc}^{ref} to provide a frequency reference for stable PHES operation, so that the flow of power on PHES-VSC is fully controlled by PHES. The reference value P_{TP}^{ref} of the active power of the reversible pump-turbine is determined by:

$$P_{TP}^{ref} = P_{RES} \pm P_{Load}^{ref} \quad (10)$$

$$P_{TP}^{ref} = \eta_{TP} . P_{TP} \quad (11)$$

The figure 6 shows the control strategies combined operation system.

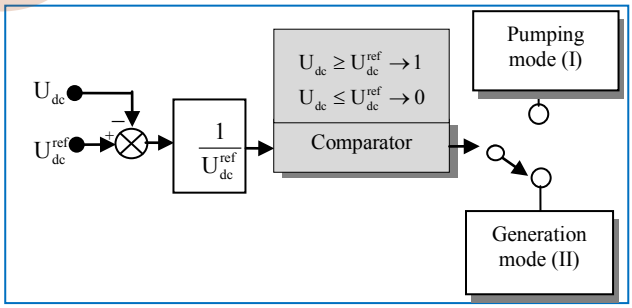

Figure 6. Ccontrol loop for PHES

IV. RESULTS AND DISCUSSION

Table 1 gives the parameters for the reversible pump-turbine, the PMSM and the electrical load. The studied system, shown in figure 1, is implemented in the Matlab\Simulink software environment. The results of simulation are obtained for load power reference $P_{Load}^{ref} = 1.6MW$ and the typical RES power given in figure 2.

A. Results in Pumping mode

The speed rotation and the power in pumping mode are given by the figures (7-8).

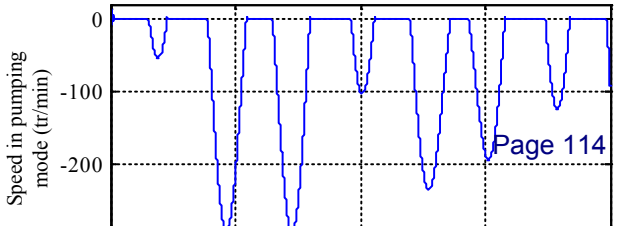

Figure 7. Speed in pumping mode

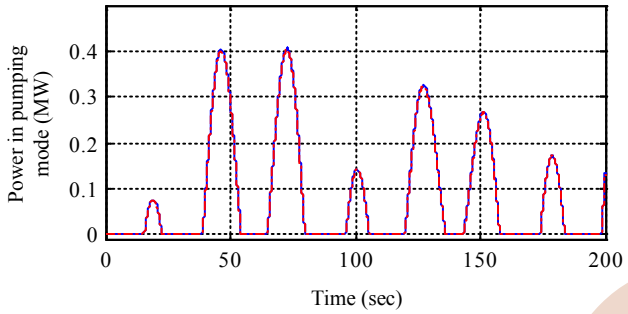

Figure 8. Power in pumping mode

B. Results in generation mode

The speed rotation and the power in generation mode are given by the figures (9-10).

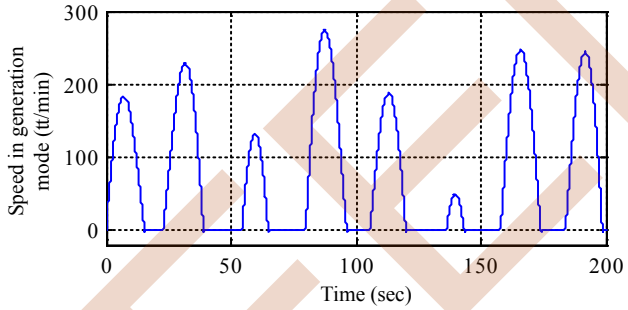

Figure 9. Speed in generation mode

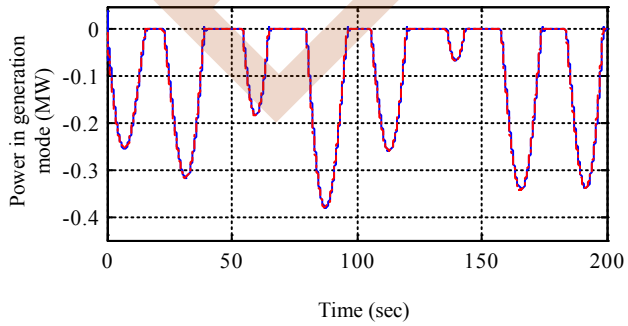

Figure 10. Power in generation mode

The results of simulation for both modes evidence the performance of the variable speed hydropower plant, showing a dynamic response excellence when the system switches from the generate mode ($\Omega_{TP} > 0$) to the pumping mode ($\Omega_{TP} < 0$) with the reversal the direction of the speed rotation. Ensure the stability of the speed control, when the reversible pump-turbine units operating state changes, in order to avoid emitted active power fluctuations of the RES.

It is clear from the figures (8 to the 11) that the droop coefficient is making the pumped storage and the pumped storage is also reacting to the speed of change of the grid frequency. The power variation for both modes follows the variation of the guide vane opening, that assuring more efficient management of available wind resources.

The power variation for both modes follows the variation of the speed, that assuring more efficient management of available wind resources.

The DC voltage is maintained at constant value of 1.5 kV as shown in figure 11.

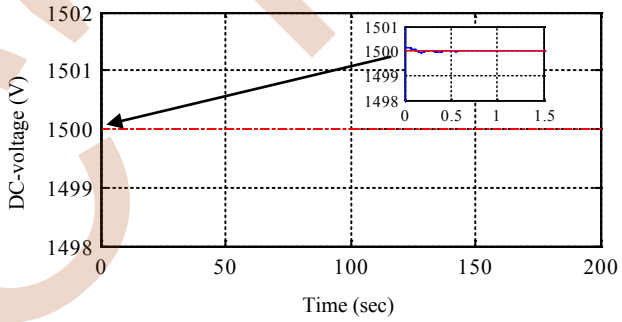

Figure 11. DC-voltage and Transitional regime

Figure 12 shows the load power remains constant at 1.6 MW.

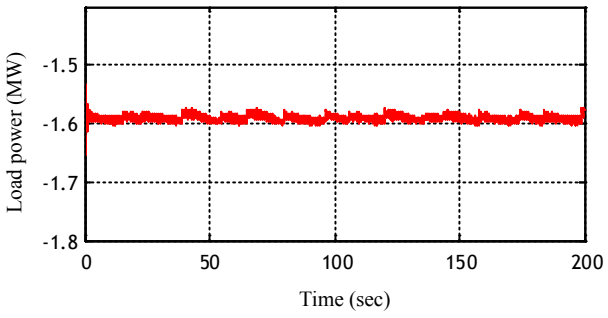

Figure 12. Load power

TABLE I. PARAMETER OF SIMULATION

name	Table of parameter		
	parameter	*Value*	*unit*
Pump-turbine	Nominal power	520	kW
	Rate speed	360	rpm
	Efficiency	0.76	
	Mass generator	834	kg
	Mass rotor	834	kg
DC- voltage	DC-Bus voltage	1.5	kV
	DC-Bus capacitor	0.015	F
	Inductance filter	0.002	H
	Resistor filter	0.01	Ω
PMSM	Frequency	50	Hz
	Stator winding resistance	12	mΩ
	Stator inductance	0.13	mH
	Rotor inductance	0.13	mH
	Excitation Flux	2.5	Wb

CONCLUSION

The Pumped-Storage Hydropower associated to the Renewable energy Source has been presented in this paper. The simulation results have confirmed the reversible pump-turbine operation in that variable speed technology allows for rapid transition between the two operating modes. This advantage of the pumped hydroelectric energy storage system offers a high performance for the compensation of the power fluctuation of renewable energies sources.

The variable speed technology in pump-turbines permits the energy storage and production with a fast reactivity (seconds), the grid frequency regulation (in both regimes pump and turbine) and the optimization of the efficiency of the hydraulic power plants.

REFERENCES

[1] M.H.Mahmoud, S.Tomonobu, O. Mohamed, A.A.M. Mohamed, M.H. Mohamed, amada M.M, Control of a Stand-Alone Variable Speed Wind Energy Supply System, applied sciences journal 2013, vol.3, pp.437-456.

[2] S. Kaiqi, KJ.LI, J.Pan,Y.Liu, Y.Liu, An optimal combined operation scheme for pumped storage and hybrid wind-photovoltaic complementary power generation system, Applied Energy (2019), Vol.242, pp.1155–1163.

[3] CEER. Status Review of Renewable Support Schemes in Europe for 2016 and 2017. Status Review of Renewable Support Schemes in Europe for 2016 and 2017. Ref: C18-SD-63-03, 14 December 2018.

[4] B. Getachew, P. Björn, Feasibility study for a standalone solar–wind-based hybrid energy system for application in Ethiopia, Appl Energy 2010., vol.87, pp.487–95.

[5] N.E.M. Rozali, S.R.W. Alwi, Z.A. Manan, J.J. Klemeš M.Y.Hassan, Optimisation of Pumped-Hydro Storage System for Hybrid Power System Using Power Pinch Analysis. Chemical Engineering Transactions 2013., vol. 35, pp 85-90.
DOI: 10.3303/CET1335014

[6] S.Rehman, L.M. Al-Hadhrami, M.M. Alam, Pumped hydro energy storage system: A technological review. Renewable and Sustainable Energy Reviews; December 2015; vol. 44,pp. 586-598.
http://dx.doi.org/10.1016/j.rser.2014.12.040

[7] S.R. hanrajan, S.Vamsi Krishna, L.Narayana Reddy, A. Surya Teja, B.Vishal, A Study of Motor - Generator Topologies for Pumped Storage Applications, Conference on Advances In Engineering And Technology - ICAET-2014; pp. 627-635.

[8] T. Ma, H. Yang, L. Lu, J. Peng, Technical feasibility study on a standalone hybrid solar-wind system with pumped hydro storage for a remote island in Hong Kong, Renewable Energy journal 2014; Vol. 69, pp. 7-15.

[9] M. Manish, O. Abdelhamid, H. Rob, L.Yusheng, S. Mohit, M. Eduard, G.Vahan, D.Peter, Real-time co-simulation of adjustable-speed pumped storage hydrofor transient stability analysis, Electric Power Systems Research journal 2018, vol.154, pp.276–286.

[10] Lott, Melissa, Kim, Sangll, Tam, Cecilia, Elzinga, David. Technology roadmap: energy storage; 2014.

[11] X. Luo, J. Wang, M. Dooner, J. Clarke, Overview of current development in electrical energy storage technologies and the application potential in power system operation, Appl Energy 2015, vol. 137, pp.511–36.

[12] B. Lakhdar, B.Seddik, R.Daniel, Optimisation du contrôle commande d'un système hydraulique réversible à vitesse variable. Thèse doctorat, Ecole Doctorale Electronique, Electrotechnique, Automatique & Traitement du signal, Laboratoire de Génie Electrique de Grenoble 8 juillet 2013.

[13] G. Zhao, Q.Zhao, J.Ren, X.Song, M.Han, Modelling and control of doubly fedvariable-speed pumped storage units for grid power regulation. The 6th International Conference on renewable Power Generation (RPG) 19–20 October 2017, J. Eng. 2017, Vol.2017(Issue13), pp. 745–750. Doi :10.1049/joe.2017.0430

[14] N.N.Phuc Diem, Optimisation de systèmes de production intermittents et non conventionnels couplés au réseau électrique. Thèse de doctorat, université de GRENOBLE, Laboratoire G2ELAB, l'École Doctorale EEATS, France 20 avril 2011.

[15] P.A.Eduardo, J.F. Adria, L.F. David,G.B. Oriol, Decentralized Control of a Nine-Phase Permanent Magnet Generator for Offshore Wind Turbines, IEEE transactions on energy conversion 2015, pp.1-10. DOI: 10.1109/TEC.2015.2412550

Anew power management technique for a standalone wind energy conversion system based on SCIG with storage battery

Toufik Laddi *, Djamal Aouzellag
Laboratoire de Maitrise des Energies Renouvelables (LMER).
Faculté de Technologie
Université de Bejaia 06000, Algérie
ladditoufik@yahoo.fr; aouzellag@hotmail.com

Oussama Khoudour, Nabil Taib
Laboratoire de technologie industrielle et de l'information (LTII).
Faculté de Technologie
Université de Bejaia 06000, Algérie
Oussama.kh89@yahoo.fr; taib_nabil@yahoo.fr

***Abstract* — This paper presents the dynamic behavior of autonomous and variable speed wind energy conversion system with storage battery based on induction generator. The wind turbine extracts the maximum power from the wind using the MPPT technique, to meet the load requirements and the excess power is used to charge the batteries for the future used.**

A novel power management strategy is proposed, when the batteries are fully charged, the proposed control system disconnects the batteries immediately for protect them. In this moment, the power generated is greater than that consumed by the load, this power difference must be canceled in order to protect the generator and the power converters, in this case, the proposed control system deactivates the MPPT technique, and the wind turbine is released to rotate with can reach twice the nominal speed to generates just a power to meet the needs of the load.

***Keywords* —** *SCIG generator, stand-alone, power converters, variable speed, wind turbine, power control, battery.*

I. INTRODUCTION

Electricity generation plants have become a daily environmental issue, as they present a source of pollution. As a result, resources that use green energy have a very strong growth. Among renewable energies, wind energy is one of the most used for the production of electrical energy [1-2].

The use squirrel cage induction generator (SCIG), permanent magnet synchronous generators (PMSG) and doubly-fed induction generators (DFIG) is recently preferred in the wind energy conversion system (WECS) units. However, the PMSG suffers from high cost of materials and manufacturing [3] and the use of DFIG has the disadvantage of requiring a system of rings and brushes inducing important maintenance costs mostly for offshore projects located in a saline medium [4].

Therefore, the squirrel cage induction generator (SCIG) has many advantages over other generators, such as robustness, low installation and maintenance costs which making it an ideal candidate to be used in WECS [5-6].

In the variable speed (WECS), the use of maximum power point tracking algorithm (MPPT) has a great importance, to extract the maximum power available in the wind [7]. So far, the MPPT algorithms researched can be classified into three main control methods, namely tip speed ratio (TSR) control, power signal feedback (PSF) control and hill-climb search (HCS) control. The first control method (TSR) is used in this paper, which used to regulate the rotation speed of the generator, in order to maintain the TSR to an optimum value at which power extracted is maximal. This method requires both the wind speed and the turbine speed in addition to requiring the knowledge of optimum TSR of the turbine in order for the system to be able extract maximum possible power [8].

In the grid connection mode, all power extracted using the MPPT algorithm will be injected into the grid [9]. Nevertheless, in stand-alone mode, the WECS system must meet the power requirements for the loads and the excess power will be stored in a storage system for future use [10]. In this context, several works carried out in stand-alone variable speed WECS using the MPPT algorithm and storage unit (batteries).

However, to approach the system to the reality, the batteries have a maximum state of charge (SOC) which must not exceed. Beyond this, the life of the batteries is reduced, which leads to their deterioration, the same thing for the discharge of the batteries below the SOC.

Unfortunately, this assumption is not taken into account in all the works carried out for the stand alone WECS using the MPPT and batteries as storage unit. Therefore, in this paper, a new power management and control (PMC) algorithm is proposed to ensure a reliable satisfaction of the load requirement and to protect the batteries as follow.

At the beginning, The WECS operates using the MPPT mode to supply the load, and the excess power is exploited to charge the batteries. In the case of full charging of batteries, to protect them, the PMC will disconnect them immediately, in this moment, the power generated by the WECS becomes greater than that consumed by the load. So, the MPPT mode loses its physical sense at this moment. Therefore, this power difference can be dangerous to power converters, to rebalance the generated and consumed power, the PMC will deactivate the MPPT mode and activates the FREE mode Fig.2.

For the FREE mode, the wind turbine will release to generate a wind torque following the generator electromagnetic torque, which has its turn following the load power. So that, the WECS will only generates the

power to supply the load. In this operating zone, each change in electrical load will cause an imbalance in the dynamic equation of wind turbine, and the later will increase or decrease its rotational speed to find a new operating point.

The main decision factors for the proposed power management system are the provided and demand powers and the state of charge (SOC) of the batteries. The studied system is modeled and tested using the MATLAB/Simulink software. The control of global system and the proposed power management are done for different operating conditions, such as sudden load variation and randomly fluctuations of the wind speed at the same time to approach the system to the reality. Moreover, the operation of the system in free and in MPPT mode, the results obtained are discussed.

II. The Studied System

The global system studied in this paper consists of a wind turbine, an induction generator, three power converters with a PWM control, and an accumulator battery. In the case of variable speed stand-alone operation with balanced load, the regulation of the voltage at the DC level is ensured by generator side converter (GSC), and the regulation of frequency is ensured by the load side converter (LSC), because the wind and the load are randomly variable, a storage system is added at the DC voltage level after a back-Boost converter taken account the maladjustment of load. The proposed power management is used to ensure all the production/consumption balance, the charging and discharging of the batteries, the connection and disconnection them (full charging or critical discharging level), and determines the operating mode of the wind turbine with or without MPPT, the system studied is then simplified as shown in Figure 1.

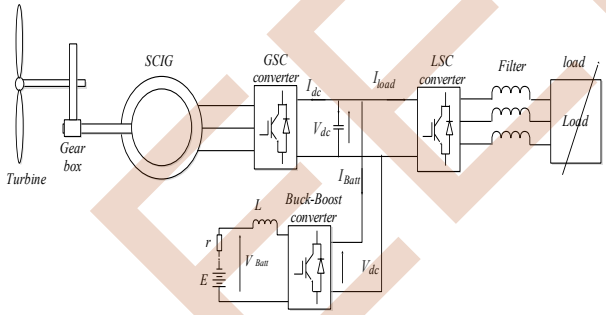

Figure 1. Schematic diagram of the system studied

A. Turbine Modeling

The wind turbine converts part of the kinetic energy of the wind into a useful mechanical energy. The power extracted from the wind can be expressed in (1) as follows:

$$P_m = \frac{1}{2}\pi\rho C_p(\lambda,\beta)R^2v^3 \qquad (1)$$

Whereρ is the air density, C_p is the power coefficient, whichis a function of λ, the tip speed ratio and β, the pitch angle.$R$is the radius of the turbine and v is the wind speed.The tip speed ratio and the power coefficient are given respectively by(2) and (3)respectively as follows:

$$\lambda = \frac{\Omega_t R}{v} \qquad (2)$$

$$Cp(\lambda,\beta) = 0.4 - 0.0167\beta\, sin\left(\pi\frac{\lambda + 0.1}{12.8 - 0.43\beta}\right) - 0.00184(\lambda - 3)\beta \qquad (3)$$

Where Ω_t is the angular speed of turbine, neglecting the friction forces, the dynamic equation of the wind turbine is given by:

$$\frac{d\Omega_r}{dt} = \frac{1}{J}(T_t - T_{em}) \qquad (4)$$

Where Ω_r , the angular speed of the generator, $J$is the moment of inertia of the generator and the turbine, T_t is the torque developed by the wind turbine and T_{em} is the generator electromagnetic torque.

The functional diagram of the turbine model is established in figure 2. It shows that the speed of turbine is controlled by action on the electromagnetic torque, which depends on the choice of the operation mode of the turbine (with or without MPPT). In the case of MPPT mode, the electromagnetic reference torque is imposed depending on the optimum parameters of the turbine λ_{opt} and $Cp_{\max}$, the wind turbine develops a torque T_m equal to the electromagnetic torque to rebalance the dynamic equation of wind turbine and stabilize at a maximum operating point, and as the wind speed is variable with time and considered as a disturbing input in this system, the wind turbine speed must be adjusted continuously to that of the wind for ensure maximum collection of wind energy. And in the case of operation without MPPT, the electromagnetic reference torque is depend on the parameters of the generator (stator currents and rotor fields), the rotor field is kept at its nominal value by the *dq* rotor reference frame control, the electromagnetic torque has a direct relationship with the stator current, the later depends on the load currents via the DC bus, so any increasing the load current will increase the call of the stator currents and increases the electromagnetic torque of the generator, the operating point will move to rebalance the dynamic equation of the turbine. In our work, the choice of operating mode of the turbine (with or without MPPT) is decided by the proposed optimization and power management algorithm.

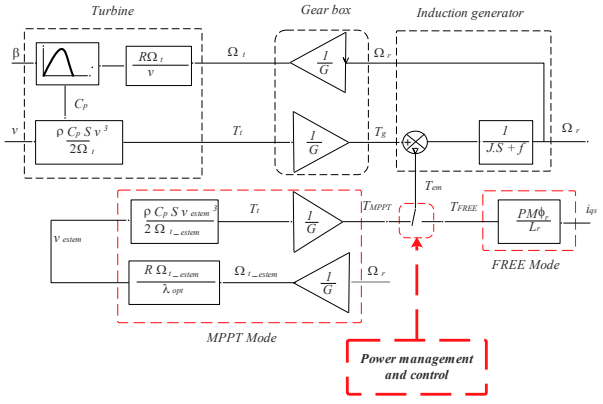

Figure 2.The functional block diagram of the turbine model

B. *Model Of Induction Generator*

In order to obtain a dynamic model for the electric generator which allows us to easily define the control system of the generator, we use the Park's transformation (dq), in this frame, the inductance parameters become constant, independent of position. The dq model ofthe squirrel-cage asynchronous machine provides a powerful physical interpretation of the interactions of currents and fields of such fate to produce voltages and torques, more importantly it leads to an easy adaptation with the proposed control strategies.

$$\begin{cases} \frac{d}{dt} i_{ds} = \frac{1}{\sigma L_s}\left[-R_{sr} i_{ds} + \omega_s \sigma L_s i_{qs} + \frac{MR_r}{L_r^2}\varphi_{dr} + \frac{M}{L_r}\omega_r \varphi_{qr} + v_{ds}\right] \\ \frac{d}{dt} i_{qs} = \frac{1}{\sigma L_s}\left[-R_{sr} i_{qs} - \omega_s \sigma L_s i_{ds} + \frac{MR_r}{L_r^2}\varphi_{qr} - \frac{M}{L_r}\omega_r \varphi_{dr} + v_{qs}\right] \\ \frac{d}{dt}\varphi_{dr} = \frac{MR_r}{L_r} i_{ds} - \frac{R_r}{L_r}\varphi_{dr} + \omega\varphi_{qr} \\ \frac{d}{dt}\varphi_{qr} = \frac{MR_r}{L_r} i_{qs} - \frac{R_r}{L_r}\varphi_{qr} - \omega\varphi_{dr} \end{cases} \quad (8)$$

Where: $R_{sr} = \left(R_s + R_r \frac{M^2}{L_r^2}\right); \sigma = \left(1 - \frac{M^2}{L_s L_r}\right)$

WhereR_s, R_r, are the stator and rotor resistances and L_s , L_r, are the stator and rotor cyclical inductances respectively, M is the mutual inductance,ω_s and ω are the pulsation of stator and rotor quantities respectively, which are linked by the following relationship:

$$\omega_s - \omega_r = \omega \quad (9)$$

$$\omega_r = P\Omega_r \quad (10)$$

When, Ω_r the mechanical speed of the generator.

III. CONTROL OF THE ASYNCHRONOUS GENERATOR

In vector control algorithms, the rotor field is kept constant at its rated value. Thus the torque can be adjusted according to the active power demand. The DC bus voltage V_{dc} is kept at its desired value, it is possible to express the reference power by:

$$P_{dc}^* = V_{dc}^* . i_{dc} \quad (11)$$

Where, i_{dc} is the output current of the generator side converter. Neglecting the losses, we obtain the electromagnetic torque expression by:

$$T_{em}^* = \frac{P_{dc}^*}{\Omega_r} \quad (12)$$

The control of V_{dc} voltage can be carried out through the electromagnetic torque, in our present work, the orientation of thedq frame is chosen so that ϕ_{dr} =ϕ_r,ϕ_{qr} =0and controlling the field$\phi_r$to keep it constant. The implementation of the control requires estimating the electromagnetic torque, the rotor field and ω_s. The electromagnetic torque is expressed from the current i_{qs} by:

$$T_{em} = P\frac{M}{L_r}\phi_r i_{qs} \quad (13)$$

The rotor field is expressed from the currenti_{ds} as follows:

$$\phi_r = \frac{M}{1+T_r.S} i_{ds} \quad (14)$$

Knowing of ω_s ensures the validity of the equations because the dq reference must constantly monitor the rotating field. For this, one uses the internal angular relationship ω_s= ω+$P\Omega_r$. The rotational speed of the machine is measured and that the rotor field is estimated. Is then obtained for ω_s :

$$\omega_s = \frac{Mi_{qs}}{T_r.\phi_r} + P\Omega_r \quad (15)$$

The rotor field is adjusted by thei_{ds} current, and the electromagnetic torque is adjusted by i_{qs} current. The figure 3 resumes the adopted vector control algorithm:

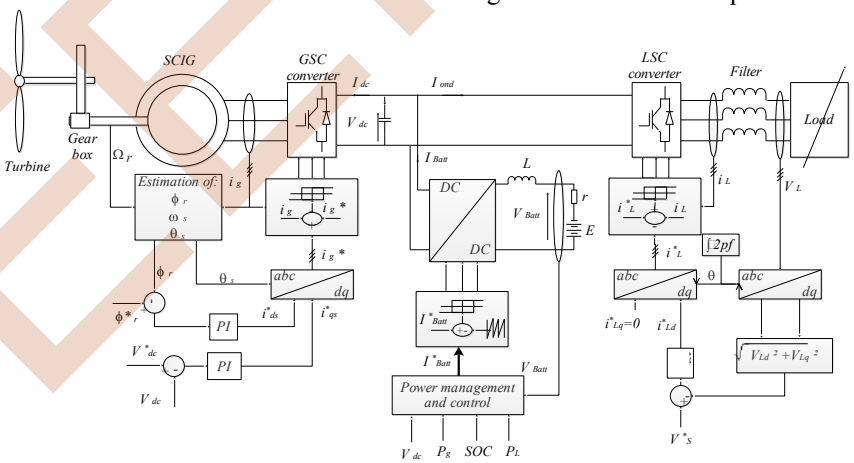

Figure 3.The adopted vector control algorithm

IV. THE PROPOSED POWER MANAGEMENT STRATEGY

The studied system using the proposed power management strategy has the advantage of being able to operate in two operating zones, the operation with or without the use of the MPPT technique.

Zone I: this zone corresponds to the operating mode of the studied system using the MPPT technique, provided that the power generated by the wind conversion system is sufficient to satisfy the needs of the load, so the power difference is positive, this difference is invested to charge the batteries as long as they are not fully charged ($SOC < SOC_{max}$), or in the case where the power difference is negative i.e. the power demand by

the load is greater than that generated by the wind conversion system, this power difference will be compiled by the batteries as long as they are not completely discharged ($SOC > SOC_{min}$). In this case, the power coefficient and the tip speed ratio of the turbine are maintained at the maximum and optimum values, respectively, $Cp = Cp_{max}$ and $\lambda = \lambda_{opt}$.

Zone II: At the time of disconnection of the batteries (fully charged), the power of the wind conversion system is greater than that demanded by the load, the MPPT technique is disabled by the control system, the wind turbine operates with a power coefficient and a tip speed ratio below and above the maximum and the optimum values respectively $Cp < Cp_{max}$ and $\lambda > \lambda_{opt}$. At this moment the speed of the turbine will continue to increase to reduce the torque generated by the wind turbine which makes a displacement of the operating point corresponds only to the power demanded by the load.

The overall system works for a long time. Therefore, the functioning of the studied system involves a number of decisions concerning the management of the powers. The key indicators that govern the operation of the system are the state of charge of the batteries and the sign of the difference of the powers. The dynamics of charging and discharging batteries is much faster, so it can effectively cover the fluctuations of wind energy due to the random nature of the wind, given the importance of batteries in the proper functioning of the global system.

V. Simulation Results

The nominal parameters of the squirrel-cage asynchronous generator, the wind turbine and the nickel-cadmium battery are written in the appendix. The battery is initially charged at50%. The value of the DC bus voltage reference is put equal to V_{dc}^{*} = 650 V. And the reference rotor field is put equal to the rated value 0.7 Wb. The load in this work is balanced and purely resistive which is initially taken equal 3 kW. At $t = 1s$, the batteries are inserted, at time $t = 10s$, the load power is increased to 4.5 kW, and it reduced to its initial value at time$t = 20\,s$. For this test, the wind speed varies randomly around the nominal speed ($v = 8\,m/s$), the wind speed profile is given in Figure 4.

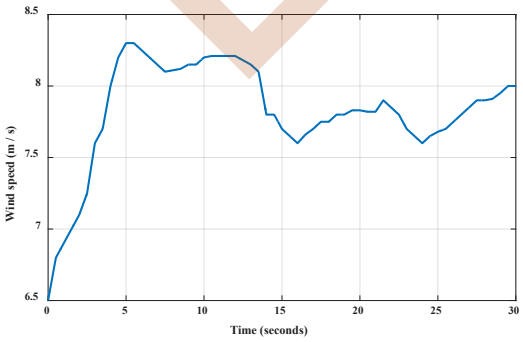

Figure 4. Wind speed profile

As shown in Figure 5 and Figure 6, the studied system can operate in two operating zones, with or without using of MPPT strategy. The operating mode with using the MPPT technique, to extract the maximum wind power, requires a maximum power coefficient equal to 0.4 (Figure 6), with an optimum rotation speed (Figure 5). In the operating mode without using of MPPT strategy, the rotational speed of the generator varies over a wide speed range which can be almost twice the nominal speed (Figure 5) with a decrease in the power coefficient, the speed decreases as load active power increases and vice-versa, in this case the operating point varies and stabilizes according to the power demanded by the load. Note that the speed variation is a slow process because it is determined by the inertia of rotating system and negative sign in generator torque shows that it operates as generator mode, in order to clearly see the variation of the power coefficient versus tip speed ratio a long test time.

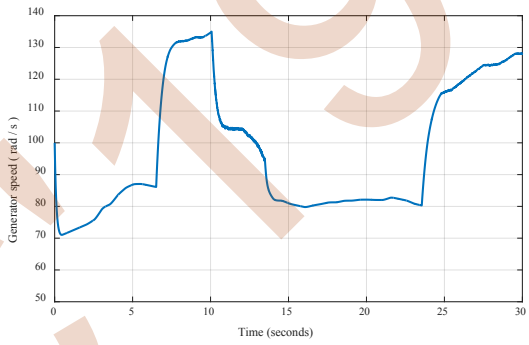

Figure 5. Generator speed (rd/sec)

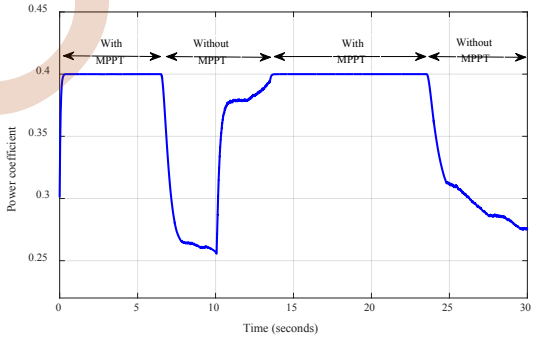

Figure 6. The power coefficient

In order to initial the excitation process, the capacitor connected at the DC side of the converters assumed that is pre-charged to a voltage of 12 V. It can be noted that this initial voltage is appropriate to implement the proposed scheme at the lowest speed, but the start-up process can be achieved with low initial voltage if rotor speed increases or sluggish DC-link voltage reference ramp is selected, and with increase in capacitor value the DC-link voltage takes longer time to reach the reference value, but at the same time the final ripple amplitude decreases, it can be seen from (Figure 7) that the DC-link voltage is well regulated and is insensitive to the variation of the load, an overrun is not exceeded by 13 % due to the disconnection of the batteries at the time of fully charging. This gives us a three-phase voltage with constant amplitude at the output of the inverter.

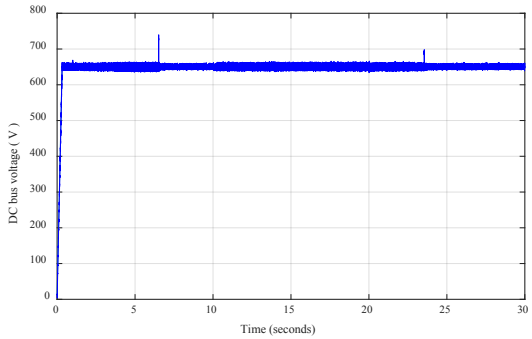

Figure 7. DC bus voltage

The stator currents are shown in Figure 8, the d axis stator current is kept at its reference value, to ensures the magnetization of the generator whatever the load and the wind variations, the q axis stator current is the picture of the active power delivered by the generator if the stator voltage is properly regulated and kept constant, it depends on the variation of the load power, the rotational speed of the rotor and the charge and discharge of the battery. The generator must provide sufficient power to satisfy the needs of the load and the batteries during the charging period of the latter by using the MPPT technique, if the batteries are disconnected (fully charged), the generator operates without using the MPPT technique, and it provides just the power required by the load.The generator torque changes accordingly to the load and follows the torque supplied by the turbine, it have the same curve that the q-axis current (Figure 9).

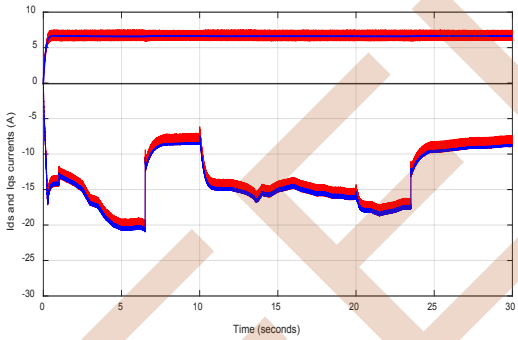

Figure 8. i_{ds} and i_{qs} currents and heirs references

The state of charge of the battery is one of the important key decisions of control strategy proposed, in our work the battery is initially charged and inserted in the global system at $t = 1s$, as shown in (Figure 10), the battery current is positive during the charging mode and negative during the discharging mode, as is known, the batteries can be charged more than 100 %, but they heat up and degrade over time, and to protect it, the SOC_{max} is set at 95%, beyond this value the batteries must be disconnected.

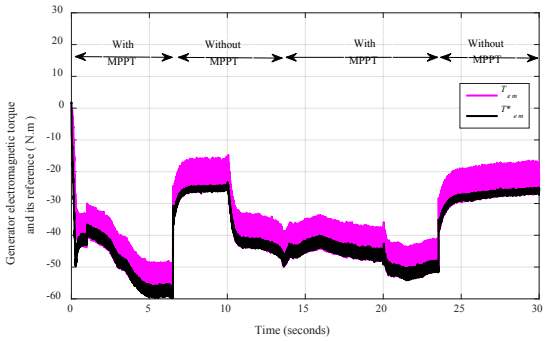

Figure 9. Electromagnetic torque and it reference behavior

The corresponding power flows in our system during the wind and the load change is shown in the figure 11, it can be seen that in every moment the generator power is equal to sum of the load and the battery power. It can be found too that the proposed control strategy plays a very important role in protecting the global wind energy conversion system, the wind turbine extract the maximum power from the wind using the MPPT technique, to power the load and the excess power will charge the batteries.

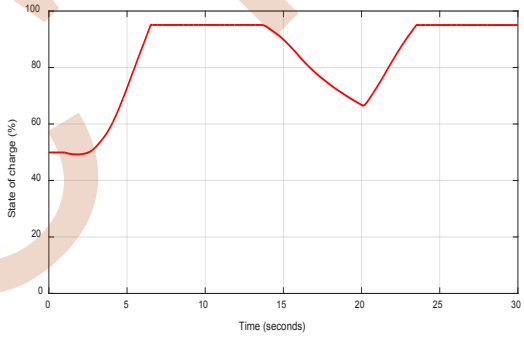

Figure 10. State of charge of battery

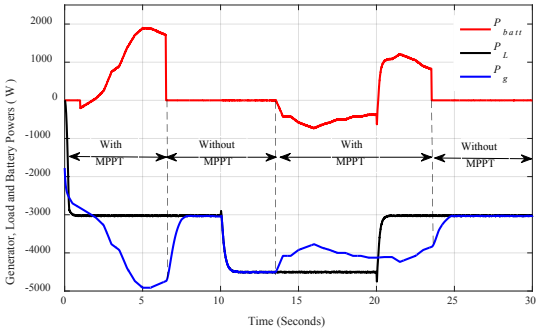

Figure 11. Generator, load and battery powers

When the batteries are fully charged, the control system disconnects them immediately to protect them. But the power generated at this time is greater than that consumed by the load, this power difference must be canceled to protect the generator and the power converter, in this case the proposed control system will disable the extraction technique of maximum power and the turbine will be released to produce just the needs of the load as shown in figure 5 and figure 11.

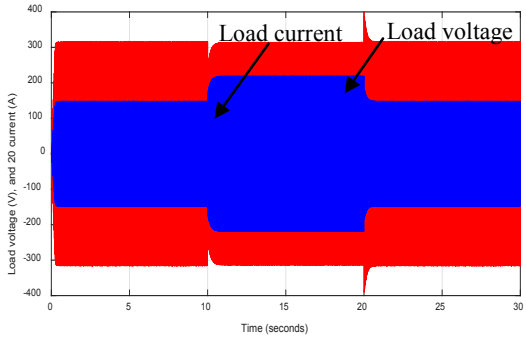

Figure 12. Load voltages and currents behavior

The Figure 12 shows the load current and voltage, it can be clearly seen that the load current depends just of the load variations, the load voltage is well controlled and established to its reference value and is insensitive to the variation of the wind speed or connection and disconnection of batteries, its frequency is fixed to 50Hz whatever the variation speed of the turbine, we can to say the term, variable speed system and constant frequency (VSCF).

VI. CONCLUSION

In this paper, a dynamic behavior of autonomous and variable speed wind energy conversion system with storage battery based on squirrel-cage asynchronous generator was studied, an analytical model of the asynchronous generator allowed us to directly extract the control laws has been presented, a vector control by the rotor field orientation was used, this strategy allows to maintain the DC bus voltage at a constant value however the speed of the wind and the abrupt variation of the load, in addition, this control makes it possible to adjust the rotor field separately from the electromagnetic torque adjustment and to maintain it at its nominal value, in order to guarantee a stable supply of the asynchronous generator by the reactive power. And on the other hand, and to protect the storage system and the asynchronous generator, an optimization and power management algorithm has been proposed to determine the limits of use and validity of the MPPT technique. The simulation results show that the proposed control system adds high performance dynamic flexibility and behavior to the conventional stand-alone wind conversion system, and is very robust with respect to wind speed or load variations. The strategy proposed in this paper is very relevant for a stand-alone wind energy conversion system based on a squirrel cage asynchronous generator.

APPENDIX

Parameters of the asynchronous machine [12]:

P_N= 5.5 kW, U_N= 220/380 V, I_N= 23.8/13.7 A, 50 Hz, R_s= 1.07131 Ω, R_r= 1.29511 Ω, p = 4, Ω_N= 690 rpm, J = 0.230 kg·m^2, K_f= 0.0025 N·m/$rads^{-1}$.

Parameters of the turbine [12]:

$G = 3.1425$, $R = 3.24\ M$, $\lambda_{opt} = 10.4$, $C_{pmax} = 0.44$

REFERENCES

[1] T. Ramji, N.R. Babu. "Recent developments of control strategies for wind energy conversion system" Renewable and Sustainable Energy Reviews 66, 2016, Pages 268-285.

[2] F. Abdoune, D. Aouzellag and K. Ghedamsi ''Terminal voltage build-up and control of a DFIG based stand-alone wind energy conversion system'' Renewable Energy. Volume 97, 2016, Pages 468-480.

[3] Y. Tang and L. Xu, "A flexible active and reactive power control strategy for a variable speed constant frequency generating system," IEEE Trans. Power Electron. vol 10, 1995, Pages 472–478.

[4] C. Carunaiselvane, Thanga RajChelliah ''Present trends and future prospects of asynchronous machines in renewable energy systems'' Renewable and Sustainable Energy Reviews. Volume 74, July 2017, Pages 1028-1041.

[5] T. Ahmed, O. Noro, E. Hiraki, M. Nakaoka,"Terminal Voltage Regulation Characteristics by Static Var Compensator for a Three-Phase Self-Excited Induction Generator" IEEE Trans. On Industry Applications, Vol. 40, No. 4, 2004, Pages 978–988.

[6] Z. Chen, Y. Hu, and F. Blaabjerg ''Stability improvement of induction generator-based wind turbine systems'' IET Renewable Power Generation 2007, Pages 81-93.

[7] G. Sihem, et al. "MPPT control in wind energy conversion systems and the application of fractional control (PIα) in pitch wind turbine." *International Journal of Modelling, Identification and Control* volume 26,2, 2016, pages 140-151.

[8] S.A. Deraz, F.E. Abdel Kader, A new control strategy for a stand-alone self-excited induction generator driven by a variable speed wind turbine. Renewable Energy, Volume 51, 2013, Pages 263-273.

[9] E. J. Novaes Menezes, A. MaurícioAraújo, N. Bouchonneau da Silva ''A review on wind turbine control and its associated methods'' Journal of Cleaner Production, Volume 174, 10 February 2018, Pages 945-953.

[10] S. S. Martin , A. Chebak , A. E. Ouafi, M. Mabrouki''Modeling and simulation of hybrid power system integrating wind, solar, biodiesel energies and storage battery''International Renewable and Sustainable Energy Conference (IRSEC), 2016, Pages 457-463.

[11] T. M. Masaud, O. Oyebanjo, P.K. Sen ''Sizing of large-scale battery storage for off-grid wind power plant considering a flexible wind supply–demand balance'' IET Renewable Power Generation, Volume 11, Issue 13, 2017, Pages 1625-1632.

[12] K.Idjdarene ''*Contribution à l'étude et la commande de génératrices asynchrones à cage dédiées à des centrales électriques éoliennes autonomes*. 2010. Thèse de doctorat. Lille 1.

Organic Solar Cells Structures and Performance

Ourida Ourahmoun
Electronic Departement, LATAGE Laboratory, Faculty of electrical engineering and computing, University of Mouloud Mammeri of Tizi-Ouzou.
Tizi-Ouzou, Algeria
ourahmounourida@yahoo.fr

***Abstract*— Polymer solar cells have attracted much attention during the last years due to their lower fabrication cost and possibility of using flexible substrates. Various parameters contribute to the stability of the performances of organic solar cells: the configuration or the structure of the cells, the materials used in their elaboration such as the active layer and the electrode contact. In this work we discuss the different structures of organic solar cells and the role of the interface layer used as hole transport layer or electron transport layer. Then the important processes which might limit the power conversion efficiency of organic photovoltaic devices are discussed. The fabrication method of organic solar cells is presented. Organic solar cells are sensitive to moisture, oxygen, and light. A solution to improve performance and protect cells from degradation is proposed.**

I. INTRODUCTION

Polymer solar cells have attracted much attention during the last years due to their lower fabrication cost and possibility of using flexible substrates [1]. However, their efficiency is usually less than 5%. The active layer morphology related to blending preparation and annealing [2], is one of the most important factors affecting solar cell efficiency. Organic solar cells undergo many degradation pathways during their lifetime [3]. Efficiency loss is due to light, oxygen and water. The exposure to oxygen leads to enhanced charge carrier concentration and a decreased charge carrier mobility. A lower mobility leads to a higher extraction time for the charge carriers and therefore to an enhanced bimolecular recombination probability which results in decreased FF. The open circuit voltage is slightly increased because the Langving recombination rate is lower when the mobility decreased. The higher charge carrier densities reduce the internal field and therefore increase the open circuit voltage. Thermal annealing improves cell efficiency [4].

Various parameters contribute to the stability of the performances of organic solar cells. The configuration or the structure of the cells, the materials used in their elaboration such as the active layer the electrode contact and the interfacial materials [5]. The current density depends in temperature, the mobility of carrier charges, and substrate type. Thermal annealing reduces interface defect, and increases crystallinity which improves the mobility of carriers then improves photocurrent. Several factors contribute to increase the series resistances when the device is left in ambient conditions such as reduction of mobility, metal corrosion at the contact or changes in the contact barrier and charge space regions.

Generally, there are six main important processes which might limit the power conversion efficiency of organic photovoltaic devices: light absorption in the film, free charge carrier generation, charge transport to the opposite electrodes and extraction by the electrodes, carrier recombination, architecture dimension, design of the device, and annealing temperature of the active layer or the final device.

In this work, the different structures and configurations of organic solar cells are presented.

II. DIFFERENT STRCTURES OF ORGANIC PHOTOVOLTAIC CELLS

A. Single layer structure

Figure 1 shows a simplified diagram of single layer cell. This type of cell has been described as Shottky because a

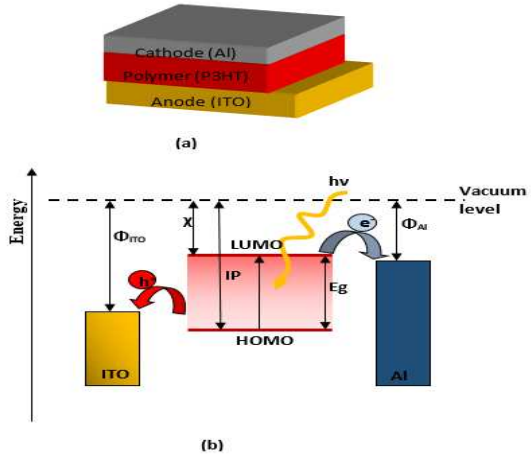

Figure.1. (a): Structure of a single-layer organic cell, (b): energy band diagram. φ : work function of electrodes, χ : electronic affinity, IP : ionization potential, Eg : optical gap of the organic material.

layer of organic material is sandwiched between two asymmetric electrodes. One with ohmic contact and the other with a rectifier contact. In general, Schottky cells are in the form of ITO/organic semiconductor/metal. The dissociation of the photogenerated carriers takes place at the interface of the semiconductor and the metal electrode. A transparent electrode (ITO, SnO_2, ZnO…) is deposited on a transparent substrate such as glass or plastic. For the cathode, a metal such as aluminum is deposited on the active layer. The single layer ITO/polymer/Al structure is shown in figure 1-a, the energy band diagram is shown in figure 1-b.

The open circuit voltage is given by the difference between the output work function of the electrodes:

$$V_{co} = \Phi_{anode} - \Phi_{cathode} \quad (1)$$

B. Planar heterojunction (two-layer structure)

The structure of the cell is shown in figure 2.a, is very similar to that of the conventional inorganic cell (homo-junction p-n). The electric field, which prevails in the active zone at the interface donor/acceptor (D-A), leads to an effective dissociation of the photogenerated electron-hole pairs. Figure 1.b represents the energy band diagram of a two-layer structure of the ITO/donor/acceptor/Al type, ITO is the cathode and Al is the anode of the planar heterojunction.

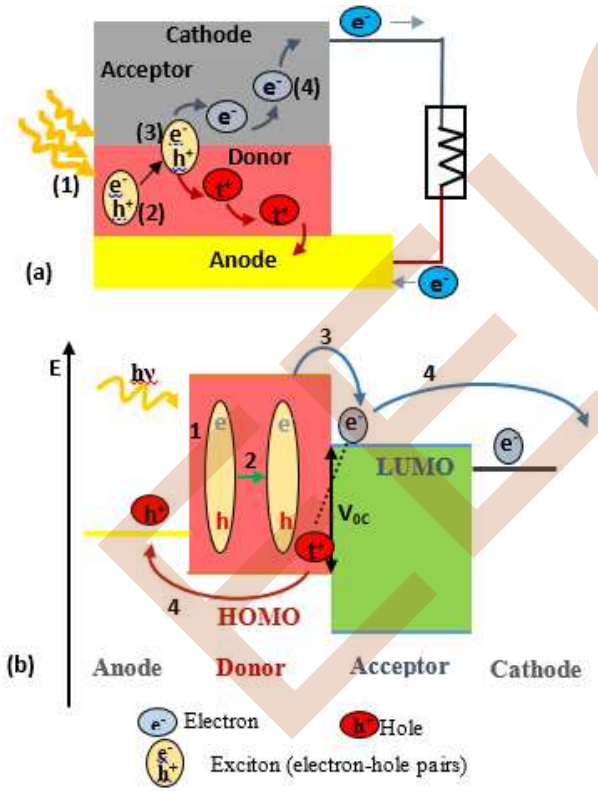

Figure. 2. (a) Structure of a two-layer photovoltaic cell, (b) its energy band diagram with the different conversion steps: (1) absorption of a photon followed by the formation of an excitons, (2) diffusion of the excitons, (3) collection of charges by the electrodes.

C. Bulk heterojunction (BHJ) solar cells

The active zone in two-layer organic cells is limited to a diffusion length around the D-A interface (around 10 nm). Only excitons created at a distance less than or equal to this length can reach the interface to dissociate, which limits the generation of free charges, and thus limits the efficiency of the cells. the idea of a bulk heterojunction is to mix the two donor and acceptor materials to form interpenetrated network as shown in figure 3. Each D-A interface in the volume of the active layer is within a distance of the

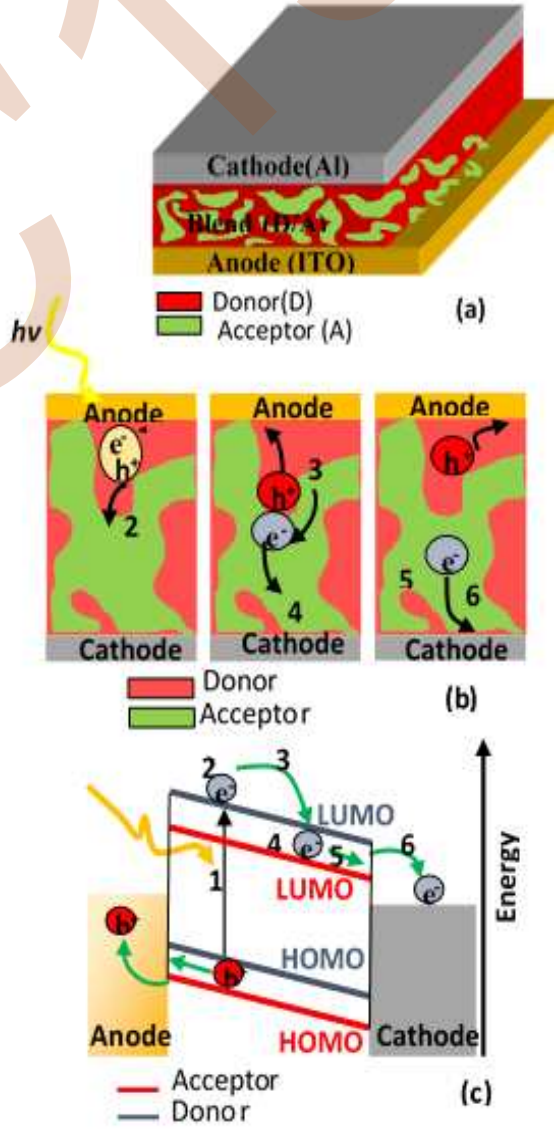

Figure.3. (a) Structure of BHJ solar cell, (b) charge photogeneration mechanisms in a D/A interface in a BHJ cell, (c) energy band diagram of the structure.

excitons diffusion length. In addition, the donor and the acceptor must form a continuous network to allow the separated charges to have a percolation path to the electrodes. The notion of electron-hole pair separation at the D-A interface is similar to that of planar heterojunctions, but the active zone where separation occurs is greatly increased, making this heterojunction more effective in terms of dissociation of excitons, generation of free charges, and thus cell efficiency. The yields of cells based on polymer:fullerene blends has increased steadily. The use of P3HT polymer donor has allowed a great advance in the performance of P3HT:PCBM based cells. performance depends essentially on the morphology of the composite layer, which should ideally have accepting donor domains of the order of the excitons diffusion length (about 10 nm), with the existence of percolation paths between each domain of the same nature to allow charges to be transported to the electrodes. Therefore, the experimental conditions, solvent nature, Polymer:PCBM ratio, annealing step are important details. Parameters such as the speed of spin spreading and the time between each step of the manufacturing protocol also contribute to changing the nature of the morphology of the mixture. This make it difficult to obtain fully reproducible results.

D. Conventional and inverted structure

The inverted structure of photovoltaic cell can be manufactured either on glass or on flexible substrates coated with transparent semiconductors (TCO). The inverted term is used to refer to the direction of the opposite displacement of charges with respect to the direct structure. The inverted structure offers several advantages over the standard structure. It shows a better stability of the device in relation to atmospheric conditions by the use of cathodes with low work function. The inverted structure created good ohmic contacts with the active layer, which improve cell performance. ITO is used as an anode an anode in the conventional structure and as a cathode in the inverted structure. Figure 4 shows the structure of an organic solar cells as function of polarity.

- *Interfacial materials*

The interfacial layers were integrated into the organic devices to select the charges extracted from the active layer and to collect them at the electrodes according to their polarity. These interface layers are called electron transport layer (ETL) if they were at the interface of the cathode and hole transport layers (HTL) if they were at the interface with the anode. The interface materials in organic solar cells allow electrons and holes to be transported to the electrodes. The creation of an electron-hole pair occurs from a photon absorbed by the active layer. At the donor/acceptor interface of the active layer, the electron-hole pair dissociates to form two distinct charges? The electron is transported to the cathode and the hole is transported to the anode via the donor material.

The interface that is formed between the active layer and the electrodes is essential to obtain high performance and stable devices. The main function of the interface materials are as follows:

- Adjust the energy barrier between the active layer and the electrodes;
- Determine the polarity of the photovoltaic device;
- Limit physico-chemical reactions between the active layer and the electrodes;
- Transport the electrons and holes to the respective electrodes;
- Act as an optical spacer.

There are many types of interface materials such inorganic metal oxides, metal salts and small molecules. The metal oxides used as an electron transport layer in solar cells must be stable in air but especially as transparent as possible because they are on the side of the transparent electrode in the inverted configuration of the devices. The main oxides used are ZnO, TiOx, SnO_2 and Nb_2O_5. The production of nanoparticles of dispersed oxides in a solvent makes It possible to manufacture devices with low annealing temperatures not exceeding 120°C. Doping of the interfacial layers increases conductivity and therefore increases cell performance.

PEDOT:PSS or poly(3,4-ethylene dioxythiophene) polystyrene sulfonate is the most commonly used polymer in organic solar cells. the doping of the PEDOT by the PSS improves conductivity and solubility in protics solvent. Generally used in standard structure due to high work function and good alignment of the HOMO band of the donor polymer P3HT, PEDOT:PSS educes the roughness of the ITO electrode and modifies the work function of the ITO

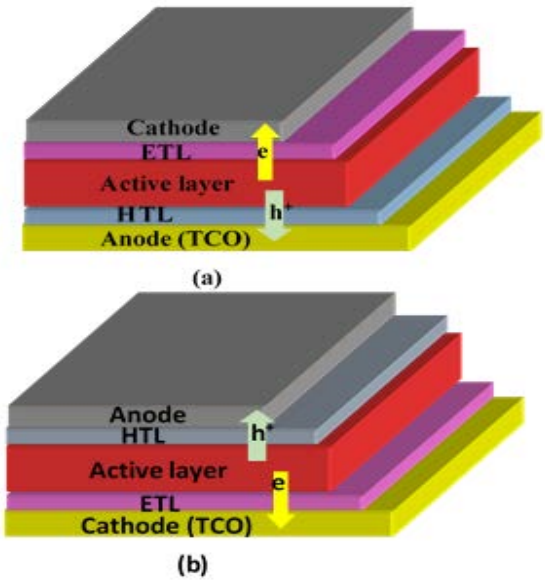

Figure. 4. Structure of an organic photovoltaic solar cells. (a) conventional, (b) inverted.

electrode, providing an ohmic contact between the active layer and the ITO. In the standard configuration, the acidic and hydrophobic nature of the PSS greatly degrades the surface of the electrode modifying the ITO/PEDOT:PSS interface and the contamination of the PEDOT:PSS by indium reduces the lifetime of the organic cell. In order to increase the performance of the devices, studies have been carried out on the plasmonic effect. The introduction of metallic nanoparticles such silver or gold into the hole transport layer increase photon absorption by the active layer. The etching of ITO by the PEDOT/PSS results in the diffusion of indium to the active layer which limits the use of this polymer in standard structure. Another approach is to invert the interface layers, where the hole transport layer acts as the electron layer and vice versa. With this new configuration the upper electrode is a non-corrosive metal with a high work function that increases the stability of the cells. the main materials used to transport holes based on metal oxides are WO_3, MoO_3, V_2O_5, and nickel oxide NiO. WO_3 plays an important role because it is considered less toxic than MoO_3.

E. Tandem structure

Improvement can still be made by stacking the cells on top of each other. The objective is to absorb most of the solar spectrum while limiting losses by thermalization. From an electrical point of view, the overall current of the tandem cell will be determined by the sub cell delivering the lowest photocurrent. The serial connection of two sub cells requires an interfaciales zone (interconnection) of electron-hole recombination to ensure the continuity the electrical circuit, the simple way being to deposit a thin metal layer at the interface of the two sub cells such as AgNWs (silver nanowires) [6]. Table one shows comparison of the performance of single-layer photovoltaic cells with tandem cells formed by interconnections between two single cells. the PCE of tandem cells is up to 9%.

TABLE I. TABLE COMPARISON OF THE PERFORMANCE OF SINGLE-CELL PHOTOVOLTAIC AND CELLS FORMED BY INTERCONECTIONS BETWEEN TWO SINGLE CELLS (TANDEM) [6].

	Type of cells	V_{OC} (V)	J_{SC} m(A)	PCE (%)
Only one cell	ITO/ZnO/P3HT:ICBA/MoO_3/Ag	0.80	11.5	5.5
	AgNWs/ZnO/P3HT:ICBA/MoO3/Ag	0.77	11.4	4.8
	ITO/ZnO/PTB7:PC_{71}BM/MoO3/Ag	0.70	17	6.9
	AgNWs/ZnO/PTB7:PC_{71}BM/MoO3/Ag	0.71	16.8	6.8
Tandem	ITO/ZnO/P3HT:ICBA/AgNWs/ZnO/ PTB7:PC_{71}BM/MoO3/Ag	1.48	11.01	9.90
	AgNWs/ZnO/P3HT:ICBA/ AgNWs/ZnO/PTB7:PC_{71}BM/MoO3/Ag	1.47	11.23	9.24

III. FABRICATION OF INVERTED BULK HETEROJUNCTION SOLAR CELLS

The inverted BHJ solar cell is based on a blend of Poly(3-hexylthiophene-2,5-diyl) (P3HT) and [6,6]-Phenyl C61 butyric acid methyl ester (PCBM). The glass substrate covered by transparent electrode of indium tin oxide (ITO) with sheet resistance of 7Ω/square was ultrasonically cleaned in acetone, ethanol and isopropanol for 10 min respectively, then treated by UV ozone for 10 min afterwards, nanoparticles of zinc oxide (ZnO~40 nm thick) was spin coated on the substrate in order to form an electron transport layer. Having been dried at 130 °C for 15 min a film (~200 nm thick) of the blend of P3HT:PCBM with a weight ratio of (1:0.8) in 1–2 dichlorobenzene was further spin coated on ZnO. This active layer was covered with Poly(3,4-ethylenedioxythiophene)- poly(styrene sulfonate) PEDOT (F010) (~40 nm thick), this layer is used as a hole transport layer. Finally, an Ag electrode was evaporated at 10^{-6} mbar (100 nm thick) through a shadow mask delimiting a 0.18 cm^2 solar cell area. The cells are annealed at 110 °C for 30 min in the glove box. The J(V) characteristics of the cells are measured in the glove box. A power conversion efficiency (PCE) of 3.08%, open circuit voltage (V_{OC}) of 0.56V, short current density (J_{SC}) of 10.59 mA/cm² and fill factor (FF) of 50% are achieved

IV. RECENT PROGRESS IN ORGANIC SOLAR CELLS

The efficiency of inverted organic solar cells is improved by employing luminescence down-shifting layers based on tetrazine (NITZ) mixed in a matrix of polymer (polystyrene or PMMA) [7]. This verified by IPCE characterization showing enhanced performance at UV wavelengths. NITZ layers can be easily integrated on top of an encapsulating material like a UV blocking layer to improve performances and to avoid degradation of the photovoltaic cell.

The doping of metal oxides is an expedient technique for controlling the electronic band gap configurations of the electron buffer layer (EBL) in inverted organic solar cells for better performance [8]. The doping enhanced the interfacial electrical properties in terms of conductivity and carrier density. Higher yield of 7% is achieved for solar cells using PTB7 as donor and ICBA as acceptor. Utilizing quaternary strategy for simultaneous optimization of donor and acceptor phases is a feasible way to realize high efficient organic solar cells [9]. Cathode interface layer (CIL) enhances the solar cells device performance. The devices with dual CIL showed the higher electron mobility which matches with the higher fill factor and improved current density. The dual CIL exhibited excellent impact on enhancing the photovoltaic properties of OSCs and PSCs along with long-term stability [10]. The highest power conversion efficiency (PCE) of 8.11% was achieved in ternary solar cells with 30 wt% N2200-F content, mainly due to the improved short-circuit current density (J_{sc}) and fill factor (FF). Further studies showed that the improved J_{sc} could attribute to the complementary absorption of the two acceptors and the enhanced FF was originated from the higher hole mobility and the fine-tuned morphology in the ternary system. The combination of fullerene and non-fullerene acceptors in ternary organic solar cells is a promising approach to achieve high-

performance organic solar cells [11]. Non-fullerene (NF) acceptors with superior optoelectronic properties, tunable morphology, and absorption characteristics have demonstrated higher PCE of over 14% in single junction and over 17% in tandem OSCs incorporating NF OSCs which is relatively higher than conventional fullerene-based counterparts [12].

To protect cells from degradation an encapsulation is required. The choice of encapsulating materials is also an important factor in improving the performance of the cells. the use of down conversion principle limits the degradation and the ageing of cells because unconverted light heats the cell, causing the degradation of the photovoltaic device.

The use of transparent plastic substrates such as PET and PEN instead of rigid substrates made of glass/ITO for the production of flexible cells in which all materials are organic.

V. CONCLUSION

There are two different architectures for organic solar cells: standard and inverted. They differ according to the role of the lower electrode as a cathode or an anode. In the standard structure the holes go towards the ITO electrode while in the reverse structure the holes go towards the ITO electrode.

Interface materials are located between the active layer and the electrodes. The advantages of these layers is the alignment of energy levels between the active layer, the electrodes and these interface materials in order to facilitate transport of charges to the electrodes and to minimize recombination.

The fabrication method of organic solar cells is presented. Organic solar cells of the structure ITO/ZnO(Np)/P3HT:PCBM/PEDOT(F010) are realized. The achieved power conversion efficiency is 3.08%.

Organic solar cells using indium free electrodes presents a higher efficiency than when an ITO electrode is used. Alternative materials are proposed such as AgNWs and multilayer electrodes such as ZnO/Ag/ZnO. These electrodes are easy to fabricate using spin coating device.

Organic solar cells are sensitive to moisture, oxygen, and light. To improve performance and protect cells from ageing and degradation, an encapsulation of the cells is required. The addition of a fluorescent layer on the front of the cell should improve performance by converting part of the light spectrum into energy absorbed by the active layer. The fluorescence materials used in matrix of polymer can be used as encapsulation of the cells.

REFERENCES

[1] V.S. Balderrama, M. Estrada, A. Cerdeira, B.S. Soto-Cruz, L.F. Marsal, J. Pallares, J. Albero, "Influence of P3HT: PCBM blend preparation on the active layer morphology and cell degradation". *Microelectronics Reliability*, *51*(3), 597-601, 2011.

[2] D. Spoltore, T. Vangerven, P. Verstappen, F. Piersimoni, S. Bertho, K. Vandewal, J. Parisi, "Effect of molecular weight on morphology and photovoltaic properties in P3HT: PCBM solar cells". *Organic Electronics*, *21*, 160-170, 2015.

[3] H. K. H. Lee, A.M. Telford, J.A. Röhr, M.F. Wyatt, B. Rice, J. Wu, J.R. Searle, "The role of fullerenes in the environmental stability of polymer: fullerene solar cells". *Energy & Environmental Science*, *11*(2), 417-428, 2018.

[4] O.K. Kwon, M.A. Uddin, J.H. Park, S.K. Park, T. L. Nguyen, H.Y. Woo, S.Y. Park, "A high efficiency nonfullerene organic solar cell with optimized crystalline organizations". *Advanced Materials*, *28*(5), 910-916, 2016.

[5] S. Banerjee, S.K. Gupta, A. Singh, A. Garg, "Buffer layers in inverted organic solar cells and their impact on the interface and device characteristics: An experimental and modeling analysis". *Organic Electronics*, *37*, 228-238, 2016.

[6] M. Raïssi, S. Vedraine, R. Garuz, T. Trigaud, B. Ratier, " Solution processed cathode and interconnecting layer of silver nanowires in an efficient inverted tandem organic solar cells". *Solar Energy Materials and Solar Cells*, *160*, 494-502, 2017.

[7] O. Ourahmoun, T. Trigaud, B. Ratier, M.S. Belkaid, L. Galmiche, P. Audebert, "An efficient tetrazine photoluminescent layer used for organic solar cells down shifting". *Synthetic Metals*, *234*, 106-110, 2017.

[8] G. Kim, J. Kong, J. Kim, H. Kang, H. Back, H. Kim, K. Lee, "Overcoming the light-soaking problem in inverted polymer solar cells by introducing a heavily doped titanium sub-oxide functional layer". *Advanced Energy Materials*, *5*(3), 1401298, 2015.

[9] Z. Bi, H.B. Naveed, X. Sui, Q. Zhu, X. Xu, L. Gou, X. Liu, "Individual nanostructure optimization in donor and acceptor phases to achieve efficient quaternary organic solar cells", Nano Energy, 104176, 2019.

[10] U.K. Aryal, V.M. Arivunithi, S.S. Reddy, J. Kim, Y.S. Gal, S.H. Jin, "Efficient dual cathode interfacial layer for high performance organic and perovskite solar cells", Organic Electronics, 63, 222-230, 2018.

[11] F. Liu, C. Li, J. Li, C. Wang, C. Xiao, Y. Wu, W. Li, "Ternary organic solar cells based on polymer donor, polymer acceptor and PCBM components", Chinese Chemical Letter, 2019s.

[12] L. Duan, N.K. Elumalai, Y. Zhang, A. Uddin, "Progress in non-fullerene acceptor based organic solar cells. Solar Energy Materials and Solar Cells", 193, 22-65, 2019.

Power management strategy based on utilisation cost of stand-alone hybrid system PV/battery/hydrogen with associated hydrogen storage

1) *Nourredine Zidane and Sofia Lalouni Belaid*
   a) *Laboratoire de Technologie Industrielle et de l'Information (LTII), Faculté de Technologie*
   b) *Université de Bejaia*
   c) *Bejaia, Algerie*
   d) *nourredinezidane@hotmail.fr;lalouni_sofia@yahoo.fr*

***Abstract*— This document proposes a new hourly power management strategy for an autonomous renewable energy system. The latter, consists of photovoltaic solar generator as the main energy source and two energy storage systems: a hydrogen subsystem and a battery. The evaluation of the energy management system was simulated in a MATLAB-Simulink environment with real conditions over a typical period of one thousand hours for the installation area located in the North of Algeria. The management method is based on the technical-economic aspect and the cost/life cycle of each component. The simulation results show that the proposed management method is able to provide the energy required by the loads, while favoring the cheapest components according to the exchanged power.**

I. INTRODUCTION

Solar energy is now widely used because it is free, abundant and non-polluting [1]. The main problem with generation facilities depends on the intermittent nature of renewable resources (e. g. sun and wind), which results in a power generation curve that generally does not match the load curve. In order to reduce the gap between the production curve and the demand curve, as well as the sudden variations in production, many solutions have been proposed such as the use of a backup generator set or a conventional battery storage system.

In stand-alone applications, solar batteries and hydrogen systems are the most common energy storage systems [2,3,4]. In references [5,6], a battery and a super capacitor were used. This configuration improves the dynamic response of the system, but reduces the energy storage capacity compared to the hydrogen system, which consists of a fuel cell (FC), electrolyzer (EZ) and hydrogen tank. The hydrogen system can stabilize the flow of energy from renewable sources if power management is adequate.

A lot of research has been done on energy management for stand-alone applications [7–11]. In [9], three energy management strategies (EMS) for a photovoltaic (PV)/wind/FC/battery hybrid system have been proposed, the main decision factors in EMS are the power supplied by renewable energy sources and the state of charge (SOC) of the batteries. In [10], three autonomous hybrid systems (PV/Battery, PV/FC, PV/FC, PV/FC/Battery) using different energy storage technologies were presented, the energy management strategy is based on the energy balance throughout the year and a link between maximum efficiency and minimum system cost was implemented. An energy management method for a PV/FC/battery hybrid system based on the cost of the battery and FC has been developed by [11], the strategy is to reduce the number of starts of the FC and battery by introducing measurement and timing elements into the conventional strategy. These strategies are based either on the technical or the economic aspect.

In this work, the PV source is connected to a storage subsystem composed of a fuel cell, electrolyzer, hydrogen tank and batteries. A control strategy based on operating modes and combining technical and economic aspects while respecting the cost/life function of the components is proposed in order to optimize the profitability and energy efficiency of the system.

The structure of the paper is as follows: after an introduction, section 2 briefly describes the mathematical models used for each subsystem. Section 3 presents the proposed management approach for the hybrid system and a flowchart provides details on implementation. Section 4 presents the simulated results and evaluate performances of the proposed power management strategy (PMS) against some criteria.

II. SYSTEM DESCRIPTION AND MODELING

The studied hybrid system is depicted in Fig. 1, it contains the PV generator, batteries, PEM fuel cell, water electrolyzer, a hydrogen tank, and the power electronic converters interconnected to a DC bus to supply the AC load.

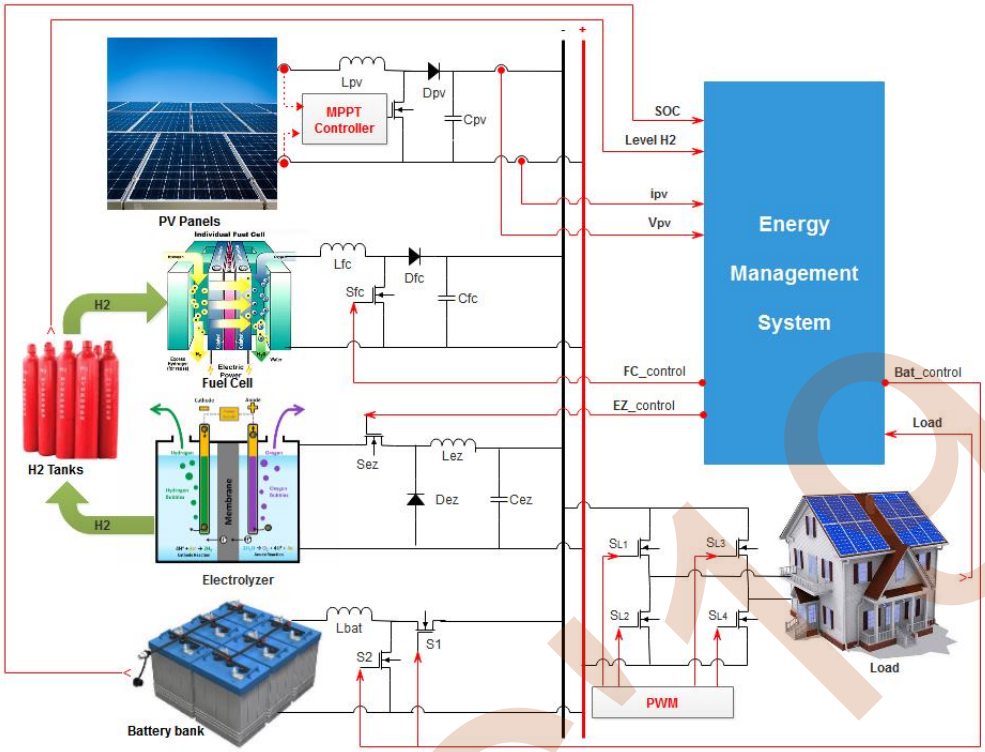

Figure 1. Configuration of the hybrid system under stud.

A. PV Model

Insolation data are converted into power output from the PV array using the following equation [12]:

$$P_{PV}(t) = E(t).A.\eta_{PV} \quad (1)$$

Where E(t) is the insolation data at time t (kW/m²), A is the area of a PV panel (m²), and η_{pv} is the overall efficiency of the PV panels and the DC/DC converter.

The v-i characteristic of a solar cell is highly nonlinear and is given in [13].

B. Fuel Cell Model

Various fuel cell types are available today and a great effort is concentrated in their modelling concerning equivalent electrical operation [12]. A brief presentation of the proton exchange membrane fuel cell (PEMFC) modelling is made in this section.

The output voltage V_{FC} of a single cell can be defined in Eq. (2)

$$V_{FC} = E_{Nernst} - V_{act} - V_{ohm} - V_{con} \quad (2)$$

Where E_{Nernst} is the thermodynamic potential of the cell and it represents its reversible voltage; V_{act} is the voltage drop due to the activation of the anode and of the cathode; V_{ohm} is the ohmic voltage drop and V_{con} represents the voltage drop resulting from the concentration or mass transportation of the reacting gases [15, 16].

C. Electrolyzer Model

In this work, the hydrogen production rate of the electrolyzer is calculated from Faraday's law. According to this law, the hydrogen production rate of the electrolyzer cells is directly proportional to the electrical current in the equivalent electrolyzer circuit [17]. The hydrogen produced in the electrolyzer, n_{H2}(mol/s) is given in Eq. (3) [17].

$$n_{H_2} = \frac{n_F.n_c.i_e}{2.F} \quad (3)$$

Where n_c is the number of cells in series; i_e (A) is the electrolyzer current (C/mol), F is the Faraday constant; and n_f is the Faraday efficiency. Faraday efficiency is the ratio between the actual and the theoretical maximum amount of hydrogen produced in the electrolyzer, which can be expressed by Eq. (4).

$$n_F = 96,5.\exp\left(\frac{0,09}{i_e} - \frac{75,5}{i_e^2}\right) \quad (4)$$

D. Hydrogen tank model

Hydrogen energy produced by the electrolyzer provides another option for storing solar energy in excess of demand. Equation (5) and Eq. (6) give the method of transforming the capacity unit mol of hydrogen tanks to the unit kWh and liter. The mole mass of hydrogen gas is 2 (g/mol) [18].

$$E_{\tan k} = \frac{M_{\tan k}.2.LHV}{1000} \quad (5)$$

$$V_{\tan k} = \frac{M_{\tan k}.T_{\tan k}.R}{P_{\tan k}} \quad (6)$$

Where E_{tank} (M_{tank}, V_{tank}) is the size of hydrogen tanks in units of kWh (mol, liter), T_{tank} is the temperature of the hydrogen tanks (°K), P_{tank} is the pressure of the hydrogen tanks (atm), R is the gas constant (0.08211 atm/mol/K) and LHV (-33 kWh/kg) is the low heat value of the hydrogen.

E. Battery Model

In this work, the battery is used as an auxiliary generator to improve the flexibility, speed and life time of the PEM FC. The model of the battery can be expressed in Eq. (7), [19].

$$E_b = \int \left(P_{b.dish\arg} - P_{b.ch\arg}.\eta_b \right).dt \quad (7)$$

Where $P_{bdischarging}$ represents battery power when it is discharging, $P_{bcharging}$ represents battery power when it is charging and η_b is the battery efficiency.

The battery SOC can be written as follows: Eq. (8) [19,20].

$$SOC(\%) = 100\left(1 - \frac{\int i_{bat}.dt}{Q}\right) \quad (8)$$

Where Q (Ah) is the maximum battery capacity, and i_{bat} is the battery current.

F. Optimal sizing system

In our case, we used the loss of power supply probability (LPSP), this sizing method has been studied in [21].

This method determines the optimal number of hydrogen storage tanks and PV module status based on two optimization criteria namely: reliability, which is based on the concept of the loss of power supply probability and the cost of the system [21, 22, 23].

III. POWER MANAGEMENT STRATEGY

This strategy, presents a control scheme based on technical-economic operating modes, as shown in Fig. 2. It determines the appropriate operation mode, taking into account the excess of renewable power P, battery SOC, hydrogen tank level, and the costs of cycling the energy of battery, FC and electrolyzer. This strategy is described as follows using four operating modes:

A. Mode I

The power generated by the PV system (P_{PV}) is given priority to satisfy the power demand (P_{Load}) compared to the one provided by the fuel cell or battery bank.

The total power generated by the PV system is greater than the load ($P_{PV} > P_{Load}$ or $P > 0$), the surplus power will be compared to the charge power limits (P_{ch}^{lim}), $P > P_{ch}^{lim}$, two cases may occur:

If then level of hydrogen storage tank (L,H2) is greater or equal to level max of hydrogen storage ($L,H2_{max}$ = 100%), the power surplus will be stored in battery bank taking into account the instantaneous maximum power of the battery ($P^{ch}_{Bat,,max}$) and its soc.

If $L,H2 < L,H2_{max}$ the power surplus will be stored in favour of hydrogen storage taking into account the instantaneous maximum power of the electrolyser (P^{EZ}_{max}) and L,H2. If $P > P^{EZ}_{max}$ and $SOC < SOC_{max}$ (SOC_{max} = 100%) the power surplus will be stored in battery bank. If $P < P^{EZ}_{min}$ the battery will discharge to recover the power surplus that is the minimale power electrolyzer (P^{EZ}_{min}). In this case:

$P_{EZ} - P^{EZ}_{min}$, $P - P^{EZ}_{min}$.

B. Mode II

If $P_{PV} > P_{Load}$ or $P > 0$, the surplus power will be compared to the charge power limits, and this power generated by the system is lower than the charge power limits ($P < P_{ch}^{lim}$), two cases may occur:

If $soc < soc_{max}$, the power surplus will be stored in battery bank taking into account the instantaneous maximum power of the battery ($P^{ch}_{Bat,max}$) and the soc of the battery bank, If $P^{ch}_{Bat,max} > P$ and $L,H2 < L,H2_{max}$, the power surplus will be stored in battery bank taking and hydrogen storage tank.

If $SOC \geq SOC_{max}$, the power surplus will be stored in favour hydrogen storage taking into account P^{EZ}_{max}, P^{EZ}_{min} and L,H2. If $P < P^{EZ}_{min}$ the battery will discharge to recover the power surplus that is lower power electrolyzer min (P^{EZ}_{min}). In this case: $P_{EZ} - P^{EZ}_{min}$, $P_{bat} - P - P^{EZ}_{min}$.

C. Mode III

The total power generated by the PV system is lower than the load ($P < 0$), the necessary power to satisfy the load is provided by the lead-acid accumulator or the fuel cell.

Total power generated by the system is lower than the discharge power limits (P^{lim}_{dis}), the deficit will be filled by favouring the batteries, taking into account their SOC. If $SOC \leq SOC_{max}$ (SOC_{min} = 40%), the necessary power to satisfy the load is provided by the fuel cell taking into account L,H2.

D. Mode IV

Total power generated $P > P^{lim}_{dis}$, the deficit will be filled by favouring the fuel cell, taking into account L,H2. If $L,H2 < L,H2_{min}$ ($L,H2_{min}$ = 2%), the necessary power to satisfy the load is provided by the battery bank until $soc \leq soc_{min}$.

IV. UTILIZATION COST OPTIMIZATION CONTROL

The cost of delivering or absorbing a certain quantity of energy through the RES can be optimized by using the charge and discharge power limits. The charge power limit is

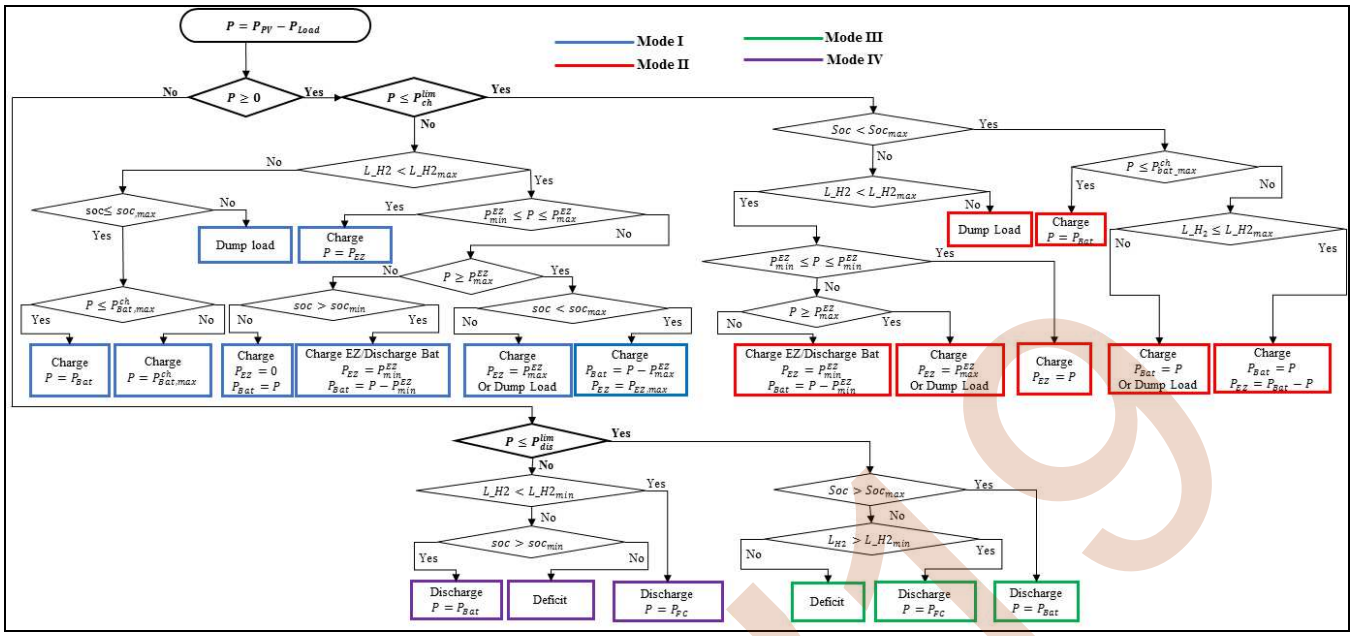

Figure 2. Proposed power management system algorithm.

defined as the power from which is cheaper to use the electrolyzer than the battery to store the available net power. Analogously, the discharge power limit represents the power from which is cheaper to use the FC than the battery to deliver the required power. Otherwise, as previously mentioned, the battery utilization cost depends on the power, whereas the utilization costs of the FC and electrolyzer are always independent from the power.

The charge and discharge power limits are calculated in Eq. (9,10) [22]:

$$P_{ch}^{\lim} = \frac{C_{EZ}^{h}.E_{bat}^{year}.SPWF}{NPC_{bat}}; P_{ch}^{\lim} \geq P_{EZ,\min} \quad (9)$$

$$P_{dis}^{\lim} = \frac{C_{FC}^{h}.E_{bat}^{year}.SPWF}{NPC_{bat}} \quad (10)$$

Where: E_{bat}^{year} is the total energy that the battery can deliver in a year, NPC_{bat} is the net present cost of the battery, SPWF is the series present worth factor, C^{h}_{EZ} and C^{h}_{FC} are the electrolyzer and fuel cell utilization cost respectively [21] expressed in Eq. (11) and Eq. (12).

$$C_{EZ}^{h} = \frac{\left(NPC_{EZ} + NCP_{EZ}^{OM}\right)/SPWF}{N_{EZ,hour}^{year}} \quad (11)$$

$$C_{FC}^{h} = \frac{\left(NPC_{FC} + NCP_{FC}^{OM}\right)/SPWF}{N_{FC,hour}^{year}} \quad (12)$$

Where: NPC_{EZ} is the net present cost of the electrolyzer, NPC_{EZ}^{OM} and NPC_{FC}^{OM} are the net present cost of operation and maintenance of the electrolyzer and fuel cell respectively, $N^{year}_{EZ,hour}$ and $N^{year}_{FC,hour}$ are the number of working hours of the electrolyzer and fuel cell respectively during a year.

V. SIMULATION RESULTS

The EMS based on utilization cost proposed for the stand-alone hybrid system was tested for the load profile presented in Fig. 3 and using real weather data (solar irradiance), as shown in Fig. 4.

Table I. presents the component characteristics of the stand-alone power system.

TABLE I. COMPONENT CHARACTERISTICS

	PV system	Battery Bank	PEM fuel cell	PEM electrolyzer	H2 Storage tank
Power	17 kW_P	11.7kWh	3 kW_P	3 kW_P	5.4 kW
Efficiency	14.5%	85%	50%	76%	99.98%
Cost	13175 §	700 §	11570 §	7895 §	3780 §

The evolution of powers during the simulation are presented in Fig. 5 and Fig. 6. Figure 7 and Fig. 8 show the hydrogen level in the tank and the battery SOC respectively, during the performed simulation. In the majority of cases, it is found that the hydrogen level and battery SOC exceeds 40%.

Figure. 9, show the hydrogen inventory in the system, during the simulated time period for the PMS. Figure 10 show the hydrogen energy storage, battery bank and hybrid system effeciency.

The results demonstrated that the designed hybrid system assures reliable electricity supply for the stand-alone

application under study in this work. However, although the configuration under study in this work is technically feasible, it is not the best option from the economic point of view. Further research in hydrogen technology is still needed to develop low-cost and highly efficiency hydrogen devices, which make this technology more competitive.

Figure 11. presents the main components cost of the hybrid system during lifetime cycle.

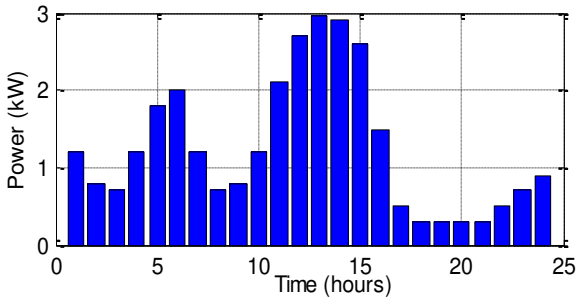

Figure 3. Profile of consumption.

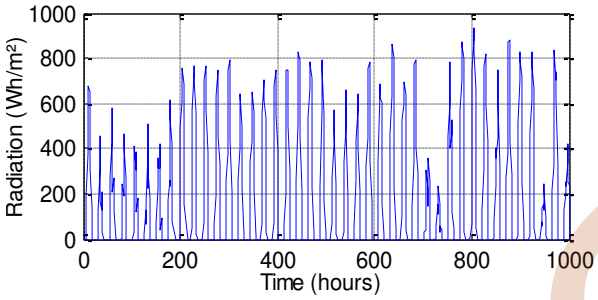

Figure 4. Solar irradiance.

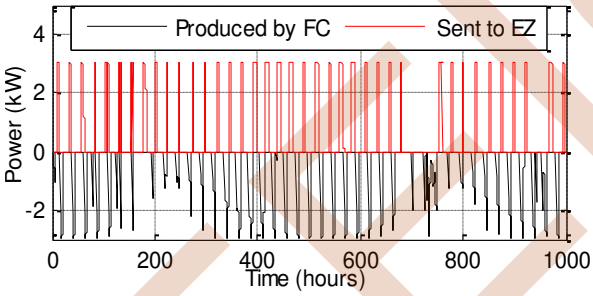

Figure 5. Power sent to electrolyzer and produced by fuel cell.

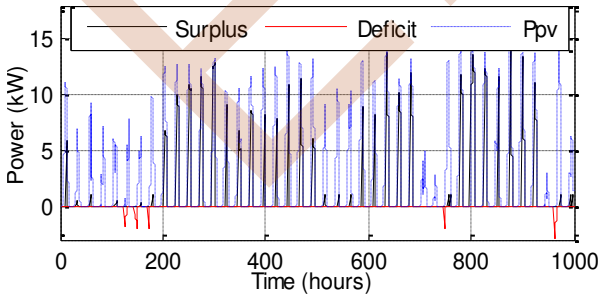

Figure 6. PV produced, deficit and surplus power.

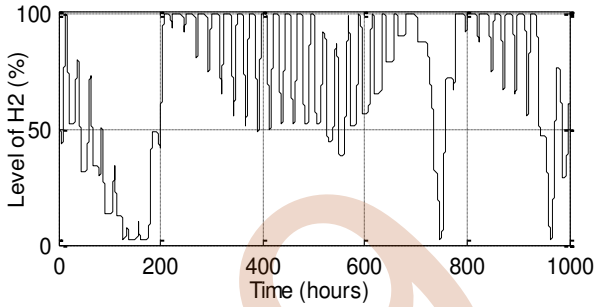

Figure 7. Hydrogen tank level (%).

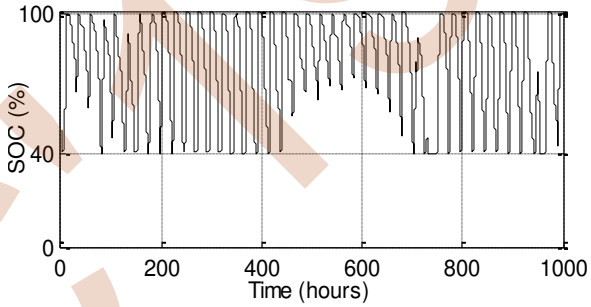

Figure 8. Battery SOC (%).

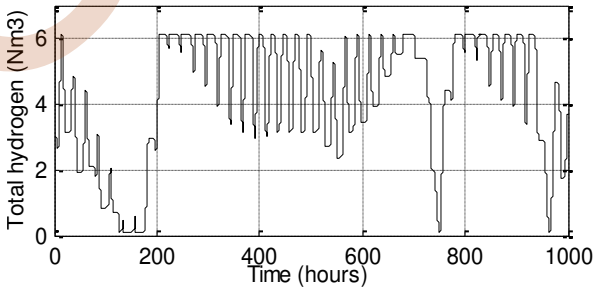

Figure 9. Hydrogen inventory.

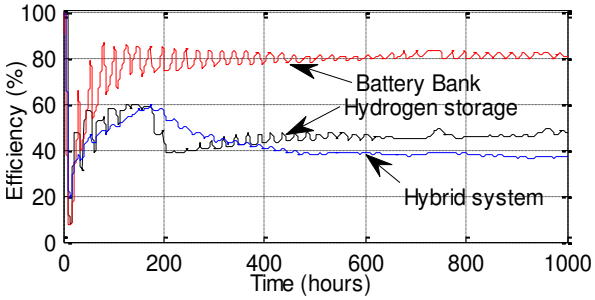

Figure 10. Hybrid system, hydrogen storage and battery bank efficiency.

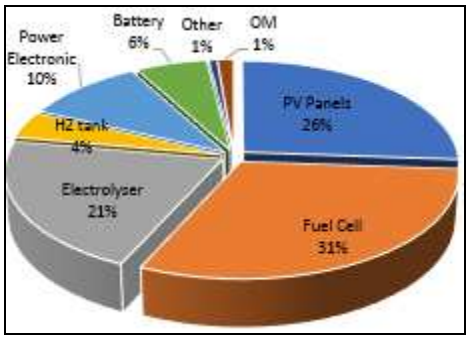

Figure 11. main components cost of the hybrid system during lifetime cycle.

VI. CONCLUSION

This paper presents and evaluated a new hourly EMS for a stand-alone renewable energy system, composed by PV panels renewable energy sources, battery bank and hydrogen system (FC, electrolyzer and tank) as energy storage system. The management strategy determines the power to be exchanged between the components of the hybrid system and uses as the main decision variable, the net power, the charge and discharge power limit, as well as the maximum and minimum levels of battery and hydrogen.

The simulation results clearly show that, for a load of 30 kWh/day, and a sunlight profile adopted at the site implantation, the demand is largely satisfied as indicated by the hydrogen level, the battery SOC and the overall efficiency of the system, which is around 40%.

REFERENCES

[1] M. J-Kwon, K. H. Nam, and B. H Kwon, "Photovoltaic power conditioning system with line connection," IEEE Trans Ind Elec, vol. 53, pp.1048–54, 2006.

[2] A. M. Thameem and S. Velusami, "Dual mode linguistic hedge fuzzy logic controller for an isolated windediesel hybrid power system with superconducting magnetic energy storage unit," Energy Convers Manag, vol. 51(1), pp. 169–81, 2010.

[3] I. Gonzalez, A. Ramiro, M. Calderon, A. J. Calderon, and L. F. Gonzalez, "Estimation of the state-of-charge of gel lead-acid batteries and application to the control of a stand-alone wind-solar test-bed with hydrogen support," Int J Hydrogen Energy, vol. 37(15); pp. 11090–103. 2012

[4] L. Chun-Hua, Z. Xin-Jian, C. Guang-Yi, S. Sheng, and H. Ming-Ruo, "Dynamic modeling and sizing optimization of stand-alone photovoltaic power systems using hybrid energy storage technology," Renew Energy, vol. 34(3), pp. 815–26, 2009.

[5] A. Etxeberria, I. Vechiu, H. Camblong, and J. Vinassa, "Comparison of three topologies and controls of a hybrid energy storage system for microgrids," Energy Convers Manag, vol. 54(1), pp. 113–21, 2012.

[6] P. Thounthong, V. Chunkag, P. Sethakul, S. Sikkabut, S. Pierfederici, and B. Davat, "Energy management of fuel cell/solar cell/supercapacitor hybrid power source," J Power Sources, vol. 196(1), pp. 313–24, 2011.

[7] K. Zhou, J. Ferreira, and S. W. H. de Haan, "Optimal energy management strategy and system sizing method for standalone photovoltaic-hydrogen systems," International Journal of Hydrogen Energy," vol. 32, pp. 477–89, 2008.

[8] R. Dufo-Lopez, J. L Bernal-Agustın, and J. Contreras, "Optimization of control strategies for stand-alone renewable energy systems with hydrogen storage," Renewable Energy, vol. 32, pp. 1102–26, 2007.

[9] D. Ipsakis, S. Voutetakis, P. Seferlis, F. Stergiopoulos, C. Elmasides, "Power management strategies for a stand-alone power system using renewable energy sources and hydrogen storage," Int J Hydrogen Energy, vol. 34(16), pp. 7081–95, 2009.

[10] L. C-H, X. J. Zhu, G. Y. Cao, S. Sui, M. R. Hu, "Dynamic modeling and sizing optimization of stand-alone photovoltaic power systems using hybrid energy storage technology," Renew Energ, vol. 32(3), pp. 815–26, 2009.

[11] K. H. Kang and D. J. Won, "Power management strategy of stand-alone hybrid system to reduce the operation mode changes," In: Transmission & Distribution Conference & Exposition: Asia and Pacific, 2009. pp. 1–4.

[12] A. Tofighi and M. Kalantar, "Power management of PV/battery hybrid power source via passivity-based control," Renewable Energy, vol. 36, pp. 2440-2450, 2011.

[13] H. Deboucha and S. Lalouni Belaid, "Improved incremental conductance maximum power point tracking algorithm using fuzzy logic controller for photovoltaic system," Rev. Roum. Sci. Techn.– Électrotechn. et Énerg, vol. 62 (4), pp. 381–387, 2017.

[14] M. H. Nehrir and C. Wang, "Modeling and control of fuel cells, distributed generation applications," John Wiley & Sons, Inc., Hoboken, New Jersey, 2009, pp. 57–83.

[15] J. M. Corrêa, F. A. Farret, J. R Gomes and M. G Simoes, "Simulation of Fuel-Cell Stacks Using a Computer-Controlled Power Rectifier with the Purposes of Actual High-Power Injection Applications," IEEE transactions on industry applications, vol. 39 (4), pp. 1136–1142, 2003.

[16] F. Z. Zerhouni, and M. Telidjane, "Branchement direct d'une pile à combustible à membrane échangeuse de protons à une charge et modelisation," Rev. Roum. Sci. Techn. – Électrotechn. et Énerg, vol. 60 (4), pp. 387–396, 2015.

[17] M. Uzunoglua, O.C. Onar, and M.S. Alam, "Modeling, control and simulation of a PV/FC/UC based hybrid power generation system for stand-alone applications," Renewable Energy, vol. 34, pp. 509–520, 2009.

[18] M.J. Khan, M.T. Iqbal, "Dynamic modeling and simulation of a small wind–fuel cell hybrid energy system," Renewable Energy, vol. 30, pp. 421–439, 2005.

[19] M. Castaneda, A. Cano, F. Jurado, H. Sanchez, and L.M. Fernandez, "Sizing optimization, dynamic modeling and energy management strategies of a stand-alone PV/hydrogen/battery-based hybrid system, International journal of hydrogen energy," vol. 38, pp. 3830-3845, 2013.

[20] J. Lagorse, D. Paire, and A. Miraoui, "Sizing optimization of a stand-alone street lighting system powered by a hybrid system using fuel cell, PV and battery," Renewable Energy, vol. 34, pp. 683–691, 2009.

[21] N. Zidane and S. Lalouni, "Optimal sizing of hybrid PV/FC/EZ/BAT system using LPSP concept," 5th International Conference on Electrical Engineering in Boumerdes, Algeria, 2017.

[22] B. Ai, H. Yang, H. Shen, and X. Liao, Computer-aided design of PV/wind hybrid system, Renewable Energy," vol. 28 (10), pp. 1491–1512, Aout 2003.

[23] B. Borowy and Z. M. Salameh, "Methodology for optimally sizing the combination of a battery bank and PV array in a wind/PV hybrid system," IEEE Transactions on Energy Conversion, vol. 11, pp. 367–373, 1996.

A new signal filtering strategy for photovoltaic controller improvement

Walid Rahmouni, Ghalem Bachir
Laboratoire de développement durable de l'énergie électrique (LDDEE)
Université des sciences et de la technologie d'Oran (USTO-Oran, Algeria
walid.rahmouni@univ-usto.dz

Michel Aillerie
Laboratoire Matériaux Optiques, Photonique et Systèmes (LMOPS)
Université de Lorraine
Metz, France

***Abstract*— One of the major challenges concerning grid integration of a photovoltaic system is the harmonics it generates. To minimize their impact on power quality, the control strategy adopted is crucial. For such system the most widely used controller is the PI controller based on the synchronous reference frame. These controllers are simple but have major drawbacks. Amongst them is the Feedforward voltage term. It makes it vulnerable to the grid disturbances which in turns lower the power quality.**

This paper proposes a simple improvement to the PI controller. By filtering the voltage signal in Feedforward, its impact is reduced and the controller performs better in terms of harmonics.

First, an overview of the systems main components is presented. Then, the validity of the proposed method is proved through simulations on Simulink-Matlab. The Fast Fourier Transformation is used for power quality assessment. A comparison to the PI controller and to the PR controller is made. The results obtained clearly show the validity of the proposed strategy.

I. INTRODUCTION

The rapid increase in energy consumption and the growing global warming phenomena cause the necessity of urgent search for alternative energy sources [1]. Among these sources, solar photovoltaic technology plays a vital role.

The Photovoltaic industry has grown more than 40% per year since last decades due to rapid decrease in PV technology cost [2].

Nowadays, the concern in photovoltaic energy focuses on interconnection with the grid. Generally, such system mainly consists of a boost DC/DC converter, a DC/AC inverter and a passive filter to attenuate current harmonics caused by switching frequency [3 4]. The DC/AC inverter can be considered as the core of the whole system because of its important role in grid connected operations [3]. However, its interaction with the grid produces power quality implications such as harmonic generation [5].

The quality of the current supplied by the inverter is significantly affected by the current controller, and therefore it is important that the controller provides a high quality sinusoidal output with minimal distortion to avoid creating harmonics [6].

In the literature, the conventional current controller is designed in the Synchronous Reference Frame (*SRF*) of the fundamental component (*dq*-frame) and uses two Proportional-Integral (PI) controllers in order to generate the reference signal [7]. Another controller that is gaining popularity is the Proportional Resonance (PR). This controller designed in stationary reference frame ($\alpha\beta$) performs better then the PI controller and have fewer drawbacks [8].

One major drawback in PI controllers is that the grid voltage is Fed-forward. This has a negative impact due to the presence of background harmonics [9].

In this paper a simple filtering technique is used to reduce the negative impact of the feed-forward term in PI controllers. The main focus concerns the harmonics injected to the grid.

The strategy proposed is compared to the classical PI controller and to the PR controller in terms of Total Current Harmonic Distortion. The simulations are carried out in Simulink Matlab to assess the effectiveness of the proposed strategy.

II. SYSTEM'S STRUCTURE

Photovoltaic is the technology that converts solar energy into electricity [10]. The system under consideration represents a two-stage topology of the grid-tied PV system. The PV array converts solar irradiation into electrical energy.

The DC-DC boost converter with a Maximum Power Point Tracker (MPPT) optimizes the PV output. A DC-link capacitor enhances the DC output voltage stability, and therefore, reduces the effect of fluctuation on the AC output [11]. A two-level three-phase inverter transfers the generated PV power from the boost converter to the main grid through a passive filter [12].

A. *Photovoltaic array*

A PV array is mainly constituted of PV cells, which converts the sunlight falling on it directly into electricity by photovoltaic effect [13]. The simplest equivalent circuit of a solar cell is a current source in parallel with a diode. The output of the current source is directly proportional to the light falling on the cell [14].

The single diode model of PV cell is shown in fig 1.

The mathematical model of the PV cell can be presented by the following equations [15 16]

$$I_{pv} = I_{PH} - I_d - I_{sh} \quad (1)$$

When supposing the parallel shunt resistor R_{sh} is not infinite, the shunt current I_{sh} can be calculated as follows:

$$I_{sh} = \frac{V_d}{R_{sh}} = \frac{V_{pv} + I_{pv} R_s}{R_{sh}} \quad (2)$$

The Shockley diode equation is:

$$I_d = I_{sat}\left[\exp\left(\frac{V_{pv} + (I_{pv} R_s)}{A U_T}\right) - 1\right] \quad (3)$$

The expression of the current supplied by the cell I_{pv} is then defined by:

$$I_{pv} = I_{PH} - I_{sat}\left[\exp\left(\frac{V_{pv} + (I_{pv} R_s)}{A U_T}\right) - 1\right] - \frac{V_{pv} + (I_{pv} R_s)}{R_{sh}} \quad (4)$$

Knowing that :
I_{sat} : Diode Current (A);
I_{ph} : The photo-generated current;
R_s: The series resistor;
R_{sh} :The shunt resistor;
U_T: The thermal potential;
A : Ideality factor;

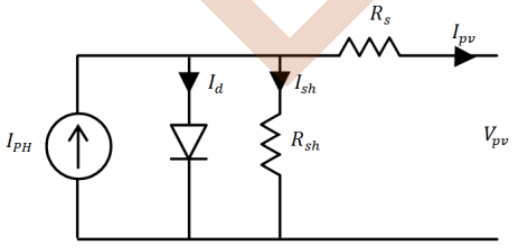

Figure 1. Equivalent model of a photovoltaic cell

B. *DC/DC – Boost converter*

The power output of the Solar PV module varies with solar irradiation and solar cell temperature [13].

To extract the maximum power from the panel, a DC-DC converter is used. It is the interface that allows adaptation between the PV panel and the load or the grid [16]. The topology of a DC-DC boost converter is shown in Fig 2.

The most commonly used MPPT technique is the Perturb and Observe algorithm (P&O), due to its ease of implementation in its basic form [14]. Its flow chart is given in Fig 3.

C. *DC/AC- Inverter*

An inverter is a power electronic device, which generates a sinusoidal AC output with controllable frequency and magnitude from a DC input. The inverter in the grid-tied PV system acts as an interface between energy sources and the utility grid [11]. In our work a voltage source inverter (VSI) is used, its general structure is shown in Fig 4.

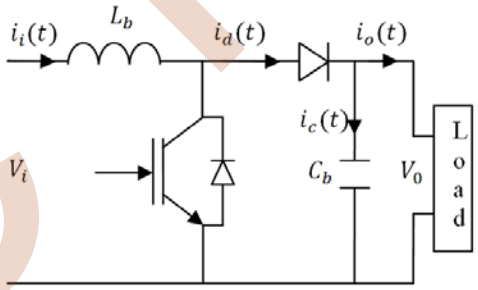

Figure 2. DC-DC boost converter

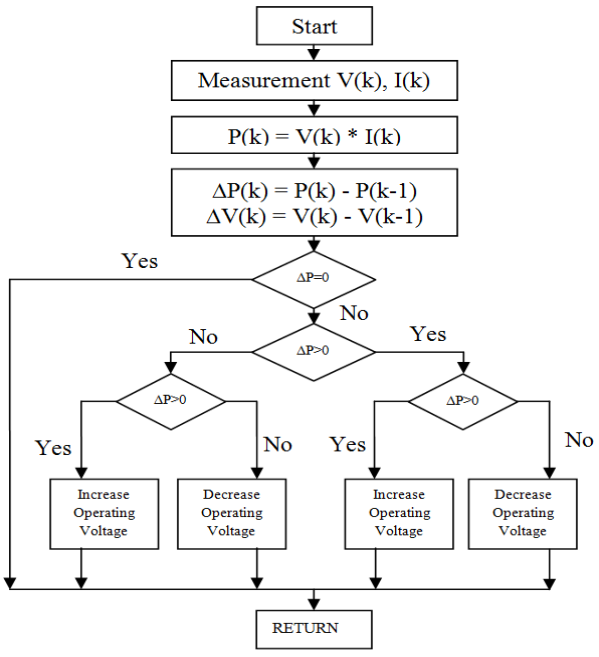

Figure 3. Flowchart of P&O algorithm

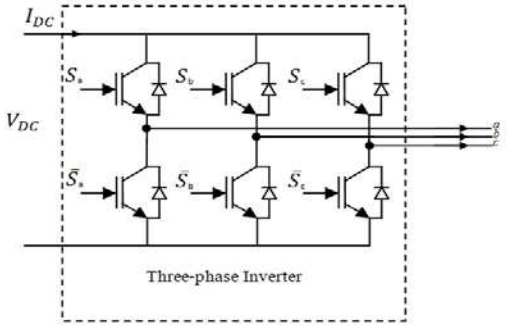

Figure 4. Three phase Voltage Source Inverter

The power circuit of the three-phase inverter consists of six bidirectional switches to connect the three-phase grid through a passive filter. The two switches of each inverter leg must operate in a complementary mode to avoid the short circuit of the DC-Link [12].

The switch is controlled by a PWM generator in order to obtain the same waveform as the reference signal. The PWM signal is obtained by comparing a triangular signal (carrier) to the reference signal obtained from the controller [17].

III. THE CONTROL STRUCTURE

The control strategy applied to the grid-tide converter consists mainly of two cascaded loops. Usually, there is a fast internal current loop, which regulates the grid current, and an external voltage loop, which controls the DC-link voltage [18]. The DC-link voltage control aims at balancing the active power flow in the system [19].The synchronization of the system with the grid is done by a Phase-Locked Loop (PLL) [20].

A. PI controller

Current control strategy using proportional integral (PI) controller is normally based on "*dq"* control structure as it is superior in DC variable control. This control transforms the grid voltage and current in the "*abc"* natural frame into a "*dq"* reference frame as shown in (5) [21]. In this way, I_d and I_q, respectively are regulated by the controller.

$$\begin{bmatrix} d \\ q \\ 0 \end{bmatrix} = \frac{2}{3}\begin{bmatrix} \cos(\theta) & \cos(\theta-\frac{2\pi}{3}) & \cos(\theta+\frac{2\pi}{3}) \\ -\sin(\theta) & -\sin(\theta-\frac{2\pi}{3}) & -\sin(\theta+\frac{2\pi}{3}) \\ \frac{1}{2} & \frac{1}{2} & \frac{1}{2} \end{bmatrix}\begin{bmatrix} a \\ b \\ c \end{bmatrix} \quad (5)$$

The matrix transfer function of the controller can be written as

$$G_{PI}^{(dq)}(s) = \begin{bmatrix} K_p + \frac{K_i}{s} & 0 \\ 0 & K_p + \frac{K_i}{s} \end{bmatrix} \quad (6)$$

For improving the performance of the controller, cross-coupling terms and voltage feed-forward are usually used [18].The controller is depicted in Fig 5.

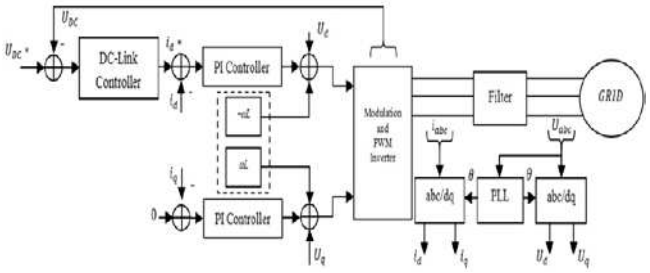

Figure 5. PI Controller model for grid tied inverter

B. PR controller

The Proportional-Resonant (PR) controller uses an "*abc-αβ*" module to transform the grid currents in the natural "*abc*" frame into a stationary reference "*αβ*" frame [21]. This can be achieved by Clark transformation [22]

$$\begin{bmatrix} \alpha \\ \beta \end{bmatrix} = \frac{2}{3}\begin{bmatrix} 1 & -\frac{1}{2} & -\frac{1}{2} \\ 0 & \sqrt{\frac{3}{2}} & -\sqrt{\frac{3}{2}} \end{bmatrix}\begin{bmatrix} a \\ b \\ c \end{bmatrix} \quad (6)$$

The controller matrix in the stationary reference frame is given by

$$G_{PR}^{(\alpha\beta)}(s) = \begin{bmatrix} K_p + \frac{K_i s}{s^2+\omega^2} & 0 \\ 0 & K_p + \frac{K_i s}{s^2+\omega^2} \end{bmatrix} \quad (7)$$

A PR controller is able to track sinusoidal reference signals and reject the disturbance within the system in high performance. At the fundamental frequency, the PR controller produces an infinite gain; therefore, the steady state error can be eliminated [5].

The proportional gain basically determines the dynamics of the system in terms of bandwidth phase and gain margin. For harmonic compensation, it determines the order of harmonics that can be regulated without violating the stability limit [9]. The controller is shown in fig 6.

C. Noise filtering

A drawback of using feedback is that measurement noise is injected into the system [23].Most of the measured converters' signals are affected by switching noise and other disturbances [24]. Filtering reduces their effects and eliminates the undesired control activity [23].

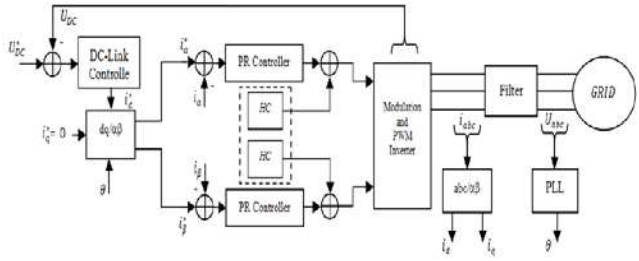

Figure 6. PR Controller model for grid tied inverter

The PI controller used in the grid tied PV system gets its control variables directly from measurement of the grid voltage and current values. They are subject to the effect of noises coming from the grid. To reduce this effect on the controllers' performance, filtering techniques will be used.

A filter may be chosen in several different ways. It has normally a low-pass character. It must have the property $F_r(0) = 1$ to ensure that the process output equals the set-point in steady state.

In this work a simple first order filter structure is adopted as suggested in [25]. Equation (8) refers to its transfer function and its Bode plot is given in Fig 7.

$$F_y = \frac{1}{1+sT_f} \quad (8)$$

One way to determine the filter time constant T_f is to design ideal controllers and to add the filter afterwards. An iterative procedure also known as trial and error will be used [24]. Controllers with different filter constants will be designed and the value of T_f will be chosen as a trade-off between robustness and noise attenuation [23].

Fig 8 shows a random system's step response without filter and with filters of different time constants T_f.

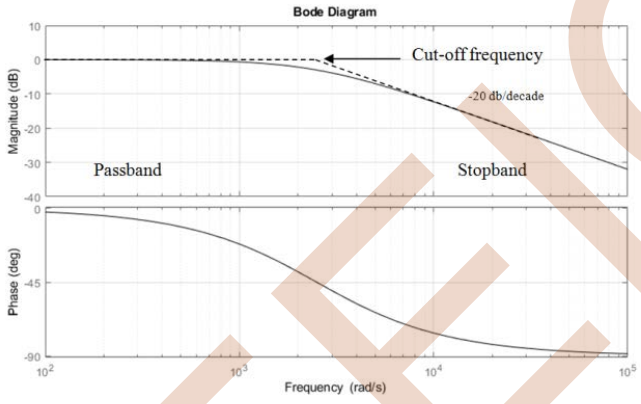

Figure 7. Bode plot of a first order filter

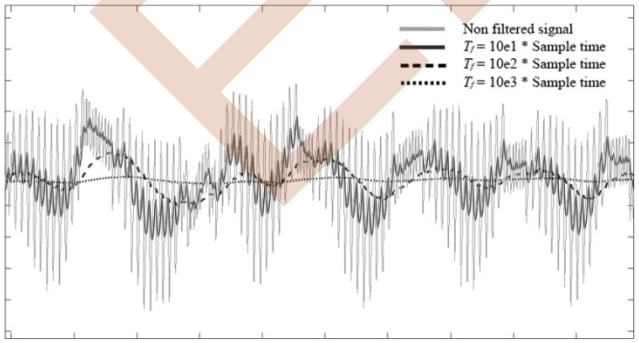

Figure 8. Random noise signal filtered

IV. SIMULATIONS

Numerical simulations using MATLAB-Simulink environment are carried out to confirm the performances of the proposed strategy. A Soltech 1Sth-215-P solar array is chosen for this task. Its data are borrowed from [26]. The module is made of 60 cells in series and provides 213.15W of nominal maximum power. The system is designed to deliver 8.5Kw to the grid at unity power factor. The systems specifications are given in table 1.

The proposed strategy is implemented by filtering the feedforward voltage signal of a PI controller. The results obtained are compared to a PI controller and a PR controller in terms of Total Harmonic Distortion through FFT (Fast Fourier Transformation) calculations on steady state.

Fig. 9 presents the three phase current waveforms of the system using the PI controller with filtered FeedForward signal compared to the PI and PR controllers.

Figs. 10 to 12 show the Fast Fourier Transformation for the system using the PI controller, the PI controller with filtered feedforward and the PR controller respectively.

In Fig. 13 a comparison between the Total current harmonic distortions of each system is presented.

When comparing the current waveforms it can be seen that the PI controller generates the most distorted signal. The PR controller performs better, with a cleaner signal. The proposed strategy reduces the distortion and gets the PI controller closer to the clean sinusoidal waveform.

The Fast Fourier Transformation shows that the harmonics generated by the PR controller have lower magnitude compared to the PI controller. Also, it can be seen that the proposed strategy greatly lowers the 5th, 7th and 9th harmonics when compared to the PI controller.

TABLE I. STUDIED SYSTEM SPECIFICATIONS

Pv array	
Open circuit voltage (V_{oc})	36.3 [V]
Optimum operating voltage (V_{mpp})	29.0 [V]
Short circuit current (I_{oc})	7.84 [A]
Optimum operating current (I_{Mpp})	7.35 [A]
Maximum power (P_{mpp})	213.15 [W]
Number of cells connected in series (N_s)	60
Number of panels connected in series (N_{ss})	10
Number of panels connected in parallel (N_{pp})	5
Boost converter	
Inductance (L_b)	0.250 [mH]
Input capacitor (C_b)	564 [µF]
Output capacitor (C_{dc})	200 [µF]
LCL filter	
Input inductance (L_i)	1.69 [mH]
Filter Capacitor (C_f)	16.56 [µF]
Damping resistor (R_d)	2.05 [Ω]
Grid-side inductance (L_g)	0.001 [H]
Simulation	
Switching frequency (f_s)	5 [KHz]
Grid frequency (f_g)	50 [Hz]
Simulation time-step (t)	1e-6 [s]

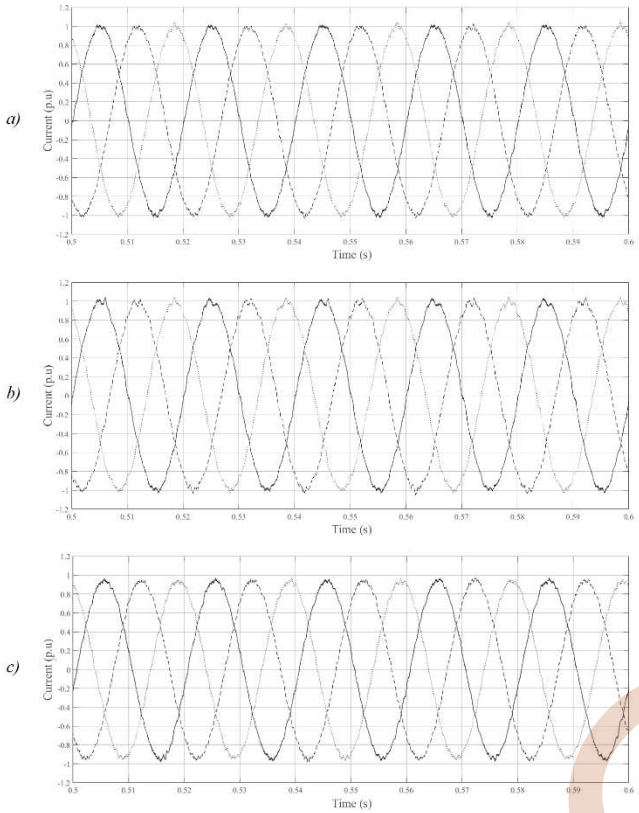

Figure 9. Current waveform of the photovoltaic system a) PI with feedforward filter, b) PI controller, c) PR controller

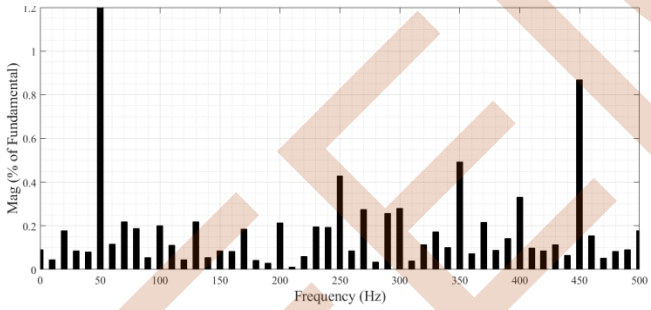

Figure 10. Fast Fourier Transform for the system with PI controller

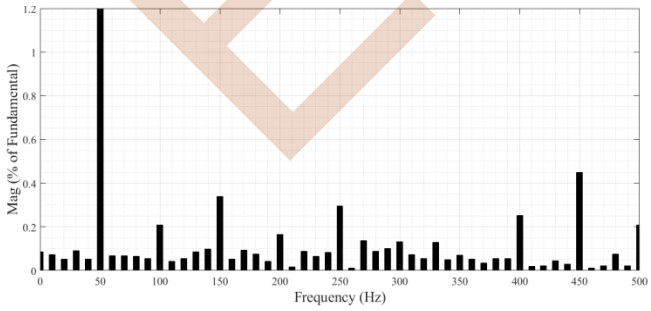

Figure 11. Fast Fourier Transform for the system with filtered PI controller

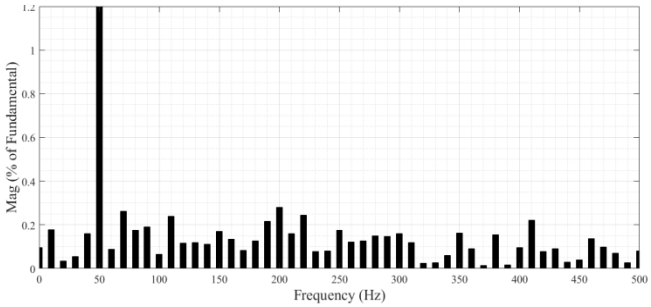

Figure 12. Fast Fourier Transform for the system with PR controller

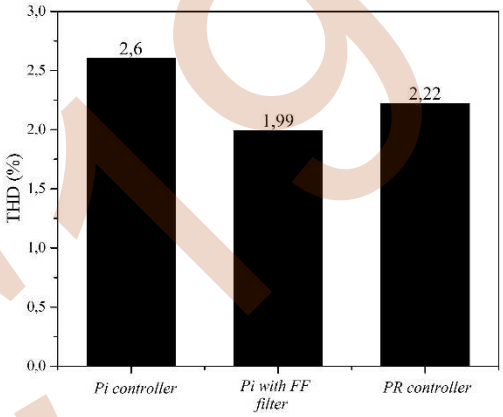

Figure 13. THD comparison for filtered PI controller compared to the PI and PR controllers

In terms of Total Harmonic Distortion, the proposed strategy clearly performs better with the lowest THD. It is 23.5% lower compared to the PI controller. The PR controller's THD is only 14.6% lower.

V. CONCLUSION

This paper proposes a simple strategy to improve the harmonic performances of PI controllers. The strategy takes advantage of filtering techniques to reduce the impact of grid noises and disturbances in the voltage signal in Feedforward. First, an overview of a photovoltaic system and its control schemes were presented. The PI controllers, the PR controllers and the noise filtering technique were discussed.

The viability of the proposed strategy was investigated through Simulations on Matlab Simulink by comparison to the PI and PR controllers. The Fast Fourier Transformation gave informations about the harmonics generated by the system for each case. The feed-forward injects the grid voltage directly to the controllers output and so injects the grid harmonics to the reference signal. Filtering this signal improved the overall performances of the controller.

The proposed strategy is suitable for grid tied photovoltaic systems. It has the advantage of being simple and easy to implement. It offers a high improvement in terms of harmonic reduction. Further studies are necessary for assessing its viability on more complex power systems while taking into account the dynamics of the solar source.

REFERENCES

[1] N. Zhang,H. Tang, and C. Yao, "A systematic method for designing a PR controller and active damping of the LCL filter for single-phase grid-connected PV inverters". Energies, 7(6), pp.3934-3954. 2014.

[2] S. Alsadi and T. Khatib, "Photovoltaic power systems optimization research status: A review of criteria", Constrains, Models, Techniques, and Software Tools. Applied Sciences, 8(10), pp.1761, 2018.

[3] H. Cha, T.K. Vu, J.E. Kim, "Design and control of proportional-resonant controller based photovoltaic power conditioning system", Proc. IEEE Energy Convers. Congr. Expo., pp. 2198-2205, Sep. 2009.

[4] E. Avci and M. Ucar, "PR control of grid-connected 3-level inverter with LCL filter", International energy technologies conference, ENTECH'17, pp. 17-24, 2017.

[5] H. Khalfalla, et al: "An adaptive proportional resonant controller for single phase PV grid connected inverter based on band-pass filter technique". IEEE Int. Conf. Compatibility, Power Electronics and Power Engineering (CPE-POWERENG), Gadiz, Spain, pp. 436–441, April 2017.

[6] D. Zammit, C. Spiteri Staines, M. Apap and J. Licari, "Design of PR current control with selective harmonic compensators using Matlab", Journal of Electrical Systems and Information Technology, vol. 4, no. 3, pp. 347-358, 2017. Doi: 10.1016/j.jesit.2017.01.003.

[7] Z. Ali, N. Christofides, L. Hadjidemetriou, E. Kyriakides, "An advanced current controller with reduced complexity and improved performance under abnormal grid conditions" in PowerTech 2017 IEEE Manchester, IEEE, pp. 1-6, June. 2017..

[8] M. W. Alzahlan, K. M. Alawasa and H. D. Al-Majali, "Performance evaluation of different optimal-tuned current controllers for voltage-source converter connected to a weak AC grid", 2019 IEEE Jordan International Joint Conference on Electrical Engineering and Information Technology (JEEIT), Amman, Jordan, pp. 198-203, 2019, doi: 10.1109/JEEIT.2019.8717376.

[9] R. Teodorescu, F. Blaabjerg, "Proportional-Resonant controllers. A new breed of controllers suitable for grid-connected voltage-source converters", The 9th International Conference on Optimization of Electrical and Electronic Equipments, pp. 9-14, 2004.

[10] L. Atik et al, "Maximum power point tracking algorithm based on sliding mode and fuzzy logic for photovoltaic sources under variable environmental conditions", 2017. doi: 10.1063/1.4976282.

[11] M. Shayestegan, "Overview of grid-connected two-stage transformer-less inverter design", Journal of Modern Power Systems and Clean Energy, vol. 6, no. 4, pp. 642–655, Jan. 2018, doi: 10.1007/s40565-017-0367-z.

[12] A. Kihal, F.krim, B.Talbi, A. Laib, A.Sahli, "A robust control of two-stage grid-tied pv systems employing integral sliding mode theory." Energies, vol. 11, no. 10, pp. 2791, Oct. 2018, doi:10.3390/en11102791.

[13] A. Ahlawat, D. Gupta, S. K. Gupta, "Modeling of a PV array and implementation of an efficient MPPT based control mechanism in stand-alone photovoltaic systems", I-Manager's Journal on Circuits and Systems, vol. 5, no. 2, pp. 51, 2017, doi:10.26634/jcir.5.2.13665.

[14] N. Derbel and Q. Zhu, "Modeling, identification and control methods in renewable energy systems", Green Energy and Technology, Singapore, Springer Singapore, 2019.

[15] M. Fares, L. Atik, G. Bachir and M. Aillerie, "Photovoltaic panels characterization and experimental testing", Energy Procedia, vol. 119, pp. 945-952, 2017. doi: 10.1016/j.egypro.2017.07.127.

[16] L. Atik, et al, "Comparison of four MPPT techniques for PV systems", AIP Conference Proceedings 1758, 030047, 2016; doi: 10.1063/1.4959443.

[17] T. Z. Touhami, P. Petit, G. Bachir, M. Aillerie, "New topology of photovoltaic microinverter based on boost converter", Energy Procedia, vol. 119, pp. 938–944, July 2017, doi:10.1016/j.egypro.2017.07.106.

[18] F. Blaabjerg, R. Teodorescu, M. Liserre, A. V. Timbus, "Overview of control and grid synchronization for distributed power generation systems", IEEE Transactions on Industrial Electronics, vol. 53, no. 5, pp. 1398–1409, Oct. 2006, doi:10.1109/tie.2006.881997.

[19] L. Hassaine, E. OLias, J. Quintero, V. Salas, "Overview of power inverter topologies and control structures for grid connected photovoltaic systems", Renewable and Sustainable Energy Reviews, vol. 30, pp. 796–807, Feb. 2014, doi:10.1016/j.rser.2013.11.005..

[20] M. Chabakata M. Petit, F. Costa, R. Marouani, A. Mami, "Optimized design of an LCL Filter for grid connected photovoltaic system and analysis of the Impact of neighbors' consumption on the system", Journal of Electrical Systems, 13, pp 618-632, 2017.

[21] O. A. Ajeigbe, et al., "Harmonic control strategies of utility-scale photovoltaic inverters" , International Journal Of Renewable Energy Research, vol. 8, no. 3, pp. 1354-1368, 2018.

[22] M. Janaszek, "Extended clarke transformation for n-phase systems", proceedings of electrotechnical institute, vol. 63, pp. 5-26, 2016. doi: 10.5604/01.3001.0009.4333..

[23] V. R. Segovia, T. Hägglund, K. J. Aström, "Measurement noise filtering for PID controllers", Journal of Process Control, vol. 24, no. 4, pp. 299–313, Apr 2014, doi:10.1016/j.jprocont.2014.01.017.

[24] S. Haitao, M. J. Mnati, M. N. Ibrahim, A. Van der Bossche, "A tuning method for PID controller for an integrating system with time delay", MATEC Web of Conferences, vol. 249, p. 03007, 2018, doi:10.1051/matecconf/201824903007.

[25] T. Hägglund, "Signal filtering in PID control", IFAC Proceedings Volumes, vol. 45, no. 3, pp. 1–10, 2012, doi:10.3182/20120328-3-it-3014.00002.

[26] A.M. Farayola, A.N. Hasan, A. Aili, "Comparison of modified incremental conductance and fuzzy logic MPPT algorithm using modified CUK converter", 8th International Renewable Energy Congress (IREC), Mar 2017, doi:10.1109/irec.2017.7926029.

Design and Comparison of Two Intelligent Controllers for Global Maximum Power Point Tracking of PV System under Partial Shading Conditions

Faiza Belhachat[1*], Cherif Larbes[2]
[1,2] Laboratoire des Dispositifs de Communication et de Conversion Photovoltaïque, Ecole Nationale Polytechnique, Alger, Algérie.
*faiza.belhachat@g.enp.edu.dz
cherif.larbes@g.enp.edu.dz

Rachid Bennia[3]
[3] Laboratoire des Dispositifs de Communication et de Conversion Photovoltaïque, Ecole Nationale Polytechnique, Alger, Algérie.
bennia.rachid@g.enp.edu.dz

Abstract—In the presence of partial shading, the characteristic curves of a PV module have several peaks, which makes the tracking of the maximum power point more difficult. Traditional algorithms fail to locate correctly the global maximum among multiple local peaks under such conditions. Therefore, to overcome this problem, reliable algorithms must be implemented to improve the efficiency of the PV module and consequently increase the efficiency of the whole PV system. To achieve our goal, we designed two intelligent MPPT algorithms using an Artificial Neural Network (ANN) and Adaptive Neural Inference System (ANFIS). The effectiveness of the two proposed methods is investigated for 4S configuration under partial shading conditions for various shading scenarios. The results show that both proposed methods can track the global MPP efficiently within very short convergence time and negligible oscillation at GMPP. The comparison carried out between the neural network and neuro-fuzzy controllers shows a superiority of the neuro-fuzzy controller compared to the neural controller in term of convergence speed. The proposed technique can be also applied to any PV configuration type and or size.

I. INTRODUCTION

Solar photovoltaic (PV) energy is one of the most important renewable energy generations that directly produce electric energy from solar irradiance. Despite its range of advantages, partial shading significantly decreases the overall PV system performance. It may occur due to multiple reasons, such as dirt and dust, clouds, trees and buildings… etc. [1, 2].

When a partial shading occurs, multiple maximum power points can arise on the characteristics curve of the PV array caused by the use of bypass diodes that avoid the hotspot effect. The appearance of these multiple peaks makes the extraction of the maximum power point under these conditions a hard task, which requires the development of reliable and more efficient tracking methods able to locate the true maximum among the other local maxima to increase the efficiency of the PV field [2].

From literature, a variety of recent GMPPT methods for maximum power point tracking under partial shading based on optimization algorithm, hybrid algorithm, mathematical model and other GMPPT have been developed [3] and can be found from literature reviews in Refs [3–9].

Other new methods have been also proposed in literature such as a modified cat swarm optimization (MCSO) [10], improved chicken swarm optimization (ICSO) [11], improved gravitational search algorithm (IGSA) [12], modified artificial wolf pack (MAWP) [13], modified artificial whale optimization algorithm (MAKWO) [14], improved differential evolution algorithm (IDE) [15], hybrid grey wolf optimization (GWO) and Beta method (GWO-Beta) [16], a hybrid particle swarm optimization and artificial neural network (PSO-ANN) [17], a genetic algorithm (GA) and the firefly algorithm (FA) [GA-FA) [18], monte carlo (SMC) filtering assisted by the prediction of MPP via an artificial neural network (ANN) (SMC-ANN) [19], enhanced bayesian function [20], power-increment algorithm [21], bypass diode scanning algorithm [22], method based on the maximum power delivered by the series and parallel configuration of PV cells [23] and modified particle velocity based PSO technique (MPV-PSO) [24]…etc.

Despite, the emergence of various optimization algorithms and different techniques to deal with problem of GMPP tracking under partial shading, soft computing methods based on artificial intelligence are still widely used in PV system application for their multiple benefits.

Soft computing methods based on artificial intelligence (AI) concepts such as artificial neural network (ANN), fuzzy logic control (FLC) and their hybrids have been employed to extract of global MPP from partial shaded PV system [2].

Artificial neural network has taken special attention because of its ability to use non-linear models, ability to learn and generalize from examples, no necessity of knowledge of rules, universal approximation that allow for solving complicated control problems.

Adaptive Neuro-Fuzzy Inference System (ANFIS) is a hybrid intelligent approach, which combines ANN with Fuzzy system. The ANFIS takes advantage of the learning capability of neural networks and allows for automatic generation of adequate rules (with respect to input and output data),

The main aim of this paper is to design efficient MPPT controllers for PV system under partial shading conditions. To achieve our goal, we propose two intelligent approaches, namely: the Artificial Neural Network and Neuro-Fuzzy (ANFIS) networks.

The main advantage of the proposed controller is the improvement of performances compared to other methods published in literature. In addition, the proposed intelligent MPP controllers can be applied for any PV configuration type or size.

This paper is organized as follow: The PV module modelling and partial shading effect on PV array characteristic are presented in section 2 and 3 respectively. Section 4 describes the proposed neural and neuro-fuzzy MPPT controllers. Simulation results of proposed GMPPT methods performed under different shading scenario are discussed and compared in section 5. Finally, a conclusion is given in section 6.

II. MODELING OF PV MODULE

To study the effects of shading on the electrical characteristic of solar cells, we must take into account the whole of its characteristic, whatever its mode of operating. The phenomenon referred to the "bishop effect" takes into account the breakdown voltage in the expression of the characteristic (I-V) of a photovoltaic cell [1, 25, 26]. The electrical behavior of the PV cell over the whole voltage range can be expressed by Eq. (1).

$$I = I_{ph} - I_{s1}\left[\exp\left(\frac{V+R_sI}{m_1V_t}\right) - 1\right] - I_{s2}\left[\exp\left(\frac{V+R_sI}{m_2V_t}\right) - 1\right] - \left(\frac{V+R_sI}{R_p}\right)\left[1 + a\left(1 - \frac{V+R_sI}{V_b}\right)^{-n}\right] \quad (1)$$

This model is represented by equivalent circuit shown in Fig.1.

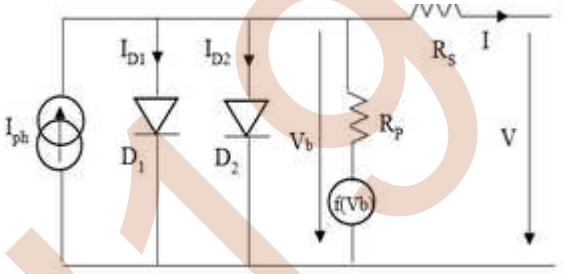

Fig.1. Equivalent circuit of photovoltaic cell.

Where I_{ph}: is the photon current, I_{s1} and I_{s2}: are inverse saturation currents of the first and second diode respectively. m_1 et m_2: are the ideality factors of the diode D_1 and D_2 respectively, Vt: is the junction thermal voltage, R_s and R_p: are series and parallel resistances respectively, Vb: is the breakdown voltage, a and n are constants.

III. PARTIAL SHADING EFFECT ON PV MODULE CHARACTERISTICS

A typical PV module is connected in series to form a string. When the PV module is subjected to the shading, the exposed part of the solar cell due to shading will no longer generate power and the module become as a load. The shaded module current will force the output current of the whole string. In extreme cases, the shaded modules will generate excess heat due to reverse current flow. The excessive heat generated in certain part of PV modules leads to creation of the hot spots. In order to overcome this problem bypass diodes are connected in parallel with group of PV cells. The bypass diode will bypass the cell current subjected to shading and protect the module failure due to hot spots [2].

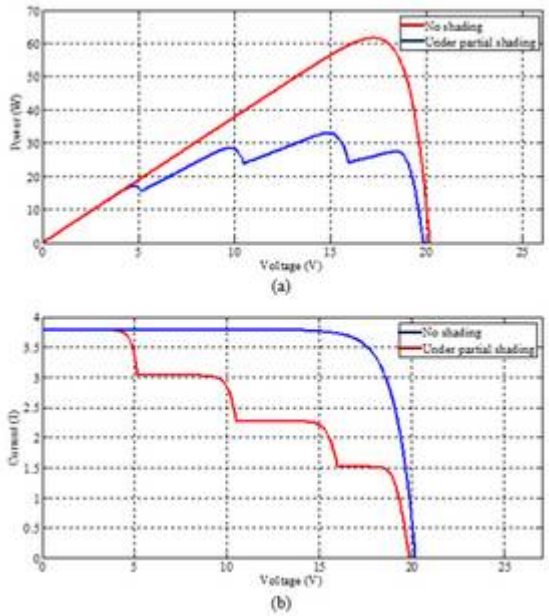

Fig.2. Characteristics curves obtained under STC and partial shading conditions.
(a) P-V. (b) I–V

Module current versus voltage (I–V) and power versus voltage (P–V) characteristics curves are shown in Fig.2 obtained by using Matlab/Simulink. These curves are obtained at standard test condition (STC) (under the irradiation of 1000 W/m^2 and temperature of 25°C) and under partial shading conditions for following irradiance levels: 6 cells are exposed to an irradiance of 400 W/m^2, 10 cells are exposed to 600 W/m^2, 10 cells are exposed to 800 W/m^2 and 10 cells are exposed to an irradiance of 1000 W/m^2. The following parameters are used: m_1 = 1, Is_1 = 1.26x10^{-9} A, m_2 = 2, Is_2 =2.53x10^{-6}A, R_s =1x10^{-3} Ω, R_p =1000Ω; I_{ph}=3.798A. Bishop's term: V_b = -15V, a = 2 x10^{-3}, n = 3. [27].

The maximum power points obtained under standard and partial shading conditions are shown in Table 1.

Table I Maximum power points obtained under standard and partial shading conditions.

Condition	Maximum power point		
	Voltage (V)	Current (A)	Power (W)
STC	17.23	3.59	61.78
Partial shading	14.90	2.23	33.16

Under partial shading conditions, the P–V characteristic exhibits multiple peaks power and the maximum output power is 33.16 W.

IV. INTELLIGENT GMPPT CONTRLLERS DESIGN

In this section, the designed MPPT controllers are described. To achieve this, the databases should be created in order to learn the neural and neuro-fuzzy models. The data bases witch include input-output parameters are taken from a simulation of 4S PV configuration for various partial shading scenarios.

A. The proposed neural network based GMPPT

For our application, the first used MPPT controller is a multilayer perceptron. It has two inputs and one output corresponding to the parameters: Voltage (V), current (I) and power (P) respectively, the number of hidden neurons selected for this model is 6, with sigmoid transfer function. The output layer has a linear activation function. Fig.3 shows the structure of the proposed neural network.

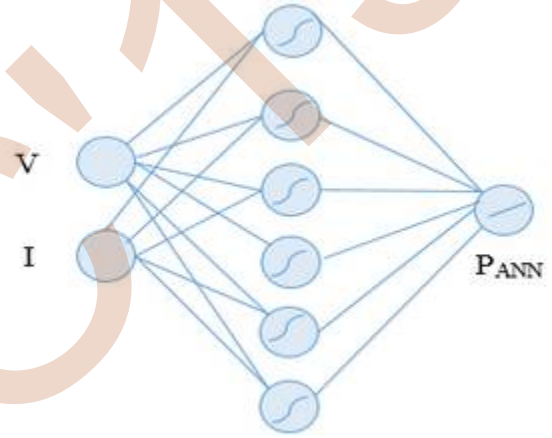

Fig.3. Architecture of the proposed ANN controller.

During the learning phase, each output neuron compares its computed activation to the desired value to determine the associated error and adjusts thereafter the synaptic weights to minimize the squared error. For the learning phase, we applied the method of Levenberg Marquardt. Fig.4 shows the evolution of the learning error during training of the neural network based on the iterations number.

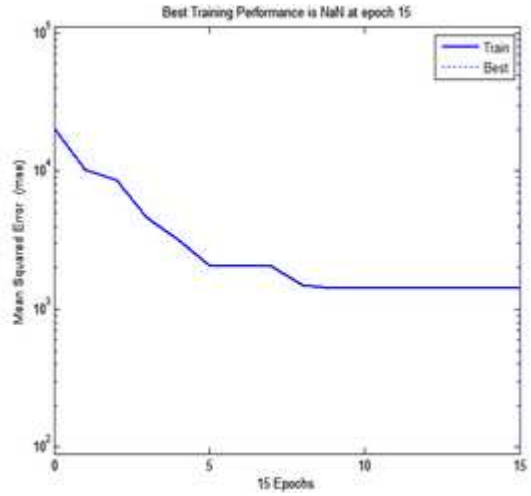

Fig.4. Evaluation of the squared error based on the number of iterations.

The generated neural network structure is shown in Fig.5.

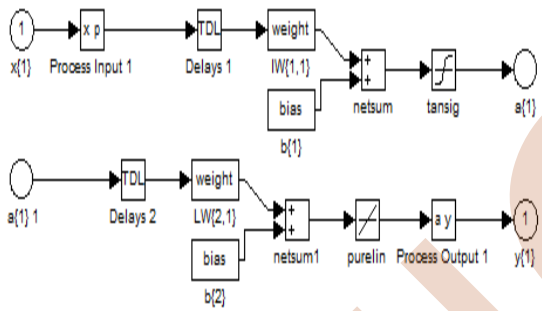

Fig.5. The generated neural network structure.

B. The proposed neuro-fuzzy based GMPPT

The ANFIS network has five layers with two inputs (voltage and current) and one output (series configuration power). Each input parameter has 5 membership functions "Gaussian" which are learned by ANFIS method. Fuzzy rules is constructed by the ANFIS network from a given input-output data set with appropriate membership functions. The parameters of membership function's shape are adjusted during learning process. Consequently, 25 fuzzy rules are generated to produce output power for each input set. The ANFIS network employs the hybrid learning algorithm to identify membership function parameters, which combines the least squares method and back propagation gradient descent method with maximum number of iteration equal to 2500 (epochs). Figs.6 and 7 show the training error and the generated ANFIS network structure from Matlab respectively.

Fig.6. The training error.

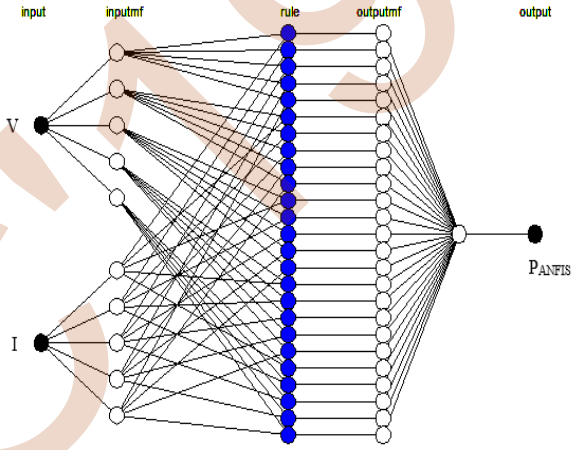

Fig.7. Structure of ANFIS network.

V. SIMULATION RESULTS AND DISCUSSION

To verify the effectiveness of the proposed intelligent controllers, a photovoltaic system is simulated using Matlab/Simulink environment. Fig.8 shows the overall PV system integrated with the intelligent controllers. Four PV modules were used, each PV module comprises 36 PV cells connected in series and protected by bypass diode. The used sampling period is equal to 0.0001s, and the switching frequency is selected equal to 20 kHz. The buck-boost parameters values are: L=5.6mH, $C_1 = C_2 = 3.5$ mF, $R_L = 60\ \Omega$.

To test the effectiveness of the proposed controllers, we will consider the following shading scenarios shown in Fig.9.

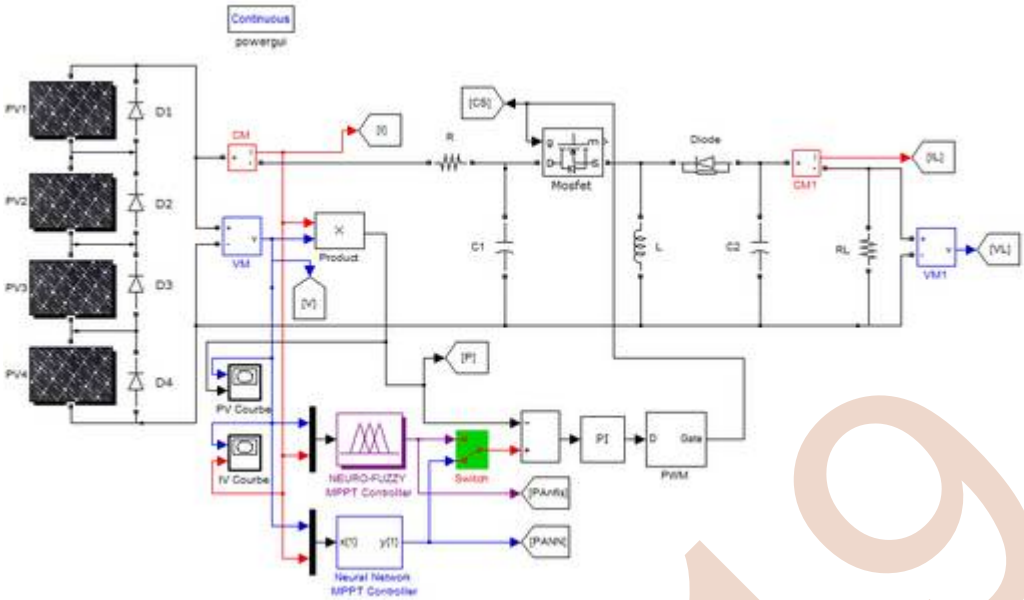

Fig.8. Simulink model of the overall PV system integrated with MPPT for 4S configuration.

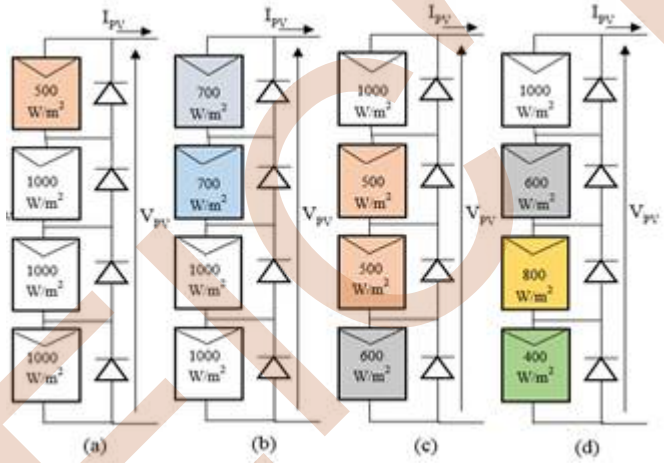

Fig.9. A string of four panels in series (4S) with different scenarios:
(a): Scenario SP_2 (weak shading). (b): Scenario SP_3 (weak shading). (c): Scenario SP_4 (strong shading). (d): Scenario SP_5 (strong shading).

Table 2 shows different patterns for PV array connected in series configuration for various considered scenarios.

Table II Uniform irradiance and different partial shading patterns for 4S configuration (W/m^2).

Pattern (W/m^2)	Scenario				
	SP_1	SP_2	SP_3	SP_4	SP_5
G_{PV1}	1000	500	700	1000	1000
G_{PV2}	1000	1000	700	500	600
G_{PV3}	1000	1000	1000	500	800
G_{PV4}	1000	1000	1000	600	400

The (P-V) and (I-V) characteristics under standard and partial shading conditions for different scenarios are shown in Fig.10.

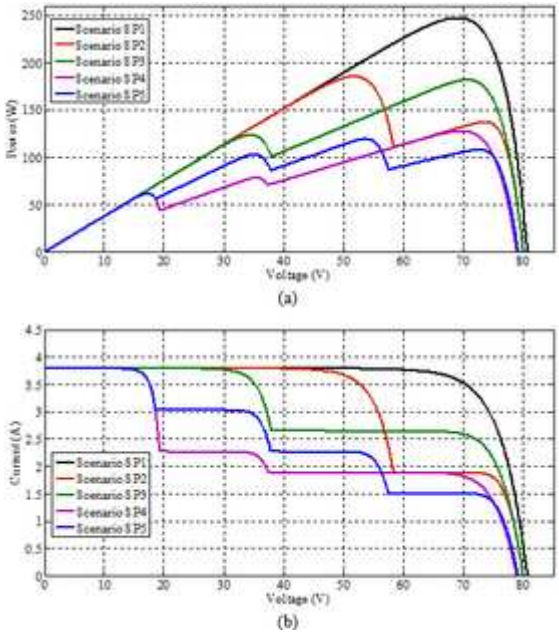

Fig.10. Simulated characteristics for 4S configuration for different scenarios.
(a) P–V. (b) I–V

Table 3 shows the obtained global maximum powers points for PV array connected in series configuration for all considered scenarios.

Table III Simulation results of a PV module under standard conditions.

Scenario	Maximum power point		
	Voltage (V)	Current (A)	Power (W)
SP_1	68.99	3.58	247.21
SP_2	51.67	3.59	185.40
SP_3	70.59	2.57	181.71
SP_4	69.55	1.84	127.62
SP_5	53.61	2.23	119.40

a. *Scenario SP_1 (without shading):*
The MPPT curve under standard conditions (scenario SP_1) illustrated in Fig.10 employing ANN and ANFIS are depicted in Fig.11. Since there exists a single peak at 247.21 W, reaching peak in this case is a simple task for both methods. From the results, it can be seen that ANN method takes 0.038s to converge whereas ANFIS method reaches to a global peak within 0.0392s.

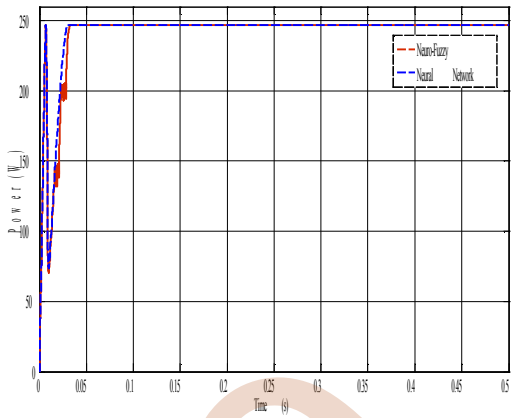

Fig.11. Power tracking curve of 4S PV configuration under standard condition (scenario SP_1).

b. Scenario SP_2 (Weak shading):
The power curve corresponding to the scenario SP_2 (weak shading) illustrated in Fig.10 is shown in Fig.12.a. In this case, ANFIS converges to GMPP of 185.4W in less than 0.033s while ANN takes 0.08s to converge at GMPP.

c. Scenario SP_3 (Weak shading):
The power curve that corresponds to the scenario SP_3 (weak shading) illustrated in Fig.10 is shown in Fig.12.b. In this case, ANN and ANFIS controllers take 0.032s to converge to GMPP.

d. Scenario SP_4 (Strong Shading):
In this case, more number of panels is exposed to different irradiances. This condition is realized in scenario SP_3 shown in Fig.10. The shade in this case has led to have three different peaks with two local maximum power points occurring (LMPP) at 61.78W, 78.1W and one GMPP at 127.62W. The power curve corresponding to this case is illustrated in Fig.12.c. The graphs indicate that both ANFIS and ANN methods are able to track GMPP and successfully reach GMPP in less than 0.045s.

e. Scenario SP_5 (Strong Shading):
This case is realized in scenario SP_5 shown in Fig.10. The shade in this case has led to have four different peaks with three LMPP occurring at 61.8W, 103.17W, 108.1W and one GMPP at 119.4W. The power corresponding to this case is illustrated in Fig.12.d.
From Fig.12.d, it is clear that ANFIS algorithm tracks a power of 118.8 W while the ANN tracks 119.9W. In this case, the ANN controller tracks more power than ANFIS controller. However, the time taken by the ANFIS to reach GMPP is shorter than ANN controller.

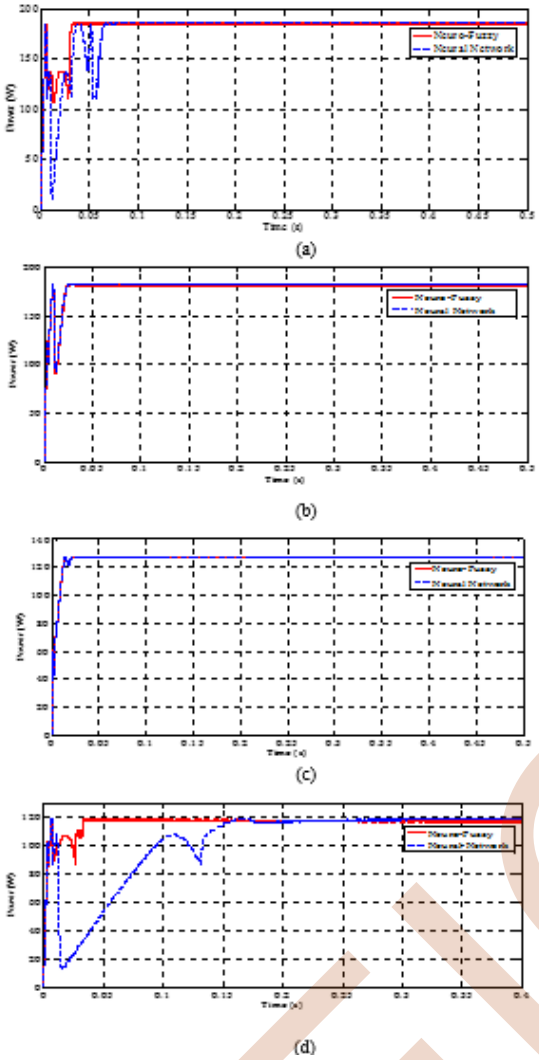

Fig.12. Power tracking curve of 4S PV configuration under partial shading for different scenarios: (a) SP_2. (b)SP_3. (a) SP_4. (b)SP_5.

The performances of the proposed MPPT controllers for various scenarios are listed in Table 4.

It is clear, that the both ANFIS and ANN methods can track accurately the real maximum power within very short time under uniform and partially shaded conditions for all tested cases. The average efficiency of tracking for each controller is around 99.90%. Generally, the convergence time of ANFIS is better than that in ANN.

Hence, by examining the simulation results, it is evident that the ANN and ANFIS algorithms are able to extract the maximum available power. Both methods succeed to locate the MPP with the same efficiency under various conditions (with slight difference). However, the proposed ANFIS method presents a shorter convergence speed compared to the ANN method.

V. CONCLUSION

Maximum power point tracking (MPPT) process play a vital role in efficiency improvement of photovoltaic (PV) systems. It is mainly used to extract maximum possible power of the PV modules under both uniform and partial shaded conditions.
In this paper, two intelligent algorithms are presented and applied to extract the global maximum power from the partially shaded PV system: these algorithms are ANN and ANFIS networks. A Simulink/SimPower model of PV array comprising four modules connected in series is built. Different shading patterns are used and tested. The obtained results from each MPPT algorithm are compared and discussed. The obtained results from ANFIS and ANN are closely matched to those obtained from the Simulink/SimPower model. Generally, the convergence time of ANFIS controller in almost studied cases is better than that in ANN controller. The proposed intelligent controllers can be implemented for any array configuration type or size.

Table IV Comparison between the ANN and the ANFIS based MPPT algorithms for different scenarios.

Pattern n°	Ideal output Power (W)	Output power obtained (W)		Accuracy (%)		Tracking speed (s)	
		ANN	ANFIS	ANN	ANFIS	ANN	ANFIS
SP_1	247.21	247.17	247.20	99.98	100	0.038	0.0392
SP_2	185.4	185.4	185.4	100	100	0.08	0.033
SP_3	181.71	181.6	181.6	99.94	99.94	0.032	0.032
SP_4	127.62	127	127.40	99.51	99.83	0.050	0.045
SP_5	119.4	119.4	118.8	100	99.50	0.18	0.044

REFERENCES

[1] Belhachat, F., Larbes, C.: 'Modeling, analysis and comparison of solar photovoltaic array configurations under partial shading conditions', Sol Energy., 2015, 120, pp 399-418
[2] Belhachat, F., Larbe, C. : 'Global maximum power point tracking based on ANFIS approach for PV array configurations under partial shading conditions', Renew Sustain Energy Rev., 2017,77, pp 875-889
[3] Belhachat, F., Larbes, C.: 'A review of global maximum power point tracking techniques of photovoltaic system under partial shading conditions', Renew and Sustain Energy Rev., 2018, 92, pp 513–553
[4] Lian, LJ., Srivatsan, R., Douglas, LM. : 'Computational intelligence techniques for maximum power point tracking in PV systems: A review', Renew and Sustain Energy Rev., 2018, 85, pp 14–45
[5] Danandeh, M.A., SM. Mousavi, G.: 'Comparative and comprehensive review of maximum power point tracking methods for PV cells', Renew and Sustain Energy Rev., 2018, 82, pp 2743–2767
[6] Li, G., Jin, Y., Akram, M.W., Chen, X., Ji, J.: 'Application of bio-inspired algorithms in maximum power point tracking for PV systems under partial shading conditions – A review', Renew and Sustain Energy Rev., 2018, 81, pp 840–873
[7] Ramli Makbul, A.M., Twaha, S., Ishaque, K., Al-Turki Yusuf, A.: 'A review on maximum power point tracking for photovoltaic systems with and without shading conditions', Renew and Sustain Energy Rev., 2017, 67, pp 144–159
[8] Joshi P, Arora S.:' Maximum power point tracking methodologies for solar PV systems – A review', Renew and Sustain Energy Rev., 2017, 70, pp 1154–1177
[9] Mohapatra, A., Nayak, B., Das, P., Mohanty, KB.:' A review on MPPT techniques of PV system under partial shading condition', Renew and Sustain Energy Rev., 2017, 80, pp 854–867
[10] Guo, L., Meng, Z., Sun, Y., Wang, L.: 'A modified cat swarm optimization based maximum power point tracking method for photovoltaic system under partially shaded condition', Energy 2018, 144, pp 501-514.
[11] Wu, Z., Yu, D., Kang, X.:' Application of improved chicken swarm optimization for MPPT in photovoltaic system', Optimal Control Applications and Methods journal., 2018, pp 1–14
[12] Li, LL., Lin, GQ., Tseng, ML., Tan, K., Lim, MK.:' A maximum power point tracking method for PV system with improved gravitational search algorithm', Appl Soft Comput., 2018, 65, pp 333–348
[13] Gupta, S., Saurabh K.:' Modified artificial wolf Pack method for maximum power point tracking under partial shading condition'. Proc. Int. Conf. Power and Embedded Drive Control (ICPEDC), 2017, pp. 60-65
[14] Gupta, S., Saurabh, K.:' Modified artificial killer whale optimization algorithm for maximum power point tracking under partial shading Condition'. Proc. Int. Conf. Recent Trends in Electrical, Electronics and Computing Technologies, 2017, pp. 87-92
[15] Kok Soon, T., Mekhilef, S., Seyedmahmoudian, M., Horan, B., Than Oo, A., Stojcevski A.:' Improved differential evolution-based MPPT algorithm using SEPIC for PV systems under partial shading conditions and load variation', IEEE Transactions on Industrial Informatics, 2018
[16] Rocha, MV., Sampaio, LP., Da Silva, SAO.:' Maximum power point extraction in PV array under partial shading conditions using GWO-assisted beta method'. Proc. Int. Conf. Renewable Energies and Power Quality (ICREPQ'18), Salamanca. Spain, 2018, 1, (16), pp. 450-455
[17] Zakaria Said, S., Thiaw, L., Wekesa Wabuge, C.:' Maximum power point tracking of photovoltaic generators partially shaded using a hybrid artificial neural network and particle swarm optimization algorithm', International Journal of Energy and Power Engineering, 2017, 6, (6), pp 91-99
[18]Yu-Pei Huang, Xiang Chen, Cheng-En Ye. :' A hybrid maximum power point tracking approach for photovoltaic systems under partial shading conditions using a modified genetic algorithm and the firefly algorithm', International Journal of Photoenergy., 2018, pp 1-13
[19] Leian, C., Xiaodong, W.:' An enhanced MPPT method based on ANN-assisted sequential monte carlo and quickest change detection', Electrical Engineering and Systems Science: Signal Processing, 2018
[20] Keyrouz, F.:' Enhanced bayesian based MPPT controller for PV systems', IEEE Power and Energy Technology Systems Journal, 2018, 5, (1), pp 11-17
[21] Li, X., Wen, H., Chu, G., Yihua, H., Jiang L.:' A novel power-increment based GMPPT algorithm for PV arrays under partial shading conditions', Sol Energy, 2018, 169, pp 353–361
[22] Prince Winston, D., Praveen Kumar, B., Cynthia Christabel, S., Chamkha, AJ., Sathyamurthy, R.:' Maximum power extraction in solar renewable power system- a bypass diode scanning approach', Computers and Electrical Engineering., 2018, pp 1–15
[23] Ashouri-Zadeh, A., Toulabi, M., Dobakhshari, AS., Taghipour-Broujeni S, Ranjbar AM.:' A novel technique to extract the maximum power of photovoltaic array in partial shading conditions', Electr Power. Energy Systems., 2018, 101, pp 500–512
[24] Sen, T., Pragallapati, N., Agarwal, V., Kumar R.:'Global maximum power point tracking of PV arrays under partial shading conditions using a modified particle velocity-based PSO technique', IET Renew. Power Gener., 2018, 12, (5), pp 555-564
[25] Bishop, JW. :'Computer simulation of the effects of electrical mismatches in photovoltaic cell interconnection circuits', Sol Cells., 1988, 25, pp 73–89
[26]Quaschning, V., Hanitsch, R. Numerical simulation of current-voltage characteristics of photovoltaic systems with shaded solar cells. Sol Energy., 1996, 56, (6), pp 513–20
[27] Silvestre, S., Boronat, A., Chouder A.:' Study of bypass diodes configuration on PV modules', Appl Energy., 2009, 86, pp 1632–1640

Reactive Power Control for Power Improvement in Wind Farms Unsing STATCOM

Radia Abdelli
Faculty of Technologies,
Abderrahmane Mira Université
of Bejaia, 06000 Bejaia, Algeria
E-mail: Abdelli_radia@yahoo.fr

Ahcene Bouzida and Aimad Boudouda
Laboratoire de Recherche sur
l'Électrification des Entreprises
Industrielles (LREEI)
University de Boumerdes, 35000
Boumerdes, Algeria.
E-mail:ah_bouzida@univ-boumerdes.dz

M'hamed Ouadah
National Polytechnic School
of Algiers, 16200 Algiers,
Algérie
E-mail: ouadah@gmail.com

Abstract: **In this paper, a new control system for power compensation, voltage regulation and transient stability enhancement have been studied and discussed for wind conversion systems based on variable-speed doubly fed induction generators (DFIGs) under severe low voltage conditions. Calculations and simulations show the effectiveness of the STATCOM in providing the voltage regulation and increased transient stability.**
Keywords: Statcom, Transient stability, DFIG, Reactive power compensation, Voltage regulation.

1 INTRODUCTION

A static compensator (STATCOM) is a member of the flexible alternating current transmission system (FACTS) devices. It is a power-electronics-based regulating device which is composed of a voltage source converter and connected to AC current distribution networks. The voltage source is created from a DC super capacitor. The STATCOM exchange reactive power with the power network and usually installed in the electric networks with poor power factor or poor voltage regulation in order to improve the voltage stability [1].

The penetration of wind generation in the power network is the leading source of renewable energy in the power industry, Wind farms totalling hundreds, even thousands, of MW are now being considered [2-5]. The high penetration of wind renewable energy in the power systems, accuracy in predicting power system state under various conditions is really important. The reactive compensation has been used extensively in the power industry to provide voltage regulation, improve transient stability and aid in power system oscillation damping [6-10]. Marge capacitors and inductors have been replaced by static compensators (STATCOM) and recently, the development of the power electronic switches; STATCOMs are replacing more and more the SVCs for the same rating.

In this paper, the impact of STATCOM on stability of power system with connected wind turbine is studied. For this investigation, stability and voltage regulation are discussed. This work clarifies some important roles and concerns about power system quality improvement using the STATCOM.

2 CONVERSION SYSTEM PRESENTATION

The studied system is presented in Figure, where a wind turbine (20 MW) is connected to a local power grid via a power transformer (69 kV).

A studied system consists of integration of both wind energy system and the STATCOM based on three levels inverter in power system network. The wind turbine besed on a Doubly-Fed Induction Generator (DFIG) and a back-to-back PWM converter modelled by voltage sources. The stator winding of a DFIG is directly connected to the grid and the rotor one is fed at variable frequency through the back-to-back converter. The controlled DFIG allows extracting maximum energy from the wind for different speeds.

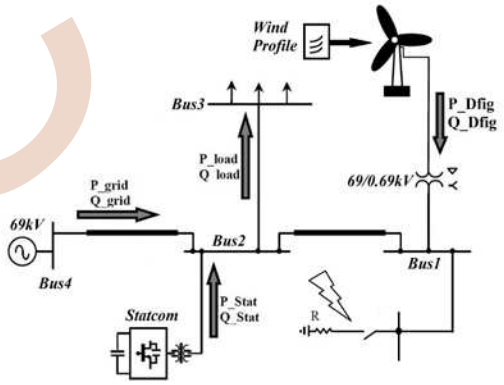

Figure 1 Studied Conversion System

3 DFIG MODEL AND CONTROL

The DFIG model in a dq0 reference frame is given by the following equations [5]:

$$\begin{cases} V_{sd} = R_s I_{sd} + \dfrac{d}{dt}\phi_{sd} - \omega_s \phi_{sq} \\ V_{sq} = R_s I_{sq} + \dfrac{d}{dt}\phi_{sq} - \omega_s \phi_{sd} \\ V_{rd} = R_r I_{rd} + \dfrac{d}{dt}\phi_{rd} - (\omega_s - \omega)\phi_{rq} \\ V_{rq} = R_r I_{rd} + \dfrac{d}{dt}\phi_{rq} - (\omega_s - \omega)\phi_{rd} \end{cases} \quad (1)$$

$$\begin{cases} \phi_{sd} = L_s I_{sd} + L_m I_{rd} \\ \phi_{sq} = L_s I_{sq} + L_m I_{rq} \\ \phi_{rd} = L_r I_{rd} + L_m I_{sd} \\ \phi_{rq} = L_r I_{rq} + L_m I_{sq} \end{cases} \quad (2)$$

The electromagnetic torque is given by

$$\begin{cases} C_e = PL_m(I_{rd}I_{sq} - I_{rd}I_{sd}) \\ C_e - C_r = J\frac{d}{dt}\Omega + F\Omega \end{cases} \quad (3)$$

where $\Phi_{sd}, \Phi_{sq}, V_{sd}, V_{sq}$ are respectively the stator flux and voltage components, $\Phi_{rd}, \Phi_{rq}, V_{rd}, V_{rq}$ are respectively rotor flux and voltage components, R_s, R_r are stator and rotor resistances, L_s, L_r are stator and rotor inductances, L_m is the mutual inductance ω_s, ω are the stator and the rotor pulsations, f is the friction coefficient, C_r is the load torque, J is total inertia, P is number of pole pairs and Ω is mechanical speed.

Direct Power Control (DPC) strategy is used in this work to control a DFIG, it's principle is the same with the principle of a DTC technique where the directly controlled variables are torque and flux, the unique difference in the DPC is that the controlled variables are the stator active and reactive powers.

In this strategy, the direct flux component is aligned with the stator flux vector [1][5][11] as follows:.

$$\phi_{sd} = \phi_s, \text{ and } \phi_{sq} = 0, \quad (4)$$

To simplify, we neglect the phase stator resistances, the stator voltages will be:

$$V_{sd} = 0, \text{ and } V_{sq} = V_s \cong \omega_s \phi_s, \quad (5)$$

By taking Eq.4 and Eq.5 into account in the DFIG model, we find the following equations giving a new generator model:

$$\begin{cases} V_{rd} = R_r I_{rd} + (L_r - \frac{L_m^2}{L_s})\frac{dI_{rd}}{dt} - g\omega_s(L_r - \frac{L_m^2}{L_s})I_{rq} \\ V_{rq} = R_r I_{rq} + (L_r - \frac{L_m^2}{L_s})\frac{dI_{rq}}{dt} - g\omega_s(L_r - \frac{L_m^2}{L_s})I_{rd} + g\frac{L_m V_s}{L_s} \end{cases} \quad (6)$$

$$\begin{cases} \frac{dI_{rd}}{dt} = -\frac{1}{\sigma T_r} I_{rd} + g\omega_s I_{rq} + \frac{1}{\sigma L_r} V_{rd} \\ \frac{dI_{rq}}{dt} = -\frac{1}{\sigma}(\frac{1}{T_r} + \frac{L_m^2}{L_s T_s L_r})I_{rq} + g\omega_s I_{rd} + \frac{1}{\sigma L_r} V_{rq} \end{cases} \quad (7)$$

Where $Tr = \frac{L_r}{R_r}; Ts = \frac{L_s}{R_s}; \sigma = 1 - \frac{L_m^2}{L_s L_r}$, σ is leakage factor, , g is the slip. T_S and T_R are stator and rotor time-constant The conventional DPC of a DFIG based on PID is shown in Figure 2.

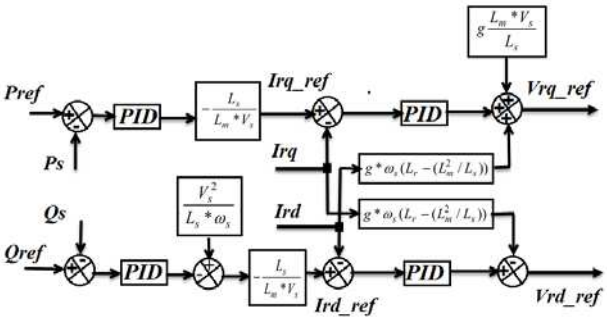

Figure 2 The conventional DPC of a DFIG based on PID

4 Reactive Compensation Principles

The principle and the benefits of the reactive power compensation benefits will be investigated in this paper. For self-commutated system, reactive compensation can be consederated as the connection of an ideal voltage source, either in shunt, by injecting reactive current or in series, in order to control directly the line current, ic [1][12].

In this work, the case of a shunt compensation is considered where the injected voltage is connected to the system via a coupling transformer. The connection of the Statcom is usually made at approximately the midpoint of the transmission line but connection near the load is also possible [3].

5 STATCOM MODELLING

The three-level inverter structure possesses the advantage that it has the same waveform quality as a two-level inverter converter operating at twice the switching frequency [12]. The three level voltage source converters differ from conventional voltage source converters in that it has four self-com mutated switches in each leg instead of the traditional as in fig. 3.

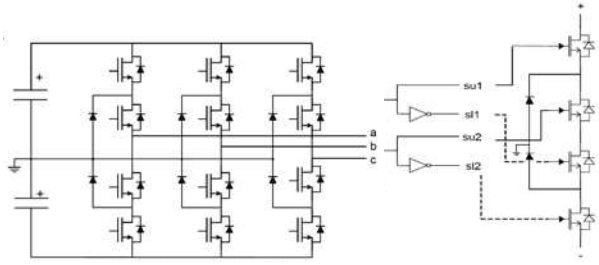

Figure 3 The three-level PWM signals of a three-levels converter

Table.1 gives the corresponding voltages to each control signal:

TABLE 1 INVERTER OUTPUT VOLTAGE

SU1	SU2	SL1	SL2	Vout
0	0	1	1	-Vd/2
0	1	1	0	0
1	1	0	0	Vd/2

6 STACOM MODELLING AND CONTROL

The reactive power control is divided into two parts [1-2][4][11][13]:

1- Generating the reactive power reference by the voltage regulation.

2- Generating the converter output voltage magnitude by the Power oscillation damping and the reactive current control.

The principle of reactive current control is based on the two-bus system detailed in (Fig.4), where V_{st} is the fundamental component of the STATCOM voltage, V_{PCC} is the voltage at the PCC, and X is the leakage inductance of the coupling transformer.

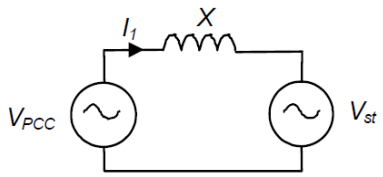

Figure.4. Two-bus system representing the fundamental components of STATCOM system

The two following equations give the active and reactive power flowing from the PCC to the STATCOM

$$\begin{cases} P = \dfrac{V_{PCC}^2 V_{st}}{X}\sin(\delta) \\ Q = \dfrac{V_{PCC}^2 - V_{PCC}V_{st}\cos(\delta)}{X} \end{cases} \quad (8)$$

By assuming the angle, δ, between the two voltages small in Eq.8, we find:

$$\begin{cases} P \cong \dfrac{V_{PCC}V_{st}}{X}\delta \\ Q \cong \dfrac{V_{PCC}(V_{PCC} - V_{st})}{X} \end{cases} \quad (9)$$

We can now see how the reactive current can be controlled easily by adjusting the relative voltage of the fundamental component of the V_{st}. In addition, this has shown that introducing a phase shift between the two voltages allows real power to flow and thus can be used to regulate the dc bus voltage. Derivation of the state space model of the real and reactive components of the current can then be used to determine the controller gains (Fig.5).

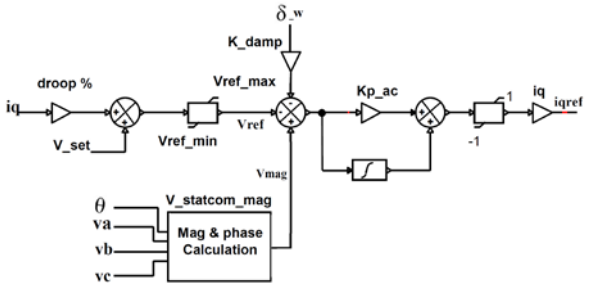

Figure 5 Reactive current control

The fundamental component of the current, I1 can be divided into two components, denoted i_d and i_q, respectively corresponding to that in phase with the V_{PCC} and that in quadrature to the voltage. The state-space representation of the system is given by:

$$\frac{d}{dt}\begin{bmatrix} i_d \\ i_q \end{bmatrix} = \begin{bmatrix} \dfrac{-R}{L} & \omega_0 \\ -\omega_0 & \dfrac{-R}{L} \end{bmatrix}\begin{bmatrix} i_d \\ i_q \end{bmatrix} + \frac{1}{L}\begin{bmatrix} V_{std} \\ V_{stq} \end{bmatrix} - \frac{1}{L}\begin{bmatrix} V_{PCC} \\ 0 \end{bmatrix} \quad (10)$$

Where, R is the lumped losses, L is the leakage inductance, and ω_0 is the nominal system frequency. d and q denote respectively the components in phase with and quadrature to the V_{PCC} space vector. we can denote that there is no quadrature component of V_{PCC}.

The regulation of the direct bus voltage is done by imposing a small phase shift between V_{PCC} and the STATCOM voltage. This phase shift is the output of a PI block that controls an error between the Vdc and its reference value. The sum of the obtained phase shift and the adjusted PLL angle is used in the STATCOM voltage transformation to phase quantities (Fig.6).

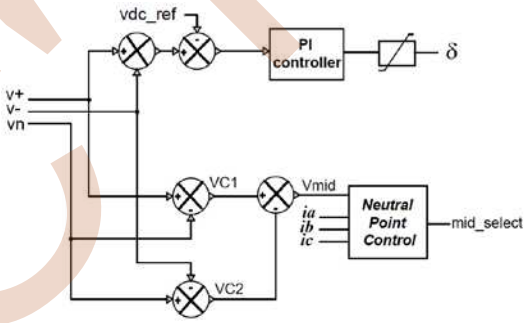

Figure 6 Dc bus control

The transfer function of Eq.11 gives a linear relation between a change in the dc voltage a phase shift:

$$\frac{\Delta V_{dc}(s)}{\Delta\delta(s)} = \frac{3m^2\omega_0 L V_{dc0}}{CL^2s^3 + 2RLCs^2 + (\omega_0^2L^2C + R^2C + 3m^2L) + 3m^2R} \quad (11)$$

Where: V_{dco} is the nominal DC voltage and m is the modulation index.

Reactive Compensator control

The voltage regulation control uses a droop characteristic in order to find the reference voltage. The benefits of this characteristic consist of promote stable operation, prevent the compensator from operating always at its limits and lend itself to sharing of compensation between different reactive power sources.

Fig.7 shows the droop characteristic where the set point is *1.0 pu* with the droop which allows the reference voltage to varying.

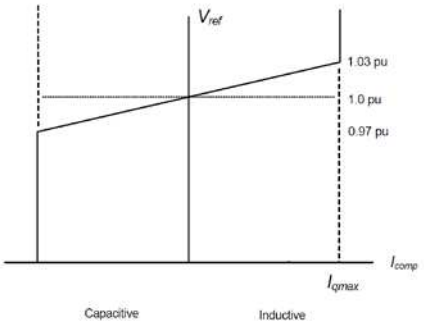

Figure 7 Statcom strategy control

The reactive power control is based on a PI compensator that generates the reference reactive current based on the error between the ac system reference and the magnitude of the positive sequence component. The droop characteristic produces the reference voltage based upon the amount of reactive compensation provided and varies from its nominal value to the upper and lower limit which is set by the slope of the line. The $\Delta\omega$ signal can be added to the voltage reference in order to realize an increase in the damping of the power system oscillations. The reactive compensation control block is given in detail here:

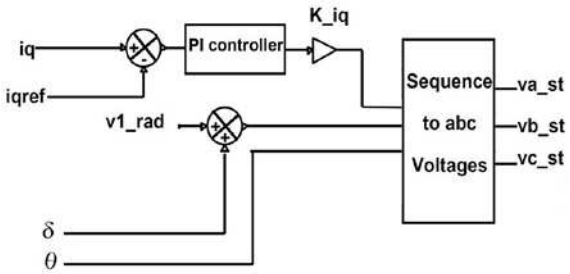

Figure 8 reactive current control

The simulation block diagram of the control strategy is depicted in Figure 9. The required quantities values for compensation are calculated using three phase supply voltages and line currents. It controls the output voltage of

STATCOM. The reference sinusoidal signal is produced by the PLL circuit using line to line supply voltages. Reference sinusoidal voltage will have a same phase shift with the corresponding supply voltage. The phase shift controls the real power flow to balance the converter.

Power losses and dc link capacitor voltages regulation is made using PI controllers as shown in the scheme (Figure 9). The obtained phase shift amount to reference voltage, the swapping algorithm is also applied to balance DC bus voltages. and then, STATCOM control signals are obtained by a PWM strategy.

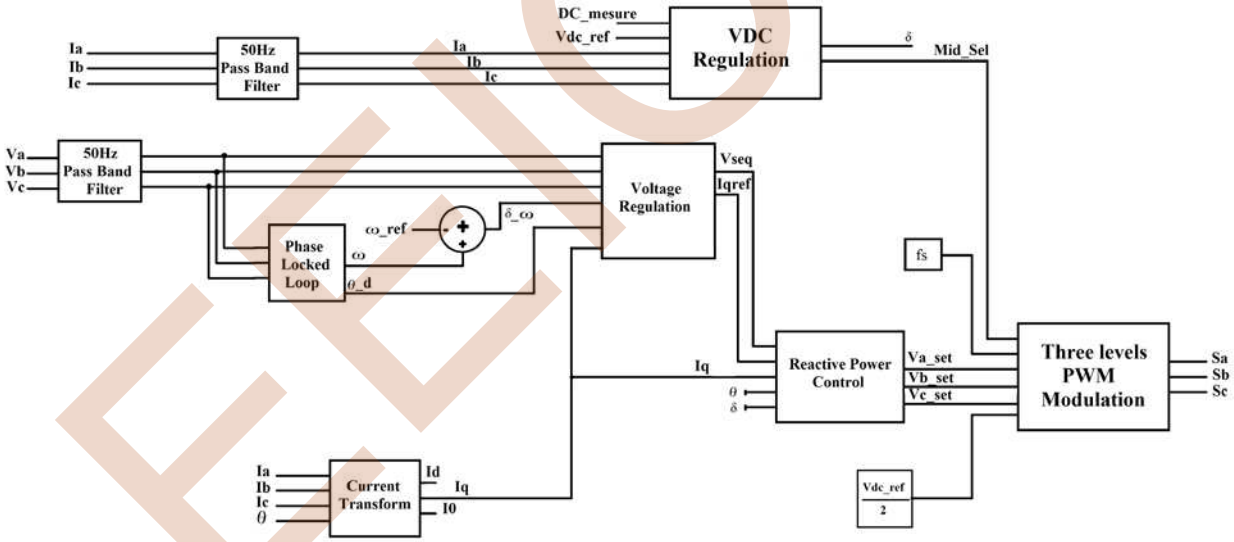

Figure 9 Statcom strategy control

7 Simulation Results

In this section, a comparison between the different quantities of the studied system during faulty conditions are presented and discussed, these simulation results of different quantities are

obtained and compared with and without STATCOM super capacitor with a wind turbine model. Active and reactive power, voltages and currents are calculated at different buses. The simulation results are given in Figures 10 to 19.

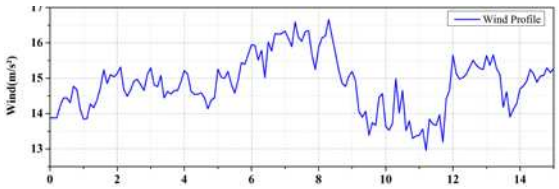

Figure 10 Wind speed profile

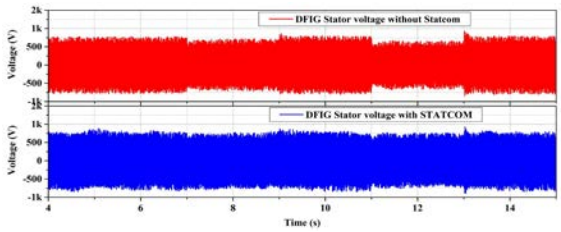

Figure 11 DFIG Stator output voltage during three phase fault

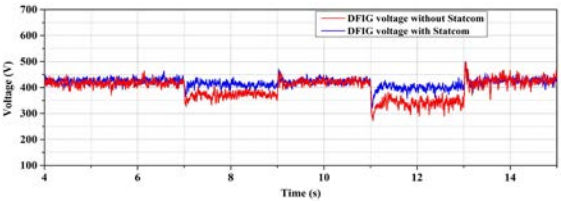

Figure 12 DFIG RMS output voltage during three phase fault

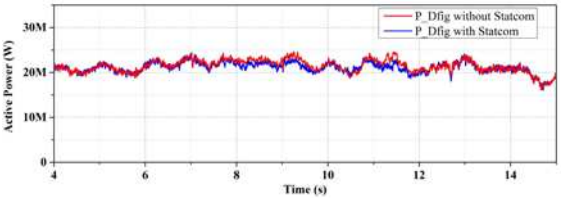

Figure 13 DFIG injected active power during three phase fault

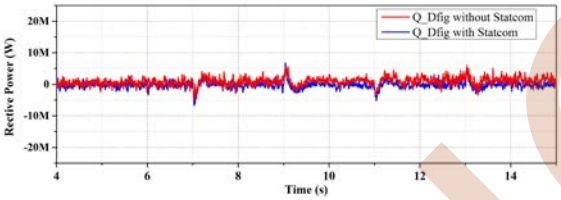

Figure 14 DFIG injected reactive power during three phase fault

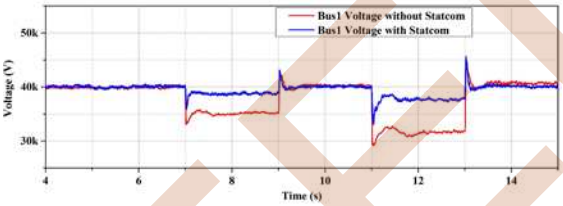

Figure 15 Bus1 RMS output voltage during three phase fault

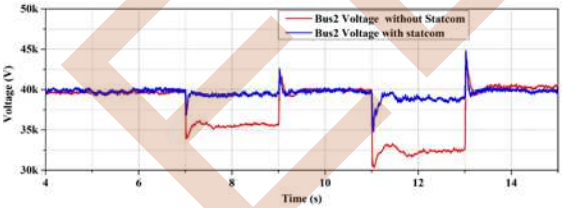

Figure 16 Bus2 RMS output voltage during three phase fault

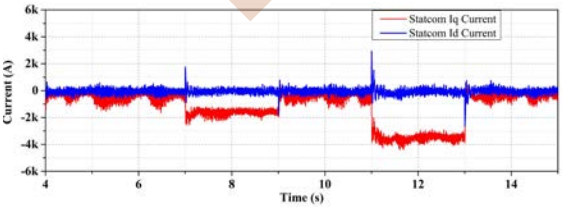

Figure 17 STATCOM Id and Iq currents during three phase fault

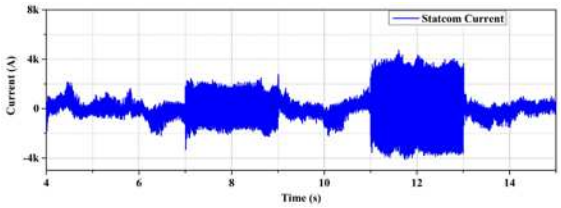

Figure.18 STATCOM injected current during three phase fault

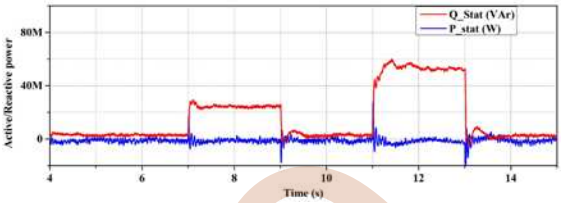

Figure 19 Active and reactive power injected by the STATCOM during three phase fault

Figures 11 to 14 show that the DFIG behaviour has been improved especially during fault with a contribution of the STATCOM, where we notice an improvement the voltage RMS of about 25% without STATCOM to 2.4% with a STATCOM contribution. We notice from Fig.13 and Fig.14 that the active and reactive powers follow their references. It can be observed that, STATCOM can mitigate the voltage dip and current surges in the DFIG and different buses connected to PCC voltage (Fig.15 and Fig.16).

The STATCOM power corresponds directly to the injected current to the grid (Fig.17 to Fig.19), the principle is that during the first and second fault stages, the STATCOM detects the new voltage amplitude and generates the necessary reactive power to maintain the voltage closed to the reference value. Fig.19 shows how the reactive power is injected by STATCOM and the active power is maintained zero.

8 CONCLUSION

By analyzing the obtained simulation results, we can conclude that STATCOMs improve the connection of wind convresion systems to the grid by helping the wind generator to ride through low voltage conditions.

Finally, we can improve the power quality and the transient stability by optimizing the parameters of the STATCOM such as increasing capacity and critical clearing time.

REFERENCES

[1] SHAHNIA, F., RAJAKARUNA, S. & GHOSH, A. 2015. Static compensators (STATCOMs) in power systems, Springer.
[2] CASTRO, L. M., ACHA, E. & FUERTE-ESQUIVEL, C. R. 2013. A novel STATCOM model for dynamic power system simulations. IEEE Transactions on Power Systems, 28**,** 3145-3154.
[3] WARTANA, I. M., SINGH, J. G., ONGSAKUL, W. & SREEDHARAN, S. 2013. Optimal placement of FACTS controllers for maximising system loadability by PSO. International Journal of Power and Energy Conversion, 4**,** 9-33.
[4] BALIKCI, A. & AKPINAR, E. 2015. A multilevel converter with reduced number of switches in STATCOM for load balancing. Electric Power Systems Research, 123**,** 164-173.
[5] AMRANE, F. & CHAIBA, A. 2016. A Novel Direct Power Control for Grid-Connected Doubly Fed Induction Generator Based on Hybrid Artificial Intelligent Control with Space Vector Modulation. Revue

Roumaine des Sciences Techniques-Serie Electrotechnique et Energetique, 61**,** 263-268.
[6] WANG, L. & TRUONG, D.-N. 2013. Stability enhancement of DFIG-based offshore wind farm fed to a multi-machine system using a STATCOM. IEEE transactions on power systems, 28**,** 2882-2889.
[7] TAYYEBIFAR, T., SHAKER, M. & AGHABABAIE, M. Performance comparison of STATCOM versus SVC to improve reactive power control in wind power based DFIG under short circuit fault. Ecological Vehicles and Renewable Energies (EVER), 2014 Ninth International Conference on, 2014. IEEE, 1-7.
[8] ANANTH, D. & KUMAR, G. N. 2015. Mitigation of voltage dip and power system oscillations damping using dual STATCOM for grid connected DFIG. Ain Shams Engineering Journal.
[9] VARMA, R. K., RAHMAN, S. A. & VANDERHEIDE, T. 2015. New control of PV solar farm as STATCOM (PV-STATCOM) for increasing grid power transmission limits during night and day. IEEE transactions on power delivery, 30**,** 755-763.
[10]HEYDARI-DOOSTABAD, H., KHALGHANI, M. R. & KHOOBAN, M. H. 2016. A novel control system design to improve LVRT capability of fixed speed wind turbines using STATCOM in presence of voltage fault. International Journal of Electrical Power & Energy Systems, 77**,** 280-286.
[11] NIAN, H., CHENG, P. & ZHU, Z. 2016. Coordinated direct power control of DFIG system without phase-locked loop under unbalanced grid voltage conditions. IEEE Transactions on Power Electronics, 31**,** 2905-2918.
[12] JAVADI, M. S. 2011. Flicker mitigation approach based on three-level statcom. International journal of multidisciplinary sciences and engineering, 2.
[13] NOURELDEEN, O., RIHAN, M. & HASANIN, B. 2011. Stability improvement of fixed speed induction generator wind farm using STATCOM during different fault locations and durations. Ain Shams Engineering Journal, 2**,** 1-10.
[14] OLAMAEI, J., JAVAN, J., YAVARTALAB, A. & KHEDERZADEH, M. 2012. Advanced control of FACTS devices for improving power quality regarding to wind farms. Energy Procedia, 14**,** 298-303.

Direct Torque Control based on Fuzzy Switching Table of IM for PV Pumping System

Sofia Lalouni Belaid, Sahri Younes
Laboratoire de Technologie Industrielle et de l'Information (LTII),
Faculté de Technologie, Université de Bejaia, Algérie
lalouni_sofia@yahoo.fr

Abstract— **This paper presents an improved direct torque control (DTC) based on fuzzy logic switching table of induction motor (IM) for photovoltaic pumping application. Conventional DTC provides high performances comparing to the field oriented control but its major drawback is the high torque and flux ripples generated by the hysteresis comparators. To overcome this problem, fuzzy switching table is used to replace the hysteresis controllers and the conventional switching tables. Using Fuzzy direct torque control (FDTC), the inputs (torque error, flux error and stator flux angle) can divide into more subsections instead of hysteresis controllers state's (0 and 1), which result in optimal selection of the voltage space vector. Simulation was performed in MATLAB/SIMULINK to validate the effectiveness of the proposed FDTC, the results show a significant reduction in torque and flux ripples and in current total harmonic distortion.**

Keywords: **PV energy, Induction motor (IM), Direct torque control (DTC); Fuzzy Direct Torque control (FDTC);**

I. INTRODUCTION

The increasing of the world energy demand encourage a lot of investments in renewable energy solutions. One of the most used renewable energy is photovoltaic energy. This latter is clear, free, and abundant, has less environmental impact and proved to be an economical renewable energy source in many applications. The most used application is for water pumping. However, the PV pumping system efficiency is still low; then, maximum power point tracking (MPPT) control must be introduced in order to maximize the efficiency of the photovoltaic array. Also, several authors were interested in the control of the photovoltaic pumping system in order to improve performance of such system [1,2]

Direct Torque Control (DTC) of induction motors is proposed as a new fast response technique, robust and efficient control technique [3,4]. Good dynamic performances has made DTC popular and widely used in industrial applications [5,6]. The conventional DTC (CDTC) suffers from disadvantages related to the high torque and flux ripples due to the hysteresis controllers especially at low speed [3,6], that generate mechanical vibrations and undesirable acoustic noise, and therefore, deteriorates the induction motor performances [7]. The variable switching frequency causes switching losses and current distortions [7].

Several solutions were proposed in many papers to improve the CDTC. Some authors propose improvements by using multi level inverters [8], but this solution results in high switching losses and increases cost [9,10]. Other researcher propose improvement by using Space Vector Modulation (SVM) control [11] that needs several motor parameters and increases the complexity system control [9]. Application of AI techniques like Fuzzy logic controller in electrical drives gained great attention in recent years [3-9]. In Ref[3], the fuzzy logic controller proved a significant reduction in torque and flux undulations.

In this paper, direct torque control based on fuzzy logic witching table of the induction motor is used to improve the performances of the photovoltaic umping system. The proposed control design doesn't depend on accurate mathematical model of the system [5]. Through the simulation results, performances improvement are shown, significant reduction in torque / flux ripples and current THD.

II. PV PUMPING SYSTEM MODELLING

A. *Modelling of PV array and MPPT Control*

Diverse models of PV array were presented in the literature. [1,2]. Those models vary according to the calculation method, the used parameters and precision. The model taken in this paper is developed in [1], the photovoltaic current I_{pv} is given by the following equation:

$$I_{pv} = I_{sc}.\{1 - K_1[\exp(K_2 V_{pv}^{K_3}) - 1]\} \quad (1)$$

Where, K_1= 0.01175 is determined experimentally and the coefficients K_2 and K_3 are defined as:

$$K_2 = \frac{\ln\left[\frac{1+K_1}{K_1}\right]}{V_{oc}^{K_3}} \quad (2)$$

$$K_3 = \left[\frac{\ln\left[\frac{I_{sc}(1+K_1) - I_{mpp}}{K_1 I_{sc}} \right]}{\ln\left[\frac{1+K_1}{K_1} \right]} \right] \Bigg/ \ln\left[\frac{V_{mpp}}{V_{oc}} \right] \quad (3)$$

Where V_{mpp} and I_{mpp} are PV voltage and current at maximum operation, V_{oc} is the open circuit voltage and I_{sc} the short circuit current.

The photovoltaic parameters (V_{pv} and I_{pv}) change, when environmental conditions (G and T) varie, according to the following equations:

$$V_{pv,new} = V_{pv} - \beta_{oc}\Delta T_c - R_s \Delta I_{pv} \quad (4)$$

$$I_{pv,new} = I_{pv} + \alpha_{sc}\left(\frac{G}{G_{stc}}\right)\Delta T_c + \left(\frac{G}{G_{stc}} - 1\right) I_{sc,stc} \quad (5)$$

Where: ΔT_c the temperature variation, α_{sc} and β_{oc} are respectively I_{pv} and V_{pv} temperature coefficients and R_s the cell resistance.

The PV characteristics $P_{pv}(V_{pv})$ are presented in Fig.1 for different levels of irradiance, the non-linear nature of the PV array is shown from those characteristics. Then, an MPPT control must be introduced to force the PV generator to always delivers the maximum available power. Fuzzy logic control (FLC) is used in this paper for MPPT purpose [1,2].

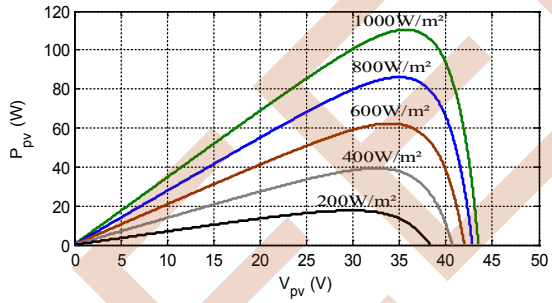

Figure 1. PV array characteristics $P_{PV}(V_{PV})$.

B. Fuzzy logic MPPT controller

The fuzzy MPPT controller (FLC) has better advantages over conventional methods; it is robust, adaptive and doesn't need exact mathematical models of the system [1], but to have a good control, experience of designer is required to choose fuzzy parameters [4]. The fuzzy logic MPPT controller measures the PV array voltage, current and calculates PV power, then perturbs the operating voltage with either positive or negative increment ($\Delta V_{pv,ref}$) in a small or respectively large way in the direction which makes possible to increase the power P_{pv}. The fuzzy logic MPPT controller structure is shown in Fig. 2. The MPPT fuzzy logic controller consists of three main modules: the fuzzification process, the inference and the defuzzification process. The inputs variables are (ΔP_{pv} and ΔV_{pv}) and output is ($\Delta V_{pv,ref}$). Those variables are triangular and have seven fuzzy subsets. The membership functions values are assigned to the linguistic variables (BN (Big Negative), MN (Medium Negative), SN (Small Negative), Z (Zero), SP (Small Positive), MP (Medium Positive), and BP (Big Positive)).The control rules are indicated in Table.1. The fuzzy inference used is Mamdani's method based on min-max decision and a centre of gravity is used for defuzzifizcation [1,2].

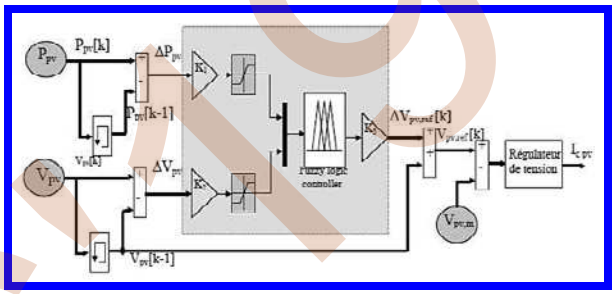

Figure 2. Fuzzy MPPT controller structure.

TABLE 1. FUZZY CONTROLLER RULE FUZZY [2].

ΔPpv / ΔVpv	BN	MN	SN	Z	SP	MP	BP
BN	BP	BP	MP	Z	MN	BN	BN
MN	BP	MP	SP	Z	SN	MN	BN
SN	MP	SP	SP	Z	SN	SN	MN
Z	BN	MN	SN	Z	SP	MP	BP
SP	MN	SN	SN	Z	SP	SP	MP
MP	BN	MN	SN	Z	SP	MP	BP
BP	BN	BN	MN	Z	MP	BP	BP

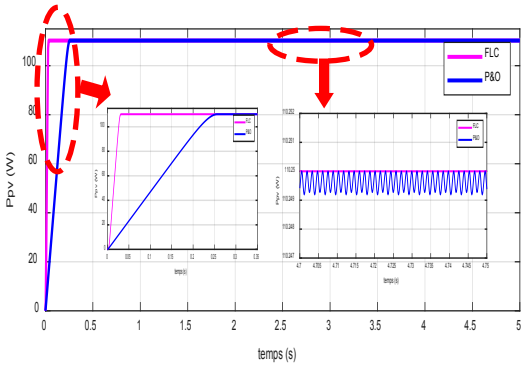

Figure 3. Photovoltaic power waveform with zoom.

The result of Fig.3 shows that the fuzzy MPPT controller (FLC) gives us a fast response since it reaches its optimal value at 0.027 s compared to (P&O) methods which

required 0.25s to track the maximup of power and presents a lot of oscillations at steady state.

B. Induction machine modeling

The mathematical dynamic model of the IM in the stator frame is described by eq. (6).

$$\begin{cases} V_{s\alpha} = (R_s + L_s \frac{d}{dt}) i_{s\alpha} + M \frac{di_{r\alpha}}{dt} \\ V_{s\beta} = (R_s + L_s \frac{d}{dt}) i_{s\beta} + M \frac{di_{r\beta}}{dt} \\ 0 = (R_r + L_r \frac{d}{dt}) i_{r\alpha} + M \frac{di_{s\alpha}}{dt} + \omega M i_{s\beta} + + \omega L_r i_{r\beta} \\ 0 = (R_r + L_r \frac{d}{dt}) i_{r\beta} + M \frac{di_{s\beta}}{dt} - \omega M i_{s\alpha} - \omega L_r i_{r\alpha} \end{cases} \quad (6)$$

Where $V_{s\alpha}$, $V_{s\beta}$, $i_{s\alpha}$, $i_{s\beta}$, are α-β axis stator voltage and current respectively, $i_{r\alpha}$ and $i_{r\beta}$ are the rotor's currents along the α-β axis. Ω is the machine speed (pΩ=ω), R_s, R_r, L_s, L_r, M *and* p are respectively, stator and rotor main resistances, inductances, magnetizing inductance and pair pole number of the IM [11].

The electromagnetic torque developed by IM is function on the stator flux and currents and given by [3]:

$$T_e = \frac{3}{2} p(\varphi_{s\alpha} . i_{s\beta} - \varphi_{s\beta} . i_{s\alpha}) \quad (7)$$

The mechanical speed equation is given by the following Equation:

$$J . \frac{d\Omega}{dt} + f . \Omega = T_e - T_r \quad (8)$$

The opposed resistive torque *Tr* of the centrifugal pump is given by:

$$T_r = K_r \, \Omega^2 \quad (9)$$

Where: J, f and T_r are respectively the moment of inertia, the viscous friction coefficient and ($K_r = \frac{P_n}{\Omega_n^3}$) deponds on the nominal power and speed of the induction motor.

III. CONVENTIONAL DIRECT TORQUE CONTROL (DTC)

The direct torque control (DTC) of induction machines is initially proposed in 1985 by Takahashi and Depenbrock and after developed by Noguchi (1998) [11]; Its goal is the elimination of the PWM modulation block and internal current control loop by replacing them with a switching table. Using torque and rotor flux informations, the motor electromagnetic torque and rotor flux is controlled by selecting the optimal inverter switching states [6]. The bloc diagram of conventional DTC induction motor is shown in Fig. 4.

Using the inverter voltage vector (inverter's switching states) and the DC voltage, the stator voltage space vector components in the stationary reference frame (α,β) are calculated as follow [4]:

$$\begin{cases} v_{s\alpha} = \sqrt{\frac{2}{3}} V_{dc} (S_a - \frac{S_b + S_c}{2}) \\ v_{s\beta} = \sqrt{\frac{1}{2}} V_{dc} (S_b - S_c) \end{cases} \quad (10)$$

The (α,β) components of stator current space vector are calculated as follow:

$$\begin{cases} i_{s\alpha} = \sqrt{\frac{3}{2}} i_{sa} \\ i_{s\beta} = \frac{1}{\sqrt{2}} (i_{sb} - i_{sc}) \end{cases} \quad (11)$$

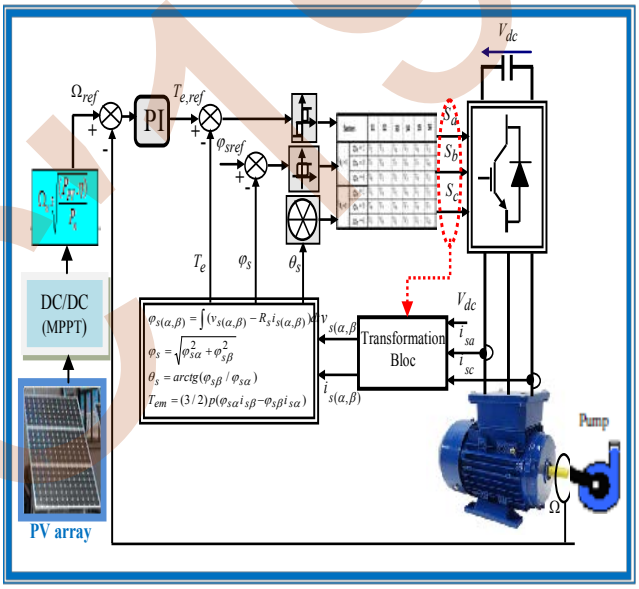

Figure.4: Block diagram of conventional direct torque control.

The stator flux vector is estimated from the measurements of the voltages and currents of the IM [7,9].

$$\begin{cases} \varphi_{s\alpha} = \int_0^t (v_{s\alpha} - R_s . i_{s_\alpha}) dt \\ \varphi_{s\beta} = \int_0^t (v_{s\beta} - R_s . i_{s_\beta}) dt \end{cases} \quad (12)$$

Then, the magnitude of the stator flux is calculated by [4]:

$$\varphi_s = \sqrt{\varphi_{s\alpha}^2 + \varphi_{s\beta}^2} \quad (13)$$

The switching table inputs are the errors between the reference and the estimated values of the stator flux and electromagnetic torque provided by respectively two and three levels hysteresis comparators. The torque and flux errors are defined as:

$$\begin{cases} \Delta\varphi_s = \varphi_{sref} - \varphi_s \\ \Delta T_e = T_{eref} - T_e \end{cases} \quad (14)$$

The selected sector is based upon the stator flux angle (θ_s) by dividing flux in (α, β) plane into six sectors of 60^0 each [1]. The stator flux angle is calculated as follow [3]:

$$\theta_s = \tan^{-1}\left(\frac{\varphi_{s\beta}}{\varphi_{s\alpha}}\right) \quad (15)$$

The sectors can be numerically determined by the following equation:

$$(n-2)\frac{\pi}{3} < \theta_n < (n-1)\frac{\pi}{3} \quad (16)$$

Where n the number of sector, n=1,2 ,...,6.

Finally, an appropriate inverter voltage vector is selected from the switching table (Table 1) according to the outputs of the comparators and the stator flux sector.

Table 1. The switching table of CDTC [9]

θs		θ1	θ2	θ3	θ4	θ5	θ6
$\Delta\varphi_s$	ΔT_e						
1	1	V_2	V_3	V_4	V_5	V_6	V_1
	0	V_7	V_0	V_7	V_0	V_7	V_0
	-1	V_6	V_1	V_2	V_4	V_4	V_5
0	1	V_3	V_4	V_5	V_6	V_1	V_2
	0	V_0	V_7	V_0	V_7	V_0	V_7
	-1	V_5	V_6	V_1	V_2	V_3	V_4

The selected voltage vector will be applied to the induction motor in order to control the rotor flux and torque and to maintain the rotor flux vector extremity in a circular trajectory [9]. The switching table (Table.1), includes eight vectors : $V_0(000)$, $V_1(100)$, $V_2(110)$, $V_3(010)$, $V_4(011)$, $V_5(001)$, $V_6(101)$, $V_7(111)$. Where V_1 to V_6 are the active vectors and V_0,V_7 the zero voltage ones.

IV. DTC BASED ON FUZZY LOGIC (FDTC)

To improve the PV pumping system performances and to minimize flux and electromagnetic torque ripples, intelligent controllers based on fuzzy logic are used. Those controllers' design doesn't depend on accurate mathematical model of the system and they can handle non linearity of arbitrary complexity [5].

The conventional DTC drawback can be minimized by replacing the hysteresis comparators and switching table by fuzzy inference system. In this system, flux error, torque error and flux angle are considered as inputs of fuzzy logic controller [7].Using Fuzzy logic DTC controller (FDPC) we can divide the flux error and the torque error into more subsections instead of two states (0, 1) of the hysteresis controller [5]. Then, the generated switching vector will be based on the different levels of flux and torque errors and the sector that is selected. The block diagram of the fuzzy inference system is shown in Fig.5.

The stator flux error input is characterized by three linguistic variables: negative (N), zero (Z) and positive (P) . The torque error, need to be minimized, is depicted by five linguistic variables: positive large (PL), positive small (PS), zero (Z), negative small (NS) and negative large (NL). The stator flux angle position (θ_s) is divided into six 12 sectors each of 30_0 and represented by twelve fuzzy sets (θ_1-θ_{12}) distributed between 0^0 and 360^0. Each control rule can be formulated as follows:

If ΔTe is X_i & $\Delta\varphi$s is Y_i & θs is θ_i then V is V_i.

Where X_i, Y_i and θ_i are the fuzzy sets of ΔTe, $\Delta\varphi$s and θs. The rule table of the proposed strategy is indicated in Table.2, it consists on 144 rules [3, 9]. The fuzzy inference is carried out by Mamdani's method and the maximum criterion is used for defuzzification. The outputs is applied to switches S_a, S_b and S_c [3].

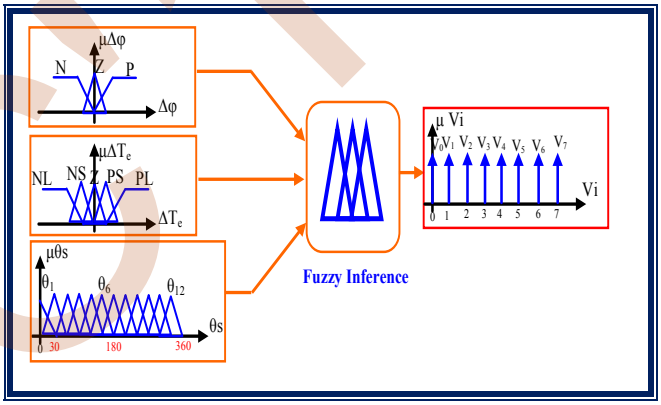

Figure .5 : Inputs and output variables of fuzzy inference system.

Table 2. Fuzzy rule base of FDTC [3]

θ		θ1	θ2	θ3	θ4	θ5	θ6	θ7	θ8	θ9	θ10	θ11	θ12
e_T	e_φ												
PL	P	V_1	V_2	V_2	V_3	V_3	V_4	V_4	V_5	V_5	V_6	V_6	V_1
	Z	V_2	V_2	V_3	V_3	V_4	V_4	V_5	V_5	V_6	V_6	V_1	V_1
	N	V_2	V_3	V_3	V_4	V_4	V_5	V_5	V_6	V_6	V_1	V_1	V_2
PS	P	V_1	V_2	V_2	V_3	V_3	V_4	V_4	V_5	V_5	V_6	V_6	V_1
	Z	V_2	V_3	V_3	V_4	V_4	V_5	V_5	V_6	V_6	V_1	V_1	V_2
	N	V_3	V_3	V_4	V_4	V_5	V_5	V_6	V_6	V_1	V_1	V_2	V_2
ZE	P	V_0	V_0	V_0	V_0	V_0	V_0	V_0	V_0	V_0	V_0	V_0	V_0
	Z	V_0	V_0	V_0	V_0	V_0	V_0	V_0	V_0	V_0	V_0	V_0	V_0
	N	V_0	V_0	V_0	V_0	V_0	V_0	V_0	V_0	V_0	V_0	V_0	V_0
NS	P	V_6	V_6	V_1	V_1	V_2	V_2	V_3	V_3	V_4	V_4	V_5	V_5
	Z	V_0	V_0	V_0	V_0	V_0	V_0	V_0	V_0	V_0	V_0	V_0	V_0
	N	V_4	V_5	V_5	V_6	V_6	V_1	V_1	V_2	V_2	V_3	V_3	V_4
NL	P	V_6	V_6	V_1	V_1	V_2	V_2	V_3	V_3	V_4	V_4	V_5	V_5
	Z	V_5	V_6	V_6	V_1	V_1	V_2	V_2	V_3	V_3	V_4	V_4	V_5
	N	V_5	V_5	V_6	V_6	V_1	V_1	V_2	V_2	V_3	V_3	V_4	V_4

V. SIMILATION RESULTS AND DISCUTION

The PV pumping system is composed of (11) photovoltaic array of 110W connected in parallel. The bloc diagram of fig.4 associated to fig.5 are used to verify the performance

of the proposed fuzzy direct torque control of the induction motor with FLC optimization. The reference speed is variable with the variation of the PV power obtained from the fuzzy MPPT algorithm. The flux and V_{dc} reference values are Φ_{ref} = 0.8Wb and V_{dc} = 570V. In order to test the robustness of the proposed algorithm, conventional DTC and proposed FDTC techniques were developed and tested using Matlab/Simulink, the IM parameters are given in [8]. Initially, the irradiance level is fixed to 1000W/m², change to 700W/m² at t=2sec then returns to its initial value at t=4sec, while the temperature is fixed to 25°C intill t=6sec where it varies to 15 °C and come back to its initial value at t=8sec. The motor is started on load with pump resistive torque. The speed response of the IM controlled with the Fyzzy direct torque control (FDTC) tracks perfectly its reference value abtained from the PV power (fig.6) as shown in fig.7. Torque response for both control strategies (DTC and FDTC) is shown in figs. 8 and 9, comparing curves illustrates clearly a significant reduction in torque ripples using fuzzy logic controller, as shown in figure 10.

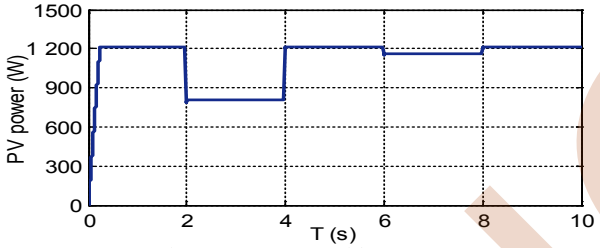

Figure.6: PV power with Fuzzy MPPT.

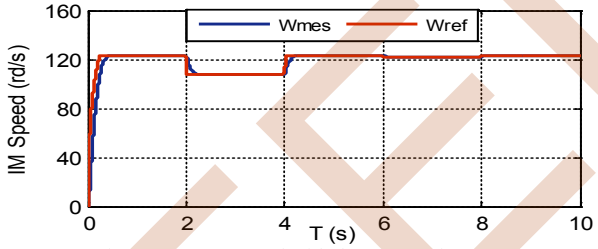

Figure.7: Motor speed with the proposed FDTC.

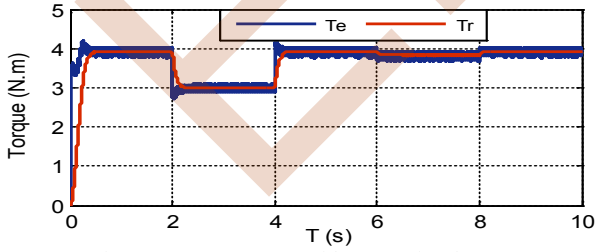

Figure .8: Motor Torque with conventional DTC.

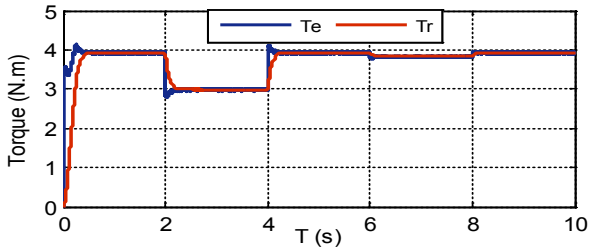

Figure .9: Motor Torque with the proposed FDTC.

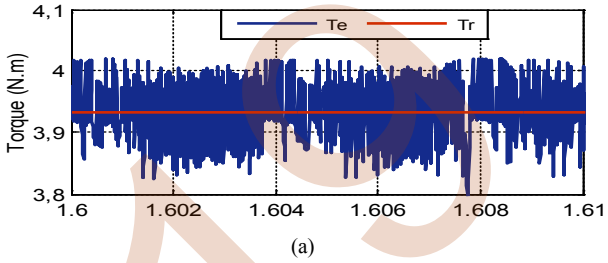

(a)

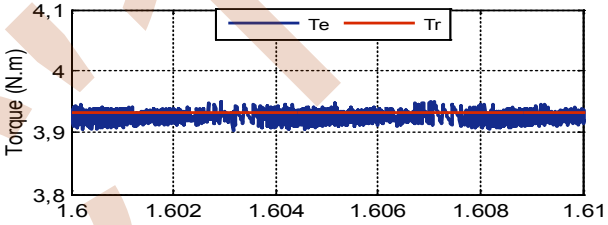

(b)

Figure .10: Motor Torque zoom for both control strategies (a) CDTC and (b)FDTC.

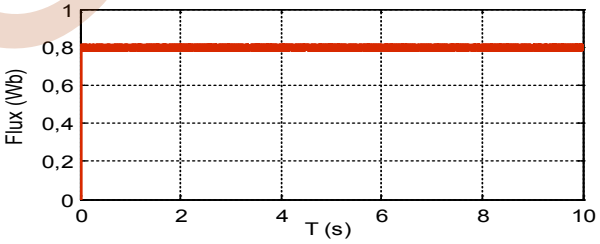

Figure .11: Stator flux response with Conventional DTC.

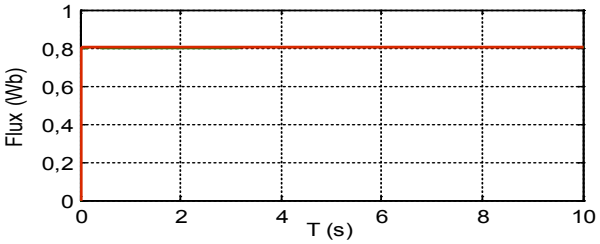

Figure .12: Stator flux response with the proposed FDTC.

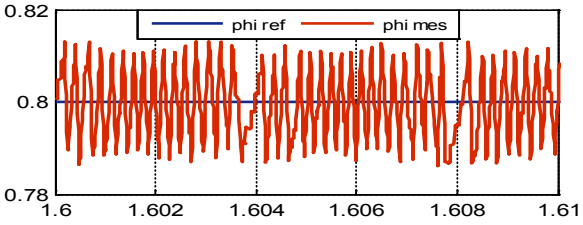

(a)

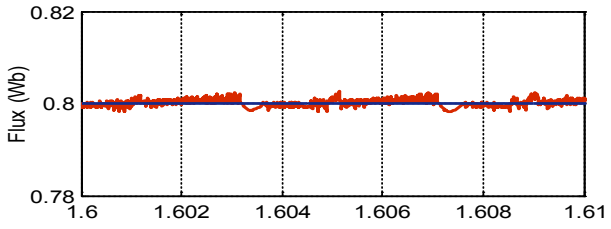

(b)

Figure .13: Zoom in stator flux (a)CDTC and (b)FDTC.

Figs. 11 and 12, show the stator flux magnitude response for the conventional technique and the improved one, the estimated stator flux tracks closely its reference value, the zooms of those figures show that the FDTC gives us a better response with less ripples (fig.13).

As we ca seen in Figs.14 and 15, the stator flux trajectory is kept circular for both control techniques, smooth trajectory is observed using the proposed FDTC compared to conventional DTC. The stator current waveform for (DTC and FDTC) is sinusoidal is sinusoidal (fig.16) with a THD respectively of 2.49 % and 0.65 % .

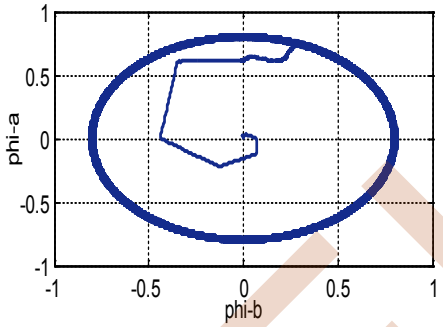

Figure .14: Stator flux trajectory of CDTC.

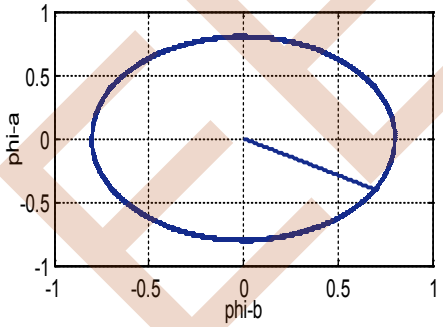

Figure .15: Stator flux trajectory of FDTC.

VI. CONCLUSION

This paper has presented fuzzy direct torque control of IM for PV pumping application. The optimal operation of the system was insured by fuzzy logic MPPT controller in order to speed-up the procedure of reaching the accurate maximum PV power. The proposed FDTC technique is based on replacing the hysteresis controllers and the look-up table by a fuzzy switchin table. Simulation has been performed under Matlab/Simulink to compare the proposed FDTC with the conventionnal DTC. The obtained results illustrate clearly a considerable reduction in torque ripples, consequently fewer problems for the motor (mechanical vibration and heating), and smooth flux trajectory. The harmonics in stator current are significantly reduced; a THD of 0.65 % is obtained using fuzzy direct torque control.

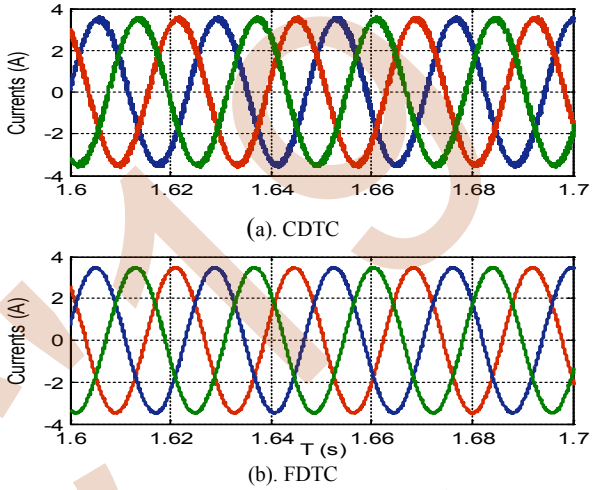

(a). CDTC

(b). FDTC

Figure .16: Zoom of stator current waveform.

REFERENCES

[1] S. Lalouni, d. Rekioua, t. Rekioua, E. Matagne, "Fuzzy logic control of stand-alone photovoltaic system with battery storage", Journal of Power Sources, Vol. 193, pp:899–907, 2009.

[2] S .Lalouni, d. Rekioua, "control of photovoltaic water pumping system with battery storage", International Journal Of Electrical Engineering & Technology (IJEET), vol. 4, issue 1, pp. 190-199, 2013.

[3] Sudheer H, Kodad SF, Sarvesh B, "Direct Torque and Flux control of Induction Machine using Fuzzy Logic controller", International Conference on Advances in Electrical, Electronics, Information, Communication and Bio-Informatics (AEEICB16), pp :1-5. 2016.

[4] A. Idir & M. Kidouche, Direct Torque Control of Three phase Induction Motor drive using Fuzzy Logic controllers for low Torque ripple, International Conference on Control, Engineering & Information Technology (CEIT'13), Proceedings Engineering & Technology - vol.2, pp.78-83, 2013.

[5] C.Vignesh,S.Shantha Sheela,E.Chidam Meenakchi Devi,R.Balachandar, Direct Torque Control of Induction Motor Using Fuzzy Logic Controller, International Refereed Journal of Engineering and Science (IRJES),vol. *3, issue 2 (January 2014), pp.56-61, 2014.*

[6] W. Ayrir, M. Ourahoua, B. El Hassounia, A. Haddi, Direct torque control improvement of a variable speed DFIG based on a fuzzy inference system, Mathematics and Computers in Simulation, May 2018, DOI: 10.1016/j.matcom.2018.05.014

[7] Najib El Ouanjli, Saad Motahhir, Aziz Derouich, Abdelaziz El Ghzizal, Ali Chebabhi, Mohammed Taoussi, Improved DTC strategy of doubly fed induction motor using fuzzy logic Controller, Energy Reports 5;pp.271–279, 2019.

[8] Salah tamalouzt, performances of direct reactive power control Technique applied to three level-inverter under Random behavior of wind speed *Rev. Roum. Sci. Techn.– electrotechn. Et energ.* vol. **64**, *1*, pp. 33–38, Bucarest, 2019

[9] Sudheer H., Kodad S.F, Sarvesh.Improvements in direct torque control of induction motor for widerange of speed operation using fuzzy logic, Journal of Electrical Systems and Information Technology 2017.

[10] Saber Krim, Soufien Gdaim, Abdellatif Mtibaa and Mohamed Faouzi Mimouni, Design and Implementation of Direct Torque Control Based on an Intelligent Technique of Induction Motor on FPGA, J Electr Eng Technol.; vol.10: pp.30-40, 2015.

[11] Idir Issad, Kassa Idjdarene, Sofia Lalouni, Direct Torque Control Using Space Vector Modulation of Wind Pumping System with Storage, *Rev. Roum. Sci. Techn.– Électrotechn. et Énerg.* vol. **63**, *4*, pp. 397–402, Bucarest, 2018.

An Optimal energy management strategy to increase the autonomy of a fuel cell hybrid electric vehicle

Said Belhadj
Laboratoire de Maitrise des Énergies Renouvelables Renouvelables
University of Bejaia
Bejaia, Algeria
belhadj_said_1976@yahoo.fr

Kaci Ghedamsi
Laboratoire de Maitrise des Énergies Renouvelables Renouvelables
University of Bejaia
Bejaia, Algeria
kghedamsi@yahoo.fr

Karim Belmokhtar
Nergica
Gaspé, Canada
kbelmokhtar@nergica.com

Abstract*—This paper presents a new proposed energy management strategy (EMS) based on the using of photovoltaic solar panels as a secondary source for a Fuel Cell Electric Vehicle (FCEV). This solution is considered as a very attractive option for electric vehicles. The design phase, as well as the determination of the electrical topology, was achieved to meet driving conditions. The carried out simulations show the effectiveness contribution of solar PV panels to better management of hydrogen consumption for different driving cycles. Indeed, the results show that the hybridization allows a significant improvement of the economy of hydrogen thanks to the new EMS proposed as well as the contribution of the solar PV panels, especially during prolonged stops of the vehicle. In addition, the results show the relevance of the new EMS with better management of fuel cell in cold starting, and the fast and strong accelerating phases by prioritizing battery bank. The conclusion is that the hybridization of the FCEV with the PV solar panels and using a smart EMS could be a promising solution for the electrification of transport.

Keywords—***Hybrid electric vehicle, energy management strategy, fuel cell, photovoltaic source, vehicle acceleration, high power demand, Battery SOC.***

I. INTRODUCTION

Demand for oil has increased significantly, leading to a limitation of fossil fuel resources. The transportation sector is ranked first in terms of oil consumption over the last decade. The rate of this consumption is increasing faster than any other sector. Zero-Carbon transport is feasible with Hydrogen and electricity, which will constitute in the near future the two main fuels. In order to contribute to a significant reduction in greenhouse gas emissions, it is necessary to reduce the consumption of oil by combining biofuels and rechargeable hybrid electric vehicles (PHEV). It is important to favor certain types of fuels used in power plants to generate electricity, depending on the region. In the long run, to achieve societal goals in a meaningful way, 100% electric vehicles powered by fuel cells or batteries will be the best solution.[1].

In an FCEV, the power distribution between the FC system and the other energy sources must fulfill the power demand regardless of various operating constraints. The control strategy makes it possible to define this power distribution appropriately. Energy management and optimization strategies can be classified into two categories: off-line optimization strategies and real-time energy management strategies. Offline optimization strategies are based on a priori knowledge of operating conditions and pre-established driving cycles. These strategies have an important advantage. They allow evaluating the quality of the strategies of management in real-time since they determine the minimum hydrogen consumption achievable in real-time.[2].

This work proposes a new energy management strategy in a Hybrid Electric Vehicle (HEV), combining a solar photovoltaic (PV) panels and a fuel cell. This strategy is based on the continuous monitoring of the state of charge (SOC) of the Battery. We brought an efficient solution to the problem of energy autonomy in a hybrid vehicle. Moreover, we have improved the hydrogen consumption, especially during stops. Thus, this work contributes to improving the overall performance of hybrid vehicles. This strategy is very easy to use and has advantages in terms of memory and computing time requirements. We have developed an algorithm to reduce the consumption of hydrogen while maintaining a level of SOC determined in advance. The strong point of this method is the improvement of the lifespan of the FC and its dynamics.

II. HYBRID VEHICLE SYSTEM MODELING AND THE PROPOSED ENERGY MANAGEMENT STRATEGY

A. Hybrid Electric Vehicle Model with Photovoltaic/F.Cell

We will model and simulate the various components of the used system to validate this work. Fig. 1 gives a schematic diagram of the complete system. It consists of two energy sources: a fuel cell and solar PV panels. First, the fuel cell is a proton exchange member fuel cell (PEMFC) that is connected to the DC bus via a DC-DC boost converter. The battery bank is directly connected to the dc-bus to maintain its voltage within the desired range.

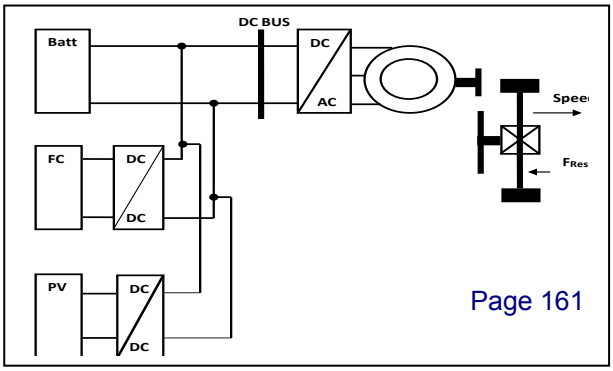

Fig. 1. General Hybrid Electric Vehicle Diagram with FC/Photovoltaic

The system also contains a three-phase permanent magnet synchronous machine (PMSM), powered by a three-phase inverter in order to interface dc and ac and allowing a bidirectional power flow. Fig. 2 also shows the various control blocks as well as the optimal block. The needed power during a road trip is calculated as a function of the speed and the electromagnetic torque of the electric motor. The power of the fuel cell is calculated in the block of energy management. The reference current of the FC is deduced using a command based on the set point on the power of the latter. The obtained current is then compared with the measured value to control the boost converter using a proportional-integral regulator (PI). The reference current is also used to define both hydrogen and oxygen consumption and regulate their flow rates. Fig. 2 shows the overall Simulink schema of the dynamic model of the system. The MATLAB / Simulink environment and its SimPowerSystems and SimDriveline toolboxes are used to carry out the electrical model as well as the mechanical model of the hybrid vehicle. It consists of three blocks: the block of the mechanical part of the vehicle, the block of the electrical part containing the electrical machine, power converters and the energy sources (the fuel cell and the solar PV panels) and the last one represents the part of the management of energy. In the following paragraphs, we will detail the contents of each block.

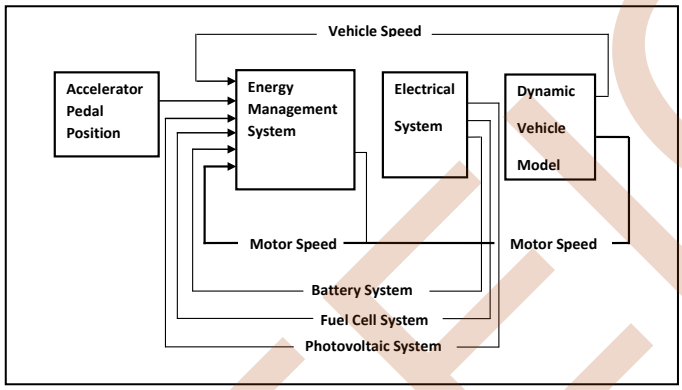

Fig. 2. Overall Simulink scheme of the dynamic model of the proposed system

a. *Dynamic model of vehicle*

The MATLAB / Simulink SimDrive toolkit provides the mechanical model of the electricvehicle as a block. Fig. 3shows the dynamic model of the vehicle under SimDrive. The vehicle is considered to be a solid point when it moves and is subjected to forces along the longitudinal axis: the pulling force F_t is caused by the action of the two drive wheels, the friction force due to the F_{roll} advancement, the effort of the aerodynamic resistance F_{aero} and the resistance F_{slope}. Resistance forces are given by the equations contained in [3].

The parameters of the HEV model are given in Table I.

b. *Dynamic model of the fuel cell*

The FC is an electrochemical device that generates electrical energy and heat through a chemical reaction. Electrical energy is produced without emission of gas. Moreover, FC has high efficiency and good performance.Fuel cells operate at high power, which favors their use in the automotive field and in the distribution of energy. The fuel cell is capable of converting hydrogen directly into electrical energy without using polluting combustion and can operate at low temperatures. Its voltage varies as a function of the load and is given byequation (1) [4]. The FC is the secondary energy source for the vehicle.

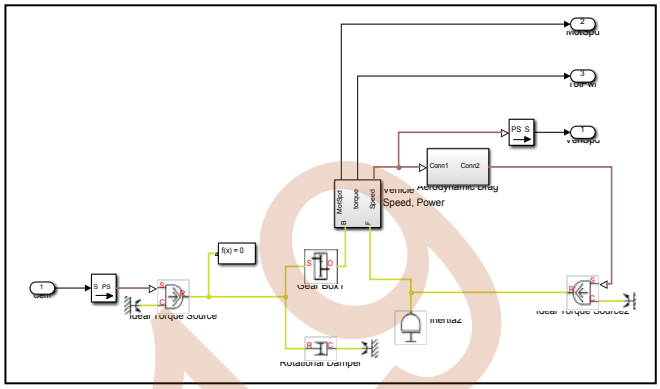

Its cell voltage and total power are defined by the following equations[5]:

Fig. 3. Dynamic model of the vehicle under SimDrive

$$V_{FC} = N_0 V_{Cell} \quad (1)$$

$$V_{FC,cell} = E_{Nernst} - U_{act} - U_{ohm} - U_{conc} \quad (2)$$

The different losses in the FC can be expressed as follows:

$$U_{ohm} = R_{FC} I_{FC} \quad (3)$$

$$U_{act} = b_1 + b_2 T_{FC} \ln(I\, 5{,}2\, 10^{-3}) \quad (4)$$

$$U_{act} = B_{FC} \ln(0{,}0136\, I_{FC}) \quad (5)$$

The voltage generated by the thermodynamics of the electrochemical reactions is given by the Nernst equation, having as expression according to [6].

The parameters of the FC model are given inTable II.

c. *Model of solar PV system*

For an operating voltage (equal to V_{mpp}) in the solar cells, given on the power/voltage curve, there will be a case of maximum power, which is considered a disadvantage when using solar photovoltaic cells. In the fast-response autonomous control of a solar panel, the processing of its power by the electronic interface will be able to provide significant benefits. For the simulation of the photovoltaic generator, it is essential to develop a mathematical model. [7].

The equivalent circuit of a solar cell is shown in Fig. 4. Where I_{PV} and V_{PV} are respectively the current and the voltage of the photovoltaic generator. The photocurrent of the cell is noted I_{ph}. R_{sh} and R_s are the intrinsic shunts and series resistances of the cell. In order to simplify the electric model, we will neglect the terms given by R_{sh} and R_s given their great difference in terms of numerical value. The current-voltage characteristic function of the photovoltaic generator is given by[7]:

$$I_{PV} = n_p I_{ph} - I_{rs}\left[\exp\left(\frac{q(V_{PV}+I_{PV}R_S)}{AKTn_S}\right) - 1\right] - \frac{V_{PV}}{R_{Sh}} \quad (6)$$

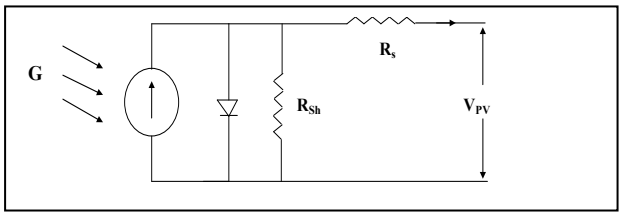

Fig. 4. PV Cell

The parameters of the PV model are given in Table III.

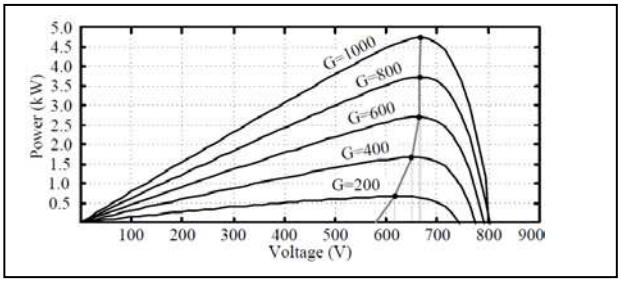

Fig. 5. P-V characteristics of PV system under various irradiances [8]

d. Model of the electric machine (PMSM)

The chosen electric machine in this work is a permanent magnets synchronous machine.

Table IV contains the parameters of the electrical machine used in this research work.

e. Model of batteries

The construction of this dynamic model will be based on the technical sheets of the batteries, where the parameters will be obtained in a practical and simple way. This model is applicable in charge and discharge regime. [9]

$$V_{batt} = E_0 - K\frac{Q}{Q-it}.it - R.i + Aexp(-B.it) - K\frac{Q}{Q-it}.i^* \quad (7)$$

Where:

$K\frac{Q}{Q-it}.it$: Polarization voltage

$K\frac{Q}{Q-it}.i^*$: Polarization resistance

V_{batt} = battery voltage (V)
E_0 = battery constant voltage (V)
K = polarization constant (V/(Ah)) or polarization resistance (Ω)
Q= battery capacity (Ah)
i_t = actual battery charge (Ah)
A = exponential zone amplitude (V)
B = exponential zone time constant inverse (Ah)−1
R = internal resistance (Ω)
i= battery current (A)
i*= filtered current (A)
The parameters of the Battery model are given in Table V.

III. Proposed Energy Management Strategy

This article deals with energy management in an HEV. The proposed method consists in finding the best distribution of the power between the solar PV panels and the FC. The main objective is to minimize hydrogen consumption by prioritizing solar PV energy during HEV shutdown phases. The problems encountered in this work reside in the design of this method were in the work of dimensioning of the elements of the system as well as the respect of a state of charge of the battery, which must vary within the desired range. The energy management strategy must thus respond toinstantaneous power demand. An optimal solution is proposed.Many optimization strategies have been developed, with some improvements. The performance of each strategy

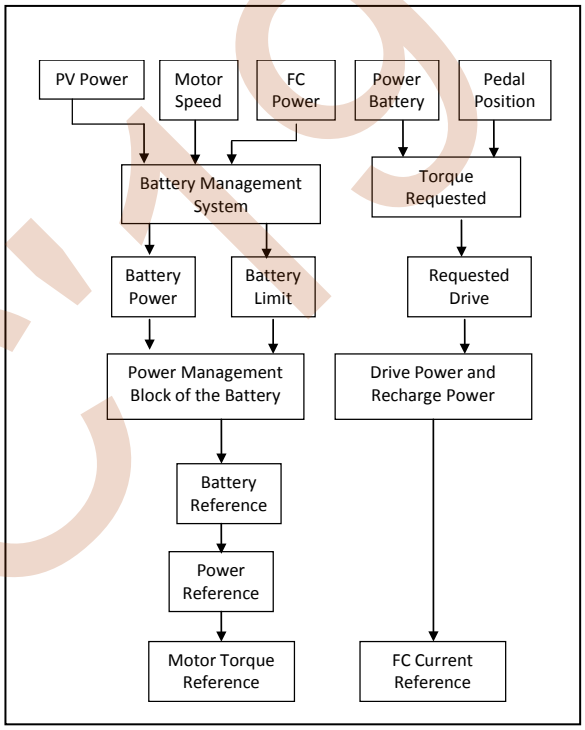

is analyzed according to several criteria such as hydrogen consumption, the state of charge of the Battery and the overall efficiency of the system.

Fig. 6. Flowchart explaining the method of energy management of the system

Several criteria were taken into consideration during the study of the energy management strategy, in order to judgeperformances and propose improvements. The economy ofthe fuel is taken care of according to the SOC of the bank ofthe battery and delimiting it to a range defined previously.

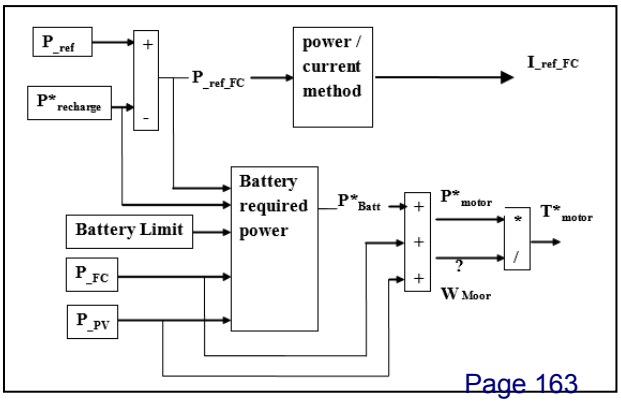

Fig. 7. Energy Management System

A. control of the fuel cell

The main role of the fuel cell is to maintain the state ofcharge (SOC) of the battery in a previously chosen range. For this purpose, the fuel cell will contribute to increasing the autonomy of the vehicle and will increase the life of the battery by reducing the factors due to aging. FC control and its principle are illustrated inFig. 8.

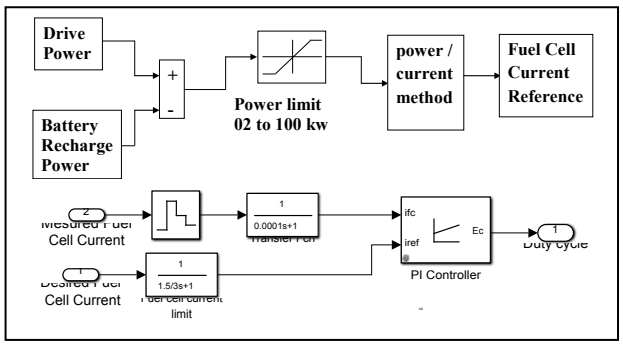

Fig. 8. Diagram illustrating the control of the fuel cell

B. control of the solar pv Panels

Maximum power point tracking (MPPTs) algorithm is, therefore, employed to reach the power peak regardless the variation of solar irradiance. An MPPT consists basically to control dc–dc boost converter by adjusting continuously its duty cycle [6].Several algorithms were proposed in the literature for an optimal adjustment of the duty cycle, and the most popular technique is the real-time realization of the gradient following method termed Perturb and Observe P&O algorithm and used extensively for the MPPT, which is shown in Fig. 9.

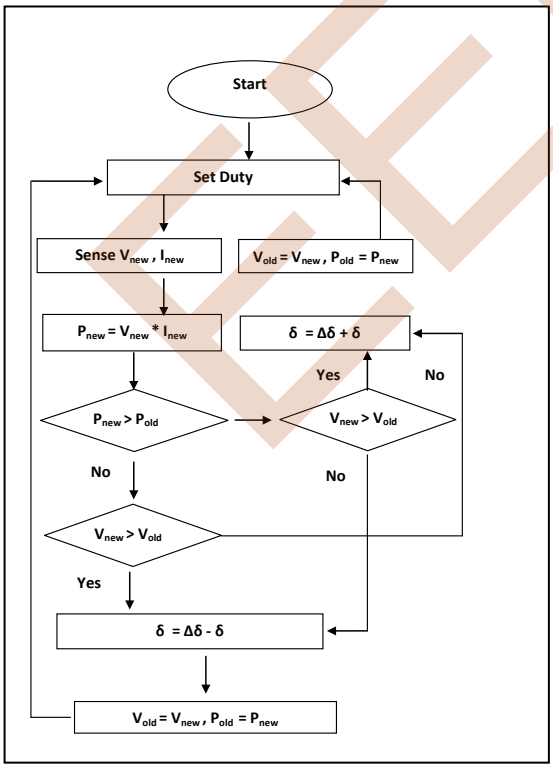

Fig. 9. Flowchart of P&O Method. [6]

C. Control of the electric motor

In order to respond effectively to the road cycle having different constraints during the simulation, control is designed for this purpose. A reference torque of the engine is generated using two nested loops. It is shown in Fig. 10, a reduction in the acceleration of the vehicle by an external loop, also another internal is responsible for controlling the reference torque of the engine.

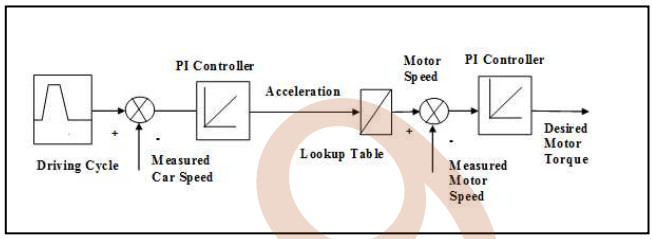

Fig. 10. Diagram illustrating the determination of the reference torque of the motor

IV. SIMULATION RESULTS AND DISCUSSION

In this article, a numerical simulation was carried out by using Matlab/Simulink environment in order to show the performance or the proposed EMS for HEV applications.

The last figure represents the objective of this work where the stopping phase of the vehicle (zero speed) is tested to recharge the battery by the photovoltaic source, noting the good precision of the control designed. System control is effective.

Fig. 11gives us information on the comparison between the two vehicle speeds: reference and measured. On is especially concerned with the time range between 50 and 250 [S], depending on the requested power (Fig.12).

Figures 13and14show the powers of the fuel cell, and the photovoltaic source. From these two figures, we note the good sizing of these two sources depending on the battery life and the speed profile requested. The battery intervenes during the acceleration phase, while the photovoltaic source recharges the battery continuously, in particular during the stopping phase of the vehicle.

In the region from 50 to 250 [s] the battery is not charged, we notice the state of the battery that has remained constant. This region is the most important in our study where the photovoltaic source intervenes alone. We notice well the decrease of the SOC of the battery when it intervenes. The results in Fig. 15, shows a charging region of the battery despite the vehicle is stopped, where the state has gone from 41,28 % to almost 42,20 % in 3 minutes and 20 seconds only. There is an evolution of the state of charge with the power supply of the photovoltaic panel. This confirms an interest in the proposed strategy.

In Fig. 16, 17, we found the fixed values of the voltage and current in the sizing phase of the fuel cell.It can be seen that during a strong acceleration of the vehicle, the photovoltaic source provides additional energy to the battery (see Fig. 19), which leads to an increase in autonomy of the latter. Another advantage is the hydrogen saving of the fuel cell.In this Fig. 19, the battery is discharged during phases of high powerdemands (vehicle acceleration, period from 5 to 15 (S). The battery starts to charge in all other phases exceptionally stop phase, resulting in increasing its autonomy.Fig. 19illustrated the states of recharging and discharging of the battery according to the different phases of the vehicle, where the contribution of the photovoltaic source is put to contribution, the results are satisfactory, in particular during prolonged stops of the vehicle. This will increase battery life, minimize hydrogen consumption, and increase fuel cell and battery life.

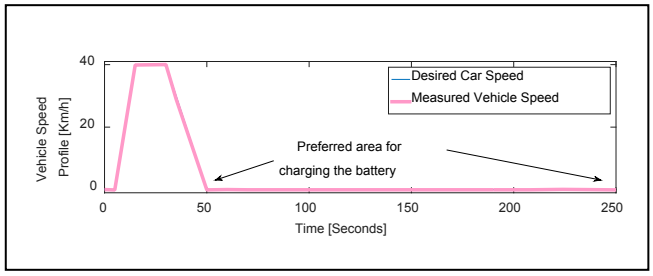

Fig 11. Comparison between the two speeds of the vehicle: reference and measured

Fig. 12. The requested power

Fig. 13. The power of the fuel cell

Fig. 14. The power of the Photovoltaic System

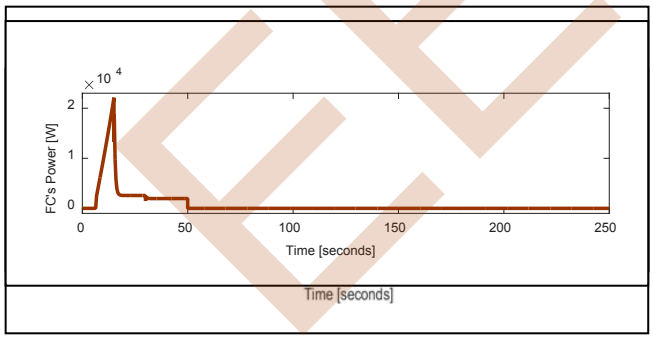

Fig. 15. State of the charge (SOC) of the Battery without and with the PV Source

Fig. 16. Fuel cell's voltage

Fig. 17. Fuel cell's current

Fig. 18. Power of Battery

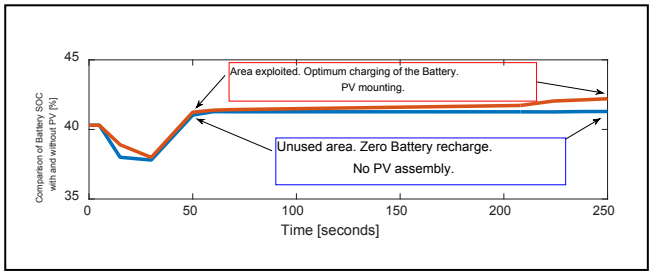

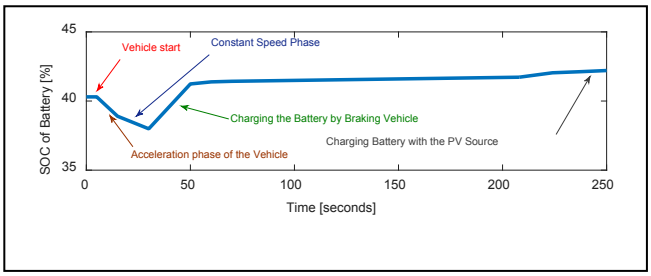

Fig. 19. Phases of charging the Battery in the System

TABLE I. PARAMETERS OF THE HEV MODEL

Parameters	Vehicle		
	Symbol	*Values*	*Units*
Vehicle total mass	M_v	3500	Kg
Rolling resistance force constant	f_r	0,01	S^2/m^2
Air density	P	1,20	$Kg.m^3$
Frontal surface area of the vehicle	A	2,711	m^2
Tire radius	R_w	0,25	M

TABLE II. PARAMETERS OF THE FC MODEL

Parameters	Fuel Cell		
	Symbol	*Values*	*Units*
N^{br} of cells series in the stack	N0	400	-
Nominal Current	In	285	A
Nominal Voltage	Vn	300	V
Fuel cell resistance	RFC	0,1757	Ohm
Operating temperature	TFC	95	C°
Nominal power Pnominal	Pnominal	85	kW
Maximal power Pmaximal	Pmaximal	100,0224	kW

TABLE III. PARAMETERS OF THE PV MODEL

Parameters	Photovoltaic		
	Symbol	*Values*	*Units*
Open circuit voltage	*Voc*	66	V
Electrical series resistance	R_s	2,2	Ω
Maximum power	$P_{PV,max}$	1260,15	W
Temperature	*T°*	25	C°
Irradiance	*G*	400	W/m^2

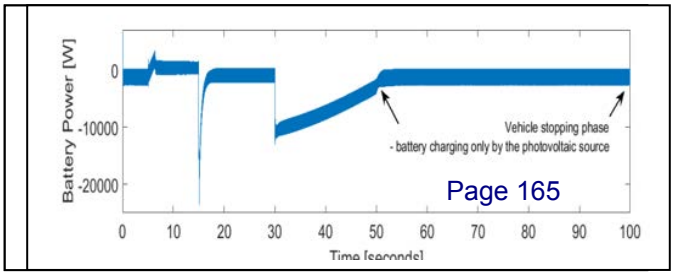

TABLE IV. PARAMETERS OF THE ELECTRICAL MACHINE

Parameters	PMSM	
	Values	*Units*
Flux induced by magnets	0,07111	Wb
Stator phase resistance	0,0083	Ω
Number of poles pairs	4	-
Inductance Ld	0,00017	H
Inductance Lq	0,00029	H
Maximal speed	12500	rpm
Maximal power	100	kW

TABLE V. PARAMETERS OF THE FC MODEL

Parameters	Battery		
	Symbol	*Values*	*Units*
Battery constant voltage	*Eo*	312,0125	V
Internal resistance	R	0,20719	Ohms
PolarizationResistance	K	0,11696	

V. CONCLUSION

Energy management of multiple sources has been proposed as a solution for a hybrid energy system using renewable energy from solar cells, fuel cells with energy storage device. A PV source can improve the storage device according to the characteristics of the vehicle requests and the main sources by providing an optimal solution, in order to respond to changes in the phases of the vehicle.In this article, a strategy is presented, aimed at improving energy management in a fuel cell hybrid vehicle. During the essential stages of the vehicle phases, the PV source provides the energy balance needed during these periods. The contribution of the photovoltaic source is demonstrated, which is particularly important in the context of the study of the availability of the battery, in terms of vehicle autonomy and the life of the fuel cell, adding an optimum energy storage level, improving the supply of quality and efficiency.

Simplicity in control, where we have exploited the advantages of control by the integration of the PI regulators, as well as the modeling of the PV source, constitutes the major advantage of this technique presented. We gained in terms of space, cost, at the level of the energy management block. Without forgetting, a considerable gain for hydrogen consumed, given the limitation of the solicitation of the fuel cell.The validation of the MPPT model of the PV source, while verifying the supply and storage phases, demonstrated the excellent performance of the entire system and validated the principle of the proposed energy management, while respecting the compatibility of connections with other subsystems such as the battery, the fuel cell, as well as the dynamic model of the vehicle.

REFERENCES

[1] C.E. Thomas. Fuel cell and battery electric vehicles compared. international journal of hydrogen energy 34 (2009) 6005–6020.
[2] Zhengchen, chrischunting mi, ruixiong, jun Xu, and Chenwen You. Energy management of a power-split plug-in hybrid electric vehicle based on genetic algorithm and quadratic programming. Journal of Power Sources, 248 :416-426, 2014.
[3] Hwang Jenn Jiang, Chen Yu Jie, Kuo Jenn Kun. The study on the power management system in a fuel cell hybrid vehicle. Int J Hydrogen Energy 2012;205:86e92.
[4] Zheng CH, Oh CE, Park YI, Cha SW. Fuel economy evaluation of fuel cell hybrid vehicles based on equivalent fuel consumption. Int J Hydrogen Energy 2011; 37, 2; 1790-1796.
[5] RekiouaDjamila, BensmailSamia, Bettar Nabila. Development of hybrid photovoltaic-fuel cell system for stand-alone application. J Hydrogen Energy 2014; 35: 1604-1611.
[6] Melero-Perez Agustin, GaoWenzhong, Jesu´ s Fern_andez-Lozano J. Fuzzy logic energy management strategy for fuel cell/ultracapacitor/battery hybrid vehicle with multiple input DC/DC converter. IEEE Trans 2009: 199-206.
[7] Ashish Pandey, NiveditaDasgupta, and Ashok Kumar Mukerjee, "High-Performance Algorithms for Drift Avoidance and Fast Tracking in Solar MPPT System", IEEE Transactions on Energy conversion, Vol. 23, No. 2, June 2008.
[8] Solar-Hydrogen Energy based Hybrid ElectricVehicle Dr. Siva Ganesh Malla, MIEEE, JayadeepuDadi ,Pavan Kumar Dadi, International Conference on Energy, Communication, Data Analytics and Soft Computing (ICECDS-2017).
[9] Zhang Xiaoguang, Zhao Ke, Sun Li, AnQuntao. Sliding mode control of permanent magnet synchronous motor based on a novel exponential reaching law[J]. Proceedings of the CSEE 2011-2015.

Grey Wolf Optimizer-Based MPPT Algorithm Under Partial Shading Conditions for PV Systems

Houssam Deboucha, Sofia Lalouni Belaid
Laboratoire de Technologie Industrielle
et de l'Information (LTII),
Faculté de Technologie,
Université de Bejaia, Algérie
houssamelt@yahoo.fr, lalouni_sofia@yahoo.fr

Saad Mekhilef
Power Electronics and Renewable Energy Research
Laboratory (PEARL),
Department of Electrical engineering, Faculty of Engineering,
University of Malaya, Kuala Lumpur 506003, Malaysia
Saad@um.edu.my

***Abstract*—The partial shading condition (PSC) is considered an unavoidable problem in the PV system, which the power-voltage (P-V) characteristic shown numerous local maximum peak (LMPs) and one global maximum peak (GMP). The conventional maximum power point tracking (MPPT) methods fail to track the GMP, which effect the efficiency of the PV system. Hence, in this paper theGrey Wolf Optimizer (GWO) based MPPT algorithmis proposed to track the GMP under PSC. The proposedGWO algorithmis performed in MATLAB/Simulink in comparison to the PSO and P&O techniques under different PSC patterns. The obtained results have clearly shown the superiority of the proposed GWO algorithm overall in terms of efficiency and tracking time.**

keywords—Partial Shading Condition PSC, Grey Wolf Optimization (GWO)algorithm, Maximum Power Point Tracking (MPPT), PV system

I. INTRODUCTION

The photovoltaic generation systems(PVGS) technology have known a significant development due to several pros such as: clean, low cost maintenance, noiseless and the solar energy is available in all the earth planet. Additionally, to reduce the greenhouse effect [1]. However, there are some cons such as, low efficiency of the PV arrays, $7-19\%$[2], depending at environmental conditions, temperature and solar irradiance, that effect the efficiency of the PVGS. Therefore, the maximum power point tracking (MPPT)must be presented in the PV system to ensure the extraction of the maximum power yields from the PV panel[3].

Many traditional MPPT techniques have been proposed in the literature to track the maximum power point MPP, which include Hill climbing (HL), Perturbation and Observation (P&O), Incremental Conductance (INC), Fractional Short Circuit (FSC), Fractional Open Circuit (FOC) and Ripple Correlation Control (RCC) [4]. These MPPT techniques are suitable in uniform irradiance where the P-V curve consists of a single peak. However, when the PV arrays subjected to no uniform irradiation known as partially shaded condition (PSC) the P-V curve exhibits multiple peaks, one global maximum peak (GMP) and several local maximum peaks (LMPs), all the aforementioned techniques fail to track the GMP [5],whicheffect the PV system efficiency.

Recently, several MPPT based on meta-heuristic algorithms are employed in the literature as an alternative methods to track the GMP, such as Ant Colony Optimization [6], Artificial Bee Colony (ABC) [7], Simulated Annealing (SA) [8], Whale Optimization Algorithm (WOA) [9], Flower Pollination Algorithm (FPA) [10], Particle Swarm Optimization (PSO) [11], which is the most widely used in the literature due to the capability to address the PSC and own simple structure, but take long time to track the GMP, power oscillation and may trap into the LMP. Therefore, many modified PSO have been proposed, such as Deterministic PSO (DPSO) [12], an improved PSO[13], Leader PSO (LPSO) [14]. This modification smoothly improved the performances but still lagging and depends on tuning parameters.

In this paper,a new method based on Grey Wolf Optimizer (GWO) algorithm [15]is proposed for MPPT of PV systems to mitigate the PSC. This algorithm is inspired by mimic the grey wolves' hunting mechanism of the prey, which has less parameters for tuning compared to other meta-heuristic algorithms, which make it a suitable solution to track efficiently the GMP under PSC. The performances of the proposed method are proven through simulation by MATLAB/Simulink under different partial shading patterns in comparison to the PSO and the P&O algorithms in the same conditions. The results have shown the effectiveness and superiority of the proposed algorithm which takes a few iterations to track the GMP.

The remainder of this paper is organized as follows: Section II describes the modeling of the PV system under partial shading conditions, an overview of the proposed

algorithm is described in section III. The simulation results and discussion are presented in section IV. Finally, the conclusion is presented in section V.

II. CHARACTERISTICS OF THE PV SYSTEM UNDER PSC

A. Modeling of PV cell

The single diode modelapproach is considered in this study to modulate and simulate the PV cell [16], as illustrated in Fig.1. By applying the KCL the output current (I_{PV}) of a PV module is described as:

$$I_{PV} = I_{Ph} - I_o \left[e^{\left(\frac{(V_{pv}+R_S I_{Pv})q}{AnkT}\right)} - 1 \right] - \left(V_{pv} + \frac{R_S I_{Pv}}{R_{sh}} \right) \quad (1)$$

Where, I_{Ph} represents the photovoltaic current,Io is the cell reverse saturation current,V_{pv} is the output cell voltage, A is the diode ideality factor, R_S and R_{sh} are equivalent series and shunt resistance, q is the electron charge, k is the Boltzmann's constant, T is module temperature (in kelvin), n is the number of the series cells.

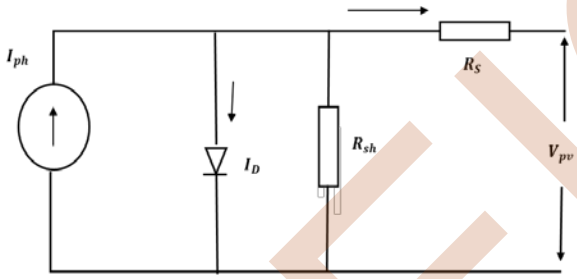

Figure 1. Equivalent Single diode model of PV cell.

B. Effect of PSC over the PV array

Typically, the PV modules connected in series to elevate the voltage and parallel to increase the current in order to match the load energy demanded. Practically the PV array installation will not be subjected to the same level of irradiation which create PSC (due to clouds, trees, buildings…etc.) [17]. In this study, a string of three panels connected in series is considered as shown in Fig.2. The bypass diode connected in parallel with each module to prevent the hot spotdue to the mismatch between modules. the parameters of the panel used are given in table I. from fig.2 three different PSC patterns, pattern (1), pattern (2), pattern (3) are considered. Under PSC the P-V curve exhibits multiple local peaks LMPs and singleglobal peak GMP due to the conduction of the bypass diode[18], which the GMP is located in different area of the search space, middle, left extremity and the right extremity.

TABLE I. Parameter of PV module of Shell Solar SQ80 at STC

Parameters		*Values*
Maximum power	P_{mpp}	$80\ W$
Short Circuit Current	I_{sc}	$4.848\ A$
Open Circuit Voltage	V_{oc}	$21.8\ V$
Maximum Power Current	I_{mmp}	$4.579\ A$
Maximum Power Voltage	V_{mpp}	$17.5\ V$

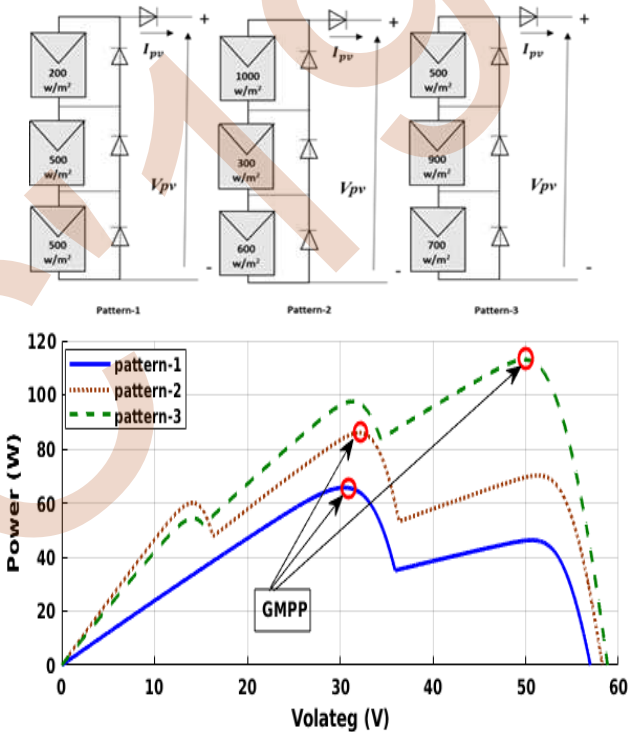

Figure 2. P-V curves of under different PSC. (a) patter-1, (b) pattern-2, (c) pattern-3

III. GWO AND ITS APPLICATION IN MPPT

A. Overview of GWO algorithm

The Grey Wolf Optimizer (GWO) is considered as new meta-heuristic algorithm proposed by Mirjalili and al [19], this algorithm is inspired by emulate the leadership hierarchy and hunting prey technic of grey wolves in wildlife. Mostly, the grey wolves prefer to live in pack with a particular dominant hierarchy as depicted in fig.4. where, the pyramid leader hierarchy has four levels such as: the leaders wolves called alpha (α), and the subleaders called beta (β), and delta (δ), and the remains called omega (ω). There are there main steps for deign the GWO algorithm namely chasing, encircling and attack. The mathematical model of encircling the prey can be formulated by the following equation:

$$\vec{E} = \left|\vec{C}.\vec{X}p(t) - \vec{X}(t)\right| \quad (2)$$

$$\vec{X}p(t+1) = \vec{X}p(t) - \vec{A}.\vec{D} \quad (3)$$

Where A, C and D represent the coefficient vectors, t represent the current iteration, Xp denotes the position of the prey, and X represent the position of a grey wolf. The vectors A and C can be estimated as follows:

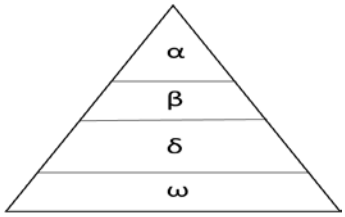

Figure 4. Hierarchy of Grey wolves

$$\vec{A} = 2\vec{a}.\vec{r}1 - \vec{a} \quad (4)$$

$$\vec{C} = 2.\vec{r}2 \quad (5)$$

Where the coefficient a linearly decreases during the course of iteration from 2 to 0 and r1, r2 are random numbers in [0,1].

B. GWO algorithm based MPPT

The optimization problem of MPPT in the PV system can be expressed as follows:

$$P(d^{k+1}{}_i) > P(d^k{}_i) \quad (6)$$

$$\text{dmin} < di < dmax \quad (7)$$

The objective function is maximizing the power generated from the PV array, considering the duty cycle (d) as the decision variable and the $dmin$ and $dmax$ are the limits of the duty cycle. The main steps of design the GWO based MPPT algorithm are:

*Step1) initialization parameters:*send three duty cycle $(0.1,0.5,0.9)$, $0.1 \leq di \leq 0.9$ to cover all the search space [0,1].

*Step2) fitness evaluation:*evaluate the value of the power corresponding to each duty cycle di, the duty cycle corresponds to the best fitness value considered as the best solution $di, best$.

Step3) update the particle solutions: adjust the position of the grey wolves which are the duty cycles d_i as follow:

$$d_i\,(k+1) = d(k) - A.D \quad (8)$$

*Step4)*repeat steps 2 and 3 until all the particles achieve the global maximum solution.

*Step5) Re-initialization:*if the deviation of the output power and the optimal power satisfies the condition (9)

$$\left|\frac{P_{PV,New} - P_{PV,old}}{P_{PV,old}}\right| > \Delta P \quad (9)$$

The ΔP is set 0.01.

The flowchart of the GWO algorithm for MPPT is depicted in fig.4.

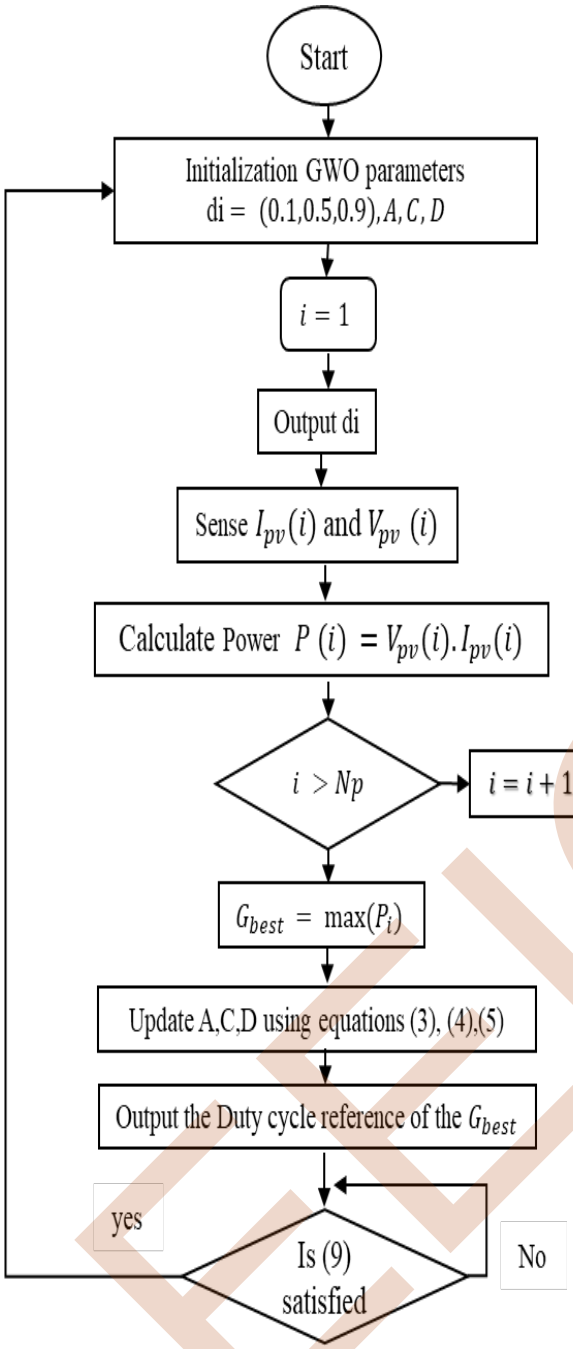

Figure.4. Flowchart of GWO

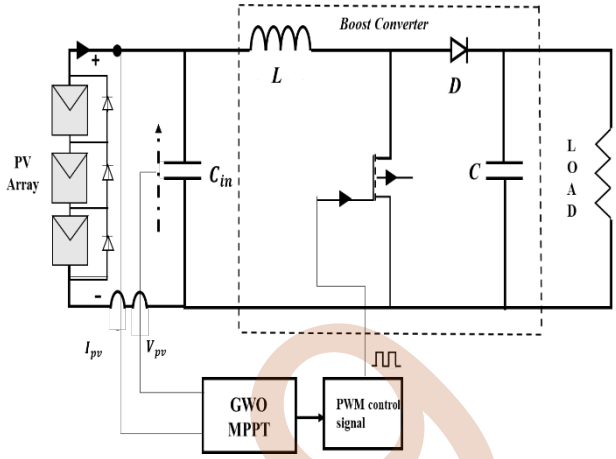

Figure 5. Block diagram of PV system with MPPT

IV. RESULTS AND DISCUSSION

To evaluate the effectiveness of the proposed GWO based MPPT algorithm, the PV system simulation of 3S PV panels configuration as depicted in Fig.5 is done. The PV array is subjected to three different PSC patterns namely pattern-1, pattern-2, and pattern-3 as shown in Fig.2, which the GMP is located in different area of the search space, in the left extremity for the first pattern, in the middle for the second pattern and in the right extremity for the third pattern. The proposed algorithm is compared with the PSO and the P&O algorithms under the same conditions, the results of the power waveforms of all the algorithms under differentPSC are shown in Fig.5,6,7.

TABLE II. SIMULATION PERFORMANCES OF DIFFERENT PSC

patterns	Simulation results				
	Power(w) at GMP	Method	Power (W)	Tracking time (s)	Oscillation
Pattern (1)	**65.683**	GWO	65.675	2.7	Low
		PSO	65.663	3.1	Medium
		P&O	65	0.06	High
Pattern (2)	**85.973**	GWO	85.954	1.3	Low
		PSO	85.905	3	Medium
		P&O	70	0.05	High
Pattern (3)	**113.015**	GWO	112.985	2.7	Low
		PSO	112.968	3.2	Medium
		P&O	112	0.015	High

In addition, the numerical results are summarized in Table II.

It can be seen clearly from the results that the proposed method and the PSO reached the GMP in all the PSC patterns with different tracking time, which the GWO algorithm has taken an average of 1.1s where the PSO algorithm has taken an average of 2s, while the P&O trapped into LMP in pattern-2, moreover produce huge oscillation in the steady-state, it's noticeable that the proposed GWO algorithm is superior to the PSO and the P&O methods.

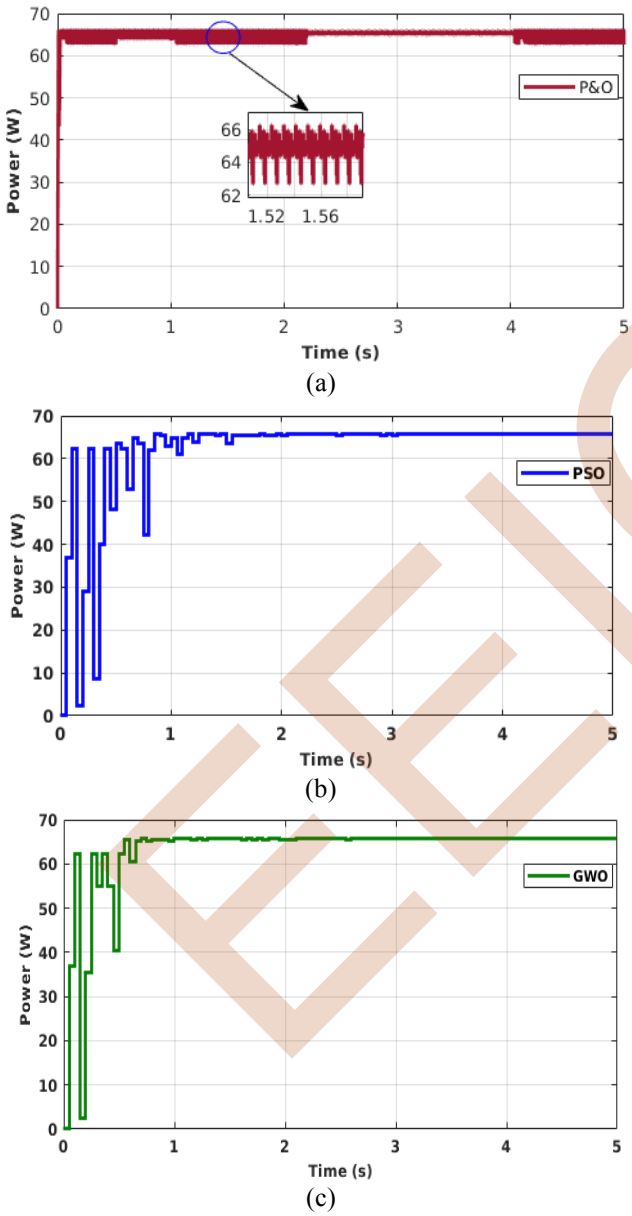

Figure.5. Results of power waveforms of pattern-1, (a) P&O, (b) PSO, (c) GWO

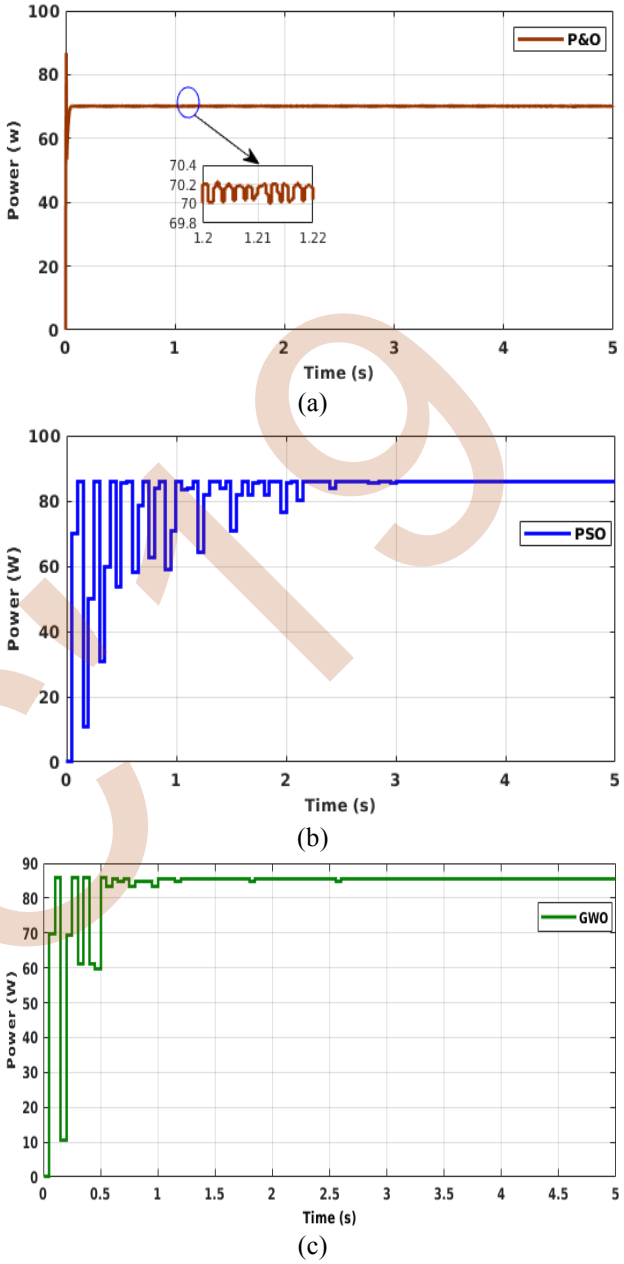

Figure 6. Results of power waveforms of pattern-2, (a) P&O, (b) PSO, (c) GWO

V. CONCLUSION

In this paper, the GWO based MPPT algorithm has been proposedto track the GMP, in order to evaluate the performance of the GWO method, simulation has been conducted and compared with the PSO and P&O methods under different PSCs. The proposed GWO method has mitigated the PSC problem effectively with short tracking time, all the results clearly show the superiority and the reliability of the proposed method against the P&O and the PSO methods. The future work is to make more

improvement at the position update formula that affected directly by the convergence factor *a*, and the experimental validation will carry out.

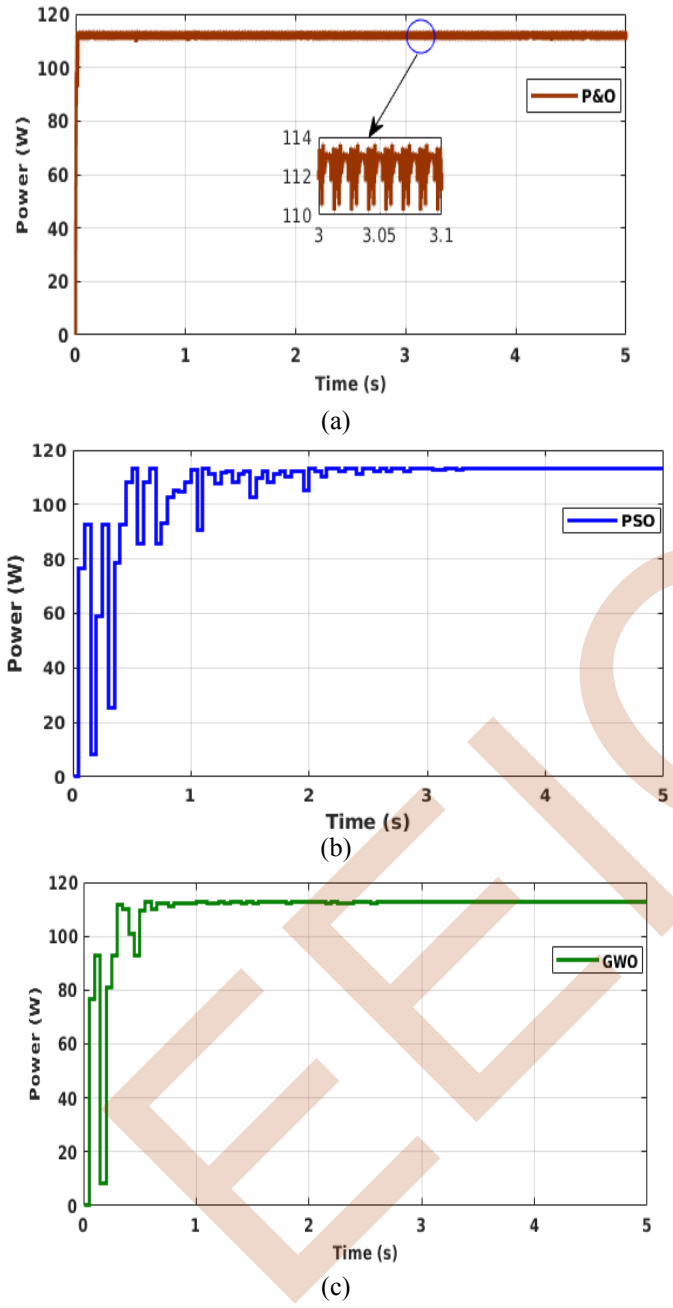

Figure 7. Results of power waveforms of pattern-3,
(a) P&O, (b) PSO, (c) GWO

REFERENCES

[1] L. Liu, X. Meng, and C. Liu, "A review of maximum power point tracking methods of PV power system at uniform and partial shading," *Renew. Sustain. Energy Rev.*, vol. 53, pp. 1500–1507, 2016.

[2] A. G. Gaglia, S. Lykoudis, A. A. Argiriou, C. A. Balaras, and E. Dialynas, "Energy efficiency of PV panels under real outdoor conditions–An experimental assessment in Athens, Greece," *Renew. Energy*, vol. 101, pp. 236–243, 2017.

[3] C. Manickam, G. P. Raman, G. R. Raman, S. I. Ganesan, and N. Chilakapati, "Fireworks enriched P&O algorithm for GMPPT and detection of partial shading in PV systems," *IEEE Trans. Power Electron.*, vol. 32, no. 6, pp. 4432–4443, 2017.

[4] Y. Wang, Y. Li, and X. Ruan, "High-Accuracy and Fast-Speed MPPT Methods for PV String under Partially Shaded Conditions," *IEEE Trans. Ind. Electron.*, vol. 63, no. 1, pp. 235–245, 2016.

[5] K. S. Tey, S. Mekhilef, M. Seyedmahmoudian, B. Horan, A. T. Oo, and A. Stojcevski, "Improved Differential Evolution-Based MPPT Algorithm Using SEPIC for PV Systems Under Partial Shading Conditions and Load Variation," *IEEE Trans. Ind. Informatics*, vol. 14, no. 10, pp. 4322–4333, 2018.

[6] J. Ahmed and Z. Salam, "An Enhanced Adaptive P&O MPPT for Fast and Efficient Tracking Under Varying Environmental Conditions," *IEEE Trans. Sustain. Energy*, vol. 9, no. 3, pp. 1487–1496, 2018.

[7] D. Pilakkat and S. Kanthalakshmi, "Artificial Bee Colony Algorithm for Peak Power Point Tracking of a Photovoltaic System under Partial Shading Condition," *Proc. 2018 Int. Conf. Curr. Trends Towar. Converging Technol. ICCTCT 2018*, pp. 1–7, 2018.

[8] S. Lyden and M. E. Haque, "A Simulated Annealing Global Maximum Power Point Tracking Approach for PV Modules under Partial Shading Conditions," *IEEE Trans. Power Electron.*, vol. 31, no. 6, pp. 4171–4181, 2016.

[9] M. Premkumar and R. Sumithira, "Humpback whale assisted hybrid maximum power point tracking algorithm for partially shaded solar photovoltaic systems," *J. Power Electron.*, vol. 18, no. 6, pp. 1805–1818, 2018.

[10] J. Prasanth Ram and N. Rajasekar, "A Novel Flower Pollination Based Global Maximum Power Point Method for Solar Maximum Power Point Tracking," *IEEE Trans. Power Electron.*, vol. 32, no. 11, pp. 8486–8499, 2017.

[11] Y. H. Liu, S. C. Huang, J. W. Huang, and W. C. Liang, "A particle swarm optimization-based maximum power point tracking algorithm for PV systems operating under partially shaded conditions," *IEEE Trans. Energy Convers.*, vol. 27, no. 4, pp. 1027–1035, 2012.

[12] K. Ishaque and Z. Salam, "A deterministic particle swarm optimization maximum power point tracker for photovoltaic system under partial shading condition," *IEEE Trans. Ind. Electron.*, vol. 60, no. 8, pp. 3195–3206, 2013.

[13] S. M. Mirhassani, S. Z. M. Golroodbari, S. M. M. Golroodbari, and S. Mekhilef, "An improved particle swarm optimization based maximum power point tracking strategy with variable sampling time," *Int. J. Electr. Power Energy Syst.*, vol. 64, pp. 761–770, 2015.

[14] J. Prasanth Ram and N. Rajasekar, "A new robust, mutated and fast tracking LPSO method for solar PV maximum power point tracking under partial shaded conditions," *Appl. Energy*, vol. 201, pp. 45–59, 2017.

[15] S. Mohanty, B. Subudhi, and P. K. Ray, "A new MPPT design using grey Wolf optimization technique for photovoltaic system under partial shading conditions," *IEEE Trans. Sustain. Energy*, vol. 7, no. 1, pp. 181–188, 2016.

[16] J. Ahmed and Z. Salam, "A soft computing MPPT for PV system based on Cuckoo Search algorithm," *Int. Conf. Power Eng. Energy Electr. Drives*, no. May, pp. 558–562, 2013.

[17] N. Kumar, I. Hussain, B. Singh, and B. K. Panigrahi, "Rapid MPPT for Uniformly and Partial Shaded PV System by Using JayaDE Algorithm in Highly Fluctuating Atmospheric Conditions," *IEEE Trans. Ind. Informatics*, vol. 13, no. 5, pp. 2406–2416, 2017.

[18] M. Seyedmahmoudian, T. K. Soon, B. Horan, A. Ghandhari, S. Mekhilef, and A. Stojcevski, "New ARMO-based MPPT Technique to Minimize Tracking Time and Fluctuation at Output of PV Systems under Rapidly Changing Shading Conditions," *IEEE Trans. Ind. Informatics*, vol. PP, no. c, pp. 1–1, 2019.

[19] S. Mirjalili, S. M. Mirjalili, and A. Lewis, "Grey Wolf Optimizer," *Adv. Eng. Softw.*, vol. 69, pp. 46–61, 2014.

Characterization and Optimization of Germanium Nanowires-based Silicon Solar Cells: Design and simulation

Fatiha Benbekhti
Technology Depatment. Khemis Miliana university
Djillali Bounama- Khemis Miliana
Khemis Miliana, Algeria
Fatiha.benbekhti@univ-dbkm.dz

Souaad Tahraoui
Electronic Engineering Department, Chlef University Chlef, Algeria
s.tahraoui@univhb-chlef.dz

Habiba Houari
Electronic Engineering Department, Tlemcen University
Tlemcen, Algeria
habiba.haouari @univ-tlemcen.dz

Hayate Khouani
Electronic Engineering Department, Tlemcen University
Tlemcen, Algeria
Hayate.khouani@univ-tlemcen.dz

***Abstract*—The work we have presented in this paper is the modeling, simulation and optoelectronic characterization of photovoltaic cells based on germanium nanowires and microcrystalline silicon substrate in order to achieve high efficiency and low cost solar cells. The main objective is to improve the conversion efficiency of this type of solar cells by integration of germanium nanowires. The hydrogenated amorphous silicon-germanium films, to be used as low band gap absorber material in thin film solar cells. This was achieved through modeling and simulation using Tcad-Silvaco Athena, advanced virtual wafer-fabrication tool. A model Silvaco-Tcad Athena was created using actual solar cell parameters (such as layer thicknesses, doping levels and material properties) documented in various papers to optimize parameters in order to make a compromise between amelioration conversion efficiency and lowest cost of manufacture.**

Keywords-silicon; germanium; thin films; optimization; nanowires.

I. INTRODUCTION

Fortunately there exist many alternative forms of energy production that are both clean and renewable. They are clean means no pollutant and renewable, means not dependent on substances. Such renewable energy sources include solar (both photovoltaics and solar thermal), wind, hydro, geothermal, tidal, and biofuels [1]. Due to the enormous potential of solar energy it may well become a significant contributor for clean and renewable electricity in the future [2].

Solar cells convert sunlight directly into electricity using the photovoltaic effect. They are a promising technology for satisfying current and future energy demands in a sustainable and environmentally friendly way [3]. The main focus of this paper was to study the effect of dwindling of the compounds for fabricate solar cells. To make solar cells competitive fossil fuels and achieve the stated goals many improvements in cost and efficiency must progress [2].

Photovoltaic power generation has been receiving considerable attention as one of the most promising energy generation alternatives. It can hold the world electricity consumptions. The photovoltaic market which is powerfully dominated by crystalline silicon technology [4], which accounts for about 86% (53% multicrystalline (mc) and 33% monocrystalline cells) of the global cell production [5], has been growing strongly over the past few years. Scientists are pushed to develop quicker some methods and technologies by the growth, at the same time, achieving both an improvement in efficiency and a reduction in the production costs of photovoltaic cells [6]. New PV technologies with cheaper manufacturing cost compared to traditional silicon crystalline based modules are available in the international market these days such as; amorphous silicon (a-Si), Cadmium Telluride (CdTe) and Copper Indium Selenium (CIS) [4].

Another way of photovoltaic appeared after the dominant technology of crystalline Silicon, which is replaced by another more absorbent material. These second generation photovoltaic cells or say thin film reduce the massive amount of silicon used and improve their conversion efficiency by the testimony of the effective amount [7].

Semiconductor nanowires have recently emerged as a new class of materials with significant potential to reveal new fundamental physics and to propel new applications in quantum electronic and optoelectronic devices. Semiconductor nanowires show exceptional promise as nanostructured materials for exploring physics in reduced dimensions and in

complex geometries, as well as in one-dimensional nanowire devices.

Nanowires have significant regarding relaxation problem properties, transmission and electronic optical confinement. Due to their controllable morphology (length, density and diameter) and their light trapping effect, nanowires have attracted the attention and considered good candidates for many applications [8]. Their integration in devices meets the miniaturization of physical exigencies, quantum confinement and helps improve the performance of devices.

The nanowires structure is full cylindrical, has a length generally on the order of a few microns and its diameter is submicron. The ratio length/diameter is 25 (~5µm/200 nm) [9]. The methods of making nanowires vary depending on the types of nanowires and according to the robustness and depletion of various tools available [10].

II. MATERIALS AND METHODS

The simulation software Athena of Tcad-Silvaco provides general possibilities for the simulation of processes used in the semiconductor industry, such as diffusion, oxidation, ion implantation, etching, lithography, deposition processes. It allows fast and accurate simulations of all manufacturing steps used in optoelectronics and power components.

Figure 1 shows the solar cell under study; is hetero-structure based on using of silicon nanowires on an oriented microcrystalline silicon substrate (111) and thin films of amorphous silicon. A microphah solar cell with the following structure was used in the simulation:

SiO_2 (30 nm) /ZnO: Al (20 nm)/n-a-SiGe:H (10 nm)/ i-a-SiGe:H(10 nm)/p-µc-NWs-Ge:H(L=2.5µm-D=100 nm)/p-µc-Si:H (2.5 µm) /Al (1 µm).

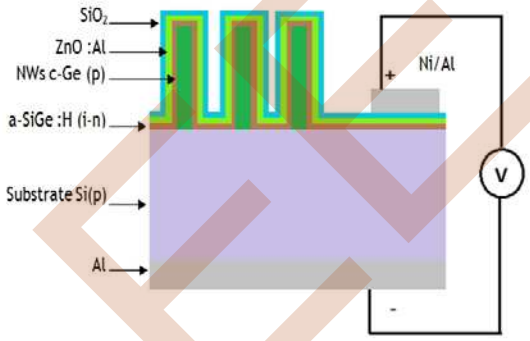

Figure 1. Schematic of Germanium nanowires based Silicon Solar Cell

A. Substrate preparation

The main dopants silicon thin-film is boron, p-type and arsenic n-type. Other dopants, phosphorus, gallium, aluminum, etc., are used occasionally for very specific applications or even marginal. In this case, the oriented multi-crystalline silicon substrate (111) is p-doped with a low boron concentration (Na = 10^{15} at/cm^3) and a logger 5 microns.

B. Nanowires preparation

For creation of new nanowire-based structures with new properties and functionalities, the most central qualities of nanowires are: [11]

- Degree of confinement including possible quantum confinement;
- Large surface-to-volume ratio intrinsic to nanowires;
- Length scale defined by the nanowire diameter which has dramatic consequences for the excitation and emission of electronic states in nanowires;
- Successful growth of nanowires involves careful control of quality, alloy composition, diameter, and electronic properties.

The manufacture of semiconductor nanowires is made by several technological ways. Microelectronics is conventionally noted two approaches, bottom-up and top-down approach.

- *Bottom-up Approach*

Bottom-up is to assemble individual components such as atoms, molecules and aggregates to form more complex structures by synthesis (self-assembly). Bottom-up methods, involve the chemical synthesis of nanowires whose properties can be carefully controlled and tuned during growth [11].

- *Top-down Approach*

Top-down consist to machine structures in solid substrate by lithography techniques and etching. The position of the nanowires is well-controlled on the substrate [12]. The procedure for making nanowires is as follows: A pattern is part of a resin (optical lithography, electronic, near field, or by nano-imprint) to form an etching mask. The pattern is then transferred by etching into a substrate to form nanostructures. Lithography is used as a preliminary step to define, after deposition and removal of the resin a hard mask formed from a set of pads. The etching substrate results in the production of vertical nanowires [13]. Furthermore, the process is intrinsically wasteful and there are large challenges to overcome before these technologies become high- throughput, cost-effective means of nanowire fabrication. [6]

After the substrate preparation, a multi-crystalline Germanium layer p-doped with a high concentration of boron (N_a=10^{20} at/cm^3) is deposited by epitaxy with length 2.5 microns on the substrate. An etching is done to eliminate undesirable parts, so to have very thin layers of 2.5 µm of length and diameter of 100 nm on the substrate.

C. Hydrogenated Amorphous Silicon Germanium

After etching of the nanowires on the substrate, an intrinsic amorphous silicon thin-film is deposited of 100 nm thickness. Then etching is made to remove unwanted part.

D. Electrodes

Due to the low conductivity of the a-Si: H compared with c-Si, the addition of a conductive layer over its all surface is essential for current collection. In concern the illuminated face

of the cell, the conductive transparent oxide (CTO) collects current, plays both the role of the conductive layer and the antireflection layer and consequently provides good contact with the metal electrodes (Figure 1). In the absence of illumination of the back face of the cells, the conductive transparent oxide is replaced by a simple metal deposited on the amorphous layer [10, 12].

The Zinc oxide has very interesting electrical properties, its electronic structure has been widely studied, that the zinc oxide is a direct gap semiconductor at room temperature. The band gap of pure ZnO is about 3.37 eV, superior to conventional semiconductors, therefore ZnO has a gap about 367 nm which is therefore located in the near UV, ZnO is therefore transparent in the visible spectrum.

In addition, the zinc oxide can be doped with a high concentration and it is possible to obtain high electrical conductivities of the order of 2×10^{-4} Ω cm^{-1}. These properties of transparency in visible light and good electrical conductivity are very interesting for applications requiring transparent electrodes [11, 13].

E. Antireflection Coating

The use of an antireflection coating (ARC) combined with silicon substrate textured, greatly reduces optical losses drastically affecting the power output of the solar cell by reducing the short-circuit current. Silicon oxide (SiO_2) and silicon nitride (Si_3N_4) have complementary properties. Silicon oxide with refractive index 1.46, has good transparency in the visible, good dielectric properties (Eg~10 eV) and low mechanical stress but it is bad barrier to the diffusion of ions and dopants, the silicon nitride with 2.02 refractive index, is denser and therefore provides a better diffusion barrier. The final step is to deposit a thin layer of the oxide silicon with thickness of 100 nm and addition of electrodes.

III. RESULTATS AND DISCUSSION

The amorphous nature of a-SiGe:H makes it easier to achieve conformal growth of thin films on rough or nanostructured surfaces than is the case with µc-Si:H. Combined with the relatively high deposition rate of hotwire chemical vapor deposition (HWCVD) as compared to PECVD, HWCVD a-SiGe:H is a feasible option for thin film silicon PV on textured light-scattering substrates [14]. The recent developments in advanced light-scattering structures such as textures created with nano-imprint lithography and naturally grown ZnO nanorods, have motivated us to investigate whether a-SiGe:H HWCVD can be considered as active material for low cost thin film a comparison of a conventional and an unconventional method to improve the quality of forming electrodes on silicon solar cells [15].

The antireflection coating prevents the reflection of rays of sunshine and a loss of energy, as well creates a barrier into the connection zone, which increases the resistance between the electrode layer and the silicon substrate. The thickness of the deposited layer has an influence on the structure of the obtained electrode layer and resistance value of the resistance electrode [16].

In solar cells, the minority carrier lifetime, internal quantum efficiency and the solar cell efficiency are also affected by germanium despite although it is, electrically inactive in the silicon lattice [2].

Germanium nanowires were incorporated in single junction between hydrogenated amorphous Silicon Germanium thin films and microcrystalline Silicon substrate for forming heterostructure solar cell with an efficiency of 13.23 %.

The simplest semiconductor junction that is used in solar cells for the separation of photogenerated charge carriers is the p-n junction, an interface between the p-type region and a n-type region of the semiconductor. Therefore, the basic semiconductor property of a material is the possibility of varying its conductivity by doping, must be demonstrated before the raw material can be considered a suitable candidate for solar cells, this was the case for amorphous silicon.

Indeed, the interest in germanium stems from the fact that it has a high mobility of carriers and a Bohr radius (11 nm) wider than that of silicon (by 4.3 nm). The quantum confinement effects are all the more important as the radius of the nanostructures is smaller than the Bohr radius. Thus, these effects are achieved for a nanowire diameter larger for germanium than for silicon.

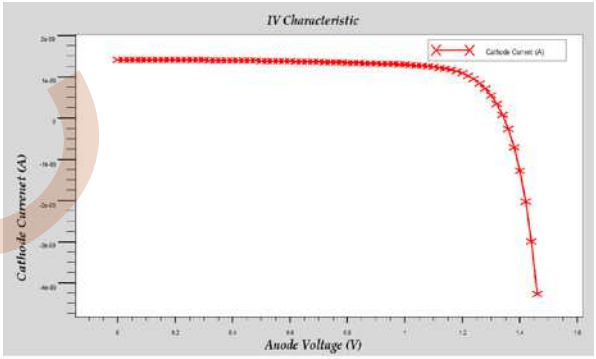

Figure 2. IV Characteristic of cell obtained after simulation

The pervious figure (figure 2) represents the characteristic IV obtained of the cell after simulation. The value of the open-circuit voltage is 1.467 V and the short-circuit current value is 11.69 mA / cm2, giving a form factor of 77.69% and a yield of about 13.12%.

The following figure (Figure 3) presents the IV characteristic of the solar cell with and without germanium to see the effect of germanium incorporation in the substrate.

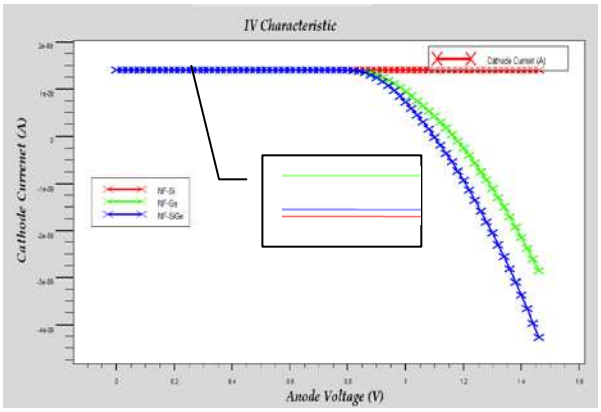

Figure 3. IV Characteristic of cell for Si, Ge and SiGe Nanowires

From the figure above (Figure 3), we also see that the maximum short-circuit current and the highest efficiency are given by the germanium nanowires. Due to the incorporation of germanium in the silicon, the nanowires of SiGe increase the current value and approach to germanium value, their efficiency reaches 13.14%.

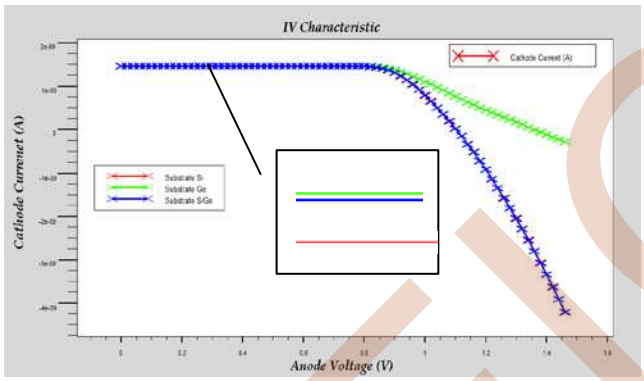

Figure 4. IV Characteristic of cell for Si, Ge and SiGe substrate

From the figure above (Figure 4), we also see that the values of the short-circuit current and the efficiency are higher for germanium substrate compared with the silicon substrate and by using the SiGe substrate, the value of the short-circuit current is moved a little upwards which gives a slight increase in the efficiency value. We therefore come to the conclusion that the incorporation of germanium in a silicon substrate increases the efficiency of the cell, it reaches 13.17%.

The same work is done and realized for the amorphous layer. Following Figure (Figure 5) shows characteristic IV of the cell by varying the material of the amorphous layer.

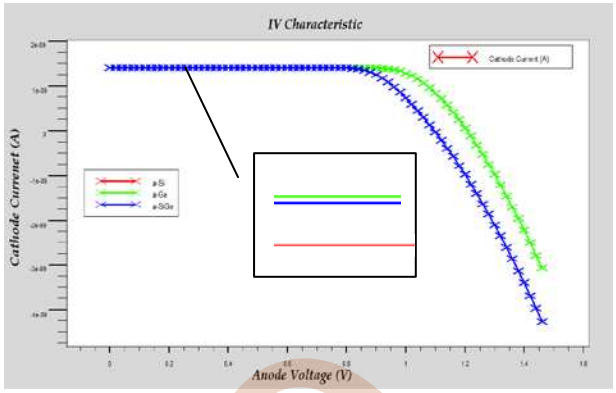

Figure 5. IV Characteristic of cell for Si, Ge and SiGe substrate

From the figure above (Figure 5), we also see that the highest short-circuit and efficiency values are given by germanium. We therefore conclude that the amorphous germanium layer has the highest value of the short-circuit current compared with the amorphous silicon layer and by introducing the germanium into the silicon the value of the short-circuit current -circuit and moved a little upwards, which increases their conversion efficiency, it reaches 13.16%.

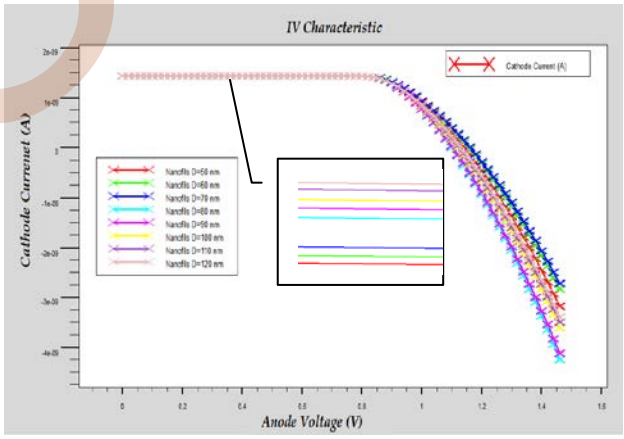

Figure 6. IV Characteristic of cell for different diameters of the nanowires

From the results obtained in the previous figure (Figure 6), the highest value of the short-circuit current is obtained for nanowires diameter of 120 nm. Typically, when the diameter decreases the electrical conductivity also decreases. We therefore conclude that for the diameter of nanowires, the best efficiency will be obtained when the diameter of nanowires is 120 nm, it reaches 13.47%.

Research has proved the existence of a critical size of change of direction of nanowires for two families of diameters 60 and 100 nm [5]. It is estimated at 80 nm on Silicon substrate (111). From Figure we see that a remarkable jump in the value

of the short-circuit current is obtained at a diameter of 80 nm, which has the critical diameter.

IV. Conclusion

The aim of our work was to be able to make significant improvements to the performance of silicon-based solar cells by the inclusion of germanium nanowires on the one hand, and on the other hand, by incorporating germanium into the amorphous silicon thin film. Our strategy consisted in particular of ordering the nanowires of germanium perpendicularly to the electrodes in order to improve significantly the collection of the photogenerated charges. Because of lower bandgap of hydrogenated microcrystalline silicon, it constitutes a useful complement to amorphous silicon-germanium. Its basic stability light-induced degradation made it an attractive for photovoltaic and optoelectronic applications. The optimization of the cell parameters is therefore a compromise between optimization of the optical absorption and the optimization of the collection of carriers. Nanowires-based solar cells are good candidates to reduce thickness solar cells and cost, due to their high surface-to-volume ratio permitting to enhance significantly light absorption.

REFERENCES

[1] N. Jain, "Design of III-V Multijunction Solar Cells on Silicon Substrate," Virginia Polytechnic Institute And State University, 2013.

[2] B. Dridi Rezgui, "Etude des propriétés optiques, électriques et structurales de nanoparticules de silicium insérées dans une matrice diélectrique et étude de leur intégration pour des cellules photovoltaïques à haut rendement, " L'institut national des sciences appliquees de Lyon, 2010.

[3] N. Brahimi, "Influence du PH sur les propriétés optiques et morphologiques des nanofils de silicium," Université de Boumerdès, 2012.

[4] H. J. Joyce, Q. Gao, H. H. Tan, C. Jagadish, Y. Kim, J. Zou, L. M. Smith, H. E. Jackson, J. M. Yarrison-Rice, P. Parkinson, M. B. Johnston, "III–V semiconductor nanowires for optoelectronic device applications," Elsevier, Progress in Quantum Electronics, vol 35, 2011, pp. 23–75.

[5] R. Boukhicha, "Croissance et caractérisation de nanofils de silicium et de germanium obtenus par dépôt chimique en phase vapeur sous ultravide," Université Paris-Sud 11, 2011.

[6] K.V. Maydell, K. Grunewald, M. Kellermann, O. Sergeev, P. Klement, N. Reininghaus, T. Kilper, "Microcrystalline SiGe Absorber Layers in Thin-Film Silicon Solar Cells," E-MRS Spring Meeting 2013 Symposium D- Advanced Inorganic Materials and Structures for Photovoltaics," 27-31 May 2013. Strasbourg, France : Journal Elsevier, Energy Procedia 44, pp. 209 – 215, 2014.

[7] Y. Leprince-Wang, "Élaboration et caractérisation des matériaux à l'échelle micro- et nanométrique," université de Marne La Vallée, 2003.

[8] L. A. Dobrzański, M. Musztyfaga and A. Drygała, "Final Manufacturing Process of Front Side Metallisation on Silicon Solar Cells Using Conventional and Unconventional Techniques," Strojniški vestnik-Journal of Mechanical Engineering 59, 3, 2013, pp. 175-182.

[9] S. Zeman "Amorphous and Microcrystalline Silicon Solar Cells".

[10] Q. Peng, Y. Qin, "ZnO Nanowires and Their Application for Solar Cells," Hangkong University, China.

[11] L. W. Veldhuizen, C. H. M. vander Werf, Y. Kuang, N. J. Bakker, S. J. Yun and R. E. I. Schropp, "Optimization of hydrogenated amorphous silicon germanium thin films and solar cells deposited by hot wire chemical vapor deposition," Thin Solid Films 595, 2015, pp. 226-230.

[12] K. Laurent, "Etude expérimentale de la microstructure et des propriétés électriques et optiques de couches minces et de nanofils d'oxydes métalliques (d-Bi_2O_3 et ZnO) synthétisés par voie électrochimique," Université de Paris-Est, 2008.

[13] L. A Dobrzański, M. Musztyfaga and A. Drygała, "Final Manufacturing Process of Front Side Metallisation on Silicon Solar Cells Using Conventional and Unconventional Techniques," Strojniški vestnik-Journal of Mechanical Engineering 59, 3, 2013, pp. 175-182.

[14] S. Emin, S. P. Singh, L.Han, N. Satoh, A.Islam, "Colloidal quantum dot solar cells," Elsevier Solar Energy 85, 2011, pp 1264–1282.

[15] S. E Jenks, Selecting Semiconductor Materials for the Quantum Dot Intermediate Band Solar Cell, Drexel University, 2012.

[16] B. Padmanabhan, "Modeling of solar cells," Arizona state University, 2008.

Application of the Indirect Adaptative Control on a Photovoltaic System

OUARET Ahmed[1], LEHOUCHE Hocine[2]
[1, 2] Laboratoire de Technologie Industrielle et de l'Information (LTII), Faculté de Technologie, Université de Bejaia, 06000 Bejaia, Algérie
[1] ahmed201189@hotmail.fr

HADDOUFI Lamia[3] and MECHEROUH Meriem[4]
[3, 4] Département de Génie Electrique
Faculté de Technologie, Université de Bejaia, 06000 Bejaia, Algérie

***Abstract*— The output power produce in photovoltaic modules depends on the temperature of the solar cells and the solar radiation. To maximize the efficiency of the system, it is indispensable to follow the maximum power point of the photovoltaic generator. The main objective of this work is to use indirect adaptive control to assure a tracking of a setpoint to obtain maximum power, despite the presence of different disturbances. This method is simple and robust to variations in temperature and irradiance. The simulation results obtained with Matlab/Simulink show the efficiency, robustness and performance of the control strategy applied to photovoltaic systems.**

I. INTRODUCTION

Due to global concern over climate change and rapid increase in electricity demand, renewable energy sources play an important role in electric power generation [1]. Various renewable sources such as solar energy, wind energy, geothermal, are harnessed for electric power generation. Solar energy is a good alternative to electricity production due to its cleanliness and availability [2, 3]. Solar energy is directly converted into electricity by solar photovoltaic (PV) module. PV modules have maximum power points (MPP) corresponding to the surrounding condition such as PV modules temperature, solar irradiance and cell area. In order for the PV module to deliver its maximum power, Many methods of tracking the maximum power point have been developed since the 1970s, starting with simple techniques such as MPPT controllers based on voltage and current feedback [4], to more powerful controllers using algorithms to calculate MPP of GPV, among the most used techniques, the method of Disturbance and Observation (P&O) and the method of Conductance Incrementation (IC) [5, 6, 7, 8].

The main objective of this paper is to develop an indirect adaptive control technique applied to photovoltaic systems. The main idea behind this control strategy is to track maximum power of photovoltaic cells, the most used, are detailed, a particular interest is to track the maximum power point of the PV array despite the presence of deferent disturbances and constraints without the presence of oscillations such as other techniques that have already been applied, and other advantage such as: robustness and good precision.

Remainder of the paper is structured as follows: Section 2 presents the choice of a model; Description of indirect adaptive control is shown in section 3; Section 4 devoted to the application of indirect adaptive control to the PV system; Section 5 is dedicated to the study of robustness. Conclusions and perspectives are drawn in the last section.

II. CHOICE OF A MODEL

A. *Photovoltaic system*

In our study we choose a solar panel type SIEMENS SM110-24, whose characteristics are given in Table I.

TABLE I. PARAMETERS OF A SIEMENS SM110-24 PHOTOVOLTAIC MODULE [9]

Parameters	**Values**
Photovoltaic Power (P_{pv})	110 W
Maximum current at PPM (I_{mpp})	3.15 A
Maximum voltage at PPM (V_{mpp})	35 V
Short circuit current (I_{cc})	3.45 A
Open circuit voltage (V_{co})	43.5 V
Temperature coefficient of short circuit current (a_{oc})	1.4 mA/°C
Temperature coefficient of open circuit voltage (B_{oc})	-152 mV/°C
Maximum power (P_{mpp})	110 W

B. *Model photovoltaic array*

The model used in this work is represented by an equivalent circuit given in Figure 1. This one contains a diode to optimize the modeling of some phenomena at the cell level, the series resistor (R_s) which models the ohmic losses and a shunt resistor (R_{sh}) which is used to model the losses around the junction due to the impurities and on the corners of the cell [10-11].

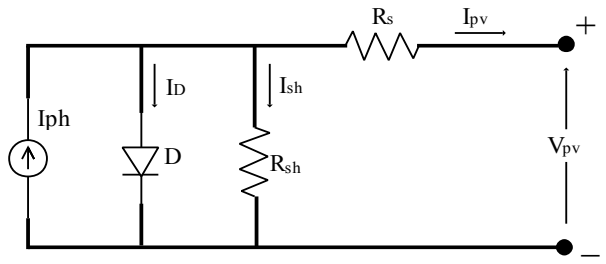

Figure 1. Equivalent circuit of solar cell with one diode

This model is expressed by the following equations [12]:

From Figure 1, the equation for the output current can be given by:

$$I_{PV} = I_{ph} - I_D - I_{sh} \quad (1)$$

- **Calculate** I_{ph}

The photocurrent I_{ph} is depends on the illumination and the panel temperature.

$$I_{ph} = P_1 E_s (1 + P_2 (E_s - E_{sref}) + P_3 (T_j - T_{jref})) \quad (2)$$

Where E_{ref} is the illuminance under STC conditions. T_j the jonction temperature of the panel and T_{jref} the reference temperature of the panel (K). P_1, P_2 and P_3 are constant parameters.

- **Calculate** I_D

The current of the diode is given by the equation:

$$I_D = I_s \, e^{\left(\frac{q(V_{ph} + R_s I_{ph})}{KAN_s T_j}\right) - 1} \quad (3)$$

$$I_s = P_4 T_j^3 e^{\left(\frac{-E_g}{KT_j}\right)} \quad (4)$$

With I_s the saturation current (A), q the elementary charge (1.6×10^{-19} C), k the Boltzmann constant (k=1.38*10^{-23} J/K), A the ideality factor of the junction and R_s and R_{sh} the series and shunt resistances respectively. N_s corresponds to the total number of cells connected in series and/or in parallel. E_g the gap energy (1,76×10-19) and P_4 is the constant parameter.

- **Calculate** I_{sh}

The saturation current is given by the equation

$$I_{sh} = \frac{V_{sh}}{R_{sh}} \quad (5)$$

From equations 2, 3 and 5 we get the overall equation:

$$I_{PV} = P_1 E_s \left(1 + P_2 (E_s - E_{sref}) + P_3 (T_j - T_{jref})\right) - P_4 T_j^3 e^{\left(\frac{-Eg}{KT_j}\right)} e^{\left(\frac{q(V_{ph} + R_s I_{ph})}{kAN_s T_j}\right) - 1} - \frac{V_{sh}}{R_{sh}} \quad (6)$$

III. INDIRECT ADAPTATIVE CONTROL

The basic philosophy of this methodology is to estimate the parameters of the unknown plant from input-output data and, in turn, use these estimates to adjust the parameters of a controller such that the transfer function of the controlled plant evolves to that of a model [13].

Figure 2 shows the bloc diagram for indirect adaptive control.

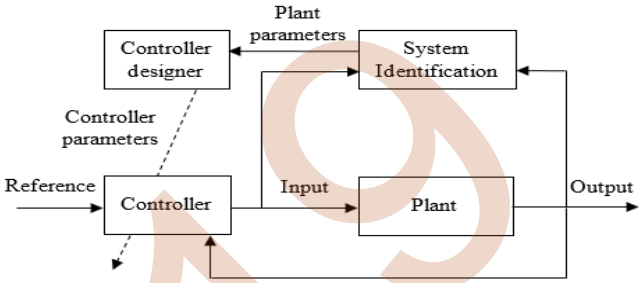

Figure 2. Indirect adaptive control

A. *Process identification*

1. *Model of the process* [14]

Considering a mono-variable linear invariant discrete model described by:

$$A(z^{-1}) y(k) = B(z^{-1})(u(k-d) + v(k-d)) \quad (7)$$

$$A(z^{-1}) = 1 + a_1 z^{-1} + \cdots + a_n z^{-n} \quad (8)$$

$$B(z^{-1}) = b_0 + b_1 z^{-1} + \cdots + b_m z^{-m} \quad (9)$$

with $d = n - m$

u and y are respectively input and output of the process.

v : disturbance

2. *Recursive Least Squares Algorithm* [14]

The objective is to minimize a mean square error corresponding to the sum of the squares of the gap between the output of the process to identify and that of the model obtained at each sampling instant.

$$V(\hat{\theta}, k) = \frac{1}{2} \sum_{i=1}^{k} \lambda^{k-i} \left[y(i) - \varphi^T(i) \hat{\theta} \right]^2 \quad (10)$$

where $0 < \lambda \leq 1$ is the forgetting factor

The form of the algorithm (RLS) in general is as follows:

$$\hat{\theta}(k) = \hat{\theta}(k-1) + K(k) \left[y(k) - \varphi^T(k) \hat{\theta}(k-1) \right] \quad (11)$$

$$K(k) = \frac{P(k-1)\theta}{\left[\lambda + \varphi^T(k) P(k-1) \varphi(k) \right]} \quad (12)$$

$$P(k) = \frac{1}{\lambda} \left\{ P(k-1) - \frac{P(k-1)\varphi(k)\varphi^T(k)P(k-1)}{\lambda + \varphi^T(k)P(k-1)\varphi(k)} \right\} \quad (13)$$

$$\hat{y}(k) = -a_1 y(k-1) \cdots - a_n(k) y(k-n) + b_0(k) u(k-d) + \cdots + b_m(k) u(k-m-d) \quad (14)$$

$$\theta = \left[a_1 \cdots a_n, b_0 \cdots b_m \right] \quad (15)$$

$$\varphi^T(k) = [-y(k-1)... -y(k-n), u(k-d)... u(k-m-d)] \quad (16)$$

$$\hat{y}(k) = \varphi^T(k)\theta \quad (17)$$

B. The RST control

An RST corrector is synthesized by an algebraic pole placement method. The goal is to give the closed loop the behavior of a system described by a model transfer function, expressed as a rational fraction in z^{-1}. Generally, this function is of the second order, defined on the basis of criteria of the type: damping, static gain, angular frequency, overshoot ... etc [14].

These criteria generally used to define the denominator $A_m(z^{-1})$ of the transfer function of the model. The choice of $B_m(z^{-1})$ on the other hand can not be completely imposed. Since the influence of the zeros of the transfer function is less than that of the poles, these constraints will not have an excessive effect on the behavior of the system [14].

This function is in the form

$$H_m(z^{-1}) = \frac{z^{-d} B_m(z^{-1})}{A_m(z^{-1})} \quad (18)$$

where z^{-d} is the pure delay of the process.

1. Structure of RST controller

The structure of a RST controller is given in the following figure where R, S and T are polynomials in z^{-1} [14] :

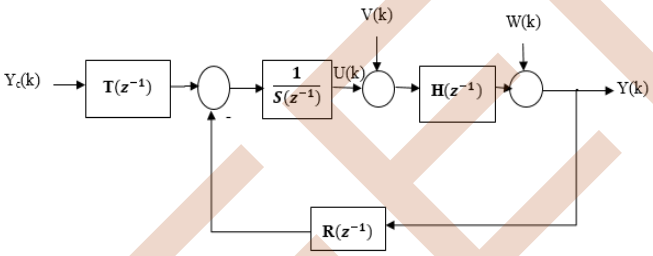

Figure 3. RST controller structure

The general form of the control law is given by:

$$S(z^{-1})U(z) = T(z^{-1})Y_c(z) - R(z^{-1})Y(z) \quad (19)$$

Where Y_c represents the setpoint and Y represents the output of the system.
Where the input $U(z)$ can be put in the form:

$$U(z) = \frac{T(z^{-1})}{S(z^{-1})}Y_c(z) - \frac{R(z^{-1})}{S(z^{-1})}Y(z) \quad (20)$$

From Figure 3, the output of the closed-loop process given by the according equation

$$Y(z) = \frac{B(z^{-1})}{A(z^{-1})}U(z) + \frac{B(z^{-1})}{A(z^{-1})}V(z) + W(z) \quad (21)$$

Where $V(z)$ and $W(z)$ are disturbances.

We will take back equations (20) and (21), only the terms (z^{-1}) and (z) will not be written just to lighten the shape of the equations [15] :
So :

$$SU = TY_c - RY \quad (22)$$

$$AY = BU + BV + AW \quad (23)$$

By multiplying (22) and (23) by A and R successively, then replace (23) in (22) we obtain:

$$(AS + BR)U = ATY_c - BRV - ARW$$

$$U = \frac{AT}{AS+BR}Y_c + \frac{BR}{AS+BR}V + \frac{AR}{AS+BR}W \quad (24)$$

By multiplying this time (22) by B, and (23) by S we'll have

$$(AS + BR)Y = BTY_c + BSV + ASW$$

$$Y = \frac{BT}{AS+BR}Y_c + \frac{BS}{AS+BR}V + \frac{AR}{AS+BR}W \quad (25)$$

C. Simulation parameters of the PV system used

It is very important to define the system parameters used, so that we can see its evolution over time, and for this the parameters of the system that we will use from now on are fixed with respect to the type of the panel used in the simulation (see Table I in Section II).

D. Identification of the process

Whatever the control approach, it is essential to identify the process. This is the most delicate part, where the automation engineer should define the excitation signals of the process and ensure the quality of the measurements.

This is why a pseudo random binary sequence (SBPA) is commonly used as the excitation signal because the quality of the identification is directly related to the richness of the input signal.

Indeed at each pole of the process corresponds to a pulsation, if it is not present in the input signal it will obviously unreal and this, whatever the method of identification used [16].

❖ **Parameters of the recursive least squares algorithm:**

The implementation of the recursive least squares algorithm presented above is used to approximate the process by a second-order model given by the following transfer function:

$$H(z^{-1}) = z^{-d}\frac{B(z^{-1})}{A(z^{-1})} = \frac{b_0 z^{-1} + b_1 z^{-2}}{1 + a_1 z^{-1} + a_2 z^{-2}}$$

After several tests during the simulation with different values of the parameters of the identification algorithm, it was noted that the best result found from the point of view of error and convergence of model parameters (See Table II).

TABLE II. IDENTIFICATION PARAMETERS AND RESULTS

1.Initialization :

- $A(q^{-1}) = 1 + 0.5q^{-1} + 0.5q^{-2}$
- $B(q^{-1}) = 0.5q^{-1} + 0.5q^{-2}$

2. Parameters of the identification algorithm

- $F(0) = 10^6, \lambda = 0.956.$
- The sampling time T_e=0.1 sec.

3. Simulation time 24s
4. The transfer function of the model

$$H(z) = \frac{0.00323z + 0.0007561}{z^2 + 0.001064z - 0.00177}$$

The model identified in this case is without delay (d=0), hence its transfer function can be given by:

$$H(z^{-1}) = z^{-d}\frac{B(z^{-1})}{A(z^{-1})} = \frac{0.00323z^{-1} + 0.0007561z^{-2}}{1 + 0.001064z^{-1} - 0.00177z^{-2}}$$

The parameters of the identified model are given in the following figure:

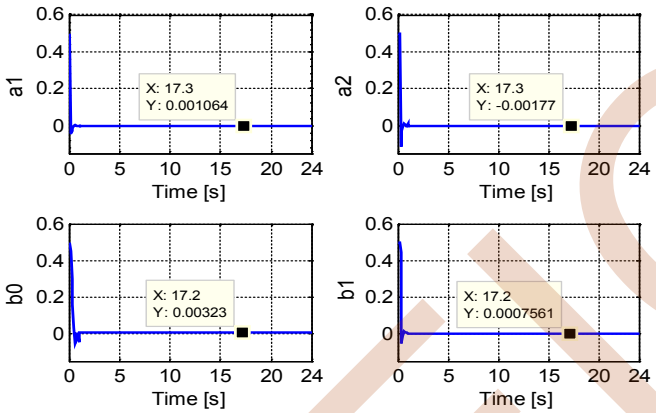

Figure 4. The parameters of the identified model

From Figure 4, the parameters of the identified model converge at a certain value so we can say that the identification step is validated.

IV. APPLICATION OF INDIRECT ADAPTATIVE CONTROL ON THE PV SYSTEM

The system in this case includes, the identifier by the LMS algorithm, the adaptive controller, the process and the RST polynomials. The recursive approach with a fixed forgetting factor has been adopted to estimate in real time the parameters of the system, and to adapt simultaneously the parameters of the RST controller, and at each instant t the coefficients of the RST regulator polynomials are updated. The principle is illustrated in the Figure 5.

The parameters of identification and RST controller are given in the table below.

TABLE III. PARAMETERS OF IDENTIFICATION AND RST CONTROLLER

1. Initialization

- $A(q^{-1}) = 1 + 0.5q^{-1} + 0.5q^{-2}$
- $B(q^{-1}) = 0.5q^{-1} + 0.5q^{-2}$

2. Parameters of the identification algorithm

- $\alpha = 10^6, \lambda = 0.956, d = 0 et\ T_e = 0.1\text{sec}$

3. Simulation time 24s
4. RST polynomials

- $R(q^{-1}) = \begin{bmatrix} 1 & -0.33672446714 & -4.14600796735e-005 \end{bmatrix}$
- $S(q^{-1}) = \begin{bmatrix} 98.3401255755 & -15.4654023733 & 0.836989869629 \end{bmatrix}$
- $T(q^{-1}) = \begin{bmatrix} 85.2367329234 & -1.53426119262 \ldots \\ 0.00920556715572 & 1.84111343114e-005 \end{bmatrix}$

A. Extraction of Pmax, Imax et Vmax

In order to extract the maximum available power and recover the reference signal applied for our control. We simulated the open loop panel for an irradiation of 1000W/m² and a temperature of 25°C.

After simulation, the following results were obtained:

P_{max}=109.2092w, I_{max}=3.1204A et V_{max}=34.9980V

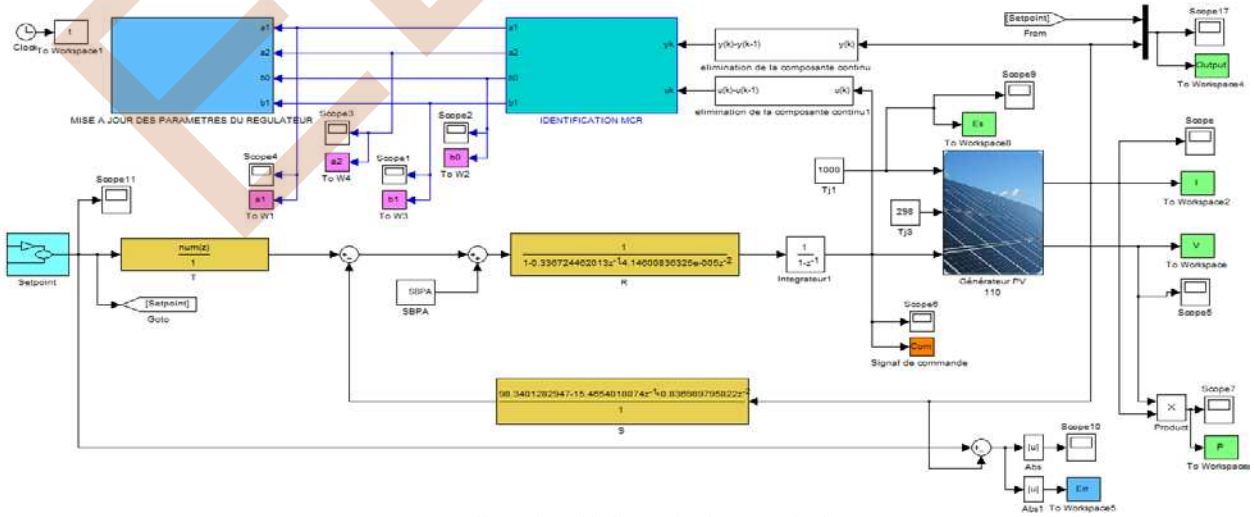

Figure 5. Illustrative of indirect adaptive control scheme

B. *Simulation of indirect adaptive control*

The simulation results for an irradiation of 1000W/m² and a temperature of 25°C are given in the following figures

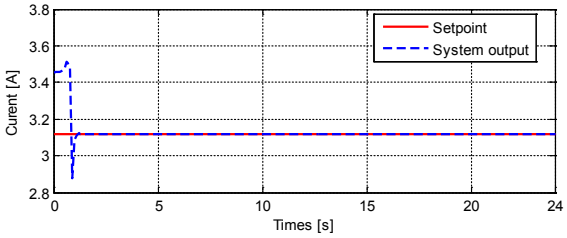

Figure 6. PV current

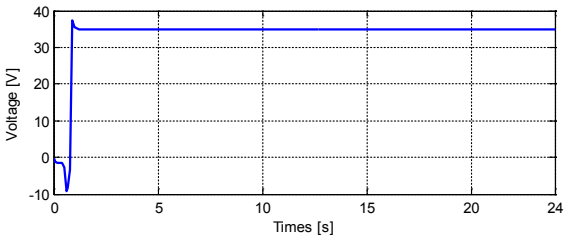

Figure 7. PV voltage

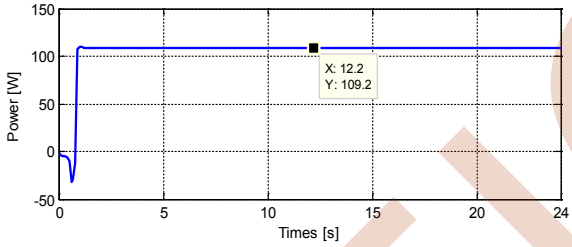

Figure 8. PV power

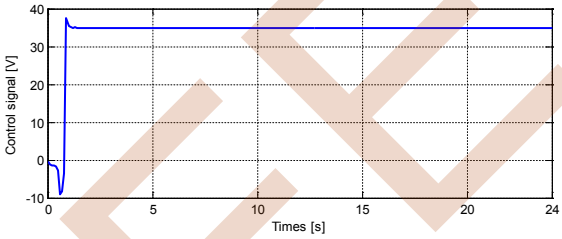

Figure 9. Control signal

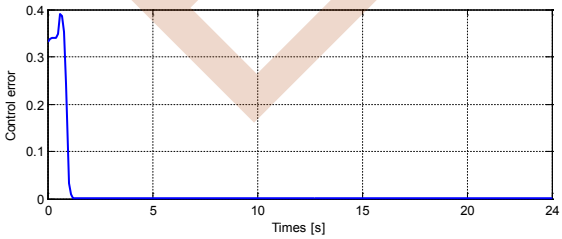

Figure 10. Control error

C. *Discussion of the results*

According to several tests that we have carried out, we note that the system output perfectly follows that of setpoint (see Figure 6) with a control error which equals to zero (see Figure 10). Figure 8 shows that the maximum power is reached. Concerning the control signal, oscillations are observed at the beginning of the simulation because of the adaptation of the parameters (a1, a2, b0, b1), then the signal stabilizes and without any exceeding of the max value of the voltage (see Figure 9).

V. STUDY OF THE ROBUSTNESS OF THIS CONTROL

In order to test the robustness of the indirect adaptive control, we have studied the case of the variation of the irradiance and the case of the variation of the temperature.

1. *Simulation results for irradiation variation*

In this case we applied to a setpoint corresponding to the irradiation given in Figure 11. The temperature is set at 25°C. The simulation results are shown in the figures below

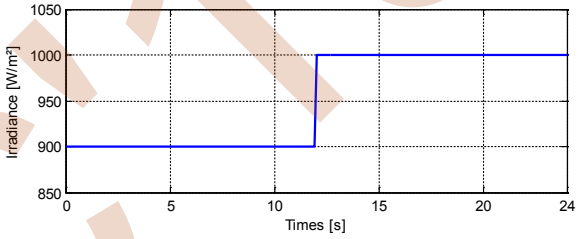

Figure 11. Irradiation variation

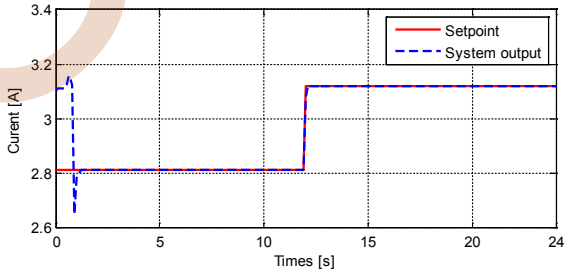

Figure 12. PV current

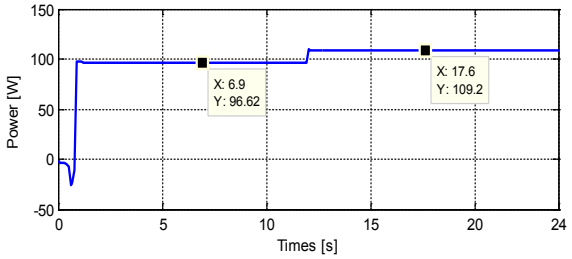

Figure 13. PV power

2. *Simulation results for temperature variation*

In this case we applied to a setpoint corresponding to the temperature given in Figure 14. The irradiation is set at 1000W/m². The simulation results are shown in the figures below

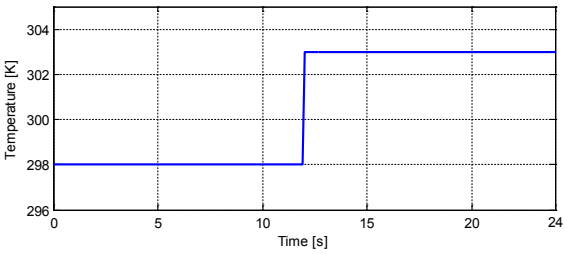

Figure 14. Temperature variation

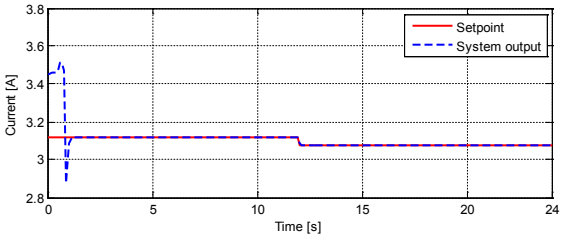

Figure 15. PV current

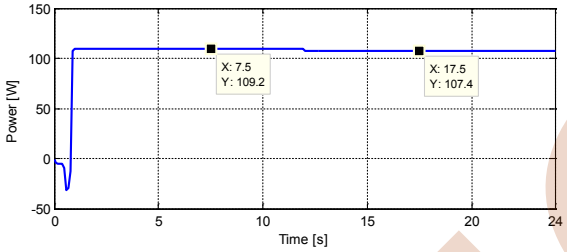

Figure 16. PV power

3. *Discussion of the results*

From the results obtained, we notice that the output of the system perfectly follows that of setpoint despite the variation of the irradiation and the temperature (see Figures 12 and 15), from where the error is almost zero in both cases and the desired maximum power is reached with the variation of the irradiation and the temperature (see Figures 13 and 16).

VI. CONCLUSION AND PERSPECTIVES

In this article, an advanced control method, namely the indirect adaptive control has been developed and applied to a photovoltaic system.

We have come to design a robust control that improves system performance despite the presence of various disturbances. Several simulations have been done which show that the automatic adjustment of the controller parameters, the permanent pursuit of the setpoint in order to recover the desired maximum power. The results obtained show the robustness and the effectiveness of this control strategy in improving performance in terms of stability, speed and accuracy.

As perspectives, this work can be improved by adding converters, battery and load. The implementation of this control on a photovoltaic panel will be very interesting.

REFERENCES

[1] Kaundinya, D. P., Balachandra, P., & Ravindranath, N. H. (2009). Grid-connected versus stand-alone energy systems for decentralized power—A review of literature. Renewable and Sustainable Energy Reviews, 13(8), 2041-2050.

[2] Parida, B., Iniyan, S., & Goic, R. (2011). A review of solar photovoltaic technologies. Renewable and sustainable energy reviews, 15(3), 1625-1636.

[3] Mellit, A., Kalogirou, S. A., Hontoria, L., & Shaari, S. (2009). Artificial intelligence techniques for sizing photovoltaic systems: A review. Renewable and Sustainable Energy Reviews, 13(2), 406-419.

[4] Salas, V., Olias, E., Barrado, A., & Lazaro, A. (2006). Review of the maximum power point tracking algorithms for stand-alone photovoltaic systems. Solar energy materials and solar cells, 90(11), 1555-1578.

[5] Femia, N., Petrone, G., Spagnuolo, G., & Vitelli, M. (2005). Optimization of perturb and observe maximum power point tracking method. IEEE transactions on power electronics, 20(4), 963-973.

[6] Ghassami, A. A., Sadeghzadeh, S. M., & Soleimani, A. (2013). A high performance maximum power point tracker for PV systems. International Journal of Electrical Power & Energy Systems, 53, 237-243.

[7] Zou, Y., Yu, Y., Zhang, Y., & Lu, J. (2012). MPPT control for PV generation system based on an improved inccond algorithm. Procedia Engineering, 29, 105-109.

[8] Hadji, S., Gaubert, J. P., & Krim, F. (2014, October). Experimental analysis of genetic algorithms based MPPT for PV systems. In 2014 International Renewable and Sustainable Energy Conference (IRSEC) (pp. 7-12). IEEE

[9] Rekioua, D., Achour, A. Y., & Rekioua, T. (2013). Tracking power photovoltaic system with sliding mode control strategy. Energy Procedia, 36, 219-230.

[10] Tsai, H. L., Tu, C. S., & Su, Y. J. (2008, October). Development of generalized photovoltaic model using MATLAB/SIMULINK. In Proceedings of the world congress on Engineering and computer science (Vol. 2008, pp. 1-6).

[11] Sera, D. (2009). Real-time modelling, diagnostics and optimised MPPT for residential PV systems. Institute of energy technology-Alborg university, Denmark.

[12] Anis, W. R., & Metwally, H. M. (1994). Dynamic performance of a directly coupled PV pumping system. Solar Energy, 53(4), 369-377.

[13] Narendra, K. S., & Valavani, L. S. (1978). Direct and indirect adaptive control. IFAC Proceedings Volumes, 11(1), 1981-1987.

[14] L. D. Landau. "Introduction to adaptive control". Edition Springer. London. 2011. 1-33.

[15] E. Godoy and E. Ostertag. "Commande numérique des systèmes : Approches fréquentielle et polynomiale : Supélec". Edition Ellipses. Paris.2003.

[16] H. Lehouche. "Commande supervisée des systèmes hybrides". Thèse de doctorat. Université de Bejaia. 2014.

The photovoltaic generation system impact on the energy demand and its financial analysis in the USTO campus

Nessim Abderrahim Bourahla
Department of Electrotechnics, Laboratory « LDDEE »
University of Sciences and Technology of Oran,''USTO-MB''
Oran , Algeria
nessim.bourahla@gmail.com

Mustapha Benghanem
Department of Automatics, Laboratory « AVCIS »
University of Sciences and Technology of Oran,''USTO-MB''
Oran , Algeria
mbenghanem69@yahoo.fr

Ali Tahri
Department of Electrotechnics, Laboratory « LGE»
University of Sciences and Technology of Oran,''USTO-MB''
Oran , Algeria
alitahri.dz@gmail.com

***Abstract*-- The photovoltaic energy of a microgrids has shown great advantages due to the reliable operation of the distribution networks with high flexibility and robustness and also to enable efficiency.The purpose of this study is to analyze the economic impact of photovoltaic energy generation through a microgrid to be installed on the campus of the University of Science and Technology (USTO). In this work, hourly solar and temperature data provided by the local weather service are used to study the distribution and duration of solar radiation on campus. The photovoltaic solar energy generated is analyzed taking into account economic aspects such as the investment cost in the photovoltaic system and the annual energy production cash flow. The installed power of the photovoltaic system has been calculated and the energy produced estimated. The feasility analysis shows an internal rate of return of 5%, a payback year of 10,3, and a profitability index of 1,78.**

Keywords -- Hybrid power systems - PV array - Microgrid - Renewable energy - Radiation distribution - Grid-connected photovoltaic system–Economic analysis

I. INTRODUCTION

The production of electricity from fossil resources has adverse effects on the environment such as global climate change and air pollution. The rising cost of fossil fuels and increased consumption of energy resources will play a crucial role in the use of clean energy in many parts of the world in the near future. Over the past decade, the trend of electricity generation from renewable energy has taken the place of conventional fossil fuels worldwide. [1]

Advances in power electronics have also contributed more effectively and more reliably to the integration of renewable resources into power grids [2]. The cost reduction of photovoltaic (PV) technology and related components, such as inverters and batteries, and the sharp decline in the cost of large wind turbines have made these energy sources more attractive in many countries.

The large-scale development of renewable energy systems and their integration to utility grid are considered as the most important challenges for the sustainable environment. The electric energy industry restructuring and the introduction of the concept of a smart grid have also led to new technologies (distributed energy resources and decentralized generation) become more and more widely adopted [2]. Since the industrial and residential sectors are among the largest consumers of electrical energy, decentralized electricity generation has now become a potential solution for satisfying the energy needs locally. In comparison to large-scale wind energy, the cost of deploying a PV system is much higher, and therefore implying that a larger financial subsidy is needed to increase the PV installation capacity by customers [3-5].

The use of photovoltaics as a renewable source for reliable electricity production has been increasing rapidly for more than 30 years thanks to specific national and transnational incentive schemes [6]. In addition, PV as the use of renewable energy sources is becoming a popular account of the high degree of modularity, the lack of additional resources, the absence of moving parts and the low cost of maintenance. Another advantage of using PV is that as the increasing rate of PV use increases, the cost of generating PV electricity decreases steadily [7]. Studies have shown that photovoltaic systems will be widely used in the future, given the rapidly declining cost of photovoltaic systems. [8].

An economic analysis must be carried out to evaluate the profitability to ensure that the investment cost can be recovered throughout the life cycle. More studies on the profitability analysis have been carried out. The main factors affecting PV deployment are the initial capital cost of the system, the feed-in tariff and the capital cost subsidy rate [9].

Several works in the field of photovoltaic micro-networks have been carried out around the world to analyze their economic benefits. Examples of these studies were carried out on 1 MWp photovoltaic power plant in Farafenni (Gambia) [10]. PV system having an installed capacity of 5 MWp in Jordan, and on a photovoltaic plant of 1 MWp in Osmaniye [1].

II. DIMENSIONING OF PHOTOVOLTAIC SYSTEM AND ESTIMATION OF CAMPUS SOLAR POTENTIAL

The Algerian government has adopted a series of support measures for the promotion of renewable energies through the establishment of a favorable legal framework and a National Fund for Energy Management and Renewable Energies and

Cogeneration (FNMEERC) which is supplied annually with 1% of the oil royalty and the product of certain taxes [11]. Highest potential of solar resources in the world are situated in Algeria because of its geographical location. The average annual solar radiation and the sunshine duration across the whole country, are estimated at 5.7 kWh / m2 / day and 2000 hours per year, this latter can reach 3900 hours (highlands and Sahara). The energy received daily on a horizontal surface of 1m2 is around 5 KWh over most of the national territory, we can see the highest regions are the Sahara and the highlands and the coastal region to the north have respectively 2263 kwh / m2 / yr and 1700KWh / m2 / yr, this latter is less important than the southern regions but remains sufficient to provide solar energy. This solar field exceeds 5 billion GWh [12].

The support proposed by the government for the promotion of solar energy is done through the mechanism of feed-in tariff guaranteed (Table I). This system allows solar energy producers to profit from tariffs granting them a reasonable return on their investment over a 20 year eligibility period. During this period, the producer receives, in the first five years period, a fixed single purchase tariff which is calculated based on an estimated reference potential of 1 500 hours of full operation charge. In the second phase, and for the remaining duration of the contract, this single tariff can be readjusted, according to the real potential of the site [13]. Beyond this period, facilities can still operate without benefiting from this mechanism. However, the solar energy produced payback will be evaluated at the market rate. The additional costs generated by these rates will be borne by the FNER as diversification costs, the distributor who buys this energy at the guaranteed purchase rate is therefore reimbursed for the difference between the guaranteed purchase price and a tariff of reference which is the average price of conventional electricity [11], Solar radiation is influenced not only by the solar position, but also by the weather condition.

The characteristics of solar radiation variation for a position are determined by measuring solar radiation in that position. Maximum and minimum total solar radiation observed in 2015 are shown in Fig. 1. In addition, the highest monthly average radiation of 5,0 kWh/m^2/day was recorded in May 2015, while the lowest monthly average solar radiation was 2,45 kWh/m^2/day in December 2015.

As can be seen in Fig. 1, the monthly mean values of global solar radiation remain almost constant every month and each year. As a result, the total value of solar radiation measured based on 2015 was about 1,65 MWh/m^2/year for a full year.

Table III shows the monthly measured average radiation and the average temperature. Moreover, Oran has a significant solar energy potential to produce electricity. To provide the specific power at a specified voltage and current, PV modules can be collocated to form a PV array. For this purpose, 245 W peak PV modules which contain monocrystalline silicon solar cells are used [15]. The data acquisition system and software tools used in this study can import weather data from a dozen different sources as well as personal data. It will allow us to size the photovoltaic installation on campus. In this way, it can be deduced that the total installed capacity of the solar power plant consisting of 1 845 modules and calculated using the technical specifications of Table IV is 452 kW. The PV system will be installed on the campus buildings roofs.

These roofs have plane surfaces, the inclination of each photovoltaic panels is 36 °, which represents the optimal angle for the whole year,the total covered surface is approximately 3000m2 for a total of 20 roofs. To determine the total generation electricity from the PV system accurately, the PV module, inverter and external transformer losses are taken into consideration. The calculated energy injected into the local grid is 604 102 kWh/year in Oran. A basic evening power consumption of about 150 kW corresponding to lights and devices in standby can be noticed [16,19]. The power consumption for a winter day can reach almost 1 000 kW unlike a summer day where it reaches to 550 kW. As shown in Fig. 2, the daily consumed power over the year presents important peaks in the winter from January to March but also in the summer during the month of June. A drastic decrease of consumption can be observed during the weekend and represents the lowest energy consumption. According to Fig. 2, the maximum power peaks that can be reached is 1 050 kW in winter period and 700 kW in summer period. The minimum power is 150 kW during weekends.

TABLE I. GUARANTEED FEED-IN TARIFF PER POWER RANGE AND ACCORDING TO THE POTENTIAL IN EURO / KWH

Regulatory adjustment limit	**Number of hours of operation (kWh / kW / year)**	**Guaranteed feed-in tariff (DA/kWh)**	
		Phase I	Phase II
-15%	1275-1349	15.94	20.08
	1350-1424		18.83
	1425-1499		17.45
Reference potential	1500-1574		15.94
+15%	1575-1679		14.43
	1650-1724		13.06
	≥1725		11.80

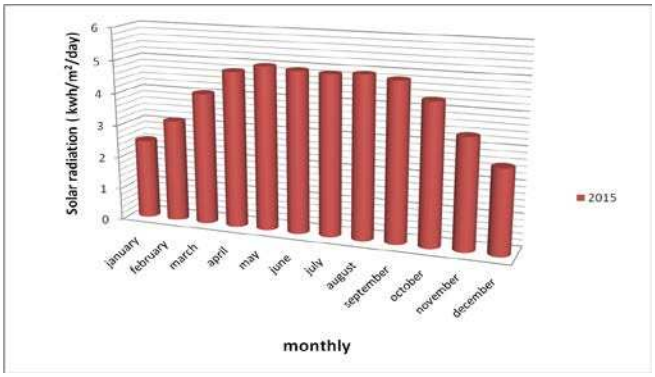

Fig .1. Monthly averages of daily solar radiation throughout 2015.

Global radiation, sunshine duration, and temperature as measured datas are generally necessary to produce electricity with a photovoltaic power plant in a selected region. Therefore, the values of the daily measurement datas at Oran city are given in Table II. The table shows that the value of

monthly measured average radiation is 125.183 kWh/m2; and the value of annual average temperature is 18.75°C.Moreover, it is clear that Oran has a significant solar energy potential to produce electricity.

PV modules can be collocated to form a solar array to provide the specific power at a specified voltage and current. For this purpose we choose a 245W peak PV module, which contains monocrystalline silicon solar cells [15]. Pvsyst is a software that can import weather data from a dozen different sources as well as personal data, it allows a project to be studied, dimensioned and simulated. It will allow us to size the photovoltaic installation on to campus, In this way we deduce that the capacity which can be installed is 452 KW of a power plant constituted by 1845 modules calculated with using the technical specifications of table III. The PV system will be installed on the campus buildings roofs, these roofs have plane surfaces, the inclination of each photovoltaic panels is 36 °, which represents the optimal angle for the whole year, the total covered surface is approximately 3000m2 for a total of 20 roofs. In this study, it is seen from Figure 3 and 4 that measured annual average solar radiation to the horizontal surface is 1502 kWh/m2. As shown in Figure 5, for determining total generation electricity of a PV system, we take into account PV and module loss, inverter loss, and external transform. With using the study of Verma and Singhal [17], the calculated energy injected into grid is 604102KWh/year in Oran.

TABLE II. THE VALUES OF DAILY AVERAGE MEASUREMENT DATA

Months	Daily average radiation (kWh/m2)	Daily average temperature (C°) [14]
January	2,45311488	10,3
February	3,14340703	11,4
March	4,06018611	13,7
April	4,79475285	18
May	5,00881897	20,7
June	4,93664186	22,5
July	4,8976206	27,3
August	4,95154414	27,6
September	4,84672324	23,7
October	4,32233579	21
November	3,39003843	15,4
December	2,58747094	12,8

TABLE III. TECHNICAL SPECIfiCATIONS OF A PHOTOVOLTAIC MODULE USED [15]

Module specifications for standard conditions of 1000w/m^2,25°C and AM=1.5	
Rated power (Pmax)	245 W
Current at Pmax	8.2 A
Voltage at Pmax	30.1 V
Short-circuit current	8.7 A
Open-circuit current	37.7 V
Coefficient of current (Ki)	0.032 A/C°
Coefficient of voltage (Kv)	-0.32 V/C°
Number of cells in series (ns)	60

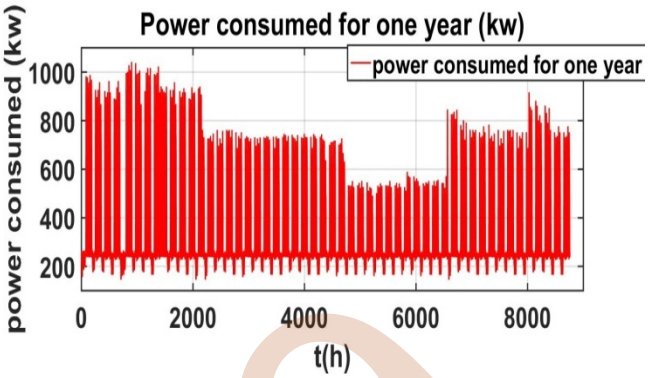

Fig .2. Power consumption data for one year

The campus electrical network combined with the PV system is shown in Fig. 3. This network is supplied with 10 kV from the national grid. Electrical energy is supervised by an energy center inside the campus. This electrical energy feeds the entire campus consisting of 9 zones and each zone contains different loads. Each zone is equipped with a MV/LV transformer and several protection circuits (circuit breakers, fuses, etc.). The PV generator, which consists of photovoltaic panels, will be connected to each zone via a power conversion stage (DC/DC and DC/AC). This proposed microgrid configuration contributes in the reduction of electricity bill and ensures autonomy of supply in certain situations. The PV generator consists of a total of 1 845 solar panels. Based on the calculations, the electrical energy generated by the PV panels will be sufficient to satisfy the electricity needs of all the campus facilities and will reduce the energy demand from the grid.

A series of simulation results are presented to illustrate this situation. During weekends, the electrical power generated from PVs will be sufficient to satisfy the consumption as shown in Fig. 4 and 5. Fig 6 and 7 show the electrical energy supplied by the PVs during the other days of the week, energy will not be enough but the demand from the electric provider will be less than without the contribution of the PV especially in summer where the consumption is lower than the winter.

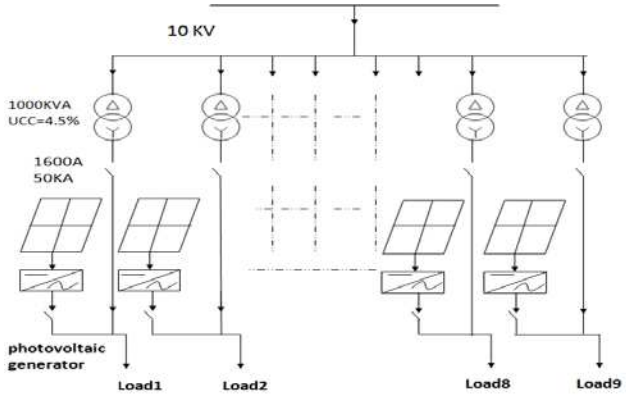

Fig .3. general electrical diagram of the microgrid

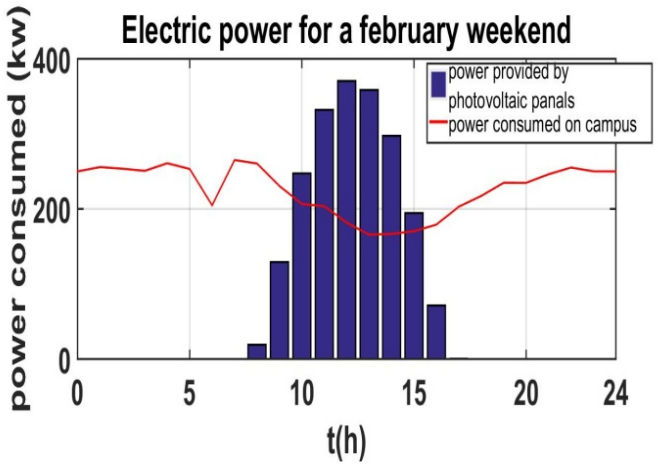

Fig .4. Power consumption and power provided by photovoltaic panels for a weekend of February

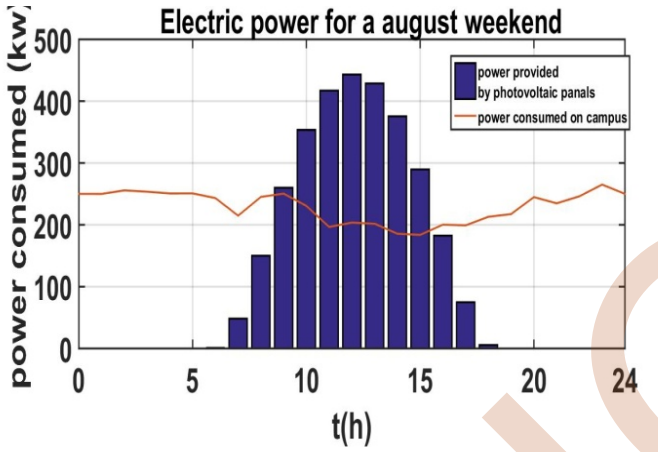

Fig .5. power consumption and power provided by photovoltaic panels for a weekend of August

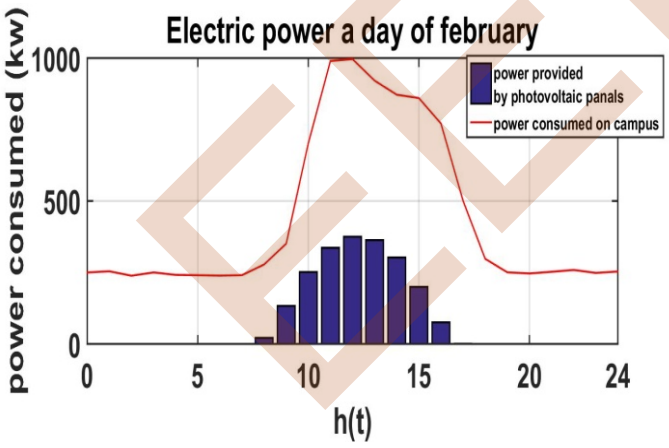

Fig .6. Power consumption and power provided by photovoltaic panels for a day of February week

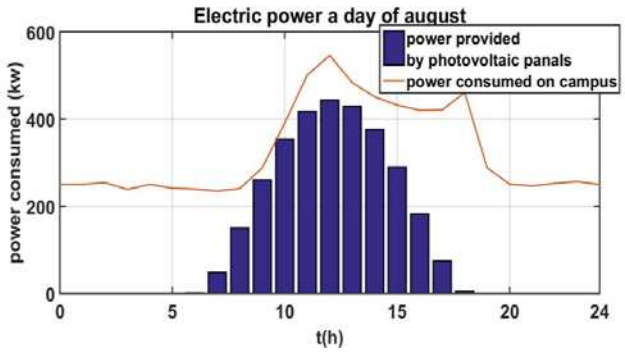

Fig .7. Power consumption and power provided by photovoltaic panels for a weekday of August on campus

The energy provided by the photovoltaic panels as well as that consumed on campus is plotted for each month as shown in Fig. 9. The contribution of this photovoltaic energy will reduce the supply of energy by the supplier. From Figure 9 we deduce that the photovoltaic production is 938 kWh for the whole year and that of the consumption is 2595 kWh. In conclusion the contribution of photovoltaic production in our case is 36%, it will play a big role in the financial aspect.

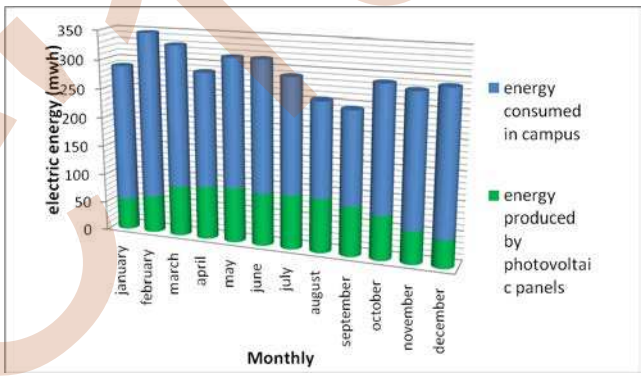

Fig .8. Monthly photovoltaic energy production and load demand for each monthly

III. FINANCIAL ANALYSIS

Several methods are used to calculate the return on the investment. For determining the economic viability of this type of project, the net present value (NPV), the internal rate of return (IRR), the payback years (PBY) and the profitability index (IP) are the most commonly used method. These methods are analyzed in this study. The NPV as an economic indicator compares the present value of all cash flows with the present value of all cash flows associated with an investment project according to equation (1) computed at the discount rate [1,5,9,18,19,20]. The positive NPV represents an indicator of a potentially feasible project. This is the most accepted standard method used in financial evaluations for long-term projects.

$$NPV = \sum_{y=0}^{Y} \frac{CF_y}{(1+r)^y} - C_0 \quad (1)$$

where: C_0 – capital investment cost of the photovoltaic system, r – annual discount rate, CF_y – net cash inflow for year y.

The internal rate of return (IRR) is an indicator which should be compared to an interest rate and may invalidate the NPV.IRR is solved by setting the NPV to zero, a high IRR indicates that the investment opportunity is favorable. Since it is higher than the discount rate, the PV project is considered satisfactory and interesting. The IRR is given by: [1,5,18,19,20].

$$0 = \sum_{y=0}^{Y} \frac{CF_y}{(1+IRR)^y} - C_0 \quad (2)$$

It is necessary to first calculate the annual cash flow (CF), which is the difference between the cash and the cash out, as indicated in the equation (3) [9,18].

$$CF_y = Cashinflow_y - Cashoutflow_y \quad (3)$$

$$CF_y = (C_{APSS,Y}) \times (1-dr)^y - C_{O\&M,y} \quad (4)$$

where : $C_{APSS,y}$ – annual power solar saving cost at year y, dr – PV performance derating rate, $C_{O\&M,y}$ – is the annual cost of operation and maintenance at the year y.

The payback years (PBY) can be obtained by equation (5) [19,22]:

$$PBY = \frac{\log(1 - \frac{C0}{CF1}.r)}{\log(\frac{1}{1+r})} \quad (5)$$

The profitability index (PI) indicates the amount of profit or loss that the project makes in a certain period. It is calculated by dividing the NPV value by the initial investment and adding 1, as shown in the equation (6) [1,18]. There is a break-even point when PI equals 1. When PI equals 2, the profit is doubled on the investment. The time of the investment assumed for this work is 25 years.

$$PI = \frac{NPV}{Initialinvestment} + 1 \quad (6)$$

IV. Results and Discussions

Several parameters were considered to calculate the economic viability of the 452 kW PV system. These include the total investment cost, the fixed operating costs, of maintenance, repair and use, the price of guaranteed purchase offered by the government and the increase in energy price. So the costs of solar PV system that will produce electricity are analyzed and evaluated on the basis of Algerian's regulations. The different solar radiation for the whole year 2015 and the average annual solar radiation measured at the horizontal surface is 1 502 kWh/m^2 (Fig. 1). Several parameters were considered for the total production of the PV system, the energy injected into the electrical network is calculated at 604 102 kWh/year for the city of Oran. The economic input parameters are summarized in Table IV (cost of afflation, discount and interest). The different costs used for this solar PV system are given in Table V.

Table V shows that PV panels and their associated equipment are the main elements for solar PV investment and represents 70,35% or 44 140 404 DA of the total investment which is 62 744 000 DA The rest of the investment will be distributed among the other equipment which will represent 29,65% (i.e. 18 603 596 DA) of the total investment. All these costs and the different rates given in Tables IV and V were used for the economic feasibility analysis of this system.

A project is considered financially feasible only if the corresponding NPV is positive. The NPV determines whether the project is generally an acceptable investment or not.

Based on the savings achieved by the PV contribution, Table VI shows the investment cost which represents the present value of the expenditures for this year, i.e. 62 744 000 DA. The NPV is a positive value, that is, 2 485 749,47 DA. Since NPV = 0, then the evaluation is feasible. Here, in Fig. 9, it is shown that PBY and NPV are 10,3 years and 49 353 070,43 DA respectively over the lifetime of the PV.

The development of a PV project would be acceptable if IRR is equal to or greater than the required rate of return. the calculated IRR value for Oran is 5% higher than the discount rate. Thus, the investment considered appears profitable. The profitability index (PI) indicates the amount of profit or loss that the project makes in a certain period of time. In this case it is equal to 1,78 which is greater than the breakeven point which is equal to 1.

TABLE IV. VARIOUS RATES USED IN ECONOMIC FEASIBILITY

Item description	value
Discount rate [23]	3,75%
Photovoltaic panel yield loss	0,8%
Initial annual system power production (kWh)	604 011,771
Project life	25 years

TABLE V. COST AND ECONOMIC ASSUMPTION FOR THE PV POWER PLANT[1].

Item description	Cost (DA)	% of total cost
Feasibility study	564 696	0,9%
Devlepoment and Engineering cost	627 440	1,0%
Solar PV equipment	44 140 404	70,35%
Other power equipment+Miscellaneous	17 411 460	27,75%
Total initial cost	62 744 000	100%
Annual operation and maintenance	1 800 000	Annual

TABLE VI. SIMULATION RESULTS OF NPV.

Years	Cash flow(DA)	Present value of cash flow(DA)	NPV (DA)
0	0	0	-62 744 000
1	7 750 924,05	7 470 770,17	-55 273 229,83
2	7 674 516,66	7 129 758,54	-48 143 471,29
3	7 598 720,52	6 804 185,66	-41 339 285,63
4	7 523 530,76	6 493 356,98	-34 845 928,65
5	7 448 942,51	6 196 609,03	-28 649 319,62
6	7 374 950,97	5 913 308,07	-22 736 011,55
7	7 301 551,36	5 642 848,72	-17 093 162,83

8	7 228 738,95	5 384 652,72	-11 708 510,12
9	7 156 509,04	4 613 149,54	-7 095 360,58
10	7 084 856,97	4 902 866,11	-2 192 494,47
11	7 013 778,11	4 678 243,94	2 485 749,47
12	6 943 267,89	4 463 819,83	6 949 569,30
13	6 873 321,75	4 259 134,00	11 208 703,30
14	6 803 935,17	4 063 747,28	15 272 450,58
15	6 735 103,69	3 877 240,19	19 149 690,76

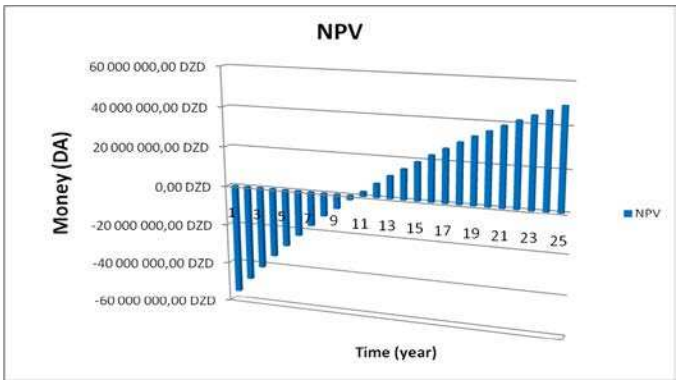

Fig. 9. NPV for the PV installation.

V. CONCLUSION

Photovoltaic solar energy is a clean and reliable source of energy. In addition, as market demand and photovoltaic system production increase the cost of photovoltaic energy technology is gradually decreasing. This study makes a comparison between the production of a photovoltaic energy and the energy consumption on the university campus of USTO. We present economic analysis of the photovoltaic generator that is connected to the local electrical network of the campus. In this paper we showed that the campus presents a high solar potential because of its high measured solar radiation. We also determine the total installed solar power. It is equal to 452 kW and represents 36% of the total power demand. The generated PV energy will mitigate the demand to the electricity supplier.

The average value of the internal rate of return (IRR) has been set at 5%, The payback year of this investment (PBY) was 10,3 which is good index for returns to cover investment costs and the profitability index (PI) is equal to 1,78, which shows that the capital budget is more appropriate for this profitable investment.

In our analysis the net present value (NPV) method is a very good way to analyze the profitability of an investment. This NPV was calculated, it corresponds to positive value of 2 485 749,47 DA. This economic analysis shows that the solar photovoltaic system project at USTO campus can be considered as profitable investment with consequent financial contribution.

REFERENCES

[1] Yaniktepe, B., Kara, O., & Ozalp, C. (2017). "Technoeconomic Evaluation for an Installed Small-Scale Photovoltaic Power Plant". *International Journal of Photoenergy*, *2017*.

[2] Moradi, H., Abtahi, A., & Zilouchian, A. (2017). "Financial Analysis of a Grid-connected Photovoltaic System in South Florida". arXiv preprint arXiv:1709.05923.

[3] J. Bebic, R. Walling, K. O'Brien, and B. Kroposki, "The sun also rises,"*IEEE Power Energy Mag.*, vol. 7, no. 3, pp. 45–54, May/Jun. 2009.

[4] European Photovoltaic Industry Association, Solar Generation V-2008.[Online]. Available: http://www.greenpeace.org/raw/content/international/press/reports/solar-generation-v-2008.pdf

[5] LIN, Chia-Hung, HSIEH, Wei-Lin, CHEN, Chao-Shun, *et al.* Financial analysis of a large-scale photovoltaic system and its impact on distribution feeders. *IEEE Transactions on Industry Applications*, 2011, vol. 47, no 4, p. 1884-1891.

[6] International Energy Agency (IEA), "Report IEA-PVPS T1-24:2014," PVPS Report Snapshot of Global PV 1992–2013 Preliminary Trends Information from the IEA PVPS Programme, 2014.

[7] Bianchini, M. Gambuti, M. Pellegrini, and C.Saccani, "Performance analysis and economic assessment of different photovoltaic technologies based on experimental measurements," Renewable Energy, vol. 85, pp. 1–11, 2016.

[8] M. S. Cengiz andM. S.Mami, "Price efficiency relationship for photovoltaic systems on a global basis," International Journal of Photoenergy, vol. 2015, Article ID 256101, p. 12, 2015.

[9] Hsu, C.-T., R. Korimara, and T.-J. Cheng, Cost-effectiveness analysis of a PVGS on the electrical power supply of a small island. International Journal of Photoenergy, 2014.

[10] S. Sowe, N. Ketjoy, P. Thanarak, and T. Suriwong, "Technical and economic viability assessment of PV power plants for rural electrification in the Gambia," Energy Procedia, vol. 52, pp. 389–398, 2014.

[11] Programme National des Energies Nouvelles et Renouvelables, Republic of Algeria ,Ministry of energy, http://www.energy.gov.dz/francais/uploads/2016/Programme-National/Programme-National-Energies-Nouvelles Renouvelables.pdf.

[12] Potentiels des Energies renouvelables, http://www.energy.gov.dz/francais/index.php?page=potentiels.

[13] Photovoltaïque : Les tarifs d'achat garantis en Algérie , JOURNAL OFFICIEL DE LA REPUBLIQUE ALGERIENNE N°23,http://www.energy.gov.dz/francais/uploads/2016/Textes_Legislatifs_et_Reglementaires/Legis_Energies_Rrenouvelables/Art2_2-Fevrier2014_tarifs_achat_garantis_conditions_application_Elect_photovoltaique.pdf

[14] Nessim A.B., Mustapha B., Hamid B., Conception and Analysis of a Photovoltaic Microgrid in the USTO Campus, The International Conference on Electrical Sciences and Technologies in Maghreb (CISTEM 2018)

[15] Bosch Solar Module c-Si M60 ,"Haute performance et stabilité élevé",Modules solaires de Bosch Solar Energy.

[16] Temperature of the city of Oran for the year 2015 with wunderground , https://www.wunderground.com/history/airport/DAOO/2015/1/1/CustomHistory.html?dayend=1&monthend=1&yearend=2016&req_city=&req_state=&req_statename=&reqdb.zip=&reqdb.magic=&reqdb.wmo=

[17] A. Verma and S. Singhal, "Solar PV performance parameter and recommendation for optimization of performance in large scale grid connected solar PV plant—case study," Journal of Energy Power Sources, vol. 2, no. 1, pp. 40–53, 2015.

[18] S. Rodrigues, R. Torabikalaki, F. Faria et al., "Economic feasibility analysis of small scale PV systems in different countries,"Solar Energy, vol. 131, pp. 81–95, 2016.

[19] Chen, C. S., Hsu, C. T., & Korimara, R. (2012). The photovoltaic generation system impact on the energy demand of a small island and its financial analysis. Energy Procedia, 14, 411-417.

[20] analysis of grid connected photovoltaic system in Spain," Renewable Energy, vol. 31, no. 8, pp. 1107–1128, 2006.

[21] LES INSTRUCTIONS - ANNEE 2017, LE TAUX DE RÉESCOMPTE, BANQUE OF ALGERIA , http://www.bank-of-algeria.dz/html/legist2017.htm

[22] Gillian Basso , 'Approche à base d'agents pour l'ingenierie et le contrôle de micro-reseaux', Grade de Docteur de l'Universite de Technologie de Belfort-Montbeliard ,

Fuzzy DPC of Grid Connected PV System Associated to an APF for Power Quality Enhancement

Sofia Lalouni Belaid, Zoubir Boudries,Amel Aoumer
Laboratoire de Technologie Industrielle et de l'Information (LTII),
Faculté de Technologie, Université de Bejaia, Algérie
lalouni_sofia@yahoo.fr

Abstract—**Solar energy is the kind of renewable power generation technologies. It is being widely used, since it is free, clean, and its technology is now well mastered. This paper presents an application of active power filter (APF) in grid connected photovoltaic (PV) system for power quality improvement. A new fuzzy direct power control (FDPC) technique has been proposed to control the injection of the available maximum active power from the PV generator into the grid, to compensate reactive power and to reduce the total harmonic distortion (THD) of grid current caused by connected nonlinear load. In this technique the switching states of the inverter are selected from a fuzzy inference system based on the errors between the active and reactive powers and their reference values and the line voltage vector position. In order to demonstrate the performance of the proposed control strategy and to study the effectiveness of APF, simulation model has been developed using Matlab/ Simulink and Sim Power System, under irradiance and load disturbances. Simulation results exhibit the effectiveness of the proposed system.**

***Keywords*-PV system; MPPT; Fuzzy Direct Power Control (DPC); Active power filter (APF).**

I. INTRODUCTION

The increase of world energy demand has seriously stimulated the search of new sources of energy since the primary sources are on the verge of extinction and causes serious environmental pollution[1-2]. Renewable energy sources have received much more attention due to the advantages such as less environmental impact and offer clean and abundant energy [3]. Photovoltaic energy is being widely used, since it is free, clean and its technology is now well developed [4]. Photovoltaic installations are classified according to their operating, namely standalone and grid connected PV systems. Standalone application, isolate areas are supplied by DC or AC power converters and energy storage equipments [5]. The grid connected PV application, has nowadays become more popular because of its reliable performance and its ability to generate power from clean energy resources [6]. Traditionally, grid connected converters are designed with controlled converters preceded by DC links. Industrial and domestic equipments use more and more electronic circuits with a nonlinear behavior responsible for grid pollution, they cause power quality deterioration and generate harmonics [2].

Passive filters were the traditional methods for harmonic filtering with advantages such as simplicity, reliability and low cost [3]. Nevertheless, in practical applications, they present many disadvantages such as large size, resonances which are the principal causes of several nuisances, and complexity in the power system[6,7]. To overcome the shortcomings of passive filters, active power filteris an interesting solution to passive ones for current harmonics elimination and reactive power compensation and power factor correction [3,7]

The structure of the active power filter (APF) consists essentially of two parts, a power and a control part [2]. The power part consists of power electronic device. These last decade, PWM converters have become the most popular electronic devices thanks to their viable advantages: bi-directional power flow, low harmonic distortion of line current [8]. Many researchers have been done on control of active power filter supplied by photovoltaic system. Voltage-oriented control (VOC), which is a well-known method of control provides a good dynamic and static performance, however, it presents some disadvantages such as coordinate transformation and power decoupling operation using internal current control loops [9]. P–Q theory, based on the harmonic current identification and instantaneous current control loops is used for harmonic currents detection and elimination [6]. Direct power control (DPC), which is based on "*p-q Theory*" and proposed by Akagi et al in 1983 for other applications, is widely used[2,7,9-11]. The DPC has many advantages such as easy to implement, quick response and robustness [9-11]. The major inconvenience of DPC is located in its variable switching frequency which mainly depends on the hysteresis bands and the structure of switching table; which introduces a wide band of harmonics into the grid line current. This problem can be minimized by averting hysteresis comparators [12].

This paper is focused on the studied of a grid connected PV-APF system with a new approach, namely Fuzzy direct power control (FDPC), in order to inject the maximum photovoltaic power into the grid, control the reactive power to provide unit power factor and minimize harmonics in grid line current.

II. DESCRIPTION OF THE CONTROL SYSTEM

The sytem under study is presented in Fig.1. It consists of a photovoltaic generator connected throughout a controlled boost converter and three-phase inverter to a grid through inductive filter and non-linear load (uncontrolled rectifier and passive elements R, L). For optimal operation of the PV array, the DC/DC converter achieves the MPPT function using a fuzzy logic controller. Whereas, the inverter is utilized to transfer the PV power to the grid, it's controlled using a fuzzy direct power controller in order to improve the performance of the injected active power and to compensate harmonic currents disturbance and reactive power.

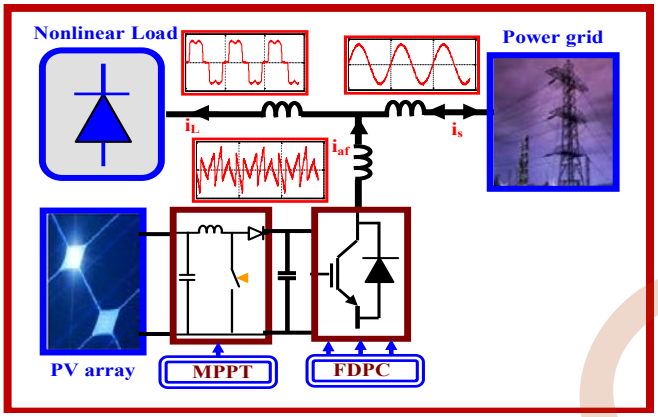

Figure 1. Block diagram of grid connected PV system with non linear load and Active Filter.

A. Modelling of the PV array

Different models of photovoltaic array are presented in the literature [1,2,4,5]. These models varyaccording to the number of parameters used to reproduce their operations, the calculation method and precision.The model chosen in this paper is a five parametric model (I_{sc}, V_{oc}, imp, V_{mpp} and R_s) of PV array of 110Wc whose electrical parameters are given in [4]. The photovoltaic current is calculated as follows:

$$I_{pv} = I_{sc}.\{1 - K_1[\exp(K_2 V_{pv}^{K_3}) - 1]\} \quad (1)$$

Where, $K_1 = 0.01175$ is determined experimentally and the coefficients K_2 and K_3 are defined as:

$$K_2 = \frac{\ln\left[\frac{1+K_1}{K_1}\right]}{V_{oc}^{K_3}} \quad (2)$$

$$K_3 = \left[\frac{\ln\left[\frac{I_{sc}(1+K_1) - I_{mpp}}{K_1 I_{sc}}\right]}{\ln\left[\frac{1+K_1}{K_1}\right]}\right] \Big/ \ln\left[\frac{V_{mpp}}{V_{oc}}\right] \quad (3)$$

Where V_{mpp} and I_{mpp} are PV voltage and current at maximum operation, V_{oc} is the open circuit voltage and I_{sc} the short circuit current.

The photovoltaic voltage and current change,when environmental conditions vary, according to the following equations:

$$V_{pv,new} = V_{pv} - \beta_{oc}\Delta T_c - R_s \Delta I_{pv} \quad (4)$$

$$I_{pv,new} = I_{pv} + \alpha_{sc}\left(\frac{G}{G_{stc}}\right)\Delta T_c + \left(\frac{G}{G_{stc}} - 1\right) I_{sc,stc} \quad (5)$$

Where: α_{sc} and β_{oc} are respectively the current and the voltage temperature coefficient, ΔT_c the temperature variation and R_s the cell resistance.

The PV array is simulated using Matlab/Simulink software. The $P_{pv}(V_{pv})$ and $I_{pv}(V_{pv})$ characteristics, for different irradiance levels, are presented in Fig.2. From those characteristics, the non-linear nature of the PV array apparent. An MPPT control must be introduced for maximum operation of PV generator. Fuzzy logic control (FLC) is used in this paper to optimize the efficiency of PV system [4,5].

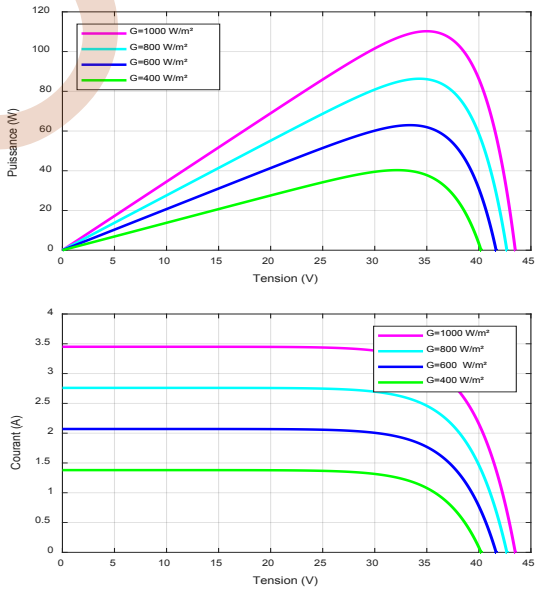

Figure 2. PV array characteristics $P_{PV}(V_{PV})$ and $I_{PV}(V_{PV})$.

B. Fuzzy logic MPPT controller

The fuzzy MPPT controller (FLC)has better advantages over conventional methods; it is robust, adaptive and doesn't need exact mathematical models of the system [5], but to have a good control, experience of the designer is required to choose fuzzy parameters [4]. The fuzzylogicMPPT controller measures the PV array voltage and currentthen calculates PV power,the operating voltageis

perturbed with either positive or negative increment ($\Delta V_{pv,ref}$) in a small or respectively large way in the direction which makes possible to increase the power $P_{pv.}$The fuzzy logic MPPT controller structure and the control rules are indicated in [4].

The results of Fig.3 show that the fuzzy MPPT controller (FLC) gives a fast response since it reaches its optimal value at 0.027 s compared to (P&O) methods which required 0.25s. It, also, ensure better steady-state performance in that it permitts toéliminate oscillations present with (P&O) methods.

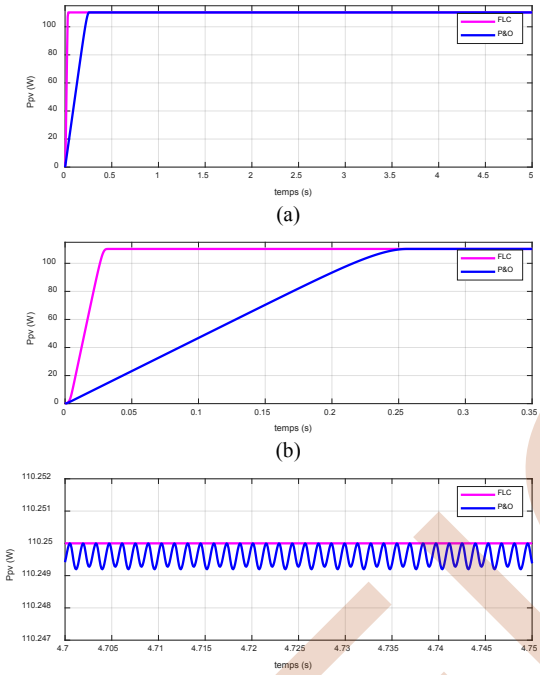

Figure3.photovoltaic power waveform,
(a). Global waveform, (b)Transient state, (c) Steady state.

C. *Active power Filter (APF)*

The structure of the active power filter (APF) consists essentially of two parts, power and control part [2,4] The power part consists of power electronic device (inverter) coupling to an RL filter and a PV generator. The control part used fuzzy direct power control (FDPC) to generate the optimal switching states of the inverter. The APF goal is to compensate harmonic pollution caused by the non linear load, and the reactive power flowing in the power grid [1,10].

D. *Fuzzy direct power control (FDPC)*

The direct power control (DPC) was originally proposed by Ohnishi (1991) and after developed by Noguchi (1998) [11]. Its goal is the elimination of the PWM modulation block and internal current control loops used in indirect control methods that are voltage oriented control (VOC) and virtual flux oriented control (VFOC). In DPC methods,the optimal inverter switching states are selected using the errors between the reference and the measured values of the active and reactive powers provided by hysteresis comparators and an angular position of the voltage vector.

The major inconvenience of DPC is located in its variable switching frequency which mainly depends on the hysteresis bands and the structure of switching table, it introduces a wide band of harmonics into the grid current. This problem can be minimized by replacing the hysteresis comparators and switching table by afuzzy inference system.Using Fuzzy logic DPC controller (FDPC), we can divide the active and reactive power errors into more subsections instead of two states (0, 1) that provides the hysteresis controller [12]. Then, the generated switching vector will be based on the different levels of power errors.The block diagram of the fuzzy inference system is shown in Fig.4.

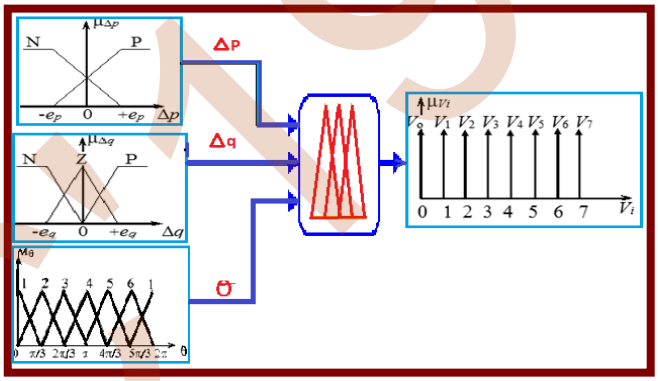

Figure 4. Inputs and output variables of fuzzy inference system.

The fuzzy inference system has three inputs: active power error, reactive power error and line voltage vector position. The voltage space vector represents the controlled output.

Active and reactive power errors are defined as:

$$\begin{cases} \Delta p = p_{ref} - p \\ \Delta q = q_{ref} - q \end{cases} \quad (6)$$

The estimations of active and reactive powers are obtained using the value of voltage and grid line current after Concordia transformation. These are given by the following equation:

$$\begin{cases} p = i_\alpha . v_\alpha + i_\beta . v_\beta \\ q = i_\alpha . v_\beta - i_\beta . v_\alpha \end{cases} \quad (7)$$

The active power error input is characterized by two linguistic variables: negative (N) and positive (P), represented by trapezoidal membership function. The reactive power error is depicted by three linguistic variables: negative (N), zero (Z) and positive (P).

The voltage source vector position (θ) is given by:

$$\theta = \arctan \frac{v_\beta}{v_\alpha} \quad (8)$$

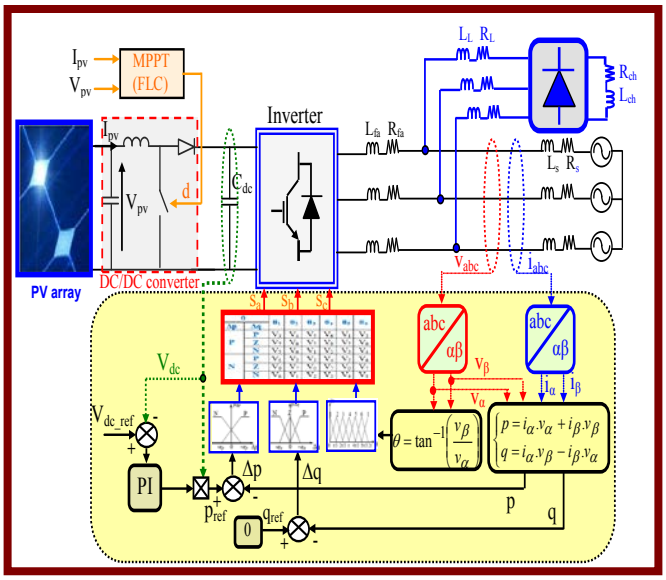

Figure 5. The global system controlled by FDPC.

The voltage vector position (θ) is divided into six 06 sectors and represented by six fuzzy sets (θ_1-θ_6) represented by triangular membership functions distributed between 0^0 and 360^0. The block diagram of the grid connected PV-APF system with fuzzy direct power control is shown in Fig.5.

The rule table of the proposed strategy is indicated in Table.1, it consists of 36 rules [12]. The fuzzy inference is carried outby Mamdani's method and the maximum criterion is used for defuzzification. Each control rule can be formulated as follows:

ifΔp is X_i&Δq is Y_i&$\theta$is θ_i then V is V_i.

Where X_i, Y_i and θ_i are the fuzzy sets of Δp, $\Delta q$and θ.

The optimal outputs vector from the eight combination vectors :V_0(000), V_1(100), V_2(110), V_3(010), V_4(011), V_5(001), V_6(101), V_7(111) are applied to the inverter switches S_a, S_b and S_c. Where V_1 to V_6 are the active vectors and V_0,V_7 the zero voltage ones.

TABLE I. SWITCHING TABLE OF FDPC [12]

θ		θ1	θ2	θ3	θ4	θ5	θ6
Δp	Δq						
P	P	V3	V4	V5	V6	V1	V2
	Z	V7	V0	V7	V0	V7	V0
	N	V5	V6	V1	V2	V3	V4
N	P	V1	V2	V3	V4	V5	V6
	Z	V0	V7	V0	V7	V0	V7
	N	V6	V1	V2	V3	V4	V5

III. SIMULATION RESULTS AND ANALYSIS

The global system (PV and APF) has been modeled and developed using Matlab/Simulink and Sim Power System. The study consists to test the proposed FDPC technique performances in operations such as the injection of theavailable maximum PV power to the grid and/or the load and the compensation of harmonic currents disturbance and reactive power. The system is composed of PV generator made of 4 strings of 5 series connected in parallel. This gives a total PV power around 2.2kW. All modules are considered identical and work in the same operating conditions. The MPPT is controlled using fuzzy logic controller (FLC). The main system parameters used in the simulation are indicated in [10].

To verify the robustness of the proposed FDPC, different level of irradiance are applied like shown in Fig.6. We first consider the non linear load disconnected, then we introduce it at t=5s.

The results of Fig.(7-9)show the PV voltage, current and powerand indicatesthat the fuzzy logic controller ensures a fast response until variations of irradiance.

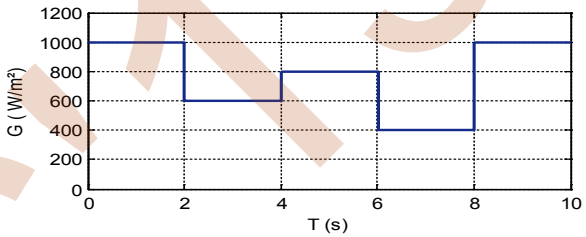

Figure 6.Solar irradiance.

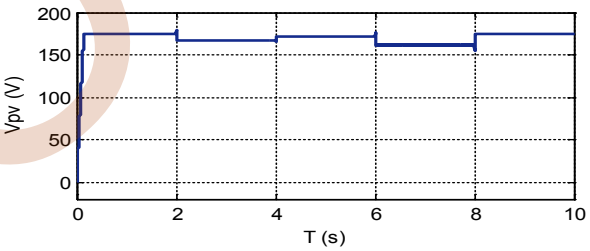

Figure 7.PV generator voltage.

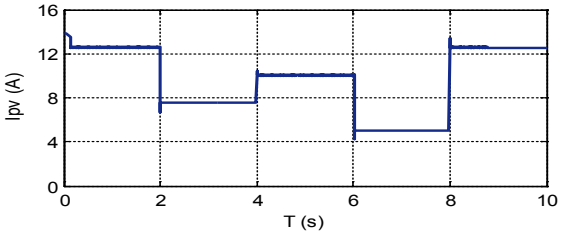

Figure 8.PV generator current.

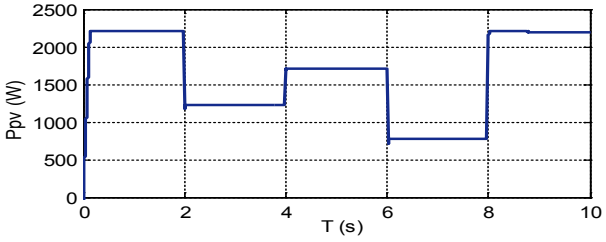

Figure 9.PV generator power.

As can be seen from Fig. 10, the DC voltage is well controlled to it's reference value of 212V. It reaches its steady state in a short time with negligible oscillations.

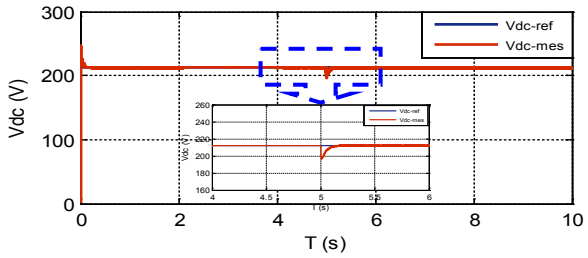

Figure 10.DC bus voltage.

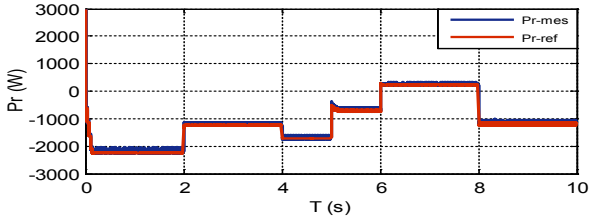

Figure 11.Waveform of grid active power with (FDPC).

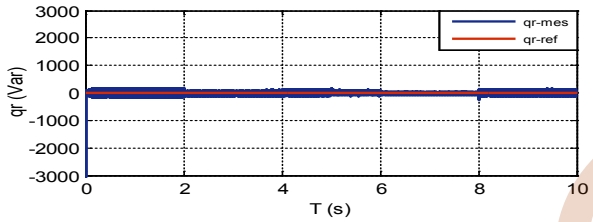

Figure 12.Waveform of grid reactive power with (FDPC).

The grid active and reactive powers responses are shown in Figs. 11 and12. The powers are decoupled and are following their reference values, where the reactive power tends toward zero and remains null even when irradiance levels change.During the interval [0 5], the three-phase diode rectifier with RL load is disconnected, the PV power is totally injected into the grid, which is represented by the negative sign of grid active power (the grid is in receiver mode).

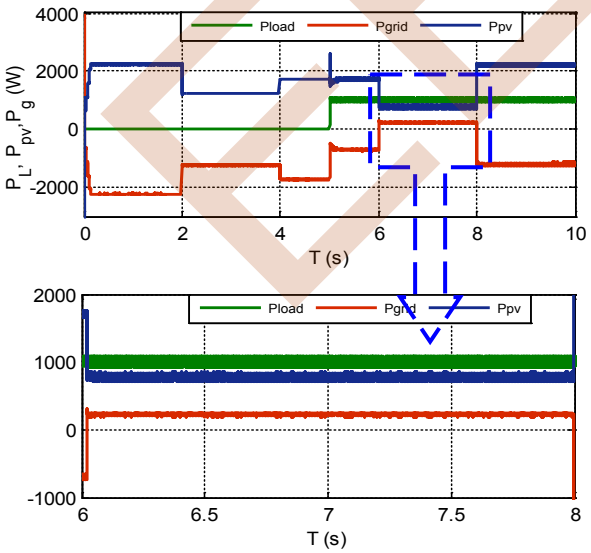

Figure 13. Waveform of active power: grid, PV and load with zoom.

At t=5s, the non-linear load is connected, then, the PV generator supply the load and injects the remaining energy to the grid. During the interval [6 8], the non-linear load consumption will be furnished at the same time by the PV generator and grid as shown in Figure 13. P_{grid} has a positive sign (the grid is in generator mode).Figures 14 show source current, APF current and load current waveform with their zooms.

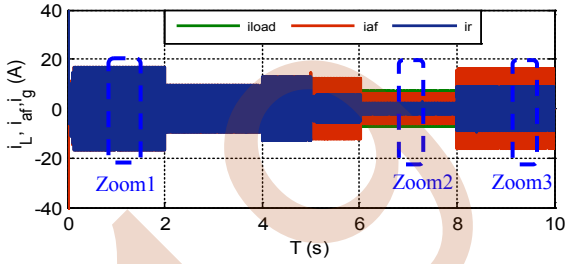

(a) Global waveform of currents

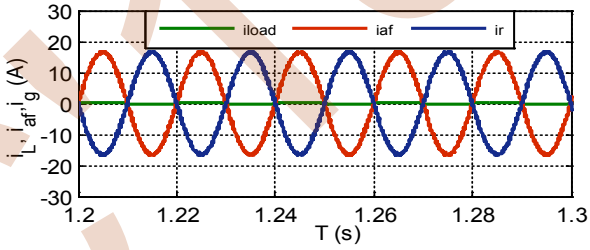

(b) Zoom 1

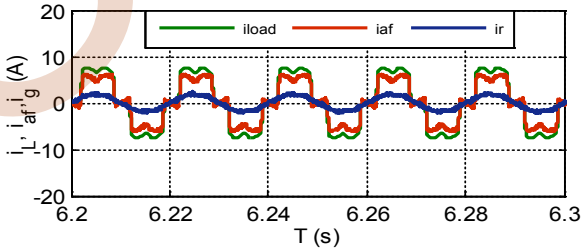

(c) Zoom 2

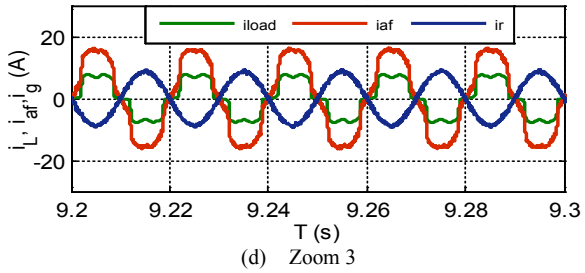

(d) Zoom 3

Figure 14.Currents waveform of: Source, APF and load with zooms.

In the first zoom, the non-linear load is disconnected, the produced PV power is injected to the grid, then, the active power filter current and grid current are sinusoidal and in opposition of phase. When the load is connected, it becomes energized by a PV generator and grid (zooms 2) and in zoom 3, the PV generator supplies the load and the power rest is sent to the grid. During both the operating modes, the

current of the APF compensates load harmonic currents and the source line current becomes sinusoidal.

When (p_{load}=0), the source line current is quasi-sinusoidal, in opposition of phase to the source phase voltage, thatmeans that the grid is receiving powerfrom the PV generator. When the load is connected and (P_{pv}<P_{load}) the grid became generator, then, voltage and current are synchronized since the PV-APF compensated reactive powers of the non-linear load as shown in Fig.15.

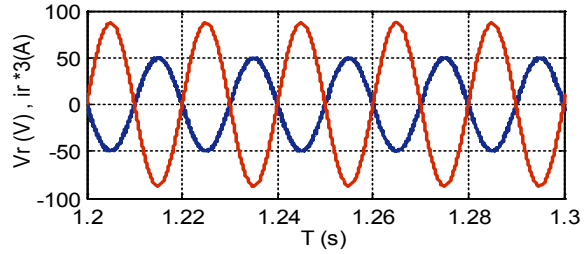

(a)

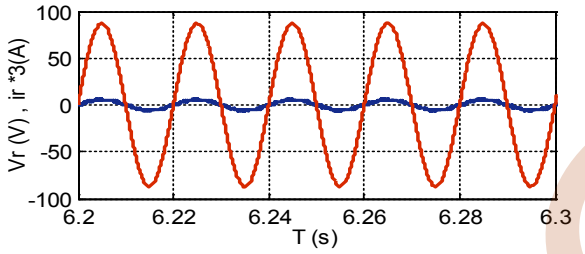

(b)

Figure 15.Source voltage and current.

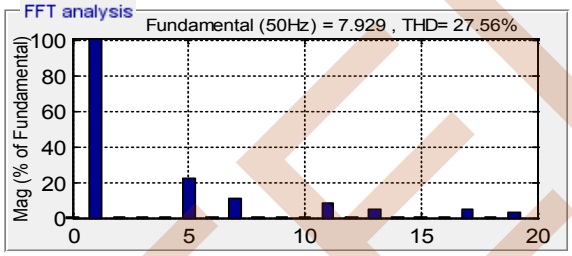

Figure 16.The grid current harmonic before filtering.

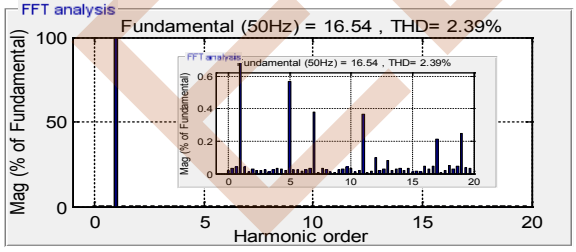

Figure 17.The grid current harmonic spectrum after filtering.

The THD of line currents is analyzed using fast Fourier transform (FFT) as shown in Figs.16-17. Before filtering, the total harmonic distortion source current source is equal to 27.56% higher than 5% (limit specified by IEEE standard 519-1992)[10].After introducing the APF, the source current becomes sinusoidal with THD*i*% = 2.39%.

IV. CONCLUSION

In this paper, the effectiveness of the proposed FDPC of active power filter in the grid connected photovoltaic system is demonstrated. The studied system supplies the load and injects the rest of photovoltaic energy into the grid, compensates reactive power and harmonic currents caused by the non-linear load. An MPPT based fuzzy logic controller is applied for photovoltaic power optimization. The obtained results, under irradiance and load variation, show that the active power filter compensates the non linear load harmonics current, the source currents have sinusoidal waveform with a THD of 2.39%, which is less than the limit specified by (IEEE standard 519-1992) and in phase or opposition of phase to the source phase voltage according to the operating mode of the grid (generator or receiver). As evident from the simulation results, the grid connected PV based APF is effective for power quality improvement.

REFERENCES

[1] B. Boukezata, A.Chaoui, J.P. Gaubert, and M. Hachemi, "Active power filter in a transformerless grid connected photovoltaic system",Balkan journal of electrical & computer engineering, , Vol.2, N°3, 2014

[2] M.r. Bengourina, M. Rahli and L. Hassaine, "Direct power control of a grid connected photovoltaic system, associated with an active power filter", Revue des Energies Rnouvelables,Vol. 20 N°1, pp:99 – 109, 2017.

[3] R.Belaidi, A.Haddouche, D.Ghribi, M.MghezziLarafi."A three-phase grid-connected PV system based on SAPF for power quality improvement",Telkomnika, Vol.15, N°.3, september 2017.

[4] S. Lalouni, d. Rekoua, t. Rekioua, E. Matagne, "Fuzzy logic control of stand-alone photovoltaic system with battery storage", Journal of Power Sources, Vol. 193, pp:899–907, 2009.

[5] S .Lalouni, d. Rekoua, "Optimal control of a grid connected photovoltaic systemwith constant switching frequency", Energy Procedia Vol.36, pp. 189 – 199, 2013.

[6] Nguyen Duc Tuyen, Goro Fujita, "PV-active power filter combination supplies power to nonlinear load and compensatesutility current", IEEEPower And Energy Technology Systems Journal, Vol.2, pp.1-11, 2015.

[7] Chaoui, J-P. Gaubert, A. Bouafia, "Direct power control switching table concept and analysis for three-phase shunt activepower filter", J Electrical SystemsVol.9, N°.1, pp. 52-65, 2013.

[8] Zoubir Boudries, Djamila Rekioua Ziani, "Study on Decoupling Direct Power Control of PWM Rectifier Using Space Vector Modulation", Arabian Journal of Science and Engineering, Vol.38, Iss. 4, pp. 875-882, Dec. 2012.

[9] M.N.Amrani, A.Dib, "Direct power control for a photovoltaic conversion chain connected to a grid", rev. Roum. Sci. Techn.– Electrotechn. et Energ. vol. 61, 4, pp. 378–382, Bucarest, 2016.

[10] B. Boukezata, A.Chaoui, J.PGaubert, and M.Hachemi, "Power quality improvement by an active power filter in grid-connected photovoltaic systems with optimized direct power control strategy",Electric Power Components and Systems, Vol:44, N°18, pp.2036–2047, 2016.

[11] Tapan A. Trivedi, Ajendrasinh Jadeja, Praghnesh Bhatt, "A review on direct power control for applicationsto grid connected PWM converters, engineering", Technology & Applied Science Research, Vol. 5, no. 4, pp.841-849, 2015.

[12] H. Hamdaoui, A. Semmah, A. Masssoum, P. Wira, Aa. Ayad, A. Meroufel, "Elaboration d'une table de commutation floue Pour la commande d'un filtre actif de puissance", Rev. Roum. Sci. Techn.– Électrotechn. et Énerg., Vol :**58**, N°4, pp : 405–414, Bucarest, 2013.

Control of Photovoltaic Grid Connected System Associated with an Active Filter

Amel AOUMER, Sofia BELAID LALOUNI, Zoubir BOUDRIES
Laboratoire de Technologie Industrielle et de l'Information (LTII)
Faculté de Technologie, Université de Bejaia, Algérie
amel_aoumer@outlook.fr

***Abstract*—Industrial and domestic equipment most often has electronic circuits that behave like non-linear loads. They are the main cause of harmonic currents in the grid, which causes deterioration in power quality, losses and malfunctions at the grid and consumers level. In this work, an active power filtering (APF) with its control system is associated with a grid-connected photovoltaic (PV) system, it is processed to improve the quality of energy fed into the grid. The proposed system has been verified using MATLAB/Simulink and Power System. The results show the efficiency of the APF, the total harmonic distortion rate (THD) of the source current is reduced to 1.91% and the reactive power tends toward zero and remains null even when irradiance levels change which guarantees a unit power factor.**

***Keywords*—Photovoltaic energy; Active filter; Quality of energy, THD.**

I. INTRODUCTION

Photovoltaic energy system is one of the inexhaustible power generating technologies available today with advantages such as: clean, producing no air pollution, waste, or noise that decreases our dependence on fossil fuels [1]. Due to its intermittent nature, the increasing penetration of PV energy to the grid produce different problems like harmonics, which inspire the designers to develop power electronics devices with different control strategies [2].

The growth of development in the field of power electronics, and their ease of control, has led to the wide use of non-linear loads, such as: chopper, inverter, rectifier, etc. The use of these devices is the major cause of harmonic disturbances and unbalanced currents injected into the electricity grid. Harmonics reduce efficiency and power factor, increase losses and cause electromagnetic interference with adjacent communication lines and other harmful consequences [3].

In order to reduce the impact of these harmonics on the power supply system, active power filters (APF) are installed. The APF injects the compensation current at the common connection point to cancel the harmonics and to make the source current sinusoidal [4].

In this paper, a photovoltaic system connected to the grid associated to an active power filtering is proposed, where active filter has the task to eliminate disturbances in the grid.

II. DESCRIPTION OF THE STUDIED SYSTEM

The system studied of Fig.1, consists of a PV generator, a boost chopper, an MPPT control, an inverter coupled to the grid through a passive filter RL feeding a non-linear receiver constituted by a PD3 rectifier bridge having as load a resistance in series with an inductance.

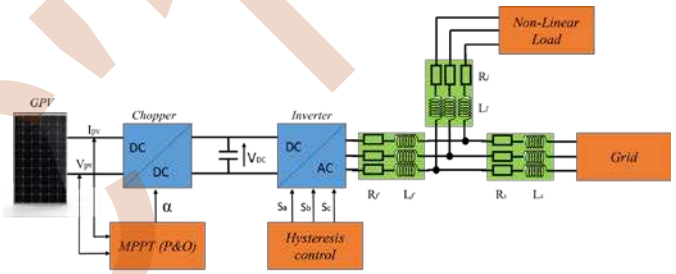

Figure 1. Overview of the grid-connected PV system

A.Modeling of the photovoltaic generator

The model chosen is a five-parameter model (Isc, Voc, Impp, Vmpp and Rs), of the SIEMENS 110Wp type, whose electrical parameters are illustrated in Table 1.

Table 1. Parameters of the PV panel SIEMENS SM 110 [5]

Parameters	**Values**
Panel power Pmpp	110 W
Current at the point of maximum power Impp	3.15 A
Maximum power point voltage Vmpp	35 V
Short-circuit current Isc	3.45 A
Open circuit voltage Voc	43.5 V
Increment coefficient of the current Isc (αcc)	1.4
Increment coefficient of the voltage Voc (βco)	-152

The expression of the photovoltaic module current is given by [3]:

$$I_{pv} = I_{sc}.\{1 - K_1[\exp(K_2 V_{pv}^{K_3}) - 1]\} \quad (1)$$

Where $K_1 = 0.01175$ *and* the coefficients K_2 and m are given by:

$$K_2 = \frac{K_4}{V_{co}^m} \quad (2)$$

$$m = \frac{ln\left[\frac{K_3}{K_4}\right]}{ln\left[\frac{V_{mpp}}{V_{co}}\right]} \quad (3)$$

$$K_3 = ln\left[\frac{I_{cc}(1+K_1) - I_{mpp}}{K_1 I_{cc}}\right] \quad (4)$$

$$K_4 = ln\left[\frac{1+K_1}{K_1}\right] \quad (5)$$

When the irradiance and temperature vary, the parameters in Table 1 change according to the following equations:

$$\Delta T_{PV} = T_c - T_{stc} \quad (6)$$

$$\Delta I_{pv} = \alpha_{cc}\left(\frac{G}{G_{stc}}\right)\Delta T_c + \left(\frac{G}{G_{stc}} - 1\right) I_{cc,stc} \quad (7)$$

$$\Delta V_{pv} = -\beta_{co}\Delta T_c - R_s \Delta I_{pv} \quad (8)$$

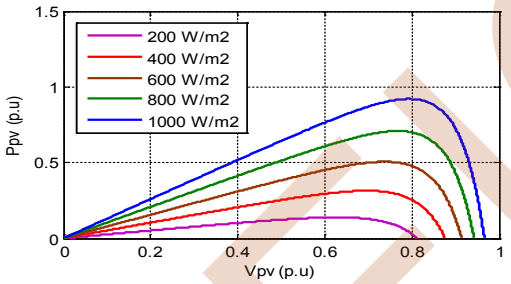

Figure 2. *P–V* characteristics of a PV array for different irradiance.

As shown in Fig. 2, the photovoltaic power varies with the irradiance. The photovoltaic voltage needs to be adjusted according to the irradiance level to extract the maximum photovoltaic power using an MPPT control strategy.

B.The MPPT control

The MPPT (Maximum Power Point Tracking) control is an essential control for optimal operation of the photovoltaic system. To increase the efficiency of PV array, an MPPT algorithm is applied to the DC/DC converter. In this paper the P&O algorithm is used, it is adopted for its simplicity and ease of implementation [6].

The P&O algorithm is explained in the flowchart of Fig. 3, it is based on the perturbation the photovoltaic panel voltage with a fixed perturbation step (c) until the optimal power is reached as explain in Fig. 4.

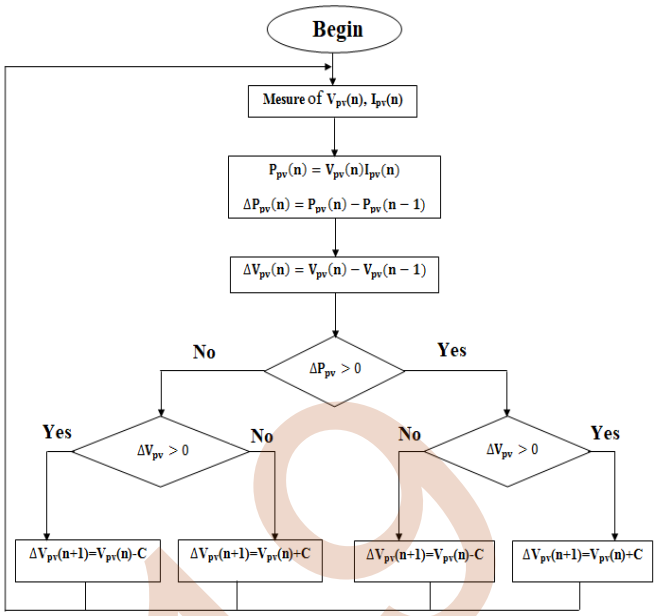

Figure 3. Organization chart of the P&O method.

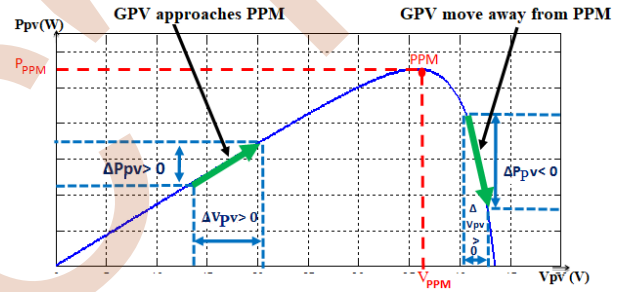

Figure 4. Operation of the algorithm (P&O) on the $P_{pv}(V_{pv})$ characteristic.

III. THE ACTIVE POWER FILTER STRUCTURE

The parallel active filter consists of a voltage inverter, an output filter (R_f-L_f) and a capacitive energy storage circuit C which represents the DC bus at the output of the photovoltaic generator. Fig. 5 shows the structure of an active filter connected in parallel to the grid through a passive filter (R_S-L_S), feeding a non-linear load.

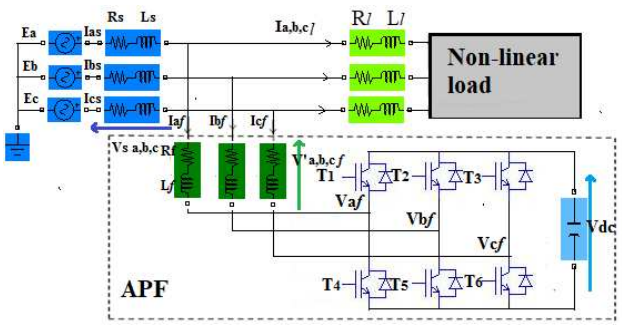

Figure 5. Structure of the parallel active filter

IV. DIRECT CURRENT CONTROL

Its principle is to measure the DC bus voltage (V_{dc}) and compare it with a reference voltage V_{dc_ref}, then regulate it using an IP regulator (Integral-Proportional), the output of this regulator produces the current I_c, then from I_c the current I_{pv} is subtracted at the output of the DC-DC converter, then it gives the current I_{ond}, which will be multiplied by a three-phase sinusoidal signal of unit amplitude : (sin (ωt), (sin (ωt- 2π/3) and (sin (ωt-4π/3))) obtained from the grid voltages, thus establishing the reference currents $I_{s\,a,b,c\text{-}ref}$ which will be compared to the measured currents of the $I_{s\,a,b,c}$ grid, then applied to the input of the hysteresis controllers, which produce the inverter control signals at their outputs. The diagram of direct current control is shown in Fig. 6.

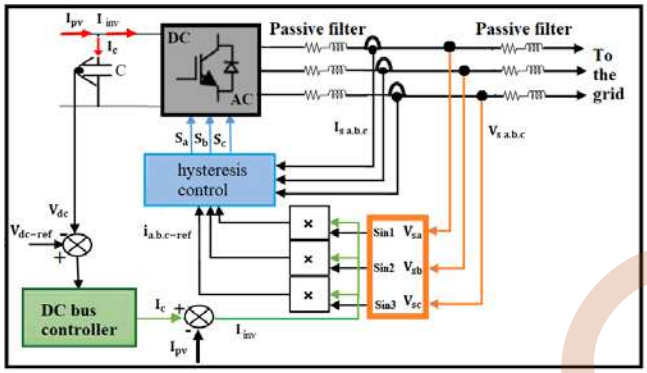

Figure 6. Diagram of direct current control.

The control of the continuous bus is an essential procedure for the control of the FAP. The following figure shows the regulation block diagram. An (IP) regulator is used as a voltage corrector to V_{dc}.

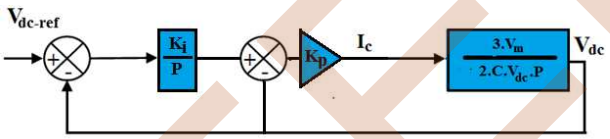

Figure 7. Block diagram of the DC bus control.

The closed loop transfer function is given by:

$$H(p) = \frac{k_p.k_i / k}{p^2 + \left(k_p / k\right)p + \left(k_p.k_p / k\right)} \qquad (9)$$

This transfer function represents a second-order system, its canonical form is written:

$$H(p) = \frac{w_n^2}{p^2 + 2\xi.w_n p + w_n^2} \qquad (10)$$

After identification, the parameters of the IP controller are obtained:

$$k_p = 2.k.\xi.w_n \qquad (11)$$

$$k_i = w_n / 2.\xi \qquad (12)$$

V. SIMULATION RESULTS

The global power section was programmed by using the SimPower Systems modules and setting them with the same values as the real components. The simulation parameters are given in [7].

In order to study the response of the grid-connected photovoltaic system under climate change, variable irradiance is applied, with a fixed temperature of 25°C. Fig. 8 illustrates the irradiance profile (G) selected for the study.

The waveform of the output power of the photovoltaic generator is shown in Fig. 9, the variations in the power of the GPV are in accordance with the applied irradiation profile. It is zero in the absence of sunlight and then follows the evolution of the irradiance. So the maximum power point moves to the new maximum point corresponding to each irradiation.

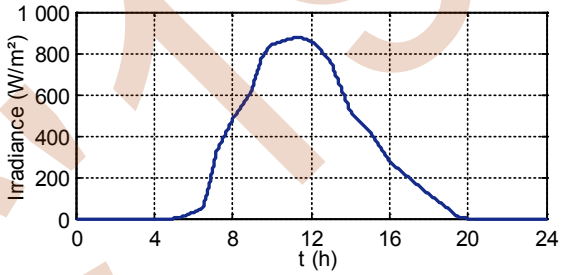

Figure 8. Irradiance profile.

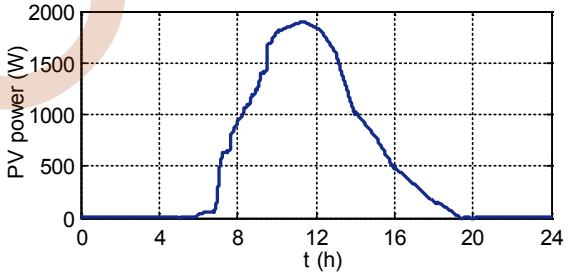

Figure 9. Photovoltaic power waveform.

Fig. 10 shows the DC bus voltage V_{dc} waveform, it can be seen that it is well regulated to its reference value, even during a variation in irradiance. The disturbances on the voltage V_{dc} appear when there are strong evolutions of the irradiance, but it reaches its reference value.

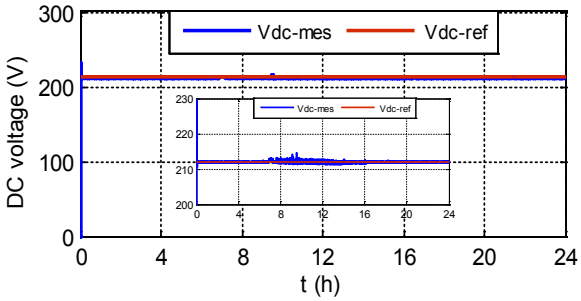

Figure 10. DC bus voltage Vdc.

Fig. 11 represents active powers. The grid active power follows the path imposed by the control, it is clear

that the power of the inverter corresponds to the power of the GPV. Between (0 s to 5 s) at zero irradiation, the grid power equal to the load power means that the grid provides all its power to the non-linear load. Between (5 s to 20 s) the GPV injects energy into the polluting load and the grid at the same time, and from (20s to 24s) the load power is higher than that produced by the GPV, the power deficit is supplied by the grid.

In the other hand, the reactive power of the grid is cancelled when the FAP is operational Fig. 12, which means that it is the active filter that provides the reactive power to the load.

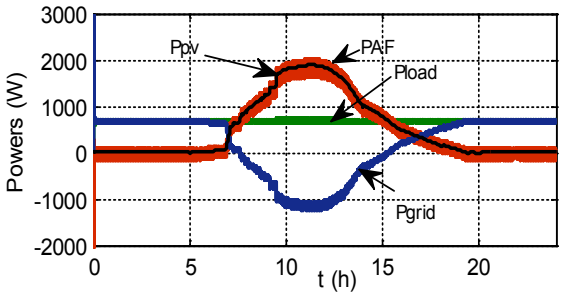

Figure 11. PV power, grid active power and active filter power.

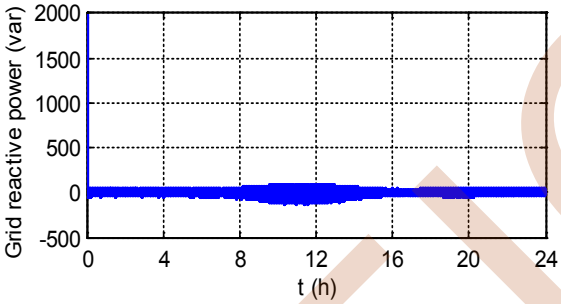

Figure 12. Reactive power waveform.

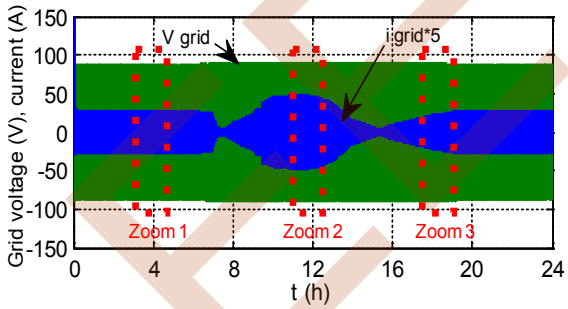

Figure 13. Line current and voltage of a grid phase.

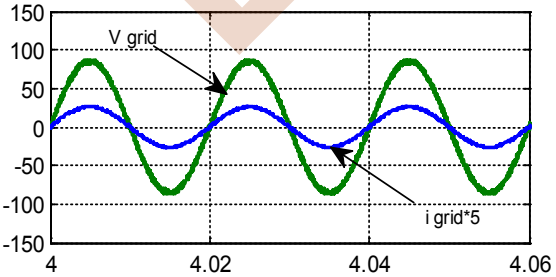

Figure 13.a. Zoom1: Grid in generator mode.

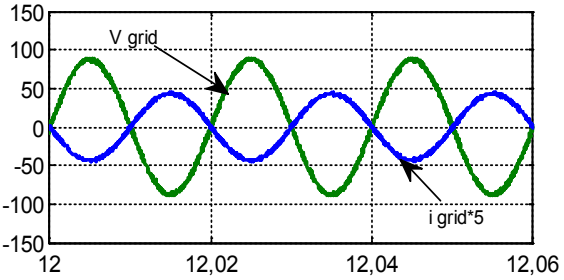

Figure 13.b. Zoom2: grid in receiver mode.

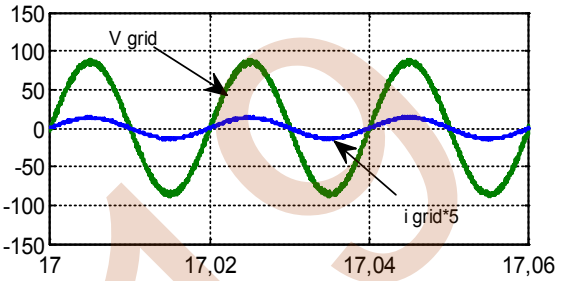

Figure 13.c. Zoom3: grid in generator mode

The figures (13, 13.a, b and c) represent the current and voltage rates of the grid phase as well as their zooms during the different operating phases. When the current and voltage are in phase, the grid behaves like a generator; otherwise (in opposition phase) it becomes a receiver.

Fig. 14 illustrate the harmonic spectrum of the grid current, it has a total harmonic distortion rate THD = 28.22% and the line source current after filtering has a THD of 1.91% which is an acceptable value following the standard (IEC-1000) [6].

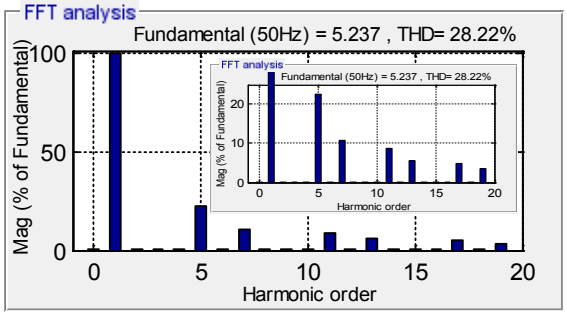

Figure 14.a. Harmonic spectrum of the load current.

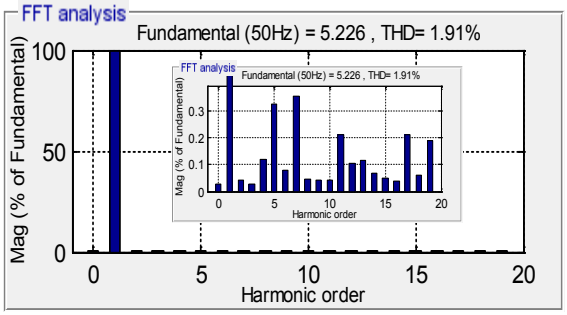

Figure 14.b. Harmonic spectrum of the grid line current.

Fig. 15 represents the current rates (I_l a, I_{inv}, I_{grid}), this figure determines the evolution of the grid currents as well as the currents produced by the GPV and that of the load current.

In the absence of the generated PV power, the source current is almost sinusoidal and in phase with the load current, the FAP injects currents to compensate the harmonic currents caused by the nonlinear load as shown in Fig. 15.a.

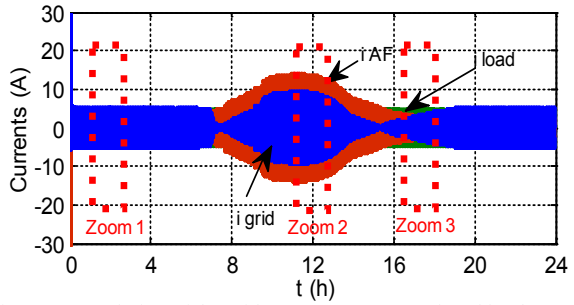

Figure 15. Evolution of the grid current, current produced by the GPV and the one of the

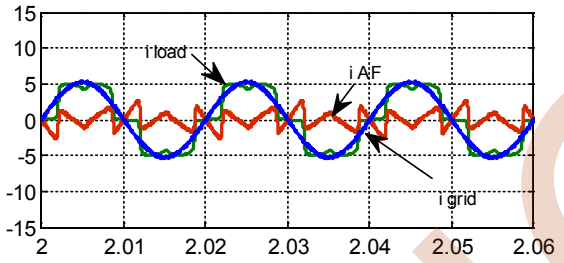

Figure 15.a: Zoom1

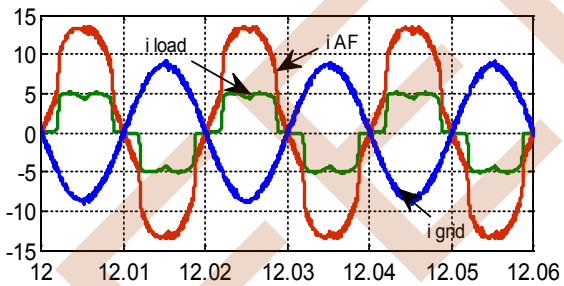

Figure 15.b. Zoom2

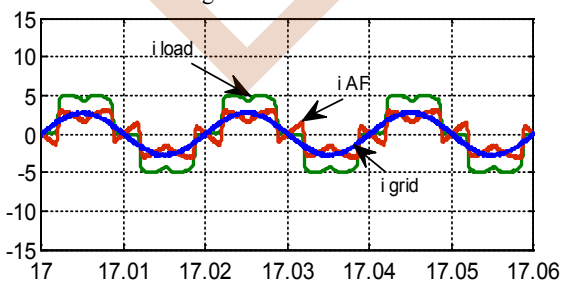

Figure 15.c. Zoom3

In the case where (PPV > Pch) the source current remains almost sinusoidal but in phase opposition to the non-linear charge current, Fig. 14.b, the FAP current contains the information of the harmonic compensation and injection of the LPI current. This phase shift proves that the grid receives well the active power from the PV source after subtracting the value consumed by the load.

We see that the grid current becomes in phase with the charging current, so the grid switches to generator mode, since the power required by the load is higher than the one produced by the GPV ($P_{GPV}<P_{load}$).

VI. CONCLUSION

In this paper, a grid-connected photovoltaic system with active power filtering has been studied, in which a direct current control is applied. The obtained simulation results were presented, analyzed and proved the effectiveness and the robustness of the applied control technique.

The FAP has reduced the effects of disturbances and harmonics caused by the nonlinear loads to an acceptable value (THD= 1.91%). The results also showed a quasi-sinusoidal current absorption with an almost unitary power factor.

REFERENCES

[1] Bouzelata Yahia, Djeghloud Hind, Chenni Rachid, "The application of an active power filter on a photovoltaic power generation system", International Journal of Renewable Energy Research, vol.2, no.4, pp.1-8, 2012

[2] B. Boukezata, A.Chaoui, J.P Gaubert, And M.Hachemi, "Power quality improvement by an active power filter in grid-connected photovoltaic systems with optimized direct power control strategy", Electric Power Components and Systems, Vol:44, N°18, pp.2036–2047, 2016.

[3] A.Betka, S.Ouchen, S.Abdeddaim, and R. Mechouma " Design and experimental validation study on direct power control applied on active power filter",2nd Int. Conf. Intell. Energy Power Syst., pp. 1–5, Jun. 2016.

[4] S.Ouchen "Contribution à la Commande Directe de Puissance Dédiée au Filtrage Actif, Associé à une Source Photovoltaïque", Thèse de doctorat, Université de Biskra 2017.

[5] H. Deboucha, S. Lalouni Belaid "Improved incremental conductance maximum power point tracking algorithm using fuzzy logic controller for photovoltaic system", Rev. Roum. Sci. Techn.–Électrotechn et Énerg. Vol.62, N.4, pp. 381–387, 2017.

[6] N.Aouchiche, M.S.Ait Chikh, A.Malek "Poursuite du Point de Puissance Maximale d'un Système Photovoltaique par les Méthodes de l'Incrémentation de Conductance et la Perturbation Observation", revue des Energies Renouvelables. Vol. 16 N.3, pp 485-498, 2013.

[7] A. Chaoui, J-P. Gaubert, A. Bouafia "Direct Power Control Switching Table Concept and Analysis for Three-phase Shunt Active Power Filter" J. Electrical Systems 9-1: 52-65, 2013

[8] C.Dewez "Modélisation d'un Filtre Actif Parallèle Triphasé pour la Dépollution d'harmoniques et Synthèse d'une Commande basée sur le rejet de perturbation", Thèse de Doctorat, Université de Poitiers, France, 2007.

Fuzzy logic control of dual-star induction generator in stand-alone wind energy system

*Samira AIT OUARETCHEKKAL, Djamal AOUZELLAG, Kaci GHEDAMSI
Laboratoire de maitrise des énergies renouvelables, faculté de technologie, université de Bejaia 06000, Algérie
*Corresponding author. Tel: +213-775-728-202; Fax: +0-000-000-000
E-mail address: samirachekkal12@gmail.com

***Abstract*—This paper presents the operation of a stand-alone wind energy conversion system using a Dual-Star Induction Generator (DSIG) as well as the contribution they can make to its application in an energy production chain for dedicated operation for isolated sites. The role of stand-alone systems is to supply one or more consumers located in an isolated area of the electricity grid. The proposed system is modeled and simulated using Matlab / Simulink software to examine the dynamic characteristics of the system with the proposed control strategy. The controlled voltage source is performed by using a controller flou, this controller is specifically designed to maintain constant DC- link voltage under wind speed and electrical load variations. The results of the modeling and simulations show that most of the isolated sites can be supplied with clean energy. Dynamic control of the DC- link voltage has also been successfully demonstrated under varying load. A ramp DC- link voltage reference is chosen and it is shown that the ramp slope is a deciding factor for successful current build-up. The simulation results ensure good dynamic control of the DC- link voltage with very small changes around its reference value.**

I. INTRODUCTION

The balance between production and the demand for power is one of the main challenges of stand-alone installations. The next exhaustion of fossil fuels has contributed to the development of renewable energy in general and wind energy in particular [1]. In wind energy conversion system dual-stator induction generator (DSIG) is a better choice especially for isolated power generation, because of its robustness and low maintenance requirement [2]. Shunt capacitors were traditionally used to supply reactive power but back-to-back voltage source converters were necessary to ensure maximal power extraction under variable wind speed. Initial voltage in the dc bus is derived from the terminal voltage of the unexcited machine, derived from remanent magnetism of the magnetic core. Machine flux was ramped up from this small initial voltage using scalar control although no analytical justification of the ramp slope was provided [3-4]. For voltage build-up, a ramp reference of Defined slope is used for the dc voltage and the selection of slope is explained analytically.

The present work is inserted in this context, which consists of control in stand-alone wind energy conversion system using vector control of Dual-Stator Induction Generator (DSIG). This last shows, in addition to the advantages of cage induction motors, other benefits, such as conventional segmentation power, high reliability [5]. The mathematical model of the turbine and the DSIG, vector control, sharing of powers between the wind system and the stand-alone network will be studied and detailed. The simulation results are presented to shown the performance of the proposed system figure1. The above study offers various possibilities of power generation in isolated system.

II. SYSTEM CONFIGURATION AND MODELING

The basic device to be studied is that of figure 1. This device is made up of a double stator induction generator, converter and a capacitor is connected on the power supply side of controlled converter, this makes it possible to obtain a standalone operation.

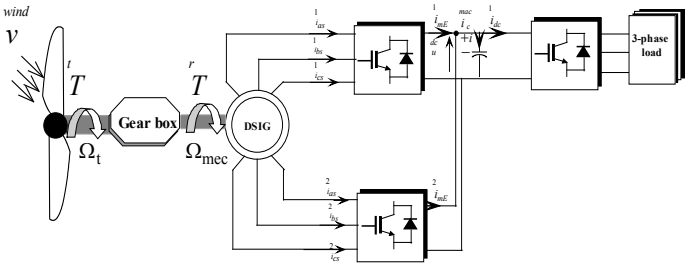

Figure1. Scheme of the studied device

III. SYSTEM MODELLING

A. Wind turbine model

The A wind turbine can only convert a certain percentage of the captured wind power. This percentage is represented by C_p which is a function of the wind speed, the turbine speed and the pitch angle of any specific wind turbine blades [6-7]. The mechanical power (P_t) extracted from the wind is

mainly governed by three quantities namely: the area swept by rotor blades (S), the upstream wind velocity (v_{wind}) and the rotor power coefficient (C_p)by following equation:The mechanical power (P_t) extracted from the wind is mainly governed by three quantities namely: the area swept by rotor blades (S), the upstream wind velocity (v_{wind}) and the rotor power coefficient (C_p)by following equation [5-6]:

$$P_t = \frac{1}{2} C_p(\lambda) S v_{wind}^3 \quad (1)$$

$$\lambda = \frac{R\Omega_t}{v_{wind}} \quad (2)$$

The rotor efficiency curve $C_p(\lambda)$ is a nonlinear function of the tip speed ratio (TSR), λ which is determined by the blade design, and the pitch angle [7].

The turbine torque is the ration of the output power to the shaft speedΩ_t :

$$T_t = \frac{P_t}{\Omega_t} = C_p(\lambda) \frac{\rho}{2} S v_{wind}^3 \frac{1}{\Omega_t} \quad (3)$$

In this paper, a functional block diagram model of the turbine and power coefficient for the wind turbine model reported in [8] is used.

B. Modeling of dual-star induction generator (DSIG)

DSIG depends on the rotational speed of the rotor. If the latter is slightly greater than that of the magnetic field of the stator, it then develops an electromagnetic force similar to that obtained with a synchronous generator. On the other hand, the machine does not generate its own excitation energy. For that, it will be necessary to bring this energy either by a battery of capacitors, or by a static converter control, which will stabilize its output voltage. The model of dual-star induction machine (DSIM) is composed of a two-phase electrical phase windings shifted by an electric angle α = 30 °, and a rotor cage squirrel. [9-10].

$$\begin{cases} v_{ds1} = R_{s1} i_{ds1} + \frac{d\varphi_{ds1}}{dt} - \omega_s \varphi_{qs1} \\ v_{qs1} = R_{s1} i_{qs1} + \frac{d\varphi_{qs1}}{dt} + \omega_s \varphi_{ds1} \\ v_{ds2} = R_{s2} i_{ds2} + \frac{d\varphi_{ds2}}{dt} - \omega_s \varphi_{qs2} \\ v_{qs2} = R_{s2} i_{qs2} + \frac{d\varphi_{qs2}}{dt} + \omega_s \varphi_{ds2} \\ v_{dr} = R_r i_{dr} + \frac{d\varphi_{dr}}{dt} - (\omega_s - \omega_r)\varphi_{qr} = 0 \\ v_{qr} = R_r i_{qr} + \frac{d\varphi_{qr}}{dt} + (\omega_s - \omega_r)\varphi_{dr} = 0 \end{cases} \quad (4)$$

The expressions for stator and rotor flux linkages are

$$\begin{cases} \varphi_{ds1} = L_{s1} i_{ds1} + L_m (i_{ds1} + i_{ds2} + i_{dr}) \\ \varphi_{qs1} = L_{s1} i_{qs1} + L_m (i_{qs1} + i_{qs2} + i_{qr}) \\ \varphi_{ds2} = L_{s2} i_{ds2} + L_m (i_{ds1} + i_{ds2} + i_{dr}) \\ \varphi_{qs2} = L_{s2} i_{qs2} + L_m (i_{qs1} + i_{qs2} + i_{qr}) \\ \varphi_{dr} = L_r i_{dr} + L_m (i_{ds1} + i_{ds2} + i_{dr}) \\ \varphi_{qr} = L_r i_{qr} + L_m (i_{qs1} + i_{qs2} + i_{qr}) \end{cases} \quad (5)$$

The electrical model is completed by this mechanical equation:

$$T_{em} - T_r = J \frac{d\Omega_{mec}}{dt} + k_f \Omega_{mec} \quad (6)$$

The electromagnetic torque expression as a function of stator currents and rotor flux is as follows:

$$T_{em} = p \frac{L_m}{L_m + L_r} \left[(i_{qs1} + i_{qs2})\varphi_{dr} - (i_{ds1} + i_{ds2})\varphi_{qr} \right] \quad (7)$$

IV. FIELD-ORIENTED CONTROL OF THE DUAL-STAR INDUCTION GENERATOR

The main objective of the vector control to independently control the torque and the flux [9].

The rotor currents in terms of the stator currents are divided from (4) as:

$$i_{dr} = \frac{\phi^*_r}{L_m + L_r} - \frac{L_m}{L_m + L_r} (i_{ds1} + i_{ds2}) \quad (8)$$

$$i_{qr} = -\frac{L_m}{L_m + L_r} (i_{qs1} + i_{qs2}) \quad (9)$$

$$\omega^*_{gl} = \frac{R_r L_m}{(L_m + L_r)} \frac{(i_{qs1} + i_{qs2})}{\varphi^*_r} \quad (10)$$

The final expression of the electromagnetic torque is

$$T^*_{em} = p \frac{L_m}{L_m + L_r} (i_{qs1} + i_{qs2}) \varphi^*_r \quad (11)$$

Consequently, the electrical and mechanical equations for the system after these transformations in the space control may be written as follows:

$$\frac{d}{dt}\varphi_r = -\frac{R_r}{(L_m + L_r)} (\varphi_r + L_m (i_{ds1} + i_{ds2})) \quad (12)$$

$$\frac{d}{dt}\Omega_{mec} = \frac{1}{J} [T^*_{em} - T_g - f\Omega_{mec}] \quad (13)$$

Dynamic equation for the DC- link voltage, shown in figure 2, is derived as follows. Equating currents at the DC- link voltage, the following governing equation is obtained:

$$i_{dc} = C_{dc} \frac{d}{dt} u_{dc} \quad (14)$$

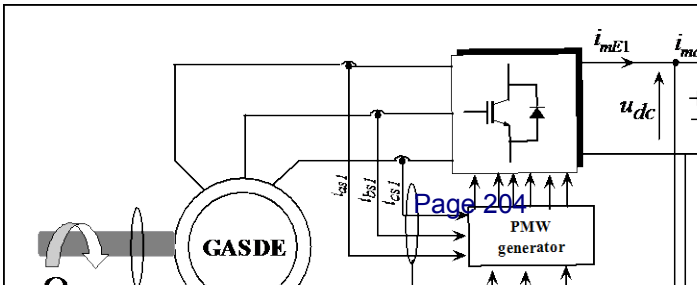

V. FUZZY-PI CONTROLLER DESIGN

A fuzzy logic controller is used to alleviate the problem of voltage regulation for DSIG, by acting the switching unit and injecting the needed the current, in varying the capacitance value. There are two inputs of fuzzy control. Input parameters error (figure 3).For both the error and P (Positive) N (Negative), Z (Zero) for its derivative. For the output signals, five triangular membership functions denoted by NB (Negative Big), NM (Negative Middle), Z (Zero), PM (Positive Middle), and PB (Positive Big) are used [11]. The elements of this rule base table are related to e and de as represented in figure. 4. Big errors need big voltage step; however, small errors need fine control, which requires fine input/output variables. The rule table is obtained as shown in table 1, with error and change in error as inputs.

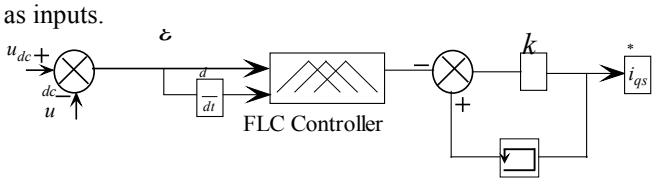

Figure.3. The Fuzzy-PI controller structure.

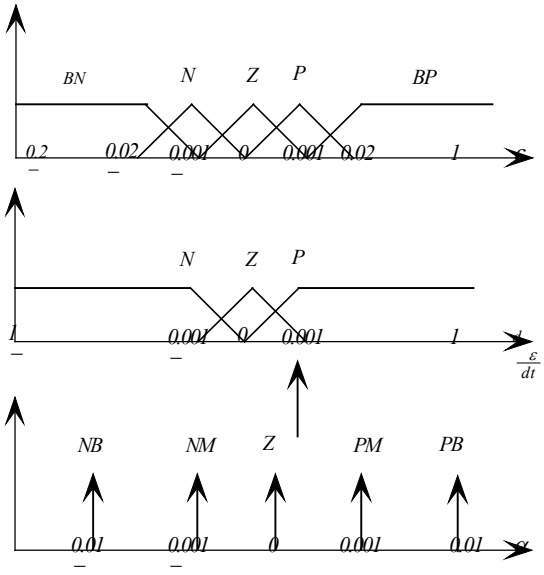

Figure 4 Inputs and outputs membership functions

Table1. The rule table

	The error Ɛ			
		N	Z	P
dƐ	N	NB	PM	PB
	Z	NB	Z	PS
	P	Z	NS	Z

VI. RESULTS AND DISCUSSION

Influence of the variation of the resistive load

The overall system to be studied consists of a DSIG connected to a rectifier / inverter and controlled according to the control strategy presented above. In what follows, a simulated test is performed in order to analyze the performance of the control, this test dedicated to the behavior of the fixed speed control and purely resistive load variable.The generator is driven at a speed of 314 rad/s with a value of voltage straightened reference $u_{dc}^{*}=622V$ throughout the entire duration of the simulation. The priming of the generator has taken place an empty, the presence of a remanent magnetic flux is essential or else loaded up the capacity at an initial value. In order to do this, we opted to loaded up initially the capacity an value 10 µF to *12V*, to provide the reactive energy needed for priming,The q-axis current reference, generated from the voltage controller is kept at small value during starting by using the ramp voltage reference figure 5. At the moment t = 2s, a balanced pure resistive three-phase load is inserted at 50% of its nominal value *(64Ω)*. At the moment t = 4s, another load of the same characteristic as the first one is inserted at 100% of its nominal value *(64Ω)*. The DC- link voltage follows the reference as shown in figure 5.
Figure 6 illustrates the pace of the active power that reaches almost its nominal value which is the main advantage of the studied structure. The analysis of the figures (6-9) made it possible to see the behavior of the current, the voltage and the electromagnetic torque according to the variation of the load, where we notice that the voltage is insensitive to this variation, unlike the current and the electromagnetic torque. We notice that the torque is still in the nominal operating range.

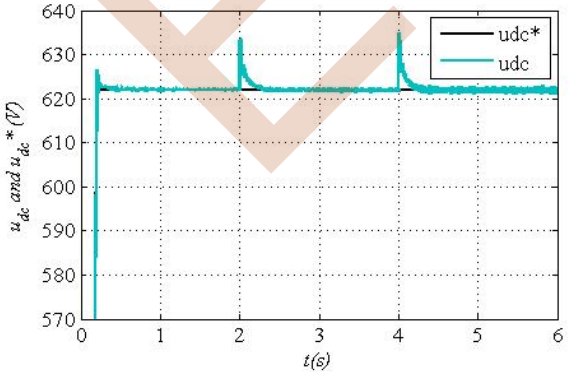

Figure.5 DC-link voltage

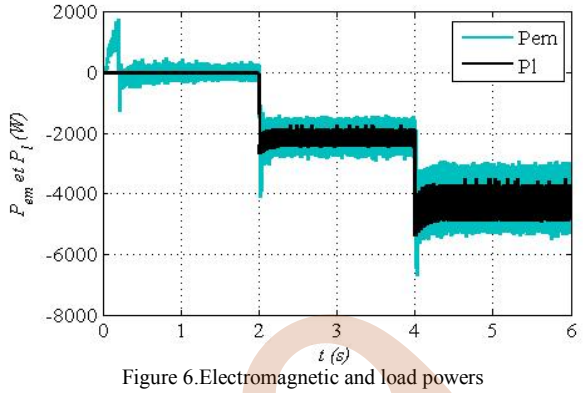

Figure 6.Electromagnetic and load powers

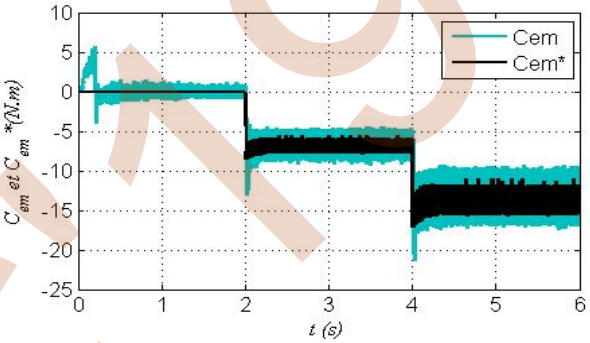

Figure7. Electromagnetic torque and its reference.

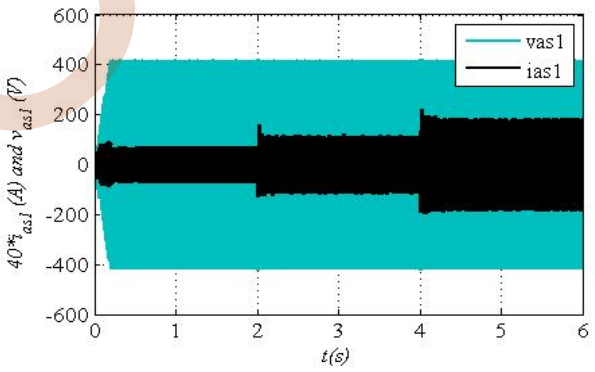

(a)

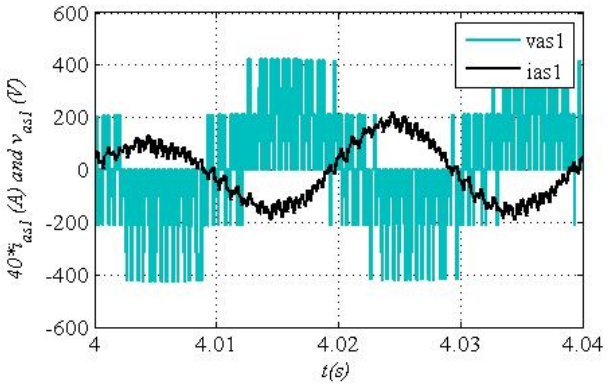

(b)

Figure 8. (a) Stator voltage and current for star 1. (b) Zoom of the stator voltage and current for star 1.

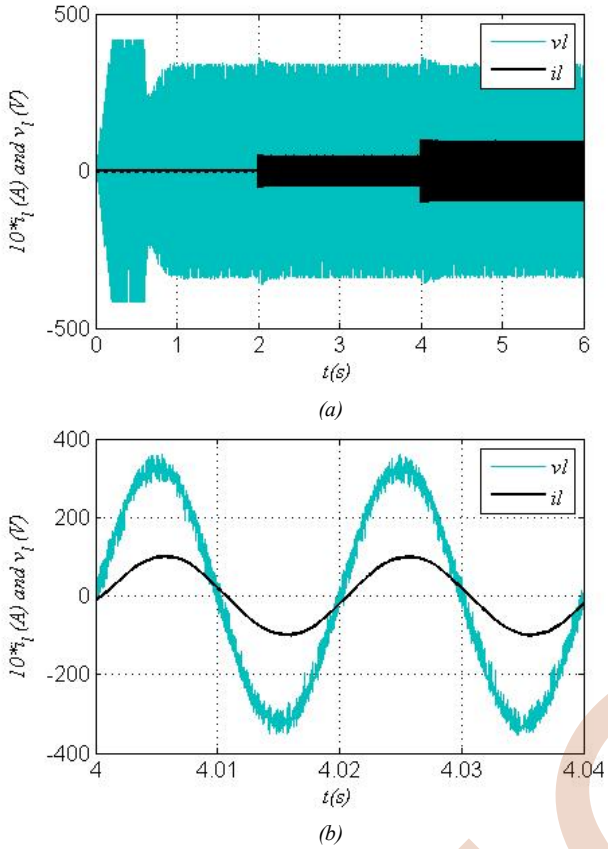

Figure 9 Voltage and current for load

VII. CONCLUSION

In this paper, the subject consists of improving the performance of wind turbines based on double-star asynchronous machines operating on isolated load. A control structure of DSIG operating in autonomous sites is presented.

The description of the latter is presented, adopting a mathematical model that defines the different equations describing the operation of the machine. The generator is connected to the converter for the control of the voltage in the presence of the variations of the load. The control of the DC- link voltage has been demonstrated under varying load.

A ramp of the DC-link voltage has been selected. The ramp slope is a decisive factor for a successful current.The simulation results ensure good dynamic control of the DC-link voltage with very small changes around its reference value.

REFERENCES

[1] D. Seyoum, C. Grantham, MF. Rahman, "The dynamic characteristics of an isolated self-excited induction generator driven by a wind turbine". IEEE Trans on Indus Appl. 2003;39: 936–944.

[2] R. Cardena, R. Pena, "Sensorless vector control of induction machines for variable-speed wind energy applications" IEEE Trans Energy Convers 2004; 19:196–205

[3] S.Hazra, P. Sensarma, "Vector approach for self-excitation and control of induction machine in stand-alone wind power generation" IET Renew. Power Generation 2011: 5:397–405.

[4] S. Hazra, P.S. Sensarma, "Self-excitation and control of an induction generator in a stand-alone wind energy conversion system" IET Renew. Power Gener 2010; 4: 383–393.

[5] D. Hadiouche, H. Razik, A. Rezzoug, "On the Modeling and Design of Dual-Stator Windings to Minimize Circulating Harmonic Currents for VSI fed AC Machines" IEEE Trans. Ind. Appl 2004; 40.

[6] K. Ghedamsi ,D. Aouzellag, "Improvement of the performances for wind energy conversions systems". Int J Electr Power Energy Syst 2010;32(9):936–945.

[7] D. Aouzellag , K. Ghedamsi, EM. Berkouk, "Network power flux control of a wind generator". J Renewable Energy 2009;34:615–622.

[8] F. Poitiers, T. Bouaouiche, M. Machmoum, "Advanced control of a doubly-fed induction generator for wind energy conversion". Electric Power Syst Res 2009;79:1085–1096.

[9] S. Chekkal, N. AouzellagLahaçani, D. Aouzellag, K. Ghedamsi," Fuzzy logic control strategy of wind generator based on the dual-stator induction generator", International Journal of Electrical Power and Energy Systems IJEPES 2014: 59:166–175.

[10] S. Chekkal, D. Aouzellag, K. Ghedamsi, H. Amimeur,"New control strategy of wind generator based on the dual-stator induction generator". 10th International Conference on Environment and Electrical Engineering (EEEIC), Italy; 2011; 268-271.

[11] T. Mhamdi, A. Barhoumi, L. Sbita," Stand-alone self-excited induction generator driven by a wind turbine", Alexandria Engineering Journal 2018; 57: 781–786.

Voltage Build up and Control in Self-excited Stand-alone Doubly fed Induction Generator Wind Energy System

Kaddour abdoune, Fateh abdoune, Djamal Aouzellag
Laboratoire de Maitrise des Energies Renouvelables
Faculté de Technologie, Université de Bejaia
Bejaia 06000, Algeria

***Abstract*— This paper presents the start-up and operation of a stand-alone wind energy conversion system using a doubly-fed induction generator (DFIG). The proposed scheme obviates the use of any auxiliary source in DC bus, such as excitation capacitor or batteries. The DC bus voltage is ramped to the rated value from a small initial voltage produced by remanent magnetism of the machine core which enables minimizing energy loss during the starting. Stator side converter (SSC) and rotor side converter (RSC) are designed specifically to maintain constant DC bus voltage and machine flux under wind speed and electrical load variations. The load side converter (LSC) is operated in a voltage-controlled mode to impose the terminal reference voltage amplitude and frequency. The proposed control scheme has been validated through simulation using Matlab/Simulink software program.**

Keywords—Stand-alone DFIG; Double side converters control; Self-excitation; DC bus voltage build up control

NOMENCLATURE

$V, I, \emptyset$	Voltage, current and flux quantities, respectively
V_{dc}	DC-link voltage
C_{dc}	DC-link capacitor
L_t	Filter inductance
R_s, R_r	Machine resistance per phase
p	Machine pair pole number
ω_s ,ω_m , ω_r	Synchronous, rotational rotor, and slip speeds
θ_s,θ_m , θ_r	Synchronous, rotational rotor, and slip angles
T_g	Generator torque
Ω_g	Generator speed
(d, q)	Synchronous rotating coordinates
(a, b, c)	Stationary three-phase coordinates

I. INTRODUCTION

In recent years, wind energy conversion systems for both grid-connected and stand-alone have been developed based on doubly-fed induction generators (DFIG) which offers several advantages when compared to other generators [1-5]. These advantages include ease of speed control, decoupled active and reactive power capability. An interesting structure of DFIG with converters on the stator as well as the rotor side is presented. This configuration ensures the power extract over wide range speed, offers the possibility of full control on both sides (stator and rotor) of the machine to an equal extent and possibility to share the excitation current equally between the sides of the machine.

In stand-alone generation systems, the generator should be controlled to build-up a constant output voltage and frequency to support the connected loads [4,6,7]. In addition, the machine needs a reactive power for setting up the magnetic field in the machine. To overcome this, various authors have suggested the use of some additional source for charging the DC-link capacitor of power electronics converter during starting. In reference [8], two methods were described to provide the initial power for the excitation. One method was to connect an energy-storage (small battery or super-capacitor) to the DC-link part via separation diode. The second method was to utilize the remanence of the magnet circuit and additional AC stator capacitance. Initially, DC-link capacitor was charged when the DFIG operated as a squirrel cage induction generator with the rotor circuit shorted. Thereafter, the rotor circuit was opened and a power electronics converter provides the excitation power from the charged DC-link capacitor. Another method proposed in references [9] and [10] uses a permanent magnet generator placed on the same shaft. According to the PMG rated power, it can be used for only preliminary DC-link charging via diode rectifier or for recover and supply the slip power through the rotor power converters, and thus feeds the DFIG with its magnetizing reactive power.

In this paper, a novel scheme for voltage build-up is proposed without any auxiliary source. The voltage build-up process is initiated from a small amount of initial energy in the DC-link capacitor coming from the voltage generated by the remanent magnetism of the machine core and thereafter rectified by the anti-parallel diodes of the converters. The use of an appropriate voltage reference ramp is proposed for the

success of the startup process. Indirect stator flux-oriented vector control is proposed to keep the load terminal voltage constant by means of converters connected to the stator and rotor sides, irrespective of the rotational speed and the loading variations. The machine side converters (MSCs) are used to control the DC-link voltage and flux in the machine at its reference values and keeping the modulation index of PWM inverter within a reasonably practical limit. As far as output AC voltage is concerned, it is controlled by LSC.

II. SYSTEM MODELING AND CONTROL METHODOLOGIE

Fig.1 shows the general configuration and control scheme of a stand-alone double side converter fed wound rotor induction machine wind energy conversion system. The stator and the rotor are connected to the load through PWM voltages sources converters composed of the stator side converter, rotor side converter and the load side converter with a common DC bus capacitor. The modeling of the focal components of the studied power system is explained below. The positive polarity convention of important system variables is shown in Fig. 1.

A. *Induction Machine Model*

The modeling of DFIG is carried out in the d-q synchronous reference frame considering symmetrical and isotropic magnetic conditions. Using the concept of flux linkage the basic machine electrical equations are well known and given by Refs. [1, 6]:

$$\overline{V}_s = R_s.\overline{I}_s + \frac{d}{dt}\overline{\phi}_s + j.\omega_s.\overline{\phi}_s \quad (1)$$

$$\overline{V}_r = R_r.\overline{I}_r + \frac{d}{dt}\overline{\phi}_r + j.\omega_r.\overline{\phi}_r \quad (2)$$

The stator and rotor flux linkages could be determined using

$$\overline{\phi}_s = L_s.\overline{I}_s + L_m.\overline{I}_r \quad (3)$$

$$\overline{\phi}_r = L_r.\overline{I}_r + L_m.\overline{I}_s \quad (4)$$

where superscript ($^-$) denotes the vector form of flux linkage, voltage and current. The parameters L_s and L_r represent respectively the stator and rotor winding cyclic inductances, L_m is the mutual cyclic inductance between stator and rotor windings which is kept constant in linear modeling.

The electromagnetic torque as a function of the stator flux and current is given by equation (5):

$$T_g = p.Im\left(\overline{\phi}_s.\overline{I}_s^*\right) \quad (5)$$

where superscript (*) denotes the complex conjugate operator, (Im) represents the imaginary component of the result and p is machine pole pair number.

B. *Modelling of Converters and DC Side Circuitry*

Using the notation and current flow definitions of the Fig.1, the voltages of AC and DC side of each voltage source converter are related as

$$v_{ra} = \frac{1}{3}.(2.\lambda_a - \lambda_b - \lambda_c).V_{dc}$$

$$v_{rb} = \frac{1}{3}.(2.\lambda_b - \lambda_c - \lambda_a).V_{dc} \quad (6)$$

$$v_{rc} = \frac{1}{3}.(2.\lambda_c - \lambda_a - \lambda_b).V_{dc}$$

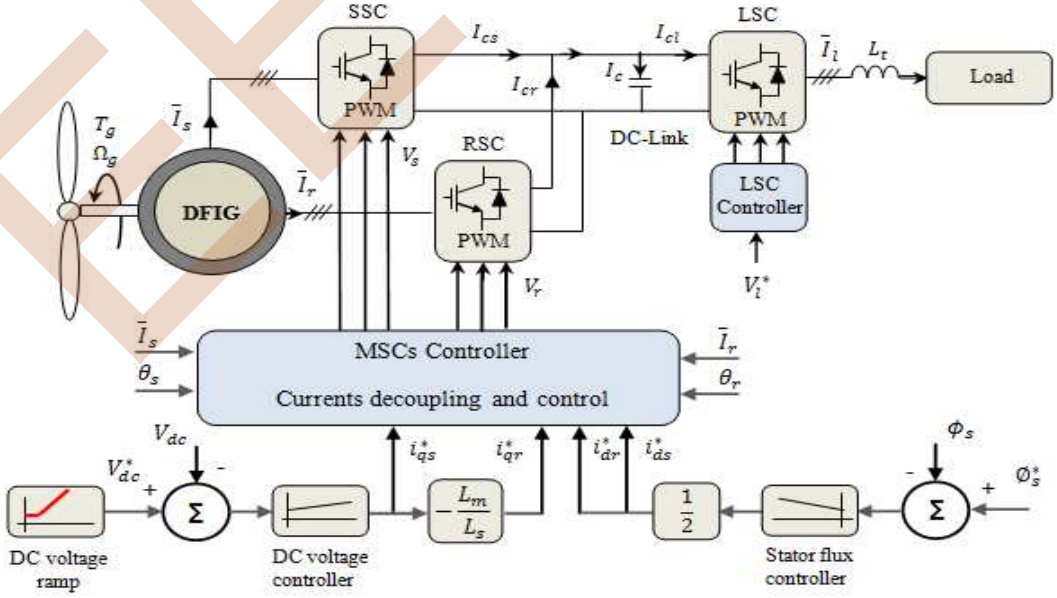

Fig. 1. Global configuration and control scheme

where λ_1, λ_2 and λ_3 are the corresponding switching function of the converter legs. Any of the three switching functions takes the value of '1' if upper switch in the given converter leg is on and lower switch is off, and value '0' if lower switch in the same converter leg is on, while upper switch is off.

The DC-link circuitry is an energy storage element, represented by a capacitor which serves as an energy buffer between the stator, the rotor and load converters. The dynamic of the voltage across the capacitor is derived as follow:

$$V_{dc} = \frac{1}{C_{dc}} \cdot \int_0^t (I_{cs} + I_{cr} - I_{cl}).dt \qquad (7)$$

where I_{cs}, I_{cr} and I_{cl} are respectively the current through the DC side of the stator, the rotor and the load converters.

C. *Control Methodology*

The control aim of the proposed energy conversion system is to maintain the terminal load voltage amplitude and frequency constant irrespective of the rotational speed and the loading conditions. Also, control the voltage build-up owing to the self-excitation process at start-up. The system control is carried out using vector control and the reference frame is oriented along the stator flux vector position. The control aim of the MSCs is used to control the DC-link voltage and flux in the machine at its reference values under rotor speed and load disturbances. The LSC is controlled by PWM technique to impose the terminal reference voltage amplitude and frequency at the load.

The DC bus voltage control loop is designed according to the model defined by Equation (7). As it can be seen in Fig. 1, to maintain DC-link voltage constant, the measured voltage is compared to the reference value and the error is fed into a PI controller to get at their output the q-axis stator currents reference. The rotor component q-axis current reference is automatically generated as the reflection of i_{qs}. To control the DC bus voltage in the start-up, the reference ramp is selected for minimizing the total energy loss.

The reference currents for d-axis are created by means of closed loop stator flux amplitude control and they enable excitation of the machine. The total magnetizing current can be supplied by an arbitrary sharing between the two converters.

III. VOLTAGE BUILD UP PROCESS AND SLOPE OF RAMP VOLTAGE REFERENCE

To start the self-excitation process of induction generator, a small amount of initial energy is required to be supplied to the generator. For the proposed scheme, in which obviates the use of any additional electrical energy source, this is assured by the presence of sufficient residual magnetism in the machine core. As the machine runs and the voltage source converters control is kept switched off, the voltage produced by the remanent magnetism is rectified by the anti-parallel diodes of the converters and therefore charges the DC bus up to a small voltage. In case that the voltage produced is not sufficient to start the voltage build up, an external low-voltage low-power DC source is required for initial charge of the DC bus. After that, the terminal voltage buildup process can be started by introducing the controllers in action.

During the voltage build-up process, a small current from the charged capacitor is injected to the machine windings through the stator and rotor side converter, thereby supplies the necessary magnetizing ampere-turns to provide the air-gap flux of the machine. As a result of stator and rotor winding currents, machine flux and torque are produced. The currents flowing in the machine circuit dissipate power in the circuit resistances, and increasing currents dissipate increasing power, which implies some energy source is required to supply this power. At the starting, because of the low machine flux the power generation remains at low value, but at the same time high currents result high resistive loss in the machine. So, the total loss in the machine is higher than the generated power and that net power loss is assured by the presence of sufficient initial energy in the DC capacitor, causing an initial voltage dip at the DC bus. If the initial machine currents, which are mainly decided by the voltage controllers, remain at low values, the energy loss becomes less during the starting. Whereas the generation increases because of continuous increment of the flux, when the generated power overtakes the loss component, the energy gets stored in DC capacitor and voltage build-up is started.

The purpose of using a reference ramp for DC bus voltage is to control the machine currents at a low values during voltage build-up. In the absence of the starting ramp, the machine currents continue to be high and the DFIG continues to draw power from DC bus, to result in total DC bus voltage collapse. So, the reduction of resistive loss can be achieved by decreasing the machine currents. The choice of the ramp slope is a compromise between the voltage build-up time and the total energy loss occasioned, which is supported by the initial energy in the DC capacitor. For a given rotor speed, the ramp slope by which self-excitation can occur will depend essentially on initial voltage and DC capacitance value. In practice, the minimum initial voltage required in the DC capacitor is dependent on the components used in the converters, their combined forward voltage drop in the converter arrangement and the parameters of the induction generator.

IV. SIMULATION RESULT

The entire system is modeled and simulated using MATLAB/ Simulink. The parameters are given in the appendix. Simulated tests for different transient conditions such as dynamic self-excitation process, sudden application of load and disturbances in wind speed have been carried out to demonstrate the effectiveness of the proposed system. The obtained results are discussed in the following sub-sections.

A. *DC bus voltage Build-up Owing to Self-excitation Process*

In this test, the voltage build-up of the generation system is studied for one DC-link capacitor value. The generator is

operating to run at a constant speed of 1000 rpm under no-load condition. In order to initiate the excitation process, the capacitor connected at the DC bus of the converters is charged initially to a voltage of 12 V, and the DC bus voltage reference ramp is selected.

Fig. 2 shows the DC bus voltage build-up according to the ramp voltage reference and the DC bus capacitor value. The reference DC voltage is set at 700 V. The initial stage of the build-up is shown enlarged in scale in Figure 3. DC-link capacitor is charged initially to provide the air-gap flux of the machine, during the voltage build-up process, a small current from the charged capacitor is injected to the stator and rotor windings through the converters, thereby supplies the necessary magnetizing ampere-turns to provide the air-gap flux of the machine. The d-q stator flux components are shown in Fig. 4. The q-axis stator flux is close to zero and the d-axis flux remains in its reference value, reflecting the correct orientation of the vector control system and performance of proposed control. The currents in DC capacitor and in stator and rotor windings of machine are shown in Fig. 5 and Fig. 6 respectively. It is seen that the necessary machine excitation power is provided in equality from the stator and rotor converter, which explains the equal sharing of the excitation currents between the two sides of the machine. The generated Joule losses are provided by stator and rotor windings. A ramp reference is used to control terminal voltage build-up with minimum energy loss during the starting by controlling the DC capacitor current. In Fig.7 and Fig. 8 are shown the dynamic build-up of the terminal voltage. The results confirm good tracking of the used start-up ramp. The obtained voltage magnitude and frequency are equal to the values imposed by the reference. The stator voltage magnitude reaches its nominal value within 380 V with a good stability and without overshoot. The evolution of the generator torque owing to self-exitation process is shown in Fig. 9. It is seen that the evolution of the torque is the same as that of DC capacitor-discharge. The control of capacitor discharge and the currents in machine sides minimizing energy loss during the starting and generate a stable torque.

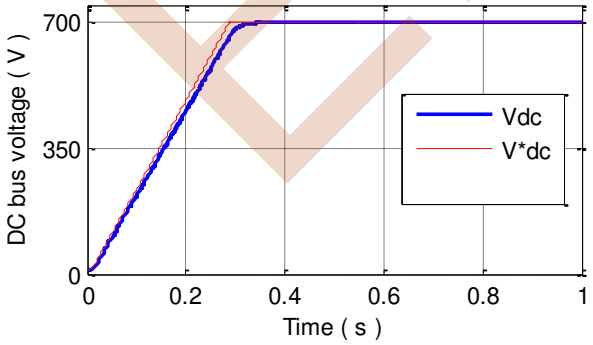

Fig. 2. DC bus voltage build-up

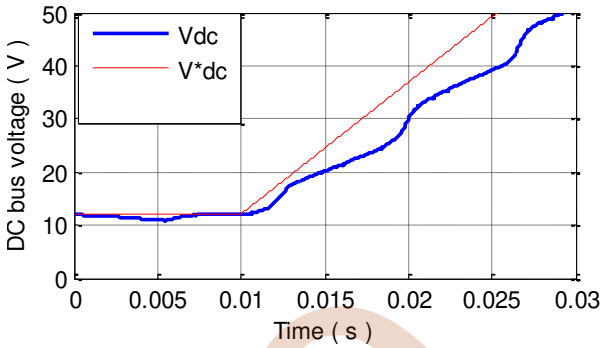

Fig. 3. Initial stage of DC bus voltage build-up

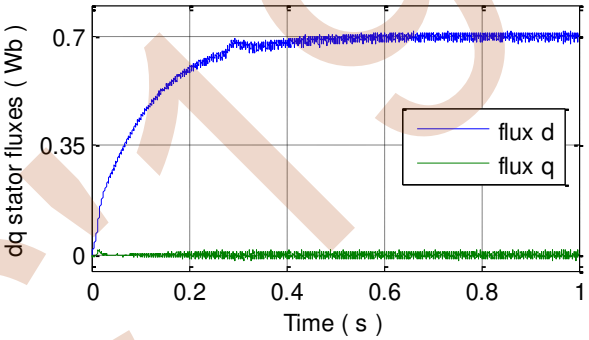

Fig. 4. Stator flux components

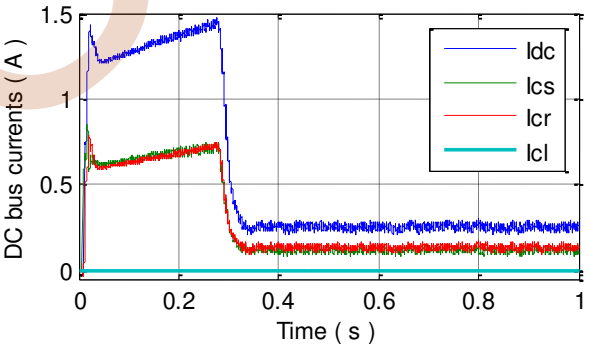

Fig. 5. Currents in DC bus

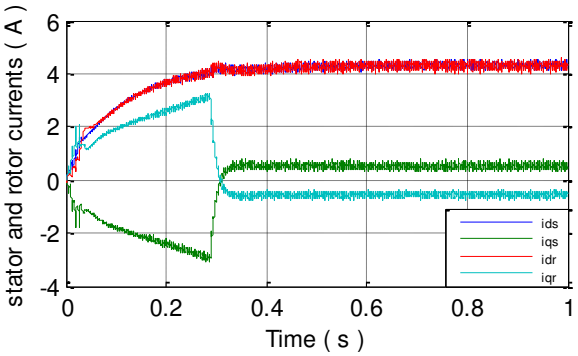

Fig. 6. Stator and rotor currents

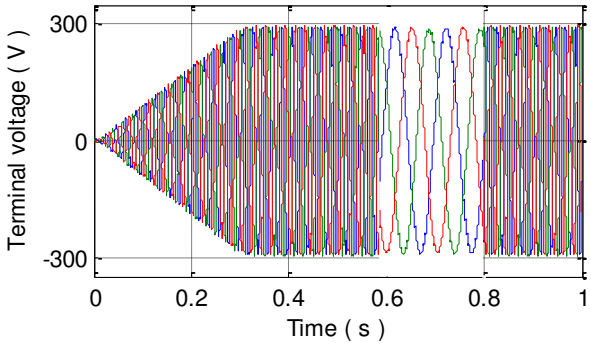

Fig. 7. Three-phase terminal voltage

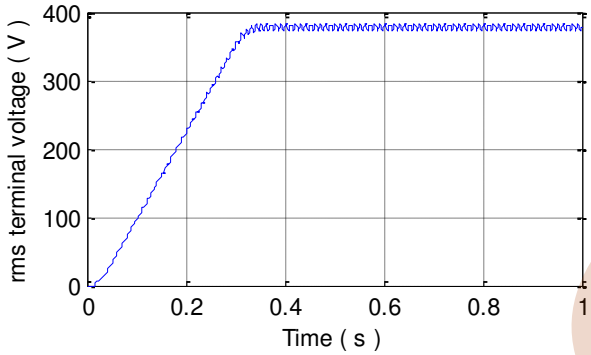

Fig. 8. RMS line-to-line terminal voltage

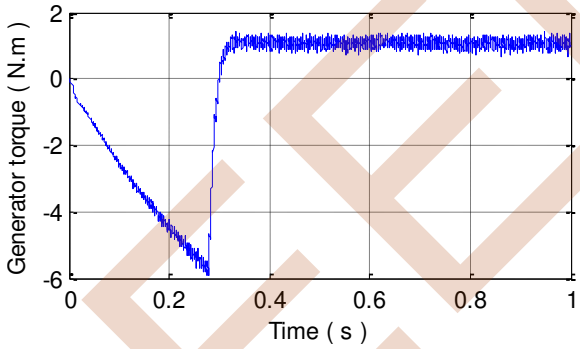

Fig. 9. Generator torque evolution owing to self-excitation process

B. Control under Wind and load Disturbances

In this section, the system is tested for sudden application of load on the generator terminals, when the model is actuated by a variable generator speed profile presented on Fig. 10. A 25% nominal resistance load is applied at t = 3s. The obtained simulation results of the proposed control scheme under the mentioned conditions are shown in Figs. 11-14.

The regulation capabilities of the proposed control strategy during the whole speed profile and load variation can be observed in Figs. 11-14. Fig. 11 and Fig. 12 illustrate respectively the response of DC-link voltage and the stator flux components to variation in load and to wind speed. There is a drop in DC bus voltage of approximately 6%. However the regulation capabilities of the proposed control strategy can be observed, the control is able to recover magnitude of DC voltage and flux. The correct orientation of the stator flux vector is obtained despite the large variations of speed and load. The ability of the system to supply constant load voltage during the load variations and wind speed is illustrated in Fig. 13 and Fig. 14. The rms line-to-line load voltage shown in Fig. 13 is fixed whatever be the load and speed. A short drop in the voltage amplitude at the load switching points can be observed. It can be seen from Fig. 14 that the load is supplied with fixed voltage amplitude and a fixed frequency (50 Hz) irrespective of the load variation and wind speed.

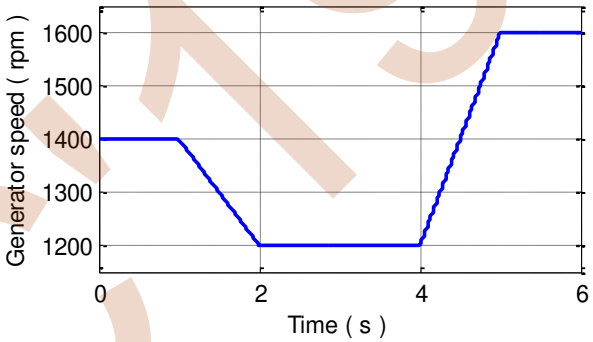

Fig. 10. Generator speed

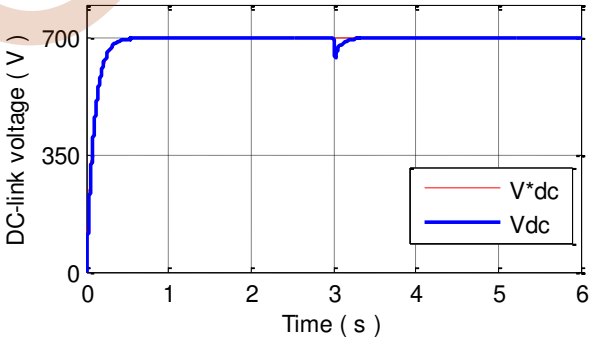

Fig. 11. DC bus voltage

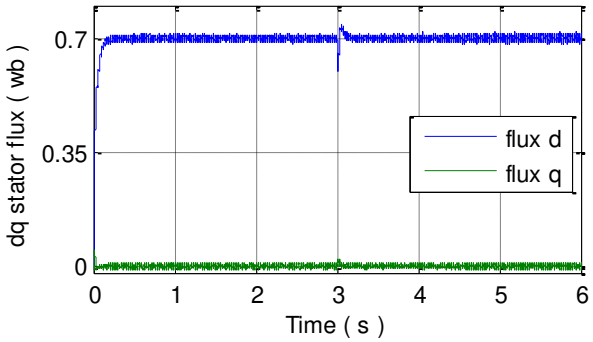

Fig. 12. Stator flux components

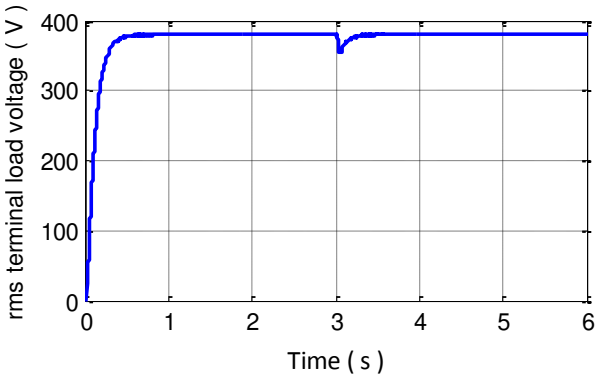

Fig. 13. RMS line-to-line terminal load voltage

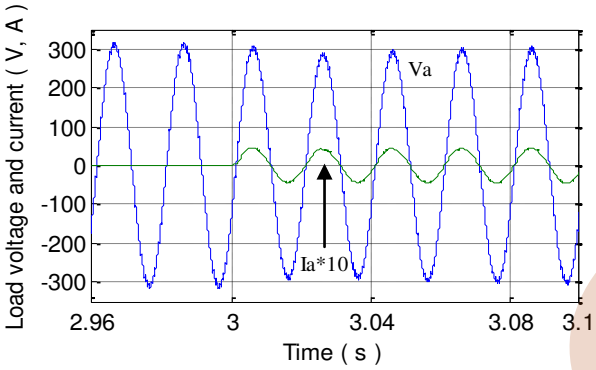

Fig. 14. Terminal load voltage and current

V. CONCLUSION

In this paper, A novel structure for voltage build-up is presented where precludes the use of any additional hardware support like battery or capacitor bank. The DC bus has been charged from a small initial voltage, which is derived from the rectification of small terminal voltage of the induction generator because of remanent magnetism. A ramp reference is chosen to control DC-link voltage and terminal load voltage build-up with minimum energy loss during starting.

Dynamic behavior of DFIG has been tested under varying load and wind speed conditions. The test results ensure good dynamic control of the terminal voltage at the load. For the entire tests carried out in this work, the performance of the proposed control system is effective.

APPENDIX

Parameters for the simulated DFIG [11]

Rated voltage	380 V
Rated Power	7.5 KW
Frequency	50 Hz
Number of poles	4 poles
Stator winding resistance	0.445 Ohm
Rotor winding resistance	0.620 Ohm
Magnetism inductance	0.078 H
Stator inductance	0.084 H
Rotor inductance	0.081 H
DC-link capacitor	50 µF
DC-link voltage	700 V

REFERENCES

[1] D. Aouzellag, K. Ghedamsi, E.M. Berkouk, "Terminal Network power flux control of a wind generator," Renew. Energy 34, 2009,pp. 615-622.

[2] R.D. Shukla, R.K. Tripthi, "Topologies for stand-alone DFIG based wind energy conversation system," In: second International Conference on Power on Control and Embedded Systems IEEE, 2012.

[3] R.D. Shukla, R.K. Tripathi, "wind power supply system using double fed induction generator for remote areas," Energy Convers. Manag. 96, pp. 473-489, 2015.

[4] F.Abdoune, D. Aouzellag, K. Ghedamsi, "Terminal voltage build-up and control of a DFIG based stand-alone wind energy conversion system," Renewable Energy 97, pp. 468-480, June 2016.

[5] J. Chen, W. Zhang, Y. Chen, Y. Ma," Improved vector control of brushless doubly fed induction generator under unbalanced grid conditions for offshore wind power generation,"IEEE Transaction on Energy Conversion, vol. 31, no. 1, 2016, pp. 293-302.

[6] R. Pena, R. Cardenas, "Vector control of a diesel-driven doubly fed induction machine for a stand-alone variable speed energy system," The 28th Annual Conference of the Industrial Electronics Society, pp. 985-990, 2000.

[7] W. Xu, O.M.E Mohammed, Y. Liu, M.R. Islam,"Negative Sequence Voltage Compensating for Unbalanced Standalone Brushless Doubly-fed Induction Generator," IEEE Transactions on Power Electronics, 2019, DOI: 10.1109/TPEL.2019.2912820

[8] A. Ansel, B. Robyns, "Modelling and simulation of an autonomous variable speed micro hydropower station,"Math Comput Simul, pp. 320-332, 2006.

[9] G. Iwanski, W. Koczara, "Sensorless direct voltage control method for standalone slip ring induction generator,"11th European Conference on Power Electronics and Applications, 2005.

[10] T. Mesbahi, A. Ouari, T. Ghennam, "A stand-alone wind power supply with a Li-ion battery energy storage system,"Renewable and Sustainable Energy Reviews, pp. 204-213, 2014.

[11] F. Poitiers, Study of Induction Generators for Wind Energy Conversion Systems (PhD thesis), University of Nantes, 2003

Voltage control Improvement of a STATCOM-assisted Self-excited Induction Generator-based Wind Turbine

BERABEZ Kahina
Department of Electrical Engineering
Laboratory LTII. University of Bejaia, Algeria
kberabezpg2015@gmail.com

IDJDARENE Kassa
Department of Electrical Engineering
Laboratory LTII. University of Bejaia, Algeria
idjdarene@yahoo.fr, kassa.idjdarene@univ-bejaia.dz

HAMOUDI Farid
Department of Electrical Engineering
Laboratory LMER. University of Bejaia, Algeria
f hamoudi@yahoo.fr

HACINI Ismail
Department of Electrical Engineering
Laboratory LTII. University of Bejaia, Algeria
hacinismail@yahoo.fr

Abstract: This work has for objective maintains the voltage to be constant and improves power quality in the system of Self-Excited Induction Generator (SEIG) by mean of STATCOM in order to improve its role in wind energy conversion systems in remote areas. In addition to the induction generator and the STATCOM, the System presented here is constituted with capacitor bank.The regulation of the voltage is carried out by a (STATCOM) connected in parallel with (SEIG). To accomplish that, it is proposed the use of proportional-integral (PI) controllers to control the compensation currents processed by STATCOM. The aim simulation tests have been carried out using MATLAB Simulink, under wind speed variation, load variation and load unbalance. The test results are presented to demonstrate its performance.

Key words: STATCOM, saturation effect, self-excited induction generator (SEIG), Voltage control, PI controller, unbalanced load.

1. INTRODUCTION

The wind is a clean, free, and readily available renewable energy source. Each day, around the world, wind turbines are capturing the wind's power and converting it to electricity. This source of power generation plays an increasingly important role in the way we power our world. For several decades,the use of wind turbine as renewable energy source hasincreased considerably in remote and isolated area[1].Furthermore, a Self-Excited Induction Generators (SEIG) are largely used for wind energy due to its low cost, less maintenance, ruggedness, little maintenance needs and has been the subject of many researches [2,7].However, this machine have need the reactive power to bemagnetized. So maintaining voltage and frequency of (SEIG) has become a very challenging task and has been extensively worked upon by researchers [2, 3].The model used is a diphase one obtained by the application of the Park transform. This model permits, when adopting some simplifying hypothesis, to take account of the saturation effect based on the approximation of the magnetizing inductance with regards to the current. Different methods can be adopted to approximate the magnetising inductance with regards to the current. In our case, we use a polynomial function, of 12th degree to achieve this approximation. This approach is simple and very accurate [2]. Many researches use this model to study the induction generator when a capacitive bank is connected to the stator windings. The disadvantages of this type of generator are its relatively poor voltage regulation. The magnitude of voltage generated by the SEIG is highly influenced by the rotor speed, the excitation and the load[4, 9]. However, a static and dynamic analysis of a Self-Excited Induction Generator has led several researchers to conduct investigations in order to improve the efficiency of the quality of the energy provided [3, 7].Different system configurations and control strategies are proposed in the literature in order to overcome these problems.Static synchronous compensator (STATCOM) in parallel is more efficient to compensate reactive power for regulating magnitude of terminal voltages[8, 9].This added STATCOM is the topic of the analysis presented in thiswork and will be used mainly to improve the efficiency and to regulate the generated voltage by the self-excited induction generator.The performance of a STATCOM greatly depends upon the controller used in the system. Generally PI controllers are used for the control of STATCOM [6, 10].

This system is described in section, while its modelling and control will be detailed respectively in sections three and four. In section five, the main results will be presented and discussed. Finally, this paper will be ended by a conclusion in section six.

2. SYSTEM DESCRIPTION

Schematic diagram of the STATCOM based SEIG to regulate voltage is shown in Fig.1.The whole system consists of an induction machine a self-excited induction generator (SEIG) system under varying loads and SIEG parameters is proposed, capacitor bank for excitation, loadis coupled in delta and STATCOM for regulating voltage.The STATCOM consists of a three-phase current controlled IGBT-VSI, with DC bus capacitor, and connected to the SEIG through AC filtering inductors.

3. SYSTEM MODELING

a. Induction Machine model:

The electrical equations of the induction machine are expressed in the d-q frame and then written in a matrix form such as [2]

$$\begin{bmatrix} V_{sd} \\ V_{sq} \\ 0 \\ 0 \end{bmatrix} = \begin{bmatrix} R_s & -P\Omega.L_s & 0 & -P\Omega.L_m \\ P\Omega.L_s & R_s & P\Omega.L_m & 0 \\ 0 & 0 & R_r & 0 \\ 0 & R_r & 0 & R_r \end{bmatrix} . \begin{bmatrix} i_{sd} \\ i_{sq} \\ i_{md} \\ i_{mq} \end{bmatrix} + \begin{bmatrix} l_s & 0 & L_m + L_m' . \frac{i_{md}^2}{|i_m|} & L_m' . \frac{i_{md} . i_{mq}}{|i_m|} \\ 0 & l_s & L_m' . \frac{i_{md} . i_{mq}}{|i_m|} & L_m + L_m' . \frac{i_{mq}^2}{|i_m|} \\ -l_r & 0 & l_r + L_m + L_m' . \frac{i_{md}^2}{|i_m|} & L_m' . \frac{i_{md} . i_{mq}}{|i_m|} \\ 0 & -l_r & L_m' . \frac{i_{md} . i_{mq}}{|i_m|} & l_r + L_m + L_m' . \frac{i_{mq}^2}{|i_m|} \end{bmatrix} . \begin{bmatrix} \frac{di_{sd}}{dt} \\ \frac{di_{sq}}{dt} \\ \frac{di_{md}}{dt} \\ \frac{di_{mq}}{dt} \end{bmatrix} \quad (1)$$

In this equation Rs,Rr,ls and lr are phase resistances and leakage inductances in stator and rotor. Magnetizing inductance and its derivative with respect to the magnetizing current are represented respectively by Lm and Lm'. ωs and ωr represent respectively the electrical pulsation in the stator and the rotor respectively. Besides, the stator voltage and current are noted in dq axis by V_{sd},i_{sd},$V_{sq}$and i_{sq}. Finally, in dq axis, the magnetizing currents imd and imq are given as:

$$i_{md} = i_{sd} + i_{rd} , \qquad i_{mq} = i_{sq} + i_{rq} \quad (2)$$

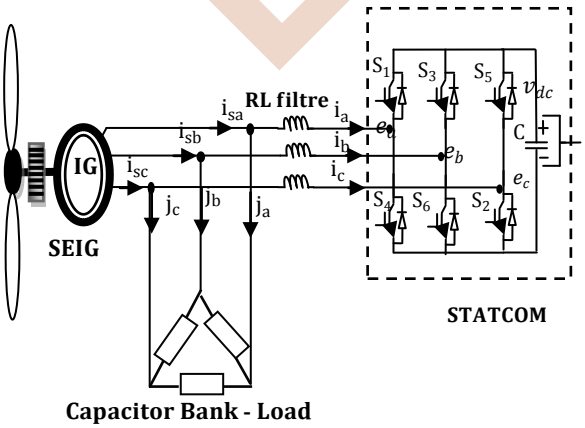

Fig.1: Schematic diagram of STATCOM based SEIG system.

with ird and irq the rotor currents in dq axis. The magnetizing current im defined as:

$$|i_m| = \sqrt{i_{md}^2 + i_{mq}^2} \quad (3)$$

The expression of Lmas function of i_m, is approximated with a 12th degree polynomial by [2]:

$$\begin{cases} L_m = f(|i_m|) = \sum_{j=0}^{n} a_j . |i_m|^j \\ L_m' = f(|i_m|) = \sum_{j=0}^{n} j . a_j . |i_m|^{j-1} \end{cases} \quad (4)$$

b. Modeling of the STATCOM:

The STATCOM DC-bus voltage vdc can be expressed with respect to AC side currents (ia,ib and ic), and commutation functions Sa, Sb andSc by the following equation

$$p\, v_{dc} = \frac{S_a i_a + S_b i_b + S_c i_c}{C_{dc}} \quad (5)$$

Where C_{dc} represents the DC-bus capacitance. The DC current i_{dc} can be expressed in terms of switching functions of the inverter as:

$$i_{dc} = S_a i_a + S_b i_b + S_c i_c \quad (6)$$

The three phase voltages of the SEIG can be determined as follows:

$$\begin{bmatrix} v_{sa} \\ v_{sb} \\ v_{sc} \end{bmatrix} = R_f . \begin{bmatrix} i_a \\ i_b \\ i_c \end{bmatrix} + L_f . \frac{d}{dt} . \begin{bmatrix} i_a \\ i_b \\ i_c \end{bmatrix} + \begin{bmatrix} e_a \\ e_b \\ e_c \end{bmatrix} \quad (7)$$

In which Rf and Lf represent the resistance and the inductance of the filter between the STATCOM and the SEIG.

Moreover, this voltage is given line-to-line as:

$$\begin{cases} U_{sab} = (v_{sa} - v_{sb}) \\ U_{sbc} = (v_{sb} - v_{sc}) \\ U_{sca} = (v_{sc} - v_{sa}) \end{cases} (8)$$

The output voltages of the inverter (STATCOM), noted ea,b and ec are formulated with respect to switching functions and DC-bus voltage as follows:

$$\begin{bmatrix} e_a \\ e_b \\ e_c \end{bmatrix} = \frac{V_{dC}}{3} \begin{bmatrix} 2 & -1 & -1 \\ -1 & 2 & -1 \\ -1 & -1 & 2 \end{bmatrix} \begin{bmatrix} S_a \\ S_b \\ S_c \end{bmatrix} \quad (9)$$

The dynamic equations relating voltage to current of the STATCOM are written as:

$$U_{sab} = R_f i_a + L_f P i_a + e_{ab} - R_f i_b - L_f P i_b \quad (10)$$

$$U_{sbc} = R_f i_b + L_f P i_b + e_{bc} - R_f i_c - L_f P i_c \quad (11)$$

When balanced, the line currents are normally related as:

$$i_c = -i_a - i_b \quad (12)$$

The control scheme is shown in Fig 2. To regulate the terminal voltage of the SEIG is based on the control of source currents is using a decoupled controlled strategy which has two control loops a active power control loops and a reactive power control loops(which have two components in phase and quadrature with ac voltage).The in-phase sinusoidal unit vectors(ua,ub,uc)are obtained from the three-phase AC voltages(V_{sa}, V_{sb}, V_{sc})with respect to equivalent voltage amplitude (Vt). Another set of quadrature unit vectors(w_a, w_b, w_c)is then obtained from in-phase vectors (u_a, u_b, u_c). The AC terminal voltage is regulated using PI controller, from the comparison of the vector $V_{t\text{-réf}}$ its reference. The PI output is in-quadrature term i^*_{sq}corresponding to the reactive current to be generated by the STATCOM. Multiplying this term by the quadrature unit vectors(w_a, w_b, w_c), the corresponding three phase currents

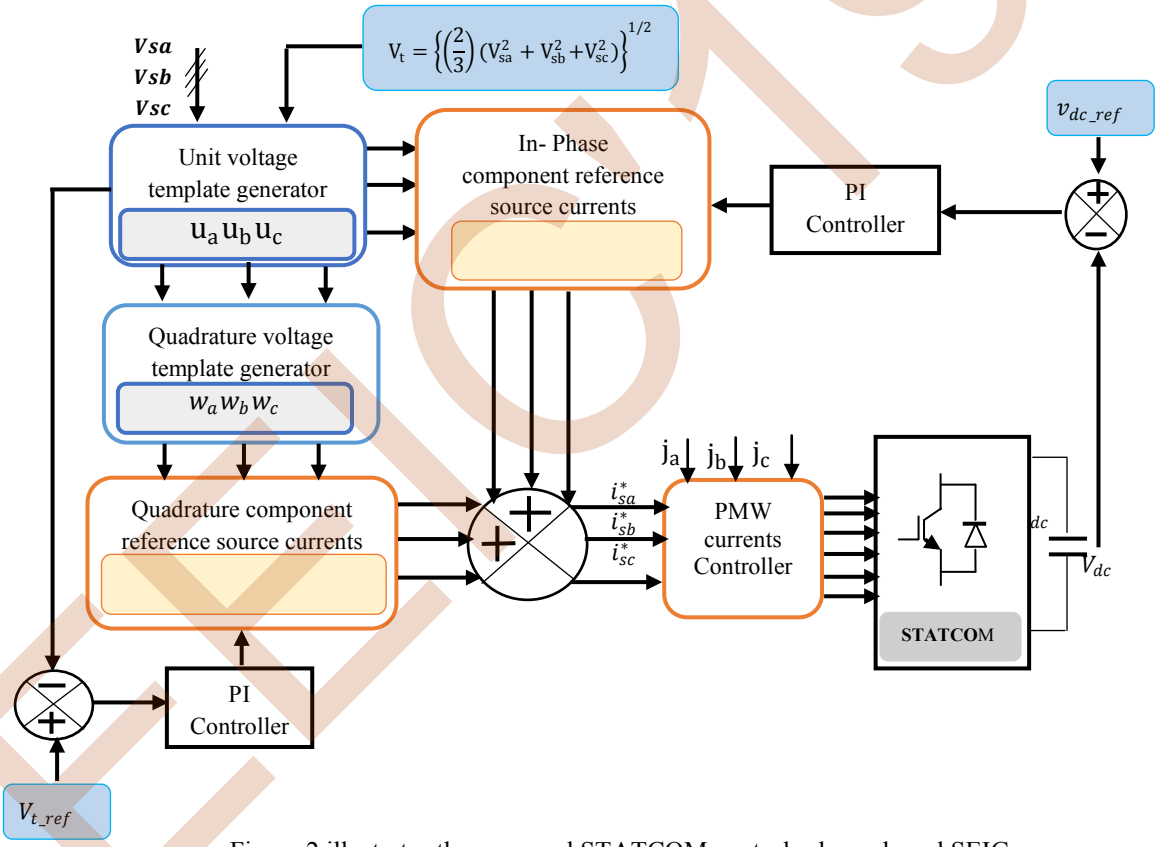

Figure 2 illustrates the proposed STATCOM control scheme based SEIG

According to the above equation, the time derivative of STATCOM currents are given by:

$$Pi_a = \{U_{sbc} - e_{bc} + 2(U_{sab} - e_{ab}) - 3R_f a\}/3L_f \quad (13)$$

$$Pi_b = \{U_{sbc} - e_{bc} - (U_{sab} - e_{ab}) - 3R_f i_b\}/3L_f \quad (14)$$

4. CONTROL OF STATCOM

are then obtained. To provide self-supporting DC bus, its voltages sensed to be regulated with its reference value using another PI controller. This one provides a current termi^*_{sd}corresponding to the active current magnitude. The in-phase references for the source currents (i^*_{sad}, i^*_{sbd}, i^*_{scd})are then obtained after multiplying this term by the in-phase unit vectors(u_a, u_b and u_c). (ua,ub and uc). Finally, from the in-phase and in-quadrature components, the source reference currents (i^*_{sa}, i^*_{sb}, i^*_{sc})are constituted and compared with the sensed line currents (j_a, j_a, j_a).to perform the current control of the STATCOM [6,10]. The equation associated with STATCOM are given below.

The voltage amplitude Vt or SEIG terminal voltage is obtained from (Vsa, Vsb, Vsc) by:

$$V_t = \left\{\left(\frac{2}{3}\right)(V_{sa}^2 + V_{sb}^2 + V_{sc}^2)\right\}^{1/2} \quad (15)$$

The in-phase unit vectors are derived as,

$$u_a = \frac{V_{sa}}{V_t}\ ; \qquad u_b = \frac{V_{sb}}{V_t}\ ; \qquad u_c = \frac{V_{sc}}{V_t} \quad (16)$$

The quadrature unit vectors from these in-phase vectors are,

$$\begin{bmatrix} w_a \\ w_b \\ w_c \end{bmatrix} = \begin{bmatrix} 0 & \frac{-1}{\sqrt{3}} & \frac{1}{\sqrt{3}} \\ \frac{\sqrt{3}}{2} & \frac{1}{2\sqrt{3}} & \frac{-1}{2\sqrt{3}} \\ \frac{-\sqrt{3}}{2} & \frac{1}{2\sqrt{3}} & \frac{-1}{2\sqrt{3}} \end{bmatrix} \begin{bmatrix} u_a \\ u_b \\ u_c \end{bmatrix} \quad (17)$$

In-phase components of the source reference currents are given as:

$$i_{sad}^* = i_{sd}^* * u_a;\ \ i_{sbd}^* = i_{sd}^* * u_b\ i_{scd}^* = I_{sd}^* * u_c \quad (18)$$

In-quadrature components of the source reference currents are given as:

$$I_{saq}^* = I_{sq}^* * w_a\ ;\ \ I_{sbq}^* = I_{sq}^* * w_b;\ \ I_{scq}^* = I_{sq}^* * w_c \quad (19)$$

Finally,Reference compensating current of STATCOM is the sum of In-phase current & In-quadrature current, which can be expressed as:

$$\begin{cases} i_{sa}^* = i_{sad}^* + i_{saq}^* \\ i_{sb}^* = i_{sbd}^* + i_{sbq}^* \\ i_{sc}^* = i_{scd}^* + i_{scq}^* \end{cases} (20)$$

The switching functions$(s_a, s_b, s_c)$to the STATCOM are generated through hysteresis current controller from the currents errors:

$$\begin{cases} i_{aer}^* = i_{sa}^* - j_a \\ i_{ber}^* = i_{sb}^* - j_b \\ i_{cer}^* = i_{sc}^* - j_c \end{cases} (21)$$

5. SIMULATION RESULTS AND DISCUSSION

The studied system has been implemented with different operating conditions in the MATLAB/SIMULINK environment. The system is subjected to two different types of tests (Effect of balanced and unbalanced load, effectof speed variation)

a. Step change in load:

In this step, The generator is initially driven at a speed Ω= 750 (rad/s). In the simulation, the performance of the system is tested under two types of load change resistive load and an inductive load.

Effect of balanced load

For this test, the load is fixed constant with its resistance at 120 Ω, and changed to 180Ω at t= 3s. a the other step of changing inductive load a 50mH introduced at t = 6 s.

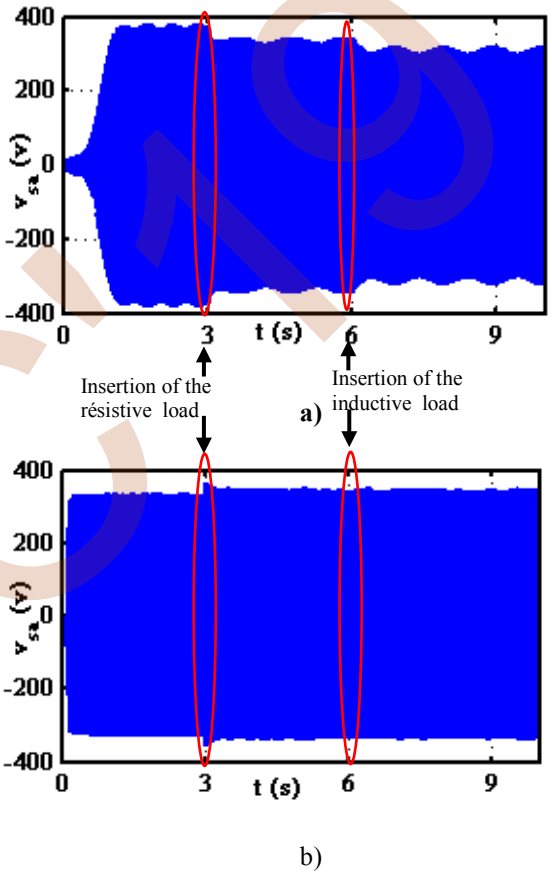

Figure.3: Output voltage generator.

Fig.3 at shows the output voltage of system without STATCOM. The voltage changes with the change of state of charge; this result ensures the sensitivity of the generated phase voltage to the load variations. This is controlled by STATCOM. This is mainly due to the demagnetization of the machine and the lack of reactive energy necessary on the one hand for the magnetization of the machine and on the other hand, for the supply of the load, in particular the inductive one that is consuming the reactive energy.

As shown in Fig. 3 b Waveforms of generator terminal voltage with STATCOM. The voltage is controlled

perfectly and returns to its rated value after to load change.

In Figures 4 and 5, the SEIG voltage magnitudeVt is compared to its reference Vt_ref, the DC bus voltage Vdc compared to its reference value Vdc_ref are respectively represented.

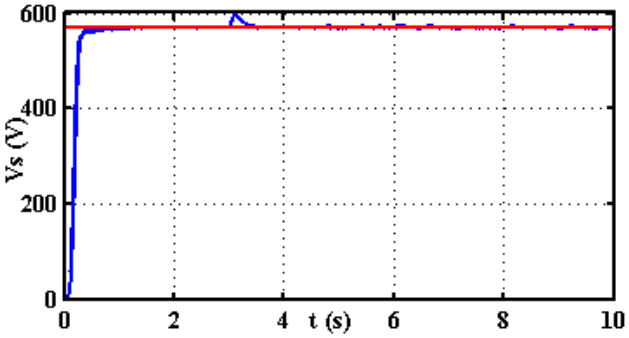

Figure 4. AC Voltage magnitude.

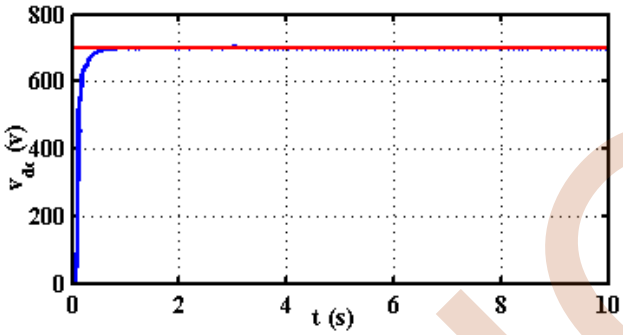

Figure 5. Vdc waveform.

The voltage of the DC bus is kept constant around 700 V, but for the magnitude of terminal voltage, we can observe an overshoot at startup of about 4% at t=3s.

Effect of load unbalance

In this section the system performance is evaluated by subjecting it to loadunbalance as:

- Phase a: Ra = 120Ω and La=30mH.
- Phase b:Rb = 140Ω and Lb=40mH.
- Phase c : Rc=180Ω and Lc=50mH.

Figures 6 and 7 show a perfect reference tracking for SEIG stator and STATCOM DC-bus voltages, and therefore, these voltages are almost insensitive to load unbalance. Moreover rapid response is observed in case of perturbation.

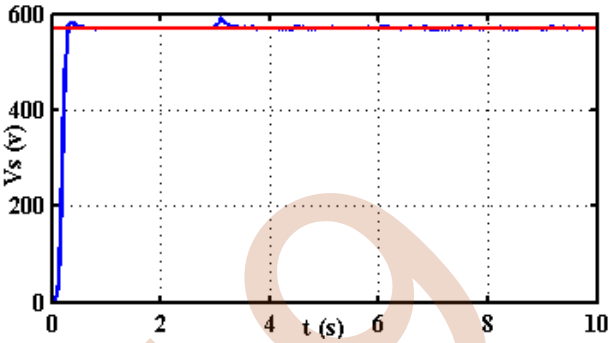

Figure 6. AC Voltage magnitude.

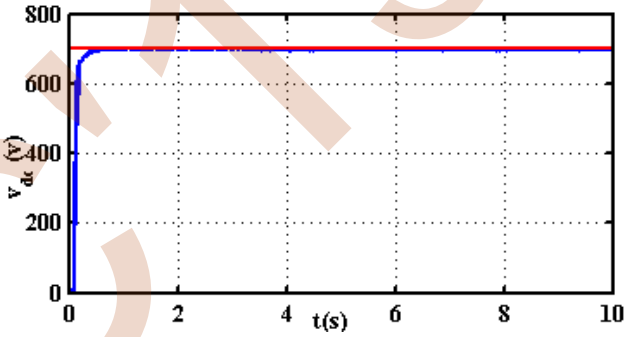

Figure 7. *DC bus voltage.*

a. Effect of speed variation :

In this part the speed and the load are varied at the same time. The speed profile is shown in figure 8. the variations of the load are similar to that of first test (balanced load).

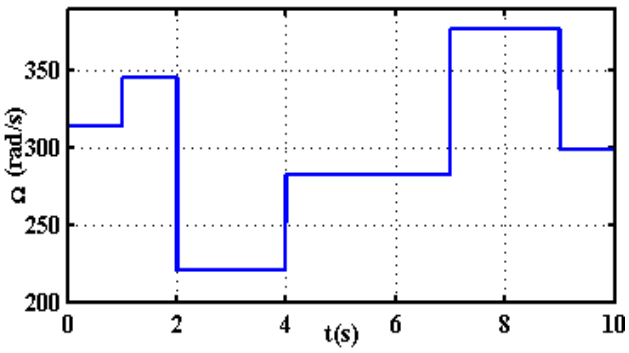

Figure 8. waveform of Generator speed.

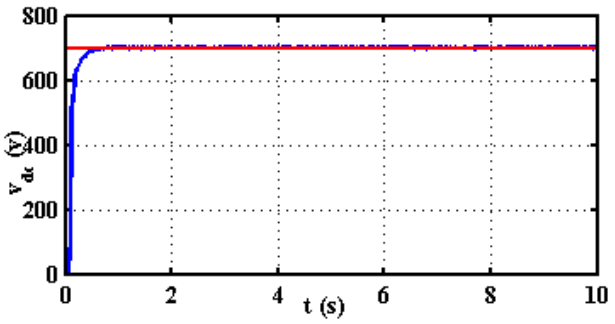

Figure 9. DC bus voltage.

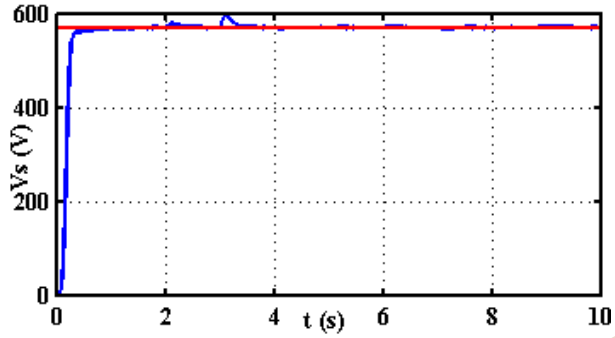

Figure 10. Ac Voltage magnitude.

Figures 9–10 show the waveforms of DC-bus voltages and the AC Voltage magnitude; It can be seen that the DC-bus voltage is well regulated and totally insensitive loadand speed change. Slightly sensitive to load change, the AC voltage is also correctly regulated.

6. CONCLUSION

This communication presents a proposal for voltage regulation for a Self-Excited Induction Generator (SEIG), and therefore to improve the performances of wind energy conversion systems in remote areas. The voltage profile is maintained constant and being controlled by a simple PI controller. All with different load conditions (changes and unbalance). The simulation results indicate that the controller proves its robustness by maintaining always SEIG voltage at the desired value.It appears that under steady-state condition, following each perturbation, the terminal voltage is maintained at normalized values.

References

[1] A. R. Choudhury, S. Pati, A. Choudhury "Control of Voltage & Frequency of a Hybrid Microgrid Using a FLC based Bidirectional Converter equipped with BESS" IEEE International Conference on Technologies for Smart-City Energy Security and Power (ICSESP-2018), March 28-30, 2018, Bhubaneswar, India.

[2] K. Idjdarene, D. Rekioua, T. Rekioua, A. M. Tounzi, "Performance of an Isolated Induction Generator Under Unbalanced Loads," IEEE Trans. on Energy Conversion, vol. 25, No. 2, pp. 303–311, 2010.

[3] A. S. Satpathy, D. Kastha , K. Kishore"Control of a STATCOM-assisted self-excited induction generator-based WECS feeding non-linear three-phase and single-phase loads" IET Power Electron., 2019, Vol. 12 Iss. 4, pp. 829-839. 2019.

[4] K. Idjdarene, D. Rekioua, T. Rekioua, A. M. Tounzi "Vector Control of Autonomous Induction Generator with Battery Storage System", International Renewable and Sustainable Energy Conference, IRSEC, 2017.

[5] A. N Patil, S. Angadi, A.B.Raju"Voltage control of PWM-VSI Assisted Standalone Self Excited Induction Generator" IEEE International Conference on Current Trends toward Converging Technologies, Coimbatore, India 2018.

[6]S. Pati, S.K.Kar, K.B.Mohanty, S. Mishra " A Sliding mode Controller based STATCOM with Battery storage for Voltage and Frequency Stabilization in a Micro-Grid" IEEE Conference, International Conference on Circuit, Power and Computing Technologies (ICCPCT), 18-19 March 2016 .

[7] R. El Akhrif, A. Abbou, M. Barara, Y. Majdoub"Modeling and simulation for a three-phase voltage source inverter using a self-excited induction generator"IEEE7th International Renewable Energy Congress (IREC) 2016.

[8]S. Khatua, S. Mishra, S. Pati "Voltage & Frequency Stabilisation of a SEIG based Micro-Hydro System through a DFIG based WECS equipped with BESS" IEEE International Conference on Technologies for Smart-City Energy Security and Power (ICSESP-2018), March 28-30, 2018, Bhubaneswar, India.

[9] S.A. Deraz , F.E. Abdel Kader "A new control strategy for a stand-alone self-excited induction generator driven by a variable speed wind turbine" Renewable Energy, Elsevier, Vol. 51, March 2013, pp. 263-273.

[10]B.Singh, S. S. Murthy,S. Gupta, "STATCOM-Based Voltage Regulator for Self-ExcitedInduction Generator Feeding Nonlinear Loads"IEEE transactions on industrial electronics, vol. 53, no. 5, october 2006.

[11] B.Singh, S. S. Murthy, S. Gupta "A Stand-Alone Generating System Using Self-Excited Induction Generators in the Extraction of Petroleum Products" IEEE transactions on industry applications, vol. 46, no. 1, january/february 2010.

Thermal Modeling of an Integrated Circular Inductor Using Separation of Variables Method

BENHADDA Yamina
Electrical engineering department,
University of Science and Technology
Oran, Algeria
benhadda_yamina@yahoo.fr

ALLAOUI Abdelhak
Electrical engineering department,
University of Science and Technology
Oran, Algeria
abdelhakallaoui@yahoo.fr

HAMID Azzedine
Electrical engineering department
University of Science and Technology
Oran, Algeria
hamidazdean@yahoo.fr

***Abstract*— The purpose of this article is to study the thermal modeling of an integrated circular inductor using separation of variables method. We have presented an analytical solution of a problem of transient heat conduction in a one-dimensional three-layer composite slab in a contact perfect at the interfaces. In the solution of transient heat conduction problems expansion technique, the contribution of nonhomogeneous terms of the boundary conditions in the solution generally gives rise to convergence difficulties when the solution is evaluated near the boundary. Therefore, whenever possible, it is desirable to transform the nonhomogeneous boundary conditions into homogeneous ones. The Green's function approach is used for solving the nonhomogeneous problem with energy generation in a plate. Finely, we treat the thermal phenomena in an inductor using the finite element method.**

I. INTRODUCTION

The integration of passive components has grown up considerably in the recent decades with the electronics industry's application. In this domain of the embedded electronics, reduced size, volume and high temperature functionality is an industrial and scientific challenge. The purpose of this paper is a thermal modeling of an integrated circular planar inductor. A mathematical formulation of one dimensional transient heat conduction in a inductor in a contact perfect at the interfaces using method of separation-of-variables is presented [1]. We determine the evolution of the temperature as a function of time and position. The transformation of the problem with nonhomogeneous boundary condition into the one with homogeneous boundary condition is described. The use of Green's function is a very convenient approach for solving nonhomogeneous problems of transient heat conduction with energy generation in a composite medium [2,5].

II. PROPERTIES OF THE INTEGRATED CIRCULAL INDUCTOR

The geometry parameters [6] characterizing the integrated inductor (Fig. 1) are the number of turns $\boldsymbol{n}$, the width of the conductor $\boldsymbol{w}$, thickness of the conductor $\boldsymbol{t}$, the spacing between conductor $\boldsymbol{s}$, length of the conductor $\boldsymbol{l}$, the outer diameter $\boldsymbol{d_{out}}$ and input diameter $\boldsymbol{d_{in}}$.

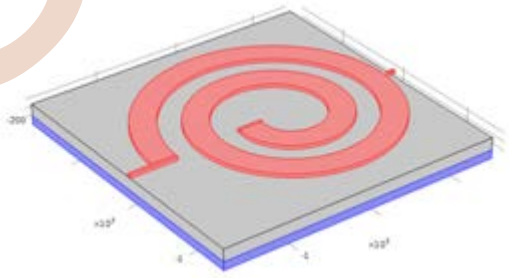

Figure 1. Geometry of integrated circular spiral inductor

Table 1 presents the geometry parameters of the integrated inductor.

Table 1 Design results of the spiral inductor

Parameter	Value
Inductance, L (µH)	0.5
Output diameter, d_{out} (mm)	3
Input diameter, d_{in} (mm)	0.9
Number of turns, n	2
Thickness of the conductor, t (µm)	40
Width of the conductor, w (µm)	280
Spacing between conductor, s (µm)	245
Length of the conductor, l (mm)	15.9

The equivalent electrical model of the integrated inductor [7] is shown in Fig. 2.

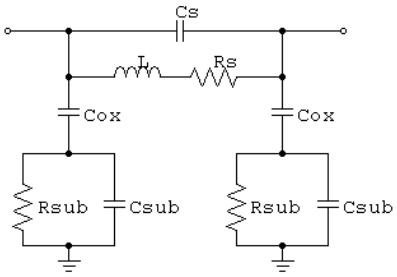

Figure 2. Equivalent electrical model

Table 2 presents electrical parameters of the integrated inductor.

Table 2 Electricals parameters of the integrated circular spiral inductor

Electricals parameters	Values
$R_s(\Omega)$	0.0241
$R_{sub}(\Omega)$	0.002
$C_s(pF)$	0.023
$C_{ox}(pF)$	15.37
$C_{sub}(pF)$	2.03

III. MATHEMATICAL EQUATIONS IN A CIRCULAR INDUCTOR

Consider a composite slab consisting of three parallel layers as shown in figure 3.

Figure 3. Sectional view of integrated circular spiral inductor

Let k_1 , k_2 and k_3 be thermal conductivities for the first layer in $0 \le x \le L_1$, second in $L_1 \le x \le L_2$ and third in $L_2 \le x \le L_3$, respectively. α_1 , α_2 and α_3 be the thermal diffusivities. Initially (t=0) the three layers has a specific, uniform temperature T_0. The boundary surface at $x = 0$ is kept at temperature T_0 and the boundary at $x = L_1 + L_2 + L_3$, dissipate heat by convection with h constant. We assume that perfect thermal contact conditions are satisfied. We assume also that the thermal conductivity and the thermal diffusivity are temperature independent and uniform within each layer. We consider the transient heat conduction problem with energy generation q .

The temperatures distributions $T_1(x), T_2(x)$ and $T_3(x)$ in the first, second and third plate respectively, is governed by the following heat conduction equations (1).
This equations has nonhomogeneous boundary conditions at the outer surfaces. In order to transform this time-dependent problem into a one with homogeneous boundary conditions.

$$\begin{aligned} \frac{\partial^2 T_1}{\partial x^2} + \frac{q}{k_1} &= \frac{1}{\alpha_1}\frac{\partial T_1}{\partial t} \\ \frac{\partial^2 T_2}{\partial x^2} + \frac{q}{k_2} &= \frac{1}{\alpha_2}\frac{\partial T_2}{\partial t} \\ \frac{\partial^2 T_3}{\partial x^2} + \frac{q}{k_3} &= \frac{1}{\alpha_3}\frac{\partial T_3}{\partial t} \end{aligned} \quad (1)$$

For solve this equation, we can determinate the solution analytical for homogeneous problem $\theta_i(x,t)$, and the solution of steady-state problem $T_s(x)$ [8,12]. Green's function approach is used to generalize the analysis to the solution of transient heat conduction nonhomogeneous problems involving energy generation. The solution is determined from (2)

$$T_i(x,t) = \theta_i(x,t) + T_s(x) \quad (2)$$

The temperature boundary conditions are determined from (3). Where $\theta_i(x,t)$, is the temperature of the layer i. For i=1,2,3.

$$\begin{aligned} &\theta_1 = 0 \ \ at \ \ x = 0 \\ &\left.\begin{aligned} \lambda_i \frac{\partial \theta_i}{\partial x} &= \lambda_{i+1} \frac{\partial \theta_{i+1}}{\partial x} \\ \theta_i &= \theta_{i+1} \end{aligned}\right\} \text{ at interface, } i = 1,2 \\ &\lambda_3 \frac{\partial \theta_3}{\partial x} + h\theta_3 \ \ at \ \ x = L_1 + L_2 + L_3 \end{aligned} \quad (3)$$

h represent the convective heat transfer coefficient. The initial condition is (4)

$$\theta_i(x,t) = T_0 \quad (4)$$

For obtain the analytic solution of each layer, we use the solution by separation of variables (5)

$$\theta_i(x,t) = \Gamma_i(t).\Psi_i(x) \quad (5)$$

Where Γ_i and Ψ_i are unknown functions (6) (7)

$$\Gamma_i = e^{-\beta_n^2 t} \quad (6)$$

$$\Psi_i = A_{in}\sin\frac{\beta_n x}{\sqrt{\alpha_i}} + B_{in}\cos\frac{\beta_n x}{\sqrt{\alpha_i}} \quad (7)$$

Where

$$\theta_i = e^{-\beta_n{}^2 t}\ (A_{in}\sin\frac{\beta_n x}{\sqrt{\alpha_i}} + B_{in}\cos\frac{\beta_n x}{\sqrt{\alpha_i}}) \quad (8)$$

While applying the boundary conditions, we have to solve the following system (9), (10)

$$\begin{cases}
B_{1n} = 0 \\
A_{1n}(\frac{\lambda_1}{\lambda_2}\frac{\sqrt{\alpha_2}}{\sqrt{\alpha_1}})\cos\frac{\beta_n L_1}{\sqrt{\alpha_1}} - A_{2n}\cos\frac{\beta_n L_1}{\sqrt{\alpha_2}} \\
+ B_{2n}\sin\frac{\beta_n L_1}{\sqrt{\alpha_2}} = 0 \\
A_{1n}\sin\frac{\beta_n L_1}{\sqrt{\alpha_1}} - A_{2n}\sin\frac{\beta_n L_1}{\sqrt{\alpha_2}} - B_{2n}\cos\frac{\beta_n L_1}{\sqrt{\alpha_2}} = 0 \\
A_{2n}\frac{\lambda_2}{\lambda_3}\frac{\sqrt{\alpha_3}}{\sqrt{\alpha_2}}\cos\frac{\beta_n(L_1+L_2)}{\sqrt{\alpha_2}} - B_{2n}\frac{\lambda_2}{\lambda_3}\frac{\sqrt{\alpha_3}}{\sqrt{\alpha_2}}\sin\frac{\beta_n(L_1+L_2)}{\sqrt{\alpha_2}} \\
- A_{3n}\cos\frac{\beta_n(L_1+L_2)}{\sqrt{\alpha_3}} + B_{3n}\sin\frac{\beta_n(L_1+L_2)}{\sqrt{\alpha_3}} = 0 \\
A_{2n}\sin\frac{\beta_n(L_1+L_2)}{\sqrt{\alpha_2}} + B_{2n}\cos\frac{\beta_n(L_1+L_2)}{\sqrt{\alpha_2}} - A_{3n}\sin\frac{\beta_n(L_1+L_2)}{\sqrt{\alpha_3}} \\
- B_{3n}\cos\frac{\beta_n(L_1+L_2)}{\sqrt{\alpha_3}} = 0 \\
A_{3n}\left[\frac{h}{\lambda_3}\frac{\sqrt{\alpha_3}}{\beta_n}\sin\frac{\beta_n(L_1+L_2+L_3)}{\sqrt{\alpha_3}} + \cos\frac{\beta_n(L_1+L_2+L_3)}{\sqrt{\alpha_3}}\right] + \\
B_{3n}\left[\frac{h}{\lambda_3}\frac{\sqrt{\alpha_3}}{\beta_n}\cos\frac{\beta_n(L_1+L_2+L_3)}{\sqrt{\alpha_3}} - \sin\frac{\beta_n(L_1+L_2+L_3)}{\sqrt{\alpha_3}}\right] = 0
\end{cases} \quad (9)$$

$$\begin{cases}
s_1 A_{1n} - s_2 A_{2n} + s_3 B_{2n} + 0A_{3n} + 0B_{3n} = 0 \\
s_4 A_{1n} - s_3 A_{2n} - s_2 . B_{2n} + 0A_{3n} + 0B_{3n} = 0 \\
0A_{1n} + s_5 A_{2n} - s_6 B_{2n} - s_7 A_{3n} + s_8 . B_{3n} = 0 \\
0A_{1n} + s_9 A_{2n} + s_{10} B_{2n} - s_8 A_{3n} - s_7 . B_{3n} = 0 \\
0A_{1n} + 0A_{2n} + 0B_{2n} - s_{11} A_{3n} - s_{12} . B_{3n} = 0
\end{cases} \quad (10)$$

We have now the following system (11)

$$\begin{bmatrix} s_1 & -s_2 & s_3 & 0 & 0 \\ s_4 & -s_3 & -s_2 & 0 & 0 \\ 0 & s_5 & -s_6 & -s_7 & s_8 \\ 0 & s_9 & s_{10} & -s_8 & -s_7 \\ 0 & 0 & 0 & -s_{11} & -s_{12} \end{bmatrix} \begin{bmatrix} A_{1n} \\ A_{2n} \\ B_{2n} \\ A_{3n} \\ B_{3n} \end{bmatrix} = \begin{bmatrix} 0 \\ 0 \\ 0 \\ 0 \\ 0 \end{bmatrix} \quad (11)$$

Which contains six equations with seven unknown coefficients: A_{1n} , B_{1n} , A_{2n} , B_{2n} , A_{3n} , B_{3n} and β_n. The solution of this system (11) consists to take $A_{1n} = 1$, and to determine the others coefficients. Thus, the system of equations to solve is now (12)

$$\begin{bmatrix} s_1 & -s_2 & s_3 & 0 & 0 \\ s_4 & -s_3 & -s_2 & 0 & 0 \\ 0 & s_5 & -s_6 & -s_7 & s_8 \\ 0 & s_9 & s_{10} & -s_8 & -s_7 \\ 0 & 0 & 0 & -s_{11} & -s_{12} \end{bmatrix} \begin{bmatrix} 1 \\ A_{2n} \\ B_{2n} \\ A_{3n} \\ B_{3n} \end{bmatrix} = \begin{bmatrix} 0 \\ 0 \\ 0 \\ 0 \\ 0 \end{bmatrix} \quad (12)$$

To determine A_{2n} , A_{3n} , B_{2n} and B_{3n} , we will take four equations. We will have to solve the following system (13)

$$\begin{bmatrix} -s_2 & s_3 & 0 & 0 \\ -s_3 & -s_2 & 0 & 0 \\ s_5 & -s_6 & -s_7 & s_8 \\ s_9 & s_{10} & s_8 & s_7 \end{bmatrix} \begin{bmatrix} A_{2n} \\ B_{2n} \\ A_{3n} \\ B_{3n} \end{bmatrix} = \begin{bmatrix} -s_1 \\ -s_4 \\ 0 \\ 0 \end{bmatrix} \quad (13)$$

In order to know the β_n arguments, we must cancel the determinant of the equation (11), which cannot be solved analytically. For that, we have used the numerical method, namely, bisection method, in order to calculate β_n . By knowing the β_n , we can easy deduce the coefficients A_{in} and B_{in}.

$$\begin{vmatrix} s_1 & -s_2 & s_3 & 0 & 0 \\ s_4 & -s_3 & -s_2 & 0 & 0 \\ 0 & s_5 & -s_6 & -s_7 & s_8 \\ 0 & s_9 & s_{10} & -s_8 & -s_7 \\ 0 & 0 & 0 & -s_{11} & -s_{12} \end{vmatrix} = 0 \quad (14)$$

We determinate $\theta_i(y,t)$ with equation (15)

$$\theta_i(x,t) = \sum\left(A_{in}\sin\frac{\beta_n . x}{\sqrt{\alpha_i}} + B_{in}\cos\frac{\beta_n . x}{\sqrt{\alpha_i}}\right)C_n \quad (15)$$

The temperature distribution (15) must satisfy the initial condition (16).

$$T_0 = \sum_i C_n . \Psi_{in}(x) \tag{16}$$

By applying the operator: $\frac{\lambda_i}{\alpha_i} . \int_{x_i}^{x_{i+1}} \Psi_{ir}$ to the both sides of equation (16), we find (17)

$$\sum_{i=1}^{M} \frac{\lambda_i}{\alpha_i} \int_{x_i}^{x_{i+1}} \Psi_{ir}(y) . T_0 . dx = \sum_n C_n \left[\sum_{i=1}^{M} \frac{\lambda_i}{\alpha_i} . \int_{x_i}^{x_{i+1}} \Psi_{ir} . \Psi_{in} d\,x \right] \tag{17}$$

Where, M is the number of layer (M=3).

$$\sum_{i=1}^{M} \frac{\lambda_i}{\alpha_i} . \int_{x_i}^{x_{i+1}} \Psi_{in} . \Psi_{ir}\, d\,x = \begin{cases} 0 & n \neq r \\ N_n & n = r \end{cases} \tag{18}$$

The N_n and C_n expressions are defined, respectively, as follows (19), (20)

$$N_n = \sum_{j=1}^{M} \frac{\lambda_i}{\alpha_j} . \int_{x_i}^{x_{i+1}} \Psi_{jn}^{\,2}\, dx \tag{19}$$

$$C_n = \frac{1}{N_n} . \sum_{i=1}^{M} \frac{\lambda_i}{\alpha_i} . \int_{x_i}^{x_{i+1}} \Psi_{in}\ .T_0 . dx \tag{20}$$

Finally, the temperature expression is now (21)

$$\theta_i(x,t) = \sum_{i=1}^{n} \frac{e^{-\beta_n^{\,2} . t}}{N_n} . \Psi_{in} . \sum_{i=1}^{M} \frac{\lambda_i}{\alpha_i} . \int_{x_i}^{x_{i+1}} \Psi_{in}\ .T_0 . d\,x \tag{21}$$

We replace Ψ_{in} by its expression, we will have (22)

$$\theta_i(x,t) = \sum_{n=1}^{\infty} \frac{1}{N_n} e^{-\beta_n^{\,2} . t} \left(A_{in} \sin \frac{\beta_n . x}{\sqrt{\alpha_i}} + B_{in} \cos \frac{\beta_n . x}{\sqrt{\alpha_i}} \right) G \tag{22}$$

The solution of a homogeneous transient heat conduction problem presented by this equation (23)

$$\begin{cases} \theta_1(x,t) = \sum_{n=1}^{\infty} \frac{1}{N_n} e^{-\beta_n^{\,2} t} \cos \frac{\beta_n x}{\sqrt{\alpha_1}} G; \\ 0 \le x \le L_1 \\ \theta_2(x,t) = \sum_{n=1}^{\infty} \frac{1}{N_n} e^{-\beta_n^{\,2} t} \left(A_{2n} \sin \frac{\beta_n x}{\sqrt{\alpha_2}} + B_{2n} \cos \frac{\beta_n x}{\sqrt{\alpha_2}} \right) G; \\ L_1 \le x \le L_1 + L_2 \\ \theta_3(x,t) = \sum_{n=1}^{\infty} \frac{1}{N_n} e^{-\beta_n^{\,2} t} \left(A_{3n} \sin \frac{\beta_n x}{\sqrt{\alpha_3}} + B_{3n} \cos \frac{\beta_n x}{\sqrt{\alpha_3}} \right) G; \\ L_1 + L_2 \le x \le L_1 + L_2 + L_3 \end{cases} \tag{23}$$

Where

$$G = \frac{\lambda_1}{\alpha_1} \int_0^{L_1} \Psi_{1n} T_0 dx + \frac{\lambda_2}{\alpha_2} \int_{L_1}^{L_1+L_2} \Psi_{2n} T_0 dx + \frac{\lambda_3}{\alpha_3} \int_{L_1+L_2}^{L_1+L_2+L_3} \Psi_{3n} T_0 dx \tag{24}$$

$$N_n = \frac{\lambda_1}{\alpha_1} \int_0^{L_1} \Psi_{1n}^2 dx + \frac{\lambda_2}{\alpha_2} \int_{L_1}^{L_1+L_2} \Psi_{2n}^2 dx + \frac{\lambda_3}{\alpha_3} \int_{L_1+L_2}^{L_1+L_2+L_3} \Psi_{3n}^2 dx \tag{25}$$

The solution of the steady-state $T_s(x)$ is determined from (26). The one-dimensional steady-state heat conduction problem with no heat generation can be solved by the separation of variables if only one of the boundary conditions is nonhomogeneous. If the problem involves more than one nonhomogeneous boundary condition, it can be split up into a set of simpler problems each containing only one nonhomogeneous boundary condition.

$$T_s(x) = \phi_i(x) . T_0 + \Psi_i(x) . T_0 \tag{26}$$

$\phi_i(x)$ satisfy the steady-state heat conduction problem, with no heat generation, but with one non-homogeneous boundary condition given as (27), (28)

$$\frac{d^2 \phi_i(x)}{dx^2} = 0 \tag{27}$$

$$\phi_i(x) = A_i + B_i x \tag{28}$$

Subject to the boundary condition (29)

$$\begin{aligned} &\phi_1 = 1 \ \ at \ \ x = 0 \\ &\left. \begin{aligned} &\lambda_i \frac{\partial \phi_i}{\partial x} = \lambda_{i+1} \frac{\partial \phi_{i+1}}{\partial x} \\ &\phi_i = \phi_{i+1} \end{aligned} \right\} at \ \text{interface}, \ \ i = 1,2 \\ &\lambda_3 \frac{\partial \phi_3}{\partial x} + h \phi_3 = 0 \ \ at \ \ x = L_1 + L_2 + L_3 \end{aligned} \tag{29}$$

The functions $\Psi_i(x)$ satisfy the steady-state heat conduction problem, with no heat generation, but with one non-homogeneous boundary condition given as (30), (31)

$$\frac{d^2 \psi_i(x)}{dx^2} = 0 \tag{30}$$

$$\psi_i = C_i + D_i y \tag{31}$$

Subject to the boundary condition (32)

$$\left.\begin{aligned}\psi_1 &= 0 \ \ at \ \ x = 0 \\ \lambda_i \frac{\partial \psi_i}{\partial x} &= \lambda_{i+1} \frac{\partial \psi_{i+1}}{\partial x} \\ \psi_i &= \psi_{i+1}\end{aligned}\right\} \ at \ \text{interface}, \ \ i = 1,2 \qquad (32)$$

$$\lambda_3 \frac{\partial \psi_3}{\partial x} + h\psi_3 = hT_0 \ \ at \ \ x = L_1 + L_2 + L_3$$

The Green's function appropriate for the solution of the nonhomogeneous heat conduction problem with heat generation [16]. Green's function is given by $G_{ij}(x,t|x',\tau)$ (33).

$$T_i(x,t) = \sum_{j=1}^{M} \int_{x_j}^{x_{j+1}} x' \left| G_{ij}\, x,t|x',\tau) \right|_{\tau=0} T_0 dx' + \int_{\tau=0}^{t} d\tau. \int_{x_j}^{x_{i+1}} x' G_{ij}(x,t|x',\tau) \left[\frac{\alpha_j}{k_j} q \right] dx' \qquad (33)$$

Where the composite medium Green's function $G_{ij}(x,t|x',\tau)$ is defined as (34)

$$G_{ij}(x,t|x',\tau) = \sum_{n=1}^{\infty} e^{-\beta_m^{2(t-\tau)}} \frac{1}{N_n} \frac{k_j}{\alpha_j} \psi_{in}(x) \psi_{jn}(x') \qquad (34)$$

where $\psi_{in}(x)$ and $\psi_{jn}(x)$ are the eigenfunctions, the β_n values are the eigenvalues. $G_{ij}(x,t|x',\tau)_{\tau=0}$ is the composite medium Green's function evaluated at $\tau = 0$, and $G_{ij}(x,t|x',\tau)$ is the composite medium Green's function. The homogeneous problem defined by:

$$\theta_i(x,t) = \sum_{j=1}^{M} \int_{x_j}^{xj+1} x' \left[\sum_{n=1}^{\infty} e^{-\beta_m^{2(t)}} \frac{1}{N_n} \frac{k_j}{\alpha_j} \psi_{in}(x) \psi_{jn}(x') \right] F_i(x') dx \qquad (35)$$

$$G_{ij}(x,t|x',\tau)\big|_{\tau=0} = \sum_{n=1}^{\infty} e^{-\beta_m^{2(t)}} \frac{1}{N_n} \frac{k_j}{\alpha_j} \psi_{in}(x) \psi_{jn}(x') \qquad (36)$$

4. Results and discussion

The temperatures distributions obtained from the analytic expressions are represented in the figures 4, 5 and 6, for the third plates, respectively. Note that the first, second and second plates are composed by the Copper (Cu), Silicon dioxide (SiO_2) and Ferrite (NiFe). We can see from these figures, that the temperature $T_1(x,t)$ increases from 25°C to 41.2°C. The temperature $T_2(x,t)$ decreases from 41.2°C to 38.9°C. After, the temperature $T_3(x,t)$ decreases at 25°C.

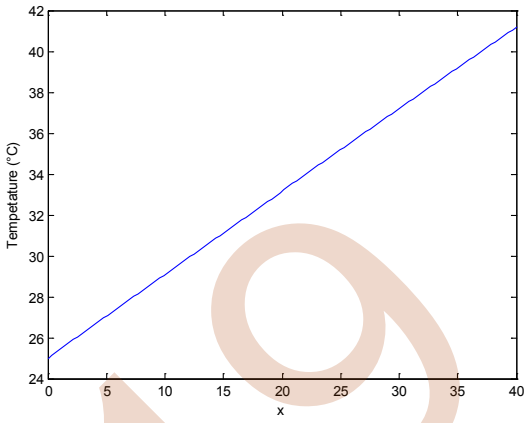

Figure 4. Temperature at the Copper, x = 40

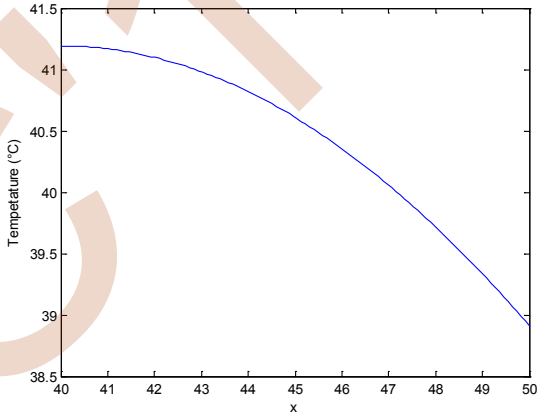

Figure 5. Temperature at the Silicon dioxide, x = 10

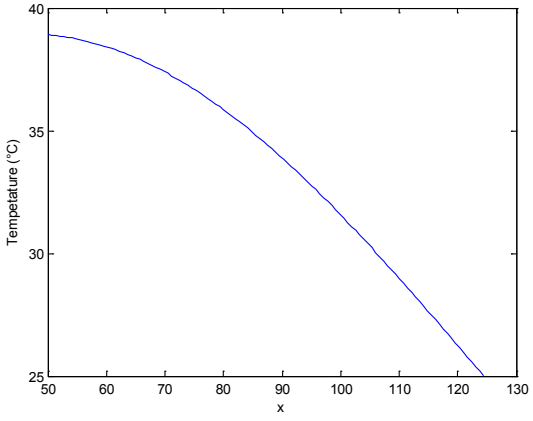

Figure 6. Temperature at the Ferrite, x = 75

In Fig. 7, we observe the temperature distribution in the inductor on substrate. We see from these figures that the temperature is about 31 °C. Our results were compared with analytical solution [13]. We notice the same evolutions therefore quite acceptable and in very good agreement.

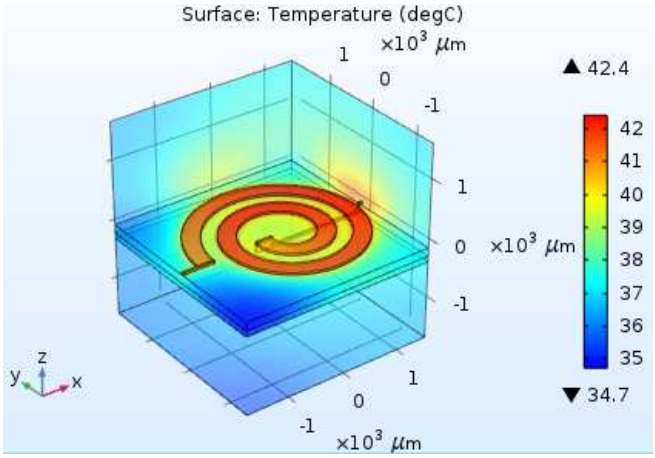

Figure 7. Temperature distribution in the inductor on substrate

VIII. CONCLUSION

In this paper we addressed the problem of thermal modeling of an integrated circular. An analytical solution to the transient heat conduction in a plate with multi-layer is presented using method of separation-of-variables that allowed us to determine the temperature evolution. The homogeneous problems are readily handled with this method. We describe the splitting up of a nonhomogeneous problem into a set of simpler problems that can be solved.
The problem of the time dependent heat conduction for a multrilayer composite medium with heat generation and nonhomogeneous outer boundary conditions can be transformed into a problem with heat generation but homogeneous boundary conditions.Green's function formalism provides an efficient, straightforward approach for developing exact analytic solutions to a broad class of transient heat conduction nonhomogeneous problems with energy generation.

For a good visualization of thermal behavior in our component, we have presented the temperature distribution in our inductor, based on the finite element method.

ACKNOWLEDGMENT

Yamina BENHADDA was born in Ain emouchent, Algeria in 1982. He obtained his Doctorate degree in electrical engineering at Mohamed Boudiaf University of Sciences and Technology of Oran in 2016.

Second Author Abdelhak ALLAOUI was born in Oran, Algeria in 1988. He obtained his master degree in electrical engineering at Mohamed Boudiaf University of Sciences and Technology of Oran in 2011. He obtained his Doctorate degree in electrical engineering at Mohamed Boudiaf University of Sciences and Technology of Oran in 2017.

Third Author Azzedine HAMID was born in Alger, Algeria in 1961. He obtained his Magister degree in electrical engineering at Mohamed Boudiaf University of Oran in 1994. He received his PhD in 2005 from Mohamed Boudiaf University of Sciences and Technology of Oran.

REFERENCES

[1] M. Derkaoui, A. Hamid, T. Lebey, R. Melati, "Design and modeling of an integratedmicrotransformer in a flyback converter, " *Telkomnika*, 11(4), pp. 669-682, 2013.
[2] Y. Benhadda, A. Hamid, T. Lebey, A. Allaoui, M. Derkaoui, R. Melati, "Thermal behavior of an integrated square spiral micro coil, " Telkomnika, 14(2), pp. 669-682, 2015.
[3] Sabrije Osmanaj , Erdet Nasufi, " Design of an integrated planar inductor using 0.35 µM fabrication technology," *17th International Research/Expert Conference*, Istanbul, Turkey, 10-11 September 2013.
[4] R. I. Hickson, S. I. Barry, G. N. Mercer, "Critical times in multilayer diffusion. Part 1: Exact solutions", Preprint submitted to International Journal of Heat and Mass Transfer 2009.
[5] Y. Hu, C. Mao, The study of one-dimensional problem of heat conduction with inhomogeneous boundary conditions, IEEE 2011, p 2738-2741.
[6] S S Mohan, M d M Hershenson, S P Boyd, and T H Lee " Simple Accurate Expressions for Planar Spiral Inductances, " *IEEE Journal of solid-state circuits*, 1999; vol. 34, no 10, pp. 1419-1424.
[7] J. M. Wright, D. W. Lee, A. Mohan, A. Papou, P. Smeys, and S. X. Wang, "Analysis of integrated solenoid inductor with closed magnetic core, " *IEEE Transactions on Magnetics*, vol. 46, no. 6, pp. 2387-2390, Jun. 2010.
[8] Y. Benhadda, A. Hamid, T. Lebey, M. Derkaoui, "Design and modeling of an integrated inductor in a buck converter DC-DC, "*Journal of Nano and Electronic Physics*, 7(2), 2015, pp. 2006 (6pp).
[9] T. G. Imre, U. Viscarret, I. E. Otadui, A. Rufer, "Transient thermal model of a medium frequency power transformer", IEEE 2008, p 1033-1038.
[10] M. S. Islam, M. R. K. Akanda , "3D Temperature distribution of SiC MESFET using Green's function", Electrical and Computer Engineering, IEEE 2010, p 13-16.
[11] M. Janicki, A. Napieralski, "Application of Green's functions for thermal analysis of electronic circuits", 2005 IEEE, p 435-438.
[12] Y. Liang, H. Chunyue, Z. Xin, L. Tianming, G. Guangkuo, X. Guoji , T. Wenliang, "Influence of compliant layer thickness on stress and strain of solder joints in wafer level chip scale package under thermal cycle", 15th International Conference on Electronics Packaging Technology, 2014 IEEE, p 577-582.
[13] A. Allaoui, A. Hamid, P. Spiterri, V. bley, T. Lebey, "Thermal modeling of an integrated inductor in a micro-converter, " Journal of Low Power Electronics, 11(1), pp. 63-73, 2015.

Modeling of Octagonal Planar Microtransformer for Integrated RF Systems

MokhtariaDerkaoui

LaRATIC laboratory,
National Institute of Telecommunications & ICT,INTTIC,
Oran, Algeria.
mderkaoui@inttic.dz

Fateh ABBAD

Electronic Department,
University of Sciences and Technology HouariBoumediene,
USTHB, Algiers, Algeria.
abadfateh@gmail.com

***Abstract*—Interest in on-chip transformer has surged for the capability of impedance conversion and low loss while occupying reduced silicon area. Transformers have been used as inter-stage connection in the power amplifier, as low-loss devices in the ASK modulator, as feedback elements in the low-noise amplifier …etc.The modeling of planar transformer for very high frequencies is the subject of this paper. Square, polygonal and circular shapes of the planar windings are the important difference regarding transformer topologies. In this work, comparison was restricted to a square and an octagonal shape of the windings. In this study, we opted for calculation method developed by Wheeler to evaluate the inductance of different planar geometrical shapes of transformer windings. Besides, we determined the geometrical parameters of the transformer and from its π-electrical model; we highlighted all parasitic effects generated by stacking of different material layers. By using the S-parameters, we calculated the technological parameters. The important characteristics of a transformer are its inductances values and its parasitic capacitances and resistances, which determine its Q factor and self-resonant frequency. Furthermore, we carried out the electromagnetic simulation using COMSOL Multiphysics 4.3 software to show current density and electromagnetic field in the windings of the transformer for high frequencies.**

Keywords*— *Integration;transformer; on-chip; planar; RF.

I. INTRODUCTION

It is well known that the integrated circuit (IC), since its introduction in 1958, has affected nearly all parts of contemporary life. The major application of integrated circuits is in microprocessor design. When digital circuitry became relatively small, the next logical step was to move the analog part onto the on-chip domain [1]. The decreased size and increased operational frequency caused off-chip passive devices to be the major obstacle in the way to reducing the overall system size. The common sense solution is to move the passive components, like capacitors, inductors, and transformers, from the board to the chip realm. The first implementation of monolithic inductors on silicon substrates for mixed-signal radio-frequency ICs circuits was achieved [2-4], making the use of integrated passive components practical A few years later, advantages of using monolithic transformers in the design of low-voltage silicon bipolar receivers were demonstrated by [5],[6]. In recent years, monolithic transformers have been successfully implemented in RFIC designs. At the time of this writing, monolithic transformers fabricated on silicon substrates areused in silicon RFICs enabling the implementation of high frequency circuits such as low noise amplifiers, voltage-controlled oscillators, and mixers. Because of the wide application of transformers in RF systems circuits, modelling for transformers has become more and more essential.

II. WINDINGS MODELING OF AN INDUCTIVE DEVICE

A transformercan be considered a device, whose operation is based on mutual inductive coupling between two inductors. Fig. 1 shows a schematic diagram of an ideal transformer.

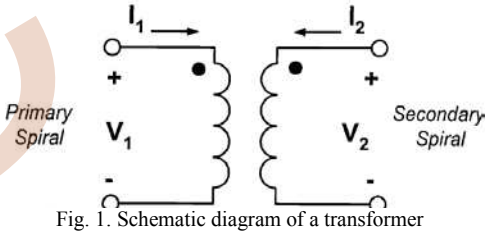

Fig. 1. Schematic diagram of a transformer

In high frequencies (from 100 MHz), inter-winding capacitive couplings can no longer be neglected. The behavior of the inductor can be represented by an ideal inductance L in series with a resistance Rs and in parallel with an ideal capacitance Cs for the global taking into account of the capacitive coupling between turns (Fig. 2).

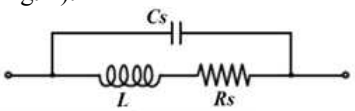

Fig.2. Model of a high frequency inductor

Nguyen and Meyer [7] were the first to propose a simple model in ''π'' to describe the behavior of an integrated planar inductor on silicon (Fig.3), Ashby and al [8] developed an improved model. Whereas, the parameters of the model need to be adjusted from the experimental data. Then, Yue and Yong [9] present a similar model (Fig. 4.a), but with more appropriate parameters for the geometry of the inductance. The electrical diagram of a planar spiral inductor is derived from its cross-section (Fig. 4.b). In this case, the capacitance Cs makes it possible to take into account the capacitive

couplings betweenthe turns. Capacitance Cox represent the coupling between the conductor and the substrate.

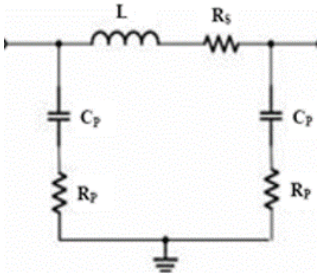

Fig. 3. Model in π developed by Nguyen etMeyer [7]

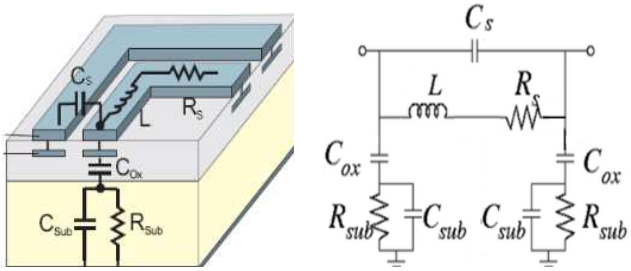

(a) (b)

Fig.4. Planar inductor developed by Yue and Yong[9]: (a) Cross-section, (b) Model in π.

When a magnetic material layer is placed above or below the inductance, the model becomes very complicated because of the interactions between the stacking layers constituting the inductor (winding-magneticmaterial-substrate). The first equivalent scheme (Fig. 5) was proposed by Yamaguchi and al. [10-14].

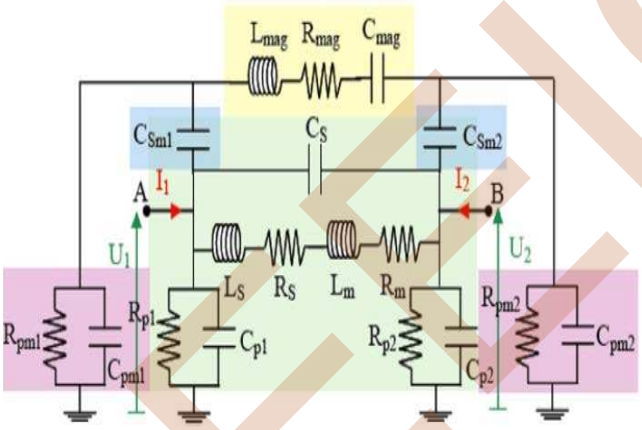

Fig. 5. π electrical model of a ferromagnetic inductor [10][11].

The work proposed by [15] shows the integrated transformer, which is composed of two planar windings of spiral square form. The two copper windings are deposited on a layer of ferrite magnetic material (NiZn), isolated therefrom by an insulating layer of silicon dioxide (SiO_2). The three layers aredeposited on asilicon layer (Si) which serves as a substrate. A silicon dioxide layer of (SiO_2) which ensures the magnetic coupling separates the two stacks. The combination of the equivalent electrical circuits of two windings form the equivalent electrical circuit of transformer (Fig.6).

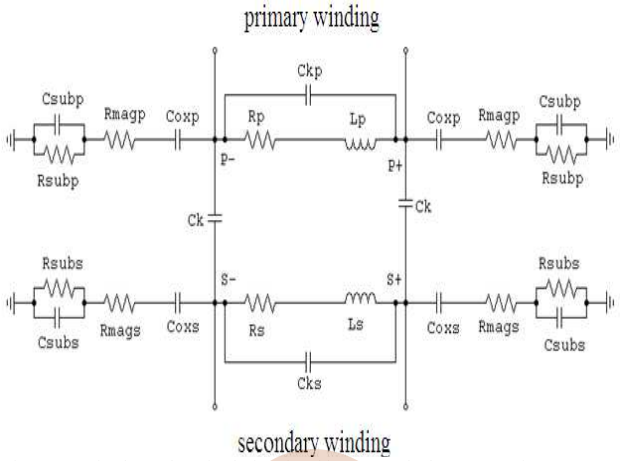

Fig. 6. Equivalent electrical circuit of integrated planar transformer [15]

In this work, we present the model of a transformer whose windings are of octagonal planar shape (Fig.7.a). The transformer is composed of two octagonal winding superimposed on a ferrite layer and isolated by a dioxide layer of silicon dioxide, all the layers of the different materials are superimposed on a layer of silicon, which serves as a substrate, this transformer operates at a high frequency of the order of 100 MHz. The (Fig.7.b) presents the equivalent electrical circuit of the octagonal transformer.

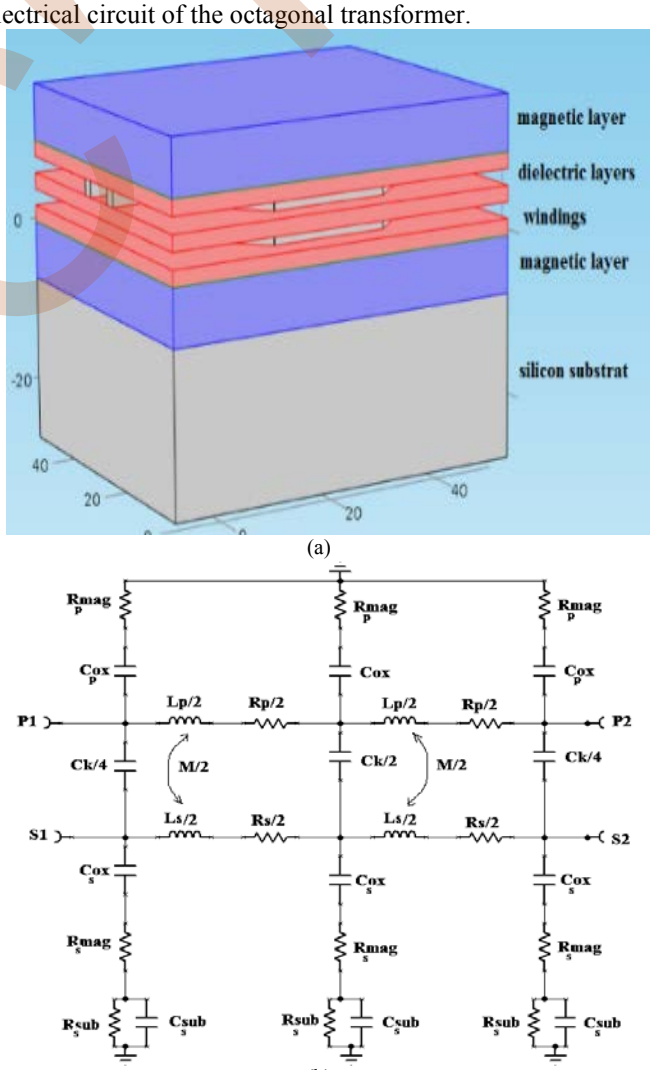

Fig. 7. Integrated planar octagonal transformer: (a) cross section, (b) equivalent electrical circuit

III. ELECTRICAL PARAMETERS CALCULATION

The equivalent circuit of Fig. 4 contains for the two windings the inductances L_p and L_s, serial resistances R_p and R_s, oxide capacitances C_{oxp}, C_{oxs}, magnetic layer resistances R_{magp}, R_{mags}, silicon substrate resistances R_{subp}, R_{subs}, silicon substrate capacitance C_{subp}, C_{subs}, coupling capacitance C_k between the two windings.

The analytical expressions of different elements are:

- Serial resistanceof the two windings

$$R_p = \rho_{cu}.\frac{lt_p}{w_p.t} = 0.74\ \Omega \quad (1)$$

$$R_s = \rho_{cu}.\frac{lt_s}{w_s.t} = 0.045\ \Omega \quad (2)$$

$\rho_{Cu} = 1.7 .10^{-8}\ \Omega.m$

- Resistance of the magnetic layer,

$$R_{magp} = 2.\rho_{NiZn}.\frac{e_{NiZn}}{w_p.l_{tp}} = 3.6\ k\Omega \quad (3)$$

$$R_{mags} = 2.\rho_{NiZn}.\frac{e_{NiZn}}{w_s.l_{ts}} = 2.06\ k\Omega \quad (4)$$

$\rho_{NiZn} = 10^3\Omega.m$

- Resistances associated to the silicon substrate

$$R_{subp} = 2.\rho_{Si}.\frac{e_{Si}}{w_p.l_{tp}} = 2.15\ k\Omega \quad (5)$$

$$R_{subs} = 2.\rho_{Si}.\frac{e_{Si}}{w_s.l_{ts}} = 1.22\ k\Omega \quad (6)$$

$\rho_{Si} = 18.5\ \Omega.m$

- Oxide capacitance

$$C_{oxp} = \frac{1}{2}.\varepsilon_0\varepsilon_{rox}.\frac{w_p.l_{tp}}{t_{ox}} = 2.97\ pF \quad (7)$$

$$C_{oxp} = \frac{1}{2}.\varepsilon_0\varepsilon_{rox}.\frac{w_s.l_{ts}}{t_{ox}} = 5.2\ pF \quad (8)$$

$\varepsilon_{rox} = 3.9$

- Capacitance associated to the silicon substrate,

$$C_{subp} = \frac{1}{2}.\varepsilon_0\varepsilon_{rSi}.\frac{w_p.l_{tp}}{e_{si}} = 0.89\ pF \quad (9)$$

$$C_{subs} = \frac{1}{2}.\varepsilon_0\varepsilon_{rSi}.\frac{w_s.l_{ts}}{e_{si}} = 1.57\ pF \quad (10)$$

$\varepsilon_{rSi} = 11.8$

- Coupling capacitance Between the two windings

$$C_k = \varepsilon_0\varepsilon_{r\,air}.\frac{d_{out}^2}{t_{ox}} = 0.34\ fF \quad (11)$$

$\varepsilon_{r\,air} = 1$

In this work, we let the same values of the different geometric parameters (primary and secondary thickness t_p, t_s;width w_p, w_s;spacings$_{p,}s_s$ and total length $lt_{p,}$ lt_s)calculated by [15]; we change the square form into an octagonal form.

In the expressions 1 to 11, we notice that all the values of the capacities are very weak; oxide capacities serve to avoid current infiltration into the magnetic core and into the substrate; inter-turns and coupling capacities avoid short-circuits between windings. Concerning the resistances, we see that the values of the resistances of magnetic core and the substrate are very high because they serve to limit the induced current by capacitive effect. However, the values of the series resistances of the windings are very weak to minimize the losses by Joule effects and facilitate the circulation of the current in the windings.

IV. CALCULATION OF THE INDUCTANCES VALUES

The windings of the transformer are planar and the inductance value of each one depend of the inner and outer diameters d_{in} and d_{out} and their average d_{avg} (expression 12)

$$d_{avg} = (d_{out} + d_{in})/2 \quad (12)$$

The method of calculation developed by Wheeler allows an evaluation of the inductance of hexagonal, octagonal or square coil, realized in a discrete way [16]. A simplification can be made when one transposes in the integrated planar case [17]. The inductance L_{mw}given by Wheeler method is represented by (expression 13),

$$L_{mw} = k_1\mu_0\frac{n^2 d_{avg}}{1+k_2 A_m} \quad (13)$$

A_m: the form factor (expression 14),

$$A_m = \frac{d_{out} - d_{in}}{d_{out} + d_{in}} \quad (14)$$

The coefficients k_1 and k_2 depend on the geometrical form used. The values of these coefficients are given in Table 1.

TABLE I. Values of coefficients k_1 and k_2 used in Wheeler method

Form	k_1	k_2
Square	2.34	2.75
Hexagonal	2.33	3.82
octagonal	2.25	3.55

According to the form factor A_m, it is possible to obtain so called "hollow" or "full" inductors (d_{out}>>d_{in}). Thus, a "full" inductor has a lower inductance than a "hollow" one because the turns located near the center of the spiral contribute to decrease the mutual positive inductances and increase the mutual negative inductances [18].

We have opted for an outer diameter of 2000 µm and a width of 50 µm. The shape of the windings is an important distinction regarding transformer topologies. Circular,square and polygonal spirals have already been reported to constitute inductors and transformers. In this study, comparison was hence restricted to a square (Fig. 8.a) and an octagonal transformer (Fig.8.b) and angles are limited to multiples of 45 degrees.

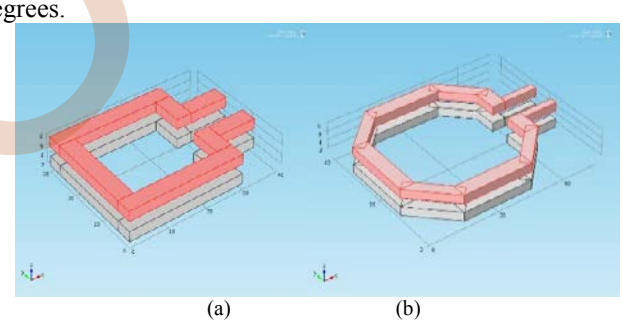

(a) (b)

Fig. 8. (a) Square and (b) octagonal topologies.

V. S-PARAMETERS CONCEPT

From the localized modelwe can easily obtainthe scattering parameters of the transformer. The S-parameters of Fig. 7.b are calculated as follows [19]:

a) We calculate the ABCD matrices for each block.

$$\begin{bmatrix} A & B \\ C & D \end{bmatrix}_\alpha = \begin{bmatrix} 1 & 0 \\ \frac{1}{\frac{1}{j\omega C_{oxp}} + R_{magp} + \frac{R_{subp}}{1+j\omega R_{subp} C_{subp}}} & 1 \end{bmatrix} \quad (15)$$

$$\begin{bmatrix} A & B \\ C & D \end{bmatrix}_\beta = \begin{bmatrix} 1 & R_{sp} \\ 0 & 1 \end{bmatrix} \quad (16)$$

$$\begin{bmatrix} A & B \\ C & D \end{bmatrix}_\gamma = -\begin{bmatrix} \frac{L_p}{M} & j\omega\left(\frac{L_p.L_s}{M} - M\right) \\ \frac{1}{j\omega M} & \frac{L_s}{M} \end{bmatrix} \quad (17)$$

$$\begin{bmatrix} A & B \\ C & D \end{bmatrix}_\delta = \begin{bmatrix} 1 & R_{ss} \\ 0 & 1 \end{bmatrix} \quad (18)$$

$$\begin{bmatrix} A & B \\ C & D \end{bmatrix}_\varepsilon = \begin{bmatrix} 1 & 0 \\ \frac{1}{\frac{1}{j\omega C_{oxs}} + R_{mags} + \frac{R_{subs}}{1+j\omega R_{subs} C_{subs}}} & 1 \end{bmatrix} \quad (19)$$

$$\begin{bmatrix} A & B \\ C & D \end{bmatrix}_\varphi = \begin{bmatrix} 1 & \frac{1}{j\omega C_k} \\ 0 & 1 \end{bmatrix} \quad (20)$$

Where $M = k.\sqrt{L_p.L_s}$ (21)

b) We can combine the blocks α, β, γ, δ, ε, φ in cascade:

$$\begin{bmatrix} A & B \\ C & D \end{bmatrix}_I = \begin{bmatrix} A & B \\ C & D \end{bmatrix}_\alpha \cdot \begin{bmatrix} A & B \\ C & D \end{bmatrix}_\beta \cdot \begin{bmatrix} A & B \\ C & D \end{bmatrix}_\gamma \cdot \begin{bmatrix} A & B \\ C & D \end{bmatrix}_\delta \cdot \begin{bmatrix} A & B \\ C & D \end{bmatrix}_\varepsilon \cdot \begin{bmatrix} A & B \\ C & D \end{bmatrix}_\varphi \quad (22)$$

c) We can combine the large intermediate block I with block φ in parallel. The final ABCD matrix of the entire transformer F is given below:

$$\begin{bmatrix} A & B \\ C & D \end{bmatrix}_F = \frac{1}{B_I + B_\varphi} \cdot \begin{bmatrix} A_I B_\varphi + A_\varphi B_I & B_I . B_\varphi \\ (C_I + C_\varphi).(B_\varphi + B_I) + (D_I - D_\varphi).(A_\varphi - A_I) & D_\varphi B_I + D_I B_\varphi \end{bmatrix} \quad (23)$$

d) We can convert the A, B, C, D parameters to S-parameters as follows:

$$S_{11} = \frac{A_F + \frac{B_F}{Z_0} - C_F.Z_0 - D_F}{A_F + \frac{B_F}{Z_0} + C_F.Z_0 + D_F} \qquad S_{12} = \frac{2.(A_F.D_F - (B_F.C_F))}{A_F + \frac{B_F}{Z_0} + C_F.Z_0 + D_F} \quad (24)$$

$$S_{21} = \frac{2}{A_F + \frac{B_F}{Z_0} + C_F.Z_0 + D_F} \qquad S_{22} = \frac{-A_F + \frac{B_F}{Z_0} - C_F.Z_0 + D_F}{A_F + \frac{B_F}{Z_0} + C_F.Z_0 + D_F} \quad (25)$$

Z_0 is the characteristic impedance of the line. We note that due to reciprocity, we will have $A_F.D_F - B_F.C_F = 1$; thus, S_{12}=S_{21}.

From the S-parameters, we can determine the Z-parameters such that:

$$Z_{11} = Z_0 . \frac{(1+S_{11}).(1-S_{22}) + S_{21}.S_{12}}{(1-S_{11}).(1-S_{22}) - S_{21}.S_{12}} \quad (26)$$

$$Z_{12} = Z_0 . \frac{2.S_{12}}{(1-S_{11}).(1-S_{22}) - S_{21}.S_{12}} \quad (27)$$

$$Z_{21} = Z_0 . \frac{2.S_{21}}{(1-S_{11}).(1-S_{22}) - S_{21}.S_{12}} \quad (28)$$

$$Z_{22} = Z_0 . \frac{(1-S_{11}).(1+S_{22}) + S_{21}.S_{12}}{(1-S_{11}).(1-S_{22}) - S_{21}.S_{12}} \quad (29)$$

From the Z-parameters, we can determine the primary and secondary inductances and resistances (expressions 30 and 31),

$$L_p = \frac{\mathrm{Im}(Z_{11})}{\omega} \qquad L_s = \frac{\mathrm{Im}(Z_{22})}{\omega} \quad (30)$$

$$R_p = \mathrm{Re}(Z_{11}) \qquad R_s = \mathrm{Re}(Z_{22}) \quad (31)$$

The measurement results for square [15] and octagonal transformers are shown in Fig. 9. Those two transformers present the same diameter and the same trace width. It is observed that for the same diameter, square windings present a higher inductance value. This difference is due to the greater total length the square device presents.

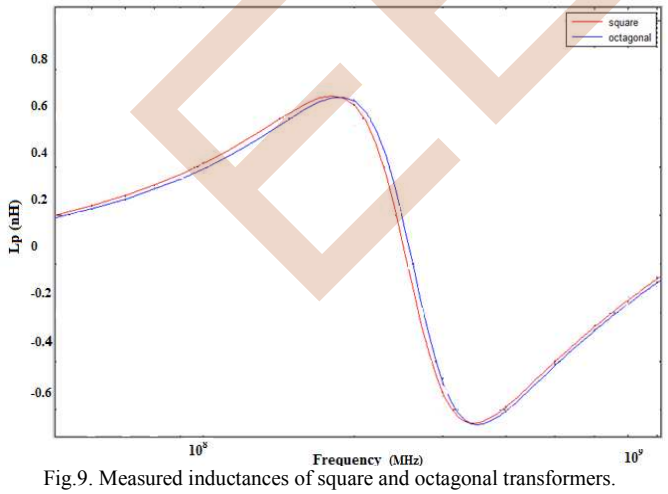

Fig.9. Measured inductances of square and octagonal transformers.

We also observe the characteristics of inductance behavior. We notice that there are three distinct zones: The inductive behavior up to 100 MHz operating frequency, a transition zone in which the value of the inductances becomes negative with a zero crossing corresponding to the own resonant frequency of the inductance and finally the capacitive behavior.

VI. QUALITY FACTOR

The quality factor expresses losses of power in the windings of the transformer; it is defined as following [20]:

$$Q = 2\pi . \frac{\text{stocked energy}}{\text{dissipate denergy}} \quad (32)$$

For the inductor, only the stored energy in magnetic form is interesting. The quality factor is also proportional to the difference between the maximum magnetic energy and the energy supply, therefore the quality factor will be represented by the following relation [21][22]:

$$Q = \frac{\omega.L}{R_s} . \frac{R_p}{R_p + \left[\left(\frac{\omega.L}{R_s}\right)^2 + 1\right] R_s} . \left[1 - \frac{R_s^2 (C_s + C_p)}{L} - \omega^2 L (C_s + C_p)\right] \quad (33)$$

In expression 33, we note that the first term corresponds to the simplified quality factor, the second term represents the losses substrate and the third expresses the self-resonance factor, ω is the pulsation, L is the inductance, Rs is the serial resistance, Cs is the serial capacitance, Rp is the coupling resistance and Cp the coupling capacitance. Rp and Cpare related to the resistance of the substrate R_{Si}, the capacitance of the substrate C_{si} and the oxide capacitance C_{ox} by the following expressions 34 and 35:

$$R_p = \frac{1}{\omega^2 C_{ox}^2 R_{si}} + \frac{R_{si} (C_{ox} + C_p)^2}{C_{ox}^2} \quad (34)$$

$$C_p = C_{ox} \frac{1 + \omega^2 (C_{ox} + C_{si}) C_{si} R_{si}^2}{1 + \omega^2 (C_{ox} + C_{si})^2 R_{si}^2} \quad (35)$$

The following expressions determine thequality factors of primary and secondary windings;

$$Q_p = \frac{\mathrm{Im}(Z_{11})}{\mathrm{Re}(Z_{11})} \qquad Q_s = \frac{\mathrm{Im}(Z_{22})}{\mathrm{Re}(Z_{22})} \quad (36)$$

The measurement results of quality factors of secondary square [15] and octagonal windings are shown in Fig. 10. The two components present the same diameter and the same trace width. We note that octagonal transformers have lightly better qualityfactor. This means that the reduction of this topology brings to the resistance and capacitance of the windings is proportionally more substantial than the reduction on the inductance.

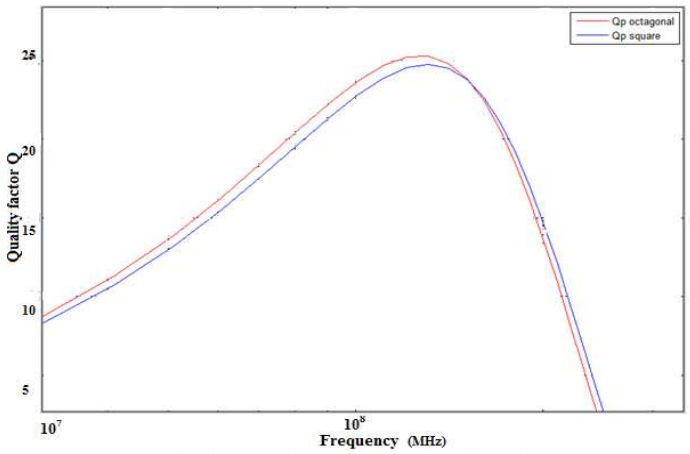

Fig.10.Quality factors of square and octagonal transformers.

We also note that the quality factor increases with the frequency until reaching a maximum value which corresponds to the losses. The first part of the curve corresponds to the zone where the windings have an inductive behavior. Beyond

this frequency, the quality factor decreases to zero at an operating point corresponding to the resonant frequency.

VII. FEED LINES POSITION

As the stacked topology is adopted, the relative position between primary and secondary is also considered in terms of the location of their respective leads. One approach is to have the secondary completely covered by theprimary, so that their feed lines overlap (Fig.11.a). Another flipped transformer possibility consists in a 180-degree rotation of one of the windings (Fig.11.b). This configuration results in an uncovered zone of the windings, which tends to weaken their coupling. The choice between these structures should be made not only in function of their performance but also considering which one is better suited to the layout of a specific circuit.

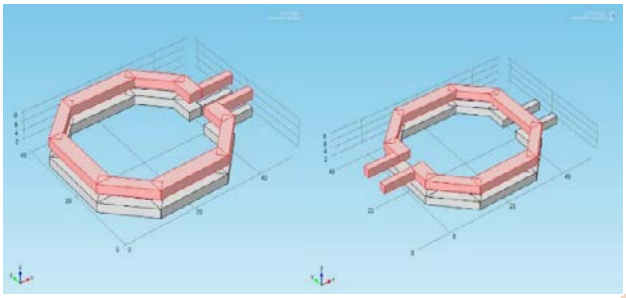

(a) (b)

Fig.11. (a) Non-flipped and (b) flipped transformer topologies.

The measurement results for transformers with those two topologiesare presented in Fig. 12. The obtained curves show a significant reduction of the resonant frequency of the transformer when the flipped topology is adopted. Since low frequency, self-inductances remain unchanged and magnetic coupling is weakened, this reduction results mostly from the augmented oxide and substrate capacitance that this topologypresents. Even though magnetic coupling is significantly lower, global coupling including capacitive effects presents similar results beyond 100 MHz. It is also noticed that the flipped transformerdemonstrates a lower minimum insertion loss for frequencies greater than 100 MHz,however the non-flipped transformer presents a proper performance for a wider band.

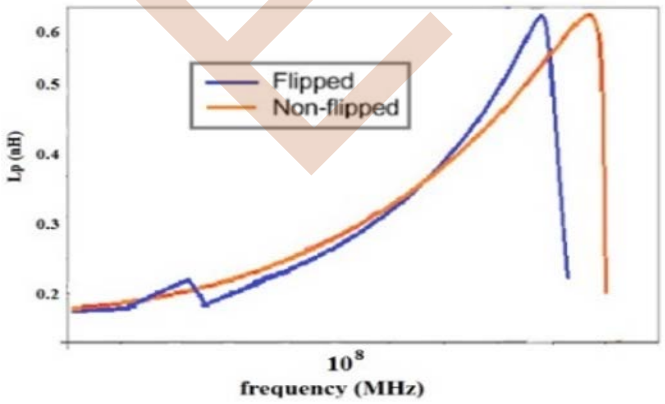

Fig.12.Flipped and non-flipped inductances.

VIII. 3D SIMULATION OF THE ELECTROMAGNETIC EFFECTS

In this section, we present 3D simulation of electromagnetic effects on the transformers at 100 MHz using software COMSOL Multiphysics 4.3 which is basedon finite elements method.

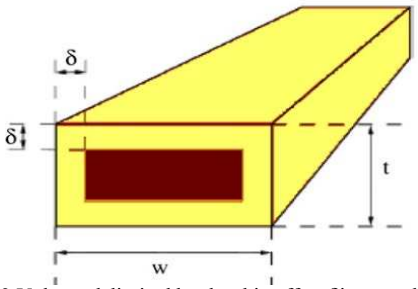

Fig. 13.Volume delimited by the skin effect δin a conductor

In the conductor, the current density whose section is rectangular (Fig. 13), is expressed by the following expressions [23],

$$j(x) = j_0 . e^{-i\left(\frac{x}{\delta}\right)} . e^{-\left(\frac{x}{\delta}\right)} \quad (37)$$

$$\|j(x)\| = j_0 . e^{-\left(\frac{x}{\delta}\right)} \quad (38)$$

The average value of the current density is given by:

$$j_{moy} = j_0 . \frac{\left[e^{-\left(\frac{t}{2\delta}\right)}+1\right]}{2} \quad (39)$$

The current flowing in the winding of the transformer that we want to integrate is a function of the cross section of the conductor S_c and the current density j_{moy}. It is given by the following expression:

$$i_p = S_c . j_{moy} \quad (40)$$

The section S_c of the turn of the transformer is rectangular; it is given by the following expression:

$$S_c = w . t \quad (41)$$

Skin effect is patent for the considered conductors. Fig. 14 shows the electromagnetic simulation of the current density on the two transformers at 100 MHz. It is clearly noticed how, even for the 4µm width of transformer, current is mostly concentrated on the edges of the conductors. This effect contributes to limiting the attainable insertion losses.

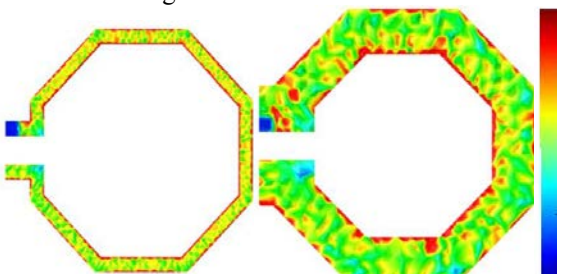

Fig.14. Simulated current density at 100 MHz with different widths

In Fig. 15, we observe 3D mesh of octagonal integrated transformer alone and with the different layers.

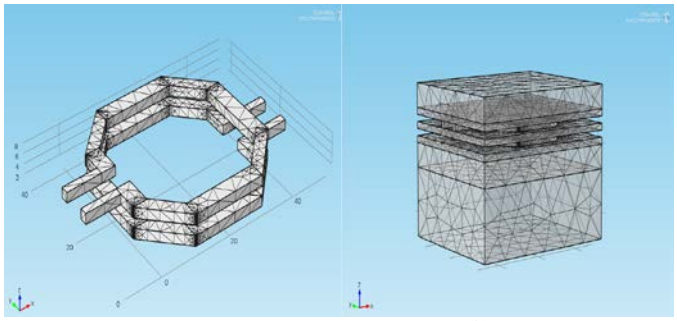

(a) (b)

Fig. 15. 3D mesh transformer: (a) Octagonal windings geometry, (b) Global structure

Fig. 16 shows the distribution of magnetic field in transformer composed of two octagonal windings of copper, deposited on ferrite NiZn magnetic layer and isolated by a dioxide layer, all these layers are deposited on a silicon substrate.

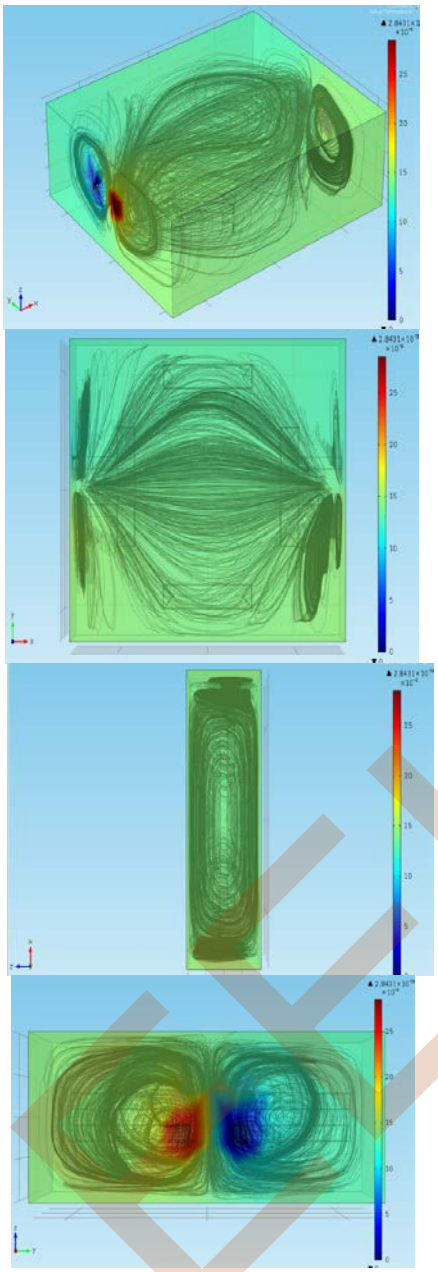

Fig. 16. Distribution of magnetic field in the transformer.

IX. CONCLUSION

This paper present the design of RF transformer. The first considered parameter was the direction in which coupling between windings takes place. It was shown that a vertical coupling is more advantageous, as it provides distinctively better coupling coefficients and minimum insertion loss. Concerning the shape of windings, octagonal transformers were shown to present higher quality factors than their square counterparts. Moreover, the effect of the position of the feed lines of the two windings was investigated. It was shown that while flipped transformers can achieve lower losses, the non-flipped topology allows a stronger magnetic coupling and a more wideband behavior. The conclusion drawn in this paper constitute an important base to allow the definition of the best-suited topologies for application in specific integrated circuits. Moreover, the results obtained throughout this paper were taken into account in order to guide the development of an electric model for RF transformers.

REFERENCES

[1] J. Aguilera, R. Berenguer, «Design and test of integrated inductors for RF applications», Kluwer Academic Publishers, 2004.
[2] B. Estibals, J.L. Sanchez, C. Alonso, H. Camon et J.P. Laur, « Vers l'intégration de convertisseurs pour l'alimentation des microsystèmes », J3EA, Journal sur l'Enseignement des sciences et technologies de l'information et des systèmes, Vol 2, 2003.
[3] Y. Maycvskiy, «Analysis and modeling of monolithic on-chip transformers on silicon substrates», Master Thesis, Oregon State University, United States of America, 10 June 2005.
[4] A. S. Ezzulddin, M. H. Ali, M.S. Abdulwahab, « On-chip RF transformer performance improvement technique », Eng. & Tech. Journal, Vol.28, N°.4, 2010.
[5] Z. Ouyang, Ole C. Thomsen, M. A. E. Andersen, «Optimal design and tradeoff analysis of planar transformer in high-power DC–DC converters», IEEE Transactions on Industrial Electronics, January 25, 2010.
[6] M. Derkaoui, A. Hamid, T. Lebey, R. Melati, « Design and modeling of an integrated transformer in a flyback converter», Telecommunication, Computing, Electronics and Control, TELKOMNIKA, SCOPUS Vol.11, N° 4, pp. 669~682, December 2013. ISSN: 1693-6930
[7] N.M. Nguyen, R.G. Meyer, «Si IC-compatible inductors and LC passive filters», IEEE Journal of Solid-State Circuits (25) (1990) 1028–1031.
[8] K.B. Ashby, W.C. Finley, J.J. Bastek, S. Moinian, I.A. Koullias, «High Q inductors for wireless applications in a complementary silicon bipolar process», in: Proc. Bipolar/BiCMOS Circuits and Technology Meeting, 1994, pp. 179–182.
[9] C. Patrick Yue, S. Simon Wong, «Physical modeling of spiral inductors on silicon», IEEE Transactions on Electron Devices 47 (3) (2000).
[10] M. Yamaguchi, T. Kuribara, K.-I. Arai, «Two port type ferromagnetic RF integrated inductor», in: IEEE International Microwave Symposium, IMS-2002, TU3C-2, Seattle, USA, 2002, pp. 197–200.
[11] Ali Telli, SimsekDemir, Murat Askar,«Practical Performance of Planar Spiral Inductors». IEEE, 2004, pp.487-490.
[12] Y. Benhadda, A. Hamid, T. Lebey, M. Derkaoui, «Design and modeling of an integrated inductor in a Buck converter DC-DC», Journal of Nano- and Electronic Physics, Vol. 7, No. 2, 10 June 2015.
[13] M. Derkaoui, R. Melati, A. Hamid, «Modeling of a planar inductor for converters low power», Global Conference on renewables and Energy Efficiency for Desert Regions GCREEDER'11, 2011, Jordanie.
[14] R. Melati, A. Hamid, T. Lebey, M. Derkaoui, «Design of a new electrical model of a ferromagnetic planar inductor for its integration in a micro-converter», Mathematical and Computer Modelling, Vol 57, pp 200–227, Janvier 2013.
[15] M. Derkaoui, A. Hamid, T. Lebey, R. Melati, « Design and modeling of an integrated transformer in aflyback converter», Telecommunication, Computing, Electronics and Control, TELKOMNIKA, SCOPUS Vol.11, N° 4, pp. 669~682, December 2013. ISSN: 1693-6930
[16] H-A. Wheeler & al., «Simple inductance formulas for radio coils», Proc. IRE, 16, n° 10, pp. 1398-1400.
[17] S. Mohan & al., «Simple Accurate Expressions for Planar Spiral Inductances», IEEE Journal of Solid -State Circuits, 34, n° 10 (1999), pp. 1419-1424.
[18] B. Estibals , A. Salles, «Design and realization of integrated inductor with low DC-resistance value for integrated power applications», HAIT Journal of Science and Engineering B, Vol. 2, Issues 5-6, pp. 848-868, 2005.
[19] ShwetabhVerma, Jose M. Cruz, «On-chip Inductors and Transformers», SMLI TR-99-79 December 1999.
[20] Y. K. Koutsoyannopoulos, « Systematic Analysis and Modeling of Integrated Inductors and Transformers in RF IC Design », Analog and Digital Signal Processing, Vol. 47, No. 8, August 2000 699.
[21] D. Belot, B. Leite, E. Kerherve, and J. B. Begueret, «Millimeter-wave transformer with a high transformation factor and a low insertion loss», U.S. Patent Application12/787,782, 2010.
[22] C. Wang, H. Liao, Y. Xiong, C. Li, R. Huang, and Y. Wang, «A physics-based equivalent-circuit model for on-chip symmetric

transformers with accurate substrate modeling», IEEE Transactions on Microwave Theory and Techniques, vol. 57, no. 4, pp. 980–990, 2009.
[23] J. Gautier, « Modèles électriques pour la conception des circuits intégrés sur silicium », Lavoisier, 2004.

A Three Phase Input-Six phase Output Indirect Matrix Converter and Space Vector Modulation.

Ahmed AZIB
Laboratoire de Technologie Industrielle et de l'Information,
Faculté de Technologie,
Université de Bejaia, 06000 Bejaia, Algérie
ahazib@gmail.com

Djamel ZIANE
Faculté de génie électrique et informatique,
Université de Tizi ouzou, 15000 Tizi ouzou, Algérie
ziane.djamel27@gmail.com

***Abstract*—In this research report, our goal is to study and control a new reduced-switch converter structure called the three phase input-six phase output indirect matrix converter (IMC) using a Bi-directional current-source rectifier (CSR) and dual-output inverter (nine switch inverter). This converter is controlled by space vector modulation (SVM) and will be dedicated to supply dual three-phase load. The results of simulation of the dynamic behavior obtained make it possible to validate the structure.**

***Key words*— Indirect Matrix Converter (IMC), Current Source rectifier (CSR), Space Vector Modulation (SVM).**

I. INTRODUCTION

Many industrial applications require new converter topologies to power its loads, for this several independent converters are usually required and developed towards small, high reliability and low cost trends. Recently, a new topology with reduced active components, named the nine switch inverter has been developed [1-6].

The control of dual three-phase load is traditionally done by two three-phase back-to-back inverters controlled by space vector modulation (SVM). With the progress of power electronics, other converter structures are appearing and moving towards increasingly smaller topologies like the five-arm inverter and nine switch inverter [7].

The control of the amplitude, the frequency and the absence of intermediate storage element, add to this the possibility to control the power factor at the input of the converter are the mean advantages of the indirect matrix converter (IMC) [8-10], for all these we purpose to study and control the three phase input-six phase output indirect matrix converter which is AC-AC converter and based on two stages a current source rectifier (CSR) at the input of the converter as the one used in the conventional IMC and in the other hand the stage of the inverter based on nine switch inverter at the output to supply dual three phase load. So to obtain this we began by modeling this converter in order to study it then we develop a control strategy based on SVM to control it. To validate this structure, we present the simulation results of the dynamic behavior of the converter.

II. MODELING AND CONTROL OF THE INDIRECT MATRIX CONVERTER WITH NINE SWITCHES

A. *Presentation of the converter with nine switches*

Indirect Matrix Converters (CMIs) are AC-AC converters. They comprise two stages such as a rectifier stage and a stage of the inverter without intermediate circuit.

As shown in Figure (1) and contrary to the conventional topology, the structure of the nine-switch converter has three arms, each arm of which consists of three switches as shown in the figure where the upper converter (q_1, q_2, q_3, q_a, q_b and q_c), and the lower converter (q_a, q_b, q_c, q_4, q_5, q_6,) are integrated by sharing three switches (q_a, q_b, q_c). So, we can say that it is a fusion of two three-phase inverters reduced by three switches.

The switches that make up the nine-switch converter are of the IGBT type, this choice was made to overcome switching losses as well as for quick use.

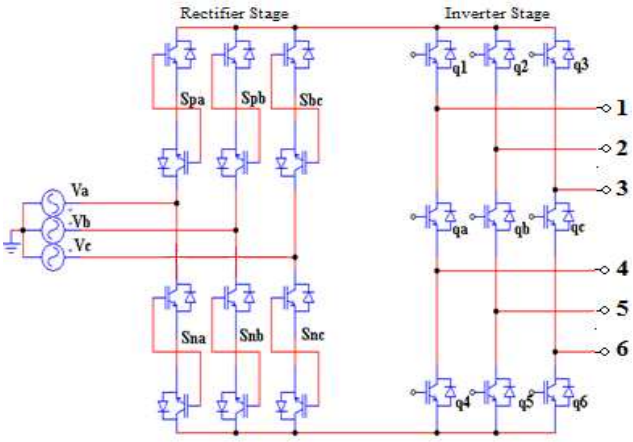

Figure 1. Power diagram of the IMC based on nine-switch converter

B. Modeling of the converter with nine switches

In this section, we will present the steps to follow for the modeling of this converter. In order to simplify the reasoning, we assume:

- The switches is supposed to be perfect
- The voltage drop across the semiconductors is negligible compared to the supply voltage.

a) For rectifier

The equations of the output voltages as a function of the input voltages for the rectifier stage and the inverter with nine switches are given by the following equations:

$$\begin{bmatrix} V_p \\ V_n \end{bmatrix} = \begin{bmatrix} S_{ap} & S_{bp} & S_{cp} \\ S_{an} & S_{bn} & S_{cn} \end{bmatrix} \begin{bmatrix} V_a \\ V_b \\ V_c \end{bmatrix} \quad (1)$$

b) For inverter

To fully understand its operating principle, a suitable mathematical model must be presented for this converter.

Using the compound voltages we obtain the system of equation which translates the operation of the converter (opening and closing of the switches) as shown in "(2)". Subsequently we will have to deduce the simple voltages from the expressions connecting the simple voltages to the compound voltages.

$$v_{12} = v_1 - v_2 = \begin{cases} E \text{ if } & (q_1 = 1 \text{ et } q_b.q_5 = 1) \\ -E \text{ if } & (q_2 = 1 \text{ et } q_a.q_4 = 1) \\ 0 \text{ if } & (q_1.q_2 = 1 \text{ or } q_a.q_4.q_b.q_5 = 1) \end{cases} \quad (2.a)$$

$$\text{So} : v_{12} = E(q_1.q_b.q_5 - q_2.q_a.q_4)$$

$$v_{23} = v_2 - v_3 = \begin{cases} E & if \quad (q_2 = 1 \text{ et } q_c.q_6 = 1) \\ -E & if \quad (q_3 = 1 \text{ et } q_b.q_5 = 1) \\ 0 \text{ if } & (q_2.q_3 = 1 \text{ or } q_b.q_5.q_c.q_6 = 1) \end{cases} \quad (2.b)$$

$$\text{So} : v_{23} = E(q_2.q_c.q_6 - q_3.q_b.q_5)$$

$$v_{31} = v_3 - v_1 = \begin{cases} E & if \quad (q_3 = 1 \text{ et } q_a.q_4 = 1) \\ -E & if \quad (q_1 = 1 \text{ et } q_c.q_6 = 1) \\ 0 \text{ if } & (q_1.q_3 = 1 \text{ or } q_a.q_4.q_c.q_6 = 1) \end{cases} \quad (2.c)$$

$$\text{So} : v_{31} = E(q_3.q_a.q_4 - q_c.q_6.q_1)$$

$$v_{45} = v_4 - v_5 = \begin{cases} E & if \quad (q_5 = 1 \text{ et } q_1.q_a = 1) \\ -E & if \quad (q_4 = 1 \text{ et } q_2.q_b = 1) \\ 0 \text{ if } & (q_4.q_5 = 1 \text{ or } q_1.q_a.q_2.q_b = 1) \end{cases} \quad (2.d)$$

$$\text{So} : v_{45} = E(q_5.q_1.q_a - q_4.q_2.q_b)$$

$$v_{56} = v_5 - v_6 = \begin{cases} E & if \quad (q_6 = 1 \text{ et } q_2.q_b = 1) \\ -E & if \quad (q_5 = 1 \text{ et } q_3.q_c = 1) \\ 0 \text{ if } & (q_5.q_6 = 1 \text{ or } q_2.q_b.q_3.q_c = 1) \end{cases} \quad (2.e)$$

$$\text{So} : v_{56} = E(q_6.q_2.q_b - q_5.q_3.q_c)$$

$$v_{64} = v_6 - v_4 = \begin{cases} E & if \quad (q_4 = 1 \text{ et } q_3.q_c = 1) \\ -E & if \quad (q_6 = 1 \text{ et } q_1.q_a = 1) \\ 0 \text{ if } & (q_4.q_6 = 1 \text{ or } q_1.q_a.q_3.q_c = 1) \end{cases} \quad (2.f)$$

$$\text{So} : v_{64} = E(q_3.q_c.q_4 - q_6.q_1.q_a)$$

The expressions of the simple voltages as a function of the compound voltages are given by:

$$\begin{cases} v_1 = \dfrac{v_{12} - v_{31}}{3} \\ v_2 = \dfrac{v_{23} - v_{12}}{3} \\ v_3 = \dfrac{v_{31} - v_{23}}{3} \\ v_4 = \dfrac{v_{45} - v_{64}}{3} \\ v_5 = \dfrac{v_{56} - v_{45}}{3} \\ v_6 = \dfrac{v_{64} - v_{56}}{3} \end{cases} \quad (3)$$

C. Modeling for control

The space vector modulation consists of synthesizing the output voltages of the input voltages and the input currents of the output currents and separating between the control of the input currents and the control of the output voltages, thus the IMC can be represented by an equivalent circuit that includes a rectifier at the input and an inverter at the output but without any intermediate circuit for storing energy (Fig.1).

a) Control of the rectifier stage

The rectifier stage not only produces the DC bus voltage at the inverter stage, but it must also maintain the sinusoidal input currents with the possibility of controlling the power factor.

The switches can have nine combinations and this to avoid the open circuit and these nine combinations are divided into six active vectors of the input current and three null vectors (Fig.2).

The output voltage $U_{dc} = V_p - V_n$ of the rectifier is found from the input voltages (V_a, V_b, V_c) "(1)", and the input currents (I_a, I_b, I_c) from the current fictitious.

$$\begin{bmatrix} I_a \\ I_b \\ I_c \end{bmatrix} = \begin{bmatrix} S_{ap} & S_{an} \\ S_{bp} & S_{bn} \\ S_{cp} & S_{cn} \end{bmatrix} \begin{bmatrix} I_p \\ I_n \end{bmatrix} \quad (4)$$

The rectifier switches (S_{ap}, S_{bp}, S_{cp}, S_{an}, S_{bn}, S_{cn}) may have only six possible combinations to avoid the open circuit, these six combinations are divided into six active vectors I_1 to I_6 (Fig.2.a).

The bidirectional switches of the rectifier are controlled so that the input lines must never be short-circuited.

$$S_{ap} + S_{bp} + S_{cp} = 1 \quad (5)$$

$$S_{an} + S_{bn} + S_{cn} = 1 \quad (6)$$

During a switching period T_c, is synthesized from the adjacent active vectors I_γ and $I_{\delta\ with}$ the cyclic ratios d_γ and d_δ respectively (Fig.2.b). If the input currents are considered constant during a switching period T_c, the reference vector is expressed as follows:

$$I_{in} = d_\gamma . I_\gamma + d_\delta . I_\delta + d_0 . I_0 \quad (7)$$

The computation of the cyclic ratios d_γ and d_δ are relative to the currents I_γ and d_δ, are given by the following equations:

$$\begin{cases} d_\gamma = m_R \sin(\frac{\pi}{3} - \theta_{in}) \\ d_\delta = m_R \sin(\theta_{in}) \\ d_0 = 1 - d_\gamma - d_\delta \end{cases} \quad (8)$$

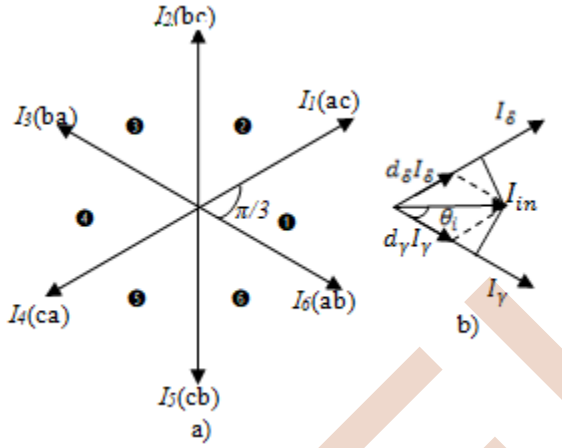

Figure 2. (a) The seven positions of the spatial vector of the input current, (b) The synthesis of a reference vector in a given sector

However, the fact that the DC bus voltage can not be negative, three of these combinations are not usable (zero current vectors). As a result, the new adjusted duty cycles of the rectifier stage are determined by the relationship:

$$\begin{cases} d_\gamma^R = \frac{d_\gamma}{d_\gamma + d_\delta} \\ d_\delta^R = \frac{d_\delta}{d_\gamma + d_\delta} \end{cases} \quad (9)$$

b) Control of the Inverter stage

The control signals of the upper switches remain unchanged and are obtained as in the conventional configuration, as for the lower signals they are also generated conventionally but, they are reversed by means of a logical operator NOT.

The control signals of the common switches (q_a, q_b, q_c) are generated by applying an XOR or NXOR logic operator to these derived signals by the upper switches (q_1, q_2, q_3) and the lower switches (q_4, q_5, q_6) (Fig.3).

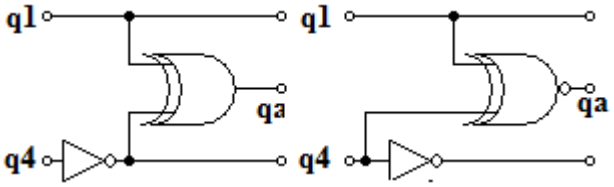

Figure 3. Two ways to generat q_a

A combinatorial analysis of all the states (open or closed) of the switches of the inverter (q_1, q_2, q_3, q_a, q_b, q_c) allows to have only eight possible combinations to avoid the short circuit of the DC voltage fictional V_{pn}.

The eight combinations are divided into six active vectors V_1 to V_6, two of which are zero V_0 to V_7, which makes it possible to calculate the corresponding output voltage vectors.

Using vector modulation (SVM), the output voltage generated by the first six combinations is transformed into six spatial vectors of output voltages as shown in the following figure (Fig.4.a).

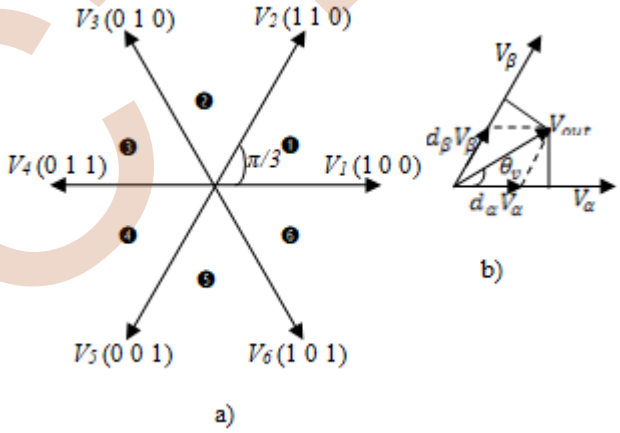

Figure 4. (a) The seven positions of the spatial vector of the output voltage, (b) The synthesis of a reference vector in a given sector

The reference vector can be synthesized by two adjacent spatial vectors V_α, V_β and the voltage vector no V_0, in a given sector. During a switching period T_c, the output reference vector can be synthesized as follows (Fig.4.b):

$$V_{réf} = d_\alpha V_\alpha + d_\beta V_\beta + d_0 V_0 \quad (10)$$

The calculation of the cyclic ratios d_α, d_β and d_0 are given by the following expressions:

$$\begin{cases} d_\alpha = m_1 \sin(\frac{\pi}{3} - \theta_{out}) \\ d_\beta = m_1 \sin(\theta_{in}) \\ d_0 = 1 - d_\alpha - d_\beta \end{cases} \quad (11)$$

c) Complete modulation of the CMI

To achieve the control of the indirect matrix converter under the constraints of an adjustable power factor to the

input, the bidirectional transit power and the zero-current switching, it must be applied has a coordination between the control switches of the rectifier and that of the switches of the inverter. Switching at the rectifier occurs when the current is zero. To illustrate this coordination, a control cycle during sector I as well as the cyclic ratios relating to the inverter stage can be determined by the following relationships:

$$\begin{cases} t_{r1} = d_\gamma^R * T_{s\omega} \\ t_{i1} = \frac{1}{2} d_\gamma^R * d_0 * T_{s\omega} \\ t_{i2} = d_\gamma^R * d_\alpha * T_{s\omega} \\ t_{i3} = d_\gamma^R * d_\beta * T_{s\omega} \\ t_{i4} = \frac{1}{2} d_\delta^R * d_0 * T_{s\omega} \\ t_{i5} = d_\delta^R * d_\beta * T_{s\omega} \\ t_{i6} = d_\delta^R * d_\alpha * T_{s\omega} \end{cases} \quad (12)$$

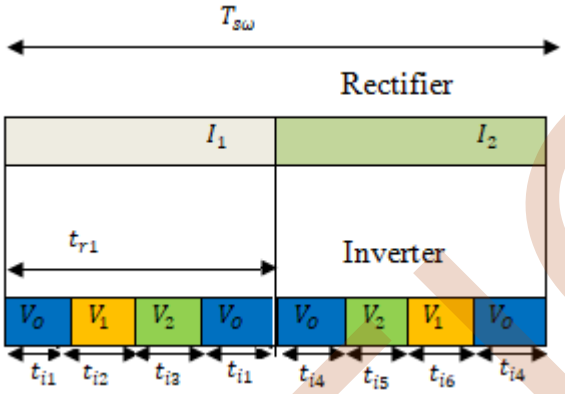

Figure 5. A control cycle during sector I as well as the cyclic ratios relating to the inverter stage

III. Simulation Results and Interpretation

To study the performance of the matrix converter controlled by the vector modulation feed a load -L, we use the following simulation parameters:

- The effective value of the supply voltage is = 220V.
- The supply frequency f = 50 Hz.
- R = 5Ω.
- L = 10mH.

The simulation results obtained for an inductive load (R, L) and an output frequency of the IMC is 50 HZ are represented in the following figures:

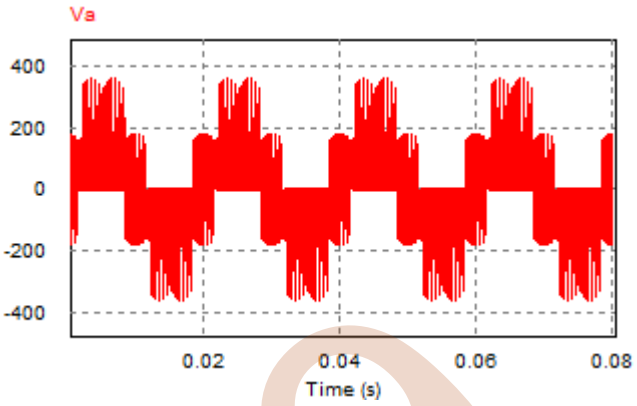

Figure 6. Simulation results of Output phase voltage of Upper load

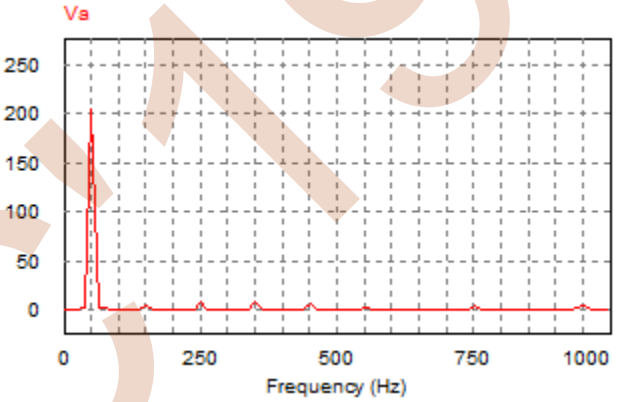

Figure 7. Spectrum of Output phase voltage of Upper load

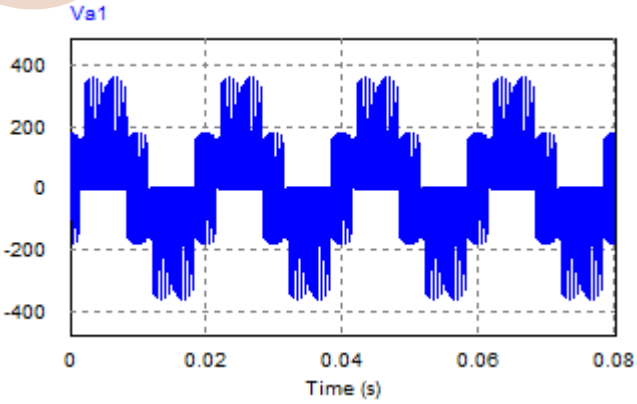

Figure 8. Simulation results of Output phase voltage of Lower load

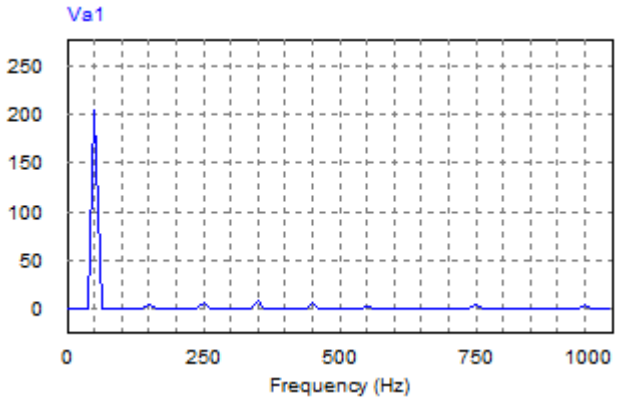

Figure 9. Spectrum of Output phase voltage of Lower load

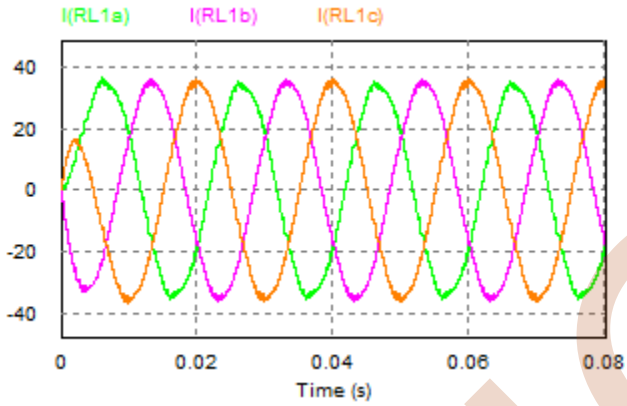

Figure 10. Simulation results of Upper load currents for IMC

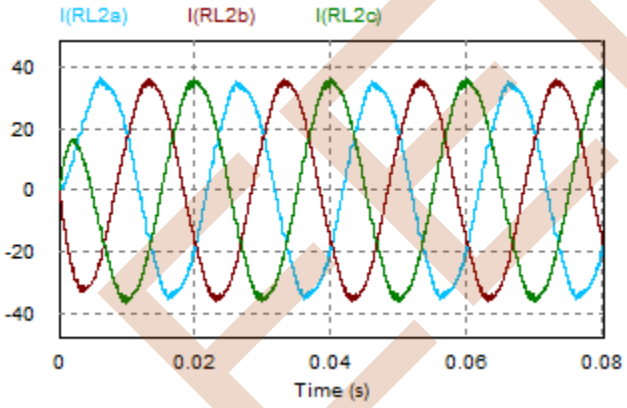

Figure 11. Simulation results of Lower load currents for IMC

The figures (Fig.6,7 and Fig.8,9) represent the first output phase voltage of the IMC of each load system so its harmonic spectrum with a power frequency of 50 Hz for an inductive load, it can be seen that the waveform of the voltage is acceptable despite the appearance of some harmonics.

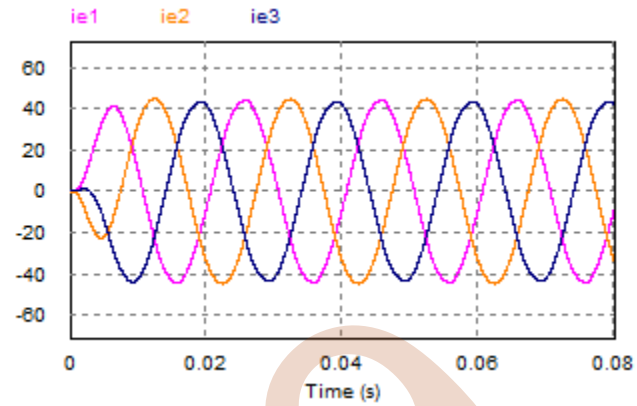

Figure 12. Simulation results of Input currents for IMC

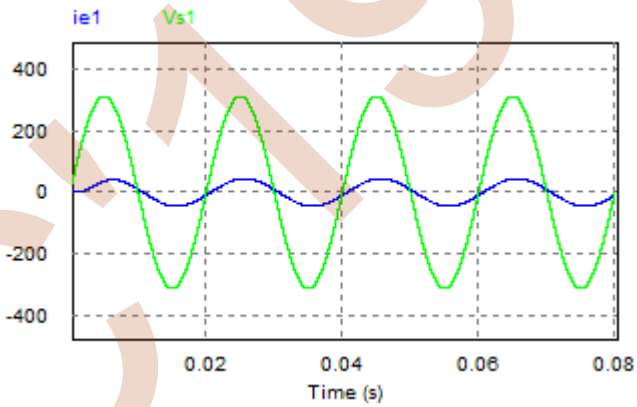

Figure 13. Simulation results of the first Input current with the volatge source for IMC

The Fig.10 and Fig.11 show both the IMC output currents for upper and lower load, the waveform of currents is sinusoidal.

In Fig.12 is represented the input currents of the converter which are also sinusoidal.

The Fig.13 shows the input voltage and the filter input current of the IMC for 50 Hz supply frequency, we note that the current is in phase with the voltage and this shows the property of IMC to be able to control the power factor at the input.

IV. CONCLUSION

This article presents a new topology of the matrix converter, the theoretical results of analysis and simulation show that IMC satisfies the following performances:

- Waveforms of almost sinusoidal input.
- The converter can provide a unit power factor at the input.
- Requires no intermediate storage element.

- The converter offers a better efficiency than the direct matrix converter, since the commutations of the rectifier stage take place at zero current.

REFERENCES

[1] E. C. dos Santos Jr., C. B. Jacobina and O. I. da Silva « Six-phase Machine Drive System with Nine-switch Converter » Federal University of Campina Grande (UFCG),58109-970 Campina Grande - PB – Brazil , 03 January 2012.

[2] S. Ahmed Salem, A. Ragi. Hamdy, S. Ayman. F. Abdel-Khalik, Ibrahim El Arabawy,S. Mostafa. Hamad, « Performance of nine-switch inverter-fed asymmetrical six- phase induction machine under machine and converter faults » MEPCON, 2016.

[3] F. Gao,Lei Zhang, Poh Chiang « Dead-Time Elimination of Nine-Switch Converter » Shandong University Jinan, China , Nanyang Technological University Singapor , 07 April 2011.

[4] F. Gao, Lei Zhang, Ding Li, Poh Chiang Loh « Optimal Pulse width Modulation of Nine-Switch Converter » Agency for Science, Technology, and Research, Singapore, 25 mars 2010.

[5] Y. Chen, G. Wen « Sliding Mode Pulsewidth Modulation (SMPWM) for Nine-Switch Converter » State Key Laboratory of Advanced Electromagnetic Engineering and Technology (AEET) also the College of Electrical and Electronic Engineering (CEEE) Huazhong University of Science and Technology (HUST), Mai 2013.

[6] T. Kominami, Y. Fujimoto « A Novel Nine-Switch Inverter for Independent Control of Two Three-phase Loads »Yokohama National University,octobre 2007.

[7] H.Xu, H.A. Toliyat, L. J. Peteren, "Modelling and control of five-phase induction motor under asymmetrical fault conditions", Electric Machines & Power Electronics Laboratory- Department of Electrical Engineering Texas A&M University, IEEE, 2001.

[8] D. Casadei, G. Serra, A. Tani, L. Zarri, "A review on matrix converters," Przeglad Elek-trotechniczny (Electr Rev)., 2, pp. 15–25, 2006.

[9] A. Quawi, M. Haseeb Khan « A Novel Three Phase Three Leg AC/AC Converter Using Nine IGBTS » International Journal of Innovative Research in Science,Engineering and Technology,janvier 2017.

[10] M. Chai, D. Xiao, R. Dutta, and J. E. Fletcher, "Space vector PWM techniques for three-to-five phase indirect matrix converter in the over modulation region," IEEE Trans. Ind. Electron., vol. 63, no. 1, pp. 550–561,Jan. 2016.

Design and Implementation of Shunt Active Power Filter using STM32F4 Board

AYACHI AMOR Yacine [1], DEKARI Cherif [2], DAHMANI Seif-Eddine [2], KHELDOUN Aissa [2], METIDJI Brahim [2], HAMOUDI Farid [1], AMMAR Abdelkarim [2], SLAMI Abdelhadi [3]

[1]Laboratoire de Maitrise des Energies Renouvelables (LMER), Faculté de Technologie, Université de Bejaia 06000 Bejaia, Algeria.
[2]Signals and Systems Laboratory Institute of Electrical and Electronic Engineering, University M'hamed Bougara of Boumerdes 35000, Boumerdes, Algeria.
[3]University of Tlemcen, Faculty of Sciences, Department of Physics Unité de Recherche « Matériaux et Energies Renouvelables », URMER BP: 119, Fg Pasteur, Tlemcen, 13000, Algeria.

Abstract— This paper proposes a simple yet cost-effective implementation of three-phase two-level inverter based shunt active power filter (SAPF) using STM32F4 discovery board. A similar system is mostly implemented using either DSP card or Dspace platform, which increase the cost of the system. The control algorithm has been chosen based on the simplicity and flexibility features, that is the instantaneous power PQ theory. Simulation work of SAPF with the proposed algorithm was conducted and assessed in MATLAB–Simulink. The simulation results have been confirmed by the implementation part where the STM32F4 provides a great flexibility interfacing between the Matlab environment and the board. The results are obtained to be met the power quality requirement by the international standards, where the THD of the grid current drawn by a nonlinear load is kept below 5%.

Keywords—*Power quality, THD, Shunt Active power filter, STM32F4 discovery.*

I. INTRODUCTION

Power quality has become of utmost importance for the power systems owners. Where, the power electronics systems are found nowadays in all systems, such as industrial applications, appliances and telecommunications. These systems, which use power switching devices, are source of harmonics and consequently deteriorate the quality of voltage and current in the grid utilities. Harmonics can be defined as "a sinusoidal component of a periodic wave or quantity which having a frequency that is an integral multiple of the fundamental supply frequency" [1]. These harmonics are caused by a certain type of loads known as nonlinear loads. Traditionally passive filters have been used to compensate harmonics and reactive power; but passive filters are large in size, aging and tuning problems exist and can resonate with the supply impedance. Recently active power filters are designed in order to protect the electrical equipment from getting damaged due to harmonic voltage distortion. They can also be used for the compensation of power quality problems such as reactive power control, harmonic filtering, load balancing, voltage regulation and flicker reduction [2, 3].

Active power filters (APF) can be classified based on the type of converter, configuration, control scheme, and compensation characteristics. In this work, a shunt active power filter based on two-level inverter using P-Q theorem is adopted for both power quality and reactive power compensation. The instantaneous P-Q theory is a popular theory used as the control algorithm for shunt APFs, undesirable powers can conveniently be selected and compensated. It is most widely used as it offers a very precise reference compensation, current template and allows obtaining a clear difference between instantaneous active and reactive powers. However, it is criticized as a disappointment under non-ideal supply conditions [4]. The main configuration of the proposed APF is shown in Figure 1.

The control of APF is usually implemented using software based on DSP card or Dspace platform [5] that are fast processors. However, they are costly. To this, it is proposed in the present work to investigate a very economic microcontroller with almost has the same computation performance. This low cost Microcontroller, STM32F4, is based on the high-performance ARM Cortex-M4 32-bit RISC core operating at a 210 DMIPS. The Cortex-M4 core features a Floating Point Unit (FPU) single precision that supports all ARM single precision data-processing instructions and data types. It also implements a full set of DSP instructions and a memory protection unit (MPU), and also incorporates high-speed embedded memories and an extensive range of enhanced I/Os and peripherals some of them dedicated to power electronics converters and electrical machines control such as ADCs, DACs, PWMs outputs and Encoders inputs [6].

In this paper, we will cover the VSC shunt active power filter based on the instantaneous active and reactive power (p-q) control technique, where both the simulation and experimental results are validated.

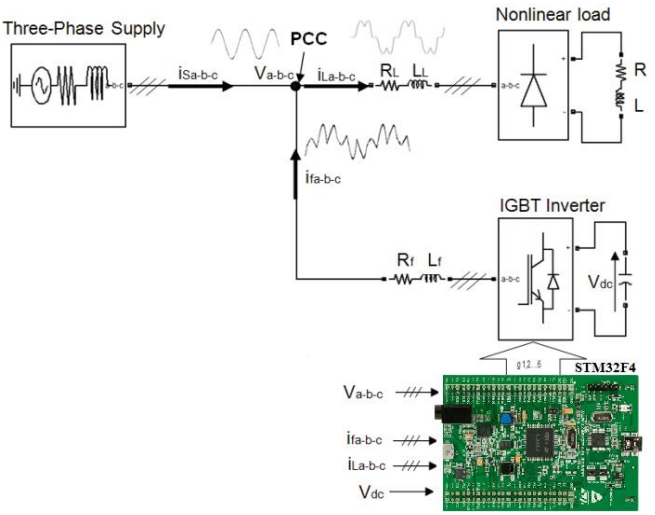

Figure 1: scheme of a shunt active filter

II. The Instantaneous Active And Reactive Power (p-q) Control Technique

The p-q theory, or "Instantaneous Power Theory", was developed by Akagi *et al* in 1983, with the objective of applying it to the control of active power filters [7]. Using sensors, we track the source voltages (V_{sa}, V_{sb}, V_{sc}) and the load currents (I_{sa}, I_{sb}, I_{sc}). As shown in the Figure.3, the Clark transformation is applied on voltages and the currents in order to compute the active and reactive power by the upcoming steps.

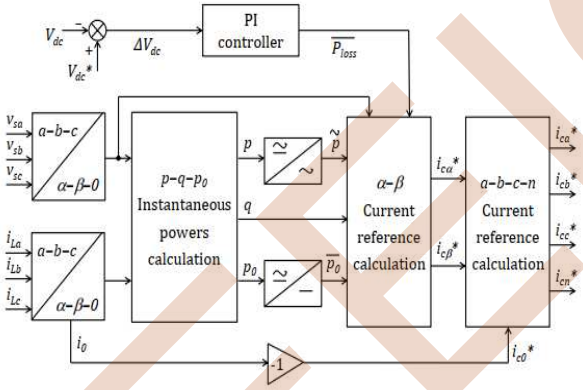

Figure 3: Control block diagram of the p-q scheme.

The Clark transformation matrix applied for transforming source voltages and load currents from (a,b,c) to ($\alpha,\beta,0$) references is defined as:

$$\begin{bmatrix} V_0 \\ V_\alpha \\ V_\beta \end{bmatrix} = \sqrt{\frac{2}{3}} \begin{bmatrix} \frac{1}{\sqrt{2}} & \frac{1}{\sqrt{2}} & \frac{1}{\sqrt{2}} \\ 1 & -\frac{1}{2} & -\frac{1}{2} \\ 0 & \frac{\sqrt{3}}{2} & -\frac{\sqrt{3}}{2} \end{bmatrix} \begin{bmatrix} V_a \\ V_b \\ V_c \end{bmatrix} \quad (1)$$

$$\begin{bmatrix} I_0 \\ I_\alpha \\ I_\beta \end{bmatrix} = \sqrt{\frac{2}{3}} \begin{bmatrix} \frac{1}{\sqrt{2}} & \frac{1}{\sqrt{2}} & \frac{1}{\sqrt{2}} \\ 1 & -\frac{1}{2} & -\frac{1}{2} \\ 0 & \frac{\sqrt{3}}{2} & -\frac{\sqrt{3}}{2} \end{bmatrix} \begin{bmatrix} I_a \\ I_b \\ I_c \end{bmatrix} \quad (2)$$

According to the p-q theory, the active, reactive and zero-sequence powers are defined as shown in equation 3:

$$\begin{bmatrix} p_0 \\ p \\ q \end{bmatrix} = \begin{bmatrix} V_0 & 0 & 0 \\ 0 & V_\alpha & V_\beta \\ 0 & V_\beta & -V_\alpha \end{bmatrix} \begin{bmatrix} I_0 \\ I_\alpha \\ I_\beta \end{bmatrix} \quad (3)$$

Where p,q and p_0 have DC components ($\bar{p}, \bar{q}, \bar{p}_0$) and AC components ($\tilde{p}, \tilde{q}, \tilde{p}_0$).

As shown in the scheme of p-q method, the entire reactive power (q) and oscillating component of active power ($\tilde{p}$) are utilized for calculation of reference filter currents in α,β coordinates using equation 4:

$$\begin{bmatrix} I_{c\alpha^*} \\ I_{c\beta^*} \end{bmatrix} = \frac{1}{\sqrt{{V_\alpha}^2 + {V_\beta}^2}} \begin{bmatrix} V_\alpha & -V_\beta \\ V_\beta & V_\alpha \end{bmatrix} \begin{bmatrix} -\tilde{p} + \Delta\bar{p} \\ -q \end{bmatrix} \quad (4)$$

Once we get reference currents ($I_{\alpha\beta 0}{}^*$) we can transform them into ($I_{abc}{}^*$)using the inverse Clarke transformation:

$$\begin{bmatrix} I_{ca^*} \\ I_{cb^*} \\ I_{cc^*} \end{bmatrix} = \sqrt{\frac{2}{3}} \begin{bmatrix} \frac{1}{\sqrt{2}} & 1 & 0 \\ \frac{1}{\sqrt{2}} & -\frac{1}{2} & \frac{\sqrt{3}}{2} \\ \frac{1}{\sqrt{2}} & -\frac{1}{2} & -\frac{\sqrt{3}}{2} \end{bmatrix} \begin{bmatrix} I_{c0^*} \\ I_{c\alpha^*} \\ I_{c\beta^*} \end{bmatrix} \quad (5)$$

The next step after getting the reference currents ($I_{abc}{}^*$) is to compare them to the filter actual currents using a hysteresis controller which has a hysteresis band (HB) (Fig.4).

Therefore, the 6 IGBTs gates of the two-level inverter can be controlled using the following conditions:

If $ica < (ica,ref - HB)$

The upper switch is *off* and the lower switch is *on*.

If $ica > (ica,ref + HB)$

The upper switch is *on* and the lower switch is *off*.

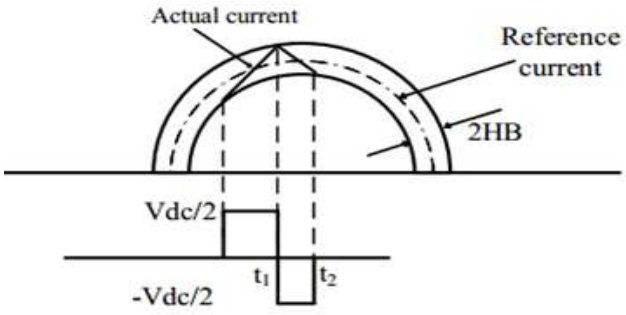

Figure 4: Principle of the hysteresis current controller

III. Simulink Model Of The SAPF

The overall system simulation model containing the power source, the APF and the nonlinear load as shown in Figure5.

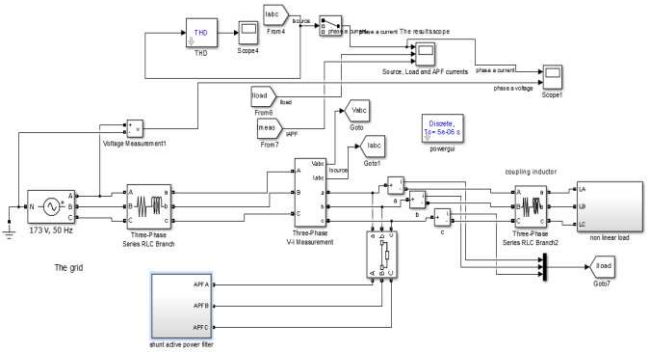

Figure 5: The simulation block of the proposed system.

The main components of the system are the following ones:
-The power source which was designed as a 3 single phases 180V/50Hz. Voltage source connected to the load.
-The load designed as a full wave rectifier ends by an RL branch.
-The SAPF designed based on two level inverter using the instantaneous active and reactive power theorem control.

The following table summarizes the system parameters:

Table1: System parameters used for simulation.

ELEMENTS	PARAMETERS	VALUES
SAPF Converter	DC LINK VOLTAGE	300 V
	COUPLING INDUCTOR	*2 mH*
	DC LINK CAPACITOR	2200 µF
AC POWER GRID	GRID VOLTAGE	180 V
	GRID FREQUENCY	50 HZ
NONLINEAR LOAD	R LOAD	20 Ω
	L LOAD	*20 mH*

IV. SIMULATION RESULTS

After studying the SAPF theoretically, the simulation has been performed in order to investigate the presented theoretical aspects with the simulating results. First, we will see the system without any filtering process, the results is shown in Figure.6.

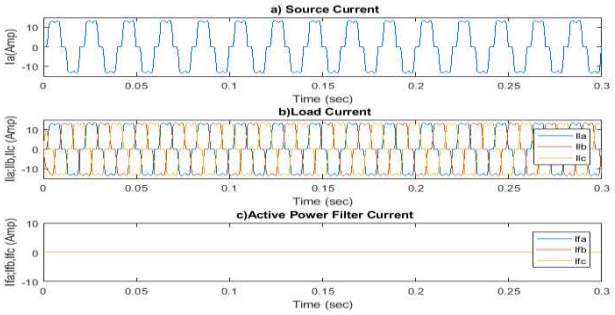

Figure 6: a) The source current, b) the load current, c) APF currents with an open breaker.

The THD of the phase A grid current is 21.51% as shown in Figure.7 which is high as it should be because the non-linearity of the load. Therefore, the objective here is to set the THD of the source current to be less than 5% according to IEEE 519-1992.

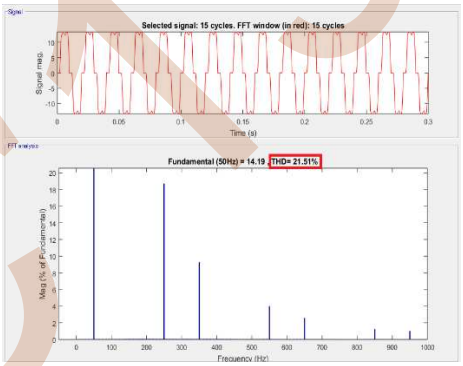

Figure 7: FFT analysis of the grid current before the filtering.

The shunt APF is turned on at t = 0.05s and the source currents become sinusoidal, balanced and in-phase with its perspective phase voltage. After compensation, the THD of the phase *A* grid current becomes to 1.62% as demonstrated in Figure. 8.

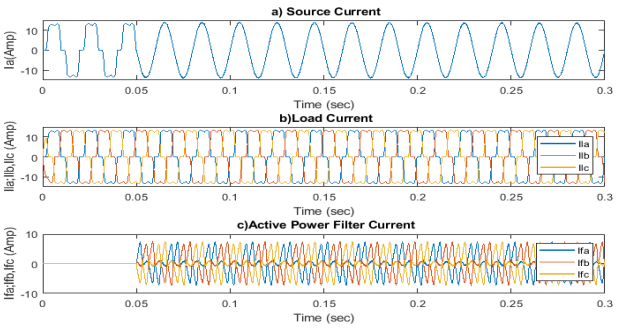

Figure 8: a) The source current, b) load current, c) APF current with a closed breaker.

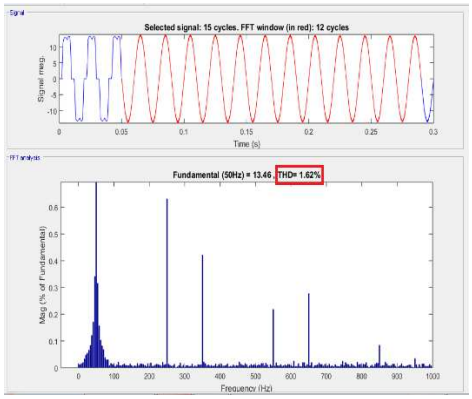

Figure 9: FFT analysis of the grid current after filtering.

V. Implementation Results

To validate the proposed SAPF practically, a prototype was built in the laboratory, based on the parameter values listed in Table I and slightly modified in order to get a reasonable result. The circuit connection is shown in Figure.10 as per earlier used for simulation. The developed control algorithm was executed in STM32f4 microcontroller.

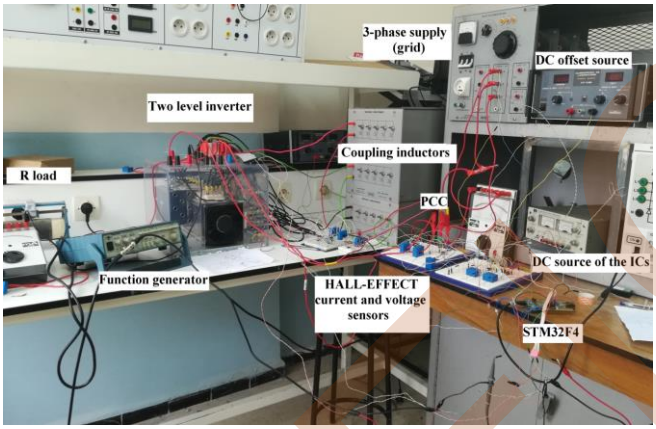

Figure 10: Hardware setup of the shunt active power filter.

Figure. 11 (A, B, C and D) represents the co-simulation results where it shows respectively the grid current, the active filter compensation current, the load current and the inverter DC voltage. (The results are shown based on phase A).

So far, only co-simulation have been performed in this work which is not the final implementation results, this is due to the lack of desired coupling power inductance value (Lf), till then the final results will be performed.

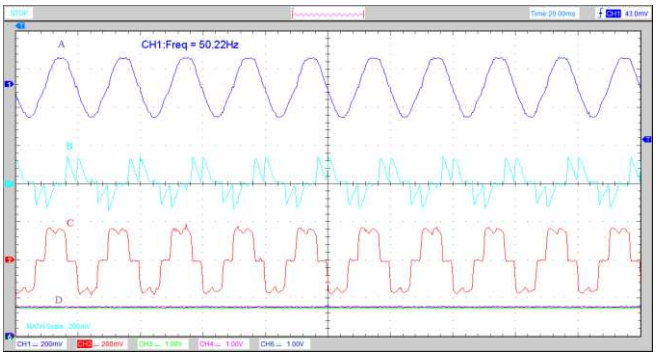

Figure 11: A) grid current, B) APF current, C) the load current, D) the DC voltage.

It is clearly shown that the co-simulation results based on the real elements exactly match the simulation results. Consequently, the results show the effectiveness and capability of using STM32F4 board in controlling such a complex system like a SAPF.

VI. Conclusion

In this work, a tow level inverter based SAPF using the instantaneous active and reactive power theorem control is simulated and implemented. Both the simulation and experimental results show that the proposed shunt APF was able to compensate the harmonic current and improve the power quality where the source current became sinusoidal and the THD was reduced below 5%.
The main contribution of this work is the ability the use of cost-effective microcontroller such as STM32F4 to control a system like APF.
In the future, the desired coupling inductor will be provided and the final experimental results will be conducted.

References

[1] "IEEE standard dictionary of electrical and electronics terms," IEEE Standard 100,1984.

[2] H.Akagi, "Active harmonic filter," in *Proceedings of IEEE*, Vol 93, No 12, Dec 2005.

[3] T.C. Green and J.H. Marks, "Control techniques for active power filter" in *IEE Proceedings - Electric Power Applications*, Vol. 152 , No. 2 , 2005.

[4] M. Kale and E. Ozdemir, "Harmonic and reactive power compensation with shunt active power filter under non-ideal mains voltage", *Electric Power Systems Research*, Vol. 74, No. 3, pp. 363-370, 2005.

[5] E. Sundaram, M. Venugopal, "On design and implementation of three phase three level shunt active power filter for harmonic reduction using synchronous reference frame theory", *Electrical Power and Energy Systems* Vol.81 pp. 40–47, 2016.

[6] STM32F4Discovery – Discovery kit with STM32F407VG MCU, pdf file, www.st.com/en/evaluationtools/stm32F4discovery.html

[7] H. Akagi, Y. Kanazawa, A. Nabae, "Generalized Theory of the Instantaneous Reactive Power in ThreePhase Circuits" Vol. 103, No.4, 1983.

Integration of a Planar Micro-Transformer

BENHADDA Yamina
Electrical engineering department,
University of Science and Technology
Oran, Algeria
benhadda_yamina@yahoo.fr

ALLAOUI Abdelhak
Electrical engineering department,
University of Science and Technology
Oran, Algeria
abdelhakallaoui@yahoo.fr

HAMID Azzedine
Electrical engineering department
University of Science and Technology
Oran, Algeria
hamidazdean@yahoo.fr

***Abstract*— The objective of our work is the integration of a planar micro-transformer presented in a converter Flyback based on a square spiral inductor. This paper is decomposed into five parts. First of one concern a presentation of model for converter Flyback. Then the geometric dimensions and electrical model of an integrated planar micro-transformer are calculated. The third part concerns simulation of our Flyback coupled with ideal transformer and coupled with integrated planar micro-transformer. Subsequently, a magnetic modeling, using the finite element method is carried out to study effects of the electric field and magnetic field lines in our component. The last part concerns simulation results of thermal modeling, using the finite element method that allowed us to determine the operating temperature in the materials of this integrated component.**

I. INTRODUCTION

The integration of passive components has grown up considerably in the recent decades with the electronics industry's application. In this domain of the embedded electronics, reduced size, volume and high temperature functionality is an industrial and scientific challenge. The purpose of this paper is to design and modeling a square planar micro-transformed integrated in converter Flyback.

II. PRESENTATION OF THE FLYBACK CONVERTER

A Flyback converter model is shown in Figure 1. Input voltage, $V_{in} = 14Volt$. Output voltage, $V_{out} = 12Volt$. Duty cycle $\alpha = 0.5$. Output power, $P_{out} = 5W$. Frequency of operation, $f = 100MHz$.

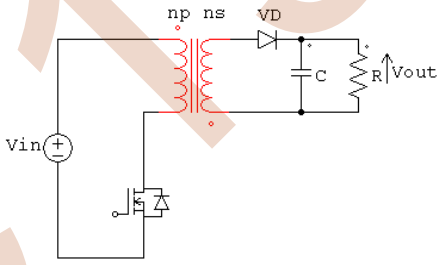

Figure 1. schematic diagram of flyback converter

III. DIMENSIONING OF THE MICRO-TRANSFORMER

Dimensioning of the planar micro-transformer requires sizing the magnetic circuit and the geometrical parameters of two square wading of our component, primary and secondary [5].
Turn ratio

$$m = \frac{\alpha}{\alpha - 1}\frac{V_{out}}{V_{in}} = 0.85 \qquad (1)$$

The primary inductance L_p is given by relation (2)

$$L_p = \frac{V_{in}^2 \alpha^2}{2fP_{out}} \qquad (2)$$

The secondary inductance L_s is derived from the relation (3)

$$L_s = m^2 L_p \qquad (3)$$

The maximum energy stored in the inductor is given by relation (4)

$$W = \frac{1}{2}L_p I_{in}^2 = \frac{1}{2}L_s I_{out}^2 \qquad (4)$$

The volumetric energy density of the ferrite is given by the equation (5)

$$W_{v\max} = \frac{B_{\max}^2}{2\mu_0 \mu r} \quad (5)$$

$B_{\max}$: The maximum magnetic induction supported by the ferrite

μ_r : The relative permeability

μ_0 : The magnetic permeability of the free space

The volume of the ferrite is given by relation (6)

$$Vol = \frac{W}{W_{v\max}} \quad (6)$$

The ferrite's thickness is t_{Sub}=74µm, thus the volume of the magnetic core, NiFe will be $500 \times 500 \times 74 \mu m^3$.

The electrics characteristics of materials are shown in table I.

TABLE I. ELECTRICS CHARACTERISTICS OF THE MATERIALS

Element	Materiel	Characteristics
Conductor	Copper (Cu)	Electrical conductivity: $\sigma = 5.998\ 10^7\ \Omega^{-1}m^{-1}$ Relative permeability: Relative permittivity: $\varepsilon_r = 1$
Substrate	Ferrite (NiFe)	Electrical conductivity: $\sigma = 2.2\ 10^4\ \Omega^{-1}m^{-1}$ Relative permeability: $\mu_r = 800$ Relative permittivity: $\varepsilon_r = 10$
Oxide	Silicon dioxide (SiO_2)	Electrical conductivity: $\sigma = 1\ \Omega^{-1}m^{-1}$ Relative permeability: $\mu_r = 3.9$ Relative permittivity: $\varepsilon_r = 1$
Dielectric	Air	Electrical conductivity: $\sigma = 1\ \Omega^{-1}m^{-1}$ Relative permeability: $\mu_r = 1$ Relative permittivity: $\varepsilon_r = 1$

Since a micro-transformer is nothing else than two coupled inductors, a solid knowledge of the characteristics and limitations of the integrated inductors will be an excellent starting point for the analysis of integrated micro-transformer.

The square inductor is geometrically defined by this parameters (Figure 2), the number of turns **n**, the width of the conductor **w**, thickness of the conductor **t**, the spacing between conductor **s**, length of the conductor **l**, the outer diameter $\mathbf{d_{out}}$ and input diameter $\mathbf{d_{in}}$ [6].

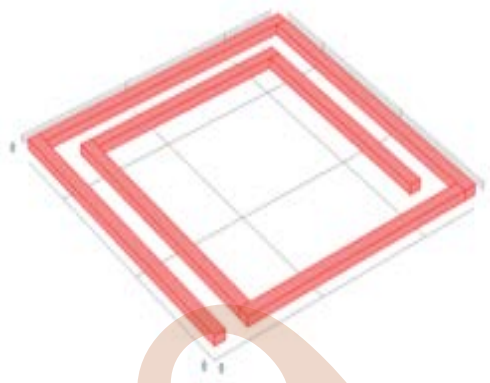

Figure 2. Geometry of square spiral inductor

Figure 3 shows an integrated square spiral planar micro-transformer.

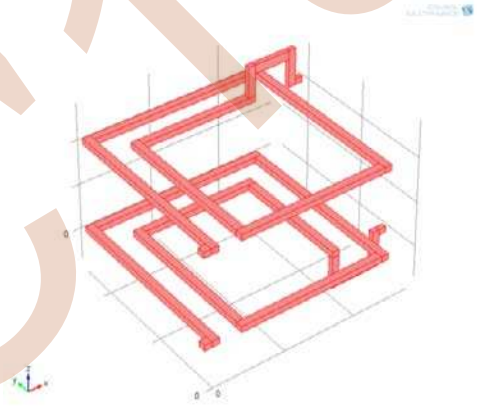

Figure 3. Integrated planar micro-transformer

Table II contains the specifications and the design results of the integrated micro-transformer.

TABLE II. DESIGN RESULTS OF THE INTEGRATED MICRO-TRANSFORMER

Parameter	Value
Outer diameter: d_{out}	500 µm
Inner diameter: d_{in}	450 µm
Primary turns: n_p	1.75
Secondary turns: n_s	1.25
Thickness of winding: t	13 µm
Width of primary winding: w_p	20 µm
Width of secondary winding: w_s	20 µm
Inter-spacing of primary winding: s_p	4.2 µm
Inter-spacing of secondary winding: s_s	6. 5 µm
Total length of primary winding: l_p	3.2 µm
Total length of secondary winding: l_s	2.8 µm

IV. ELECTRICAL MODEL

Planar micro-transformer is built on the integrated inductor model (figure 4).

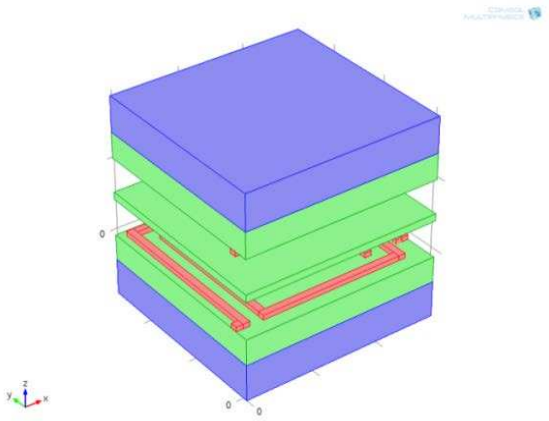

Figure 4. Geometry of integrated micro-transformer on substrate

of an integrated planar micro-transformer contains the following electrical parameters [10]:

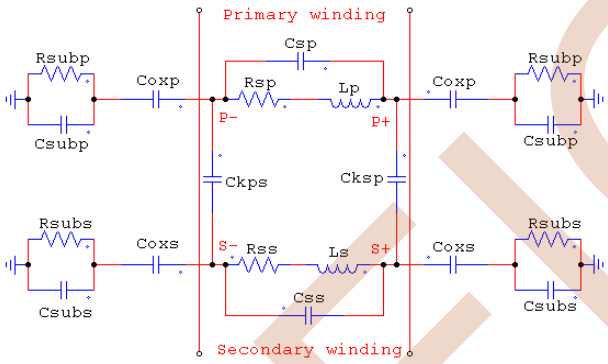

Figure 5. Equivalent circuit of an integrated planar micro-transformer

Table III shows the electrical parameters calculated.

TABLE III. ELECTRICAL PARAMETERS RESULTS

Electrical parameters	values
Primary inductance: L_p	49 nH
Secondary inductance: L_s	36 nH
Primary serial resistance: R_{sp}	0.21 Ω
Secondary serial resistance : R_{ss}	0.18 Ω
Primary serial resistance: R_{sACp}	0.48 Ω
Secondary serial resistance : R_{sACs}	0.42 Ω
Primary resistance of silicon substrate R_{subp}	0.10 Ω
Secondary resistance of silicon substrate : R_{subs}	0.11 Ω
Primary coupling capacitance : C_{sp}	346.59 pF
Secondary coupling capacitance : C_{ss}	191.86 pF
Coupling capacitance between the primary and secondary: C_{kps}	44.83 pF
Coupling capacitance between the secondary and primary : C_{ksp}	38. 79 pF
Primary oxide capacitance : C_{oxp}	44.83 pF
Secondary oxide capacitance : C_{oxs}	38.79 pF
Primary capacitance of silicon substrate : C_{subp}	38.79 pF
Secondary capacitance of silicon substrate : C_{subs}	33.56 pF
Quality factor Q_p	43.94
Quality factor Q_s	37.33

Figure 6 shows the evolution of the quality factor as a function of frequency for the primary and secondary winding.

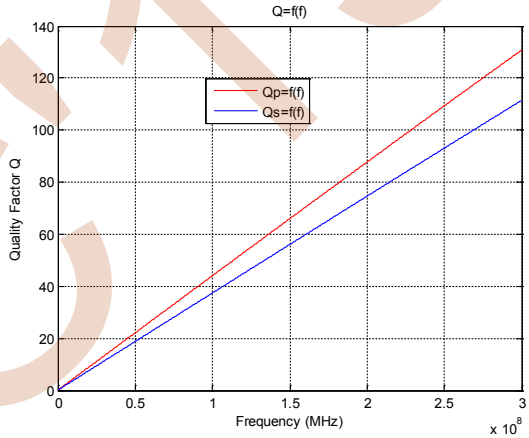

Figure 6. Quality factor of the primary and secondary windings versus frequency

V. SIMULATION OF THE OF THE FLYBACK CONVERTER

In this section, an electrical model of Flyback converter contains an ideal micro-transformer (figure 7) is presented.

Figure 8 shows the waveform of the output voltage and current of the transistor and diode of the Flyback.

When the switch is closed, the primary of the transformer is directly connected to the input voltage source. The primary current and magnetic flux in the micro-transformer increases, storing energy in the micro-transformer. The voltage induced in the secondary winding, so the diode is reverse-biased. The output capacitor supplies energy to the output load.

When the switch is opened, the primary current and magnetic flux drops. The secondary voltage is positive, forward-biasing the diode, allowing current to flow from the transformer. The energy from the transformer core recharges the capacitor and supplies the load.

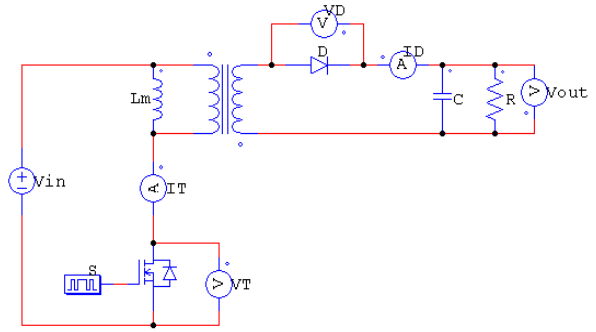

Figure7. Schematic of Flyback coupled with ideal transformer

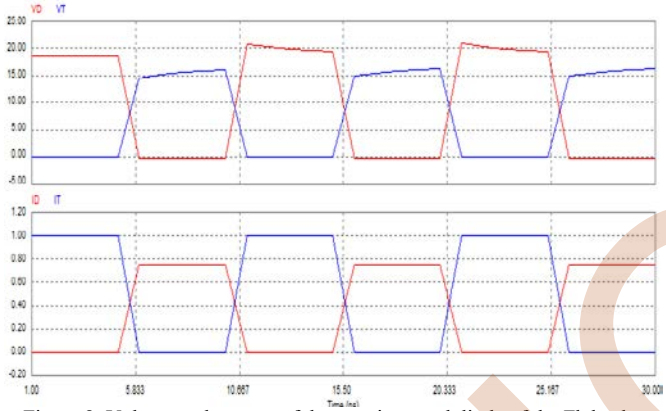

Figure 8. Voltage and current of the transistor and diode of the Flyback with an ideal micro-transformer

Figure 9 shows the schematic of converter simulated coupled with integrated micro-transformer. Figure 10 shows the waveform of the output voltage and current of the transistor and diode of the Flyback. We observe the same result with ideal transformer and integrated planar micro-transformer.

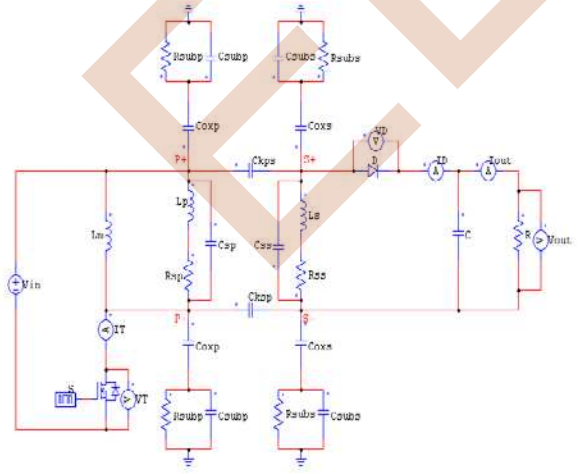

Figure 9. Schematic of Flyback coupled with an integrated micro-transformer

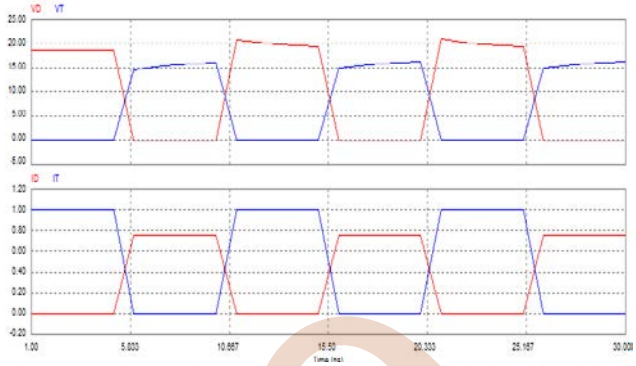

Figure 10. Voltage and current of both transistor and diode of the Flyback with an integrated micro-transformer

VI. MAGNETIC EFFECT IN A PLANAR MICRO-TRANSFORMER

In this section, we present the distribution of the magnetic field in a planar micro-transformer in the air and on substrate using finite elements method [12,19].
Figure 11 shows the distribution of the electric field and magnetic field lines in the planar micro-transformer in the air. This electric field is important to the input of the integrated planar micro-transformer. The magnetic flux density lines are concentrated around the component and are bounded by the borders.

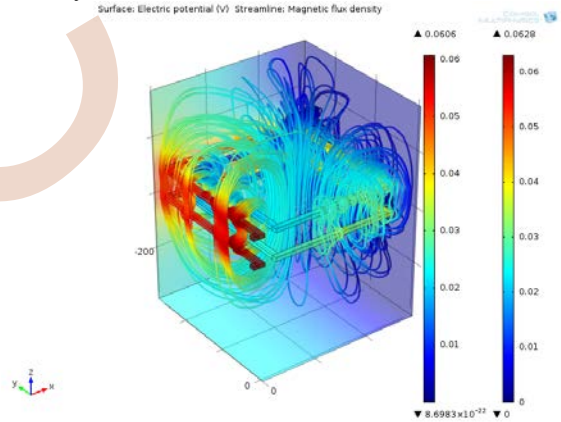

Figure 11. Distribution of magnetic field lines in the planar micro-transformer in the air

Figure 12 shows the distribution of the electric field and the magnetic field lines in the planar micro-transformer on substrate. When we insert a multi-layer of the insulating, the majority of the magnetic field lines are concentrated at the substrate. These layers can reduce the value of resistance. So, we conclude that the substrate is required to have a good electromagnetic compatibility in the case of the integration of a planar micro-transformer.

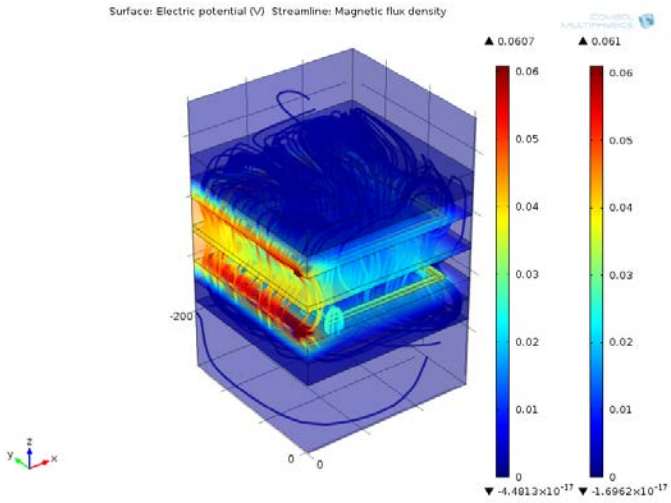

Figure 12. Distribution of magnetic field lines in the planar micro-transformer on substrate

VII. THERMAL EFFECT IN A PLANAR MICRO-TRANSFORMER

In this section, we present the temperature distribution in our integrated micro-transformer, based on the finite element method [20]. This distribution is obtained by solving the equation (7) of heat taking into account certain boundary conditions [21].

$$\rho.C_p \frac{\partial T}{\partial t} - \nabla(k\nabla T) = q \quad (7)$$

For an integrated micro-transformer in the air, the heat source can be expressed as (8)

$$q = \frac{P_j}{V} \quad (8)$$

For an integrated micro-transformer on substrate, the heat source is defined as (9)

$$q = \frac{P_{j+}P_{ed} + P_f}{V} \quad (9)$$

In figure 13, we observe the temperature distribution in the micro-transformer on the air. We see that the temperature attained is from 43 °C.

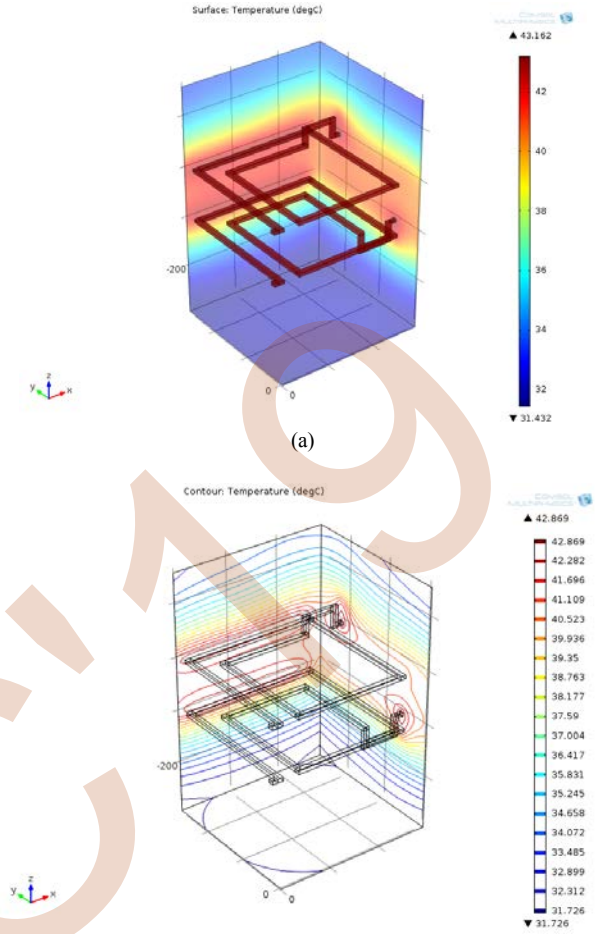

Figure 13. Temperature distribution in the micro-transformer on the air, (a) on general surface, (b) on contour

In figure 14, we observe the temperature distribution in the planar micro-transformer on substrate. We see from these figures that the temperature is about 33°C. It is shown that the temperature is reduced.

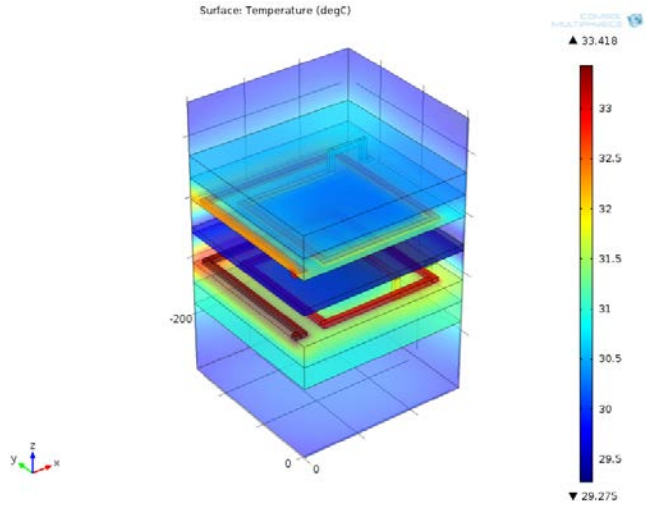

(a)

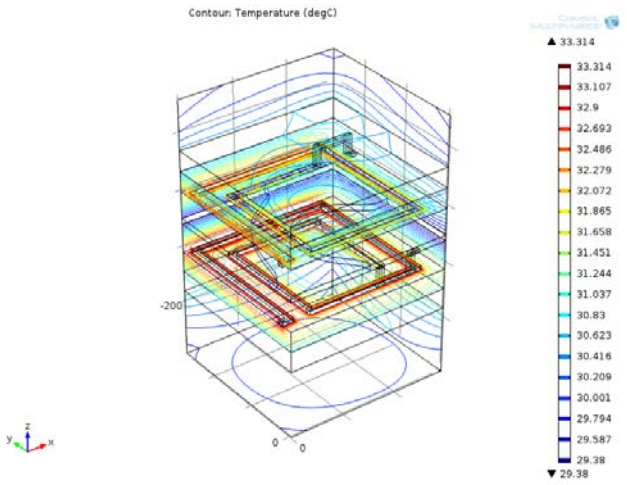

(b)

Figure 14. Temperature distribution in a planar micro-transformer on substrate, (a) on general surface, (b) on contour

VIII. CONCLUSION

This paper contains an integration of square spiral planar micro-transformer presented in a converter Flyback.

We have visualized the magnetic phenomenon in our integrated micro-transformer in the air and on substrate. When we insert a magnetic core, the majority of the magnetic field lines are concentrated at the walls of the magnetic block. We conclude that the substrate layer is required to have a good electromagnetic compatibility in the case of the integration planar micro-transformer.

For a good visualization of thermal behavior in our component, we have presented the temperature distribution, based on the finite element method. When we insert a substrate, the losses decrease. So, the heat source decrease and the value of the temperature decrease.

ACKNOWLEDGMENT

Yamina BENHADDA was born in Ain Temouchent, Algeria in 1982. He obtained his Doctorate degree in electrical engineering at Mohamed Boudiaf University of Sciences and Technology of Oran in 2016.

Second Author Azzedine HAMID was born in Alger, Algeria in 1961. He obtained his Magister degree in electrical engineering at Mohamed Boudiaf University of Oran in 1994. He received his PhD in 2005 from Mohamed Boudiaf University of Sciences and Technology of Oran.

REFERENCES

[1] J. Kim, J-. k. Kim, M. Kim, F. Herrault, M. G. Allen, "Microfabrication of totoidal inductors integrated with nanolaminated ferromagnetic metallic cores,» *Journal of Micromechnics and Microengineering*, vol. 23, no. 11, pp. 114006, Nov. 2013.

[2] J. Kim, M. Kim, F. Herrault, J. Y. Park, and M. G. Allen, "Electrodeposited nanolaminated CoNiFe cores for ultracompact DC-DC power conversion, " *IEEE Transactions on Power Electronics*, vol. 30, no. 9, pp. 5078-5087, Sep. 2015.

[3] D.D. Yaya, M.B. Bechir, M.K. Youssouf, M. Soultan, F. Kahlouche, S. Capraro, A. Siblini, J.P. Chatelon and J.J. Rousseau, " Characterization of integrated inductors with one and two YIG layers for low-power converters (1W), " *published by EDP Sciences*, 2014.

[4] M. Derkaoui, A. Hamid, T. Lebey, R. Melati, "Design and modeling of an integratedmicrotransformer in a flyback converter, " *Telkomnika*, 11(4), pp. 669-682, 2013.

[5] Sabrije Osmanaj , Erdet Nasufi, " Design of an integrated planar inductor using 0.35 µM fabrication technology," *17th International Research/Expert Conference*, Istanbul, Turkey, 10-11 September 2013.

[6] S S Mohan, M d M Hershenson, S P Boyd, and T H Lee " Simple Accurate Expressions for Planar Spiral Inductances, " *IEEE Journal of solid-state circuits*, 1999; vol. 34, no 10, pp. 1419-1424.

[7] J. M. Wright, D. W. Lee, A. Mohan, A. Papou, P. Smeys, and S. X. Wang, "Analysis of integrated solenoid inductor with closed magnetic core, " *IEEE Transactions on Magnetics*, vol. 46, no. 6, pp. 2387-2390, Jun. 2010

[8] C. R. Sullivan, D. V. Harburg, J. Qiu, C. G. Levey, and D. Yao, "Integrating magnetic for on-chip power: a perspective, *" IEEE Transactions on Power Electronics*, vol. 28, no.9, pp. 4342-4353, Sep. 2013.

[9] Haitao Gan, "On-chip transformer modeling, characterization, and applications in power and low noise amplifiers, " *these of stanford university*, March 2006.

[10] H. Yun, J. M. Kikkawa, J.Kim,T. Paik, C. R. Kagan, L. Meng, Mark G. Allen, P.S. Jo, and C. B. Murray, "Alternate current magnetic property characterization of nonstoichiometric zinc ferrite nanocrystals for inductor fabrication via a solution based process, " *Journal of applied physics 119*, p 113901-1 113901-9 (2016)

[11] Ichiro Aoki, "Distributed Active Transformer—A New Power-Combining and Impedance-Transformation Technique, " *IEEE Transactions on microwave theory and techniques*, Vol. 50, No. 1, January 2002, p 316-331

[12] Ichiro Aoki, "Fully Integrated CMOS Power Amplifier Design Using the Distributed Active-Transformer Architecture, " *IEEE Journal of solid-state circuits*, Vol. 37, NO. 3, March 2002, p 371-383

[13] J. Muhlethaler, J. Biela, J.W.Kolar, and A. Ecklebe, "Improved core-loss calculation for magnetic components employed in power electronic systems*," IEEE Transactions on Power Electronics*, vol.27, no.2, pp.964-973, Feb 2012.

[14] P. Viarouge, J.C .Fagundes, ETourkhani, H.Le-Huy, "Comportement thermique et conception des composants magnétiques dans les convertisseurs statiques de fréquence élevée, " 1995 IEEE, p 582-585

[15] C. Feeney, N. Wang, and S. C. O'Mathuna, "A 20-MHz 1.8-W DC-DC converter with parallel microinductors and improved light-load efficiency, " *IEEE Transactions on Power Electronics*, vol. 30, no. 2, pp. 771-779, Jan. 2015.

[16] Y. Benhadda, A. Hamid, T. Lebey, M. Derkaoui, "Design and modeling of an integrated inductor in a buck converter DC-DC, "*Journal of Nano and Electronic Physics*, 7(2), 2015, pp. 2006 (6pp).

[17] S. Lim, J. Ranson, D. M. Otten, and D. J. Perreault, "Two-stage power conversion architectures suitable for wide range input voltage, " *IEEE Transactions on Power Electronics*,vol. 30, no. 2, pp. 5078-5087, Feb. 2015.

[18] C. F. Foo, X. H. Gong, " determination of winding losses of high frequency planar-type transf0rme:r using finite-element method, "*Power Electronics and Variable Speed Drives*, 23-25 September 1996, Conference Publication No. 429, IEE, 1996, p 477-482.

[19] A. Allaoui, A. Hamid, P. Spiterri, V. bley, T. Lebey, "Thermal modeling of an integrated inductor in a micro-converter, " Journal of Low Power Electronics, 11(1), pp. 63-73, 2015.

[20] Y. Benhadda, A. Hamid, T. Lebey, A. Allaoui, M. Derkaoui, R. Melati, "Thermal behavior of an integrated square spiral micro coil, " Telkomnika, 14(2), pp. 669-682, 2015.

MAGNETOTHERMIC BEHAVIOR OF THE MICRO-TRANSFORMER

Medjaoui Fatima Zohra
Department of Electrical Engineering
University of Sciences and Technology of Oran, Mohamed BOUDIAF, Oran, Algeria
e-mail: medjaouifaz@yahoo.fr

Mokhefi Abderrahim
Department of Electrical Engineering
University Tahri Mohamed, Béchar
abderahimmokhefi@yahoo.fr
Hamid Azzedine
Department of Electrical Engineering
University Centre Nour Bachir, El Bayadh
hamidazdean@yahoo.fr

Abstract: The miniaturization, integration and collective manufacturing of passive components is a major current issue, especially for embedded devices to reduce volumes and costs. Among the so-called passive components, magnetic components (inductors and transformers) are receiving more and more attention. Indeed, these components in their conventional manufacturing technology occupy a large area and do not lend themselves to integration. In addition, advances in telecommunications require new components that can operate at increasingly higher frequencies. Thus reduce the space occupied by the inductor on a chip, improve its performance, limit its electromagnetic radiation and use manufacturing technologies compatible with those of microelectronics are important issues that mobilize many researchers.

I. INTRODUCTION

The design of an integrated transformer requires the study of the magneto thermal behavior to determine an optimum distribution of current and electrical potential in the conductor and to visualize the distribution of the temperature of the assembly, coil and substrate.

II. DIMENSIONNEMENT DU MICRO-TRANSFORMATEUR

From the specifications, we define the microconverter specifications which constitutes the starting point for the dimensioning of the micro transformer. This is consisting of two inductions deposited on a magnetic material and separated by a dielectric that also ensures the magnetic coupling. The literature shows that the magnetic core not only increases the value of inductances, confines magnetic field lines, stores more energy, but also greatly reduces the number of turns. This favors the attenuation of various spurious effects, whether at the level of the conductive ribbons or at the level of the substrate. The judicious choice of the magnetic material determines the size of the component and makes it possible to increase the value of the inductance from 10% to 100%, for the same number of turns, and the same occupied surface [1][2][3].

A. Physical model

Figures 1 (a) and (b) present the physical model of micro-transformer object of our study, including the stages of design and sizing

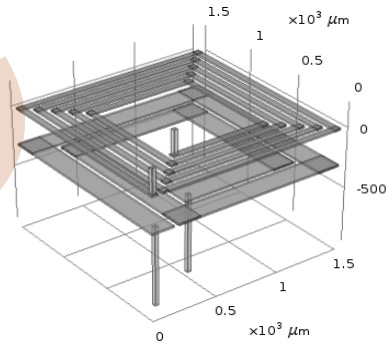

(a)

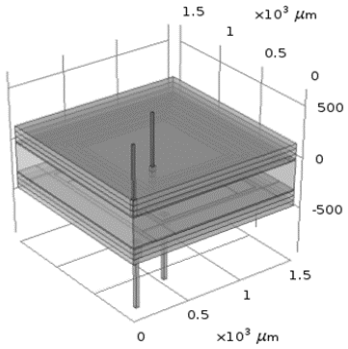

(b)

Figure 1 Physical model of micro-transformer
(a) with substrate (b) without substrate

B. Mathematical Model

Dimensioning of the micro-coils of primary and secondary: The expression (II.1) shows that the primary and secondary inductances of the micro-transformer are directly connected to the energy stored. For a maximum current, that is to say for t = αT, the expression (II.1) can be written as follows:

$$W = \frac{1}{2} L_p i_{1max}^2 = \frac{1}{2} L_s i_{2max}^2 \quad \text{(II.1)}$$

From the energy over a period we can calculate the power

$$P = \frac{W}{T} = \frac{1}{2T} L_p I_{1max}^2 \quad \text{(II.2)}$$

Let's replace I1max with its value

$$I_{1max} = \frac{V_e . \alpha T}{L_p} \quad \text{(II.3)}$$

This power is transmitted to the load

$$P = V_s . I_s = \frac{V_e^2 \alpha^2 T}{2 L_p} \quad \text{(II.4)}$$

The value of the primary inductance Lp of the micro-transformer is derived therefrom:

$$L_p = \frac{V_s^2 \alpha^2 T}{2 . V_s I_s} \quad \text{(II.5)}$$

The transformer ratio m is given by the expression:

$$m = \frac{\alpha}{\alpha - 1} . \frac{V_s}{V_e} \quad \text{(II.6)}$$

With α = 0.5 then m equals 0.42

From the value of the primary inductance Lp and the transformation ratio m, the value of the secondary inductance Ls of the micro-transformer can be determined:

$$L_s = m^2 . L_p \quad \text{(II.7)}$$

Sizing of the magnetic core

Sizing of the magnetic core depends on the volume of the core needed to store the energy that is calculated from the density of energy and the energy stored in the windings. [4] The volume density of energy is a function of the maximum induction Bmax that the material can withstand and its relative permeability μr. To determine the volume of material required for this storage, we will have to know the density of energy characterizing this material. The density of energy is given by the equation:

$$W_{V.max} = \frac{B_{max}^2}{2 . \mu_0 . \mu_r} \quad \text{(II.8)}$$

- B_{max} : maximum magnetic field that can support the material,
- μ_r : the relative permeability of the material

C. Maxwell equations

The electromagnetic phenomenon is governed by the maxwell equations, [5] the resolution of the latter will allow us to visualize the distribution of the electric potential on the conductor and the electrical current density and that of magnetic flux. The equations are:

$$\nabla \times \vec{H} = \vec{J} \quad \text{(II.9)}$$

$$\nabla \times \vec{A} = \vec{B} \quad \text{(II.10)}$$

$$\vec{E} = -\nabla V - j\omega \vec{A} \quad \text{(II.11)}$$

$$\vec{J} = \sigma \vec{E} + j\omega \vec{D} \quad \text{(II.12)}$$

$$\nabla . \vec{J} = 0 \quad \text{(II.13)}$$

$$\vec{B} = \mu_0 \mu_r \vec{H} \quad \text{(II.14)}$$

$$\vec{D} = \varepsilon_0 \varepsilon_r \vec{E} \quad \text{(II.15)}$$

$\vec{H}$: Magnetic field [A / m] [A/m]

$\vec{B}$: Density of magnetic flux [T]

$\vec{J}$: Density of electric current [A/m2]

$\vec{A}$: Magnetic vector potential [Wb/m]

$\vec{E}$: Electric field [V/m]

$\vec{D}$: Standard of the electric displacement field [c/m2]

D. Conditions to the limits

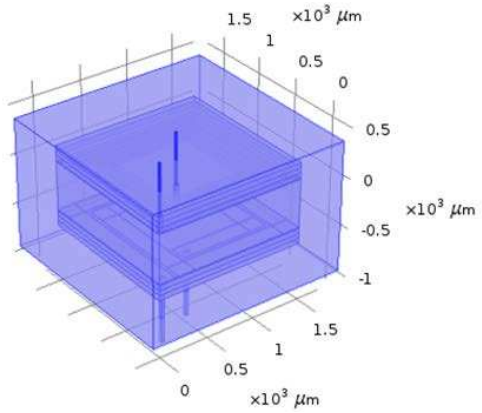

Figure .2 Domain boundaries study of the micro-transformer

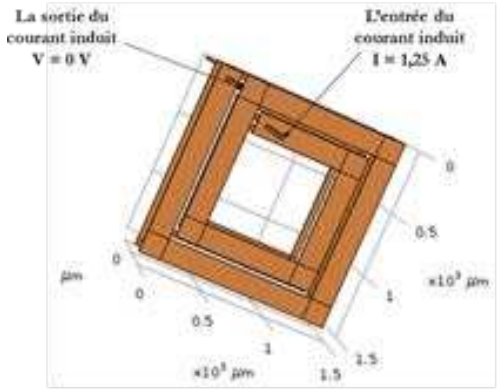

Figure.3 Initial operating conditions of the micro-transformer
(a) Input and output of the primary current (b) Input and output of the secondary power

E. *Mesh of the field of study*

The principle of the mesh [6] consists in cutting the geometric model in several triangles or figures IV.4. The operating frequency is imposed for the resolution process. The finer the mesh, the more accurate the calculation results are, however the computation time becomes larger and the data size will be larger. To have a good accuracy we proceed to an extremely fine tetrahedral mesh.

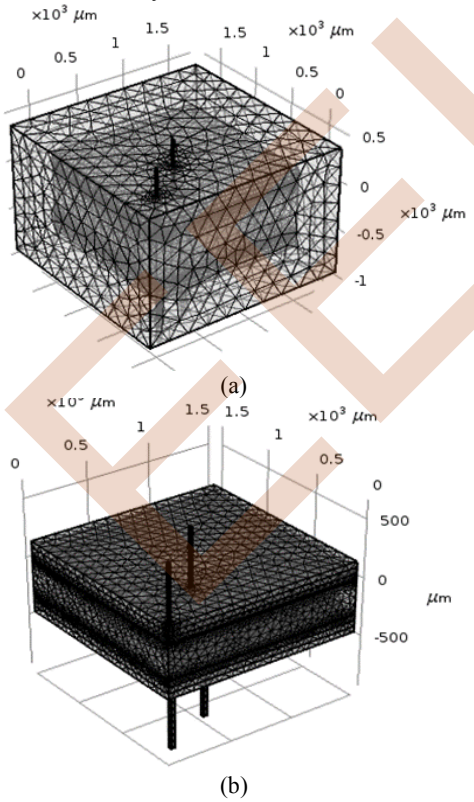

(a)

(b)

Figure .4 (a) Mesh of the field of study, (b) Mesh of the micro-transformer with substrate

III. SIMULATION RESULTS AND DISCUSSION

A. *Distribution of the electric potential*

The figure below shows the distribution of potential in the primary and secondary coils. We notice that the electric potential is maximum at the entry of the current, and decreases along the spiral because of the resistance of the driver.

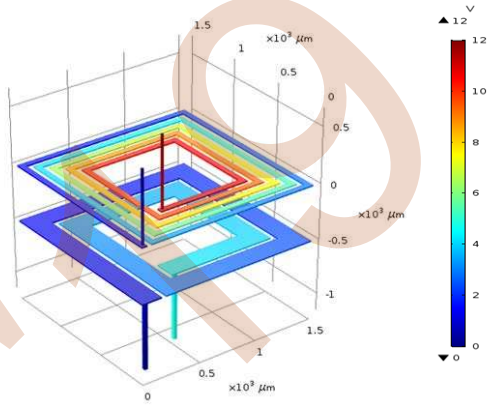

Figure .5 Potential distribution in the coils of the micro-transformer

1) *Influence of the gap on the distribution of the magnetic field*

Figures 6 and 7 show the distribution of the density of the magnetic field in our micro-transformer, 3D and 2D. These field lines are first confined to the small gaps and disperse in the gap space as the gap increases.

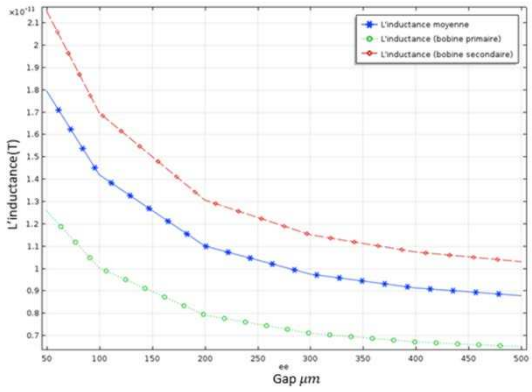

Figure .6 Variation of the inductance of the coil according to the gap

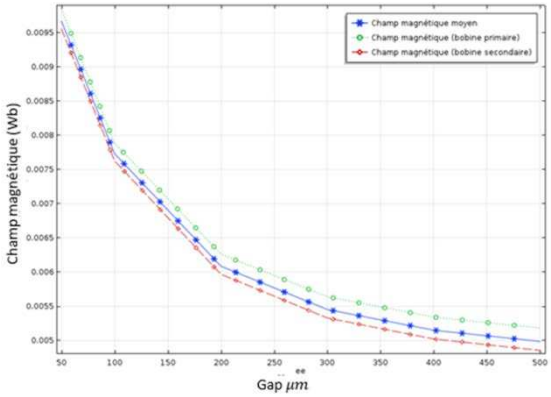

Figure.7 Variation of the density of the field according to the gap

IV.STUDY OF THE THERMAL BEHAVIOR OF THE MICRO-TRANSFORMER

The objective of this study is to visualize the distribution of the temperature in our device

A. Physical model

Figure 8 shows the physical model of the micro-transformer. In this case, the following considerations must be taken into account:

• Isotropy of different materials in the field of study
• The coefficient of thermal conductivity depends on the temperature.
• Thermal convection is introduced as a boundary condition of the substrate-micro coil assembly.1 Contours des iso-températures.

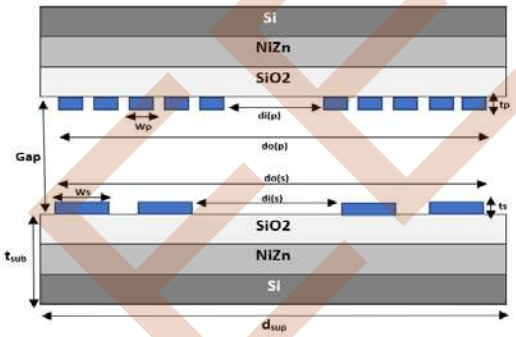

Figure.8 Longitudinal section of a micro-transformer

1) Influence of the gap on the distribution of the temperature in the micro-transformer

a) Contours of iso-temperatures

The temperature contours clearly show the way in which the temperature is distributed in the study set, they visualize the places where the temperature is high or low.

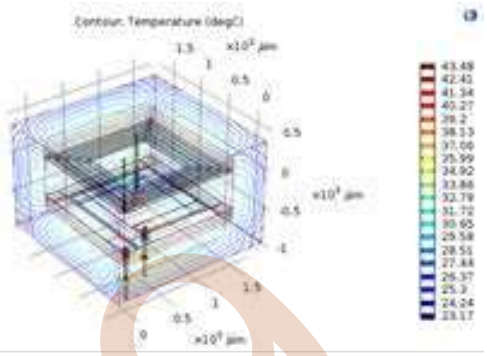

Figure.8 Distribution of the temperature in the micro-transformer iso values of the temperature in the field.

b) Distribution of the temperature in the different layers of the primary and secondary

In this section, we present the transverse distribution of the temperature in the micro-transformer.

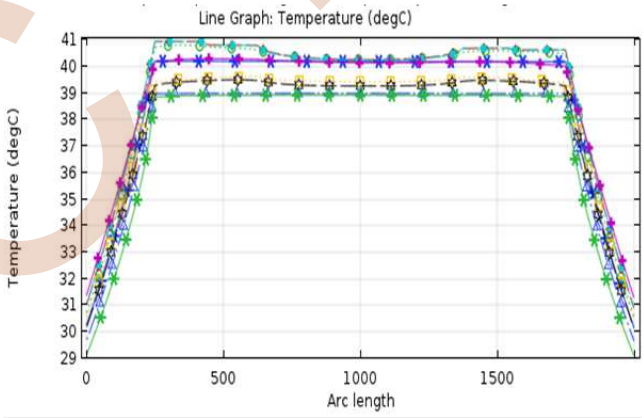

(a)

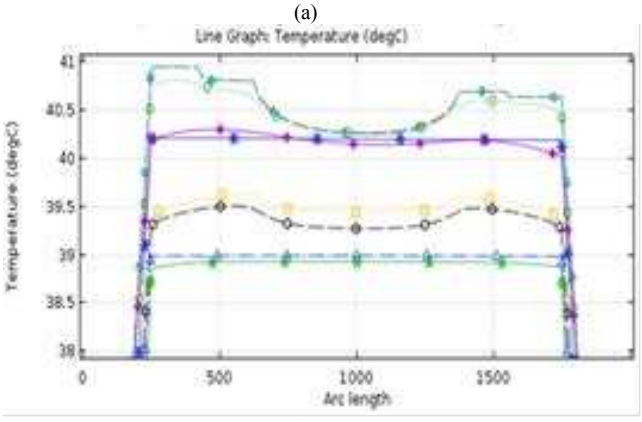

(b)

Figure.10 (a) global graphs of the temperature slices, (b) visualization of the upper part of the graph

From the analysis of the above curves, it can be deduced [7] that the thermal behavior of the secondary and primary coils

are of the same qualitative appearance, but their values are different.

CONCLUSION

In this work we have contributed numerically to the electrothermal study of a planar micro-transformer where the primary with five turns and the secondary with two turns. The numerical simulation done by introducing the electromagnetism equations combined with the heat equation was solved by the finite element method using COMSOL Multiphasics software. These simulations allowed us to deduce the following points: There is a very important relationship between the field of power electronics and the field of energetics in mechanical engineering where this work consolidates the physical aspects connecting the two fields in the near future. Most of the electrical function optimizations have been done considering only the electromagnetic aspects which would have been still reliable and consistent if one had introduced the thermal aspects.

The studied transformer is characterized by the existence of a layer of SiO2 between the primary and the secondary, the thickness of this layer plays a role inversely proportional to the magnetic field.

The magnetic field increases in the transformer by comparing its results with those of a planar micro-coil.

The thermal behavior of the transformer is totally related to the density of the electric current where the latter has a positive influence on the increase of the temperature on the conductor which favors the conductive transfer throughout the field of study.

The maximum temperatures have occurred at the entry and exit of the primary and secondary since the small section of the conductor wires (hereinafter called vias) that contribute to a considerable increase in heat flow generated.

Our thermal simulation would have been well optimized thermally (reduced temperature) if we had taken input and output son (vias) of the same section as the planar coil, resulting in an almost identical generation of heat flow by the Joule effect.

This work is an extension of a micro-coil design dimensioned by [7] from which we had the idea to constitute a transformer by the same micro-coil to determine the effect of the physical quantity interference (electromagnetic and thermal) where it was noted that the temperature to increase and all other aspects have changed relatively.

REFERENCES

[1] Jean-Paul Ferrieux et François Forest, *Alimentations à découpage : Convertisseurs à résonance, principes, composants, modélisation*, Dunod, 2006.

[2] C.C. Tang, C.H. Wu, S.I. Liu, «Miniature 3-D inductors in standard CMOS process, IEEE Journal of Solid-State Circuits, 2002.

[3] A. Salles, "Conception d'éléments passifs pour convertisseurs de faible puissance," Ph.D.Dissertation, Université Toulouse III - Paul Sabatier, 2008. 16, 137

[4] Y..Benhadda "*Modelisation thermique des composants Magnétiques integres dans les microsystemes*" These de Doctorat soutenue à l'Université de 'université de Mohamed boudiaf,soutenue Juin 2016

[5] A.Allaoui, "Etude des phénomènes thermiques dans une micro-bobine planiare", Thèse de Doctorat soutenue à l'université Mohamed Boudiaf d'Oran, 2017.

[6] FZ.Medjaoui "Conception d'une inductance planaire sur nife application : micro convertisseur abaisseur DC/DC", Thèse de Doctorat soutenue à l'université Mohamed Boudiaf d'Oran, 2019.

[7] Y. Yorozu, M. Hirano, K. Oka, and Y. Tagawa, "Electron spectroscopy studies on magneto-optical media and plastic substrate interface," IEEE Transl. J. Magn. Japan, vol. 2, pp. 740–741, August 1987 [Digests 9th Annual Conf. Magnetics Japan, p. 301, 1982].

Cyclic Venturini Modulation based Matrix Converter in Wind Energy Conversions Applications

Yazid BERKANI, Nabil TAIB
Laboratoire LTII, Département de Génie Electrique
Université de Bejaia
06000, Bejaia, Algeria
berkaniyazid@gmail.com

***Abstract*—This paper discusses the benefits of cyclic Venturini modulation controlled Direct Matrix Converter (DMC) in wind energy conversions system based on three phase squirrel cage induction generator. Three to three phase DMC and the proposed modulation control technique were presented. The global model of the proposed system was tested by simulation under Matlab/Simpowersys environment. The obtained results show clearly the contribution of DMC advantages and the proposed modulation technique on wind energy, such as good input and output current waveforms and operation with unity input power factor, bidirectional power flow and better quality of injected power to the grid.**

Keywords: Direct matrix converter, Venturini modulation, cyclic Venturni modulation, squirrel cage induction generator.

I. INTRODUCTION

Matrix converter (MC) is one of the direct frequency converters the most promising, thanks to their advantages compared to Back To Back (BTB) converter such as the lack of DC-link stage which makes it small, very, robust and reliable. It also offers a bidirectional power flow capability, sinusoidal input/output current and adjustable input power factor [1-4]. It is composed by bi-directional semiconductor switching elements connected in a matrix between the input and output lines.

In the literature, many research papers have been published on the development of several MC topologies such as Indirect Matrix Converter (IMC) [2], Sparse Matrix Converter (SMC) [3], Ultra Sparse Matrix Converter (USMC) [4], in the aim to reduce the number of semiconductor switches and Hybrid Matrix Converter (HMC) that allows increasing the voltage ratio[5]. Also on the applications of these kinds of converters in drive system [2] and in renewable energy system [6-7]. Hence, developing new modulation strategies [2][8]. It can be find scalar approach such as Venturini and Roy [1][8] and Space Vector Modulation (SVM) approaches [8-9].

Attention was given to cyclic Venturini modulation technique [10-12]. It is a modified Venturini modulation method with a double-sided symmetrical switching sequence that changes cyclically according to the input vector position. This method has been used in this work.

Several studies were carried out on the use of MC and their different topologies on Wind Energy Conversions System (WECS) instead of BTB converter. In [7], DMC is used for WECS based Doubly Fed Induction Generator (DFIG) and Squirrel Cage Induction Generator (SCIG) in [13-16]. In [17], an HMC which consists on quasi-Z-source matrix converter used to interface Permanent Magnet Synchronous Generator (PMSG) to the grid. Three level sparse topology was proposed in [6] for DFIG.

WECS based SCIG has been used in this work due to simple structure, robustness, low cost and better reliability [13-16][18]. Space Vector Pulse Width Modulation strategy (SVPWM) is used in [16]. In [15], authors used SVM and Venturini modulation techniques to control DMC. The obtained results show that there are a spikes in line to line output voltage of DMC when Venturini modulation is applied. This spikes can be removed using the proposed modulation strategy.

This paper presents DMC interfaces the SCIG with grid. Cyclic Venturini modulation is used to control DMC. In the other word, the advantages of both matrix converter and SCIG are combined and presents the interest of using cyclic Venturini modulation method.

II. DESCRIPTION OF THE GLOBAL SYSTEM

Fig. 1 presents the global scheme of the system to be studied, consisting of a three phase SCIG connected to the grid through direct matrix converter that is formed of nine bidirectional switches.

SCIG modeling is performed using electrical, mechanical and electromagnetic equations in the *dq* synchronous reference frame as it is discussed in [18]. The gear box is inserted between wind turbine and SCIG which steps up the shaft speed to extract maximum power over a wide range of wind velocity [15]. Mathematic models of wind turbine and gear box are developed in [13].

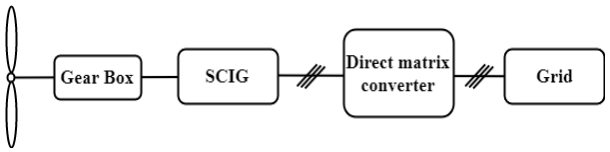

Figure 1. Block diagram of the proposed system.

Cyclic Venturini modulation technique is applied to DMC. It consists to calculte duty cycles for nine switches using Venturini technique and changing switching sequence according to input voltage space vector.

III. THREE TO THREE PHASE DIRECT MATRIX CONVERTER

The three to three phase DMC allows to connect any of the three input phases on any of the three output lines, as shown Fig. 2. Each power switch is equipped with two anti-parallel connected IGBTs and diodes; it is characterized by a switching function, that if $S_{Kj}=1$ the switch is closed and if $S_{Kj}=0$ the switch is opened.

With $K=\{A,B,C\}$ and $j=\{a,b,c\}$.

MC is fed by a voltage source, for this reason, the input terminals should not be short-circuited. On the other hand, the load has typically an inductive nature so an output phase must never be opened. The constraints discussed above can be expressed by (1).

$$S_{Aj}+S_{Bj}+S_{Cj}=1 \tag{1}$$

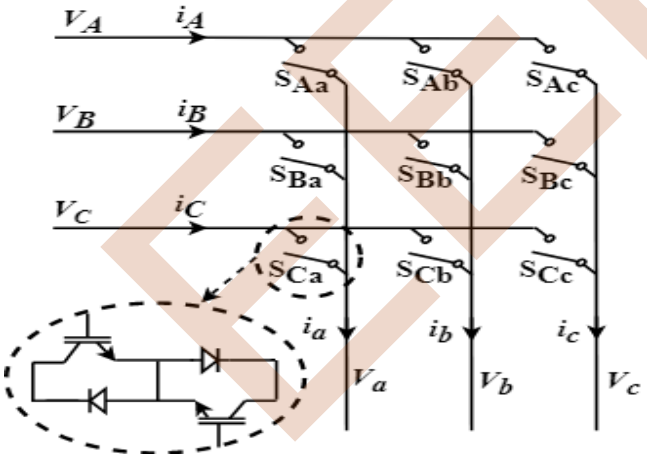

Figure 2. Three to three phase matrix converter topology.

The inputs and outputs voltages and currents of MC are expressed by (2),(3),(4) and (5).

$$v_K=\left\{V_{in}\cos(\omega_i t+(l-1)\frac{2\pi}{3})\right\}_{l=1}^{3} \tag{2}$$

$$i_K=\left\{I_{in}\cos(\omega_i t+(l-1)\frac{2\pi}{3})\right\}_{l=1}^{3} \tag{3}$$

$$V_j=\left\{qV_{in}\cos(\omega_o t+(n-1)\frac{2\pi}{3})\right\}_{n=1}^{3} \tag{4}$$

$$i_j=\left\{I_{om}\cos(\omega_o t+(n-1)\frac{2\pi}{3}+\varphi)\right\}_{n=1}^{3} \tag{5}$$

Where V_{in},V_{om} are peak values of input and output voltages; I_{in},I_{om} are peak values of input and output currents; ω_i,ω_o are input and output frequency respectively; φ is the load p.f angle; $q=V_{om}/V_{in}$ is voltage ratio.

The relation between the output voltages and the input voltages and that the input currents and output currents is defined in (6).

$$V_j(t)=[M(t)].v_K(t) \quad i_K(t)=[M(t)]^T.i_j(t) \tag{6}$$

$[M(t)]$ is modulation matrix and can be expressed by (7).

$$M(t)=\begin{bmatrix} m_{Aa}(t) & m_{Ba}(t) & m_{Ca}(t) \\ m_{Ab}(t) & m_{Bb}(t) & m_{Cb}(t) \\ m_{Ac}(t) & m_{Bc}(t) & m_{Cc}(t) \end{bmatrix} \tag{7}$$

$[M(t)]^T$ is the transpose matrix of $[M(t)]$.

Where duty cycle m_{Kj} of switch S_{Kj} is expressed by (8).

$$m_{Kj}=t_{Kj}/T_s \tag{8}$$

t_{Kj} is switch ON time for switch S_{Kj}, $T_s=1/f_s$ is switching period and f_s is switching frequency.

IV. CYCLIC VENTURINI MODULATION STRATEGY

Venturini modulation method allows to connect each output phase to the input phases for a fixed time t_{Kj} in a single sided fixed switching sequence, for example, output phase a is connected to input phase A then B then C during each switching sequence T_s as shown Fig.3.

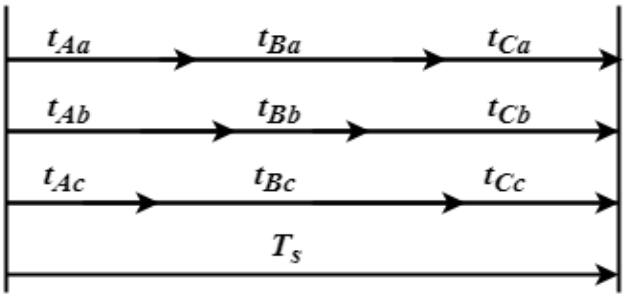

Figure 3. Switching sequence.

The nine duty cycles are calculated by (9).

$$m_{Kj} = \frac{1}{3}\left[1 + \frac{2v_k V_j}{V_{in}^2}\right] \quad (9)$$

The limitation of the solution presented in (9) is that the voltage ratio of the converter cannot exceed *q=0.5*.

By injecting the third harmonic of the input voltage and the third harmonic of the output voltage, the desired output voltages will be recalculating in (10) and the voltage ratio will increase to *q=0.866*. The desired output voltages waveforms after injecting the harmonics are shown in Fig. 4 where $V_{in} = 220\sqrt{2}$, $f_i = 50Hz$ and $f_o = 100Hz$.

$$V_j = \left\{ \begin{array}{l} qV_{in}\cos(\omega_o t + (n-1)\frac{2\pi}{3}) \\ -\frac{1}{6}\cos(3\omega_o t) + \frac{1}{2\sqrt{3}}\cos(3\omega_i t) \end{array} \right\}_{n=1}^{3} \quad (10)$$

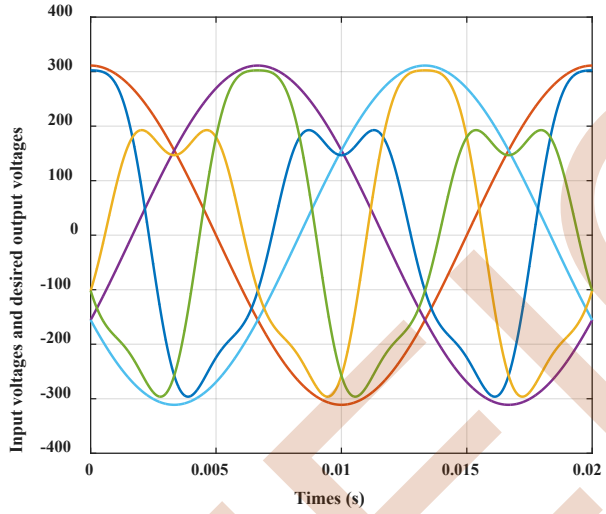

Figure 4. Desired ouput voltages waveforms.

For *q=0.866* the duty cycles are recalculated by (11).

$$m_{Kj} = \frac{1}{3}\left[1 + \frac{2v_k V_j}{V_{in}^2} + \frac{4q}{3\sqrt{3}}\sin(\omega_i t + \beta_k)\sin(3\omega_o t)\right] \quad (11)$$

where $\beta_k = \left\{0, \frac{-2\pi}{3}, \frac{2\pi}{3}\right\}$ for $K = \{A, B, C\}$ respectively.

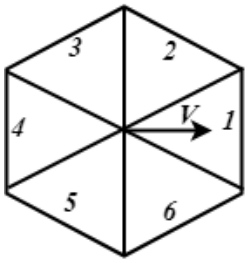

Sector	Sequence
1 , 4	C-A-B-B-A-C
2 , 5	B-C-A-A-C-B
3 , 6	A-B-C-C-B-A

Figure 5. Input voltage space vector and Switching sequence.

The principle of cyclic Venturini method is to use the same duty cycles that are calculated earlier by Venturini modulation method but with a double sided symmetrical switching, for example, A-B-C-C-B-A as illustrated in Fig. 6. The sequence changes cyclically according to the sector in which the input space vector is located, as shown in Fig. 5. The input voltages are expressed as space vector using (12).

$$V = \frac{2}{3}\left(v_A + e^{j\frac{2\pi}{3}}v_B + e^{j\frac{4\pi}{3}}v_C\right) \quad (12)$$

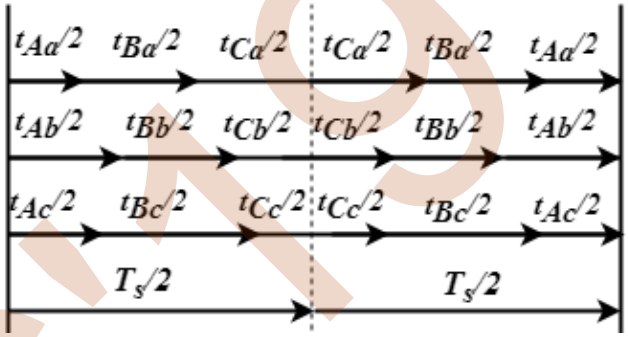

Figure 6. Switching sequence.

V. SIMULATION RESULTS AND DISCUSSION

The proposed system performances are analyzed using Matlab/simpowersys environment. A switching frequency of $f_s = 5kHz$ was considered. The parameters of the three phase SCIG are summarized in Table I.

It is worth noticing that the behavior of the wind turbine and its gear box are substituted by a variable mechanical torque input.

TABLE I. SCIG PARAMETERS

Parameters	Values
Rated power	7500 VA
Rated speed	1440 rpm
Voltage (line-line)/frequency	400 V / 50 Hz
Stator resistance/inductance	0.7384 Ω / 0.003045 H
Rotor resistance/ inductance	0.7402 Ω / 0.003045 H
Mutual inductance	0.1241 H
Inertia	0.0343 kg.m^2
Friction	0.000503 N.m.s
Pole pairs	2

The initial torque value was set to -25 *N.m*, then at *t=1s* the mechanical torque input was doubled as it is shown in Fig.7.

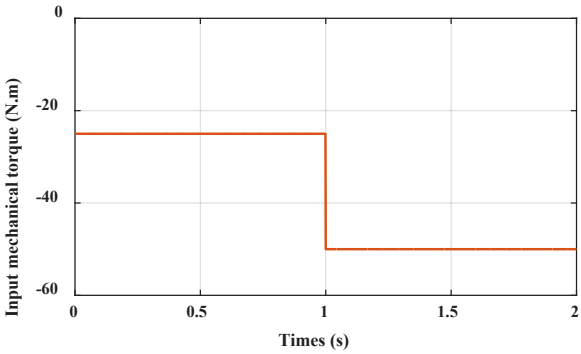

Figure 7. Input mechanical torque.

Fig. 8 shows mechanical speed of SCIG. When mechanical torque is applied, it can be seen that SCIG is in hyper-synchronism mode. The developed electromagnetic torque tracks imposed mechanical torque as it is illustrated in Fig. 9.

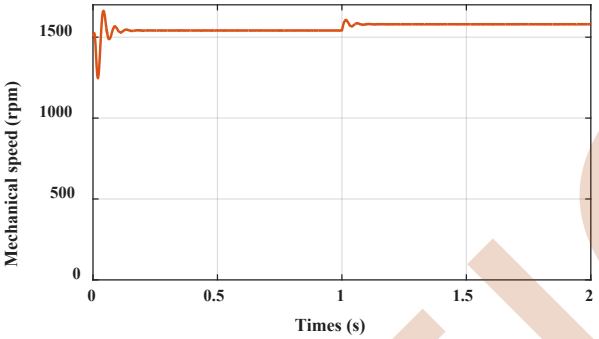

Figure 8. Mechanical speed.

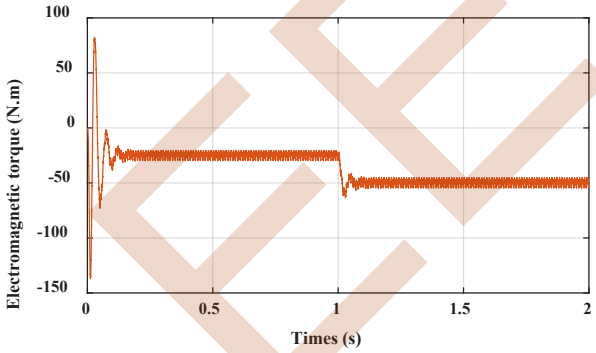

Figure 9. Electromagnetic torque.

Stator currents of SCIG present good waveforms as illustrated in Fig.10. Fig.11 gives the active power produced by SCIG that is equal to -3760 *W* and -7348 *W* from 1 *s*. The reactive power is positive sign that means the need for this energy for operating in generator mode.

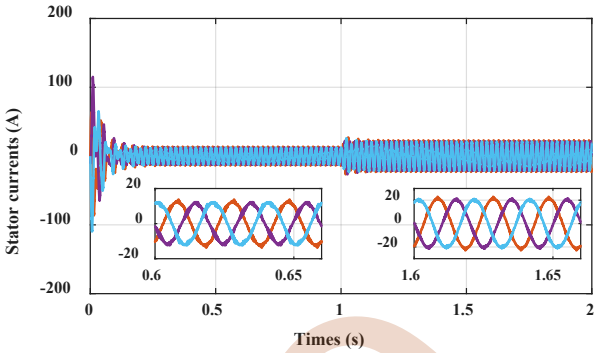

Figure 10. Stator currants of SCIG.

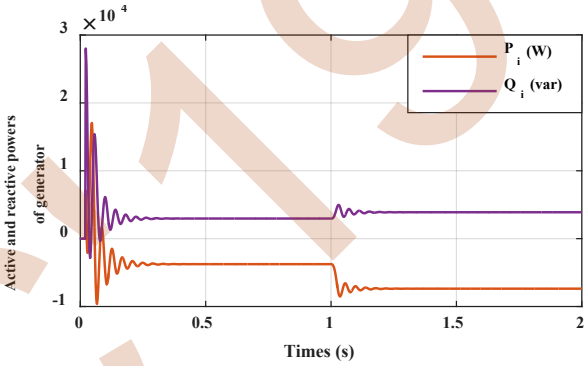

Figure 11. Active and reactive powers of SCIG.

Figs. 12 and 13 show the output voltage and output line to line voltage respectively. It can be seen that the output line to line voltage has a very good waveform thanks to the use of cyclic Venturini method. The switching sequence is changed according to the sector in which the input space vector is located as it is shown in Fig. 14.

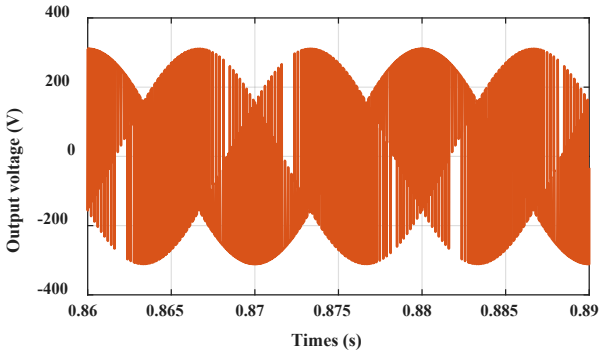

Figure 12. Ouput line to neutral voltage.

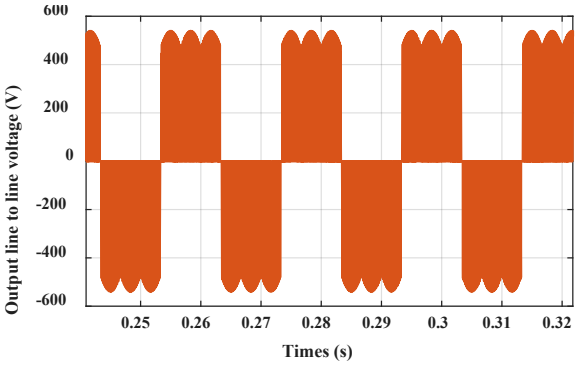

Figure 13. Ouput line to line voltage.

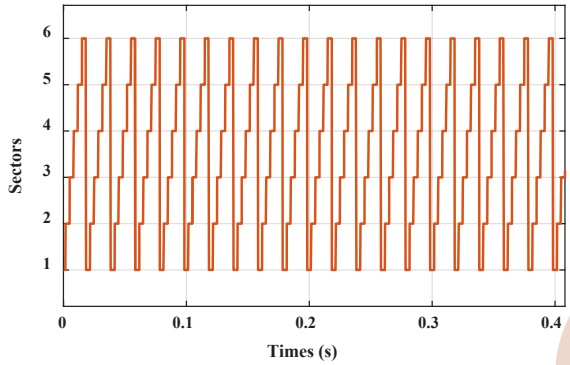

Figure 14. Sectors.

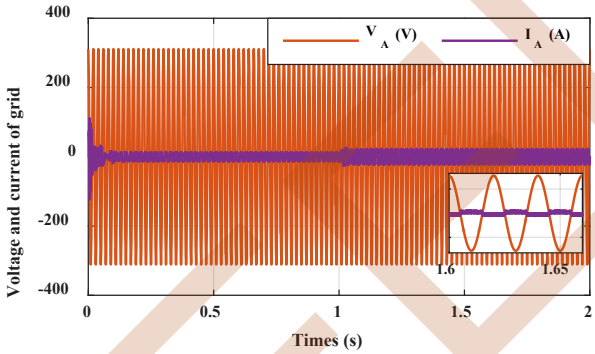

Figure 15. Unfiltered current and corresponding phase voltage.

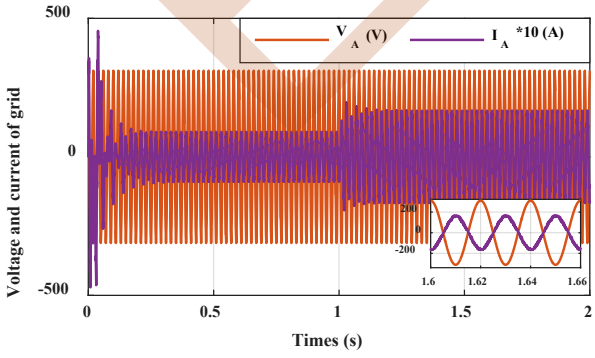

Figure 16. Filtered current and corresponding phase voltage.

Fig. 15 shows the input line-to-neutral voltage and its corresponding line current. By inserting the LC filter, the input line current has a sinusoidal waveform as shown in Fig. 16. As can be seen, the input line current and input phase voltage are in phase opposition. So, the active power is negative which means that the power generated by SCIG is injected to the grid via MC as it is shown in Fig. 17.

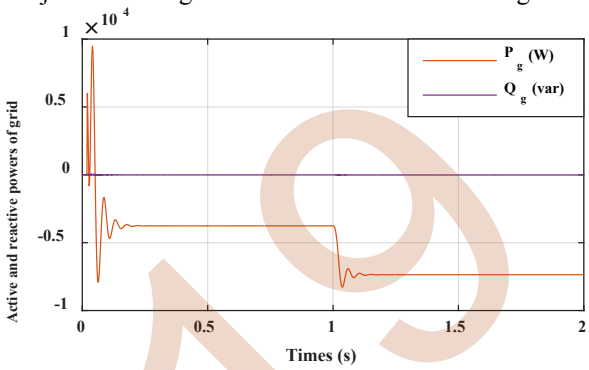

Figure 17. Active and reactive power grid side.

The THD value of output current is 2.5% and that of input current is equal to 4.92% as it is mentioned Figs. 18 and 19. The obtained THD values are lower than the value imposed by international standards (<5%). Thus, the use of cyclic Venturini modulation method gives a good input and output current waveforms.

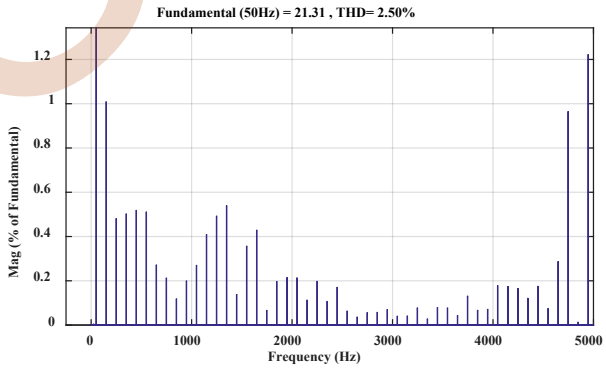

Figure 18. Output current spectrum.

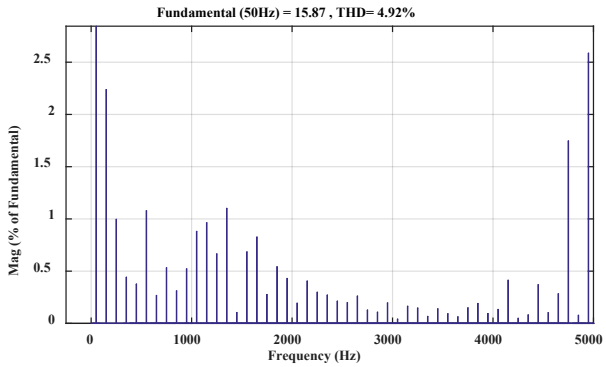

Figure 19. Input current spectrum.

VI. CONCLUSION

In this paper, cyclic Venturini modulation strategy used to control three to three phase direct matrix converter is presented. The SCIG is interfaced to the grid through a DMC. The system was tested by simulation on Matlab/Simpowersys environment. The simulation results highlighted the interesting characteristics of the matrix converter and cyclic Venturini modulation in grid connected WECS based on SCIG, such as good input and output current waveforms, bidirectional power flow and operation with unity input power factor, also the better quality of injected power.

REFERENCES

[1] M. Venturini and A. Alesina, "The generalized transformer: a new bidirectional, sinusoidal waveform frequency converter with continuously adjustable input power factor," in IEEE Power Electronics Specialists Conference, 1980, pp. 242-252.

[2] N. Taïb, B. Metidji and T. Rekioua, "A fixed switching frequency direct torque control strategy for induction motor drives using indirect matrix converter, " in Arabian Journal for Science and Engineering, 2014, vol.39, no.3, pp. 2001-2011.

[3] J.W. Kolar, F. Schafmeister, S.D. Round and H. Ertl, "Novel Three-Phase AC-AC Sparce Matrix Converters, " in IEEE Transactions on power electronics, September 2007, vol.22, no.5, pp. 1649-1661.

[4] J. Schonberger, T. Friedli, S.D. Round and J.W. Kolar, "An ultra sparse matrix converter with a novel active clamp circuit, " in IEEE Power Conversion Conference, Nagoya, appril 2007, pp. 784-791.

[5] C. Klumpner and C. Pitic, "Hybrid matrix converter topologies: An exploration of benefits, " in IEEE Power Electronics Specialists Conference, Rhodes, 2008, pp. 2-8.

[6] N. Taib, B. Metidji, and T. Rekioua, "Performance and efficiency control enhancement of wind power generation system based on DFIG using three-level sparse matrix converter, " in International Journal of Electrical Power & Energy Systems, 2013, vol.53, pp. 287-296.

[7] K. Ghedamsi and D. Aouzellag, "Improvement of the performances for wind energy conversions systems," in International Journal of Electrical Power & Energy Systems, 2010, vol.32, no.9, pp. 936-945.

[8] J. Rodriguez, M. Rivera, J.W. Kolar and P.W. Wheeler, "A Review of Control and Modulation Methods for Matrix Converters, in IEEE Transactions on power electronics, January 2012, vol.59, no.1, pp. 58-70.

[9] L. Huber and D. Borojevic, "Space vector modulated three-phase to three-phase matrix converter with input power factor correction, " in IEEE transactions on industry applications, 1995, vol.31, no.6, pp. 1234-1246.

[10] M. Apap, J.C. Clare, P.W. Wheeler and K.J. Bradley, "Analysis and comparison of AC-AC matrix converter control strategies, " in IEEE Power Electronics Specialist Conference,34th Annual, 2003, pp. 1287-1292.

[11] W.M. Rohouma, S.L. Arevalo, P. Zanchetta and P. Wheeler, "Repetitive control for a four leg matrix converter, " in 5th IET International Conference on Power Electronics, Machines and Drives, 2010. pp. 1-6.

[12] W.M. Rohouma, P. Zanchetta, P.W. Wheeler and L. Empringham, "A four-leg matrix converter ground power unit with repetitive voltage control, " in IEEE Transactions on Industrial Electronics, 2015, vol.62, no.4, pp. 2032-2040.

[13] S.M. Barakati, J.D. Aplevich and M. Kazerani, "Controller design for a wind turbine system including a matrix converter, " in IEEE Power Engineering Society General Meeting, June 2007, pp. 1-8.

[14] S.M. Barakati, M. Kazerani and X. Chen, "A new wind turbine generation system based on matrix converter, " in IEEE Power Engineering Society General Meeting, June 2005, pp. 2083-2089.

[15] V. Agarwal, R.K. Aggarwal, P. Patidar and C. Patki, "A novel scheme for rapid tracking of maximum power point in wind energy generation systems," in IEEE Transactions on Energy Conversion, 2009, vol.25, no.1, pp. 228-236.

[16] M.T Athulya and S. Subramanian, "SVPWM based control of Matrix Converter for gearless operation of wind energy power conversion system, " in IEEE Biennial International Conference on Power and Energy Systems: Towards Sustainable Energy, January 2016, pp. 1-6.

[17] M. Alizadeh and S.S. Kojuri, "Modelling, control, and stability analysis of quasi-Z-source matrix converter as the grid interface of a PMSG-WECS," in IET Generation, Transmission & Distribution, 2017, vol.11, no.14, pp. 3576-3585.

[18] M. Rahimi and M. Asadi, "Control and dynamic response analysis of full converter wind turbines with squirrel cage induction generators considering pitch control and drive train dynamics, " in International Journal of Electrical Power & Energy Systems, 2019, vol.108, pp. 280-292.

Two-level Voltage Source Converter for High-Voltage Direct Current Transmission Systems

Khadidja CHENNA
Laboratoire de Maitrise des Energies Renouvelables, Faculté de Technologie, Université de Bejaia 06000, Algérie
chennakhadidja@gmail.com

Mouloud ADLI
Laboratoire de Génie Electrique, Faculté de Technologie, Université de Bejaia 06000, Algérie
mulud_adli@yahoo.fr

Kaci GHEDAMSI
Laboratoire de Maitrise des Energies Renouvelables, Faculté de Technologie, Université de Bejaia 06000, Algérie
kghedamsi@yahoo.fr

***Abstract*— In the context of a future global grid, High Voltage Direct Current (HVDC) links will play a central role. New technologies of semi-conductors and control devices have made possible HVDC project with Voltage Source Converters. This technology has several advantages, allowing it to make a growing presence in the HVDC projects. A new topology of VSC has been developed in recent years. This paper presents two-level voltage source converter for dc transmission systems. We will introduce HVDC. The models and results are presented and tested by simulations using Matlab Simulink and its toolbox SimPowerSystems.**

Keywords: **HVDC; VSC-HVDC; control design.**

I. INTRODUCTION

The traditional electric power system based on 3-phase ac transmission technology in general functions well and with good levels of availability and reliability[2]. There are however challenges mainly arising from the increasing share of renewable generation, which will most likely increase the level of variability and unpredictability in electric power grid operation, increased needs for reserve power for power balancing, and will require more flexible power flow control[1]. Other challenges include requirements from the electric power market, such as relieving transmission bottlenecks, and the difficulties of obtaining new transmission corridors because of the environmental impact[2]

High Voltage Direct Current (HVDC), especially the Voltage Source Converter (VSC) HVDC, is a feasible and attractive technology to fulfil almost all above challenges, due to its distinct advantages in the areas of controllability and flexibility. The benefits from applying VSC-HVDC in the traditional ac grid include independent control of active and reactive power, very fast control response, using cable, ability to connect to weak system, black start ability, and facilitating the construction of multi-terminal system or even complete dc grids.

The need for utilities to understand the issues surrounding interconnection of remote resources – in particular offshore wind located out at sea or in freshwater – via HVDC in a planning context is growing worldwide as implementation becomes more common

II. THE COMPONENTS OF AN HVDC TRANSMISSION SYSTEM

The HVDC technology is used in transmission systems to transmit electric bulk power over long distances by cable or overhead lines. It is also used to interconnect asynchronous AC systems having the same or different frequency. Figure 1 shows a simplified schematic picture of an HVDC system, with the basic principle of transferring electric energy from one AC system or node to another, in any direction. The system consists of three blocks: the two converter stations and the DC line. Within each station.[5]

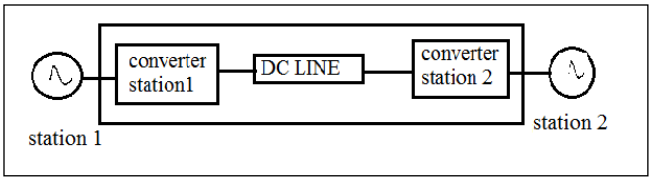

Figure 1. Basic configuration of classical HVDC systemHVDC Configurations

Different configurations of HVDC systems can be determined according to the particular application and the project considered. The main configuration lay outs are shown in this section. Independently from the converter technology, there are two main topologies for HVDC transmission systems: monopolar and bipolar[6]

A. Monopolar HVDC

As the name suggests, this configuration has only one pole, mostly of negative polarity to reduce corona effects

monopolar topologies, as well as bipolar topologies, can be further classified according to the return path used [3]

1) Symmetric Monopole: This configuration either uses no grounding at the dc circuit side or – in VSC-HVDC systems the dc link capacitors are grounded at their middle point. Due to its symmetry, this is the only topology in which the ac transformer is not subjected to dc voltage stresses, which simplifies its design. Additionally, it is the only topology in which in case of a pole-to-ground fault, the dc side is not fed by ac side currents. However, it has higher costs since it requires two fully insulated conductors.

2) Asymmetric monopole with ground Return:This topology is advantageous from a cost perspective due to the presence of only one fully insulated conductor and the possibility of expansion to a bipolar if necessary. However, it requires permission for installation of electrodes and continuous ground current, which can raise environmental concerns.[7] [3]

*3) Asymmetric monopole with metallic Return:*This topology has no ground currents, as the return is made via the metallic conductor, which does not require high-voltage insulation. This topology can be easily expanded to a bipolar.[4] [1]

All monopolar HVDC topologies lack redundancy as, in case of a dc fault, all terminals are affected by the high fault currents. Unless selective protection methods – able to isolate the faulty HVDC line in time – are implemented, the MTDC network has to be de-energized before operation is restored.

B. Bipolar HVDC topologies

Bipolar configuration employs at least two converters at each network terminal, which makes it a more costly alternative than the monopolar one[3]. However, bipolar topologies can achieve double the power rating of monopolar topologies. Each converter is connected to the ac grid via two different transformer groups, or by a transformer with two secondary windings. Usually one pole uses a Yg-Δ transformer configuration whereas the other uses a Yg-Y configuration, to reduce the ac side harmonic distortion.

As long as the DC side of the transmission system is grounded, the transformers secondary indings need to be designed for high direct-voltage stresses, namely half the direct-voltage nominal value. Hence, special attention has to be paid to their insulation. The main advantage of the bipolar configuration is its redundancy, which can be more than half the total transmission capacity if poles can be overloaded whenever one converter suffers a fault. However, there are disadvantages for each of the available bipolar topologies[3]

*1) Bipole with ground return:*Additionally to the higher costs, when compared to respective monopolar configurations, the bipolar configuration also raises environmental concerns due to ground currents when both poles are not balanced, e.g. pole outages or maintenance periods. Even though not necessary, grounding is often provided for the bipolar configuration. If there is no return path for the current, the whole HVDC transmission system will be made unavailable during faults.

*2) Bipole with metallic return:*Compared to the bipolar with ground return, this topology needs an extra low-voltage insulated neutral conductor. If injecting current in the ground

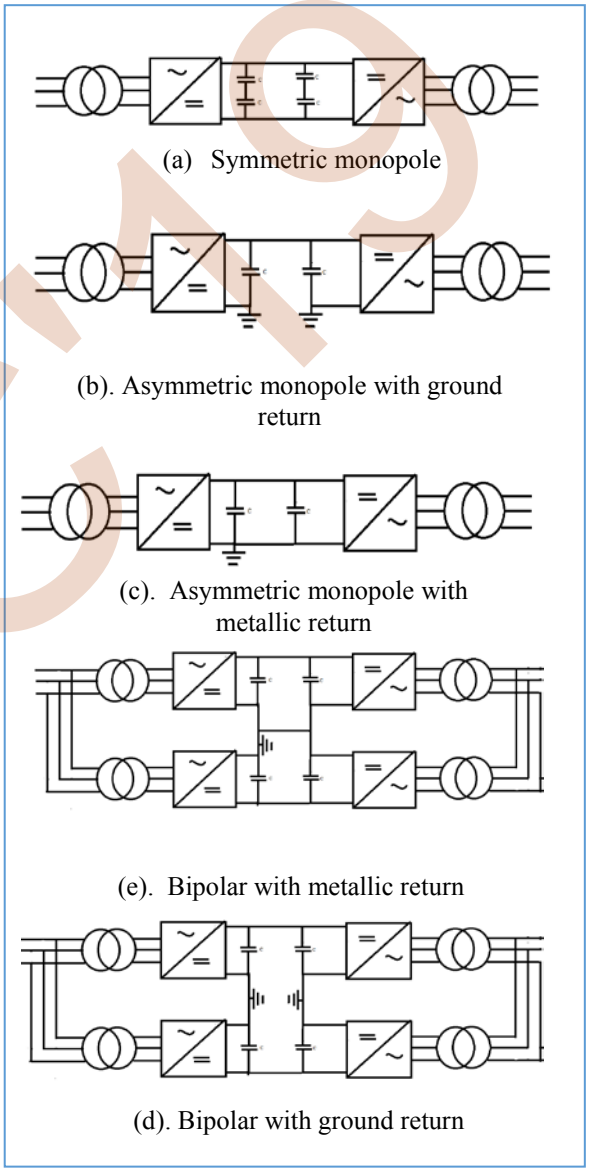

Figure 2. HVDC configurations.

III. VSC-HVDC SYSTEM-OPERATION AND CONTROL

The typical configuration of a two-terminal VSC-HVDC transmission link is illustrated in Figure 3. where two VSC stations connect two ac systems via a dc-transmission system. The two ac systems can be independent networks,

isolated from each other, or nodes of the same ac system where a flexible power transmission link is to be established. The interconnection point between a VSC station and its adjacent ac system is called the Point of Common Coupling (PCC). The main operating mechanism of a VSC station considers the ability of the VSC

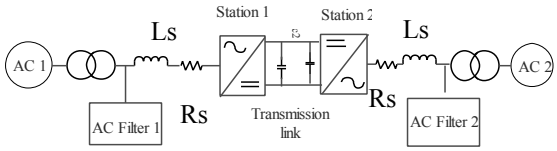

Figure 3. Twot terminal VSC-HVDCtransmission

IV. CONVERTER MODELING

This two-level topology is the simplest to use in VSC-HVDC transmission, and as shown in Figure 4, the converter can generate only two voltage values (Vdc) and (Vdc). To model the converter correctly, we assumed that the power source is defined as an infinite bus which is characterized by a three-phase voltage source and s v, line resistances R and line inductances L. Let us designate by V_{c_abc} voltage, the voltage on the network side and by V_{s_abc}, the current leaving the infinite bus. We represent the system by the following equations [1].

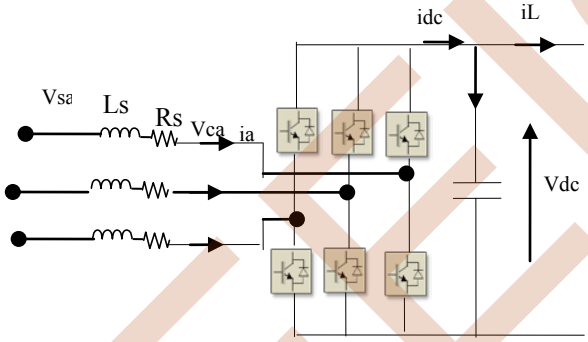

Figure 4. Figure. two-level topology with 6 switches

$$\begin{cases} L_s \dfrac{di_a}{dt} = V_{sa} - V_{ca} - R_s i_{ca} \\ L_s \dfrac{di_b}{dt} = V_{sb} - V_{cb} - R_s i_{cb} \\ L_s \dfrac{di_c}{dt} = V_{sc} - V_{cc} - R_s i_{cc} \end{cases} \quad (1)$$

V_{Sabc} : network voltage

V_{cabc} : line voltage

after the transformation of the park

$$\begin{cases} L_s \dfrac{di_d}{dt} = V_{sd} - V_{cd} - Ri_d + Lwi_q \\ L_s \dfrac{di_q}{dt} = V_{sq} - Vcq - Ri_q - Lwi_d \end{cases} \quad (2)$$

V. CONTROL STRATEGY

Generally the control strategy of a two terminal VSC-HVDC transmission line is to keep one terminal DC voltage constant as operation point, and adjust the other terminal DC current or active power order. The AC voltage or the reactive power of the two terminals can be controlled. Always in the interest of simplicity, the converter is considered ideal in the sense that it does not involve any losses[3]

Its control is that of the Figure

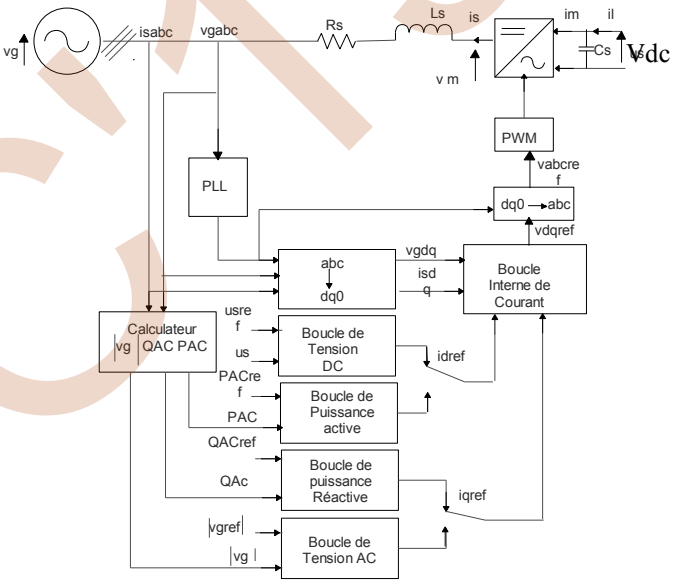

Figure 5. Overview diagram of the VSC control system

A. *Phase locked loop*

The phase locked loop (PLL) shown in fig.5 is used to synchronize the converter control with the line voltage and also to compute the transformation angle used in the d-q transformation. The PLL block measures the system frequency and provides the phase synchronous angle Θ for the d-q transformations block. In steady state, sin (Θ) is in phase with the fundamental (positive sequence) of the α component and phase A of the point of common coupling voltage (Uabc).[7]

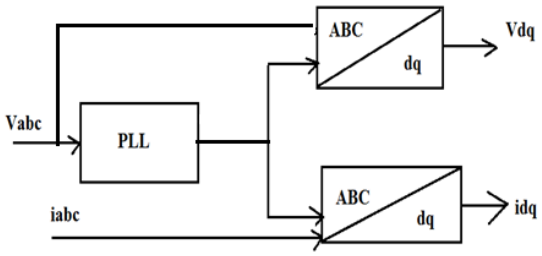

Figure 6. Phase locked loop block

The active and the reactive power

The converter is controlled in plane dq0, which is synchronized with phase a of the AC grid, using a Phase Locked Loop (PLL), so that $V_{gq} = 0$. Thus, since in plan dq0, we have

$$\begin{cases} P_{AC} = V_{gd}.i_{sd} + V_{gq}.i_{sq} \\ Q_{AC} = V_{gq}.i_{sd} - V_{gd}.i_{sq} \end{cases} \quad (3)$$

For $V_{gq=0}$:

$$\begin{cases} P_{AC} = V_{gd}.i_{sd} \\ Q_{AC} = -V_{gd}.i_{sq} \end{cases} \quad (4)$$

Thus, active power and reactive power can be controlled separately as long as we remain within the operating limits of the converter (controllability and maximum allowable voltage/current threshold).[1]

In addition, the DC voltage is linked to the active power passing through the converter, and is therefore controlled by acting on I_{sdref}.

Finally, the internal current loop generates the control signal (sent to the PWM) of v_{mabc} voltages while ensuring that the i_{sabc} currents do not exceed the maximum current of the converter. It also makes it possible to decouple i_{sd} and i_{sq}.

In the context of a future global grid, High Voltage Direct Current (HVDC) links will play a central role. New technologies of semi-conductors and control devices have made possible HVDC project with Voltage Source Converters. This technology has several advantages, allowing it to make a growing presence in the HVDC projects. A new topology of VSC has been developed in recent years.

VI. RESULTS AND DISCUSSION

The simulation parameters are gathered in table 1. The studied system, shown in figure 5, is implemented in the Matlab\Simulink software environment. The results of simulation are obtained for U_{dcref}=308kV.

The grid voltage and current are given by the figures (7-8).

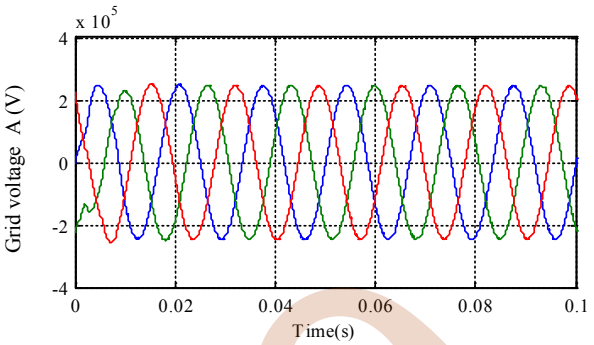

Figure 7. Grid voltage station1

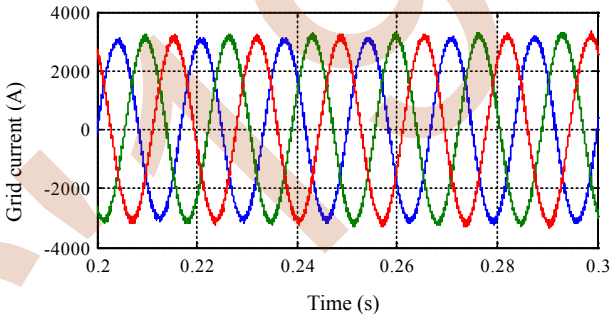

Figure 8. Grid current station1

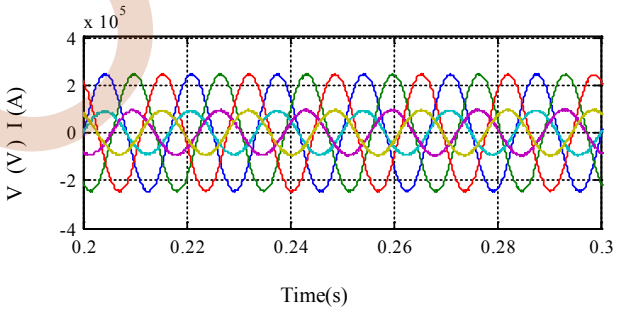

Figure 9. . Voltage and courant station 1

All the figures above show the waveforms of the alternating voltages and currents

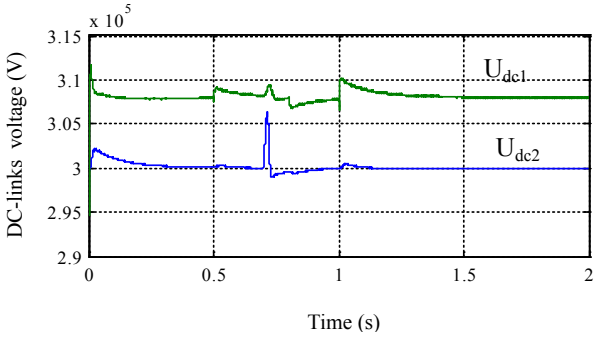

Figure 10. DC voltage

The DC side voltage of both stations is shown in figure 9. It shows that the slack bus is able to keep the DC side voltage close to its reference.

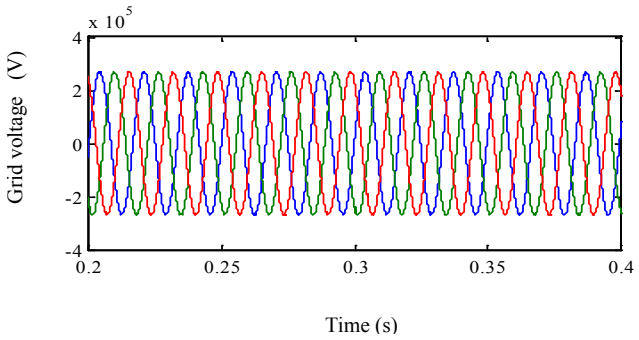

Figure 11. Grid voltage station 2

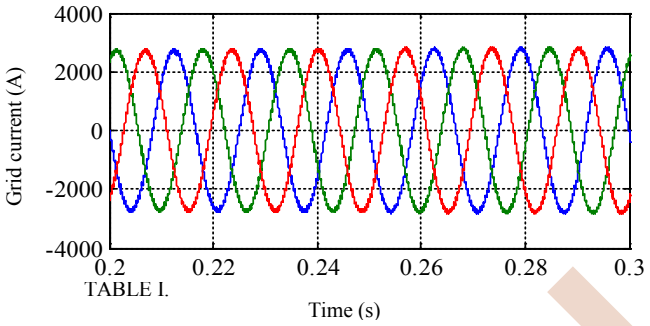

TABLE I.

Figure 12. Courant station 2

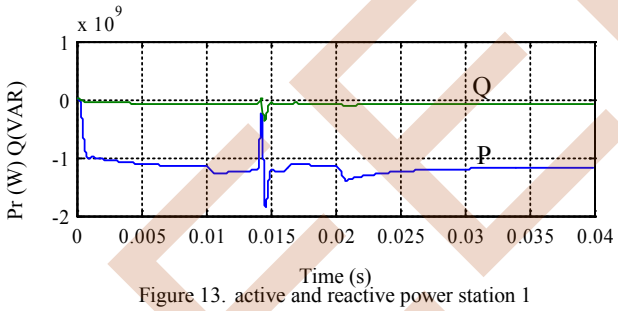

Figure 13. active and reactive power station 1

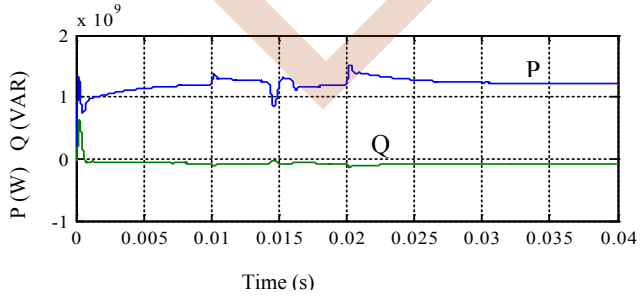

Figure 14. active and reactive power station 2

TABLE II. TABLE. PARAMETER OF SIMULATION

name	Table of parameter		
	parameter	*Value*	*unit*
Station1	VSC rated power	120	MVA
	Resistor	12.4	Ω
	Inductor	23.46	mH
	Frequency	60	Hz
DC- Line	Cable resistance	0.0139	Ohms/km
	Cable Inductance	0.00015	H/km
	Cable capacity	0.23	µF/km
	Line length	75	km
Station 2	VSC rated power	120	MVA
	Resistor	12.4	Ω
	Inductor	23.46	mH
	Frequency	60	Hz

VII. CONCLUSION

This paper has given study to the HVDC technology, with its motivations and applications. The main configurations and components in a typical HVDC system have been shown. A model of a two-terminal VSC-HVDC system is presented regulating the DC voltage while the others converters control the active power flow independently and bi-directionally.

[1] M. Barnes; D. Hertem; S.P.Teeuwsen; M.callavik;"HVDCsystems in smart grid"ieee;

[2] J.Setreus; T.Berlling"introduction to HVDCtechnology for reliable electrical power systems "ieeeexplore; 29 may 2014.

[3] A. Barket; B.Marinesw; C.Join; M.Fliss; "model free control for VSC based HVDC systems" 8th PES innovation smart grid technology coference ISGT Europe 2018 .

[4] M.Barner; D.Hertem; S.Teeuwen; M.Callvi "HVDCsystems in smart grid " ieeeworking groupe 02/2017DOI101109/JRROC. 2017

[5] N.Yen; C.Hongkuw; N.Giang;"study onVSC-HVDCgrid topology offshore windfarms" springer science +busines Media

[6] Z.Cheng; X.Wang; G.Du; F.Yanli" simulation stady of dynamic fault recover performance of VSC-HVDCsystems" energy and power engineering DOI104236;2013.

[7] Modeling of a Multi-level Converter Based VSC HVDC Supplying a Dead Load", 1st International Conference on Electrical and Information Technologies ICEIT'2015,pp. 218-223

Effect of tasks reallocation on the performance of a multi robot system in goods transportation

Ali Djenadi
Laboratoire de Technologie Industrielle et de l'Information
Faculté de Technologie
Université de Bejaia, 06000 Bejaia, Algeria
a.djenadi@yahoo.com

Boubekeur Mendil
Laboratoire de Technologie Industrielle et de l'Information
Faculté de Technologie
Université de Bejaia, 06000 Bejaia, Algeria
bmendil@yahoo.fr

***Abstract*— This paper proposes a multi-robot transportation task allocation strategy that aims to maximize the productivity and minimize energy consumption. A designed Iterative Local Search metaheuristic is used to optimize the task allocation. A reallocation mechanism is embedded into the strategy to adapt the system to dynamic environments. The proposed approach is compared to three heuristics in a simulated environment. The impact of the reallocation mechanism on the productivity and the energy consumption is evaluated**

I. INTRODUCTION

The design of multi-robot system (MRS) includes key elements such as, group architecture (centralized, decentralized, hybrid), cooperative mechanisms, resource conflicts, task allocation, learning, and geometric problems [1]. However, in industrial applications such as transportation, more specific details should be considered [2]. One important aspect is the battery management [3], [4].

In goods transportation task, like warehouse logistics scenarios [5], the main objective is to maximize the number of goods transported. However, if each task is associated with a priority value, the robot may be constrained to fulfill the most urgent tasks first. On other hand, it is crucial to design strategies to ensure optimal energy consumption. The obvious strategy, to consume less energy, is to choose tasks with the shortest travelling distance or the nearest tasks from the robot. However, the tasks chosen may not be the most urgent. The solution then is to optimally allocate the tasks to robots considering the energy consumption and the priority of the tasks, which involve solving the Multi-robot Task Allocation problem (MRTA).

The MRTA problem addresses the question of which robot should be allocated to which task? [1], [6]. The MRTA may be considered as a dynamic decision problem that may be solved iteratively over time [6]. Besides, in goods transportation scenarios, the number of available tasks may be dynamic. Therefore, the robots have to adapt to changes. Thus, A reallocation mechanism may handle this issue. This mechanism allows the robots, while executing tasks, to find a better allocation, which leads to a change in their destinations. However, the more the robots are allowed to reallocate, the more they may consume energy. Hence, the reallocation mechanism has to be constrained to benefit the system.

Literature summarize three major approaches for MRTA, including optimization techniques (deterministic and stochastic) [7], [8]. behavior-based approaches [9], [10] and market-based approach [11], [12].

In this paper, we propose a tasks allocation strategy based on a designed Iterative Local Search metaheuristic (ILS) for MRS involved in goods transportation tasks. Also, we discuss the impact of a tasks reallocation mechanism on the productivity and energy consumption of the system.

This paper is organized as follow: Section 2 discusses the related work. Section 3 details transportation tasks allocation formulation. Section 4 proposes a task allocation strategy based on ILS. Section 5 describes the simulation experiments conducted and presents the results and discussion. Finally, Section 6 concludes the paper.

II. RELATED WORK

Several works have been done to improve the productivity of MRS in goods transportation. Chaimowicz et al, proposed in [13], a behavior-based paradigm, using roles, for dynamic coordination of a multi-robot system involved in transportation tasks. A decentralized auction based task allocation for cooperative transportation mission is developed using a coupled constraint consensus based bundle algorithm [14]. More recently, Farinelli et al proposed a graphical method for multi-robots transportation tasks in logistic scenarios to solve the spatial coordination between robots [15]. In industrial environment, the Automated Guided Vehicles, and the Robotic Mobile Fulfillment System are widely studied [2], [4], [5], [16], [17]

Most the above literature focuses on aspects, such as: path planning, vehicle routing, tasks allocation and coordination, and does not include energy management in their approaches. In other hand, the literature addressing energy management in MRS, mostly investigate recharging methods and logistic matters and consider energy

management in the task execution, rather than in the task allocation process [4], [18], [19].

This paper contribution focuses on presenting an energy management strategy that maximize the profit of MRS involved in goods transportation, by considering the energy management constraints in the task allocation process.

III. TRANSPORTATION TASK ALLOCATION FORMULATION

A. Problem statement

This paper framework is inspired from backgrounds such as robotized warehouse management system [5]. However, our work is stressed on robot task allocation and reallocation mechanisms. A set of incapacitated homogenous mobile robots, with wide communication range, is considered in a simulated transportation task, from loading to unloading stations. In the simulated scenarios, each task is weighted with a priority value.

In goods transportation applications, the energy consumption for the robots depends on its activities (e.g. travelling, pickup, drop off, ...). In our scenarios, we only consider the energy consumption of the travelling activity, since the latter consumes the most energy as stated in [3]. Hence, the robot travelling distance is used to emulate the energy consumption in the framework.

B. Formal model of tasks allocation

According to the taxonomy proposed by Gerkey et al. [20], our MRTA model is a single-task, single-robot, and instantaneous assignment problem (SR-ST-IA).

In the task allocation process, we consider a set of m tasks $T=\{t_1, t_2, ..., t_m\}$ and a set of n robots $R=\{r_1,..., r_n\}$. We estimate the utility u_{ij} of each robot r_i for performing each task t_j. Assuming that each robot can compute its own utility for each available task, an utility matrix $U=\{ u_{ij} \}$ with $1\leq i \leq n$, and, $1\leq j \leq m$, can be constructed. The objective is to find robot-task pairs $(i_1, j_1)...(i_k, j_k)$, $1\leq k \leq \min(n, m)$ that maximize the overall utility of the system (1).

$$\max \sum_{m=1}^{k} u_{i_m j_m} \qquad (1)$$

Given the assumption of SR-ST-IA, the pairs (i_k, j_k) have to be unique.

C. Heuristic-based utility function

From the above issues (robot energy consumption management, throughput maximization, task priority constraint), an utility function (2), is designed based on, the number available robots *nbrR*, number of available task *nbrT* and their priorities Q_j, the Cartesian distance estimation d_{ij}, that a robot needs to travel to perform a task from his current position, the robot accumulated travelled distance $Traveld_i$, and, the maximal travelling distance $Traveldmax_i$, that a robot can performs before reaching the battery depletion.

$$h_{ij} = \frac{nbrR/nbrT}{\exp(d_{ij})} + (\frac{nbeT}{nbeR})Q_j^2 - (d_{ij}^2 - 1)(\frac{Traveld_i}{Traveld\max_i} + 0.1) - (\frac{Traveld_i}{Traveld\max_i}^2 - 1)(d_{ij} + 0.1) \qquad (2)$$

In case the robot doesn't have enough energy to achieve the task, his utility is null. Hence, the complete heuristic-based utility function is:

$$u_{ij} = \begin{cases} h_{ij} & if\ Traveldmax_i - Traveld_i \geq d_{ij} \\ 0 & Otherwise \end{cases} \qquad (3)$$

In this work, we assume that: $\frac{nbrT}{nbrR} \geq 1$.

IV. TASK ALLOCATION STRATEGY BASED ON ILS ALGORITHM

A. Distributed Task Allocation mechanism

In the proposed approach, each available robot, involved in MRTA, participates in the decision making in a distributed cooperative process. Fig. 1 shows the flowchart of the task allocation process that each robot runs.

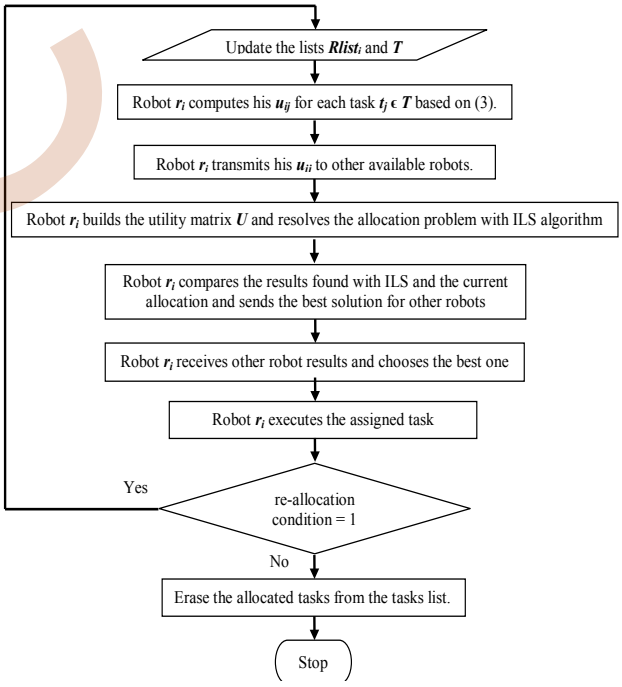

Figure 1. Flowchart of the task allocation process

B. The proposed Iterative Local Search (ILS)

The ILS constructs sequence of solutions, using, iteratively, the Local Search as an embedded guided heuristic [21], to explore the search space *S* by moving from a solution *s* to a better (improved) solution s^*.

Algorithm 1 shows the ILS in our approach, as presented by Lourenço et al [21]. Five components are considered

including, Generate Initial Solution, Local Search, Perturbation, Acceptance Criterion, and Termination Conditions.

Algorithm 1: Procedure for Iterative Local Search (ILS)

$s_0 = GeneratInitialSolution()$

$s^* = LocalSearch(s_0)$

Repeat

$s' = Perturbation(s^*)$

$s^{*'} = LocalSearch(s')$

$s^* = Accep\tan ceCriterion(s^*, s^{*'})$

Until (Termination Conditions met)

During the task allocation, the available robots will have the same utility matrix $U=\{u_{ij}\}$, the same list of available robots *Rlist* and the same list of tasks *T*, with $1 \le i \le p \le n$ (*p* the number of available robots) and $1 \le j \le m$. The solution $s \in S$ is constructed as in (4), (See also, table 1):

$$s = \{U, Rlist, T\} \quad (4)$$

We note that the allocation corresponds to the pairs (r_i, t_j) with $i = j = k$ and, $1 \le k \le \min(p, m)$.

TABLE I. ILS SOLUTION REPRESENTATION

	t_1	⋯	t_m
r_1	u_{11}	⋯	u_{1m}
⋮	⋮	⋱	⋮
r_p	u_{p1}	⋯	u_{pm}

In our approach, the Local Search uses a swap move on the utility matrix columns and elements of the task list by exchange positions between a random *ith* and *jth*, column from the utility matrix ***U*** and the same *ith* and *jth*, element of the list ***T***, with $(i, j) \le \min(p, m)$.

In other hand, the perturbation, considered as a high order move in the search space than the Local Search [21], the proposed ILS, uses a rotation move mechanism on the columns and the rows of the utility matrix ***U***, the task list ***T*** and robots list ***Rlist***. In our approach, we assume that the rotations number is min (*p*, m).

The acceptance criterion determines if the solution given by the Local Search and the perturbation is accepted as new current best solution. Here, a new solution is accepted if it is better than the current. The acceptance criterion is expressed by (5) and (6). With *s* the current solution, *s′* the new found solution, and, $1 \le k \le \min(p, m)$.

$$Better(s, s') = \begin{cases} s' & if\ G(s') > G(s) \\ s & Otherwise \end{cases} \quad (5)$$

$$G(s) = \sum_{i=j=1}^{k} u_{ij} \quad (6)$$

We indicate that the initial solution of the algorithm s_0 is constructed randomly and The termination condition is the number of iterations.

C. Task reallocation embedded in the proposed MRTA

Most of literatures addressing MRTA consider a mechanism for tasks reallocation to ensure that the system, is fault-tolerant, robust and more flexible. However, to embed a reallocation mechanism, the system has to allow it, also, the tasks must permit that robots may exchange tasks or even abandon tasks for others.

The transportation tasks presented in this work, as stated previously, consists, when allocated to a task, robots move from their initial positions to loading stations to pick-up an objects, then transport them to unloading stations. Assuming that a robot with a loaded object can't transfer it to another robot or left it in a random place. The task reallocation is only possible between robot initial position and current allocated task loading station position. In our approach, the reallocation mechanism is constraint with the following two conditions:

$$\begin{cases} nbrT > nbrR \\ and \\ \left\| r_i CurrPos - r_i InitPos \right\| \le \beta \left\| r_i InitPos - T_j LoadPos \right\| \end{cases} \quad (7)$$

We assume that the task T_j has been allocated to the robot r_i previously located at $r_i InitPos$. The positions $r_i CurrPos$ and $T_j LoadPos$ refer to robot current location and the task location. The constant β, with $0 \le \beta \le 1$, is a design parameter.

The first condition allows reallocation when the number of available tasks is greater or equal to the number of available robots. The second condition compares the robot traveled distance and the whole distance needed to reach the allocated task. When β =1, the robot is allowed to participate in reallocation, from his position until he arrives to the loading station. However, for β =0.5 , the reallocation is permitted only for the first half of the whole distance.

The parameter β, is a control parameter for the reallocation for each robot, from no reallocation allowed with β =0, to fully reallocation with β =1. Consequently, we can manage the robot search for a new allocation, hence, we can control the commitment of the robots to their current allocated tasks. However, as expressed above, the more the robots reallocate, the more they may consume energy, therefore, it is crucial to choose the convenient β.

V. EXPERIMENTS

A. Experiments design

The proposed approach is tested on the Player/Stage simulator [22]. Tasks priorities are generated randomly between 0 and 5 (0 as lowest and 5 as the highest priority). In each scenario, the experiment continues until the tasks are completed or the maximum travelling distance for each robot is reached. Each scenarios were carried out 20 times.

The environment topology (Fig. 2) is designed in order to have a simple framework to test our approach. Therefore, we assume that in simulated scenarios, five loading stations and five unloading stations are used . The obstacles are limited as possible. Given that our study's is about task allocation, rather than the obstacles avoidance or path planning.

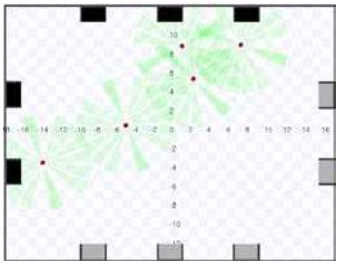

Figure 2. The environment simulation with 5 loading stations (black), 5 unloading stations (grey), and 5 robots.

B. Evaluation methodology

The aim of the simulations were to evaluate first, the performance of the proposed strategy that maximize the productivity and minimize the energy consumption considering priority constraint. Secondly, the reallocation mechanism impact on energy consumption and productivity.

1) Multi-robot transportation task allocation strategy evaluation

The approach is compared to three heuristics inspired from Automated Guided Vehicles dispatching rules [2]. The heuristics are used as task allocation strategy without reallocation.

The first heuristic is the Nearest Task-First (NTF). It allocates tasks near the robot without considering the priorities. The heuristic minimizes the energy consumed by minimizing the travelling distance. The second heuristic is the Shortest Travel Distance-First (STDF). similar to NTF. However, STDF compares the total travelling distances required to complete the task. The third heuristic is the High Priority Task-First (HPTF). It allocates tasks with highest priority first, which will maximize system efficiency, by allocating according to the priority, regardless to the travelling distance.

In all three heuristics, A random choice is made If more than one task is presented with the same parameters.

The proposed strategy and the three heuristics are tested, with 5 robots, numbers of tasks (i.e. 20 and 80 tasks), and a travelling distance of 500 units.

2) Reallocation mechanism evaluation

To assess the impact of the reallocation on energy consumption and productivity, we simulate three scenarios. In two scenarios, the number of available tasks is dynamic. A comparison was conducted between those scenarios and a third scenario, in which the number of tasks is static. Each scenario is tested for different values of parameter β (i.e. 0, 0.1, 0.25, 0.5 and 1).

The scenarios 1, 2, and, 3, were simulated with 5 robots with a travelling distance of 500 units. The scenario 3, is considered as the control test, the simulation start with 80 total tasks. In the scenarios 1, and 2, the simulation starts with a fixed number of tasks and for each period of time, tasks are added until reaching a certain amount. A description is detailed in table 2.

TABLE II. PARAMETERS FOR SCENARIOS USED IN THE EXPERIMENT

	Initial task	Tasks added	Period to add tasks (second)	Total tasks
Scenario 1	10	5	120	80
Scenario 2	5	1	60	20

3) Evaluation scales

The system performance is analyzed with two scales. The first is the mean of robots travelled distance. In our case, it emulates the average energy consumed. The second scale is the productivity of the system (8), that corresponds to the weighted (priority) arithmetic mean of the completed tasks. Considering $nbrT_{Qi}$ the completed task for each priority.

$$productivity = \sum_{i=0}^{5} (i \cdot nbrT_{Q=i}) \Big/ \sum_{i=0}^{5} i \qquad (8)$$

C. Results and discussion

Fig. 3 illustrates, the average distance travelled (energy consumed) by the system to complete all 20 tasks, with a travelling distance of 500 units (maximum energy units to consume). The results show that the proposed approach is slightly minimizing the travelling distance (energy consumption).

Fig. 4, and 5 show the robots performances to complete 80 tasks with 500 units travelling distance. The results show that the proposed approach travels less distance (consumes less energy) than HPTF. However, it travels more distance (consume more energy) than STDF and NTF. However, the results reported in the fig. 5 denote that our algorithm is more productive. Such performance is due to the fact that the robots cannot achieve the 80 tasks with the travelling distance allowed. Therefore, our algorithm manages the energy consumption to complete most high priority tasks.

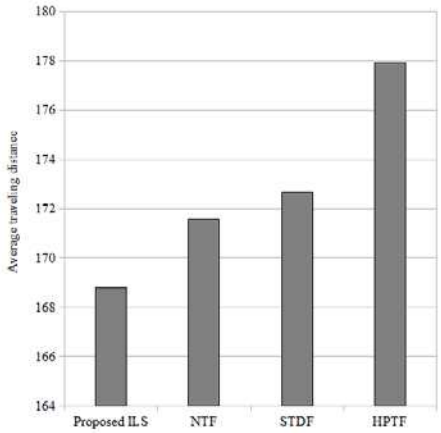

Figure 3. Average travelling distance to complete 20 tasks with maximum travelling distance of 500 units.

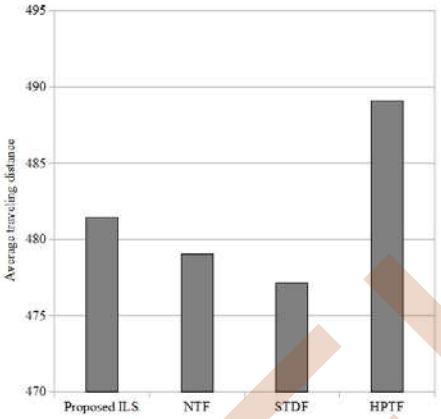

Figure 4. Average travelling distance with for 80 available tasks and maximum travelling distance of 500 units.

Regarding reallocation impact, the results of the scenario 3, without dynamic in task availability, shown in fig. 6, confirm the assumption that with β=1 (full reallocation), the system consumes the more and produces the less. In this scenario the robots waste a lot of energy reallocating several times, which causes depletion of the system energy reserve, leading to less production as shown in fig. 7. However, in the same scenario 3, with $0.25 \leq \beta \leq 0.5$, the robots consume less energy and are more productive.

In the scenario 1 case, with a dynamic in the task availability, the robots system, with β=0 (without reallocation), consumes the more and produce less than some cases with reallocation allowed (i.e. β=0.5 and β=0.25). The robots in this case, without reallocation, are not able to adapt to changes in the environment. The same results, show that with β=0.25 and β=0.5, the system produces the more, however, it consumes more than with β=0.1. In this scenario, the robots cannot achieve the total 80 tasks with the available energy. Therefore, the proposed algorithm manages the energy consumption to complete most tasks with high priority. The values of β, that offers the best result in that case are $0.25 \leq \beta \leq 0.5$.

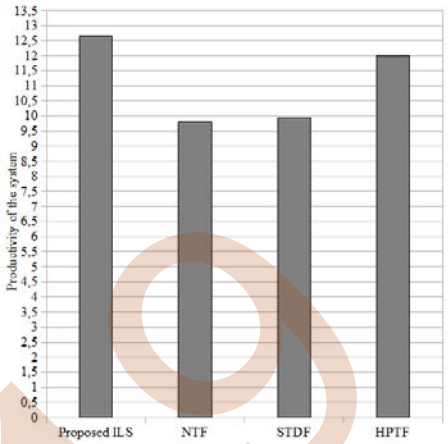

Figure 5. Productivity of the system for 80 available tasks with a maximum travelling distance of 500 units

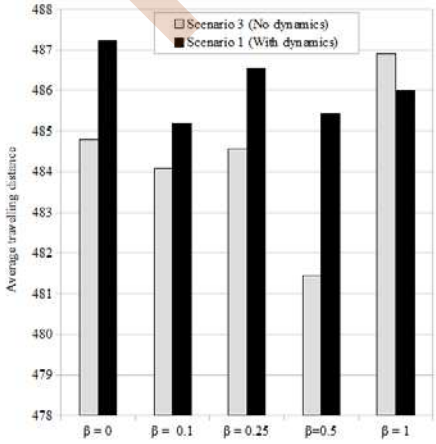

Figure 6. Average travelling distance for 80 available tasks with maximum travelling distance of 500 units.

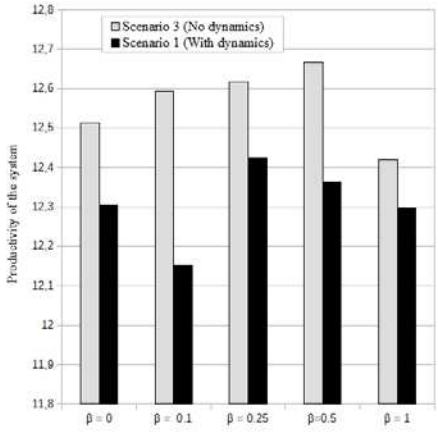

Figure 7. Productivity of the system for 80 available tasks with a maximum travelling distance of 500 units.

Fig. 8, shows the energy consumed to complete a total 20 available tasks as simulated in scenario 2 with a dynamic tasks availability. This scenario asses the performance of the system to manage the energy consumption to complete all the available 20 tasks. The results indicate that the reallocation with β=0.1, and the case without reallocation (β=0), consumes more energy. However, a reallocation with β=0.5 and β=0.25 consumes the less energy. As in the previous scenarios the optimal value for β are $0.25 \leq \beta \leq 0.5$

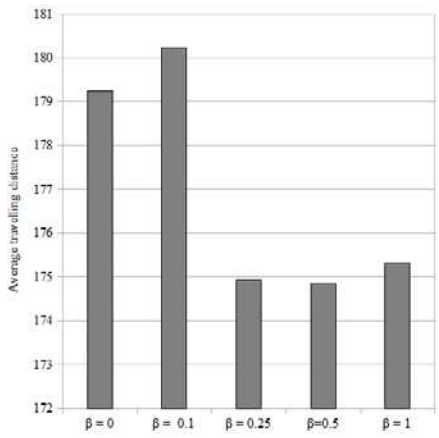

Figure 8. Average travelling distance to complete 20 tasks with travelling distance of 500 units (with a dynamic task availability).

VI. CONCLUSION AND FUTURE WORKS

This paper introduces a multi robot transportation task allocation strategy embedded with a reallocation mechanism. A designed Iterative Local Search metaheuristic is used to optimize the tasks allocation. In this work ,two objectives were investigated: the performances of the proposed approach compared to three heuristics, and, the reallocation mechanism impact on the productivity and the energy consumption of the system.

The results show that our approach successfully manage the energy consumption in order to balance between spending energy to maximize the productivity and saving energy to minimize the consumption. Furthermore, the results on the reallocation mechanism denote that, task reallocation with the right parameters β, has a positive outcome on the performances of our system. Thus, as future works, include evaluating the approach on important number of robots in realistic warehouse environments. Another extension will concern other MRS such as multi unmanned aerial vehicle (multi-UAV).

VII. REFERENCES

[1] Y. U. Cao, A. S. Fukunaga, and A. Kahng, 'Cooperative Mobile Robotics: Antecedents and Directions', *Autonomous Robots*, vol. 4, no. 1, pp. 7–27, Mar. 1997.

[2] I. F. A. Vis, 'Survey of research in the design and control of automated guided vehicle systems', *European Journal of Operational Research*, vol. 170, no. 3, pp. 677–709, May 2006.

[3] R. McHANEY, 'Modelling battery constraints in discrete event automated guided vehicle simulations', *International Journal of Production Research*, vol. 33, no. 11, pp. 3023–3040, Nov. 1995.

[4] M. Ebben, 'Logistic control in automated transportation networks', Twente Univ. Press, Enschede, 2001.

[5] J. J. Enright and P. R. Wurman, 'Optimization and Coordinated Autonomy in Mobile Fulfillment Systems', in *Proceedings of the 9th AAAI Conference on Automated Action Planning for Autonomous Mobile Robots*, 2011, pp. 33–38.

[6] B. P. Gerkey and M. J. Mataric, 'Multi-robot task allocation: analyzing the complexity and optimality of key architectures', in *2003 IEEE International Conference on Robotics and Automation (Cat. No.03CH37422)*, Taipei, Taiwan, 2003, vol. 3, pp. 3862–3868.

[7] N. Atay and B. Bayazit, 'Mixed-Integer Linear Programming Solution to Multi-Robot Task Allocation Problem', 2006.

[8] M. N. Rastgoo, B. Nakisa, and M. Z. Ahmad Nazri, 'A Hybrid of Modified PSO and Local Search on a Multi-Robot Search System', *International Journal of Advanced Robotic Systems*, vol. 12, no. 7, p. 86, Jul. 2015.

[9] L. E. Parker, 'ALLIANCE: an architecture for fault tolerant multirobot cooperation', *IEEE Transactions on Robotics and Automation*, vol. 14, no. 2, pp. 220–240, Apr. 1998.

[10] B. B. Werger and M. J. Mataric, 'Broadcast of Local Eligibility: Behavior-based Control for Strongly Cooperative Robot Teams', in *Proceedings of the Fourth International Conference on Autonomous Agents*, New York, NY, USA, 2000, pp. 21–22.

[11] B. P. Gerkey and M. J. Mataric, 'Sold!: auction methods for multirobot coordination', *IEEE Transactions on Robotics and Automation*, vol. 18, no. 5, pp. 758–768, Oct. 2002.

[12] M. B. Dias, 'TraderBots: A New Paradigm for Robust and Efficient Multirobot Coordination in Dynamic Environments', Jan. 2004.

[13] L. Chaimowicz, V. Kumar, and M. F. M. Campos, 'A Paradigm for Dynamic Coordination of Multiple Robots', *Autonomous Robots*, vol. 17, no. 1, pp. 7–21, Jul. 2004.

[14] K.-S. Kim and H.-L. Choi, 'A decentralized task allocation approach for cooperative transportation missions', *2014 13th International Conference on Control Automation Robotics & Vision (ICARCV)*, pp. 1479–1483, 2014.

[15] A. Farinelli, N. Boscolo, E. Zanotto, and E. Pagello, 'Advanced Approaches for Multi-robot Coordination in Logistic Scenarios', *Robot. Auton. Syst.*, vol. 90, no. C, pp. 34–44, Apr. 2017.

[16] H. Martínez-Barberá and D. Herrero-Pérez, 'Autonomous navigation of an automated guided vehicle in industrial environments', *Robotics and Computer-Integrated Manufacturing*, vol. 26, no. 4, pp. 296–311, Aug. 2010.

[17] D. Stavrou, S. Timotheou, C. G. Panayiotou, and M. M. Polycarpou, 'Assignment and Coordination of Autonomous Robots in Container Loading Terminals', *IFAC-PapersOnLine*, vol. 50, no. 1, pp. 9712–9717, Jul. 2017.

[18] B. Zou, X. Xu, Y. (Yale) Gong, and R. De Koster, 'Evaluating battery charging and swapping strategies in a robotic mobile fulfillment system', *European Journal of Operational Research*, vol. 267, no. 2, pp. 733–753, Jun. 2018.

[19] Q. S. Kabir and Y. Suzuki, 'Increasing Manufacturing Flexibility Through Battery Management of Automated Guided Vehicles', *Comput. Ind. Eng.*, vol. 117, no. C, pp. 225–236, Mar. 2018.

[20] B. P. Gerkey and M. J. Matarić, 'A Formal Analysis and Taxonomy of Task Allocation in Multi-Robot Systems', *The International Journal of Robotics Research*, vol. 23, no. 9, pp. 939–954, Sep. 2004.

[21] H. R. Lourenço, O. C. Martin, and T. Stützle, 'Iterated Local Search', in *Handbook of Metaheuristics*, F. Glover and G. A. Kochenberger, Eds. Boston, MA: Springer US, 2003, pp. 320–353.

[22] 'Player Project', 16-Feb-2014. [Online]. Available: http://playerstage.sourceforge.net/. [Accessed: 21-Feb-2019].

Job Shop and parallel machine scheduling problems: minimization of Makspan

Houari habiba
Manufacturing Engineering Laboratory of Tlemcen (MELT)
Abou bakr Belkaïd University of Tlemcen, Algeria
Tlemcen Algeria
houari_habiba@yahoo.fr

Fatiha Benbekhti
Technology Depatment. Khemis Miliana university
Djillali Bounama- Khemis Miliana
Khemis Miliana, Algeria
fatiha.benbekhti@univ-dbkm.dz

Tahraoui Souad
Department of Electronic, Hassiba Benbouali University of Chlef, Algeria)
University of Chlef, Algeria)
Chlef, Algeria
s.tahraoui@univhb-chlef.dz

Ahmed Hassam
Manufacturing Engineering Laboratory of Tlemcen (MELT)
Abou bakr Belkaïd University of Tlemcen, Algeria
Tlemcen Algeria
hassam.ahmed@yahoo.fr

***Abstract*—A heuristic algorithm is advanced for the classic programming problem in which independent jobs are programmed non-preventively on identical parallel machines in order to minimize the makepan with load balancing. The algorithm utilizes iteratively the LPT procedure to be effective computational tools in many hard Combinatorial Optimization problems. We present an approximation algorithm built on balance which are a type of assignment variables for the classical deterministic scheduling problem of minimizing the makespan on identical machines. These problems are differentiated by their complexity, known as NP-hard in most situation. Computational results signalize that the suggest algorithm is very competitive with esteem to well-known deductive algorithms for a large number of benchmark.**

Keywords— Flexible Manufacturing System (FMS), metaheuristic, Identical parallel machines, makespan, genetic algorithm (GA) approach, The LPT procedure, shortest processing time (SPT) heuristic

Current production systems are growing in complexity. This complexity results from the demands of the market, competition, quality as well as the density and diversity of the products they process. In this type of problem, we are faced with a scheduling problem. The choice of the resolution method strongly depends on the size and complexity of the problem. If the problem is large and of significant complexity, it is not possible to provide an exact algorithm for such systems. We are naturally interested in non-exact algorithms called 'heuristics' which present more interesting alternatives. Among the problems that are often classified NP-Difficile, those of scheduling form a large part, which justifies the use of the approximate methods for their resolution.

The system should be flexible, productive and should be able to meet the demands within time bounds at a reasonable cost. An FMS can be considered flexible, if it is able to process parts when they arrive into the system to changing the world as flexibility is the way to stay ahead in business [1].

The FMS scheduling is among the hardest and interesting combinational optimization problem. For this raison,researche used different approaches to solve this problem such as mathematical programming, simulation, and heuristic algorithms… [2]. The choice of the resolution method of the optimization problems depends strongly on the size and complexity on the problem. If the problem is of small size and reduced complexity, an exact method can suffice and lead for an optimal solution. For complex problems, the approached methods, in particular the heuristic ones present an interesting alternative [1].

A parallel machines job-shop problem is a generalization of a job-shop problem to the case when there are identical machines of the same type. Job-shop problems encountered in a flexible manufacturing system, train timetabling, production planning and in other real-life scheduling systems. This paper presents an developed algorithm for solving the parallel machines job-shop problem.

In a classical job shop problem, the elementary product operations follow a completely ordered sequence according to the product to be manufactured. In some structures, each elementary operation may be carried out on several machines, from where, thanks to the versatility of the machines, a greater flexibility is obtained. We can talk about total flexibility if all the machines are able to carry out all the operations, otherwise, it is a partial flexibility. This is what we call the hybrid job

shop or the flexible job shop. Multiprocessor Scheduling, Theory and Applications [3].

This work is part of solving the scheduling problems of flexible production systems. We were particularly interested in those with routing flexibility. This kind of flexibility that can be found in every system that includes identical, alternate or redundant parallel machines offers several advantages in balancing machine loads better, allowing the system to continue to operate and maintain its high performance despite occurrence of certain unexpected events such as machine failures, ... [4]

These properties are pushed many researchers to take into account during the implementation and configuration of the systems, which explains the existence of many works that deal with scheduling problems in manufacturing systems with presence of flexibility.

The idea of a better balancing of the loads on the machines of the job shop, pushed us to try it on a system of parallel machines which contains a flexibility in the selection of the machines. For this we developed an algorithm that was called MMIPMH to select the best makespan for a system of identical parallel machines.

The results of this algorithm are compared to those of the LPT rule which is one of the methods that gives the best results for the scheduling problem P || C max (the minimization of Cmax for the problem of identical parallel machines without constraints) which is an NP-complete problem.

These results confirmed that the MMIMPH method we developed almost always gives better results than those given by the LPT rule and results in worst case worst case. The power of this method is in the manner in which the load balancing is done on the different machines of the system [5].

I. RESENTATION OF FLEXIBLE MANUFACTURING SYSTEM ENVIRONMENT

The FMS model studied is drawn from the literature (Saygin and Kilick, 1999; Hassam and Sari, 2010 [6]). It is composed from seven machines and two stations, one is a loading station and the other is an unloading one. The system will process six kinds of parts. Each machine has an input and an output queue. The loading station also has an input queue. Fig. (1) represents the model's configuration, and Table 1 shows possible alternative routings for each parts kind with the processing time for each machine.

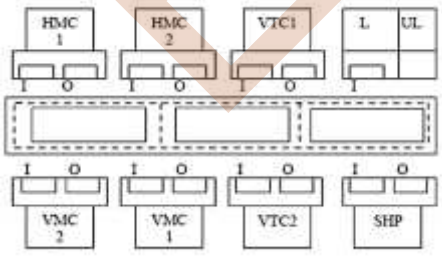

Figure 1. Model FMS configuration.

L: Loaded Station
UL: Unloaded Station
VTC1, VTC2: vertical turning centers
VMC1, VMC2: vertical milling machines
HMC1, HMC2: horizontal milling machines
SHP: shaper
I: input buffer,
O: output buffer

A group of colleagues and I have developed several metaheuristics in order to improve the work of the job Shop operator and gave us a good result there is a table showing that

But that is not enough, which made me think about developing a balanced machine operator, which is part of the job Shop.

Table I. Production rate of parts for a queues capacity equal to 2.

T.A.A(1/min)	1/5	1/10	1/15	1/20	1/25
(AG)	23,12	46,22	69,02	92,00	99,99
(MA)	23,84	47,42	71,21	94,34	99,99
(MA|PM).	23.95	47.83	71.61	94.66	99.99
(SS)	23,98	47,90	72,02	95,21	99,99

MA|PM: memetic algorithm with management of population.
MA: memetic algorithm
GA: genetic algorithm
SS: Scatter search

Table I gives the evolution of the rate of production for various values of the queues capacity. It is clear that the Scatter search (SS) gives better results compared with those of the algorithms.

II. PARALLEL MACHINES SCHEDULING

This paper considers the problem of scheduling independent jobs on identical parallel machines. the partition jobs to machines and sequence jobs for each machine are the two essential issues in classical parallel machine scheduling problem [7]. The aim of machine scheduling is to assign jobs to the machines based on related objective function to minimize operating time and increase productivity [8]. The problem can be described as follows: we are given n jobs when each operation has to start and finish on each one of the identical parallel m machines and using available resources in efficient manners to execute (assign) jobs or tasks on machines during a fixed processing time without preemption. The schematic representation of a typical identical parallel processing environment involving three identical machines, required to produce eight jobs, is shown in Figure

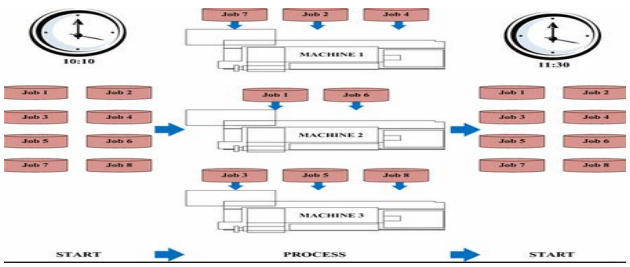

Figure 2. Structure of parallel machine process

A. Formulation of the Problem

The paper considers the problem of finding an appropriate allocation of jobs to machines that would optimize the performance criterion, for the classical deterministic scheduling problem of minimizing the makespan which is defined as the total completion time of all the jobs. The performance of MMIPMH heuristic is compared with LPT heuristic approach by Hu [9]. We will use this notation in what follows:

n: number of jobs
m: number of machines
J: job i, i Є N={1,...,n}
Mi : machine j, j Є M={1,...,m}
pj: processing time of J
Ci: completion time of J
C_{max}: makespan, the maximum completion time of all jobs
Cm=Completion time or workload of machine m
Cmin: Minimum of workloads (completion times).
X_{ij}: The assignment (decision) variable.
In this paper, the solution can be obtained in two steps: The LPT algorithm is used to find (generate) the initial solution, while the developed algorithm is used to improve the initial solution.

- The LPT rule of Graham [10], one of the most popular heuristics, to distribute jobs among identical machines so as to minimize the makespan of the resulting schedule. This rule always puts the smaller jobs towards the end of schedule, such that P_1≥P_2≥P_3≥⋯≥P_nand then successively assigns jobs to the least loaded machine.

According to the (LPT) algorithm, whenever one of the (m) machines is freed, the longest job among number of jobs (N) in decreasing order waiting for processing is selected to be next [20]. The next job (j) will be scheduled on machine (i*) according to the equation

$$i^* = argmin\{C_i + P_j, j = 1, \dots, m\} \quad (1)$$

The LPT algorithm is summarized below:

Step 1. Sort then n jobs according to the non- increasing order of their processing time

Step 2. Set j=1.

Step 3. Assign job i to machine j according to (1)

Step 4. If i=n (i.e. all jobs are allocated) then go to the next step, otherwise set i=i+1 and go to Step3.

Step 5. Calculate C_max^LPT=max{C_(j,),j=1,…,m}

- Algorithm The algorithm, called elimination of load balancing MMIPMH Job and Machine Sets (MMIPMH), solves P||Cmax by using LPT approaches, many times in sequence. This method is inspired by Hopfild neuron network; it does not take all the loads of the machines because before we suppress many cases for active the calculation. we posed the bound each step

step 1: 1<=Number the jobs in each lines <n-m+1

step2 : : $\propto = C_{max}^{LPT} - C_{min}^{LPT}$, α and

$$C_{max} = C_{min}^{LPT} + \propto/2 \quad (2)$$

$$C_{min}^{LPT} < C_{max}^{*} < C_{max} \quad (3)$$

non-increasing order (15, 9, 8, 7, 7, 6, 6, 5, 4, 3, 3)

Step 2: set j=1

Step3: Construct a matrix of which the number of rows is equal 2n (n the number of jobs) and the number of columns = n and Converting this matrix to a binary matrix.

Step4: Delete all lines after using the formula (4).

1<=Number the 1 in each lines <n-m+1 (4)

That is to say all the lines, which contains more n-m + 1 of 1 and less than 1. The 1 these are the job. Multiply each row by jobs using step 1.

Step5: We compute at each line the Cmax*. Delete lines according to formula (2).

The feasibility of the load is checked by equation (3). If the construction is successful (all machines are loaded and all conditions are satisfied), both the upper bound and lower bound are updated.

Step6: print the results and stop.

B. Computer program

The developed algorithms have been coded in delphi and executed for CPU 2.30 GHz, RAM 6.00 GH. System type (64bit) in order to remain comparable in terms of the computational time. The program is designed to solve variety of problems depending on number of machines (m) and number of jobs (N).
Many computational applications with different levels of difficulties have been carried out to evaluate the performance of the MMIPMH algorithm. Then we will make a comparison between these algorithms and the LPT algorithm previously used to solve the same problem to get an idea on the most efficient methods for this problem and choose the most effective.
Find the optimal schedule (solution) by using the (LPT) and the algorithms to minimize maximum completion time (Cmax) for (12) jobs their processing times (Pj) given bellow:
Pj= [3, 6, 3, 15, 6, 7, 9, 7, 8, 9 , 4, 5]
The jobs processed by (4) identical parallel machines, each machine each job is assigned to exactly one of the machines and permission of a job on another machine is not allowed.
Using LPT algorithm to find the initial schedule (solution):
Step1: sort the jobs in non-increasing order (15, 9, 8, 7, 7, 6, 6, 5, 4, 3, 3)
Step 2: set j =1
Step 3: assign job (1) to the machine (i) according to equation:

$$j^* = argmin\{C_j, P_i \;\; j = 1, \dots, m\} \quad (1)$$

The load on machines:
C1= P4 + P6 + P10 + P12= 8+7+4+3 = 22
C2= P3 + P5+ P11= 9+ 7+3 =19

C3= P2 + P8 + P9= 9+ 6+5 = 20
C4=P1+P7=15+6=21
Step 4: j = N = 12 (all jobs are assigned (allocated)).
Step 5: calculate C by using equation (2).

$$C_{max} = max\{C_i : i = 1,2,3,4\}$$
$$C_{max} = max\{C_1, C_2, C_3, C_4\}$$
$$C_{max} = max\{22,19,20,21\} \rightarrow C_{max}^{LPT} = 22 ; C_{min}^{LPT} = 19$$

Using the algorithm to improve the initial solution:
Use (LPT) algorithm to find the initial solution (upper bound)

The lower bound (LB) can be found by equation (2) as follows: $\propto = C_{max}^{LPT} - C_{min}^{LPT} = 22 - 19 = 3$

Therefore:

$$C_{max}^{*} = C_{min}^{LPT} + \propto \frac{1}{2} = 19 + \frac{3}{2} = 21{,}5$$

Since we can not divide the execution time of jobs, we will take the entire part of
That means the algorithm is going to look for in the meantime [19,21]:

$$19 \leq C_{max} \leq 21$$

III. RESULTS AND DISCUSSIONS

TABLE II: The solution for number of (4) Machines and (12) Jobs

MMIPMH algorithm				
Machine	Jobs	C	C_{ma}	iteration
M_1	P_1P_7	21	21	4
M_2	$P_4P_5P_8$	21		
M_3	P_2 ,P_3P_{11}	21		
M_4	P_1,P_7	21		
LPTalgoritm				
Machine	Jobs	C	C_{xax}	Iteration
M_1	P_1P_7	22	22	1
M_2	P_2 , P_8 P_9	19		
M_3	P_3 , P_5 P_{11}	20		
M_4	P_4,$P_6P_{10}P_{12}$	21		

According to the results in table (II) the solution of the problem (Cmax) which obtained by LPT algorithm CmaxLPT=22 but we observed the optimal solution obtained by the MMIPMH algorithm Cmax=21 with different distribution of jobs on machines and number of solution iterations.

Table II give a summary of the results for the first and second data sets respectively. The summary shows the performance of proposed MMIPMH approach with the LPT heuristic proposed by Hu [9].

TABLE III: The solution for number of (m) Machines and (N) Jobs

MMIPMH algorithm

N°	Machine	Jobs	C_{max}		Iteration
	(m)	(N)	LPT	H	
1	2	8	24	24	5
2	3	11	24	23	5
3	4	9	15	12	4
4	5	15	26	23	3

Table III gives the evolution of the various numbers of jobs for a fixed number of machines. It is clear that the MMIPMH algorithm gives better results compared with those of the algorithm (LPT).

IV. CONCLUEIONS

The idea of a better balancing of the loads on the machines of the job shop, pushed us to try it on a system of parallel machines which contains a flexibility in the selection of the machines. For this we developed an algorithm that was called MMIPMH to select the best makespan for a system of identical parallel machines. This work was presented in this papier, where we presented and explained the algorithms by giving explanatory examples.

The results of this algorithm can be compared to those of the LPT rule which is one of the methods that gives the best results for the scheduling problem P || Cmax (the minimization of Cmax for the problem of identical parallel machines without constraints) which is an NP-complete problem. Several methods such as dynamic programming, integer method for branching and linking, Hopfild, GA have been used to solve Identical parallel machine scheduling problem in order to reduce the disruption of workload between machines and the makespan has been

Our objective is to determine the performance of heuristic MMIPMH based the loading problems in Identical parallel machine compared to the LPT algorithm for a scheduling problem in an FMS, many experiments are used with random number of machines (m) and jobs (N) to prove effectiveness of the algorithm solution.

These results confirmed that the MMIMPH method that we developed almost always gives better results than those given by the LPT rule and results equal to those of the LPT in the worst case.
The power of this method is in the manner in which the load balancing is done on the different machines of the system. We also note that this method gives its results in a fairly reasonable computation time compared to other methods because of the reduction of the search space of the makespan.

All in order to balance the workload which reduces the makepan this result from finding a better sequence of the types within reasonable time application.

ACKNOWLEDGMENT *(Heading 5)*

This work was financial supported by the University Tlemcen (Algeria.2019) Authors wish to thank the head of

Electrical Engineering Department in Tlemcen and all member of the Manufacturing Engineering Laboratory.

REFERENCES

[1] H. Houari, Y. Houbad, M. Souier, and Z. Sari, "Adaptation of Memetic Algorithm with Population Management for the Improvement of the Performances of Flexible ManufacturingSystems," The Open Automation and Control Systems Journal, 2017, 9, (Suppl-1, M2) 2-14

[2] O.A. Joseph, and R. Sridharan, "Effects of routing flexibility: sequencing flexibility and scheduling decision rule on the performance of aflexible manufacturing system", In: Int J Adv Manuf Technol, vol. 56. Springer-Verlag London Limited, 2011, no. 1-4, pp. 291-306.

[3] F. Dugardin, Edited by Eugene LevnerISBN 978-3-902613-02-8Hard cover, 436 pagesPublisher I-Tech Education and PublishingPublished online 01, December, 2007,

[4] H. Houari, A. Hassam, S. Tahraoui and Z. Sari ,"Minimizing Makespan on Identical Parallel Machines," in Magnetism, vol ELECTROTEHNICĂ, ELECTRONICĂ, AUTOMATICĂ,, 2018, pp. 271-350.

[5] H. Houari, " L'intelligence artificielle pour résoudre les problèmes d'ordonnancement des systèmes flexibles de production," Thèse de Doctorat en Sciences en Productique Intitulée :

[6] A. Hassam, and Z. Sari, "Selection of alternative routings in real time: DMM and modified DMM rules", Int. J. Prod. Dev., vol. 10, no. 1/2/3, pp. 241-258..

[7] I.. Chaudhry, M. Sultan. and A. Riaz. ." Minimizing Makespan for Machine Scheduling and Worker Assignment Problem in Identical Parallel Machine Models Using GA" Proceedings of the World Congress on Engineering 2010 Vol III WCE 2010, June 30 - July 2, 2010, London, U.K.

[8] D. Eren Akyol and M. Bayhan , G."Minimizing Makespan on Identical Parallel Machines Using Neural Networks ". I. King et al. (Eds.): ICONIP, 2006, Part III, LNCS 4234, pp. 553.

[9] P-C. Hu., "Minimizing total tardiness for the worker assignment scheduling problem in identical parallel-machine models", 2004.,International Journal of Advanced Manufacturing Technology, vol. 23(5–6), pp. 383-388.

[10] R. Graham, R., Lawer, E., Lenstra, J., & Rinnooy Ken, A. 1979. Optimization and approximation in deterministic sequencing and scheduling. Annals of Discrete Mathematics, 5, 287–326.

Predictive Functional Control of Building HVAC Systems

OUARET Ahmed[1], LEHOUCHE Hocine[2], OUALI Nassima[3]
[1, 2, 5] Laboratoire de Technologie Industrielle et de l'Information (LTII), Faculté de Technologie, Université de Bejaia, 06000 Bejaia, Algérie
[1] ahmed201189@hotmail.fr

GUEGUEN Hervé[4] and MENDIL Boubekeur[5]
[3] Département de Génie Electrique
Faculté de Technologie, Université de Bejaia, 06000 Bejaia, Algérie
[4] IETR – CentraleSupelec, Rennes, France

***Abstract*— Nowadays the balance between occupant thermal comfort and energy efficiency in the tertiary building is considered as a target of the world. An important energy consumption is associated to building heating systems. In this paper, we have proposed a new approach to control the ambient temperature inside the working office in order to minimize energy consumed without reduce the comfort of occupants. To achieve this compromise, a predictive functional controller has been used. This control algorithm is applied to a building heating system. Simulations results found using the SIMBAD toolbox, demonstrate the validity, the performance and the effectiveness of this control strategy.**

I. INTRODUCTION

The building sector is considered as a more consumer of energy and represents approximately 40% of the world's energy consumption. This is due to rapidly growing of population and the increasing demand of living comfort. Nearly half of the energy use is associated to heating, ventilation and air-conditioning (HVAC) systems [1, 2]. Reducing the building energy costs has become an urgent task, due to the increasing environmental concerns and energy prices. Despite, the most HVAC systems at the existing buildings are not operating in the efficient way. Therefore, the main objective of this work is to develop and design a control strategy that can be used to reduce the energy consumption and improve thermal comfort in the tertiary buildings.

Even if many studies were carried out in order to optimize the energy efficiency of the heating systems, the control algorithms that are used for this objective remain basic or stand for local control problems, such as on/off type or PID controllers, auto-tuning methods of PID parameters [3, 4]. The major problem of thermal systems is their slow dynamics and the presence of time delays [5]. Therefore, other approaches have been proposed in the literature like fuzzy logic controllers [6], genetic algorithms [7] or neural networks [8, 9].

This work enrolled in the context of our research project, which is the expansion of the previous works [10, 11, 12], a predictive functional control (PFC) methodology has been used. The PFC algorithm is considered as a promising technique to solve the optimization problem in the building sector. Briefly, this advanced method consists to solve the industrial complex problems. It is based on the use of a dynamic model of the system inside the controller in order to anticipate its future behavior of the process.

The main objective of this paper is to develop a control strategy based on predictive functional controller for regulating the ambient temperature in the building zone. This zone is a working office that can be considered as a highly unknown nonlinear complex model, which is taken from *Simbad toolbox* [13]. Our goal is to make the temperature inside tracks perfectly the desired one, despite the presence of different disturbances and environmental constraints.

The remainder of this paper is organized as follows. Section 2 describes the complete process; in the same section, the main control problem is stated. Section 3 devoted to restoring the operating principle of the predictive functional control of the heating system. Section 4 presents the application of PFC for regulating the temperature in a building zone; Conclusions are drawn in the last section.

II. THE BUILDING ZONE WITH ELECTRICAL HEATER CASE STUDY

A. *Zone Model Description*

The room model consists of a detailed envelope model, simplified radiation model and simplified convection model. It uses a central node to represent the resultant temperature in the zone. The different inputs and outputs of the model are described in Figure 1.

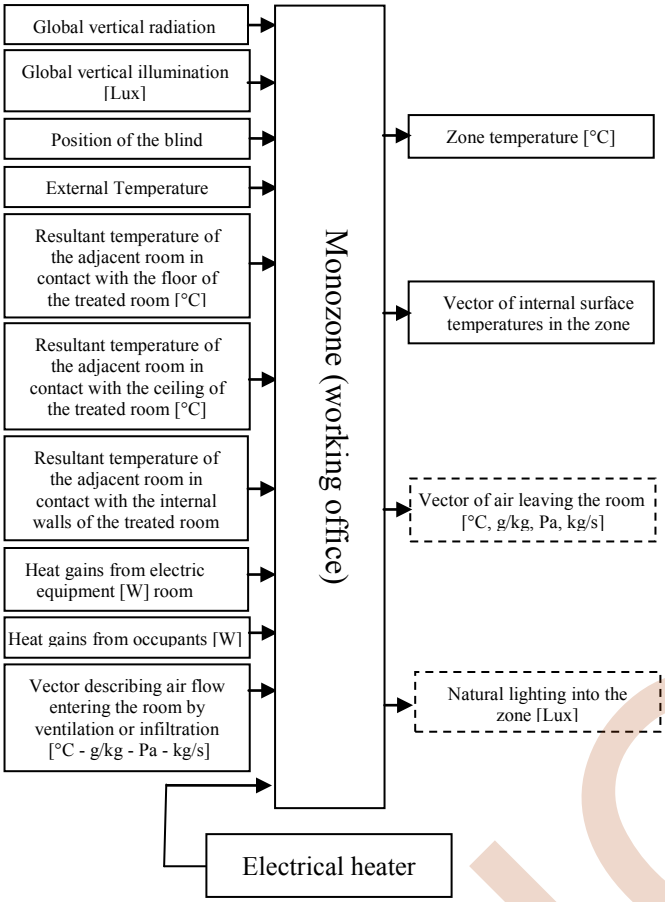

Figure 1. The simulation model of the room with different perturbations and electric heater

B. Electric Heater Model Description

This is first order model of an electric heater.

1) Input:

- *Com:* Command from controller limited between 0 and 1.

2) Outputs:

- *Heat flux:* Heat dissipated to surroundings [W]
- *P_elec:* Electric consumption of heater [W]

C. Performance indicators

To verify the effectiveness of the method and compare it with other methods, we defined four performance indicators. The first two translate the energy consumed and the comfort of the occupants. They are naturally defined as:

1. The energy consumption, in [kWh], during the study period:

$$I_{cons} = \int_{t_0}^{t_f} P(t)\,dt \qquad [kWh] \tag{1}$$

2. The comfort index penalizes the difference between the temperature of the room and the reference temperature, but only during the periods of occupation of the room, which gives, in [°Ch]:

$$I_{comf} = \int_{t_0}^{t_f} \left| T_{ref}(t) - T_{amb}(t) \right| dt \quad [°Ch] \tag{2}$$

The last two indices do not have a direct impact on consumption or comfort but are also important from a more automation point of view. They measure the oscillatory phenomena of the temperature and the continuous aspect of the command:

3. The temperature stability index. It measures the temperature oscillations and is constructed from the differences between the local maximums of the room temperature and the desired temperature during the occupancy period. Which gives in [° C]:

$$TSI = \underbrace{\sum \left(local\max \left(\left| T_{amb}(t) - T_{ref}(t) \right| \right) \right)}_{while\ occupancy} \quad [°C] \tag{3}$$

4. The stability index of the control corresponds to a weighted average of the control variation, and depends on the sampling period T_s :

$$CSI = \frac{mean\left(\left| u(t+1) - u(t) \right| \right)}{T_s} \tag{4}$$

Now that these indicators have been clearly defined, the next step is to define the principle and the parameters necessary for the implementation of the PFC, so that these indicators are the best ones possible.

III. PREDICTIVE FUNCTIONAL CONTROL (PFC)

Predictive functional control has been designed to solve control problems for medium complexity processes. In the industry, PFC has been very successful compared to other MPC control strategies.

It uses a non-aligned model (independent) divided into two parts: one autoregressive and the other forced. The forced response is projected on a function basis.

The goal is to rally the output of the process to the set point in the future. The prediction calculation is done with the help of a numerical model of the process that one wants to control. The calculation of the future terms of the order is made on a prediction horizon formed of a sequence of points that are called coincidence points. The predicted output is then supposed to coincide with a reference trajectory [14].

To set up such a control, we must follow the following steps [15].

- Obtain and represent the model of the system.
- Look for the prediction formula (sometimes called preacher).
- Obtaining the analytical expression of the control to be applied.

A. *Principle of functional predictive control*

In general, we consider the system to be regulated as a model that can be modeled according to the ARMA representation:

$$y(k) = \sum_{i=1}^{n} \alpha_i y_p(k-i) + \sum_{j=1}^{m} b_j u(k-j) \quad (5)$$

α_i and b_j are the model parameters

Then the PFC is based on principles that are specific to its implementation.

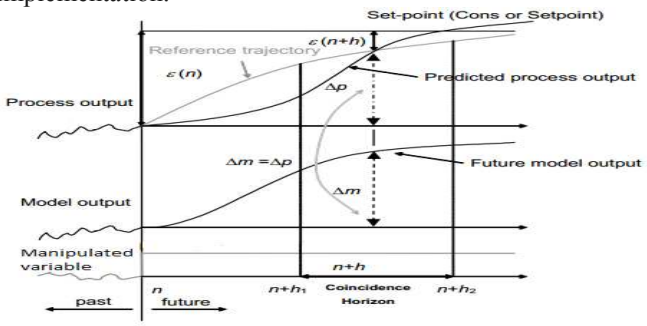

Figure 2. Principle of the PFC [16]

1. *Internal model*

The behavior of a process will be simulated by an internal model. It is said internal because it is located in the control. The parameters of this model are obtained by different techniques of modeling and/or identification of the process.

The goal is to know the future behavior of the process if it is submitted to a certain input [17].

2. *Reference trajectory*

The setpoint (consigne) is the target of the control, but this specification is not sufficient and it should be defined how to achieve this. The reference trajectory is the future path that one would ideally want the regulated process to take in order to reach the imposed set point. It is she who will impose the dynamics of the closed loop.

3. *Coincidence horizon*

It is necessary to define a time interval [H1, H2] in which we find at least a point of coincidence between the known reference trajectory and the output of the process.

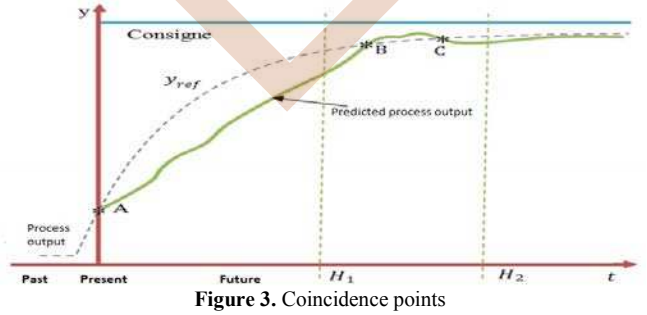

Figure 3. Coincidence points

In Figure 3, the points B and C are the points of coincidence Between the reference trajectory $y_{ref}(t)$ and the output of the process $y_p(t)$ in the interval [H1, H2].

4. *Purpose of the control*

It is considered that the increment of the output of the process at the point of coincidence is presented by the following relation:

$$\Delta_P(k) = y_P(k+H) - y_P(k) \quad (6)$$

where k represents the present time.

As on the other hand, the model simulates the behavior of the process, one can also set the desired increment in the model space.

$$\Delta_M(k) = y_M(k+H) - y_M(k) \quad (7)$$

In the end, the control to be applied to the process is obtained from the equality between the two increments presented, that is to say:

$$\Delta_P(k) = \Delta_M(k) \quad (8)$$

B. *The calculation of the control*

One of the characteristics of the PFC control is the structuring of the control law.

This corresponds to choosing the type of setpoint signal from basic functions such as step, ramp, parabola, etc. These basic functions are used in the prediction part of the predictive control.

As mentioned previously, the predictive control is obtained from the equality between the reference trajectory and the predicted output of the process at a point of coincidence *H*.

Thus, the relation (8) allows to find the expression of the control.

The model:

$$G(p) = \frac{K_p}{1+\tau_p P} = \frac{y_p(t)}{u_p(t)} \quad (9)$$

$$G_p(z^{-1}) = \frac{k_M(1-e^{-T_e/\tau})z^{-1}}{1-e^{-T_e/\tau}z^{-1}} = \frac{y_M(z^{-1})}{u(z^{-1})} \quad (10)$$

where T_e is the sampling time.

From the previous sampled model, remembering that Z^{-1} is equivalent to a delay of a sample and noting $\alpha = e^{-T_e/\tau}$ (where τ is the time constant), it comes:

$$y_p(k) = \alpha y_p(k-1) + K_M(1-\alpha)u(k-1) \quad (11)$$

By doing the same thing for the model, we can write:

$$y_M(k) = \alpha y_M(k-1) + K_M(1-\alpha)u(k-1) \quad (12)$$

If we consider the control as constant at a value $u(k)$ after its application at time *k*, we have:

$$u(k+1) = u(k+2) = \ldots = u(k+H) = u(k) \quad (13)$$

It is therefore possible to calculate the output at the instant $k+H$ by incrementing in the equation (13).

This approach leads to the predictor equation:

$$y_M(k+H) = \alpha^H y_M(k) + K_M(1-\alpha^H)u(k) \quad (14)$$

The reference trajectory can be set by specifying the desired closed loop response time (T_{Bf}) and choosing an exponential decay difference (see the Figure 3).
From the Figure 3, we can write:

$$\varepsilon(k) = C - y_{ref}(k) \quad (15)$$

where $\varepsilon(k)$ is the difference between the set-point C and the reference trajectory at time k.
The reference trajectory is chosen exponentially, the decrement of the difference between the set-point and the output is given by:

$$\varepsilon(k+H) = \varepsilon(k)e^{-T_e H/\tau_{bf}} = \varepsilon(k)\lambda^H \quad (16)$$

with $\lambda = e^{-T_e H/\tau_{bf}}$ and τ_{bf} represents the time constant of the reference trajectory.
If it is assumed that at the instant $k+H$ there is a coincidence between the output of the process and the reference trajectory, under these conditions, the increment of the output of the process $\Delta_p(k)$ can be determined by:

$$\Delta_p(k) = y_{ref}(k+H) - y_{ref}(k) = C - \varepsilon(k+H) - y_{ref}(k) \quad (17)$$

Using relations (15) then (16), the expression of the increment of the output becomes:

$$\Delta_p(k) = (1-\lambda^H)(C - y_{ref}(k)) \quad (18)$$

Given the coincidence between the two trajectories in $k+H$, y_{ref} can be replaced by measuring the output of the process in equation (18).

In the same way as for the method, we can determine the increment of the output of the model by using equation (14):

$$\Delta_M(k) = (1-\alpha^H)k_M u(k) - y_M(k)(1-\alpha^H) \quad (19)$$

Since the objective is to have $\Delta_p(k) = \Delta_M(k)$, we can derive from equations (18) and (19) the expression of the control:

$$u(k) = \frac{(1-\lambda^H)(C(k) - y_p(k))}{(1-\alpha^H)k_M} + \frac{y_M(k)}{k_M} \quad (20)$$

This control corresponds to the scheme described in Figure 4

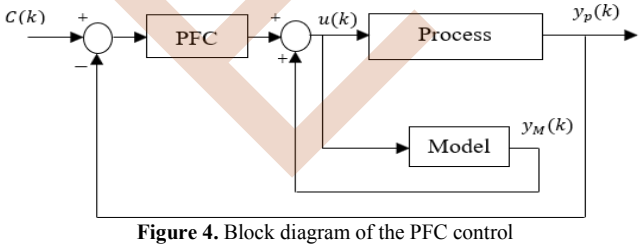

Figure 4. Block diagram of the PFC control

C. *Parameters needed to implement the PFC*

The preceding paragraph makes it possible to determine the shape of the control law, the closed loop time constant (τ_{bf}) and the coincidence horizon are necessary for the final calculation.

These parameters are defined as follows:
Let's note first that the response time in open loop (T_{Bo}) is defined from the time constant of the model: $T_{Bo} = 3\tau$
If we define an acceleration factor of the response called F_{accel}, this factor makes it possible to specify the desired response time in closed loop by the relation:

$$T_{Bf} = \frac{T_{Bo}}{F_{accel}}$$

with : $1 < F_{accel} < 3$
Thus, the time constant in closed loop is obtained by:

$$\tau_{bf} = \frac{T_{Bf}}{3}$$

Finally, the coincidence point H is taken equal to:

$$H = ceil\left(\frac{\tau_{bf}}{3T_e}\right)$$

IV. Identification of the Building Heating System

The identification of a system is the most difficult part for the implementation of a predictive control, specifically the heating system that is defined as a non-linear system and also because of its slowness.

For this, we took a linear model that perfectly represents the behavior of the heating system, which will be used in the following for the application of the PFC control.

The linear model that identifies our system is that of a third order defined by the following continuous transfer function [18]:

$$G(p) = \frac{k(T_z p + 1)}{p(T_w^2 p^2 + 2\varepsilon T_w p + 1)} \quad (21)$$

with: $k = 0.000226$; $T_z = 61741$; $T_w = 834$; $\varepsilon = 1.1606$

V. Application of PFC Control to Building Heating System

We have taken the example of an office (36m^3) occupied from 8h00 to 17h00 from Monday to Friday with the following parameters:

TABLE I. Simulation Parameters

Designation and Heat Transfer Factor	Dimension
Window surface	2 m^2
Convective heat transfer coefficients (wall – floor – ceiling)	[0.25 0.0001 0.25] W/m^2/k
Initial zone temperature	10 °C
Reference temperature while occupancy	19 °C
Electric heater nominal power	1000 W
Number of occupants	2 persons
Weather data	Rennes (region in France)
Simulation time	1 day
Equipment heat emission per m^2	1 W/m^2
Fresh air supply	40 m^3/h/pers
Mean outside temperature	6.5 °C

The structure of the PFC control is shown below

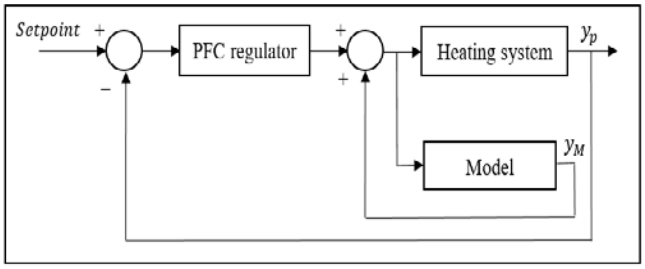

Figure 5. The structure of PFC control applied to heating regulation of building zone

A. The control algorithm

The following steps give the control law of the PFC:

Step 1: Formulation of the internal model

- *The decomposition of the model*

Using as an internal model equation (21), which will be decomposed into simple elements of three sub-models M_1, M_2 and M_3.

$$G(p)=\frac{k_1}{p}+\frac{k_2}{1+T_2 p}+\frac{k_3}{1+T_3 p} \tag{22}$$

The parameters of the model:

$$\begin{cases} k_1 = 2.26\times10^{-4} \\ k_2 = -6.9286 \\ k_3 = 20.4403 \end{cases} \qquad \begin{cases} T_1 = 1 \\ T_2 = 476.1906 \\ T_3 = 1428.600 \end{cases}$$

The figure below shows the parallel decomposition of the model:

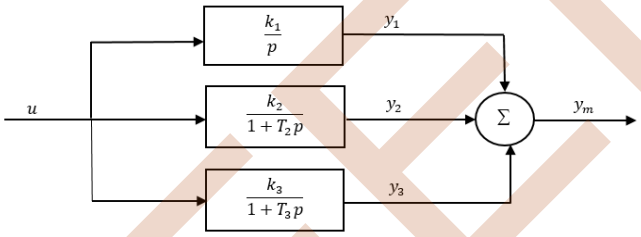

Figure 6. Parallel internal model

Since the model includes an integrator, it is advisable to break down the integrating term which is unstable into two models M_{01} and M_{02} of the first order in parallel [16].

In order to implement the model in the control computer one must transform the model into discrete; so the parallel model plus the BOZ with a sampling period $t_e = 70s$ gives us:

$$\begin{cases} \begin{cases} M_{01}(z^{-1}) = \dfrac{k_1 z^{-1}}{1-\alpha_1 z^{-1}} \\ M_{02}(z^{-1}) = \dfrac{(1-\alpha_1)z^{-1}}{1-\alpha_1 z^{-1}} \end{cases} \\ M_2(z^{-1}) = \dfrac{k_2(1-\alpha_2)z^{-1}}{1-\alpha_2 z^{-1}} \\ M_3(z^{-1}) = \dfrac{k_3(1-\alpha_3)z^{-1}}{1-\alpha_3 z^{-1}} \end{cases} \tag{23}$$

with: $\alpha_1 = e^{-t_e/T_1}$; $\alpha_2 = e^{-t_e/T_2}$; $\alpha_3 = e^{-t_e/T_3}$

- *The output of the model*

From the Figure 6, the global output of the model $y_M(k)$ is given by:

$$y_M(k) = y_1(k) + y_2(k) + y_3(k) \tag{24}$$

with:

$$\begin{cases} y_1(k) = \alpha_1 y_1(k-1) + (k_1 + (1-\alpha_1))(1-\alpha_1)u(k-1) \\ y_2(k) = \alpha_2 y_2(k-1) + k_2(1-\alpha_2)u(k-1) \\ y_3(k) = \alpha_3 y_3(k-1) + k_3(1-\alpha_3)u(k-1) \end{cases}$$

Step 2: Formulation of the reference trajector

$$y_R(k+H) = C - \lambda^H (C - y_p(k)) \tag{25}$$

with: $\lambda^H = e^{-T_e * H * 3/T_{Bf}}$

Step 3: Calculation of the predicted output
The estimated output of the model id given by:

$$y_p(k+H) = \sum_{i=1}^{3} y_i(k+H) + (y_p(k) - \sum_{i=1}^{3} y_i(k)) \tag{26}$$

Step 4: Calculation of the order law
The expression of the control law is:

$$u = \frac{(1-\lambda^H)(C(k) - y_p(k))}{\sum_{i=1}^{3} k_i(1-\alpha_i^H)} + \frac{\sum_{i=1}^{3} y_i(k)(1-\alpha_i^H)}{\sum_{i=1}^{3} k_i(1-\alpha_i^H)} \tag{27}$$

B. PFC controller parameters

$T_{Bf} = 4000s$; $T_e = 50$; $F_{accel} = 2$; $H = 10s$

The closed loop response time is the major setting parameter of the PFC that is set by the reference path, and the dynamics of the system depends on the latter. For that, we tested different values of the T_{Bf}, so that H would be short, which has the consequence of the control which will be very active and more stable comparing to a distant H, and we could note that the value of $T_{Bf} = 4000s$ ensures a good result for the order.

To evaluate the performance of this strategy of the control, we have simulated the process for one day the parameters and different inputs are given in Table II.

TABLE II. THE INPUTS USED IN OUR CASE

Inputs	**Parameters**
E_vert [W/m²]	Connected to weather data (Rennes, France)
E_vert [luxe]	Connected to weather data (Rennes, France)
Blind_pos	Closed during the period of occupation
Text [°C]	Connected to weather
(Tlower, Tupper, Tadj) [°C]	Temperature of lower, upper and adjacent zones
Q_elec [W]	Heat given by the electrical equipements
Q_occ [W]	Heat given by the occupants
Air in	Air conditionning vector of zone
Q_EM [W]	Power given by the heater
Control input signal	In the interval [0,1]

C. Simulation results

The simulation results are illustrated in Figure 7, Figure 8 and Figure 9.

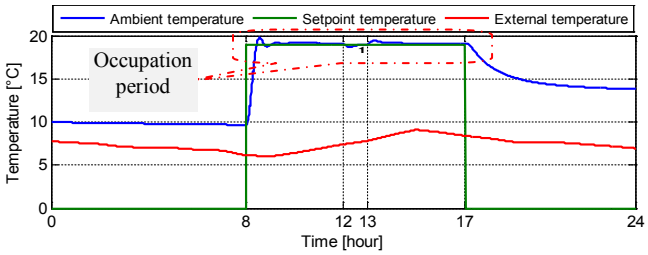

Figure 7. The output of the process and the reference

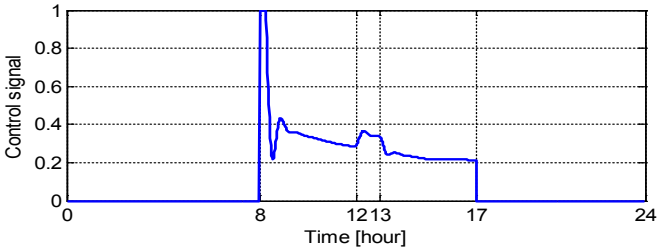

Figure 8. Control signal

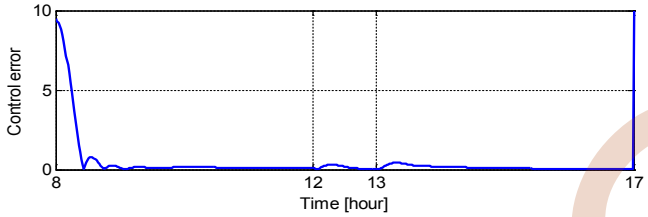

Figure 9. Control error

Table III shows the performance indices for PFC approach

TABLE III. PERFORMANCES INDEX

Comfort index [°Ch]	Consumption index[kWh]	Temperature stability index[°C]	Command stability index
3.3370	3.0835	12.827	4.0852×10^{-5}

D. Discussion of the results

Figure 7 shows the output of the system and that of the reference model, it can be seen that during the occupation period the ambient temperature follows perfectly the set point with very small as shown in the Figure 9. The gap in beginning of the occupation period due to inertia of the heating system.

From Figure 8 it is clear that the control has weak oscillations only at the beginning of the occupation period due to the abrupt change of the temperature, which dispersed at the rest of time. For this reason, we conclude the stability of the control signal.

The numerical evaluation of the different indices showed in Table III indicate the satisfactory of the comfort inside the zone and the optimization of the energy consumption. We can conclude that with a minimum consumption of 3.0835 kWh, we have guaranteed a good comfort.

VI. CONCLUSION

In this paper, we proposed a method of predictive functional control to regulate the temperature in a building zone. The main objective addressed herein is a control of building heating system in the presence of different types of disturbances such as neighborhood temperatures, external temperature and weather data. The results obtained after the simulation in Matlab/Simulink, show the efficacy of this strategy in the control of very complex nonlinear systems. The future work will focus on the application of other control strategies to reduce the temperature inertia gaps and to consider a multizones heating process.

REFERENCES

[1] Al-Sanea, Sami A., M. F. Zedan, and S. N. Al-Hussain. "Effect of masonry material and surface absorptivity on critical thermal mass in insulated building walls." Applied energy 102 (2013): 1063-1070.

[2] L. Prez-Lombard, J. Ortiz, C. Pout, A review on buildings energy consumption information, Energy Build. 40 (2008) 394–398.

[3] R. Yusof, H. Selamat and S. Attaran. (2014) "Short review on HVAC components, mathematical model of HVAC system and different PID controllers", International Review of Automatic Control, vol. 7, no. 3, pp. 263-270.

[4] S. Soyguder, M. Karakose, H. Alli, Design and simulation of self-tuning PID type fuzzy adaptive control for an expert HVAC system, Expert Systems with Applications 36 (2009) 4566–4573.

[5] J. Bai, S. Wangb, X. Zhang, Development of an adaptive Smith predictor-based self-tuning PI controller for an HVAC system in a test room, Energy and Buildings 40 (2008) 2244–2252.

[6] R. Parameshwaran, R. Karunakaran, C. Vinu Raja Kumar & S. Iniyan, "Energy conservative building air conditioning system controlled and optimized using fuzzy-genetic algorithm", *Energy and Buildings*, 42(2010), pp. 745-762.

[7] N. Nassif, S. Kajl, R. Sabourin, Optimization of HVAC control system strategy using two-objective genetic algorithm, HVAC&R Research 3 (2005) 459–486.

[8] A. Berry and H. Alaskr. (2018) "Using Artificial Neural NetworkTechnique to Save Energy Consumption in HVAC Systems ", International Journal of Applied Engineering Research, vol. 1 3, no. 12, pp. 10517-10524.

[9] J. Liang, R. Du, Design of intelligent comfort control system with human learning and minimum power control strategies, Energy Conversion and Management 48 (2008) 517–528.

[10] A. Ouaret, H. Lehouche, B. Mendil, L. Brikh, F. Yahiaoui. "Identification and Control of a Heating System Building Based RBF Neural Networks", *3rd International Conference on Green Energy and Environmental Engineering* (GEEE 2016), 23-25 April 2016 - Hammamet, Tunisia.

[11] A. Ouaret, H. Lehouche, B. Mendil, S. Fredj and H. Guéguen. "Comparative study Between Two Architectures of Neural Networks Used for Identification and Control of a building Heating System", *8th International Conference on modelling, identification and control* (ICMIC), IEEE, pp. 845-850, 2016.

[12] Ahmed Ouaret, Hocine Lehouche, Boubekeur Mendil, Siham Fredj and Hervé Guéguen. "Supervisory Control of a Building Heating System Based on Radial Basis Function Neural Networks", *5th International Conference on Electrical Engineering – Boumerdes (ICEE-B)* October 29-31, 2017, Boumerdes, Algeria. DOI : 10.1109/ICEE B.2017.8192182

[13] SIMBAD Building and HVAC Toolbox, Version 4.0 ed, CSTB, 84, avenue Jean Jaurés- Champs-sur-Marne-B-P 2- F-77421 Marne-la-Vallée Cedex 2, March 2005.

[14] L. Matoug, M.T. Khadir et M. Djeghaba,. «Modélisation et commande prédictive d'une station de production d'eau froide basée sur un compresseur scroll et des échangeurs à plaques brassées.» université badji mokhtar , Annaba, Algerie.

[15] Matoug, Lamia. «Modélisation et commande prédictive d'une station de production d'eau glacée basée sur un compresseur scroll.» mémoire de magister, Université Badji Mokhtar-, Annaba, Algerie, 2008.

[16] Jacques, Richalet. *Pratique de la commande prédictive,*. Paris: éditions Hermès, 1993.

[17] Petru-Daniel Morosan, Romain Bourdais, Hevré Guéguen. «Apports de la commande prédictive pour la régulation thermique des bâtiments.» *Traitement de l'information et de l'environnement* : 479-492, 2010.

[18] Hossein FALLAHSOHI, Modélisation dynamique des échangeurs diphasiques, appliquée aux groupes frigorifiques contrôlés par une commande avancée, thése doctorat Institut national des sciences appliquées de Lyon, France, 26 Avril 2011.

Design and voltage control of an automatic voltage regulator using partcile swarm optimization

Adel OUBELAID, Nabil TAIB, Toufik REKIOUA
Laboratoire LTII, Département de Génie Electrique
Université de Bejaia, 06000, Bejaia, Algeria

***Abstract*— This paper presents a study about an intelligent tuning approach of a PID controller which is to be used in the voltage control system of synchronous generator (AVR system). The tuning was performed using particle swarm optimization (PSO) and it is found that the obtained PID parameters strongly depend on the used cost function and the ability of the optimizer to explore well the search space. The PID controller is used within a closed loop consisting of an amplifier, exciter, generator, and the voltage sensor. The objective of this optimization design is to achieve high performance voltage control of the generator. The performance measures of the PID controlled system are investigated by considering the characteristics of the step response. This study was strengthened by a statistical study which shows that the designed optimum AVR system is robust against parameter variations.**

Keywords: Automatic voltage regulator, Particle swarm optimization, PID controller

I. INTRODUCTION

Generator excitation system maintains output voltage and adjusts the reactive power flow using an automatic voltage regulator [1-2]. Voltage regulation is almost importance for the power system as its performance can seriously affect the security of the power system and the optimal operation of equipments connected to it. Owing to its performance, robustness and ease of implementation, the Proportional, Integral and Derivative regulator is still mostly used in the industry. Various systematic methods are used to design PID when plant's transfer function has an order less or equal than two. However, due to the uncertainties, nonlinearities and high order of transfer functions describing the dynamic of the power plant, tuning PID parameters of its AVR becomes a difficult task. To overcome this, more attention nowadays is given to heuristic tuning methods which consider the plant's transfer function as a black box. Amongst these methods, one can find PSO [3-5] and GA [6-7] which have been applied for various engineering optimization problems. They are based on seeking the optimum of cost functions which well model the desired performances of the AVR. However selection of the appropriate cost function to be optimized as well as the best parameters of the optimizer is not always an easy task. In this paper, it is proposed to use PSO algorithm to optimize PID gains and subsequently improve AVR system response.

II. AVR SYSTEM

An AVR is set of many components connected together in such a way the voltage measured at the terminal of the generator is maintained close to its nominal value. These components are the PID regulator, the amplifier, the exciter, the generator and the sensor as depicted in fig.1.Therefore designing the PID controller needs the knowledge of transfer function of each of the above components. For the sake of design, the mathematical model of each component is linearized and the obtained transfer function takes into account the major time constant and ignores the saturation or other nonlinearities. Used AVR parameters are shown in Table I [8].

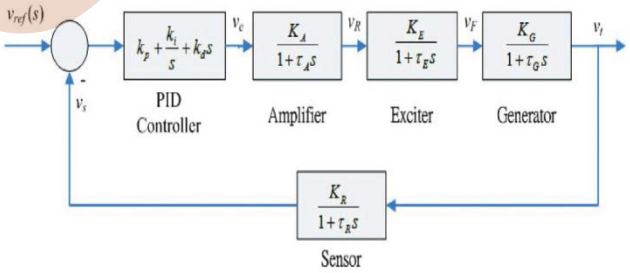

Figure 1. AVR closed loop system.

TABLE I. AVR SYSTEM INFORMATIONS

Component	Transfer function	Interval
Controller	$K_p + K_i/s + K_d s$	Optimum values
Amplifier	$K_A/(1+T_A)$	Ka=[10 40] Ta=[0.02 0.1]
Exciter	$K_E/(1+T_E)$	Ke=[1 10] Te=[0.4 1]
Generator	$K_G/(1+T_G)$	Kg=[0.7 1] Tg=[1 2]
Sensor	$K_S/(1+T_S)$	Ks=[0.7 1] Ts=[1 2]

III. PARTICLE SWARM OPTIMIZATION

Particle swarm optimization is a population-based algorithm inspired from the social behavior of organisms such as birds and fishes. It was first introduced by Eberhart and Kennedy in 1995[9-11]. It is similar to other population-based algorithms like (GA) in that the algorithm is initialized with a population of random solutions. PSO is aimed to find an optimal solution for a specified optimization problem under use of appropriate fitness function. It is based on the assumption of optimum existence inside the considered search field. Furthermore, it uses finite number of decentralized intercommunicating particles (solutions or agents) initialized to positions in this search space moving to hopefully converge to the optimal solution as precise and fast as possible.

For a population of N particles, The personal and global bests are respectively given by equation (1) and (2):

$$P_{best,i}^{t+1} = \begin{cases} P_{best,i}^{t} & if \quad f(x_i^{t+1}) > P_{best,i}^{t} \\ x_{best,i}^{t+1} & if \quad P_{best,i}^{t} \geq f(x_i^{t+1}) \end{cases} \tag{1}$$

$$G_{best}^{t} = \text{Min}\left(P_{best,1}^{t} P_{best,2}^{t} \dots P_{best,n}^{t}\right) \tag{2}$$

$P_{best,i}^{t}$ and G_{best}^{t} are the personal and global best position of particle i at iteration t .The particles' position is updated using equation (3).

$$v_i^{t+1} = w^t v_i^t + c_1 r_1 \left[P_{best,i}^{t} - x_i^t\right] + c_2 r_2 [G_{best}^{t} - x_i^t] \tag{3}$$

w^t is the inertia weighting factor which is linearly decreasing [0.4, 0.9]. r_1, r_2 are random coefficients. c_1 emulates the individual or the cognitive behavior of a given particle whereas c_2 represents the swarm influence that is excerted on a given swarm agent. This phenomenon is highlighted in figure 2. The pseudocode of PSO algorithm is shown in figure 3.

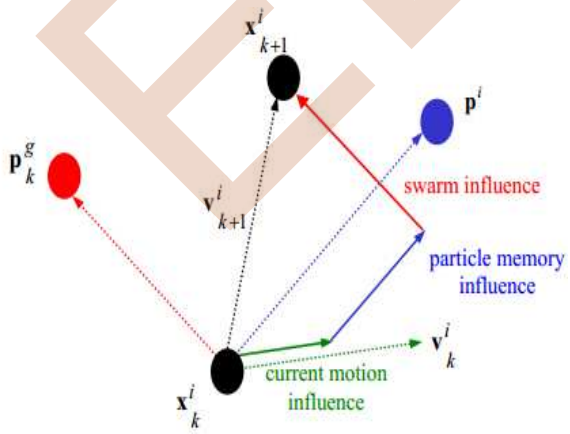

Figure 2. Velocity and position updates in PSO.

```
----------Pseudo code for PSO algorithm----------
Inialize all the particles
Do
  For each particle
    Calculate the new cost
      If the new cost is better than the one in history(Pbest)
      Set the new cost as the new Pbest value
End
Choose particle with best cost of all particles as Gbest
While max iteration or min error is not satisfied
  for each particle
    Update position and velocity based on Pbest and Gbest
  end
end
```

Figure 3. Pseudo code of PSO algorithm.

IV. PERFORMANCE MEASURE

In particle swarm optimization discussed in the previous section , terms like "best particle, best position" have been used. The measurement tool that enables us to classify swarm particles is called: cost function. It is worth noticing that the effeciency of any optimization algorithm is strongly related to the cost function [12-13]. In this work, the goodness of the AVR system response is measured using the integral absolute error given by equation (5).

$$IAE = \int_0^{\infty} |e(t)| dt \tag{4}$$

The swarm is navigating through a bounded three dimensional search space. Particles in the first dimension are seeking for the optimal proportional gain in the interval [0 2]. The search space for optimum integral gain is in the interval [0 1.5] and the derivative gain is located in [0 2].

Before integrating the PSO into the AVR system, one should make sure that the algorithm optimizes well. For this reason, two test functions given by equations (6) and (7), have been considered as cost functions to see whether or not PSO algorithm will succeed to find their optimums.

$$J_1 = x_2 \sin(4x_1) + x_1 \sin(4x_2) \tag{5}$$

$$J_2 = -\mathrm{e}^{-0.2\sqrt{x_2^2 + x_2^2} + 3(\cos(2x) + \sin(2y))} \tag{6}$$

As it is shown in figure 04 and 5, PSO algorithm has succeeded to escape the trap of local optima and converged to local optima. This means that the algorithm is ready for integration in the AVR system.

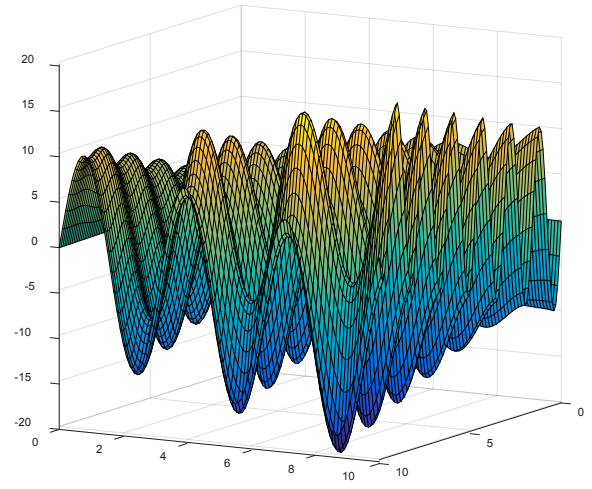

Figure 4. Graph of test function J_1

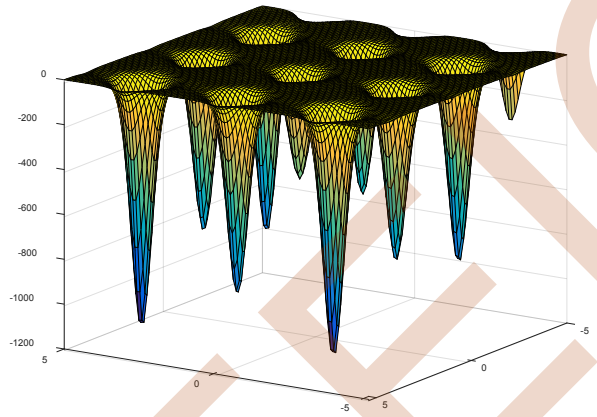

Figure 5. Graph of test function J_2

V. SIMULATION AND RESULTS

Several simulations were carried out with a swarm of 50 particles for 100 iterations. Since the tuning process is offline, the number of population and iterations can be increased for better performance.cognetive and social factors are equal and the PSO topoogy is full connected.

Figure 06 shows the optimum AVR step response. One can remark that the response is fast and smooth. Also, steady state error is very small. More information about AVR time domain performances are provided in Table II.

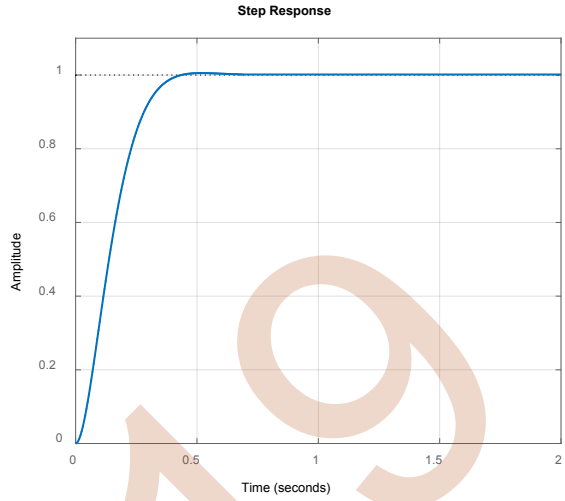

Figure 6. Optimum AVR step response.

TABLE II. AVR TRANSIENT PERFORMANCES

Transient performance	PSO
Percentage overshoot (%)	0.5358
Rising time	0.2355 s
Settling time	0.3699 s
Peak time	0.5207 s
Steady state error	0.0028 s

A. *Root locus analysis*

In order to perform frequency domain analysis, root locus of the resulting optimum AVR system is shown in figure 5. It is worth noticing that the optimum AVR system has five stable poles, four of which are complex and one real pole. The pole and zero located in the neighborhood of -100 are insignificant and can be omitted without affecting AVR system dynamics. The remaining poles are imaginary and occurring in conjugate. These poles are significant since their real part is very close to the origin of the frame.

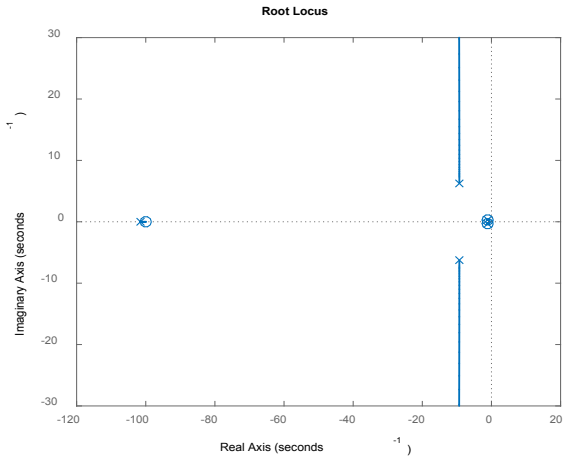

Figure 7. AVR root locus graph.

B. *Bode analysis*

The Bode plot of the optimum AVR system tuned by PSO algorithm is shown in figure 6. It could be noticed that the AVR system has a slope of -40 dB/decade. This means that the overall AVR transfer function behaves like a second order system and the order of the AVR system could be reduced.

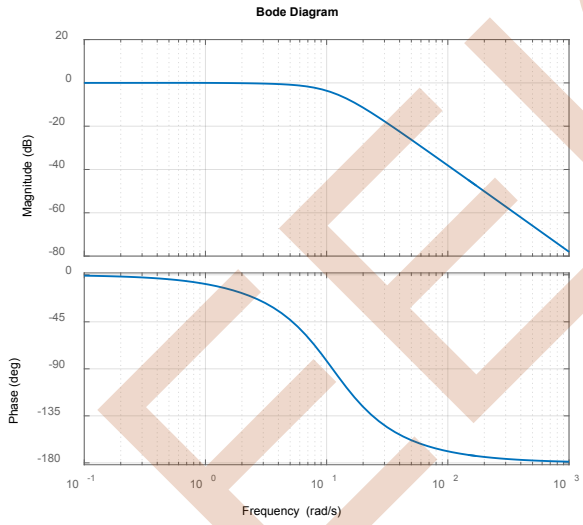

Figure 8. Bode plot of AVR system response.

C. *Robusntness and statistical analysis*

It is very important to ensure that all plant processes are safe and stable around the operating point. To check the robustness of the AVR system against external disturbances, several robustness tests have been performed to the Optimum AVR system gotten using PSO algorithm by varying the time constants of the amplifier, exciter, generator and sensor by ±50% and ±25% . Results of this test are shown in Table III. It can be noticed that time constant variation will not affect system stability. Also, large variations of time constants will cause the AVR system to have higher overshoot but always within limits.

TABLE III. AVR ROBUSTNESS TEST

Time constant	ΔT	Tr	Ts	PO(%)	Tp
Ta	**+50%**	0.1478	0.4346	6.1664	0.3047
	+25%	0.1804	0.4555	3.0515	1.2591
	-25%	0.3424	0.6024	0.2461	1.2584
	-50%	0.5779	1.0403	0.5153	2.1330
Te	**+50%**	0.3370	1.8688	4.9357	0.8960
	+25%	0.2885	1.1994	2.7405	0.7543
	-25%	0.1796	0.8778	0.000	0.3427
	-50%	0.1246	1.3512	2.6813	0.2396
Tg	**+50%**	0.3455	2.0116	4.3804	0.9555
	+25%	0.2924	1.1829	2.4022	0.8005
	-25%	0.1772	0.8443	0.6415	0.3446
	-50%	0.1214	1.4163	4.3560	0.2332
Ts	**+50%**	0.2254	0.3455	1.1578	0.4756
	+25%	0.2304	0.3573	0.8154	0.4984
	-25%	0.2409	0.3832	0.3167	0.5478
	-50%	0.2464	0.3972	0.1549	0.5840

Table IV represents a statistical test conducted to see what is the maximum deviation that occurs in a given AVR performance when the time constant of one of its components is varied. It could be concluded that the maximum percentage overshoot deviation is 5.92%, maximum settling time deviation 0.4301 sec and maximum rising time deviation is 1.1673 sec.

TABLE IV. CRITICAL AVR PERFORMANCES

Time constant	Performance	Maximum deviation
Ta	**Tr**	0.4301
	Ts	0.6057
	Po	5.9203
	Tp	1.8283
Te	**Tr**	0.2124
	Ts	1.1162
	Po	4.9357
	Tp	0.6564
Tg	**Tr**	0.2241
	Ts	1.1673
	Po	3.7389
	Tp	0.7223
Ts	**Tr**	0.210
	Ts	0.517
	Po	1.0029
	Tp	0.1048

VI. CONCLUSION

In this paper, an intelligent voltage control for an AVR system is studied. The PID controller is intelligently tuned using PSO algorithm. This tuning method has not only provided satisfactory results but it has also saved time and efforts which are usually wasted in the trial and error process. Frequency domain analysis, Robustness analysis and statistical analysis were performed on the optimum AVR system and the results are satisfactory.

VII. REFERENCES

[1] Htay M, Win KS. Design and construction of automatic voltage regulator for diesel engine type stand-alone synchronous generator. World Academy of Science, Engineering and Technology. 2008 Aug;42:652-8.

[2] Kouba NE, Menaa M, Hasni M, Boudour M. Optimal control of frequency and voltage variations using PID controller based on particle swarm optimization. In2015 4th International Conference on Systems and Control (ICSC) 2015 Apr 28 (pp. 424-429). IEEE.

[3] Madadi A, Motlagh MM. Optimal control of DC motor using grey wolf optimizer algorithm. Tech J Eng Appl Sci. 2014;4(4):373-9.

[4] Bhatt VK, Bhongade S. Design of PID controller in automatic voltage regulator (AVR) system using PSO technique. International Journal of Engineering Research and Applications (IJERA). 2013 Jul;3(4):1480-5.

[5] Nirmal JF, Auxillia DJ. Adaptive PSO based tuning of PID controller for an Automatic Voltage Regulator system. In2013 International Conference on Circuits, Power and Computing Technologies (ICCPCT) 2013 Mar 20 (pp. 661-666). IEEE.

[6] Maulik U, Bandyopadhyay S. Genetic algorithm-based clustering technique. Pattern recognition. 2000 Sep 1;33(9):1455-65.

[7] Hasanien HM. Design optimization of PID controller in automatic voltage regulator system using Taguchi combined genetic algorithm method. IEEE systems journal. 2012 Nov 10;7(4):825-31

[8] Panda S, Sahu BK, Mohanty PK. Design and performance analysis of PID controller for an automatic voltage regulator system using simplified particle swarm optimization. Journal of the Franklin Institute. 2012 Oct 1;349(8):2609-25.

[9] Eberhart RC, Shi Y. Comparing inertia weights and constriction factors in particle swarm optimization. InProceedings of the 2000 .

[10] Shi Y, Eberhart RC. Fuzzy adaptive particle swarm optimization. InProceedings of the 2001 congress on evolutionary computation (IEEE Cat. No. 01TH8546) 2001 May 27 (Vol. 1, pp. 101-106). IEEE.

[11] Sönmez Y, Unal M. Estimation of Smooth and Non-smooth Fuel Cost Function Parameters Using Improved Symbiotic Organisms Search Algorithm. Journal of Electrical Engineering & Technology. 2019:1-3

[12] Musardo C, Rizzoni G, Guezennec Y, Staccia B. A-ECMS: An adaptive algorithm for hybrid electric vehicle energy management. European Journal of Control. 2005 Jan 1;11(4-5):509-24.

[13] Eberhart RC, Shi Y. Comparing inertia weights and constriction factors in particle swarm optimization. InProceedings of the 2000 .

Neural Network for Abnormalities Detection in Radiotherapy Service

ET-Tahir Zemouri[1] and Abdelkrim Allam[2]
Centre for Development of Advanced Technologies (CDTA)
Baba Hassen - Algiers, Algeria
[1]tzemouri@cdta.dz, [2]allam@cdta.dz

***Abstract*—We present an automatic system for abnormality detection basis on machine learning techniques for radiotherapy services. The quality of services in radiotherapy remains a big challenge in the entire world. For this reason, the proposed system improves the quality of services and increase medical care. The platform consists of an ensemble of computers for server, linear accelerators and scanner simulators located in cure rooms. Computers have network connection to control the and store the data concerning check-list of the devices, the temperature, the moisture data, Users and patients management. The main contribution is the use of machine learning techniques for avoiding fatal mistakes during the treatment. An encouraging result is obtained using Neural Network (NN).**

Keywords—radiotherapy, sensors, abnormalities detection, classification, neural network

I. INTRODUCTION

The cure of cancer in radiotherapy services requires a lot of attention. Many manipulators are involved to take care and to treat patients by using dangerous devices like linear accelerators. It is difficult to control the interaction between these agents and check the quality of the apparatus (Devices and tools) in a daily basis. For example, the medical staff of the radiotherapy service in "Centre Pierre et Marie Curie hospital (CPMC)" is composed of fifty (50) people. The proposed system in this work plans to avoid some mistakes of manipulation and management. It improves the quality of the services and increases the medical care while applying some medical, technical and physical procedures. These procedures should be applied by personnel of the radiotherapy service. The developed program permits the application of these procedures. The main purpose of this work is to avoid mistakes of manipulation. They are fatal for patients once they are encountered. Accidents occur even in developed countries (USA, France, England, etc) [1-3]. Currently, the problem of quality of services and accidents in radiotherapy services in the world are not solved adequately [4-18]. The first version of the system that we propose to address this issue is implemented in the radiotherapy service of the hospital CPMC in Algiers.

II. COMPUTERS NETWORK PLATFORM

The block diagram of the control platform implemented in this study is shown in Fig. 1.

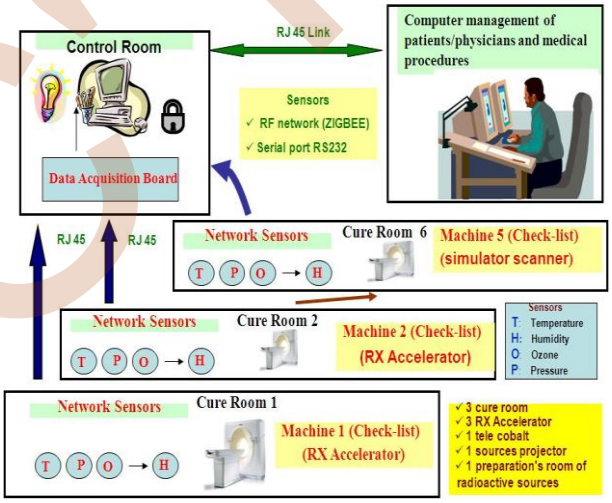

Figure 1. Control platform of the radiotherapy service.

In the first step, the system consists of set of computers (PC), Server, Linear accelerators [19-20], Scanner simulators, and temperature, moisture and pressure sensors for the cure rooms.

The PCs are connected to a network and others are used to control the check list of the apparatus (linear accelerators). These PCs are located outside the cure rooms. The Server stores the data (the check list of the devices, temperature, moisture and pressure data, Users and patients). PCs devoted to the users in order to enter their coordinates and all medical information related to patients during the sessions of the radiotherapy simulation and treatment.

The head or the technical manager of the radiotherapy services could by this means controls and supervises all the machines. Temperature, moisture and pressure sensors are located inside the cure and simulation rooms with linear accelerators and scanners simulators. This system is implemented in order to improve the quality of services and to increase the medical care.

The proposed system was built in collaboration between CDTA and CPMC. Fig. 2-3 show the real time control of cure rooms and simulation room, which consists of multiple screen solution, the system was developed under Labview [21-24].

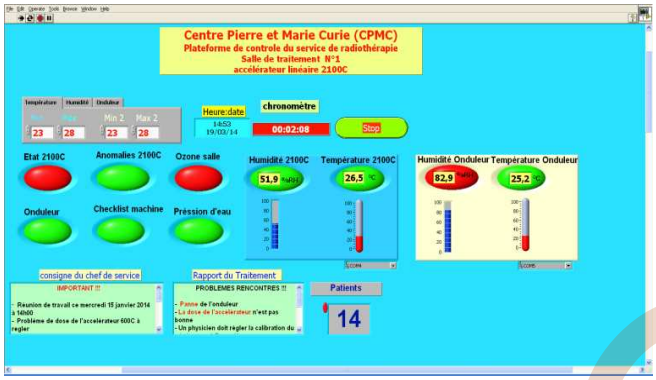

Figure 2. Real time control of one cancer treatment room(Labview).

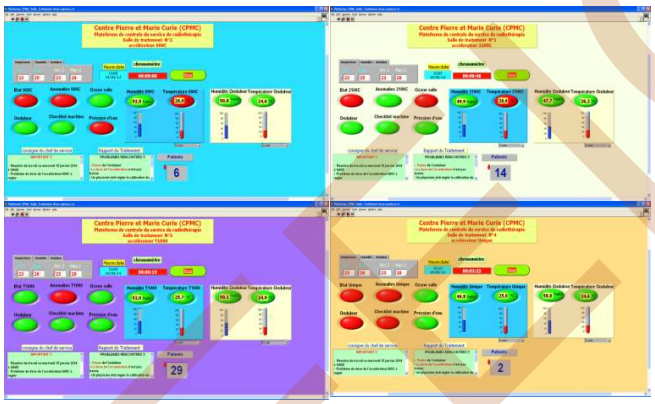

Figure 3. Real time control of four treatment rooms (Labview).

Medical treatment procedures utilizing radiation play a central role in modern health care. To ensure maximal benefits and minimal risks, it is essential that these techniques rely on adequate procedures. The available system does not guaranty mistakes of manipulations and human fatal errors for the patients during treatment. For this, we propose an automatic abnormality detection system on the basis of machine learning techniques, the proposed system function in parallel with the available platform in order to control the different procedures.

III. Description Of The Proposed Control System

The main contribution of the proposed system is to use the machine learning techniques for detecting the abnormalities in the medical chain treatment. Fig. 4 summarizes the proposed flowchart.

The proposed system first trains the input data using NN training in order to generate the NN classification model, finally the collected data are classified and the decision is done.

In this paper we exploit the supervised Neural Network (NN) classifier, which has multiple input, output and hidden layers with arbitrary number of neurons [26]. Multi-layer perception (MLP) is the famous used NN classifier with back propagation learning algorithm which is used for optimization. As shown in Fig. 5, the basic NN architecture consists of three layer types, called: input layers, hidden layers, and output layers. In general, the input layers correspond to the features set, the hidden layers are defined empirically relatively to the accuracy, and the output layer corresponds to the classes. Each class corresponds to a node in output layer. Where, the output node value should present a high output value on the correct class and a low output value otherwise.

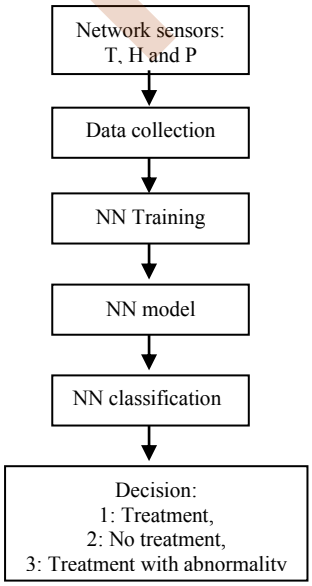

Figure 4. Flowchart of the proposed system.

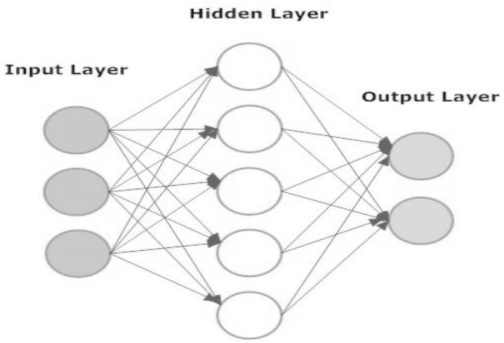

Figure 5. Multi-layer Neural Network Architecture.

As NN is supervised classifier, set of features vector and their corresponding desired output vector are presented at the input layers during the training phase. Initial random weights are assigned to the set of nodes. The NN adjusts the weights related to the connections according to the network output and the desired output in order to minimize the difference between them. A neuron in the network can be represented as:

$$y_i = f_i \sum w_{ij} x_i \quad (1)$$

where x_i is the input data, w_{ij} is the weight between i^{th} neuron of previous layer and j^{th} neuron of the current layer and f_i is the activation function.

IV. Experiment and Results

The data are collected from CPMC using three sensors: temperature (T), moisture (H) and pressure (P). The used temperature and humidity network sensors are MS6503 and PM15PS. More details about the data collection are described in [25].

The collected data (T, H, P) are labeled into three classes according to the decision of the proposed system:

- Class 1: Treatment,
- Class 2: No treatment,
- Class 3: Treatment with abnormality.

A 1-hidden layer feed forward neural network with 10 hidden layer neurons is created and trained. The input and target samples are divided into training, validation, and test sets. The training set is used to learn the network. Training continues as long as the network continues improving on the validation set. The test set provides an independent measure of the network accuracy.

Performance is shown for each of the training, validation, and test sets. It rapidly decreased as the network was trained. The best validation performance is 0.016802 at epoch 26 (See Fig. 6).

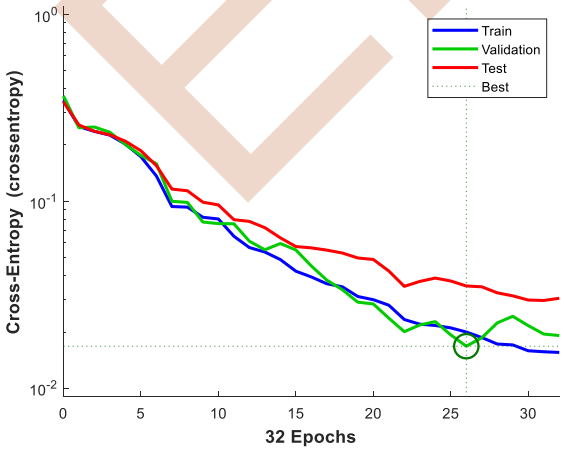

Figure 6. Best validation performance.

Fig. 7 shows the performance in term of Receiver Operating Characteristic (ROC) curve.

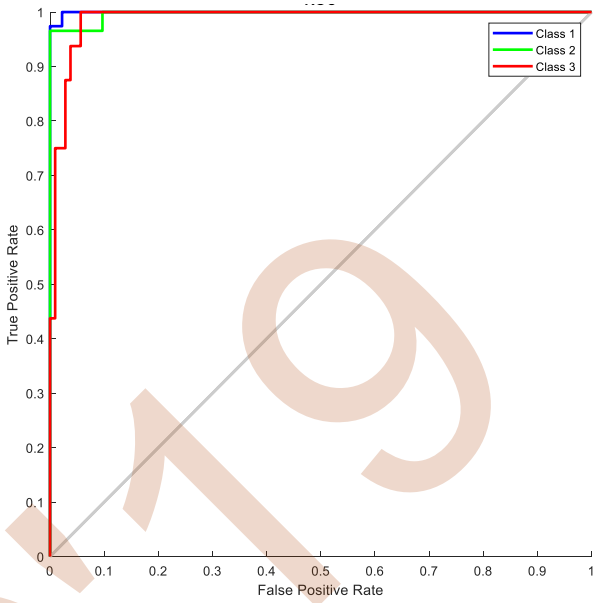

Figure 7. Receiver Operating Characteristic (ROC) curve.

Table 1 shows the confusion matrix. The network outputs are very accurate, as we can see by the high numbers of correct responses in the green squares and the low numbers of incorrect responses in the red squares. The lower right blue squares illustrate the overall accuracies.

TABLE I. Confusion Matrix (%).

Target / Output	1	2	3	
1	61.5	0	1	98.7
2	0	23	0.8	96.6
3	1.6	0.8	11.5	82.4
	97.4	96.6	87.5	**95.9**

Our proposed system achieved 95.9 % for the overall accuracies, these warrants the efficiency of the proposed protocol for abnormalities detection.

V. Conclusion

Besides chemotherapy and surgery, radiotherapy is the last step when treating cancer. We have designed and implemented a computer network platform devoted to radiotherapy services. To control the different sensors we have proposed an intelligent system based on Neural Network in order to avoid errors of manipulation which

could be fatal to patients. The objective is to detect automatically the abnormalities in the treatment process. The obtained results justified that our proposed system improved the quality of the treatment cure.

In future work we propose to implement other machine learning techniques.

ACKNOWLEDGMENT

This research has been funded under grant N° 05/DEPR/ATRSS by the Thematic Agency of Research in Health Sciences (ATRSS) and the Algerian Ministry of Higher Education and Scientific Research Authors would like to thank ATRSS for their support

REFERENCES

[1] O Holmberg, "Accident prevention in radiotherapy",Biomedical Imaging and Intervention Journal, 2007, 3(2):e27.

[2] International Atomic Energy Agency, "The overexposure of radiotherapy patients in San José, Costa Rica", Vienna, Austria: IAEA, 1999.

[3] G.Wack, F.Lalande, M.D Seligman, « Radiotherapy accident occurring at Epinal (France) », AIEA report number INIS-FR--09-0236, reference number 40032727, Feb 2007; 8 p.

[4] T. Garcia, T. Lacornerie, R. Popoff,, V. Lourenço, J.-M. Bordy, « Dose verification and calibration of Cyberknife® using EPR/Alanine dosimetry », (2011), Radiation Measurements, volume 46 issue 9, pages 952-957

[5] J.M. Bordy et al, Radiotherapy out-of-field dosimetry: « Experimental and computational results for photons in a water tank », Radiation Measurements, Volume 57, October 2013, Pages 29-34.

[6] V. D. Merwe, « Radiotherapy in Cancer Care: Facing the Global Challenge », IAEAL 17-01089 | ISBN 978–92–0–115013–4, edited by E. Rosenblatt, E. zubizarreta, International Atomic Energy Agency (AIEA), 2017.

[7] S.Thyago, P.dos, T.Flavia, C.Da Siva; D. Souza, « Radiotherapy risk analysis: Application of the FMEA tool in linear accelerator quality control », congress of the Brazilian Society of Radiotherapy, São Paulo (Brazil), August 2018.

[8] Shrivastava, K.Shyam, « Improving radiotherapy outcomes: are newer technology achieving the goal? », ICRR-HHE 2018: international conference on radiation research - impact on human health and environment and second biennial meeting of society for radiation, Hyderabad (India); 1-4 Feb 2018.

[9] A.N.Abbasi, M.Karim, B. M. Qureshi, « A Simplified Suggested Methodology for Quality Improvement in Radiation Oncology Facility », Department of Oncology, The Aga Khan University, Radiation Oncology Section, Karachi-Pakistan, Turkish Journal of Oncology, 2018;33(3):125–7, doi: 10.5505/tjo.2018.1831.

[10] N.Abbasi A, Muhammad W, Hussain A. "Implementation of quality medical physics training in a low middle income country - sharing experience from a tertiary caree" JCIA-accredited university hospital. J Appl Clin Med Phys 2016;17(6):454–6.

[11] Rosenblatt E, Fidarova E, Ghosh S, Zubizarreta E, Unterkirhere O, Semikoz N, et al. « Quality of radiotherapy services in post-Soviet countries: An IAEA survey », Radiother Oncol 2018;127(2):171–7.

[12] International Atomic Energy Agency, "Investigation of an accidental exposure of radiotherapy patients in Panama", Vienna,Austria: IAEA, 2001.

[13] International Atomic Energy Agency, "The accidental overexposure of radiotherapy patients in Bialystok", Vienna, Austria: IAEA, 2002.

[14] International Atomic Energy Agency, "Lessons learned from accidents in radiotherapy", Vienna, Austria: IAEA, 2000. (Safety Reports Series; 17).

[15] Prevention of accidental exposures to patients undergoing radiation therapy. A report of the International Commission on Radiological Protection. Ann ICRP 2000; 30(3):7-70.

[16] Cohen L, Schultheiss TE, Kennaugh RC. A radiation overdose incident: initial data. Int J Radiat Oncol Biol Phys 1995;33(1):217-24.

[17] Ash D, Bates T. Report on the clinical effects of inadvertent radiation underdosage in 1045 patients. Clin Oncol (R Coll Radiol) 1994; 6(4):214-26.

[18] The accident of the linear accelerator in the "Hospital Clínico de Zaragoza". Spanish Society of Medical Physics, 1991.

[19] Nuclear Regulatory Commission, Report to Congress on Abnormal Occurrences. Washington DC: US NRC, 1988; NUREG-0090; vol11(4).

[20] Report of an investigation by the Inspector appointed by the Scottish Ministers for The Ionising Radiation (Medical Exposures) Regulations 2000. Unintended overexposure of patient Lisa Norris during radiotherapy treatment at the Beatson Oncology Centre,Glasgow January 2006.

[21] Li Pengfei, Nie Luhua, « Remote Control Laboratory Based On LabVIEW », ICICTA conference, vol. 4, pp.84-87, 2009 Second International Conference on Intelligent Computation Technology and Automation, Changsha, Hunan, China, 2009.

[22] Xiaoyan, C., Xiaodong, Z., Xi, C."A Virtual Laboratory for Electrical and Electronics Teaching", IEEE International Symposium on Microwave, Antenna, Propagation and EMC Technologies for Wireless Communications Proceedings, pp.491-495, 2005.

[23] A. Bhandari and M. Shor. Access to an instructional control laboratory experiment trough the world wide web. In Proc. of IEEE American Control Conference, pages 1319–1325, Philadelphia, June1998.

[24] D. Gillet, A.V. Nguyen Ngoc, Y. Rekik, "Collaborative Web-Based Experimentation in Flexible Engineering Education", IEEE Transaction on Education, vol. 48, no. 4, November 2005.

[25] K.Lamamra, A.Allam, M.Afiane, "Artificial neural networks for acquisition and processing of sensors data in a radiotherapy application", Inderscience journal, IJSPM International Journal of Simulation and Process Modelling, 2018 – Vol.13, No.1 pp. 15 –23.

[26] J. Hertz, A. Krogh, and R. Palmer, Introduction to the theory of neural computation. Basic Books, 1991, vol. 1.

The slotine-Li controller for a manipulator robot has two degree of freedom

Samir IKNI
Department of Technology, University of Khemis Miliana
Algeria
s.ikni@univ-dbkm.dz

Abdelyazid ACHOUR
Laboratory of Industrial Technology and information
Faculty of Technology, University of Béjaia
Béjaia, Country

***Abstract*— In this study, a planning and motion control system of manipulator robots is proposed using adaptive control based on the slotine-Li method for the stability of nonlinear systems. The system is responsible for constantly monitoring the proper tracking of the desired trajectories for the robot. The result obtained is that the adaptive control algorithm is proposed by using a parameter estimation rule as a function of the dynamics of the manipulator robot. The effectiveness of the proposed system is evaluated through the simulation by the MATLAB software of a manipulator robot with two degrees of freedom.**

Keywords*: *Manipulator robot, control, Track planning, great precision

I. INTRODUCTION

The subject of control of robotic systems remains one of the most important topics of the news, which directs towards the imitation of the man. An imitation that leads to increasingly complex systems [1, 2], and highly nonlinear (uncertain). These systems generally do not have the mathematical model necessary for their order, which requires the availability of very effective tools [8].

For this purpose, several control methods based on various approaches have been developed. In the framework of this work, we base on the adaptive approach, which leads to the realization of very powerful control systems, which makes it possible to adjust or estimate online the values of the parameters used in the calculation of the control law.

The principle of the Slotine-LI (adaptive passive) control is based on the ability to adapt to different operating conditions thanks to an approximate knowledge of the robot model.

The objective of our work is the realization of the comparative study and simulation of a Slotine-Li control and PID control, under the MATLAB software, for a manipulator arm with two degrees of freedom.

II. THE DYNAMIC MODEL

The joint cons*ists of two chords. The first connected* with a rotary joint at the base and the second connects to the first with a rotary joint [1, 2, 3].

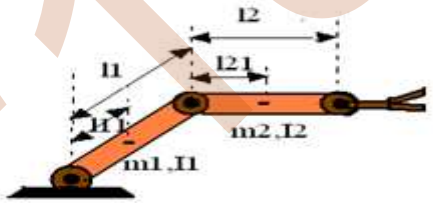

Fig.1: Robot has two degrees of freedom

With L1: languor of the first segment
L2: languor of the second segment

The dynamic model of such structure is given by the following expression:

$$\tau = M(\theta)\ddot{\theta} + C(\theta,\dot{\theta})\dot{\theta} + G(\theta) = \lambda(\theta,\dot{\theta},\ddot{\theta})\alpha \qquad (1)$$

With: M: is the inertia matrix
C: is the matrix of Coriolis forces
G: is the gravity matrix

The components of the inertia matrix [8, 9]:

$$M_{11} = m_1 \cdot I_{11}^2 + m_2 \cdot (I_1^2 + I_{21}^2 + 2 \cdot I_1 \cdot I_{21} \cdot \cos(\theta_2)) + I_1 + I_2$$

$$M_{12} = M_{21} = m_2 \cdot (I_{21}^2 + I_1 \cdot I_{21} \cdot \cos(\theta_2)) + I_2$$

$$M_{22} = m_2 \cdot I_{21}^2 + I_2$$

The components of the gravity matrix [8, 9]:

$$G_1 = (m_1 \cdot I_{11} + m_2 \cdot I_1) \cdot g \cdot \cos(\theta_1) + m_2 \cdot I_{21} \cdot g \cdot \cos(\theta_1 + \theta_2)$$
$$G_2 = m_2 \cdot I_{21} \cdot g \cdot \cos(\theta_1 + \theta_2)$$

The components of the matrix of Coriolis forces [8, 9]:

$$C_{11} = m_2 \cdot I_1 \cdot I_{21} \cdot \sin(\theta_2)\dot{\theta}_2$$
$$C_{12} = m_2 \cdot I_1 \cdot I_{21} \cdot \sin(\theta_2) \cdot (\dot{\theta}_1 + \dot{\theta}_2)$$
$$C_{21} = m_2 \cdot I_1 \cdot I_{21} \cdot \sin(\theta_2)\dot{\theta}_1$$
$$C_{21} = 0$$

The control law of this structure can be written in the following form:

$$\tau = [m_1 \cdot I_{11}^2 + m_1 \cdot (I_1^2 + I_{21}^2 + 2 \cdot I_1 \cdot I_{21} \cdot \cos(\theta_2) + I_1 + I_2]\ddot{\theta}_1$$
$$+[m_2 \cdot (I_{21}^2 + I_1 \cdot I_{21} \cdot \cos(\theta_2) + I_2]\ddot{\theta}_2 \cdots (2)$$

III. THE COMMAND OF SLOTINE-LI

In the case of conventional control methods, the identification of system parameters has been assumed possible. Normally this is not the case, more; it may be that these parameters change over time [8].

To remedy this problem, several techniques come into being; whose idea is to separate the unknown parameters of the system into a single vector [9]. Among these techniques, we find the adaptive control law proposed by Slotine and Li [8] expressed as follows:

$$\tau = M(u_r)\ddot{u}_r + C(u_r, \dot{u}_r)\dot{u}_r + G(u_r) - k_d \cdot S \ldots (3)$$

With:

$$S = \dot{\tilde{u}} + \lambda\tilde{u} \ldots (4)$$
$$\tilde{u}_r = \tilde{u}_d + \lambda\dot{\tilde{u}} \ldots (6)$$
$$\tilde{u} = u - u_d \ldots (7)$$
$$\dot{u}_r = u_d + \lambda\tilde{u} \ldots (8)$$

S, $\ddot{u}_r$, $\dot{u}_r$: are auxiliary signals

By a simple analogy between the expression (1) and (3), it is deduced that the purpose of the order is to ensure that:

$$\tilde{u} = 0 \wedge \dot{\tilde{u}} = 0 \cdots (9)$$

IV THE STATE ESTIMATOR

A state estimator is introduced to determine the vector " α " of equation (1). From the error between the measured and desired speeds [9, 4], the estimator calculates the variation of "α" which may be the cause of the error.

If $S = 0 \Leftrightarrow \tilde{u} = \dot{\tilde{u}} = 0 \cdots (10)$

And also $S = \dot{\theta} - \dot{u}_r \cdots (11)$

***Note**: equations (10) and (11) are conditions, the first of which is the cancellation of the measurement error and its variation, and the second describes closed loop.*

The variation of α is given by

$$\dot{\alpha} = \dot{\tau} \cdot \dot{\lambda}(\theta, \dot{\theta}, \dot{u}_r, \ddot{u}_r) \cdot (\dot{\theta} - \dot{u}_r) \cdots (12)$$

The closed loop of the equation we will have:

$$M(\theta)\ddot{\theta} + C(\theta, \dot{\theta})\dot{\theta} + G(\theta) = M(u_r)\ddot{u}_r +$$
$$C(u_r, \dot{u}_r)\dot{u}_r + G(u_r) - k_d \cdot S \cdots\cdots\cdots (13)$$

Given the condition (9), the choice of the Laypunov function is make as follows:

$$V(t) = \left(\frac{1}{2}\right)(S^T MS + \alpha^T \gamma^{-1}\alpha) \cdots\cdots (13)$$

The goal to search is that: $\dot{V}(t) \le 0 \cdots\cdots (14)$

Deriving the equation (13) it comes:

$$\dot{V}(t) = S^T M\dot{S} + \left(\frac{1}{2}\right)(S^T MS + \dot{\alpha}\gamma^{-1}\alpha) \cdots\cdots (15)$$

From the expression (11) draws:

$$\dot{\theta} = S + \dot{u}_r \cdots\cdots (16)$$

Deriving equation (16) will have:

$$\ddot{\theta} = \dot{S} + \ddot{u}_r \cdots\cdots (17)$$

Replacing $\ddot{\theta}$ of equation (17) in equation (13) and after simplification will result in:

$$M\dot{S} = \lambda(\theta, \theta, \dot{u}_r, \ddot{u}_r)\alpha - (k_d \cdot S + C)S \cdots\cdots (18)$$

Replacing MS 'in equation (15) comes:

$$\dot{V}(t) = S^T \lambda(\theta, \theta, \dot{u}_r, \ddot{u}_r)\alpha - S^T (k_d \cdot S + C)S$$
$$+\left(\frac{1}{2}\right)(S^T MS + \dot{\alpha}\gamma^{-1}\alpha) \cdots\cdots (19)$$

The term: $\left(\frac{1}{2}\right)\dot{M} - C = 0 \cdots\cdots (20)$

Because the matrix is antisymmetric.

To ensure that (14); it is necessary to choose:

$$S^T \lambda + \alpha\gamma^{-1} = 0 \cdots\cdots (21)$$

From equation (21) finds the expression of the estimator given by equation (12).

Note: In our case (the output of the Slotine-Li command) is given as follows:

$$\tau_0 = M \cdot \ddot{u}_r + C \cdot \dot{u}_r + G - k_d \cdot S \cdots\cdots (22)$$

The following figure illustrates the Simulink scheme of the Slotine control

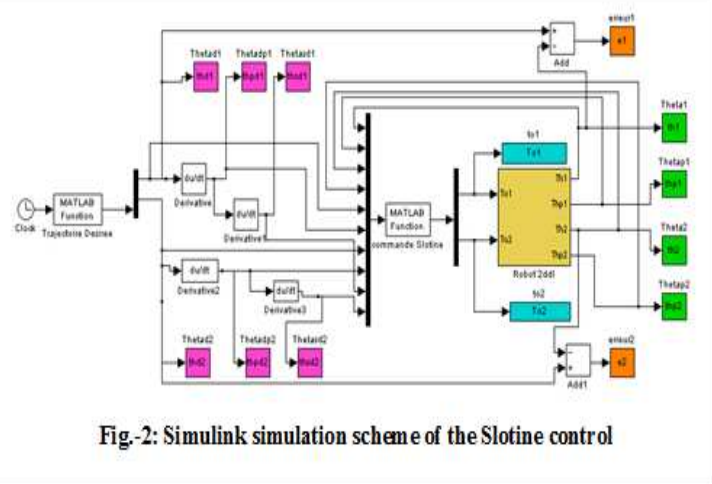

Fig.-2: Simulink simulation scheme of the Slotine control

V Simulation results

After the realization of the different source codes of the different blocks of the two type of the command PID and the Slotine control, after the execution (simulation) we obtained the following results.

A. Use case of PID control

The simulation was performed with a PID whose gain values are as follows: K_{p1}=100, K_{v1}=20, K_{p2}=100, K_{v2}=20,

The following figures (fig.3 and fig.4) shows the behavior of the measured variables (joint position and articular velocity) relative to the desired ones.

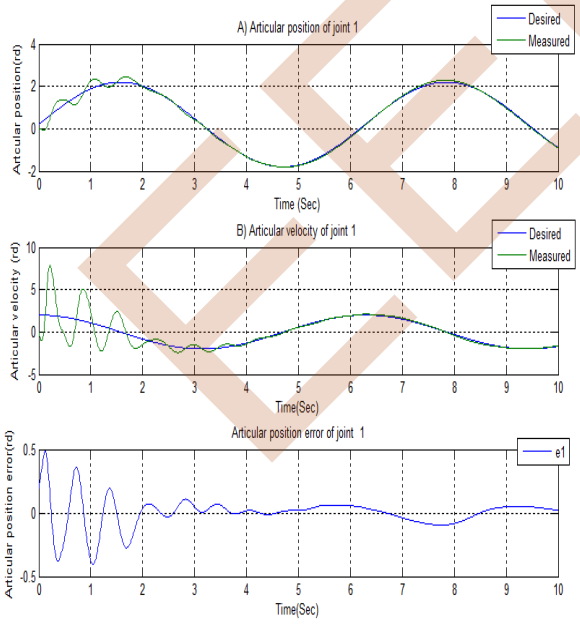

Fig.3 : The paces of articular position/velocity and articular position error of joint1

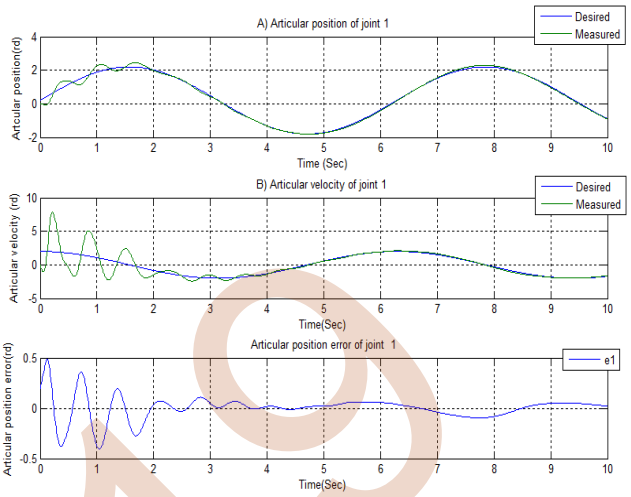

Fig.4: The paces of articular position/velocity and articular position error of joint2

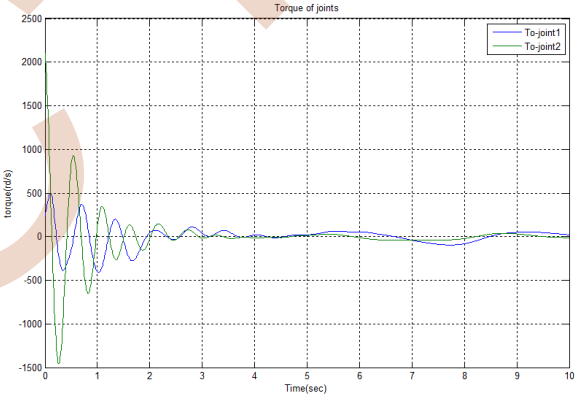

Fig.5: Torque of joints

A.1 Results interpretation

From the results obtained as illustrated in fig.3 (A, B, C), note the signals corresponding to the measured magnitudes namely th1 and th2, oscillate around the desired signals respectively thd1 and thd2, during a considerable period (about 4 seconds) during the simulation. This indicates that the error in position is considerable. Then in other words, the outputs (th1 and th2) do not adapt quickly to the inputs (thd1 and thd2). Moreover, that the control used in this case, does not ensure the stability of the system, as shown in fig.5. Whose torque values are very high during the first 4 seconds of the simulation, which is justified by the oscillation around the desired signals (as illustrated in fig3 (A, B)), and that these values do not converge to zero during the remainder of the simulation time.

B. Simulation using the Slotine-Li controlled

The following figures (fig.6 and fig.7) shows the behavior of the measured variables (joint position and articular velocity) relative to the desired ones.

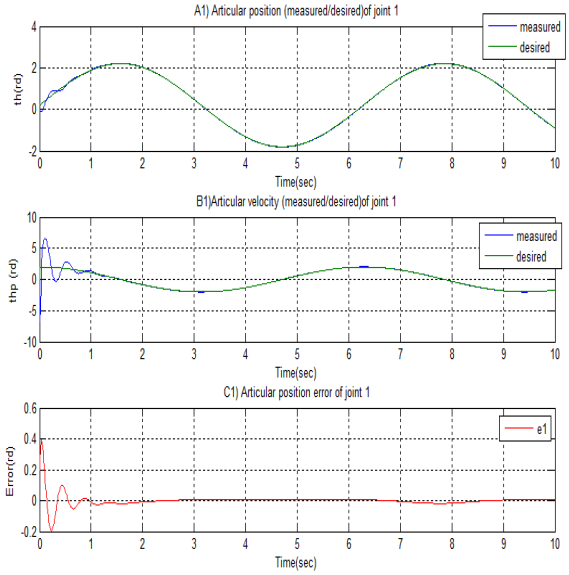

Fig.6: The paces of articular position/velocity and articular position error of joint1

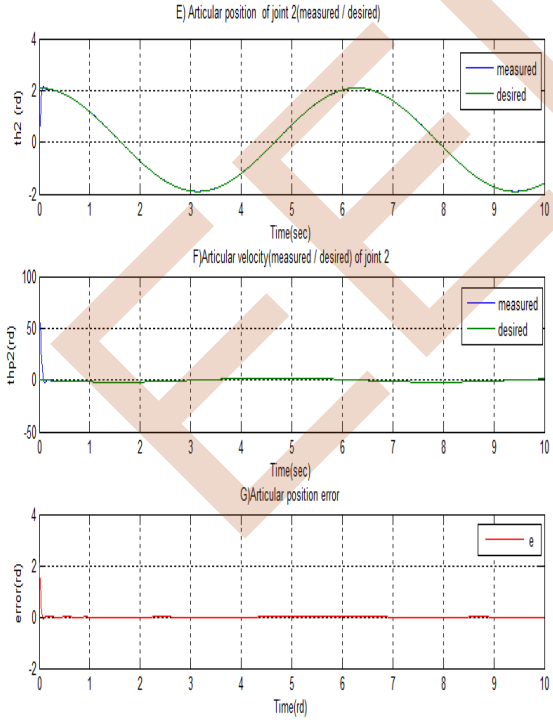

Fig.7:The paces of articular position/velocity and articular position error of joint2

B.1 Results interpretation:

From the results obtained as illustrated in fig.6 (A1, B1), using the Slotine's command, there is a clear resemblance between the signals corresponding to the measured quantities namely th1 and th2, to the desired signals respectively thd1 and thd2. This indicates that the error in position is almost zero (fig.6 (C1)). Then in other words the outputs (th1 and th2) adapts very quickly to the inputs (thd1 and thd2).

The error recorded is almost negligible, which can been caused by slight variations in speeds (fig.6 (C1)), while ensuring good stabilization, the torque To1 and To2 tends to zero, as illustrated in fig8.

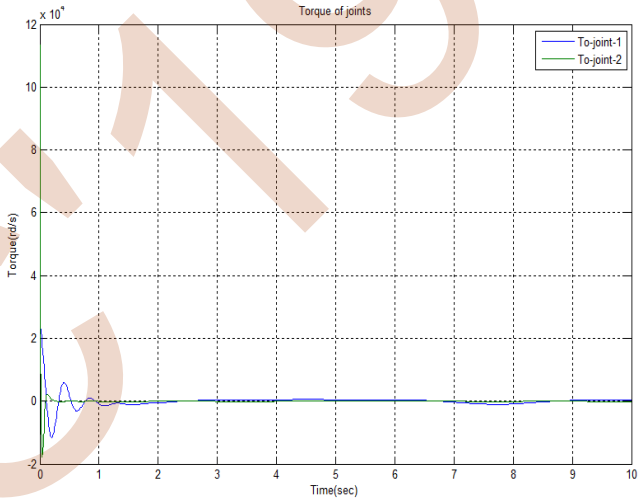

Fig.8 : Torque of joints

VI Conclusion

The results obtained during the previous study show that with the Slotine-Li controller, the outputs (in position or in speed) imitate the reference very quickly. Indeed, when it directly controls the error generated by the current position of the manipulator and that desired by the manipulator, the control signal acts with a high torque, given the dynamics of the error. Another variable to consider is a system that follows the reference behaves without oscillations and whose position error does not exceed 10^{-4} radians, this due to the compensation of the vector of the inertia matrix, the vector of forces of centrifugal and Coriolis, the vector of gravitational forces and the vector of friction forces presented in equation (9). In conclusion, the performances (speed, stability) of the systems are considerably improved thanks to the Slotine-Li controller. This will enable us to consider the adaptation of this technology in our future work, to more complicated systems such as mobile manipulative robots.

REFERENCES

[1] Etienne Dombre et Wisama Khalil « Modélisation et commande des robots » Editions Hermes paris, 1988.

[2] M. GIORDANO & J. LOTTIN. Description et fonctionnement des robots industriels. Livre 1er edition. France.1990.

[3] S.B.NIKU. Introduction to Robotics Analysis, control applications. Livre second edition.USA. 1998.

[4] R. Burkan & I. Uzmay. A model of parameter adaptive law with time varying function for robot control. Article de Elsevier. Applied Mathematical Modelling 29/361–371. Kayseri/Turkey. 2005.

[5] W.KHALIL, E.DOMBRE. Modeling, Identification & Control of Robots. Livre/New York/USA 2002.

[6] Bordon, C. & Camacho, EF. A generalized predictive controller for a wide class of industrial processes. IEEE Transactions on Control Systems Technology 6(3), pp. 372-387. (1998).

[7] Spong, MW. Hutchinson, S. & Vidyasagar, M." Robot modeling and control. John Wiley & Sons, USA. (2006).

[8] Jean-Jacques E. Slotine and Weiping Li. "On the Adaptive Control of Robot Manipulators". The International Journal of Robotics Research .1987

[9] Jean-Jacques E. Slotine, Weiping Li. « Applied nonlinear control » .book ISBN 0-13-040890-5.1991.

EEIC'2019 University of Bejaia

Fractional Order Adaptive Model Predictive Control

Imen Deghboudj
Signal Processing Laboratory, Department of Electronics
University Mentouri Brothers, Constantine
Route de Ain Elbey 25000 Constantine, Algeria
E-mail: imde44@hotmail.fr

Samir Ladaci
National Polytechnic School of Constantine
Department of E.E.A., Nouvelle ville Ali Mendjli,
BP 75 A, 25100 Constantine, Algeria
E-mail: samir_ladaci@yahoo.fr

***Abstract*—This paper proposes a fractional-order adaptive Model Predictive Control (FO-AMPC) design in order to command a conical tank level with nonlinear dynamics. The plant model is estimated online using the Recursive Least Square (RLS) algorithm. The predictive model is set to be a fractional order system approximated by rational transfer functions using the singularity function approach in the frequency domain. Simulations on the conical tank model illustrate the effectiveness of the proposed control scheme.**

Keywords— Model Predictive Control; fractional-order system; fractional adaptive control, Fractional order adaptive MPC, RLS, singularity function technique.

I. INTRODUCTION

Recently, fractional-order calculus has been extensively studied and applied in many areas of science and engineering (see for instance [1], [2], [3]). In control theory, the objective of using fractional calculus is to apply the FOC to enhance the system control performance. Research activities are based on developing new analysis and design methods for fractional order controllers as an extension of classical control theory. Fractional $PI^{\lambda}D^{\mu}$ (Podlubny [4]) , CRONE controller (Oustaloup et al. [5]) and Fractional adaptive control (Ladaci et al. [6]) are examples of popular Fractional order controllers.

In most cases, however, researchers consider the fractional order controller applied to the integer order plant to enhance the system control performance. Fractional order systems; could model various real materials more adequately than integer order ones and thus provide an excellent modeling tool in describing many actual dynamical processes.

One of the recent applications of fractional order systems and operators in automatic control concerns the model predictive control (MPC) framework [7–11]; as for the integer order case, this topic focused important attention of the control engineering research community for its high potential for applications [12], [13]. Many fractional order control structures based on MPC configuration have been developed in literature. An MPC setting for Takagi-Sugeno fuzzy fractional-order systems was introduced in [14] and switched MPC of fractional-order systems in [15]. Deng et al. [16] proposed a predictive control scheme for the power regulation of a fractional order dynamic model for solid oxide fuel cell. For these fractional order systems, the control engineer has to approximate the fractional order plant model with a rational transfer function using some approximation techniques and then the MPC control design is performed as for an integer model.

At the other hand, and according to [17], "MPC predicts future behavior using a linear-time-invariant (LTI) dynamic model. In practice, such predictions are never exact, and a key tuning objective is to make MPC insensitive to prediction errors. In many applications, this is sufficient for robust controller performance. If the plant is strongly nonlinear or its characteristics vary dramatically with time, LTI prediction accuracy might degrade so much that MPC performance becomes unacceptable".

Many authors suggested another solution for this problem by using the adaptive MPC (AMPC) which has the ability to update the linearized model at each control interval [18-20]. This means that the controller employs a process model which approaches that of the true system over time. Conventional adaptive MPC is a linear MPC method that uses a nonlinear model to update the linear model only at each sample time, k .

In this investigation, we consider that the prediction model is of fractional order, and the identified parameters using the RLS estimator are the coefficients of the approximating transfer function, using the singularity function technique. The proposed fractional order adaptive linear MPC method (FOAMPC) can offer an attractive alternative to existing predictive control methods for mildly nonlinear systems. The main advantages of the proposed approach are that the usually tedious and time-consuming modeling task can be eliminated and that the controller can adapt to changing process conditions with a certain improvement of plants performance and robustness.

The remaining part of this paper is organized as follows. Section II presents some theoretical background on fractional order systems. The proposed fractional order adaptive MPC control strategy is presented in Section III, whereas simulation results of its application to a conical tank level

control are given in Section IV. Finally, Section V is dedicated to concluding remarks and future researches.

II. Fractional Order Systems

Fractional calculus is the field of mathematical analysis which deals with the investigations and applications of integrals and derivatives of arbitrary order [21]. Fractional order operators are the integrals and derivatives operators with a non integer order. They are a generalization of the integrations and derivatives of integer order. In recent years considerable interest in the concepts of fractional order operators has been simulated by their applications in system and control theories [22-23].

A. Definitions

The commonly used definitions of the fractional order integrals and derivative are the Riemann-Liouville (R-L) and Grunwald-Letnikov (G-L) definitions [21].

The R-L fractional order integral of order $\lambda>0$ is defined as:

$$I_{RL}^{\lambda} f(t) = D^{-\lambda} f(t) = \frac{1}{\Gamma(\lambda)} \int_0^t (t-\tau)^{\lambda-1} f(\tau) d\tau \quad (1)$$

and the expression of the R-L fractional order derivative of order $\mu>0$ is:

$$D_{RL}^{\mu} f(t) = \frac{1}{\Gamma(n-\mu)} \frac{d^n}{dt^n} \int_0^t (t-\tau)^{n-\mu-1} f(\tau) d\tau \quad (2)$$

with $\Gamma(.)$ is the Euler's gamma function and the integer n is such that $(n-1) < \mu < n$. This fractional order derivative of equation (2) can also be defined from equation (1) as:

$$D_{RL}^{\mu} f(t) = \frac{d^n}{dt^n} \left\{ I^{(n-\mu)} f(t) \right\} \quad (3)$$

The G-L fractional order integral of order $\lambda > 0$ is given by:

$$I_{GL}^{\lambda} f(t) = D^{-\lambda} f(t) = \lim_{h \to 0} h^{\lambda} \sum_{j=0}^{k} (-1)^j \binom{-\lambda}{j} f(kh - jh) \quad (4)$$

Where h is the sampling period and the coefficients and $\omega_0^{(-\lambda)} = \binom{-\lambda}{0} = 1$ the coefficients of the following binomial:

$$(1-z)^{-\lambda} = \sum_{j=0}^{\infty} (-1)^j \binom{-\lambda}{j} z^j = \sum_{j=0}^{\infty} \omega_j^{(-\lambda)} z^j \quad (5)$$

The G-L fractional order derivative of order $\mu > 0$ is also given by:

$$D_{GL}^{\mu} f(t) = \frac{d^{\mu}}{dt^{\mu}} f(t) = h^{-\mu} \sum_{j=0}^{k} (-1)^j \binom{\mu}{j} f(kh - jh) \quad (6)$$

where h is the sampling period and the coefficients $\omega_j^{(\mu)} = \binom{\mu}{j} = \frac{\Gamma(\mu+1)}{\Gamma(j+1)\Gamma(\mu-j+1)}$ with $\omega_0^{(\mu)} = \binom{\mu}{0} = 1$ are the coefficients of the following binomial:

$$(1-z)^{\mu} = \sum_{j=0}^{\infty} (-1)^j \binom{\mu}{j} z^j = \sum_{j=0}^{\infty} \omega_j^{(\mu)} z^j \quad (7)$$

B. Linear approximation of fractional order transfer function

For the purpose of our approach we need to use an integer order model approximation of the fractional order model reference in order to implement the adaptation algorithm. For this aim we use the so-called singularity function method proposed by Charef et al. [25], and precisely for fractional second order system of the form

$$G(s) = \frac{1}{\left(\frac{s^2}{w_n^2} + 2\xi \frac{s}{w_n} + 1 \right)^m} \quad (8)$$

with *m* a positive real number such that $0<m<1$, there are two cases:

- For $0<m<0.5$, we can express:

$$H(s) = \frac{1}{\left(\frac{s^2}{\omega^2} + 2\xi \frac{s}{\omega} + 1 \right)^m}$$

as:

$$H(s) = \frac{\left(\frac{s}{\omega} + 1 \right) \left(\frac{s}{\omega + 1} \right)^{\beta}}{\left(\frac{s^2}{\omega^2} + 2\alpha \frac{s}{\omega} + 1 \right)} \quad (9)$$

with $\alpha = \xi^m$ and $\beta = 1 - 2m$, which can also be approximated by the function,

$$H(s) \approx \frac{\left(\frac{s}{\omega}+1\right)}{\left(\frac{s^2}{\omega^2}+2\alpha\frac{s}{\omega}+1\right)} \frac{\prod_{i=1}^{N-1}(1+\frac{s}{z_i})}{\prod_{i=1}^{N}(1+\frac{s}{p_i})} \quad (10)$$

The singularities are given by:

$$p_j = (ab)^{j-1} a.z_1 \qquad j = 1, 2, 3,... N$$

$$z_i = (ab)^{i-1} z_1 \qquad i = 2, 3,... N-1$$

with, $z_1 = w\sqrt{b}$, $a = 10^{\frac{\varepsilon_p}{10(1-\beta)}}$, $b = 10^{\frac{\varepsilon_p}{10\beta}}$, $\beta = \frac{\log(a)}{\log(ab)}$

and where ε_p is the tolerated error in dB

The order of approximation N is computed by fixing the frequency band of work, specified by $\omega_{\max}$, so that:

$p_{N-1} < \omega_{\max} < p_N$. This leads to:

$$\text{N= integer part of } \left[\frac{\log\left(\frac{\omega_{\max}}{p_1}\right)}{\log(ab)}+1\right]+1 \quad (11)$$

H(s) can then be written under a parametric shape function of order N+2:

$$H(s) = \frac{b_{m0}s^N + b_{m1}s^{N-1} + ... + b_{mN}}{s^{N+2} + a_{m1}s^{N+1} + ... + a_{mN+2}} \quad (12)$$

a_{mi} and b_{mi} are calculated from the singularities p_i, z_i and α, ω.

- For $0.5<m<1$, the approximating function is given as follows :

$$H(s) = \frac{\left(\frac{s}{\omega}+1\right)}{\left(\frac{s^2}{\omega^2}+2\alpha\frac{s}{\omega}+1\right)\left(\frac{s}{\omega}+1\right)^{\beta}} \quad (13)$$

Where $\alpha = \xi^m$ and $\beta = 2m-1$, which by the same reasoning the approximating function (10), but with the following singularities values:

$$p_j = (ab)^{j-1} p_1 \qquad j = 1, 2, 3,... N$$

$$z_i = (ab)^{i-1} a p_1 \qquad i = 2, 3,... N-1$$

with, $p_1 = w\sqrt{b}$, $a = 10^{\frac{\varepsilon_p}{10(1-\beta)}}$, $b = 10^{\frac{\varepsilon_p}{10\beta}}$,

$$\beta = \frac{\log(a)}{\log(ab)} \quad (14)$$

H(s) can then be written under the parametric function (12).

III. Fractional Order Adaptive Model Predictive Control (FO-AMPC)

In the following paragraph, we present the proposed methodology for fractional order MPC control design.

A. Model Predictive Control scheme

For a control system, the reference trajectory r(k) is defined as the ideal trajectory along which a plant should return to the set-point trajectory w(k), at any instant k [26]. The current error between the output signal y(k) and the set point is an error represented as:

$$e_{rr}(k) = w(k) - y(k). \quad (15)$$

Then the reference trajectory is chosen such that if the output followed it exactly, then the error after *i* steps would be

$$e_{rr}(k+i) = exp^{-iT_s/T_{ref}} e_{rr}(k), \quad (16)$$

where T_{ref} is the time constant of exponential assuming that reference trajectory approaches the set-point exponentially and Ts is the sampling interval. Therefore, the reference trajectory is defined as

$$r(k+i/k) = w(k+i) - y(k+i). \quad (17)$$

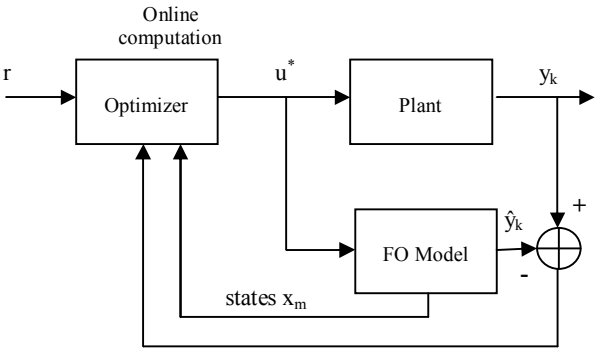

Figure 1. Block Diagram for MPC controller

The notation $r(k + i/k)$ implies that the reference trajectory depends on the conditions at time k [9].

At this stage, the predictive controller uses an internal model to estimate the future behavior of the plant. This process starts at the current time k and carries over a future prediction horizon H_P. This predicted behavior depends on the assumed control effort trajectory $\hat{u}$ that is to be applied over the prediction horizon and we have to select the input which promises the best predicted behavior (See Fig. 1).

The notation $\hat{u}$ represents the predicted value input at time $k+i$ at instant k; the actual input $u(k+i)$ may be different than $\hat{u}$. After a future trajectory is decided, only the first element of the trajectory is required as the control input to the process. Hence $u(k)$ becomes $\hat{u}$ $(k|k)$. The tasks of prediction, measurement of output and determination of input trajectory are repeated at every sampling instant. This is known as the receding horizon strategy, since prediction horizon slides along by one sampling interval at each step while its length remains the same.

B. *Problem statement*

The most important element in MPC is the model of the process/plant, which is required for prediction of the future states. Since the decisions that is, the optimal control effort is updated regularly, any model uncertainty can be dealt with in a fair range [24]. Hence, accuracy of the model used for the prediction can be compensated with regular updating of states. When MPC is applied to a real process, its output y_k is measured in real time at every instant for evaluation of optimal control effort. The main contribution of this paper is to use a fractional order system as prediction model, whereas the plant model is of integer order and unknown. The following recursive least-squares estimator (RLS) with exponential forgetting is used to estimate the actual plant model:

$$\begin{aligned}
&\breve{\theta}(t)=\breve{\theta}(t-1)+K(t)\varepsilon(t)\\
&\varepsilon(t)=y(t)-\varphi^T(t-1)\breve{\theta}(t-1)\\
&K(t)=P(t-1)\varphi(t-1)\times\left(\lambda+\varphi^T(t-1)P(t-1)\varphi(t-1)\right)^{-1}\\
&P(t)=I-K(t)\varphi(t-1)P(t-1)/\lambda
\end{aligned} \tag{18}$$

The fractional order prediction model is implemented after its approximation using the singularity function approach [25]. This fractional order adaptive MPC scheme allows us to improve the prediction control dynamics and thus the plant output when compared to the classical scheme. However, this algorithm is very sensitive to the initial values of parameters θ. Thus, we will consider the re-initialization of the algorithm when the reference input signal is varied.

IV. Simulation Results

In this Section, we will apply the proposed FOAMPC scheme to the conical tank system shown in Figure. 2. The water is pumped from the bottom of the recirculating tank to the upper part of the conical tank by means of a pump driven by an induction motor of variable speed driven by a variable frequency drive. The water flows from the bottom of the conical tank to the input of the recirculating tank by gravity through a pipe with a valve whose opening can be fixed manually [26-27].

From [28] the nonlinear model for the conical tank is governed by the following equation:

$$h=\frac{5.43f-78.23-20.63\sqrt{h}}{0.65h^2+11.4h+17.1}=\mathrm{g}(h,f) \tag{19}$$

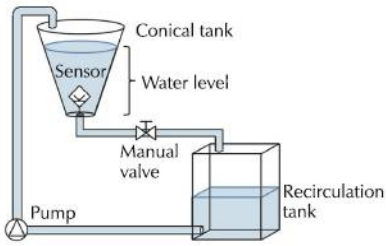

Figure 2. Conical tank configuration.

where f is the input, h is the output and $g(h, f)$ is a nonlinear function of these two variables. In [26], this nonlinear model (18) is approximated by the first order Taylor approximation around different operating points. These approximations are given by,

$$h=A(h-h_{op})+B(f-f_{op}) \tag{20}$$

With $A=\left.\frac{\partial \mathrm{g}(h,f)}{\partial h}\right|_{(h_{op},f_{op})}$ and $B=\left.\frac{\partial \mathrm{g}(h,f)}{\partial f}\right|_{(h_{op},f_{op})}$.

where h_{op} and f_{op} are the different operating points to be considered. The operating points are determined by dividing the whole operation range 15 cm–60 cm into three segments, as illustrated in Table I.

TABLE I. Conical Tank in Linearized Models

	Low level	Medium level	High level
Interval (cm)	15–30	30–45	45–60
h_{op} (cm)	22.5	37.5	52.5
f_{op} (%)	32.42	37.66	41.92
A	−0.0036	−0.0012	−0.0006
B	0.009	0.004	0.0022

These three linearized models can be used as predictive models for the classical integer order MPC control.

A. *Controller settings*

Prediction Horizon: N_p=18, N_U=3, Pondering factor = 0.2.

Adaptive control:

We used the RLS algorithm to estimate the model of the conical tank level system. As the system has a first order model, the transfer function H(z) could be represented as,

$$H(z) = b/(z+a) \tag{21}$$

And set θ the parameters vector as: θ=[a b], Such that the initial values are: θ_0 =1, φ_0=1, p=20000.

B. *Results :* Two strategies are considered,

Case 1- Without parameters re-initialization:

θ(n+1) = θ(n) ; thus when the reference level changes we maintain the last value of θ, as Initial value for the next level. The simulation results are given in Figures 3 to 6 respectively for the system response, a zoom for the transition response, the control signal and the parameter estimation.

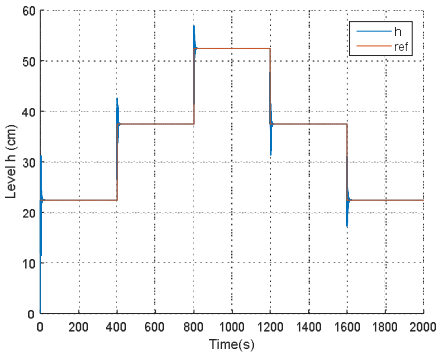

Figure 3. Tank level response without re-initialization.

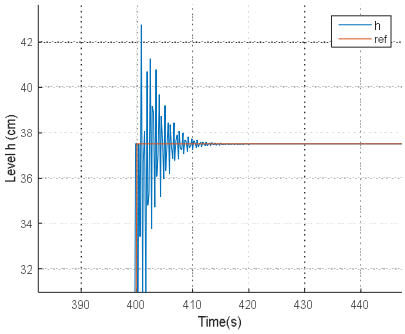

Figure 4. Zoom of Conical tank step response without re-initialization.

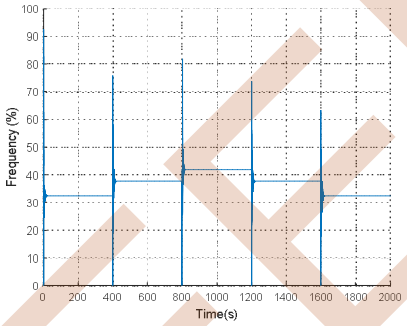

Figure 5. Control signal without re-initialization.

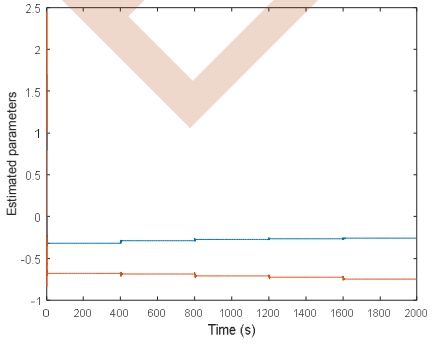

Figure 6. Parameters estimation without re-initialization.

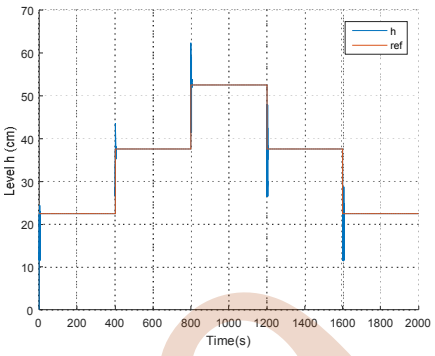

Figure 7. Tank level response with re-initialization.

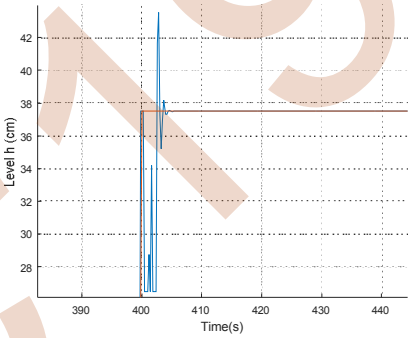

Figure 8. Zoom of Conical tank step response with re-initialization.

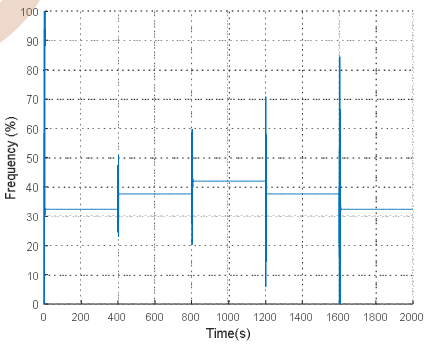

Figure 9. Control signal with re-initialization.

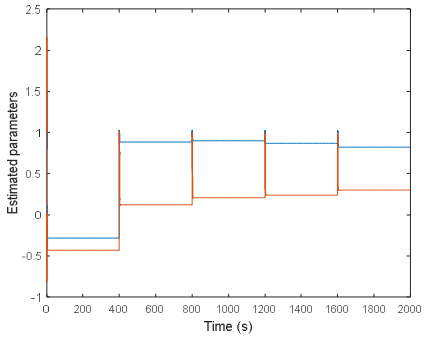

Figure 10. Parameters estimation with re-initialization.

Case 2- With parameters re-initialization:
$\theta(n+1) = \theta_0$; thus when the reference level changes we reinitialize the parameters vector θ to the initial value θ_0, for the next level. The simulation results are given in Figures 7 to 10 respectively for the system response, a zoom for the transition response, the control signal and the parameter estimation.
It is obvious that the proposed adaptive approach is able to stabilize the nonlinear conical tank and improve the dynamical behavior of the AMPC regulator, with more rapidity of convergence and less static error.

V. CONCLUSION

A fractional-order Adaptive Model Predictive Control has been designed in order to command plants with linear or linearized models. The predictive model is set to be a fractional order system approximated by rational transfer functions using the singularity function approach in the frequency domain. This model is updated periodically using the RLS algorithm. Simulations on a conical tank identified model illustrate the effectiveness of the proposed control scheme. Further researches will concern the application this approach to plants with delays, and investigate the MPC robustness enhancement.

REFERENCES

[1] R. Hilfer (Ed.), Applications of Fractional Calculus in Physics. World Scientific Publishing, Singapore, 2000.

[2] I. Podlubny, "Fractional-order Systems and fractional-Order Controllers". Technical Report UEF-03-94, Slovak Academy of Science. Kosice, 1994.

[3] I. Podlubny, Fractional Order Systems and $PI^{\lambda}D^{\mu}$ Controllers. IEEE Transactions on Automatic Control, vol. 44, no. 1, pp. 208-214, 1999.

[4] I. Podlubny, Fractional Differential Equations. Academic Press. San Diego, 1999.

[5] A. Oustaloup, La commande CRONE (in French). Herm-es, Paris, 1991.

[6] S. Ladaci, J.J. Loiseau, and A. Charef, "Fractional Order Adaptive High-Gain Controllers for a Class of Linear Systems" Communications in Nonlinear Science and Numerical Simulations, vol 13, no. 4. pp. 707-714, July 2008.

[7] M. Romero, A de Madrid, C. Manoso, and R. Berlinches, "Generalized predictive control of arbitrary real order," in New Trends in Nanotechnology and Fractional Calculus Applications (D. Baleanu, Z. B. Guvenc, and J. A. T. Machado, eds.), pp. 411–418, Springer Netherlands, 2010.

[8] M. Romero, A. de Madrid, C. Manoso, and B. Vinagre, "Fractional-order generalized predictive control: Formulation and some properties," in Control Automation Robotics Vision (ICARCV), 2010 11th International Conference on, pp. 1495–1500, Dec 2010.

[9] D. Boudjehem and B. Boudjehem, "The use of fractional order models in predictive control," in 3rd Conference on Nonlinear Science and Complexity, symposium: Fractional Calculus Applications, (Ankara, Turkey), July 2010.

[10] Z. Deng, H. Cao, X. Li, J. Jiang, J. Yang, and Y. Qin, "Generalized predictive control for fractional order dynamic model of solid oxide fuel cell output power," Journal of Power Sources, vol. 195, no. 24, pp. 8097 – 8103, 2010.

[11] M. Romero, A . de Madrid, C. Man˜oso, V. Milane´s, and B. Vinagre, "Fractional-order generalized predictive control: Application for low-speed control of gasoline-propelled cars," Mathematical Problems in Engineering, vol. 2013, pp. 1–10, 2013. Article ID 895640.

[12] A. Rhouma, B. Bouzouita, and F. Bouani, "Model predictive control of fractional systems using numerical approximation," in Computer Applications Research (WSCAR), 2014 World Symposium on, pp. 1–6, Jan 2014.

[13] M. Romero, A . de Madrid, C. Man˜oso, and B. Vinagre, "A survey of fractional-order generalized predictive control," in Decision and Control (CDC), 2012 IEEE 51st Annual Conference on, pp. 6867–6872, Dec 2012.

[14] S. Domek, "Fuzzy predictive control of fractional-order nonlinear discrete-time systems," Acta mechanica et automatica, vol. 5, no. 2, 2010.

[15] S. Domek, "Switched state model predictive control of fractional-order nonlinear discrete-time systems," Asian Journal of Control, vol. 15, no. 3, pp. 658–668, 2013.

[16] Z. Deng, H. Cao, X. Li, J. Jiang, J. Yang, and Y. Qin, "Generalized predictive control for fractional order dynamic model of solid oxide fuel cell output power," Journal of Power Sources, vol. 195, no. 24, pp. 8097 – 8103, 2010.

[17] A. Albalasiea, G. Seliger, and A. Abu Hanieh, "Using Adaptive Model Predictive Technique to Control Underactuated Robot and Minimize Energy Consumption". 13th Global Conference on Sustainable Manufacturing - Decoupling Growth from Resource Use. Procedia CIRP, vol. 40, pp. 407 – 412, 2016.

[18] V. Adetola, and M. Guay, Adaptive Model Predictive Control for Constrained Nonlinear Systems. Proceedings of the 17th World Congress of The International Federation of Automatic Control Seoul, Korea, July 6-11, 2008.

[19] S. Karra, R. Shaw, S. C. Patwardhan, and S. Noronha, Adaptive Model Predictive Control of Multivariable Time-varying Systems. Ind. Eng. Chem. Res. Vol. 47, pp. 2708-2720, 2008.

[20] M. Tanaskovic, L. Fagiano, R. Smith and M. Morari, "Adaptive model predictive control for constrained MIMO systems". 11th IFAC International Workshop on Adaptation and Learning in Control and Signal Processing July 3-5, 2013. Caen, France.

[21] K.B. Oldham, J. Spanier, The Fractional Calculus, Academic Press, New York, 1974.

[22] A. Neçaibia, S. Ladaci, and S. Mekhilef, "ABS Braking Control Enhancement via Fractional Order Extremum Seeking Method". International Journal of Automation & Systems Engineering, vol. 9, no, 1, pp. 23-36, 2015.

[23] K. Rabah, S. Ladaci, and M. Lashab, "A Novel Fractional Sliding Mode Control Configuration for Synchronizing Disturbed Fractional order Chaotic Systems". Pramana, vol. 89, no. 3, 46. 2017.

[24] Rossiter, J. A. Model - Based Predictive Control: A Practicle Approach. CRC Press. 2003.

[25] A. Charef, H.H. Sun, Y.Y. Tsao, B. Onaral, 'Fractal system as represented by singularity function,' IEEE Trans. On Automatic Control, vol. 37, pp. 1465-1470. 1992.

[26] C. Jauregui, M. A. Duarte-Mermoud, R. Orostica, J. C. Travieso-Torres, O. Beytia, "Conical tank level control using fractional order PID controllers: a simulated and experimental study", Control Theory Tech, Vol. 14, No. 4, pp. 369–384, 2016.

[27] I. Deghboudj, and S. Ladaci, "Fractional Order Model Predictive Control of Conical Tank Level", In: International Conference on Automatic control, Telecommunication and Signals (ICATS'17) University of Annaba, Algeria, 11-12 December 2017.

[28] C. Jauregui, M. A. Duarte, R. Orostica, et al. "Conical tank level control with fractional PID". IEEE Latin America Transactions, vol. 14, no. 6, pp. 2598 – 2604, 2016.

Fault Diagnosis and Fault Tolerant Control for Mobile Robot Based on Multi-sensors Data Fusion.

Linda HACHEMI, Abedlkrim NEMRA and Mohamed GUIATNI

Intelligent Autonomous Systems Research Unit
Ecole Militaire Polytechnique
Bordj E Bahri, Algiers, Algeria
salyhachemi@hotmail.fr, karim_nemra@yahoo.fr,
mohamed.guiatni@gmail.com,

***Abstract*— In this paper, we propose an approach for tolerating faults in multisensors data fusion on a unicycle-type mobile robot, that is requires two basic tasks: duplication– comparison, and that offers detection and redesign services. We propose an architecture a Multi Sensor Fusion Based on two extended Kalman filter. This architecture contains two independent localization systems using two extended Kalman filters between the sensors pairs: (INS / GPS) and (ODO / CAM). This study uses sensors data in V-rep software and fault injection with Matlab software.**

Keywords—Unicycle-type mobile robot, Diagnosis, FTC, multisensors data fusion ,EKF, V-rep.

I. FINTRODUCTION

Multi-sensors data fusion has played a significant role in diverse areas ranging from local robot guidance to global military theatre defense etc. Various multi-sensors data fusion methods have been extensively investigated by researchers, of which Kalman filtering is one of the most important. Kalman filtering is the best-known to optimally estimate the unknown states of a dynamic system, which has found widespread application in many areas [1].

In general, the location of a mobile is to determine its (position, speed and attitude) [2]. The sensors used in navigation are divided into two main categories: internal sensors (inertial unit, odometer, gyroscopic, etc.), and external sensors (GPS, laser, camera, etc.)[3].

DRS systems: Dead Rocking System (INS, Odometer), provide reliable and fast navigation for short-term applications, however the rapid degradation of the navigation solution caused by the accumulation (through integration) of errors [4].

The GPS system (Global Positioning System), meanwhile, delivers absolute position information and offers low-cost precision, a significant degradation of the ability of the solution provided by this system is observable when submitted to a urban environment, a forest area or covered areas [4].

In such situations, and in order to take advantage and characteristics of the two systems and to make the best use of the sensor data provided, particularly for the development of a reliable and continuous navigation system, the researchers thought of a solution to this problem which consists in making a fusion of multi-sensor data using an estimator, or we have to resort to several sensors of the same nature or heterogeneous.

Precisely, in our work we want to realize a system able to estimate in real time, the position, the speed and the orientation of a mobile robot. This system relies on the multi-sensor data fusion, which uses the extended Kalman filter (FKE), because its ability to estimate parameters of a nonlinear system evolving over time. The data fusion that we have exploited is between the sensors pairs (INS / GPS) and (Odom / Cam).

To ensure the safe operation of multi-sensors perception systems, in particular their tolerance to internal faults, we propose a standard fault tolerance method (duplication and comparison) in data fusion which consists of adding a comparison mechanism and diagnostic.

Data acquisition ensure with V-Rep, rejection of data and injection of faults with Matlab.

II. KINEMATIC MODEL OF UNICYCLE MOBILE ROBOT

A unicycle is a robot powered by two independent wheels and owning eventually a number of crazy wheels ensuring its stability. The scheme of unicycle type robots as given in Fig. 1.

Where: **v** is linear velocity ,**θ**is the orientation of the robot, R is the radius of each wheel, 2L is the distance between two wheels and (x_i , y_i) are the position of the mobile robot.

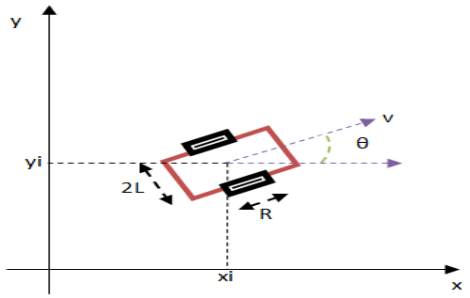

Fig. 1. Unicycle-type mobile robot.

The kinematic model of the robot is given by:

$$\begin{bmatrix}\dot{x}_c\\ \dot{y}_c\\ \dot{\theta}\end{bmatrix}=\begin{bmatrix}\cos\theta & 0\\ \sin\theta & 0\\ 0 & 1\end{bmatrix}\begin{bmatrix}v\\ \omega\end{bmatrix} \quad (1)$$

III. LOCALIZATION ARCHITECTUR OF THE MOBILE ROBOT

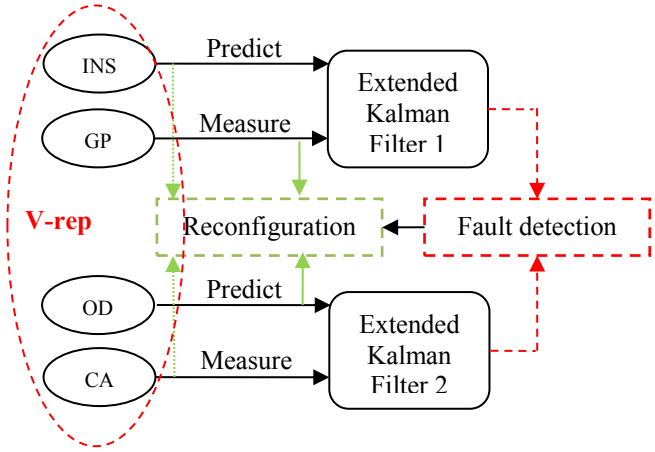

Fig. 2. Synoptic diagram : Multi Sensor Fusion Based on extended Kalman filter

IV. MULTI SENSOR FUSION

A) *Extended Kalman filter*

The extended Kalman filter can be viewed as a nonlinear version of the Kalman filter that linearized the models about a current estimate.

$$X_K = f(X_{K-1}, U_{K-1}) + W_K \quad (2)$$
$$Z_K = h(X_k) + V_K$$

The model and implementation equations for extended Kalman filter are defined as following equation:

Prediction:

$$\hat{X}_{K/K-1} = f(\hat{X}_K) \quad (3)$$
$$P_{K/K-1} = F(\hat{X}_K) P_K F^T(\hat{X}_K) + Q$$

Update:

$$K_K = P_{K/K-1}\, H^T (H.P_{K/K-1}.H^T + R)^{-1} \quad (4)$$
$$\hat{X}_K = \hat{X}_{K/K-1} + K_K\,[Z_K - h(\hat{X}_{K/K-1})]$$
$$P_K = P_{K/K-1} - K_K H P_{K/K-1}$$

Where $\hat{X}_k$represents the predicted state vector and Xk/k-1 denotes the estimated state vector, k is the Kalman gain matrix, P represents the covariance matrix; F are the Jacobian matrices of the state equation f with respect to the state vector Xk+1 and the noise variable Wk, respectively; Hk+1 is the Jacobian matrix of the measurement h with respect to the state vector Xk+1 and the noise variable Vk, respectively.[5]

The measurement model describes what the sensors measure. GPS and camera measures the position of the robot, encoder measures the wheel's velocity, and the INS measures the angular velocity and acceleration rate in gyroscope and accelerometer, respectively [6]. Process and measurement model for each sensor as follows :

A. *INS/GPS*

Prediction:

The process INS model

$$\mathrm{Xk+1} = \begin{bmatrix}\mathrm{x}\\ \mathrm{y}\\ \mathrm{z}\\ \mathrm{u}\\ \mathrm{v}\\ \mathrm{w}\\ \emptyset\\ \theta\\ \psi\end{bmatrix}_K + \mathrm{Te}^*\, \mathrm{f(xk, uk)} + \mathrm{Wk} \quad (5)$$

Where x is the state vector, which contains the position, velocity and euler angles,and u represents the Imu outputs (angular rates and accelerations)

$$x = [x \quad y \quad z \quad u \quad v \quad w \quad \emptyset \quad \theta \quad \psi]^T$$
$$u = [p \quad q \quad r \quad ax \quad ay \quad az\ ]^T$$

The nonlinear INS process state model is given by equation ().

$$\mathrm{f(x,u)} = \begin{bmatrix}\mathrm{A}\begin{bmatrix}\mathrm{u}\\ \mathrm{v}\\ \mathrm{w}\end{bmatrix}\\ \mathrm{b}\\ C\begin{bmatrix}\mathrm{p}\\ \mathrm{q}\\ \mathrm{r}\end{bmatrix}\end{bmatrix} \quad (6)$$

where:

$$A = \begin{bmatrix}\cos(\theta)\cos(\Psi) & \cos(\theta)\sin(\Psi) & -\sin(\theta)\\ a21 & a22 & \sin(\emptyset)\cos(\theta)\\ a31 & a32 & \cos(\emptyset)\cos(\theta)\end{bmatrix}$$

$$\mathrm{b}=\begin{bmatrix}\mathrm{ax+vr-wq+gsin(\theta)}\\ \mathrm{ay-ur+wp-gcos(\theta)\cos(\emptyset)}\\ \mathrm{az+uq-vp-gcos(\emptyset)\cos(\theta)}\end{bmatrix}$$

$$\mathrm{C}=\begin{bmatrix}1 & \sin(\emptyset)\tan(\theta) & \cos(\emptyset)\tan(\theta)\\ 0 & \cos(\emptyset) & -\sin(\emptyset)\\ 0 & \sin(\emptyset)\sec(\theta) & \cos(\emptyset)\sec(\theta)\end{bmatrix}$$

and

$$\mathrm{a21} = \sin(\theta)\sin(\emptyset)\cos(\Psi) - \sin(\Psi)\cos(\emptyset)$$
$$a31 = \sin(\theta)\cos(\emptyset)\cos(\Psi) + \sin(\Psi)\sin(\emptyset)$$
$$a22 = \sin(\Psi)\sin(\theta)\sin(\emptyset) + \cos(\Psi)\cos(\emptyset)$$
$$a32 = \sin(\Psi)\sin(\theta)\cos(\emptyset) - \cos(\Psi)\sin(\theta)$$

The Jacobian matrix of *f* with respect to Xk+1 is $F = \frac{\partial f(x,u)}{\partial x}$.

And WK is a covariance matrix Q. Where Q_K=BQB^T

$$B = \frac{\delta f}{\delta u} = \begin{bmatrix}0 & 0 & 0 & 0 & 0 & 0\\ 0 & 0 & 0 & 0 & 0 & 0\\ 0 & 0 & 0 & 0 & 0 & 0\\ 0 & -dt\,\omega & dt & dt & 0 & 0\\ dt\,\omega & 0 & -dt\,u & 0 & dt & 0\\ -dt\,v & dt\,u & 0 & 0 & 0 & dt\\ dt & s\phi T\theta & c\phi T\theta & 0 & 0 & 0\\ 0 & dtc\phi & -dts\phi & 0 & 0 & 0\\ 0 & dts\phi sec\theta & dt\,rc\phi sec\theta & 0 & 0 & 0\end{bmatrix} \quad (7)$$

$$Q = \begin{bmatrix} \delta_p^2 & 0 & 0 & \begin{pmatrix} 0 & \cdots & 0 \\ \vdots & \ddots & \vdots \\ 0 & \cdots & 0 \end{pmatrix} \\ 0 & \delta_q^2 & 0 & \\ 0 & 0 & \delta_r^2 & \\ \begin{pmatrix} 0 & \cdots & 0 \\ \vdots & \ddots & \vdots \\ 0 & \cdots & 0 \end{pmatrix} & & & \begin{matrix} \delta_{ax}^2 & 0 & 0 \\ 0 & \delta_{ay}^2 & 0 \\ 0 & 0 & \delta_{az}^2 \end{matrix} \end{bmatrix} \quad (8)$$

δ: are diagonal elements of covariance matrix Q of WK.
Update:

GPS measures the position of the robot, then the measurement matrix is:

$$Z_K = [x_{gps} \quad y_{gps} \quad z_{gps} \quad V_{xgps} \quad V_{ygps} \quad V_{zgps}]_K^T = h(X_K) + V_K \quad (9)$$

V_k are Gaussian noises for the measurement model with covariance R.

$$R = \begin{bmatrix} \delta_x^2 & 0 & 0 \\ 0 & \delta_y^2 & 0 \\ 0 & 0 & \delta_z^2 \end{bmatrix}$$

With :

$$h = \begin{bmatrix} x \\ y \\ z \\ Uc\theta s\psi - Vc\emptyset s\psi + Vs\emptyset c\psi + W(s\emptyset c\psi + c\emptyset s\theta c\psi) \\ Uc\theta s\psi + Vc\emptyset c\psi + Vc\emptyset s\theta c\psi - W(s\emptyset c\psi + c\emptyset s\theta c\psi \\ -Us\theta + Vs\emptyset c\theta + Wc\emptyset c\theta \end{bmatrix}$$

The Jacobian matrix of h with respect to Xk+1 is $H_K = \frac{\partial h(x,v)}{\partial x}$ given by:

B. Odometer/ Visual odometry

Prediction:
The odometer model equation is given by:

$$\begin{bmatrix} \dot{x}_c \\ \dot{y}_c \\ \dot{\theta} \end{bmatrix} = \begin{bmatrix} \cos\theta & 0 \\ \sin\theta & 0 \\ 0 & 1 \end{bmatrix} \begin{bmatrix} v \\ \omega \end{bmatrix} \quad (10)$$

Where: **v** is linear velocity and **θ** is the orientation of the robot represents the odometer outputs. The system model is shown:

$$X_{K+1} = f(X_K, U_K) + W_K \quad (11)$$

X_K is the state vector $x = [x \quad y \quad z \quad]^T$

$$\begin{bmatrix} x \\ y \\ \theta \end{bmatrix}_{K+1} = \begin{bmatrix} x \\ y \\ \theta \end{bmatrix}_K + \begin{bmatrix} vcos\theta \\ vsin\theta \\ w \end{bmatrix} Te + W_K \quad (12)$$

The Jacobian matrix of f with respect to Xk+1 is $F = \frac{\partial f(x,u)}{\partial x}$, given by:

$$F = \begin{bmatrix} 1 & 0 & -TeVsin\theta \\ 0 & 1 & TeVcos\theta \\ 0 & 0 & 1 \end{bmatrix}$$

With

$$u = [v \quad w]^T$$

W_K : is Gaussian noise for the process model with covariance Q :

$$Q_K = BQB$$

With:

$$Q = \begin{bmatrix} \delta_v^2 & 0 \\ 0 & \delta_w^2 \end{bmatrix}$$

.

$$B = \frac{\partial f(x,u)}{\partial u} = \begin{bmatrix} Tecos\theta & 0 \\ TeVsin\theta & 0 \\ 0 & \text{Te} \end{bmatrix} \quad (13)$$

Update:

The measurement visual odometer matrix is:

$$Z_K = [x_{cam} \quad y_{cam} \quad z_{cam} \quad]_K^T = h(X_K) + V_K$$

V_k are Gaussian noises for the measurement model with covariance R.

$$R = \begin{bmatrix} \delta_x^2 & 0 & 0 \\ 0 & \delta_y^2 & 0 \\ 0 & 0 & \delta_z^2 \end{bmatrix}$$

The Jacobian matrix of h with respect to Xk+1 is $H_K = \frac{\partial h(x,v)}{\partial x}$ giv en by:

$$H_K = \frac{\partial h(x,v)}{\partial x} = I_3 \quad (14)$$

V. FAULT TOLERANT CONTROL

In this section we present fault tolerant control method that is constituted by two basic tasks, fault detection and fault diagnosis and control redesign.

A) Fault detection: To detect errors in the systems, we compare the estimated positions by the two extended Kalman filters. than we calculate the Euclidean distance between the fiters's positions (EKF1, EKF2).

$$\text{Dis}_{(EKF1,EKF2)} = \sqrt{(x_{EKF1} - x_{EKF2})^2 + (y_{EKF1} - y_{EKF2})^2} \quad (15)$$

We compare this distance to a specific threshold Th_{rd} . If $Dis_{(EKF1,EKF2)}$ exceeds the threshold the system detect an error else no error is detected.

A) Fault diagnosis and control redesign

We need two steps to diagnose the error and redesign the system in case of faults:

- In the first step we compare the outputs of similar sensors, to identify the wrong branch. The sensors used in the prediction models (INS / ODO) on one side, and the sensors used in the correction models (GPS / CAM) on the other side.

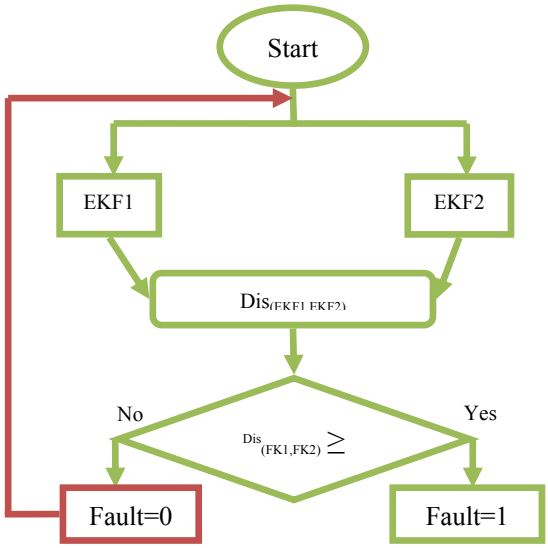

Fig. 3. Fault diagnosis flowchart

- If the output of a sensor deviates from its dual, the diagnostic system a material faults on one of these two sensors of the same type. The defective sensor will then be identified in the comparison of the sensors of the same branch.
- If the sensor outputs are similar, the system will diagnose a software fault.

- In the second step we compare the sensors of the same branch, to identify the wrong sensor. The first branch is (INS / GPS) and second branch is (ODO/ CAM).

B) System decisions :

- ➔ If a material error is detected in the first branch, the output will be the EKF2 position.
- ➔ If a material error is detected in the second branch, the output will be the EKF1 position.
- ➔ If no error is detected, the output will be tow branches average.
- ➔ If a software error is detected, an alert is generate indicating that the location is wrong

VI. SIMULATION RESULTS

In this section we propose to evaluate the fault tolerance mechanisms described above. This study uses sensors data in V-rep software and fault injection with Matlab software. First, we present (Software environment, Faults, Measures) that we used to perform these experiments. Second, we present the results of our fault injection.[7]

A) Software environment

Our evaluation environment is based on simulated data acquisition using V-rep software. Data replay and fault injections were implemented using Matlab. V-rep is Virtual robot experimentation platform, it is general purpose robot simulator with integrated development environment, Sensors, mechanisms, robots and whole systems can be modeled and simulated in various ways.[7]

B) Faults

Hardware faults are simulated by altering and modifying sensor output values, while software faults are simulated through mutation by modifying the models and gains of the Kalman filters. [7]

- ❖ Hardware faults: based on feedback from our engineers, we identified three categories of hardware faults that the sensors embedded in our vehicle may be subject to: bias faults, frozen data fault.
- ❖ Software faults are in most cases introduced during the software development phase (specification, design, coding, etc.).

C) Measures

The five thresholds Thrs1, Thrs2, Thrs3, Thrs4 and Thrs5 were defined here from experimental values using the system's nominal behavior.

Thresholds	Designation	Value [m]
$Thrs_1$	Position between the two Extended Kalman filters (PosEKF1 , PosEKF2)	3
$Thrs_2$	Position between the two similar sensors (INS/Odo)	4.5
$Thrs_3$	Position between the two similar sensors (GPS/Cam)	5.5
$Thrs_4$	Position between the two sensors (INS/GPS)	2
$Thrs_5$	Position between the two sensors (ODO/CAM)	2

D) Simulation and results

In this section, we present simulations and results of scenarios proposed for evaluated our fault tolerant control architecture, The first simulation scenario of the robot is to follow an circular trajectory without faults (nominal behavior).

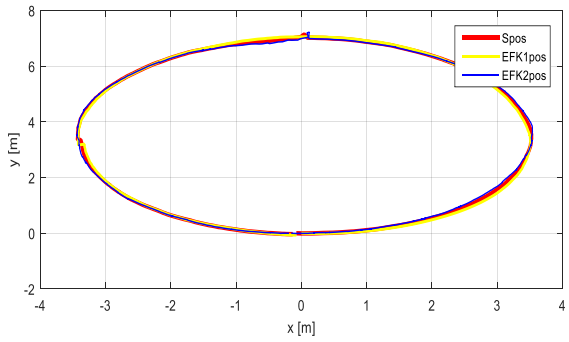

Fig. 4. Nominal behavior: Position estimated by the two extended Kalman filters and the system output.

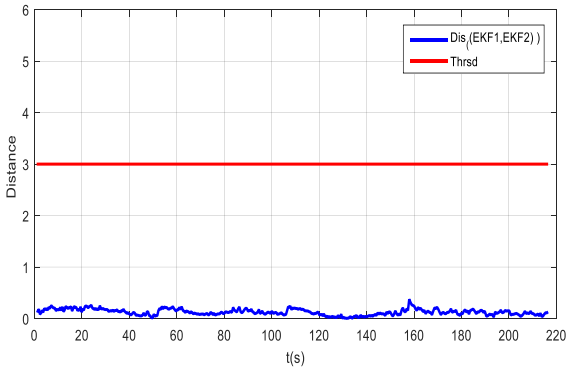

Fig. 5. Nominal behavior: Distance between the positions given by the two Extended Kalman filters.

The second simulation scenario of the robot is to follow the same trajectory, at t=93.75s we inject simulated hardware fault in the GPS sensor: we added a jump of 10 m on the yGPS:

$$y_{GPS}(tk) = y_{GPS}(ti) + 10$$

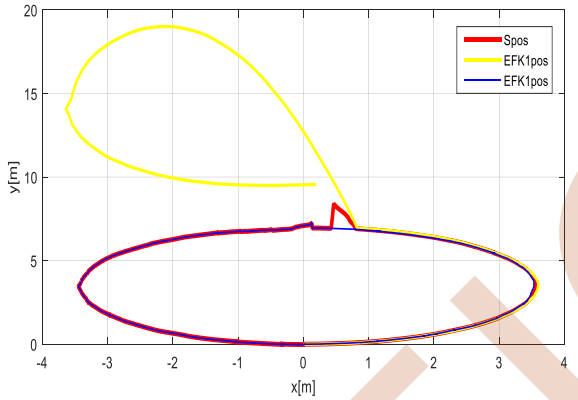

Fig. 6. .Additive fault in GPS: Position estimated by the two extended Kalman filters and the system output.

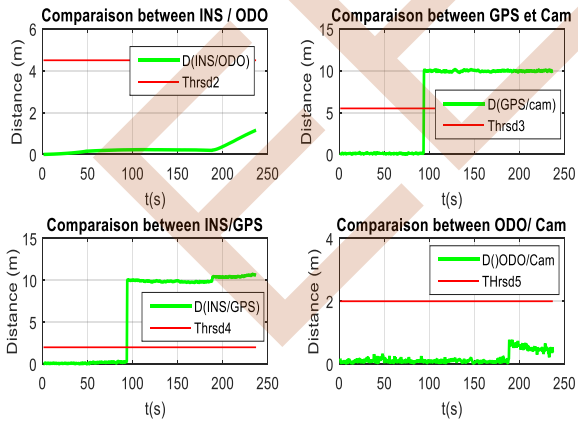

Fig. 7. Additive fault in GPS: Comparaison between sensors

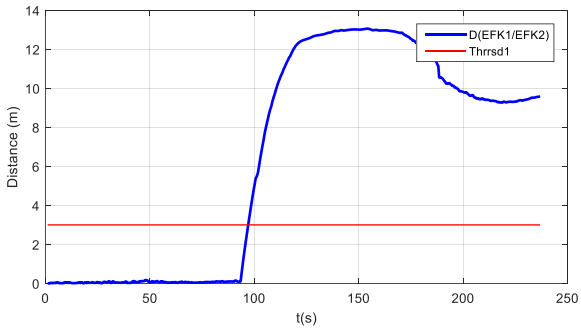

Fig. 8. Additive fault in GPS: Distance between the positions given by the two Extended Kalman filters.

The third simulation scenario of the robot is to follow the same trajectory, at t=0s we injected several types of mutations: (a) numerical value substitution: a numerical value may be replaced by a specific value in its domain (such as 0, 1, and−1 for integers); (b) unary operator: aunary operator may be replaced by another (cos become sin for instance . . .); (c) binary operator: a binary operator may be replaced by an operator from a specific set (− instead of+ and vice versa . . .)[7].

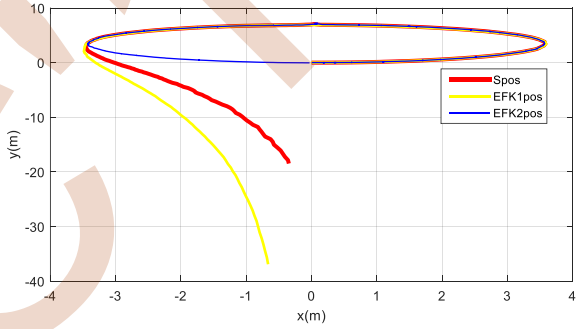

Fig. 9. Software fault in Kalman filter 1: Position estimated by the two extended Kalman filters and the system output.

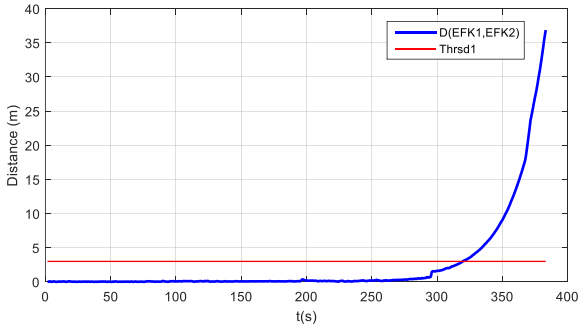

Fig. 10. Software fault in Kalman filter 1: Distance between the positions given by the two Extended Kalman filters.

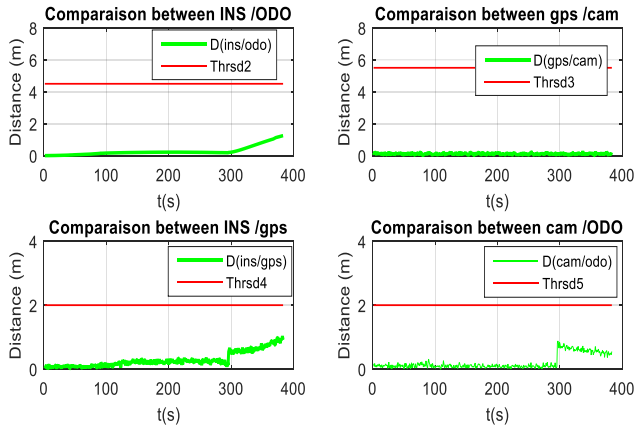

Fig. 11. Software fault in Kalman filter 1: Comparaison between sensors

*

VII. CONCLUSION

In this paper, we have proposed an approach diagnosis of faults using multisensors data fusion on a unicycle-type mobile robot. This approach use four sensors namely the GPS, Camera, INS, and odometry for the robot localisation. The fault diagnosis on two basic tasks: duplication and comparison. A sensor fusion stratery has been implemented based on two extended Kalman filters which allow for two independent localization systems. The proposed approach has been validated in simulation using the Vrep environment.

REFERENCES

[1] Q. Gan and C. J. Harris, "Comparison of two measurement fusion methods for Kalman-filter-based multisensor data fusion," in *IEEE* Transactions on Aerospace and Electronic Systems, vol. 37, no. 1, pp. 273-279, Jan 2001.

[2] I. Abuhadrous, Onboard real time system for 3D localization and modelling by multi-sensor data fusion," Theses, Ecole Nationale Superieure des Mines de Paris.Jan. 2005.

[3] A. O. Djekoune, Localisation et guidage du robot mobile dans un environnement naturel."Ph.D. dissertation, Universitée des Sciences et de la Technologie Houari Boumediene, 2010.

[4] S. Sakhi, Centrale d'acquisition temps reel pour le trace d'engins mobiles,Theses,2016.

[5] Fethi Demim, Abdelkrim Nemra, Kahina Louadj, Mustapha Hamerlain &Abdelouahab Bazoula, Cooperative SLAM for multiple UGVs navigation using SVSF filter, (2017).

[6] Ehab I. Al Khatib1, Mohammad A. Jaradat2, 3, Mamoun Abdel-Hafez2, and Milad Roigari1, Multiple sensor fusion for mobile robot localization and navigation using the Extended Kalman Filter,2015.

[7] Kaci Bader *, Benjamin Lussier, A fault tolerant architecture for data fusion: A real application of Kalman filters for mobile robot localization. Walter Schön Sorbonne Universités, Université de Technologie de Compiègne,2017.

Control and supervision of the didactic FESTO Compact Workstation via EasyPort interface

Boucetta Lakdhar Nadjib Djennane Sami Rebai Karima
GEII Department, ENST
Algiers-Algeria
l_boucetta@enst.dz s_djennane@enst.dz Karima.rebai@enst.dz

***Abstract*— The work represented in this paper aims to develop an application to control and supervise the FESTO Compact Workstation via EasyPort interface. This station available at the National School of Technology allows the study of several types of control loops (level, flow, pressure, temperature) and aids students to learn several concepts in process automation. The objective of this work is to develop a LabVIEW application that allows the data acquisition (measurements) and digital and analogical control of the various actuators transmission from PC to the station. The developed application aims can be used for training conventional PID regulator and as a base for the implementation of advanced control theories.**

Keywords*— *Didactic system for process automation; LabVIEW; Control loops, FESTO Compact Station; EasyPort USB.

I. INTRODUCTION

An important component in engineering education, in particular in the field of process automation and control, is the formation of students to deal with real industrial process. The needed skills can be acquired by the interaction and the manipulation of didactic systems that mimic real industrial process. Therefore, the National high school of technology (ENST) has the Festo "Compact Workstation" for training students on topics related to process control design and industrial automation.

The Festo Compact Workstation [1] is a didactic station developed by the German company "FESTO". It has been designed to allow students practice by experimentation basic and advanced control theories. This station represents one of an attractive system for both education [2] [3] and research [4] [5] in process control. It is composed of several loops of regulation (Level, Flow, Pressure and Temperature). These loops can be controlled by a PC via an EasyPort interface and FluidLab®-PA software. The current available software is a closed source demo software that allows students to use the predefined controller and to change their parameters; however, it is not possible to access to the elementary components of the station and to change the controller structure. This software limits the exploitation of this station to the predefined (PID) controller and it can't be used for the implementation of other control strategies. To tackle with the above-cited problems, this work has been focused in the development of our proper LabVIEW application that allows the control and the supervision of different elements composing the Festo Compact Workstation.

The remainder of this paper is organized as follows. The next section gives an overview description of the station. The third section presents the used procedure to ensure the communication between the station and LabVIEW via EasyPort USB. The section four describe the developed application for process control and supervision. An experimental test is presented in section 5 while the last section of this paper concludes this work and discusses the possible future work.

II. FESTO COMPACT STATION DESCRIPTION

The FESTO Compact Workstation didactic station represented by Fig. 1 is dedicated mainly to the study of the four control loops (Level, Flow, Pressure and Temperature). These variables represent the four basic control variables currently used in industrial process.

Fig. 1: FESTO compact Workstation [1]

The control of this station and the supervision of its operation impose the exploitation of Input/ Output interface between the station and the control PC.

Therefore, the EasyPort USB [6] is a module that offers the possibility of data change (digital/ analogical) between the station and the LabVIEW. These data can be measurements or controls signals. Fig. 2 shows the different connections between PC, EasyPort USB and the other components of the station.

In the next subsections, we give a brief description of the four loops that compose it and identify their inputs and outputs. The next section describes how these data can be exchanged with the developed LabVIEW application.

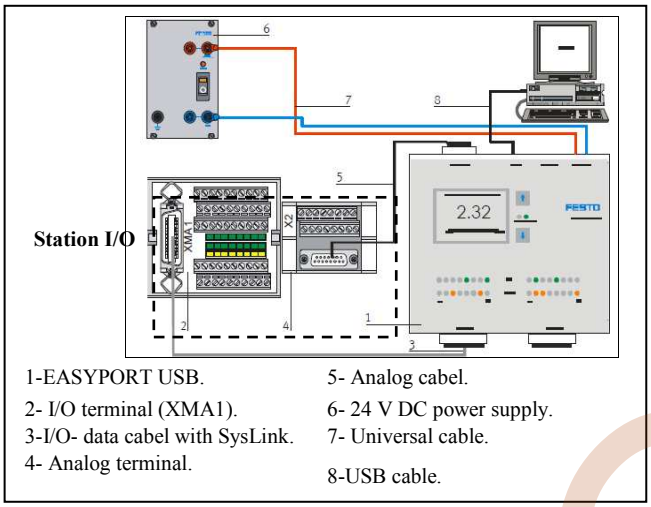

1-EASYPORT USB.
2- I/O terminal (XMA1).
3-I/O- data cabel with SysLink.
4- Analog terminal.
5- Analog cabel.
6- 24 V DC power supply.
7- Universal cable.
8-USB cable.

Fig. 2: Different connections PC-EasyPort USB-station

A. *Level control loop*

The station is composed of two tanks B101 and B102. The aim of this regulation loop is to maintain the level inside the tank B102 at a fixed value (Setpoint). For this purpose, the pump P101 is used to deliver the fluid from the tank B101 to the tank B102 via a piping system and an analog ultrasonic sensor is used for level measurement as shown in fig. 3. Disturbances to this control loop can be created by the full (opening / closing) of the ball valve V102 or by using the manual valve V104 to empty the water from the upper tank B102 into the lower tank B101.

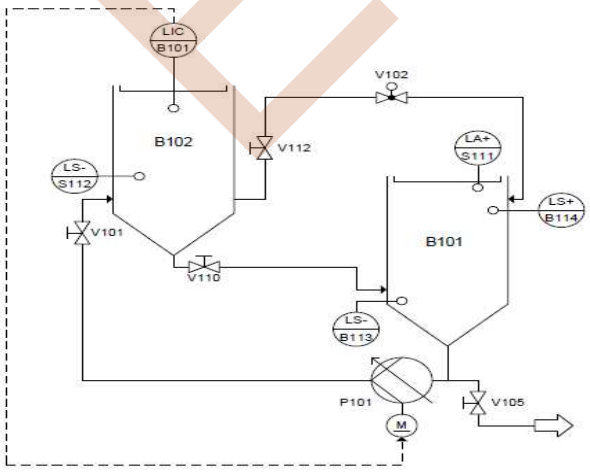

Fig. 3: P&ID Diagram of the level control system [1]

The ultrasonic sensor transmits the level value as a current (4 ... 20 mA), which is then converted into a standard voltage (0...10VDC) by the converter (current / voltage) (A1). This measurement can be transmitted to the EasyPort through the X2 analog terminal. The level control is done by the pump P101 actuated by the motor M1. For this, the control program will generate a setting value and transmits it to the station via EasyPort as a voltage between (0...10VDC). This command is then transmitted to the motor (M1) of the pump via the relay K1 and the terminal for analog signals. This terminal will adapt the standard voltage (0...10VDC) to a voltage (0...24VDC) required for motor control.

B. *Flow Control Loop*

The purpose of this control loop (Fig. 4) is to maintain the flow value fix even in the presence of disturbances. Flow measurement is carried out in the measurement point "FIC B101" linked to an optoelectronic pallets sensor. The flow control can be performed using the P101 pump or the proportional valve V106. In the first case, the voltage of the pump defines its speed of rotation while in the second case it's the voltage of the coil of the valve V106 which defines the stroke of the valve piston. Noting that when the flow control is done through the V106 valve, the P101 pump runs at a constant speed.

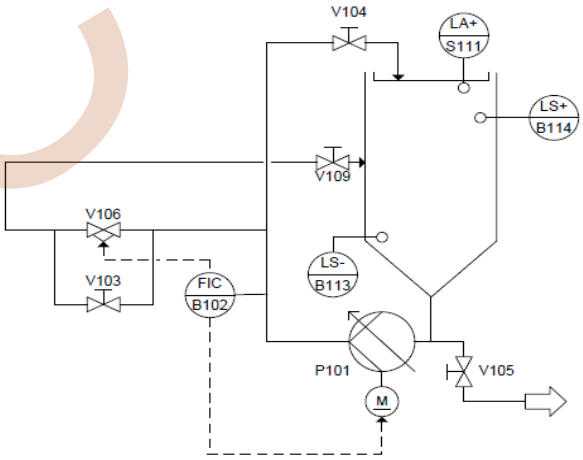

Fig. 4: P&ID Diagram of the flow control system [1]

It is possible to generate disturbances by the partial or total (opening/closing) of the manual valve V104.

The optoelectronic sensor measures the value of the flow and sends it in the form of a square wave (0...1200Hz). Its frequency is then converted into a standard voltage (0...10V) (DC) by the (frequency/voltage) converter (A2) and transmitted to EasyPort via the terminal for analog signals (X2).

The control program generates the command signal and transmits it in the form of a voltage (0...10 VDC) via EasyPort to the proportional valve V106 or the pump motor, the procedure here is identical to that of the level control where the relay K1 and the analog signal conversion terminal are operated.

C. *Prussure Control Loop*

In this loop, the pressure is controlled in a pipeline system. There are two pressure control systems depending on the control element: using pump P101 or proportional valve V106 as illustrated the Fig. 5.

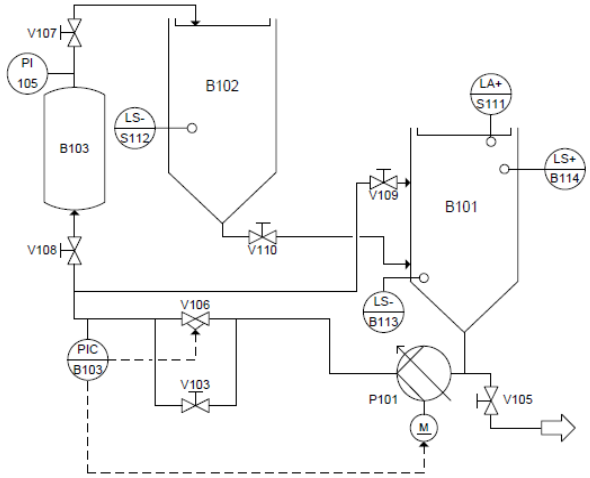

Fig. 5: P&ID Diagram of the pressure control system [1]

D. *Temperature control loop*

The temperature control is done in the lower tank B101. The fluid stored in this tank can be heated by a heat exchanger E104 and circulates under the effect of the pump which rotates at constant speed as shown in fig. 6. It is important to mention here that for using this loop, the operating temperature of the B101 tank must not exceed 65 °C and the heating resistor must be completely immersed in the fluid.

The ignition period of the heating resistor, which is the control variable, determines the quantity of heat supplied at the output by the heat exchanger E104.

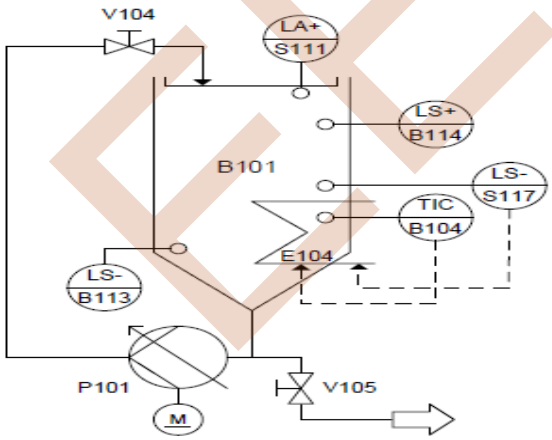

Fig. 6: P&ID Diagram of the temperature control system

The resistance of the PT100 sensor is connected to the (PT100/Voltage) converter (A3). This voltage is transmitted to the analog terminal (X2). The heating resistor is controlled via an internal relay connected directly to the EasyPort through the O1 output of XMA1.

III. Communication Between the FESTO Compact Sation and LabVIEW via EasyPort USB

EasyPort USB is a process interface for bidirectional transmission of signals between a control process and a PC [6].

The use of this interface allows the realization of the following tasks:

- Control of a real process by PC.
- Control of a process model simulated by a real API.
- Acquisition and analysis of measurements obtained on a real process.

Data is transmitted to and from an EasyPort USB process interface by means of addressed write and read commands. There exist different access levels that can be used for executing these write and read commands depending on how to incorporate EasyPort USB into application.

Our objective in this work is to develop an application with LabVIEW to control the FESTO Compact workstation. Therefore, we adopted the use of the ActiveX Control as a software interface.

To establish the communication between FESTO Compact Workstation and LabVIEW via EasyPort USB, we have used some functions that allow the use of this station as ActiveX object in LabVIEW and consequently data exchange between LabVIEW application and EasyPort USB such as *Automation Open, Invoke Node, Property Node* and *Automation Close.*

IV. Developing the LabVIEW Application

In this section, we describe our LabVIEW developed application for the control and the supervision of the FESTO Compact Workstation via the EasyPort USB. This application contains a start Virtual Interface (VI) giving access to 4 other VI that allow the control and the supervision of the 4 control loops in real time. Fig. 7 shows the overall architecture of the developed application.

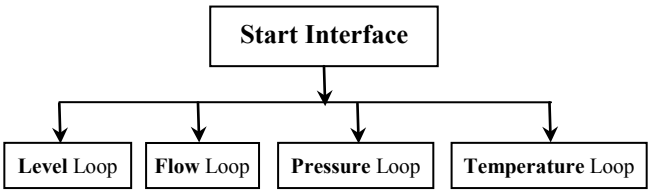

Fig. 7: The application architecture

The first and common step, between the different loops, in the development of this application is how to manipulate the analogical and digital data. Fig. 8 and 9 show the developed code for reading and writing numerical values in LabVIEW. These data describe the sensors states (Fig. 8) and On/Off actuators (Fig. 9).

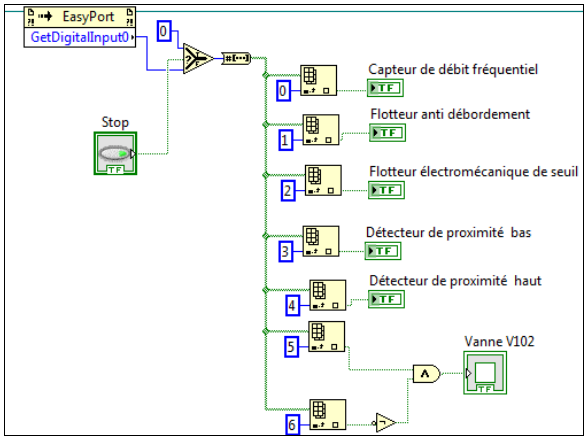

Fig. 8: Reading sensors states

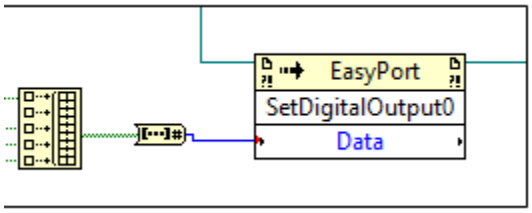

Fig. 9: Numerical Actuator control

Reading and sending analogical signals like sensor measurement and control of actuators are carried out using the code illustrated in Fig. 10. This figure presents an example of how to read level measurement (Fig. 10.a) and write the pump command (Fig. 10.b).

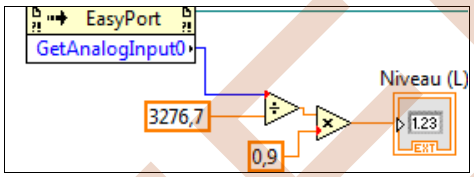

(a) Reading level measurement

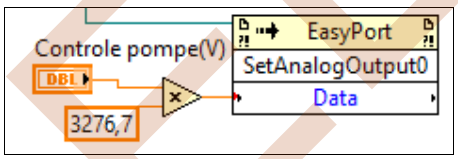

(b) Writing the Command of the pump P101

Fig. 10: Reading and writing analogical data

The table below shows different functions that are used to read the analog values:

TABLE I. Different functions used to read analogical data

Function	Values output
GetAnalogInput0	Level of water in the tank B102
GetAnalogInput1	Flow of water in the canalisation
GetAnalogInput2	Pressure in the tank B103
GetAnalogInput3	Temperature in the tank B101

We have applied a set of mathematical operations to the values sent by ***"GetAnalogInput"*** function because they do not represent the actual values of the measurements. Each value sent by this function is represented in the numeric range (0 ... 32767) and is equivalent to a voltage value between (0-10 V). It is therefore necessary to apply a scaling measure.

In the remainder of this section, we describe the pressure interface as an example of the developed VI. It has two operating modes: control by pump P101 or proportional valve V106. The flowchart represented by figure 11 illustrates the different steps carried out for the realization of 2 VI named "Pressure Regulation" and "Supervision: Pressure".

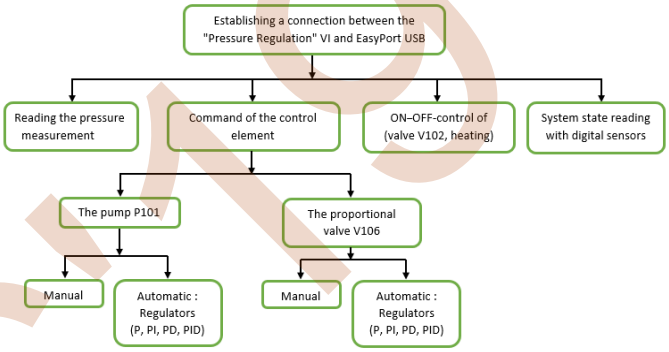

Fig. 11: Different steps followed for the realization of the VI of the pressure loop

The control interface of the pressure loop offers to the user the choice of the control element and the PID controller to be used. Depending on the choice of the control element as well as the controller (P, PI, PD, PID), a control signal is sent to the actuators through EasyPort USB using the ***"SetAnalogOutput1"*** action for the V106 proportional valve or the ***"SetAnalogOutput0"*** action for pump P101. The LabVIEW code that performs the two modes of control are presented in the Fig. 12 and Fig. 13.

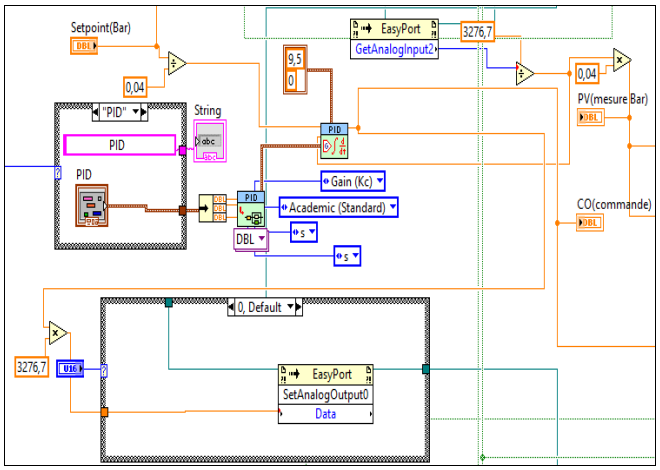

Fig. 12: LabVIEW code of the pressure loop using proportional valve V106 as a control element

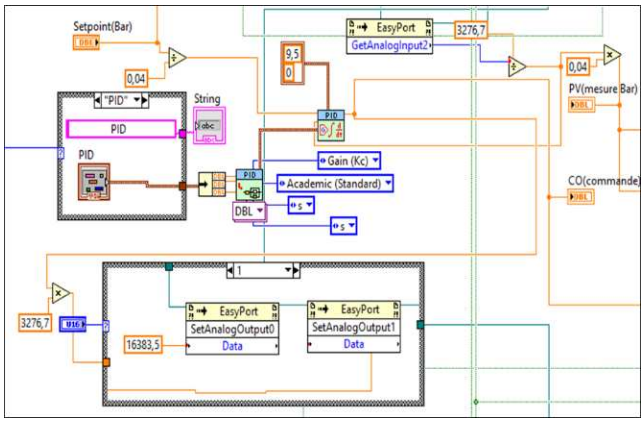

Fig. 13: LabVIEW code of the pressure loop using P101 Pump as a control

These figures shows the possibility of using this code with small modifications for the implementation of other controllers.

The sub-VI "Supervision: Pressure" offers to the student the possibility of visualizing the states of the sensors recovered in real time as shown in the fig. 14.

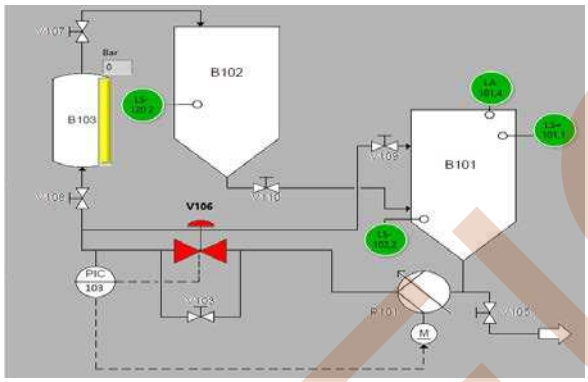

Fig. 14: The sub-VI "Supervision: Pressure"

Fig. 15 illustrates the developed interface for pressure control.

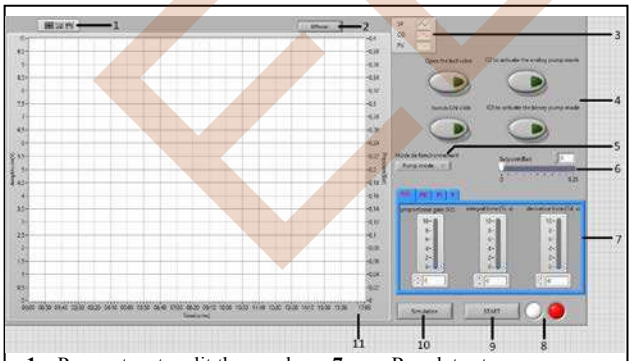

1	Parameters to edit the graph	**7**	Regulator type
2	Clear the curves	**8**	Leds
3	Curves	**9**	Start and Stop
4	Digital controls	**10**	Supervision window
5	Select the control system	**11**	The Graph
6	Setpoint		

Fig. 15: Pressure interface

V. Experimental Results

After completing the application design and development, it was necessary to test it to validate our work. The Fig. 16 shows an example of the obtained result when testing the pressure loop test. In this experiment (Fig. 16.a), we tested a PI regulator using a pump as control element for different value of set point (Blue). This figure shows how the developed application aid student to improve their skills in process control with experimentation and in interactive approach. The Supervision VI represented in Fig. 16.b get information about the real process in real time that can help student to understand the considered process.

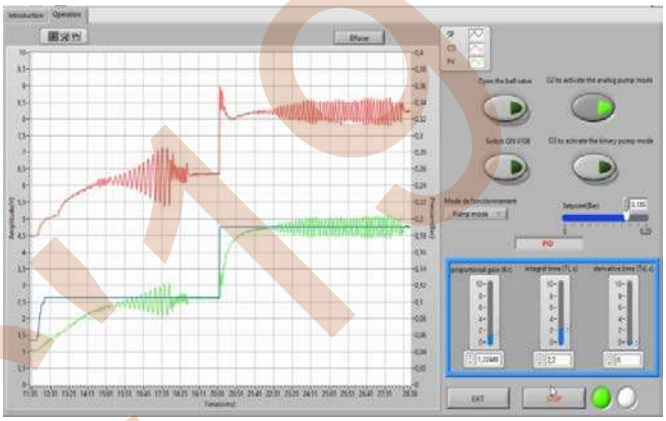

(a) Pressure loop test

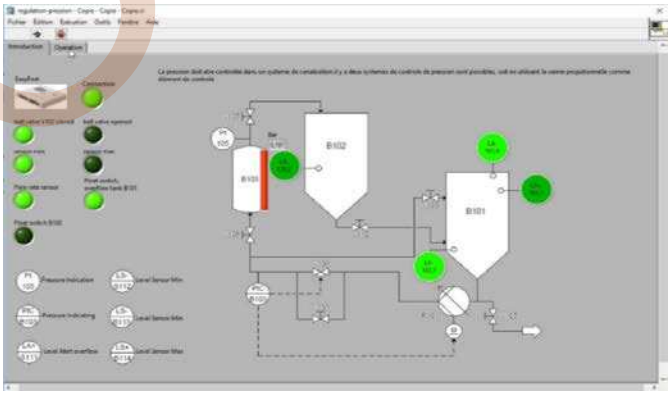

(b) Supervision of the pressure loop

Fig. 16: The result of the pressure loop test

VI. Conclusion and Future Work

This paper presents the developed LabVIEW application for FESTO Compact workstation control and supervision. The design and development of this application starts by the study of the considered process and all the control loops that compose. The issue of how to establish communication between the station and LabVIEW has been also addressed using EasyPort USB and ActiveX. Different VI have been developed in this work for the control and the supervision of the four control loops.

The current version of the developed application can be viewed as an interactive teaching system that allows an improvement in basic industrial control education and

training. Its use for practical experimentation touch on the important basic notions and problems. This application has didactic properties such as friendly graphical user interfaces, modular architecture, data storage and graphical visualization of real measurements. The final interactive system composed of the station and the application helps students to understand and compare different identification and control methods. This application can be easily extended with the implementation of other advanced control methods in future works.

REFERENCES

[1] J. Helmich, "Compact Workstation Manual," FESTO, 2008.

[2] D. Sendrescu, M. Roman, D. Selisteanu, "Interactive teaching system for simulation and control of electropneumatic and electrohydraulic systems," Proceedings of the 24th EAEEIE Annual Conference (EAEEIE), pp. 151-156, 2013.

[3] M. Vinatoru, G. Canureci, C. Maican, E. IANCUI, "Level and Temperature Control Study Using Festo Kit in a Laboratory Stand," Proceedings of the 3rd WSEAS/IASME International Conference on Dynamical Systems and Control, Arcachon, France, October 13-15, 2007, pp. 247-252

[4] V. Skopis, I. Uteshevs and A. Pumpurs, "Advanced Control System Development on the Basis of Festo Training Laboratory Compact Workstation," Journal of Energy and Power Engineering 8(5), 2014

[5] Koszewnik, T. Nartowicz and E. Pawłuszewicz, "Fractional order controller to control pump in FESTO MPS® PA Compact Workstation," Conference: 2016 17th International Carpathian Control Conference. DOI: 10.1109/CarpathianCC.2016.7501124.

[6] Eberhardt, et Löffler, « EasyPort USB Manual », FESTO, 2008.

Fractional order PI-$I^{\lambda}D^{\mu}$ regulator design for high-accuracy position control of an industrial robot

Seghiri Tounes
Department of Mechanical Engineering
University of 20th Auust 1955 – Skikda
Elhadaiek, Skikda 21000 Algeria.
E-mail: seghiritounes@gmail.com

Samir Ladaci
Department of E.E.A.
National Polytechnic School of Constantine
N.V. Ali Mendjli, Constantine 25100, Algeria.
E-mail: samir_ladaci@yahoo.fr

Salim Haddad
Department of Mechanical Engineering
University of 20th Auust 1955 – Skikda
Elhadaiek, Skikda 21000 Algeria.
E-mail: salimhad@yahoo.fr

***Abstract*—In this paper we propose a new methodology for a fractional order PID-like controller in order to supervise a high-precision position of a industrial robot arm loading round steel blocks from inside a rotary hearth furnace. The novel fractional order PII$^{\lambda}$D$^{\mu}$ control configuration involves a standard integrator joined to fractional order integral and derivative actions. The design procedure begins with the use of relay method to tune an integer order PID controller that stabilizes. Then the fractional order integral and derivative of orders λ and μ approximated with rational functions using the singularity function method are introduced and the new parameters are tuned by optimizing performance criteria. Simulation results illustrate the efficiency of the proposed controller and its ability to fulfill the performance constraints and avoid undesirable overshoots with a bounded range of input currents variation.**

Key word: Fractional order PI-$I^{\lambda}D^{\mu}$, Singularity function method, industrial robot, relay method, Performance.

I. INTRODUCTION

Fractional order control is focusing a great research effort and touching a widening field of applications [1-2]. In particular, fractional order PID controllers have been intensively studied and developed this last decade [3-4]. Since the first design of Podlubny [5], many fractional order PID-like structures and parameter tuning techniques have been proposed in literature. Numerous fractional order PID control studies considered mechanical systems applications [6-7] and particularly on robotic manipulators [8-10].

Indeed, many dangerous or difficult tasks are realized in industrial processes through robots manipulators. In this paper, we consider supplying and discharging heavy steel blocks, from an industrial furnace [11].

The industrial robot moves horizontally inside the furnace in order to remove the heated blocks from the furnace with minimum fuel consumption. An important issue is to correctly discharge the steel blocks without hitting them with the gripper, which requires an automatic control structure for the positioning of the industrial robot [12]. In the initial classical control system, the current positioning of the robot is made with an 11% overshoot, which has to be reduced in order to minimize the possible stroke.

The aim of this work is to design a fractional order PID-like control configuration, for the automatic positioning of the discharging robot, in order to obtain the desired performance such as no overshoot and a settling time of maximum 3 seconds, and to be able to guarantee the rhythm of rolling of 4 peaces/ minute.

The proposed fractional order controller combines an integer order integral action with a couple of fractional order integral and derivative operators. We maintained the original integral in order to eliminate the steady state position error.

This paper is organized as follows. Section II comprises two main parts: the fractional order systems definitions and the approximation methods are presented. In section III the industrial robot model is presented. Section IV gives the fractional order PID-like controller design method and in Section V numerical simulations of its application to the position control of the robot are given to verify the effectiveness of the proposed scheme. To complete the paper conclusions and discussions are added in Section VI.

II. FRACTIONAL ORDER SYSTEMS

A. *Fractional Calculus and fractional order systems*

Fractional calculus where the integration and differentiation are arbitrary (fractional) order is an old concept which dates back to Cauchy, Riemann Liouville and Leitnikov in the 19th century. Fractional calculus is extending of the concept of integer order integral and derivative, the fractional integral and derivative have been defined. Fractional order calculus also provides a good tool for describing dynamic process. In a general way, fractional order calculus refers that orders of differentials and integrals can be arbitrary or fractional [13-14].

$$ {}_{t_0}D_t^{\alpha} = \begin{cases} \dfrac{d^{\alpha}}{dt^{q}} & \alpha > 0 \\ 1 & \alpha = 0 \\ \displaystyle\int_{t_0}^{t} (d\tau)^{-\alpha} & \alpha < 0 \end{cases} \tag{1} $$

Here, t_0 is the initial value, α is the fractional order which can also be complex, and *R(q)* is the real part of the fractional order.

There are several definitions for fractional order derivatives of which three most commonly used definitions are the Grünwald–Letnikov's, Riemann–Liouville's, and Caputo's derivative definition.

if *f(t) is* a continuous time function, for the order *n* where $n \in [0\ 1]$, there are some definitions for fractional derivatives of *f(t)* [13]:

- The Grünwald–Letnikov's derivative definition can be written as;

$$ D_t^{\lambda} f(t) = \lim_{h \to 0} \frac{1}{h^{\lambda}} \sum_{j=0}^{[\,]} (-1)^k \binom{\lambda}{j} f(t - jh) \tag{2} $$

Where, *h* is the sampling period with the coefficients $\omega_j^{-\lambda}$

Verifying $\omega_0^{(-\lambda)} = \binom{-\lambda}{0} = 1$ w here the coefficients

(2) is given as follows

$$ D_t^{\lambda} f(t) = \lim_{h \to 0} h^{\mu} \sum_{j=0}^{[\,]} (-1)^k \binom{\lambda}{j} f(t - jh) \tag{2.a} $$

$$ \omega_j^{(-\lambda)} = \binom{-\lambda}{j} = \binom{\mu}{j} = \frac{\Gamma(\mu+1)}{\Gamma(j+1)\Gamma(\mu - j + 1)} \tag{2.b} $$

The Caputo's derivative definition has the following Form;

$$ D_t^{m} f(t) = \frac{1}{\Gamma(n-m)} \int_c^t \frac{f^{(n)}(\tau)}{(t-\tau)^{m-n+1}} d\tau \tag{3} $$

The Riemann–Liouville's m[th] derivative of function f(t) is described as,

$$ D_t^{m} f(t) = \frac{d^n}{dt^n} \left[\frac{1}{\Gamma(n-m)} \int_c^t \frac{f^{(n)}(\tau)}{(t-\tau)^{m-n+1}} d\tau \right] \tag{4} $$

Where n is the first integer larger than m

$n-1 < m < n$, $n \in N$ and $\Gamma(n)$ is the gamma function.

In the analysis and synthesis of automatic control systems, the Laplace transform method is used commonly.

The Laplace transform of the differ-integral operator ${}_a D_t^{\alpha}$ is given by the expected form [14-15]:

$$ L\left\{ {}_0 D_t^{\alpha} f(t), s \right\} = s^{\alpha} . F(s) \tag{5} $$

where $F(s) = £\{ f(t) \}$ is the normal Laplace transformation, *n* is integer that satisfies $n-1 < \gamma \le n$.

A fractional-order system is defined by the system which is better described by the fractional order mathematical models. Contrary to the conventional approach, the fractional-order system has the transfer function of an arbitrary real order.

B. *Approximation method*

Many approximations methods have been developed in the fractional calculus literature. The most popular are those of Charef et al. (1992) called the singularity function method and Oustaloup's method (1995) [15].

The singularity function method is based on the fractional order poles powers function approximation in the frequency domain with a rational one. This method is very easy to implement and is based on the approximation of a function of the form:

$$ H(s) = \frac{1}{s^{\lambda}} \tag{6} $$

where λ is a positive number such that $0 < \lambda < 1$. In a given bandwidth $[\omega_b, \omega_h]$, this fractional operator can ba approximated as,

$$ H(s) \approx \frac{K_I}{\left(1 + \dfrac{s}{\omega_c}\right)^{\lambda}} \approx K_I \frac{\displaystyle\prod_{i=0}^{N-1} \left(1 + \frac{s}{z_i}\right)}{\displaystyle\prod_{i=0}^{N} \left(1 + \frac{s}{p_i}\right)} \tag{7} $$

with $K_I = \dfrac{1}{\omega_c^{\lambda}}$ and ω_c, is the cutting frequency given by,

$$ \omega_c = \omega_b \sqrt{10^{\left(\frac{\varepsilon}{10\lambda}\right)} - 1} \tag{8} $$

and ε is the maximal error in dB.

The singularities are given by:

$$ p_j = (ab)^{j-1} p_0 \qquad j = 1, 2, 3, \ldots N $$

$$ z_i = (ab)^{i-1} a p_0 \qquad i = 2, 3, \ldots N-1 $$

with, $p_0 = w_c \sqrt{b}$, $a = 10^{\frac{\varepsilon}{10(1-\lambda)}}$, $b = 10^{\frac{\varepsilon}{10\lambda}}$, $\beta = \dfrac{\log(a)}{\log(ab)}$

The order of approximation N is computed by fixing the frequency band of work, specified by $\omega_{\max}$, so that:

$p_{N-1} < \omega_{\max} < p_N$. This leads to:

$$\text{N= integer part of } \left\lfloor \frac{\log\left(\frac{\omega_{\max}}{p_0}\right)}{\log(ab)} + 1 \right\rfloor + 1 \qquad (9)$$

.

III. Robot Positioning System Model

The positioning system of the industrial robot is electro-hydraulically driven because of the heavy and hot blocks of steel it has to properly handle. After the discharge robot's position is measured using a linear incremental encoder, the value is converted in millimeters. The robot is positioned above the block in relation to the center of the round block of steel at discharge.

A video camera is used in order to measure this displacement, and special software calculates the distance from the block center to the industrial robot's axis in millimeters. The positioning system model has been obtained using a parametric identification method, based on a set of experimental data [11,16].

The model transfer function is given as,

$$H(s) = \frac{18.153}{0.75\,s^2 + 3.25s + 1} \qquad (10)$$

IV. Fractional Order Controller Design

The fractional order PID-like controller is obtained in two steps, as follows:

A. *Standard PID control design*

In order to tune an integer PID control system that stabilizes the industrial robot positioning system, one can use the Relay method. The controller's parameters are obtained after the analysis of the simulated positioning signal's step response, using simple formulas. The Relay method consists of implementing a feedback closed-loop structure that has the relay block and the fixed part model of the process to be controlled on the direct path, and a unitary feedback path as represented in Figure 1.

The reference signal represents the billet displacement and is set at 1 mm. A relay with hysteresis is used as the relay block, having the error signal as the input signal, the switch point value *eps* and the relay output signal given in (11). The relay's parameters need to be set in such a way that the output signal *p(t)* exhibits maintained oscillations.

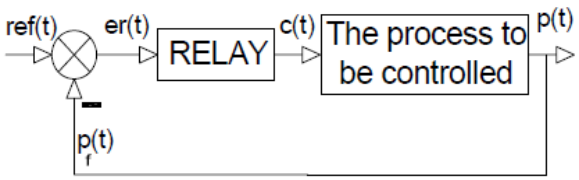

Figure 1. The relay step test configuration

$$\begin{cases} c(t) = b, & if \quad er(t) \geq eps \\ c(t) = -b, & if \quad er(t) \leq -eps \end{cases} \qquad (11)$$

The PID controller parameters are determined quite easily as [11],

$$H_{PID}(s) = k_p\left(1 + \frac{1}{T_i s} + T_d s\right) \qquad (12)$$

with

$$k_p = 1.18938, \quad T_i = 0.387\ \text{sec}, \quad T_d = 0.0929\ \text{sec} \qquad (13)$$

For the simulation of the industrial robot functionality a billet displaced to the right of the robot axis with 100 mm is considered. The simulated position of the robot, generated by the PID automated control structure, is depicted in Figure 2.

It shows that the obtained step response presents an overshoot of 36% for the positioning system, which needs further improvement.

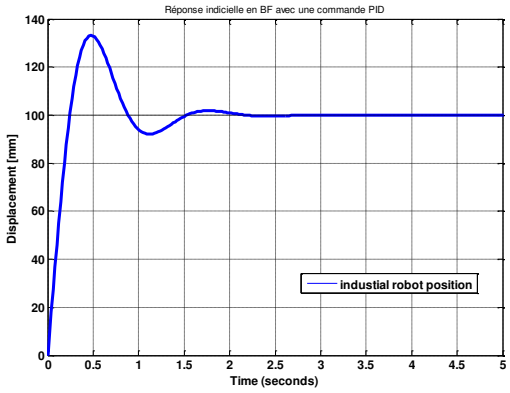

Figure 2. The robot position usin the relay based PID controller

B. *Proposed fractional order PI$^{\lambda}$D$^{\mu}$ control design*

In recent years, it is remarkable to see the increasing number of studies related to the theory and application of fractional order controller (FOC), especially PI$^{\lambda}$D$^{\mu}$ controller, in many areas of science and engineering. Research activities are focused on developing new analysis and design methods for fractional order controllers as an extension of classical control theory [17-18].

In this paper, a new tuning method for fractional order proportional, integral and derivative (PII$^{\lambda}$D$^{\mu}$) is proposed , in order to decrease the position error and the control input energy and ensure the same overall performances for the positioning of the industrial robot, even if the block of steel is located at the maximum stroke. The general form of a feasible FOPID controller is presented in (14),

$$H_{FOPID}(s) = \frac{k_p}{Ts+1}\left(1+\frac{1}{T_i\, s}+\frac{1}{T_i\, s^{\lambda}}+T_d\, s^{\mu}\right) \qquad (14)$$

where the controller parameters are the same as those presented for the PID controller in the previous section and λ represents the fractional integral effect's order, μ represents the derivative effect's order. The controller parameter's values are equal to the PID controller that generates no overshoot, obtained through trial and error.

In order to keep a zero steady state error the integral effect order is kept, while for the integral and derivative effect's order a factional form is used, as to decrease the effect of the derivative action over the control signal and decrease J_e and J_{eu}.

The values of the fractional-order λ and μ are determined by means of successive computer simulations of the proposed FOPID control system.

V. Simulation Results

The proposed FOPID closed-loop control structure is simulated via computer simulation, using MATLAB Simulink. The fractional order integrator and derivative, of order λ respectively μ, are approximated using the Charef's method so-called the Singularity function.
In order to verify the IO model's accuracy the quadratic error criterion and the combined quadratic criterion between the process and the simulated response is computed, using the following criteria involving the output error and the input energy and a combined one respectively,

$$J_e = \sqrt{\sum er(t)^2} \qquad (15)$$

$$J_{eu} = \sqrt{\alpha \sum er(t)^2 + \beta \sum c(t)^2} \qquad (16)$$

With α = 0.6 and β = 0.4.

In Table 1, the authors present the values obtained for the criteria J_e and J_{eu} when applying the proposed controller to the robot manipulator model. Different values were chosen for the two non–integer parameters, according to the procedures steps. It can be noted, from the values presented in Table 1 that the best value resulted for λ is 0.1 and μ is 0.8, for which the quadratic error criterion and the combined quadratic criterion is equal to J_e=143.873 , J_{eu}=115.840. After applying the results of the previously presented identification procedure, the fractional order transfer function model of the positioning system, for which the smallest value for the J_e, J_{eu} is obtained, is given as,

$$H_{FOPID}(s) = \frac{k_p}{Ts+1}\left(1+\frac{1}{T_i\, s}+\frac{1}{T_i\, s^{0.1}}+T_d\, s^{0.8}\right) \qquad (17)$$

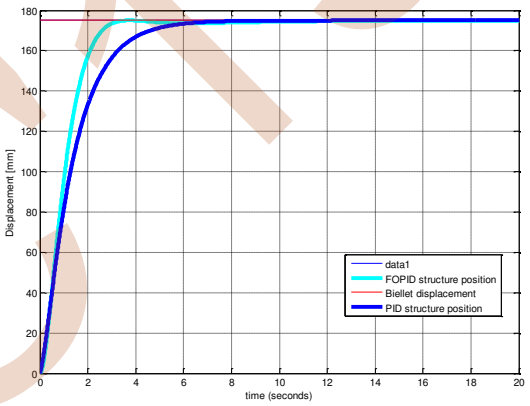

Figure 3. Comparison between the position of the robot generated by the integer order PID control structure and the FOPID control structure.

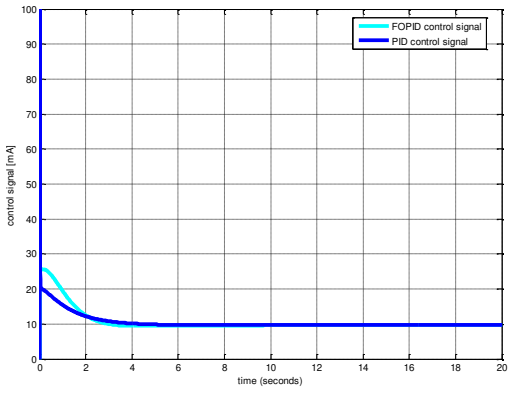

Figure 4. Comparison between the control signal of the robot generated by the integer order PID control structure and the FOPID control structure.

TABLE I. QUADRATIC CRITERIA VALUES OBTAINED FOR DIFFERENT VALUES OF THE FRACTIONAL PARAMETERS

	μ = 0.1	0.2	0.3	0.4	0.5	0.6	0.7	0.8	0.9
λ = 0.1	J_e=142.907 J_{eu}=113.42	142.896 113.408	142.851 113.371	142.810 113.337	142.762 113.301	142.728 113.268	142.694 113.245	142.651 113.227	142.629 113.227
0.2	142.848 113.392	142.826 113.371	142.770 113.325	142.721 113.283	142.671 113.242	142.626 113.205	142.590 113.179	142.545 113.159	142.521 114.835
0.3	142.878 113.426	142.840 113.393	142.761 113.330	142.699 113.278	142.640 113.229	142.589 113.187	142.550 113.158	142.505 113.139	142.479 102.373
0.4	142.975 113.519	142.922 113.475	142.824 113.396	142.749 113.334	142.680 113.277	142.623 113.231	142.582 113.201	142.537 113.181	142.510 380.783
0.5	143.178 113.684	143.110 113.638	142.993 113.546	142.910 113.477	142.836 113.416	142.778 113.369	142.74 113.341	142.699 113.325	142.673 374.495
0.6	143.515 113.9714	143.433 113.9066	143.300 113.804	143.213 113.732	143.137 113.669	143.0818 113.624	143.0514 113.602	143.0212 113.594	142.998 371.877
0.7	144.000 114.376	143.913 114.300	143.772 114.189	143.684 114.117	143.612 114.058	143.565 114.019	143.545 114.005	143.530 114.009	143.512 366.842
0.8	144.872 115.057	144.767 114.969	144.621 114.859	144.544 114.795	144.486 114.747	144.458 114.722	144.459 114.725	144.475 114.753	144.464 107.259
0.9	145.565 115.600	145.457 115.535	145.327 115.432	145.262 115.378	145.220 115.342	145.208 115.331	145.226 115.346	145.261 115.389	145.261 109.655

The comparative graph between the IO and the FO controller's step response at the same billet displacement of 175 millimeters is presented in Figure 3. From this figure analysis, it is deducted that the overall performances remain the same, meaning there is a zero steady state error and a settling time is lower than 2.6 seconds, also the control signal presented in Figure 4 has been reduced comparatively with the IO model.

It can be noted that the quadratic error criterion and the combined quadratic error between the curves from Figure 5 has a much smaller value than in the case of the IO model, resulting in the fact that the model from Eq. (17) is much more accurate than the model from Eq. (12). This proves that the usage of a fractional order transfer function, as the robotic arm's positioning system model, is justified [19].

VI. CONCLUSION

The positioning system of an industrial robot is controlled using a proposed fractional order PID-like controller in order. The novel fractional order $PII^{\lambda}D^{\mu}$ control configuration involves a standard integrator joined to fractional order integral and derivative actions. The design procedure begins with the use of relay method to tune an integer order PID controller that stabilizes. Then the fractional order integral and derivative of orders λ and μ approximated with rational functions using the singularity function method are introduced and the new parameters are tuned by optimizing performance criteria. Simulation results illustrate how with the developed control system, the positioning accuracy of industrial robots can be greatly improved.

REFERENCES

[1] M. Dulău, A. Gligor, and T.-M. Dulău, "Fractional Order Controllers Versus Integer Order Controllers", Procedia Engineering, vol. 181, pp. 538-545, 2017.

[2] S. Ladaci, and A. Charef, On Fractional Adaptive Control, Nonlinear Dynamics, vol. 43, no. 4, pp. 365-378, 2006.

[3] P. Shah, and S. Agashe, "Review of fractional PID controller", Mechatronics, vol. 38, pp. 29-41, September 2016.

[4] M. Silas, and S. Bhusnur, "A survey on fractional order PID controller", Res. J. Engineering Sci., vol 6, no. 7, pp. 39-43, August 2017.

[5] I. Podlubny, "Fractional-order systems and $PI^{\lambda}D^{\mu}$-controllers", IEEE Transaction on Automatic Control, vol. 44, no. 1, pp. 208–214, 1999.

[6] A. Pal Singh , T. Srivastava , H. Agrawal and P. Srivastava, "Fractional Order Controller Design and Analysis for Crane System", Progress in Fractional Differentiation and Applications, vol.3, no. 2, pp. 155-162, 2017.

[7] A. Pal Singh, H. Agarwal, P.Srivastava, "Fractional Order Controller Design for Inverted Pendulum on a Cart System (POAC)", WSEAS Transactions on Systems and Control, vol. 10, pp. 172-178, 2015.

[8] P. Ostalczyk, and M. Stolarski, "Fractional-Order PID Controllers in a Mobile Robot Control", IFAC Proceedings Volumes, vol. 42, no. 13, pp. 268-271, 2009.

[9] A. J. Muñoz-Vázquez, F. Gaxiola, F. Martínez-Reyes, and A. Manzo-Martínez, "A fuzzy fractional-order control of robotic manipulators with PID error manifolds", Applied Soft Computing, Volume 83, 105646, October 2019.

[10] L. Bruzzone, V. Belotti, and P. Fanghella, "Implementation of a Fractional-Order Control for Robotic Applications". In Advances in Service and Industrial Robotics, C. Ferraresi, and G. Quaglia, Eds. RAAD 2017. Mechanisms and Machine Science, vol. 49, Springer, 2018.

[11] I. Clitan, V. Muresan, M. Abrudean, A. Clitan and R. Miron, "Position control of an industrial robot using fractional order controller", International Conference on Robotics and Machine Vision, A. V. Bernstein, A. Olaru, J. Zhou, Eds, Proc. of SPIE, vol. 10253, 2016.

[12] V. Mureşan, and M. Abrudean, "Control System Optimization of Rotary Hearth Furnace Charging/Discharging", Proc. 5th Int. Symp. on Applied Computational Intelligence and Informatics, pp. 277-282, 2009.

[13] Y. Tang, H. Liu, Wang and X. Guan "Parameter identification of fractional order systems using block pulse functions". Signal Processing, 107, 272–281. 2015.

[14] B. Bourouba. and S. Ladaci and A. Chaabi "Reduced order model approximation of fractional order systems using differential evolution algorithm". J. Control Autom. Electr. Syst,Vol. 29, 32–43. 2018.

[15] K. Rabah, S. Ladaci, and M. Lashab, "State feedback with fractional $PI^{\lambda}D^{\mu}$ control structure for genesio-tesi chaos stabilization," in Proc. 16th IEEE Int. Conf. on Sciences and Techniques of Automatic control & computer engineering- STA'2015, Monastir, Tunisia, December 21-23, 2015, IEEE, pp. 328-333. 2015.

[16] Y. Liu, N. Xi, and Y. Shen, "High-accuracy positioning of an industrial robot using image/psd-based hybrid servo control", International Journal of Optomechatronics, vol. 5, pp. 170–187, 2011.

[17] K. Rabah, S. Ladaci, and M. Lashab, "Bifurcation-based fractional-order $PI^{\lambda}D^{\mu}$ controller design approach for nonlinear chaotic systems", Frontiers of Information Technology & Electronic Engineering, vol. 19, no. 2, pp. 180–191, 2018.

[18] H.S. Li, and Y.Q. Chen, "A fractional order proportional and derivative (FOPD) controller tuning algorithm", 2008 Chinese Control and Decision Conference, Yantai, Shandong, China, 2-4 July 2008.

[19] Y. Bensafia, S. Ladaci, K. Khettab, and A. Chemori, "Fractional Order Model Reference Adaptive Control for SCARA Robot Trajectory Tracking". International Journal of Industrial and Systems Engineering, vol. 30, no. 2, pp.138-156 September 2018.

Robot arm control using a single neuron trained by the BAT algorithm

LADJOUZI Samir
Department of Electrical Engineering
University of Bouira
Bouira, Algeria
ladjouzi_samir2001@yahoo.fr

GROUNI Said
Department of Industrial Maintenance
University of Boumerdes
Boumerdes, Algeria
said.grouni@yahoo.com

SOUFI Youcef
Department of Electrical Engineering
University of Tébessa
Tébessa, Algeria
y_soufi@yahoo.fr

KIRAT Abderrahmen
Department of Industrial Maintenance
University of Boumerdes
Boumerdes, Algeria
kiratauto@gmail.com

***Abstract*— Proportional-integral-derivative (PID) controllers have now been widely used in industrial control systems for their high reliability and usability. The major task in PID control theory is how to find optimal values of the parameters Kp, Ki and Kd. In this paper, a novel approach to determine the optimal values of a PID controller is presented. The proposed method is based on using a Single Neuron (SN) which its weights represent the PID parameters. To update these weights we use the BAT optimization algorithm. Our approach is tested on robot arm position control and a comparison is made with the classic tuning PID method Ziegler-Nichols.**

Keywords*— PID controller, Single Neuron , BAT algorithm, robot arm, Ziegler-Nichols.

I. INTRODUCTION

Industrial and commercial systems have been taking advantage of robot technology in recent years. Over the past few years, a wide range of control research and numerous control applications have been presented. One of the areas of interest in industrial, educational and medical applications is robotic manipulator.

It is very important to design and evaluate robot manipulators and to apply control techniques before using them to work with high accuracy in these circumstances [1]. Several industrial robot manipulators are controlled by linear methods (e.g. Proportional-Derivative (PD) controller, Proportional- Integral (PI) controller or Proportional- Integral-Derivative (PID) controller)

In the field of control technology, the use of PID control has been a long history, typically the three controller gain parameters, proportional gain KP, integral gain KI, and derivative gain KD are usually tuned by several methods [2].

Many articles have been proposed solutions to this problem, like the famous Ziegler-Nichols tuning method [3]. In [4], the pole placement technique was used to adjust PID parameters and a combination of pattern recognition with expert systems was applied in [5] on an industrial PID controller. Recently with the apparition of evolutionary, bio-inspired and intelligent algorithms researches on PID tuning become improved. Among papers talking about introducing these algorithms in PID parameters adapting, we can cite: Particle Swarm Optimization algorithm [6, 7], Genetic Algorithm [8, 9], Fuzzy logic [10], BAT algorithm [11] and others. Artificial Neural Networks have also been used for the PID tuning with the advantage of reduction the method complexity to find optimal parameters of the PID by using a single neuron [12-15]. In this paper we propose to apply a Single Neuron (SN) to adapt parameters of the PID to control the robot arm. The weights of this neuron are adapted with the BAT algorithm.

This paper is arranged as follows: Section 2 describes the system. The neuron model used in this work is depicted in section 3 describes. In section 4, we give an overview about the BAT algorithm. Simulations, results are given in section 5. Finally, we finish with conclusion in Section 6.

II. ROBOT JOINT SYSTEM

Degrees of freedom generally describe the robot arms. Usually this number indicates the number of single-axis rotational joints in the arm. In our work we use a single joint robot arm which is given in Fig.1.

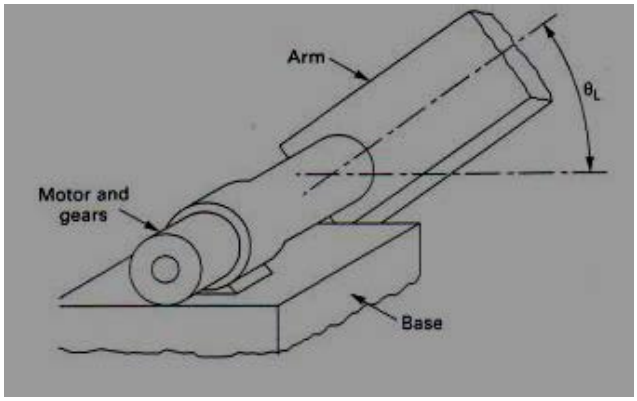

Fig.1- Schematic representation of a single joint robot arm

The following formula gives the dynamic behavior of the robot arm control system [16]:

$$e_a(t) = R_m i_a(t) + L_m \frac{di_a(t)}{dt} + e_m(t) \quad (1)$$

$$e_m(t) = K_m \frac{d\theta_m(t)}{dt} \quad (2)$$

$$T_m = J \frac{d^2\theta_m(t)}{dt^2} + B \frac{d\theta_m(t)}{dt} \quad (3)$$

$$J = J_m + n^2 J_m l \quad (4)$$

$$B = B_m + n^2 B_m l \quad (5)$$

$$\theta_L = n\theta_m \quad (6)$$

After simplifications, we will get the transfer function as below:

$$\frac{\theta_L(s)}{E_a(s)} = \frac{K_T}{JL_m s^3 + (R_m J + BL_m)s^2 + (K_T K_m + R_m B)s} \quad (7)$$

Where.
R_m : armature- winding resistance in ohm.
L_m : armature – winding inductance in Henry.
I_a : armature – winding current in ampere.
E_a :armature voltage in volt .
e_m :back emf voltage in volt.
K_m :back emf constant in volt / (rad/sec)
T_m :torque developed by the motor in N.m
K_T :motor torque constant in N.m/A
J : moment of inertia of motor and robot arm in kg. 2 m /rad.
B : viscous – friction coefficient of motor and robot arm in N.m/rad /sec.
θ_m :angular displacement of the motor shaft in rad.
θ_L :angular displacement of the robot arm in rad.
N : gear ratio

For our work we get the following parameters:
R_m =21 Ω , L_m =2 H , K_T =38 N.m/A , J = 2 kg.m^2 /rad
B = 1 N.m/rad/sec , K_m =0.5V/(rad/sec) and n =0.05
Thus the transfer function becomes:

$$G(s) = \frac{\theta_L(s)}{E_a(s)} = \frac{38}{4s^3 + 44s^2 + 40s} \quad (8)$$

III. THE NEURON MODEL

We begin in this section by describing the neuron model used in this work. The neuron used in this study is composed of a simple neuron which receives external inputs as depicted in Fig.2.

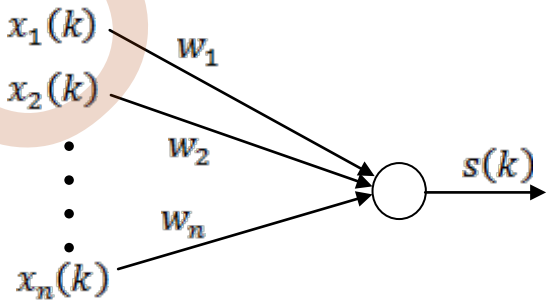

Fig.2- The neuron model

We use the following notations relative to our work:
x_i(k) : the ith input of the neuron. ($1 \le i \le n$)
s(k) : the output of the neuron.
w_i(k) : the weight of the connection from the ith input x_i(k) to the input of the neuron.
f : the activation function of the neuron.
n: number of the inputs to the neuron.
The output of the neuron is given by this equation:

$$s(k) = f\left(\sum_{i=1}^{n} w_i(k) x_i(k)\right) \quad (9)$$

The PID controller is by far the most common control algorithm. Most feedback loops are controlled by this algorithm or minor variations of it. Many thousands of

instrument and control engineers worldwide are using such controllers in their daily work [17].

The classic PID feedback control structure is shown in Fig. 3.

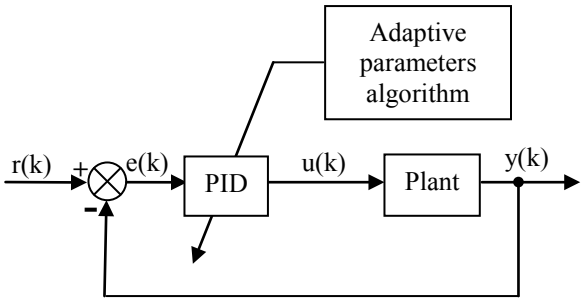

Fig.3- Structure of an adaptive PID controller

The objective is to find an optimal control signal so we minimize the following objective function:

$$E = \frac{1}{2}\sum_{k=1}^{T} e(k)^2 = \frac{1}{2}\sum_{k=1}^{T}\big(r(k) - y(k)\big)^2 \qquad (10)$$

T is the total number of epochs.

The continuous analog PID controller using the Laplace transform is given by:

$$U(s) = \left[K_p + \frac{K_I}{s} + K_d s\right] E(s) \qquad (11)$$

Using the approximation: $s \approx 1\text{-}z^{-1}$, we obtain the form of the PID controller using the z transform as:

$$U(z) = \left[K_p + \frac{K_I}{1-z^{-1}} + K_d(1 - z^{-1})\right] E(z) \qquad (12)$$

After a short modification:

$$(1 - z^{-1})U(z) = \left[K_p(1 - z^{-1}) + K_I + K_d(1 - z^{-1})^2\right]E(z) \qquad (13)$$

By applying the inverse z transform to this equation, the discrete time PID algorithm can be written as follows:

$$\Delta u(k) = K_p \Delta e(k) + K_I e(k) + K_d \Delta^2 e(k) \qquad (14)$$

Where:

$$\Delta u(k) = u(k) - u(k-1) \qquad (15)$$

We can write:

$$\Delta^2 e(k) = \Delta\big(\Delta e(k)\big) = \Delta\big(e(k) - e(k-1)\big) = \big(e(k) - e(k-1)\big) - \big(e(k-1) - e(k-2)\big) = e(k) - 2e(k-1) + e(k-2) \qquad (16)$$

Finally, equation (14) becomes:

$$\Delta u(k) = K_p[e(k) - e(k-1)] + K_I e(k) + K_d[e(k) - 2e(k-1) + e(k-2)] \qquad (17)$$

In our work, we use the single neuron as an incremental controller to compute the increment term Δu(k).

The neuron has three inputs:

$$\begin{cases} x_1(k) = e(k) \\ x_2(k) = \Delta e(k) = e(k) - e(k-1) \\ x_3(k) = e(k) - 2e(k-1) + e(k-2) \end{cases} \qquad (18)$$

And the output of the neuron will represent the increment of the control signal. It is given by:

$$s(k) = \Delta u(k) = f\big(inp(k)\big) \qquad (19)$$

The variable *inp* is the input of the neuron given by the following summation:

$$inp(k) = w_1(k)x_1(k) + w_2(k)x_2(k) + w_3(k)x_3(k) \qquad (20)$$

The control signal applied to the system is given by:

$$u(k) = u(k-1) + \Delta u(k) \qquad (21)$$

The structure of the single neuron controller is given in Fig.4.

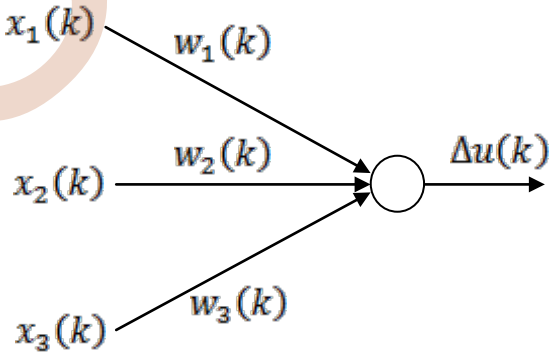

Fig. 4- Design of the single neuron controller

The different weights $w_i(k)$ (i = 1, 2, 3) represent the parameters K_I, K_p and K_d respectively.

The frame form of the PID controller using the single neuron is depicted in Fig.5.

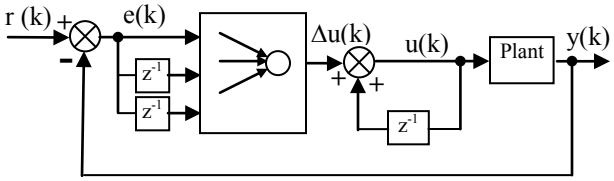

Fig. 5- Block diagram of the single neuron PID controller

IV. THE BAT ALGORITHM

Bat algorithm was developed by Xin-She Yang in 2010 as a metaheuristic optimization algorithm. This new technique is based on micro-bats echolocation with varying emission and loudness pulse levels.

Bats use sonar echoes to identify and avoid obstacles: they determine the size of an object, how far away it is, how fast it is moving, and even its shape, all separated in a second. Bats turn their own pulse into useful information after reaching and reflecting to gage how far the target is [18].

Yang used three abstract rules to translate these bats ' actions into algorithms:

1- To sense space, all bats use echolocation, and they also conveniently guess the difference between food / prey and ambient barriers.

2- Bats travel spontaneously at velocity v_i at location x_i with a set frequency f_{min}, varying wavelength λ and loudness A_0 to search for prey. They can change the wavelength of their emitted pulses automatically and adjust the pulse emission frequency r from [0, 1], depending on their target's proximity.

3- While the loudness can differ in many ways, we presume that the loudness ranges from a large positive value A_0 to a constant minimum value A_{min}.

The initial position x_i for each bat, including velocity v_i and frequency f_i, is initialized. Using the following equations, the movement of virtual bats is given for each time step t by updating their velocity and position.

$$f_i = f_{min} + \rho\left(f_{max} - f_{min}\right) \quad (22)$$

$$v_i^j(t) = v_i^j(t-1) + \left[x_{gbest}^i - x_i^j(t-1)\right] f_i \quad (23)$$

$$x_i^j(t) = x_i^j(t-1) + v_i^j(t) \quad (24)$$

Where:

ρ∈ [0,1] refers to the random number provided

x^j_{gbest} refers to the current best global solutions

For the local search part, once a solution is selected among the current best solutions, a new solution for each bat is generated locally using random walk:

$$x_i^{new} = x_i^{old} + \sigma A_{mean}^{old} \quad (25)$$

With :

σ ∈ [0,1] is a random number and represents direction and intensity of random-walk.

A_{mean}^{old} is the average loudness of all the bats.

The BAT algorithm procedure can be resumed in different steps in Fig.6.

Objective function $f(x)$, $x= (x_1, x_2, \ldots, x_d)^T$
Initialize the Bat population x_i and v_i for i=1, 2, ….,n
Define pulse frequency $Q_i \in [Q_{min}, Q_{max}]$
Initialize pulse rates r_i and the loudness A_i
while ($t < T_{max}$) // number of iterations
Generate new solutions by adjusting frequency, and updating velocities and locations/solutions
if (rand (0,1) > r_i)
Select a solution among the best solutions
Generate a local solution around the best solution
end if
Generate a new solution by flying randomly
If (rand (0,1) < A_i and $f(x_i) < f(x)$)
Accept the new solutions
Increase r_i and reduce A_i
end if
Rank the bats and find the current best
end while
Post process results and visualization

Fig. 6- The BAT algorithm procedure

For our case the BAT algorithm is used to find optimum values of the three weights w_1, w_2 and w_3.
The schematic diagram of the neuron PID controller trained by the BAT algorithm is given in Fig. 7.

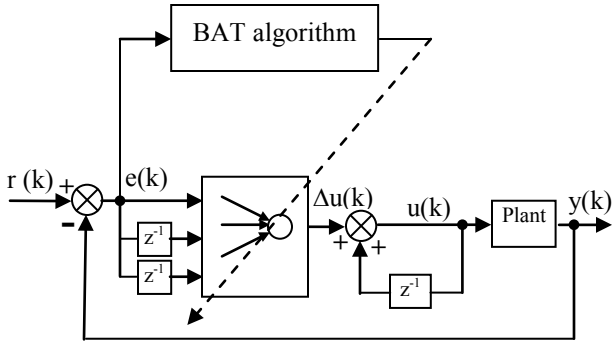

Fig. 7- Neuron PID controller trained by BAT algorithm

V. SIMULATION AND RESULTS

For simulation, we take the following sigmoid bipolar transfer function for the neuron:

$$f(x) = \frac{1-e^{-x}}{1+e^{x}} \qquad (26)$$

For the BAT algorithm parameters, we use the following values:

Table I. Parameters of the BAT algorithm

Parameter	Value
Population size (n)	20
Number of generations (ng)	100
Range of the weight w_1 (K_i)	[0 20]
Range of the weight w_2 (K_p)	[0 0.1]
Range of the weight w_3 (K_d)	[0 10]
Minimum frequency (f_{min})	0
Maximum frequency (f_{max})	2
Loudness (A)	0.5
Pulse rate (r)	0.5

Each individual in the BAT population is formed of three parameters: K_I, K_p and K_d representing, respectively, the neuron weights w_1, w_2 and w_3.
We use the following notation:
ZN-PID: the Ziegler Nichols based PID controller.
BAT-SN-PID: the BAT algorithm Single Neuron based PID controller.

Table II shows the optimal values obtained with the different methods ZN-PID and BAT-SN-PID with the parameters performance.

Table II. Parameters results

Parameter	ZN-PID	BAT-SN-PID
K_p	6.94	3.7943
K_i	6.94	0.0721
K_d	1.73	7.6929

Fig. 8 shows the obtained system responses using the ZN-PID and the BAT-SN--PID methods for a unit step reference.

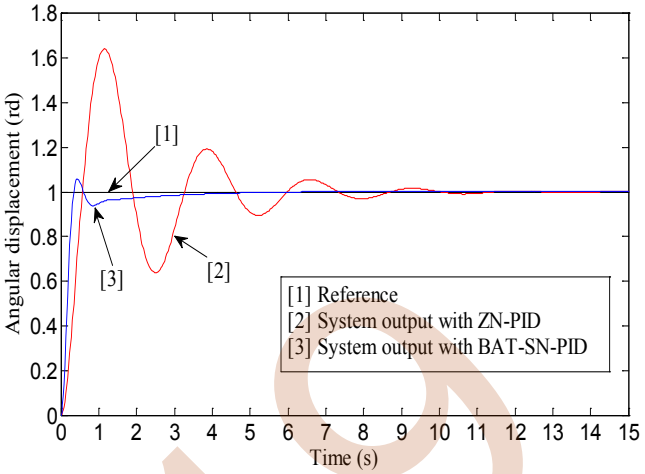

Fig. 8. Set point responses using the ZN-PID and the BAT-SN-PID with a constant reference

From the simulation results showed in Fig. 8 we can see that:
- There is an important overshoot with the ZN-PID method but with the BAT-SN -PID the overshoot is reduced considerably.
- The response to the set point is faster using the BAT-SN-PID than the ZN-PID.

For evaluate the diverse performances of the two methods, we use the following main parameters using in analyzing the performance of a PID controller:

Rise time : time required for a signal to reach from 10% to 90% of the final value.
Overshoot : normalized difference between the time response peak and steady output.
Settling time : time required for the response to reach and stay within the specified range of its final value.
Peak time : time at which the peak value occurs.

Table III shows the parameters performance obtained with the different methods ZN-PID and BAT-SN -PID.

Table III. Parameters performance

Parameter	ZN-PID	BAT-SN-PID
Settling time (s)	8.4029	2.4723
Rise time (s)	0.4011	0.3036
Overshoot (%)	62.9828	2.5891
Peak time (s)	1.2125	0.4021

As point out from the table III all the parameters: settling time, rise time, overshoot and peak time are reduced with the BAT-SN-PID controller in comparison to the ZN-PID.

In the second part of the simulation, we take a variable reference and the obtained results are shown in Fig.9.

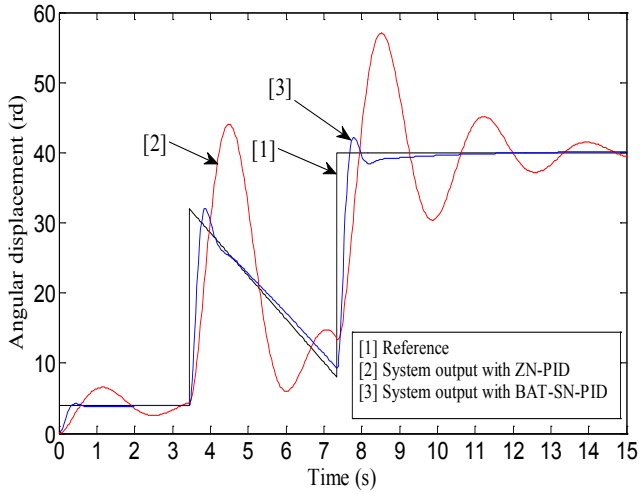

Fig. 9. Set point responses using the ZN-PID and the BAT-SN-PID with a variable reference

In the case of a variable reference, the controller BAT-SN-PID gives a good tracking of the reference, while we can see that the ZN-PID controller cannot follow the variable trajectory

VI. CONCLUSION

PID controller is the most and practical controller used in many applications to achieve a desired response. The difficulty in a PID controller is to find optimum values for the three parameters (K_p, K_i and K_d).

In this paper, we propose a method for the PID control based on a Single Neuron (SN). The SN weights (PID gains) were tuned using the metaheuristic BAT algorithm. Our technique was tested to control a robot arm and the obtained results are very suitable.

The results show clearly the efficiency of our approach and it was hopeful to apply this method on other industrial applications.

REFERENCES

[1] S. Al-Marzoqi and A. E. Mansour, " Comparative study of different control techniques applied on 6 dof robot arm," Journal of Al Azhar University Engineering Sector, 12(42), 2017, 25-36.

[2] A. C. Emmanuel and H. Inyiama, "A Survey of Controller Design Methods for a Robot Mainpulator in Harsh Environments," European Journal of Engineering and Technology, 3, 2015, 64-73.

[3] Ziegler J G, Nichols N B. Optimum settings for automatic controllers. Trans ASME 1942; 64 :759–68.

[4] Åström K J, WESTERBERG B, Wittenmark B. , "Self-tuning PID Controllers Based on Pole Placement," Department of Automatic Control, Lund Institute Technical Report, TFRT-7179 1979.

[5] Da Silva M A , Gomide F A C, Amaral W C. , " A rule based procedure for self tuning PID controllers,"Proc 27th Conf on Decision and Control 1988; 1947-51.

[6] Solihin M I, Tack L F, Kean M L. , "Tuning of PID controller using particle swarm optimization (PSO) ," Proc Int Conf on Advanced Science, Engineering and Information Technology 2011; 458-61.

[7] Nayak A, Singh M. , "Study Of Tunning Of PID Controller by Using Particle Swam Optimization," Int J Of Advanced Research And Studies 2015; 346-50.

[8] Ayman A A. , "PID Parameters Optimization Using Genetic Algorithm Technique for Electrohydraulic Servo Control System," Intelligent Control and Automation 2011; 2: 69-76.

[9] Patel M V, Pathak R M. , "PID Tuning Using Genetic Algorithm For DC Motor Positional Control System,"Int J of Innovations in Engineering and Technology 2015 ; 6 : 141-47.

[10] Li M, Wang L, Liu J, Ye J. , "Method study on fuzzy-PID adaptive control of electric-hydraulic hitch system," Conf. Proc Advances in Materials, Machinery, Electronics 2017.

[11] Fister D, Šafarič R, Fister I Jr. , "Parameter tuning of PI-controller with bat algorithm," Informatica 2016; 40(1):109–16.

[12] Sheng Q, Xianyi Z, Changhong W, Gao X Z, Zilong L. , " Design and Implementation of An Adaptive PID Controller Using Single Neuron Learning Algorithm," Proc 4th World On Intelligent Control and Automation, 2002; 2279-83.

[13] Minzhi J, Chao G, Xiaomin S. , "Study on the application of the single neuron adaptive PID controller in prestressed tension device," Proc IEEE 10th Int Conf on Electronic Measurement & Instruments 2011; 4:16-19.

[14] Zuo S, Song Y, Wang L, Zhou Z. , "Neuron-adaptive PID based speed control of SCSG wind turbine system," Abst Appl Analysis 2014.

[15] Hang L, Yu L, Quan S, Huang L, Chen Q, Xiong Y, Quan J. , " Design of voltage loop for three-phase PWM rectifier based on single neuron adaptive PID control," 32nd Youth Academic Annual Conference of Chinese Association of Automation 2016; 171-75.

[16] M.D. Youns S.M. Attya and A.I. Abdulla , "Position Control of Robot Arm Using Genetic Algorithm Based PID Controller," *Al-Rafidain Engineering*, 21 (6), 2013,19-30.

[17] Åström K J, Hägglund T. , "PID Controllers: Theory, Design, and Tuning," Instrument Society of America; 1995.

[18] N. Talbi,'' Bat Algorithm Optimization for Fuzzy Rule Base Design of a Fuzzy Controller,'' International Conference on Automation & Signal Processing, 35, 2018, 95-100.

Stabilizing Controller Design for Discrete-Time Takagi-Sugeno Descriptor Models with Actuator Saturation

Ines Righi
Faculty of Sciences and Technologies
Univ. Souk Ahras-LEER- BP 1553
Souk-Ahras, 41000. Algeria
e-mail: i.righi@univ-soukahras.dz

Sabrina Aouaouda and Khelil Khaled
Faculty of Sciences and Technologies
Univ.Souk Ahras-LEER-BP 1553
Souk-Ahras,41000. Algeria
e-mail:sabrina.aouaouda @univ-soukahras.dz
khaled.khelil @univ-soukahras.dz

***Abstract*— this paper treats the stabilization analysis for a class of nonlinear descriptor systems subject to input saturation and unknown disturbance. The synthesized control strategy is based on the Takagi-Sugeno design approach and a non-parallel distributed compensation (non-PDC) control law. Stabilization conditions are derived using non-quadratic Lyapunov functions to ensure the closed-loop system stability despite the given saturation constraint on the control input. The optimization problem is formulated in terms of linear matrix inequalities (LMIs). The technique is illustrated through numerical examples.**

Keywords—Takagi-Sugeno descriptor models; Actuator saturation; Stability; non-PDC; Linear matrix inequalities (LMIs).

I. INTRODUCTION

Recently, Takagi-Sugeno (T-S) models have been widely investigated to study nonlinear models [1]. Among nonlinear control theory, the T-S model-based approach has attracted great interest since it constitutes universal approximation of any smooth nonlinear function by a "blending" of some local linear system models. This method greatly facilitates observer/controller synthesis for complex nonlinear systems [2]. Based on this modeling technique, stability conditions have been obtained directly from Lyapunov methodology [3, 4]. For control design, the so-called parallel distributed compensation (PDC) has been the most commonly used scheme and remain to associate inferred state of output feedback to each local subsystem. Stabilization of T-S systems and the control design are investigated via the direct Lyapunov method. In fact, various works deal with stability analysis using either quadratic Lyapunov functions [1] where common matrices to each subsystem have to be found, piecewise Lypunov functions [3], more recently non quadratic Lyapunov functions [4, 5]. The derived conditions are formulated into a set of linear matrix inequalities (LMIs). These LMIs can be solved, when a solution exists, by classical convex optimization algorithms [2, 4-6]. In practice, many systems are physically described by nonlinear descriptor models [6]. The T-S descriptor model representation has the advantage to decrease the number of LMI constraints since it conserves nonlinearities in the left-hand side will keeping the original structure of the nonlinear model [7, 11-15].

Usually real physical applications suffer from actuator saturation and/or sensor saturation. Thus, a great attention has been given to the control design of T-S models with input saturation constraints [8-9]. Among the most popular works dealing with saturated input constraints, the convexity based approach to the saturation function (see [9-10] and the references therein). The interest of this approach is to consider a bounded ellipsoidal symmetric region of stability solved by a set of LMIs. Moreover, descriptor design approaches has been recently studied in [11] to deal with problem of input saturated T-S systems using a polytopic representation of the saturation function. The T-S descriptor fuzzy system is affected by unknown exogenous disturbances ω_k ,the main contribution of the new method can be summarized as the proposed result, can be applied to T-S systems subject to H_2 approach. In the present paper, stability analysis for discrete-time T-S descriptor system subject to input saturation is proposed. New LMIs conditions are derived based on two Lyapunov functions with the Finsler's lemma [12] which allows decoupling the control law from the Lyapunov function.

This paper is organized as follows: Section 2 provides some useful notation and properties, it also introduces the discrete-time T-S descriptor model; Section 3 presents the main results for controller design of saturated discrete-time T-S descriptor models subject to disturbances; Finally in section 4 two examples are given to demonstrate the effectiveness of the proposed approaches.

II. NOTATION AND PROBLEM STATEMENT

Given a set of nonlinear functions $h_i(.) \geq 0, i \in \{1...r\}$, $v_k(.) \geq 0, k \in \{1...r_e\}$ having the convex sum property , $\sum_{i=1}^{r} h_i(.) = 1$, $\sum_{i=1}^{r_e} v_k(.) = 1$,a shorthand notation will be used in the sequel to represent convex sum of matrix expressions: $Y_h = \sum_{i=1}^{r} h_i(z(k))Y_i$ and $Y_v = \sum_{i=1}^{r} v_k(z(k))Y_k$ for single convex sum; $Y_{h+} = \sum_{i=1}^{r} h_i(z(k+1))Y_i$ for a delayed convex sum ; $Y_{h-} = \left(\sum_{i=1}^{r} h_i(z(k))Y_i \right)^{-1}$ for the inverse of a convex sum. $M(A)$ the Hermitiann of the

matrix A ,i.e $M(A) = A + A^T$ for a vector x, x_k denotes its *k-th* entry, and x_{k+} denotes $x(k+1)$. N_r denotes the set {1…r},*I* denotes the identity matrix.(*) stands for the terms deduced by symmetry in symmetric block matrices.

Let us consider the following discrete-time TS fuzzy model in the descriptor form subject to input saturation and external disturbances:

$$E_v x_{k+} = A_h x_k + B_h sat(u_k) + B_\omega \omega_k \quad (1)$$

Where $x_k \in \Re^n$ is the state vector, $u_k \in \Re^m$ is the control input vector, k is the sample. Matrices A_i and $B_i, i \in N_r$ represent the *i-th* linear right-hande side model and $E_v, k \in \{1...r_e\}$, represents the *k-th* linear left-hand side model of T-S descriptor models. The membership functions $h_i(z(k))$ and $v_k(z(k))$ satisfy the convex sum property and depend on the known premise variables. The MFs depend on the premise variables grouped in the vector $z(k)$ which is known and usually depends on the state vector. The dead zone nonlinearity $\psi(.) : \Re^{nu} \to \Re^{nu}$ is defined by:

$$\psi(u_k) = u_k - sat(u_k) \quad (2)$$

However the saturation function $sat : \Re^{nu} \to \Re^{nu}$ is defined as:

$$\begin{cases} sat(u_k) = [sat_1(u_{tk}).....sat_t(u_{tk}).....sat_{nu}(u_{nk})] \\ sat_t(u_{tk}) = sign(u_{tk}) \min(|u_{tk}|, u_t^{\max}) \end{cases} \quad (3)$$

With $u_t^{\max} \geq 0$ designate the saturation level.

Relaxation Lemma [14]: Let T_{ij}^k be matrices of appropriate dimensions, then for $i, j \in \{1...r\}, k \in \{1...r_e\}$:

$$T_{ij}^k < 0$$

$$\frac{2}{r-1} T_{ii}^k + T_{ij}^k + T_{ji}^k < 0, i \neq j \quad (4)$$

Finsler's Lemma [16]. Let $x_k \in \Re^n, \theta = \theta^T \in \Re^n$ and $R \in \Re^{mxn}$ such that $Rank(R) < n$; the following expression are equivalent:

$$a) x_k^T \theta x_k < 0; \forall \{x_k \in \Re^n; x_k \neq 0; Rx_k = 0\}$$

$$b) \exists \aleph \in \Re^{mxn} : \theta + \aleph R + R^T \aleph^T < 0$$

Congruence Lemma: Let Π a positive definite matrix, symmetric of the appropriate dimension, Y is a nonsingular matrix compatible with Π then, the product $Y^T \Pi Y > 0$ is called the congruence transformation of Π .

Property 1. Let X and Y matrices of the appropriate size, the following expressions holds:

$$(Y - X)^T X^{-1} (Y - X) \geq 0 \Leftrightarrow Y^T X^{-1} Y \geq Y + Y^T - X$$

Saturation Lemma [16]: Given matrices $F_{jk} \in \Re^{mxn}$, $H_{jk} \in \Re^{nxn}$ and $W_{jk} \in \Re^{mxn}$, for $i, j, k \in N_r, t \in N_m$, let us define the following set:

$$P_u = \left\{ x_k \in \Re^n : \left| \left(G_{jk} \Im_{jk}^{-1} - W_{jk} \Im_{jk}^{-1} \right) x_k \right| \leq u_{\max(t)} \right\}$$

If $x_k \in P_u$ then $\psi(u_k)^T S_{jk}^{-T} \left[\psi(u_k) - (W_{jk} \Im_{jk}^{-1}) x_k \right] \leq 0$

holds of any positive diagonal matrices $S_{jk} \in \Re^{mxn}$ and for any scalar function $\Im_{ij}, i, j \in N_r$, satisfying the convex sum property.

Assumption 1. The validity domain Ω_x of the system (1) is defined by: $\Omega_x = \{x_k \in \Re^n; Q_m x_k \leq 1, m \in N_q\}$ (6)

Where the vectors $Q_m \in \Re^{mxn}$ are corresponding to the state constraints of system (1).

Assumption 2. The disturbance signal ω_k belongs to the following class of function:

$$\omega_\delta^2 = \left\{ \omega_k : \Re^+ \to \Re^{nu}, \sum_{i=1}^{\infty} \omega_k^T \omega_k \leq 0 \right\} \quad (7)$$

In order to mitigate the effect of ω_k on the state space x_k we will use the H_2 -approach. We want to guarantee:

$$\|x_k\|_2 \leq \gamma \|\omega_k\|_2, \gamma > 0, \omega_k \neq 0 \quad (8)$$

III. MAINS RESULTS

In this section, the objective is to design a non-PDC control law ensuring the desired control performance and guarantying the stability of the closed loop perturbed system, despite the presence of input control saturation. Accordingly, the proposed non-PDC controller law is designed as follows:

$$u_k = F_{hv} H_{(.)}^{-1} x_k \quad (9)$$

The combination of the T-S descriptor model (1) with the control law (9) yields:

$$E_v x_{k+} = A_h x_k + B_h (F_{hv} H_{(.)}^{-1} x_k - \psi(u_k)) + B_\omega \omega_k \quad (10)$$

Expression (8) can be rewritten as an equality constraint:

$$\begin{bmatrix} A_h + B_h F_{hv} H_{(.)}^{-1} & -E_v & -B_h & B_\omega \end{bmatrix} \begin{bmatrix} x_k \\ x_{k+} \\ \psi(u_k) \\ \omega_k \end{bmatrix} = 0 \tag{11}$$

In the following, two different Lyapunov functions will be considered:

$$V(x_k) = x_k^T P_h^{-1} x_k \quad \text{with } P_h = P_h^T > 0, P_h^{-1} = X_h .$$

$$V(x_k) = x_k^T H_h^{-T} P_h H_h^{-1} x_k \quad \text{with } P_h = P_h^T > 0 .$$

A. Case 1

The H_2 gain denoted γ of the transfer ω_k to x_k is bounded, and defined in equation (8). By considering the saturation lemma and H_2 norm, the dynamic of considered system is given by:

$$x_{k+}^T P_{h+}^{-1} x_{k+} - x_k^T P_h^{-1} x_k - 2\psi(u_k)^T S_{hv}^{-1} \psi(u_k) + \psi(u_k) S_{hv}^{-1} W_{hv} H_{hv}^{-1} x_k + x_k^T x_k - \gamma \omega_k^T \omega_k < 0 \tag{12}$$

The inequality (12) written as:

$$\begin{bmatrix} x_k \\ x_{k+} \\ \psi(u_k) \\ \omega_k \end{bmatrix}^T \begin{bmatrix} -(X_h - I) & 0 & 0 & 0 \\ 0 & X_{h+} & 0 & 0 \\ S_{hv}^{-1} W_{hv} H_{hv}^{-1} & 0 & -2S_{hv}^{-1} & 0 \\ 0 & 0 & 0 & -\gamma I \end{bmatrix} \begin{bmatrix} x_k \\ x_{k+} \\ \psi(u_k) \\ \omega_k \end{bmatrix} < 0 \tag{13}$$

Via the Finsler's Lemma, equality (11) and inequality (13) results in:

$$\begin{bmatrix} -(X_h - I) & 0 & 0 & 0 \\ 0 & X_{h+} & 0 & 0 \\ W_{hv} & -B_h^T N^T & -2S_{hv}^T & 0 \\ 0 & B_\omega^T & 0 & -\gamma I \end{bmatrix} + \begin{bmatrix} M \\ N \\ 0 \\ 0 \end{bmatrix} \begin{bmatrix} A_h + B_h F_{hv} H_{(.)}^{-1} & -E_v & -B_h & B_\omega \end{bmatrix} + (*) < 0 \tag{14}$$

Where matrices $M \in \Re^{nxn}$ and $N \in \Re^{nxn}$ are free matrices fixed later on. Let us select $H_{(.)} = H_{hv}$ .Now, the results can be obtained depending and is stated in the following Lemma.

Lemma 3. The closed-loop T-S descriptor model (1) is asymptotically stable, if there exist matrices $P_j = P_j^T > 0, H_{jk} \in \Re^{nxn}, F_{jk}, W_{jk} \in \Re^{mxn}$ a matrix $Q_m \in \Re^{mxn}, m \in N_q$,a positive diagonal matrix $S_{jk} \in \Re^{mxm}$ for $i, j \in \{1 \ldots r\}, k \in \{1 \ldots r_e\}$, and positive scalar $\bar{\gamma} = \sqrt{\gamma}$ such as conditions 4 are satisfied with:

$$T_{ij}^k = \begin{bmatrix} \begin{pmatrix} -H_{jk}^T - H_{jk} + \\ P_j \end{pmatrix} & * & * & * & * \\ H_{jk} & -I & * & * & * \\ \begin{pmatrix} A_i H_{jk} + \\ B_i F_{jk} \end{pmatrix} & 0 & \begin{pmatrix} -M(E_k P_j) + \\ P_j \end{pmatrix} & * & * \\ W_{jk} & 0 & -S_{jk}^T B_i^T & -2S_{jk}^T & * \\ 0 & 0 & B_\omega^T & 0 & -\gamma I \end{bmatrix} < 0 \tag{15}$$

$$\begin{bmatrix} -P_j & * \\ Q_m P_j & -1 \end{bmatrix} \le 0, m \in N_q, j \in N_r \tag{16}$$

And,

$$\begin{bmatrix} \begin{pmatrix} -M(H_{jk}) + \\ P_j \end{pmatrix} & * \\ F_{jk(t)} - W_{jk(t)} & -(u_t^{\max})^2 \end{bmatrix} \le 0, m \in N_q, j \in N_r \tag{17}$$

Proof. From inequality (16) it can be deduced that $x_k \in \Omega_x$.

Furthermore, by Schur complement lemma [16] and matrix property 1, it can be deduced from (17) that :

$$H_{jk}^T P_j H_{jk} - \frac{(F_{jk(t)} - W_{jk(t)})^T (F_{jk(t)} - W_{jk(t)})}{(u_t^{\max})^2} \ge 0 \tag{18}$$

Pre and post-multiplying (18) with H_{jk}^{-T} yields:

$$P_j - \frac{(F_{jk(t)} H_{jk}^{-T} - W_{jk(t)} H_{jk}^{-T})^T (F_{jk(t)} H_{jk}^{-T} - W_{jk(t)} H_{jk}^{-T})}{(u_t^{\max})^2} \ge 0 \tag{19}$$

Then, it is easily observed that condition (19) implies the inclusion $\Omega_x \subseteq P_u$ .Now by using the congruence lemma property with the full rank matrix $diag(H_{hv}^T \quad P_{h+} \quad S_{hv}^T \quad I)$, (14) yields:

$$\begin{bmatrix} -H_{hv}^T(X_h - I)H_{hv} & 0 & 0 & 0 \\ 0 & P_{h+}X_{h+}P_{h+} & 0 & 0 \\ W_{hv} & -S_{hv}^T B_h^T & -2S_{hv}^T & 0 \\ 0 & B_\omega^T & 0 & -\gamma I \end{bmatrix} + \begin{bmatrix} H_{hv}^T M \\ P_{h+}N \\ 0 \\ 0 \end{bmatrix} \begin{bmatrix} A_h H_{hv} + B_h F_{hv} & -E_v P_{h+} & -B_h S_{hv} & B_\omega \end{bmatrix} + (*) < 0 \quad (20)$$

In order to derive an LMI optimization problem, a good choice is to consider $M = 0$ and $N = X_h$ then (20) yields if:

$$\begin{bmatrix} -H_{hv}^T(X_h - I)H_{hv} & * & * & * \\ A_h H_{hv} + B_h F_{hv} & -M(E_v P_h) + P_h & * & * \\ W_{hv} & -S_{hv}^T B_h^T & -2S_{hv}^T & * \\ 0 & B_\omega^T & 0 & -\gamma I \end{bmatrix} < 0 \quad (21)$$

Theorem 1. Given T-S descriptor system (1) whose validity domain is characterized by a matrix $Q_m, m \in N_q$. If there exist positive definite matrix P_j, a positive diagonal matrix S_{jk} and a matrices $H_{jk}, F_{jk}, W_{jk}; i, j, k \in N_r$ and positive scalar $\bar{\gamma} = \sqrt{\gamma}$,solutions of the optimization problem defined as (23) :

$$T_{ij}^k = \begin{bmatrix} \left(-M(H_{jk}) + P_j\right) & * & * & * & * & * \\ H_{jk} & -I & * & * & * & * \\ \begin{pmatrix} A_i H_{jk} + \\ B_i F_{jk} \end{pmatrix} & 0 & -M(E_k P_j) & * & * & * \\ 0 & 0 & 0 & -P_j & * & * \\ W_{jk} & 0 & -S_{jk}^T B_i^T & 0 & -2S_{jk}^T & * \\ 0 & 0 & B_\omega^T & 0 & 0 & -\gamma I \end{bmatrix} < 0 \quad (22)$$

$$\begin{cases} \min \gamma \\ LMI(4) \\ LMI(16) \\ LMI(17) \\ LMI(22) \end{cases} \quad (23)$$

Proof: The result of theorem 1 is derived from the proof of Lemma (3) by choosing $M = 0$ and $N = P_h^{-T}$ .Thus, this proof is omitted here for brevity.

B. Case 2

Consider $H_{(.)} = H_h$ in (9). Then the variation of the Lyapunov functions in case 2 by considering the saturation lemma and H_2 -norm yields:

$$\Delta V(x_k) - 2\psi(u_k)^T S_{hv}^{-1}\psi(u_k) + \psi(u_k)S_{hv}^{-1}W_{hv}H_h^{-1}x_k + x_k^T x_k - \gamma\omega_k^T\omega_k < 0 \quad (24)$$

With: $\Delta V(x_k) = x_{k+}^T H_h^{-T} P_{h+} H_h^{-1} x_{k+} - x_k^T H_h^{-T} P_h H_h^{-1} x_k$

Developping inequality (24) one can obtain :

$$\begin{bmatrix} x_k \\ x_{k+} \\ \psi(u_k) \\ \omega_k \end{bmatrix}^T \begin{bmatrix} \Gamma^{(1,1)} & 0 & 0 & 0 \\ 0 & \Gamma^{(2,2)} & 0 & 0 \\ \Gamma^{(3,1)} & 0 & -2S_{hv}^{-1} & 0 \\ 0 & 0 & 0 & -\gamma I \end{bmatrix} \begin{bmatrix} x_k \\ x_{k+} \\ \psi(u_k) \\ \omega_k \end{bmatrix} < 0 \quad (25)$$

$\Gamma^{(1,1)} = -H_h^{-T} P_h H_h^{-1} + I$, $\Gamma^{(2,2)} = H_h^{-T} P_{h+} H_h^{-1}$ and $\Gamma^{(3,3)} = S_{hv}^{-1} W_{hv} H_h^{-1}$.

The same proof is used as theorem 1 but using $diag\left(H_h^T \quad P_{h+} \quad S_{hv}^T \quad I\right)$ in congruence application, we conclude the following theorem:

Theorem 2. Given T-S descriptor system (1) whose validity domain is characterized by a matrix $Q_m, m \in N_q$. If there exist positive definite matrice $P_j = P_j^T > 0$, a positive diagonal matrices S_{jk} and a matrices $H_j, F_{jk}, W_{jk}; j, k \in N_r$, and positive scalar $\bar{\gamma} = \sqrt{\gamma}$ solutions of the optimization problem defined as (28):

$$T_{ij}^k = \begin{bmatrix} -P_j & * & * & * & * \\ H_j & -I & * & * & * \\ \begin{pmatrix} A_i H_j \\ + B_i F_{jk} \end{pmatrix} & 0 & \begin{pmatrix} -M(E_k P_j) \\ + P_j \end{pmatrix} & * & * \\ W_{jk} & 0 & -S_{jk}^T B_i^T & -2S_{jk}^T & * \\ 0 & 0 & B_\omega^T & 0 & -\gamma I \end{bmatrix} < 0 \quad (26)$$

$$\begin{bmatrix} \begin{pmatrix} -M(H_j) + \\ P_j \end{pmatrix} & * \\ F_{jk(t)} - W_{jk(t)} & -(u_t^{\max})^2 \end{bmatrix} \le 0, m \in N_q, j \in N_r \quad (27)$$

$$\begin{cases} \min \gamma \\ LMI(4) \\ LMI(16) \\ LMI(26) \\ LMI(27) \end{cases} \quad (28)$$

Proof. The result of Theorem 2 is derived from the proof of Lemma 2 by choosing $M = 0$ and $N = H_{h+}^{-T} = P_{h+}^{-1}$.Thus, this proof is omitted here for brevity.

IV. ILLUSTRATIIVE EXAMPLE

Two examples and their computer simulation results are provided to show the effectiveness of the proposed methods. The first one is a numerical example given to illustrate the validity of the control design. The second one is a Benchmark of an inverted pendulum system used for comparison with other methods proposed in recent published papers. Simulation results with initial conditions $x(0) = \begin{bmatrix} \pi/2 & -\pi/3 \end{bmatrix}$.Saturation limits is: $u_t^{\max} = 1$.The number of rules is 2^{nl}, then nl represent the number of nolinearities in the left /right hand side of T-S model. The membership function $h_i(z_k)$ are calculated as follows :

For exemple :

$\mu_{1j}(z_k) = \dfrac{z_{1k} - z_{1k\min}}{z_{1k\max} - z_{1k\min}}$ and $\mu_{2j}(z_k) = 1 - \mu_{1j}(z_k)$

Then, $h_i(z_k) = \mu_{1j}(z_k).\mu_{2j}(z_k).\mu_{3j}(z_k)$, $j = 1,2$

Example 1: Let us consider the following academic nonlinear descriptor system:

$$E(x)x = A(x)x + B(x)sat(u) + B_\omega \omega$$

$E(x) = \begin{bmatrix} 1 & 1 \\ -1 & z_1 \end{bmatrix}$; $A(x) = \begin{bmatrix} 0 & z_1 - z_2 \\ -\frac{3}{2} & -3 + b(1+z_2)z_3 \end{bmatrix}$;

$B(x) = \begin{bmatrix} 1+z_2 \\ az_1 - 2 \end{bmatrix}$; $B_\omega = \begin{bmatrix} -0.25 \\ -0.25 \end{bmatrix}$. By using the sector nonlinearity approach [2], and the descretization with the Euler's Method, the previous nonlinear system can be expressed on the T–S fuzzy descriptor form (1) as follows:

$$A(z_k) = \begin{bmatrix} 1 & Te(z_1 - z_2) + 1 \\ -(1 + \frac{3}{2}Te) & z_1 - 3Te + bTe(1+z_2)z_3 + z_1 \end{bmatrix};$$

$B(z_k) = \begin{bmatrix} Te(1+z_2) \\ Te(az_1 - 2) \end{bmatrix}$; $E(z_k) = \begin{bmatrix} 1 & 1 \\ -1 & z_1 \end{bmatrix}$; $b \in \begin{bmatrix} -3.5 & 1 \end{bmatrix}$.

$a \in \begin{bmatrix} -4 & 4 \end{bmatrix}$; With: $z_1 = \cos^2(x_{2k})$; $z_2 = \dfrac{1}{1+x_1^2}$;

$z_3 = \dfrac{\sin(x_{2k})}{x_{2k}}$.

This leads to $r_e = 2$ and $r = 8$ submodels, for the left and the right part respectively of T-S fuzzy model, the domain of attraction is: $\Omega_x = \left|x_{1k}\right| \le 2; \left|x_{2k}\right| \le 2$, the disturbance signal is : $\omega(t) = \sin(10 * t)$, and the sampling period chosen $T_e = 0.1$ .Simulation results are presented in figure (1) and 2) :

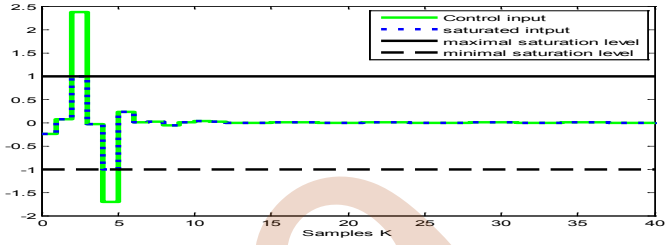

Fig.1. System control input.

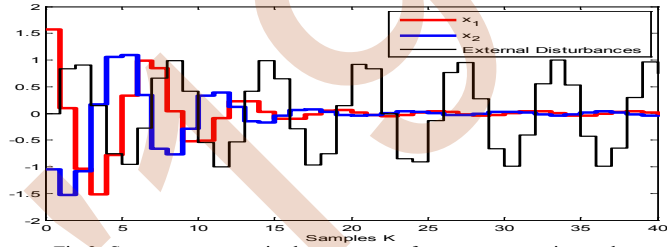

Fig.2. System responses in the presence of actuator saturation and disturbances.

The Theorem 1 gives the following gain: $\bar{\gamma} = 1.3432$

Example 2: Let us now consider the benchmark of an inverted pendulum on a cart given by Fig. 3. The motion equations obtained from the Newton's second law are given by {see [17]}:

$m = 2kg; M = 8kg; g = 9.8m/s^2; l = 0.5m; a = 1/(m+M)$

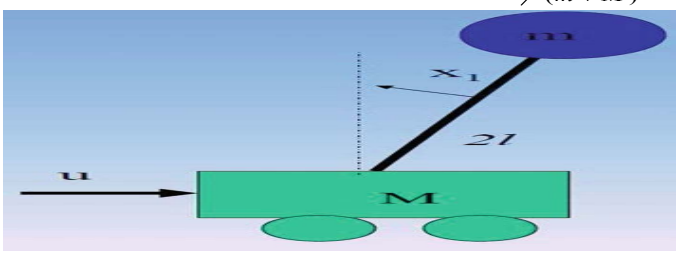

Fig.3. Inverted pendulum.

Via the sector nonlinearity approach, we have:

$A(z_k) = \begin{bmatrix} 1 & \frac{Te}{2} \\ Tegz_1 & 1 - \frac{aml}{2}Tez_2 \end{bmatrix}$; $B(z_k) = \begin{bmatrix} 0 \\ aTez_3 \end{bmatrix}$

$E(z_k) = \begin{bmatrix} 1 & 0 \\ 0 & \frac{4}{3}l - amlz_4 \end{bmatrix}$; $B_\omega = \begin{bmatrix} 0 \\ 0.3Te \end{bmatrix}$. With :

$z_1 = \dfrac{\sin(x_{1k})}{x_{1k}}$; $z_2 = x_{2k}\sin(2x_{1k})$; $z_3 = \cos(x_{1k})$;

$z_4 = \cos^2(x_{1k})$. $r_e = 2$ and $r = 8$ linear model for the left

and the right part of T-S fuzzy model, the domain of attraction is: $|x_{1k}| \leq 22\pi/45; |x_{2k}| \leq \sqrt{3}$, $T_e = 0.5$ is the sampling period. The disturbance signal is : $\omega(t) = \sin(t)$. Simulation results are presented in figure (4) and (5) :

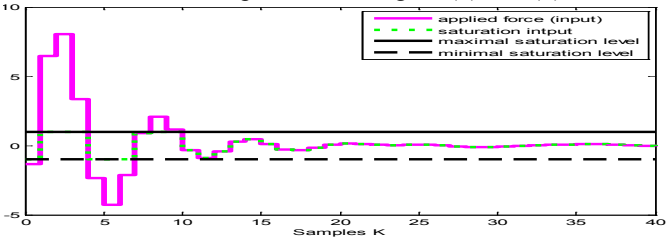

Fig.4. System control input.

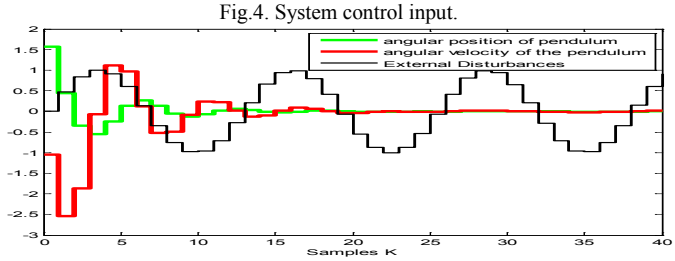

Fig.5. System responses in the presence of actuator saturation.

The Theorem 2 gives the following gain matrices: $\overline{\gamma} = 3.0825$

$$P_i = \begin{bmatrix} 1.2904 & -0.5079 \\ -0.5079 & 0.9630 \end{bmatrix}; i = 1...8$$

$$F_{jk} = \begin{bmatrix} 137.5338 & 30.2767 \end{bmatrix}; j = 1,3,5,7; k = 1,2$$

$$F_{jk} = \begin{bmatrix} -243.0218 & 193.9856 \end{bmatrix}; j = 2,4,6,8; k = 1,2$$

$$H_1 = H_3 = \begin{bmatrix} -0.0513 & -0.0659 \\ -0.2295 & -0.1566 \end{bmatrix};$$

$$H_2 = H_4 = \begin{bmatrix} 0.0810 & -0.7708 \\ -0.3347 & -0.0737 \end{bmatrix};$$

$$H_5 = H_7 = \begin{bmatrix} 0.1001 & -0.0142 \\ -0.3324 & -0.0550 \end{bmatrix};$$

$$H_6 = H_8 = \begin{bmatrix} 0.0998 & -0.0142 \\ -0.3342 & -0.0559 \end{bmatrix}.$$

Figure 2 and 5 shows the different control inputs applied to the proposed system, where represent the derived non-PDC controller input. The closed-loop disturbed discrete-time T-S responses derived with the controller gain matrices, are depicted in Figure 1 and 4. It can be deduced that the designed controller allows achieving a stable closed-loop performance.

V. Conclusion

This paper proposes a novel LMI-based framework for controller synthesis of discrete-time disturbed descriptor T-S systems with state and input constraints. Based on non-quadratic Lyapunov functions and non-PDC controllers, new stability conditions have been designed. The controller gains are then obtained by solving an optimization problem under LMI constraints. Through two numerical examples, the efficiency of the approaches has been demonstrated.

References

[1] K.Tanaka, T.Ikeda. and H.O.Wang, "Fuzzy regulators and fuzzy observers : relaxed stability conditions and LMI-based designs, "IEEE Transactions on Fuzzy Systems, vol.6,pp:250-265,1998.

[2] K.Tanaka and H.O.Wang Fuzzy Control system, design and Analysis: a Linear Matrix Inequality Approach. Wiley-Interscience, 2001.

[3] M. Johansson, A. Rantzer, and K.E. Arzen, "Piecewise quadratic stability of fuzzy systems, " IEEE Transactions on Fuzzy Systems, vol. 7, no.6, pp. 713-722, 1999.

[4] T.M.Guerra and L.Vermeiren., « LMI based relax non-quadratic stabilization for non-linear systems in the Takagi-Sugeno's form, », Automatica, 40(5):823-829, May 2004.

[5] T.M.Guerra,M.Bernal, K.Guelton, and S.Labiod, "Non-quadratic local stabilization for continous-time Takagi-Sugeno models, "Fuzzy Sets and Systems,2012.

[6] T.Taniguchi, K.Tanaka and H.O.Wang, " Fuzzy Descriptor system and nonlinear model following Control," IEEE transactions on Fuzzy Systems, vol.8,no.4,pp,442-452,2000.

[7] V.E.Manzo,Z..Lendek,T.Guerra, and P.Pudlo, "Control design for discret-time descriptor models: a systematic LMI approach, "IEEE Trans.On Fuzzy Systems, Early Access Online 2015.

[8] A-T.Nguyen,M.Damrine,J.Lauber,"Simulataneous design parallel distributed output feedback and anti-windup compensators for constrained Takagi-Sugeno fuzzy systems, "Asian.J. Control, Vol.18,pp-1641-1654,2006.

[9] A.Benzaouia,A.El hajjaji,A,and R.Oudah."Fault tolerant saturated control for T-S fuzzy discrete-system with delay, "Nonlinear analysis:Hybrid systems, 1²8,pp:60-71,2015.

[10] D.Saifia,M. Chadli,S.Labiod, and T.M.Guerra, "Robust H∞ static output feedback stabilization of T-S fuzzy system subject t actuator saturatio,"Inter.J.Conf,Automation and System, vol.10(3), pp.613-622,2012.

[11] S. Bezzaoucha, S., Marks, B., Maquin, D., & Ragot, J. "Stabilization and output feedback control for Takagi-Sugeno with saturated actuators". Inter.J.Adaptive control and signal Processing. Vol.30, pp.888-905.

[12] T.M. Guerra, V.Estrada-Manzo, and Z.Lendek, "Observer design for Takagi-Sugeno descriptor models: An LMI approach" Automatica, vol.52,pp.154-159,2015.

[13] K.Guelton, S.Delprat,and T.M.Guerra, "An Alternative to inverse dynamics joint torques estimation in human stance based on a Takagi-Sugeno unknow-inputs observer in the descriptor form, "Control Engineering Practice, vol.16(12),pp.1414-1426,2008.

[14] S. Aouaouda, M. Chadli, M. Boukhnifer, H.R. Karimi, "Robuste fault tracking controller design for vehicle dynamics: A descriptor appraoch", Mechatronics, vol. 30, pp. 316-326, 2015.

[15] M.Chadli and M.Darouach, "Novel bounded real lemma for discrete-time descriptor systems: Application to control-design, "Automatica, vol.48, no.2, pp.449-453,Feb.2012.

[16] Q.V. Dang, L.Vermeiren, A. Dequidt, M. Dambrine, "Robust stabilizing controller design for Takagi-Sugeno fuzzy descriptor systems under state constraints and actuator saturation," Fuzzy Sets and Systems, vol. 329, pp. 77-90, 2017.

[17] Mansouri B, Manamanni N, Guelton K, Kruszewski A, Guerra TM. Output feedback LMI tracking control conditions with H1 criterion for uncertain and disturbed T_S models. Inform Sci 2009;179(4):446_57.

Electromyography Based Identification and Prediction of the Knee Joint Continuous Movement

Ait Ghezala Amel
University of science and technology HouariBoumediene
Automation and Instrumentation Department
Algiers, Algeria
amelaitghezala@gmail.com

Guiatni Mohamed,
Complex Systems & Simulators Control Laboratory
Ecole Militaire Polytechnique
Algiers, Algeria
mohamed.guiatni@gmail.com

***Abstract*—Surface EMG signals are found to be very effective in identifying the intent of the voluntary movement. First of all because they are generated by human will and can be acquired in a non-invasive way. Then, they can also help in estimating and predicting the continuous motion of a joint. However, predicting methods of continuous motion founded on EMG signals, are mainly based on the quality of the EMGs, and can lead to incorrect estimates.**

In this work, a method of identification and predicting knee movement was proposed. This method uses a dynamic model of the complex tendon-muscle as a function of EMG signals based on the HILL model. As a model of the human muscle, it establishes a link between the dynamics of the knee joint and EMG signals. The model parameters identification is based on an optimization algorithm (the trust region algorithm).

Since the HILL model is open-loop, we propose an inertial sensor and neural network approach to estimate knee joint position and speed as feedback information. These are then used as a corrective measure in a closed-loop correction-prediction algorithm, such as the extended Kalman algorithm.

I. INTRODUCTION

Intent is at the origin of any voluntary movement. It is generated through a series of operations controlled by the central nervous system, which ensures its diffusion to the skeletal muscles allowing motor skills.

For people with a motor disability, the intention is interrupted according to the rupture zone of the neural pathways, giving rise to two approaches of strategy of identification of the intention for the control of an exoskeleton. The first approach is considering that the muscle is active, i.e. the patient suffers from muscle weakness but still manages to develop very little effort. The latter triggers an identification and estimation process based on force sensors that will serve as feedback to the controller, who will in turn generate the assistance torque required to execute the movement[1],[2],[3]. The second approach, it considers that the interruption is at the tendon, so the patient cannot develop any effort, therefore, the strategy is based on the measurement of physiological signals, EMG and EEG. Several studies use classification algorithms for intention estimation [4]. these algorithms consist of two steps, the first is the extraction of the EMG signal characteristics and the second step classifies the different target movements according to the set of selected information. These algorithms, such as support vector machines [5], neural networks [6] and many others, are discrete methods and limit the number of movements. Currently, research is interested in estimating intention, to have any movement in a continuous way, a kind of desired trajectory. A model of the muscle-tendon complex exists, which allows the EMG electromyographic signal to be directly linked to the necessary torque developed by each muscle to generate the assisting torque to be applied to the joint. In the literature, the Hill model and the transformed Hill model are most often used[7].

In this work, the Intent identification is based on the second approach, because it is much more intuitive than the first approach, it allows to anticipate movement and also with good control, the realization of the monolithic function of the exoskeleton.

This paper is organized as follows. The second section will focus on the modeling of the muscle-tendon complex. The estimation of the continuous movement of the knee joint a closed loop will be presented in the third section. The fourth section will include the results of the simulation and experimentation, followed by a conclusion in the last section.

II. OPEN-LOOPESTIMATION FORTHE INTENT OF CONTINUOUS JOINT MOVEMENT

In this section, we will briefly explain Hill's model.

A. Muscle activation dynamics

Muscle activation represents the amount of electrically stimulated muscle fibers that is sufficient for a muscle to

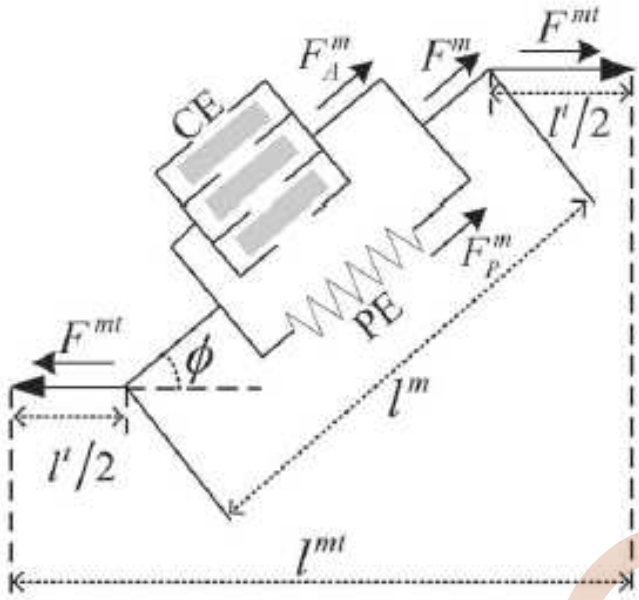

Figure 1. Hill muscle–tendon complex model.

contract. This is also equivalent to the amount of active force produced by the muscle. However, there is a gap between muscle activation and strength development. The amplitude of muscle activation is represented by an interval varying between[0 1]. The best way to achieve muscle activation is to proceed in three steps, first the EMG signal is filtered, thenrectified, processed and smoothed using the square root mean square (RMS) value, in order to eliminate any negative amplitude. Then it is normalized[8]. There are several ways to normalize the EMG signal. The most common method in the literature is the MVC method (maximum voluntary contraction). Once we have quantified the EMG signal, we move on to the second step, which consists of transforming the EMG signal to neural activation, then the third step, the transition from neural activation to muscle activation [8]. These transformations are respectively defined by these following equations:

$$u(k)=\alpha\cdot e(k-d/Temg)-\beta1\cdot u(k-1)-\beta2u(k-2) \quad (1)$$

Where dand Temg respectively represent the electromechanical delay and sampling time of the EMG signal, α, β1 and β2 are the coefficients that define the dynamics of the second-order equation[8],[9]. To obtain a stable solution for (1), these coefficients must comply with the following constraints:

$$\begin{cases} \beta1=\gamma_1+\gamma_2 \\ \beta2=\gamma_1.\gamma_2 \\ \alpha-\beta1-\beta2=1 \end{cases} \quad (2)$$

where $|\gamma_1|<1$ and$|\gamma_2|<1$

The relationship between neural activation u(k) and muscle activation a(k) is the following formula [8], [9].

$$a(k)=\frac{e^{A.u(k)}-1}{e^{A}-1} \quad (3)$$

A is a non-linearity factor, which varies between -3 and 0.

B. Hill's model

Hill's model, describes approximately the behavior of human muscle during contraction and extension. it establishes also a link between the dynamics of the knee joint and EMG signals.

Hill's model consists of three main components:

- The contractile component: It represents the source of the active force that is generated by the muscle.
- The parallel elastic component: This component is placed in parallel with the contractile element. It represents the elastic aspect of the muscle.

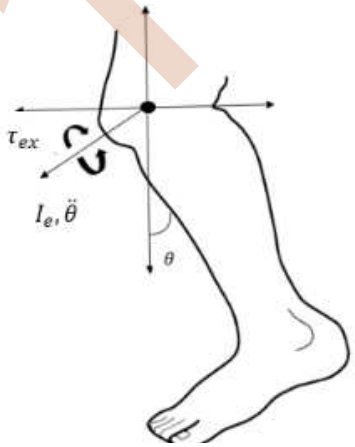

Figure 2. Knee joint motion.

- The series elastic component: Placed in series with respect to the contractile element, it represents the elongation of the tendon that transmits the force exerted on the joint.

Following the model proposed by Hill, several models were implemented, including the Hill model transformed and proposed by Zajac[7], [8], which can be defined by the following equations:

$$F^{mt}=[F_A^m.+F_P^m].\cos(\varphi) \\ =\left[F_A(l).F_V(l).a(k).F_0^m+f_p(l)\right].F_0^m.\cos(\varphi) \quad (4)$$

In order to calculate (4), the physiological parameters can be approximated as follows:

Where$F_A(l)$, $F_V(v)$ and $F_p(l)$represents respectively, the nominal active force as a function of the nominal length of the muscle, the force as a function of speed and the nominal elastic force as a function of the nominal length of the

muscle. V is the nominal speed of muscle contraction. F_0^m is the maximum isometric force and a(k) represents muscle activation. Finally we can estimate the assistance torque with the Hill model by this following relationship:

$$\tau = F^{mt}.r \quad (5)$$

C. The state-space EMG model of continuous knee joint movement

In this work we used the knee joint with the Rectus femoris of the quadriceps muscle as a case study, however the procedure can be used for any muscle-tendon complex[9]. We have therefore opted for the Hill model transformed by Zajac, in order to establish a direct link between the EMG signal and angular acceleration. The figure below illustrates the benchmarks used for the modified Hill model[9].
Fig. 2 shows that the angular acceleration of the knee can be calculated as follows:

$$\ddot{\theta} = \frac{1}{I_e}.(\tau - \tau_{ex}) \quad (6)$$

Where

$$\tau_{ex} = \tau_{ex8\_max}\ .\sin(\theta)(7)$$

I_e represents the moment of inertia of the leg which is assumed to be constant for a given weight. τ_{ex} is a combination between the moment developed by the tip of the leg and the moment developed at its center of gravity. Finally, by combining equations (4), (5) and (6), we will have the dynamic model of knee joint motion[8], [9]:

$$\ddot{\theta} = (S_0 + S_1\ .\theta + S_2\ .\ \theta^2).a(k) + S_3\ .e^{s_4.\theta} - S_5\ .\ \sin(\theta) \quad (8)$$

With

$$\begin{cases} S_0 = \frac{q_0.F_0^m.b_1.\cos(\varphi)}{I_e} + \frac{q_1.F_0^m.b_1.(b_0-l^t).b_1}{I_e.l_0^m} + \frac{q_2.F_0^m.b_1.(b_0-l^t)^2.b_1}{I_e\ .(l_0^m)^2.\cos(\varphi)} \\ S_1 = \frac{q_1.F_0^m.b_1.(b_1)^2}{I_e.l_0^m} + \frac{2.q_2.(b_1)^2.(b_0-l^t)^2}{I_e\ .(l_0^m)^2.\cos(\varphi)} \\ S_2 = \frac{q_2.(b_1)^3.F_0^m}{I_e\ .(l_0^m)^2.\cos(\varphi)} \\ S_3 = \frac{F_0^m.b_1.\cos(\varphi)}{I_e}.\exp\left(\frac{10.(b_1)^2.(b_0-l^t)^2}{l_0^m.\cos(\varphi)} - 15\right) \\ S_4 = \frac{10.b_1}{l_0^m.\cos(\varphi)} \\ S_5 = \frac{\tau_{ex\_max}}{I_e} \end{cases}$$

We obtain now the state-space EMG model of continuous knee joint movement

$$\begin{cases} \ddot{\theta}_{k+1} = \left(S_0 + S_1\ .\theta_k + S_2\ .\ \theta_k^2\right).a(k) \\ \quad +S_3\ .e^{s_4.\theta_k} - S_5\ .\ \sin(\theta_K) \\ \dot{\theta}_{k+1} = \dot{\theta}_k + \ddot{\theta}_k.\ Ts \\ \theta_{k+1} = \theta_k + \dot{\theta}_k.\ Ts \end{cases} \quad (9)$$

III. CLOSED LOOP ESTIMATION OFTHE CONTINUOUS KNEE JOINT MOTION

The relationship (9) represents Hill's simplified model, which describes the continuous movement of the knee joint depending on the muscle activation. The S_i parameters are identified and stored in offline, however the continuous estimation of motion can be performed in real time.

It is only a hypothesis that the physiological parameters are constant.Indeed, theseparameters change according to the human, skincondition and the measurement, which implies uncertainties at the model,therefore it will generate an accumulation of errors during recursive calculation and willlead the system to diverge. Also, (9) is an open-loop model, i.e. in addition to the EMG electrodes, we do not have a sensor, which could provide joint motion measurements as feedback information.

The main contribution of this work is thefeedback information extraction method, based on measurements of an inertial central unit (IMU) and artificial neural network, which will then be used to correct continuous movement.

A. construction of measurement feedback equations

1) ***Data collection:***In order to collect information from the states of the knee joint as feedback, we use an artificial neural network technique, with an acquired database containing IMU data placed on the quadriceps and constituting the RNA input vector and the target vector, which
represents the kinematic measurement of the knee from a potentiometer.

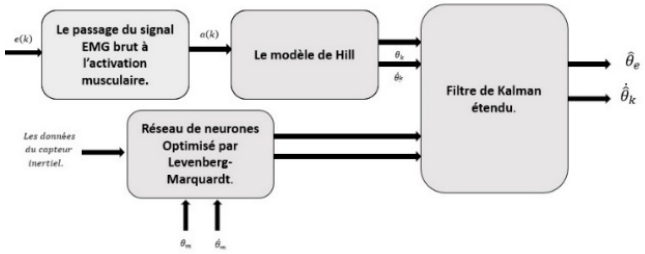

Figure 3. Block diagram of the holistic state estimation of the Hill model.

2) ***ANN****:* A downstream network was selected with an input layer consisting of a node, a hidden layer of 20 nodes and a single node output layer. The network used performs supervised learning to modify the network weights so that the output best matches the target vector. The updating of the network weight values has been optimized using the Levenberg-Marquardt optimization algorithm.Selection:

*3) **Closed-loop Hill's model**:* In order to achieve the feedback information, we propose these following measurement equations for the model (9):

$$\begin{cases} h1_k = \theta \\ h2_k = \dot{\theta} \end{cases} \quad (10)$$

Where,$[\theta_k ; \dot{\theta}_k]$ represents the state vector of our system, $h1_k$and $h2_k$represents the measurement equations. In order to correct the behavior of the model (9). Fig. 3 illustrates the diagram of Hill closed-loop model.

B. *Open-loop system identification*

For the identification of the Hill model we applied the trust region algorithm, this method was used to optimize and solve a non-linear problem [10], applied to an objective function such as:

$$\min_{x \in \mathbb{R}^n} \mathbf{E(x)}$$

C. *Estimation and prediction of continuous motion by the extended Kalman algorithm*

The extended Kalman filter is an algorithm that estimates the optimal states of a stochastic non-linear system from a reference model and also through the combination of available measurements (Input/Output). Also, its strong point is to be able to predict parameters and it corrects errors from the sensors and the model itself [11].

In the following we present our approach based on the extended Kalman filter to estimate the states of the knee joint. We can now write the system in the form of a model in the state space:

$$x_{k+1} = f(x_k, a_k) + W_k \quad (11)$$

$$y_{k+1} = h(x_k) + v_{k+1} \quad (12)$$

$$f(x_k, a_k) = \begin{bmatrix} \ddot{\theta}_{k+1} = (S_0 + S_1 . \theta_k + S_2 . \theta_k^2).a(k) \\ +S_3 . e^{s_4 . \theta_k} - S_5 . \sin(\theta_K) \\ \dot{\theta}_{k+1} = \dot{\theta}_k + \ddot{\theta}_k . Ts \\ \theta_{k+1} = \theta_k + \dot{\theta}_k . Ts \end{bmatrix}$$

$$h(x_k) = \begin{bmatrix} \theta_k \\ \dot{\theta}_k \end{bmatrix}$$

To use the EFK algorithm, we first linearize the model (13) around the last estimated state.

$$F_k = \frac{\partial f}{\partial x}|_{x=\hat{x}_k} = \begin{bmatrix} 0 & 0 & (S_1 + 2.S_2 . \theta_K).a(k) + S_3.s_4 . e^{s_4.\theta_k} - S_5 . \cos(\theta_K) \\ Ts & 1 & 0 \\ 0 & T & 1 \end{bmatrix} \quad (14)$$

$$H_{k+1} = \frac{\partial h}{\partial x}|_{x=\hat{x}_{k+1,k}} = \begin{bmatrix} 1 & 0 \\ 0 & 1 \end{bmatrix} \quad (15)$$

The algorithm of the extended Kalman filter is as follows:

- Prediction step:

$$x_{k+1} = f(x_k, a_k)$$

$$y_{k+1} = F_k . x_k . F_k^T + Q \quad (16)$$

- Update step:

$$\begin{cases} K_{k+1} = P_{k+1,k} H_{k+1}^T (H_{k+1} P_{k+1,k} H_{k+1}^T + R)^{-1} \\ \hat{x}_{k+1} = \hat{x}_{k+1,k} + K_{k+1}(y_{k+1} - h(\hat{x}_{k+1,k})) \\ P_{k+1} = (P_{n\,x\,n} - K_{k+1} . H_{k+1}) P_{k+1,k} \end{cases} \quad (17)$$

IV. RESULTS AND DISCUSSION

A. *The experimental protocol*

In order to evaluate the performance of the proposed intention model, we collected EMGs signals as well as signals from the reference movement, from 2 healthy people, one male and one young woman aged 24 years.

The acquisition system consists of 3 sensors: the EMG signal measurement sensor, the inertial sensor and the potentiometer-based sensor. The processing is carried out using the Dspace 1103 card. Fig. 4 illustrates the signal acquisition protocol.

EMG signals are acquired using a MyoWare sensor (AT-04-001). This one is designed for direct use, as the output signal from this sensor is amplified, filtered and rectified. The acquisition frequency can be up to 2kHz.

To be able to measure EMG signals correctly, we go through the following steps:

After determining the femoral straight muscle, we clean the skin thoroughly, to remove all this debris, we place the measuring electrodes in the center of the muscle belly and the reference electrode in a non-depolarized area.

The (flexion/extension) movements must be with an average speed. The experiment is done in 20 tests per person, to test the accuracy of the sensor. A recording lasts 60 seconds, during which the person must make non-stop (flexion/extension) movements.

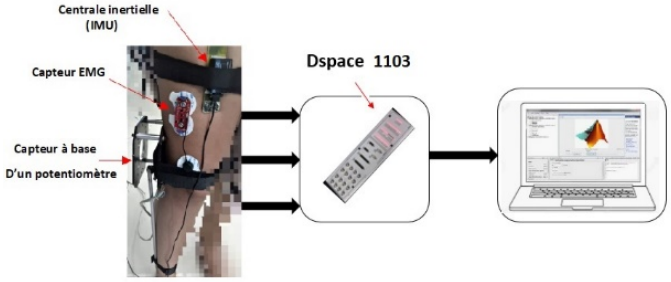

Figure 4. Diagram of the acquisition protocol.

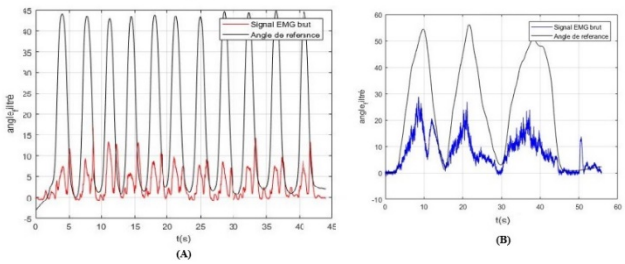

Figure 5. Acquisition of EMGs signals and reference angle - (A): subject 2, (B): subject 1.

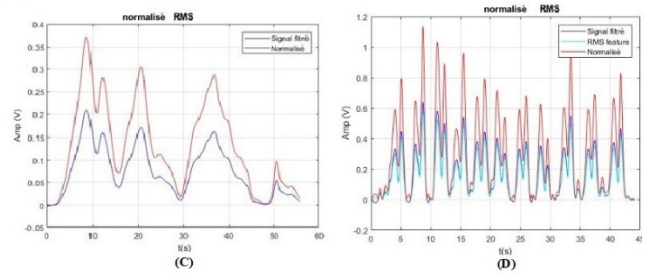

Figure 6. Filtering of the raw EMG signal and its normalized. (C): subject 1, (D): subject 2.

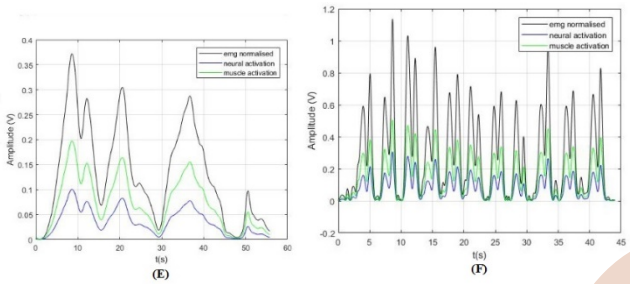

Figure 7. Transition from EMG signal to muscle activation - (E): subject 1, (F): subject 2.

Between each test the person must rest for 10 minutes to avoid muscle fatigue. Once the signals are acquired, they will be digitized by an analog-digital module of the Dspace card, with a sampling frequency of 1 kHz. Then the signal will be filtered with a Chebyshev low pass filter of order 2, for this freed of Frequencies carrying measurement noise. Finally, a time window of 30 ms has been defined in order to extract the RMS characteristic vector from the EMG signal, which is supposed to contain the distinctive information specific to each test. In order to avoid the compatibility problem of the

Parameters	S_0	S_1	S_2	S_3	S_4	S_5
Initial	0.0100	-2	10	0.0100	0.1000	0.4000
Best (Sub1)	1.9701	-1.3173	-0.1144	0.0865	-1.57	0.3161
Best (Sub2)	2.4	-1.529	-1.3	0.09	-1.223	0.390

TABLE I. OPTIMAL IDENTIFICATION OF THE OPEN LOOP HILL MODEL

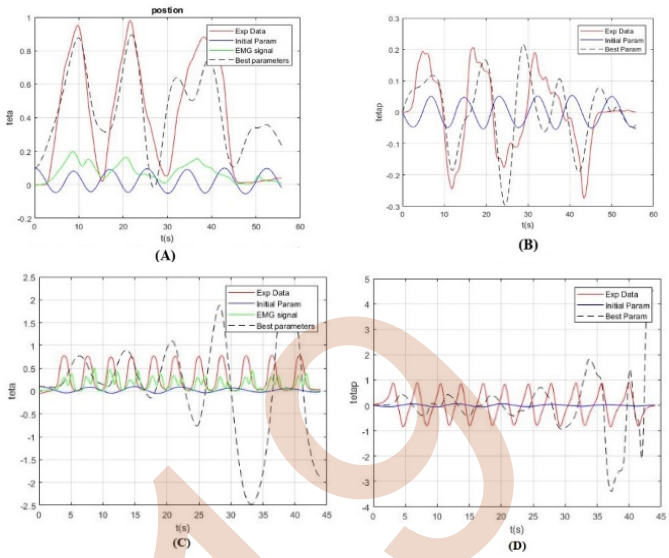

Figure 8. Estimation of Hill model parameters. -Subject 1 (A): The position of the knee joint, (B): The speed of the knee joint. -Subject2 (C) : the position of the knee joint, (D) : the speed of the knee joint.

EMG signals of different people, we normalize the EMG signal with the method (MVC).

B. Identification of the open-loop Hill's model

The $S_i$represents the physiological parameters of the muscle-tendon model, which have been identified using a confidence

region optimization algorithm, minimizing the following criterion:

$$E(x) = \sqrt{\sum(Y(X) - \hat{Y})^2} \qquad (17)$$

With Y represents the vector of the system states, X represents the vector of the parameters to be estimated and $\hat{Y}$represents the measurement vector. Tab.1 shows the performance of the identification results.

The experimental results of the identification of the Hill model in open loop, with the comparison between the real measurement by the potentiometer and the estimated Output. We notice that the two graphs of subject 1 are getting closer but we notice an estimation error that is important, due to the accumulation of inaccuracies of the Hill model during the
recursive calculation. As a result, the open-loop system may diverge as in the case of subject 2.

TABLE II. PERFORMANCE EVALUATION OF THE THREE NEURAL NETWORKS (SUBJECT 2)

Subject 2	RMSE(deg)	RMSE(deg/s)	Cc(deg)	Cc(deg/s)
No-	3.651	1.814	0.989	0.968

recurssive				

Subject 1	RMSE(deg)	RMSE(deg/s)	Cc(deg)	Cc(deg/s)
No-recurssive	3.457	4.532	0.988	0.975
Input Recurssive	1.951	4.273	0.996	0.986
I/O recurssive	0.781	3.747	0.999	0.9903
Input Recurssive	2.122	1.736	0.994	0.9706
I/O recurssive	2.798	2.389	0.991	0.940

TABLE III. PERFORMANCE EVALUATION OF THE THREE NEURAL NETWORKS (SUBJECT 1)

C. Experimentation of the Hill closed-loop model

By substituting the estimated parameters of Hill's open-loop model, we were able to improve the estimation of its states, using the constructed measurement equations and the extended Kalman filter algorithm.

In order to evaluate the performance of the neural network we studied 3 types of networks: a non-recursive neural network, with an input layer with a node, a recursive network

with an input layer composed of 3 nodes, the latter represent the input vector shifted by 1 then 2 sampling steps and finally the last network is recursive at input and output, it includes an input layer with 5 nodes, namely: an input node, 2 input nodes offset by 1-2 sampling steps and 2 output nodes offset by 1-2 sampling steps. The performance of the 3 networks is compared and presented in tab.2 and tab.3.

The performance of the different neural networks is evaluated by the root mean square error (RMSE) and the correlation coefficient.

$$RMSE = \sqrt{\frac{1}{n}\sum(y_m - y_e)^2}\,.\ \rho = \frac{C_c}{\sigma_{y_m}.\sigma_{y_e}} \qquad (18)$$

Where, Ym and Ye represent the measured signal and the estimated signal of knee joint movement respectively. tabl 2 and 3, present a comparison between the performance of learning networks. The latter show that the most efficient network is the input recursive network for subject 1 Fig. with an estimate of the real angle including a correlation coefficient of Cc=0.994 and a root mean square error of RMSE = 2.122 deg. For subject 2 the most efficient network is the recursive input and output network with a RMSE=0.7816 and a Cc= 0.9997. The Fig. curves illustrate the estimates of the measures as feedback.

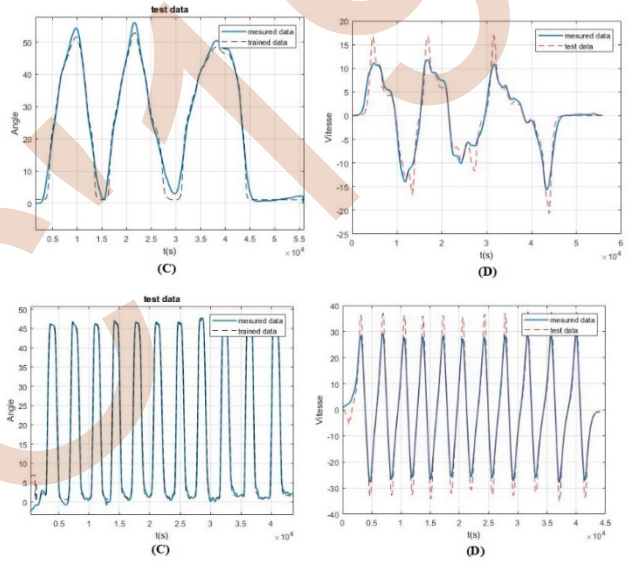

Figure 9. Estimation of feedback measurements-Subject 1 (A) : position of knee joint, (B) : speed of knee joint. -Subject2 (C) : the position of the knee joint, (D) : the speed of the knee joint.

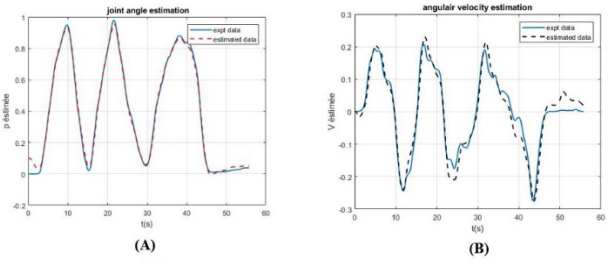

Subject1	RMSE(rd/s)	RMSE (rad)	Cc(rd/s)	Cc(rd)
OP MODEL	3.08	2.1817	0.74	0.846
CP MODEL	0.0265	0.0209	0.9779	0.9985

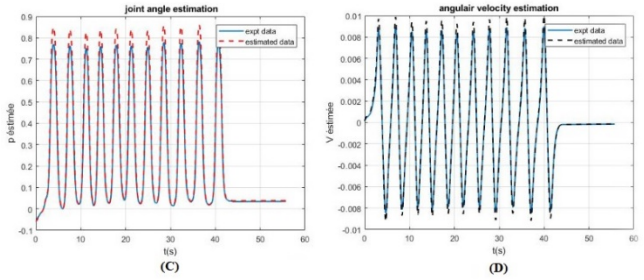

Figure 10. Estimation of Hill model states by EFK -Subject 1 (A) : position of knee joint, (B) : speed of knee joint. -Subject2 (C) : the position of the knee joint, (D) : the speed of the knee joint.

D. Estimation of continuous knee joint movement by EFK

Once the feedback measurement equations were constructed, we used the extended Kalman filter algorithm to estimate the states of the knee joint. The Q and R covariance matrices are chosen by tattooing and compromise. Fig.11 shows the experimental results of the estimation of the angle and speed of the knee joint, or comparison. The measurement of the potentiometer serves as the real value for the comparison

TABLE IV. COMPARISON BETWEEN THE ESTIMATION OF THE OPEN-LOOP AND CLOSED-LOOP SYSTEM (SUBJECT 1)

TABLE V. COMPARISON BETWEEN THE ESTIMATION OF THE OPEN-LOOP AND CLOSED-LOOP SYSTEM (SUBJECT 2)

Subject2	RMSE(rd/s)	RMSE (rad)	Cc(rd/s)	Cc(rd)
OP MODEL	3.08	2.1817	0.74	0.846
CP MODEL	0.0265	0.0209	0.9779	0.9985

In order to verify the improvement brought by the constructed measurement equations, tab.3 and Tab.4 show the results obtained when identifying the Hill model in open and closed loop.

We can see that the estimation of the Hill open loop model is much less efficient due to the accumulation of model errors.

The closed-loop model has been successful in overcoming accumulation errors and has maintained convergent estimation while improving the accuracy.

V. CONCLUSION

In this work, we have identified the intent of the continuous movement of the knee joint with a Hill model. This allows a direct link to be established between the dynamics of the knee joint and the EMG signal. A system for estimating the behavior of the knee joint based on inertial sensors and neural networks has been built to provide measurement equations as feedback information. A trust-region optimization algorithm was used for optimal identification of the Hill model. A condition estimation algorithm (the extended Kalman filter) was also proposed to reject all uncertainties in the model and improve the estimation. Extensive experiments have been carried out, as well as comparisons between model-based estimates and actual measurements from a potentiometer, confirm the effectiveness of the proposed methods. As part of the future prospects, we will introduce a method based on EEG (electroencephalographic) signals, to increase the speed of detection of the intention of movement and apply it to prostheses or orthoses.

REFERENCE

[1] Cao, Hua. Modélisation et évaluation expérimentale de la relation entre le signal EMG de surface et la force musculaire. Diss. Université de Technologie de Compiègne, 2010.

[2] Hassani, Walid. *Contribution à la modélisation et à la commande assistive basée, intention d'un exosquelette du membre inférieur*. Diss. Paris Est, 2014.

[3] Zhang, Chao, et al. "Human–machine force interaction design and control for the HIT load-carrying exoskeleton." *Advances in Mechanical Engineering* 8.4 (2016).

[4] Kiguchi, Kazuo, and Yoshiaki Hayashi. "Motion estimation based on EMG and EEG signals to control wearable robots." 2013 IEEE International Conference on Systems, Man, and Cybernetics. IEEE, 2013.

[5] Gudiño-Mendoza, Berenice, Gildardo Sanchez-Ante, and Javier M. Antelis. "Detecting the intention to move upper limbs from electroencephalographic brain signals." Computational and mathematical methods in medicine 2016 (2016)

[6] Orjuela-Cañón, Alvaro David, Andrés F. Ruíz-Olaya, and Leonardo Forero. "Deep neural network for EMG signal classification of wrist position: Preliminary results." 2017 IEEE Latin American Conference on Computational Intelligence (LA-CCI). IEEE, 2017.

[7] Hoy, Melissa G., Felix E. Zajac, and Michael E. Gordon. "A musculoskeletal model of the human lower extremity: the effect of muscle, tendon, and moment arm on the moment-angle relationship of musculotendon actuators at the hip, knee, and ankle." Journal of biomechanics 23.2 (1990): 157-169.

[8] Buchanan, Thomas S., et al. "Neuromusculoskeletal modeling: estimation of muscle forces and joint moments and movements from measurements of neural command." Journal of applied biomechanics 20.4 (2004): 367-395.

[9] Han, Jianda, et al. "A state-space EMG model for the estimation of continuous joint movements." IEEE Transactions on Industrial Electronics 62.7 (2015): 4267-4275.

[10] Byrd, Richard H., Robert B. Schnabel, and Gerald A. Shultz. "A trust region algorithm for nonlinearly constrained optimization." SIAM Journal on Numerical Analysis 24.5 (1987): 1152-1170.

[11] López-Delis, Alberto, et al. "Continuous Estimation Prediction of Knee Joint Angles Using Fusion of Electromyographic and Inertial Sensors for Active Transfemoral Leg Prostheses." Advances in Data Science and Adaptive Analysis 10.02 (2018): 1840008.

Distributed State Feedback Controller for Heat Exchanger Network

HABRACHE Nouara
Laboratoire de Conception et de Conduite des Systèmes de Production (L2CSP)
Tizi-Ouzou, Algérie
E-mail: nouara.habrache90@gmail.com

MEGHERBI Ouerdia
Laboratoire de Conception et de Conduite des Systèmes de Production (L2CSP)
Tizi-Ouzou, Algérie
E-mail: meg_ouer@yahoo.fr

Abstract—**In this paper, a control approach is proposed for controlling the internal fluid temperature in a heat exchanger network at the boundary by manipulating its velocity. This approach consists to design a distributed state feedback controller using the geometric control, based on the concept of the characteristic index, in the framework of the late lumping approach. Numerical simulations illustrate the effectiveness of the proposed control approach.**

I. INTRODUCTION

Heat exchanger is a device in which heat transfer is realized across the separating wall between two fluids at different temperatures. According to the fluids flow direction there are several configurations such as counter-current heat exchanger, where the fluids flow in the opposite direction, and the co-current heat exchanger, in which the fluids flow in the same direction [1]. Thesetwo configurations represent the basic structure for heat exchangers. Generally, in practice, we find the combination of these last to form a heat exchanger network.

Heat exchanger is a Distributed Parameter System (DPS) since the fluid temperatures are not uniform with respect to the space variable along the heat exchanger [2]. Consequently, the modelling of this system leads to Partial Differential Equations (PDE's). The fluid temperature in heat exchanger can be controlled by manipulating the inlet temperature or the velocity (flow rate) of a fluid [3]. Considering the velocity of one of the heat exchanger fluids as the control variable, a very common case in practice, leads to a bilinear system which represents a particular class of nonlinear systems [4], [5]. Bilinear systems are characterized by the product of the state variable and the control variable, that is, they are linear with respect to the state variable and linear with respect to the controlvariable when they are considered independently, but not jointly linear in both [4]. For this system class, the spatial operator has a particular structure that can be easily exploited to develop control laws [6].

In recent years, the late lumping approach is the obvious choice for the DPS's control. This approach consists in designing the controller directly using the PDE's without any approximation; the controller is of distributed nature that enhances the performance in closed-loop [7], [8] ,[9]. This approach is very developed in the case of linear DPSs, thanks to the semi-group theory [10]. The control theory of nonlinear DPS's remains very challenging due to the complexity of formulated control problems and the absence of a general theory. The study is usually done case by case [11].

The late lumping approach is moderately used for the control of heat exchangers. In [3] and [12], the geometric control was used for the control at the boundary of a co-current and counter-current heat exchanger, respectively. The Backstepping control was used in [13] to control a co-current heat exchanger. In [14], the internal model control for a heat exchanger network has been proposed. These proposed control techniques are based on the choice of the fluid inlet temperature as a control variable.

The paper is organized as follows: In Section II, we present the heat exchanger network model. The control design, based on the geometric theory, is developed in section III. Section IV is devoted to show the obtained simulation results. Finally, we end the paper with a summarizing conclusion

II. HEAT EXCHANGER NETWORK MODEL

The tubular heat exchanger network, of length$2L$,considered is a cascade of two heat exchangers as shown in Figure **1**. The first is a co-current heat exchanger andthe second is a counter-current one. The internal tube, in which the cold fluid flows and enters at temperatureT^0, is common between the two exchangers. This tube is in the contact with the environment over a distance2μ before being transferred to the second heat exchanger. The hot fluids of the co-currentheat exchanger (enters at temperatureT_1^0) and the counter-current heat exchanger (enters attemperatureT_3^{2L}) flow in external tubes.

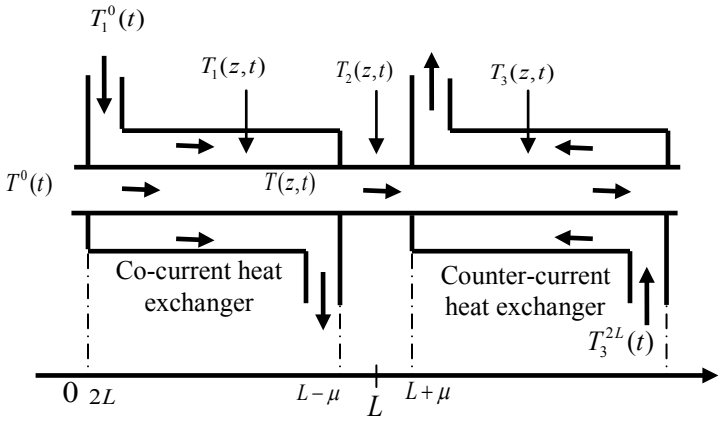

Fig.1. Heat exchanger network.

The dynamic behavior of the heat exchanger network is described by a set of coupled partial differential equations, when the diffusion phenomenon is neglected, given as follow [14]:

$$\frac{\partial T(z,t)}{\partial t} = -v_0 \frac{\partial T(z,t)}{\partial z} + \sum_{i=1}^{3} h_i\big(T_i(z,t) - T(z,t)\big) \quad (1)$$

$$\frac{\partial T_1(z,t)}{\partial t} = -v_1 \frac{\partial T_1(z,t)}{\partial z} + h_1\big(T(z,t) - T_1(z,t)\big) \quad (2)$$

$$T_2(z,t) = 0 \quad (3)$$

$$\frac{\partial T_3(z,t)}{\partial t} = -v_3 \frac{\partial T_3(z,t)}{\partial z} + h_3\big(T(z,t) - T_3(z,t)\big) \quad (4)$$

With $h_i \equiv 0$on $\Omega_{j\neq i}$for$i,j = 1,2,3$.
The initial conditions are

$$T(z,0) = T^*(z) \quad (5)$$
$$T_1(z,0) = T_1^*(z) \quad (6)$$
$$T_3(z,0) = T_3^*(z) \quad (7)$$

$T^*(z)$,$T_1^*(z)$ and $T_3^*(z)$are the initial spatial temperature profiles of the internal fluid, external fluid of the co-current heat exchanger and external fluid of the counter-current heat exchanger, respectively.
The boundary conditions that represent the fluid inlet temperatures are defined as follows:

$$T(0,t) = T^0(z) \quad (8)$$
$$T_1(0,t) = T_1^0(z) \quad (9)$$
$$T_3(2L,t) = T_3^{2L}(z) \quad (10)$$

The temperatures of the internal fluid, the external fluid of the co-current heat exchanger, the environment temperature and the external fluid of the counter current heat exchanger are defined, respectively, in the following zones:

$T, \quad z \in \Omega_1 = (0,2L)$
$T_1, \quad z \in \Omega_2 = (0, L-\mu)$
$T_2, \quad z \in [L-\mu, L+\mu]$
$T_3, \quad z \in \Omega_3 = (L+\mu, 2L)$

Such as $T(z,t)$, $T_1(z,t)$, $T_3(z,t) \in \mathcal{L}_2([0,2L])$. $\mathcal{L}_2(.)$is the space of square-integrable functions in interval[0,2L]. v_0, v_1, and v_3, are the velocities of the internal fluid, the external fluid of the co-current heat exchanger and the external fluid of the counter-current heat exchanger respectively.$h_i$are the heat transfer coefficients. $t \in [0,\infty) \subset \Re$and$z \in [0,2L] \subset \Re$ are the time and spatial variables, respectively.$\Re$is the set of real numbers.

The open-loop simulation is performed using the method of lines. This method consists in transforming the EDP's into ordinary differential equations by discretizing them with respect to the space variable z [15]. Method of lines principle is based on dividing the space domain Ω into N points, using a discretization stepΔz. Then, a finite difference scheme will be chosen to discretize the partial derivative with respect to $z$leading to a Lumped parameter system (LPS) of dimension$N$.
For open-loop simulation, the finite difference scheme used is givenas follow:

$$\frac{\partial X(z_J,t)}{\partial z} = \frac{X(z_J,t) - X(z_{J-1},t)}{\Delta z} \quad j = 1,\dots,N \quad (11)$$

The parameters of the heat exchanger network are given in Table 1 as follow:

Table 1: Exchanger network parameters

Parameter	h_1	h_2	h_3	v_0	$\boldsymbol{v_1}$	v_3	μ
value	$1s^{-1}$	$1s^{-1}$	$2s^{-1}$	$2ms^{-1}$	$5ms^{-1}$	$1ms^{-1}$	0.16m
Parameter	N	L					
value	100	2m					

The values of the inlet fluid temperatures are given in the following Table

Table 2: Boundary condition values

Boundary condition	$T^0(z)$	$T_1^0(z)$	T_3^{2L}
Value	25°C	50 °C	70°C

For the given parameters and boundary conditions values, the spatial temperature profiles in the heat exchanger network are shown in Figure 2. Note, that thespatial temperature profiles of the exchanger network are a series of two heat exchangers temperatureprofiles, the co-current and counter-current, respectively. The internal tube contact with the environment causes a drop in the internal fluidtemperature.

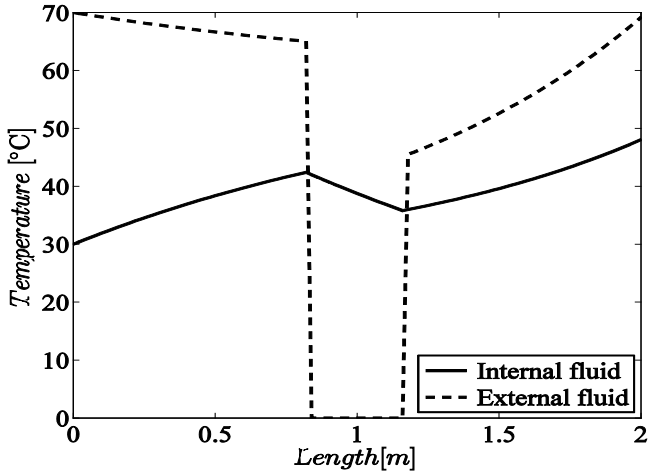

Fig.2. Open-loop spatial temperature profiles of the heat exchanger network.

III. CONTROL APPROACH DESIGN

In this section, divided in two parts, we propose our control approach. We formulate at first the control problem then we develop in more details the control design.

A. *Control problem formulation*

The main purpose of controlling heat exchangers is to maintain an output temperature fluid at a desired value. In this work, the objective is to control the internal fluid temperature at the boundary$z = 2L$, by manipulating its velocityv_0.

The controlled output and the manipulated variable are given, respectively, as follows:

$$y(t) = T(z,t)|_{z=2L} \quad (12)$$

$$u(t) = v_0(t) \quad (13)$$

The choice of the fluid velocity as a control variable leads to a particular class of nonlinear DPS's called the bilinear systems [5].

B. *Control law design*

The control strategy is developed using the geometric control, introduced in [9]and based on the characteristic index, denotedρ, following the late lumping approach. The geometric control is an interesting and appropriate approach for designing control laws for DPS's following the late lumping approach. This strategy consists on the design of the control laws directly using PDE's, which leads to a distributed controller that improves the performance of closed-loop system [9], [11].

The characteristic index represents the smallest order of the time derivative of the controlled output $y(t)$when the manipulated variable$u(t)$appears explicitly [9]. For this, the first time derivative of the controlled output is calculated as follow:

$$\frac{dy(t)}{dt} = \frac{\partial T(z,t)}{\partial t}\Big|_{z=2L}$$

$$= -v_0(t)\frac{\partial T(z,t)}{\partial z} + h_1(T_1(2L,t) - T(2L,t)) + h_2\big(T_2(2L,t) - T(2L,t)\big) + h_3\big(T_3(2L,t) - T(2L,t)\big) \quad (14)$$

The coefficients $h_1 = h_2 = 0$at the boundary$z = 2L$then,

$$\frac{\partial T(z,t)}{\partial t}\Big|_{z=2L} = -\underbrace{v_0(t)}_{u(t)}\frac{\partial T(z,t)}{\partial z}\Big|_{z=2L} + h_3\big(T_3(2L,t) - T(2L,t)\big) \quad (15)$$

The spatial temperature profile of the internal fluid is not constant then,

$$\frac{\partial T}{\partial z}\Big|_{z=2L} \neq 0 \quad (16)$$

The manipulated variable appears linearly in the first time derivative of the controlled output. Consequently, the characteristic index $\rho$is equal to 1.

A first order dynamic behavior will be imposed, in closed-loop, between the desired set-point $T_d(t)$ and the controlled output $y(t)$given as follows,

$$\tau\frac{dy(t)}{dt} + y(t) + T_d(t) \quad (17)$$

where$\tau$is a desired time constant in closed-loop.

Thereafter, the substitution of first time derivative of the controlled output $y(t)$ by its expression given in Equation (15) into Equation (17), yields:

$$\tau\left[-v_0\frac{\partial T(z,t)}{\partial z}\Big|_{z=2L} + h_3\big(T_3(z,t) - T(z,t)\big)\Big|_{z=2L}\right] + y(t) = T_d(t) \quad (18)$$

According to the Equation (18), the expression of the control law is deduced and given as follows

$$v_0(t) = -\left[\frac{T_d(t) - y(t) - h_3\big(T_3(z,t) - T(z,t)\big)\big|_{z=2L}}{\tau\frac{\partial T(z,t)}{\partial z}\Big|_{z=2L}}\right] \quad (19)$$

V. SIMULATION RESULTS

In order to evaluate the effectiveness of the control law given in Equation (19), by simulation, the method of lines is used. The exchanger network parametersand the boundary

conditions values are given in Table 1 and Table 2, respectively.

To avoid undesirable behavior of the controlled output y(t) caused by sudden changes of the set point $T_d(t)$, a first order filter, given by the following equation, is used to smooth the controlled output

$$\tau \frac{dT_f(t)}{dt} + T_f(t) = T_d(t) \qquad (20)$$

T_f is the filtered set point and τ_f is the time constant of the filter. The filtered control law is then written as follows

$$v_0(t) = -\left[\frac{T_f(t) - y(t) - h_3\left(T_3(z,t) - T(z,t)\right)\big|_{z=2L}}{\tau \frac{\partial T(z,t)}{\partial z}\Big|_{z=2L}}\right] \qquad (21)$$

Two simulation tests namely trajectory tracking and the disturbance rejection for two different values of μ are performed. The aim is to evaluate the ability of the control law, given by Equation (21), to reach the objective fixed in each of the simulation tests when μ is important (a significant drop in the internal fluid temperature appears).

A. Trajectory Tracking

The first simulation test is done when the desired output is varied. Therefore, two set points $T_d(t) = 65$ °C and $T_d(t) = 50$ °C are imposed at $t = 10$s and $t = 100$s respectively. For $\mu = 0.16$m, Figure 3 shows that the controlled output $y(t)$ tracks suitably the set point $T_d(t)$. The variations of the manipulated variable $u(t)$ shown on Figure 4, are admissible. The temperature profiles obtained at time $t = 200$s are realist as illustrated on Figure 5. The trajectory tracking is also performed when $\mu = 0.24$m, as shown in Figure 6, with a low variation of the manipulated variable (see Figure 7). In this case, the temperature profiles are given by Figure 8.

B. Distrubance rejection

In practice, all systems are subject to disturbances during their operation. Consequently, it is necessary to evaluate their influences on the system dynamics in closed-loop.This is indeed done in the second simulation test.

The test consists in applying a variation of −50% on both the velocity v_1 of the external fluid of the co-current heat exchanger and the velocity v_3 of the external fluid of the counter current heat exchanger at $t = 200$s which are now considered as a disturbance. Figure9 and Figure 12 show that the controlled output $y(t)$ is not affected by the disturbance for $\mu = 0.16$m and $\mu = 0.24$m, respectively. For this, an insignificant variation is produced on the manipulated variable shown in Figure 10 and Figure 13 for $\mu = 0.16$m and $\mu = 0.24$m,respectively. The temperature profiles obtained at time $t = 200$ s are realist as we can notice from Figure 11 and Figure 14 for $\mu = 0.16$m and $\mu = 0.24$m,respectively.

V. CONCLUSION

In this paper, a distributed state feedback controller is developed to control the internal fluid temperature at the boundary of a heat exchanger network, described by a set of PDE's, when the velocity is assumed as the manipulated variable.

The control problem formulated leads, in a closed loop, to a bilinear DPS. The controller is designed in the framework of the geometric control theory, based on the characteristic index, using directly the PDE's without any approximation. The simulation results show the effectiveness of the control law designed for the trajectory tracking problem and disturbance rejection. This is verified in case of an important value of μ.

REFERENCES

[1] T. KAKAC and H. LIU,"Heat exchangers selection, rating and thermaldesign," CRC Press, USA, 2002.

[2] S. POHJOLAINEN and I. LATTI, "Robust controller for boundary control systems," International Journal of Control, vol.38(6), pp.1189-1197, 1983.

[3] A. MAIDI, M. DIAF andJ-P.CORRIOU, "Boundary control of parallel-flow heat exchanger by input-output linearization,"Journal of Process Control, vol. 20(10), pp.1161–1174, 2010.

[4] E. BUHLERand D. FRANKE, "Topics in identification and distributed parameter systems," Springer Fachmedien Wiesbaden, 1980.

[5] N. HABRACHE, A. MAIDI and J-P.CORRIOU, "Feedback control of bilinear distributed parameter system by input-output linearization,"International Journal of Modeling, Identification and Control, vol. 31(4), pp. 323-330, 2019.

[6] M. OUZAHRA, "Stabilization with Decay Estimate for a Class of Distributed Bilinear Systems," European Journal of Control, vol. 5(10), pp. 509-515, 2007.

[7] J. P. BABARY and W. PELCZEWSKY, " Commande optimale des systèmes continus déterministes," Masson, Paris, 1985.

[8] W. H. RAY, "Advanced Process Control," Butterworth's, Boston, 1989.

[9] PD. CHRISTOFIDES and P. DAOUTIDIS, "Feedback control of hyperbolic PDE systems,"AIChE Journal,vol. 42(11), pp.3063–3086, 1996.

[10] A. EL JAI and M. AMOUROUX, "Automatique des Systèmes Distribués,"Hermes, Paris, 1990.

[11] A. MAIDI and J. -P. CORRIOU, " Distributed control of nonlinear diffusion systems by input-output linearization,"International Journal of Robustand Nonlinear Control, vol.24(3), pp.389-405, 2014.

[12] A. MAIDI, M. DIAF and J-P. CORRIOU, " Boundary geometric control of a counter-current heat exchanger,"Journal of Process Control, vol. 19(2), pp. 297-313, 2009.

[13] H. SANO, "Output tracking control of a parallel-flow heat exchange process,"Systems and Control Letters, vol. 60(11), pp.917-921, 2011.

[14] Y. TOURE and L. JOSSERAND, "Semigroupformalism and internal model control for a heatexchanger,"Revue électronique des sciences ettechnologies de l'automatique, e-STA, vol. 1(2), 2004.

[15] A. VANDE WOUWER, Ph. SAUCEZ, and W. E. SCHIESSER, "Adaptive Method of Lines," Chapman and Hall/CRC,New York, 2001.

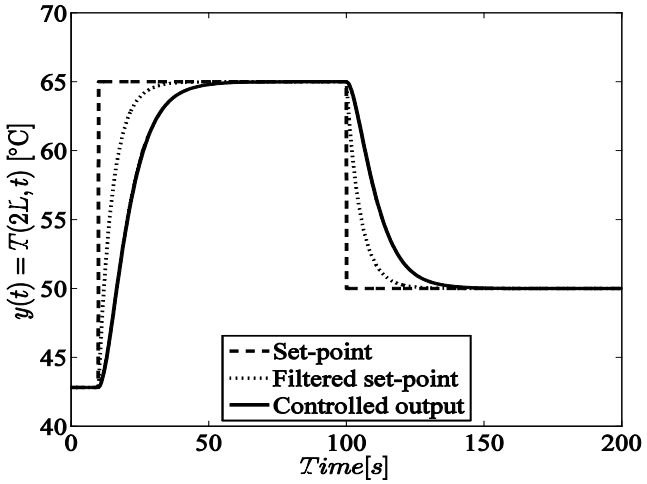

Fig. 3. Tracking problem: evolution of the controlled output T(2L, t) with μ = 0.16m.

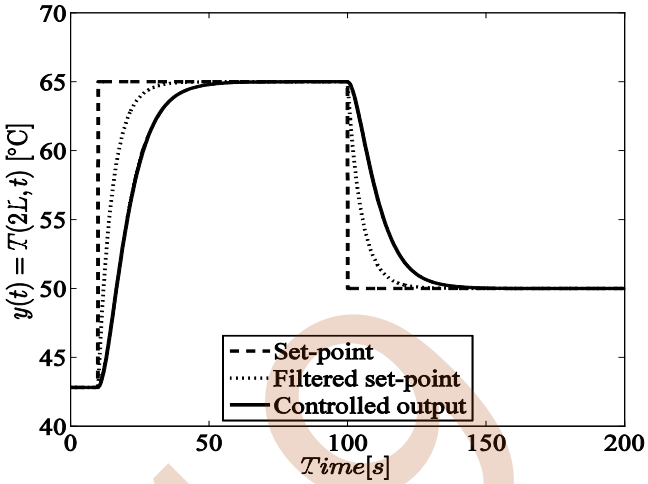

Fig. 6. Tracking problem: evolution of the controlled output T(2L, t) with μ = 0.24m.

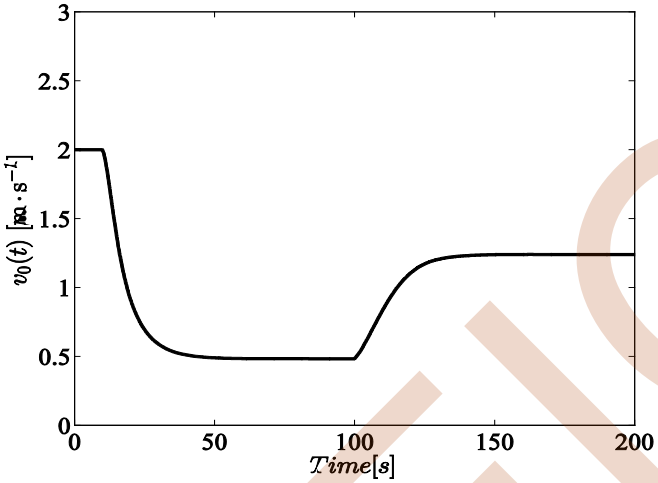

Fig. 4. Tracking problem: evolution of the manipulated variable $v_0(t)$ with μ = 0.16m.

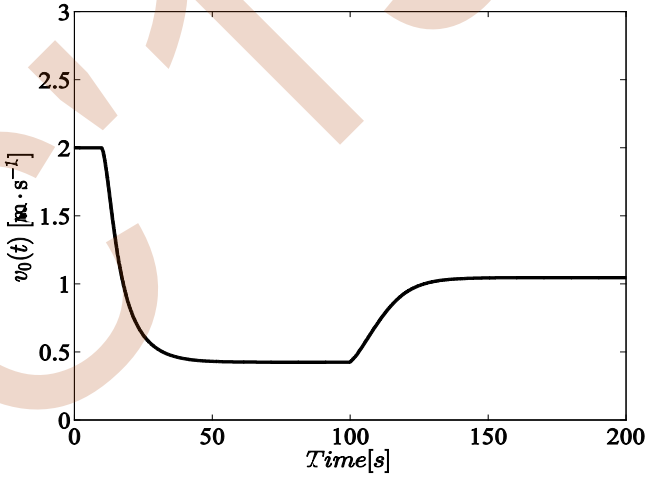

Fig. 7. Tracking problem: evolution of the manipulated variable $v_0(t)$ with μ = 0.24m.

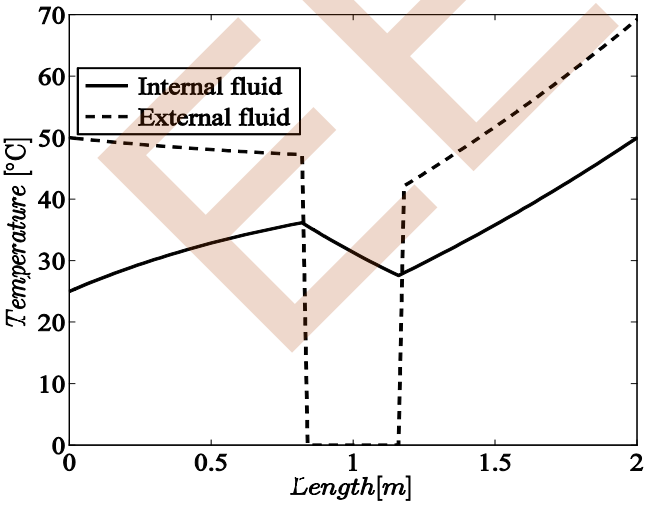

Fig. 5.Tracking problem: spatial temperature profiles at t=200s with μ = 0.16m.

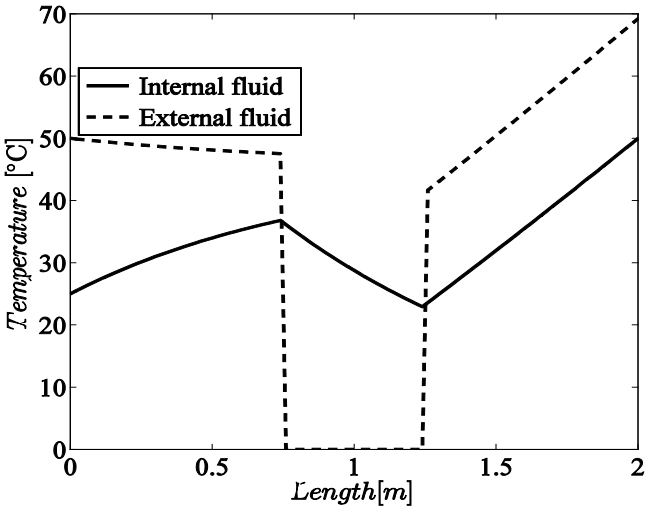

Fig. 8.Tracking problem: spatial temperature profiles at t=200s with μ = 0.24m.

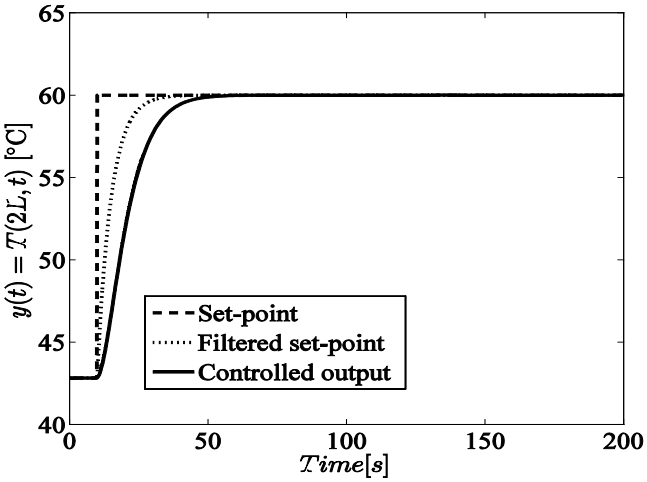

Fig. 9. Regulation problem: evolution of the controlled output T(2L, t) withμ = 0.16m.

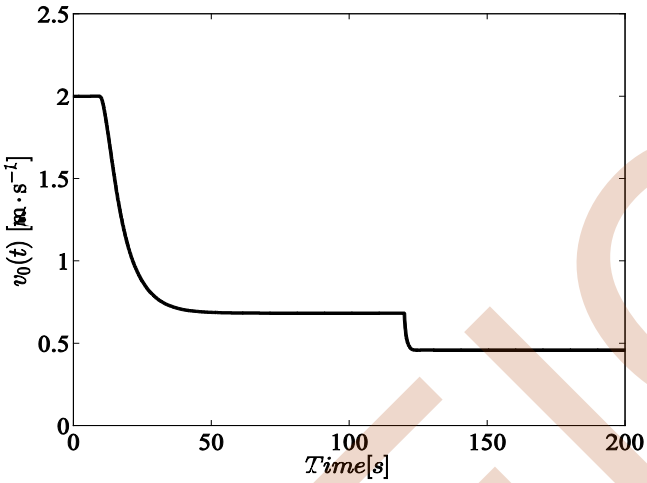

Fig. 10. Regulation problem: evolution of the manipulated variable $v_0(t)$ with μ = 0.16m.

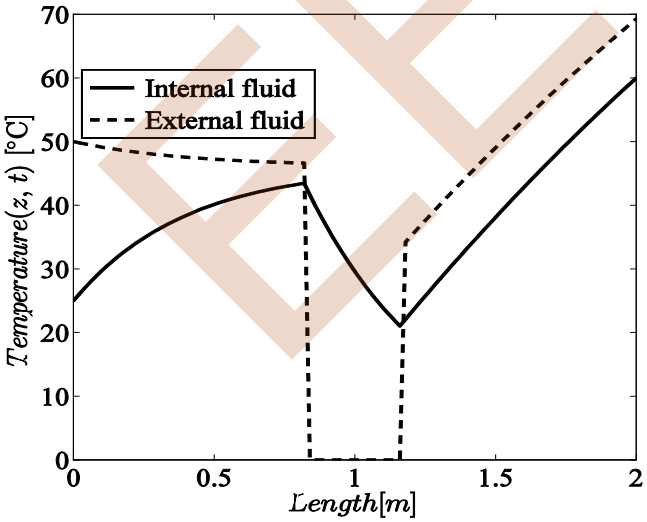

Fig. 11.Regulation problem: spatial temperature profiles at t = 200s withμ = 0.16m.

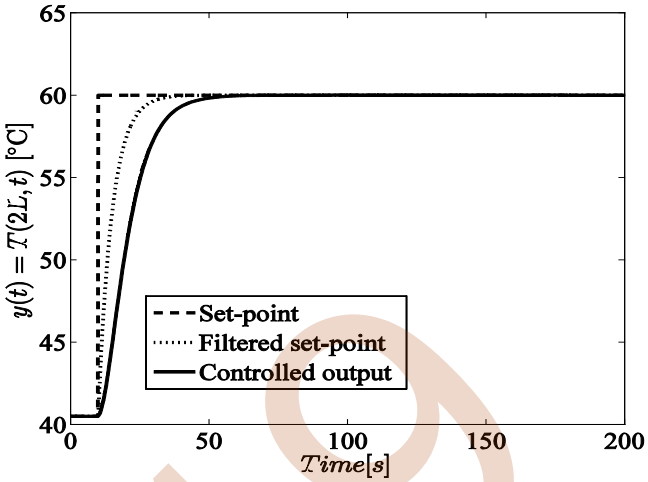

Fig. 12. Regulation problem: evolution of the controlled output T(2L, t) withμ = 0.24m.

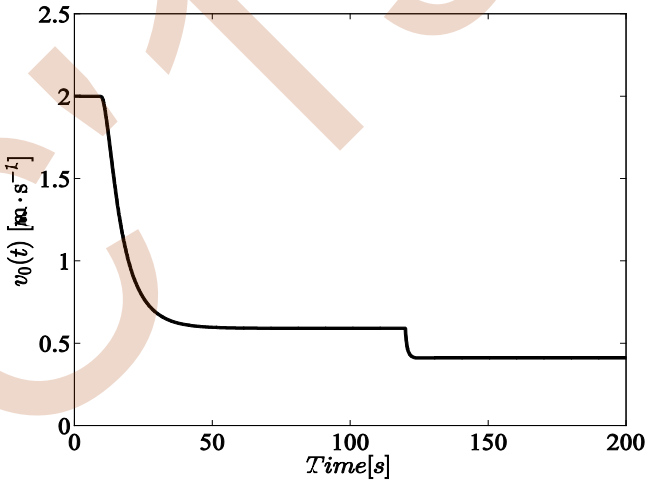

Fig. 13. Regulation problem: evolution of the manipulated variable $v_0(t)$ with μ = 0.24m.

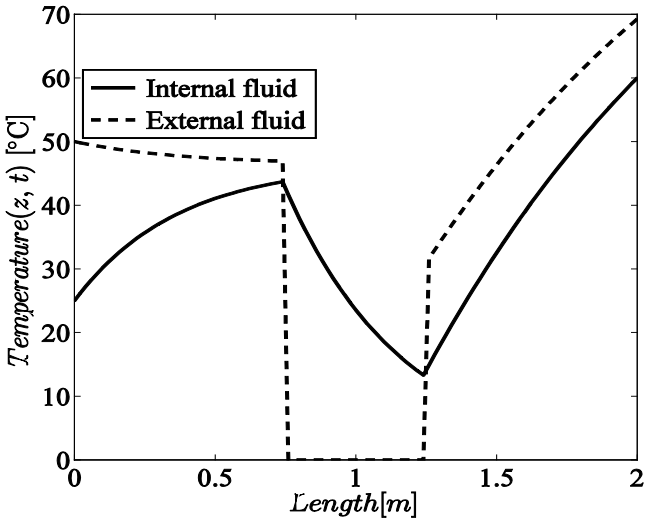

Fig. 14. Regulation problem: spatial temperature profiles at t = 200s withμ = 0.24m.

Performance Comparison of APD and PIN Photodiodes using RZ and NRZ

Hadjira HAMADOUCHE
Department of Electrical Engineering
Mustapha Stambouli University of Mascara, Algeria
hadjira.hamadouche@univ-mascara.dz
LSTE Lab, Mascara univ, Algeria

Boualem MERABET
Department of Electrical Engineering
Mustapha Stambouli University of Mascara, Algeria
b.merabet@univ-mascara.dz

Mouweffeq BOUREGAA
Department of Electrical Engineering
Mustapha Stambouli University of Mascara, Algeria
m.bouregaa@univ-mascara.dz

Abstract— In this paper, we have studied the quality factor (Q), bit error rate (BER) and eye diagram of a gigabyte passive optical network (GPON) used modulation formats, and compare Q, BER performance. Analysis performed for non return to zero (NRZ) and RZ line codes by using avalanche photo diode (APD) and P-Insulator-N (PIN) photodiodes receivers, revealed an improved Q-Factor by changing encoding techniques at different length optical fiber, bit rate, CW laser power and number of users.

Keywords— EDFA, FTTH, GPON , BER, Q-Factor, APD, PIN, Optisystem.

I. INTRODUCTION

Predicting the performance of fiber optic communication systems through numerical simulations has began to be an increasingly important way to complement expensive system experiments, and explore large variations in system designs that are difficult to study experimentally. Measuring an optical signal quality is the most important task in optical communication systems. Optical system quality evaluated by Q-factor BER is mainly depending on input power, bit rate, channel length, modulator, wavelength and receiver type [1]. Hence, the capacity demands for data transmission and optical fiber communication (OFC) technology have undergone an enormous growth. During long distance transmission in OFC systems, light signals get attenuated; and to recover from this problem we need an optical amplifier such as erbium doped fiber amplifiers (EDFA) [2]. In this paper the system performance is measured in terms of Q-factor, BER and eye diagram by varying the system component with and without EDFA[1], The network layout is designed and simulated with Optisystem 7 software.

II. FTTH-GPON SYSTEM

Optical line terminals (OLTs), optical splitters and optical network terminals (ONTs) are the three main components of fiber to the home (FTTH)-GPON access network (Fig.1):

- OLT is the main element of a network, usually placed in the local exchange, and the engine driving the FTTH-GPON system. Traffic planning [3].
- Splitter having one input from port and multiple output ports is passive because it requires no external energy source other than the incident light beam. It is only add loss and broadband, mostly due to the fact that it divides the input (downstream) power. Such loss is called "splitter loss" or "splitting ratio"[3].
- ONT, deployed at the customer premises, is connected to the OLT by means of optical fiber and no active elements are present in the link [3].

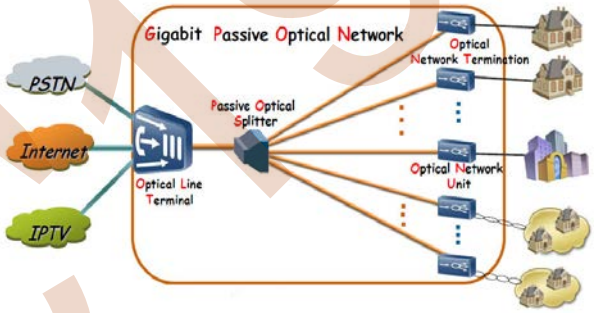

Fig. 1. FTTH-GPON network (Ref .1)

The system could degrade becoming weaker in the channel, and signal is hence attenuated when some part of this is lost, and we need for that to use EDFAs. Using Optisystem software different modulation formats have been made, such as RZ and NRZ, and a comparison between both photodiodes APD and PIN photodiodes has been here performed [2].

1. EDFA

Because of its high gain and low noise feature, a great preference is given to the EDFA that enhances the quality of the signal and it helps to encounter the problems like attenuation and distortion, due to the used doping material: erbium (Er). EDFA has two bands named as L-Band and C-Band, which are very commonly used these days, and a uniform gain at the wavelength range of 1550nm, hence it is the most suitable amplifier for this wavelength[2].

2. PIN Photodiode

PIN consists of three zones: the first zone in order to create a hole excess is called as P-doped, the second zone has an intrinsic region called absorption zone and the third zone is N-doped which creates an electron excess[4].

3.APD Photodiode

The avalanche effect is used to multiply the electrons in a photodiode. Such effect is used to increase the electrical signal power by generating several photoelectrons.[5] APDs are widely used in laser-based fiber optic systems to convert

optical data into electrical form. They are high-sensitivity, high-speed semiconductor light sensors[6].

III. SIMULATION SETUP

The study of Q-factor and BER of GPON using Optisystem is summarized in Fig. 2 showing an EDFA schematic design in GPON system, s that consists of :

- Transmitter section including a pseudo random bit sequence generator (PRBSG), a continuous wave (CW) laser whose frequency and input power 0 dBm are respectively 193.1THz, an NRZ pulse generator (PG) and a Mach-Zehnder modulator

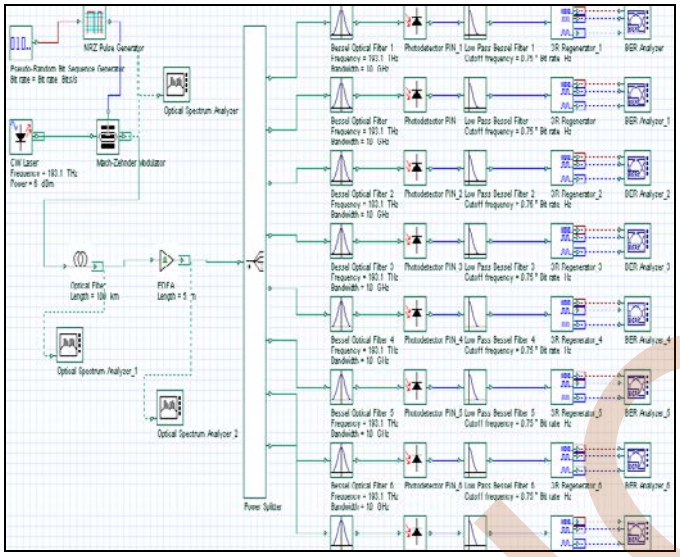

Fig 2 . FTTH-GPON simulation setup

- Channel section :

Optical fiber with length and attenuation of 100Km and 0.2dB/Km and an EDFA whose length is 5m.

- Receiver section which consists of a Bessel optical filter whose frequency and bandwidth of 193.1THz and 10GHz respectively, a PIN photo- detector, a low pass Bessel filter (LPBF), with a Cut off frequency of 0.75*Bit, a rate and 3R Regenerator, and a BER Analyzer.

A. Q- factor

Q-factor is a parameter that directly shows the quality of the optical communication system, indicating how good (low loss) the system quality will be. The high the value of Q, better the quality of the system. Q-factor should be the best judgment, defined as the ratio of the signal and noise [3] :

$$Q = \frac{|\mu_1 - \mu_0|}{\sigma_1 + \sigma_0} \qquad (1)$$

where $|\mu_1-\mu_0|$ denotes the separation between the intensity levels of "1" and "0", and $\sigma_1+\sigma_0$ is the sum of the standard deviations of the intensities around the levels of "1" and "0". Based on the Gaussian approximation for the noise distribution in the received signal.

B. BER

BER is one of a key indicator to measure optical properties, in terms of which the system performance is estimated. It is not counted directly but measured by the evaluation of statistical fluctuations that are characterized by Q-factor as:

$$BER = \frac{1}{2} erfc\left(\frac{Q}{\sqrt{2}}\right) = \frac{1}{\sqrt{2\pi}} \frac{1}{Q} e^{-\frac{Q^2}{2}} \qquad (2)$$

A transmission might have a BER of 10^{-6} for example., means that out of 1,000,000 bits transmitted, one bit was in error [2].

IV. RESULTS AND DISCUSSION

1 / GPON with and without EDFA(8 Users)

Fig 3 shows the results of the optical fiber input which power is 0 dBm (*a*), optical fiber output whose power is -20 dBm (*b*), and EDFA amplifier output which is maximum value 0 dBm, but inversely in terms of noise figure(*c*).

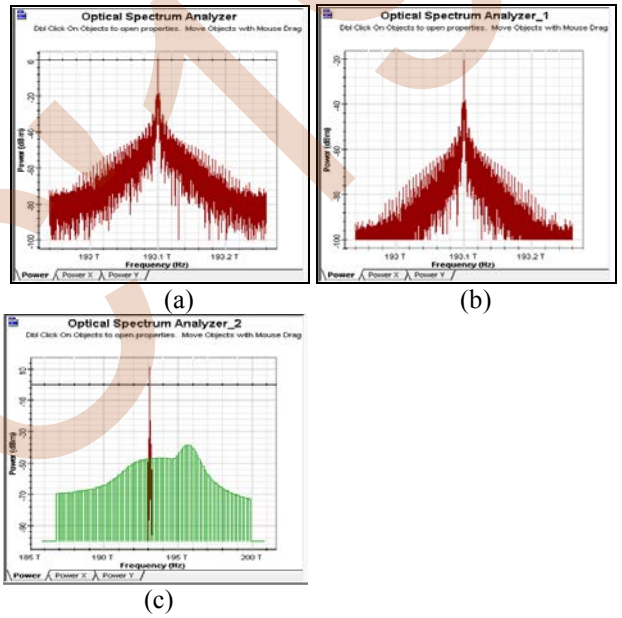

(a) (b)

(c)

Fig 3: Optical Spectrum Analyzer (*a*) Optical fiber input , (*b*) Optical fiber Output, and (*c*) EDFA Output.

The green curve in the graph represents the noise, while the red one shows the sample wavelength. Bit Rate used was 8 Gbps. Analyzing results, it can be concluded that EDFA should be used to compensate the loss of optical signal to increase the transmission length. In this model we are analyzing the Q-factor and BER by varying fiber length between 20 Km and 200Km (see Fig.4).

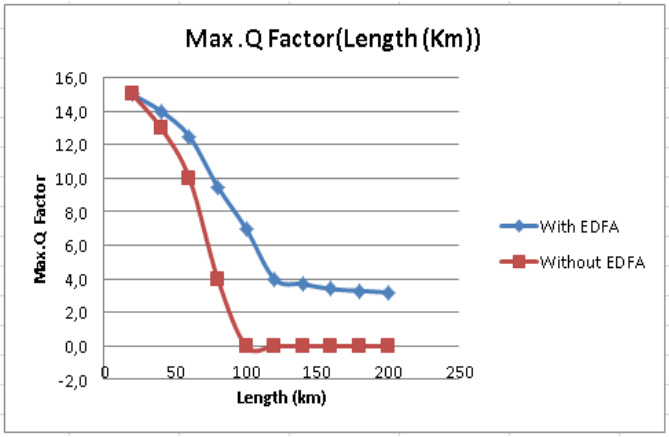

Fig4. Q factor vs. L with and without using EDFA

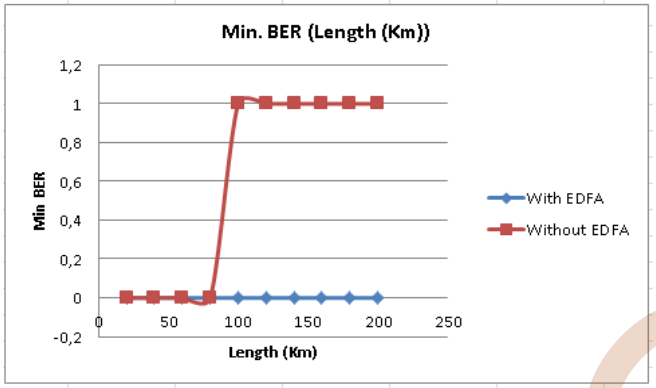

Fig 5. Min BER vs. L with and without using EDFA.

As appearing (Fig. 4 and 5), Q-factor and BER performance by using EDFA is better than without using it.

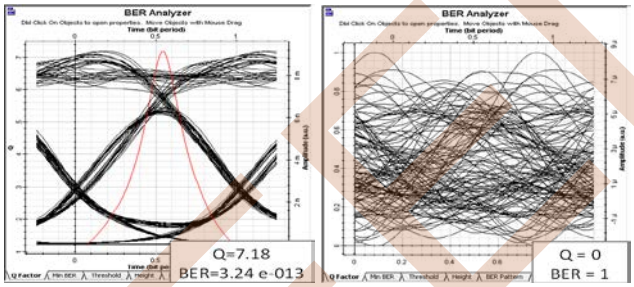

(a) (b)

Fig 6. Eye diagram of downlink shown in BER analyzer (the red curve shows Q-factor) for L=100Km (a) with EDFA, (b) without EDFA.

2 / GPON with EDFA (32 users)

Our model has analyzed the Q-factor and BER, using PIN and APD, and NRZ and RZ modulation formats.

A. Impact of CW laser Power :

To estimate the impact of power CW laser, simulated Q-factors and BER are shown for different transmitted powers (P) varying from -6 to10dBm, with a data rate set at 8Gbps for a link length of 60km and 100Km. For a users' number of 32 communicating simultaneously, the results show a signal quality increasing and a BER decreasing when P increases (Fig. 7 (a, b) and Fig. 8 (a, b)).

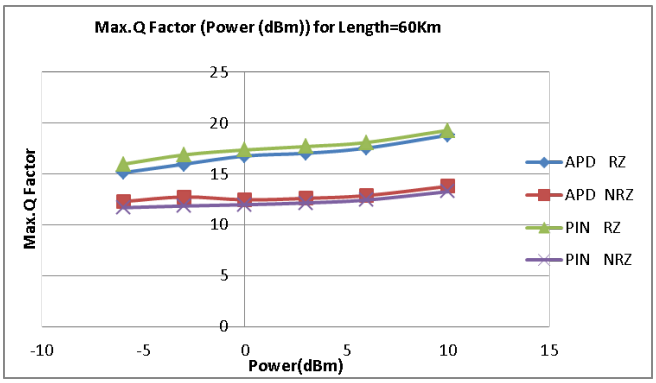

(a)

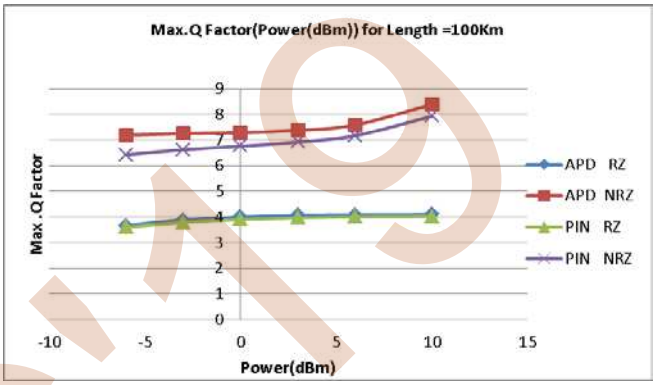

(*b*)

Fig 7. Max Q-factor vs P with and without using EDFA, for: a) L = 60Km, b) L = 100Km.

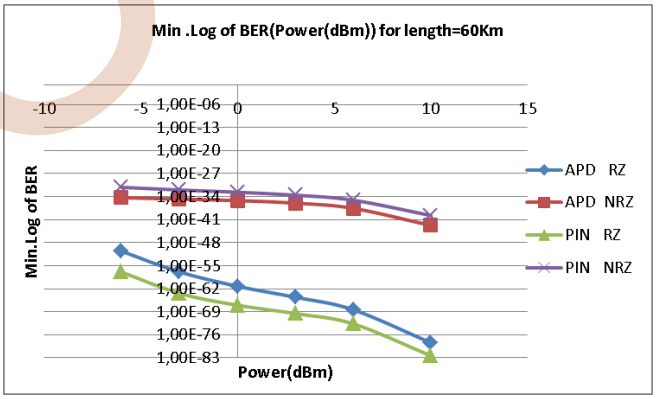

(a)

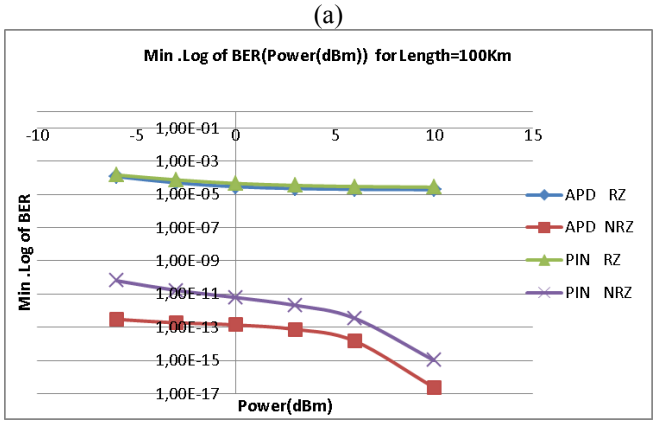

(b)

Fig8. Min Log of BER *vs* P with and without using EDFA, for (a) L = 60Km, (b) L = 100Km.

Fig. 7 and 8 show that the BER and Q-factor performance of the modulation RZ and NRZ by using PIN and APD is shown in Figure 7 and 8. One can clearly mention that using modulation RZ with APD and PIN is suitable for the system performance for length up to 60Km. For L farther than 60Km (for ex.,100Km) the modulation NRZ with APD and PIN is convenient for the system, and using APD is much better than PIN. As for the eye diagram results, when the data bit rate is 8Gbps, P is about 10dBm and L equals to 60/100Km with APD Photodiodes (see figure 9 (a -d)).

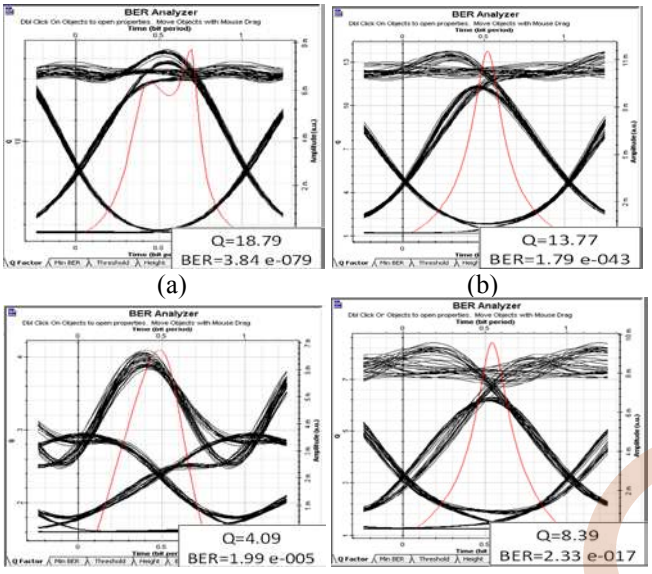

(a) (b)

(c) (d)

Fig 9 . Eye diagram of downlink shown in BER analyzer (the red curve represents Q-factor) using APD with : a) RZ (60Km), b) NRZ(60Km), c) RZ(100Km), d) NRZ(100Km).

B. Impact of Transmission Distance

In the following, we assume that P=6dBm, D=8Gbps and users' number of 32, using PIN photodetectors, are assumed. Fig. 12 (a and b) shows how eye diagrams of downlink changes with fiber lengths of 60 and 100km, respectively. With a transmission distance (i.e. L) varying between 10 and 200Km, the results of Q-factor and BER are shown in Fig. 10 and Fig.11.

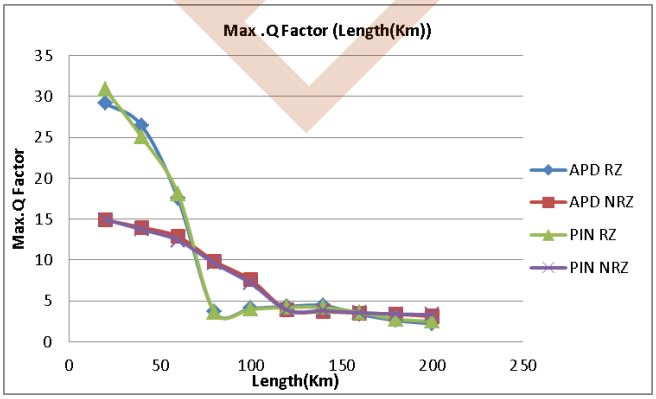

Fig 10. Max Q-factor vs L

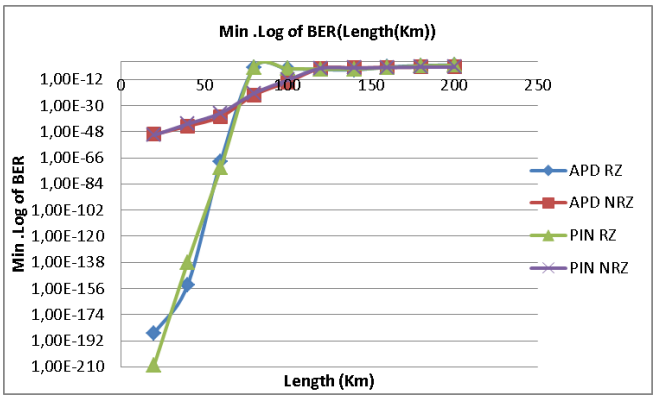

Fig. 11. Min Log of BER *vs* L

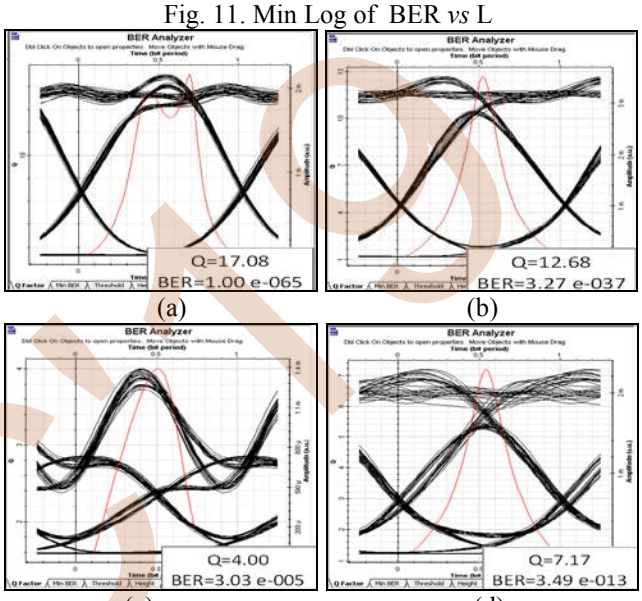

(a) (b)

(c) (d)

Fig. 12. Eye diagram of downlink shown in BER analyzer (red curve represents Q-factor) with PIN: a) RZ (60Km) NRZ(60Km), c) RZ(100Km), d) NRZ(100Km).

Fig. 10 and 11 show that using modulation RZ with APD and PIN is better for the system performance for length up to 60Km. so for lengths beyond 60Km, the modulation NRZ with APD and PIN is more convenient for the system.The modulation NRZ is better than RZ in the long distances.

C. Impact of Bite rate (D)

To evaluate the impact of data rate between the transmitter and receiver, we have studied the performances in terms of Q-factors and BER for different values of D,and P of 6dBm. The results are shown in Fig. 13 and 14.

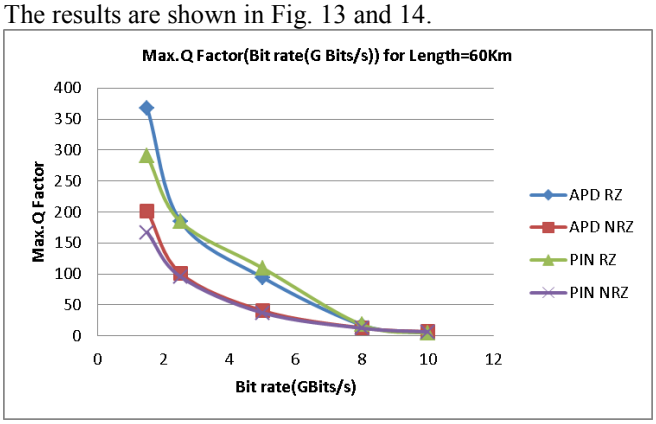

(a)

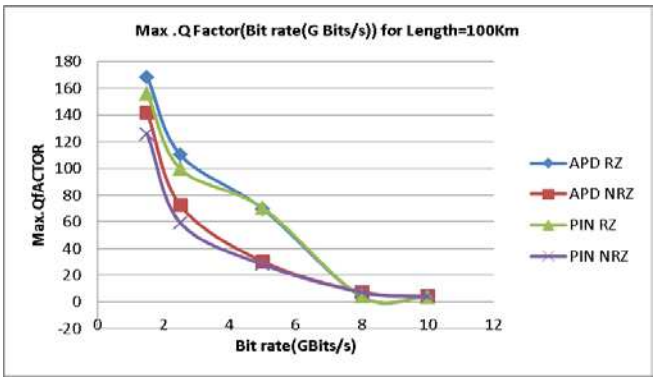

(b)

Fig13. Min Log of BER vs D for L: a) 60Km, b) 100Km.

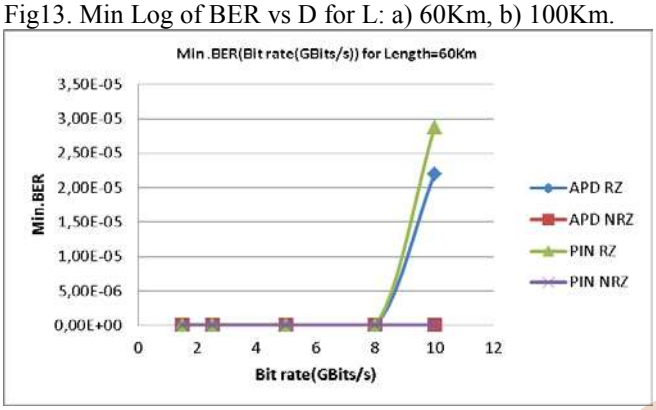

Fig 14. Min Log of BER *vs* D for L=60Km.

Fig. 13 and 14 show a decreasing of the signal quality when the bit rate increases and BER increases. The Q-factor and BER performance are shown in Fig. 13 and 14. One can clearly mention that using RZ modulation with APD and PIN is better for the system performance, and Q-factor performance of APD is higher than that of PIN. Comparing PIN with APD photodiodes reveals that the APD is more advantageous than the PIN photodiode for the low bit rate.

D. Impact of number of users :

To evaluate the performance impact of the number of users, we tested the GPON architecture by calculating Q and BER values for many subscribers simultaneously communicating. We considered the data rate D=8Gbps, power P=6dBm. The simulated results are shown in Fig. 15 and 16.

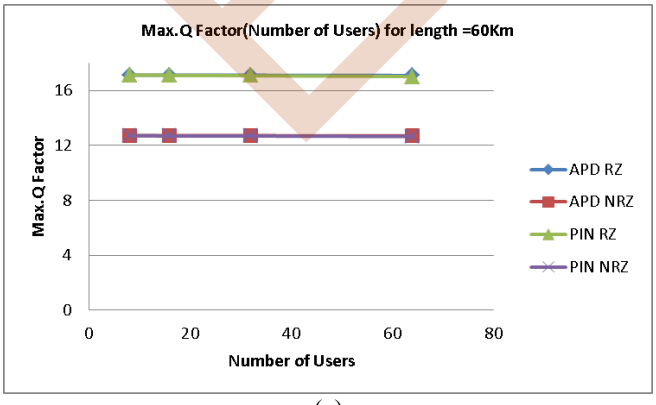

(a)

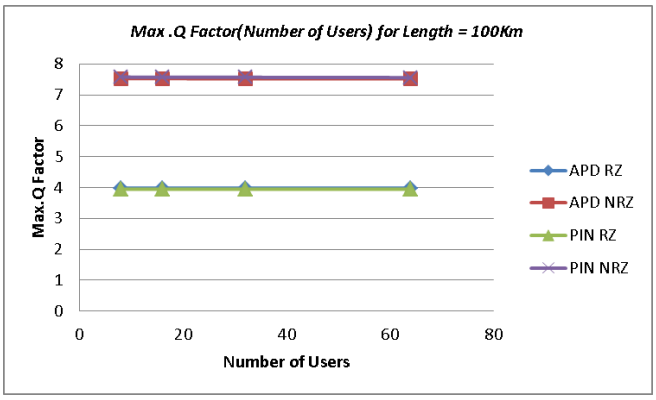

(b)

Fig15. Q-factor *vs* users' number for L: a) 60Km, b) 100Km

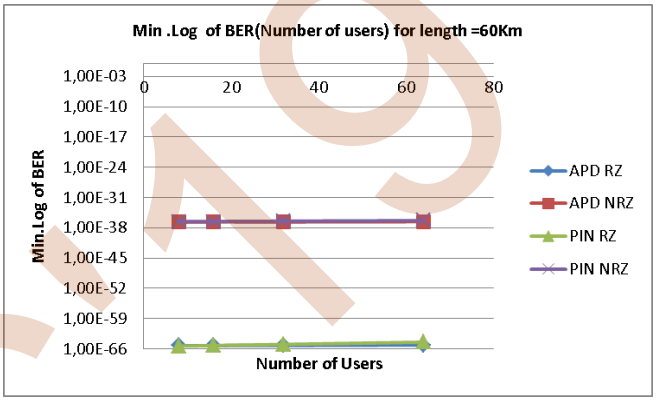

(a)

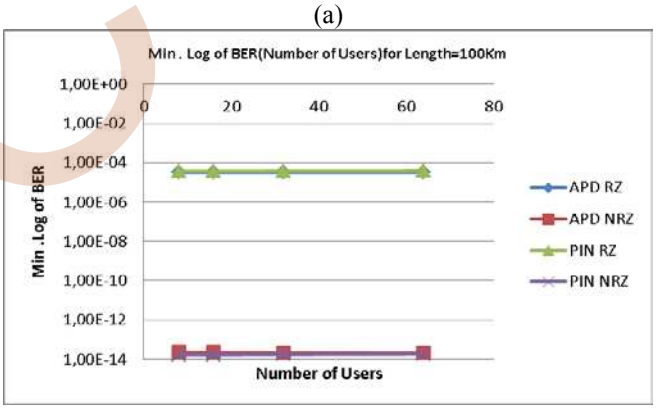

(b)

Fig.16. Min Log of BER vs users' number for L: a) 60Km, b) L=100Km

As shown in Fig. 15 and 16, the use of modulation RZ with APD and PIN is better for the system performance for L up to 60KM, but for L beyond 60KM (for ex.,100Km) the modulation NRZ with APD and PIN is better for the system.

V. CONCLUSION

Optical fiber-based communication as a modern medium of transmission provide high bit rate that fulfill the demand of high speed internet. Performance of GPONs system using different modulation techniques such as NRZ, RZ has been analyzed by Optisystem software with PINs and APDs. The comparison between different modulation technique and Photodiode has been performed and GPON with and

without EDFA reveals a great preference proviede by using EDFA. It can be concluded that EDFA could be used to compensate the optical signal loss in order to increase the transmission length. Using modulation RZ with APD and PIN is much convenient for the system performance for length up to 60Km. For length about100Km, the modulation NRZ with APD and PIN is better for the system. Also, the comparison between the PIN and APD photodiodes prouves that APDs are more advantageous than PINs, especially for a low bit rate, which may provide more effective results for APDs that can show less BER than PINs at similar powers. And the modulation NRZ is better than RZ in the long distances.

REFERENCES

[1] R. Mehra, V. Joshi, Effect on Q Factor of Fixed Bit Pattern and Encoding Techniques in Intensity Modulated Optical Networks, International Journal of Computer Applications (0975 – 8887), Volume 106 – No. 13, November 2014.

[2] J.Gujral and M.Singh, " Performance Analysis of 4-Channel WDM System with and without EDFA", International Journal of Electronics & Communication Technology, IJECT Vol. 4, Issue Spl - 3, April - June 2013

[3] M. Bouregaa, M. Chikh Bled, and M. Debbal, "Optical Code Division Multiple Access for a FTTH system," Journal of Photonics Letters Of Poland, Vol. 10 (4), pp.121-123, 2018.

[4] A.Boudkhil,A.Ouzzan and B.Soudini, Analysis of Fundamental Photodetection Noises and Evaluation of PIN and APD Photodiodes Performances using an Optical High Debit Transmission Chain Simulated by Optisystem, International J. of Computer Applications (0975 – 8887) Vol. 115 No.18, 2015.

[5] I.Mashrur Islam1, A.Shahriar and I. Anisul , "Performance Analysis of 2.5 Gbps PIN and APD Photodiodes to Use in Free Space Optical Communication Link", International Journal of Thin Films Science and Technology, Int. J. Thin.Fil. Sci. Tec. 8, No. 2, 53-58 (2019)

[6] P.Sharma and H.Sarangal, " Perfo rmance Comparison of APD and PIN Photodiodes using Different Modulation and Different Wavelengths",International Journal of Signal Processing, Image Processing and Pattern Recognition, Vol.9, No.4 (2016), pp.257-264.

Plasmonic nano-sensor and band-pass filter based on metal-insulator-metal waveguide with a hexagonal ring based cavity

Hocine Ben salah, Abdesselam Hocini, Djamel Khedrouche, Noureddine Melouki
Laboratoire d'Analyse des Signaux ET Systèmes, Department of Electronics, University of M'Sila, BP.166, Route Ichebilia, M'sila, 28000 Algeria
hocine.bensalah@univ-msila.dz

***Abstract*— In this paper, a high sensitivity metal-insulator-metal (MIM) waveguide based plasmonic sensor, coupled by a hexagonal ring resonator is proposed. The sensing characteristics of the device are analyzed by the finite-difference time-domain (FDTD) method embedded in the commercial simulator R-Soft. The results show a linear correlation between the refractive index of the material and its wavelength resonances. Moreover, the maximum linear sensitivity is S = 1743 nm/RIU for the second mode and it is S = 836 nm/RIU for the first mode, its corresponding sensing resolution is 5.73 × 10^{-6} RIU for mode 2 and 1.19 × 10^{-5} RIU for mode 1. The proposed sensor can be implemented in high performance nano-sensors and bio-sensing devices. The positions of transmission peaks can be easily manipulated by adjusting the inner side lengths of the hexagonal ring resonator, this structure can be used as an adjustable band pass filter. In addition, introducing another small hexagonal ring within the base resonator decreased the full width of half maximum (FWHM) of the resonance peak.**

I. INTRODUCTION

Surface plasmon polaritons (SPPs) are electromagnetic fields propagating along the interface of metal-insulator, and have been of great interest for several decades due to the ability to modulate light in nano-scale, as well as break the diffraction limit [1]. In addition, the size of the SPP based model is so small, that a nanoscale optical transmission, processing, and control can be realized [2, 3]. Optical devices based on SPP waveguide structures have been of a great interest, such as in filters [4], diodes [5], optical switches and sensors [6, 7]. In the field of biomedical and clinical development, surface Plasmon resonance (SPR) sensors have been focused on for a series of applications such as proteins [8], DNA [9], and drugs [10]. Because of their high sensitivity, simple fabrication and their nanoscale size, SPR sensors are used widely to examine and determine the refraction index of a wide range of materials [11, 12]. Among different plasmonic structures, metal-insulator–metal (MIM) based structure is one of the most promising choices for realization of the mentioned requirements [13]. The confinement of light in sub-wavelength insulator regions is highly achievable, so a prominent transmission efficiency and simplicity in fabrication procedure made the MIM-based devices a good candidate in nanoscale photonic devices [14]. As one of the most innovating devices in optical circuits, MIM waveguide based plasmonic sensors and filters for wavelength selection has been investigated numerically and experimentally, and different types of plasmonic sensors and filters such as nanodisk resonators [15], ring resonators [16-19] and tooth-shaped waveguide [7,20].

Plasmonic ring resonators are important components in integrated circuits. They have attracted attention in recent years due to their compactness, high-quality factor, and simplicity of fabrication [21]. Resonance frequencies are highly tunable by dynamically adjusting the ring's geometric parameters [22, 24].

The sensor's sensitivity is one of the most important features that are used to analyze its performance according to the changes of the refraction index in different materials. The goal is to improve the sensitivity factor by applying different topologies in a small area, and to determine the effective sensitivity and transmission characteristics.

In this study, an MIM waveguides coupled with the stub and hexagonal ring resonators based structures, is applied as a plasmonic refractive index nano-sensor. The perfectly matched layer absorbing boundary condition is applied and was calculated using the finite-difference time-domain (FDTD) method implemented in the commercial simulator R-SOFT, we varied the inner side length of the hexagonal ring resonator, and the distance between the hexagonal ring resonator and the waveguide, to study the effect on its sensing characteristics and refractive index sensitivity. The proposed structure showed a promising result in both sensitivity and quality factor, which makes our design a perfect candidate for a tunable band-pass filter and a plasmonic based nano-sensor.

II. THE STRUCTURAL AND THEORETICAL ANALYSIS

The proposed MIM based plasmonic structure is depicted in Figure 1. It consists of a slit (waveguide) with w =50 nm as a width and fixed to that value so the only excited mode is (TM_0) in the MIM waveguides [25], and a hexagonal ring resonator (HRR), with L_1=200nm and L_2 =125nm as an inner and outer side lengths respectively, g =10 nm, is the distance between the HRR and the waveguide, The gray area represents the silver layer and the white one represents the dielectric material. The silver's frequency dependent dielectric constant is calculated and expressed by Lorentz–Drude model [26]:

$$\varepsilon_m(\omega) = \varepsilon_\infty - \frac{\omega_p^2}{\omega(\omega + i\gamma)} \quad (1)$$

Where ε_∞ is the dielectric constant at the infinite angular frequency with a value of 3.7, ω_p is the bulk plasma frequency (ω=1.38 x 10^{16}*Hz*), and γ is the electron collision frequency (γ=2.73 x 10^{13} *Hz*) and ω is the angular frequency of the incident wave in vacuum [27].

The incident light for excitation in our simulation process of the SPP Mode is TM-polarized; this led to the magnetic field being parallel to y axis [28].

The resonance wavelength λm of the single plasmonic hexagonal cavity can be obtained theoretically by [29]:

$$\lambda_m = \frac{(6L_{eff})x\ \mathrm{Re}(n_{eff})}{m - \varphi 2\pi} \quad (2)$$

Where L_{eff} is side lengths of hexagonal cavity, Re (n_{eff}) is the real part of the effective refraction index of the hexagonal cavity. The positive integer m represents the order of the standing SPP wave in the cavity; φ also presents the total phase shift in the corners of the hexagonal cavity.

III. SIMULATION RESULTS

The commercial simulator R-Soft, is used in all carried out simulations, it's based on the FDTD method [30]. The Perfectly Matched Layers (PML) is imposed and applied on the structure to simulate its transmission characteristics, as the absorbing boundary condition for all sides of the computational window to absorb outgoing waves.

The grid size in both the x and z directions were chosen as Δx = Δz = 5 nm [7], with a continuous TM polarized Gaussian modulated wave based input type. The transmitted light was collected at the right side of the waveguide which is defined as T = P_{out}/P_{in}. The incident power Pin and the transmitted power Pout are observed at positions A and B respectively.

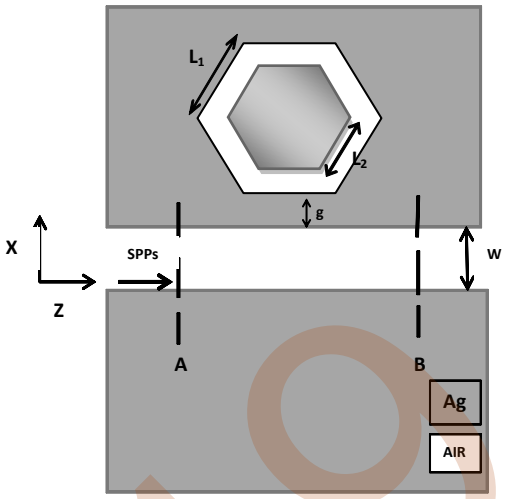

Figure 1. Schematic diagram of the proposed MIM Based plasmonic structure.

First, both the insulator in the dielectric core and the cavities has a refractive index n of 1.

Figure 2(a) Shows the transmission spectra of both the hexagonal based cavity (side length L_1=200nm) and the proposed hexagonal ring resonator (L_1=200nm and L_2=125nm).

The structure with hexagonal shaped cavity exhibits a low transmission peak at the resonance wavelengths of 742.6 nm, whereas the case of the MIM waveguide is coupled with the HRR, the two transmission peaks is observed at the resonance wavelengths of 742.6 nm and 1388.4 nm, corresponding to the first and second resonance modes of the HRR. Figure 2(b) depict the field distributions of $|H_y|$ for the on and off resonance wavelengths of the proposed structure.

It's clearly noticed that the incident light within the wavelengths of both 742.6 nm and 1388.4 nm, couples to the HRRs resonance wavelengths, so it's prohibited to pass through the waveguide, contrary to the rest of the wavelengths which are transmitted to the output.

To investigate the influence of the coupling distance g, we set it as a state variable from 10 nm to 20 nm with a step of 5 nm, while keeping the other structural parameters fixed (L_1=200nm, L_2 =125nm, and n = 1.0).

From Figure 3, it's noted that when the coupling distance g is increased, the wavelengths of the peaks shift slowly towards short wavelengths and the bandwidth become narrower. In the other hand, the maximum transmittances are reduced accordingly, due to the fact that the MIM coupler losses are increased also with increasing of the distance g [31].

Figure 4(a) illustrates the transmission spectra of the proposed structure for different refractive indices varying from 1 to 1.2 in steps of 0.05.

(a)

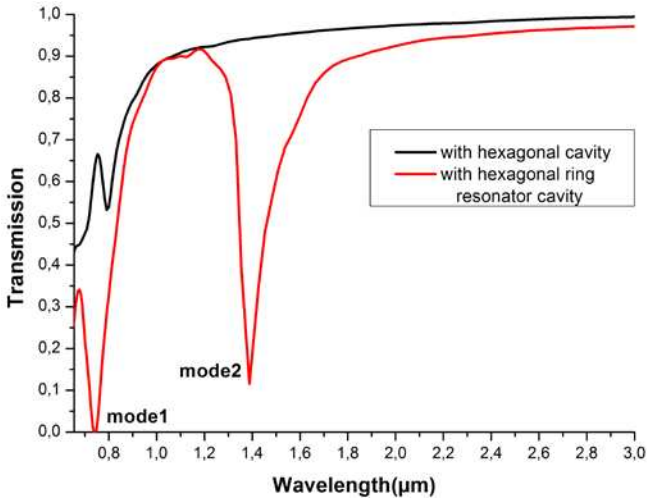

(b)

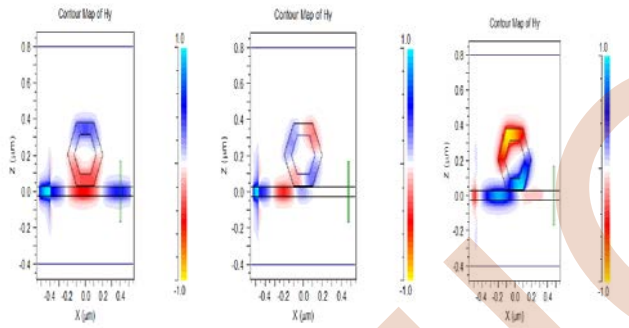

Figure 2. (a) The transmission spectra of MIM plasmonic structure with n = 1, L_1=200nm, L_2=125nm and g=10nm. (b) Magnetic-filed patterns of the MIM plasmonic structure at resonance wavelengths of = 742.6 nm (center), 1338.4 nm (right) and at wavelength 1200nm (left).

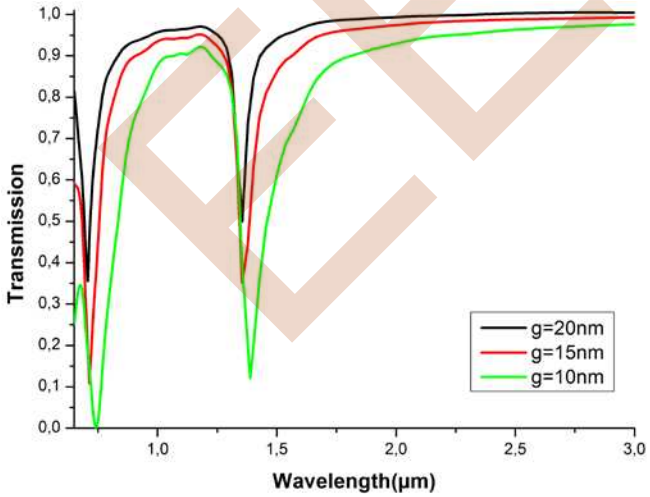

Figure 3. The transmission spectrum of the structure versus wavelength with different coupling distance g at n = 1, L_1=200nm, and L_2=125nm.

Increasing the refractive index n results in a red-shift of resonance wavelengths of the transmitted spectra, with a larger shift in mode 2 in comparison to mode 1. Figure 4(b) represents the maintained linearity relation between the resonance wavelengths and the refractive indices for both the first and the second modes.

Sensitivity (S), is an important aspect in the designing and analyzing of the SPR based sensors, it can be calculated as $S = \Delta\lambda/\Delta n$ (nanometer per refractive index (nm/RIU))[32], where $\Delta\lambda$ denotes the shifting rate of resonant peak wavelength of transmittance, and Δn represents the changing rate in the refraction index in the plasmonic sensor structure. Keeping the other existing parameters fixed, and increasing the refraction index between n = 1 and n = 1.2, the sensitivity for the first mode is around 670 nm/RIU and for the second mode is around 1380 nm/RIU.

(a)

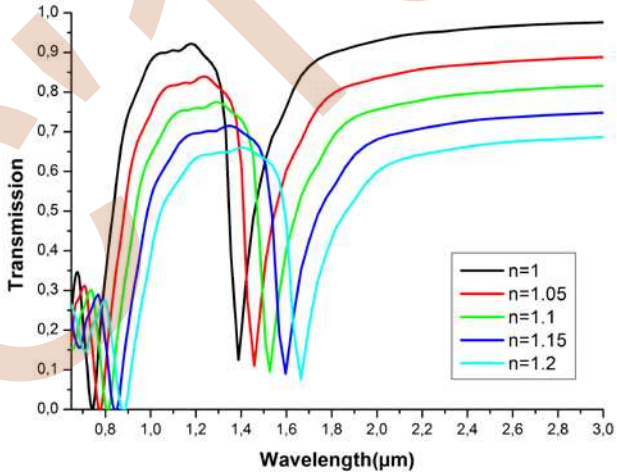

(b)

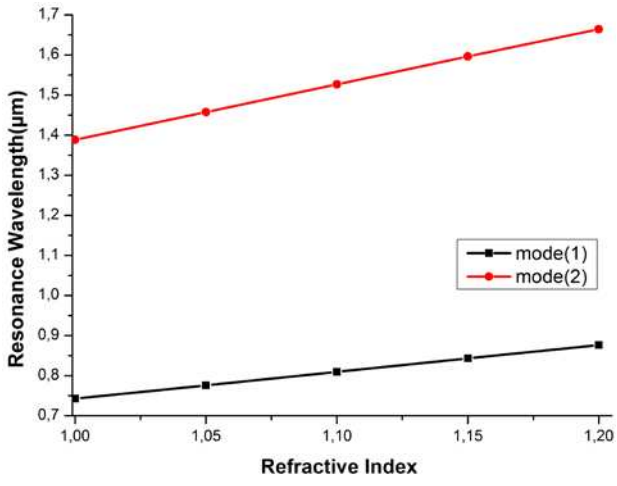

Figure 4. (a) The transmission spectrum of the structure for different refractive index n, (b) the resonance wavelength versus the refractive index n of the material under sensing.

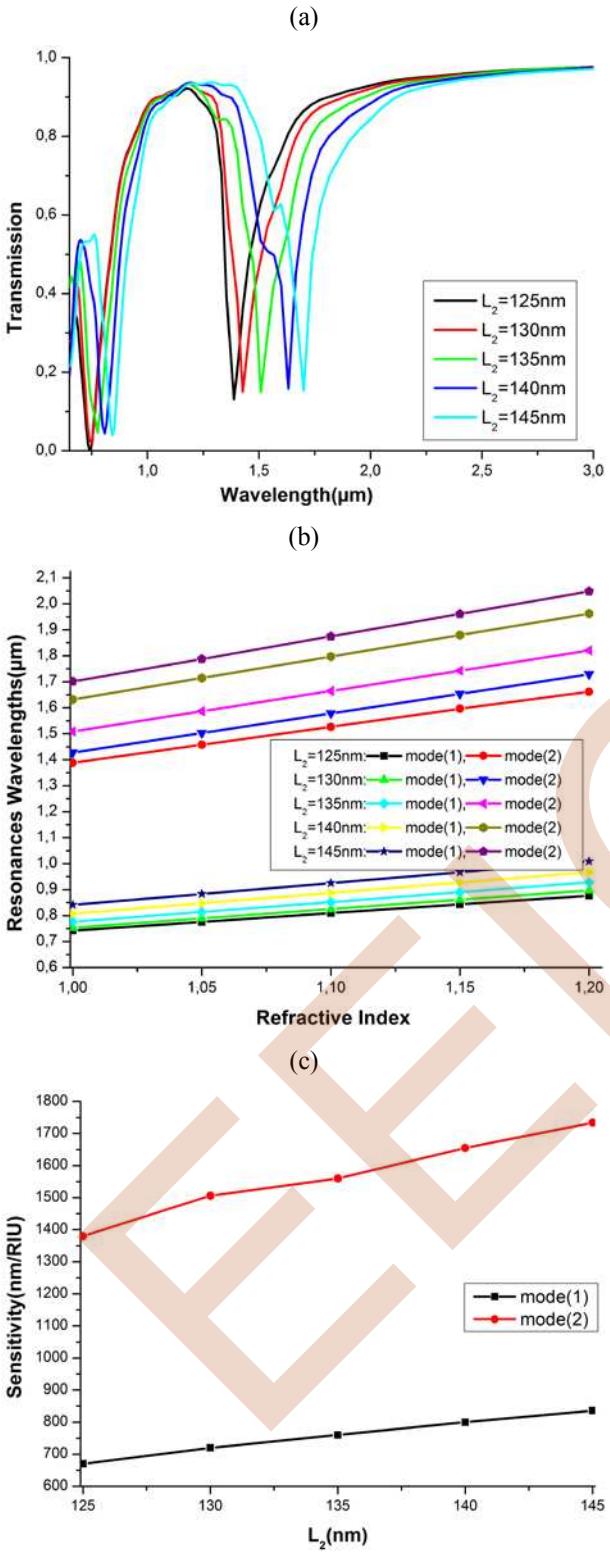

Figure 5. Sensing properties as functions of L_2. (a) Transmission spectra of index 1 for L_2 varying from 125 to 145 nm. (b) The resonance wavelengths versus the refractive index for different L_2. (c) Sensitivities of the plasmonic sensors for L_2 varying from 125 to 145 nm.

In Figure 5, the increase in the value of L_2 from 125 to 145 nm with a step of 5 nm is associated with an increase in the resonance wavelength. Meaning, the value of L_2 causes a shift in resonance wavelength, and the shift for mode 2 is larger than that for mode 1 as shown in Figure 5(a). According to Figure 5(b) the linearity of wavelength resonances versus the refractive indices is maintained in spite of the increase in the value of L_2. Moreover, an enhancement of the sensor's sensitivity is achieved by increasing the value of L_2, for mode 1 the sensitivity is 836 nm/RIU whereas in the case of mode 2, the sensitivity was 1743 nm/RIU, i.e. sensing resolution of 1.19×10^{-5} RIU for mode1 and 5.73×10^{-6} RIU for mode2, is achieved corresponding to value of L_2 =145 nm, in comparison to sensitivity of 670 nm/RIU for mode1 and 1380 nm/RIU for mode2 where the value of L_2 was 125 nm. In Figure 5(c) it is clearly shown that the greater the value of L_2 is, the better the sensor's performance.

The proposed MIM based plasmonic structure can be used as a tunable band-pass filter for a wide range of wavelengths. The positions of transmission peaks can be easily manipulated by adjusting the inner side length of the HRR. As mentioned before, one of the main metrics for a narrow-band filter is its quality factor that depends mainly on its operation bandwidth. So a narrower bandwidth leads to a higher quality factor [33].

Using a secondary hexagonal ring inside the main one, as illustrated in Figure 6, narrowed down the bandwidth, hence the higher quality factors, especially for higher wavelengths discussed previously. Figure 6(a) depicts the proposed hexagonal shaped double-ring resonator with L_3=100nm and L_4=70nm. As illustrated in Figure 6(b), and for the wavelength of λ_r = 1701 nm, this hexagonal shaped double-ring resonator enhanced the quality factor.

The Figure 6(b) shows the output transmission of the filter without using a secondary hexagonal ring resonator with a quality factor of 15. Whereas for the case of employing the secondary hexagonal ring inside the main one, the calculated quality factor after utilizing the proposed method increased to 31, so a promising results for enhancing the quality factor.

Figure 6(c) depict the field distributions of $|H_y|$ for the on and off resonance wavelengths states of the proposed structure. It's clearly observed that the incident light within the wavelength of 841.5nm and 1701 nm, couples the hexagonal shaped double-ring resonator and it's prohibited to pass through the waveguide, while the rest of the wavelengths are transmitted to the output freely.

Table 1 compares the sensitivity (S) for different reported MIM plasmonic sensors in literatures with our present work.

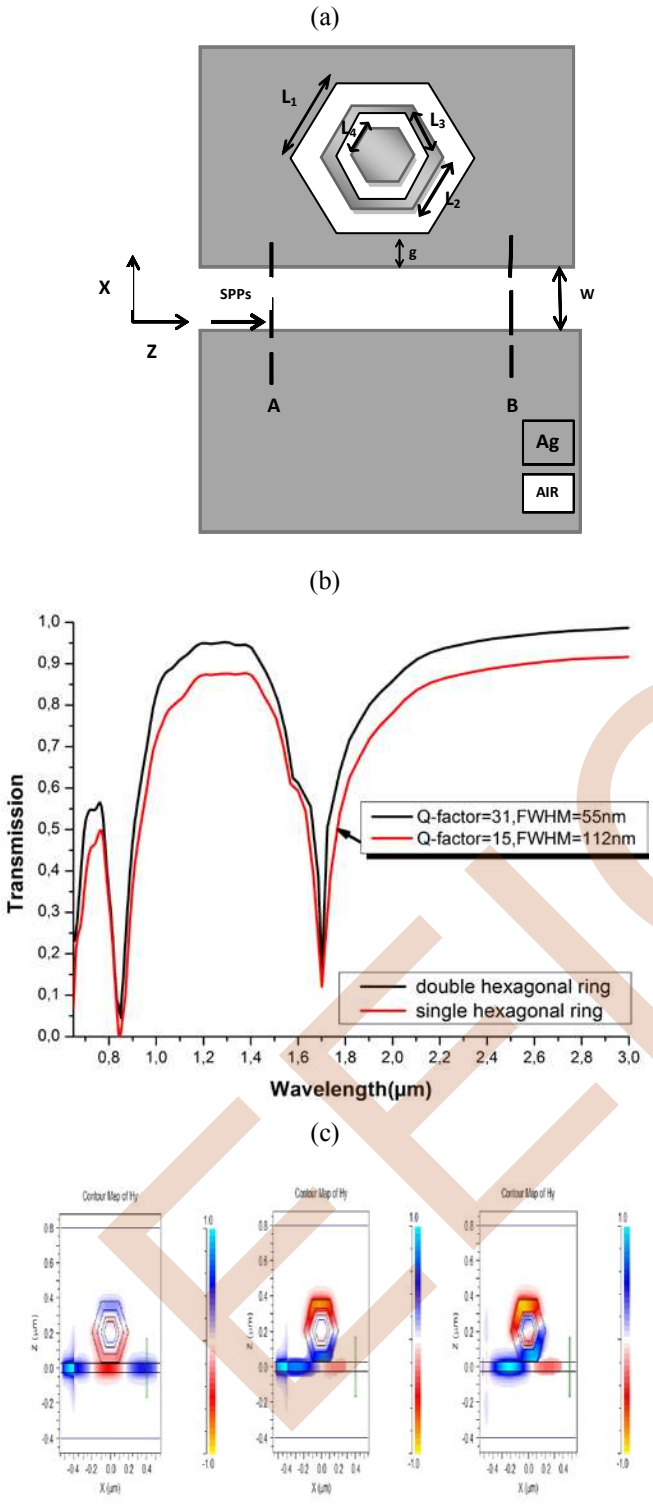

Figure 6. (a), schematic of the proposed structure with double-hexagonal ring resonators , (b) transmission of the structure proposed with double-hexagonal rings with corresponding FWHM and quality factors (c) Magnetic-filed patterns of the structure proposed at resonance wavelengths of = 841.5 nm (center), 1701 nm (right) and at wavelength 1200nm (left).

TABLE I. SENSITIVITY COMPARISON OF DIFFERENT SENSOR STRUCTURES.

Reference	Sensitivity	Year
[34]	1125	2017
[35]	1540 for mode 1 and 1010 for mode2	2018
[18]	1160	2018
[7]	2602.5	2019
This work	1743 for mode 2 and 836 for mode 1	2019

IV. CONCLUSION

An MIM based waveguide structure coupled by a hexagonal shaped ring resonator for both a refractive index based sensor and a filter is proposed. The sensing characteristics of the device were analyzed by 2D finite element method embedded in the commercial simulator R-Soft. The positions of transmission peaks have linear relations in respect to the refractive index of the material under sensing, and can be easily manipulated by adjusting the inner side length of HRR. In this proposed structure, the maximum linear sensitivity is S = 1743 nm/RIU and S = 836 nm/RIU for both mode 2 and mode 1 respectively, after optimizing the structural parameters. Also, by introducing another hexagonal shaped ring inside the main one enhanced the quality factor which makes the proposed MIM based plasmonic structure a promising candidate for a tunable band-pass filter for a wide range of wavelengths.

ACKNOWLEDGMENT

This work was supported by the Algerian Ministry of Higher Education and Scientific Research via funding through the PRFU project No. A25N01UN280120180001.

REFERENCES

[1] Barnes, W.L.; Dereux, A.; Ebbesen, T.W. Surface plasmon subwavelength optics. Nature 2003, 424, 824–830.

[2] Yin, Y.; Qiu, T.; Li, J.; Chu, P.K. Plasmonic nano-lasers. Nano Energy 2012, 1, 25–41.

[3] Ozbay, E. Plasmonics: Merging photonics and electronics at nanoscale dimensions. Science 2006, 311, 189.

[4] Y. Gao, G. Ren, B. Zhu, L. Huang, H. Li, B. Yin, S. Jian, Tunable plasmonic flter based on graphene split-ring, Plasmonics 11 (1) (2016) 291–296.

[5] Fan, C.; Shi, F.; Wu, H.; Chen, Y. Tunable all-optical plasmonic diode based on fano resonance in nonlinear waveguide coupled with cavities. Opt. Lett. 2015, 40, 2449–2452.

[6] J.S. Gómez-Díaz, J. Perruisseau-Carrier, Opt. Express 21 (2013) 15490–15504.

[7] H. Ben salah, A. Hocini, M.N. Temmar, D. Khedrouche. Design of mid infrared high sensitive metal- insulator-metal plasmonic sensor. Chinese Journal of Physics 61 (2019) 86–97.

[8] D. Etezadi, I.V. J. B. Warner, F.S. Ruggeri, G. Dietler, H.A. Lashuel, H. Altug, Nanoplasmonic mid-infrared biosensor for in vitro protein secondary structure detection, Light Sci. Appl. 6 (2017) 17029.

[9] M.F.O. Hameed, A.S. Saadeldin, E.M. Elkaramany, S.S. Obayya, Label-free highly sensitive hybrid plasmonic biosensor for the

detection of DNA hybridization, J. Light. Technol. 35 (2017) 4851–4858.

[10] W. Kong, D. Wu, N. Hu, N. Li, C. Dai, X. Chen, Y. Suo, G. Li, Y. Wu, Robust hybrid enzyme nanoreactor mediated plasmonic sensing strategy for ultrasensitive screening of anti-diabetic drug, Biosens. Bioelectron. 99 (2018) 653–659.

[11] Jin X, Huang X, Tao J, Lin X and Zhang Q 2010 A novel nanometeric plasmonic refractive index sensor IEEE Trans. Nanotechnol. 9 134–7.

[12] Zou S, Wang F, Liang R, Xiao L and Hu M 2015 A nanoscale refractive index sensor based on asymmetric plasmonic waveguide with a ring resonator: a review IEEE Sens. J.15 646–50.

[13] Wang, Y.; Wang, T.; Han, X.; Zhu, Y.; Wang, B. Plasmon induced Transparency Effect in Metal–Insulator–Metal Waveguide Coupled with Multiple Dark and Bright Nanocavities. Opt. Eng. 2016, 55, 027108.

[14] Lei, J.; Ji, B.; Lin, J. High-performance Tunable Plasmonic Absorber Based on the Metal–Insulator–Metal Grating Nanostructure. Plasmonics 2016, 1 , 151–156.

[15] G. Wang, H. Lu, X. Liu, Y. Gong, L. Wang, Optical bistability in metal-insulator-metal plasmonic waveguide with nanodisk resonator containing Kerr nonlinear medium, Appl. Opt. 50 (2011) 5287–5290.

[16] G. Zheng, Y. Chen, L. Xu, M. Lai, Y. Liu, Metal–insulator–metal waveguide-based band-pass filter with circular ring resonator containing Kerr nonlinear medium, Opt. Commun. 305 (2013) 164–169.

[17] V.F. Nezhad, S. Abaslou, M.S. Abrishamian, Plasmonic band-stop filter with asymmetric rectangular ring for WDM networks, J. Opt. 15 (2013) 055007.

[18] X. ZHANG, Q.I. Yunping, P. ZHOU, H. GONG, H.U. Bingbing, C. YAN, Refractive index sensor based on fano resonances in plasmonic waveguide with dual side coupled ring resonators, Photon. Sens. 8 (4) (2018) 367–374.

[19] M.R. Rakhsani, M.A. Mansouri-Birjandi, High-sensitivity plasmonic sensor based on metal- insulator-metal waveguide and hexagonal-ring cavity, IEEE Sens. J. 16 (2016) 3041–3046.

[20] D. Xiang, W. Li, MIM plasmonic waveguide splitter with tooth-shaped structures, J. Mod. Opt. 61 (2014) 222–226.

[21] Rafiee E, Emami F, Nozhat N. Coupling coefficient increment and free spectral range decrement by proper design of microring resonator parameters. Opt Eng. 2014;53:123108-1–123108-7.

[22] Zou S, Wang F, Liang R, Xiao L and Hu M 2013 A nanoscale refractive index sensor based on asymmetric plasmonic waveguide with a ring resonator IEEE Sensors J. 15 646–50.

[23] Li B 2015 Tunable flter and optical buffer based on dual plasmonic ring resonators J. Mod. Opt. 62 212–20.

[24] Wu T, Liu Y, Yu Z, Peng Y, Shu C and Ye H 2014 The sensing characteristics of plasmonic waveguide with a ring resonator Opt. Express 22 7669–77.

[25] H.F. Gai, J. Wang, Q. Tian, "Modified debye model parameters of metals applicable for broadband calculations", Appl. Opt. 46 (12) (2007) 2229–2233.

[26] A. Taflove, S.C. Hagness, Computational Electrodynamics: The FiniteDifference Time-Domain Method, 3rd ed., Artech House, Boston, MA, USA, 2005.

[27] R. Zafar, M. Salim. "Enhanced figure of merit in Fano resonance based plasmonic refractive index sensor". IEEE Sensors J. 2015;15(11):6313-6317.

[28] P.K. Wei, Y.C. Huang, C.C. chieng, F.G. Tseng, W. Fann, "Off angle illumination induced surface plasmon coupling in subwavelength metallic slits", Opt. 253 Express. 13 (26) (2005) 10784–10794.

[29] Xie, Y.; Huang, Y.; Zhao, W.; Xu, W.; He, C. A novel plasmonic sensor based on metal-insulator-metal waveguide with side-coupled hexagonal cavity. IEEE Photon. J. 2015, 7.

[30] Q. Zh Aang, X.G. Huang, X.S. Lin, J. Tao, X.P. Jin, "A subwave length coupler-type MIM optical filter, " Opt. Express 17 (9) (2009) 7549–7555.

[31] H. Zhao, X. Guang, and J. Huang, "Novel optical directional coupler based on surface plasmon polaritons," Physica E 40(10), 3025–3029 (2008).

[32] Wu, T.; Liu, Y.; Yu, Z.; Peng, Y.W.; Shu, C.G.; He, H.F. The sensing characteristics of plasmonic waveguide with a single defect. Opt. Commun. 2014, 323, 44–48.

[33] Mahdi Zavvari, Milad Taleb Hesami Azar & Armin Arashmehr (2017): Tunable band-stop plasmonic filter based on square ring resonators in a metal-insulator-metal structure, Journal of Modern Optics, DOI: 10.1080/09500340.2017.1349195

[34] Tang, Y.; Zhang, Z.; Wang, R.; Hai, Z.; Xue, C.; Zhang, W.; Yan, S. Refractive Index Sensor Based on Fano Resonances in Metal-Insulator-Metal Waveguides Coupled with Resonators. Sensors 2017, 17, 784.

[35] S. Ghorbani, M. Ali Dashti, M. Jabbari. Plasmonic nano-sensor based on metal dielectric-metal waveguide with the octagonal cavity ring. Laser Phys. 28 (2018) 066208 (6pp).

The impact of jitter on the HEVC video streaming with Multiple Coding

Farouk BOUMEHREZ

Department of Electronics,
Abbes Laghrour University,
Laboratoire des Télécommunications (LT)
8 Mai 1945 University, Guelma, Algeria.

boumfarouk@yahoo.fr

A.Hakim SAHOUR

Department of Electronics,
Abbes Laghrour University,
Route de Constantine, Khenchela 40000, Algeria

hakim-sahour1@yahoo.fr

Noureddine DOGHMANE

Department of Electronics,
Badji Mokhtar University,
BP 12, Sidi Amar, Annaba, Algeria.
Laboratoire d'Automatique et Signaux
d'Annaba (LASA), Annaba, Algeria.
ndoghmane123@yahoo.fr

***Abstract*— In this paper, we assessed the new and emerging video coding standard HEVC/H.265 from the viewpoint of quantization parameter (QP) impact, the video content, and the degradation brought about by the transmission channel on the quality of the experience (QoE). Also, a study of the quality of service (QoS) and QoE that will allow us to evaluate multimedia applications in wireless Ad-Hoc Networks is proposed.**

The main contribution of this paper is the performance evaluation of the codec HEVC/H.265 based on the QP variation values for different video content. This can be used to reduce their impacts on video transmission through a corrupted wireless channel. In this work, we also studied the effects of jitter on the QoE of the transmitted video sequences. The results prove that the use of the QP value can recover the jitter impacts and ameliorate the received video quality. Finally, an HEVC encoder parameter adaptation scheme based on MDC (Multiple Description Coding) is modeled with the encoder parameter and QoE model. A comparative study shows that the proposed MDC technique is efficient for better transmission.

Keywords*— *HEVC/H.265; Multiple Description Coding (MDC); Quantization Parameter (QP); Jitter, Video content.

1. I. INTRODUCTION

Nowadays, video transmission over all kinds of networks is a field that has kept growing in the last years. the improvements in network properties together with a larger efficiency of video codecs and an increase in processing ability and storing capacity of all kinds of devices (desktop computers, smart-phones, tablet computers, ...) help to make video streaming feasible. Lots of applications use video streaming [1][2].

Digital uncompressed videos contain large amounts of data. This is the reason why video codecs plays an important role, as they are able to compress video sequences with large frame sizes and frame rates into relatively small bit-streams while keeping the quality of perception acceptable.

Video has been for a long time a very important media for communications, and many other applications. Originally the video is analog since its generation, using sensors, up to its transmission via radio or cable and its reception. With the evolution of techniques and digital technologies this led to the digitization of this type of content .This digitization allowed us to have high quality and high definition videos. Only, this was accompanied by a huge quantity of digital data to process, transmit or store. The solution adopted is of course the compression. Video compression has emerged as an area of research vital and much solicited from the end of the 1980s.

The popularity of the internet from the mid-1990s encouraged the digital video to be transmitting under IP. Only, this diffusion under IP has been facing several problems and handicaps [2][3]. Among these handicaps the bandwidth of communication used under IP systems is generally low and variable in time. Also, the principle of a transmission under IP often favors losses of packets and delays [4].

The term QoE is actually most used. QoE represents the set of objective and subjective characteristics that satisfy, which determinate the interaction between the user's perception (light intensity, color, etc.), and the video presented with expression in words, such as bad, poor, fair, good or excellent[2]. In contrast, the measurement of QoE is done by a subjective assessment of a person or a consistent population of users on a service they use. QoE is generally used alongside QoS. Moreover, delay, jitter, PLR (Packet Loss ratio), and bandwidth, are some of the most common parameters used to measure QoS [5]. Now, the QoS considered weakly in determining the quality, the term QoE is dominant to represent it [6].

Indeed, jitter is one of the important parameters that deteriorate the QoS. Jitter is the variation of delays, or the difference in transmission delay of packets transmitted between two systems of multimedia data communication over a network.

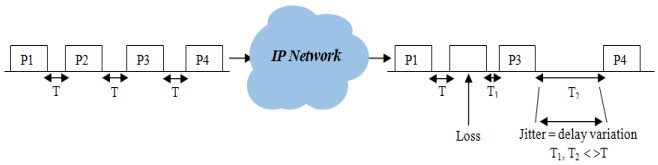

Figure.1 IP Network with packet loss and Jitter.

The HEVC (H.265) standard is the successor of H.264/AVC (Advanced Video Coding), which was developed similarly to H.264 by a joint effort between ISO/IEC Moving Picture Experts Group, and ITU-T video coding experts group (VCEG). The main objective of the new codec is to provide 50% better compression efficiency than H.264 encoding[7], as well as support for display resolutions up to 8192 X 4320 with better network transmission [6] [7].

Real-time video transmission over wireless channels is a big defiance in the last few years. The transmission of the raw video is impossible because of the large bandwidth required, that's why the video compression is inevitable. Moreover, compressed video is very sensitive to packet loss delay, and jitter happening in best-effort networks like the Internet.

MDC is an efficient method established to deal with the transmission of data through disturbed networks [8]. It encodes a signal in several bit-streams, every bit-stream is a description, and every description is independently decodable [8]. The received signal can be reconstructed with several descriptions which give a quality improvement. Indeed, MDC minimizes the impacts of QoE parameters by transporting the descriptions with diversified paths. As well, various error concealment techniques can be developed to recapture the lost information [03] [8]. The advantages of the MDC are obtained to the detriment of additional redundancy in the descriptions. Thus, one of the principal objectives of the MDC technique is to minimize redundancy [8]. In the temporal domain MDC category; mainly the frames are divided between the descriptions; the odd frames in one description and the even frames in the other description. On the decoder side, decoding the lost frames are replaced by frames freezing or estimated by concealment methods [8] [15]. The motion estimation/compensation is performed intra description, which means that even (odd) frames are predicted from odd (even) frames.

In [10][11] the authors explain the impact of video content and transmission impairments on QoE of a MPEG-2 (Moving Picture Experts Group-2) video stream transmitted through a wired network. The MPEG-2 video standard is involved and found that the loss and the jitter parameters have a significant influence on the user experience, and the impact of codec and network settings on QoE is dependent on the video content.

Previous works have also addressed studies employing the codec H.264/AVC, using subjective and objective evaluation methods. In [5], the video sequences encoded using the H.264/AVC and transmitted via a typical noisy wireless channel with transmission interruption, the results have been saved and analyzed.

In [6] it examines the impact of video content types and the encoding parameters based on QP in HEVC video quality, with objective and subjective tests. Therefore, the obtained results have shown that encoding parameters and the variety of video content types affect the video quality.

In [3], the author has proposed the use of MDC methods for video compression through the use of Multiple Description, a novel system was presented, whose main idea was the use of H.264/AVC based on MDC for wireless video transmission.

The authors of [8] demonstrated that the temporal MDC scheme is a simple alternative for video streaming where methods that use error control schemes such as Forward Error Correction (FEC) or Automatic Repeat Request (ARQ) are not suitable for transmission impairments. Thus, they evaluate the performance of the proposed MDC image/video coder for two descriptions.

The rest of this paper is organized as follows: Section II describes the system block diagram. Section III introduces the HEVC encoder parameter model. Section VI describes the system tested on wireless IP transmission solutions. The objective QoE prediction model for HEVC encoded video streaming. Section V discusses the collected results. Finally, the conclusion of the paper is found in section VI.

II. SYSTEM DESCRIPTION

This paper includes three parts, i.e. Part A: HEVC encoder parameter model, Part B: objective QoE prediction model and Part C: HEVC encoder adaptation scheme. The overall system block diagram is shown in Fig 2.

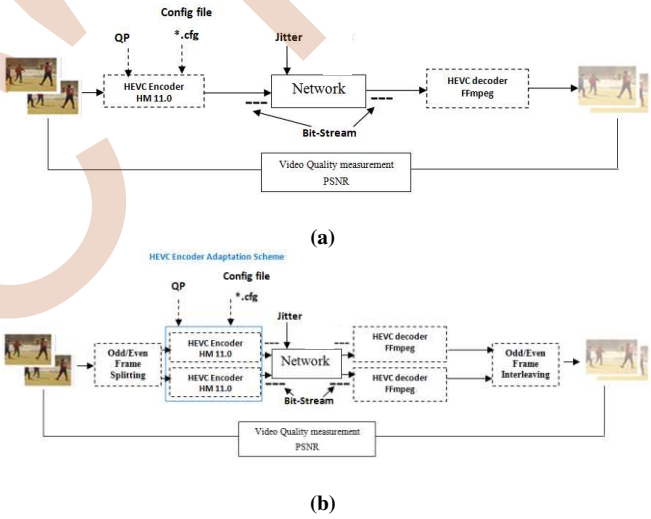

Figure.2 Adaptation Scheme for objective assessment of video sequence: (a) Without MDC and (b) with MDC.

Our contributions can be outlined as:

A) Analyze the impact of video content (characterized by motion activities and complexity of video sequences) and encoding parameters (QP, resolution, frame rate...) on the new and emerging standard of video coding HEVC.

B) Concentrate specifically on source level protection, such as MDC as an approach which is fighting the loss of video packets and delay variation. The proposed model discusses the reliable transmission issues of video HEVC/H.265 over wireless communication environments. Objective video quality evaluation according to QoE prediction model in wireless IP network scenarios.

III. HEVC ENCODER PARAMETER MODEL

The defined video content type is used with different QP values to model the impact of the HEVC encoding process for a given test scenario. The video sequences have been coded using the full range QP (17, 32 and 42) as recommended by JCT-VC [12]. The conditions under which HEVC should be tested [7] are chosen to obtain different objective metrics such as PSNR.

A. Experiment Settings

The JCT-VC defines many encoder configurations [7] in the reference software HM 11.0[12], such as all intra mode (AI), random access mode (RA), and low delay mode (LD) [7] [12].In this experiment, each frame in the test video sequences is coded in the Low delay with B slices (LB) because it's suitable for live streaming and video conferencing applications [7].

The input data is six standard test video sequences. They had 4CIF spatial resolutions were used from the ReTRiEVED video quality Database [10] [11]. The source videos had different characteristics like context, motion, temperature, color and camera movements, etc. The uncompressed video sequence format is YUV4:2:0, and represented as 8 bits per sample. Table 1 presents the characteristics of standard test video sequences obtained for experiments and sample frames extracted from each video sequence are shown in Fig.3. Figure.4 shows the spatial perceptual information (SI) and temporal perceptual information (TI) planes as recommended by ITU [10], it can be noticed that the SI and TI indexes vary from relatively small to relatively large values for the selected content.

Table 1 Original video sequences include resolution, frame rate (fps), length and frames.

Videos	Resolution (Pixel)	FR (fps)	Length (s)	Frames
Duckstakeoff	704 x 576	25	9	250
Ice	704 x 576	30	7	240
Crowdrun	704 x 576	25	9	250
Harbour	704 x 576	30	9	300
Soccer	704 x 576	30	7	300
Parkjoy	704 x 576	25	8	250

In this paper, video quality evaluation is divided into three steps,

1. The video should be encoded.
2. We are streaming with FFmpeg to the destination via a disturbed channel accumulated by the network emulator (NetEM) [10].
3. Stream the video from the transmitter to the receiver by a wireless LAN architecture configured at the "ad-hoc" mode. The used computer is HP laptop with a CPU Intel (R) Core (TM) i7-4790S, Processor Speed @3. 20GHZ, RAM 8 GO, system type 64-bit, processor architecture running Ubuntu 14.04LTS Linux. Moreover, the distance between the two computers is 100 m. The emulation setup is as in Fig.5.

Figure.3 Sample frames from considering videos.

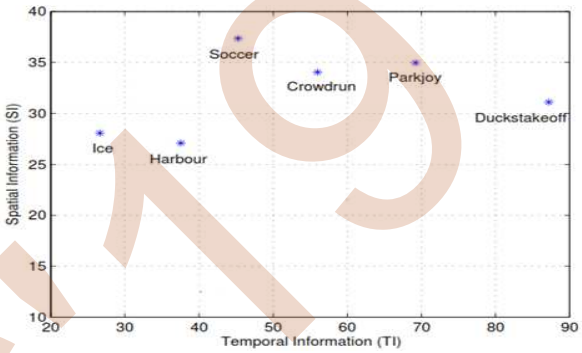

Figure.4 TI and SI planes for raw videos.

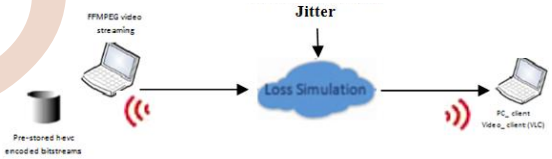

Figure.5 Proposed Testbed System.

The effect of jitter has been added by introducing a fixed delay of 100 ms plus five variable delays (1, 2, 3 4, and 5 ms), the selection of Jitter values are based on the ITU recommendation [11]. On the receiver side, a VLC player was used.

Therefore, to study the effect of the jitter, the video content, and the quality perception, the impact jitter variations at a time was considered, i.e., when study de jitter effect, we didn't take into account the impact of the delay, packet loss and bandwidth limitation.

In this paper, we have used principally the objective metrics, Thus, PSNR is an objective quality assessment most used; it performs a pixel by pixel comparison between the reference and the deformed content [6].

PSNR is defined using the mean square error (MSE)

$$MSE = \frac{1}{mn}\sum_{i=0}^{m-1}\sum_{j=0}^{n-1}[I(i,j) - k(i,j)]^2 , \qquad (1)$$

$$PSNR = 10\ log_{10}\left(\frac{MAX_I^2}{MSE}\right) \qquad [dB] \qquad (2)$$

Where, MAX is the maximum value of the pixel which can take (for example, 255 for the 8-bit image).
This criterion provides the error between the original video and the reconstructed video; a higher PSNR usually indicates better quality.

B- HEVC Encoder Parameter Model without MDC

By applying the QP values 17, 32 and 42, we extract the corresponding PSNR from the encoding process. The obtained results are presented in Fig. 6, for the test video sequences with HEVC encoder.

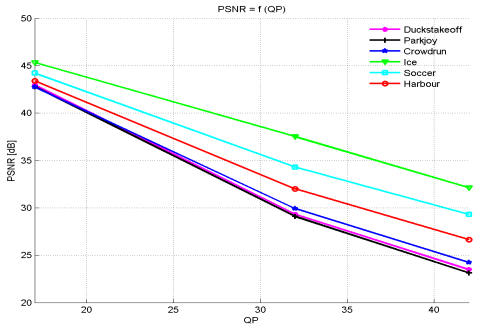

Figure.6 Impact of QP on HEVC Model without MDC.

All obtained results demonstrated that when encoding different videos with the same codec parameters such as QP, frame rate, and spatial resolution, produced different PSNR values as shown in Fig. 6. Moreover, as the QP increases the bitrate reduces resulting in a degradation in video quality, thing proved in several studies [6][10]. On the contrary, the lowest QP values result in higher bitrates, which leads to increased video quality. As the PSNR varies with different video sequences, it can be asserted that the content type has an impact on PSNR values; this indicates that other parameters must be influencing in the PSNR values than the encoding parameters.

C- HEVC Encoder Parameter Model based on MDC

By MATLAB language tool, two descriptions (sub-streams) of the same video are created; these two latter's take the even frames and the odd frames respectively. Then, in the same conditions mentioned earlier, the HEVC /H.265 encoder has been applied to each description. On the decoder side, the central description is reconstructed from the bit-streams with HEVC/H.265 decoder. Generally, each side decoding correlated with side distortion, while the decoding of all descriptions is called central decoding with the smallest central distortion [8]. Figure.7 shows the graph of the PSNR, according to the QP.

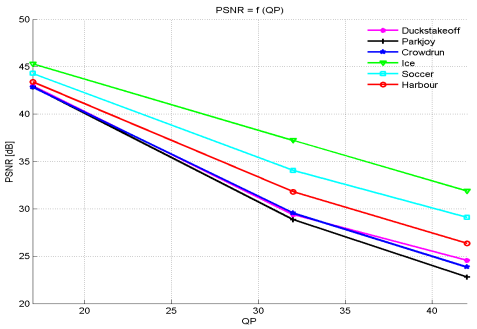

Figure.7 Impact of QP on HEVC Model based on MDC

From the Fig. 7, it can be observed that the PSNR decreases gradually with the increased of QP values such as indicated in the previously obtained results as shown in Fig. 6. Also, the PSNR takes the same downtrend in both cases. It can be noted that when QP increases, there is some slight difference between them that can be considered negligible. This behavior was found in other studies [3][8]. Also, we can see that the PSNR is positively correlated with video quality as shown in Figs. 6 and 7.

The video sequences with the lowest PSNR presented in both cases are respectively the Duckstakeoff, Parkjoy, and Crowdrun. The PSNR of video sequences Ice, Soccer, and Harbour are rather high, and then it seems that there is a big variation between Crowdrun sequence and Ice sequence. Thus, all encoded videos contain various content types (motion activities (TI) and complexity of video (SI)) [6] as shown in Fig. 4. Additionally, it should be noted the video quality declining with the increase in QP value (compression). However, it seems clear in the Figs.6 and 7 that the drop is at most intensity whenever the video has higher motion activities compared to the video which has a lower motion. Also, you should keep in mind the level of compression because it determines the video quality. Furthermore, all sequences need a different compression level for the same quality in motion characteristics. Thus, Ice, Soccer and Harbour video sequences require lower compression and the transmission bandwidth requirement for the same quality when compared to Duckstakeoff, Parkjoy, and Crowdrun video sequences. Therefore, this is important because it will enable us to know the QP effect and how it should be used in designing an improved video quality without disturbance model. Also, the frame rate has an impact on the encoded video, in the same QP, the video quality increases as the frame rate increases. As a result, encoded and designed video quality in our prediction model depends on HEVC/H.265 video codec, video content type of video sequences as also indicated by authors in [4] and [6] and the QP as the initial encoding settings determines the initial video quality.

VI- OBJECTIVE QOE PREDICTION MODEL FOR HEVC ENCODED VIDEO STREAMING

A- Packet loss and Jitter impact on HEVC Video Streaming

Previous researches have demonstrated that the most popular network impairment are jitter and PLR [5][10][11]. Thus, to study the video quality assessment; it has used the HEVC encoder settings are discussed in Sec.III, the video sequences which are presented in table 1. Then, it's transmitted over an emulated wireless IP-network as shown in Fig.5. However, the Fig.8 shows that the smallest jitter values give higher values of PSNR, indicating the better use of the video perception. As jitter values increases the PSNR drops steeply, but it remains acceptable until the values of the jitter are superior to 2ms, after that the video sequence will be degraded. Therefore, if videos with high values of jitter were provided as a service, users might consider stopping watching. The videos are more sensitive to jitter [5][6][11]. It is proved that jitter can deteriorate the video quality and results in a severe degradation in the perceived video quality.

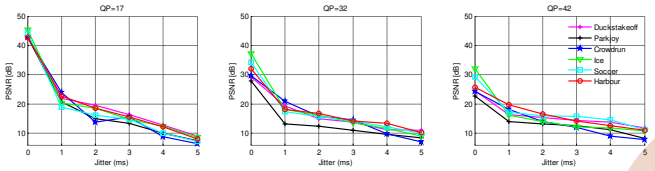

Figure.8 Impact of Jitter on perceived quality without MDC Scheme.

It is evident that when the jitter values are smaller than 1ms, there are significant differences in PSNR values for all video sequences. Also, we have noticed that, if the video is affected so much by jitter, the perceived quality associated depends on the HEVC encoding process. Moreover, the results of the impact of them are seemed clear on the graph. Consequently, HEVC codec has a significant impact on the compression rate and the visual quality of videos compared to H.264 [5], and MPEG-2 [10][11].

B- Jitter impact on HEVC Video Streaming based on MDC

In this section, we have proposed a QoE model to use the HEVC encoder adaptation scheme based on MDC technique as shown in Fig. 2. Figure 9 presented the results in terms of PSNR when applied the more robust temporal domain MDC approach using HM11.0 and transmitted over the emulated wireless IP-network. Then, on the decoder side, the video sequences are reconstructed from odd/even frames. In the same way, Figs.10 and 11 show that the variations of PSNR with jitter are dropping trend similar from the most of the cases.

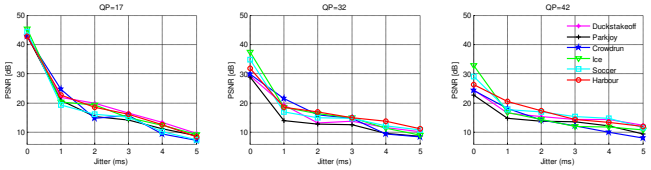

Figure.9 Impact of Jitter on perceived quality with MDC scheme.

V- DISCUSSION

From the Fig 9, it can be seen that the perceived quality degrades significantly in all considered videos for high values of jitter [5][6][10] associated with a significant improvement compared to HEVC encoder without MDC scheme, as shown in Fig.8.

In addition, we have found that the PSNR decreases gradually by increasing the QP values. This, with a significant variation depending on video content types which have different characteristics like motion level, context, temperature, color and camera movements[10][11], as indicated below (see Figs. 8 and 9), the video sequences Ice, Soccer, and Harbour, are more resistant to jitter than Duckstakeoff, Parkjoy, and Crowdrun video sequences.

Furthermore, the QP has a significant impact on the video quality and compression rate; it regulates how much spatial detail is maintained [6]. For all video content types, there is a decrease in video quality when QP and jitter values increase. For instance, there is a relationship between QP, jitter and the quality degradation. Thus, the jitter impact on video quality can be considered a factor of video quality assessment as the QP (Bitrate), content Type, etc.

In this paper, we have demonstrated that when the Jitter increases, it can minimize the impairment impact on a video quality metric by a QP increasing (reducing the encoding bitrate) (see also Figs. 8 and 9).

Moreover, the choice of a QP value in the HEVC encoder represents an essential thing for the bitrate control and the impairment impact on a video quality, as in the older video compression techniques, e.g., H.264/AVC [5][13][14] and MPEG-2[10][11].

Also, this study has shown that for the smallest jitter values (1ms, and 2ms), the PSNR with or without the MDC remains the same, as shown in Figs. 8 and 9, as expected from theoretical results [3][8]. It can be seen that for higher values, the MDC scheme leads to better results, indicating that the MDC method is a solution used to counter the higher values of PLR and Jitter.

To prove the MDC importance, we compared the impact of Jitter on HEVC Video Streaming based on MDC scheme with the impact of Jitter on HEVC Video Streaming without MDC scheme. For this purpose, the obtained results can help us to achieve a comparison between the obtained averages PSNR of each QP value for all videos in both cases. Moreover, it has been found that there are higher values of PSNR in the presence of the MDC when jitter is increasing because it's a technique for combating the packet losses as detailed in [8], i.e., it's one of the big advantages of this approach. It can be noted that the use of MDC is an effective way to improve the transmission with a PSNR gain 1dB to 2dB for Jitter.

CONCLUSION

The use of multimedia services has become widespread in the daily life. Video streaming with its various uses are the typical example. The QoE is strongly recommended

especially for certain types of networks like ad-hoc wireless networks. Indeed, these networks have the particularity of introducing even more errors disturbances and losses, compared to the other types of networks essentially wired. In this work, a simple MDC method is proposed to improve the performance of the video quality; HEVC encoder scheme is applied to encode and designed the end-to-end video quality, which depends essentially on the video content type and the QP as the initial encoding settings. This method gives better results in terms of the PSNR. This paper has demonstrated that when the Jitter increases, it can minimize the video degradation in terms of video quality metrics by the QP increasing. Thus, the comparative study shows that for video transmission over wireless channels, the MDC technique gives an improved solution for good transmission.

REFERENCES

[1] Y. M. Saputra and Hendrawan, "The effect of packet loss and delay jitter on the video streaming performance using H.264/MPEG-4 Scalable Video Coding," *2016 10th International Conference on Telecommunication Systems Services and* Applications *(TSSA)*, Denpasar, (2016), pp. 1-6. Doi: 10.1109/TSSA.2016.7871094

[2] J. Nightingale, Q. Wang and C.Grecos, "The impact of network impairment on quality of experience (QoE) in H.265/HEVC video streaming," *IEEE Transactions on Consumer Electronics*. **60** (2), 242-250(2014).

[3] C. M. Chen, C.W.Lin, H.C.Wei and Y.C. Chen, "Robust video streaming over wireless LANs using multiple description transcoding and prioritized retransmission," *J. Vis. Commun. Image R*.**18,** 191-206 (2007).

[4] J. Frnda, M. Voznak and L. Sevcik, "Impact of packet loss and delay variation on the quality of real-time video streaming", *Telecommun Syst* .**62**,265–275 (2016).

[5] S.Paulikas, D.Gursnys, A. Anskaitis, A. Šaltis, " The Impact of Packet Loss on Quality of H.264/AVC Video Streaming", *ELEKTRONIKA IR ELEKTROTECHNIKA*, ISSN 1392-1215.**22**(2), 81-85 (2016).

[6] L. Anegekuh, L. Sun, and E. Ifeachor, "Encoding and video content based HEVC video quality Prediction, " *Multimed Tools Appl*. **74**, 3715-3738 (2015).

[7] B. Bross, "High Efficiency Video Coding (HEVC) text specification draft 10," *Joint Collaborative Team on Video Coding (JCT-VC), Geneva (Switzerland)*, *Tech. Rep*. JCTVC-L1003 (2013).

[8] M. Kazemi, h. H. Sadeghi, and S. Shirmohammadi, "A Review of Multiple Description Coding Techniques for Error-Resilient Video Delivery," *Multimedia Systems*. **20**, 283-309 (2014).

[9] D. Hands, and M. Wilkins, "A study of the impact of network loss and burst size on video streaming quality and acceptability," *in Interactive Distributed Multimedia Systems and Telecommunication Services*, M. Diaz, P. Owezarski, and P. Snac, Eds. Berlin, Heidelberg, Springer Berlin Heidelberg, **1718**, pp, 45-57 (1999).

[10] P. Paudyal, F. Battisti, and M. Carli, "Evaluation of the effects of transmission impairments on perceived video quality by exploiting ReTRiEVED dataset," *J. Electron. Imaging(SPIE)*. **26**(2), 023003 (2017).

[11] P. Paudyal, F. Battisti, and M. Carli, "Impact of video content and transmission impairments on quality of experience," *Multimedia Tools Appl* .**75**(23), 16461-16485 (2016).

[12] F. Bossen, "Common HM Test Conditions and Software Reference Configurations", document JCTVC-H1100, JCT-VC, San Jose, CA (2012).

[13] F. Tommasi, V. D. Luca, and C. Melle, "Packet losses and objective video quality metrics in H.264 video streaming ," *J. Vis. Commun. Image* R. **27,** 7-27 (2015).

[14] R. Kibria, and J. Kim,"H.264/AVC-based multiple description coding for wireless video transmission," *Paper presented at the International Conference on Communications* pp. 429-432 (2008).

[15] E. Baccaglini, T. Tillo, and G. Olmo, "A Comparison Between ULP and MDC With Many Descriptions for Image Transmission," *Signal Processing Letters, IEEE* .**17** (1):75-78(2010).

Enhanced Performances of SAC-OCDMA System Operating with Different Codes.

Walid Sahraoui[1, 2], Hakim Aoudia[1], Smail Berrah[1], Angela Amphawan[2, 3], Rafah Naoum [4]

[1] Laboratoire de Maitrise des Energies Renouvelables (LMER), Faculté de Technologie, Université de Bejaia, Bejaia 06000, Algérie.

[2] Optical Technology Research Laboratory, School of Computing, Universiti Utara Malaysia, 06010 Sintok, Kedah, Malaysia.

[3] Research Laboratory of Electronics, Massachusetts Institute of Technology, Cambridge, MA, USA.

[4] Laboratoire de Télécommunications et Traitement Numérique du Signal (LTTNS), Faculté des Sciences de l'Ingénieur, Université de Sidi Bel Abbés, Sidi Bel Abbés 22000, Algérie.

***Abstract*— Herein, Spectral Amplitude Coding-Optical Code Division Multiple Access (SAC-OCDMA) technology is investigated and simulated. Thus, a comparative analysis is done between the random diagonal (RD), modified double weight (MDW) and enhanced double weight (EDW) codes, aiming to obtain results with better performances. The suggested system that exploits lasers as transmitter shows significantly perfect performances as compared to the Bit Error rate (BER), Eye's diagram and Q factor of others standard SAC-OCDMA.**

***Key words*—SAC-OCDMA, RD, EDW, MDW, BER, optical fiber.**

I. INTRODUCTION *(HEADING 1)*

Optical fiber communication is the key technology behind the endless growth of internet. However, such technology suffers from some phenomena like the linear and nonlinear effects (attenuation, dispersion, Kerr effect…etc.). These effects degrade the signal's quality and increase noises during the transmission. Therefore, the optical fiber communication requires multiplexing techniques that support a large number of simultaneous users demanding voice, video, and data services [1]. Also, reduce the linear and nonlinear phenomena's influence.

The optical code-division multiple-access (OCDMA) technique is getting attention which allows multiple users to share the same transmission medium by assigning different optical codes (OCs) to different users [2][3]. Nowadays, OCDMA cannot be considered as a competitor of wavelength division multiplexing (WDM), but it can be considered as a complementary multiplexing technique to improve optical access networks in terms of all-optical processing [4].These systems have special features which make them suitable for this purpose, such as enhanced information security, simplified and decentralized network control, improved spectral efficiency [1]. In the other side, the OCDMA systems suffer from different noises like the phase-induced intensity noise (PIIN), thermal noise, shot noise, the dark current, add to that the multi-access interference (MAI) [5] who represents a complicated problem. In order to eliminate the MAI effect, various encoding techniques are proposed by many researchers, some researchers proposed the use of Spectral phase coding to obtain the orthogonality of bipolar codes, but it was very difficult to preserve in fiber. Therefore, the Spectral Amplitude Coding was proposed [6].

There are many different codes whose have been considered for the SAC–OCDMA networks. In particular, the optical orthogonal code, prime code, enhanced double weight (EDW) code, Khazani–Syed (KS) code, modified frequency hopping (MFH) code, a random diagonal (RD) code, modified quadratic congruence (MQC) code and modified double weight (MDW) code [5].

In this paper, a system based on the SAC-OCDMA technique was created. The RD, MDW and EDW codes was applied. The aim of this work is to obtain enhanced performances, where a comparative analysis will be done between those codes.

II. CONSTRUCTION OF CODES

A. The Random Diagonal

The Random Diagonal (RD) code uses unipolar code (0,1) sequences. It is denoted by (N, W, λ) which N is the code length, W is the code weight and λ represents in-phase cross correlation that has two proprieties. The first propriety is the zero cross-correlation that will minimize the λ and reduce the PIIN (Phase Induced Intensity Noise) and the second propriety is the no cross-correlation in data level. The design of the RD code can be performed by dividing the code sequence into two parts, the code segment and the data segment [6][7].

1) Data segment

This part is represented by (K*K) identity matrix, where K represents the number of users and only one '1' is contained in each code (W=1) to keep the cross-correlation zero at the data level (λ=0). For K=3, so (K*K) matrix can be expressed as [Y1].

$$[Y_1]=\begin{bmatrix}0&0&1\\0&1&0\\1&0&0\end{bmatrix}$$

2) Code segment

This second part will be represented by [Y2] matrix, which is two matrices combination (weight and basic matrix). The weight matrix [M] = [M1 M2 M3…Mi], is responsible for increasing the value of 'W'[6]. Where i = W-3 and for W=4, the weight matrix is given by [M]=[M1] and it is represented as follow:

$$[M]=\begin{bmatrix}1&0\\0&1\\1&0\end{bmatrix}$$

The basic matrix [B] can be expressed as:

$$[B]=\begin{bmatrix}1&1&0\\0&1&1\\1&0&1\end{bmatrix}$$

To increase the number of users or the code length, just repeat each range of the [M] and [B] matrices, and to get the $[Y_2]$ matrix we will just combine the [B] and [M] matrices.

$$[Y_2]=\begin{bmatrix}1&1&0&1&0\\0&1&1&0&1\\1&0&1&1&0\end{bmatrix}$$

The combination of $[Y_1]$ and $[Y_2]$ gives the total code sequence [Z] with N=8 and K=3.

$$[Z]=\begin{bmatrix}0&0&1&1&1&0&1&0\\0&1&0&0&1&1&0&1\\1&0&0&1&0&1&1&0\end{bmatrix}$$

B. MDW Code

The Modified Double Weight (MDW) code is developed based on the Double Weight (DW) code of (W=2) that has a large number of weight. This code is denoted by (N, W, λ) and it has an ideal cross-correlation (λ =1) [8][9]. MDW code can be represented by the [K*N] matrix where k is the number of users, N is the length code. For (W=4), it is denoted by (N, 4, 1) where the code length 'N' is related to the number of users 'K' through:

$$N=3K+\frac{3}{8}\left[\sin\left(\frac{K\pi}{3}\right)\right]^2 \quad (1)$$

The basic MDW code of three users is given as follow[8]:

$$[K*N]=\begin{bmatrix}0&0&0&0&1&1&0&1&1\\0&1&1&0&0&0&1&1&0\\1&1&0&1&1&0&0&0&0\end{bmatrix}$$

C. EDW Code

This code is an enhanced version of the Double Weight code. The DW code weight can be any even number that is greater than two. The Enhanced DW code weight can be any odd number greater than one[9]. EDW code is denoted by (N, W, λ), as in the RD and MDW codes. It has an ideal cross-correlation(λ =1) where the relation between the number of users and the length code is given by[10]:

$$N=2K+\frac{4}{3}\left[\sin\left(\frac{K\pi}{3}\right)\right]^2\frac{8}{3}\left[\left(\sin\frac{(K+1)\pi}{3}\right)\right]^2+\frac{4}{3}\left[\left(\sin\frac{(K+2)\pi}{3}\right)\right]^2 \quad (2)$$

The EDW code is represented by [K*N] matrix where the basic codes of three users is given as follow[10]:

$$[K*N]=\begin{bmatrix}0&0&1&1&0&1\\0&1&0&0&1&1\\1&1&0&1&0&0\end{bmatrix}$$

III. SYSTEM DESCRIPTION

The SAC-OCDMA system's architecture employs different codes (RD, EDW and MDW) consisting of three active users, where the performances of these codes are tested, using Optisystem7.0 software [11]. The data signal of each user is generated from the pseudo random bit generator before using the NRZ coding. Then, the data signal is modulated with different codes using the external modulation (Fig.1). In this system, the transmitted power is based on laser sources representing the sending wavelengths with 1.2 nm spacing between two adjacent wavelengths, to represent the code words (Tab.I-III). After the combination of signals, one signal travels through the single mode fiber (SMF) and broadcasts to the receivers, where it influenced by different linear and nonlinear phenomena (attenuation, dispersion and Kerr effects). Tab.IV shows different used parameters during the simulations.

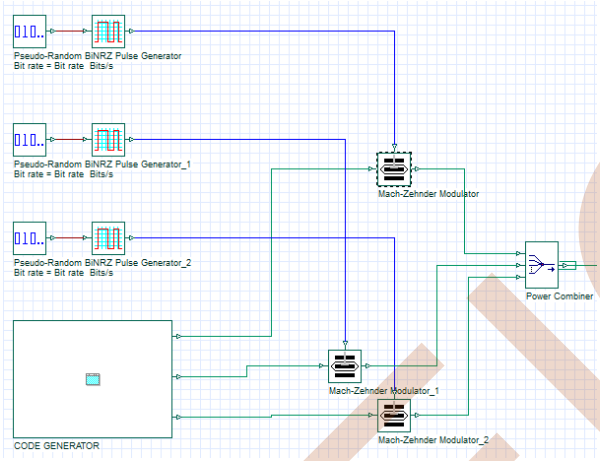

Fig. 1. The transmitter block of SAC-OCDMA system

TABLE I
WAVELENGTHS USING IN THE RD CODE

Wavelength / Users	λ_1 (nm)	λ_2 (nm)	λ_3 (nm)	λ_4 (nm)
User.1	1552.4	1553.6	1554.8	1557.2
User.2	1551.2	1554.8	1556	1558.4
User.3	1550	1553.6	1556	1557.2

TABLE II
WAVELENGTHS USING IN THE MDW CODE

Wavelength / Users	λ_1 (nm)	λ_2 (nm)	λ_3 (nm)	λ_4 (nm)
User.1	1554.8	1556	1558.4	1559.6
User.2	1551.2	1552.4	1557.2	1558..4
User.3	1550	1551.2	1553.6	1554.8

TABLE III
WAVELENGTHS USING IN THE EDW CODE

Wavelength / Users	λ_1 (nm)	λ_2 (nm)	λ_3 (nm)
User.1	1552.4	1553.6	1556
User.2	1551.2	1554.8	1556
User.3	1550	1551.2	1553.6

In the receiver side (Fig.2), the signal is decoded using the fiber bragg grating (FBG), where the same wavelengths in the encoding part for each user are employed. Then, the photo detector (PIN) is used to convert the optical signal to an electrical signal. The resultant signal is filtered by fourth order Bessel low pass filter, which is used to reject noise and interference components that lie outside the information signal spectrum [10]. Finally, each signal is analyzed by the BER analyzer.

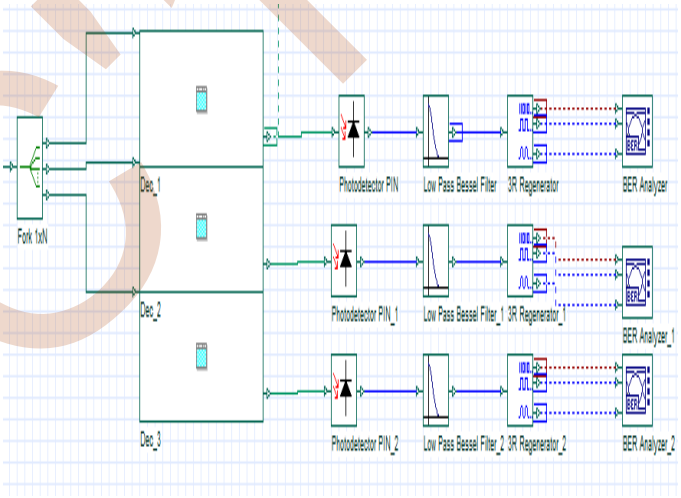

Fig. 2. The receiver block of SAC-OCDMA system

TABLE IV
TYPICAL PARAMETERS USED IN THE SIMULATION

Parameters	Value
Number of users	3
Signal Data	128 PN sequence
Chip spectral width	1.2 nm
Signal format	NRZ
External modulator extinction ratio	30 dB
Attenuation	0.2 dB/Km
Dispersion	16.75 ps/nm/km
Dark current	10 nA
Thermal noise coefficient	1.8e-023 W/Hz
Receiver filter bandwidth	0.75×Bit Rate

IV. RESULTS AND DISCUSSION

In this paper, SAC-OCDMA system containing three users was created. The performance parameters like the bit error rate (BER), Q factor and the eye's diagram were tested by exploiting different codes (RD, EDW and MDW). A comparative analysis between those codes was realized. The performance parameters were tested according to different criteria such as the fiber length, the bit rate and the source power.

Fig.3 and Fig.4 respectively show the BER and Q factor of three codes over the fiber length.

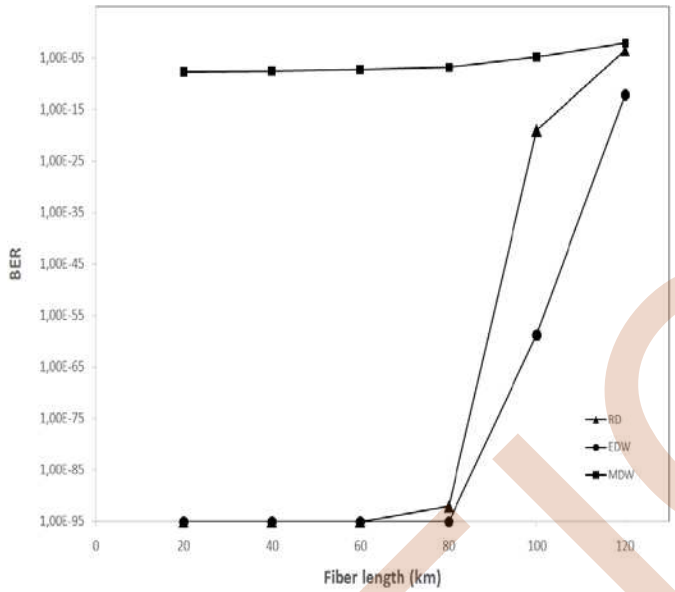

Fig. 3. BER versus fiber length at data rate of 622 Mbps

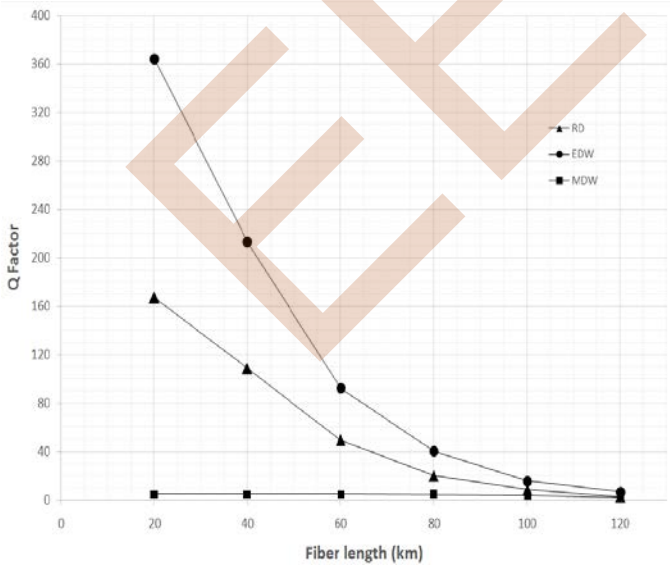

Fig. 4. Q factor versus fiber length at data rate of 622 Mbps

At each code simulation, the source power is fixed at 0 dBm and the data rate at 622 Mbps. It can be seen that BER value of all codes increases with fiber length due to different effects like attenuation. The EDW code gives better results than the other codes with a perfect BER value (BER=0) until a distance of 80 km and it is around 10^{-13} at a length of 120 Km. Even the RD code has too good results with perfect BER value until a length of 60 Km and around 10^{-4} at 120 Km. Similarly, the Q factor was obtained, except that it decreases with the increasing of the fiber length. In [6], the AGW, FGB and Thin film filter have been tested as decoders. They have used the RD code. For the FBG, the BER was around 10^{-15} at length of 40 km.

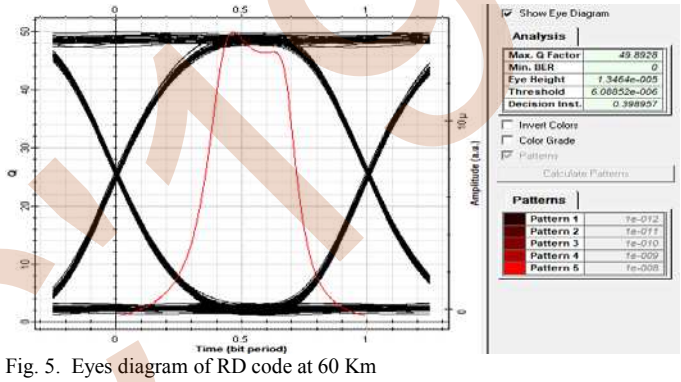

Fig. 5. Eyes diagram of RD code at 60 Km

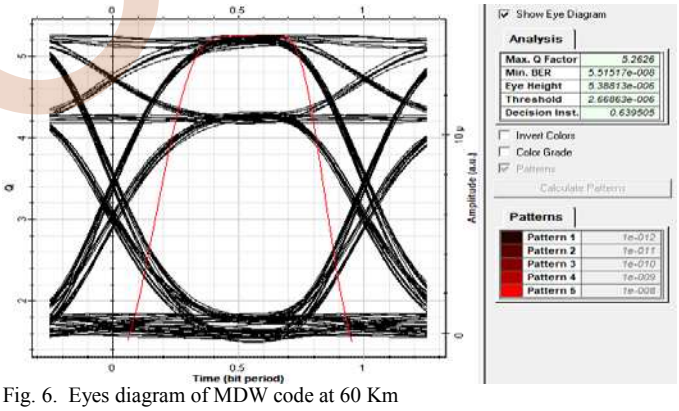

Fig. 6. Eyes diagram of MDW code at 60 Km

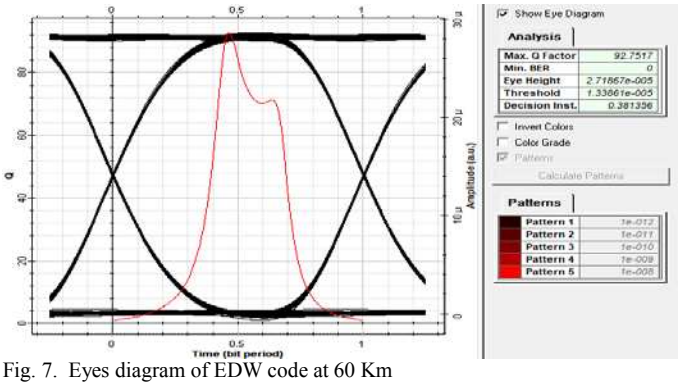

Fig. 7. Eyes diagram of EDW code at 60 Km

The eye's diagrams represented in Fig.5-Fig.7 clearly show that EDW code performs better with very large eye opening. Even RD code has too a large eye opening, which means there is no overlap between users. In this test, MDW always gives bad results comparing to the other two codes.

The second test is according to the data rate at length of 80 km and a source power of 0 dBm.

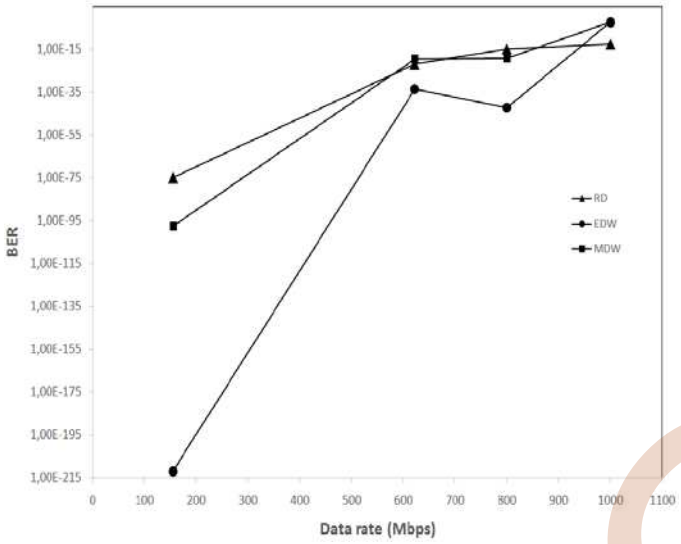

Fig. 8. BER versus data rate at length of 80 km

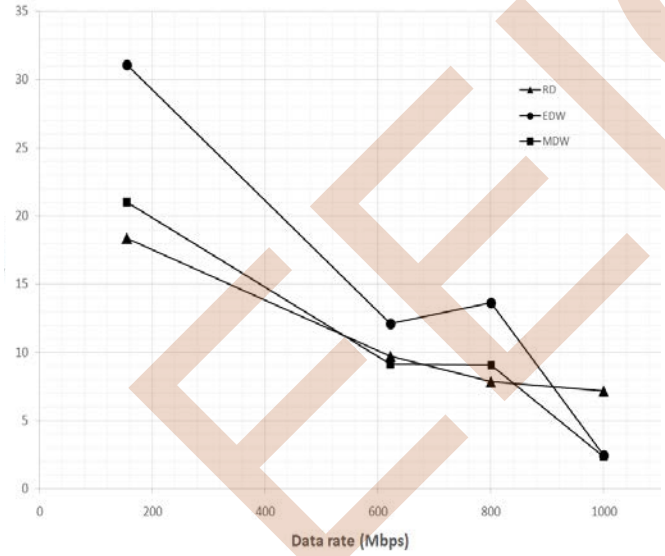

Fig. 9. Q factor versus data rate at length of 80 km

Fig.8 shows the BER of the three codes at different data rates. It is clear that there is an increasing in the BER value whenever the data rate increases. The results given by the EDW code is the best, where the lowest BER value is around 10^{-212} at 155 Mbps. MDM and RD codes have good results too. In [8], The BER versus data rate employing the MDW code at fiber length of 70 Km. In the case when the FBG was used, the BER value was around 10^{-35} at 155 Mbps. Despite in our case, we have used 80 Km as fixed length parameter, which means the influence of the linear and nonlinear effects on the transmission links like the attenuation, dispersion and SPM.

Fig.9 shows the Q factor parameter where the highest value is given at 155 Mbps. Then, whenever there is an increasing in the data rate, the decreasing in the Q factor value can be observed.

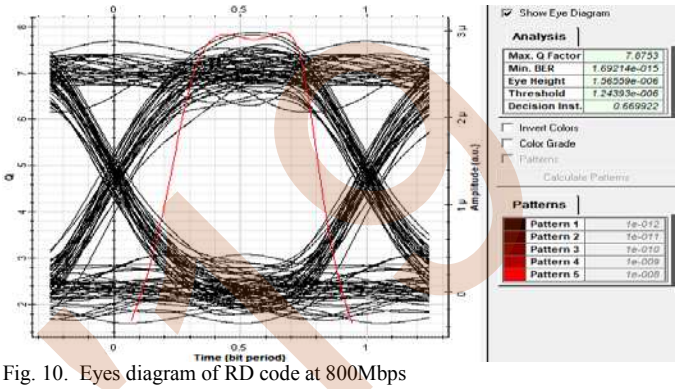

Fig. 10. Eyes diagram of RD code at 800Mbps

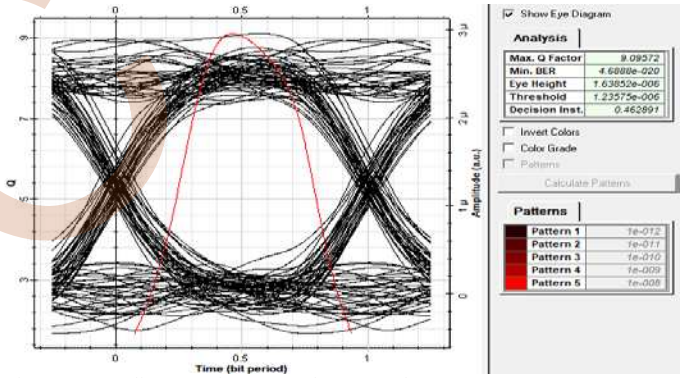

Fig. 11. Eyes diagram of MDW code at 800Mbps

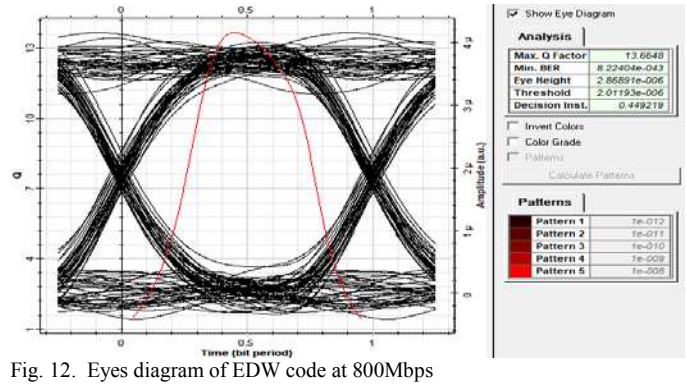

Fig. 12. Eyes diagram of EDW code at 800Mbps

The eye's diagram of the RD, MDW and EDW codes at speed of 800 Mbps are represented respectively in Fig.10, Fig.11 and Fig12. It seems that they are clear and have a large opening, but not as when a lower data rates are used.

The last test is based on the source's power, where the fiber length of 80 Km and a data rate of 622 Mbps are set as link parameters.

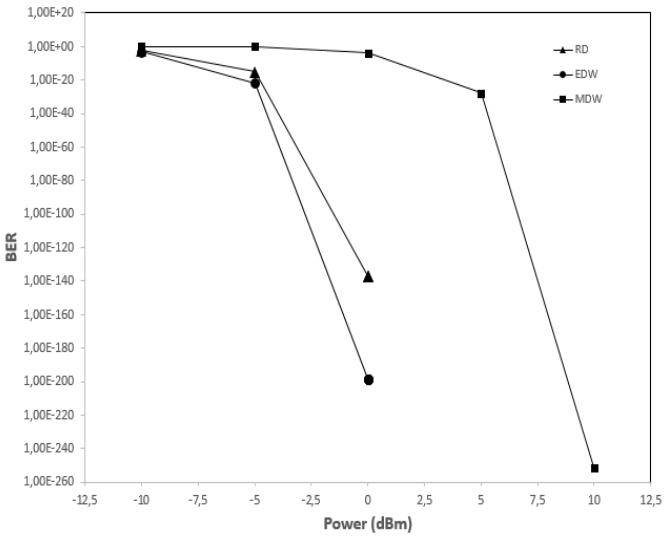

Fig. 13. BER versus the power of source

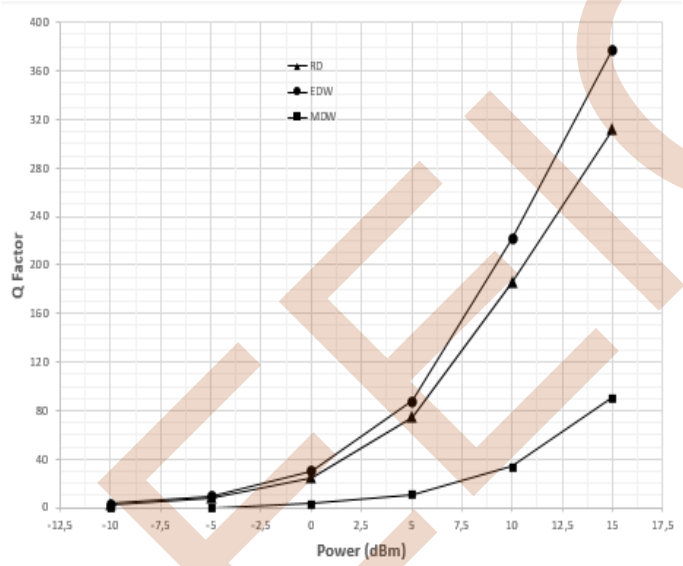

Fig. 14. Q factor versus the power of source

Fig.13 shows the BER parameter of different power values. The results that were found, show the decreasing of values, which means that there is an enhancement in the transmission performance whenever there is an increasing in the source's power, where a perfect result (BER=0) is reached in both RD and EDW codes from a source's power of 5dBm. The same thing about the Q factor, that is represented in Fig.14, except that The Q factor values increase whenever the increasing of the power values of source. This increasing requires more cost and high energy which are considered as disadvantages. For that, it is preferable to use a 0 dBm source's power as an optimal solution.

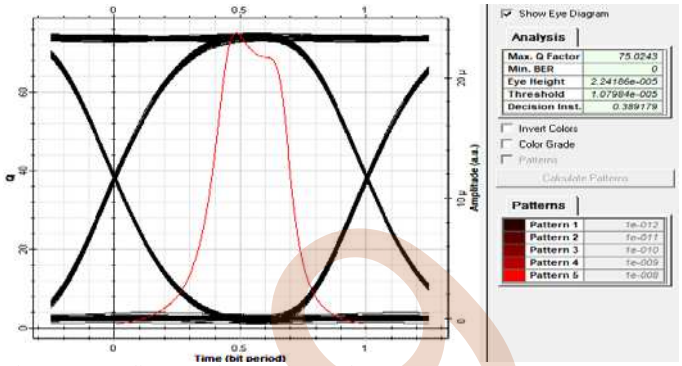

Fig. 15. Eyes diagram of RD code at 5 dBm

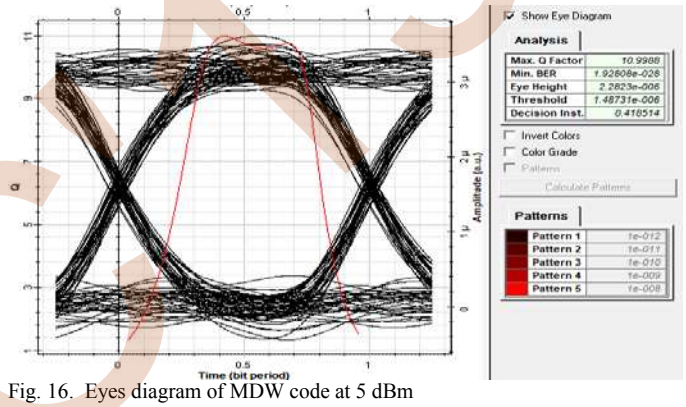

Fig. 16. Eyes diagram of MDW code at 5 dBm

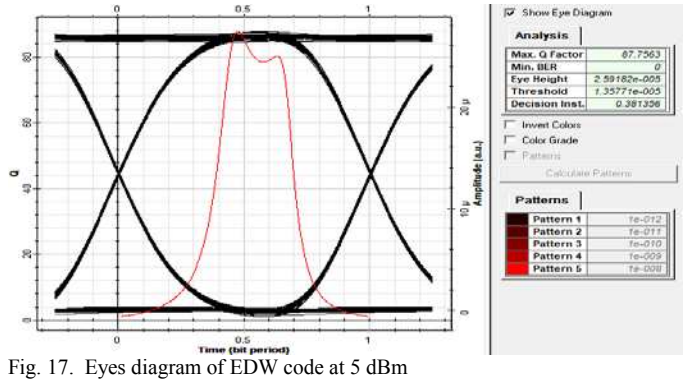

Fig. 17. Eyes diagram of EDW code at 5 dBm

The eye's diagrams of each code at a source's power of 5dBm are represented in Fig.15-Fig.17. As in all simulations, the best results are given by the EDW code regardless of the tested parameter. Even the RD code has good results. It is clearly to see that those both codes have a larger opening of the eye's diagram than the MDW code.

V. CONCLUSION

In this paper, an SAC-OCDMA system containing three users was created, where the following performance parameters like the bit error rate (BER), Q factor and the eye's diagram were tested by exploiting different codes which are the RD, EDW and MDW. This study had the object of reach enhancement performances of the optical link than the others standard SAC-OCDMA. Therefore, a comparative analysis between these codes has been done. Based on this analysis, the EDW had always the better results than the other codes, despite it exploited the minimum number of wavelenghts. The performance parameters tests were according to different criteria like the fiber length, the bit rate and the source's power.

REFERENCES

[1] X. Chen, D. Chen, and Z. Wang, "Performance improvement of bandwidth-limited coherent OCDMA system," Photonic Netw. Commun., vol. 16, no. 2, pp. 149–154, 2008.

[2] H. Yan, K. Qiu, and Y. Ling, "Performance analysis of a hybrid OCDMA/WDM system," Front. Optoelectron. China, vol. 2, no. 1, pp. 15–20, 2009.

[3] A. O. Aldhaibani, T. A. Rahman, S. A. Aljunid, M. N. Hindia, and E. B. Hanafi, "A new model to enhance the QoS of spectral amplitude coding-optical code division multiple access system with OFDM technique," Opt. Quantum Electron., vol. 48, no. 10, pp. 1–12, 2016.

[4] X. Chen and X. Yuan, "Investigation of superstructured fiber Bragg grating-based OCDMA system," Photonic Netw. Commun., vol. 20, no. 3, pp. 242–246, 2010.

[5] T. Abd, S. Aljunid, H. Fadhil, R. Ahmad, and M. Junita, "Enhancement of performance of a hybrid SAC-OCDMA system using dynamic cyclic shift code," Ukr. J. Phys. Opt., vol. 13, no. 1, p. 12, 2012.

[6] H. Adhil, S. Aljunid, and B. Ahmed, "Performance of OCDMA systems using random diagonal code for different decoders architecture schemes," Int. Arab J. Inf. Technol., vol. 7, no. 1, pp. 1–5, 2010.

[7] F. Su and H . Jin, "Research of Code Construction for OCDMA System" in Advances in Mechanical and Electronic Engineering, vol. 178, no. VOL. 3. 2013, pp. 265-270.

[8] S. G. Abdulqader, S. A. Aljunid, H. M. R. Al-khafaji, and H. A. Fadhil, "Enhanced performance of SAC-OCDMA system based on SPD detection utilizing EDFA for access networks," J. Commun., vol. 9, no. 2, pp. 99–106, 2014.

[9] Feras N. Hasoon, Mohammed H. Al-Mansoori and Sahbudin Shaari, "Different Detection Schemes Using Enhanced Double Weight Code for OCDMA Systems," in Systems IAENG Transactions on Engineering Technologies IAENG Transactions on Engineering Technologies, vol. 170. 2013, pp. 287-299

[10] Somaya A. Abd E, Mottaleb, Heba A. Fayed, Ahmed Abd El Aziz, and Moustafa H.Aly, "SAC- OCDMA System Using Different Detection Techniques," IOSR J. Electron. Commun. Eng., vol. 9, no. 2, pp. 55–60, 2014.

[11] https://optiwave.com/

A Microstript Coupler With Improving the Characteristic Transmission

R. EL-BOUSLEMTI
TTNS Laboratory
ENPO, Maurice Audin
Oran, Algeria
rahmouna.elbouslemti@enp-oran.dz

F. Salah-Belkhodja
TTNS Laboratory
Djillali Liabes university
Sidi Bel Abbes, Algeria
fouzi.salahbelkhodja@univ-sba.dz

A. K. SAYAH
Laboratoire de Simulation,
Commande, Analyse et Maintenance
des Réseaux électriques
ENPO, Maurice Audin, Oran, Algeria
Abdelkader.sayah@enp-oran.dz

***Abstract*— Couplers are widely used as combiner or power dividers. To miniaturize the device, we have used a meandered line. The coupler demonstrates a coupling level of 2.29 dB with a reflection level of 25.39 dB and an isolation level as 42.41 dB. This compact coupler operates at 3.26 GHz. The meandered coupler have compact sizes of 23×34.6 mm^2, with impedance Z0 is 50.60 Ω. To validate our model, the compact coupler is designed and fabricated using microstrip technology on FR4 substrat. Good agreement is achieved between the simulated and measured results.**

I. INTRODUCTION

The telecommunications was initially restricted to public and military services, later they became commonplace in recent years.

Driven by the enthusiasm of the public, wireless communications systems are experiencing tremendous growth worldwide, they became cheaper and faster and the microwave components became miniaturized. The use of directional couplers [1,2] has become commonplace in radio frequency systems and the modern optical communications systems. It therefore becomes important to present this "coupler" in the microwave research.

The perfect integration of the coupler in the design of RF and digital circuits requires the miniaturization of the device, which naturally leads to define the new design methodologies associated with new hardware and software tools which gives a novel enhanced and miniaturized coupler which is presented in [3-5].

This article presents a concrete case of realization of a directional coupler with meander transmission line in the microstrip technology.

This study led us to conceive, simulate, realize and characterize a compact meandered coupler.

The manipulation (electromagnetic simulations and measurements) guided us to determine the influence of the geometry on the transmission *characteristics* and to deduce all the parameters and rules of behavior.

Objectives of the study

- to highlight a design rule and a reliable process which aims to describe a geometric dimensioning
- To ensure a miniaturization of the component without having a performance degradation.

II. PARAMETERS CHARACTERISTICS OF A COUPLER

The concept of the planar transmission line was proposed from 1950, According to Pozar, from the 1960s, much thinner substrates began to be used, which promotes microstrip lines for microwave integrated circuits. Differents waveguide couplers were invented and characterized at the MIT Radiation Laboratory in the 1940s [6].

The concept of couplers in microstrip technology has been proposed since 1950, but it was not possible to achieve them effectively until 1960, when low-loss dielectrics arrived on the market [6]. Since then, research in this field has continued to intensify to exploit the many advantages of directional couplers:

A. Advantages:

- Simple to realize, suitable for two-layer circuits
- Simple connectivity,
- low-loss connector

Unfortunately, these components also have disadvantages ;

B. disadvantages

- Inhomogeneous propagation environments
- Sensitivy to electromagnetic disturbances
- Larger losses, only the substrate that is chosen
- Controlled phase shift

State space can be equivalent to the form showed Fig. 1 and the following functional form:

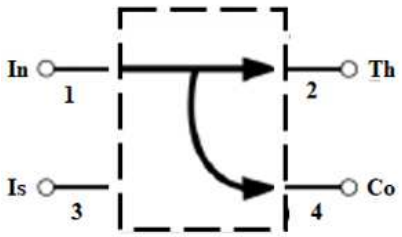

Figure 1. Functional definitions of a classical coupler with Input (In), through (Th), isolation (Is) and coupled port (Co).

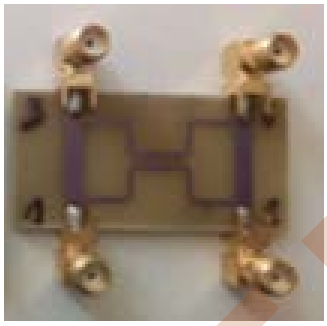

Figure 2. Three types of COD directional couplers with Input, through, isolation and coupled port.

The simplest coupler to study is probably given in Fig. 2 which is defined by:

- **Its transmission characteristics**: S-parameters, S11 (reflection coefficient), S21 (isolation), S31 and S41 (characteristics transmission: coupled and through).
- **Its usage parameters:** the resonance frequency f1, its input impedance and its bandwidth B.
- **Its internal parameters:** The first step is the choice of the substrate and the conductor for which the characteristics to be known are:

✓ **For the substrate:** its relative permittivity and the dielectric losses of the substrate tan ∂, and its thickness h.

✓ **For the conductor:** its conductivity σ and its thickness t.

The baseline design of coupler consists to determine: the S-parameters, input impedance which must be adapted and the phase difference between the Coupler Output Ports of 90 degree.

In this article only one type feeding is presented. It's about an microstrip line excitation.

In order to formalize our design optimization, the following specification is provided:

- FR4 epoxy glass substrates (it is chosen for cost reasons): relative permittivity ε_r = 4,6 , tan ∂ = 0,018 , h = 1,6*mm*
- The conductor: it is copper, *t* = 35 µ*m* .
- The type of excitation chosen is the Wave Port for simulation in HFSS.
- The resonance frequency is f1= 3.26 GHz.

The S31 and S41 (characteristics transmission: coupled and through) are given by:

$$S_{41} = \frac{\sqrt{1-k^2}}{\sqrt{1-k^2}.\cos(\vartheta) + j\sin(\vartheta)} \quad (1)$$

$$S_{31} = \frac{jk\sin\vartheta}{\sqrt{1-k^2}.\cos\vartheta + j\sin\vartheta} \quad (2)$$

θ=β*l* denotes the electrical length of the coupler and k is given by :

$$k = \frac{Z_{0e} - Z_{0o}}{Z_{0e} + Z_{0o}} \quad (3)$$

where Z_{0e} and Z_{Oo} denote the characteristic impedance of the even-mode ans odd mode of symmetrical coupled lines respectively, which verify this condition [7] :

$$Z_{0e}Z_{0o} = Z_0{}^2 \quad (4)$$

We can write Z_{0e} /Z_{0o} in terms of a voltage coupling coefficient *k* as [7]:

$$\frac{Z_{0e}}{Z_{0o}} = \frac{1+k}{1-k} \quad (5)$$

If the coupling from port 1 to port 3 is given as *C* dB (where *C* is a positive quantity), then *k* is related to *C* as [7]:

$$k = 10^{-C/20} \quad (6)$$

The geometric parameters: given in the figure below:

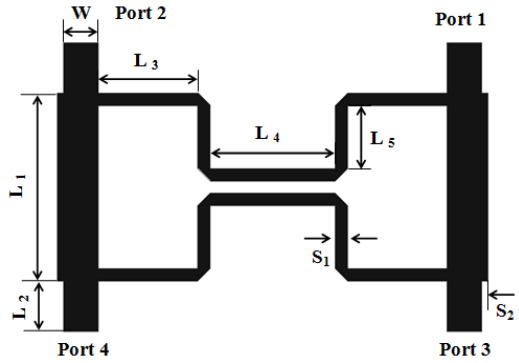

Figure 3. Geometry and dimension of the proposed coupler with:

L1=15mm; L2=4mm; L3=8mm; L4=10m; L5=5mm; S1=1mm; S2=0.5mm; and W=1.8mm.

The simulations were performed using the high-frequency structure simulator (HFSS) software who owns an electromagnetic simulator. It is based on Finite Element Method (FEM), also it requires the use of mesh patterns.

Figure 4. (left) Measurement setup: a network analyzer E5071C being used for *S*-parameter measurement, (right) component under test.

This stage of coupler measures validates the simulation steps (see Fig. 5).

These measurements are made using Vector Network Analyzers E5071C being used for *S*-parameter.

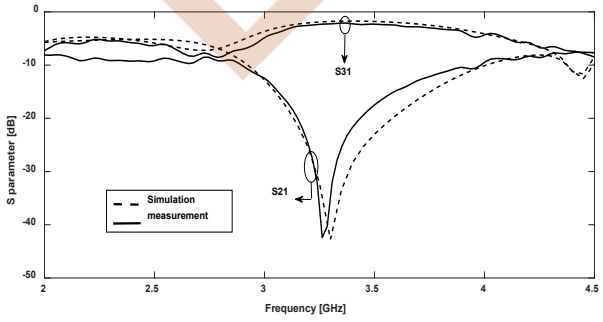

(a)

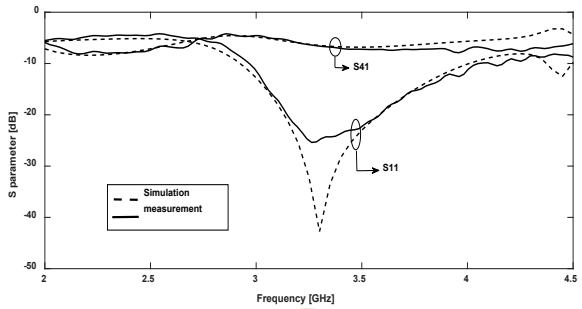

(b)

Figure 5. Simulated and measured *S*-parameters: (a) *S*11 and *S*21, and (b) *S*31 and *S*41.

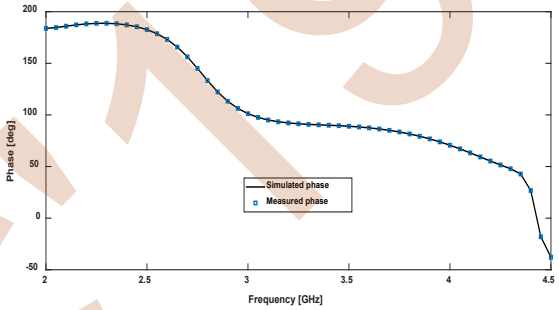

Figure 6. Measured phase difference between Port 3 and Port 4.

The measurement results shows that the branch line coupler can operate at $f = 3.26$ GHz which are selected as the operating frequency.

The comparison of the performances of the proposed coupler is summarized in Table 1.

Table 1 Performance of Branch line meandered Coupler.

	Frequency GHz	S21 dB	S31 dB	S41 dB	S11 dB	Phase Diff	$\lvert S_{41}\rvert - \lvert S_{31}\rvert \leq \pm 1dB$
Simulation	**3.30**	**33.04**	**1.74**	**6.45**	**42.74**	**90.87°**	**4.71**
Measurement	**3.26**	**42.41**	**2.29**	**6.40**	**25.39**	**91.22°**	**4.11**

The frequency shifting may be caused by weld of SMA connectors.

At the center frequency of 3.26 GHz, th*e* return loss S11 is -25.39 dB and the isolation S21 is -42.41 dB.

In the range of bandwidth, the insertions losses and S31 is -2.29 dB, it is under -3 dB and S41 is - 6.40 dB. Above all, the fabricated coupler only occupies 23×34.6 mm^2 which work at the center frequency of 3.26 GHz. Measured phase difference between Port 3 and Port 4 is 91.22° at operating bandwidth, shown in Fig. 6.

III. CONCLUSION

In this study, a new miniaturized compact coupler proposed. The main purpose of this study is used meandering transmission-line section to replace the shunt arms of the classical coupler. For improved accuracy, the frequency response of the couple was optimized by numerical simulation and fabricated on the FR4-substrate.

The simulated results are in agreement with those measured which demonstrates the interest and efficiency of numerical modeling with HFSS. This work made it possible to highlight the feasibility of the realized coupler RF and Microwave Coupled-Line Circuits

REFERENCES

[1] R. K. Mongia, I. J. Bahl, P. Bhartia and J. Hong, "RF and Microwave Coupled-Line Circuits, " 2007 Artech House, INC.

[2] Samuel. Liao, Y., "Microwave Devices and Circuits", 3rd ed., Prentice Hall, Englewood Cliffs, USA: New Jersey 07632,1990, pp. 150-160.

[3] Maktoomi, M. A., Mohammad S. Hashmi, and Fadhel M. Ghannouchi, "A Dual-Band Port-Extended Branch-Line Coupler and Mitigation of the Band-Ratio and Power Division Limitations" , IEEE Trans on components, packaging and manuf tech, Vol 7,2017, pp. 1313-1323.

[4] H. Liu, S. Fang, and Z. Wang, "A Compact Trans-Directional Coupler With Wide Frequency Tuning Range and Superior Performance," IEEE Trans On Components, Packing and Manufacturing Technology, 2017.

[5] O. D. Gurbuz and G. M. Rebeiz, "A 1.6-2.3 GHz RF MEMS reconfigurable quadrature coupler and its application to a 360° reflectivetype phase shifter," *IEEE Trans. Microw. Theory Techn.*, vol. 63, no. 2, pp. 414–421, Feb. 2015.

[6] Pozar, D. M., "Microwave engineering",4rd ed., John Wiley & Sons, Inc, USA :Amherst, 2011, pp. 320–379.

Study of the Structural and Optical Properties of Binaries(GaAs, InAs, GaN et InN)

Lyakout Achour
Laboratoire de Maitrise des Energies Renouvelables
A. Mira University
Bejaia, Algeria
yakout.achour@gmail.com

Smail Berrah
Laboratoire de Maitrise des Energies Renouvelables
A. Mira University
Bejaia, Algeria
Sm_berrah@yahoo.fr

***Abstract*—Electronics and more specifically optoelectronics are present in multiple domains and take an increasingly important place especially in fiber optic telecommunications and energy conversion systems. The rapid development of optoelectronics would not have occurred without an excellent knowledge of the materials used. The study of semiconductor materials has therefore been a special place for some years and always represents the essential step in the design of any optoelectronic device.**

I. INTRODUCTION

The III-V compound semiconductor materials and their advantageous optical and electronic properties have been a driving force in fundamental research on this type of material for decades [1]. These have excellent transport and optical properties, and thus include a wide range of mesh parameter choices that allow the development of new devices or improve them taking into account the engineering of bandwidth [2]. The elements of the III-V semiconductor group can be mixed with other atoms to adapt the band gap to achieve desirable electronic and optical properties for the realization of desired devices. Advances and studies on III-V nitride-based semiconductors have led to an exponential increase in activity oriented towards optoelectronic applications [3]. In addition to new possibilities in device applications provided by this new class of materials, many distinctly different interesting physical properties have been discovered [4].

II. COMPUTATIONNEL DETAILS

A. Method of calculating the electronic structure

Quantum mechanics defines a particle of matter as a wave, that is to say, it does not have a well-defined trajectory, rather distributed to the space [5]. The data of the wave function of the particle allows describing his condition. To find the wave function of a system, the Austrian physicist Schrödinger proposed a time-independent equation which is written as follows [6]

$$H\Psi(r) = E\Psi(r). \qquad (1)$$

Where:
H : The Hamiltonien
E : The total energy of the system.
Ψ : the wave function.

The resolution of the Schrödinger equation with an electron number N greater than or equal to 2 is not exact. For such a system, it is necessary to use approximate methods, if one wishes to access a realistic solution of H. The theory of the functional density (DFT) thus offers interesting perspectives [7].
The Hamiltonien is of form:

$$H = T_n + T_e + V_{n\_n} + V_{n\_e} + V_{e\_e}. \quad (2)$$

Where:
T_n: The kinetic energy of the nuclei.

T_e : The kinetic energy of electron.

V_{n_n}: The potential energy of interaction between the nuclei.

V_{n_e} : The potential energy of attraction nuclei-electron.

V_{e_e} : The potential energy of repulsion between electrons.

The solution of the equation leads to the resolution of a N-body problem [7]. It is impossible to solve this problem exactly. In order to find acceptable approximated states, we need to make approximations. The first approximation that can be introduced is the approximation of Born-Oppenheimer [8].

B. *Optical properties*

To obtain a better understanding of the optical properties in our semiconductors, it is important to calculate the expressions of the two basic optical constants, the real and imaginary part of the dielectric function ε (ω).

$$\varepsilon(\omega) = \varepsilon_1(\omega) + i\varepsilon_2(\omega) \qquad (3)$$

To deduce the real part ε_1 (w), we use the Kramers-Kronig transformation:

$$\varepsilon_1(\omega) = 1 + \frac{2}{\pi} p \int_0^{\infty} \frac{\omega' \varepsilon_2}{\omega'^2 - \omega^2} d\omega'. \qquad (4)$$

The imaginary part is given by:

$$\varepsilon_2(\omega) = \frac{4e^2\pi^2}{m^2\omega^2} \times \sum \int \frac{2dk}{(2\pi)^3} \left|\langle \varphi_{fk} | e.p | \varphi_{ik} \rangle\right|^2 \times \partial(E_v(\omega) - Ec\omega - \hbar\omega. \qquad (5)$$

Where e is the electron charge, m its mass, p the principal value of the Cauchy integral, ω the volume of the crystal and E_v, E_c are the energies respectively, φ_{fk} is the Fermi distribution function, φ_{ik} is the wave function of the crystal considered, corresponding to the same eigenvalue of k.

III. RESULT AND DISCUSSION

A. *Volum optimization and sructural parameters*

The Figure 1 represents the variation of the energy as a function of the volume for the various binary composants.

By comparing our results of the mesh parameters calculated by the approximation (LDA) with the experimental values, we find that this parameter a_0 is lower than the latter by approximately 0.58 for GaAs and for the three other binary compounds (GaN, InAs, InN) the error is zero.

In TABLE I, we summarize the computed equilibrium lattice constant *a*

TABLE I. THE LATTICE CONSTANT OF THE BINARY COMPOUNDS COMPARED TO EXPEROMENTAL AND THEORETICALVALUES

Materials	Our results (A°)	Other theoretical works	Experimental results
GaAs	5,607	5,66 [7]	5,64 [8]
GaN	4,5	4,46 [7]	4,50 [9]
InAs	6,03	6,026 [9]	6,036 [9]
InN	4,98	4,946 [10]	4,98 [10]

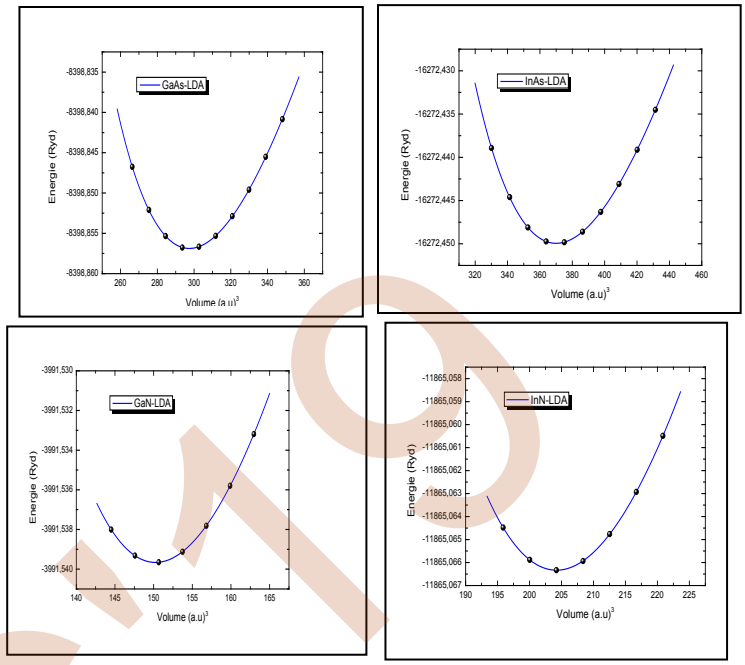

Figure 1. Total energy variation by volume for the four compounds binary GaAs, InAs, GaN and InN.

B. *Bands structure*

From the band structure of GaAs, InAs, GaN and InN semiconductors, we determined their electronic properties and their gap energy.

The results of calculations by the TB-mBJ approximation for the four binary compounds were carried out along lines of high symmetry of the first Brillouin zone. The calculation was performed using the network parameter calculated in the previous section. The resulting band structure is illustrated in Figure 2 and Figure 3. From these figures we see that all our compounds have a direct energy

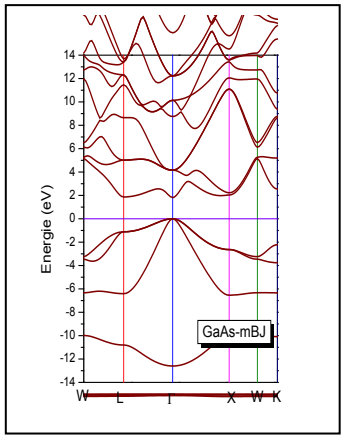

Figure 2. Band structure of the binary compound GaAs obtained by the mBJ approximation

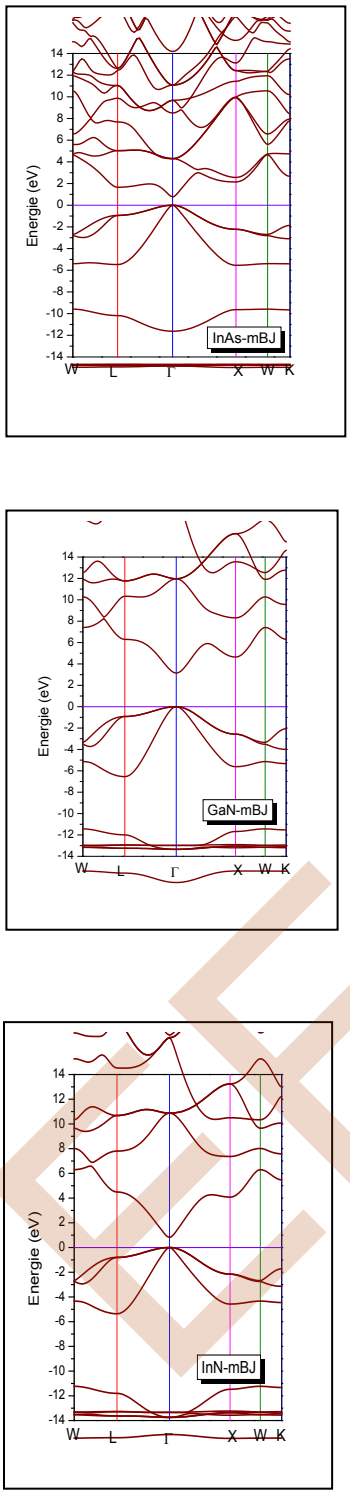

Figure 3. Band structure of the binary compounds InAs, GaN and InN obtained by the mBJ approximation

C. Optical properties

The calculation of the spectral variations of the dielectric function of the imaginary part for the GaAs, InAs, GaN et InN binary compounds are represented in Figure 4.

After analyzing the spectrum of the imaginary dielectric function $\varepsilon_2(\omega)$., we note that the two arsenide-based binary GaAs and InAs are characterized by three peaks in the energy range between the absorption threshold and 8 eV. These peaks occur at 3.14, 4.88 and 6.20 eV for GaAs; in the case of the InAs compound, the three peaks being at 2.81, 4.71 and 6.08 eV by a TB-mBJ calculation.

In the case of nitride compounds, GaN and InN, it is observed that the optical spectrum of the $\varepsilon_2(\omega)$ part of the dielectric function contains three small groups of peaks instead of three major peaks. The first small group of peaks is presented in the threshold energy range at 10 eV. This last contains two major peaks at 7.80 and 8.66 eV.

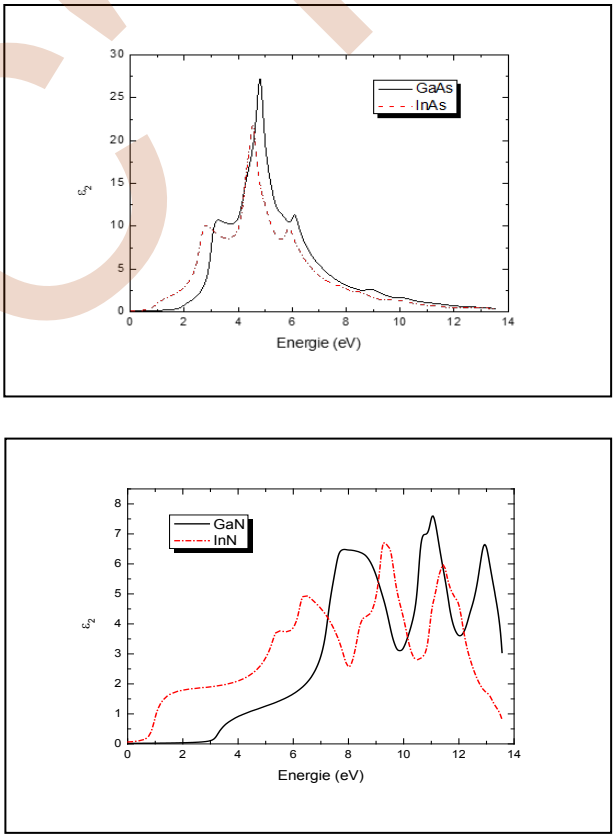

Figure 4. The spectral variation of the imaginary part of the dielectric function for GaAs, InAs, GaN and InN calculated by the TB-mBJ

From the absorption spectrum shown in the Figure 5, there is no absorption for the two GaAs and InAs binaries of 0 to 2 eV. From 2 to 10 eV, absorption increases and reaches its maximum value in the region ultraviolet (UV); the highest peak appears at 4.93 eV and 4.77 for GaAs and InAs, respectively, then decreases considerably to 14 eV.
An absence of absorption of 0 to 2.6 and 0.69 eV is observed for the binary compounds based on nitride GaN and InN respectively. above these last values, the light is absorbed to a maximum absorption of 340 and 225 × 10^4 cm^{-1} for GaN and InN, respectively.

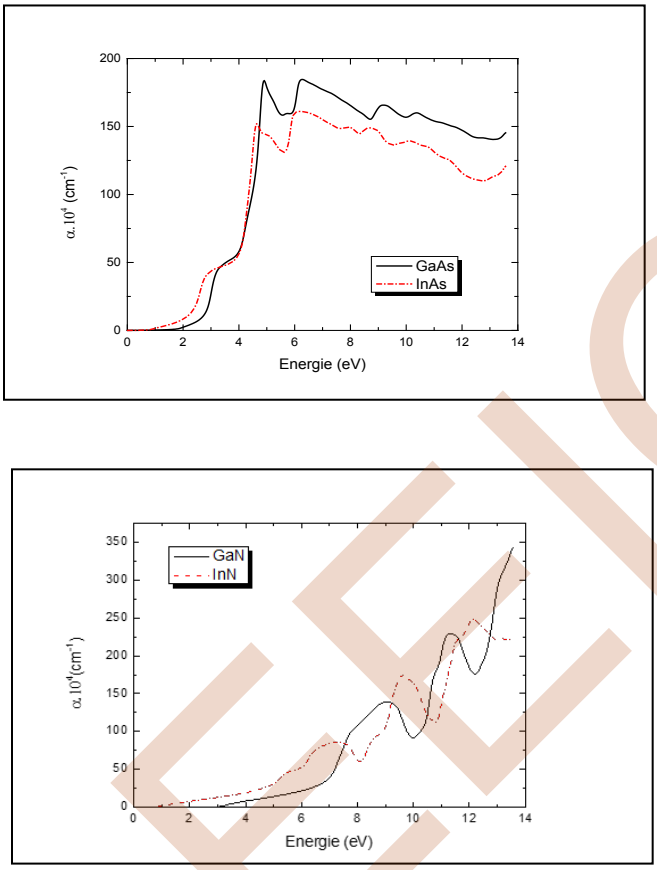

Figure 5. The spectral variation of the absorption coefficient for the GaAs, InAs, GaN and InN binary compounds calculated by the TB-mBJ

CONCLUSION

Our objective in this work is to calculate the structural, electronic and optical properties of the GaAs, InAs, GaN and InN binary compounds in the ground state. The linear augmented plane wave method with full potential (FP-LAPW) in the framework of density functional theory (DFT) has proven effective in the calculation of structural and electronic properties. Our results concerning the structural properties are in good agreement with the experimental values, the calculation of the band structure, gave a direct gap at the point Γ. For optical properties, we calculated the dielectric function in order to identify the optical transitions, which made it possible to determine other quantities (absorption coefficient, refractive index and reflectivity). It has been noticed that our materials have a high absorption coefficient and a high reflectivity. That said, these materials are predisposed to the manufacture of optical transmitters.

REFERENCES

[1] S. Adachi, Properties of semiconductor alloys: Group IV, III-V and II-VI semiconductors, Jhon Wiley and Sons, 2009.

[2] J.A. Camargo-Martinez, R. Baquero, "The modified Becke-Johnson potential analyzed", Superf. Y Vacio, Vol. 26, Issue 2, pp. 54-57, 2013.

[3] B. Amin, I. Ahmad, M. Maqbool, S. Goumri-Said, R. Ahmad, " Ab initio study of the bandgap engineering of $Al_{1-x}Ga_xN$ for optoelectronic applications", J. Appl. Phys., Vol. 109, Issue 2, 2011.

[4] M. I. Ziane, Z. Bensaad, B. Labdelli and H. Bennacer, "First-principles study of tructural, electronic and optical properties of III-arsenide binary GaAs and InAs and III-nitrides binary GaN and InN: improved density-functional-theory study", Sensors & Transducers, vol. 27, Special Issue, pp. 374–384, May 2014.

[5] Z. B. Feng, H. Q. Hu, S. X. Cui, W. J. Wang and C. Y. Lu "First principles study of electronic and optical properties of InAs", Central European Journal of Physics, vol. 7, Issuse 4, pp.786–790, 2009.

[6] I. Vurgaftman, J. R. Meyer and L. R. Ram-Mohan, "Band parameters for III-V compond semiconductors and their alloys", APPL. J. Phys, Vol. 89, pp. 5815- 5875, 2001.

[7] A. Assali, M. Bouslama, H. Abid, S. Zerroug, M. Ghaffour, F. Saidi, "Materials science in semiconductor processing optoelectronic properties of cubic $B_xIn_yGa_{1-x-y}N$ alloys matched to GaN for designing quantum well lasers: first-principles study within mBJ exchange potential", Mater. Sci. Semicond. Process., Vol. 36,pp. 192-203,2015.

[8] M. Aslan, B. G. Yalcin, M. Ustundag,"Structural and electronic properties of $Ga_{1-x}In_xAs_{1-y}N_y$ quaternary semiconductor alloy on GaAs substrate", Journal of Alloys and Compounds, Vol. 519, pp. 55-59, 2012.

[9] M. Yousaf, M. A. Saeed, R. Ahmed, M.M. Alsadria, A.R:M. Isa, A. Shaari, "An improved study of electronic band structure and optical parameters of X-Phosphides (X=B, Al, Ga, In) by modified Becke-Johnson potential", Theor. Phys., Vol. 58, Issue 5, pp. 777-784, 2012.

[10] M. Hadjab, S. Berrah, H. Abid, M: I. Ziane, H. Benacer, B. G. Yalcin, "Full-potential calculations of structural and optoelectronic properties of cubic indium gallium arsenide semiconductor alloys", Optik, Vol. 127, pp. 9280-9294, 2016.

Design of a New SIW-DGS band-pass Filter Configuration for C-band

CHERIF Nabil
Department of electrotechnical
Mustapha Stambouli University
Mascara, Algeria
nabil.cherif@univ-mascara.dz

ABRI Mehadji
Department of Telecommunications
Abou Bekr Belkaid University
Tlemcen, Algeria
abrim2002@yahoo.fr

FELLAH Benzarga
Department of electrotechnical
Mustapha Stambouli University
Mascara, Algeria
fellahbenzerga@gmail.com

KHIAL Chahira
Department of Telecommunications
Abou Bekr Belkaid University
Tlemcen, Algeria
chahira-khial@hotmail.com

BOUABDALLAH Roumeiça
Department of Telecommunications
Abou Bekr Belkaid University
Tlemcen, Algeria
roumeissa13@gmail.com

Abstract*— In this paper, a C-band band-pass filter based on substrate integrated waveguide-to-defected ground structure (SIW-DGS) cell is presented. Microstrip to SIW transition is used to provide smooth transition between the structures. Using two cascading DGS cells in the top of the plane cavity to constitute a multiple mode resonator and two cascading slots in the bottom plane for enhance the filter's performances by using CST and HFSS software. The filter is developed on FR4 substrate with dielectric constant of 4.3 and thickness of 1.54mm. Good selectivity and Low insertion loss are achieved and good agreement between CST and HFSS simulation results.

Keywords*— Substrate integrated waveguide, band-pass filter, defected ground structure, microstrip transition.

I. INTRODUCTION

Recently development of communication systems is towards minimized weight, reduced size, and increased reliability with low cost. Microwave components such as waveguide filters, antenna and power divider are a very important part of modern telecommunications systems: embedded satellite systems, telecommunication systems in general [1].

The rectangular waveguide is one of the most used microwave components, however due to its bulky structure it is difficult to manufacture at low cost and integrate it into planar structures. To answer this problem and for a Clutter less, scientists have opted for the development of planar structures. A promising new technology has emerged substrate integrated waveguide (SIW) [5].

The SIW technologies are used for the design of various components serving hyperfrequency systems such as: WIFI antenna [3], leaky wave antenna [4] antipodal antenna [2] band-pass filter using reactive longitudinal periodic structures [7].

Another promising approach is the defected ground structure (DGS), which is etched as cells in the ground plane of planar circuit board to generate resonance, increase stop-band reduction and reduce size of the circuit.[6][8]

The half mode substrate integrated waveguide (HMSIW) is an integrated waveguide with modified the proposed structure. It shows similar propagation characteristic to that of SIW and smaller size. Moreover, and it also retains the same advantages of low loss, compact size and high Q quality factor [10].

II. SIW WAVEGUIDE DESIGN METHOD

The main problem in SIW circuit design is related to minimizing losses. It is just necessary to modify geometrical parameters, namely the thickness of the substrate "h", the diameter "d" of the metal vias and their spacing "s" and the SIW waveguide width "as" [9]. To design a good SIW structure, you must adhere to certain design rules.

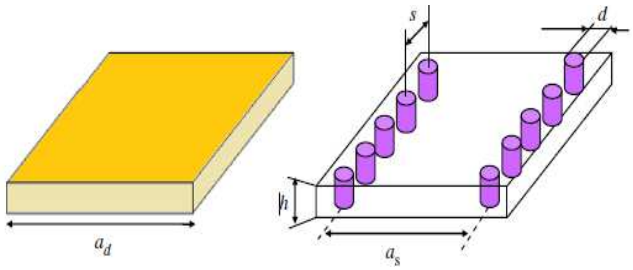

Figure 1. Dielectric filled waveguide DFW with SIW configurations.

For dielectric filled waveguide DFW, the dimension "ad" of the waveguide is calculated by Equation 1 where ε_r is the relative dielectric constant of the dielectric that fills the waveguide and "*a* "is dimension of classic waveguide [1].

$$a_d = \frac{a}{\sqrt{\varepsilon_r}} \quad (1)$$

The same cut-off frequency (f_c) for the dominant TE10 mode for a DFW can be obtained by equation 2[5].

$$f_c = \frac{c}{2a_d} \quad (2)$$

Aiming to work at the same cut-off frequency the first empirical design equation of a SIW is related to its width "as", and it is given by equation 3[7].

$$a_s = a_d + \frac{d^2}{0.95s} \quad (3)$$

To minimize the radiation and return loss due to the field leakage from the gaps between vias, two conditions are required: d < λg/5 and S ≤ 2d where λg is the guided wavelength [7].

$$\lambda g = \frac{2\pi}{\sqrt{\frac{(2\pi f)^2 \varepsilon_r}{c^2}\left(\frac{\pi}{a}\right)^2}} \quad (4)$$

The transition between the micro-ribbon line and the substrate integrated waveguide and the improvement of their performance requires the calculation of the output impedances Z_{pi} from the input impedance which is equal to: 50Ω. The Impedance is calculated using the following equations [1].

$$Z_{pi} = Z_{TE}\frac{\pi^2 h}{8a_s} \quad (5)$$

Z_{TE}: represent the wave impedance for the TE10 mode it's given by following equation [1].

$$Z_{TE} = \sqrt{\frac{\mu}{\varepsilon_r}} \times \frac{\lambda_g}{\lambda} \quad (6)$$

III. BAND-PASS SIW FILTER DESIGN

Using the CST we designed a new SIW-DGS band-pass filter structure for C-band on FR4 based substrate having a loss tangent approximately 0.018, a relative permittivity of 4.3, a thickness h of 1.54 mm and the thickness of the conductor equal to 0.05mm. The DGS cells inserted at the top plane and bottom plan are shown in the figure 2.

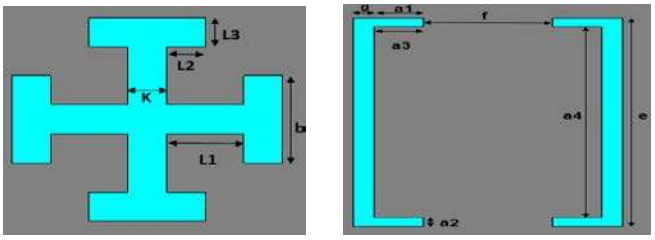

(a) (b)

Figure 2. The proposed DGS structure in the (a) top plan and (b) bottom plan for SIW filter with : L1=1 mm, L2=0.5 mm L3=0.5 mm, b=1.5 mm K=0.5 mm, g=0.5 mm, a1=1.13 mm, a2=0.5 mm, a3=1.13 mm, a4=11 mm f=3 mm, e=12 mm.

We take the structure of the filter with two cascading DGS cells in the top plane with a distance between them equal to 5.5 mm, and two cascading DGS cells in the middle of the bottom plane with a distance between them equal to 1.61mm. The simulation results is shown in the Figure 4.

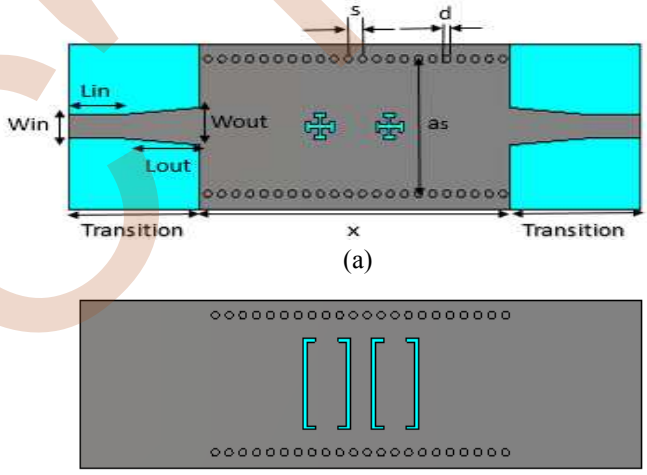

(a)

(b)

Figure 3. Structure of the DGS-SIW band-pass filter, (a) top view (b) bottom view with Win=3.2 mm, Wout=5 mm, Lin=7.4 mm, Lout=10.5 mm, as=20 mm, s=1.8 mm, d=1 mm, x=40 mm.

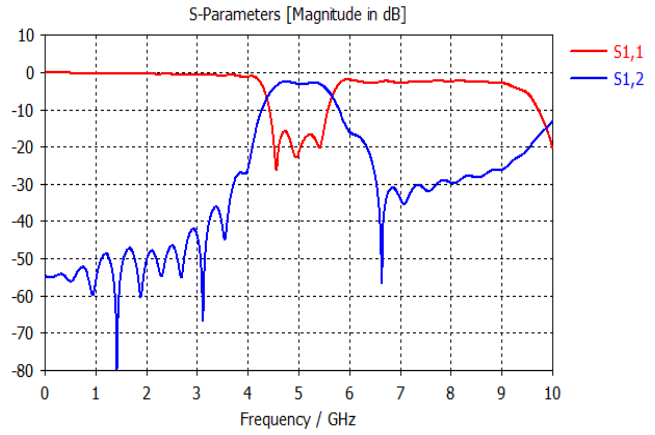

Figure 4. Transmission coefficient and return loss of SIW DGS filter.

From Figure 4 we observe that the transmission power is very good in the frequency band [4.3-5.8 GHz], and the reflection is weak, we observe many peaks, the best reaches -28 dB at the frequency of 4.5 GHz. The rejection is very good and it reaches -56 dB around the frequency of 6.6 GHz. From this analysis it can be said that this SIW filter is functional in the C band with good performance.

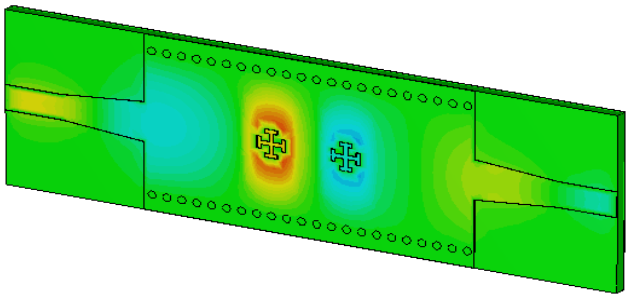

Figure 5. Distribution of the electric field at the frequency of 4.5 GHz.

Depending on distribution of the electric field, most of the energy is confined in the DGS cells, so that most of the transmission can be done around the cells, which can reduce the transmission loss resulting from the coupling opening in a conventional cavity filter.

VI. HMSIW BAND-PASS FILTER DESIGN

For The half-mode SIW filter, simply cut of the previous structure in two and eliminate one half and keep the other half. We use the parametric study by CST software for optimized the filter performance. The half mode SIW band pass filter structure is shown in the Figure 6 with the optimized value.
The distance between DGS cells in the top plan is: 0.50 mm and between DGS cells in the bottom plan is 0.24mm.

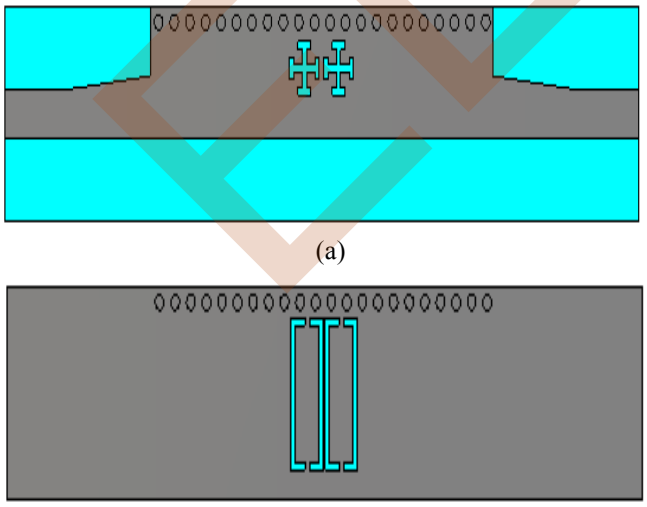

(a)

(b)

Figure 6. Structure of Half mode SIW filter (a) top view (b) bottom view.

The simulation results by the CST software are shown in the following figure:

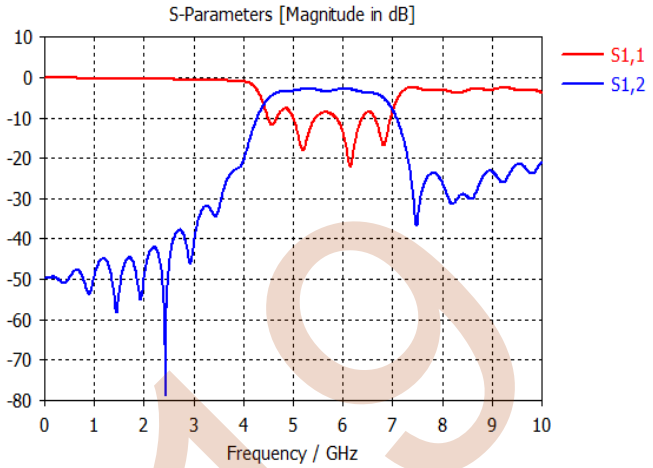

Figure 7. Transmission coefficient and return loss of HMSIW filter.

From the previous figure we observe that: the transmitted power is zero and the reflected power is total in the band ranging from 0.1 to 4.2 GHz. In the band [4.3-6.8 GHz] the transmission power increases and it reaches -1.8 dB and the reflected power has several peaks the best reaches - 22 dB around the frequency 6.1 GHz. about the rejection it is good and it reaches -39 dB at a frequency of 7.5 GHz.

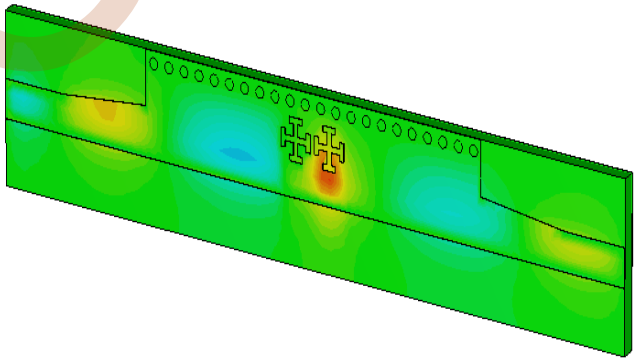

Figure 8. Distribution of the electric field at the frequency of 6.1 GHz.

We observe from distribution of the electric that the energy restrained in the DGS cells so that most of the transmission can be carried out around the DGS cells which can reduce the transmission loss resulting from the coupling opening in a conventional cavity filter

V. COMPARAISON OF THE RESULTS

In Figure 9 and Figure 10, the results of comparisons are made between CST Microwave Studio and Ansoft HFSS respectively transmission coefficient and return loss. HFSS tool based on the finite element method (FEM) and CST Microwave studio uses FIT (finite integration technique, a relative of FDTD) for its transient solver.

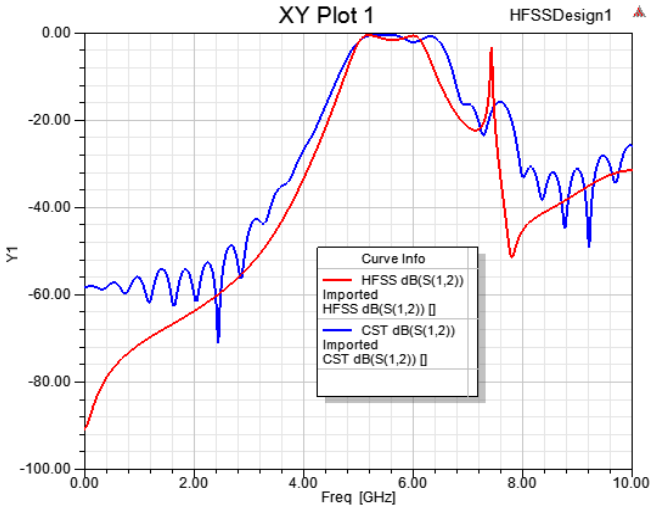

Figure 9. Transmission coefficient of SIW DGS filter.

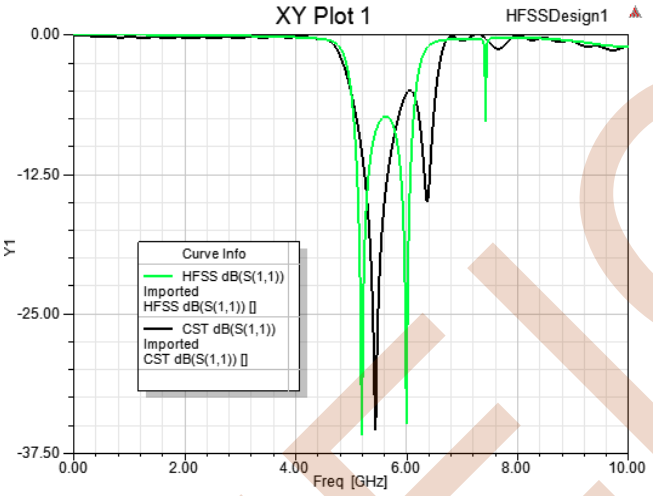

Figure 10. Return loss of the SIW DGS filter.

From the figure 9 and figure 10 it is show that excellent results are obtained. The simulation results show a good agreement of the cut-off frequency that is of 4.6 GHz. We observe a good agreement in the filtered band ranging from 4.6 to 6.4 GHz with an insertion loss of about −0.95 dB in the transmitted bandwidth and the recorded return loss reaches until −36 dB at the frequency 5.2 GHz and 6 GHz. It can also be noted that we have an agreement in the rejection bands that ranging from 1 to 4.5 GHz and from 6.5 to 8 GHz. A gap of several dB is observed because each software program use different numerical methods. We obtained a good agreement between the obtained results by CST Studio and Ansoft HFSS software which demonstrates our proposal.

VI. CONCLUSION

In this work a DGS SIW band-pass filter is designed and simulated for C-band applications, the design method is discussed. CST and HFSS software are used for the simulation and we compared between obtained results. The proposed filter possesses better out of band properties using cells DGS and he has better overall performance in insertion loss, return loss and size. The HMSIW filter has a size reduction of 50% compared to a similar SIW filter. This type of filter is easy for integration with other planar circuit compared by using conventional waveguide. This SIW DGS band-pass filter has high-rejection so it is suitable for practical applications.

The results from our work are in good agreement with previous research done on this topic and we will work to miniaturize the size of this filter with high performance in return loss, insertion loss and rejection.

REFERENCES

[1] Ahmed Noura. Mohamed Benaissa. Mehadji Abri. Hadjira Badaoui Tan-Hoa Vuong. Junwu Tao, "Miniaturized half-mode SIW band-pass filter design integrating dumbbell DGS cells," microwave and optical technology letters Volume 61, Issue 6 June 2019 Pages 1473-1477.

[2] Fellah B, Abri M. Design of antipodal linearly tapered slot antennas (ALTSA) arrays in SIW technology for UWB imaging. Springer: Recent Adv Electr Eng Control Appl. PP381-389 ICEECA 2016.

[3] Arora R, Rana SB, Arya S. Performance analysis of Wi-Fi shaped SIW antennas. AEU-Int J Electron C.94, P 168-178, september 2018

[4] Agrawal T, Srivastava S. Ku band pattern reconfigurable substrate integrated waveguide leaky wave horn antenna. AEU-Int J Electron C.87, P 70-75, 2018.

[5] Mohamed Amine Rabah, Mehadji Abri, Hadjira Abri Badaoui, Junwu Tao, and Tan-Hoa Vuong, 'Compact Miniaturized Half-Mode Waveguide/High Pass-Filter Design Based On Siw Technology Screens Transmit-IEEE C-Band Signals', Volume58, Issue2, Pages 414-418, February 2016.

[6] Ahn, D., J.-S. Park, C.-S. Kim, J. Kim, Y.-X. Qian, and T. Itoh,"A design of the low-pass filter using the novel microstrip defected ground structure," IEEE Trans. on Microw. Theory and Tech., Vol 49, No. 1, 86-93, Jan. 2001.

[7] Moitra S, Sarathee Bhowmik P. Modelling and analysis of substrate integrated waveguide (SIW) and half-mode SIW (HMSIW) band-pass filter using reactive longitudinal periodic structures. AEU-Int J Electron C.70 P 1593-1600, 2016.

[8] Gupta, N., P. Ghosh, and M. Toppo, "A miniaturized Wilkinson power divider using DGS and fractal structure for GSM application," Progress In Electromagnetics Research Letters, Vol. 27, P 25-31 2011.

[9] Y. Huang, Z. Shao, and L. Liu, "A substrate integrated waveguide bandpass filter using novel defected ground structure shape" Progress In Electromagnetics Research Vol. 135 pp. 201-213, 2013

[10] Yuanqing Wang, Wei Hong, Yuandan Dong, Bing Liu, Hong Jun Tang, Jixin Chen, Xiaoxin Yin, Ke Wu," Half Mode Substrate Integrated Waveguide (HMSIW) Bandpass Filter" IEEE Microwave and Wireless Components Letters VOL. 17, No. 4, April 2007.

Two-channel Noise Reduction Techniques Based on Efficient Sparseness Recursive Algorithm

Rédha Bendoumia
Dept. Electronics
Blida 1 university
Blida, Algeria
r.bendoumia@yahoo.fr

***Abstract*— recently, several adaptive filtering algorithms have been combined with dual blind source separation (BSS) technique for acoustic noise reduction and speech signal enhancement. This smart combination gives good results in term of speech quality and convergence rate when the acoustic environments are characterized by dispersive impulse responses. However in videoconference applications, the impulse responses are non-dispersive (i.e. sparse). In this paper, we propose a new implementation of dual Backward BSS technique based on μ-law proportionate algorithm for speech enhancement. This new implementation is proposed exactly to resolve the problem of non-proportionate backward algorithm when the acoustic environment is characterized by sparse impulse responses. To validate the performance of proposed algorithm, we do intensive experiments based on several criteria.**

Keywords*— *Speech quality; μ-law proportionate algorithm; Backward BSS structure, Convergence speed.

I. INTRODUCTION

Noise cancellation (NC) is often used in many applications in telecommunication systems such as hand-free telephony. To improve the robustness of telecommunication systems [1-2], several techniques are proposed to resolve this problem [3-5]. Recently, blind source separation (BSS) technique has been used exactly in two-channel convoluted dispersive systems to separate the speech and acoustic noise [6-7]. A very important works have investigated in NC subject by using different adaptive filtering algorithms combined with the BSS techniques [8-10]. These approaches are proposed to improve the behavior of NC systems in terms of speed convergence and steady state [8]. The dual backward BSS is important structure that is used to enhance the speech signal. Full analyses of this method are described previously [8-15].

In all these works, the two-channel backward adaptive filtering algorithms have been proposed in time and frequency domains [8]. These algorithms are used to identify the dispersive impulse responses (IRs). The two-channel backward normalized least mean square (NLMS) algorithm presents an important solution for acoustic noise reduction. However, the main drawback of this algorithm is their poor performance when the IRs are sparse. This inconvenience is well observed in transient phase. To overcome these problems, this algorithm have to consider the following notes, (i) need to adapt a relatively long filter, and (ii) unavoidable adaptation noise occurs at the inactive region of the tap weights [16].

In this paper, we propose a two-channel backward NLMS algorithm based on μ-law proportionate version (noted BMP_{NLMS} for Backward μ-law Proportionate NLMS). This algorithm based on specific normalized step-sizes and proportionate technique. The BMP_{NLMS} algorithm allows improving convergence speed and the misadjustement.

This paper is presented as follows: in section 2, the two-channel convoluted system is detailed. In section 3, we present the classical backward NLMS algorithm (BNLMS). The proposed BMP_{NLMS} algorithm is presented in Section 4. In section 5, we present the simulation results part and finally the conclusion is presented in section 6.

II. TWO-CHANNEL CONVOLUTIVE SYSTEM

In this system, we consider a first source of speech $s(n)$ and a second source is punctual noise signal $b(n)$. These two source signals are convolutedly mixed with two impulses responses of mixture system ($h_{12}(n)$ and $h_{21}(n)$) [3-4]. The output signals of this model are given by

$$p_1(n) = s(n) + b(n) * h_{21}(n) \quad (1)$$

$$p_2(n) = b(n) + s(n) * h_{12}(n) \quad (2)$$

where (*) represents the convolution operation.

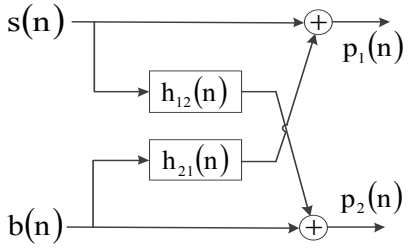

Figure 1. Two-channel convolutive mixing system

We assume that, the first microphone is close to the speaker and the second microphone is close to the noise source, thus, the direct acoustics paths are equal to the Kronecker unit impulse [3, 4, 8].

III. ACOUSTICS IMPULSE RESPOSE TYPES

In several situations as a conference system or a hands-free communication system, where an acoustic noise canceler is required to estimate an acoustic impulse response. The length of an acoustic impulse response is related to the reverberation time of an enclosed space, while the reverberation time is proportional to the volume of the space and inversely proportional to the absorption area [6].

Dispersive impulse response (DIR): A dispersive impulse response (DIR) has distributed most of its energy more or less evenly across all of the coefficients.

Sparse impulse response (SIR): Conversely, a sparse impulse response (SIR) is that in which a large percentage of the energy is distributed to only a few coefficients, while the remaining are zero or small enough to be ignored.

Figure 2 illustrates two examples of DIR and SIR [17-18].

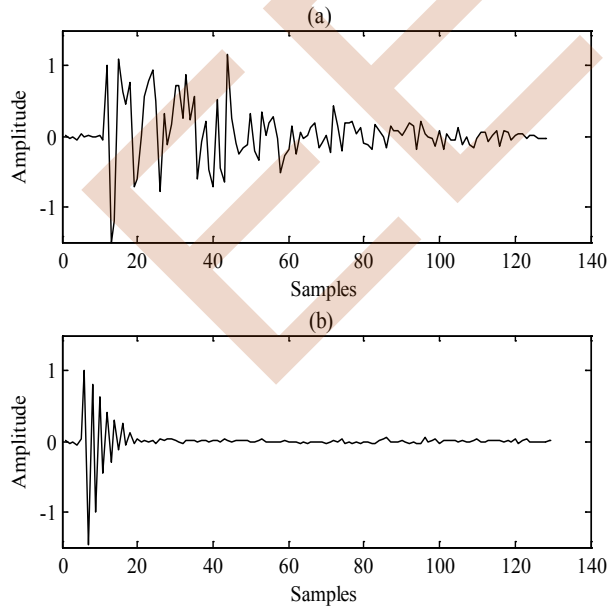

Figure 2. Impulse responses with $L = 128$, (a) DIR and (b) SIR.

IV. BACKWARD BSS STRUCTURE BASED ON NLMS ALGORITHM

In this section, we present the backward adaptive filtering NLMS algorithm (BNLMS). Firstly, we presents the dual backward BSS structure that is presented in Fig. 3. At the output of this structure, the estimated speech and acoustic noise signals are estimated as:

$$\tilde{s}(n) = p_1(n) - \tilde{b}(n) * w_{21}(n) \quad (3)$$

$$\tilde{b}(n) = p_2(n) - \tilde{s}(n) * w_{12}(n) \quad (4)$$

The optimal solutions for the two adaptive filters are given as

$$w_{21}^{opt}(n) = h_{21}(n) \quad (5)$$

$$w_{12}^{opt}(n) = h_{12}(n) \quad (6)$$

By inserting (1) and (2) in (3) and (4), as we consider the optimal solutions for the two adaptive filters, see (5) and (6). The output signals relations of can be rewritten as

$$\tilde{s}(n) = s(n) \quad (7)$$

$$\tilde{b}(n) = b(n) \quad (8)$$

The adaptation relations by NLMS algorithm of $w_{12}(n)$ and $w_{21}(n)$ are given by the following expressions:

$$\mathbf{w}_{12}(n) = \mathbf{w}_{12}(n-1) + \mu_{12} \frac{\tilde{\mathbf{s}}(n)\,\tilde{b}(n)}{\tilde{\mathbf{s}}^T(n)\tilde{\mathbf{s}}(n) + \xi_{nlms}} \quad (9)$$

$$\mathbf{w}_{21}(n) = \mathbf{w}_{21}(n-1) + \mu_{21} \frac{\tilde{\mathbf{b}}(n)\,\tilde{s}(n)}{\tilde{\mathbf{b}}^T(n)\tilde{\mathbf{b}}(n) + \xi_{nlms}} \quad (10)$$

where $\tilde{\mathbf{s}}(n) = [\tilde{s}(n), \ldots, \tilde{s}(n - L + 1)]^T$,

and $\tilde{\mathbf{b}}(n) = [\tilde{b}(n), \ldots, \tilde{b}(n - L + 1)]^T$.

μ_{12} and μ_{21} are the step-sizes of $w_{12}(n)$ and $w_{21}(n)$, which must be chosen between 0 and 2 to achieve convergence of adaptive filters.

V. PROPOSED BACKWARD μ-LAW PROPORTIONATE NLMS ALGORITHM (BMP_{NLMS})

In this part, we present an efficient version of the backward NLMS algorithm based on μ-law proportionate and normalized step-sizes for speech signal enhancement and acoustic noise reduction.

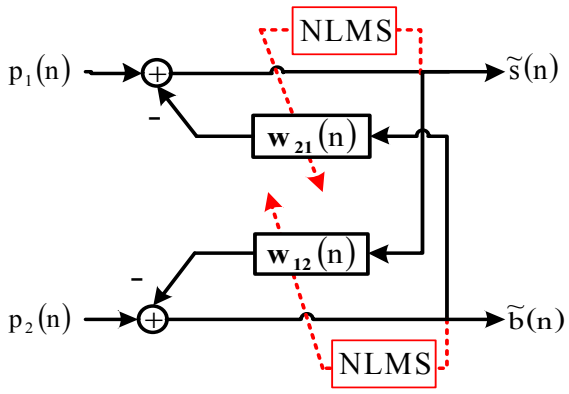

Figure 3. Dual backward NLMS algorithm.

In this algorithm, the adaptive step-sizes are calculated from the last estimate of the filter coefficients in an efficient way that the step-size is proportional to the size of the filter coefficients [16-18]. This is resulted to adjust the active coefficients faster than the non-active ones.

We propose the BMP_{NLMS} algorithm to improve the convergence rate of adaptive filters tend their optimal solutions and to enhance the speech quality, exactly in two-channel sparse system. The updating formula of adaptive filters $\mathbf{w}_{12}(n)$ and $\mathbf{w}_{21}(n)$ are given by:

$$\mathbf{w}_{12}(n) = \mathbf{w}_{12}(n-1) + \mu_{12} \frac{\mathbf{Q}_{12}(n-1)\,\tilde{\mathbf{s}}(n)\,\tilde{b}(n)}{\tilde{\mathbf{s}}^{T}(n)\mathbf{Q}_{12}(n-1)\tilde{\mathbf{s}}(n)+\xi} \quad (11)$$

$$\mathbf{w}_{21}(n) = \mathbf{w}_{21}(n-1) + \mu_{21} \frac{\mathbf{Q}_{21}(n-1)\tilde{\mathbf{b}}(n)\,\tilde{s}(n)}{\tilde{\mathbf{b}}^{T}(n)\mathbf{Q}_{21}(n-1)\tilde{\mathbf{b}}(n)+\xi} \quad (12)$$

where $\mathbf{Q}_{12}(n)$ and $\mathbf{Q}_{21}(n)$ represent the diagonals step-size control matrix (L x L) that are introduced here to determine the step-sizes of each filter coefficient. This approach used an approximation of the optimal proportionate step-size in order to achieve the fastest convergence during the whole adaptation process until the filter reaches its steady state [18]. $\mathbf{Q}_{12}(n)$ and $\mathbf{Q}_{21}(n)$ presented in two equations (13) and (14) are calculated as:

$$q_{12,l}(n) = \frac{\gamma_{12,l}(n)}{\sum_{i=0}^{L-1}\gamma_{12,i}(n)} \qquad 0 \le l \le L-1 \quad (13)$$

$$q_{21,l}(n) = \frac{\gamma_{21,l}(n)}{\sum_{i=0}^{L-1}\gamma_{21,i}(n)} \qquad 0 \le l \le L-1 \quad (14)$$

where the modified $\gamma_{12,l}(n)$ and $\gamma_{21,l}(n)$ are given by

$$\gamma_{12,l}(n) = \max\left\{\rho \times FF_{12}\,,\, F\left(\left|w_{12,l}(n)\right|\right)\right\} \quad (15)$$

$$\gamma_{21,l}(n) = \max\left\{\rho \times FF_{21}\,,\, F\left(\left|w_{21,l}(n)\right|\right)\right\} \quad (16)$$

with

$$FF_{12} = \max\left\{\delta,\, F\left(\left|w_{12,0}(n)\right|\right), F\left(\left|w_{12,1}(n)\right|\right), \ldots, F\left(\left|w_{12,L-1}(n)\right|\right)\right\} \quad (17)$$

$$FF_{21} = \max\left\{\delta,\, F\left(\left|w_{21,0}(n)\right|\right), F\left(\left|w_{21,1}(n)\right|\right), \ldots, F\left(\left|w_{21,L-1}(n)\right|\right)\right\} \quad (18)$$

ρ and δ are positive numbers with theirs typical values are ρ = 5/L and δ = 0.01. ρ presents a very small coefficient from stalling. δ regularizes the updating when all coefficients are zero at initialization.

Noting in the proposed algorithm that ξ is the regularization parameter is given by, $\xi = \xi_{nlms}/L$.

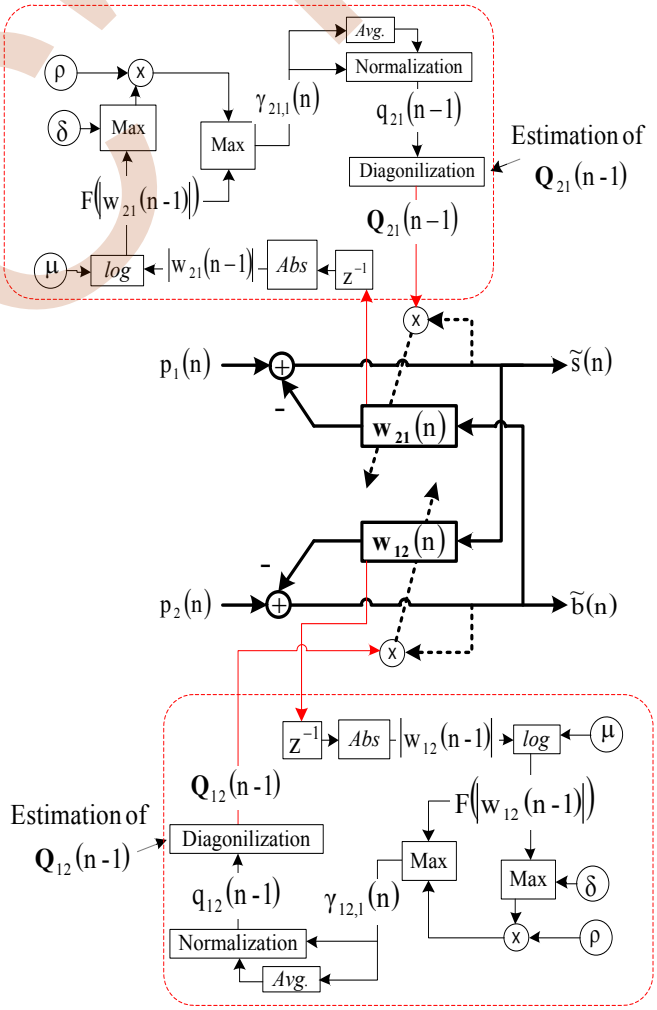

Figure 4. Detailed diagram of proposed BMP_{NLMS} algorithm.

The proposed BMP_{NLMS} algorithm was derived such that all coefficients attain a converged value to within a vicinity ε of their optimal value in the same number of iterations [16].

$$F\left(\left|w_{12,l}(n)\right|\right)=\frac{\ln\left(1+\mu\left|w_{12,l}(n)\right|\right)}{\ln(1+\mu)} \qquad 0\le l\le L-1 \quad (19)$$

$$F\left(\left|w_{21,l}(n)\right|\right)=\frac{\ln\left(1+\mu\left|w_{21,l}(n)\right|\right)}{\ln(1+\mu)} \qquad 0\le l\le L-1 \quad (20)$$

The constant 1 inside the logarithm is to avoid obtaining negative infinity at the initial stage. The denominator $\ln(1+\mu)$ normalizes $F\left(\left|w_{12,l}(n)\right|\right)$ and $F\left(\left|w_{21,l}(n)\right|\right)$ to be in the range [0, 1].

The vicinity ε is a very small positive, and its value should be chosen based on noise level. Practically, $\varepsilon = 0.001$ in sparse impulse response identification field, and μ represents $1/\varepsilon$.

VI. Simulation Results Analysis

In this section, we present the simulation results of classical backward NLMS and proposed BMP_{NLMS} algorithms. In order to qualify the performance of this proposed algorithm, we are interested on the estimated speech that we get in first output (i.e. $\tilde{s}(n)$) and the second adaptive filter (i.e. $\mathbf{w}_{21}(n)$).

We consider the convolutive mixing model presented in Fig. 1 with,

$s(n)$ is a speech signal phonetically equilibrated,

$b(n)$ is a punctual noise.

The sampling frequency is $Fs = 8\,kHz$.

In the mixing model, we have used two sparse impulse responses $h_{12}(n)$ and $h_{21}(n)$ that are convoluted with the original signals to generate the two noisy signals $p_1(n)$ and $p_2(n)$ with input SNR equal -6 dB. The length of impulse responses is L=512.

In order to evaluate the convergence time of proposed algorithm in comparison with non-proportionate algorithm, we have used the System Mismatch criterion that is calculated as follows:

$$SM(n)_{dB} = 20\log_{10}\left[\frac{\left\|\mathbf{h}_{21}(n)-\mathbf{w}_{21}(n)\right\|}{\left\|\mathbf{h}_{21}(n)\right\|}\right] \qquad (21)$$

For evaluate the quality of estimated speech signal obtained by the proposed algorithm, we have done other simulations based on objective speech quality measures which are the Segmental signal-to-noise ratio (SegSNR) criteria. The SegSNR criterion is given by:

$$\left(SegSNR_{\lambda}\right)_{dB} = 10\ \log_{10}\ \frac{\sum_{i=0}^{B-1}|s(i)|^2}{\sum_{i=0}^{B-1}|s(i)-\tilde{s}(i)|^2}\,VAD_{\lambda} \qquad (22)$$

where $s(n)$ and $\tilde{s}(n)$ are the original speech signal and the enhanced output, respectively. The parameter B represents the number of sample needed to obtain the average values of the output SNR (in all simulations of output SegSNR, we have used B = 128). The $\{VAD_{\lambda}\}$ is a voice activity detector that detects the presence/absence of speech sequences.

To confirm the good performance of the proposed algorithm in terms of distortion, we have used the Cepstral Distance that is estimated as follows:

$$CD_{dB} = \sum_{p=1}^{U} ISFT\left[\log\left(\left|S(\omega,p)\right|\right)-\log\left(\left|\tilde{S}(\omega,p)\right|\right)\right]^2 \qquad (23)$$

where $ISFT[.]$ denote the inverse-short-Fourier-transform. $S(\omega,p)$ and $\tilde{S}(\omega,p)$ are, respectively, the short-Fourier-transform (SFT) of the original speech signal $s(n)$ and the enhanced output $\tilde{s}(n)$.

In Table 1, we have summarized all selected optimal parameters of classical and proposed algorithms. The original speech signal and the estimated speech signals $v_1(n)$ obtained by the classical BNLMS and proposed BMP_{NLMS} algorithms are presented in Fig. 5.

We have reported in Fig. 6, the SM evolution. Each point corresponds to a smoothing of 256 consecutive frames. As we have done others experiments according to the input SNR and CD criteria, by using four types of acoustic noise (white, USASI, babble and street) with the length of the real and adaptive filters is large, i.e. L=512.

TABLE I. Table Type Styles

Algorithms	Parameters values
Classical BNLMS	$\xi_{nlms} = 10^{-6}$
Proposed BMP_{NLMS}	$\xi = \xi_{nlms}/L$, ρ= 5/L $\delta = 0.01$, $\mu = 1/\varepsilon$, $\varepsilon = 0.001$

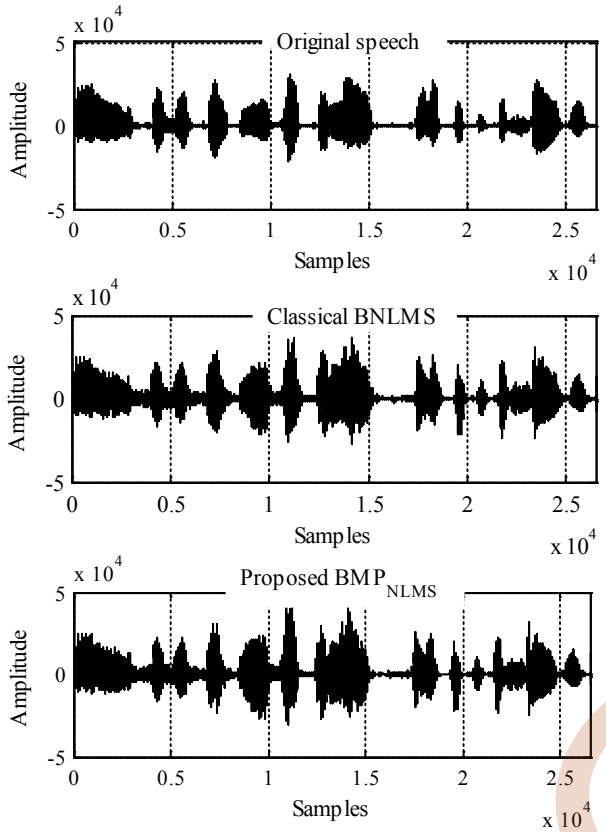

Figure 5. Detailed diagram of proposed BMP_{NLMS} algorithm.

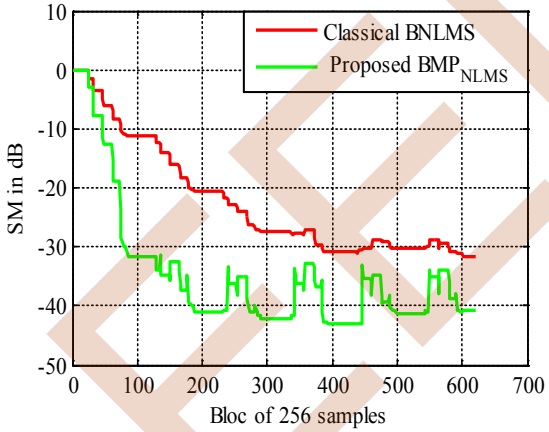

Figure 6. Detailed diagram of proposed BMP_{NLMS} algorithm.

From Fig. 6, we note the good convergence speed performance of the proposed backward µ-law proportionate NLMS algorithm (BMP_{NLMS}) compared with classical non-proportionate backward NLMS algorithm in very noisy environment. As we note that the best values of final SM are obtained by proposed BMP_{NLMS} algorithm in sparse convolutive system.

The obtained values of SegSNR and CD evaluation are reported respectively on Table 2 and Table 3.

TABLE II. OUTPUT SNR EVALUATION FOR BNLMS AND BMP_{NLMS} ALGORITHMS

Noise type	Input SNR (dB)	SegSNR in dB	
		Classical BNLMS	*Proposed BMP_{NLMS}*
White	-6	46,75	50,92
	0	48,22	52,1
	6	50,02	54,80
USASI	-6	45,38	50,05
	0	48,69	51,77
	6	49,79	54,43
Babble	-6	44,01	50,23
	0	45,08	52,98
	6	48,89	53,71
Street	-6	45,03	50,22
	0	46,93	52,12
	6	49,25	54,99

TABLE III. CD EVALUATION FOR BNLMS AND BMP_{NLMS} ALGORITHMS

Noise type	Input SNR (dB)	CD in dB	
		Classical BNLMS	*Proposed BMP_{NLMS}*
White	-6	-6.80	-7.3
	0	-7.01	-7.98
	6	-7.75	-8.53
USASI	-6	-5.95	-6.76
	0	-6.51	-7.21
	6	-6.96	-7.69
Babble	-6	-6.61	-6.98
	0	-6.69	-7.33
	6	-7.70	-8.76
Street	-6	-6.42	-7.00
	0	-7.09	-7.91
	6	-7.33	-8.24

From the obtained results presented in Tables 2 and 3, we note the good behavior of proposed backward µ-law proportionate NLMS algorithm (BMP_{NLMS}) compared with other ones (BNLMS). This behavior is noted in different situations, noisy types (i.e. white, USASI, babble and street) and different input SNR (i.e. SNR = -6 dB, 0 dB and 6 dB). We conclude that the proposed BMP_{NLMS} algorithm had given the higher output SNR and low CD values.

VII. CONCLUSION

In this study, we have proposed the dual backward µ-law proportionate NLMS algorithm (noted: BMP_{NLMS}) for speech quality enhancement and acoustic noise reduction. This algorithm is mainly proposed exactly to improve the convergence speed in initial phase, when the two-channel convolutive mixing model is characterized by sparse impulses responses as in conference room. Intensive simulations are carried out to validate the superiority of the new proposed algorithm. Basing on the SM criterion results,

we have noted the fast convergence speed in initial phase of proposed algorithm compared to the non-proportionate algorithm. The superiority of proposed algorithm in term of estimated speech quality is proven by output SegSNR and CD criterion exactly in two-channel sparse convolutive system.

REFERENCES

[1] K. Ozeki, T. Umeda, "An adaptive filtering algorithm using an orthogonal projection to an affine subspace and its properties," Electron. Commun. Jpn., vol. 67-A, n°. 5, pp. 19–27, (May) 1984.

[2] M.J. Al-Kindi, J. Dunlop, "Improved adaptive noise cancellation in the presence of signal leakage on the noise reference channel," Signal Processing, vol. 17, n°. 3, pp. 241-250, (July) 1989.

[3] R. Bendoumia, "Two-channel forward NLMS algorithm combined with simple variable step-sizes for speech quality enhancement," Analog Integrated Circuits and Signal Processing, vol. 98, pp. 27–40, 2019.

[4] E. Weinstein, M. Feder, A.V. Oppenheim, "Multi-channel signal separation by decorrelation," IEEE Trans Speech Audio Process, vol. 1, n°. 4, pp. 405–413, 1993.

[5] G. Mirchandani, R.L. Zinser, J.B. Evans, "A new adaptive noise cancellation scheme in the presence of crosstalk," IEEE Transactions on circuits and systems II: Analog and Digital Signal Processing, vol. 39, pp. 681–694, Oct. 1992.

[6] S. Haykin, "Adaptive Filter Theory," NJ: Prentice Hall, 1996.

[7] A.H. Sayed, "Fundamentals of Adaptive Filtering," Wiley, 2003.

[8] M. Gabrea, "Double affine projection algorithm-based speech enhancement Algorithm," In: Proc. ICASSP Montréal. Canada: IEEE, pp. 904–907, 2003.

[9] M. Djendi, R. Bendoumia, "A new adaptive filtering subband algorithm for two-channel acoustic noise reduction and speech enhancement," Comput.Elect.Engi.,vol.39, n°.8, pp. 2531–2550, 2013.

[10] M. Djendi, R. Bendoumia, "A new efficient two-channel backward algorithm for speech intelligibility enhancement: A subband approach," Appl. acoustics, vol. 76, pp. 209-222, 2014.

[11] R. Bendoumia, M. Djendi, "Variable step-sizes new efficient two-channel backward algorithm for speech intelligibility enhancement: a subband approach," Applied Acoustics, vol. 76, pp. 209–222, 2014.

[12] S. Araki, S. Makino, R. Aichner, T. Nishikawa, H. Saruwatari, "Subband based blind source separation with appropriate processing for each frequency band," In: IEEE. ICA 2003, Japan, pp. 499–504, 2003.

[13] K. Kokkinakis, P. Loizou, "Subband-Based Blind Signal Processing for Source Separation in Convolutive Mixtures of Speech," IEEE Acoustics Speech and Signal Processing, vol. 4, pp. 917-920, 2007.

[14] R. Bendoumia, M. Kerkar, S.A. Bouzakar, "Acoustic noise reduction by new sub-band forward symmetric adaptive decorrelation algorithms," Applied Acoustics., vol. 152, pp. 118–126, 69–81, 2019.

[15] R. Bendoumia, M. Djendi, "Two-channel variable-step-size forward-and-backward adaptive algorithms for acoustic noise reduction and speech enhancement," Signal processing, vol. 108, pp. 226–244, 2015.

[16] H. Deng, M.Doroslovački, "Improving convergence of the PNLMS algorithm for sparse impulse response identification," IEEE Signal Process. Lett., vol. 12, n°. 3, pp. 181–184, Mar. 2005.

[17] Y. Huang, J. Benesty, J. Chen, "Sparse Adaptive Filters," ch. 4, Springer-Verlag New York Inc., Secaucus, NJ, USA, 2005.

[18] L. Liu, "On Improvement of Proportionate Adaptive Algorithms for Sparse Impulse Response," Ph.D. Thesis, Kochi University of Technology, Japan, September 2009.

EEIC'2019 University of Bejaia

Implementation of two strategies for Securing IP telephony at the Medical Control Department for the specialized institute of Autism

Habib Allah Bouhamida[1,2],BoualemMerabet[1],Mohammed Moulay[1] and Samir Ghouali[1,3*]

[1]Faculty of Sciences and Technology, Mustapha Stambouli University, 29000 Mascara, Algeria
[2]Laboratory of Electromagnetism, Photonics, and Optronics (LEPO), Djillaliliabes Universityof Sidi Be lAbbès, 22000Sidi Bel Abbès, Algeria
[3]Faculty of Engineering Science of Tlemcen, STIC Laboratory, Tlemcen, Algeria
[*]Corresponding Author:s.ghouali@univ-mascara.dz

***Abstract*— The telephone networks have experienced a remarkable growth and a grandiose evolution where the offered services have multiplied.To meet this evolution it was necessary to integrate the telephone data traffic on the IP network (ToIP) to benefit from an important quality of service but the telephone networks have been affected by the problems of IP networks, the protocols have become more complex and the security breaches. In this work, we focused on security breaches and their remedies in an Autism platform called Info Parole, which is free, records the speech of our autistic patients, and uses the ToIP as a support.This article is devoted to implementing a penetration test of attacks against a next generation mobile Net that emulates a telephone Net over IP of a company by the WIFI access Net and this has integrated a security lab for the ToIP of an small/large business company.**

Keywords—Telephone Networks,Security ToIP, protocols, Autism Platform

I. INTRODUCTION

Choosing a school for a mentally unbalanced kid, particularly a youngster who requires concentrated treatments is a profound obligation. The choice may have a significant and enduring effect on the youngster's life and family. Since mental imbalance can posture such serious difficulties to families, guardians are regularly ready to attempt to do pretty much anything to support their medically introverted youngster. Taking a subsequent home loan, selling one's home, and moving are normal.

The most important point we want to emphasize is that people with autism have the potential to grow and improve. Contrary to what you may hear from professionals who are out of touch with reality or read old books, autism can be treated. It is important to find effective services, treatments and education for children with autism as soon as possible.

A survey conducted in 2019 shows that more than half of the people concerned are in dire need of information. 38% of them waited more than a year before being referred to a support system. In addition, for 46%, it took more than six months to find a health professional. Faced with this situation, we want to embark on this type of platform for listening, advice and services.

Telephone or on the Internet, everyone can find answers to their questions about screening, diagnosis, different therapies, education, patient rights, as well as addresses of host institutions, associations, cultural and sports centers for people with autism. Among the treatment methods, integrate these autistic people into communication boxes where they will use video or telephony services on ip, where health professionals will try to integrate them with society and this via fictitious client servers, so we will simulate the actors (clients) to be able to force the autistic person to talk.

Therefore, we will use a number of strategies to be able to secure this ToIP and that will be the purpose of this article, tostart soon our second article, which will take intoconsideration the speech of these autistic people and study it through deep learning.

Information and communication (Com) technology markets are currently undergoing structural change, so as conventional telecoms networks (Nets) have been planned and implemented for the transfer of specific data such as telephone calls or pure data packets [1]. Recent competitive growth, new market demands, and technological developments have fundamentally changed the traditional attitudes of the telecoms industry [2]. Theseare currently characterized by the rapid growth of broadband connections, the convergence processes of various Net technologies and the emergence of a uniform IP standard for individual and mass Coms [3].Traditional telecoms operators are facing a multitude of new challenges. Their previously successful fixed Net business is under increasing pressure. [4] New Com opportunities, such as the telephone over the Internet, and the growing market share of mobile telephony are of great concern [5].

To counter these losses, Netoperators are investing more heavily in the growth driver, broadband. The consolidation of telephone, Internet and television - known in telecoms sector as Triple Play Services (TPS) - has become the driving force behind these new business models [6].

The traditional market boundaries between fixed Nets, mobile telephony and data Nets are disappearing faster and faster. This gives the customer the advantage he can have over a very wide range of services, regardless of his access technology.

This development requires a meta-infrastructure beyond the existing, subordinate Nets - a core Net for all access Nets:new Nets it called the Next Generation Net [7].

Internet Protocol is the most important integration factor because it is available worldwide and it can use almost any service and application in any Net. Customers now require EoIP (Everything over IP), which requires NGNs with the ability to serve new multimedia services on a single device.

The general idea behind NGN is that a Net transports all information and services (voice, data and all types of media such as video and IPTV broadcasting) [8] by encapsulating them in packets, similar to those used on the Internet.

NGN Nets are generally built around the Internet protocol, and therefore give rise to the expression ALL-IP by that we can integrate the telephone com (voice) into NGN Nets.Next Generation Nets (NGNs) are being implemented worldwide to radically change the cost base, agility and service capabilities of telecoms providers.

This article is devoted to implementing a penetration test of attacks against a next generation mobile Net that emulates a telephone Net over IP of a company by the WIFI access Net and this has integrated a security lab for the ToIP of an small/large business company.

II. EXPERIMENTALIMPLEMENTATION

Our implementation is to realize an IP telephony Net and then we launch hacking attacks on the Net and at the end of the implementation; we secure it so that the hacking attacks do nothing to the Nets.Two scenarios have been made:

First scenario

A company that has only one site, so the Net used for ToIP is a LAN Net with WIFI access points and a router to connect with the outside world.

We added a firewall to block attacks from the outside and in the inside, we added a hacker to test attacks on LAN users as we can see in the fig.1. The first scenario consists in creating a ToIP Net on LAN, i.e. the company has only one site.

The previous figure shows the Net topology which contains a router to connect the LAN to the Internet and to connect the access point to the asterisk server so that SIP clients can call each other.

To test the Net security, we added a hacker who attacks LAN entities. For threats coming from outside, we have placed a new generation ASA firewall between the LAN router and the ISP PE router, i.e. the Internet. That blocks all attacks from the outside to the LAN as well as for NAT.

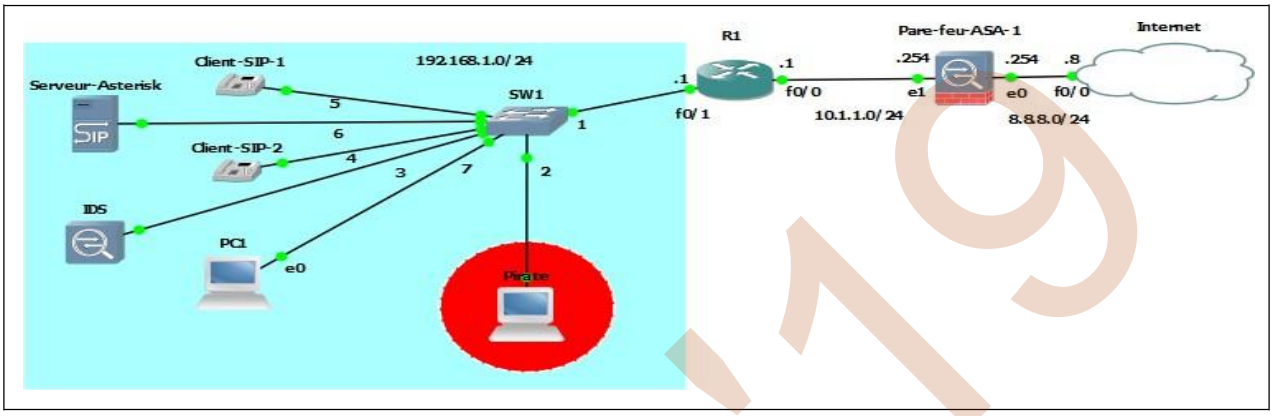

Figure.1. Schematic representation of the first scenario.

Second scenario

In this scenario we are interested in multi-site company, the two LANs represent two sites, one in Algiers and the other in Oran, the WAN represents the Internet service provider. The following topology represents the global Net:

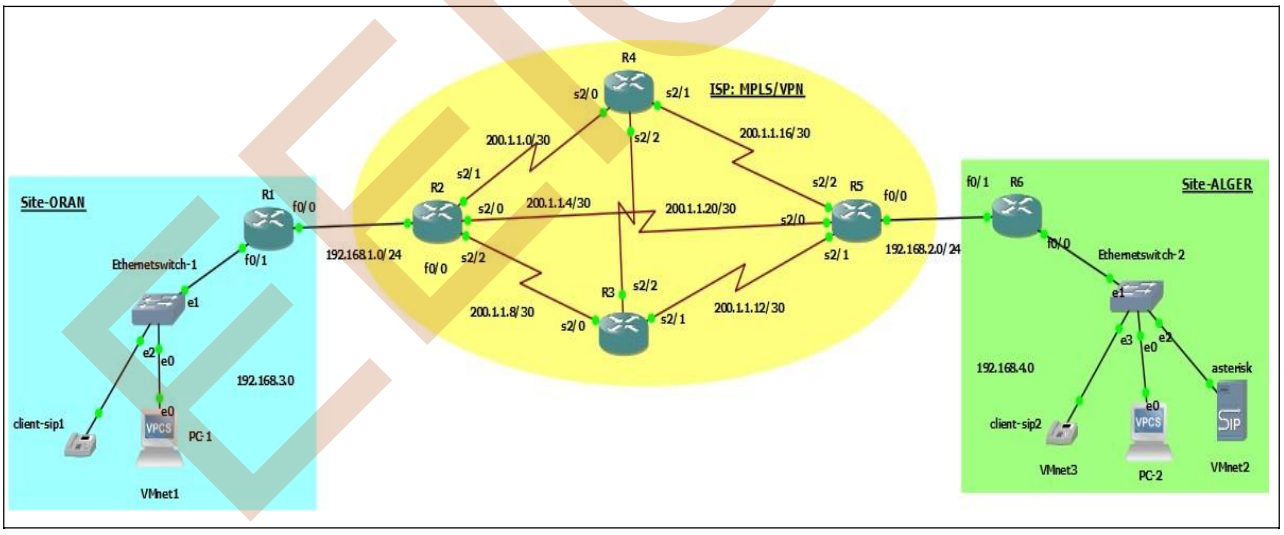

Figure.2. Schematic representation of the second scenario.

III. PROCEDURE AND USED MATERIALS

In order to carry out both scenarios, it was necessary to use GNS3 and connect the different topology entities to the

associated virtual machines (Asterisk "FreePBX" server and two machines to test the "windows 7" calls, kali Linux "pirate", ubuntu "IDS").

-A PC with an i5 5200 processor with 8Gbps of RAM.

-A TP-LINK WIFI modem to connect mobile SIP clients.

-Two smartphones with Android iOS to use as mobile SIP clients.

Note: To increase the speed of implementation execution, you need a PC with an i7 processor and at least 16 Gbps of RAM.

IV. THE SOFTWARE USED IN THIS IMPLEMENTATION

GNS 3

It is free software that runs on multiple platforms, including Windows, Linux, and MacOS X, allowing the emulation or simulation of computer Nets for advanced functions.

In order to best meet our needs, GNS3 supports a wide range of router and switch types and allows endpoint clients to connect to virtual machines. For our part, we use it mainly to test IOS features. For example, we used it to do tests around OSPF (redistribution, filtering, authentication,).

Create true Linux and Windows virtual machines and other desktop, server and tablet environments, with configurable virtual Net configuration and Netsimulation.

Asterisk server

Asterisk is an open source framework for building communication applications, it allows to transform an ordinary computer into a communication server. Asterisk powers IP PBX systems, VoIP gateways, conference servers and other customized solutions. It is used by small businesses as well as large businesses, call centers and government agencies, Asterisk is sponsored by Digium.

The server Asterisk the routing of incoming calls to their destinations, in addition it offers a wide range of services, including:

- Speed dialing to defineshortcuts.

- On-hold and on-holdmusic.

- Visual indicator of messagewaiting.

- Voice mail (automatic answeringmachine).

- Notification and listening by e-mail of messages left on your answering machine(voicemail)

- Conference management: being able to hold meetings remotely.

- Detailedinvoicing.

- Authentication of callingusers.

ASA Firewall

Next-generation Cisco ASA firewall services address these needs by integrating new features, including Application Visibility and Control (AVC) and Web Security Essentials

(WSE), into the industry's most proven stateful inspection firewall. This combination provides end-to-end Net intelligence and simplified security operations. And the ability for your company to leverage the benefits of new applications and devices to improve productivity without compromising security [9].

The next-generation ASA firewall incorporates user and application recognition features that provide users with improved visibility and control of Net traffic.

Kali Linux

Kali Linux is an open source project that is maintained and funded by Offensive Security, a provider of information security training and penetration testing services. In additionto Kali Linuxwe installed kali on a virtual machine and connected it to the gns3 to performattacks.

Snort "IDS/IPS"

It is a free intrusion detection system (or NIDS). Originally written by Marty Roesch, it now belongs to Sourcefire. Commercialversionsintegratinghardwareandsupportservices are sold bySourcefire.

Snort is also able to perform real-time traffic analyses and logpacketsonanIPNet.Itcan performprotocolanalyses, search/correspondencecontentandcanbeusedtodetectawide variety of attacks[11].

These analyses are based on rules, which are written by Sourcefire or provided by the community. Snort is provided with some basic rules but as any snort software is not infallible and therefore requires regular updating.

Zoiper

Zoiper is one of the most popular softphones on Windows, it allows you to create SIP and IAX clients compatible with all services(telephony,audioconferencing...).However,initsfree version it does not integratevideo.

To make or receive calls, you must first obtain a user ID, password and server address to use this service.

The ToIP part of the simulation performed is summarized in the following points:

1. SIP Client (1000) is connected to the LAN switchand calls the (100) which is also a SIP client and is connected to the same Net.

2. Since they have IP addresses of the same sub-Net, then the switch sends (forwards) the invitation to theasterisk server without going through therouter.

3. The server checks its database and finds that both SIP clientsexist,sotheservercreatesapathtoconnectthesetwo SIP clients and pass the invitation (1000) with the client's destination address(100).

Then switch forwards the invitation to the customer (100).

Note:ifaclientSIPinviteanotherclientSIPwichislocated in another LAN, in this case the invite request mast be routed by the router wich is our secondscenario.

Everything is done through the SIP protocol, the following figure details it:
To understand SIP messages, there are six types of responses to sent requests.

Configuration

The big part of configuration is for the second scenario it resum in four parts:

1. First,we configure the connection interfaces (each interface will have an address in the sub-Net range where itbelongs).

2. Between the CE-PE routers (between R1 and R2, R5 and R6), we configured the VRF and EIGRPprotocols.

3. Between the ISP routers (R2, R3, R4, R5), we configured the OSPF, BGP and VPNprotocols.

4. Added MPLS to ISProuters.

```
PE-ORAN(config-router)#address-family vpnv4
PE-ORAN(config-router-af)#nei
PE-ORAN(config-router-af)#neighbor 5.5.5.5 act
PE-ORAN(config-router-af)#neighbor 5.5.5.5 activate
PE-ORAN(config-router-af)#neighbor 5.5.5.5 send
PE-ORAN(config-router-af)#neighbor 5.5.5.5 send-community ex
PE-ORAN(config-router-af)#neighbor 5.5.5.5 send-community extended
PE-ORAN(config-router-af)#
```

Figure.3. VPN activation configuratio

V. Results And Discussions

The Kali linux attacks

To perform attacks on the LAN, we added a pirate pc in the first scenario using kali linux. There are many attacks and since the implementation concerns ToIP we have made attacks that threaten it.

DOS attack: (denial of service) consists in saturating the victim in order to block him (for example blocking a file server), make it impossible to access a web server or prevent the distribution of email in a company. this attack consists in sending several simultaneous requests to the victim, it is the most used. We have attacked in the first scenario the computer next to the hacker with the DOS:

First, we test the victim's connectivity by pinging to the output router. In next, we have run msfconsole on the hacker machine "kali Linux" and perform the DOS attack:

```
PE-ORAN(config)#int s2/0
PE-ORAN(config-if)#mpls ip
PE-ORAN(config-if)#int s2/2
PE-ORAN(config-if)#mpls ip
PE-ORAN(config-if)#int s2/1
PE-ORAN(config-if)#mpls ip
PE-ORAN(config-if)#
```

Figure.4. MPLS protocol addedtoISP routers interfaces.

Note: MPLS/VPN two protocols used to secure the data traffic along the route of the ISP Net.

MPLS builds a tunnel from the transmitter to the receiver and VPN allows to encrypt the data flowing into the tunnel via the IPs protocol. Against the victim PC with address 192.168.1.10 [12].

Result of the DOS attack

Figure.5. Capture showing the PC victim is out of session.

Nmap (Net Mapper):is an Open Source port scanner. It is designed to shut down open ports, hosted services and information about a remote computer's operating system.To launch it, just type "nmap @ of the victim" (For example our victim is the Asterisk server).

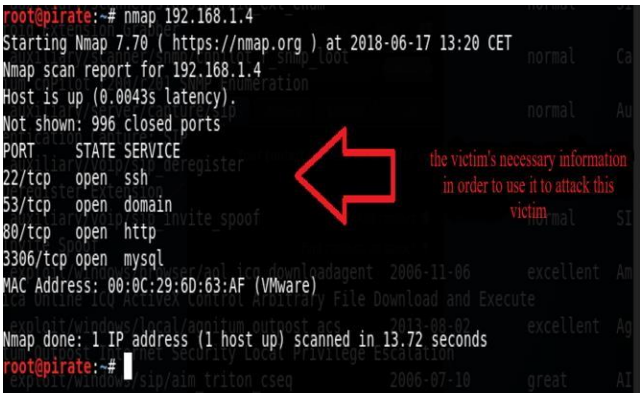

Figure.6. Capture showing the launch of the Nmap attack against

AsteriskServerwiththeaddress192.168.1.4[12], Ping of death: It is a ping that has a data length greater than the maximum size. When it is sent, the ping of death is fragmented into smaller packets. The victim PC that receives these packets must then rebuild them. Some systems do not manage this fragmentation and freeze or crash completely. Hence the name of this attack.

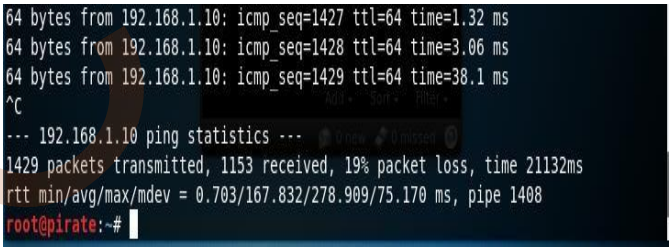

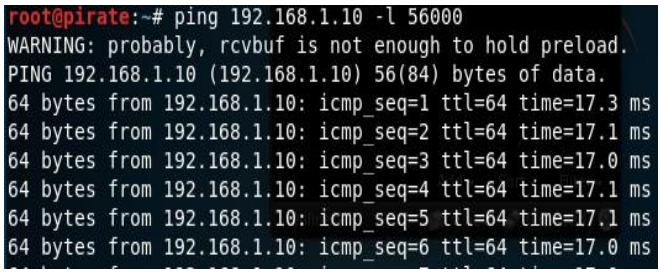

Figure.7. Ping launch of death attack against the victim PC with address 192.168.1.10 [12].

VI. Security Measures

First scenario

In our case, there are two security measures, security vulnerabilities from outside the LAN and from inside.For the outside, the security implemented consists in blocking all kinds of dangerous incoming flows for that, we installed a new generation ASA firewall.The second case consists in securing access to the LAN Net from the inside.

There are many security policies, for our most appropriate case is to limit the switch access ports according to the number of users, otherwise if a hacker has been able to connect to the LAN, there is a softwarecalled "snort" that does the detection and prevention of intrusions "but as we say: prevention is better than cure" so it remains like a security plan B.

Second scenario

We added MPLS/VPN as security part of the second scenario as we can see the following figure shows that the MPLS/VPN security works correctly since after the command line traceroute 192.168.4.1, the result displayed is none other than the end interfaces.On the other hand, the interfaces of ISP routers in the MPLS cloud are discrete; this is one of the main strengths of VPN.

VII. CONCLUSION

Our criteria for choosing the implementation for disoriented families, diagnostic wandering, unreliable or scattered information... While parents of autistic children have been denouncing for years a path of the fighter, Autism info paroles, a new national and free platform for information, guidance and listening on autism, was based on the important new features that have been introduced by the NGNs, over IP.

Telephony is one of these new features and occupies the largest share of the NGNs. Since the purpose of this article is security in next- generation mobile Nets, the WIFI wireless access Net was chosen to add mobile users and the Net was secured by adding the ASA firewall. The gradual migration of protocols from traditional mobile Nets to new-generation Nets has brought significant improvements in communication "very low latency and a high number of connected devices" as well as the security of data exchanges.

Now, the trend towards fifth generation technology has become necessary, as it provides the flexibility at the heart of its design to allow mobile operators to serve the Internet of Things (IoT) and support low-latency connections, as well as an improved high-speed mobile connection. With regard to the deployment of 5G, the NGNs control the core and access Net; this is the non-standalone mode (not autonomous) [13]. And for the security concepts currently proposed in 5G, they are based on a cloud-based approach for the core Net and for the access Net, i.e. based on very complex encryption algorithms that encrypt the flow of data carried regardless of the "wired, radio or optical" transmission technology.

REFERENCES

[1] ITU-T Y. General principles and general reference model for next-generation networks.J. Clerk Maxwell, A Treatise on Electricity and Magnetism, 3rd ed., vol. 2. Oxford: Clarendon, 1892, pp.68-73.(2011)

[2] https://www.ey.com/Publication/vwLUAssets/ey-digital-transformation-for-2020-and-beyond

[3] Mani, M. & Crespi, How IMS Enables Converged Services for Cable and 3G Technologies: A Survey, N. J Wireless Com Network (2008) 2008: 589623. https://doi.org/10.1155/2008/589623

[4] https://www.managementsolutions.com/sites/default/files/publicaciones/eng/telecommunications-digital-era

[5] M. Suryanegara, A.S. Arifin, M. Asvial, K. Ramli, M. I. Nashiruddin, and N. Hayati, What Are the Indonesian Concerns About the Internet of Things (IoT)? Portraying the Profile of the Prospective Market , IEEE Access, Vol. 7 2019

[6] Pereira, P., Ribeiro, T., & Vareda, J. Delineating markets for bundles with consumer level data: The case of triple-play. International Journal of Industrial Organization, 31(6), 760–773 (2013).

[7] Arash Kalami, Department of Electrical Engineering, Urmia Branch, Islamic Azad University, Urmia, Next Generation Networks Challenges for Ensuring the Security and Availability of NS/EP Communications, J. Basic. Appl. Sci. Res., 2(12)12694-12698, (2012).

[8] Hrovatin, N., & Švigelj, M. The interplay of regulation and other drivers of NGN deployment: A real-world perspective. Telecommunications Policy, 37(10), 836–848. (2013).

[9] Firewall Design. Designing and Building Enterprise DMZs, 207–314. (2006).

[10] Salah, K., & Kahtani, A. Performance evaluation comparison of Snort NIDS under Linux and Windows Server. Journal of Network and Computer Applications, 33(1), 6–15. (2010).

[11] Zhang, G., & Rebahi, Y. Side effects of identity management in SIP VoIP environment. Information Security Technical Report, 16(1), 29– 35. (2011).

[12] Kali Penetration Testing Tools. Hacking with Kali, 201–222. (2014).

[13] Li, S., Xu, L. D., & Zhao, S. 5G Internet of Things: A survey. Journal of Industrial Information Integration, 10, 1–9. (2018).

A modified Multi-Pulse PPM for FSO Communication Systems

Mehdi ROUISSAT
department of Electronics
Nour Bachir University Center. El-Bayadh, Algeria
mehdi.m.rouissat@gmail.com

Mohammed Belkheir
department of Electronics
LIMA Laboratory (Instrumentation and advanced materials)
Nour Bachir University Center. El-Bayadh, Algeria
belkheir_m@yahoo.fr

Abstract. *Anisochronous Synchronized Multi-Pulse PPM "AS-MPPM" is a new proposed modulation scheme based on MPPM proposed for the wireless optical systems. The proposed scheme resolves the symbol synchronization problem which may simplify the encoding and the decoding operations in the Free space Optical systems "FSO". It shows a notable improvement in term of data speed and bandwidth efficiency compared to conventional MPPM. On the other hand, and as cost of these advantages, AS-MPPM shows a moderate power efficiency.*

In this paper we present the expressions of spectral efficiency, power requirements, and the data rate improvement normalized to PPM, and we also present comparison results to conventional MPPM and to Synchronized MPPM "S-MPPM", which is a phase in the development of MPPM to AS-MPPM.

Keywords

MPPM, AS-MPPM, synchronization, spectral efficiency, power requirements.

1. Introduction

A free space optical communication system (FSO) is a telecommunication system that uses invisible beams of light to transmit and receive data information, and the free space (the atmosphere) as transmission channel. It's based on connectivity and visibility between transceiver units.

One of many challenges in designing FSO systems is the choice of modulation scheme; it is a principle factor in realizing a high performance FSO communication system at a reasonable cost and moderate complexity. Coherent modulation techniques as Phase and frequency modulation are complicated and expensive [1], on the other hand Intensity Modulation and Direct Detection (IM/DD) is widely employed in optical wireless communication systems [2] for its simple implementation and low cost.

As one of IM/DD modulation, OOK (On-Off Keying) is the simplest and the more widely adopted modulation scheme used in commercial FSO communication systems [3,4] because of ease in implementation, simple receiver design, bandwidth efficiency and cost effectiveness. As an alternative to OOK, PPM (Pulse Position Modulation) achieves higher power efficiency, but it has several drawbacks such as the complexity in implementation due to higher level of accuracy required in both slot and symbol synchronization and the rapid decline of spectral efficiency with increasing power efficiency [5]. As a new version and potential alternative to PPM, MPPM (Multi-Pulse Pulse Position Modulation) reduces the required transmission bandwidth in optical PPM to about half with the same transmission efficiency [6].

MPPM has good spectral efficiency compared to PPM; however the synchronization problem is always not solved, in order to find a solution for that problem and improve the MPPM data rate and spectral efficiency, we propose a new method of modulation "AS-MPPM" Anisochronous synchronized MPPM as a new version of the existing MPPM.

The proposed scheme solves the symbol synchronization problem in FSO systems and shows a notable improvement in term of data rate and spectral efficiency.

1. Pulse Position Modulation

Pulse position modulation (PPM) is a method to increase transmission efficiency in the FSO systems. In this scheme, each symbol interval of duration $T=\log_2 (M/R_b)$ is partitioned into M slots, each of duration T/M, and the transmitter sends an optical pulse during one of these M slots. The transmit pulse shape is given by:

$$P(t) = \begin{cases} P, & \text{for } t \in [(m-1)T/M, mT/M] \\ 0, & \text{elsewhere} \end{cases} \quad (1)$$

Where $m = \{1, 2 \dots M\}$, and P is the pulse power.

PPM is known for its power efficiency, but the PPM based systems suffer from the disadvantage of bandwidth expansion and high complexity in implementation (due to higher level of accuracy required in slot and symbol synchronization).

In this paper, the PPM scheme will be used just as a benchmark to show the data rate improvement in the other modulation schemes, on the other hand the basic modulation OOK will be used as a benchmark to compare the power requirements of the other modulation schemes.

2. MPPM (Multi-Pulse Pulse Position Modulation)

PPM based system is more power efficient than OOK, but it has several drawbacks such as the complexity in implementation due to the higher level of accuracy required in slot and symbol synchronization and the rapid decline of bandwidth efficiency with increasing the power efficiency. As a potential alternative to PPM, MPPM (Multi-Pulse Pulse Position Modulation) has been proposed; this latter reduces the required transmission bandwidth in optical PPM to about half with the same transmission efficiency.

MPPM is also called combinatorial PPM [7], is proposed as a modulation method to improve the hand-utilization efficiency and allow for significantly improved data rate in optical pulse position modulation scheme (PPM).

In MPPM, each sequence of b bits is mapped into one of $L=2^b$ symbols and transmitted to the channel, each symbol interval of duration ($T=\log_2 L/R_b$) is partitioned into M slots, each of duration T/M, and the transmitter sends w optical pulses every symbol duration, the number of possible symbols is:

$$L=\binom{M}{w}=\frac{M!}{w!(M-w)!} \tag{2}$$

Usually L is not a power of two, so generally we must discard some of the resulting signals to achieve $L=2^b$.

The average power requirement for the MPPM normalized to OOK is given by [5]:

$$\frac{P_{MPPM}}{P_{OOK}}=\frac{2w}{\sqrt{M\ d\ \log_2 L}} \tag{3}$$

d: Hamming Distance.

The bandwidth B is roughly M/T the inverse of the chip duration, this paper defines the band utilization efficiency η as the ratio of R to B, i.e.

$$\eta_{MPPM}=\frac{R_b}{B_{MPPM}}=\frac{\log_2 L}{M} \tag{4}$$

3. Synchronized MPPM "S-MPPM"

In this section and as a first step we propose synchronized MPPM "S-MPPM", where the main raison of this concept is to solve the symbol synchronization problem in MPPM. In this method, every symbol starts with a specific pulse, one time and half larger than the other pulses, Fig 1.

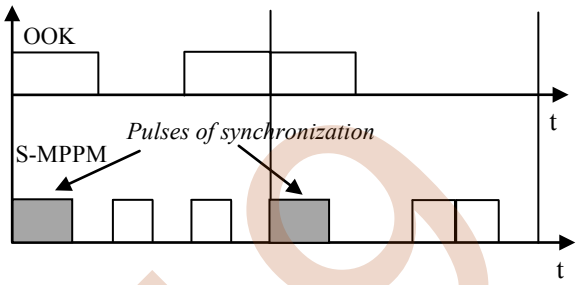

Fig.1. Encoding Example of a serial data bit to S-3MPPM.

In S-MPPM each b bit are encoded to one of $L_2 = 2^b$ symbols and transmitted in the channel, the symbol duration T is partitioned into M slots, the synchronization pulse is of duration 3/2 T_s, and the other (M-1) slots are of duration T_s.

The number of the symbols in the S-MPPM is:

$$L_2=\binom{M-1}{w-1}=\frac{(M-1)!}{(w-1)!(M-w)!} \tag{5}$$

The same case as in MPPM, usually L_2 is not a power of two, so generally we must discard some of the resulting signals to achieve $L_2=2^b$.

In the next sections and for the analysis clearness and simplicity, we will use three pulses for each symbol for all the modulation schemes.

The number of the symbols in the S-3MPPM is given by:

$$L_2=\binom{M-1}{2}=\frac{(M-1)!}{2(M-3)!}=\frac{1}{2}(M-1)(M-2) \tag{6}$$

3.1 Data rate

The data rate that can be achieved by a modulation scheme is of great importance, but it is not the only parameter to judge the performance of such scheme. The data rate that can be achieved by MPPM or S-MPPM is:

$$D=\frac{\log_2 L_M}{T}(bit/s) \tag{7}$$

L_M: L_{MPPM} or $L_{S\text{-}MPPM}$;

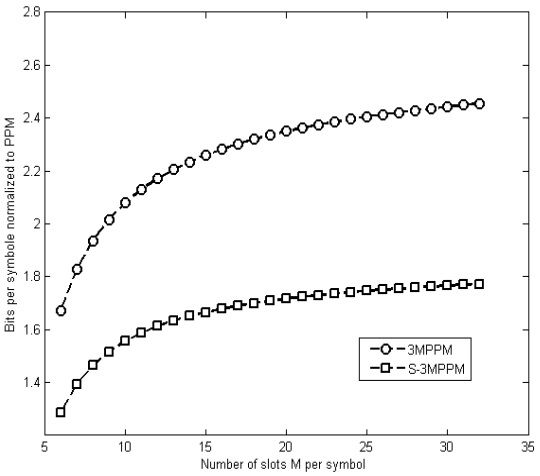

Fig.2. Number of bits per symbol for 3MPPM and S-3MPPM normalized to PPM.

To show the improvement in data rate we define the parameter *R*, which presents the ratio in term of data rate of any modulation scheme to that of PPM.

$$R = \frac{D_M}{D_{PPM}} = \frac{\log_2 L_M}{\log_2 M} \quad (8)$$

D_M: D_{MPPM} or $D_{S\text{-}MPPM}$
L_M: L_{MPPM} or $L_{S\text{-}MPPM}$

Figure 2 shows the ratio *R* of 3MPPM and S-3MPPM based on symbol length *M*. 3MPPM presents higher ratio compared to S-3MPPM where for M=6 the ratio of 3MPPM is about 1.3 times greater than that of S-3MPPM and this deference decrease as *M* increase to be at M=32 about 1.4, which makes S-MPPM so poor in term of data rate.

3.2 Power requirement and bandwidth efficiency

In the MPPM scheme, the average power requirement for each symbol is given by:

$$P_{MPPM} = wP_1 \quad (9)$$

The average power requirement for each symbol of S-MPPM modulation is given by:

$$P_{S\text{-}MPPM}=(w-1)P1+P_2 \quad (10)$$

Where $P_2=3/2\ P_1$.
From (9) and (10), the relationship between the two powers MPPM and S-MPPM is given by:

$$\frac{P_{S\text{-}MPPM}}{P_{MPPM}} = 1 + \frac{1}{2w} \quad (11)$$

In order to find the average normalized power requirement for the S-MPPM scheme, we multiply (3) by (11):

$$\frac{P_{MPPM}}{P_{OOK}} \times \frac{P_{S\text{-}MPPM}}{P_{MPPM}} = \frac{P_{S\text{-}MPPM}}{P_{OOK}} \quad (12)$$

Consequently, the average normalized power requirement for the S-MPPM scheme normalized to OOK is given by:

$$\frac{P_{S\text{-}MPPM}}{P_{OOK}} = \frac{2w+1}{\sqrt{Md\ \log_2 L_2}} \quad (13)$$

The general form of spectral efficiency of S-MPPM η is given by R_b/B:

$$\eta_{S\text{-}MPPM} = \frac{\log_2 L_2}{M} \quad (14)$$

For w=3, the spectral efficiency of S-3MPPM is given by:

$$\eta_{S\text{-}3MPPM} = \frac{\log_2 L_2}{M} = \frac{\log_2 \frac{1}{2}(M-1)(M-2)}{M} \quad (15)$$

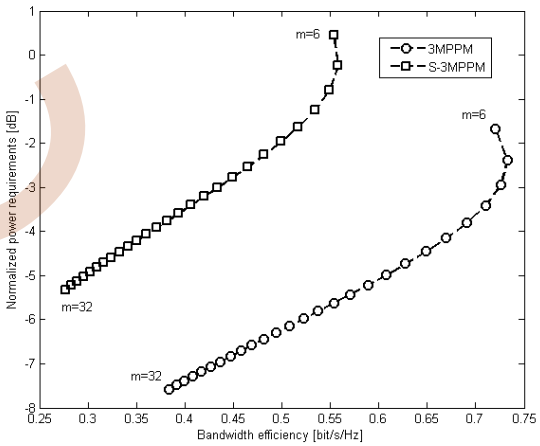

Fig.3. Normalized Power Requirement based on Bandwidth efficiency for 3MPPM and S-3MPPM.

Figure 3 shows the power requirements based on the spectral efficiency (bit/s/ Hz) for different values of *M* from 6 to 32, the figure shows that the S-3MPPM presents the higher power requirement compared to 3MPPM (lowest power efficiency), the same thing for the spectral efficiency, where S-3MPPM has the lowest efficiency (the higher bandwidth requirement), where 3MPPM has the best spectral and power efficiencies, these results shows the weakness of the S-MPPM in term of spectral and power efficiencies, and makes the symbol synchronization ability the only advantage brought by this method, which require more improvement.

4. Anisochronous S-MPPM "AS-MPPM"

Digital pulse time modulations techniques fall into two categories, namely isochronous and anisochronous. Isochronous schemes encode data by varying the position or width of a pulse, but the overall symbol structure remains constant such as MPPM and S-MPPM, in contrast, anisochronous schemes have no fixed symbol structure [8].

The proposed S-MPPM has solved the symbol synchronization problem, but it shows modest data rate, and poor spectral efficiency. As an alternative to S-MPPM, anisochronous S-MPPM "AS-MPPM" is a modified S-MPPM modulation which displays a better spectral efficiency and a higher data rate by eliminating all the unused time slots from within each symbol.

In order to avoid vicinity between a symbol ends with a pulse and another symbol starts with a pulse, an additional guard slot will be added to each symbol immediately following the last pulse.

For AS-MPPM the minimum and the maximum symbol lengths are (w+3/2) Ts and (M+1/2) Ts respectively. So the mean symbol length is given by:

$$M_{mean} = \frac{M + w + 2}{2} \tag{16}$$

The number of symbols in AS-MPPM is given by:

$$L_3 = \binom{M-2}{w-1} = \frac{(M-2)!}{(w-1)!(M-w-1)!} \tag{17}$$

The same case as S-MPPM, Usually L_3 is not a power of two, so generally we must discard some of the resulting signals to achieve $L_3=2^b$.

For w=3:

$$L_3 = \binom{M-2}{2} = \frac{(M-2)!}{2(M-4)!} = \frac{1}{2}(M-2)(M-3) \tag{18}$$

4.1 Data rate

One of the main raisons of the migration from isochronous to anisochronous scheme is the improvement in data rate, the throughput that can be achieved by AS-MPPM based on mean symbol length is:

$$D_{AS\text{-}3MPPM} = \frac{\log_2 L_3}{T_{mean}} \tag{19}$$

The ratio R based on average symbol length of AS-MPPM scheme is:

$$R = \frac{D_{AS\text{-}MPPM}}{D_{PPM}} = \frac{(2M)\log_2 L_3}{(M+w+2)\log_2 M} \tag{20}$$

For w=3, the ratio R is given by:

$$R = \frac{D_{AS\text{-}3MPPM}}{D_{PPM}} = \frac{(2M)\log_2 L_3}{(M+5)\log_2 M} \tag{21}$$

Figure 4 shows the ratio R of 3MPPM, S-3MPPM and AS-3MPPM based on symbol length M. AS-3MPPM shows better data rate than S-3MPPM from M=8, and this advantage increases as M increase, where for M=32 the ratio AS-MPPM is about 1.8 that of S-3MPPM. And compared to 3MPPM, AS-3MPPM presents low data rate for M<12, and after this value AS-3MPPM takes the advantage and outperforms 3MPPM as M increase, which makes AS-MPPM a strong scheme in term of data rate.

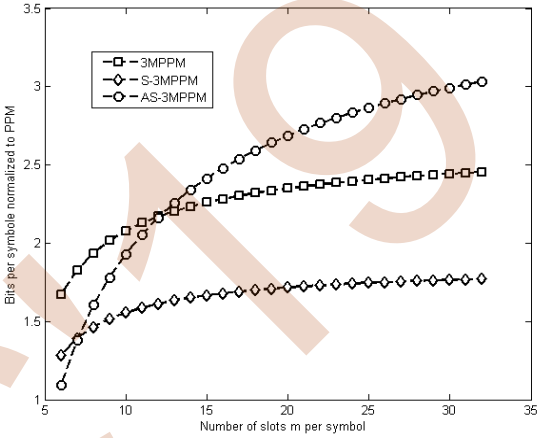

Fig.4. Bits per symbol for 3MPPM, S-3MPPM and AS-3MPPM normalized to PPM.

4.2 Power requirement and bandwidth efficiency

AS-MPPM has the same average power as S-MPPM, and the average normalized power requirement for the AS-MPPM scheme normalized to OOK given by:

$$\frac{P_{AS\text{-}MPPM}}{P_{OOK}} = \frac{2w+1}{\sqrt{M_{mean}\, d\, \log_2 L_3}} \tag{22}$$

For w=3, the normalized power requirements is given by:

$$\frac{P_{AS\text{-}3MPPM}}{P_{OOK}} = \frac{7}{\sqrt{M_{mean}\, d\, \log_2 L_3}} \tag{23}$$

Note that the data rate of AS-3MPPM is not constant, we have to use the average bit rate based on average symbol length. So the bandwidth efficiency based on the average symbol duration is given by:

$$\eta_{AS\text{-}MPPM} = \frac{\log_2 L_3}{M_{mean}} = \frac{2\log_2 L_3}{(M+w+2)} \tag{24}$$

The Normalized average power and Band width requirements of S-MPPM and AS-MPPM are shown in "Tab 1".

	S-MPPM	AS-MPPM
L	$\frac{1}{2}(M-1)(M-2)$	$\frac{1}{2}(M-2)(M-3)$
Normalized power requirement	$\frac{2w+1}{\sqrt{M\ d\ \log_2 L}}$	$\frac{2w+1}{\sqrt{M_{mean}\ d\ \log_2 L}}$
spectral efficiency	$\frac{\log_2 L}{M}$	$\frac{2\log_2 L_3}{(M+w+2)}$

Tab.1. Normalized average power and Band width requirements of S-MPPM and AS-MPPM.

Figure 5 shows the power requirement based on the spectral efficiency (bit/s/Hz) of 3MPPM, H-3MPPM and AH-3MPPM for different values of *M* from 6 to 32, as we can see, in term of spectral efficiency AS-3MPPM outperforms S-3MPPM from M=8, and compared to 3MPPM, AH-3MPPM presents low spectral efficiency for M < 13, and outperform 3MPPM in that term as *M* >13, and when it comes to power efficiency AS-3MPPM shows good power efficiency only for M=6 compared to S-3MPPM, and low power efficiency compared to 3MPPM for all *M* values, which makes AS-MPPM a promising candidate when the spectral efficiency is of great importance and the symbol synchronization is required.

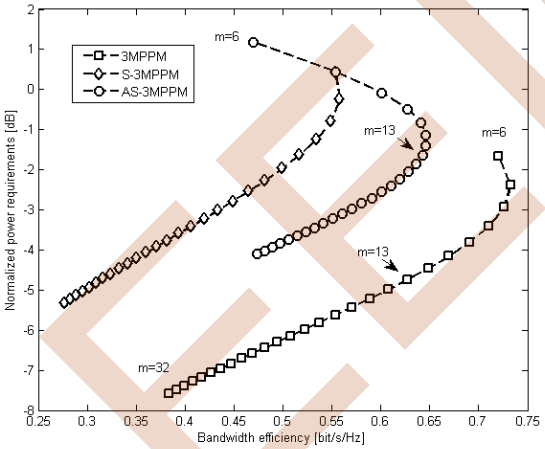

Fig.5. Normalized Power Requirement based on Bandwidth efficiency for 3MPPM, S-3MPPM, AS-3MPPM.

5. Conclusion

In this paper we presented a modified concept of modulation compatible with FSO systems, called AS-MPPM, Anisochronous Synchronized MPPM. The proposed scheme is a modified version of the existing MPPM. With AS-MPPM the symbol synchronization is solved with implantation of specific pulse in the beginning of each symbol and all the unusual slots are eliminated, beside the symbol synchronization ability the new scheme shows a notable improvement in term of data rate and spectral efficiency, and when it come to power efficiency the proposed scheme shows a modest power efficiency paid as cost of the mentioned advantages.

This method is presented to achieve a good compromise between data rate, complexity, power efficiency, spectral efficiency and synchronization possibility, which makes this scheme a viable addition in the word of the modulations and a concurrent to several schemes compatible with FSO systems.

References

[1] X. ZHU AND J. KAHN. Free-space optical communication through atmospheric turbulence channels. *IEEE Trans*. on Communications, 2003 .no. 2, pp. 1293–1300.

[2] SABI S. AND VIJAYAKUMAR N. Simulation of a Modem using Digital Pulse Interval Modulation for Wireless Optical Links. 10th National Conference on Technological Trends (NCTT09) 6-7 Nov 2009.

[3] M.IJAZ, O. ADEBANJO, S. ANSARI, Z. GHASSEMLOOY, S. RAJBHANDARI, H. LE MINH, A. GHOLAMI AND E. LEITGEB. Experimental Investigation of the Performance of OOK-NRZ and RZ Modulation Techniques under Controlled Turbulence Channel in FSO Systems. PGNet 2010.

[4] Alsowaidi, N., Eltaif, T. & Mokhtar, M. (2016). A Review on Successive Interference Cancellation-Based Optical PPM-CDMA Signaling. *Journal of Optical Communications*, 38(1), pp. 57-62.

[5] JAGTAR SINGH AND V.K.JAIN. Performance evaluation of ppm based optical communication system in atmospheric turbulence. PHOTONICS-2008: International Conference on Fibre Optics and Photonics. IIT Delhi, India. December 13-17, 2008

[6] H. SUGIYAMA AND K. NOSU. MPPM: a method for improving the band-utilization efficiency in optical PPM, *J. Lightwave Technol*., vol. 7, 1989, pp. 465-472.

[7] B. WILSON, Z. GHASSEMLOOY. Pulse time modulation techniques for Optical communications. *IEE proceedings*-J, 1993 vol. 140, no. 6, pp. 346–357.

[8] J. M. BUDINGER, M. VANDERAAR, P. WAGNER, AND S. BIBYK. Combinatorial pulse position modulation for power-efficient free-space laser communications. *SPIE Proc* Jan. 1993.vol. 1866.

Performance Comparison of APD and PIN Photodiodes using RZ and NRZ

Hadjira HAMADOUCHE
Department of Electrical Engineering
Mustapha Stambouli University of Mascara, Algeria
hadjira.hamadouche@univ-mascara.dz
LSTE Lab, Mascara univ, Algeria

Boualem MERABET
Department of Electrical Engineering
Mustapha Stambouli University of Mascara, Algeria
b.merabet@univ-mascara.dz

Mouweffeq BOUREGAA
Department of Electrical Engineering
Mustapha Stambouli University of Mascara, Algeria
m.bouregaa@univ-mascara.dz

Abstract— In this paper, we have studied the quality factor (Q), bit error rate (BER) and eye diagram of a gigabyte passive optical network (GPON) used modulation formats, and compare Q, BER performance. Analysis performed for non return to zero (NRZ) and RZ line codes by using avalanche photo diode (APD) and P-Insulator-N (PIN) photodiodes receivers, revealed an improved Q-Factor by changing encoding techniques at different length optical fiber, bit rate, CW laser power and number of users.

Keywords— EDFA, FTTH, GPON , BER, Q-Factor, APD, PIN, Optisystem.

I. INTRODUCTION

Predicting the performance of fiber optic communication systems through numerical simulations has began to be an increasingly important way to complement expensive system experiments, and explore large variations in system designs that are difficult to study experimentally. Measuring an optical signal quality is the most important task in optical communication systems. Optical system quality evaluated by Q-factor BER is mainly depending on input power, bit rate, channel length, modulator, wavelength and receiver type [1]. Hence, the capacity demands for data transmission and optical fiber communication (OFC) technology have undergone an enormous growth. During long distance transmission in OFC systems, light signals get attenuated; and to recover from this problem we need an optical amplifier such as erbium doped fiber amplifiers (EDFA) [2]. In this paper the system performance is measured in terms of Q-factor, BER and eye diagram by varying the system component with and without EDFA[1], The network layout is designed and simulated with Optisystem 7 software.

II. FTTH-GPON SYSTEM

Optical line terminals (OLTs), optical splitters and optical network terminals (ONTs) are the three main components of fiber to the home (FTTH)-GPON access network (Fig.1):

- OLT is the main element of a network, usually placed in the local exchange, and the engine driving the FTTH-GPON system. Traffic planning [3].
- Splitter having one input from port and multiple output ports is passive because it requires no external energy source other than the incident light beam. It is only add loss and broadband, mostly due to the fact that it divides the input (downstream) power. Such loss is called "splitter loss" or "splitting ratio"[3].
- ONT, deployed at the customer premises, is connected to the OLT by means of optical fiber and no active elements are present in the link [3].

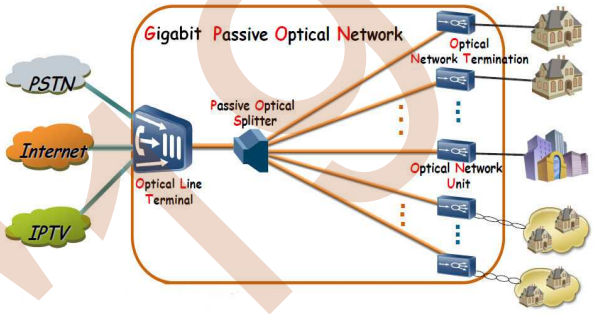

Fig. 1. FTTH-GPON network (Ref .1)

The system could degrade becoming weaker in the channel, and signal is hence attenuated when some part of this is lost, and we need for that to use EDFAs. Using Optisystem software different modulation formats have been made, such as RZ and NRZ, and a comparison between both photodiodes APD and PIN photodiodes has been here performed [2].

1. EDFA

Because of its high gain and low noise feature, a great preference is given to the EDFA that enhances the quality of the signal and it helps to encounter the problems like attenuation and distortion, due to the used doping material: erbium (Er). EDFA has two bands named as L-Band and C-Band, which are very commonly used these days, and a uniform gain at the wavelength range of 1550nm, hence it is the most suitable amplifier for this wavelength[2].

2. PIN Photodiode

PIN consists of three zones: the first zone in order to create a hole excess is called as P-doped, the second zone has an intrinsic region called absorption zone and the third zone is N-doped which creates an electron excess[4].

3.APD Photodiode

The avalanche effect is used to multiply the electrons in a photodiode. Such effect is used to increase the electrical signal power by generating several photoelectrons.[5] APDs are widely used in laser-based fiber optic systems to convert optical data into electrical form. They are high-sensitivity, high-speed semiconductor light sensors[6].

III. SIMULATION SETUP

The study of Q-factor and BER of GPON using Optisystem is summarized in Fig. 2 showing an EDFA schematic design in GPON system, s that consists of :

- Transmitter section including a pseudo random bit sequence generator (PRBSG), a continuous wave (CW) laser whose frequency and input power 0 dBm are respectively 193.1THz, an NRZ pulse generator (PG) and a Mach-Zehnder modulator

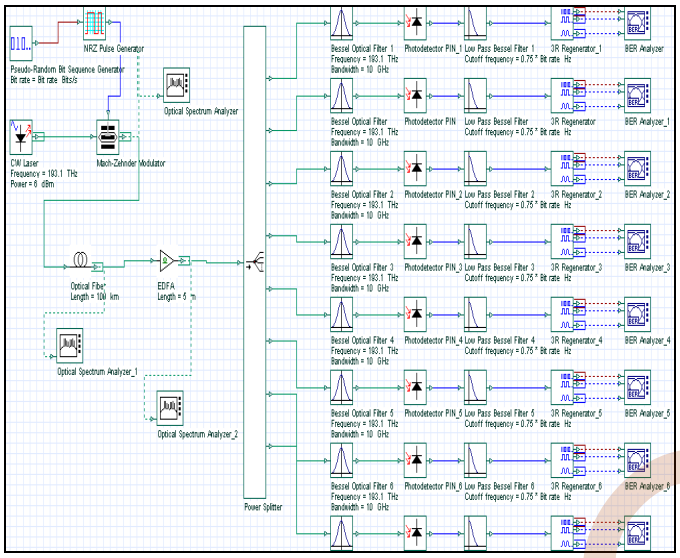

Fig 2 . FTTH-GPON simulation setup

- Channel section :

Optical fiber with length and attenuation of 100Km and 0.2dB/Km and an EDFA whose length is 5m.

- Receiver section which consists of a Bessel optical filter whose frequency and bandwidth of 193.1THz and 10GHz respectively, a PIN photo- detector, a low pass Bessel filter (LPBF), with a Cut off frequency of 0.75*Bit, a rate and 3R Regenerator, and a BER Analyzer.

A. Q- factor

Q-factor is a parameter that directly shows the quality of the optical communication system, indicating how good (low loss) the system quality will be. The high the value of Q, better the quality of the system. Q-factor should be the best judgment, defined as the ratio of the signal and noise [3] :

$$Q = \frac{|\mu_1 - \mu_0|}{\sigma_1 + \sigma_0} \qquad (1)$$

where $|\mu_1-\mu_0|$ denotes the separation between the intensity levels of "1" and "0", and $\sigma_1+\sigma_0$ is the sum of the standard deviations of the intensities around the levels of "1" and "0". Based on the Gaussian approximation for the noise distribution in the received signal.

B. BER

BER is one of a key indicator to measure optical properties, in terms of which the system performance is estimated. It is not counted directly but measured by the evaluation of statistical fluctuations that are characterized by Q-factor as:

$$BER = \frac{1}{2} erfc\left(\frac{Q}{\sqrt{2}}\right) = \frac{1}{\sqrt{2\pi}}\frac{1}{Q} e^{-\frac{Q^2}{2}} \qquad (2)$$

A transmission might have a BER of 10^{-6} for example., means that out of 1,000,000 bits transmitted, one bit was in error [2].

IV. RESULTS AND DISCUSSION

1 / GPON with and without EDFA(8 Users)

Fig 3 shows the results of the optical fiber input which power is 0 dBm (*a*), optical fiber output whose power is -20 dBm (*b*), and EDFA amplifier output which is maximum value 0 dBm, but inversely in terms of noise figure(*c*).

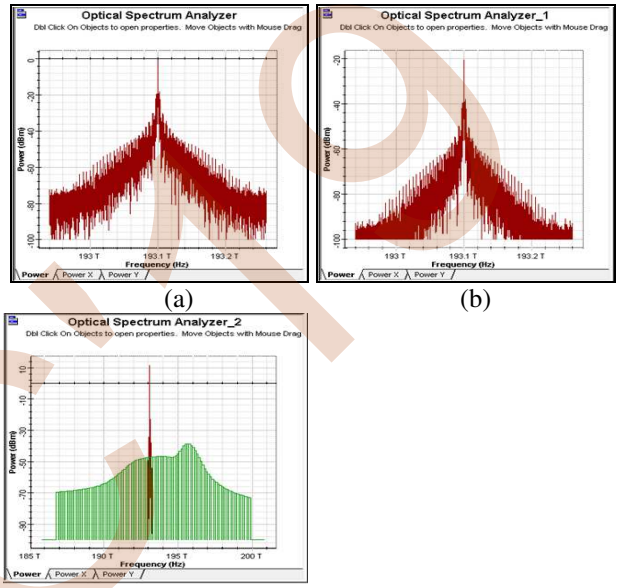

(a) (b)

(c)

Fig 3: Optical Spectrum Analyzer (*a*) Optical fiber input , (*b*) Optical fiber Output, and (*c*) EDFA Output.

The green curve in the graph represents the noise, while the red one shows the sample wavelength. Bit Rate used was 8 Gbps. Analyzing results, it can be concluded that EDFA should be used to compensate the loss of optical signal to increase the transmission length. In this model we are analyzing the Q-factor and BER by varying fiber length between 20 Km and 200Km (see Fig.4).

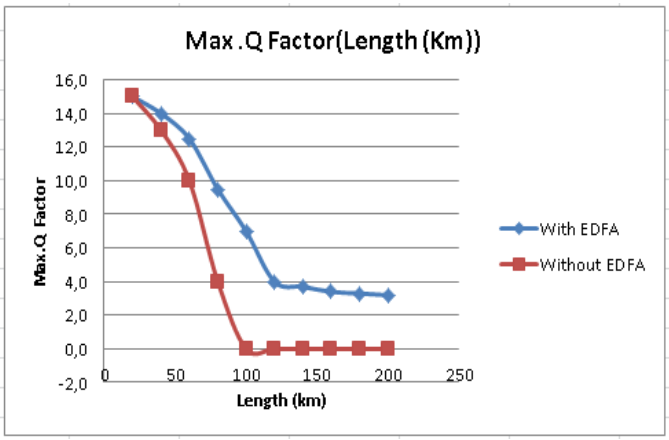

Fig4. Q factor vs. L with and without using EDFA

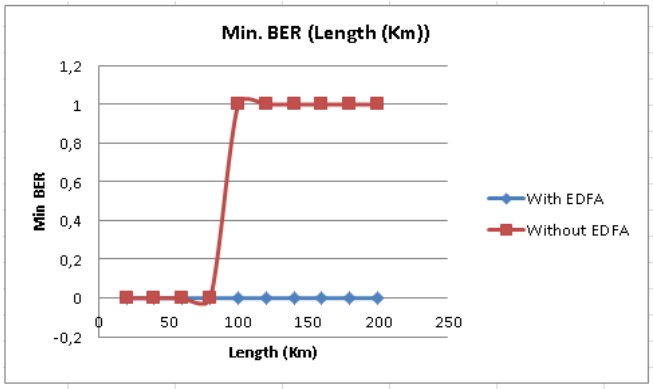

Fig 5. Min BER vs. L with and without using EDFA.

As appearing (Fig. 4 and 5), Q-factor and BER performance by using EDFA is better than without using it.

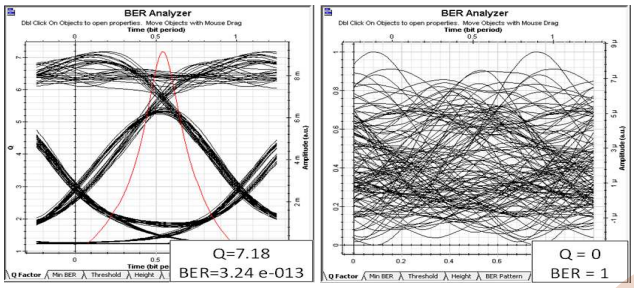

(a) (b)

Fig 6. Eye diagram of downlink shown in BER analyzer (the red curve shows Q-factor) for L=100Km (a) with EDFA, (b) without EDFA.

2 / GPON with EDFA (32 users)

Our model has analyzed the Q-factor and BER, using PIN and APD, and NRZ and RZ modulation formats.

A. Impact of CW laser Power :

To estimate the impact of power CW laser, simulated Q-factors and BER are shown for different transmitted powers (P) varying from -6 to10dBm, with a data rate set at 8Gbps for a link length of 60km and 100Km. For a users' number of 32 communicating simultaneously, the results show a signal quality increasing and a BER decreasing when P increases (Fig. 7 (a, b) and Fig. 8 (a, b)).

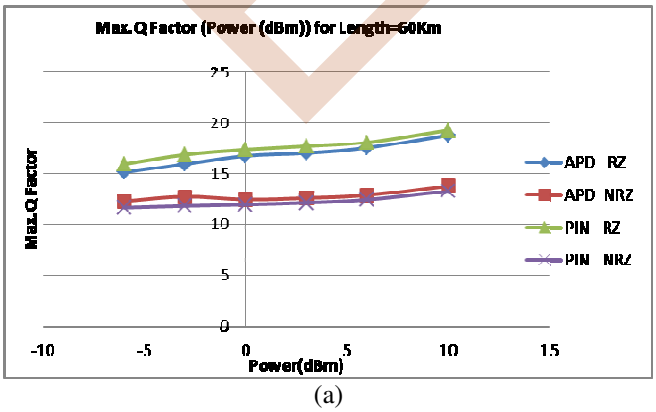

(a)

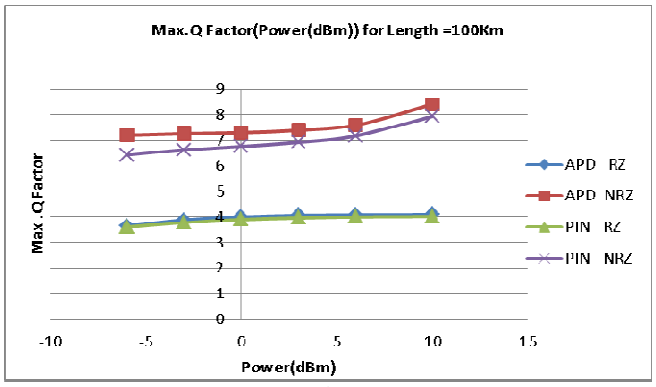

(*b*)

Fig 7. Max Q-factor vs P with and without using EDFA, for: a) L = 60Km, b) L = 100Km.

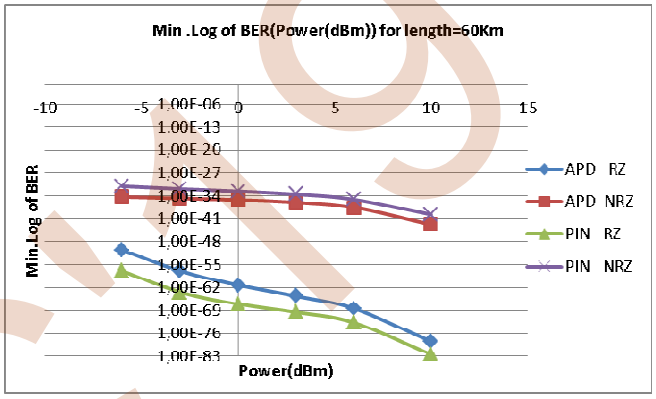

(a)

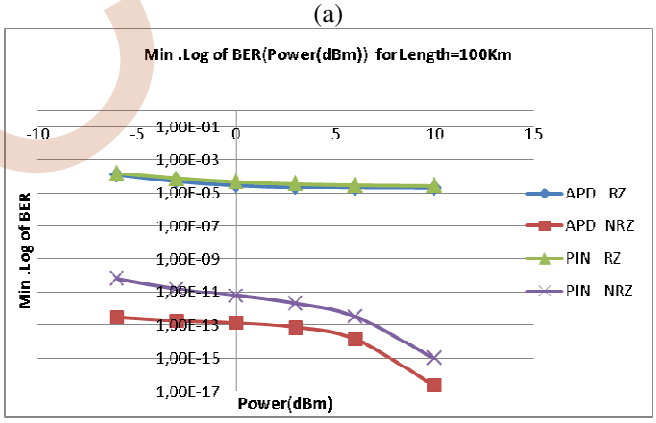

(b)

Fig8. Min Log of BER *vs* P with and without using EDFA, for (a) L = 60Km, (b) L = 100Km.

Fig. 7 and 8 show that the BER and Q-factor performance of the modulation RZ and NRZ by using PIN and APD is shown in Figure 7 and 8. One can clearly mention that using modulation RZ with APD and PIN is suitable for the system performance for length up to 60Km. For L farther than 60Km (for ex.,100Km) the modulation NRZ with APD and PIN is convenient for the system, and using APD is much better than PIN. As for the eye diagram results, when the data bit rate is 8Gbps, P is about 10dBm and L equals to 60/100Km with APD Photodiodes (see figure 9 (a -d)).

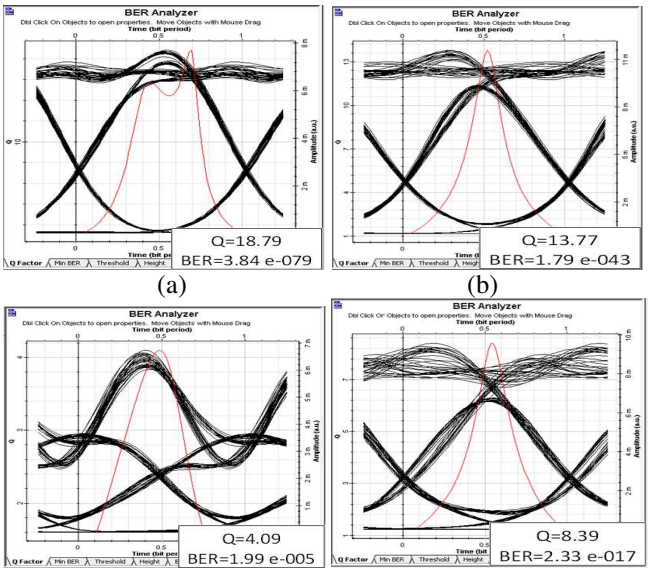

(a) (b)

(c) (d)

Fig 9 . Eye diagram of downlink shown in BER analyzer (the red curve represents Q-factor) using APD with : a) RZ (60Km), b) NRZ(60Km), c) RZ(100Km), d) NRZ(100Km).

B. Impact of Transmission Distance

In the following, we assume that P=6dBm, D=8Gbps and users' number of 32, using PIN photodetectors, are assumed. Fig. 12 (a and b) shows how eye diagrams of downlink changes with fiber lengths of 60 and 100km, respectively. With a transmission distance (i.e. L) varying between 10 and 200Km, the results of Q-factor and BER are shown in Fig. 10 and Fig.11.

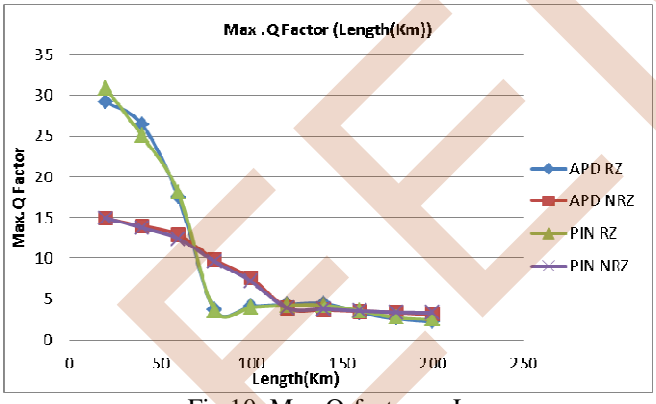

Fig 10. Max Q-factor vs L

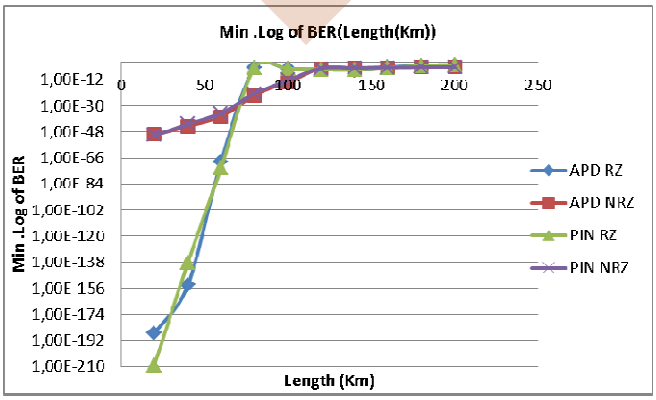

Fig. 11. Min Log of BER *vs* L

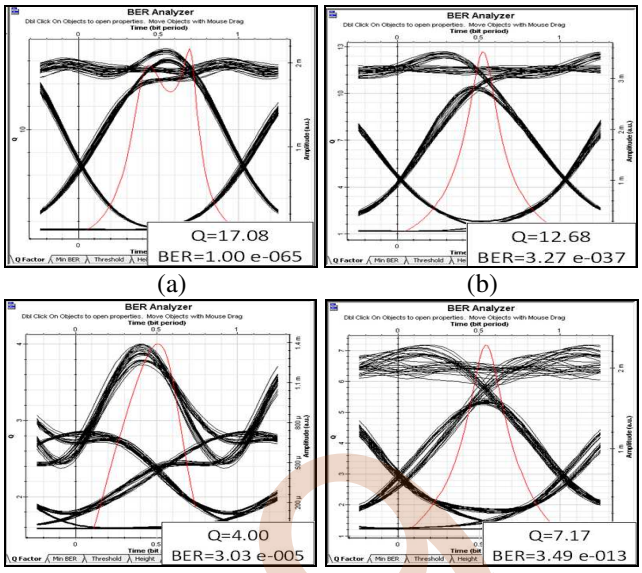

(a) (b)

(c) (d)

Fig. 12. Eye diagram of downlink shown in BER analyzer (red curve represents Q-factor) with PIN: a) RZ (60Km) NRZ(60Km), c) RZ(100Km), d) NRZ(100Km).

Fig. 10 and 11 show that using modulation RZ with APD and PIN is better for the system performance for length up to 60Km. so for lengths beyond 60Km, the modulation NRZ with APD and PIN is more convenient for the system.The modulation NRZ is better than RZ in the long distances.

C. Impact of Bite rate (D)

To evaluate the impact of data rate between the transmitter and receiver, we have studied the performances in terms of Q-factors and BER for different values of D,and P of 6dBm. The results are shown in Fig. 13 and 14.

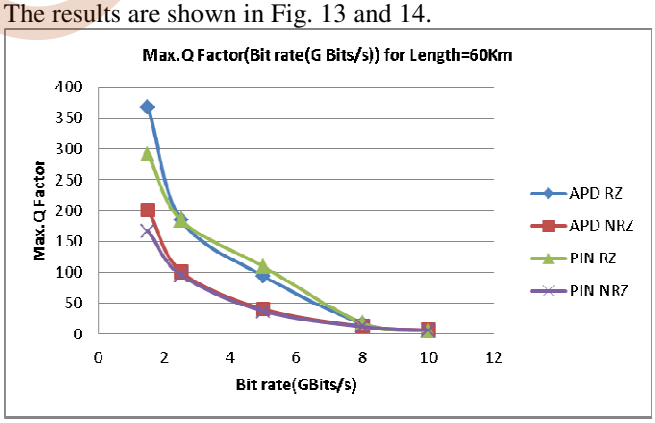

(a)

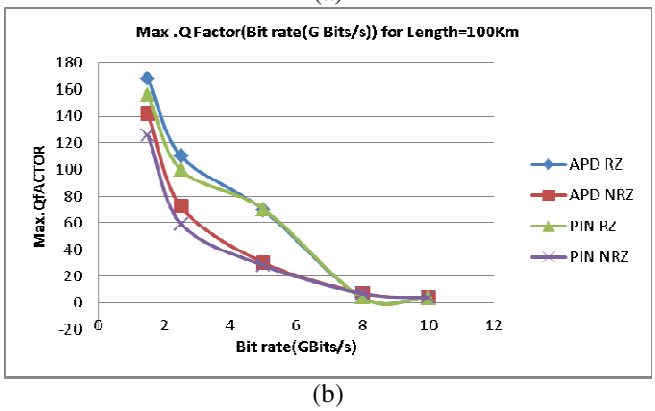

(b)

Fig13. Min Log of BER vs D for L: a) 60Km, b) 100Km.

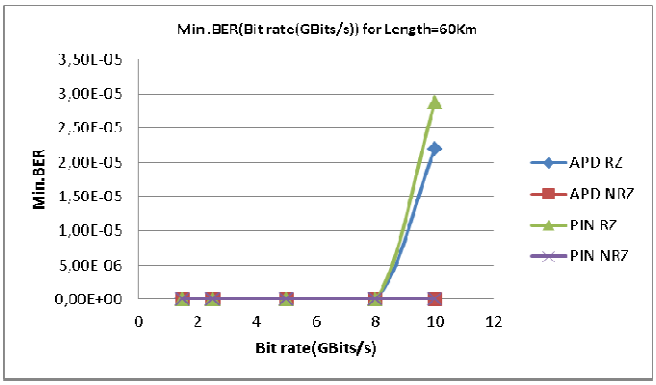

Fig 14. Min Log of BER *vs* D for L=60Km.

Fig. 13 and 14 show a decreasing of the signal quality when the bit rate increases and BER increases. The Q-factor and BER performance are shown in Fig. 13 and 14. One can clearly mention that using RZ modulation with APD and PIN is better for the system performance, and Q-factor performance of APD is higher than that of PIN. Comparing PIN with APD photodiodes reveals that the APD is more advantageous than the PIN photodiode for the low bit rate.

D. Impact of number of users :

To evaluate the performance impact of the number of users, we tested the GPON architecture by calculating Q and BER values for many subscribers simultaneously communicating. We considered the data rate D=8Gbps, power P=6dBm. The simulated results are shown in Fig. 15 and 16.

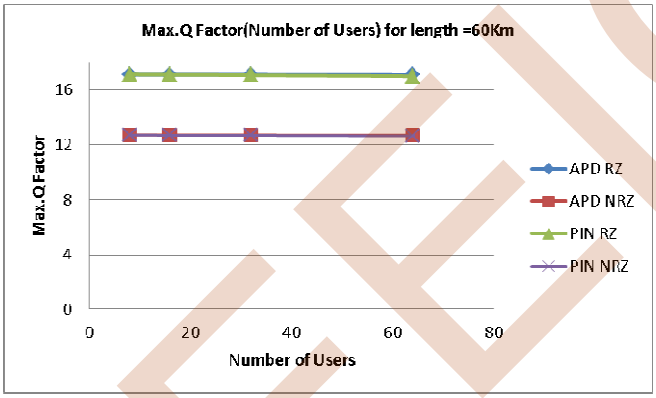

(a)

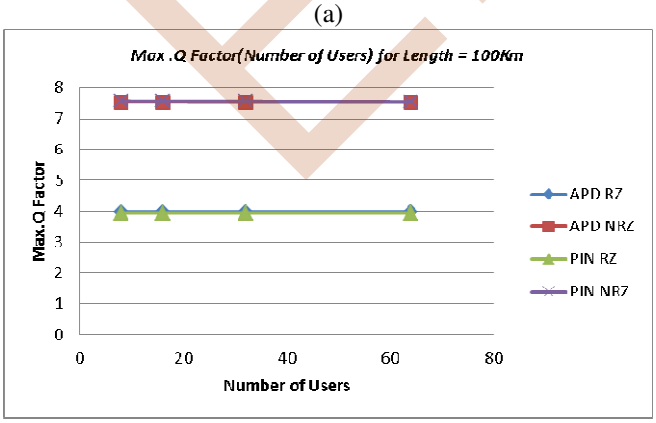

(b)

Fig15. Q-factor *vs* users' number for L: a) 60Km, b) 100Km

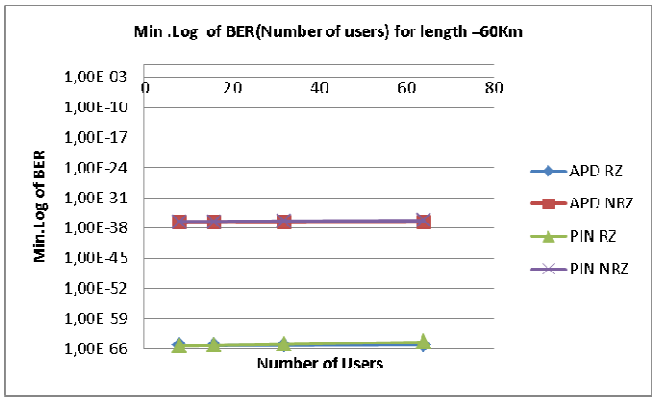

(a)

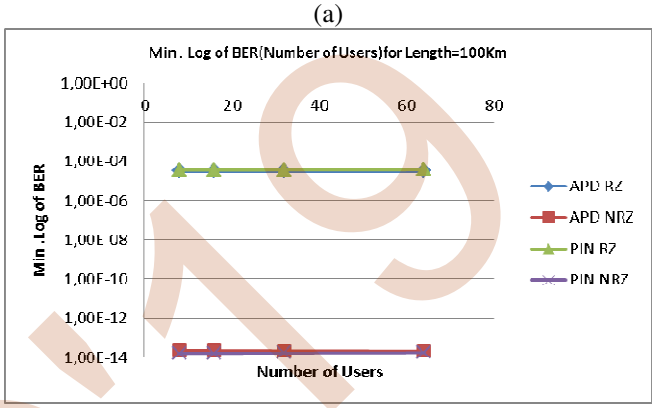

(b)

Fig.16. Min Log of BER vs users' number for L: a) 60Km, b) L=100Km

As shown in Fig. 15 and 16, the use of modulation RZ with APD and PIN is better for the system performance for L up to 60KM, but for L beyond 60KM (for ex.,100Km) the modulation NRZ with APD and PIN is better for the system.

V. CONCLUSION

Optical fiber-based communication as a modern medium of transmission provide high bit rate that fulfill the demand of high speed internet. Performance of GPONs system using different modulation techniques such as NRZ, RZ has been analyzed by Optisystem software with PINs and APDs. The comparison between different modulation technique and Photodiode has been performed and GPON with and without EDFA reveals a great preference proviede by using EDFA. It can be concluded that EDFA could be used to compensate the optical signal loss in order to increase the transmission length. Using modulation RZ with APD and PIN is much convenient for the system performance for length up to 60Km. For length about100Km, the modulation NRZ with APD and PIN is better for the system. Also, the comparison between the PIN and APD photodiodes prouves that APDs are more advantageous than PINs, especially for a low bit rate, which may provide more effective results for APDs that can show less BER than PINs at similar powers. And the modulation NRZ is better than RZ in the long distances.

REFERENCES

[1] R. Mehra, V. Joshi, Effect on Q Factor of Fixed Bit Pattern and Encoding Techniques in Intensity Modulated Optical Networks, International Journal of Computer Applications (0975 – 8887), Volume 106 – No. 13, November 2014.

[2] J.Gujral and M.Singh, " Performance Analysis of 4-Channel WDM System with and without EDFA", International Journal of Electronics & Communication Technology, IJECT Vol. 4, Issue Spl - 3, April - June 2013

[3] M. Bouregaa, M. Chikh Bled, and M. Debbal, "Optical Code Division Multiple Access for a FTTH system," Journal of Photonics Letters Of Poland, Vol. 10 (4), pp.121-123, 2018.

[4] A.Boudkhil,A.Ouzzan and B.Soudini, Analysis of Fundamental Photodetection Noises and Evaluation of PIN and APD Photodiodes Performances using an Optical High Debit Transmission Chain Simulated by Optisystem, International J. of Computer Applications (0975 – 8887) Vol. 115 No.18, 2015.

[5] I.Mashrur Islam1, A.Shahriar and I. Anisul , "Performance Analysis of 2.5 Gbps PIN and APD Photodiodes to Use in Free Space Optical Communication Link", International Journal of Thin Films Science and Technology, Int. J. Thin.Fil. Sci. Tec. 8, No. 2, 53-58 (2019)

[6] P.Sharma and H.Sarangal, " Perfo rmance Comparison of APD and PIN Photodiodes using Different Modulation and Different Wavelengths",International Journal of Signal Processing, Image Processing and Pattern Recognition, Vol.9, No.4 (2016), pp.257-264.

Colors Skin Lesions Detection for Melanoma Discrimination

S. Oukil[1,2], R. Kasmi[2,3], K. Mokrani[1,2], A. Mekhmoukh[1,2], I. Cherfa[1,2], S.S. Ghennam[1,2]

[1]Electrical engineering department
University of Bejaia,
Bejaia, Algeria

[2]Laboratory TII Bejaia
University of Bejaia,
Bejaia, Algeria

[3]Electrical engineering department
University of Bouira
Bouira, Algeria

***Abstract*— malignant melanoma is the deadliest skin cancer worldwide. The automatic detection by a computer-aided diagnosis (CAD) come as a solution to the difficulties related to the naked eye detection especially of the early lesions. The CAD of melanoma detection requires pertinent features. These lesion features include colors, textures, structures and shape of lesions. In this paper, we proposed an algorithm to detect colors that are recognized as suspicious (light brown, medium brown, dark brown, black, white, pink and blue gray) that appear on lesions. First, a set of RGB dermoscopic images are segmented by a suberpixel method. Second, we extracted the R, G and B values for each suspicious color from each blob of subpixel segmentation, the average of all extracted values of each channel color is considered as a reference color (Ref, Gref and Bref). Third, we computed the Euclidian color distance from each lesion pixel to the reference color values, the pixel is assigned to a given color if the distance to its reference is lower than an empirical threshold T, variable for each color. Finally, the surfaces occupied by each suspicious color in the lesion are used as an input to two classifiers (KNN, NN). Using KNN classifier reaches an overall accuracy of 82%, achieving sensitivity and a specificity of 82.65% and 81.39%, respectively. With NN the algorithm classified correctly 70% of lesions. The results of classification showed the importance of the color for melanoma identification.**

I. INTRODUCTION

Malignant melanoma is the most dangerous and deadliest form of skin cancer. The last estimation reported by the American Cancer Society in 2019 by [1], there is 96 480 cases affected by melanoma and 7 230 cases will pass away from melanoma. When detected in its early stage, melanoma is curable. The dermoscopic images provide suitable details and showed its efficiency in improving melanoma detection [2- 5], and allow possibility to build a computer-aided diagnosis for an automatic detection, reducing considerably the time of diagnosis and rises the number of the patient to consult. A computer-aided diagnosis requires pertinent features to be detected from the lesions. These features include colors, textures, structures and shape of lesions [6].

The presence of multiple colors in lesion presents an important biomarker of malignancy [7, 8, 9]. Mounika Lingala et al. in [10] used a blue-gray color to identify melanoma, the color is found using a fuzzy logic method to segment lesion. R. Joe Stanley et al in [11] used the relative color histogram analysis technique to evaluate skin lesion discrimination, based on color features of the skin lesion in dermoscopic images. The results show that the color features may be applicable to any set of images of benign and malignant lesions. Pathan et al. in [12] evaluate the importance of color features to discriminate malignant lesions from benign lesions. A set of fifteen color features have been extracted from the region of interest, then used as an input to a multiple classifier the best results were obtained using decision stump trees with an accuracy classification of 87.5% for classifying benign and malignant lesions

In this paper, we proposed scheme to detect most relevant colors that are recognized as suspicious and appear frequently on the malignant lesions. And demonstrates the feasibility of melanoma identification using colors

II. SUPEREPIXEL SEGMENTATION

The aim of superpixel (oversegmentation of images) is to gather a group of pixels into region according to their similarities such as color, inter region brightness, texture similarity. Since its introduction in [13], several authors have used the superpixel method to resolve different problems such as medical image segmentation [14, 15],

videos and image volumes [16, 17], 3D-reconstruction [18], saliency [19], object detection [20].
In this work, we use superpixel to segment lesions into 2500 smaller regions (blobs) as shown in figure 1. We used the manual mask segmentation of the lesion to remove the healthy skin from images.

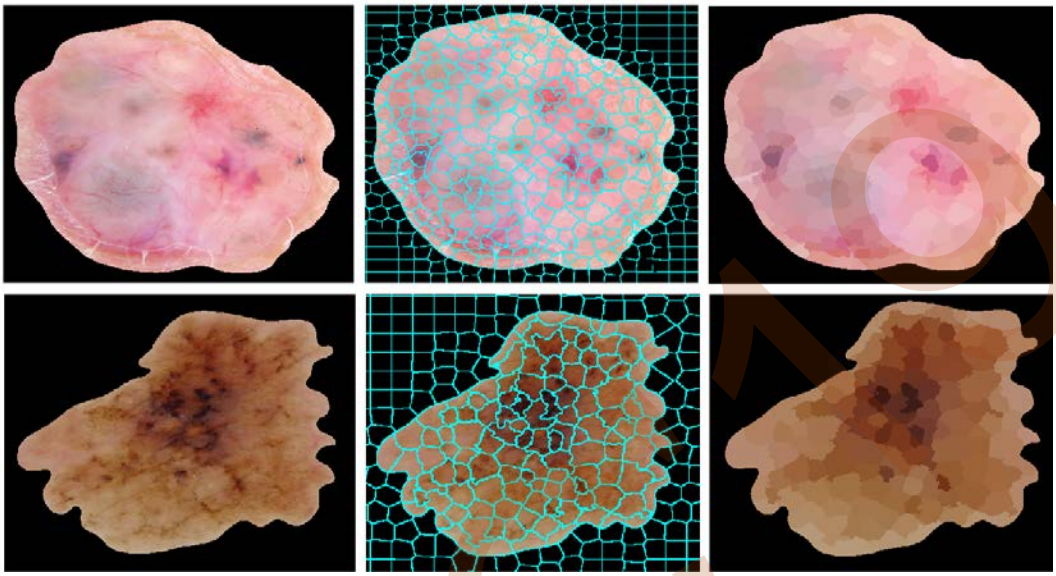

(a) (b) (c)

Figure .1 Superpixel segmentation of lesion: (a) image original (b) overlaid contours of superpixel on the original image (c) Superpixel segmentation result.

From all blobs of superpixel that visually appear as the same color, we extract and save the R-, G- and B-colors values (figure 2). The operation is repeated for all images of the test set. A similar procedure is done for six dominate suspicious colors.

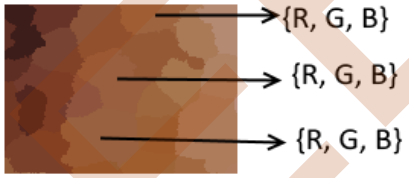

Figure 2. Extract R, G and B-color values from blobs with same color

The references color, which are the values that represent a specific color (light brown, middle brown, dark brown, black, white, and pink) are computed as the average of the extracted values from superpixel blobs.

$$R_{ref\_B} = \frac{1}{N}\sum_{1}^{N} Ri \qquad (1)$$

N: number of number of blob used
$\boldsymbol{R_{ref\_LB}}$: Red channel reference for black color

Similar procedure is used for G- and B-channel color.

The reference values of the six suspicious colors appearing in lesions are reported in the table 1

TABLE I. REFERENCE COLORS VALUES MESURED

Color	Appearance	Reference colors channel [R_{ref}, G_{ref}, B_{ref}]
Light Brown		[192, 144, 112]
Medium Brown		[160, 100, 67]
Dark Brown		[129, 67, 48]
White		[247, 221, 209]
Black		[20, 15, 14]
Pink		[255, 155, 160]
Blue-gray	Algorithm (section IV)	

III. COLORS DETECTION

We measured the color distance of each pixel in the lesion to the reference colors mentioned in the table 1 using the Euclidian distance (2).

$$Dist(i) = \sqrt{(R_i - R_{ref})^2 + (G_i - G_{ref})^2 + (B_i - B_{ref})^2} \qquad (2)$$

$Dist(i)$: distance of a given pixel i to one of the reference color (table 1)

R_i, G_i, B_i: red, green and Blue color channel of a pixel i
A pixel is said to belong to a given color if its normalized distance is lower than an empirical threshold T variable for each color and reported in the table 2. The figure 3 shows the original image and the colors detected.

TABLE II. THRESHOLDS FOR EACH COLOR

Color	Light brown	Middle brown	Dark brown	White	Black	Pink
Threshold	0.15	0.15	0.15	0.15	0.20	0.09

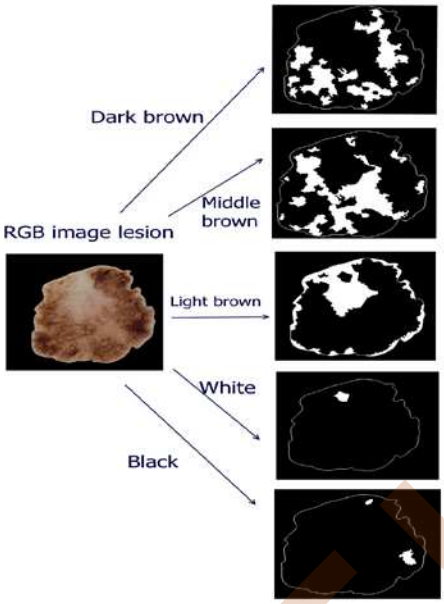

Figure .3 Color segmentation of benign skin lesion

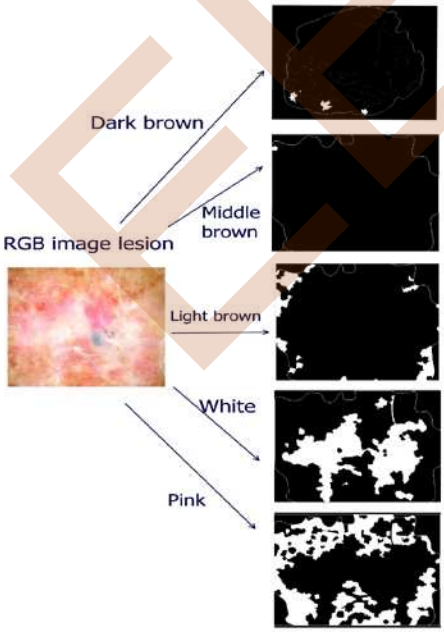

Figure .4 Color segmentation of melanoma skin lesion

To detect blue grey (Blue-white veil), we used the algorithm described by Celebi et al. in [21]. First, a pre selection of pixels are chosen by an empirical rule (R>90 $\cap$ R>B $\cap$ R>G), where R, G, and B denote the red, green, and blue channel, respectively. Second, to compute the skin color, two bands from skin are selected; the first 10% is considered to find the 20% areas outside the lesion from which the average skin colors R_S, G_S, B_S are computed. Third, chromaticity coordinates F1, F2 F3 are computed.

$$F_3 = \frac{B_L}{R_L+G_L+B_L} \quad (3)$$

$$F_{10} = R_L - R_s \quad (4)$$

Finally, a tree algorithm is used to select the blue grey pixels as shown in figure 5

```
If F3<=0.2
    No- Blue-Grey
Else
If F10 > -30
        No- Blue-Grey
    Else
If F10 < -180
        No- Blue-Grey
    Else Blue-Grey
```

Figure 5. Pseudo algorithm that detect Blue-green color with thresholds which fit to our dataset

V. DATA SET

The data set comprises 300 images of dermoscopic skin cancer with its segmentation binary mask, drawn manually by an expert. 150 are benign lesions and 150 are malignant melanomas. The images are full color 24 bit, RGB color with typical resolution of 768X1024.

VI. RESULTS AND DESCUSSION

In order to evaluate the input of colors in the classification of skin cancer lesions, two classifiers K-Nearest Neighbor (KNN) and Artificial Neural Network (ANN) are used. Each image is represented by a vector of features where each element is a percentage of the surface occupied by a given color.

A. *K Nearest Neighbor (KNN)*

K Nearest Neighbor (KNN) method which gathers closest objects measuring the Standard Euclidian distance of normalized features. K is the number of neighbors and to differentiate malignant melanoma from benign lesion [22–23]. In our case we chose K=3, the results are shown in the table 3.

$$Accuracy = \frac{TP+TN}{TP+TN+FP+FN} \quad (5)$$

$$Secsitivity = \frac{TP}{TN+FP} \quad (6)$$

$$Accuracy = \frac{TN}{TN+FP} \quad (7)$$

TABLE III. CLASSIFICATION RESULTS OF KNN

	Classified as melanoma	Classified as Benign	Sensitivity	Specificity	Accuracy
Melanoma (100)	TP=81	FP=19	82,65%	81,37%	82%
Benign (100)	FN=17	TN=83			

B. *Artificial Neural Network (NN)*

The neural network is composed by an input, hidden and an output layers as shown in figure 6.

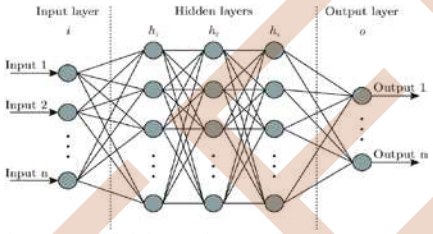

Figure.6 Artificial neural network architecture [24]

In our case the input layer is composed of 7 neurons corresponding to the number of detected colors. One hidden layer with 20 neurons and two neurons compose the output layer as shown in figure 7.

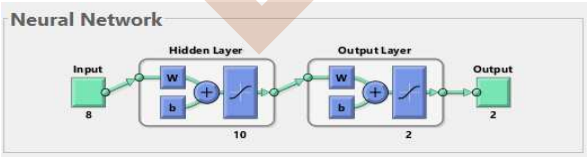

Figure.7 Architecture of the NN used

The results of the training, validation, test and all confusion matrixes are shown on the figure 8.

Figure.8 Result of classification by NN.

The limitations of the current work comprise the thresholds used to cluster pixels to as a given color (distance between pixels to the measured reference colors). The relatively small number of images used, especially, by the neural network classifier. Finally, the algorithm bases on manual segmentation. Further work includes an additional lesions and automatic segmentation to render the algorithm fully automatic.

VII. CONCLUSION

In this work we attempt to detect suspicious colors and identify melanoma. The presence of multi-colors is considered as a sign of the malignancy of the lesion. In this optic, we detected seven colors and measured the surfaces occupied by each color. The surfaces are used as an input features to two classifiers (KNN and NN). Tested on 200 dermoscopic skin lesions images, where 100 are melanomas and 100 are benign, the algorithm using KNN classifier reaches an overall accuracy of 82%, achieving sensitivity and a specificity of 82.65% and 81.39%, respectively. With NN the algorithm classified correctly 70% of lesions.

The result of this work demonstrates the feasibility of melanoma identification using colors that appears on lesions. The classification results of malignant melanomas and benign skin lesions using the incidence of colors open a perspective to improve classification accuracy by investigating more suspect colors and including additional features. Texture features have shown its importance in classification. The further work is to demonstrate the input of the texture features on classification using our data set, then combine texture and color features to optimize melanoma discrimination.

REFERENCES

[1] R. L. Siegel, K. D. Miller, and A. Jemal, "Cancer statistics, 2019," *CA: a cancer journal for clinicians,* vol. 69, pp. 7-34, 2019.
[2] A. Marghoob and R. Braun, *An atlas of dermoscopy*: CRC Press, 2012.
[3] F. Bogo, F. Peruch, A. B. Fortina, and E. Peserico, "Where's the lesion?: variability in human and automated segmentation of dermoscopy images of melanocytic skin lesions," in *Dermoscopy Image Analysis*, ed: CRC Press, 2015, pp. 82-110.
[4] M. E. Celebi, H. Iyatomi, W. V. Stoecker, R. H. Moss, H. S. Rabinovitz, G. Argenziano, and H. P. Soyer, "Automatic detection of blue-white veil and related structures in dermoscopy images," *Computerized Medical Imaging and Graphics,* vol. 32, pp. 670-677, 2008.
[5] G. Argenziano, C. Longo, A. Cameron, S. Cavicchini, J. Y. Gourhant, A. Lallas, I. McColl, C. Rosendahl, L. Thomas, and D. Tiodorovic-Zivkovic, "Blue- black rule: a simple dermoscopic clue to recognize pigmented nodular melanoma," *British Journal of Dermatology,* vol. 165, pp. 1251-1255, 2011.
[6] J. Hagerty, J. Stanley, H. Almubarak, N. Lama, R. Kasmi, P. Guo, R. Drugge, H. Rabinovitz, M. Olivero, and W. V. Stoecker, "Deep Learning and Handcrafted Method Fusion: Higher Diagnostic Accuracy for Melanoma Dermoscopy Images," *IEEE journal of biomedical and health informatics,* 2019.
[7] D. S. Gareau, J. Correa da Rosa, S. Yagerman, J. A. Carucci, N. Gulati, F. Hueto, J. L. DeFazio, M. Suárez-Fariñas, A. Marghoob, and J. G. Krueger, "Digital imaging biomarkers feed machine learning for melanoma screening," *Experimental dermatology,* vol. 26, pp. 615-618, 2017.
[8] M. C. Mihm Jr, T. B. Fitzpatrick, M. L. Brown, J. W. Raker, R. A. Malt, and J. S. Kaiser, "Early detection of primary cutaneous malignant melanoma: a color atlas," *New England Journal of Medicine,* vol. 289, pp. 989-996, 1973.
[9] R. Kasmi and K. Mokrani, "Classification of malignant melanoma and benign skin lesions: implementation of automatic ABCD rule," *IET Image Processing,* vol. 10, pp. 448-455, 2016.
[10] M. Lingala, R. J. Stanley, R. K. Rader, J. Hagerty, H. S. Rabinovitz, M. Oliviero, I. Choudhry, and W. V. Stoecker, "Fuzzy logic color detection: Blue areas in melanoma dermoscopy images," *Computerized Medical Imaging and Graphics,* vol. 38, pp. 403-410, 2014.
[11] R. J. Stanley, W. V. Stoecker, and R. H. Moss, "A relative color approach to color discrimination for malignant melanoma detection in dermoscopy images," *Skin Research and Technology,* vol. 13, pp. 62-72, 2007.
[12] S. Pathan, V. Aggarwal, K. G. Prabhu, and P. Siddalingaswamy, "Melanoma Detection in Dermoscopic Images using Color Features," *Biomedical and Pharmacology Journal,* vol. 12, pp. 107-115, 2019.
[13] X. Ren and J. Malik, "Learning a classification model for segmentation," in *null*, 2003, p. 10.
[14] B. Andres, U. Köthe, M. Helmstaedter, W. Denk, and F. A. Hamprecht, "Segmentation of SBFSEM volume data of neural tissue by hierarchical classification," in *Joint Pattern Recognition Symposium*, 2008, pp. 142-152.
[15] A. Lucchi, K. Smith, R. Achanta, V. Lepetit, and P. Fua, "A fully automated approach to segmentation of irregularly shaped cellular structures in EM images," in *International Conference on Medical Image Computing and Computer-Assisted Intervention*, 2010, pp. 463-471.
[16] R. Achanta, A. Shaji, K. Smith, A. Lucchi, P. Fua, and S. Süsstrunk, "SLIC superpixels compared to state-of-the-art superpixel methods," *IEEE transactions on pattern analysis and machine intelligence,* vol. 34, pp. 2274-2282, 2012.
[17] M. Grundmann, V. Kwatra, M. Han, and I. Essa, "Efficient hierarchical graph-based video segmentation," in *2010 ieee computer society conference on computer vision and pattern recognition*, 2010, pp. 2141-2148.
[18] A. Bódis-Szomorú, H. Riemenschneider, and L. Van Gool, "Superpixel meshes for fast edge-preserving surface reconstruction," in *Proceedings of the IEEE Conference on Computer Vision and Pattern Recognition*, 2015, pp. 2011-2020.
[19] F. Perazzi, P. Krähenbühl, Y. Pritch, and A. Hornung, "Saliency filters: Contrast based filtering for salient region detection," in *2012 IEEE conference on computer vision and pattern recognition*, 2012, pp. 733-740.
[20] J. Yan, Y. Yu, X. Zhu, Z. Lei, and S. Z. Li, "Object detection by labeling superpixels," in *Proceedings of the IEEE Conference on Computer Vision and Pattern Recognition*, 2015, pp. 5107-5116.
[21] O. Marques, *Practical image and video processing using MATLAB*: John Wiley & Sons, 2011.
[22] J. F. Alcón, C. Ciuhu, W. Ten Kate, A. Heinrich, N. Uzunbajakava, G. Krekels, D. Siem, and G. De Haan, "Automatic imaging system with decision support for inspection of pigmented skin lesions and melanoma diagnosis," *IEEE journal of selected topics in signal processing,* vol. 3, pp. 14-25, 2009.
[23] F. Bre, J. M. Gimenez, and V. D. Fachinotti, "Prediction of wind pressure coefficients on building surfaces using artificial neural networks," *Energy and Buildings,* vol. 158, pp. 1429-1441, 2018.

Breast Mass Segmentation in Mammography by Cooperation Fuzzy Possibilistic and Deformable Model

GUERROUDJI Mohamed Amine
Division Télécom
Center for Development of Advanced Technologies (CDTA)
Baba Hassen, Algeria
Email: mguerroudji@cdta.dz

***Abstract*—the breast cancer among the reasons the most common cause of death among women. Nowadays, medicine plays a vital role in our daily life. In addition, breast cancer research and computer-aided diagnosis (CAD) are considered one of the most active disciplines and an extraordinary tool of assisted diagnosis to help physicians. This work is part of an effort to develop a CAD system for the detection of mini-MIAS data masses, which can be considered as the second opinion to the radiologist. To achieve this objectively, this work aims to achieve an optimal segmentation to provide a rich information support to better guide the doctor to make a final decision especially before a surgical procedure. The proposed concept based first, on the noise suppression by anisotropic filtering to emerge all possible clear spots to be masses, and use a mathematical morphology to improve the masses contrast. Second, the segmentation of masses by Cooperation Fuzzy Possibilistic and Deformable Model (implemented by Level Set). Experimental results show that the proposed method improves and progresses significantly to successfully extract mass from the examined mini- MIAS mammography dataset.**

Keywords—mammography; CAD; masses; Level set; Fuzzy C-Means; anisotropic filtering; deformable model; Chunming Li.

I. INTRODUCTION

At the dawn of the 21st century, understanding the mechanisms that govern breast function is certainly a major challenge for basic research and its applications, particularly in the field of public health. masses is one of the most common breast diseases, so its diagnosis and treatment are of vital importance impacting 2.1 million women each year, and also causes the greatest number of cancer-related deaths among women. In 2018, it is estimated that 627,000 women died from breast cancer that is approximately 15% of all cancer deaths among women (based on the World Health Organization (WHO)) [1]. On the other hand, in recent years, the evolution of medical imaging techniques make it possible to use them in several fields of medicine, for example: Planning and simulation of surgical procedures; Navigation during an operation The preparation of radiotherapy; Monitoring the evolution of diseases. The stage of the diagnosis is a key stage in the struggle against the breast cancer as for any other pathology. Consequently, the detection of cancer, the analysis and the treatment of cancer became an orientation major of research. The modern imagery technology has already had on the rescue early cancer detection capacity, and more precisely, the diagnosis of the disease.

For this reason, the radiological technique the most effective is mammography particularly [2-4], lesions on the level of the breast. According to the radiologists an important indicator of the breast cancer, If 90% of them are benign tumors, only 15% of breast tumors are malignant tumors, is the presence of the cases diagnosed by mammography [5-8]. Consequently, the design of a system of CAD represents a system to help the radiologists in the interpretation of the mammography for the tracking of mass and calcification [9, 10]. The automation of detection of mammary pathologies remains always difficult, even for experienced radiologists. Up to now, a wide range of algorithms has been proposed for detection of masses in mammogram images. Among the method the most important are those which use the representation of mammography based on the improvement of contrast and the detection of masses by the mathematical morphology [11-13]. Other improvements of contrast based on the mathematical morphology but they are applied to different types from the images to levels of gray [14, 15]. This last provides tools for the extraction of masses even if masses are located on a non-uniform background. The application of medical image segmentation methods presentation of pathologies remains still a field of research very wide. For this reason the use of the Level set was largely documented in the literature of the medical imagery and several works were published on the segmentation of the masses in mammogram. One finds several techniques have been adopted for segmenting masses, such as Level set [16-19] and the fuzzy C-Means (FCM) algorithm is a widely used and flexible approach to automated image segmentation [20, 21]. Other studies have been conducted on mammography image for the local contrast enhancement [22, 23] and the noise equalization [24], these latter are very important process in the stage of pre-processing of the images to increase contrast between the clear and dark zones to reveal the characteristics of the limits, the main aim of clearness of the image is to highlight fine details.

In this article, a prototype of a breast disease detection system, particularly mass was used. For this reason, the Proposed a new approach to improve the detection of masses in digital mammography. This approach is based on three main stages, noise removal by the anisotropic filter and improving contrast between mass and the background digital mammography. And will make an effort in improving the morphological contrast enhancement mathematical morphology.

In the third phase, the using a segmentation of the area of interest for the identification of masses in mammography by Possibilistic / Fuzzy Cooperation- Deformable Model for that we propose a framework that is a combination of region-based and boundary-based paradigms.

This segmentation is performed in two steps: in first step, a region-based segmentation is applied, by using a new method, which exploits at the same time the information of the pixels and their neighborhood (inspired by the fields of Markov), the membership and the typicality. In second phase, the result of the first segmentation is refined by a deformable model implemented via Level Set. The proposed method has been tested on several images from the mini-MIAS database of mammography [25], noting that the results validate the superiority of our proposed approach. The rest of this paper is structured as follows: section 2 the present detection method. Section 3, present the obtained experimental results and discussion. Finally, our conclusions are presented in the last section.

II. DETECTION METHOD

In Fig. 1 we offer the several stages that our approach proposed for enhancement image of the breast.

1) Pre-processing:
In spite of effort made by the researchers, the automation of the mammary pathologies detection remains always difficult. In this work, the digital technique of pre-processing of the image based on the three following stages:

a) Stage (1): As mass spots are small and often of low intensity, the design of a filter that is able to distinguish the noise is very difficult. We applied the nonlinear anisotropic diffusion filter was introduced by Perona and Malik [26], as a filtering tool noisy images, with the particularity of preserving details and edges masses while filtering homogeneous areas [26].

Anisotropic diffusion Knowing that the main objective pursued by the anisotropic diffusion is to filter the image, to reduce noise in areas where it is present, but to avoid the smoothing of contours at the same time. It is clear that the anisotropic filter accentuates the contrast of the contours, smooths the regions and reduces the partial volume effect.

Fig. 2 represents the result and comparison of an anisotropic filter of the image mammography after and before filtering. We see that the anisotropic filter accentuates how sharp edges, smooth regions and also decreases the partial volume effect.

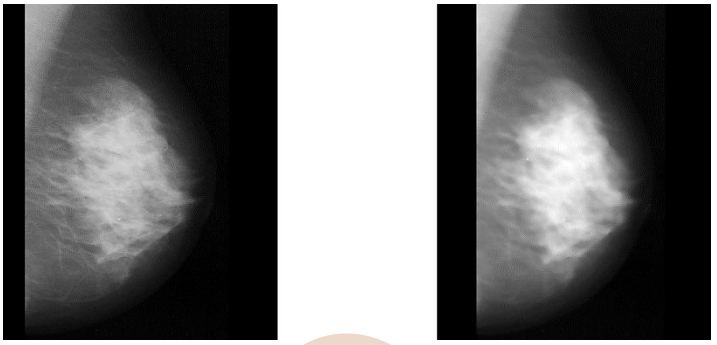

Figure 2. a) Original image. b) Result of image after the filtering.

b) Stage (2): Mathematical morphology is a science of the form and structure. The basic principle of mathematical morphology is to compare the objects, which one wants to analyze with another object of reference, with size and form known, called structuring element. To some extent, each structuring element revealed the object in a new form. The fundamental operations of mathematical morphological are erosion and dilation [27].

- From the openings and closures by reconstruction residues between the image and its open by reconstruction or residue between the closed by reconstruction and the original image, which allows finding the information eliminated by the morphological opening or, the morphological closure. This top hat transformation is called.

By applying these stages to images mammography with a choice of the structuring element used for the Top-Hat transform corresponding to a disc with a size of 3X3 [28-30] (it is the mean size, of a basic element of a mass), we obtained the following results (see Fig. 3).

2) Segmentation method: Segmentation method is regarded as the method of reference in the field of medical imaging. These methods are largely used in image segmentation mammography, in order to detect the zones of tumor or masses. In this paper, the original contribution is a masses segmentation method, we have here images [25] on which we will apply our cooperative system. The general idea is to extract the mask that contains the mass, from the initial segmentation, then apply it on the model of Chunming Li [31] and that will serve as its initial outline. This mask is not used directly; it must first undergo some morphological operations to eliminate unnecessary areas present in the mask all around the mass. We will present a global organization chart, which illustrates the steps of cooperation, associated with the results obtained from this cooperative method (see Fig. 4).

- SR: it is the total result of the segmentation.
- MR: is the final mask of the segmentation by cooperation.

Figure 1. Breast insulation flowchart.

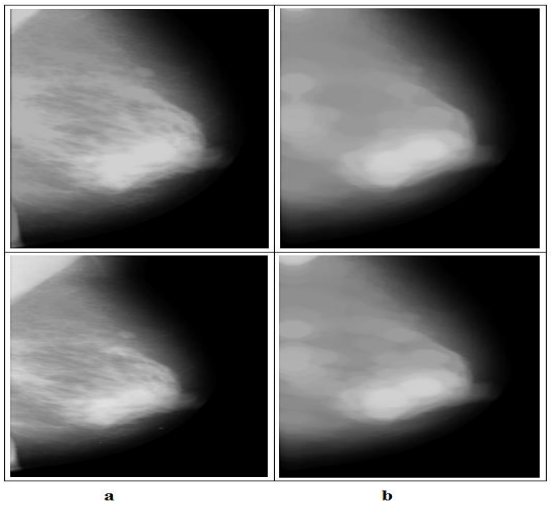

Figure 3. Results relative to each stage of the proposed algorithm for the Pre-processing image mammography: a) Original image Mammography; b) The morphological opening.

We can say, finally, that the combined use of several segmentation algorithms working in cooperation overcomes the problems encountered by the use of a single algorithm. In our case, it considerably improves the deformable model which has become an automatic method and does not require a high number of iterations to define the object of interest since it is well initialized using the FCM algorithms.

- Parameter study The parameters studied are following:

The size of the search area for the calculation of non-local weights:

$$\left|\Omega_j^{Rd}\right| = \left(2n_j + 1\right)^2 \quad (1)$$

The size of the search area for the calculation of non-local weights for regularization:

$$\left|\Omega_j^{Rr}\right| = \left(2n_{jr} + 1\right)^2 \quad (2)$$

The neighborhood size for calculating local centroids:

$$\left|M_j^{Rr}\right| = \left(2n_{jr} + 1\right)^2 \quad (3)$$

The parameters we used are: Iteration number of FCM.
Number of classes.
α: Alpha.
β : Beta.
σ: Sigma.
n_j: radius of $\left|\Omega_j^{Rd}\right|$.
n_{jr}: radius of $\left|\Omega_j^{Rr}\right|$.
m_j: radius of $\left|M_j\right|$.

III. EXPERIMENTAL RESULTS AND DISCUSSION

In this work, has been tested using the base of image mini-MIAS (Mammography Image Analysis Society) [25]. The object of our study, illustrate and segmentation of the mainly benign and malignant masses. The different mammary pathologies from the base of MIAS data which are the subject of our study, mainly illustrate benign and malignant masses distributed as follows:

- 36 images of malignant masses
- 47 images of benign masses

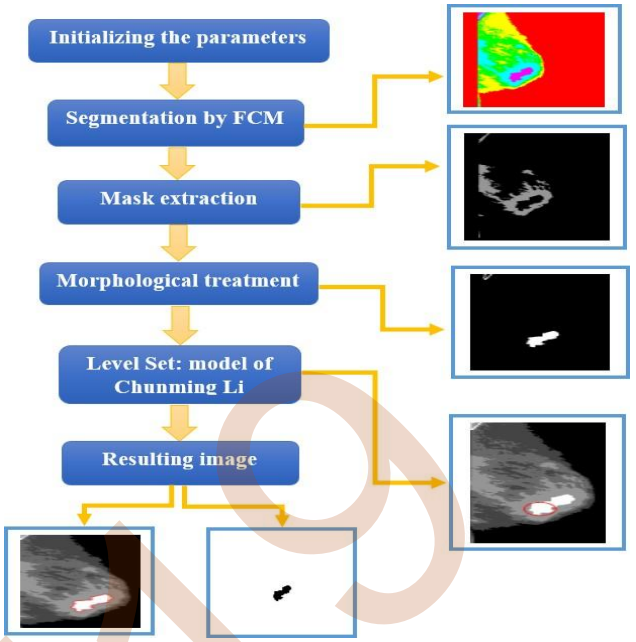

Figure 4. Global Organizational cooperation Fuzzy Possibilistic / deformable model.

The detection of cancerous masses is very complex, in one hand, to the diversity of their forms and, in the other hand the border badly definite between healthy tissue and the cancerous zone. For this reason, the striving in this work, for proposed algorithm towards the improvement of the mammography image. To highlight masses and to this end selected, several images of mini-MIAS database [25] with dense fabric and the presence of mass. The results are illustrated by the figures below: In this part, the proposed segmentation methods were implemented in the context of the identification of the main breast tissues. We first present the results obtained by using fuzzy-possibilistic classification algorithms that present the stage of the initial segmentation then the results obtained in the second stage which includes the approach contour (deformable model implemented via chunming Li) and finally the third step that concerns the results of our cooperative approach, and obtained the following results (see Fig. 5). An image histogram is a graphical representation of the number of pixels in an image as a function of their intensity. The vertical axis of the graph represents the tonal variations, that particular tonal variation [32]. Fig. 6 shows the original histogram of the image mammography and histogram of the image mammography after the segmentation. The mammogram image contains more pixels with different intensity and therefore, the histogram skew towards the right side which is closed 0 to 255.

It can be observed that the deformable model can improve the results of the initial segmentation. Although it improves the volume and surface parameters, we sometimes find that it converges to a false contour because of the bad definition (initialization) of the borders. However, the use of spatial

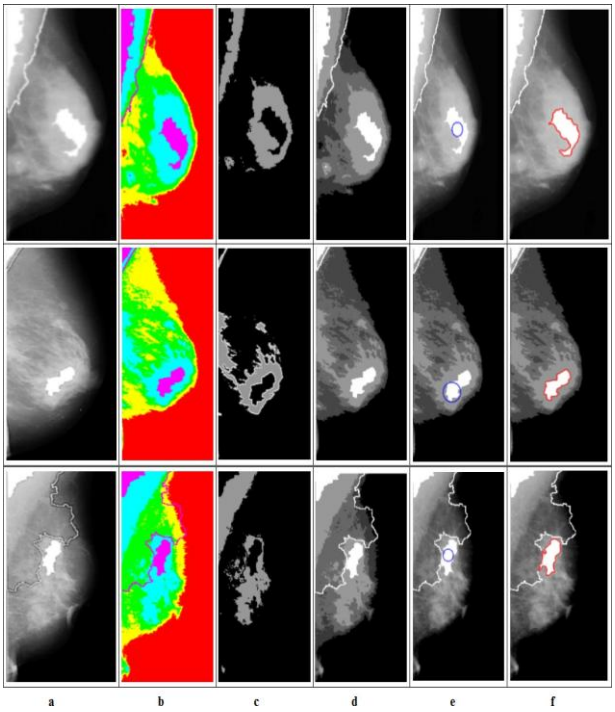

Figure 5. The results of the proposed algorithm for segmentation of the images: a) Enhancement image Mammography; b) Mask extraction; c) Segmented image by FCM; d) Segmented image by FCM in color; e) Level Set: model of Chunming Li; f) Segmentation final by cooperative approach.

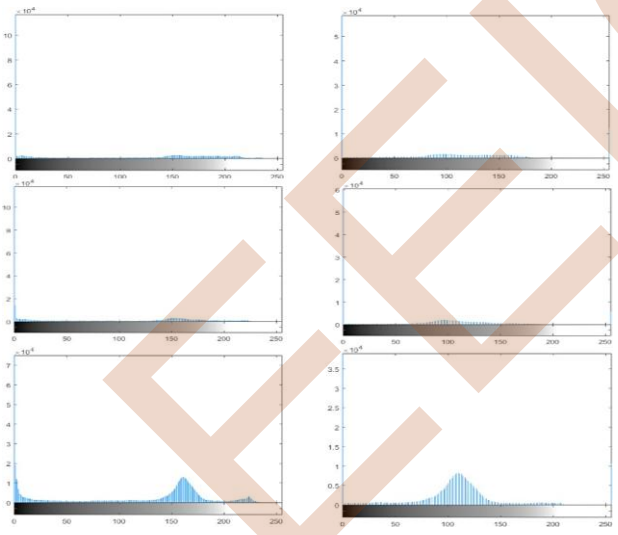

Figure 6. a) Original histogram. b) Histogram after the segmentation.

A relationship makes it possible to reduce the rate of false detections, because they prevent the escape of the contour towards the ill-defined borders. The Fig. 7 shows the convergence of deformable Model to false contour.

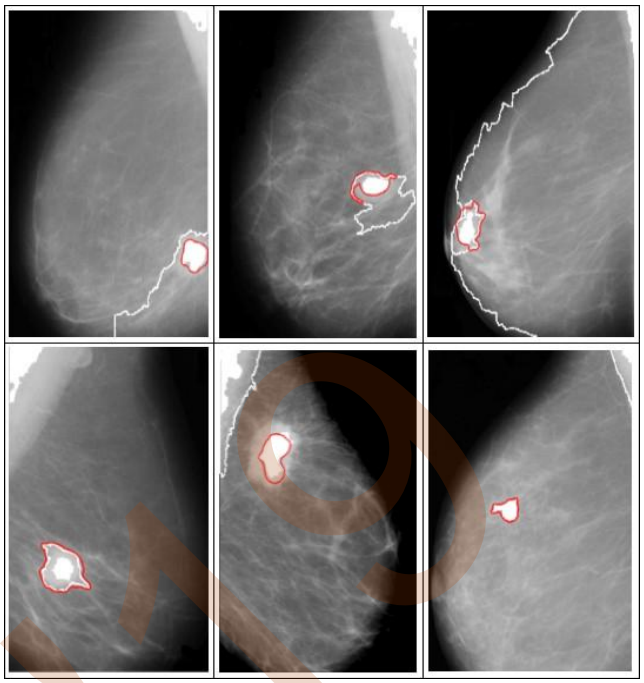

Figure 7. Results of false contour by deformable Model.

IV. CONCLUSION

The research work proposed in this article is in the context of image analysis, especially in the study of an optimized segmentation method, and apply it to mammographic medical images. These substances can be used in several applications such as morphometry (shape measurement), functional mapping, visualization and computer-assisted surgery and therefore presents an effort to develop a CAD medical imaging platform, and justifies itself by improving the quality of patient care. The information we have on mammographic images is sometimes ambiguous, either because we have unspecified boundaries (imprecise information), or we have doubts about their veracity because a pixel has attributes that assign it to one class has another (uncertain information). The addition of the blur to the classification allowed us to classify the whole of the individuals by the support of the uncertainty and the imprecision that can have a pixel. The proposed segmentation method combines contour methods and regions that push their boundaries using the advantages of each. This sequential cooperation has two main phases: initialization by a method region and refinement by a method contour. The results obtained show that the methodology used has made it possible to detect satisfactory masses.

REFERENCES

[1] Breast cancer. World Health Organization. https://www.who.int/cancer/ prevention/diagnosis-screening/breast-cancer/en/, 2019. [Online].

[2] H. Cheng, X. Shi, R. Min, L. Hu, X. Cai, and H. Du, "Approaches for automated detection and classification of masses in mammograms", Pattern recognition, vol. 4, pp. 646-668, 2006.

[3] L. Bocchi, G. Coppini, J. Nori, and G. Valli, "Detection of single and clustered microcalcifications in mammograms using fractals models and neural networks", Medical Engineering & Physics, vol. 4, pp. 303-312, 2004.

[4] F. Julian, Miller, L. Stephen, Smith, Y. Zhang, "Detection of Microcalcifications in Mammograms using Multi-chromosome Cartesian Genetic Programming", GECCO '10, 12th annual conference companion on Genetic and evolutionary computation. ACM Press, USA 2010.

[5] C. Diaz-Huerta, E. Felipe- Riveron, L. Montao- Zetina, "Quantitative analysis of morphological techniques for automatic classification of micro-calcifications in digitized mammograms", Expert Systems with Applications Elsevier, vol. 16, pp. 7361-7369, 2014.

[6] C. Marrocco, M. Molinara, F. Tortorella, P. Rinaldi, L. Bonomo, A. Ferrarotti, C. Aragno, and S. Schiano lo Moriello, "Detection of cluster of microcalcifications based on watershed segmentation algorithm In Computer-Based Medical Systems (CBMS)", 25th International Symposium on, pages 15. IEEE, 2012.

[7] H. Cheng, C. Xiaopeng, X. Chen, L. Hu, and X. Lou, "Computer-aided detection and classification of microcalcifications in mammograms: asurvey", Pattern recognition, vol.12, 2967-2991, 2003.

[8] MA. Guerroudji, Z. Ameur, "A new approach for the detection of mammary calcifications by using the white Top-Hat transform and thresholding of Otsu", optic Elsevier, vol. 3, pp. 1251-1259, 2016.

[9] B. Zheng, "Computer-Aided Diagnosis in Mammography Using Content Based Image Retrieval Approaches: Current Status and Future Perspectives", vol. 2 pp. 828-849, 2009.

[10] R. Nanayakkara, Y. P. R. D. Yapa, P. B. Hevawithana, P. Wijekoon, "Automatic Breast Boundary Segmentation of Mammograms", International Journal of Soft Computing and Engineering (IJSCE), vol. 1, pp.2231-2307, 2015.

[11]JM. Mossi, A. Albiol, "Improving detection of clustered micro-calcifications using morphological connected operators", In International Conference on Image Processing and Its Application on, pp. 498-501. IEEE, 1999.

[12]RM. Rangayyan, F. Ayres, and J. Desautels, "A review of computer-aided diagnosis of breast cancer: Toward the detection of subtle signs", Journal of the Franklin Institute, vol.3, pp. 312-348, 2007.

[13]R. Yapa, K. Harada, "Breast Skin-Line Estimation and Breast Segmentation in Mammograms using Fast-Marching Method", International Journal of Medical, Health, Biomedical, Bioengineering and Pharmaceutical Engineering, 2007.

[14]MA. Guerroudji, Z. Ameur. "New approaches for Contrast enhancement of calcifications in mammography using morphological enhancement", Proceedings of the International Conference on Intelligent Information Processing, Security and Advanced Communication - IPAC'15, 2015.

[15]X. Bai, F. Zhou, and B. Xue. "Toggle and top-hat based morphological contrast operators", Computers & Electrical Engineering, vol. 5, pp. 1196-1204, 2012.

[16]C. Hua, G. Liqun, "Geodesic active contour, inertia and initial speed", Pattern Recognition Lett, vol. 16, pp. 2197-2205, 2008.

[17]H. Shan, J. Ma, Curvelet, "based geodesic snakes for image segmentation with multiple objects", Pattern Recognition Lett, vol. 5, pp. 355-360, 2010.

[18]V. Caselles, F. Catt, T. Coll, F. Dibos. "A geometric model for active contours in image processing", Numer Math, vol. 1, pp. 131, 1993.

[19]R. Malladi, J. Sethian, B. Vemuri. "Shape modeling with front propagation: A level set approach", Pattern Anal. Machine Intell, IEEE Transactions on, vol. 2, pp. 158-175, 1995.

[20]S. Anand, V. Vinod, A. Rampure, "Application of Fuzzy c-means and neural networks to categorize tumor affected breast MR Images", International Journal of Applied Engineering Research, vol. 64, 2015.

[21]M. Kamil, A. Salih, "Mammography Images Segmentation via Fuzzy C-mean and K-mean", International Journal of Intelligent Engineering and Systems, vol. 1, 2019.

[22]A. Laine, S. Schuler, J. Fan, and W. Huda, "Mammographic feature enhancement by multi-scale analysis", Medical Imaging, IEEE Transactions on, vol. 4, pp. 725-740, 1994.

[23]W. Veldkamp, N. Karssemeije, "Normalization of local contrast in mammograms", Medical Imaging IEEE, vol. 7 pp. 731-738, 2000.

[24]K. Mcloughlin, P. Bones, N. Karssemeijer, "Noise equalization for detection of microcalcifications clusters in direct digital mammogram images", Medical Imaging IEEE, vol. 3), pp. 313-320, 2004.

[25] mini MIAS. The mini-MIAS database of mammograms. http://peipa. essex.ac.uk/info/mias.htm, 2014. [Online].

[26]P. Perona, J. Malik, "Scale space edge detection using Anisotropic diffusion", Pattern Anal, IEEE Transactions, vol. 12, pp. 629-639, 1990.

[27]X. Bai, F. Zhou, "Infrared small target enhancement and detection based on modified Top-Hat transformations", Computers Electrical Engineering Elsevier, Vol. 36, pp. 1193-1201, 2010.

[28]X. Bai, F. Zhou, Y. Xie, T. Jin, "Adaptive Morphological Method for Clutter Elimination to Enhance and Detect Infrared Small Target", Internet Computing in Science and Engineering (ICICSE), '08. International Conference IEEE, pp. 4752, 2008.

[29]X. Bai, F. Zhou, "Analysis of new top-hat transformation and the application for infrared dim small target detection", Pattern recognition Elsevier, vol. 6, pp. 2145-2156, 2010.

[30]C. Xu, D L. Pham, J L. Prince, "Chapter medical image segmentation using deformable models: medical image processing and analysis", Handbook of medical imaging, vol. 2, pp. 129-175, 2000.

[31]C. Li, R. Huang, Z. Ding, J. Gatenby, D. Metaxas, "A Level Set Method for Image Segmentation in the Presence of Intensity In homogeneities With Application to MRI", IEEE Transactions on image processing, vol. 7, 2011.

[32]A. Hussain, A. Mustapha, N. Tahir, "An analysis of x-ray image enhancement methods for vertebral bone segmentation", IEEE 10th International Colloquium on Signal Processing its Applications (CSPA2014), Kuala Lumpur, Malaysia, 2014.

EEIC'2019 University of Bejaia

Hyperspectral Feature Selection using Improved F-Score Technique

Samir L'haddad
Faculty of Electronic and Computer Science
University of Sciences & Technology Houari Boumediene
Algiers, Algeria
slhaddad@usthb.dz

Akila Kemmouche
Faculty of Electronic and Computer Science
University of Sciences & Technology Houari Boumediene
Algiers, Algeria
akemmouche@usthb.dz

Abstract— **Hyperspectral images are characterized by a large number of contiguous spectral bands. However, there are lot redundancies in the set of bands. This spectral redundancy increases computational complexity and degrades classification accuracy. Therefore, to take full advantage of the rich information provided by the hyperspectral image, a feature reduction is required before applying a classifier. For this purpose, we adapt a pattern recognition feature selection method, the Improved F-score combining with support vector machine (SVM) classifier in order to reduce dimensionality data of hyperspectral image. Six different threshold values computation techniques are used with Improved F-score feature selection method to select the most relevant spectral information. Experimental results are presented on a 125-bands Hyperion image of the Oran city (west of Algeria). The Improved F-Score, combined with SVM, significantly improves classification accuracies by using four algorithms of IFS threshold values such as mean, variance, Fuzzy Integral of Sugeno and Fisher Linear Discriminant.**

I. INTRODUCTION

Hyperspectral imaging is a well-suited technology for many remote sensing applications such as agriculture, environmental monitoring and management, etc. However, the high dimensionality of the data tends to be characterized by a complex image analysis and classification. Since the hyperspectral image is composed of hundreds of contiguous spectral bands, in which a pixel is represented with a vector of dimension equal to the number of the image bands. Hyperspectral data provide additional information for each observed area; however, classification accuracy tends to decrease as the number of features increases [1], [2]. As a matter of fact, the limited number of training samples and the high number of features restrict the performance of the supervised classification techniques. Therefore, in order to improve classification results, a dimensionality reduction process is essential to select the most relevant spectral information. Feature extraction and feature selection are two ways to achieve dimensionality reduction of the multidimensional data. Feature extraction methods transform the original spectral bands by projecting bands into new axes of data representation. On the contrary, band selection consists in finding an optimal subset of the original features that is sufficient to preserve the information of the original data. It leads to dimensionality reduction by selecting informative features, and removing redundant ones. Different feature selection methods have been proposed and investigated [3], [4], [5], [6], [7]. In this paper we propose to adapt a method, the Improved F-Score (IFS) combined with SVM classifier in order to select the most relevant bands. Classifications of the selected hyperspectral data using six different threshold values were compared to achieve the highest overall accuracy (OA).

This paper is organized as follows: In Section 2 the considered Improved F-Score approach is introduced. Section 3 discusses various strategies of threshold value computation. Experimental results obtained on Hyperion data sets from urban areas are presented in Section 4. Finally, conclusions are drawn in Section 5.

II. IMPROVED F-SCORE

The F-Score (FS) was proposed for discrimination between two sets of real numbers. Okay. [8] has applied the F-Score approach combined with SVM classifier for breast cancer diagnosis. The proposed method is to measure the discrimination of two sets of instances: positive (cancer cell) and negative (non-cancer cell) breast cancer. For this purpose, the F-Score values of all features are calculated. Then a threshold value is computed from the calculated F-Score values. The F-Score values which are greater than the threshold score value are selected. By generalization, the original F-score technique to measure the discrimination among more than two datasets, Jaganathan *et al.* [9] proposed the Improved F-Score (IFS). It has been

successfully applied for measuring the discriminating power of descriptors generated from the differential morphological profile [10]. In this study, IFS is combined with Support vector machines (SVM) for eliminating unnecessary and redundant bands. For this purpose, the IFS values of all the bands are calculated. Then a threshold value is computed from the calculated IFS values. Features with an IFS value greater than the threshold are selected and then used as input in the multichannel classification step. The set of bands of the original hyperspectral image constitutes the spectral features for which the Improved F-Score is calculated. The larger improved F-score value corresponds to the pertinent spectral feature [11].

Let's consider the classified hyperspectral image into *l* classes *(l >= 2)* without spectral feature selection and nj the number of pixels constituting the j^{th} class.

The improved F-score of the *ith* feature is defined as:

$$Fi = \frac{\sum_{j=1}^{l} [avg(x_i^j) - avg(x_i)]^2}{\sum_{j=1}^{l} \frac{1}{nj-1} \sum_{k=1}^{nj} [x_{ki}^j - avg(x_i^j)]^2} \quad (1)$$

Where

- $avg(x_i)$ is the radiometric average value of the pixels in the i^{th} spectral feature (the pixels belonging to the i^{th} band);
- $avg(x_i^j)$ is the radiometric average value of the pixels in the i^{th} spectral feature belonging to the j^{th} class;
- x_{ki}^j is the k^{th} pixel of the i^{th} spectral feature image (i^{th} band image) belonging to the j^{th} class.
- The term $[avg(x_i^j) - avg(x_i)]^2$ calculate the difference between the average of the radiometric values of the i^{th} spectral feature pixels belonging to the j^{th} class and the average of the radiometric values of all pixels in the i^{th} spectral feature (the i^{th} band pixels).

The main steps of the IFS procedure are given as below:

a) The first step is to directly use SVM classifier without feature selection.
b) Using equation (1) to calculate *Fi* of each band and then calculate the threshold value.
c) Drop bands with *Fi* below this threshold.
d) We obtain, through the threshold score, two sets of bands: the pertinent and the non-pertinent bands. The selected bands (with high *Fi*) are classified by the SVM classifier.

The selection algorithms perform differently under six different threshold values. The existence methods have focused on the mean, median and variance as thresholding value. Three other thresholding methods have been developed in this study based on Sugeno, Fisher and R-Ratio concept.

A. *Computing F-Score Threshold Value by the Mean*

The threshold value is the mean value calculated from the Improved F-Score values F_i. of all bands. We selected bands with *Fi* rather than the mean and then apply the SVM classifier. However it must be noted that from a mathematical point of view, arithmetic average is not the best measure to use with data sets containing a few extreme values or with more dispersed values in general.

B. *Computing F-Score Threshold Value by the Variance (Standard Deviation)*

Variance is the most commonly used measure of dispersion. It is a measure of propagation of data about the mean. To find standard deviation, we need to subtract the "mean" of the Improved F-Score values from each score F_i. Nevertheless, one drawback of the variance is that strongly affected by "outliers' values" (the number that are far from the mean).

C. *Computing F-Score Threshold Value by the Median*

Median is the "middle value" of a sorted list of values which separate the higher value from the lower one, in the input data. The middle score number is a less representative value because it does not depend on all values in the series of score values but it is concerned with on1y one term (i.e. the middle term).

D. *Computing F-Score Threshold Value by Fuzzy Integral of Sugeno*

Despite their limitations, the previously mentioned techniques are standard and widely used for a threshold computation from a set of numerical value. In this study, we investigate the fuzzy integral of Sugeno [12], [13], [14] for threshold value computation.

Let's consider each band of the original image as a spectral feature which has the Improved F-Score Score F_i. For each spectral feature *i* we associate a score value Per_i (called the degree of relevance of the *i* previous spectral features) that resulting from the average of the *i* previous features scores calculated by the formula:

$$Per_i = \frac{1}{i} \sum_{l=1}^{i} F_l \quad (2)$$

We sort the Improved F-Score values in descending order to obtain a new set of organized Improved F-Score values with S_i* denote the improved F-Score values of rank *i*. Each S_i* is associated with the degree of relevance Per_i. Then the fuzzy density function g^i assigned to the spectral feature *i* is calculated by the formula:

$$g^i = \begin{cases} \beta * Per_1 \ when \ i = 1 \\ (1-\beta) * \ Per_i \ when \ i \neq 1 \end{cases} \quad (3)$$

Where β is an equilibrium factor initially fixed at 0.1. A parameter λ, linked to the Fuzzy integral of Sugeno is determined by solving the following equation:

$$\lambda + 1 = \prod_{i=1}^{m}(1 + \lambda g^i) \quad (4)$$

Where m is the number of features in the original image. The resolution of equation (4) is equivalent of solving:

$$\prod_{i=1}^{m}(1 + \lambda g^i) - \lambda - 1 = 0 \quad (5)$$

The first term of equation (5) is either equal to zero or very close to zero, with g^i is the fuzzy density function of the feature i and $\lambda \in [-1,+\infty]$ with $\lambda \neq 0$.

Once the parameter λ is determinated, the fuzzy measure (or fuzzy metric) g^+ is calculated. The fuzzy measure g^+ associates a value $g^+(i)$ to each fuzzy density function g^i where $g^+ : g^i \rightarrow [0,1]$. The fuzzy metric g^+ can be obtained by resolving the equation (6):

$$\begin{cases} g^+(1) = g^1 \\ g^+(i) = g^i + g^+(i-1) + \lambda\, g^i g^+(i-1) \end{cases} \quad (6)$$

Obviously, when $\lambda = 0$, the fuzzy measure g^+ becomes a standard probability measure. The score threshold obtained by the fuzzy integral of Sugeno for the equilibrium factor β equal to 0.1 is calculated by the following formula:

$$S_\beta = Max_{(i=1:m)}[Min(S_i^*, g^+(i)] \quad (7)$$

We recall that the previously obtained threshold score S_β is calculated using a factor β fixed to 0.1. We increment the factor β by 0.05 at each step which allows obtain a new Sugeno threshold score until the factor β reach 1. Then, a final Sugeno threshold score is obtained from the average of the set of Sugeno threshold scores resulting from different values of the factor β.

E. *Computing F-Score Threshold Value by the Fisher Linear Discriminent*

The selection of the most relevant spectral features leads to a binary classification of the initial features set according to *Fi* score value. Then, two classes of features appear logically: the class of very relevant features and the class of less relevant features. So, Fisher Linear Discriminant (FLD) [15] technique can be used to identify these two classes.

Let's consider $T = \{F_1, F_2,..., F_m\}$ the set of scores *Fi* obtained for the m spectral bands of the original image. These spectral features are ranked in decreasing order of their Improved F-Score values. We then obtain the ordered set of performances $OT = \{Fo_1, Fo_2,\ldots, Fo_m\}$. From this new set of performances OT, a Fisher optimal value index F_s is determined according to the Fisher discriminating criterion.

F_s index separates the relevant feature from the irrelevant ones. To find Fisher's optimal index F_s, two values $moy_1(i)$ and $moy_2(i)$, are computed for each feature i $\forall$ $i \in [1,..,m]$, from the set of performances OT:

$$moy_1(i) = \frac{1}{i}\sum_{j=1}^{i} Fo_j \quad (8)$$

$$moy_2(i) = \frac{1}{m-i}\sum_{j=i+1}^{m} Fo_j \quad (9)$$

$moy_1(i)$ and $moy_2(I)$ represent the performances of the two classes of features (relevant and irrelevant) whose elements are respectively located on each side of the separation plan defined by the value i, $\forall i \in [1,..,m]$.

In the next step, two respective variances $Var_1(i)$ and $Var_2(i)$ are calculated $\forall$ $i \in [1,..,m]$ by :

$$Var_1(i) = \sum_{j=1}^{i}\left|Fo_j - moy_1(i)\right|^2 \quad (10)$$

$$Var_2(i) = \sum_{j=i+1}^{m}\left|Fo_j - moy_2(i)\right|^2 \quad (11)$$

Thirdly, the Fisher discriminant index $Fish_i$ is calculated by formula (12) for each feature i, $\forall$ $i \in [1,..,m]$:

$$Fish_i = \frac{|moy_1(i) - mo_{\ 2}(i)|}{|Var_1(i) - Var_1(i)|} \quad (12)$$

The maximum value of the Fisher discriminant index $Fish_i$ allows to determine the Fisher optimal index F_s: by the formula :

$$1 \leq F_s \leq m = \text{Arg}\max_i(Fish_i) \quad (13)$$

The Fisher optimal index F_s corresponds to the index of the feature k of the set OT from which the remained features are not sufficiently relevant for the classification process. Thus the selected spectral features corresponding to the performances of the set $\{Fo_1, Fo_2,\ldots, Fo_k\}$ are used as input of the classification process.

F. *Computing F-Score Threshold Value by the R-Ratio*

A threshold score can be defined by using a set of Ratio R_i [16], $\forall$ $i \in [1,..,m]$ which is computed for each feature i by:

$$R_i = \frac{F_i - ScoreMoy}{ScoreMax - ScoreMi} \quad (14)$$

where :

- *ScoreMoy* is the average of the scores obtained for different spectral features.
- *ScoreMax* is the maximum score *Fi*.
- *ScoreMin* is the minimum score *Fi*.

In this technique, the threshold score corresponds to feature score which has the R_i ratio closest to 1.

An evaluation of these proposed strategies is illustrated and discussed in the next section. The performance

measurement of each threshold calculation strategy is determined by SVM classification accuracy.

III. Experimental Results

In this section we discuss various IFS threshold value strategies used in feature selection process for the spectral image analysis and investigate their classification performance. Classification performances are assessed using classification accuracy measures such as: overall accuracy and kappa coefficient.

The Overall Accuracy (OA) is the percentage of correctly classified pixels.

The Kappa Coefficient is the percentage of agreement, i.e., correctly classified pixels, corrected by the number of agreements that would be expected purely by chance.

The high values of the OA and kappa measures (close to 100%) mean that the classification results are accurate.

To determine the optimal IFS threshold value, two sub-scenes acquired on the Oran city (west of Algeria) by Hyperion sensor on June 2017 (Fig. 1) were classified using SVM. The images have a spatial resolution of 20 *m* and a spectral resolution of 125 bands. The first sub-scene of spatial dimensions 277 × 202 pixels corresponds to the district Hai-El-Marsa which overlooks the port of the Oran city (Fig. 1.a). The second one (Fig. 2.b) of size 275 × 202 pixels is characterized by a strong urban concentration in the north and an agricultural zone in the south.

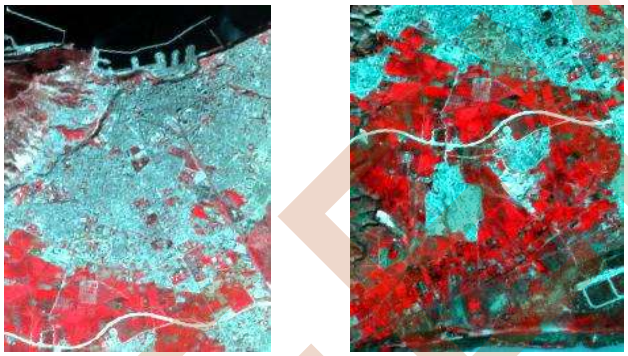

(a) (b)

Figure 1. Hyperspectral sub-scenes displayed in three-band color composite

Classification process of hyperspectral images performs differently under the different selected spectral bands with different IFS threshold values. Four classes of interest are considered for both sub-scenes. Figure 2 shows the corresponding classification maps.

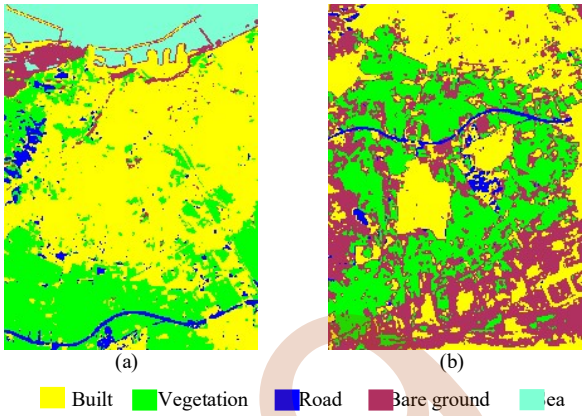

Figure 2. SVM classification maps (a) of the first sub-scene with Fisher thresholding method. (b) of second sub-scene with Sugeno thresholding method

Tables I and II list the accuracy values (Overall Accuracy OA and KAPPA rate) of the classifications, respectively, of both sub-scenes using the six different algorithms of IFS threshold values. The underlined values are the highest accuracies.

TABLE I. Classification Accuracies for the First Sub-Scene using Different IFS Theshold Values for Feature Selection

Method	First Scene		
	Number of preserved bands	*OA (%)*	*KAPPA(%)*
All Bands	125	93.69	91.15
Mean	87	94.09	91.90
Variance	81	94.15	91.97
Median	63	92.93	90.75
Sugeno	79	94.20	92.05
Fisher	76	<u>94.69</u>	<u>92.73</u>
R-Ratio	39	88.51	86.26

TABLE II. Classification Accuracies for the Second Sub-Scene using Different IFS Theshold Values for Feature Selection

Method	Second Scene		
	number of preserved bands	*OA*	*KAPPA*
All Bands	125	98.37	97.26
Mean	91	98.58	97.63
Variance	83	99.16	98.72
Median	63	97.26	96.08
Sugeno	75	<u>99.62</u>	<u>99.36</u>
Fisher	73	99.40	99.00
R-Ratio	42	89.35	88.72

As can be seen from Tables I and II, the combining of Improved F-Score with SVM classifier improves the

classification accuracies. For the first scene, the best feature subset which has highest classification Accuracy is obtained by Fisher Linear Discriminant method. However, for the second scene, the Fuzzy Integral of Sugeno method ensures the selection of the most relevant features image.

Figure 3 and 4 present the comparison of overall accuracy OA and KAPPA rate for the different algorithms of IFS threshold values used to select the optimal set of features for both sub-scenes

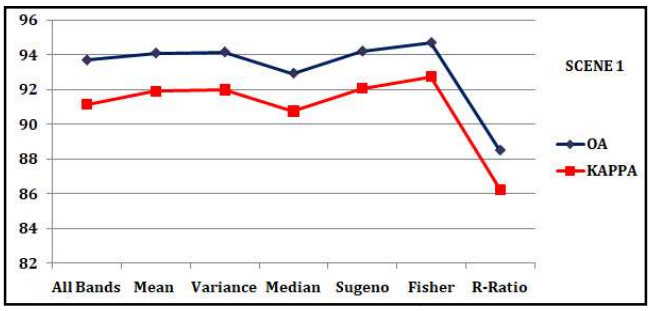

Figure 3. Overall Accuracy "OA" and KAPPA classification rate obtained by the SVM classifier from the first sub-scene

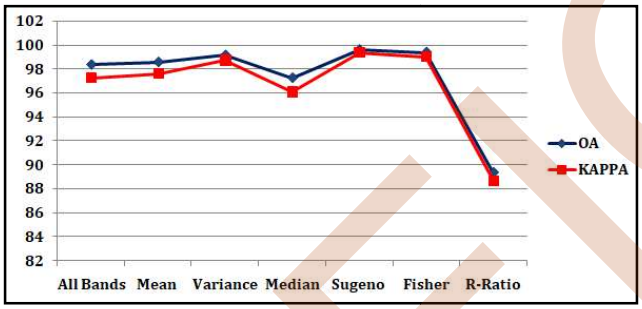

Figure 4. Overall Accuracy "OA" and KAPPA classification rate obtained by the SVM classifier from the second sub-scene

Comparative analysis of overall accuracies of different strategies of IFS threshold values, identified the Fisher and the Sugeno as the best algorithms and the worst accuracy achieved for the median and R-Ratio algorithms for both sub-scenes.

Comparison of different methods used to generate final features subset for classification task, shows that some threshold value computation strategies achieves the best classification accuracy compared to others. It also shows that not all threshold value computation method allow to have significant improvements in a spatial analysis of the image. Someone lead to loss of useful information for the spectral analysis of multivalued data.

This result also indicates a strong relation between the F-score feature selection technique and the classification rate. It demonstrates that the computation of improved F-Score values helps in discriminating the relevant and irrelevant features for classification process.

IV. CONCLUSION

Feature selection is an important issue in hyperspectral images classification because the redundancy of bands restricts the classification accuracy. In this study, Improved F-Score technique was adapted for selecting the set of pertinent bands of the hyperspectral image. Each band score was estimated by an Improved F-Score value. Since feature selection removes bands with lower IFS value, an IFS thresholding step is required. Threshold value is the factors that can be chosen to improve accuracy. Six algorithms for generating IFS threshold values were developed and tested to determine the impact of the IFS on accuracy. They are estimated from the all spectral bands IFS values. Experimental results, on two hyperspecral images acquired by Hyperion sensor, have demonstrated that the Improved F-Score combined with SVM classifier yields accurate hyperspectral image classification and largely depends on the algorithm of IFS threshold value. The six algorithms of IFS thresholding were compared to achieve the highest OA. The accuracy comparison identified Sugeno and Fisher as the optimal techniques of IFS threshold values, since they produced the highest OA (94% and 99%) when only 60% of the previous spectral bands were classified. Ratio technique tended to attenuate OA (88%) for 40 selected spectral bands.

The reported classification results are sensibly comparable for Sugeno and Fisher methods for both sub-scenes. The possible reason of this trivial difference may lie in the fact that for the SVM+IFS method the classification accuracy strongly depends not only on the chosen threshold method but also on the training and test samples used for classification.

This study provides a way for feature selection of hyperspectral images. The method developed has improved the accuracy for different IFS threshold values and is sufficiently robust for reducing multidimensional data of different kinds of images.

REFERENCES

[1] D. A. Landgrebe, Signal theory methods in multispectral remote sensing. Hoboken, New Jersey: Wiley-Interscience, 2003.

[2] David Landgrebe, "Hyperspectral Image Data Analysis as a High Dimensional Signal Processing Problem," Hyperspectral Image Data Analysis as a High Dimensional Signal Processing Problem, January 2002, pp. 17–28, 2002.

[3] P. Hansen, E. Ngai, B. K. Cheung, and N. Mladenovic, "Analysis of Global k-Means, an Incremental Heuristic for Minimum Sum-of-

Squares Clustering," Journal of Classification, vol. 22, no. 2, pp. 287–310, 2005.

[4] Y. Qian, F. Yao, and S. Jia, "Band selection for hyperspectral imagery using affinity propagation," IET Comput. Vis., vol. 3, no. 4, p. 213, 2009.

[5] C.-I. Chang, "Progressive band selection for satellite hyperspectral data compression and transmission," J. Appl. Remote Sens, vol. 4, no. 1, p. 41770, 2010.

[6] C. Cariou, K. Chehdi, and S. Le Moan, "BandClust: An Unsupervised Band Reduction Method for Hyperspectral Remote Sensing," IEEE Geosci. Remote Sensing Lett., vol. 8, no. 3, pp. 565–569, 2011.

[7] C. Kermad and K. Chehdi, "Multi-bands image segmentation: a scalar approach," in 2000 International conference on image processing: Proceedings, September 10-13, 2000, Vancouver Convention & Exposition Centre, Vancouver, British Columbia, Canada, Vancouver, BC, Canada, 2000, pp. 468–471.

[8] M. F. Akay, "Support vector machines combined with feature selection for breast cancer diagnosis," Expert Systems with Applications, vol. 36, no. 2, pp. 3240–3247, 2009.

[9] P. Jaganathan, N. Rajkumar, and R. Kuppuchamy, "A Comparative Study of Improved F-Score with Support Vector Machine and RBF Network for Breast Cancer Classification," IJMLC, pp. 741–745, 2012.

[10] S. Zemmoudj, A. Kemmouche, and Y. Chibani, "Feature selection and classification for urban data using improved F-score with Support Vector Machine," in 2014 6th International Conference of Soft Computing and Pattern Recognition (SoCPaR): 11-14 Aug. 2014, Tunis, Tunisia, Tunis, Tunisia, 2014, pp. 371–375.

[11] J. Xie and C. Wang, "Using support vector machines with a novel hybrid feature selection method for diagnosis of erythemato-squamous diseases," Expert Systems with Applications, vol. 38, no. 5, pp. 5809–5815, 2011.

[12] A. M. P. Canuto and M. C. C. Abreu, "Using Fuzzy, Neural and Fuzzy-Neural Combination Methods in Ensembles with Different Levels of Diversity," in Lecture Notes in Computer Science, Artificial neural networks: ICANN 2007 / 17th international conference, Porto, Portugal, September 9-13, 2007 / proceedings, J. Marques de Sà, L. A. Alexandre, and W. Duch, Eds., Berlin, New York: Springer, 2007, pp. 349–359.

[13] K.-C. Kwak and W. Pedrycz, "Face recognition: A study in information fusion using fuzzy integral," Pattern Recognition Letters, vol. 26, no. 6, pp. 719–733, 2005.

[14] M. Sugeno, "Fuzzy measures and fuzzy integrals: A survey. In: Gupta, Saridis and Gaines (eds.)," Fuzzy Automata and Decision Processes, 1977, pp. 89–102, 1977.

[15] R. A. FISHER, "THE USE OF MULTIPLE MEASUREMENTS IN TAXONOMIC PROBLEMS," Annals of Eugenics, vol. 7, no. 2, pp. 179–188, 1936.

[16] Y.-T. Hwang, "Finding the optimal threshold of a parametric ROC curve under a continuous diagnostic measurement," Revstat Statistical Journal, January 2018, pp. 23–43, 2018.

New aproach in vibration monitoring of bearing faults in induction motor using CSA

Tafinine Farid
Département de génie Electrique
Laboratoire LTII, Faculté de Technologie, Université A.Mira de Bejaia, 06000 Bejaia, Algérie
Bejaia, Algérie
f.tafinine@yahoo.fr

Abstract— A new signal processing technique for developing an On-line bearing fault detection based on Cyclic Spectral Analysis (CSA) is presented in this paper. The exploitation of cyclostationarity has recently been proved extremely fruitful to conceive high accuracy diagnostics tools. Cyclostationarity encompasses a subclass of nonstationary signals which exhibit some cyclical behaviour; it ideally fits the property of many rotating and reciprocating machine vibrations, due to the inherent periodic modulations that these sustain during operation. The traditional spectral analysis is not dedicated for non-stationary signals and for an on-line diagnosis. The proposed technique is tested with different bearing conditions, the results show that this technique is especially useful for non-stationary features extraction, it gives a good basis for an integrated induction motor condition monitor.

I. INTRODUCTION

Asynchronous machines are far more widely used in the industrial world for their simplicity, their robustness and their cost. The importance of detection and diagnosis of faults in machines have expanded considerably due to the increased complexity of plant equipment and high costs associated with failure and shutdown. Faults detection and isolation problems can be solved by different techniques: model based, signal based or knowledge based methods. Faults can be due to electrical or mechanical failures. The most common failure in an asynchronous machine is bearing failure [1].

Vibration analysis techniques were used for the monitoring and diagnosis of huge rotating machines. Different methods were used. Time domain statistical method such as energy monitoring (energy increases as the machine's condition deteriorate), frequency domain method such as spectrum (characteristic frequencies associated with the failure appear in the spectrum), parametric models (the parameters of the model change with the machine's condition). Vibrations can be measured by attaching displacement or velocity transducers, and thus requires direct access to the machine. In recent years much work has been carried out on the investigation of possible fault operations of electrical machines. The usual methods for detection of faults are based on vibration analysis [3-6, 10-11] or on Motor current signature analysis (MCSA) [1- 2, 12-13].

The bearings condition monitoring has received considerable attention for many years [3, 9, 14]. Many methods are available for detecting faults in bearing systems. The majority of these methods assume that faults in the bearings produce impulses [10, 11].

The Fourier analysis may be the most commonly used approach for bearing fault diagnosis. However, it is not appropriate because: first, vibration signal is generally non-stationary [5], and second, this approach cannot be applied for an on-line diagnosis, because the operator must inspect the total vibration signal spectrum in order to detect the frequency of defects.

In this paper, we will present the detection of the outer race defect using Cyclic Spectral Analysis. The results obtained confirm the effectiveness of this method in the detection of the frequency of motor bearing damage.

A non-invasive technique is now proposed. It is very practical and can be implemented at low cost. This paper is organized as follows: Section 2 presents experimental setup and the bearing faults characteristic frequencies. Section 3 reviews the theoretical background of the proposed diagnostic procedure. First we introduce the principles of the spectral domain analysis using Fourier transform. We emphasize on how the relevant information can be extracted from the spectral density using the FFT algorithm. Second, we describe the Cyclic Spectral Analysis and how it can be used for diagnosis by extracting the relevant frequencies characterizing the motor operating mode. Finally, a comparative approach of the proposed diagnostic procedure and several usual vibratory diagnostic methods are presented in section 4. And the conclusions are given in section 5.

II. EXPERIMENTAL SETUP

We have used a motor of 380 V; 50 Hz; 1.1 kW; number of pair poles (P=2). The experiments are realized with several levels of load and speed. Tests are conducted for a healthy bearing then with an outer race fault. The signals are

measured using multiple vibration sensors installed on the induction machine. Note that the all measurements are taken at stationary regime.

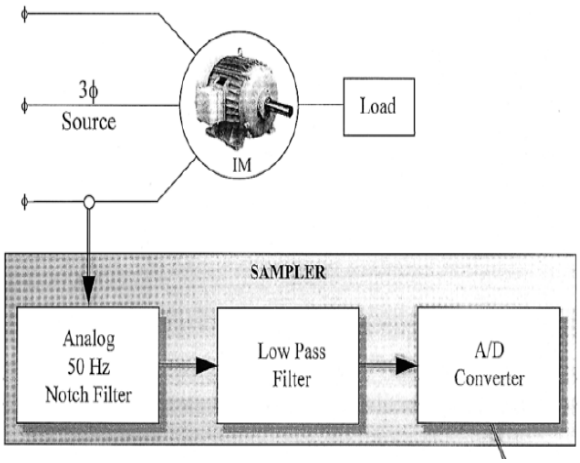

Figure 1. Scheme of the experimental setup

A. *Bearing faillure*

The vibrations frequencies depend: on the rotation speed "f_r", on the geometrical parameters of the bearing (figure 2) and on the type of defects [2, 9]. The vibration frequencies of bearing failure are given in the equations bellow [7, 8]:

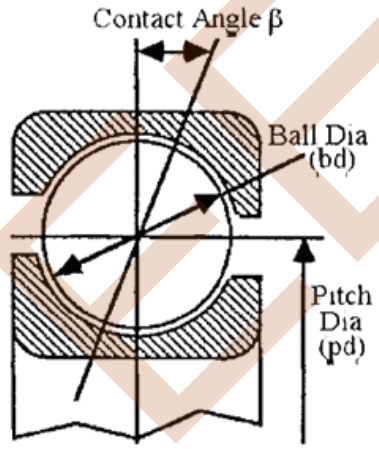

Figure 2. Geometrical parameters of the bearings.

Outer race bearing fault frequency F_0:

$$Fo=\frac{N}{2}\ f_r\left[1-\frac{BD}{PD}\cos\beta\right] \qquad (1)$$

Inner race bearing fault frequency F_i :

$$Fi=\frac{N}{2}\ f_r\left[1+\frac{BD}{PD}\cos\beta\right] \qquad (2)$$

Cage defect frequency F_c:

$$Fc=\frac{1}{2}\ f_r\left[1-\frac{BD}{PD}\cos\beta\right] \qquad (3)$$

Ball defect frequency F_b:

$$Fb=\frac{PD}{2BD}\ f_r\left[1-\left(\frac{BD}{PD}\cos\beta\right)^2\right] \qquad (4)$$

where

« BD » is the ball diameter,
« PD » is the pitch diameter,
« β » is the contact angle of the balls on the race
« N » is the number of balls.

B. *Frequency characteristics of failure*

The Benchmark is equipped with an RS bearing type 6028-2RS. The defect frequency at the speed of 3004 rpm is 4.58 Hz (see table 1).

TABLE I. FREQUENCY CHARACTERISTICS OF THE BEARING TYPE 6028-2RS.

	Frequency (Hz)			
Speed (rpm)	f_c	f_b	f_o	f_i
3004	0.28	5.43	4.58	5.81

III. APPLICATION AND RESULTS

A. *Classical spectral analysis*

The classical method converts the sampled signal to the frequency domain using a FFT (Fast Fourier Transform) algorithm. The generated spectrum includes only the magnitude information about each frequency component. Signal noise that is present in the calculated spectrum is reduced by averaging a predetermined number of generated spectra. The power spectral density is illustrated in the figure 3.

The result shows a periodic modulation of 4.6 Hz (sideband spacing = 4.6 Hz) in the defect machine spectrum. This modulation is due to the outer race defect.

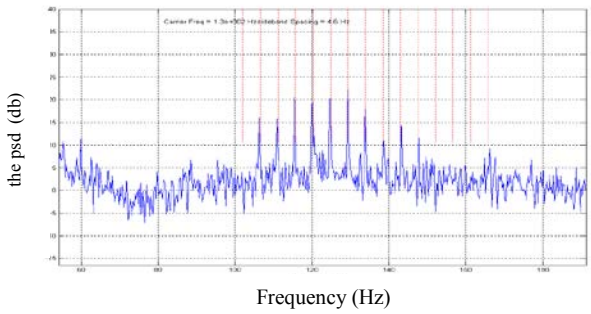

Figure 3. PSD of the vibration signal with outer race defect.

B. *Cyclical spectral analysis(CSA)*

The cyclic power spectrum. $S_x(f;\alpha)$ of signal x(t), is defined as [17], [18]:

$$S_x(f;\alpha)=\lim_{L\to\infty}\frac{1}{L}\mathrm{E}\left\{X_l\left(f+\frac{\alpha}{2}\right)X_L\left(f-\frac{\alpha}{2}\right)^*\right\} \quad (5)$$

where $X_L(f)$ is the Fourier transform of x(t) limited in the interval L.

The definition of the cyclic coherence is [15], [16]:

$$|\gamma_x(f;\alpha)|^2=\frac{|S_x(f;\alpha)|^2}{S_x\left(f+\frac{\alpha}{2}\right)S_x\left(f-\frac{\alpha}{2}\right)} \quad (6)$$

This expression presents a correlation coefficient between two components at frequencies $f+\frac{\alpha}{2}$ and $f-\frac{\alpha}{2}$. It takes values between 0 and 1, where 0 expresses nonlinear correlation, and 1 in the case of a linear relationship between the two components [17].

The diagnostics information can be revealed in the α frequency domain, the magnitude of the cyclic coherence can be used as a measure of the fault severity [19].

Cyclic coherence of the damaged bearings (figure 4) illustrates significant cyclostationary. A fundamental spectral line at $\alpha = 4.5\ Hz$ without sidebands is, according to table 1, the characterization of an outer-race fault. In the cyclic coherence, some bands located within [0; 3] *Hz* might be due to structural resonances that are excited by the impacts of the rolling elements on the faults (ie. F_c, f_r). These observations agree with the frequency band in the power spectral densities in figure 3.

IV. COMPARAISON OF THE TWO ANALYSIS TOOLS

Vibrations produced by faulty rolling-element bearing are essentially random cyclostationary [18]. In order to detect the frequency of defects it is habitual to demodulate the signal in different frequency bands in the total frequency axis. This method is the classical technique in the spectral analysis (PSD). The C*yclic Spectral Analysis(CSA)* can replace this empirical process by a precise methodology to quickly find the frequency of the faults.

The new diagnosis procedure overcomes the disadvantages related to motor parameters dependency. In contrast to the usual vibrations signal spectral analysis, the proposed diagnosis method allows also the ability to extract *quickly* the characteristic frequencies that distinguish the motor operating modes.

The *cyclic coherence* is actually the cyclic spectral quantity that offers the best fault detection tool, it reveals the discrete spectral signature of the fault. Its magnitude serves as a relative measure of the fault severity. These observations have been supported by experimental results.

.

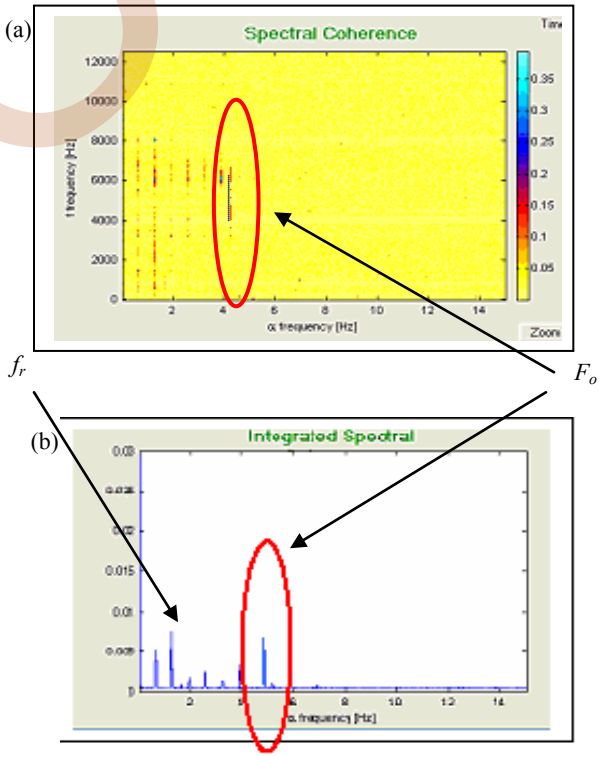

Figure 4. Estimated cyclic spectral coherence (a) and integrated spectral coherence (b) of the vibration signal with an outer-race fault.

V. CONCLUSIONS

This paper has investigated a method for detecting bearing faults using the cyclical spectral analysis. Machine fault features extraction without prior information of the fault type is important for diagnosis and maintenance planning. The Cyclic Spectral Analysis technique is qualified as a parsimonious method for exploring the information in the entire spectrum of the vibrations signal in the cyclic frequency domain. The resulting procedure is fine suitable for an on-line diagnosis, without manual research of the frequency band containing the fault.

ACKNOWLEDGMENT

The author wish to express his gratefulness to the members of the Roberval Laboratory (UTC France), for their support in the experimental setup.

REFERENCES

[1] R.R. Schoen, T. Habetler, F. Karman, R. Bartheld, " Motor Bearing Damage Detection Using Stator Current Monitoring," IEEE Trans. Ind. App. 31, 1274, 1995.

[2] M.E.H. Benbouzid, "A Review of induction Motors signature Analysis as a medium for faults detection," IEEE Trans. Ind. Electron. 47, 984, 2000.

[3] C.S. Burrus, Introduction to Wavelets and Wavelet Transforms a primer. Ed. Prentice Hall; 1998.

[4] Y. Yang, D. Yu, J. Cheng," Y. Yang, D. Yu, J. Cheng, A fault diagnosis approach for roller bearing based on IMF envelope spectrum and SVM," Measurement, Measurement, 40- 943, 2007.

[5] Antonino-Daviu JA, Riera-Guasp M, Roger-Folch J, Molina M. Validation of a New Method for the Diagnosis of Rotor Bar Failures via Wavelet Transform in Industrial Induction Machines. IEEE Transactions on Industry Applications 2006; 42: 990-96.

[6] B. Raison, G. Rostaing, O. Butscher, C.S. Maroni, "Investigations of algorithms for bearing fault detection in induction drives," in Proc. 28th Annual Conference of the Industrial Electronics Society, Sevilla, Spain, 2002.

[7] W.T. Thomson, "A review of on line condition monitoring techniques for squirrel-cage induction motors: Past present and future," in Proc. of the IEEE Symposium on Diagnostics for Electrical Machines Power Electronics and Drives (SDEMPED), Gijon, Spain, 1999.

[8] T.A. Harris, Rolling bearing analysis, (4th Edition); John Wiley & Sons, Inc, New York, USA, 2001.

[9] N.G. Nikolaou, I.A. Antoniadis, "Demodulation of vibration signals generated by defects in rolling element bearings using complex shifted morlet wavelets," Mech. Syst. Sig. Process. 16, 667, 2002.

[10] T.C. Lim, R. Singh, "Vibration transmission through rolling element bearing. Part I: Bearing stiffness formulation," J. Sound vib. 139, 179 1990.

[11] M. Blodt, Condition Monitoring of Mechanical Faults in Variable Speed Induction Motor Drives, Ph.D. Thesis, INP Toulouse, France, 2006.

[12] M. Blodt, M. Chabert, J. Regnier, J. Faucher," , Mechanical load fault detection in induction Motors by stator current time-frequency analysis," IEEE Trans. Ind. App. 42, 1454, 2006.

[13] R. Isermann," Supervision Fault-detection and fault diagnosis methods- An Introduction, Control Engineering Practice," Control Eng. Pract. 5, 639, 1997.

[14] J. Antoni, F. Bonnardot, A. Raad, M. El Badaoui, "Cyclostationary Modelling of Rotating Machine Vibration Signals," Mech. Syst. Sig. Process. 18, 1285, 2004.

[15] R.B. Randall, J. Antoni, S. Chobsaard, "The Relationship between Spectral Correlation and Envelope Analysis for Cyclostationary Machine Signals. Application to Ball Bearing Diagnostics," Mech. Syst. Sig. Process. 15, 945, 2001.

[16] A. Raad, J. Antoni, M. Sidahmed, "Indicators of cyclostationarity: Theory and application to gear fault monitoring," Mech. Syst. Sig. Process. 22, 574, 2008.

[17] A.C. McCormick, A.K. Nandi, "Cyclostationary in Rotating Machine Vibrations, Journal of Sound and Vibration ," J. Sound vib. 12, 225 1998.

[18] C. Capdessus, M. Sidahmed, J.L. Lacoume," Cyclostationary Processes: Application in Gear Faults Early Diagnosis," Mech. Syst. Sig. Process. 14, 371, 2000.

Medical Image Segmentation Using Adaptively Regularized Kernel-based Fuzzy C-Means (ARKFCM)

I. Cherfa[1,2], A. Mekhmoukh[1,2], K. Mokrani[1,2], R. Kasmi[2,3], S. Oukil[1,2], S.S. Ghennam[1,2]

[1]Electrical engineering department
University of Bejaia,
Bejaia, Algeria

[2]Laboratory TII Bejaia
University of Bejaia,
Bejaia, Algeria

[3]Electrical engineering department
University of Bouira
Bouira, Algeria

***Abstract*—Image segmentation is an important step in any automated image analysis system, especially in medical diagnostic aid. Fuzzy C Means (FCM) algorithm is the well-known soft clustering method for the segmentation of Magnetic Resonance (MR) images. However, it is sensitive to noise and does not consider the spatial information in the image. In this work, we are interested in the Adaptively Regularized Kernel-Based Fuzzy C Means (ARKFCM) algorithm, which introduces a regularization parameter to control contextual information and uses kernel function to replace the Euclidean distance metric because of its sensitivity to outliers. Tests on simulated MR images corrupted by different types of noise show the effectiveness of this method in presence of noise.**

I. INTRODUCTION

Medical image segmentation and diagnostic imaging is an invaluable tool in medicine today[1]. To achieve accurate clinical routine, automated and robust medical image computing techniques have become an active research area. Medical image segmentation techniques are specific to the imaging modality used [2]. The clinical tools allowing the observation of the brain area include X-ray CT, Magnetic Resonance Imaging (MRI), tomography, scintigraphy, etc. Among these modalities, MRI is one of the safest methods for producing data with high spatial resolution, and it is also a low risk, non-invasive modality in comparison to other diagnostic imaging techniques [3]. Segmentation is the process of dividing an image into multiple parts. This procedure is made between different tumor tissues (solid tumor, edema and necrosis) and normal brain tissues; Gray Matter (GM), White Matter (WM) and Cerebrospinal Fluid (CSF) [4]. The segmentation of brain MR images helps to detect diseases such as brain tumors, Alzheimer's disease, Parkinson's disease, etc. To study the evolution of the disease, it is necessary to know exactly the changes that have occurred in these images. In literature, different image segmentation techniques are used to segment brain MR images among which edge detection [5], region-growing [5], thresholding [6] and clustering [1] are the most known ones. Clustering methods are the most used for complex data. In clustering, Fuzzy C Means algorithm is the traditional approach used in MR image segmentation [7]. The standard FCM algorithm yields good results in the absence of noise. However, it is very sensitive to noise, since no local spatial information in the image is integrated. Many modification have been made in literature to improve the FCM algorithm and alleviate his limitations such as Spatial Fuzzy C Means (FCM-S)[8], FCM-S1 and FCM-S2 [9], Robust Fuzzy Local Information C Means (FLICM) [10], Adaptively Regularized Kernel Fuzzy C Means (ARKFCM) [11]. This paper is organized as follows; Section 2 is a background of the standard FCM and ARKFCM algorithms. In section 3, we present the results of the segmentation using these methods. Finally, a conclusion and future works are given in Section 4.

II. BACKGROUND

A. *Fuzzy C-Means (FCM) algorithm*

The FCM clustering algorithm was developed by Bezdek [12]. Let X= (x_i) an image, i= (1,2,…n) where x_i are the pixels of an image X and n is the total number of pixels to classify into K classes. The K classes are represented by a vector of the centers of the classes V = (v_1, v_2, v_3, …v_k) where v_k is the center of the class k. The FCM algorithm minimizes the objective function[12]:

$$J_m(U,v) = \sum_{i=1}^{N}\sum_{k=1}^{c}(\mu_{ik})^m \|x_i - v_k\|_A^2 \qquad (1)$$

Where:

μ_{ik} The membership function matrix;

x_i The gray value of the ith pixel;

c The number of clusters;

m The degree of fuzziness m ≥ 1;

$\|x_i - v_k\|$ The Euclidean metric distance between the pixel x_i and the cluster center v_k.

The membership degree u_{ik} should be constrained to the following:

$$\sum_{i=1}^{N} \mu_{ik} > 0; \quad \mu_{ik} \in [0,1]; \quad \sum_{i=1}^{N} \mu_{ik} = 1 \text{ for all k} \qquad (2)$$

The membership degrees are given by:

$$\mu_{ik} = \frac{1}{\sum_{j=1}^{K} \left(\frac{d(x_i, v_j)}{d(x_j, v_k)}\right)^{2/(m-1)}} \qquad (3)$$

The cluster centers are:

$$v_k = \frac{\sum_{i=1}^{N} u_{ik}^{m} * x_i}{\sum_{i=1}^{N} u_{ik}^{m}} \qquad (4)$$

The FCM algorithm is very sensitive to noise because it does not include any local information. It is also based on the Euclidean metric distance because of its simplicity, so it supposed that the data classes have the same super spherical shapes, which is not true. To overcome this problem, many modifications of the original FCM algorithm were proposed in the literature such as ARKFCM algorithm.

B. Adaptively Regularized Kernel Fuzzy C Means (ARKFCM) clustering algorithm

In ARKFCM, a regularizing parameter is introduced and Gaussian radial basis function (GRBF) is adopted to enhance segmentation and preserve image details [11]. The Euclidean distance terms $\|x_k - v_i\|$ is replaced with;

$$\|\emptyset(x_k) - \emptyset(v_i)\| = K(x_k, x_k) + K(v_j, v_j) - 2K(x_k, v_j) \qquad (5)$$

Where $\emptyset$ a nonlinear function and K the GRBF Kernel.

$$K(x_k, v_j) = \exp\left(\frac{\|x_k - v_j\|^2}{2\sigma}\right) \qquad (6)$$

The ARKFCM objective function becomes

$$J = 2\left[\sum_{k=1}^{N}\sum_{j=1}^{C} \mu_{kj}^{m}\left(1 - K(x_k, v_j)\right) + \sum_{k=1}^{N}\sum_{j=1}^{C} \varphi_k u_{kj}^{m}\left(1 - K(\overline{x_k}, v_j)\right)\right] \qquad (7)$$

The membership degrees are then

$$\mu_{ki} = \frac{\left((1 - K(x_k, v_j)) + \varphi_k (1 - K(\overline{x_k}, v_j))\right)^{-1/(m-1)}}{\sum_{i=1}^{C}\left((1 - K(x_k, v_i)) + \varphi_k (1 - K(\overline{x_k}, v_i))\right)^{-1/(m-1)}} \qquad (8)$$

The cluster centers are

$$v_j = \frac{\sum_{k=1}^{N} u_{kj}^{m}\left(K(x_k, v_j) x_k + \varphi_k K(\overline{x_k}, v_j) x_k\right)}{\sum_{k=1}^{N} u_{kj}^{m}\left(K(x_k, v_j) + \varphi_k K(\overline{x_k}, v_j)\right)} \qquad (9)$$

III. DATA AND MATERIALS

We used in this work simulated brain MR images from the Brain Web database (a database put online by the McConnel Brain Imaging Center of the Montreal Neurological Institute at McGill University). We used T1-weigthed images of dimension (217 x 181) with different types of noise. The different tests are implemented in MATLB version 2013.

IV. RESULTS AND DISCUSSION

In this section, the results of the ARKFCM algorithm are presented and compared to the FCM algorithm. Figs. 1-3 show the results of the segmentation using the FCM and ARKFCM algorithm for noisy images.

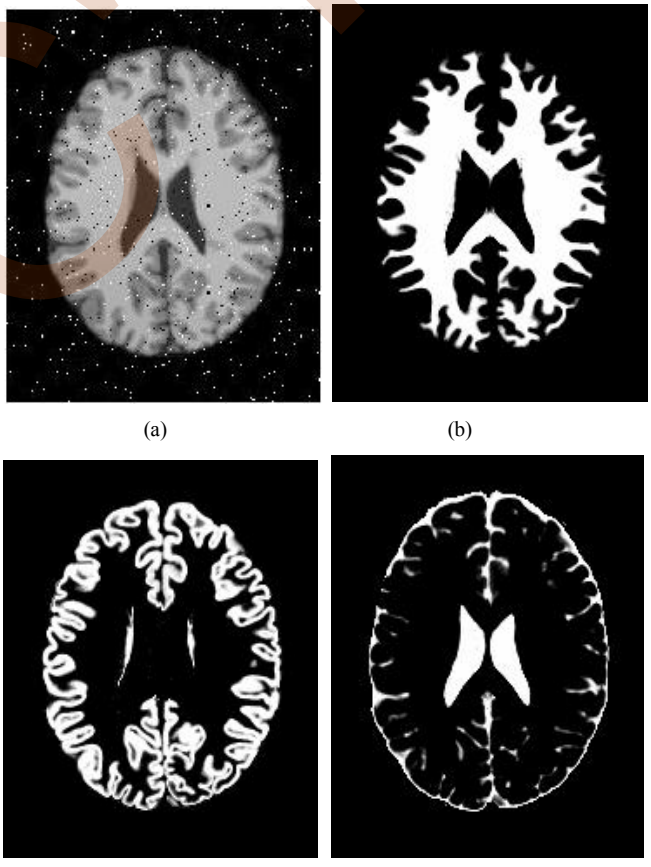

(a) (b)

(c) (d)

Figure 1. (a) Original image, (b) Ground truth of WM, (c) Ground truth of GM, (d) Ground truth of CSF.

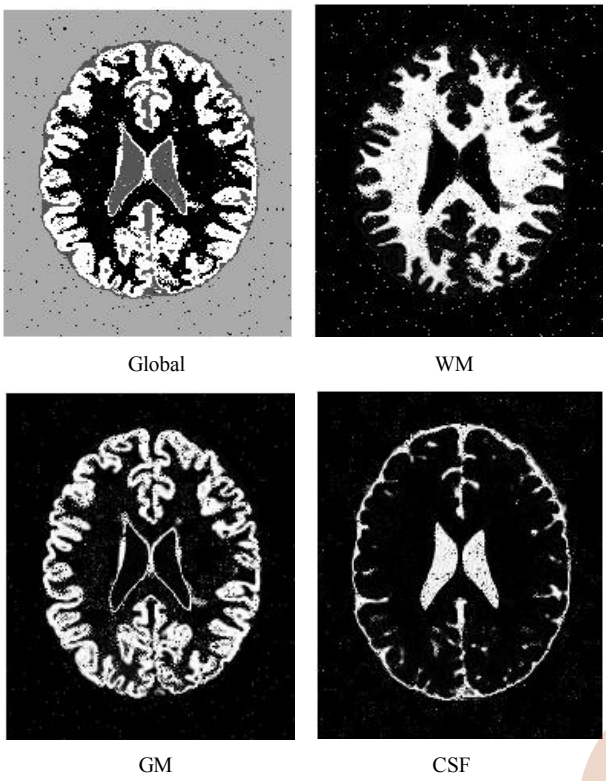

Figure 2. Results of segmentation using FCM algorithm for simulated MR brain image.

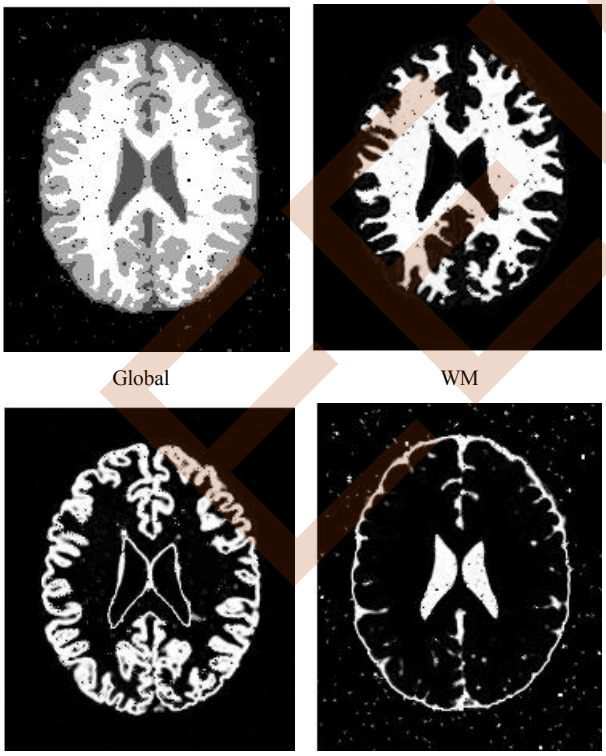

Figure 3. Results of segmentation using ARKFCM algorithm for simulated MR brain image.

A. Quantitative evaluation using ground truth

From the figures, we can see clearly that ARKFCM gives better results. Artifacts are still present, but it outperforms the FCM algorithms. For the evaluation of the segmentation results, a quantitative evaluation approach is used. A comparison is made between pixels of the resulting image and pixels of the ground truth. The following measures are usually used: Dice coefficient, Jaccard coefficient [13].

$$Dice = \frac{2|R_t \cap R_g|}{|R_t| + |R_g|} \quad ; \quad Jaccard = \frac{R_t \cap R_g}{R_t \cup R_g} \tag{10}$$

The quantitative comparison illustrated in Table.1 shows that ARKFCM outperforms FCM algorithm in the presence of noise.

B. Quantitative evaluation using validity functions

We use for this test, the 96th slice of normal T1-weighted simulated brain image Fig.4 corrupted with different types of noise: salt & pepper (2% noise level), Gaussian noise (variance = 0.01) and uniform noise (variance = 0.1). For these images, ground truth is not available to compare the results of different algorithm; a similarity measure other than Dice index should be used. To evaluate the performance of the segmentation, we use partition coefficient Vpc and partition entropy Vpe [14, 15]. A best clustering is achieved if the value Vpe is minimal or Vpc is maximal.

These functions are defined as follows

$$Vpc = \frac{1}{n}\sum_{i=1}^{c}\sum_{j=1}^{n} u_{ij}^2 \tag{11}$$

$$Vpe = \frac{1}{n}\sum_{i=1}^{c}\sum_{j=1}^{n} u_{ij}\log(u_{ij}) \tag{12}$$

Evaluation results are illustrated in Figs 5-7. Table II. Shows that Vpc is maximal and Vpe is minimal for the ARKFCM algorithm for the three types of noise. So, ARKCM outperforms and gives better results than FCM.

TABLE I. RESULTS OF QUANTITATIVE EVALUATION

Validity	**Dice coefficient**			**Vpc**	**Vpe**
Tissues	**WM**	**GM**	**CSF**		
FCM	0.9517	0.9003	0.9166	0.9071	0.2669
ARKFCM	0.9639	0.9074	0.8959	0.9155	0.2447

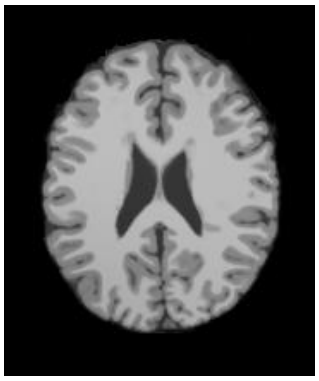

Figure 4. Original image, slice number 96 of normal T1-weighted simulated brain image.

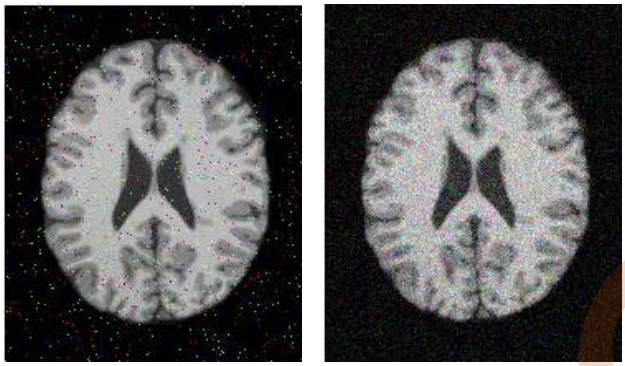

(a) (b)

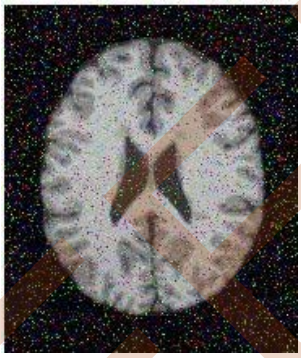

(c)

Figure 5. Noised images: (a) salt & pepper, (b) Gaussian, (c) uniform

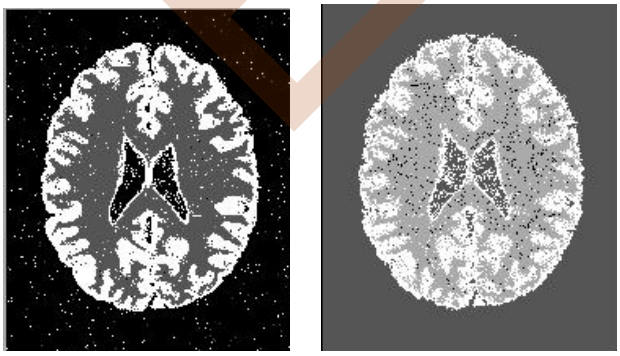

(a) (b)

(c)

Figure 6. Fuzzy C Means FCM segmentation: (a) salt & pepper, (b) Gaussian, (c) uniform

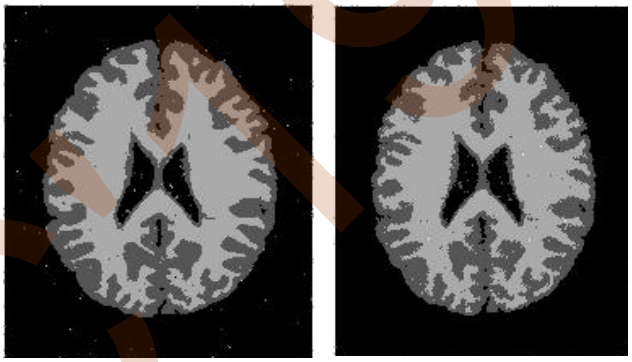

(a) (b)

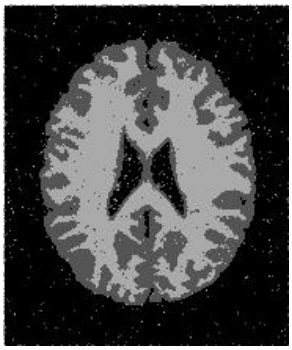

(c)

Figure 7. Adaptively Regularized Kernel-based Fuzzy C Means segmentation ARKFCM: (a) salt & pepper, (b) Gaussian, (c) uniform.

CONCLUSION

The segmentation of brain MR images is a challenging step in medical image analysis. Many techniques have been developed to perform brain image segmentation. However, not all techniques produce a high accuracy rate. In this paper, we have mentioned the ARKFCM algorithm. We showed that this algorithm is effective for brain image segmentation in presence of different types of noise compared with the standard approach. Tests offer quantitative evaluation of the segmentation results using entropy coefficient,

TABLE II. RESULTS EVALUATION FOR THE CORRUPTED IMAGES

Validity function	**Vpc**			**Vpe**		
Type of noise	**Salt & pepper**	**Gaussian**	**Uniform**	**Salt & pepper**	**Gaussian**	**Uniform**
FCM	0.9591	0.9501	0.9422	0.1161	0.1421	0.1627
ARKFCM	**0.9631**	**0.9630**	**0.9536**	**0.1069**	**0.1063**	**0.1342**

partition coefficient and Dice index. But it has some shortcomings. The one is that it chooses centers initialization randomly so the number of iteration can increase. Further work is addressed to optimize the choice of these centers by the use of metaheuristics and embedding level set technique into the clustering in order to achieve more robust segmentation results.

REFERENCES

[1] D. L. Pham, C. Xu, and J. L. Prince, "Current methods in medical image segmentation," *Annual review of biomedical engineering,* vol. 2, pp. 315-337, 2000.

[2] N. Dey and A. S. Ashour, "Chapter 1 - Computing in Medical Image Analysis," in *Soft Computing Based Medical Image Analysis*, ed: Academic Press, 2018, pp. 3-11.

[3] L. Caponetti, G. Castellano, and V. Corsini, "MR Brain Image Segmentation: A Framework to Compare Different Clustering Techniques," *Information,* vol. 8, p. 138, 2017.

[4] P. Soni and V. Chaurasia, "MRI Segmentation for Computer-Aided Diagnosis of Brain Tumor: A Review," in *Machine Intelligence and Signal Analysis*, ed: Springer, 2019, pp. 375-385.

[5] J. Xuan, T. Adali, and Y. Wang, "Segmentation of magnetic resonance brain image: integrating region growing and edge detection," in *Proceedings., International Conference on Image Processing*, 1995, pp. 544-547.

[6] H. Suzuki and J.-i. Toriwaki, "Automatic segmentation of head MRI images by knowledge guided thresholding," *Computerized medical imaging and graphics,* vol. 15, pp. 233-240, 1991.

[7] C. Li, D. B. Goldgof, and L. O. Hall, "Knowledge-based classification and tissue labeling of MR images of human brain," *IEEE transactions on Medical Imaging,* vol. 12, pp. 740-750, 1993.

[8] M. N. Ahmed, S. M. Yamany, N. Mohamed, A. A. Farag, and T. Moriarty, "A modified fuzzy c-means algorithm for bias field estimation and segmentation of MRI data," *IEEE transactions on Medical Imaging,* vol. 21, pp. 193-199, 2002.

[9] S. Chen and D. Zhang, "Robust image segmentation using FCM with spatial constraints based on new kernel-induced distance measure," *IEEE Transactions on Systems, Man, and Cybernetics, Part B (Cybernetics),* vol. 34, pp. 1907-1916, 2004.

[10] S. Krinidis and V. Chatzis, "A robust fuzzy local information C-means clustering algorithm," *IEEE transactions on image processing,* vol. 19, pp. 1328-1337, 2010.

[11] A. Elazab, C. Wang, F. Jia, J. Wu, G. Li, and Q. Hu, "Segmentation of brain tissues from magnetic resonance images using adaptively regularized kernel-based fuzzy-means clustering," *Computational and mathematical methods in medicine,* vol. 2015, 2015.

[12] J. C. Bezdek, R. Ehrlich, and W. Full, "FCM: The fuzzy c-means clustering algorithm," *Computers & Geosciences,* vol. 10, pp. 191-203, 1984/01/01/ 1984.

[13] V. Thada and V. Jaglan, "Comparison of jaccard, dice, cosine similarity coefficient to find best fitness value for web retrieved documents using genetic algorithm," *International Journal of Innovations in Engineering and Technology,* vol. 2, pp. 202-205, 2013.

[14] X. L. Xie and G. Beni, "A validity measure for fuzzy clustering," *IEEE Transactions on Pattern Analysis & Machine Intelligence,* pp. 841-847, 1991.

[15] M. R. Rezaee, B. P. Lelieveldt, and J. H. Reiber, "A new cluster validity index for the fuzzy c-mean," *Pattern recognition letters,* vol. 19, pp. 237-246, 1998.

An Intelligent Edge Linking Approach using Ants Routing

Karima BENHAMZA
LabSTIC, University 08 mai 45,
BP 401, Guelma, Algeria
Benhamza.Karima@univ-guelma.dz

Hamid SERIDI
LabSTIC, University 08 mai 45,
BP 401, Guelma, Algeria
Seridi.Hamid@univ-guelma.dz

***Abstract*— In this paper, the authors propose to enhance edge detectors results with a new variant of Ant Colony optimization (ACO) algorithm. From edge map, endpoints are extracted and used as starting pixels for ants movement. Using an intelligent ants routing mechanism, the missing edges are retraced via the pheromone traces. Obtained results are good compared to conventional Canny edge detector and affirm method's ability to recover most of broken edges.**

***Keywords*— Edge detector; endpoints; ACO; Edge linking.**

I. INTRODUCTION

In order to locate the object and extract its shape information, object's contour must be first extracted based on edge segmentation techniques. Several methods have been developed and used in various applications such as object recognition, segmentation, stereo analysis, feature extraction and image interpretation [1–4]. Oskoei and al. [5] have classified them in ten categories; from classical methods to contextual methods.

The edge detection principle is to identify areas' images which large change in intensity occurs. However, achieving an effective detection tool is a difficult target in segmentation applications because the input image is often affected by noise and the objects that define the scene have low contrast around their borders. Thus, most methods detect irrelevant and small edges, causing broken edges and hindering a good image interpretation.

Various edge linking techniques have been proposed to obtain closed objects contours, such as adaptive morphological methods, cost-based methods and ant-based methods. General principle is to find gaps then linking between endpoints. In this context, this paper introduces a new ACO variant is applied to restore true broken image edges. The rest of this article is organized as follows. Section 2 exposes most significant edge linking works. Section 3 provides details about the proposed method. Experimental results are discussed in Section 4. Finally, conclusion is given in Section 5.

II. RELATED WORKS

In Farag and Delp works [6], authors proposed a sequential search method. They consider edge linking as a graph search problem created using gradient information of each edges points. However, this method required adjusting many image-dependent parameters.

Zhu and al. [7] proposed to model the edge map as a potential force field. They used a directional potential function to guide edge linking. This method can restore small edges between broken fragments successfully, but produces unacceptable results when the image is noisy and edge gaps are significant.

Ghita and Whelan [8] specified a cost function with labeling scheme which assigns the directionality of the edge terminators based only on local knowledge. F.Y. Shih and S. Cheng [9] proposed an adaptive mathematical morphology edge linking. Broken edges are extended along their slope directions by using the adaptive dilation operation with the suitable sized elliptical structuring elements. However, this algorithm cannot be applied without a priori edge map information.

A. D. Sappa and B. X. Vintimilla [10] present a technique to generate a closed-contour representation based on global and local schemes . The global scheme computes an initial representation by connecting edge points minimizing a global measure based on spatial information. The local scheme generates closed contours by using a local cost function that takes into account both spatial and topological information. However, This approach can be used only with small gaps.

Guan Tao and al. [11] presented a Partial Differential Equation (PDE) based method to link edge points. An ending points restrained energy function is proposed to derive ending points restrained Gradient Vector Flow (ERGVF) field. Thus, the new ERGVF field can diffuse the gradient vectors in the continuous edge regions of the edge map including the broken edge regions. The method offers good performance and can recover the objects' original shapes, especially the corners.

Bastan, Muhammet and al. [12] introduced an edge linking framework based on open active contour models to mitigate the problem of broken edges. Authors exploit the local cues provided by edges and grow them under the influence of gradient vector flow to recover the missing edges. However, proposed framework is not suitable for textured images and may produce spurious edges in images with fine edge details.

D.-S. Lu and C.-C. Chen [13] proposed an ant colony optimization method to compensate broken edges. This proposed procedure adopts four moving policies to reduce the computation load. Thus, linking edges as amount of pheromone are achieved after finite iterations.

Benhamza and al. [14,15] proposed an adaptive edge detection method based on ACO. Ants in movement create a pheromone graph, which denotes edge map. Further behaviours were added in response to local stimuli. The ant can self-reproduce and lead its progenitors in appropriate directions to enhance research. Ant can die if it exceeds a specific age and thus eliminate an ineffective search.

Besides, A. Jevtic [16] uses ant colony search method that connect pairs of endpoints. A fitness function was proposed to evaluate the found segments. It depends on two variables: the pixels grayscale visibility and the edge-segment length.

M. Davoodianidaliki and A. Abedini [17] proposed an adjusted ACO algorithm using traditional edge detectors as initial ant pheromone and distribution matrixes. Image size reduction is introduced to decrease noise. Several parameters (diameter and travelled path) are converted into rules to compute the pheromone final update value.

The research in edge detection field needs more contributions. This article presents an edge map improvement based on the ACO algorithm.

III. PROPOSED APPROACH

Proposed approach uses a new variant of Ant Colony Optimization algorithm (ACO). Important improvements is introduced to diversifying edges searches performed by ants and allowed extracting global structure of the true edges [18].

The first step consists in detecting extremities points (endpoints) of the binary image obtained after application edge detector. Extracted endpoints are used as starting pixels for ants' routing process. The missing pixels edges are iteratively retraced through the movements of ants depositing pheromone trails.

III.1. Endpoints detection:

This stage consists in detecting extremities points (endpoints) of the binary image obtained after application of adaptive Canny filter. Edge pixel with only one 8-connected neighbor pixel is marked as an ending point (valid endpoints are shown in Fig.3). Its direction is labeled according to its 8-connected neighbor pixel's position.

Eight directions are defined: North (N), East (E), West (W), South (S), Northeast (NE), Northwest (NW), Southeast (SE) , and Southwest (SW).

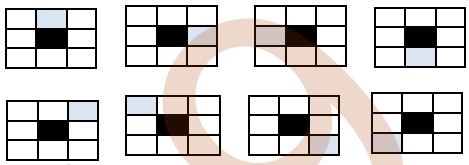

Fig. 3. Endpoints Detection

III.2. Gradient edge map

Additionally, the gradient magnitude map is computed by comparing the horizontal and vertical gradients at each pixel. Resulted gradient map is then thresholded to eliminate non-edge areas. This is achieved by applying the Canny low threshold.

III.3. Ants routing process

The proposed Ants routing process includes the following steps:

a. Initialization: The number of ants is equal the number of endpoints previously detected. To attract ant to move inside the edge area toward, initial pheromone trail matrix is set at each pixel as follows:

$$\tau_{i,j}^{0} = \frac{V_G(i,j)}{V_{Gmax}} \qquad (1)$$

V_{Gmax} is the maximum gradient magnitude variation and serves as a normalization factor. $V_G(i,j)$ is given for each pixel at (i,j) by the following formula:

$$V_G(i,j) = \max \begin{bmatrix} |G_{i-1,j-1} - G_{i+1,j+1}|, |G_{i-1,j} - G_{i+1,j}| \\ |G_{i-1,j+1} - G_{i+1,j-1}|, |G_{i,j-1} - G_{i,j+1}| \end{bmatrix} \qquad (2)$$

Where $G_{i,j}$ is the gradient magnitude value of the pixel(i,j).

b. **Pixel transition rule**: The probability for ant's movement from one pixel to another is given by probability transition matrix. So, during the nth construction step, by:

$$p^{(n)}_{(l,m),(i,j)} = \frac{(\tau^{(n-1)}_{i,j})^{\alpha} \ (\eta_{i,j})^{\beta}}{\sum_{(i,j)\in\Omega_{(l,m)}}(\tau^{(n-1)}_{i,j})^{\alpha} \ \left(\eta_{i,j}\right)^{\beta}} \quad (3)$$

$\tau^{(n-1)}_{i,j}$ defines pheromone information value of the arc connecting the node i to the node j, ηi,j is the heuristic information for pixel (x,y) of node (i,j) and Ω(l,m) is the neighborhood nodes of the node (l,m).

The parameters α and β are two constant characterizing the influence of the pheromone matrix and the heuristic matrix, respectively.

c. **Pheromone update rule**: Each time an ant visits a pixel, it performs a local pheromone update according (Eq.4).

$$\tau_{ij}{}^{n} = (1-\psi).\tau^{n-1}_{ij} + \psi.\tau^{0}_{ij} \quad (4)$$

where $\psi \in (0,1]$ is the pheromone decay coefficient used to diversify ants search. After ants movement, the pheromone is globally updated using (eq.5):

$$\tau^{n} = \begin{cases} (1-\rho).\tau^{n-1} + \rho.\Delta\tau^{k} \ \text{if } (i,j)\text{best tour}, \\ \tau^{n-1} \ \text{otherwise} \end{cases} \quad (5)$$

where $\rho \in (0,1]$ is the evaporation constant. ρ decreases the pheromone value and prevents premature convergence to sub-optimal solution. Δτk is the pheromone amount deposited by the ant.

d. **Stopping criterion**: The steps a to c are repeated in a loop. Execution is stopped when the maximum number of iterations is reached.

IV. Performance Evaluation

The proposed method is evaluated on different images: Cameraman, Peppers, Lena and Fruits.

Figure 1 shows the resulting edges maps after application of Canny operator. Proposed method offers better connected edges map compared to Canny edge detector.

In fact, achieving an effective edge detection tool with medical images is a difficult target because they are often affected by the noise and the objects have low contrast around their borders. Thus, most existing methods detect irrelevant and small edges. The proposed edge linking approach using an ant colony routing proves to be robust and adapts to the changes by generating a good distribution of true edges.

a b c

Fig. 1. Comparative results
a. *Original image* ***b.*** *Canny edge detector*
c. *Proposed method*

Figure 2 shows the algorithm convergence evolution curve for each tested image. It clearly indicates the large and significant number of edge pixels added in the smart routing step based on the processed pixels.

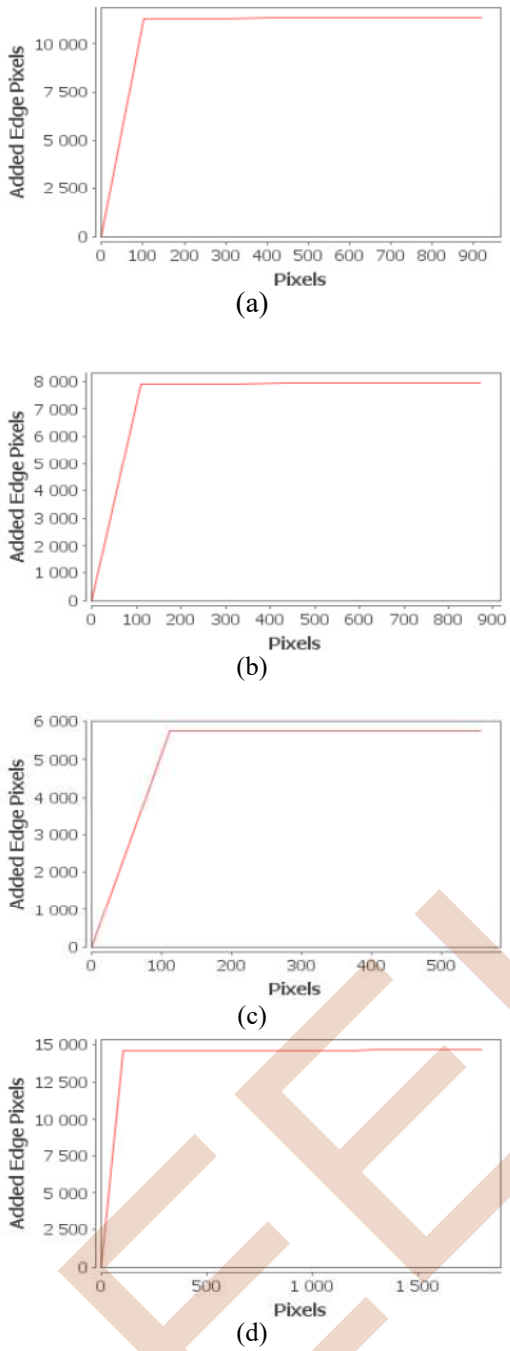

Fig.2. Algorithm Convergence Evolution
a) Cameraman, (b)Peppers, (c) Lena, (d) Fruits

The performance of the proposed method is also evaluated based on the accuracy in edge detection and the useful information obtained in the form of meaningful edges. Shannon [19] offered a measure of the amount of information in an image using an entropy function.

A higher entropy value denotes a better performance of segmentation method. The information content of the image is evaluated using the Shannon's entropy function given by the following equation:

$$H(I) = -\sum_{i=0}^{n} p_i \log p_i \quad (6)$$

Where, I represent the image whose entropy is to be measured. pi is the frequency of pixels with intensity i.

éTable 1 shows the entropy values of different test images. It is observed that the proposed method yields higher entropy as compared to Conventional Canny edge operator. The developed method offers better segmentation compared to the conventional Canny edge detector and allows to retrieve most of missed pixels for all tested images.

Table 1. Entropy values

Images\Methods	Canny	Proposed method
Lena	0.8846	**0.9189**
Peppers	0.7895	**0.8917**
Cameraman	0.8629	**0.8876**
Fruits	0.7357	**0.7436**

V. CONCLUSION

In this paper, an edge linking approach using ants colony routing is proposed to improve edge detector results. This approach is tested on different images. Visual results confirm an effective edge detection with correct edge points.

Qualitative results of the proposed method are validated using Shannon's Entropy function compared to Canny edge detector.

These results prove good edge detection of medical images. Indeed, the proposed method gives an improved solution to edge detection problem and reduce significantly broken edges even in noisy images.

REFERENCES

[1] Sonka, M., Hlavac, V., & Boyle, R. Image processing, analysis, and machine vision, Cengage Learning, 2014.

[2] Franklin, S. W., & Rajan, S. E. Diagnosis of diabetic retinopathy by employing image processing technique to detect exudates in retinal images. IET Image processing, 8(10), 601-609. 2014.

[3] Lei, T., Fan, Y., & Wang, Y. Colour edge detection based on the fusion of hue component and principal component analysis. IET Image Processing, 8(1), 44-55. 2014.

[4] Li, Y., Wang, S., Tian, Q., & Ding, X. A survey of recent advances in visual feature detection. Neurocomputing, 149, 736-751, 2015.

[5] Oskoei, M.A. and Hu, H., A survey on edge detection methods. Technical Report: CES-506. University of Essex, Colchester, 2010.

[6] Farag A. A. and Delp E. J., Edge linking by sequential search, Pattern Recognition, Vol. 28, pp. 611-633, 1995.

[7] Zhu O., Pay M., and Riordan V., Edge linking by a directional potential function (DPF), Image and Vision Computing, Vol. 14pp. 59-70, 1996.

[8] Ghita O. and Whelan P. F., Computational approach for edge linking, Journal of Electronic Imaging, Vol. 11, pp. 479-485, 2002.

[9] Shih F.Y. and Cheng S., Adaptive mathematical morphology for edge linking", Information Sciences Informatics and Computer Science: An International Journal, v.167 n.1-4, p.9-21, 2004.

[10] Sappa A. D. and Vintimilla B. X., Cost-based closed-contour representations, Journal of Electronic Imaging, Vol. 16, pp. 1-9, 2007.

[11] Guan, Tao, Zhou, Dongxiang, Peng, Keju, et al. A Novel Contour Closure Method using Ending Point Restrained Gradient Vector Flow Field. J. Inf. Sci. Eng., vol. 31, no 1, p. 43-58, 2015.

[12] Bastan, Muhammet, Bukhari, Syed Saqib, et Breuel, Thomas. Active Canny: edge detection and recovery with open active contour models. IET Image Processing, vol. 11, no 12, p. 1325-1332, 2017.

[13] Lu D.-S. and Chen C.-C., Edge detection improvement by ant colony optimization, Pattern Recognition Letters, Volume 29, Issue 4, Pages 416-425, ISSN 0167-8655, 1 March 2008.

[14] Benhamza, K., Merabti, H. and Seridi, H., Adaptive edge detection using ant colony. In: Systems, Signal Processing and their Applications (WoSSPA), 2013 8th International Workshop on. IEEE, p. 197-202, 2013.

[15] Benhamza K, Seridi H. Improvement on Image Edge Detection Using a Novel Variant of the Ant Colony System. Journal of Circuits, Systems and Computers. 2019 May 23;28(05):1950080.

[16] Jevtic A. and Li B., Ant Algorithms for Adaptive Edge Detection, open access chapter distributed under the terms of the Creative Commons Attribution License, august 2012.

[17] Davoodianidaliki M., Abedini AS. and Hankayi M., Adaptive edge detection using adjusted ant colony optimization, International Archives of the Photogrammetry, Remote Sensing and Spatial Information Sciences, Volume XL-1/W3, 2013, pp.123-126, SMPR 2013, 5-8 October 2013.

[18] Benhamza, K. and Seridi, H. Canny edge detector improvement using an intelligent ants routing. Evolving Systems, pp.1-10, 2019. https://doi.org/10.1007/s12530-019-09299-0

[19] Shannon, C. E., A mathematical theory of communication, Bell System Technical Journal. vol. 27, pp. 379–423, 1948.

Application of subMarkov random walk segmentation method to apples of type Kanzi and Pink Lady

Fatah Bouchebbah
LIMED Laboratory
Faculty of Exact Sciences
University of Bejaia
06000 Bejaia, Algeria
Email: fatah.bouchebbah@gmail.com

Hachem Slimani
LIMED Laboratory
Faculty of Exact Sciences
University of Bejaia
06000 Bejaia, Algeria
Email: haslimani@gmail.com

Hanane Boutrid
Department of Computer Science
Faculty of Exact Sciences
University of Bejaia
06000 Bejaia, Algeria
Email: boutrid.ha@gmail.com

Asma Ghilassi
LIMED Laboratory
Faculty of Exact Sciences
University of Bejaia
06000 Bejaia, Algeria
Email: asmaghilassi@gmail.com

***Abstract*— Image processing and analysis techniques are essential for modern agriculture. In this paper, we have interest in the segmentation of color images containing apple fruits. Specifically, the aim of this work is to investigate the applicability of a new graph-based semi-automatic image segmentation method, proposed by Dong et al. (2016) and named subMarkov Random Walk (subRW), to the segmentation of images containing a type of apples called Kanzi and another type of the same fruit called Pink Lady. The method essentially involves the concept of graphs and the principle of the random walk method. Moreover, we have implemented subRW in MATLAB 2014 version. Then, we have tested it on a set of real images, that have been taken from the acfr-multifruit dataset (2016), which are characterized with variable lighting conditions. Furthermore, for the purpose of subRW's accuracy estimation, we have compared its yielded results to the ones of two recent methods which address the same issue, as well as to those of the well-known level set method. The comparison results have been found favorable to subRW and have shown its accuracy comparing to the concurrent methods.**

***Keywords*—Image segmentation, Graph, Random walk, Apple of type Kanzi, Apple of type Pink Lady.**

I. Introduction

According to the *Food and Agriculture Organization (FAO)* [2], sixty nine million tonnes of fresh apple fruits were produced worldwide in 2015. These statistics rank apple as the third most produced fruit in the world after citrus fruits and bananas. Apples are edible fruits having a variant astringent property depending on the variety. Furthermore, they are considered as a public health and an economic factor for producers because of their high demand in the market. Thus, the apple is today the most cultivated fruit and presents a great varietal diversity.

In this paper, we restrict our interest to two types of apples: *Kanzi* type apple, which is a subdivision of Malus Domestica and a cross between the two types of apples *Gala* and *Braeburn*, and *Pink Lady* type apple which is actually a trademark of the variety *Cripps Pink*. Due to its high nutritional values and remarkable presence in the market, this fruit has been the subject of several research works in the literature, particularly by the computer vision community which has expressed interest in developing approaches to analyze and process images containing apples.

Nowadays, computer vision is one of the most important technologies for the domain of modern agriculture and has been widely used for inspection of the quality of agricultural and food products. The purpose of such a technology in agriculture is the contribution in developing high-tech machines which are able to replace or assist humans in traditional and manual operations that are labor intensive, slow and prone to error as affirmed by Mizushima and Lu [11]. Image segmentation is a fundamental and crucial computer vision technique, which aims to separate a region of interest (ROI) of an image from its background, hence simplify the image representation into something that is easier to understand by a machine. In this context, segmenting the apple fruits from color images has made the object of much researches during the recent years. Thus, several approaches have been proposed in the literature. For instance, Song and Yang [12] have proposed a method that is based on fractal theory and multi-thresholding to segment images containing apples of type Fuji. Specifically, relying on fractal theory the image to segment is divided into sub-images having equal surface areas, then each of the produced sub-image is segmented by an an associated threshold. Dubey et al. [7] have introduced a segmentation method to segment out infected parts from the remaining parts of an apple using K-means clustering algorithm. This latter method proceeds by grouping the pixels of an image according to their color and their spatial coordinates. Zhou et al. [15] have exhibited a new algorithm to extract apples of type Gala from an RGB color image. In their method, a

given pixel is considered as a background pixel if the (R−B) component is less than forty. Otherwise the pixel is assigned to a fruit region. Moreover, Stajnko et al. [13] have established an algorithm to estimate the diameter and the number of apples of types Golden Delicious and Jonagold on a tree that is contained in an image. The established algorithm uses two techniques: the first technique segments the image relying on color proprieties, whilst the second technique uses texture proprieties. Ji et al. [9] have proposed a method to recognize in real time apples of type Fuji for harvesting robots. The proposed method uses Adaptive Mean Shift to produce an initial segmentation, then min-cut to refine the segmentation. Lately, Bargoti and Underwood [3] have proposed a framework in which a general-purpose segmentation approach is used, involving multi-scale multilayered perceptrons (MLP) and convolutional neural networks (CNN). The proposed framework has been tested on images containing apples of types Kanzi and Pink Lady. The same authors, Bargoti and Underwood [4], have presented another framework, this time using Faster R-CNN. Despite the huge efforts that have been delivered to successfully integrate image segmentation in the field of modern agriculture, it remains important and interesting to explore and/or introduce new segmentation techniques which would be more better, specifically in terms of accuracy and precision, comparing to the existing ones to improve apple segmentation.

Recently, in 2016, Dong et al. [6] have proposed a semi-automatic image segmentation method, called *subMarkov random walk (subRW)*, that they apply for the first time to segment color images of natural scenes. In our study, we explore and investigate the applicability of the subRW method to segmentation color images containing apples of types *Kanzi*, as well as apples of type *Pink Lady*. Comparing the obtained results of subRW to the ones of two recent state-of-the-art methods, introduced in 2017, namely Bargoti and Underwood [3] and Bargoti and Underwood [4], which address the same thematic (segmentation of *Kanzi* and *Pink Lady* apples), have yielded to encouraging and promising results and have shown that it can be successfully applied to segment *Kanzi* and *Pink Lady* apples from color images.

The remainder of this paper is organized as follows: Section II presents the subRW method by giving a necessary description of the method and its pseudo-algorithm. Section III is dedicated to the exhibition of the experimental tests of the method, it incudes descriptions of the implementation environment, the used dataset, the values of the used parameter, evaluation metrics, and the obtained results of the performed tests. Finally, the last section concludes this paper by giving a recapitulation of the established work as well as some intended future works.

II. SubMarkov Random Walk segmentation method

In this section, we describe a new segmentation method that is devoted to color images so-called *subMarkov random walk (subRW)* which was proposed by Dong et al. [6] in 2016, and this by giving its principle and pseudo-algorithm. This method involves a concept of *graphes* and the principle of *random walk*. More details are given in the following subsections.

A. Description of subRW method

The image segmentation method subRW can be viewed as a semi-automatic method which is classified in graph-based methods category. Considering an image $\mathcal{I}$ having K regions of interest (ROIs) and a set of K labels $L = \{l_1, l_2, ..., l_K\}$. Each label is manually assigned to a small set of pixels of a same ROI of $\mathcal{I}$. Then, each unlabeled pixel supposedly releases a random walker which walks on $\mathcal{I}$ and computes the probability of reaching the manually pre-labeled pixels. Finally, the segmentation is obtained by assigning to each unlabeled pixel the label of the set of pre-labeled pixels having the higher mean reaching probability that is computed by the random walker that it has released [6]. The graph construction and the principle of subRW are presented as follows.

1) Graph construction: In subRW, the image $\mathcal{I}$ is seen as a weighted and non-oriented graph $G = (V, E)$, with V is the set of vertices and E is the set of edges, which is constructed by considering each vertex $v_i \in V$ as representing a pixel x_i of $\mathcal{I}$, and an edge e_{ij} of the graph connects two vertices v_i and v_j in 8-connected neighborhood system, and a weight $w_{ij} \in W$ of an edge e_{ij} measures the similarity between the two vertices that it connects. Specifically, the weight w_{ij} is calculated as follows [6]:

$$w_{ij} = \exp(-\frac{\|I_i - I_j\|^2}{\sigma}) + \epsilon, \quad (1)$$

where I_i (resp. I_j) is the intensity of the pixel x_i (resp. x_j) in the Lab space, σ is a controling parameter and ϵ is a small constant.

2) Principle of the subRW method: Let D be a diagonal degree matrix of size $N \times N$, N is the number of vertices of G. The degree of a vertex v_i is the sum of the weights of the edges that connect it to its neighbors. Thus, the i^{th} element of the diagonal of D, *i.e.* D_{ii}, is given as follows :

$$D_{ii} = d_i, \qquad d_i = \sum_{j=1; j\neq i}^{n} w_{ij}, \quad (2)$$

where n is the number of neighbors of v_i and j is the index of a vertex belonging to the n neighbors (excluding v_i).

According to Dong et al. [6], a random walker leaves the graph G from the vertex v_i (stop its random walk) with a probability c_i or walks to a neighbor vertex of v_i with a probability $1 - c_i$. In addition, a label l_k has an intensity distribution H_k for each vertex and u_i^k is the probability density that the vertex v_i belongs to H_k. This distributions are obtained by using the Gaussian Mixture Model (GMM) (for more details, the reader may refer to the article of Calinon et al. [5]).

Let $r_{im}^{l_k}$ be the probability that a random walker starting from the i^{th} unlabeled vertex reaches the m^{th} vertex $v_m^{l_k}$ that is manually pre-labeled with l_k. The vector of probability $r_m^{l_k} = [r_{im}^{l_k}]_{N\times 1} = [r_{1m}^{l_k}, r_{2m}^{l_k}, ..., r_{im}^{l_k}, ..., r_{Nm}^{l_k}]^T$, where T symbolizes the transpose, is expressed by the following formula:

$$r_m^{l_k} = (I - (I - D_c)P)^{-1}((I - D_c)u^k) + D_c b_m^{l_k}, \quad (3)$$

where $b_m^{l_k} = [b_{im}^{l_k}]_{N\times 1} = [b_{1m}^{l_k}, b_{2m}^{l_k}, ..., b_{im}^{l_k}, ..., b_{Nm}^{l_k}]^T$ is a vector that indicates if $v_i = v_m^{l_k}$, with $b_{im}^{l_k} = 1$ if $v_i = v_m^{l_k}$, otherwise $b_{im}^{l_k} = 0$.

D_c is a diagonal matrix containing the probabilities c_i, I is an identity matrix of size $N \times N$ and P is a transition matrix in which an element P_{ij}, that represents the probability of the transition from v_i to v_j, is calculated as the following:

$$P_{ij} = \frac{w_{ij}}{d_i + \lambda g_i}, \quad (4)$$

where $g_i = \sum_{k=1}^{K} u_i^k$, λ is a regularization parameter, and the vector u^k is obtained by:

$$u^k = \frac{\lambda u_i^k}{d_i + \lambda g_i}. \quad (5)$$

In order to assign the suitable label to the vertex v_i, all the manually pre-labeled vertices by a label l_k have to be taken in consideration. Therefore, the mean probability $r_i^{l_k}$ that the random walker starting from v_i reaches the vertices that are labeled with l_k is calculated. The vector r^{l_k} of this probability mean in the steady-state is obtained as the following:

$$r^{l_k} = \frac{1}{Z_k}(I - (I - D_c)P)^{-1}((I - D_c)u^k + \frac{1}{M_k}D_c b^{l_k}), \quad (6)$$

where $b^{l_k} = [b_i^{l_k}]_{N\times 1} = [b_1^{l_k}, b_2^{l_k}, ..., b_i^{l_k}, ..., b_N^{l_k}]^T$ is a vector indication if a vertex v_i has a label l_k, M_k is the number of vertices which are pre-labeled with l_k, and Z_k is a normalized constant.

The final labeling result (segmentation) of a vertex v_i is obtained by the following formula:

$$R_i = \arg\max_{l_k} r_i^{l_k}. \quad (7)$$

It is worth to note that directly computing the matrix $(I - (I - D_c)P)^{-1}$ of the formula (6) is very expensive, specifically if the number of the vertices of G is very large. To overcome this issue, the formula (6) is converted into linear equations which are solved using a sparse algorithm, for more details, the reader can consult Dong et al. [6].

B. Pseudo-algorithm of the subRW method

The pseudo-algorithm of the subRW method is given as the following:

Algorithm 1 Pseudo-algorithm of the image segmentation method subRW [6].

Input: Image $\mathcal{I}$, $L = \{l_1, l_2, ..., l_K\}$, $D_c = diag(c_1, c_2, ..., c_N)$, λ, $V_M = \{\{v_1^{l_1}, v_2^{l_1}, ..., v_{M_1}^{l_1}\}, \{v_1^{l_2}, v_2^{l_2}, ..., v_{M_2}^{l_2}\}, ..., \{v_1^{l_K}, v_2^{l_K}, ..., v_{M_K}^{l_K}\}\}$.
Output: Segmentation result R_i corresponding to the pixel x_i.

1: Obtain the indicator vectors b^{l_k}, $k = \overline{1, K}$ of the labels;
2: Define an adjacency matrix $W = [w_{ij}]_{N\times N}$, respecting an 8-connexion neighborhood system and the formula (1);
3: Obtain the probability density u_i^k;
4: Scale the probability density: $u_i^k \longleftarrow max(100 + log(u_i^k), 10^{-10})$;
5: Set $g_i \longleftarrow g_i^k$, where $g_i^k = u_i^k + \max_{t\neq k} u_i^t$;
6: Compute the transition probability matrix P by the formula (4) and the vector u^k by the formula (5);
7: Resolve the linear equations: $(I-(I-D_c)P)r^{l_k} = (I-D_c)u^k + \frac{1}{M_k}D_c b^{l_k}$;
8: Normalize the probabilities: $r^{l_k} \longleftarrow \frac{1}{Z_k} r^{l_k}$;
9: Obtain the segmentation result $R_i = \arg\max_{l_k} r_i^{l_k}$;

C. Example illustrating the subRW method

In this subsection we illustrate by an example the principle of the subRW method. To do so, we give in Fig. 1 a trivial case that is actually inspired by Grady [8]. In order to simplify the illustration, we consider each of the image's ROIs is designated with a unique pre-labeled pixel. As well, for the same raison we omit the weights of the edges.

In Fig. 1(a), we show an 8-connected graph having a set of vertices v_i, where $i = \overline{1, 16}$, among which are illustrated vertices that are representing unlabeled pixels marked with the sign (?), and vertices which are representing pre-labeled pixels having one of the labels l_1, l_2 or l_3, each of which represents a ROI.

In accordance with what we have described in Subsection II-A, each unlabeled vertex releases a random walker that walks on the graph and computes the probabilities to reach the pre-labeled vertices with l_1, l_2 and l_3. These probabilities are obtained using the formula (3). For more clarification, we show in Fig. 1(b) the probabilities that each unlabeled vertex v_i reaches the vertex pre-labeled with l_1, whilst Fig. 1(c) presents the probabilities of reaching the vertex pre-labeled with l_2, and finally Fig. 1(d) presents the probabilities of reaching the vertex pre-labeled with l_3. From the Figs. 1(b), 1(c), 1(d) we notice that for each vertex of the graph, the sum of probabilities of reaching the vertices pre-labeled with l_1, l_2 and l_3 is equal to 1, *ex.* for the vertex v_1: $0,26 + 0,71 + 0,03 = 1$.

Then, for each unlabeled vertex, the mean probability of reaching the vertices that are pre-labeled with a same label is calculated. Finally, the vertex will be labeled with the label having the largest mean reaching probability, *ex.* in our example each label has one pre-labeled vertex only, so for the same vertex v_1: the mean $r_1^{l_1}$ is equal to $0,26/1 = 0,26$, the mean $r_1^{l_2}$ is equal to $0,71/1 = 0,71$, and the mean $r_1^{l_3}$ is equal to $0,03/1 = 0,03$. Consequently, the maximum value of the means $r_1^{l_1}$, $r_1^{l_2}$, and $r_1^{l_3}$ is $r_1^{l_2}$ which corresponds to l_2, so v_1 will be labeled with l_2. This principle is applied to all the unlabeled vertices of the graph, leading to the result which is shown in Fig. 1(e).

III. Tests and Evaluations

This section is dedicated to the presentation of experimental part of the previously described method applied to images containing apple fruits. To do so, we describe the environment in which we have implemented and tested the method as well as the tools that have been necessary to accomplish the tests such as the used dataset, the adapted values of the parameters, and the evaluation metrics.

A. Implementation environment

To realize our work, we have implemented subRW in MATLAB 2014 version which is an interactive language suitable for image analysis and processing. The tests have been carried out in a DELL Inspiron, with an Intel(R) core TM i5-7200 CPU, 4GB RAM, running under Windows 10. To validate the segmentation method, we have used *acfr-multifruit* dataset [1] which contains real color images containing apple fruits of types *Kanzi* and *Pink Lady*.

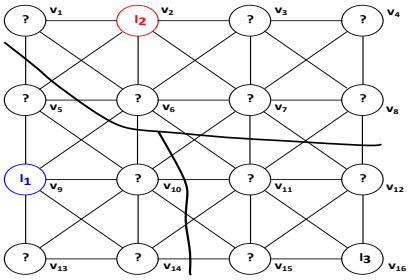

(a) Graph of the manually pre-labeling.

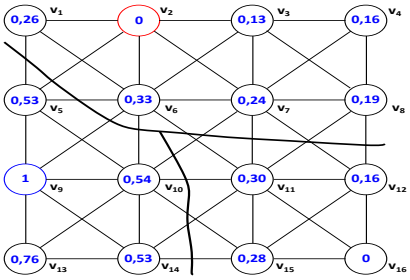

(b) Graph of showing the probabilities of reaching the vertex pre-labeled with l_1.

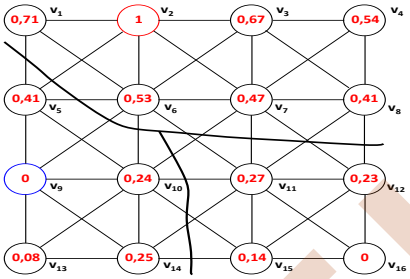

(c) Graph of showing the probabilities of reaching the vertex pre-labeled with l_2.

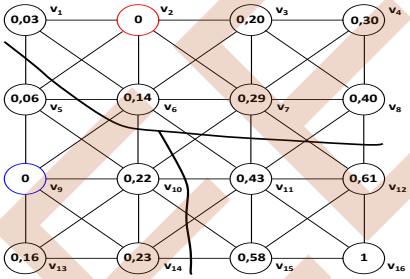

(d) Graph of showing the probabilities of reaching the vertex pre-labeled with l_3.

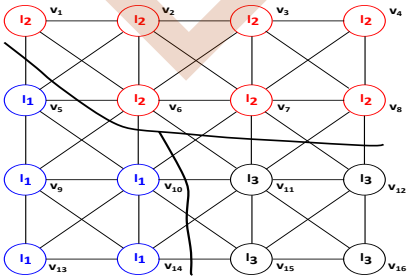

(e) Graph showing l_1, l_2 and l_3 assignment.

Fig. 1. Example illustrating the principle of the subRW method [8].

B. Acfr-multifruit dataset

The *acfr-multifruit* dataset belongs to the agriculture team of the Australian center of the ground robotic which is affiliated to the university of Sydney [3], and it is available to download at http://data.acfr.usyd.edu.au/ag/treecrops/2016-multifruit/. To the best of our knowledge, it is the only publicly available dataset that is dedicated to the evaluation of apples segmentation methods.

Moreover, the images of the dataset have been captured with preserving the natural conditions of the apples as they were in the orchard. Thus, several factors such as: the importance of intra-regions (inter-regions) variations due to the variability of the lighting conditions, the variability of the distances of the fruits from the camera, the grouping of the fruits, the different capture angle, etc. [4] constitute real challenges to test the performance of a segmentation method.

In total, the dataset contains more than 8000 images in which 1120 are images containing apples of types *Kanzi* and *Pink Lady*. All the images are 308×202 pixels. The dataset includes also manually segmented images that we have used as references to evaluate the performance of subRW.

C. Values of the used parameters

For the aim to apply subRW to segment images containing apples, we have adapted the values of the parameters of subRW to fit our goal. The new values have been determined by training the method over ten images from *acfr-multifruit* dataset and are shown in Table I. Moreover, we have used two labels: the first label to mark out pixels which belong to the apple fruits, and the second label to specify pixels of the background of the image. Additionally, it is important to point out that the subRW method is conceived in a way in which the satisfaction of some conditions when distributing labels on image's pixels is required. In fact, the label drawings should follow the overall look of the ROI for better segmentation. With this settings, the method will be called *subRW-A* abbreviation of *subMarkov random walk applied to apple fruit segmentation* in the remainder of this paper.

TABLE I. VALUES OF THE PARAMETERS USED IN SUBRW.

Parameter	δ	ϵ	λ	c
Value	$\frac{1}{60}$	10^{-6}	0.001	0.8

D. Evaluation metrics

Conventionally, the accuracy of a segmentation method is estimated by comparing its yielded segmentation results to benchmark segmentations, which are usually performed manually by experts, according to some evaluation metrics. For this purpose, we have chosen three well-known metrics in the literature namely: *Precision*, *Recall*, and *F1-score*. These metrics were introduced by Van Rijsbergen [14]. Actually, they are based on the assumption that a segmentation method is accurate if it is able to produce a maximum of correctly identified pixels and calculated using three measures that are: the *True Positive* (TP), the *False Positive* (FP), and the *False Negative* (FN). TP is the number of pixels which are simultaneously segmented by subRW-A and the experts as pixels of apples. FP is the number of pixels that are segmented

(a) Original images.

(b) Manually segmented images.

(c) Labeled images, the red label designates pixels of the region of interest and the blue label correspondes to pixels of the background.

(d) Images segmented by subRW-A.

Fig. 2. Segmentation results of subRW-A on images containing apples of type Kanzi.

(a) Original images.

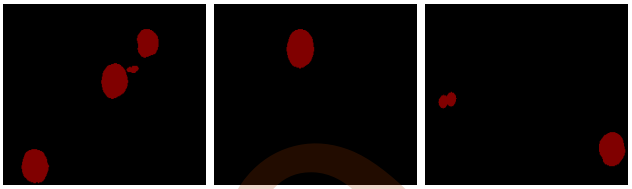

(b) Manually segmented images.

(c) Labeled images, the red label designates pixels of the region of interest and the blue label correspondes to pixels of the background.

(d) Images segmented by subRW-A.

Fig. 3. Segmentation results of subRW-A on images containing apples of type Pink Lady.

by subRW-A as pixels belonging to apples, however, they are considered by the experts as pixels of the background. Finally, FN is the number of pixels which are considered by subRW-A as pixels of the background, but actually, they are pixels that belong to the apples. The formulas of the three metrics can be found in Van Rijsbergen [14].

Note that, higher yielded result values of these evaluation metrics indicate better segmentation performance.

E. SubRW-A segmentation results

In this subsection, we take interest in the extraction of the ROI, which is in our case apples of types *Kanzi* and *Pink Lady*, by applying the subRW-A method to a set of images taken from the *acfr-multifruits* that we have described in Subsection III-B. Some segmentation results of *Kanzi* and *Pink Lady* apples are exhibited below.

1) Segmentation results of images containing Kanzi apples type: In this first part, we are interested in applying subRW-A to color images containing apples of type *Kanzi*. In Fig. 2, we show the segmentation results obtained for three images chosen from the *acfr-multifruits* dataset.

The labeled images of the three original images that are shown in Fig. 2(a) are given in Fig. 2(c) and their corresponding segmentation results by subRW-A are illustrated in Fig. 2(d). In fact, comparing these latter to those shown in Fig. 2(b) which represent the manually segmented images, we can easily notice the strong similarity between the contours of the manually segmented apples and those obtained by the application of subRW-A. Consequently, subRW-A have well extracted the ROI (the apples). And this despite of the variability of the lighting in the images that can scale from a strong lighting caused by the sun to a weak lighting due to shadows. Furthermore, we can observe that subRW-A efficiently resists to intra-apple color variability that characterizes the *Kanzi* apples.

2) Segmentation results of images containing Pink Lady apples type: In this second part, we present an exemple of segmentation results of color images containing apples of type *Pink Lady*. These latter have been obtained by applying subRW-A. In Fig. 3, we illustrate three original images containing *Pink Lady* apples (Fig. 3(a)), their manual segmentation (Fig. 3(b)), their labeled images (Fig. 3(c)), as well as their corresponding segmentation by subRW-A (Fig. 3(d)). From Figs. 3(b), 3(d) we can easily deduce that subRW-A produces good segmentation results. Actually, the segmentations shown in Fig. 3(d) tend to be the same as the manual segmentations. Moreover, it is important to mention that extracting *Pink Lady* apples from the images is a tedious task because of several

TABLE II. EVALUATION RESULTS OF SUBRW-A.

Statistic \ Metric	Precision (subRW-A)	Recall (subRW-A)	F1-score (subRW-A)	Precision (Method in [10], 2011)	Recall (Method in [10], 2011)	F1-score (Method in [10], 2011)	F1-score (Method in [3], 2017)	F1-score (Method in [4], 2017)
Max	0.9878	0.9992	0.9757	0.9831	0.9967	0.9687	/	/
Min	0.7715	0.7826	0.8474	0.4750	0.2466	0.3875	/	/
Std	0.0528	0.0474	0.0243	0.1137	0.2739	0.1956	/	/
Mean	**0.9031**	**0.9442**	**0.9219**	0.8487	0.7297	0.7526	0.7510	0.9040

issues such as the considerable lighting variability and the quasi-similarity between the apples color and the color of the leaves of the trees.

F. Evaluation of subRW-A method

For the aim of experimentations, first we have tested subRW-A on sixty images that we have taken from the *acfr-mutlifruit* dataset. The testing images have been different from those that we have used to fixe the parameters of the method which are shown in Table I. Then, we have compared its obtained results with three methods. Specifically, two recent methods of Bargoti and Underwood [3], [4], which are dedicated to the same purpose as ours (segmentation of images containing apples of types *Kanzi* and *Pink Lady*) and were evaluated using the F1-score metric over the same database (acfr-muti-fruit). And, the state-of-the-art level set that is introduced by Li et al. [10]. The evaluation results are given in Table II.

G. Interpretation of the obtained results

From Table II, we deduce that subRW-A has produced promising results. Actually, the yielded results present a mean value exceeding 0.90 for the metric Precision, and a mean value exceeding 0.94 for the metric Recall, which are better than the mean values obtained by level set for the same metrics.

For the F1-score metric, we notice that subRW-A has yielded a mean value which is approximately 0.92, that is far more large than the both mean values of the F1-score obtained by the method of Bargoti and Underwood [3], and level set (which are around 0.75). Moreover, the mean F1-score yielded by subRW-A exceeds with approximately 1,95% the mean F1-score obtained by the method of Bargoti and Underwood [4], whose score is about 0.90.

Furthermore, the tests have revealed that subRW-A has a low sensitivity to the initial positions of the pre-labels pixels. Consequently, the method presents satisfactory and encouraging performance.

IV. CONCLUSION

In this paper, we have applied for the first time the method subRW to segment color images containing apples of type *Kanzi* and other images containing apples of type *Pink Lady*. Our main aim consisted to distinguish apples from the remaining background of an image, *i.e.* extract/segment the region of interest which is in our case the apples. Moreover, we have tested and evaluated the subRW method on a set of real images that have been taken from the *acfr-multifruit* dataset, and this by comparing the obtained results of subRW to the ones of two some recent and concurrent state-of-the-art methods. Despite the unfavorable lighting variations and the quasi-similarity of the color of the Pink Lady apples to the leaves fragments, we have obtained encouraging and satisfactory results.

As future work, we intend to establish a more reliable comparison by intervening several concurrent methods and to expand the number of the testing images so that to observe the evolution of the method's performance. Furthermore, it is worth to consider the automatization of the subRW method.

ACKNOWLEDGMENT

The authors are thankful to the anonymous reviewer for his valuable comments that helped to improve the paper.

REFERENCES

[1] http://data.acfr.usyd.edu.au/ag/treecrops/2016-multifruit/. Accessed on June 25th, 2018.

[2] http://www.fao.org/home/fr/. Accessed on June 19th, 2018.

[3] S. Bargoti and J. P. Underwood. *Image segmentation for fruit detection and yield estimation in apple orchards*. Journal of Field Robotics, 34: 1039-1060, 2017.

[4] S. Bargoti and J. P. Underwood. *Deep fruit detection in orchards*. In: International Conference on Robotics and Automation (ICRA), Singapore, 3626-3633, 2017.

[5] S. Calinon, F. Guenter, and A. Billard. *On learning, representing and generalizing a task in a humanoid robot*. IEEE Transaction on Systems, Man and Cybernetics, 37:286-298, 2007.

[6] X. Dong, J. Shen, L. Shao, and L. Van Gool. *Sub-Markov random walk for image segmentation*. IEEE Transactions on Image Processing, 25: 516-527, 2016.

[7] S. R. Dubey, P. Dixit, N. Singh, and J. P. Gupt. *Infected fruit part Detection using K-Means clustering segmentation technique*. International Journal of Artificial Intelligence and Interactive Multimedia, 2:65-72, 2013.

[8] L. Grady. *Random walks for image segmentation*. IEEE Transactions on Pattern Analysis and Machine Intelligence, 28:1768-1783, 2006.

[9] W. Ji, X. Meng, Y. Tao, B. Xu, and D. Zhao. *Fast segmentation of colour apple image under all-weather natural conditions for vision recognition of picking robots*. International Journal of Advanced Robotic Systems, 13:24-33, 2016.

[10] C. Li, R. Huang, Z. Ding, J. Gatenby, D. N. Metaxas, J. C. Gore. *A level set method for image segmentation in the presence of intensity inhomogeneities with application to MRI*. IEEE Transactions on Image Processing, 20:2007-2016, 2011.

[11] A. Mizushima and R. Lu. *An image segmentation method for apple sorting and grading using support vector machine and Otsu's method*. Computer and Electronics in Agriculture, 94:29-37, 2013.

[12] X. Song and L. Yang. *The study of adaptive multi threshold segmentation method for apple fruit based on the fractal characteristics*. In: 8th International Symposium on Computational Intelligence and Design, Hangzhou, 168-171, 2015.

[13] D. Stajnko, J. Rakun, and M. Blanke. *Modelling apple fruit yield using image analysis for fruit colour, shape and texture*. European Journal Horticultural Science, 74:260-267, 2009.

[14] C. J. Van Rijsbergen. *Information Retrieval*. Butterworths, London, 1979.

[15] R. Zhou, L. Damerow, Y. Sun, and M. M. Blanke. *Using colour features of cv. Gala apple fruits in an orchard in image processing to predict yield*. Precision Agriculture, 3:568-580, 2012.

An Optimal Design of Non-Causal Recursive Digital Filters with a Zero Phase Shift Based on MiniMax Criterion

Adnane MOUFFAK
Laboratoire LGPCS,
Faculté des Sciences et de la Technologie
Université Mustapha Stambouli de Mascara - Algérie
mouffakadn@univ-mascara.dz , amouffak@gmail.com

***Abstract*— In this paper, an optimal design for the special class of Non-Causal Recursive (NR) digital filters with a zero phase shift is presented. The approximation problem is formulated as a minimax optimization. It is transformed into a linear programming, which can be solved iteratively by a well-known binary search technique. We demonstrate that the optimal frequency response of the NR filter can be better than that of the classical squared magnitude response of an optimal elliptic filter; where, we get additional attenuation in the stopband. Two examples of filter design are illustrated in agreement with our contribution. Some details of the linear programming implementation and its limits are also discussed.**

I. INTRODUCTION

As is well known, Noncausal Recursive (NR) digital filters can be realized by a cascade connection of a causal IIR filter with an arbitrary transfer function $H(z)$ (forward pass) and an anticausal time reversed version of the same function $H(z^{-1})$ (backward pass) [1-7]. The issue of designing this special class of digital filters has been discussed only slightly [1-2], and the most contributions have been focused on its real-time implementation [1-4], [6-10]. Kormylo and Jain [1] have proposed a classical design in the frequency domain based on bilinear transform and a well-known optimal design of analog elliptic filters, such that the magnitude characteristic of the causal recursive filter $H(z)$ has to agree with the square root of the desired frequency response of an NR filter $H_{NR}(e^{j\theta}) = |H(e^{j\theta})|^2$; while, its phase characteristic is inconsequential. Over these four decades, this classical design was the most commonly used in several papers [3-10], where the design procedure is fast and simple. However, despite of using an optimal elliptic digital filter $H(z)$, we are not sure that the squared magnitude response $|H(e^{j\theta})|^2$ is the optimal frequency response of the NR digital filters.

In this paper, an optimal design of NR digital filters is proposed on the basis of the minimax criterion, where the magnitude response can be better than that of the classical design. A zero phase constraint will be elaborated under some special conditions, where it can be linear. So, the approximation problem can be transformed into a linear programming, which can be solved by an iterative binary (dichotomic) search technique.

In Section II, according to the transfer function $H_{NR}(z)$ of NR digital filters, a zero phase shift constraint is developed under the special case where the poles of $H_{NR}(z)$ are located in quadrantal symmetry. The key aspect of this last assumption is the linear constraint that we can get. Section III presents a formulation of the approximation problem. The constraints as functions of the normalized frequency θ, are given in both of the passband (PB) and the stopband (SB). A linear programming formulation and details concerned with the discretization techniques are explained in section IV. In section V, we describe the optimization procedure devoted to solve iteratively the proposed linear programming; and two filter design examples are illustrated in section VI. Finally, conclusions are given in section VII.

II. A ZERO PHASE SHIFT CONSTRAINT

Consider the generalized NR filters realization [2] in Fig.1, where $H_1(z)$ and $H_2(z)$ be the transfer functions of the Nth order of causal IIR filters such that:

$$H_1(z) = \frac{\sum_{k=0}^{N} b_k z^{-k}}{\sum_{k=0}^{N} a_k z^{-k}} \quad \text{and} \quad H_2(z) = \frac{\sum_{k=0}^{N} \beta_k z^{-k}}{\sum_{k=0}^{N} \alpha_k z^{-k}} \qquad (1)$$

a_k , b_k , α_k and β_k are real coefficients.

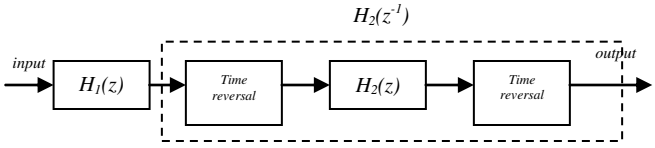

Figure 1. Generalized Noncausal Recursive (NR) digital filter realization

Thus, the equivalent transfer function $H_{NR}(z) = H_1(z)H_2\left(z^{-1}\right)$ of 2Nth order of the NR filter can be expressed as:

$$H_{Eq}(z) = \frac{\sum_{k=-N}^{N} c_k z^{-k}}{\sum_{k=-N}^{N} d_k z^{-k}} = \frac{\hat{N}(z)}{\hat{D}(z)} \tag{2}$$

Where:

$$\hat{N}(z) = \sum_{k=-N}^{N} c_k z^{-k} \quad \text{and} \quad \hat{D}(z) = \sum_{k=-N}^{N} d_k z^{-k} \tag{3}$$

For $z = e^{j\theta}$, the frequency response of the NR filter is:

$$H_{NR}\left(e^{j\theta}\right) = H_1(z)H_2\left(z^{-1}\right)\Big|_{z=e^{j\theta}} = \frac{\hat{N}(\theta)}{\hat{D}(\theta)} \tag{4}$$

$$\hat{N}(\theta) = \sum_{k=-N}^{N} c_k e^{-jk\theta} \quad \text{and} \quad \hat{D}(\theta) = \sum_{k=-N}^{N} d_k e^{-jk\theta} \tag{5}$$

According to the transfer function model (2) and (3), we are going to elaborate the constraint that can ensure a zero phase shift response. The equivalent frequency response $H_{NR}\left(e^{j\theta}\right)$ of the NR filter can be expressed as:

$$H_{NR}\left(e^{j\theta}\right) = \frac{c_0 + \sum_{k=1}^{N}\left(c_k + c_{-k}\right)\cos(k\theta) - j\sum_{k=1}^{N}\left(c_k - c_{-k}\right)\sin(k\theta)}{d_0 + \sum_{k=1}^{N}\left(d_k + d_{-k}\right)\cos(k\theta) - j\sum_{k=1}^{N}\left(d_k - d_{-k}\right)\sin(k\theta)} \tag{6}$$

If we consider the special case where all poles of the equivalent transfer function $H_{NR}(z)$ are in quadrantal symmetry. This situation can be found, where poles of $H_1(z)$ are those of $H_2(z)$. So, the set of coefficients $\{d_k\}_{-N\le k\le N}$ can be considered as an autocorrelation function, where it will have the maximum at d_0 and the others coefficients are symmetric, such as: $d_k = d_{-k}$ for $k = 1,\ldots,N$.

In this case, the denominator $\hat{D}(\theta)$ is a real function as follows:

$$\hat{D}(\theta) = d_0 + 2\sum_{k=1}^{N} d_k \cos(k\theta) \tag{7}$$

Thus, $H_{NR}\left(e^{j\theta}\right)$ can be expressed with real and imaginary parts as:

$$H_{NR}\left(e^{j\theta}\right) = \left[\frac{c_0 + \sum_{k=1}^{N}\left(c_k + c_{-k}\right)\cos(k\theta)}{d_0 + 2\sum_{k=1}^{N} d_k\cos(k\theta)}\right] - j\left[\frac{\sum_{k=1}^{N}\left(c_k - c_{-k}\right)\sin(k\theta)}{d_0 + 2\sum_{k=1}^{N} d_k\cos(k\theta)}\right] \tag{8}$$

$H_{NR}\left(e^{j\theta}\right)$ can have a zero phase shift if it is a real function, so its imaginary part equals to zero.

So, we have:

$$\sum_{k=1}^{N}\left(c_k - c_{-k}\right)\sin(k\theta) = 0 \tag{9}$$

Finally, (9) can be expressed as a linear constraint over the set of the coefficients $\{c_k\}_{-N\le k\le N}$:

$$\sum_{k=-N}^{N} c_k \sin(k\theta) = 0 \tag{10}$$

III. FORMULATION OF THE APPROXIMATION PROBLEM

Let $F(\theta)$ be the desired frequency response of the NR digital filter, where it is a specified function of frequency.

$\delta(\theta)$ is the positive tolerance function of frequency such that:

$$\delta(\theta) = \left|\frac{\hat{N}(\theta)}{\hat{D}(\theta)} - F(\theta)\right| \tag{11}$$

If we consider under the procedure of optimization that the maximum errors are respectively in the passband (PB) $\hat{\delta} = \max_{\theta\in PB}\lfloor\delta(\theta)\rfloor$, and in the stopband (SB) $\delta = \max_{\theta\in SB}\lfloor\delta(\theta)\rfloor$.

Without lose of generality, the approximation problem consists of finding the coefficients c_k and d_k $(-N\le k\le N)$; such that we get the minimum of $\hat{\delta}$ / ($\theta \in PB$) and δ / ($\theta \in SB$) under the constraints:

$$-\hat{\delta} \le \frac{\hat{N}(\theta)}{\hat{D}(\theta)} - F(\theta) \le 0 \text{ if } \theta \in PB$$

and (12)

$$0 \le \frac{\hat{N}(\theta)}{\hat{D}(\theta)} - F(\theta) \le \delta \text{ if } \theta \in SB$$

In order to keep the same sign $\le$ of inequalities after multiplication by $\hat{D}(\theta)$, we suppose that $\hat{D}(\theta) > 0$. In this situation, the constraints (12) (called principle constraints) can be expressed as a set of linear inequalities in relation with the set of the coefficients $\{c_k\}$ and $\{d_k\}$ $(-N\le k\le N)$ by writing them in the form:

$$\begin{cases}\hat{N}(\theta)-\hat{D}(\theta)F(\theta)\le 0\\ -\hat{N}(\theta)+\hat{D}(\theta)\left[F(\theta)-\hat{\delta}\right]\le 0\\ -\hat{D}(\theta)<0\end{cases} \text{ if } \theta\in PB$$

and (13)

$$\begin{cases}\hat{N}(\theta)-\hat{D}(\theta)\left[F(\theta)+\delta\right]\le 0\\ -\hat{N}(\theta)+\hat{D}(\theta)F(\theta)\le 0\\ -\hat{D}(\theta)<0\end{cases} \text{ if } \theta\in SB$$

Additional inequalities (called supplemental constraints) can be used where we take in consideration the maximum of tolerance imposed by the specifications: δ_p and δ_s respectively in the passband (PB) and the stopband (SB), such that:

$$-\hat{N}(\theta)+\hat{D}(\theta)\left|F(\theta)-\delta_p\right|\le 0 \text{ if } \theta\in PB$$

and (14)

$$\hat{N}(\theta)-\hat{D}(\theta)\left|F(\theta)+\delta_s\right|\le 0 \text{ if } \theta\in SB$$

Also, if we take in consideration that $\hat{D}(\theta)>0$ and $H_{NR}\left(e^{j\theta}\right)=\dfrac{\hat{N}(\theta)}{\hat{D}(\theta)}$ is a real function (in order to have a zero phase shift), we impose that: $\hat{N}(\theta)\ge 0$, in order to get positive magnitude frequency responses.

To simplify the problem of optimization, we consider that: $\dfrac{\hat{\delta}}{\delta}=\kappa$, so we are interesting to optimize the maximum of error in the stopband δ. We get the new formulation of the approximation problem as shown:

$$\begin{array}{l}Minimize \quad (\delta)\\ over: c_k, d_k, \delta\end{array}$$

under the constraints: (15)

$$\begin{cases}\theta\in PB\\ \hat{N}(\theta)-\hat{D}(\theta)F(\theta)\le 0\\ -\hat{N}(\theta)+\hat{D}(\theta)\left[F(\theta)-K\delta\right]\le 0\\ -\hat{D}(\theta)<0\\ -\hat{N}(\theta)\le 0\\ -\hat{N}(\theta)+\hat{D}(\theta)\left[F(\theta)-\delta_p\right]\le 0\\ \sum_{k=-N}^{N} c_k\sin(k\theta)=0\end{cases} \text{ and } \begin{cases}\theta\in SB\\ \hat{N}(\theta)-\hat{D}(\theta)\left[F(\theta)+\delta\right]\le 0\\ -\hat{N}(\theta)+\hat{D}(\theta)F(\theta)\le 0\\ -\hat{D}(\theta)<0\\ -\hat{N}(\theta)\le 0\\ \hat{N}(\theta)-\hat{D}(\theta)\left[F(\theta)+\delta_s\right]\le 0\\ \sum_{k=-N}^{N} c_k\sin(k\theta)=0\end{cases}$$

IV. LINEAR PROGRAMMING FORMULATION AND DISCRETIZATION

In order to transform the above approximation problem (15) into a linear programming, the maximum error in the stopband δ is considered as a constant during the optimization procedure; also, an auxiliary variable λ is subtracted from the left side of each inequality constraint, forming the new linear programming formulation:

The cost function to be minimized is:

$$y=\lambda$$

under the constraints: (16)

$$\begin{cases}\theta\in PB\\ \hat{N}(\theta)-\hat{D}(\theta)F(\theta)-\lambda\le 0\\ -\hat{N}(\theta)+\hat{D}(\theta)\left[F(\theta)-K\delta\right]-\lambda\le 0\\ -\hat{D}(\theta)-\lambda<0\\ -\hat{N}(\theta)-\lambda\le 0\\ -\hat{N}(\theta)+\hat{D}(\theta)\left[F(\theta)-\delta_p\right]-\lambda\le 0\\ \sum_{k=-N}^{N} c_k\sin(k\theta)=0\end{cases} \text{ ,and } \begin{cases}\theta\in SB\\ \hat{N}(\theta)-\hat{D}(\theta)\left[F(\theta)+\delta\right]-\lambda\le 0\\ -\hat{N}(\theta)+\hat{D}(\theta)F(\theta)-\lambda\le 0\\ -\hat{D}(\theta)-\lambda<0\\ -\hat{N}(\theta)-\lambda\le 0\\ \hat{N}(\theta)-\hat{D}(\theta)\left[F(\theta)+\delta_s\right]-\lambda\le 0\\ \sum_{k=-N}^{N} c_k\sin(k\theta)=0\end{cases}$$

It is clearly that the approximation problem in (16) can have a solution if and only if the minimum value of λ is 0; otherwise, no solution to the approximation problem is found, and either $F(\theta)$, or δ or both must be modified in order to obtain a solution.

Now, we are going to transform the above linear programming into its discrete version, in order to be performed under a digital machine.

The normalized frequency variable $\theta\in PB\cup SB$ can be discredited into M points (M1 is the number of points in the passband PB, such as:

$$\left\{\theta_m \,|\, 1\le m\le M_1 / \theta_m\in PB, M_1+1\le m\le M / \theta_m\in SB\right\} \quad (17)$$

The discretisation procedure is illustrated as follows:
Let we form vectors such that:

$$c=\left[c_k\right]_{-N\le k\le N}^{T},\ d=\left[d_k\right]_{-N\le k\le N}^{T},\ x=\left[c\ d\ \lambda\right]^{T} \quad (18)$$

Also, we form the matrices A and B of M lines and $(2N+1)$ columns, such that:

$$A=\left[\cos\left(k\theta_m\right)\right]_{(1\le m\le M)\times(-N\le k\le N)}$$

and (19)

$$B=\left[\sin\left(k\theta_m\right)\right]_{(1\le m\le M)\times(-N\le k\le N)}$$

If we consider the below inequalities from the principal constraints (16) in the passband (PB) and the stopband (SB), namely:

$$\begin{cases}\hat{N}(\theta)-\hat{D}(\theta)F(\theta)-\lambda\le 0\\ \hat{N}(\theta)-\hat{D}(\theta)\left[F(\theta)+\delta\right]-\lambda\le 0\end{cases} \quad (20)$$

The following vectors can be formed from the desired frequency response $F(\theta)$:

$$\begin{cases} \hat{F}_1=\left[F\left(\theta_m\right)\right]_{1\le m\le M_1} \\ F_1=\left[F\left(\theta_m\right)+\delta\right]_{M_1+1\le m\le M} \\ FF_1=\left[\hat{F}_1 \;\; F_1\right]^T_{M\times 1} \end{cases}$$

and (21)

$$\tilde{F}_1=diag\left(FF_1\right)=\begin{bmatrix} FF_1\left(\theta_1\right) & 0 & 0..... & 0 \\ 0 & . & 0..... & . \\ . & 0 & FF_1\left(\theta_m\right) & 0 \\ 0 & . & 0 & FF_1\left(\theta_M\right) \end{bmatrix}_{M\times M}$$

Also, if we consider the inequalities:

$$\begin{cases} -\hat{N}(\theta)+\hat{D}(\theta)\left[F(\theta)-K\delta\right]-\lambda\le 0 \\ -\hat{N}(\theta)+\hat{D}(\theta)F(\theta)-\lambda\le 0 \end{cases} \quad (22)$$

The following vectors can be formed from the desired frequency response $F(\theta)$:

$$\begin{cases} \hat{F}_2=\left[F\left(\theta_m\right)-K\delta\right]_{1\le m\le M_1} \\ F_2=\left[F\left(\theta_m\right)\right]_{M_1+1\le m\le M} \\ FF_2=\left[\hat{F}_2 \;\; F_2\right]^T_{M\times 1} \end{cases}$$

and (23)

$$\tilde{F}_2=diag\left(FF_2\right)=\begin{bmatrix} FF_2\left(\theta_1\right) & 0 & 0..... & 0 \\ 0 & . & 0..... & . \\ . & 0 & FF_2\left(\theta_m\right) & 0 \\ 0 & . & 0 & FF_2\left(\theta_M\right) \end{bmatrix}_{M\times M}$$

Also, with the same manner as in (21) and (23), we get from the supplemental constraints in (16):

$$\begin{cases} F_{s1}=\left[F\left(\theta_m\right)+\delta_s\right]_{M_1+1\le m\le M} \\ FF_{s1}=\left[\hat{F}_1 \;\; F_{s1}\right]^T_{M\times 1} \\ \hat{F}_{s2}=\left[F\left(\theta_m\right)-\delta_p\right]_{1\le m\le M_1} \\ FF_{s2}=\left[\hat{F}_{s2} \;\; F_2\right]^T_{M\times 1} \\ \tilde{F}_{s1}=diag\left(FF_{s1}\right) \\ \tilde{F}_{s2}=diag\left(FF_{s2}\right) \end{cases} \quad (24)$$

Finally, the approximation problem can be formulated as a linear programming such that:

$$Minimize\left(y\right), \text{ and: } y=\left[0\,0\,1\right]x \quad \text{over } x$$

Under the constraints: (25)

$$\begin{cases} Gx\le 0 \\ \left[B\,0\,0\right]x=0 \end{cases} \quad \text{and} \quad G=\begin{bmatrix} A & -\tilde{F}_1A & -1 \\ -A & \tilde{F}_2A & -1 \\ -A & 0 & -1 \\ 0 & -A & -1 \\ A & -\tilde{F}_{s1}A & -1 \\ -A & \tilde{F}_{s2}A & -1 \end{bmatrix}$$

V. PROCEDURE OF OPTIMIZATION

To determine the smallest value of δ such that the linear programming (25) has a solution, an iterative procedure should be used since δ enters into the design constraints. Before, let assume that the sum of the maximum of passband ripple $\hat{\delta}=K\delta$ and stopband ripple δ should be less than or equal to 1 [11]. If we let δ^* denote the minimum value of δ for which the approximation problem has a solution. We have:

$$0<\delta^*\le\frac{1}{K+1} \quad (26)$$

The initial lower $\delta^i_-=0$ and upper $\delta^i_+=\frac{1}{K+1}$ bounds can be used to locate δ^* by a binary search procedure, when at each step i, δ is calculated by a geometric mean ($\delta=\sqrt{\delta^i_-\delta^i_+}$). Note that, the geometric mean can reduce dynamic between these two lower δ^i_- and upper δ^i_+ bounds in comparison with the arithmetic mean. So, we get a fast binary search [11]. The procedure of optimization can be described as follows:

Step 1: initialization

Let: $\delta^i_-=10^{-15}$ (since $\delta^i_-<10^{-15}$ is unrealistic), $\delta^i_+=\frac{1}{K+1}$ and $\delta=\sqrt{\delta^i_-\delta^i_+}$

Step 2: Solve the above linear programming (26) with the value of δ. If the cost function $y=0$, a solution to the approximation problem exists and $\delta^*<\delta$. In this case, we can reduce the upper bound and we set $\delta^i_+=\delta$. Otherwise, no solution to the approximation problem exist for this value of δ and $\delta^*>\delta$. In this case, the lower bound is increased and we set $\delta^i_-=\delta$.

Step 3: set $\delta=\sqrt{\delta^i_-\delta^i_+}$, and repeat step 2 until: $\sigma=\left|\delta^i_+-\delta^i_-\right|$ reaches a predetermined accuracy. Generally, we stop processing where σ reaches a spacing floating point number [12].

Finally, polynomials $\hat{N}(z)$ and $\hat{D}(z)$ in (3) can be factorized according to the final coefficients $\left\{c_k\right\}_{-N\le k\le N}$ and $\left\{d_k\right\}_{-N\le k\le N}$ that are associated with the optimal value δ^*. Poles and zeros inside the unit circle are those of the causal minimum phase recursive filter $H_1(z)$; where, whose outside the unit circle are assigned to the noncausal maximum phase subsystem $H_2\left(z^{-1}\right)$. If zeros lie on the unit circle, the assignment to $H_1(z)$ or $H_2\left(z^{-1}\right)$ may be done arbitrary.

VI. EXAMPLES OF DESIGN

In this section, a variety of design examples are shown. In all the considered examples, the magnitude specifications were specified at equally $M = 1024$ spaced discrete frequency points, up to half the sampling frequency.

The linear programming shown in (25) can be solved first, by using the linprog() command from the optimization Toolbox of Matlab [12], with a double precision arithmetic on 64 bits machine. The commonly Simplex method is not suitable to solve a large scale problem as the filter design; so, we use this command with the option of interior point methods [12]. It seems more adequate in getting acceptable solution.

A. *Example 1: A Zero phase Low-Pass filter*

The magnitude specifications are as follows:

$$F(\theta) = 1 \quad if \ 0 \le \theta \le 0.5\pi \quad and \quad F(\theta) = 0 \quad if \ 0.6\pi \le \theta \le \pi$$

The maximum passband attenuation is $R_p = 0.5\,dB$ and the minimum stopband attenuation is $R_s = -32\,dB$. An order of 8 $(2N = 8)$ is chosen for the equivalent transfer function $H_{NR}(z) = H_1(z)H_2(z^{-1})$ of the NR filter. Fig. 2 shows the magnitude characteristics from both of the proposed and the classical designs. With the presented procedure of optimization, the optimal solution is reached after 56 iterations. We get additional 0.6 dB of stopband loss.

B. *Example 2: A Zero phase high magnitude specifications Low-Pass filter*

We keep the same above passband and stopband edges, with high attenuation requirements, such as: $R_p = 0.01\,dB$ and $R_s = -80\,dB$. An order of 14 $(2N = 14)$ is chosen for the equivalent transfer function $H_{NR}(z) = H_1(z)H_2(z^{-1})$.

With the example 2, it seems that, the linprog() command, with the large scale option, has numerical limitations for getting acceptable NR filters, where the equivalent frequency response is out of the tolerances $\delta_p = 1 - 10^{-R_p/20}$ and $\delta_s = 10^{-R_s/20}$. Also, in general, repetitive experiences confirm the same phenomena when orders are longer than 12 and high minimum stopband attenuation $(|R_s| > 60\,dB)$. In this case we can use the nonlinear solver fmincon() with the particular case of linear constraints [12]. The results are promising, and an optimal solution is reached after 56 iterations, with additional 0.02 dB stopband attenuation over that of the classical design (Fig.3). Instead of the linprog() command, with interior methods option, which uses a built-in starting point; the non linear solver fmincon() requires an initial solution that is chosen as follows: $x = [c\ d\ \lambda]^T = [0\ 0\ 1]^T$.

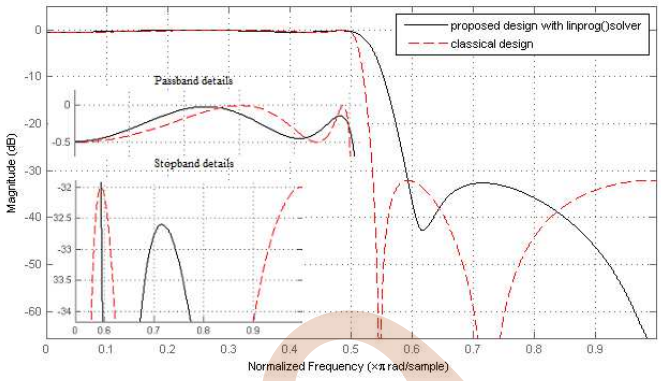

Figure 2. A Comparison between magnitude characteristics of Low-pass NR filters yielded from different designs- the proposed design (solid line) and the classical Kormylo and Jain's design (dashed line).

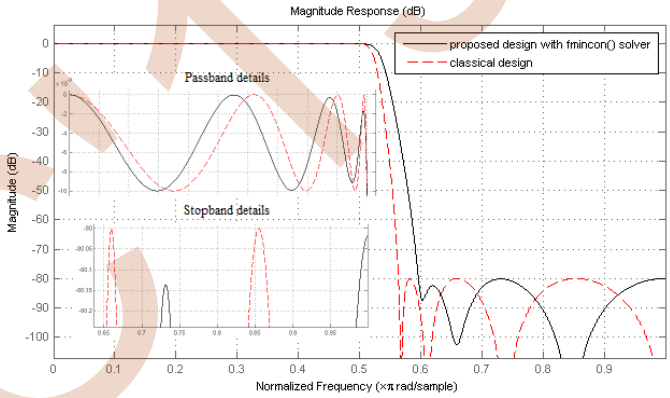

Figure 3. A Comparison between magnitude characteristics of Low-pass NR filters yielded from different designs, and under high magnitude specifications - the proposed design (solid line) and the classical Kormylo and Jain's design (dashed line).

VII. CONCLUSIONS

An optimal technique for designing NR digital filters was presented. The condition of a zero phase response was elaborated for the special case where it is linear.

The approximation problem was formulated as a linear programming, and solved iteratively using a well-known binary search technique. Two examples of filter design are illustrated. We demonstrate trough the proposed design that the optimal magnitude response of the NR filter can be different and better than that of the squared magnitude response of an optimal elliptic filter. The presented optimal design can be used for large magnitude specifications using linprog() command and/or fmincon() command with linear contraints . However, it seems limited when the minimum stopband attenuation is over than -95 dB, and the order of the NR filter is over than 2N=16. Also, when the width of the transition band is small, the coefficient sensitivity makes the proposed design unstable.

REFERENCES

[1] J. Kormylo and V.K. Jain, Two pass recursive digital filter with zero phase shift. IEEE Trans. Acoust.Speech Signal Processing, Vol ASSP-22,p-384-387, 1974.

[2] R. Czarnach, Recursive processing by noncausal digital filters. IEEE Trans.Acoust.Speech, Signal Processing, Vol ASSP-30, p.363-370, 1982.

[3] A. Mouffak, M. F. Belbachir, A new non-overlapping block processing technique for realizing linear phase two-pass recursive digital filters. Digital Signal Processing, 2013, vol. 23, no 1, p. 427-432.

[4] A. Mouffak, M. F. Belbachir, Noncausal forward/backward two-pass IIR digital filters in real time. Turkish Journal of Electrical Engineering & Computer Sciences, 2012, vol. 20, no 5, p. 769-786.

[5] A. Mouffak, M. F. Belbachir, Non-causal recursive digital filters in multi-band dysperiodicity analysis of synthetic simple vowels. In : Sciences of Electronics, Technologies of Information and Telecommunications (SETIT), 2012 6th International Conference on. IEEE, 2012. p. 792-796.

[6] E. Arias-de-Reyna, J.I. Acha, A new method for designing efficient linear phase recursive filters. Digital Signal Processing, Vol 14, p.1-17, 2004.

[7] S.R. Powell, P.M. Chau, A technique for Realizing linear phase IIR filters. IEEE Trans.Signal Processing, Vol 39,p.2425-2435, 1991.

[8] A. Kurosu, S. Miyase, S. Tomiyama, T. Takebe, A technique to truncate IIR filter impulse response and its application to real-time implementation of linear phase IIR filters. IEEE Trans.Signal Processing, Vol 51, N° 5 p.1284-1292, 2003.

[9] B. Djokic, M. Popovie, M. Lutovac, A new improvement to the Powell and Chau linear phase IIR filters. IEEE Trans.Signal Processing, Vol 46, N° 6, p 1685-1688, 1998.

[10] A.N. Willson, H.J. Orchard, An improvement to the Powell and Chau linear phase IIR filters. IEEE Trans.Signal Processing, Vol 42, p.2842-2848, 1994.

[11] L. Rabiner, N. Y. Graham, et H. D. Helms, Linear programming design of IIR digital filters with arbitrary magnitude function. IEEE Transactions on Acoustics, Speech, and Signal Processing, 1974, vol. 22, no 2, p. 117-123.

[12] T. Coleman, M. A. Branch, et A. Grace, Optimization Toolbox for use with Matlab, User's guide, version 2, The Mathworks Inc, 1999.

Diffusion segmentation approach for breast masses detection in mammography

GUERROUDJI Mohamed Amine
Telecom Division
Center for Development of Advanced Technologies (CDTA)
Baba Hassen, Algeria
Email: mguerroudji@cdta.dz

AOUACHE Mustapha
Telecom Division
Center for Development of Advanced Technologies (CDTA)
Baba Hassen, Algeria
Email: maouache@cdta.dz

***Abstract*—nowadays, medicine plays a vital role in our daily life. In addition, breast cancer research and computer-aided diagnosis (CAD) [1] are considered to be one of the most active disciplines and an extraordinary tool of assisted diagnosis to help physicians. This work is part of an effort to develop a (CAD) system for the detection of mini-MIAS data masses [2], which can be considered as the second opinion to the radiologist. The proposed concept based on the noise suppression by anisotropic filtering to emerge all possible clear spots to be masses through using an Alternating Sequential Filter (ASF). Objectively achieving thisby obtains firstly the ASF using a mathematical morphology to improve the mass contrast. Second, the segmentation approach considered here as a contribution and important task to segment the resulting spots image based geometric active contour models (Level set). Experimental results show that the proposed method improves and progresses significantly to successfully extractmass fromtheexaminedmini-MIASmammographydataset[2].**

Keywords—mammography; CAD; masses; Level set; Alternating Sequential Filter; anisotropic filtering; active contour.

I. INTRODUCTION

Recently, medical imaging (IM) is an extraordinary tool for assisting clinical diagnosis. IMs are the best way to quickly detect any type of injury and also offer new hope for a treatment for many diseases such as breast cancer. In fact, breast cancer is the leading cause of death in women [3], but it can also affect men with a much lower rate. Particular in Algeria, breast cancer is the first case reported; with 11,000 new cases per year at an advanced stage of pathology [4].The stage of the diagnosis is a key stage in the struggle againstthe breast cancer. It is also know that in early stages, the treatment is more effective. Consequently, one of the most important areas of scientific research in the detection and analysis of cancer, where the division of risk factors into three sections are the hormonal, genetic and environmental. In this case, mammography remains the essential reference technique for breast exploration, the most effective in the field of surveillance and early detection of breast cancer [5], According to radiologists, mass and calcification are parts of quiet calcium, and may appear in clusters (Micro calcification) or in cluster-shaped patterns. The growth of extra cells is usually non-cancerous but is an important indicator of breast cancer. If 80% of them are benign tumors, only 15% of breast tumors are malignant tumors, the condition being diagnosed by mammography [6]. Thus, in order to reduce the workload of radiologists, the design of a computer-assisted detection system (CAD) is based on a three-step flow of work:detection, analysisandclassification.Automateddetectionofbreastdiseases is always difficult, even for experienced radiologists. To date, some of the advantages of the algorithms described in the literature have been suggested to detect masses in the mammogram, whether benign or malignant. Among the most importantofthesemethodsarethosethatusetherepresentation of mammography based on improved contrast. The aimof this procedure is to enhance and improve the fragmentation of distinct structures and the discovery of blocks by alternating serial filtration of mathematical formation [7]. This paper at- tempts to introduce other improvements based on the pathway and mathematical morphological factors applied to different types of images to gray levels [6], [8], [10-11]. The latter provides improvements to traditional speedway methods to extract the desired masses. The application of medical image segmentation methods presentation of pathologies remains a field of research very wide. For this reason the use of theLevel set was largely documented in the literature of the medical imagery and several works were published on the segmentation of the masses in mammogram. One finds several techniques have been adopted for segmenting masses, suchas active contours [9], [12-14]. Efforts hasbeen made in other studies have been conducted on the image mammography for the local contrast enhancement for false positive reduction [15]. The main contribution of this work is the design of a new efficient segmentation method by fusion approaches for the detection of breast masses in the mini- MIAS mammography database [2]. The proposed method has been successful in achieving higher and accurate segmentation rates and the results obtained validate the superiority of our proposed approach over the advanced method [16-17]. This paper is organized into 4 sections: an introductioncoversthe review of breast pathology of interest, the motivation of research as well as the current segmentation method. Section 2 on the methodology contains the proposed detection method. The performance of the experimental simulation method is given in section 3. Concise conclusion and recommendations forfutureworkarepresentedinsection4.

II. PROPOSED DETECTIONMETHOD

Fig. 1 presents the proposed method for the detection of breast disease that helps improve and exposure masses in digital mammography. Here are the main steps conducted to achieve the proposed method. (1) Noise reduction by the anisotropic filter. (2) And will make an effort in improving the contrasts to distinguish the masses and the background using morphological Alternating Sequential Filter (ASF). In the third phase, the using a segmentation of the area ofinterest for the identification of mass and classification is the last step in a computer-assisted diagnostic system (CAD). It exploitsthe result of description (which itself exploits the result of segmentation) to be able to decide the pathological nature of themass,basedongeometricdeformablemodels(Levelset).

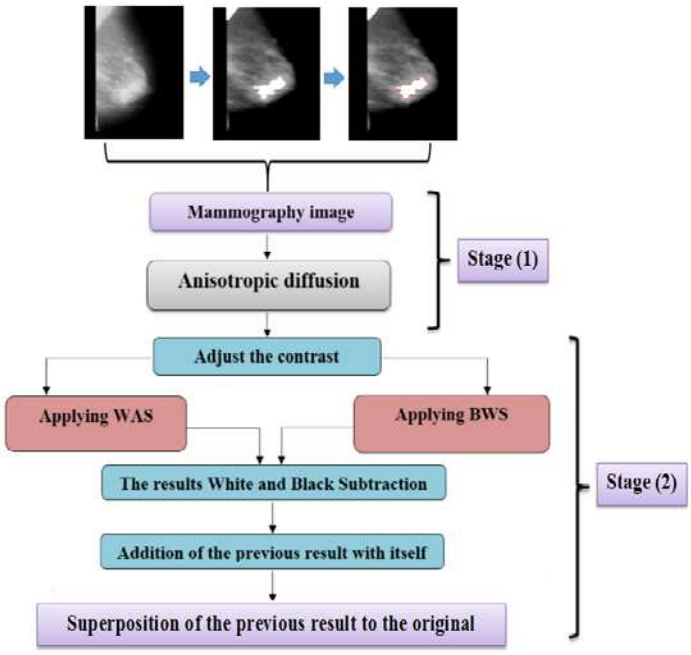

Figure 1. The proposed segmentation method by fusion approaches for masses in mammography.

A. Enhancementstage

Despite the efforts of the related work, the detection of mammary pathologies remains difficult. Thus, an additional research effort based on two main steps is examined to achieve the objective of the proposed method, as follows.

a) Step(1): Due to the small size and low intensityof the mass spots, designing a filter is a very difficult task. Here, the nonlinear anisotropic diffusion filter [18] has been applied to filter the noisy images and preserving the details and contours while filtering the homogeneous areas. The main objective pursued by the anisotropic diffusion is to filter the image by the reduction of the noise in the presented areas while avoiding the smoothing of the contours. Thus, the author in [18] modified the diffusion equation (eq.1) to achieve anisotropic diffusion based on, (1) Maximum homogenization of diffusion away from contours, and (2) Minimal diffusion on the level as ofcontours.

The heat diffusion equation:

$$\frac{du}{dt} = c.\Delta u = div\ (c.\nabla u) \qquad (1)$$

Modifying by [18]:

$$\frac{du}{dt} = div(g(|\nabla u|).\nabla u) \qquad (2)$$

With:
u: Signal / Image.
div : Divergence operator.
∇: Gradient Operator.
Δ: Laplace operator.
c :Coefficient gradient amplitude.
∇u : Gradient vector.

Where it is a decreasing function with $c(0)= 1$ and $\lim x \to \infty\, c(x) = 0$

Forexample:

$$c(x) = \frac{1}{\sqrt{1+x^2}} \qquad (3)$$

- Ifc=1,wefindtheequationofheat→diffusion.
- If c is weak, the broadcast is stopped which preserves the edges.

In [18] proposed the following two mailing functions:

$$g1(|\nabla u|) = e^{\frac{|\nabla u^2|}{c}} \qquad (4)$$

$$g1(|\nabla u|) = \frac{1}{1+\frac{|\nabla u|^2}{c}} \qquad (5)$$

It is clear that the anisotropic filter enhances the contrast of the contours with region smoothing and a partial reduction of the volume effect. Fig. 2 shows of the typical histogram of a mammogram. Clearly, we distinguish three different classes of the pixels[19]:

- Class1:thepixelsoflowofintensities.
- Class 2: the pixels having corresponding gray values within itself.
- Class 3: the pixels of high intensity, the large peak corresponding to the pectoral muscle, annotations and may be to breast lesions.

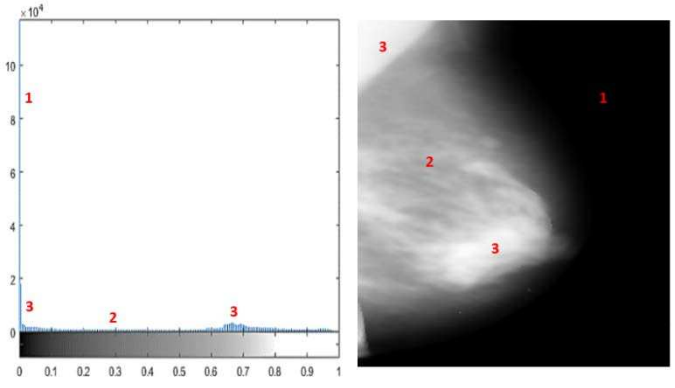

Figure 2. The typical histogram of a mammogram.

Fig. 3 shows the visual results when comparing the original mammography image before and after applying theanisotropic filter. It is clear and can easily be interpreted that the anisotropic filter accentuates the sharpness of the edges, the smoothareasandevendecreasestheeffectofpartialvolume.

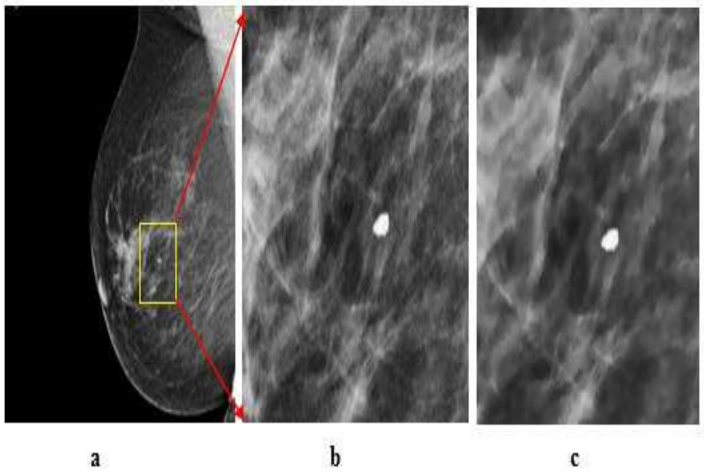

Figure 3. Visual results comparison of the: a) Original mammography image; *b)* before and (c) afterfiltering.

b) Step (2): Here, the detection of the target lesion was performed according to the sequential alternative filter (ASF) operator resulting from the mathematical morphology of [8], which allows keeping only these small structures. So, this approach was firstly adopted for mass detection using the ASF techniquetoimproveimagemammographyformassdetection. Then, the White Alternating Sequential (WAS) Filter givenas:

$$FAS_B(n) = O_n F_n \ldots\ldots O_2 F_2 O_1 F_1 \quad (6)$$

The Black Alternating Sequential (BAS) filter given as:

$$FAS_N(n) = F_n O_n \ldots\ldots F_2 O_2 F_1 O_1 \quad (7)$$

Where; $Oi$and Firespectively represent the opening and the family of the closures by a structuring element of similar shape and of increasingsize.

1) Segmentation method: The mass detection was achievedby a segmentation technique considered as a reference in the field of medical imaging for tumor or mass areas. In this paper, the original contribution is a mass segmentation method based on geometric active contours (level set). The geometric models suggested independently by [20] and [21] provide a solution to meet the limits of deformable parametric models (in particular for topological adaptation). Consequently, the changes of topology can be treated automatically. The mathematical form ofthelevelsetdefinedbyequation:

$$\frac{d\Phi}{dt} = f|\nabla\Phi| = (fint + fext)|\nabla\Phi| \quad (8)$$

Where $f$the force applied to the curve (surface) and $\Phi$is the function of the level set and $|\nabla\Phi|$it is the gradient of thefunctionΦ.Thisforcecanbebrokenupintotwoterms:

- An internal force $fint$: imposing a constraint of regularity of the curve (surface in 3D during the evolution.
- An external force $fext$: term attachment data (image data) for controlling the convergence of the shape of the shape model to the data.

III. EXPERIMENTAL RESULTS ANDDISCUSSION

In this work, the proposed method was tested using the mini-MIAS dataset from Mammography Image Analysis Society [2] to segment and illustrate primarily benign and malignant masses. A total of 83 images are examinedwith different mammary pathologies of the database mainly illustrate 36 benign masses and 47 malignant masses. The results are illustrated by the figure below (see Fig. 4): after the noise removal step (to reduce noise at themost)by the anisotropic diffusion filter, then we have moved to enhance contrast by applying these steps by mammography image [2], with a choice of structuring element used for the Alternating Sequential Filter corresponding to a disk with a sizeof4X4.
Notingthat,thisstudyconfirmstheperformance of the image mammography improvement by the Alternating Sequential Filter for the detection of masses. In the second partofexperimentalresults,theproposedsegmentationmethod has been implemented in the context of identifying the main mammography tissues and extracting the mass area (see Fig. 5). This will subsequently allow the calculation the mass characteristics in ordertoclassificationthatwillberegisteredinthedatabase.

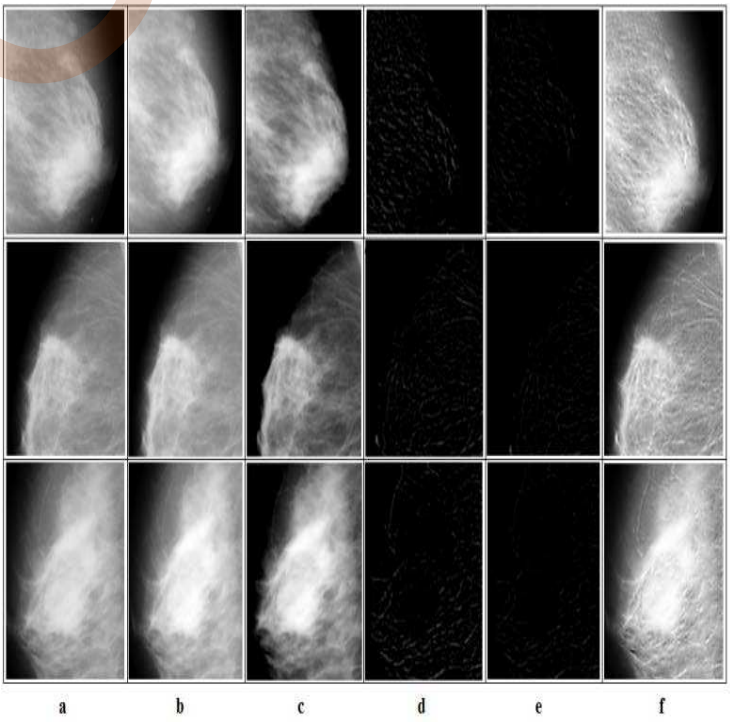

Figure 4. Illustrate the visualization results of the pre-process stagewith: a) Original mammography image; b) Noise suppression using anisotropic diffusion filter; c) Contrast adjustment; d) Subtraction results of WAS and BAS; e) Addition of the previous result with itself; f) Overlay of the previous process result with original image.

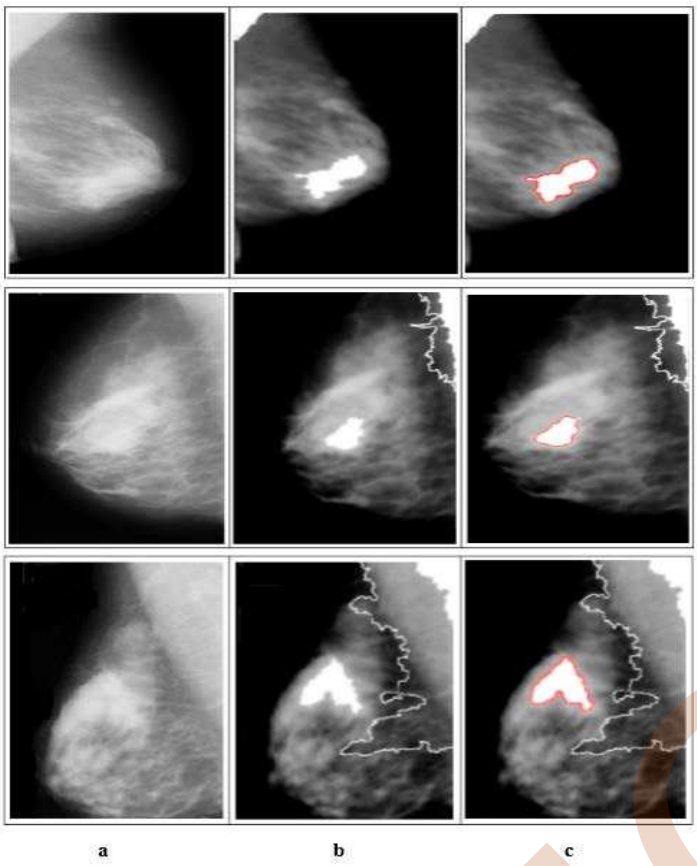

Figure 5. The results of the proposed algorithm for segmentation: a) Original mammography image after noise suppression; b) Enhancementmammography image; c) Detection of masses and segmentation of the mass by geometric deformable models (Levelset).

For performance comparison purposes our performance results with the performance results of mass detection studies in the literature. Through Receiver operating characteristic (ROC), where availability analysis and graphs are commonly used in medical decision making. The segmentation performance can be estimated by describing random errors (True positive; True negative; False positive; False negative), a measure of statistical changes(eq.9).

$$Accuracy = \frac{TP+TN}{TP+TN+FP+FN} \quad (9)$$

In addition, the obtained results show that by applying the proposed enhancement and segmentation the contour of mass, with compared other algorithms results cited in the literature (Table. I). The table summarizes the results of this work in terms of precision and shows the great performance of our approach.

TABLEI. Comparison of results obtained through our approach with other ones in theliterature.

Author	*Segmentation method*	*Database*	*Accuracy*
R. Rouhiet al [16]	Region growing algorithm	MIAS and DDSM	96.47 %
K. Burçin et al [17]	Otsu s´ algorithm	MIAS	93.2 %
Guerroudji et al	**Diffusion segmentation**	MIAS	97.09 %

IV. ICONCLUSION

The results clearly indicate that the proposed approach has achieved its goal of mass-detection mammography, in which the contrast enhancement step has the following advantages:
(1) Anisotropic scattering acts as a robust filter for additive noise suppression without affecting the pixels of the image mammography, and (2) an improved contrast making it easy to distinguish the masses from their background via sequential alternating white and black sequences. At the segmentation stage; deformable active contour models were successfully performed to extract masses from the resulting mammographic image, then a feature extraction process was examined to describe extracted regions of the images for classification and decision-making purposes. From the results obtained, the approach can easily and accurately detect the masses of mammography images with acceptable accuracy. Theproposed method is simple and suitable for other databases thatcan be easily implemented in the computer-assisted diagnosis of breastcancer.

ACKNOWLEDGEMENS

This work is supported in parts by the DGRSDT (Direction Générale de la Recherche Scientifique et du Développement Technologique), and CDTA (Centre de Développement des Technologies Avancées) via FNR (Fonds National de la Recherche), Algeria-(Project code : CAD-PACS 2019-2021).

REFERENCES

[1]B. Zheng, "Computer-Aided Diagnosis in Mammography Using Content Based Image Retrieval Approaches: Current Status and Future Perspectives", vol. 2, pp. 828-849, 2009.
[2] mini-MIAS. The mini-MIAS database of mammograms. http://peipa. essex.ac.uk/info/mias.htm, 2014. [Online].
[3] J. Mossi, A.Albiol,"Improving detection of clustered microcalcifications using morphological connected operators", In International Conference on Image Processing and Its Application on, pp. 498-501.1999.
[4] H. Maghreb,http://www.huffpostmaghreb.com/2015/04/05/cancer-sein-algérien 7007174.html,2015. [Online;].
[5] H. Zuckerman,"The role of mammography in the diagnosis of breast cancer. Breast cancer", diagnosis and treatment, pp. 152-172, 1987.
[6] C. Diaz-Huerta, E. Felipe- Riveron, L. Montao- Zetina,"Quantitative analysis of morphological techniques for automatic classification of micro-calcifications in digitized mammograms", Expert Systems with Applications Elsevier, vol. 16, pp. 7361-7369, 2014.
[7] R. Nanayakkara, Y. Yapa, P. Hevawithana, P. Wijekoon, "Automatic Breast Boundary Segmentation of Mammograms", InternationalJournal of Soft Computing and Engineering (IJSCE), vol. 1, pp. 2231-2307, 2015.
[8] J.Herredsvela, T. Gulsrud, K.Engan,"Detection of circumscribed masses in mammograms using morphological segmentation", Proceedings of SPIE - The International Society for Optical Engineering, April 2005.
[9] T. Stoji, B.Reljin,"Enhancement of microcalcificationsin digitized mammograms: Multiracial and mathematical morphology approach. FME Transactions, vol. 1, 1-9, 2010.
[10] M. Duarte, A. Alvarenga, C. Azevedo, M.Calas, A. Infantosi, W. Pereira,"Segmenting mammographicmicrocalcifications using a semiautomatic procedure based on Otsu's method morphological filters", Braz. J. Biomed. Eng, vol. 29, pp. 377-388,2013.
[11] C. laudia, D. Huerta, M.Edgardo, F. Rivern, L. Montao-Zetina,"Evaluation and Selection of Morphological Procedures for Automatic Detection of Micro-calcifications in Mammography Images", Iberoamerican Congress on Pattern Recognition CIARP 2012: Progress in Pattern Recognition, Image Analysis, Computer Vision, and Applications, pp. 575-582, Springer, 2012.
[12] C. Liu, C. Tsai, J. Liu, C. Yu, S. Yub,"A pectoral muscle segmentation algorithm for digital mammograms using Otsu thresholding and multiple regression analysis", Computers and Mathematics with Applications, vol. 1, pp. 1100-1107, 2012.
[13] N.Arikidis, A. Karajaliou, S. Skiadopoulos, P. Korfiatis,E.Likaki, G. Panayiotakis, "Size-adaptedmicrocalcification segmentation in mammography utilizing scale-space signatures", Compute. Med. Imaging Graph,vol. 34, 487-493, 2010.
[14] X. Liu, X. Xu, J. Liu, J. Tang, "Mass Classification with Level Set Segmentation and Shape Analysis for Breast Cancer Diagnosis Using Mammography", International Conference on Intelligent Computing ICIC 2011 on Advanced Intelligent Computing Theories and Applications. With Aspects of Artificial Intelligence, pp. 630-637, Springer, 2011.
[15] G. Junior, S. Vieira da Rocha, M. Gattass, A. Silva, and A. Cardoso de Paiva,"A mass classification using spatial diversity approaches in mammography images for false positive reduction", Expert Systems with Applications, vol. 40: 7534-7543, 2013.
[16] R. Rouhi, M. Jafari, S. Kasaei, P.Keshavarzian, "Benign and malignant breast tumors classification based on region growing and CNN segmentation", Expert Systems with Applications, vol. 3, pp. 990-1002, 2015.
[17] K. Burçin, V. Nabiyev, K.Turhan," A novel automatic suspicious mass regions identification using HavrdaCharvat entropy and Otsu's N thresholding", Computer Methods and Programs in Biomedicine, vol. 3, pp. 349-360, 2014.
[18] P. Perona, J. Malik, "ScalespaceedgedetectionusingAnisotropic diffusion", Pattern Anal, IEEE Transactions, vol. 12, pp. 629-639, 1990.
[19] I. HADJIDJ, "Analyse des Images Mammographiques pour laide la Détection du Cancer du Sein", Magister memory in biomedicalelectronics, aboubekrbelkaiduniversity, tlemcen Algeria 2011.
[20] V. Caselles, F. Catt, T. Coll, F. Dibos, "A geometric model for active contours in image processing", Numer. Math, vol.1, pp. 131, 1993.
[21] R. Malladi, J. Sethian, B. Vemuri, "Shape modeling with front propagation: A level set approach", Pattern Anal. Machine Intell, IEEE Transactions on, vol. 2, pp. 158-175, 1995.

Bearing Faults Diagnosis Based on Variational Mode Decomposition

A. Guedidi, A. Guettaf, W. Laala, A. Arif
Departement of Genie Electrique, Université Mohammed Khider,

Biskra 07000, Algérie
e-mail: s.guedidi@univ-biskra.dz
abderrazak.guettaf@univ-biskra.dz
aelectrot@yahoo.fr
widad.laala@univ-biskra.dz

A. J. M. Cardoso *Senior Member, IEEE*,
CISE - Electromechatronic Systems Research Centre, Universidade da Beira Interior
Calçada Fonte do Lameiro, P – 6201-001 Covilhã, Portugal
e-mail: ajmcardoso@ieee.org

Abstract — **Bearings are the most frequently used components in the vast majority of rotating machines. Their running quality influences the working performance of equipment in a large extent Consequently, the monitoring of this component is a key point to increase the reliability, security and avoiding serious damage in machine. Vibration signal is widely used for diagnosis which is considered as a powerful tool for detecting mechanical defects. In this paper, a rolling bearing fault-diagnosis method based on an improved variational mode decomposition (VMD) is proposed. The processing methodology of bearing diagnosis starts with the decomposition of the vibration signal by improved VMD technique into a set of intrinsic mode functions (IMFs). According to the aim of fault diagnosis, the selected fault indicator is calculated from the energy related to the most sensitive IMFs to the bearing defect. The proposed approach is then validated using data from the bearing data center of Case Western Reserve University. The results prove the efficient of this method to discriminating from four conditions of rolling bearing, namely, normal bearing and three different types of defected bearings: outer race, inner race, and ball.**

Index Terms —
Fault diagnosis, rolling element bearing, variational mode decomposition.

I. INTRODUCTION

In large varieties of industrial applications, increasing the reliability and availability of electrical systems is highly required. Sudden failure of electrical systems in applications such as aviation, electric traction, power plants or industrial production plants can lead to unscheduled and unwanted shutdowns that can cause damage to surrounding equipment in the same way than the staff.

In several industrial fields, the induction motor (IM) is the most used. This is due to its simplicity of construction, mass power, robustness and it's relatively low cost. According to an IM reliability survey, 45~55% of motor faults are related to bearings [1]. Which are particularly intended to support the rotating structures and facilitate their rotation [2]. Thereby, the fault detection and degradation in bearings is a research challenge where important breakthroughs are developed from signal processing techniques [3].

Typically, the vibration signal is rich with essential information on mechanical defects including rolling defects. The major challenge is to effectively separate valuable features representing fault information adequately, especially for non-stationary and noisy signatures [4]. For this reason, vibration analysis has been widely used in bearings fault diagnostic. Traditionally, the vibration detection techniques used for signal processing are realized in time [5, 6], frequency [7, 8, 9] or time-frequency domain [10, 11]. Among the most familiar approaches, in time domain, are root mean square and statistics features such as kurtosis, skewness and crest factor. It was shown that the load variation did not affect the kurtosis and crest factor values; these static characteristics can therefore be considered as a significant indicator of impulsive defects [2]. For stationary vibration signals, traditional frequency domain based on Fast Fourier Transform (FFT) method has been proved to be useful. However, due to the complex internal structure and noisy working environment of the rotating machines, the vibration signals have always been non-stationary. Hence, time frequency techniques are more appropriate to overcome this limitation. Among several time-frequency methods [13, 14, 15], the wavelet transform (WT), Hilbert Huang transform (HHT) and recently, the Variational mode decomposition (VMD) are used in bearing fault diagnosis. HHT combine the empirical mode decomposition (EMD) with the Hilbert transform to obtain both the instantaneous amplitude and frequency of each intrinsic mode function (IMF). Empirical mode decomposition (EMD) finds wide applications in the ball bearing fault diagnosis [16]. However, mode mixing and boundary distortion of intrinsic mode function affects the correctness of the decomposition result. Also, it has a strong self-adaptability which prevents us from extracting a signal relating to a previously fixed frequency band. The last

disadvantage can be surmounted by the use of Wavelet transform (WT). A WT, known as an effective tool to analyze the non-stationary signal, has good local time-frequency properties. It can provide time domain and frequency domain information by inner production between the analyzed signal and a predetermined wavelet basis. WT methods can be considered as a band-pass filter with an adjustable window size. Through the choice of the mother wavelet and different approximation scales. However, the WT is strictly limited by the selection of basic function unlike the VMD, which does not require any predefined basis function or mother wavelet.

This paper presents a contribution of rolling bearing faults diagnosis. This approach is rest on the use of an improved VMD to decompose the collected vibration signals into sets of IMFs. Then, the most sensible component to the bearing defect will be selected to extract more characteristics of fault information.

II. BACKGROUND

A. Brief introduction of VMD

Recently, a new quasi-orthogonal time-frequency signal processing technique called variational mode decomposition (VMD) was introduced by Dragomiretskiy and Zosso. VMD decompose the given signal into a collection of sub-signals (IMFs) by solving a contrained variationnal problem, where each IMF is regarded as an amplitude-modulated and frequency modulated (AM-FM) signal. It has band-limited and around a center pulsation *wk*. The constrained variational problem is formulated as follows [17]:

$$\min_{\{u_k\}\{\omega_k\}} \left\{ \sum_{k=1}^{K} \left\| \partial_t \left[\left(\delta(t) + \frac{j}{\pi t} \right) * u_k(t) \right] e^{-j\omega_k t} \right\|_2^2 \right\} \quad (1)$$

$$\text{s.t} \qquad \sum_{k=1}^{K} u_k(t) = f(t) \quad (2)$$

To solve the constrained variational problem, the augmented Lagrangian is introduced and the non-constrained variational problem is gotten by:

$$L\left(\{u_k\},\{\omega_k\},\lambda\right) = \alpha \left\{ \sum_{k=1}^{K} \left\| \partial_t \left[\left(\delta(t) + \frac{j}{\pi t} \right) * u_k(t) \right] e^{-j\omega_k t} \right\|_2^2 \right\} + \left\| f(t) - \sum_{k=1}^{K} u_k(t) \right\|_2^2 + \left\langle \lambda(t), f(t) - \sum_{k=1}^{K} u_k(t) \right\rangle \quad (3)$$

where α is balancing parameter of the data-fidelity constraint, and λ (*t*) are Lagrange multipliers

The iterative formulas of u_k and ω_k are deduced with the alternate direction method of multipliers (ADMM) as follows:

$$u_k^{n+1}(\omega) = \frac{f(\omega) - \sum_{i<k} u_k^{n+1}(\omega) - \sum_{i>k} u_k^{n}(\omega) + \frac{\lambda^n(\omega)}{2}}{1 + 2\alpha(\omega - \omega_k^n)^2} \quad (4)$$

$$\omega_k^{n+1} = \frac{\int_0^\infty \omega \left| u_k^{n+1}(\omega) \right|^2 d\omega}{\int_0^\infty \left| u_k^{n+1}(\omega) \right|^2 d\omega} \quad (5)$$

The main procedures of VMD can be summarized as follows:
Step 1: Initialize $u_k^1, \omega_k^1, \lambda_k$ and maximum iterative time N;
Step 2: Update u_k ω_k according to (4) and (5);
Step 3: Update λ based on

$$\lambda^{n+1}(\omega) = \lambda^n(\omega) + \tau\left(f(\omega) - \sum_k u^{n+1}(\omega) \right)$$

Step 3: If $\sum_k \frac{\left\| u_k^{n+1} - u_k^n \right\|_2^2}{\left\| u_k^n \right\|_2^2} < \varepsilon$ stop iterating otherwise return to step 2.

III. FAULT DIAGNOSTIC FOR ROLLING ELEMENT BEARINGKGROUND

The process methodology of fault bearing diagnosis is illustrated in Fig 1. The signal pre-processing starts with the decomposition of the vibration signal by VMD. Then, the sensitive IMFs which contain the most significant fault information are extracted. A statistical feature based on the energy moment of the selected IMFs is calculated. Finally, this fault feature is used as indicator of severity default .

Fig. 1. The Bearing fault diagnosis process methodology.

A. Experimental setup

The vibration data investigated in this work were collected from the rolling element bearing test rig obtained from the case Western Reserve University bearing data center (Case Western University). The signals are collected at the sampling rate of 12 kHz for four different load conditions(0, 1, 2 and 3 horse power) via accelerometers mounted at the drive end and fan end of the induction motor housing coupled to the load that can be varied within the operating range of motor . Four types of model were tested. The healthy condition and the defective conditions in three different places as follows: the inner race fault, the outer race fault and rolling ball fault. Single point faults (cyclic defect) were artificially induced by using an electro-discharge machining. The size of fault, for the inner, outer race and ball, is 0.007 and 0.021inch.

B. Signal task processing

Vibration analysis is a powerful tool for detecting faulty bearings. The vibration signals contain a lot of information about the operating state of a machine. However, they are often disturbed by uncertain impulses and random noises that can infect useful information. In addition, they are considered as non-stationary and non-linear signals [2]. Hence, bearing

fault diagnosis based on vibration signals require to be analyzed by robust signal processing methods.

In order to improving the accuracy and reliability of the bearing fault diagnosis, it is necessary to select the appropriate signal diagnosis which contain the significant information. For this aim, FFT (fast Fourier transform) is firstly used to study the bearing ball condition for different load levels (0, 2 and 3 hp). Fig 2 and Fig 3 show the vibration spectrum under several defects (inner, outer and ball faults) whose severity is 0.007 inches. By analyzing these vibration spectrums, it has been found that the affected frequency bandwidth can be easily localized at high frequency (resonance frequency). Thus, in term of energy, all information relating to the state's ball bearing (healthy or defect) is contained in this range. In this paper, the vibration signals are segmented by VMD. The goal of the segmentation is to obtain IMFs which represent the original signal in resonance band frequencies. Then, the most sensible IMFs are selected as diagnostic signals.

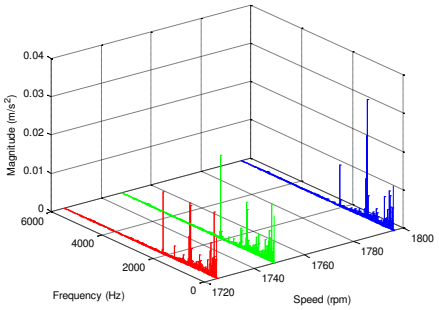

(a)

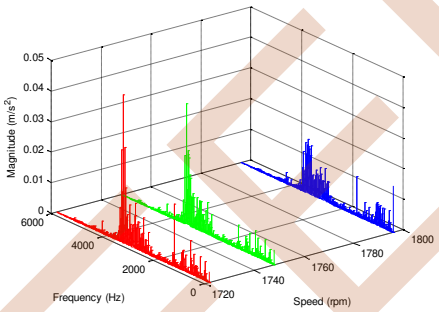

(b)

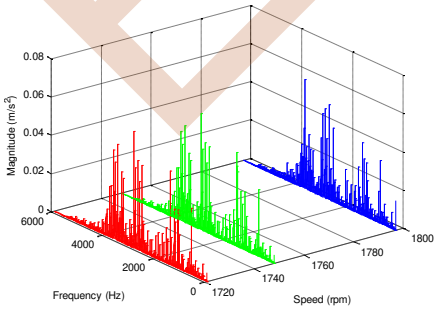

(c)

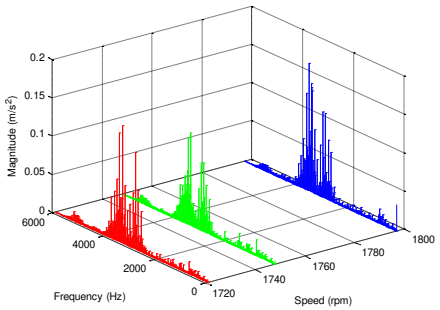

(d)

Fig.2: Vibration spectrum: (a) healthy bearing, (b) bearing with defect ball, c) bearing with defect inner race, (d) bearing with outer race.

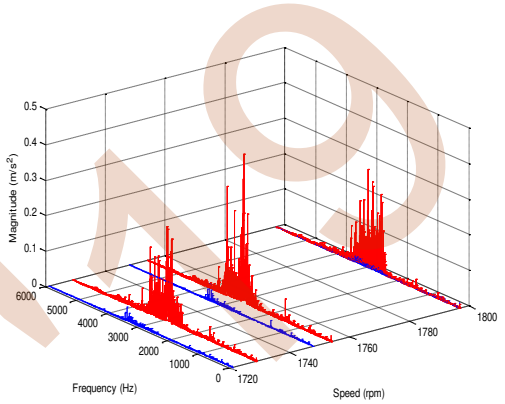

(a)

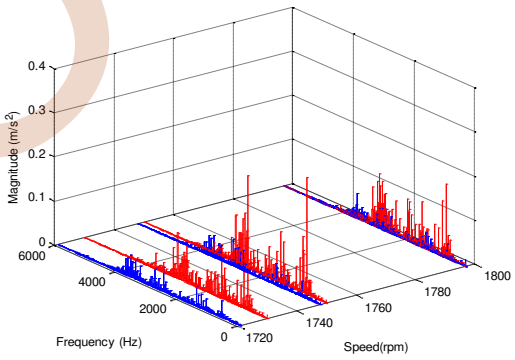

(b)

Fig. 3. Vibration spectrum (blue curve: 0.007 inch, red curve: 0.028 inch) (a) bearing with defect ball, (b) bearing with defect inner race.

It has been shown that the amplitude associated to the resonance frequency band located at [2000-4000] Hz is not clearly sensible to the load but it is more affected by the defect type. In other words, the value of the frequencies related to this range is load independent.

C. Improvement of VMD

VMD is a powerful tool for a signal decomposition, it is based on non-recursive calculations which is make it more efficient in computing algorithm than the EMD, WT and LMD. However, VMD has a major disadvantage that limits to a large extent the ability to extract features. VMD does not

have the decomposition termination condition as EMD, it is necessary to set the decomposition components *k* in advance before starting VMD calculation. In theory, the value of k is dependent on the number of frequency components included in the signal. If the value of k is too small, the data will be under-segmented, and some components will be contained in other modalities. If the value K is too large, problems such as modal copying will occur [18, 19 xiao17, xu18]. Therefore, the design of an optimal VMD should be focused on how to obtain the optimal value of key parameter of the VMD. In this paper, we are inspired by the work developed in [shi16] to determine this parameter.In order to identify the effective frequency components contained in the signal, we are exploited the FFT's spectral envelope to identify the optimal value K according to the frequency components. The steps of this method are resumed as follows [20]:

- Implement the Fourier transform of the vibration signal,
- Detect the local maxia and minima of the amplitude spectrum,
- Generate the envelope curve
- Calculate the threshold by using (6)
- Filter out those frequency components that have smaller magnitude than the threshold value through setting them to be zero.
- Identify the optimum number of modes from the resultant envelope curve.
- Then, calculate the signal correlation coefficient ratio of the modes by using (7)
- Finally, the value number of modes is determinate.

The threshold is determinate as:

$$threhold = rA_h \tag{6}$$

where A_h is the maximum magnitude that can be observed from the spectrum, *r* is a ratio used for controlling the level of the threshold.

The signal correlation coefficient ratio of the modes is given by:

$$R(n) = \sum_{k=1}^{n} corr(m_k, x) \tag{7}$$

Figures (4-6) represent respectively the frequency spectrum and the associated envelope curve, the trimmed envelope curve, and the resultant correlation coefficient ratio evolution. from the results, it is clear that the number of modes can be set to 4.

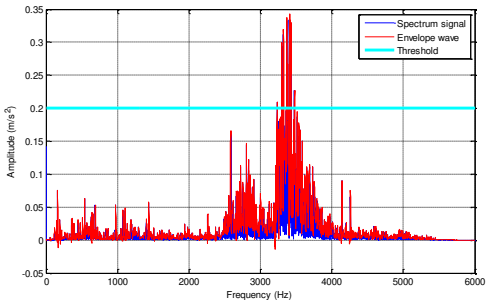

Fig 4: Envelope curve

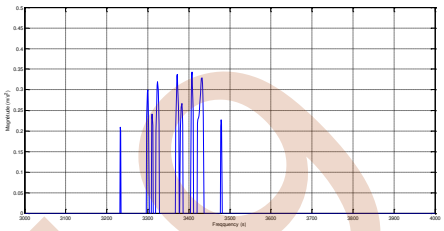

Fig. 5: Filtered envelope curve

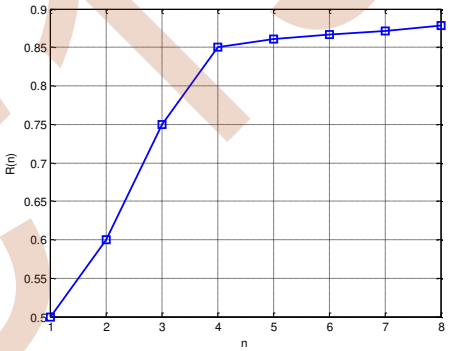

Fig.6: Evolution of the correlation coefficient ratio

As it shown in the Figures (7, 8, 9and 10), when we set the number of mode at fourth value it gives a satisfying results. The VMD method is then applied to the collected vibration signals, and the fault-related information may be decomposed into several IMF components. How to select the sensitive IMFs is important for constructing a robust fault diagnosis method. In this work, a coefficient correlation given by (8) is adopted to select the sensitive IMFs:

$$r_{u_i,x} = \left\| \frac{\sum_{t=1}^{n} \left(x(t) - \bar{x}\right)\left(u_i(t) - \bar{u}_i\right)}{\sigma_{u_i}\sigma_x} \right\| \tag{8}$$

where u_i is the *i*th decomposed IMF; σ_{u_i}, σ_x are the deviations of u_i and $x(t)$; $\bar{x}$ and $\bar{u}$ are the mean values of u_i and $x(t)$; respectively.

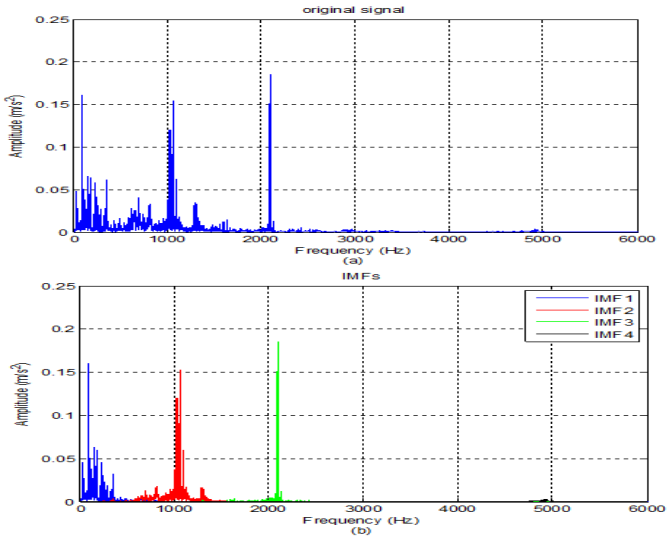

Fig. 7. Spectrum of original signal and each mode components (Healthy bearing)

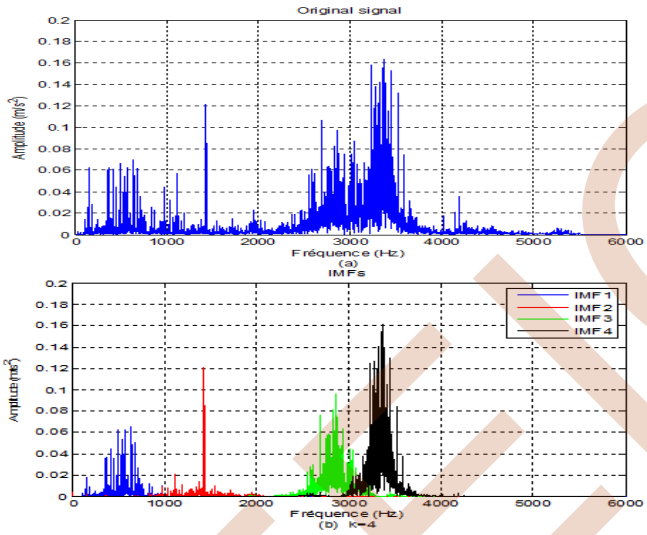

Fig. 8. Spectrum of original signal and each mode components (Ball defect)

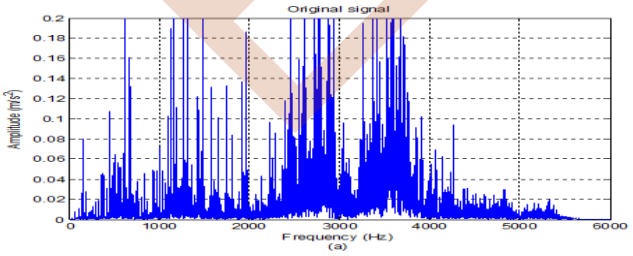

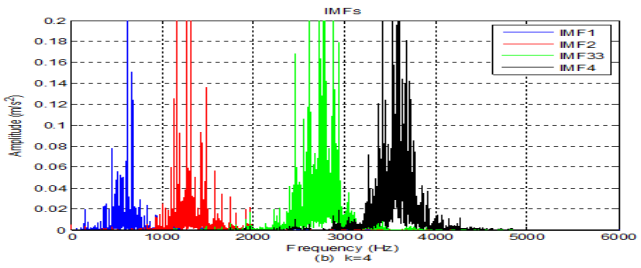

Fig. 9 Spectrum of original signal and each mode components (Inner race defect)

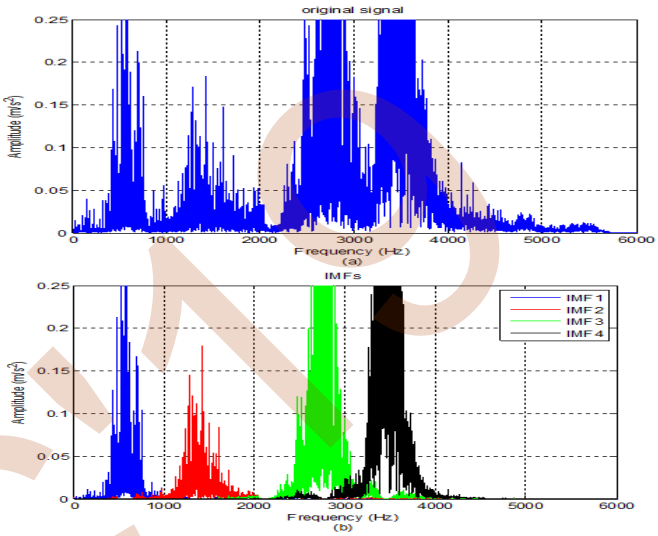

Fig. 10: Spectrum of original signal and each mode components (Outer race defect)

An evaluation criterion, based on the energy related to selected IMFs, is described below:

$$FI = \frac{1}{N_{imf}} \sum_{j=1}^{N_{imf}} \sqrt{\frac{1}{N_l} \sum_{i=1}^{N_l} (u_j)^2 [i]} \qquad (9)$$

where N_{imf} and N_l are the total number of selected IMFs and the data length of the jth selected IMF, respectively.

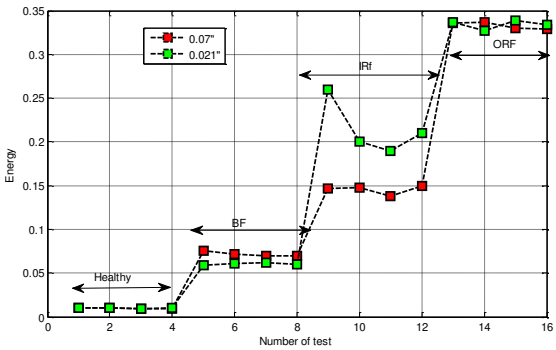

Fig. 11. Evolution of IF according to different default

Figure 11 illustrates the evolution of the feature FI according to the defect severity fault (DSF) (with 0.007 and 0.021 inch

as diameter size) at different state, healthy, BF, IRF, ORF (ball, inner race and outer race faults) and under different load (0, 1, 2, 3 Hp). The results demonstrate that the data derived from this criterion can be classified in four separate sets related to healthy and faulty behavior. Thus, it is clear that this new distinctive feature, extracted under different DSF, is an efficient indicator to discriminate between healthy and faulty bearing states. Also, it allows locating the fault type.

IV Conclusion

In this paper, a bearing fault diagnosis method based on VMD has been proposed. The experimental result obtained from the vibration signal spectrum shows the existence of the resonance frequency band located at [2000-4000] Hz which is not clearly sensible to the load but it is more affected by the defect type. Using VMD method, the raw vibration signal can be decomposed into a series of IMFs. Therefore, we can reveal the vibration modes embedded in the raw signal. Finally, a statistical feature extracted from the most sensitive IMFs has been selected as default indicator which can discriminate between healthy and faulty bearing states. The experimental results show the effectiveness of this approach to ensure a reliable and precise fault diagnosis process.

Acknowledgment

This work was supported by the European Regional Development Fund (ERDF) through the Operational Programme for Competitiveness and Internationalization (COMPETE 2020), under Project POCI-01-0145-FEDER-029494, and by National Funds through the FCT - Portuguese Foundation for Science and Technology, under Projects PTDC/EEI-EEE/29494/2017 and UID/EEA/04131/2019.

Reference

[1] W. Deng, S. Zhang, H. Zhao and X. Yang, "A novel fault diagnosis method based on integrating empirical wavelet transform and fuzzy entropy for motor bearing," IEEE Access, vol. 6, pp. 35042 - 35056, 2018.

[2] M. Diaz, P. Henríquez, M. A. Ferrer, J. B. Alonso, G. Pirlo and D. Impedovo, "Novel method for early bearing fault detection based on dynamic stability measure," in Proc. 2015 IEEE International Carnahan Conference on Security Technology (ICCST), pp. 43-47.

[3] M. Akuruyejo, S. Kowontan and J. B. Ali, "A data-driven approach based health indicator for remaining useful life estimation of bearings," in Proc. 2017 IEEE International Conference on Sciences and Techniques of Automatic Control and Computer Engineering (STA), 284-289.

[4] R. Yan, R. X.Gao and X. Chenc, "Wavelets for fault diagnosis of rotary machines: A review with applications," Signal Processing, vol. 96, pp. 1-15, 2014.

[5] D. Siegel, C. Ly and J. Lee, "Methodology and Framework for Predicting Helicopter Rolling Element Bearing Failure," IEEE Transactions on Reliability, vol. 61, pp. 846 - 857, 2012.

[6] M. Pineda-Sanchez, R. Puche-Panadero, M. Riera-Guasp, J. Perez-Cruz, J. Roger-Folch, J. Pons-Llinares, V. Climente-Alarcon and J. A. Antonino-Daviu, "Application of the teager-kaiser energy operator in bearing fault diagnosis," IEEE Transactions on Energy Conversion, vol. 28, pp. 1036 - 1044, 2013.

[7] V.K.Rai and A.R.Mohanty, "Bearing fault diagnosis using FFT of intrinsic mode functions in Hilbert Huang transform," Mechanical Systems and Signal Processing, vol. 21, pp. 2607-2615, 2007.

[8] Z. Fana and Huaizhong, "A hybrid approach for fault diagnosis of planetary bearings using an internal vibration sensor," Measurement, vol. 64, pp. 71-80, 2015.

[9] R. B.Randall, "A history of cepstrum analysis and its application to mechanical problems," Mechanical Systems and Signal Processing, vol. 97, pp. 3-19, 2017.

[10] P. Shakya and A. K. Makarand S.Kulkarni, "Bearing diagnosis based on Mahalanobis–Taguchi–Gram–Schmidt method," Journal of Sound and Vibration , vol. 337, pp. 342-362, 2015.

[11] N. HarishChandra and A.S.Sekhar, "Fault detection in rotor bearing systems using time frequency techniques," Mechanical Systems and Signal Processing, vol. 72, pp. 105-133, 2016.

[12] P. Henriquez, J. B. Alonso, M. A. Ferrer and C. M. Travieso, "Review of Automatic Fault Diagnosis Systems Using Audio and Vibration Signals," IEEE Transactions on Systems, Man, and Cybernetics: Systems, vol. 44, pp. 642 - 652, 2014.

[13] X. Zhang, H. Liu, H. Zhang and Q. Miao, "Bearing fault diagnosis based on variational mode decomposition and stochastic resonance," in Proc. 2018 IEEE International Conference on Prognostics and Health Management (ICPHM), pp 1-6.

[14] J. Jiang and W. Liu, "VMD and HMM based rolling bearing fault diagnosis," in Proc.2018 IEEE International Instrumentation and Measurement Technology Conference (I2MTC), pp 1-6.

[15] F. Jiang, Z. Zhu and W. Li, "An Improved VMD With Empirical Mode Decomposition and Its Application in Incipient Fault Detection of Rolling Bearing," IEEE Access, vol. 6, pp. 44483 - 44493, 2018.

[16] S. Liu, Y. Sun and L. Zhang, "A Novel Fault Diagnosis Method Based on Noise-Assisted MEMD and Functional Neural Fuzzy Network for Rolling Element Bearings," IEEE Access, vol. 6, pp. 27048 - 27068, 2018.

[17] Dragomiretskiy K and Zosso D 2014 Variational mode decomposition IEEE Trans. Signal Process,vol.62,pp**.** 531–44, 2016

[18] *Xiao Huaishuo, J. Wei, H. Liu, Q. Li , Yalin Shi, T. Zhang,"* Identification method for power system lowfrequency", oscillations based on improvedVMD and Teager–Kaiser energy operator," *IET Gener. Transm. Distrib.*, 2017, Vol. 11 Iss. 16, pp. 4096-4103

[19] B. Xu, F. Zhou, H. Li et al," Early fault feature extraction of bearings based on Teager energy operator and optimal VMD,". ISA Transactions (2018),

[20] Pu Shi, Wenxian Yang,''Precise Feature Extraction from Wind Turbine Condition Monitoring Signals by using Optimized Variational Mode Decomposition," IET Renewable Power Generation (2016)

AUTHORS' INFORMATION

Asma Guedidi was born in Biskra , on January 21, 1994, she is a PHD student in the Department of Electrical Engineering at Biskra University. She received the Renewable Energy master degrees in 2016 from the University of Biskra. Her research interests include condition monitoring and fault diagnosis in power electronics systems and ac machine

Abderrazak Guettaf was born in Biskra, Algeria on November 28th, 1977. He received the Engineer and Magister diploma and PHD degree in electrical engineering from University of Biskra in 2002, 2005 and 2013 respectively. His research interests are focused on design and fault analysis of switched reluctance and permanent synchronous machines.

Antonio J. Marquês Cardoso (S'98,A'95, SM'99) was born in Coimbra, Portugal, in 1962.He received the Electrical Engineering diploma, The Dr. Eng. degree and the Habilitation degree, all from the University of Coimbra, Coimbra, Portugal, in 1985 1955 and 2008, respectively. From 1985 until 2011 he was with the University of Coimbra, Coimbra, Portugal, Where he was Director of the Electrical Machines Laboratory. Since 2011 he has been with the University of Beira Interior (UBI), Covilha, Portugal, where he is a

full Professor at the Department of Electromechanical Engineering and Director of CISE Electromechatronic Systems Research Centre(http://cise.ubi.pt). From September 2013 to january 2014 he was Vice-Rector of UBI. His teaching interests cover electrical rotating machines, transformers, and maintenance of electromechatronic systems and his research interests are focused on condition monitoring and diagnostics of electrical machines and drives. He is the author of a book entitled Fault Diagnosis in Three-Phase Induction Motors (Coimbra, Portugal: Coimbra Editora,1991), (in Portuguese) and about 350 papers published in technical journals and conference proceedings

Widad Laala was born in Biskra Algeria. She received the Electrical Engineering magisterial diploma and PHD degrees from the University of Biskra in 2005,2016 respecrively. Her research interests include condition monitoring and fault diagnosis. She is an author or coauthor of several and international papers. She has been is an Assistant Professor with the University of Biskra since 200.

Ali Arif was born in Biskra, Algeria on June 19th, 1967. He received the Engineer, MSc diploma and PhD degree in electrical engineering from the University of Biskra, Algeria, in 1992, 2003 and 2013, respectively. His research interests are related to Renewable Energies; Photovoltaic, Supercapacitor, Fuel Cell and Power management of electric vehicle. Currently, Dr. Arif is an assistant professor with the University of Biskra, Algeria.

Electromagneticmodeling planar inductor for integration in a buck DC- DC

Senhadji/nisrine 1st
Dept. of electrotechnical
University of sciences and technology of Oran
Mohamed Boudiaf ,US TO
Algeria, Oran
senhadji_n@yahoo.fr

Hamid/azzedinde 2nd
dept. of technology
Nourbchir university center
Algeria, El bayadh

***Abstract*—The work presented in this article is a contribution to the work carried out in the framework of power electronics, the main objective is to see the electrical and magnetic behavior of a planar inductor with PCB substrate embedded in a buck DC-DC converter. is an electromagnetic study in which we will determine the shape of the electric field lines and the magnetic field**.

I. INTRODUCTION

The evolution of planar technologiesin the field of power electronics continues to grow. However, if we take an example of a DC-DC step-down converter, there does a problem of space between the various components constitute it Among these Passive Components, the planar inductance is mentioned in particular, and several research works (1) (2) (3) (4) have turned towards the integration and miniaturization of this type of inductance.In this work, we will focus on the electromagnetic study of a planar, spiral, square topology inductor, integrated on a PCB substrate (5) (6), (7) for introducing in a DC - DC converter. The manufacture of this type of inductance is very difficult, because a single error is sufficient for the poor quality of the product and, therefore, again, it is a very complex and very difficult job.The purpose of integrating and miniaturizing passive components is to reduce the size of the component in order to solve the congestion problem and reduce the cost of this component.

II. PRESENTATION OF THE TOPOLOGY OF MICRO COIL

The studied topologies are presented in Figure 1. It is a square spiral topology.

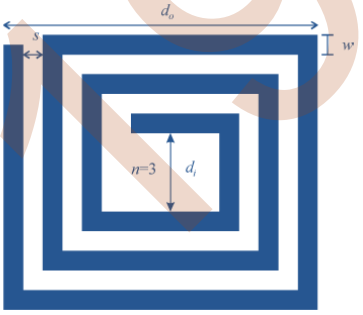

Figure 1. square planar inductor

III. PRESENTATION OF THE PARMETERS FOR OUR INDUCTANCE:

The spiral planar inductor is geometrically described by seven parameters (Figure 1). We have the width w, the thickness of the conductors t, the spacing s, the total length of the conductor lt, also the number of turns n, Its outer and inner diameter, must be chosen in order to optimize the ratio between the inductance value and the area occupied on the circuit.We present in this board the different parameters of the planar inductor in which we want to integrate on buck converter. The parameters of our planar inductor are summarized in this table.

TABLE I. GEOMETRICAL PARAMETERS USED FOR SIMULATION

Geometrical Parameters	
Parameters	*Values*
Number of turns n	3
Inner diameter Din (mm)	1
External diameter Dout (mm)	1 0
WidthW(mm)	0.9
Thickness of the conductor t (µm)	35
Permeabilitydu PCBFR4 μ_{rPcb}	1
Permittivity du PCBFR4εr_{Pcb}[8]	4.7
Substrate thickness e (mm)	0.3
	0

IV. DIMENSIONING OF THE PLANAR INDUCTOR

A. Presentation of the micro-converter parameters

We present in this board the different parameters of the converter in which we want to integrate our fixed-width micro coil. The parameters who we have chosen for our micro-converter which our micro inductance is integrated are:

Input voltage: 5 V;
Output voltage: 2.5 V;
Output power: 1 W;
Operating frequency: $100*10^7$Hz

TABLE II. BUCK CONVERTER PARAMETERS

Ve	*VS*	*Imax(A)*	*Is(A)*	*P(watt)*	*S(mm)*
5	2.5	0.8	0.4	1	0.54

a) Calculation of thecyclic ratio

the cyclic ratio is calculated by the following expression $\alpha = \frac{Vs}{Ve} = 0.5$ (1)

B. The schématic of our Buck DC-DC converter

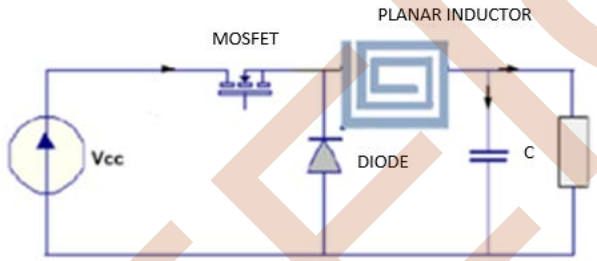

Figure 2.Diagram of buck DC-DC Converter

The buck DC-DC converter in power electronics is important and several works have been done in this area (10)(11). Figure.2 shows the converter in which we want to integrate our micro coil on a PCB substrate. A step-down is governing by the following equations:

$$\Delta I_L = \frac{\alpha.Ve.(1-\alpha)}{L.f} \quad (2)$$

$$\Delta I_L = 0.8A$$

$$L = 4.037 * 10^{-8}\ H$$

C. *Analytical expressions for diensionnement*

In the literature there are several analytic expressions to size the spiral planar inductance (12) (13) (14) among these expressions we quote (Wheeler-Mohan-Brayan, Grover).we made the difference between the two Mohan and wheeler methods. From the specifications and based on the analytical methods of Wheeler, Mohan, we will size the planar spiral inductance under a design objective with a minimum of losses and compare the value of the inductance between the two methods.

- Wheeler's expression

$$L_{mw} = K_1 \mu \frac{n^2 d_m}{1+K_2 b} \quad (3)$$

Table III. WHELEER PARAMETERS

Geometry	K_1	K_2
Square	2.34	2.75

- Mohan's expression

$$L_{Mh} = \frac{\mu_0 * n^2 * d_{avg} * c_1}{2} * \left(\ln\left[\frac{c_2}{\rho}\right] + c_3 * \rho + c_4 * \rho^2\right) \quad (4)$$

Table IV. MOHAN PARAMETERS

Geometry	C_1	C_2	C_3	C_4
Square	1.27	2.07	0.18	0.13

withthere

$$d_{avg} = \frac{d_{out} + d_{in}}{2} = 5.5mm \quad (5)$$

$$\rho = \frac{d_{out} - d_{in}}{d_{out} + d_{in}} = 0.82 \quad (6)$$

V. RESULTS OF SIMULATION

We notice that the inductance increases with the number of turns for the two methods. TheWheleer method, which gives a good approximation of the value of the inductance.

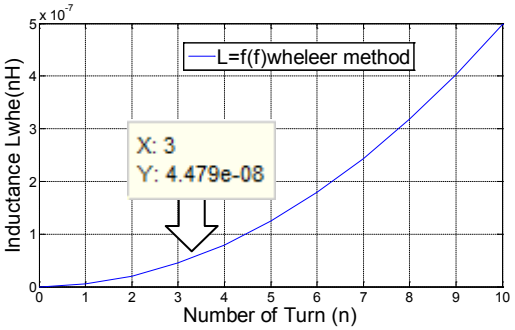

Figure 3. inductance according the number turn (Wheleer)

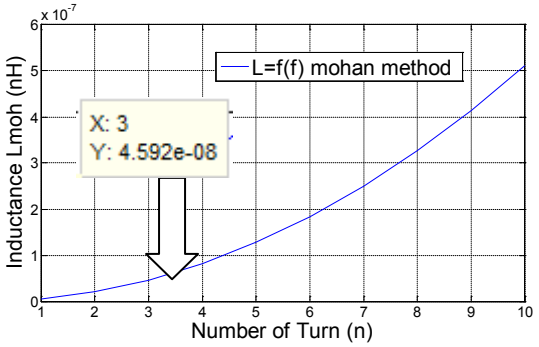

Figure 4. Inductance according the number turn (Mohan)

- The calculation of the width and thickness aredepends on the skin thickness, the skin effect is anelectromagnetic phenomenon

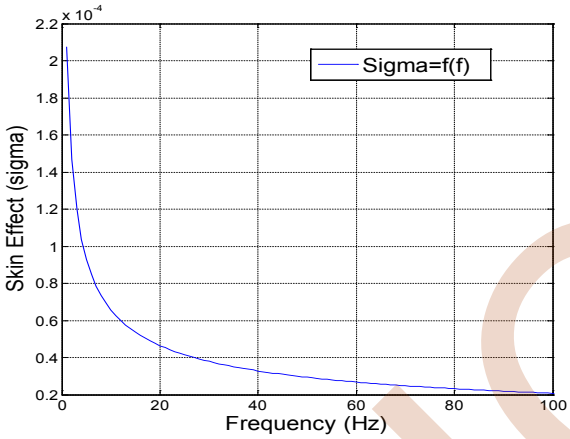

Figure 4. Results of Skin Effect according frequency

VI. ELCTRICAL PARAMETERS OF OUR MICRO COIL

1)Characteristic of copper

Thickness of conductor Material: Cu: t = 35 µm
The skin thickness: δ = 92.8 µm
Resistivity ρcu = 1.710-8Ω. m
Relative permeability: $\mu_r = 1$

2) Characteristic of sbstrate

Insulating Material: PCB

Relative PermettivityEr=4.7

VII. ELECTROMAGNETIC MODELISLATION OF OUR INDUCTOR

A. Schematization of the prototype

The prototyping of the coil requires several steps in order to schematize it in the COMSOL software:

1) STEP1: BUILD THE PROTOTYPE GEOMETRYAND DEFINE THE MATERIALS

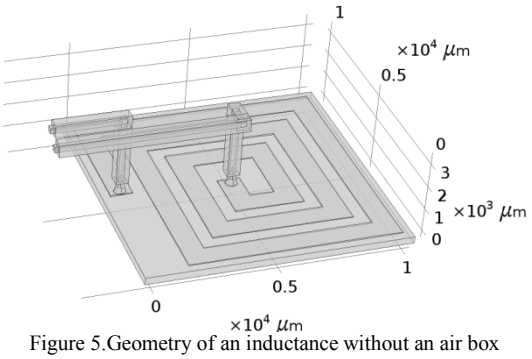

Figure 5.Geometry of an inductance without an air box

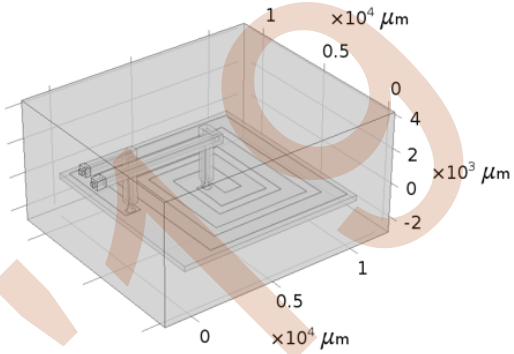

Figure 6. Geometry of an inductance with an air box

STEP2: GENERATE THE MESH

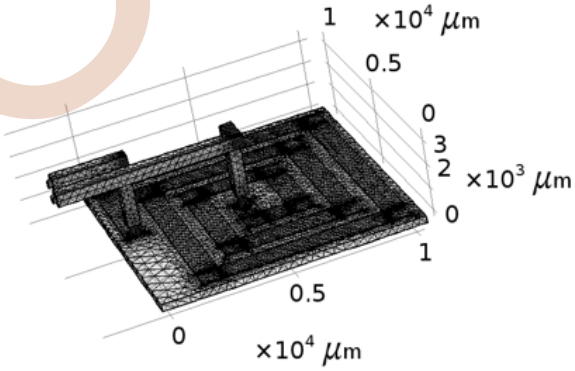

Figure7. Mesh of square spiral planaronductorwithout air box

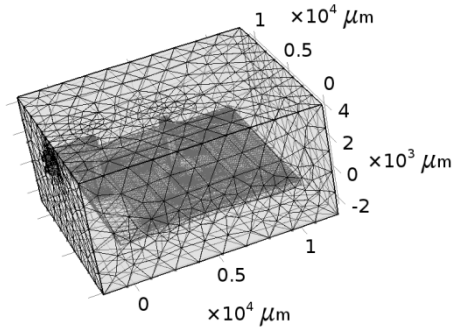

Figure 8. Mesh of square spiral planar inductorwith air box

B. Electromagnetic simulation of prototypes integrated coil:

1)We simulated the magnetic behavior of the inductor: in a frequency domain at a frequency f = 100 Hz., the results of the electromagnetic simulation :

*a) Density of the current :*According to the simulation of the density increases inside the corners of the planar inductor which is due to the peack effect.

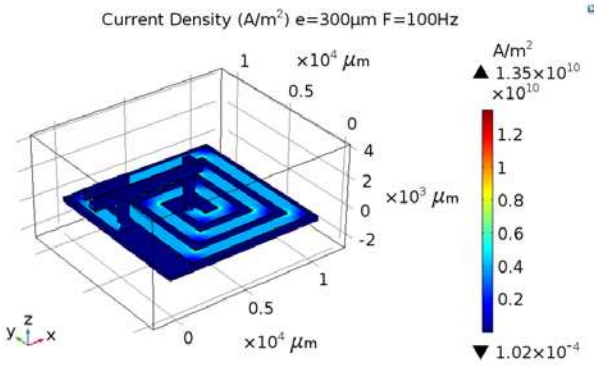

Figure 9. The Current densityof the planar inductor

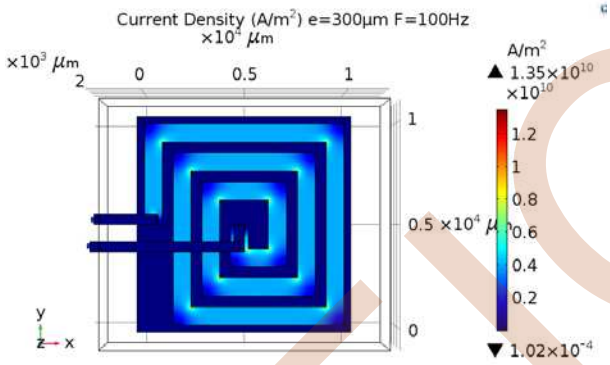

Figure 10. Front view of TheCurrent density of the planar inductor

b) Electrical field

The electric field module is more important at the input of the electric current, its value decreases as one moves away from the entrance

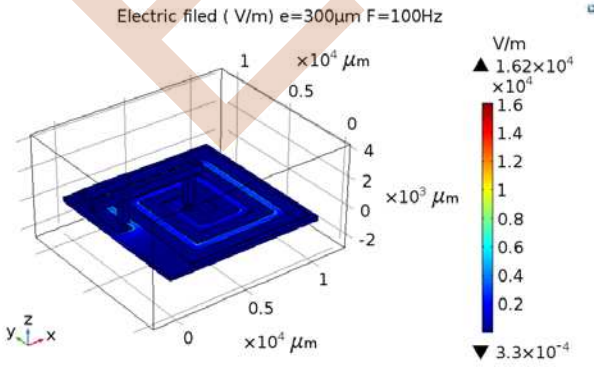

Figure 11.The electricfield ofthe planar inductor

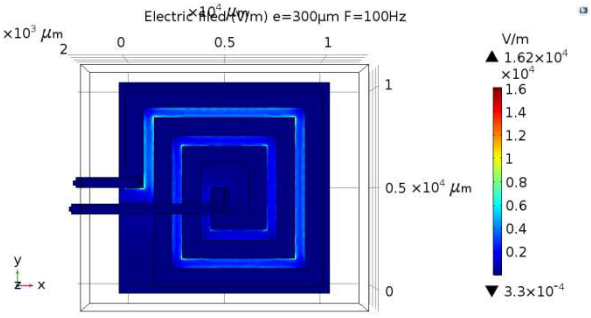

Figure 12. Front view The electricfield ofthe planar inductor

c) Electrical potential and density of magnetic flux

The figure confirms the considerations that have been taken concerning the boundary conditions, according to the current lines, the magnetic field is more important in the middle of the planar inductor

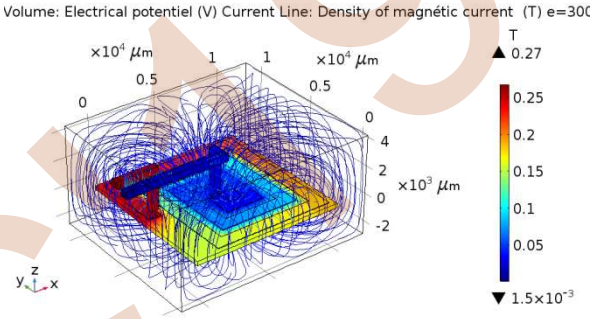

Figure 13. The electrical potential and the magnetic flux density oftheplanar inductor

d)*Electric Potential*

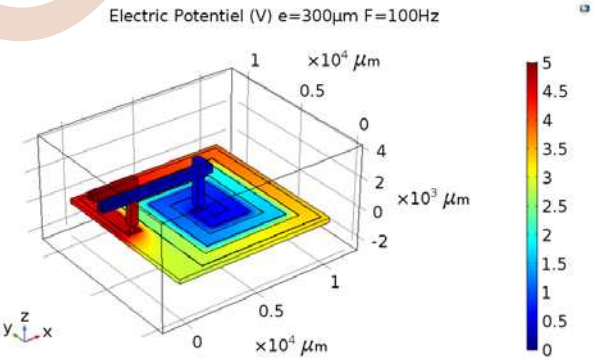

Figure14. The electricpotential ofthe planar inductor

*e) magnetic filed:*According to the simulation of the magnetic field increases inside the corners of the planar inductor which is due to the peak effect.

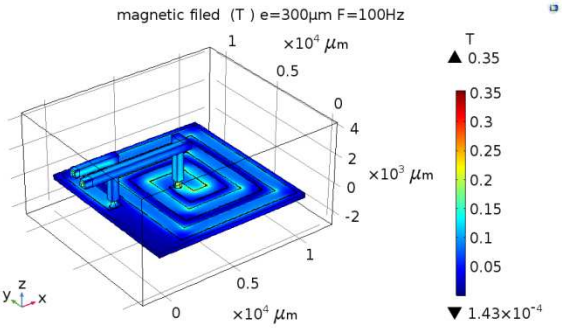

Figure 15. The emagnetic field ofthe planar inductor

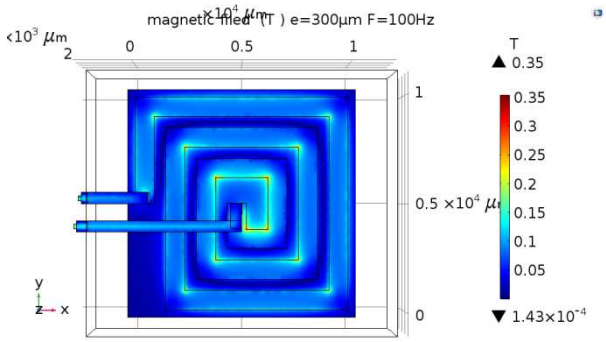

Figure 16. frontvue of The emagnetic field of the planar inductor

2) Augmentation of the frequency: we have varied the value of the frequency by taking two values [2e4 et 3e7]

we notice a drop in the potential due to the resistance of the planar conductor

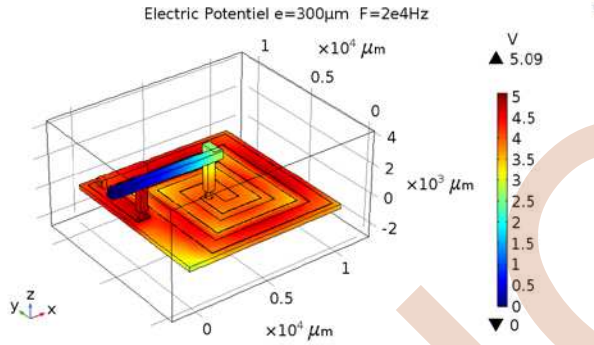

Figure 17. The electrical potential for the frequence 2e4Hz

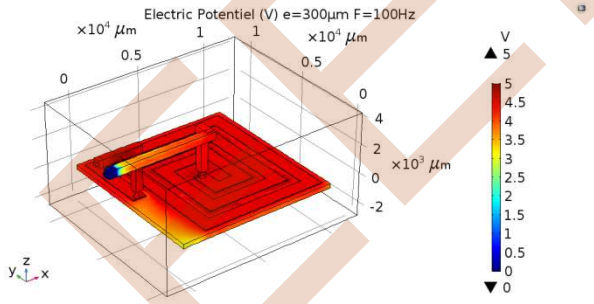

Figure 18. The electrical potential for the frequency 3e7Hz

VI. CONCLUSION

The aim of our work, was to make a electromagnetic modeling of fixed-width square-type spiral micro-inductance topologies, on a PCB-FR4 substrate who is is a passive component used in many electronic circuits such as power electronics switching power supplies). Thisplanar inductor integrated in DC buck converter DC-DC, this planar inductor topology, was realized, characterized and designed at LAPLACE laboratory of Toulouse.this contribution enters to the context of the integration and miniaturization of passive circuits including planar inductor on a PCB substrate. We have investigated the electromagnetic behavior of this planar inductance after having dimensioned it in order to integrate it into buck converter.

REFERENCES

[1] A. Désiré, ''Contribution à la réalisation d'une micro-inductance planaire ," Thèse de doctorat, Université Jean Monnet, Saint Etiene,pp.177, Novembre2010

[2] B. H. Mahamat, ''Modélisation des inductances planaires intégrées''. These de doctorat 2014

[3] B.H Mahamat., Yaya D.D., Youssouf M.K., S. Capraro, J.P Chatelon, A.Siblini, A.Désiré, J.J Rousseau, ''Inductances planaires intégrées à couches magnétiques : Conception – Fabrication –Caractérisation-Modelisation'', symposium de génie éléctrique, cachan, France2014

[4] C. Wang''Determining Dielectric Constant and Loss Tangent in FR-4''. UMR EMC, Laboratory Dept. of Electrical & Computer Engineering1870 Miner Circle,University of Missouri –RollaRolla, [MO 65409-0040, UMR EMC Laboratory Technical Report: TR00-1-041, 2000]

[5] C. Patrick Yue, S. Simon Wong, ''Physical modeling of spiral inductors on silicon",IEEE Transa.Elect. Dev, Vol. 47, No. 3, 2000

[6] A. B. Islam, S. K. Islam, F. S. Tulip , ''Design and Optimization of Printed Circuit Board Inductors for Wireless Power Transfert System''. Department of Electrical Engineering and Computer Science, University of Tennessee, Knoxville, USA, 2012

[7] D. D. Yaya,''Conception,réalisation et caractérisation d'inductancesplanairesà couches magnétiques''These de doctorat Université Jean Monnet - Saint-Etienne,pp .57, 2013

[8] G. Hérault, D. Labrousse, A. Mercier,S. Lefebvre ,''Intégration de circuit magnétique dans le PCB dédié à un convertisseur PFC''. symposium de génie ElectriqueSGE EF-EPF-MGE , GRENOBLE, France,SATIE, CNRS, ENS Cachan, Cnam, Université Paris -Saclay, 61 av. Président Wilson, 94230 Cachan, France2016

[9] O.Bushueva, ''Conception, réalisation et caracterisation d'inductances et de transformateurs tridimensionnels pour applications RF et microondes''. Physique des Hautes Energies,Université Paul Sabatier Toulouse- France, 2016

[10] O.Deleage ''Conception réalisation et mise en œuvre d'un micro-convertisseur intégré pour la conversion DC/DC'',These de doctorat, 2009

[11] S. Musunuri P.L. ''Optimization Issues for Fully-Integrated CMOS DC-DC Converters'',Chapman University of Illinois at Urbana-Champaign1406 W. Green St.Urbana, IL 61801 USA doi: 10.1109/IAS.2002.1042782 2002

[12] T.S. Johan ''Electromagnetic Design Optimization Tool for Resonant Integrated Spiral Planar Power Passives (ISP3)''. IEEE trans . power elect, vol. 20, no. 4, 2005

[13] K.Mbaitelbe,''nductance dans son environnement : caractérisation desinductances planaires intégrées dans les conditionsd'utilisation de l'électronique de puissance'',April 2019

[15] S. A. Kenari, B. A. Ganji,S. S.-Amiri,''Design and analysis of a high quality factor multipath spiral inductor'', Microsystem Technologies, Springer Nature 2018

Design of Tri_band Pass Filter using Complementary Split Ring Resonators Defected Ground Structure (CSRRs-DGS)

Mohammed MOULAY
Stic Laboratory, Department of Electrical Engineering
Faculty of sciences and Technology, Mascara University
Mascara, Algeria
moulaymed_dz@hotmail.com

Mehadji ABRI
Stic Laboratory, Department of Telecommunication
Faculty of Technology, University of Tlemcen
Tlemcen, Algeria
abrim2002@yahoo.fr

Hadjira ABRI BADAOUI
Stic Laboratory, Department of Telecommunication
Faculty of Technology, University of Tlemcen
Tlemcen, Algeria
elnbh@yahoo.fr

***Abstract*— In this paper, new dual-band and tri-band microstrip bandpass filter has been proposed by using complementary split ring resonator (CSRR). The proposed filter is realized by etching the CSRRs in the ground plane beneath a microstrip filter composed of two taper and open stub separated by simple microstrip lines. The CSRR offers the possibility of designing multi-band filters with a small size and simple structure. The CSRR as DGS can generate one passband. one transmission zeros are created to improve the selectivity of the proposed passband filter and isolation between the generated passbands. Design is simulated using ADS/Momentum and EM Simulation software (CST)and compared with HFSS Ansoft software. The simulated results show that the proposed tri-band BPF has three passbands centered at 2.69, 4.89 and 6.69 GHz with fractional bandwidth of 21.85%, 11.36% and 1.44%, respectively.**

Keywords*— Defected ground structures (DGS), CSRR, Dual band, triple band.

I. INTRODUCTION

In modern wireless communication application operating at multiband frequencies, new challenges have been presented to design and produce miniature components with high-quality. The dual and tri-band microstrip bandpass filter (BPF) with minimum insertion and enhanced selectivity are highly desirable. Extensive research works and different techniques have been introduced and reported in the literatures to meet these requirements such as stepped impedance resonator (SIR), stub loaded resonator (SLR), split ring resonator (SRR) and Geometry and defected ground structure (DGS).

Numerous filter designs for dual-bands have been recently investigated employing various shapes of defective ground planes [1]. Applying defective ground structures is found to be simple and effective. A dual wideband bandpass filter is designed in [2] by using the modified extended composite right/left-handed transmission line (ECRLH-TL) based on CSRR loaded on the ground plane. Girdhari Chaudhary et al. proposed a Dual-Band Bandpass Filter using DGS with controllable second passband, with the help of a defected ground structure (DGS) transmission line and varactor diodes, the second passband is achieved by varying the characteristic impedance of the shunt open stub of stub loaded resonator (SLR) [3]. Dual-band filter achieved by combining two different pass-bands by using open loop ring resonator (OLRR) and defected stepped impedance resonator (DSIR) [4]. In [5][6], the tri-band response is achieved by the SIR and defected ground structure (DGS) resonator. In another approaches, the compact multi-band filter has been achieved using complementary split-ring resonators (CSRRs) and defective ground structure (DGS) [7][8][9]. Three notch band are obtained in [10] by using FMRR with CSRR and the interdigital couple on the top, and etching the DGS in the ground plane. In this paper, a compact triple-band BPF is proposed. The design uses a complementary square double split ring resonator as a DGS, with two taper and open stub in the extremity and by a simple transmission line above the FR4 substrate to obtain the multi bands LPF design. As a proof of concept, the filter is designed and simulated for three different cases, with Dumbbell DGS, with and without CSRR. This results in more compact microstrip BPFs with dual pass bands and multi-band. two resonant band are attributed to the structure, while the others is a result of the embedded CSRR structure in the filter ground plane. The proposed BPF filters are successfully designed, simulated, on a FR-4, and it can be optimized by electromagnetic simulation software's.

II. FILTER DESIGN AND EQUIVALENT CIRCUIT

In this section a microstrip Dual-band bandpass filter is first designed constituted of two symmetrical tapers and open stub with same dimensions separated with a simple transmission lines. The design is based on accurate equivalent circuit model. The equivalent circuit applied to the Dual-band bandpass filter is presented and shown in figure 1.

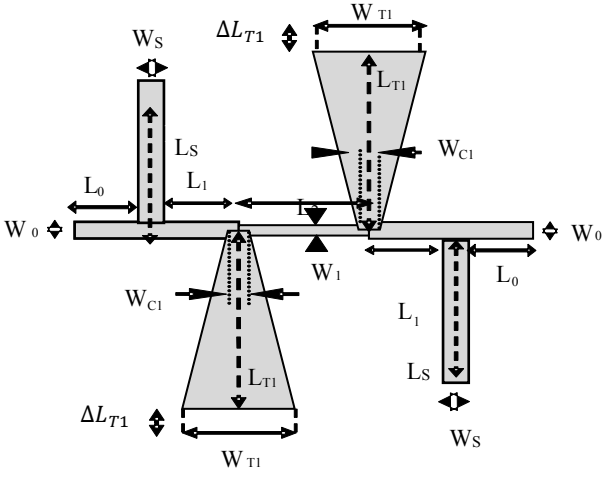

(a)

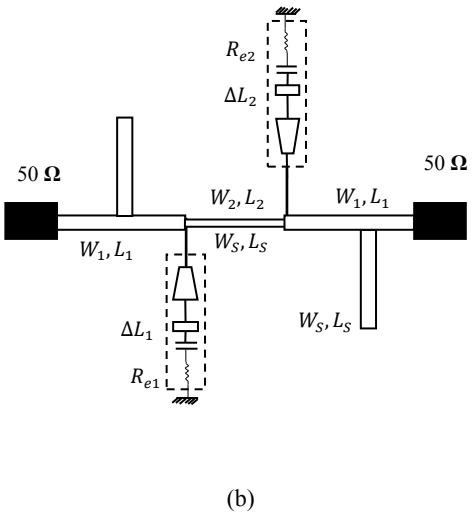

(b)

Fig 1. (a) the geometry of the proposed LPF filter. (b) Equivalent circuit model of the LPF.

Because of edge effects, the microstrip filter is greater than its physical dimensions. This is shown in Figure. 1 (b) where the size of both symmetrical tapers of the filter along its length was extended on each end by a distance ΔL_T , which is a function of dielectric constant and effective ε_{re} ratio of width W_{T1} on the thickness h.
The wavelength in the corresponding lines is given by:

$$\lambda_g = \frac{\lambda_0}{\sqrt{\varepsilon_{re}}} \quad (1)$$

Where ε_r relative dielectric constant, ε_{re}, effective dielectric constant, λ_0 wavelength in free space.
An approximate relationship very popular and convenient for the extension of the normal length is given by equation (2) [11] [12].

$$\frac{\Delta L_T}{h} = 0.412 \frac{(\varepsilon_{re}+0.3)\left(\frac{W_T}{h}+0.264\right)}{(\varepsilon_{re}-0.258)\left(\frac{W_T}{h}+0.8\right)} \quad (2)$$

Since the length of two tapers constituting the filter were extended by of each side, the length of the filter is now:

$$L_{eff} = L + 2\Delta L \quad (3)$$

The effective width of the filter is given by the following formula:

$$W_{T1} = \frac{1}{2f_r\sqrt{\mu_0\varepsilon_0}}\sqrt{\frac{2}{\varepsilon_r+1}} = \frac{v_0}{2f_r}\sqrt{\frac{2}{\varepsilon_r+1}} \quad (4)$$

The actual length of the filter can now be determined and is given by the following formula:

$$L_T = \frac{1}{2f_r\sqrt{\varepsilon_{re}}\sqrt{\mu_0\varepsilon_0}} - \Delta L_T \quad (5)$$

III. BAND-PASS FILTER DESIGN PROCEDURE BASED ON CSRR-DGS

This CSRR-DGS are obtained by cutting from the ground plane of the filter. CSSR consists of two square rings where the inner and outer slots are separated by metal strip. Presence of CSSR in the ground plane creates negative permittivity instead of negative permeability near the resonance frequency. CSRR has been successfully applied to the narrow band filters and diplexers with compact dimensions [13] [14].

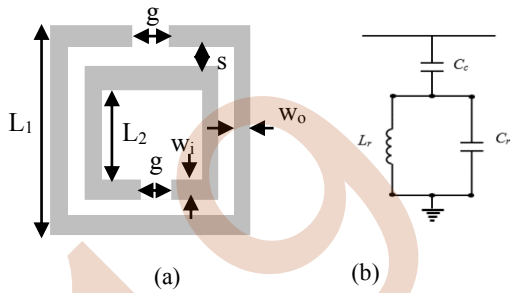

Fig. 2. (a) CSRR DGS and (b) its equivalent circuit.

The topology of CSRR DGS is shown in Figure 2 (a). From the equivalent circuit of CSRR DGS, shown in Figure 2 (b), we can get the position of the transmission zero. This is given by the frequency that nulls the shunt impedance as follows:

$$f_Z = \frac{1}{2\pi\sqrt{L_r(C_r + C_c)}}$$

IV. SIMULATION RESULTS

To design the different proposed pass bands filter without and with CSRR DGS, we have taken FR4 substrate having **εr** = 4.3 and height 1.54 mm, loss tangent (tan**δ**) = 0.018 and thickness of copper = 0.035 mm.

A. DUAL-BAND BANDPASS FILTER WITHOUT DEFECTED GROUND STRUCTURE

The filter structure, depicted in Figure 3 with no CSRR-DGS, has been modelled and analyzed at the design frequency, using ADS/Momentum and compared with the commercially available EM simulator, CST Microwave Studio. The structure exhibits a simple design with total size is 39.79 * 59.63 mm^2.

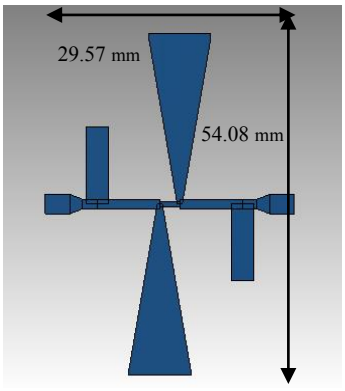

Fig. 3. Layout of the LPF without DGS.

The geometric parameters of the proposed structure are presented in the following

TABLE I. GEOMETRIC PARAMETERS VALUES OF THE BPF

W_{T1}, W_{T2}	W_{C1}, W_{C2}	L_{T1}, L_{T2}	L_0	L_1	W_0	L_s	W_s
9.91 mm	0.81 mm	25.82 mm	4.94 mm	*8.87* mm	3 mm	11.92 mm	3.58 mm

The responses of the dual-band filter obtained by moments methods and finite integration technique, respectively, are illustrated in Figure 4.

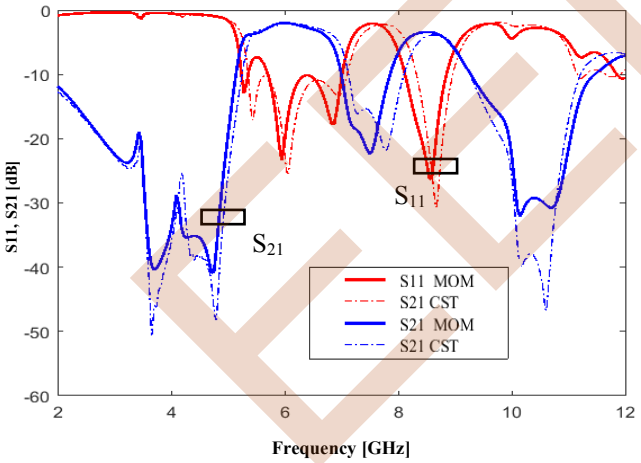

Fig. 4. Frequency response of a Dual-band bandpass filter without CSRR-DGS.

B. TRIPLE PASS BAND FILTER WITH CSRR DGS

After obtaining satisfactory dual band performance from the first design, four CSRR DGSs with same size were integrated with the BPF. The proposed triple-band bandpass filter is shown in Figure 5. The corresponding simulated results of return loss and transmission responses offered by this multi band pass filters are shown in Figure. 6. The same dimension of the filter previously studied are kept. The physical dimensions of the CSRR are obtained as width L1 = 10 mm as the length of outer loop, L2 = 6 mm as the length of inner loop, wo = 1 mm as the width of inner loop, wi = 1 mm as the width of outer loop d = 1 mm as gap between two loops and g = 1 mm as gap in loop. S=1 mm as spacing between the two loops. CSRRs etched in the ground plane or conductor strip of a planar transmission media, such as microstrip or coplanar waveguide (CPW), provide a negative effective permittivity to the structure. and thus a transmission zero (TZ) can be created.

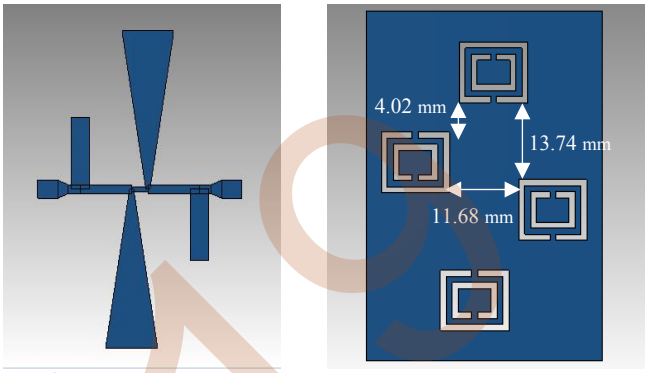

Fig.5. Final modified filter (a) top layer dimensions and (b) bottom layer dimensions.

Figure 6 shown the Frequency responses simulated by CST MW Studio and compared with HFSS Software.

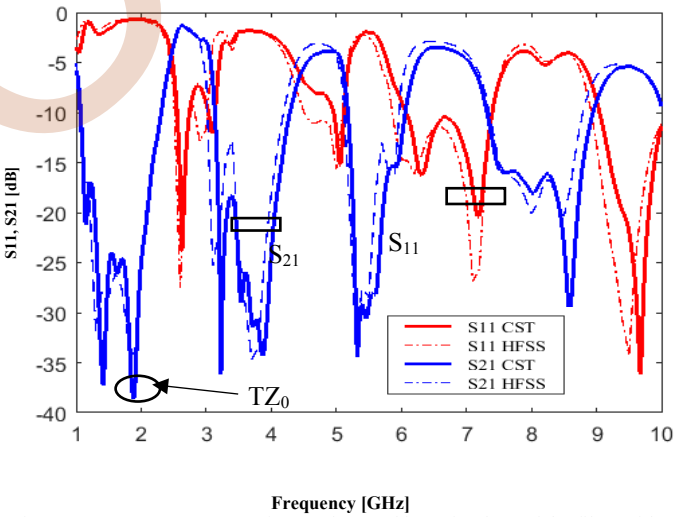

Fig. 6. Frequency responses of return loss and insertion loss of the filter with CSRR DGS.

As shown in figure 6, the CSRRs DGS cause the appearance of one lower resonant band. the two upper resonant bands which is attributed by the first dual band structure are slightly shifted. There is no such a resonant band associated with the response of the filter with non-defected ground plane. A tri-band BPF which centers at 2.69, 4.89 and 6.69 GHz with fractional bandwidth of 21.85%, 11.36% and 1.44%, respectively, is also presented. The tri-band BPF has the same miniature circuit size as the dual-band BPF. In addition, the TZ is generated at 1.89 GHz. The rejection has reached 35 dB. The simulated group delay shown in the figure 7 is less than 16 ns in the three passbands.

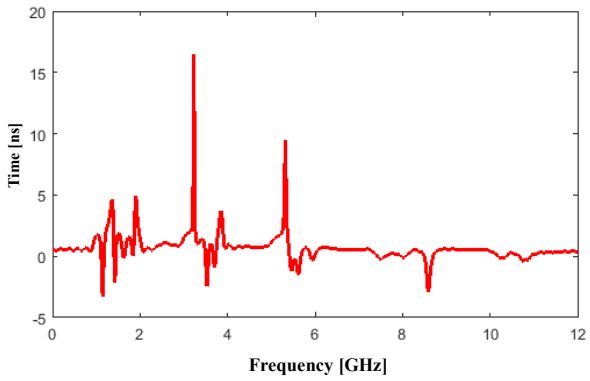

Fig. 7. Groupe delay of the filter with CSRR DGS.

V. CONCLUSION

A dual band bandpass filter based on equivalent circuit for accurate prediction was developed. A compact triple-band bandpass filter was proposed by etching four complementary square split ring resonator (CSRR) in the ground plane. The CSRR as DGS can generate the first passband, while keeping the second and third pass bands. The rejection level between the passbands is improved due to the transmission zero generated by CSRRs as DGSs. The proposed filters provide a new way to design multi-band filters with simple structures and small dimensions.

REFERENCES

[1] Yonghui Song, Guo-Min Yang, and Wen Geyi, "Compact UWB Bandpass Filter With Dual Notched Bands Using Defected Ground Structures," IEEE MICROWAVE AND WIRELESS COMPONENTS LETTERS, VOL. 24, NO. 4, APRIL 2014

[2] Parya Fathi, Zahra Atlasbaf, and Keyvan Forooraghi, "Compact Dual-Wideband Bandpass Filter Using CSRR Based Extended Right/Left-Handed Transmission Line," Progress In Electromagnetics Research C, Vol. 81, 21–30, 2018

[3] Girdhari Chaudhary, Heungjae Choi, Yongchae Jeong, Jongsik Lim, Dongsu Kim, and Jun-Chul Kim**,** "Design of Dual-Band Bandpass Filter Using DGS With Controllable Second Passband," IEEE MICROWAVE AND WIRELESS COMPONENTS LETTERS, VOL. 21, NO. 11, NOVEMBER 2011

[4] X. Lai, N. Wang, B. Wu, and C.-H. Liang, "DESIGN OF DUAL-BAND FILTER BASED ON OLRR AND DSIR," J. of Electromagn. Waves and Appl., Vol. 24, 209–218, 2010

[5] Xin Lai, Chang-Hong Liang, Hao Di, and Bian Wu**,** "Design of tri band filter based on stub loaded resonator and DGS resonator," IEEE MICROWAVE AND WIRELESS COMPONENTS LETTERS, VOL. 20, NO. 5, MAY 2010

[6] Tasher Ali Sheikh, Janmoni Borah, Sahadev Roy, "Design a Compact Tri-Band Band Pass Filter using Asymmetric SIRs and DGS," Radioelectronics and Communications Systems, 2016, Vol. 59, No. 6, pp. 269–273.

[7] Imene Sassi, Larbi Talbi, and Khelifa Hettak, "Compact Multi-Band Filter Based on Multi-Ring Complementary Split Ring Resonators," Progress In Electromagnetics Research C, Vol. 57, 127–135, 2015

[8] William Johnson, Cavin R. Nunes, Savio S. Dias, Siddhi S. Parab, and Varsha S. Hatkar , "Dual band Stepped Impedance Interdigital Microstrip Filter for LTE Bands," EJERS, European Journal of Engineering Research and Science Vol. 4, No. 7, July 2019

[9] Abu Nasar Ghazali, Srikanta Pal, "Microstrip based UWB Filter with Controllable Multiple Notches and Extended Upper Stopband,"

[10] Chin-Yen Liu, Ji-Chyun Liu, Jing-Chung Xu, "Compact Tri-Notched Ultrawideband Bandpass Filter Design Using CSRR, DGS, and FMRR Configurations,", December 2013

[11] E. H. Van Lil and A. R. Van de Capelle, "Transmission-Line Model for Mutual Coupling Between Microstrip Antennas," IEEE Trans. Antennas Propagat., Vol. AP-32, No. 8, pp. 816–821, August 1984.

[12] M. Moulay, M. Abri, and H. Abri Badaoui, "Quad-Band Bowtie Antenna Design for Wireless Communication System Using an Accurate Equivalent Circuit Model," International Journal of Microwave Science and Technology, Volume 2015

[13] Bonache,J.,I. Gil,J. Garcia-Garcia,and F. Martin, "Novel microstrip bandpass filters based on complementary split-ring resonators," IEEE Trans. Microwave Theory Tech.,Vol. 54,265– 271,2006.

[14]Bonache,J. and I. Gil,J. Garcia-Garcia,and F. Martin, "Complementary split ring resonators for microstrip diplexer design," Electron. Lett.,Vol. 41,2005.

Investigation On EM Radiation of Carbon Nanotubes Interconnects

L.Belhimer*, A.Benfdila, A.Lakhlef, M.Kessi, M.Djouder
Microelectronics and Nanotechnology Research Group, Faculty of Electrical
Engineering and Computer Sciences University Mouloud Mammeri, Tizi-ouzou, Algeria
*Corresponding author: Email: lounasbelhimer@yahoo.fr

Abstract— **The performance and reliability of an integrated circuit are largely affected by the interconnections. Carbon nanotubes have unique properties that can help address the major challenges of interconnection. In this paper, carbon nanotubes have been proposed as future VLSI interconnect material. We consider a planar interconnects line including three strips in Carbon nanotubes isolated by a high k dielectric. The main parameter evidenced is the capacitance of the transmission line which will act as a filter then attenuate to a worse level the digital signals that flow in these strips. Then we compare the CNT interconnections with the Cu interconnections. It has been found that CNT-based interconnects are suitable for high-performance applications.**

I. INTRODUCTION

Nanosystems have advantages over their antecedents microsystems. The first and most important of these benefits is miniaturization. Equivalent function, nanosystems bring again in volume and mass. Conversely, they allow performing more functions in the same volume. A second advantage is the reduction of consumption: because of the small masses involved, or even new modes of actuation (electrostatic for example). The reduction of the cost is also often put forward, the collective manufacturing techniques characteristic of the microsystems (wafer of 200mm) allow for large productions to decrease very strongly the unit cost of the produced parts. Finally, these systems can be more robust thanks to new materials such as carbon nanotubes with exceptional mechanical properties, they can be very fast and operate at very high frequencies.

Ultraminiaturization makes it possible to go from the microworld to the nanoworld through the use of more efficient microelectronics tools and techniques. Lithography techniques are pushed to the extreme with very short wavelengths to draw patterns of nanometric size.

When designing integrated circuits the designer take into consideration various parameters has become paramount, such as the temperature gradient in the micro-welding interconnects that has attracted great attention due to the requirement of miniaturization and a high integration in the electronic packaging industry [1-2], and Computation of the interconnect parameters such as matrices of capacitances and inductances per unit length is important since these parameters are essential in designing of package, lossless transmission line system and microwave circuits[3].

In this paper, we design three transmission lines in a carbon nanotube, by varying the frequency and using the finite element method we calculate the capacitance and inductance. To study the influence of the variation of frequency on the distribution of the potential and consequently the capacities between interconnection.

II. CARBON NANOTUBE

The carbon nanotubes were first identified in 1991 by Sumio Iijima [4] whereas he observed by high-resolution transmission electron microscopy the by-products, present in the form of soot, of fullerenes1 synthesized by the method. said of the electric arc. In this soot, he clearly highlighted the presence of tubes consisting solely of graphitic carbon, a few nanometers in diameter. These "nano" tubes were in fact made of several tubes nested within each other. The scientific community then called them multiwall nanotubes. In 1993, single-walled carbon nanotubes were synthesized by the same method, adding metal catalysts to the carbon electrodes between which the electric arc occurs. Today, there are two types of nanotubes: single wall and multiwall nanotubes. The SWCNT single-walled nanotubes consist of a single graphitic wall, whereas the MWCNT multiwall nanotubes consist of several graphitic walls. A multiwall nanotube can be seen as the concentric threading of several single-walled nanotubes with a well-defined inter-wall distance equal to 0.335 nm which corresponds to the interplanar distance of the graphite. Mono or multiwall nanotubes are most often arranged parallel to each other in a two-dimensional mesh of

triangular mesh, and held together by van der Waals interactions: they thus form bundles.

Nanotubes can provide a quasi-ballistic transport of electrons, a metal nanotube 1-3 nm in diameter can carry a current that can go up to ten µA which results in a current density of about 10 / ² 9 A cm. NTCs are very good candidates for the realization of interconnections [5], transistors [6], mixers [7] and diodes. In field-effect transistors, the semiconductor nanotube is used as the active area.

Carbon nanotubes are also good emitters of electrons by electric field effect, they are able to emit electrons by tunnel effect by their point when they are placed in an electric field so that their axis is parallel to field lines. Their very high form factor coupled with their thermal stability and their mechanical rigidity makes them extremely efficient transmitters capable of delivering high currents that are stable over time. Among the possible types of applications are microwave amplifiers [8], flat screens, and rear lights for passive flat screens.

III. Results And Discussion

In this study, we consider a planar interconnects line including three strips in carbon nanotube isolated by a high k dielectric. The main parameter evidenced is the capacitance and inductance of transmission line which will act as a filter and then attenuate to a worse level the digital signals that flow in these strips.

We simulated and modeled the interconnect capacitance and inductance using the finite element method.

In the finite element approach, an electromagnetic problem is solved by dividing the studied region into a set of arbitrary shapes know as finite elements.

We have solved the potential magnetic vector propagation equation, considering the finite element formulation, we have introduced the Galerkin method defined in a Cartesian coordinate system. The propagation is considered according to the oz axis, by considering the phenomenon is governed by the equation:

$$-\frac{1}{\mu}\left[\frac{\partial^2 A_z}{\partial x^2}+\frac{\partial^2 A_z}{\partial y^2}\right]+(j\sigma\omega-\varepsilon\omega^2)A_z-J_z=0 \qquad (1)$$

The per unit length capacitance of each track with respect to ground can be calculated by

$$C=\frac{2*\mathrm{W}_{dielc}}{V^2} \qquad [\mathrm{F/m}] \qquad (1)$$

the equivalent capacitance "C" per unit length, it characterizes the density of dielectric energy stored in the substrate

Where W_{dielc} is the energy per-unit length given by

$$\mathrm{W}_{dielc}=\frac{1}{2}\int_R \varepsilon\left|\nabla\phi\right|^2 dxdy \qquad (2)$$

The inductance is calculated by

$$L=\frac{2*\mathrm{W}_{mag}}{I^2} \qquad [\mathrm{H/m}] \qquad (3)$$

the equivalent inductance "L" per unit length, it characterizes the magnetic energy density stored in the medium.

Where W_{mag} is the magnetic energy per-unit length given by

$$\mathrm{W}_{mag}=\frac{1}{2}\int_R \mu\left|H\right|^2 dxdy \qquad (4)$$

To illustrate and validate the new proposed formulation, we consider a planar interconnects line including three strips in CNT, Figure 1 shows the geometry of the model.

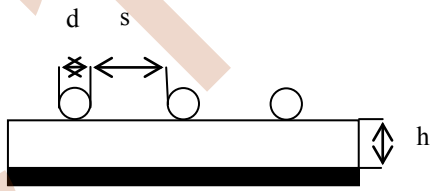

Figure 1.Symmetric microstrip coupled interconnects

This microstrip coupled interconnect has the following geometrical parameters

- d=2 µm, S=5 µm, h=4 µm

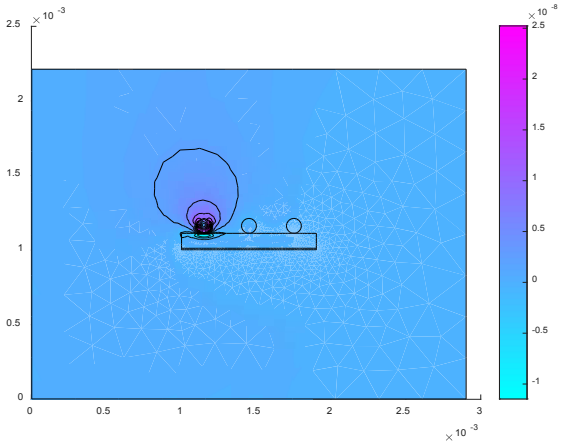

Figure 2. Surface potential distribution

The figure (2) shows the surface potential distribution we Note that the value of potential increases as it gets closer to the carbon nanotube track that is powered.

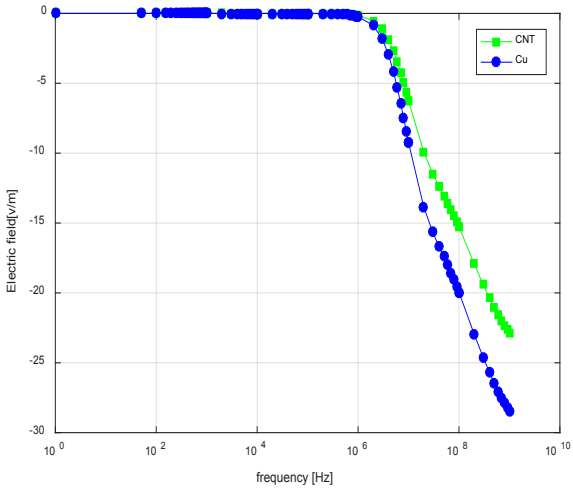

Figure 3. Electric field versus frequency

We note that the electric field decreases with the increase of the frequency and we compared the electric field to generate by tracks in a carbon nanotube with that of copper and the electric field generate by the carbon nanotube track is taller than the electric field generates by copper track.

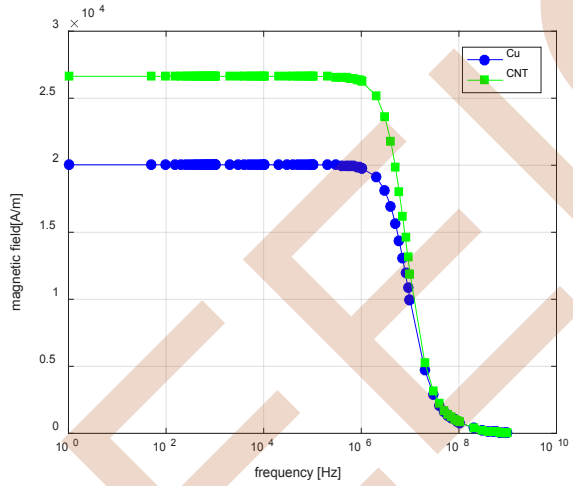

Figure 4. Magnetic field versus frequency

The figure (4) shows the magnetic field versus frequency we note that the magnetic field stabizes until a certain frequency then decreases with increasing frequency and we conclude that the magnetic field generate by carbon nanotube tracks taller than the magnetic field generate by copper tracks

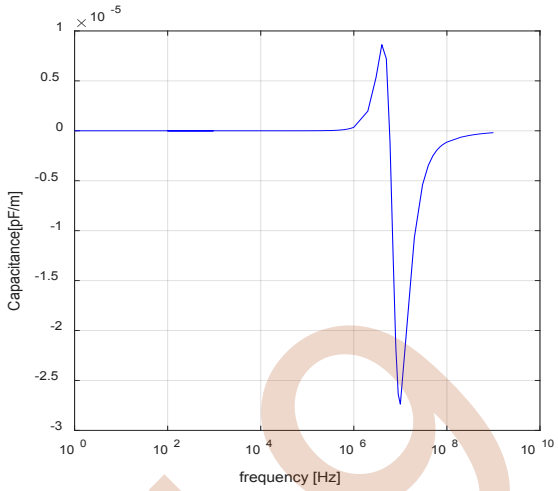

Figure 5. Capacitance versus frequency

It is found that the capacity increases with the increase of the frequency, this is explained as much as the frequency is more important the dielectric energy will tend increased consequently the capacity increases.

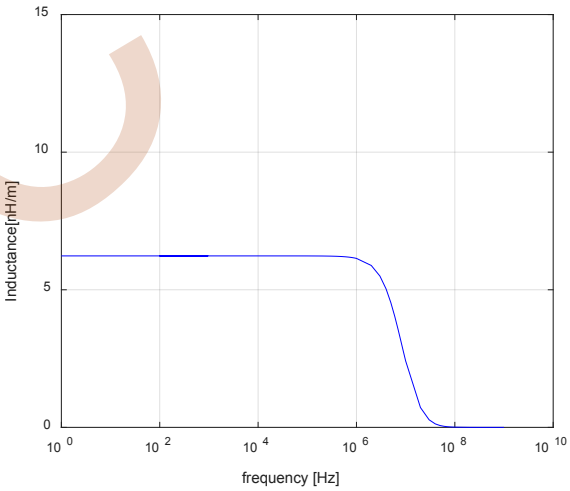

Figure6. Inductance versus frequency

We note that the inductance of the track decreases as the frequency increases. According to the relation of the inductance, it is understood that, as regards the internal volume of the conductor, the contribution to the integral of the magnetic energy is even smaller than the frequency is large.

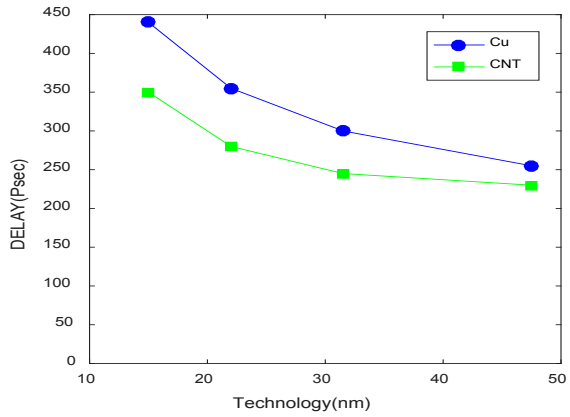

Figure 7. Delay vs technology

Figure (7) shows a comparison of interconnection delay which poses a major problem between copper interconnections and that of Carbonne nanotube and the comparison has led to the conclusion that the interconnections based on Carbonne nanotubes are less late.

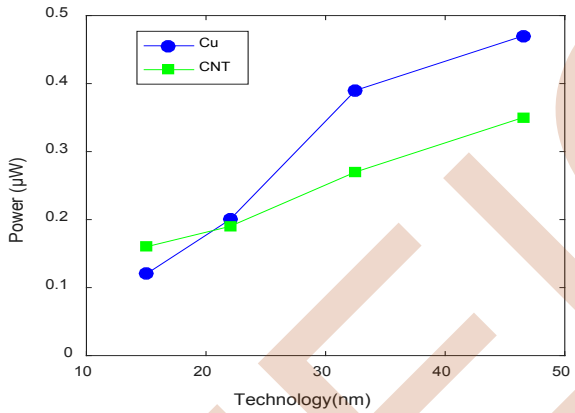

Figure 8. Power vs technology

It can be seen that there is less dissipation in terms of power in the carbon nanotubes than in the copper interconnections

ACKNOWLEDGMENT

In this paper, we have identified the electric and magnetic field of three interconnecting transmission lines and calculated the capacitance and inductance per unit length. The results obtained in this research are consistent and motivating for future study.

REFERENCES

[1] C. Chen, H.Y. Hsiao, Y.W. Chang, F.Y. Ouyang, K.N. Tu, Thermomigration in solder joints, Mater. Sci. Eng. R 73 (2012) 85–100

[2] N. Zhao, Y. Zhong, W. Dong, M.L. Huang, H.T. Ma, C.P. Wong, Formation of highly preferred orientation of ß-Sn grains in solidified Cu/SnAgCu/Cu micro interconnects under temperature gradient effect, Appl. Phys. Lett. 110 (2017) 093504

[3] Sarhan M. Musa and Matthew N.o. Sadiku, "Application of Finite Element Method in Calculating the Capacitance and Inductance of Multiconductor lines", IEEE SoutheastCon 2008.

[4] S.Iijima, "Helical Microtubules of graphitic carbon", Nature 354, 56, 1991

[5] P.J. Burke, Z. Yu and C.Rutherglen, "Carbon Nanotubes for RF and Microwaves", Gallium Arsenide applications symposium. GAAS 2005, 3-7 October 2005

[6] M.Zhang et al., "Radio-Frequency Transmission Properties of Carbon Nanotubes in a Field-Effect Transistor Configuration", IEEE Electron Device Letters, Vol. 27, No. 8, August 2006

[7] L.Rabieirad, S.Mohammadi, "Single-Walled Carbon Nanotube Mixers", IEEE 2006, 2055-2058

[8] P.Legagneux et al., "GHz Modulation of carbon nanotube cathodes for microwave amplifiers", Proceedings of 2005 5th IEEE Conference on Nanotechnology.

Study of a novel optical mirror with biisotropic slabs

Mezache Zinelabiddine

Institute of Optics and fine mechanics, University of Ferhat Abbas Setif 1, 19000 Setif, Algeria

Corresponding author mail: zinemezaache@yahoo.fr

***Abstract*— In this paper, we consider the biisotropic effects in a novel optical mirror; composed of materials with different proprieties. In these structures, we can modify; according to the various applications, the electromagnetic behavior by adjusting the number of layers, the values of permittivity and permeability for each layer. Sometimes this adjustment is not satisfactory; thus, we are obliged to adjust the material's structure to find good results.**

***Keywords*: Biisotropic media, Mirror, Multilayer, Electromagnetic fields**

I. INTRODUCTION

In a biisotropic media, the physical behavior is a consequence of chirality and non-reciprocity. Then, founding of relationships between physical and geometrical concepts developed during the nineteenth century and the beginning of the twentieth century, where concepts of chirality and optical activity were absolutely related [1–4] Main progress in the field of chirality and optical activity during the last century and the beginning of this century is attributed to A. Fresnel, J.B. Biot and L. Pasteur [1–4]. In this work, we study the chiroptical and non-reciprocity effects in a multilayer structure. For the multilayer structure, and depending on the application, the electromagnetic behavior can be adjusted by changing the number of layers, as well as the values of permittivity of each layer. This is not always satisfactory; we should customize the structure by playing on other parameters to achieve better results. The multilayer structure considered in this study, it's an alteration of biisotropic layers with high and low refractive indices.

II. RESULTS

The biisotropic mirror is a layers' arrangement of N biisotropic slabs with different proprieties and thickness of materials, while the biisotropic mirror is a general case of chiral multilayer. It's composed of an alternative periodic arrangement of biisotropic layers with high and low indexes of refraction (n_H , n_L) trapped between two homogeneous mediums and characterized by n_0 ,and n_A indexes . The constitutive relations considered in this case are expressed as following:

$$\vec{D}_H = \varepsilon_H \vec{E}_H - j\kappa_H \vec{B}_H \tag{1}$$

$$\vec{H}_H = -j\kappa_H \vec{E}_H + \left(\frac{1}{\mu_H}\right)\vec{B}_H \tag{2}$$

$$\vec{D}_L = \varepsilon_L \vec{E}_L + \gamma_L \vec{B}_L \tag{3}$$

$$\vec{H}_L = -\gamma_L \vec{E}_L + \left(\frac{1}{\mu_L}\right)\vec{B}_L \tag{4}$$

Where: γ is the non-reciprocity parameter (Ω^{-1}), and κ is the chirality parameter (Ω^{-1}).

$$E_{L+} + E_{R+} - E_{L-} - E_{R-} = E'_{L+} + E'_{R+} - E'_{L-} - E'_{R-}$$

$$-E_{L+} + E_{R+} - E_{L-} + E_{R-} = E'_{L+} + E'_{R+} - E'_{L-} - E'_{R-}$$

$$\begin{bmatrix} E_{L+} \\ E_{R+} \\ E_{L-} \\ E_{R-} \end{bmatrix} = M \begin{bmatrix} E'_{L+} \\ E'_{R+} \\ E'_{L-} \\ E'_{R-} \end{bmatrix} \qquad E = ME'$$

As P has the following form [5]:

$$P = \begin{bmatrix} \exp(jk_L d) & 0 & 0 & 0 \\ 0 & \exp(jk_R d) & 0 & 0 \\ 0 & 0 & \exp(-jk_L d) & 0 \\ 0 & 0 & 0 & \exp(-jk_R d) \end{bmatrix}$$

$$\begin{bmatrix} E_{2L+} \\ E_{2R+} \\ E_{2L-} \\ E_{2R-} \end{bmatrix} = T \begin{bmatrix} E_{4L+} \\ E_{4R+} \\ E_{4L-} \\ E_{4R-} \end{bmatrix} = T^2 \begin{bmatrix} E_{6L+} \\ E_{6R+} \\ E_{6L-} \\ E_{6R-} \end{bmatrix} = T = \ldots = T^N \begin{bmatrix} E_{(2N+2)L+} \\ E_{(2N+2)R+} \\ E_{(2N+2)L-} \\ E_{(2N+2)R-} \end{bmatrix}$$

$$\begin{bmatrix} E_{iTM} \\ E_{rTM} \\ E_{iTE} \\ E_{rTE} \end{bmatrix} = T_1 T^N M_2 \begin{bmatrix} E_{tTM} \\ E_{tTE} \end{bmatrix}$$

Where: $T_1 = M_1 P_H$, and $T = M_H P_H M_L P_L$

$M_H(M_L)$ is the correspondent matrix which founds the relation between the fields with high (low) index of refraction of the biisotropic medium and the high (low) index of refraction of the following medium [5] [6].

The matrix $P_H(P_L)$ expresses the propagation matrix of biisotropic medium fields with high (low) index of refraction. The proprieties of biisotropic mirrors are defined by the N^{th} power of T^N of T bilayers' matrix. The behavior of T matrix is defined by the eigenvalue of T [5] [6].

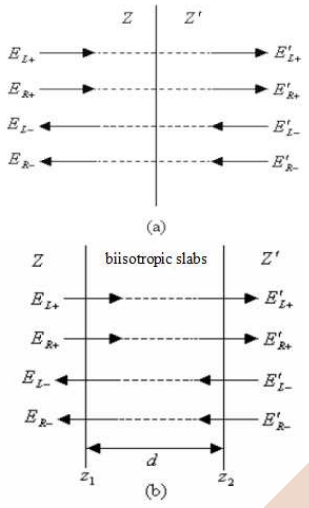

Figure.2. (a) Electric fields through the interface, (b) Electric fields through a biisotropic slabs.

In this study, we have used different values of the ratio of biisotropic parameters κ_H / γ_L , which is the ration between the chirality parameter of the high index medium and parameter of non-reciprocity of the low index medium. The thereafter figures represent the influence of the ratio of chirality parameters on reflectivity:

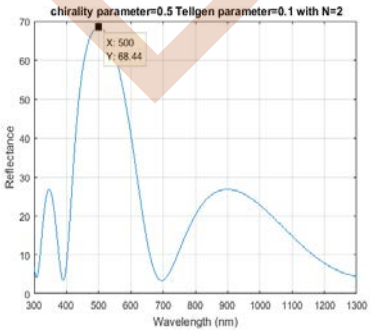

Figure.3. Reflectivity depending on the wavelength in normal incidence for: n_H (SiO), n_L (MgF_2) with $\frac{\kappa_H}{\gamma_L} = 5$

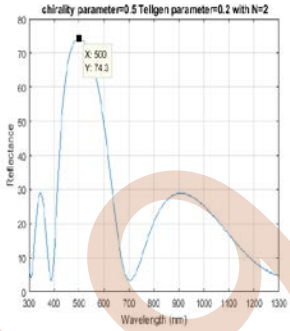

Figure.4. Reflectivity depending on the wavelength in normal incidence for: n_H (SiO), n_L (MgF_2) with $\frac{\kappa_H}{\gamma_L} = 2.5$

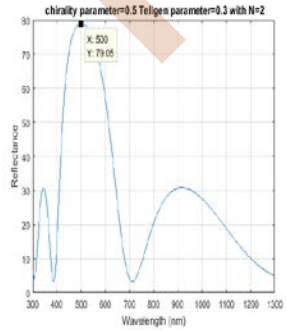

Figure.5. Reflectivity depending on the wavelength in normal incidence for: n_H (SiO), n_L (MgF_2) with

$$\frac{\kappa_H}{\gamma_L} = 1.67$$

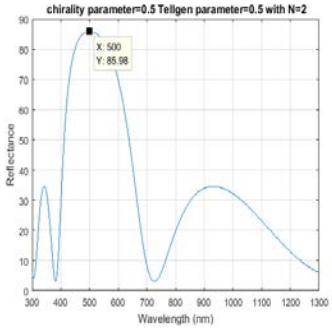

Figure.6. Reflectivity depending on the wavelength in normal incidence for: n_H (SiO), n_L (MgF_2) with $\frac{\kappa_H}{\gamma_L} = 1$

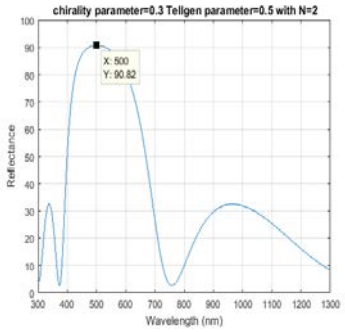

Figure.7. Reflectivity depending on the wavelength in normal incidence for: n_H (SiO), n_L (MgF_2) with $\frac{\kappa_H}{\gamma_L} = 0.6$

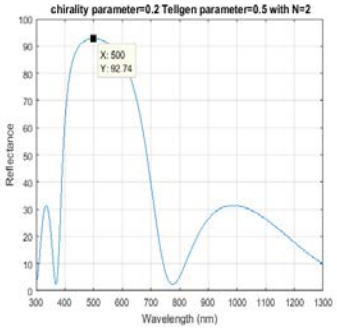

Figure.8. Reflectivity depending on the wavelength in normal incidence for: n_H (SiO), n_L (MgF_2) with $\frac{\kappa_H}{\gamma_L} = 0.4$

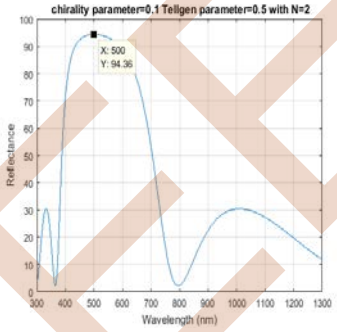

Figure.9. Reflectivity depending on the wavelength in normal incidence for: n_H (SiO), n_L (MgF_2) with $\frac{\kappa_H}{\gamma_L} = 0.2$

The figures 3 to 9 illustrate reflectivity depending on the wavelength in normal incidence. Figures 3, 4 and 5 show, a reduction in reflectivity (68.44%, 74.3%, and 79.05 %) is observed as the ratio of biisotropic parameters increases to $\kappa_H/\gamma_L = 5$, $\kappa_H/\gamma_L = 2.5$ and $\kappa_H/\gamma_L = 1.67$ respectively. According to the figures 7, 8 and 9 The highest values of reflectivity (92.36%, 92.72%, and 90.82%) are reached for the ratio of biisotropic parameters to $\kappa_H/\gamma_L = 0.2$, $\kappa_H/\gamma_L = 0.4$ and $\kappa_H/\gamma_L = 0.6$ respectively.

III. CONCLUSION

The same principle of interference mirrors is based on high number of interfaces. Thus, more the presence of bilayers fostering the improvement of reflectivity, more the total intensity will be elevated. The decrease of the thickness of the high index material at the expense of the low index material leads to the amelioration of multilayer's reflectivity. Hence, the ratio of biisotropic parameters κ_H/γ_L becomes the key factor to the amelioration of biisotropic multilayer's reflectivity.

REFERENCES

[1] D. L. Jaggard, A. R. Mickelson and C. H. Papas "On electromagnetic waves in chiral media," Applied physics, Vol. 28, pp 211 - 216, 1979.

[2] S. Bassiri, C. H. Papas and N. Engheta, "Electromagnetic wave propagation through a dielectric-chiral interface and through a chiral slab," Optical Society of America Vol. 5, No. 9, 1988.

[3] S. Ougier, I. Chenerie, A. Sihvola and A. Priou, "Propagation in biisotropic media: Effect of different formalisms on the propagation analysis," Progress in Electromagnetic Research, PIER 9, 19-30, 1994.

[4] J. Margineda, G. J. Molina-Cuberos, M. J. Núñez., A. J. García-Collado and E. Martín, "Electromagnetic characterization of chiral media," InTech, 2012.

[5] C. Sabah and S. Uçkun, "Mirrors with chiral slabs," Journal of optoelectronics and advanced materials, Vol. 8, No. 5, 2006.

[6] Z. Li, H. Caglayan, E. Colak, J. Zhou, C. M. Soukoulis and E. Ozbay, "Coupling effect between two adjacent chiral structure layers," OPTICS EXPRESS 5375, Optical Society of America, Vol. 18, No. 6, 2010

Electromagnetic effect and thermal modeling of a square inductor integrated in a Buck converter

ALLAOUI Abdelhak
Electrical engineering department,
University of Science and Technology
Oran, Algeria
abdelhakallaoui@yahoo.fr

BENHADDA Yamina
Electrical engineering department,
University of Science and Technology
Oran, Algeria
benhadda_yamina@yahoo.fr

HAMID Azzedine
Electrical engineering department
University of Science and Technology
Oran, Algeria
hamidazdean@yahoo.fr

***Abstract*—This paper presents the electromagnetic effect and thermal modeling of a square inductor for its integration in Buck converter DC-DC. The first, we descript the inductor. The second, we dimensioning our inductor. Finely, we have simulated the electromagnetic effects in two cases. An inductor in the air and an inductor with substrate. Our geometry is created in 3D space dimension. Finely, we treat the thermal phenomena in an inductor using the finite element method.**

I. INTRODUCTION

In Power electronics, modeling of passive components constitute a particularly important issue. Indeed, the magnetic components, inductors and transformers are mainly used to transmit or store energy. The passive elements volume reduction leads to a mounted in operating frequency, but this increase in frequency causes an increase in losses. If the behavior of some components is relatively insensitive to temperature changes, it is not the same thing for magnetic components whose characteristics depend strongly on the temperature. The losses freed in the form of heat are become a major concern due to the reduction of trade with the outside surfaces and increasing the density of losses. The aim of our work is a dimensioning a square inductor that will be integrated in a DC-DC micro-converter.

II. PRESENTATION OF THE BUCK CONVERTER

We have chosen a Buck micro-converter continuous-continuous step-down (Fig.1) [1-3]. The inductor to integrate will thus be dimensioned for this type of application. Input voltage, $V_{in} = 3Volt$. Output voltage, $V_{out} = 1.5Volt$. Maximum current $I_{L\max} = 0.65A$. Output power, $P_{out} = 0.6W$. Frequency of operation, $f = 1MHz$.

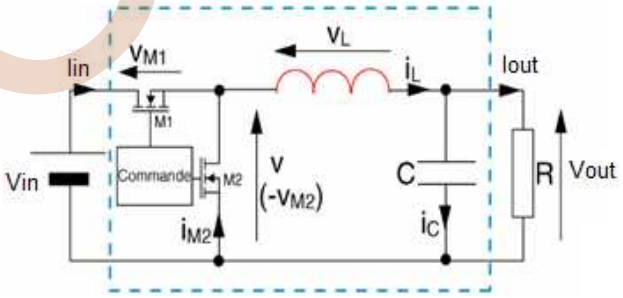

Figure 1. Buck converter

III. DIMENSIONING OF THE INTEGRATED INDUCTOR

The geometry parameters characterizing the integrated inductor (Fig. 2) are the number of turns ***n***, the width of the conductor ***w***, thickness of the conductor ***t***, the spacing between conductor ***s***, length of the conductor ***l***, the outer diameter d_{out} and input diameter d_{in}.

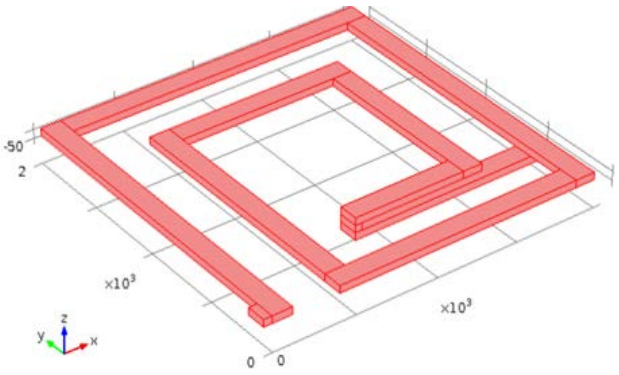

(a)

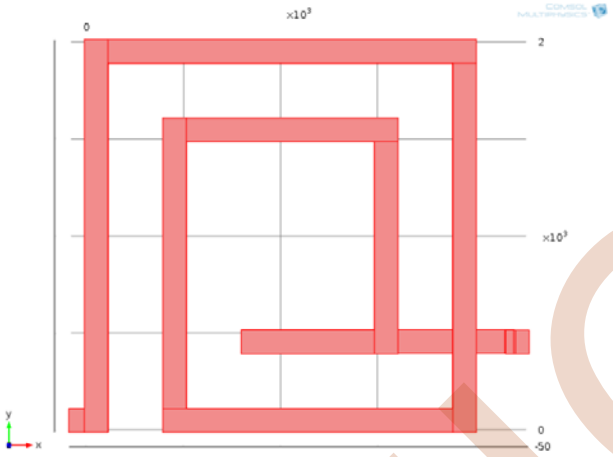

(b)

Figure 2. Geometry of a square spiral integrated inductor, (a) 3D view, (a) 2D view

The geometry of a square spiral integrated inductor on substrate [4-5] is shown in Fig. 3.

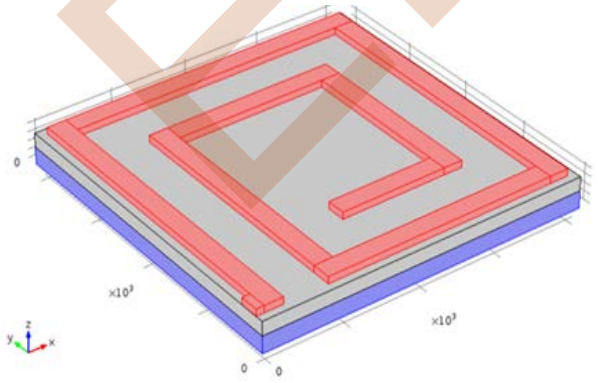

(a)

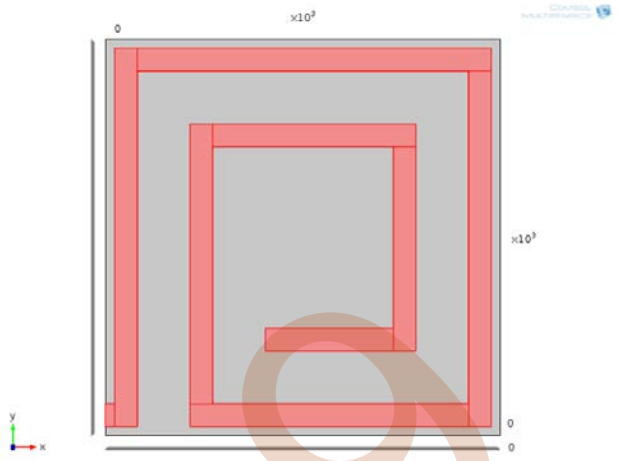

(b)

Figure 3. Geometry of a square spiral integrated inductor on substrate, (a) 3D view, (a) 2D view

Table I contains the specifications and the design results of the square spiral integrated inductor.

Table I. Design Results of the Square Spiral Integrated Inductor

Parameter	Value
Inductance, **L** (µH)	1.5
External diameter, $\mathbf{d_{out}}$ (mm)	2
Internal diameter, $\mathbf{d_{in}}$ (mm)	0.4
Number of turns, **n**	2
Thickness of the conductor, **t** (µm)	40
Width of the conductor, **w** (µm)	120
Spacing between conductor, **s** (µm)	280
Length of the conductor, **l** (m)	0.0116

IV. ELECTRICAL MODEL

The equivalent electrical model of the integrated inductor [6-16] is shown in Fig. 4.

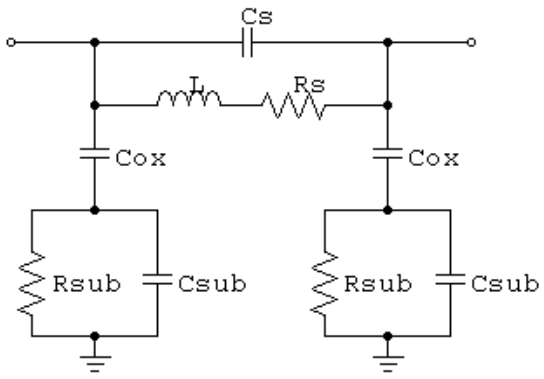

Figure 4. Equivalent electrical model

Table II shows the electrical parameters calculated.

TABLE II. ELECTRICAL PARAMETERS RESULTS

Electricals parameters	Values
$R_s(\Omega)$	0.04
$R_{sub}(\Omega)$	0.006
$C_s(pF)$	0.014
$C_{ox}(pF)$	0.598
$C_{sub}(pF)$	0.631
Q	98.56

V. MAGNETIC EFFECT IN A PLANAR INDUCTOR

In this section, we present the distribution of the magnetic field in inductor in the air and on substrate using finite elements method [17,19].
Figure 5 shows the distribution of the electric field and magnetic field lines in the inductor in the air. This electric field is important to the input of the integrated planar inductor. The magnetic flux density lines are concentrated around the component and are bounded by the borders.

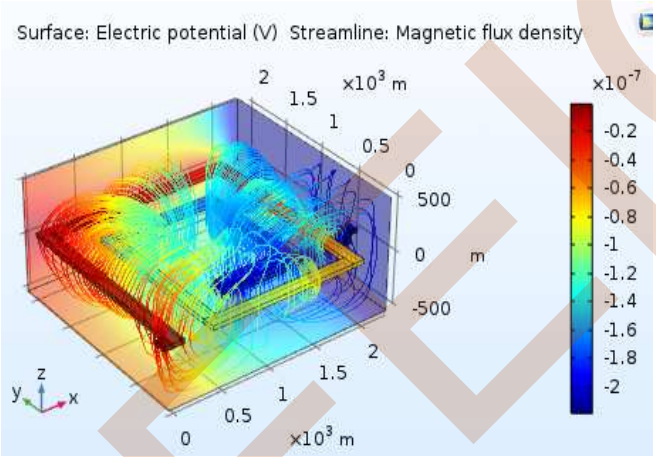

(a)

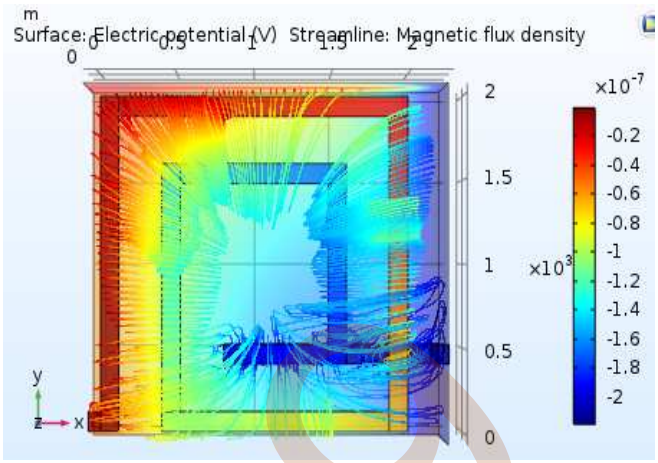

(b)

Figure 5. Distribution of magnetic field lines in the planar inductor in the air, (a) 3D view, (a) 2D view

Figure 6 shows the distribution of the electric field and the magnetic field lines in the planar inductor on substrate. When we insert a multi-layer of the insulating, the majority of the magnetic field lines are concentrated at the substrate. These layers can reduce the value of resistance. So, we conclude that the substrate is required to have a good electromagnetic compatibility in the case of the integration of a planar inductor.

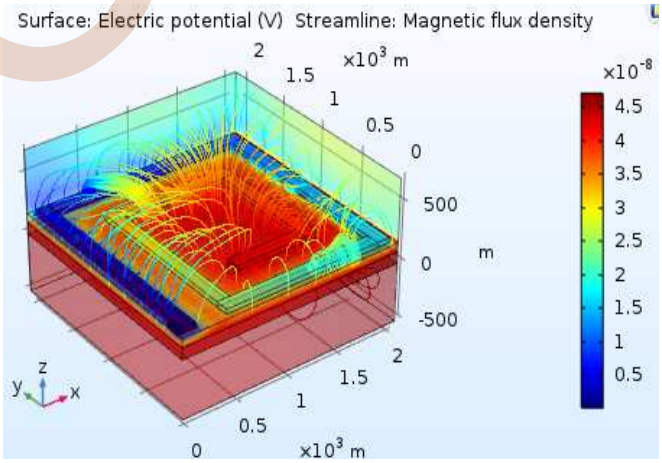

(a)

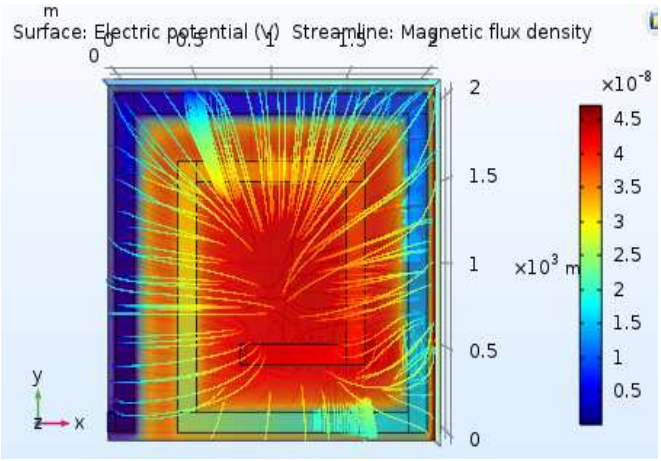

(b)

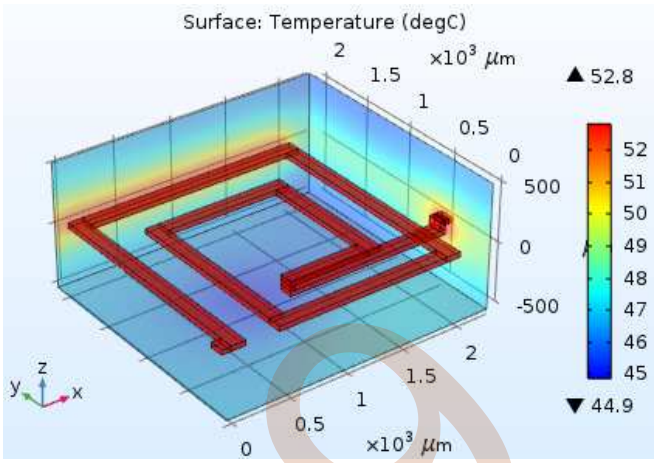

(a)

Figure 6. Distribution of magnetic field lines in the planar inductor on substrate, (a) 3D view, (a) 2D view

VI. THERMAL EFFECT IN A PLANAR INDUCTOR

In this section, we present the temperature distribution in our integrated inductor, based on the finite element method [20]. This distribution is obtained by solving the equation (7) of heat taking into account certain boundary conditions [21].

$$\rho.C_p \frac{\partial T}{\partial t} - \nabla(k\nabla T) = q \quad (7)$$

For an integrated inductor in the air, the heat source can be expressed as (8)

$$q = \frac{P_j}{V} \quad (8)$$

For an integrated inductor on substrate, the heat source is defined as (9)

$$q = \frac{P_{j+}P_{ed} + P_f}{V} \quad (9)$$

In figure 7 and figure 8, we observe the temperature distribution in the inductor on the air. We see that the temperature attained is from 52 °C.

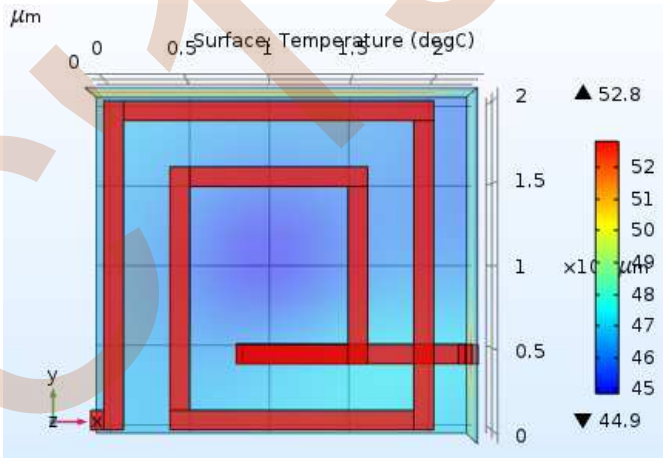

(b)

Figure 7. Temperature distribution in the inductor on the air, (a) 3D view, (a) 2D view

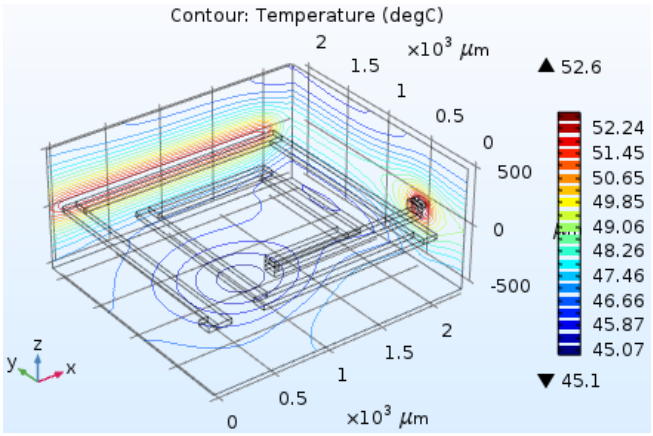

(a)

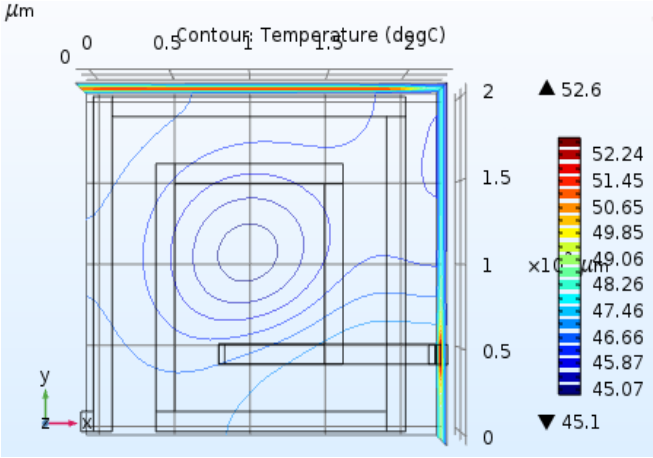

(b)

Figure 8. Temperature distribution in contour in the inductor on the air, (a) 3D view, (a) 2D view

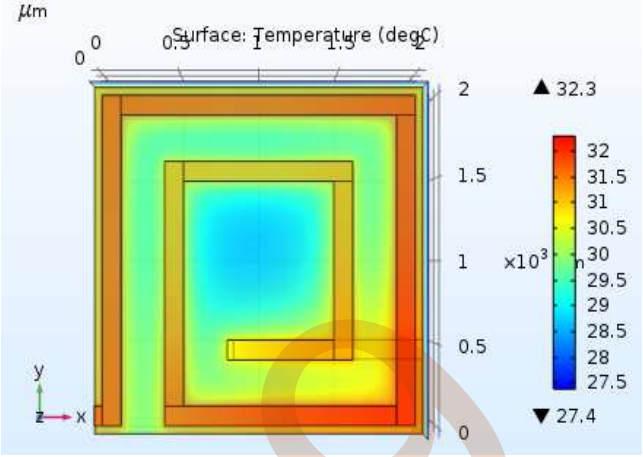

(b)

Figure 9. Temperature distribution in inductor on substrate, (a) 3D view, (a) 2D view

In figure 9 and figure 10, we observe the temperature distribution in the planar inductor on substrate. We see from these figures that the temperature is about 32°C. It is shown that the temperature is reduced.

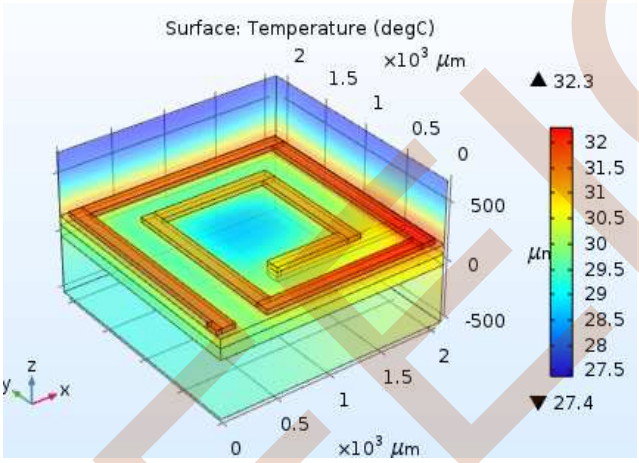

(a)

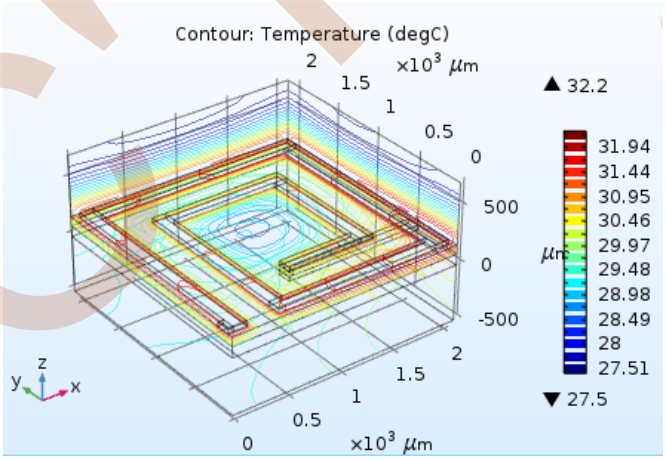

(a)

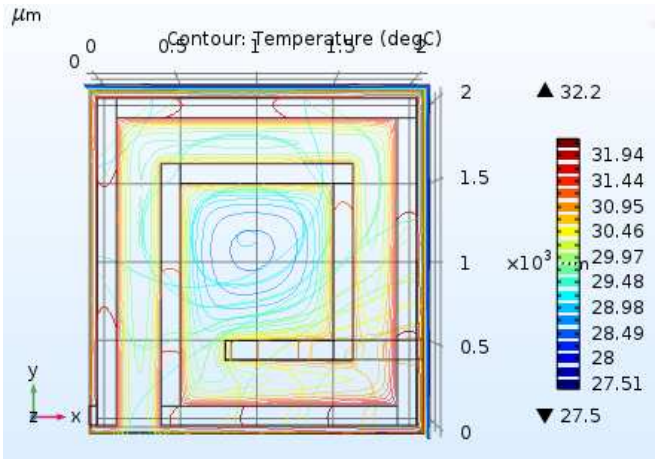

(b)

Figure 10. Temperature distribution incontour in inductor on substrate, (a) 3D view, (a) 2D view

VII. CONCLUSION

In this paper, we have presented the dimensioning, the modeling and the simulation of a square inductor. We have visualized the electromagnetic phenomenon in inductor in the air and on substrate.

When we insert a substrate, the losses decrease, the heat source decrease and the value of the temperature decrease.

ACKNOWLEDGMENT

First Author Abdelhak ALLAOUI was born in Oran, Algeria in 1988. He obtained his master degree in electrical engineering at Mohamed Boudiaf University of Sciences and Technology of Oran in 2011. He obtained his Doctorate degree in electrical engineering at Mohamed Boudiaf University of Sciences and Technology of Oran in 2017.

Second Author Yamina BENHADDA was born in Ain Temouchent, Algeria in 1982. He obtained his Doctorate degree in electrical engineering at Mohamed Boudiaf University of Sciences and Technology of Oran in 2016.

Third Author Azzedine HAMID was born in Alger, Algeria in 1961. He obtained his Magister degree in electrical engineering at Mohamed Boudiaf University of Oran in 1994. He received his PhD in 2005 from Mohamed Boudiaf University of Sciences and Technology of Oran.

REFERENCES

[1] Y. Benhadda, A. Hamid, T. Lebey, M. Derkaoui, "Design and modeling of an integrated inductor in a buck converter DC-DC," Journal of Nano and Electronic Physics, 7(2), 2015, pp. 2006 (6pp).

[2] C. Liu, H. Chang, K. Li, C. Lin, C. Hsu, T. Lin, H. Chou, H. Huang, H. Liao, " Adaptable and integrated packaging platform for mems-based combo sensors utilizing innovative wafer-level packaging technologies, " IEEE Electronic Components & Technology Conference, pp. 1675-1681, 2013.

[3] M. Derkaoui, A. Hamid, T. Lebey, R. Melati, "Design and modeling of an integrated microtransformer in a flyback converter," Telkomnika, 11(4), pp. 669-682, 2013.

[4] P. Gomes, "Monolithic power combiners in CMOS technologies for WLAN applications," l'Université de Lisboa, 2011.

[5] H. Xu, MMICs using GaN HEMTs and thin-film BST capacitors", thèse de l'Université de California, 2005.

[6] C. Somo, D. Malec, V. Bley, "New use of Mn-Zn ferrite material in power electronics integrated LC filters", IEEE Transactions on Advanced Packaging, pp. 1-9.

[7] N. Kr. Shukla, S. Birla, R. K. Singh, "New modeling technology for spiral inductors for ultra wideband applications," International Journal of Engineering and Technology, 2(1), pp. 48-51, 2010.

[8] A. Eroglu"Planar inductor design for high power applications," Progress in electromagnetics research," (35), pp. 53-67, 2011.

[9] I. Bahl, "Lumped elements for RF and microwave circuits," Boston-London, 2003.

[10] C. H. Liu, H. D. Chang, K. H. Li, C. H. Lin, C. J. Hsu, T. Y. Lin, H. H. Chou, H. C. Huang, H.-Y. Liao, "Adaptable and integrated packaging platform for MEMS-based combo sensors utilizing innovative wafer-level packaging technologies," IEEE, pp.1675-1681, 2013.

[11] J. Wei, Z. Wang, "Frequency-independent T equivalent circuit for on-chip spiral inductors," IEEE Electron device letters, 31(9), pp.933-935, 2010.

[12] P. Sharma, M. Mehta, "Analysis of RF MEMS square spiral inductor, " International Journal of Scientific & Engineering Research, 3(2), pp. 1-4, 2012.

[13] S. Couderc, "Etude de matériaux ferromagnétiques doux à forte aimantation et à résistivité élevée pour les radio-fréquences, Applications aux inductances spirales planaires sur silicium pour réduire la surface occupée, " thèse de l'Université de Limoges, 2006.

[14] A. Bejan, "Heat transfer, Second edition. Wiley, 1993.

[15] Y. Tamene, C. Bougriou and R. Bessaïh, "Thermal behaviour of a multilayer media in transient regime," Revue des Energies Renouvelables, 10(3), pp. 397-405, 2007.

[16] M. H. Belghazi, "Modélisation analytique du transfert instationnaire de la chaleur dans un matériau bicouche en contact imparfait et soumis à une source de chaleur en mouvement, " Université de Limoges, 2008.

[17] M. C. Hsieh, "Finite element analyses for critical designs of low-cost wafer-level chip scale packages, IEEE Transactions on Components, Packaging and Manufacturing Technology, 4(3), pp.451-458, 2014.

[18] L. Ying, H. Chunyue, Z. Xin, L. Tianming, G. Guangkuo, X. Guoji ,T. Wenliang, " Influence of compliant layer thickness on stress and strain of solder joints in wafer level chip scale package under thermal cycle, " IEEE 15th International Conference on Electronics Packaging Technology, pp. 577-582, 2014.

[19] T. G. Imre, U. Viscarret and I. E. Otadui, A. Rufer, "Transient thermal model of a medium frequency power transformer," IEEE, pp. 1033-1038, 2008.

[20] Y. Benhadda, A. Hamid, T. Lebey, A. Allaoui, M. Derkaoui, R. Melati, "Thermal behavior of an integrated square spiral micro coil, " Telkomnika, 14(2), pp. 669-682, 2015.

[21] A. Allaoui, A. Hamid, P. Spiterri, V. bley, T. Lebey, "Thermal modeling of an integrated inductor in a micro-converter," Journal of Low Power Electronics, 11(1), pp. 63-73, 2015.

INVESTIGATION OF FGM CYLINDER SUBJECTED TO MECHANICAL AND MAGNETIC FIELDS

Hammoum R.[1], Benslimane A.*[,1], Cheffar L.[1],
Hamoudi F.[2],
[1]Laboratoire de Mécanique Matériaux et Energétique
Department of Mechanical Engineering, University of Bejaia
Bejaia, Algeria
[2]Department of Electrical Engineering, University of Bejaia
Bejaia, Algeria
(*benslimane.ah@gmail.com)

***Abstract*— In this paper, analytical solution is presented for computing the displacements and stresses in a FGM thick-walled cylinder under a uniform mechanical and magnetic fields. An analytical model of the pressurized vessel was constructed, where the radial continuous varying of elastic modulus and permeability along the thickness was assumed. It has been assumed that the elastic modulus and permeability are varying through thickness of the FGM material according to a power law expression. The analytical solutions of distribution of displacements and stresses were obtained and illustrated in radial direction for pressurized FGM cylinder. Thus, the inhomogeneity in material properties can be exploited to optimize stress distribution.**

I. INTRODUCTION

Cylindrical hollow objects and thick-walled cylindrical vessels are common components and frequently used in engineering applications. They may be considered under the action of different types of mechanical, thermal and magnetical loadings or rotational body forces [1]. Elastic analyses of such pressure vessels subjected to internal and/or external pressures may be of great interest and importance in the design on solid mechanics.

Until recently, these spherical objects are made of isotropic homogeneous materials which can only be optimized for their applications by material selection and very limited dimensional design. In recent decades, functionally graded materials (FGM) have become widespread due to possibility they offer for optimization of the design in terms of the spatial distribution of material properties.

From viewpoints of solid mechanics, the FGM are nonhomogeneous elastic materials which have high structural performances such as high corrosion and oxidation resistant as well as great thermal resistance specification leads to the wide range of their industrial applications [2, 3]. The physical, mechanical and thermal properties of FGM vary in one or more spatial directions in such a way that for a specific application they have optimal properties variation [4,5]. FG Materials are nonhomogeneous in a microscopical scale but at macroscopic scale the material properties vary continuously in a specific spatial direction by gradually changing the volume fractions of the material constituents [6, 7]. Hence, this new class of composite materials, unlike conventional composites, has the advantage of the absence of interfaces where the stress discontinuity occurs due to the discontinuity of materials properties. Indeed, the smoothly change in microstructure of FGM may not be subjected mismatch of mechanical properties across the interface.

Many analytical studies concerning elastic problems of FGM hollow structures have been reported. For the FGM hollow cylindrical structures, previous studies on the subject considered FGM hollow cylinder including those, for example, by Lutz and Zimmerman [8], Jabbari et al. [3].

In this work, the magnetic response of a FG hollow cylinder subjected to mechanical and thermal loads was considered. Analytical solutions for stresses and perturbation of the magnetic field vector were determined using the infinitesimal theory of magneto-elasticity. The material stiffness and the magnetic permeability were considered varying continuously across the thickness direction according to power-law functions of radial direction. The aim of this work was to understand the effect of magnetic field on a FG hollow sphere subjected to mechanical and thermal loads.

II. PROBLEME FORMULATION

We consider a hollow FGM cylinder. The cylinder has inner and outer radii, respectively, R_{in} and R_{out}. It is subjected to internal/external uniform pressure loadings, respectively P_{in} and P_{out} and placed in an uniform magnetic field $\vec{H} = \begin{pmatrix} 0 & 0 & H_z \end{pmatrix}$.

The materials are assumed linearly elastic and isotropic and the graded materials Young's modulus and the magnetic permeability depend only on the radial direction while Poisson's ratio is assumed constant.

The schematization of the thick tube is shown in FIG. 1.

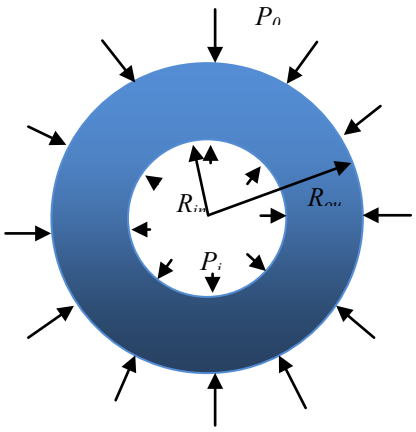

Figure 1. Thick circular cylinder with wall in FGM

For convenience, the axisymmetric load conditionsrequire considering a cylindricalcoordinate system (r, θ, z).

To ascertain the effectof the inhomogeneity, expression of Young's modulus and magnetic permeability were considered across the thickness:

$$E(r)=E_{in}\left(\frac{r}{R_{in}}\right)^{\beta}\ ;\ \alpha(r)=\alpha_{in}\left(\frac{r}{R_{in}}\right)^{\beta} \qquad (1a,b)$$

Where E_{in} , α_{in} are, respectively, the values of Young's modulus and magnetic permeability at $r = R_{in}$. β, is the parameters of the inhomogeneity material. Homogenous case is obtained when $\beta = 0$.

The length of the cylinder is sufficiently large so that we confine our attention to the plain strain problem. The stress and strain fields may be written:

$$\sigma_{ij}=\sigma_{ij}(r),\ \varepsilon_{ij}=\varepsilon_{ij}(r) \qquad (2a,b)$$

And $\boldsymbol{u}=\boldsymbol{u}(r)$, where $\boldsymbol{u}=(u_r \quad 0 \quad 0)$ is the displacement field.

The cylinder's material is graded through the r-direction, thus the material properties are functions of r. Let u_r be the displacement component in the radial direction and since the elastic field is axisymmetric and independent of z, the kinematic relations (strain-displacement) are given:

$$\begin{cases}\varepsilon_{rr}=\dfrac{\partial u_r}{\partial r}\\ \varepsilon_{\theta\theta}=\dfrac{u_r}{r}\\ \varepsilon_{zz}=\varepsilon_{rz}=\varepsilon_{r\theta}=\varepsilon_{\theta z}=0\end{cases} \qquad (3)$$

The material of the cylinder is inhomogeneous which is described by Hooke's law in the form:

$$\sigma_{ij}=2\mu(r)\varepsilon_{ij}+\lambda(r)\varepsilon_{ll}\delta_{ij} \qquad (4)$$

Where: $\mu(r)=\dfrac{E(r)}{2(1+\nu)}$ and $\lambda(r)=\dfrac{\nu E(r)}{(1+\nu)(1-2\nu)}$ are Lamé's constants, $E(r)$is Young's modulus which depends on spatial coordinates and ν the Poisson's ratio.

The relations stress-strain are given:

$$\begin{cases}\sigma_{rr}=(2\mu(r)+\lambda(r))\varepsilon_{rr}+\lambda(r)\varepsilon_{\theta\theta}\\ \sigma_{\theta\theta}=(2\mu(r)+\lambda(r))\varepsilon_{\theta\theta}+\lambda(r)\varepsilon_{rr}\\ \sigma_{zz}=\lambda(r)(\varepsilon_{rr}+\varepsilon_{\theta\theta})\end{cases} \qquad (5)$$

The governing electrodynamic Maxwell equations when applying a uniform magnetic field $\vec{H}=(0 \quad 0 \quad H_z)$ for a perfectly conducting, elastic body are given by:

$$\vec{h}=\vec{\nabla}\wedge(\vec{u}\wedge\vec{H})=(0 \quad 0 \quad h_z);$$

$$\vec{J}=\vec{\nabla}\wedge\vec{h}=\left(0 \quad -\frac{\partial h_z}{\partial r} \quad 0\right)$$

Avec : $h_z=-H_z\left(\dfrac{\partial u_r}{\partial r}+\dfrac{u_r}{r}\right)$

The electromagnetic dynamic equation of the FGM hollow cylinder, in absence of body forces, is expressed as:

$$\frac{\partial\sigma_{rr}}{\partial r}+\frac{\sigma_{rr}-\sigma_{\theta\theta}}{r}+f_z=0 \qquad (7)$$

Where f_z is defined as Lorentzs force, which may be written as:

$$f_z=\alpha(r)(\vec{J}\wedge\vec{H})=\alpha(r)H_z^2\frac{\partial}{\partial r}\left(\frac{\partial u_r}{\partial r}+\frac{u_r}{r}\right) \qquad (8)$$

To obtain the equilibrium equation in terms of the displacement component for the FGM cylinder, the functional relationship of the material properties must be known.

For convenience, we assume:

$$\lambda(r)=\zeta(\nu)\cdot E(r), \qquad 2\mu(r)+\lambda(r)=\psi(\nu)E(r)$$
$$\xi(\nu)=\frac{\nu}{(1+\nu)(1-2\nu)}, \quad \psi(\nu)=\frac{(1-\nu)}{(1+\nu)(1-2\nu)},$$

Substituting the relations in Eq. (3) and (8) into Hooke's law in Eq. (4) and then into the equations of equilibrium Eq. (7) we obtain the Navier's equation in the term of the radial displacement as:

$$r^2\frac{d^2u}{dr^2}+(1+\omega\beta)r\frac{du}{dr}-(1-\kappa\beta)u=0 \tag{9}$$

Where:

$$\omega=\frac{R_{in}\psi(\nu)E_{in}}{\psi(\nu)E_{in}+\alpha_{in}H_z^2} \;;\; \kappa=\frac{R_{in}\zeta(\nu)E_{in}}{\psi(\nu)E_{in}+\alpha_{in}H_z^2},$$

The solution of the equation (9) is given by:

$$u(r)=Ar^{a_1}+Br^{a_2} \tag{10}$$

Where:

$$a_1=-\frac{1}{2}\omega\beta+\frac{1}{2}\sqrt{\omega\beta^2-4\kappa\beta+4}\;;$$

$$a_2=-\frac{1}{2}\omega\beta-\frac{1}{2}\sqrt{\omega\beta^2-4\kappa\beta+4}$$

So,

$$\begin{cases}\sigma_{rr}=\{a_1\psi(\nu)+\zeta(\nu)\}\dfrac{E_{in}}{R_{in}^{\beta}}Ar^{\beta+a_1-1}\\ \qquad +\{a_2\psi(\nu)+\zeta(\nu)\}\dfrac{E_{in}}{R_{in}^{\beta}}Br^{\beta+a_2-1}\\ \sigma_{\theta\theta}=\{\psi(\nu)+a_1\zeta(\nu)\}\dfrac{E_{in}}{R_{in}^{\beta}}Ar^{\beta+a_1-1}\\ \qquad +\{\psi(\nu)+a_2\zeta(\nu)\}\dfrac{E_{in}}{R_{in}^{\beta}}Br^{\beta+a_2-1}\\ \sigma_{zz}=\zeta(\nu)\dfrac{E_{in}}{R_{in}^{\beta}}A\{a_1+1\}r^{\beta+a_1-1}\\ \qquad +\zeta(\nu)\dfrac{E_{in}}{R_{in}^{\beta}}B\{a_2+1\}r^{\beta+a_2-1}\end{cases} \tag{11}$$

And:

$$f_z=\frac{\alpha_{in}}{R_{in}^{\beta}}A(\alpha_1^2+a_1-1)r^{\beta+\alpha_1-2} +\frac{\alpha_{in}}{R_{in}^{\beta}}B(\alpha_2^2+a_2-1)r^{\beta+\alpha_2-2} \tag{12}$$

III. RESULTS AND DISCUSSIONS

In this section we consider numerical example in order to investigate the analytical solutions obtained in the previous section. We consider a thick cylinder whose elasticity modulus varies in radial direction and has the following characteristics: R_{in} = 0.1 m, R_{out} = 0.2 m.

The elasticity modulus and the magnetic permeability coefficient at the internal radius have values of E_{in} = 200 GPa and a_{in} = 1.2 10^{-6} H/m, respectively. Poisson's ratio was assumed to be constant and was taken as ν = 0.3 and H_z = 2.23 10^9A/m. Also, the cylinder is under an internal and external pressures and are assumed to be P_{in} =500MPa and P_{out} = 0 MPa, respectively.

The applied internal and external pressures are P_{in} = 500 MPa. and P_{out} = 0 MPa, respectively.

The parameter $\beta\in[-2,2]$ values used in this study cover the exponent values encountered in the references cited above. All the graphs including displacements and stresses have been investigated along the radial direction.

It should be noted that positive values of β lead to an increase of the modulus of elasticity and magnetic permeability in the radial direction. While negative values lead to a decrease in the Young's modulus and magnetic permeability in the radial direction.

For different values of β, the distribution of the radial displacement resulted from the analytical solution across the thickness of a cylinder is depicted in Fig. 2. It was obviously observed in Fig. 2 that the radial displacements have its maximum values in internal surface (r = R_{in}). The radial displacement values decrease gradually from inner surface through the outer surface. The increase in radial displacement with the decrease of β is due to the fact that the global stiffness of the cylinder decreases.

The variation in the displacement of heterogeneous material is similar to that of homogenous material.

The normalized radial stress, given by Eq. (11), was plotted in Fig. 3 for different values of inhomogeneity parameter β. The homogeneous case is also shown. The variation in the radial stress of heterogeneous material is similar to that of homogenous material. For all values of β considered, the magnitude of the radial stress has a monotonic behavior increasing in r-direction. It was seen that, for each fixed r in R_{in} < r < R_{0ut} the radial stress magnitude decrease as β increases. It is due to the fact that the global stiffness of the cylinder increases.

The normalized circumferential stress, given by Eq. (11), was plotted along the radial direction and shown in Fig. 4. The hoop stress along the radius decreases monotonically respect to r for all different values of β considered, due to the acting internal pressure and zero external pressure.

Fig. 8 shows the axial stress distribution plotted along the radial direction. The axial stress along the radius decreases for different negative values of β, it increases for the positive

values of β. In the homogeneous case the axial stress remains constant.

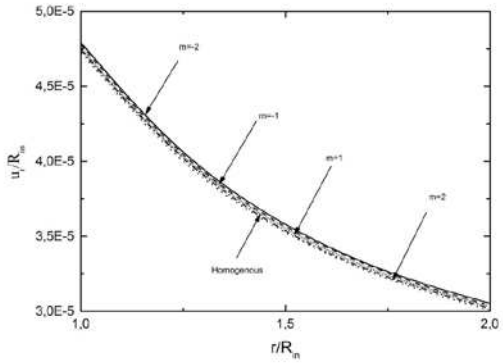

Figure 2. Radial distribution of normalized radial displacement for different values of inhomogeneity parameter

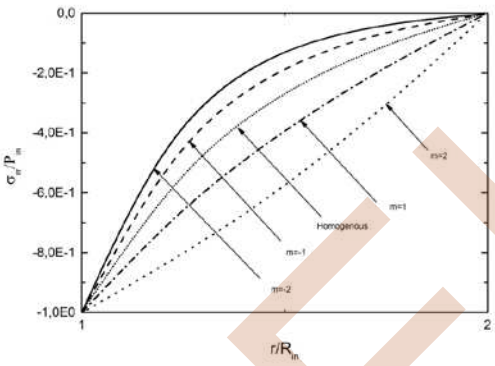

Figure 3. Radial distribution of normalized radial stress for different values of inhomogeneity parameter

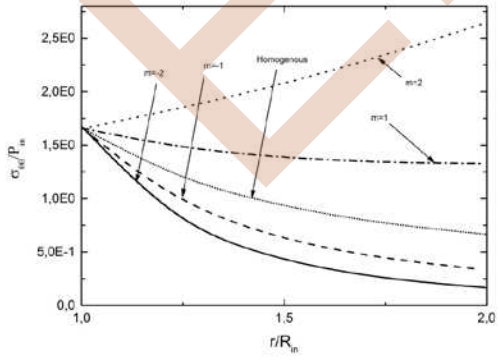

Figure 4. Radial distribution of normalized hoop stress for different values of inhomogeneity parameter

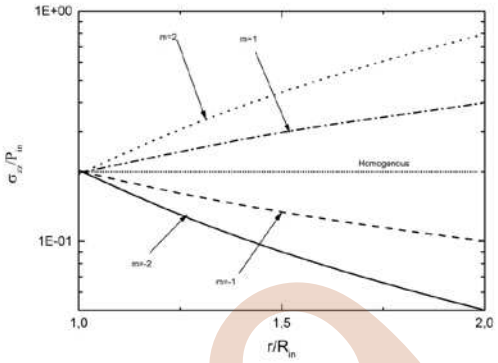

Figure 5. Axial Radial distribution of normalized axial stress for different values of inhomogeneity parameter

IV. CONCLUSION

In this work, an analytical formulation was presented to find displacements and stress components in thick-walled cylinder subjected to internal pressure and uniform magnetic field. The variation of FGM properties was supposed to be a power law expression with nonhomogeneous parameter along the thickness of the cylinder. The results obtained have been compared with results of homogenous cylinders. The results are presented as evolution of the different displacements and stress components through the radial direction and plotted for different material inhomogeneity parameter.

[1] Y. Bayat. H. E. Toussi. General thermo-elastic solution of radially heterogeneous. spherically isotropic rotating sphere. J. of Mech. Sc. And Tech. 29 (6) 2015 2427-2438.

[2] F. N. Dehnavi. A. Parzivi. Investigation of thermo-elasto-plastic behavior of thick walled spherical vessels with inner functionally graded coatings

[3] M.. Jabbari.S.. Sohrabpour.M.R.. Eslami. Mechanical and thermal stresses in a functionally graded hollow cylinder due to radially symmetric loads. International Journal of Pressure Vessels and Piping. 79 (2002) 493-497

[4] J. Dryden and K. Jayaraman. Effect of inhomogeneity on the stress in pipes. J. of Elasticity (2006) 8. 179-189.

[5] Z.W Wang. Q. Zhang. L.Z. Xia. J.T. Wu. P.Q. Liu. Stress Analysis an parameter optimization of an FGM pressure vessel subjected to thermo-mechanical loadings. Procedia Engineering 130 (2015) 374-389.

[6] K. Celebi. D. Yarimpabuc. I. Keles. A novel approach to thermal and mechanical stresses in a FGM cylinder with exponentially varying properties. Journal of theoretical and applied mechanics 55 (2017) 343-351.

[7] M.. Ghannad. G.H..Rahimi. M.. ZamaniNejad. Elastic analysis of pressurized thickcylindrical shells withvariable thickness made of functionally graded materials. Composites: Part B 45 (2013) 388-396.

[8] R.W. Zimmerman, M.P. Lutz, Thermal stresses and effective thermal expansion in a uniformly heated functionally graded cylinder, Journal of Thermal stresses 22 (1999) 177e188.

Propagation in Nonlinear Bi-isotropic media with Different formalisms

Mezache Zinelabiddine

Institute of Optics and fine mechanics, University of Ferhat Abbas Setif 1, 19000 Setif, Algeria

Corresponding author mail: zinemezaache@yahoo.fr

Abstract— **Bi-isotropic mediums present an outstanding challenge for the scientific community, their characteristics have permitted the appearance of new and stupefying applications. In this paper, we are interested in the novel effects of chirality, which characterized through proposed formalism, to highlight the nonlinear effect, is due to the magnetization vector under the influence of a strong electric field. Finally, we have done a theoretical study to define the influences of nonlinear chiral effect parameters on the propagation..**

Key words: bi-isotropic media, Schrödinger equation, nonlinear media.

I. INTRODUCTION

The theoretical studies have been conducted on chiral medium nonlinearity due to strong electric field effect generated by laser on polarization vector , without taking into account the existence of a difference between chiral and achiral media, where one must also evaluate the influence of strong electric field on the magnetization vector because the macroscopic model of electromagnetic wave interaction with chiral structures shows that the vector magnetization is a function of the magnetic and electric fields [1-10]. Our work is to highlight nonlinearity aspects of electric and magnetic fields associated with chirality. Therefore, a new mathematical approach is proposed to evaluate the nonlinear effect belong to magnetization under strong electric field influence [2]. The formalism of constitutive relations has been proposed to confirm these characteristics of this medium.

This allows us to deduce the nonlinear Schrödinger equation. This leads to a better fundamental understanding of the interaction between an electromagnetic wave and chiral media to design potential applications in microwave and optical domains. In this work, we focus on the analysis and modeling of pulse propagating, with our approach of constitutive equations [2].

II. THE CONSTITUTIVE EQUATIONS FOR A NONLINEAR BI-ISOTROPIC MEDIUM

In the bi-anisotropic media, the permittivity ($\overline{\overline{\varepsilon}}_g$), the permeability ($\overline{\overline{\mu}}$) and the coupling parameters ($\overline{\overline{\zeta}}_{EH}$, $\overline{\overline{\zeta}}^{g}_{HE}$) are described by three-dimensional complex tensor terms, so the bi-anisotropic nonlinear effect is characterized through the Mezache-Benabdelaziz formalism [2-6]:

$$\vec{D} = \overline{\overline{\varepsilon}}_g \vec{E} + \overline{\overline{\zeta}}_{EH} \vec{H} \tag{1}$$

$$\vec{B} = \overline{\overline{\mu}} \vec{H} + \overline{\overline{\zeta}}^{g}_{HE} \vec{E} \tag{2}$$

The medium effects are contained in the dyadics $\overline{\overline{\varepsilon}}_g$, $\overline{\overline{\mu}}$, $\overline{\overline{\zeta}}_{EH}$, and $\overline{\overline{\zeta}}^{g}_{HE}$ due to anisotropy.

The nonlinear bi-isotropic medium is described by in our proposed formulation of constitutive equations TABLE I.

TABLE I. Usual formalisms of bi-isotropic nonlinear medium

FORMALISM **A**	TABLE I.	$\vec{D} = \varepsilon_g \vec{E} + \zeta_{EH} \vec{H}$ $\vec{B} = \mu_A \vec{H} + \zeta^{g}_{HE} \vec{E}$
FORMALISM **B**	TABLE II.	$\vec{D} = \varepsilon^{g}_{B} \vec{E} + \sigma_E \vec{B}$ $\vec{H} = \frac{1}{\mu_B} \vec{B} - \sigma_H \vec{E}$
FORMALISM **C**	TABLE III.	$\vec{D} = \varepsilon^{g}_{C} \vec{E} + j\rho^{c}_{EH} \vec{\nabla} \times \vec{E}$ $\vec{B} = \mu_C \vec{H} - j\rho^{c}_{HE} \vec{\nabla} \times \vec{H}$

Where ε and μ are respectively the permittivity and permeability of the chiral medium. After algebraic manipulations we obtain, the relations of passage TABLE I.

TABLE II. The relations of passage between formalisms

RELATIONS OF PASSAGE BETWEEN FORMALISMS **A** AND **B**	$\varepsilon_b^g = \varepsilon_g - \frac{\xi_{EH}\xi_{HE}^g}{\mu_a}$ $\mu_b = \mu_a$ $\sigma_E = \frac{\xi_{EH}}{\mu_a}$ $\sigma_H = \frac{\xi_{HE}^g}{\mu_a}$
RELATIONS OF PASSAGE BETWEEN FORMALISMS **A** AND **C**	$\varepsilon_C^g = \varepsilon_g - \frac{\xi_{EH}\xi_{HE}^g}{\mu_A}$ $\mu_C = \mu_A - \frac{\xi_{EH}\xi_{HE}^g}{\varepsilon_g}$ $\rho_{EH}^c = \frac{\xi_{EH}}{\omega\mu_a}$ $\rho_{HE}^c = \frac{\xi_{HE}^g}{\omega\varepsilon_g}$

The linear chirality factors are given by [7, 8]:

$$\zeta_{EH} = \delta - j\kappa \tag{3}$$

$$\zeta_{HE} = \zeta_{EH}^*$$

δ and κ are respectively the non-reciprocity parameter and the chirality parameter.

$$\varepsilon_g = \varepsilon + \varepsilon_{NL} \tag{4}$$

$$\zeta_{HE}^g = \zeta_{EH}^* + \zeta_{HE}^{NL} \tag{5}$$

ε_{NL} and ζ_{HE}^{NL} are respectively the nonlinear permittivity, and the chiral nonlinear coefficient.

This work provides a modeling of propagating in chiral media with Kerr effect corresponds to the existence of nonlinear susceptibility of third order purely real, as expressed by our expressions as follows [2-6] :

$$\varepsilon_g = \varepsilon + \varepsilon_{Kerr}\left|E^2\right| \tag{6}$$

$$\zeta_{HE}^g = \zeta_{EH}^* + \zeta_{HE}^{Kerr}\left|E^2\right| \tag{7}$$

ζ_{EH}^* is the linear chirality coefficient, where the term $\zeta_{HE}^{Kerr}\left|E^2\right|$ corrects the chirality coefficient with a quantity proportional to the field intensity.

III. LIGHT PULSE PROPAGATION MODELING

A chiroptical fiber is optical fiber with a bi-isotropic core surrounded by an optical cladding (Fig. I). The chiral core has a slightly higher refractive index than that of the cladding . This difference of index will cause total reflection of the light inside the bi-isotropic core, which will allow the propagation of light with two modes of propagation: a right circular polarized wave (RCP) and a left circular polarized wave (LCP) having two different wave vectors.

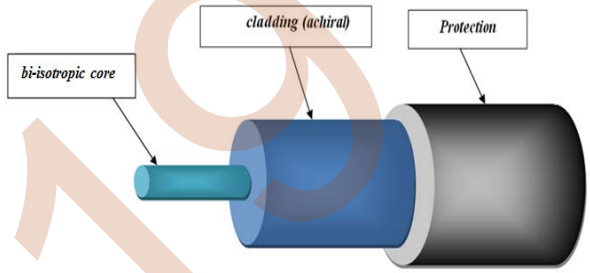

Figure. I. Conception of bi-isotropic fiber

We consider the first Maxwell equation, Maxwell-Faraday's equation:

$$\vec{\nabla}\times\vec{E} = -\frac{\partial\vec{B}}{\partial t} \tag{8}$$

we consider Maxwell-Ampere's equation, which is given by:

$$\vec{\nabla}\times\vec{H} = \frac{\partial\vec{D}}{\partial t} \tag{9}$$

After algebraic manipulations of Maxwell's equations, and constitutive relations for nonlinear bi-isotropic medium we get :

TABLE III. Propagation equation for usual Formalism

FORMALISM	PROPAGATION EQUATION
FORMALISM **A**	$\vec{\nabla}^2.\vec{E} = \left(\mu_A\varepsilon_g + \zeta_{HE}^g\zeta_{EH}\right)\frac{\partial^2\vec{E}}{\partial t^2} + \left(\zeta_{HE}^g - \zeta_{EH}\right)\frac{\partial\vec{\nabla}\times\vec{E}}{\partial t}$
FORMALISM **B**	$\vec{\nabla}^2.\vec{E} = \mu_B\varepsilon_B^g\frac{\partial^2\vec{E}}{\partial t^2} + \mu_B\left(\sigma_H - \sigma_E\right)\frac{\partial\vec{\nabla}\times\vec{E}}{\partial t}$
FORMALISM **C**	$\left(1+\rho_{EH}^c\rho_{HE}^c\frac{\partial^2}{\partial t^2}\right)\vec{\nabla}^2.\vec{E} = \mu_C\varepsilon_C^g\frac{\partial^2\vec{E}}{\partial t^2} + j\left(\rho_{EH}^c\mu_C - \rho_{HE}^c\varepsilon_C^g\right)\frac{\partial^2\vec{\nabla}\times\vec{E}}{\partial t^2}$

This permitted us to deduce the propagation equation of Formalism **A** :

$$\vec{\nabla}^2.\vec{E}-\left(\mu\varepsilon-\mu_0\varepsilon_0\kappa^2\right)\frac{\partial^2\vec{E}}{\partial t^2}-2j\kappa\sqrt{\mu_0\varepsilon_0}\,\frac{\partial\vec{\nabla}\times\vec{E}}{\partial t}=$$

$$\left(\mu\varepsilon_{Kerr}-\mu_0\varepsilon_0\kappa\kappa^{Kerr}\right)\left|\vec{E}\right|^2\frac{\partial^2\vec{E}}{\partial t^2} \qquad (10)$$

$$+j\sqrt{\mu_0\varepsilon_0}\kappa^{Kerr}\left|\vec{E}\right|^2\frac{\partial\vec{\nabla}\times\vec{E}}{\partial t}+\mu\sigma\frac{\partial\vec{E}}{\partial t}$$

Where: $\zeta_{EH}=-j\kappa\ \zeta_{HE}^{g}=j\left(\kappa+\kappa^{Kerr}\left|E^2\right|\right)$

Optical electric field in the chiroptical fiber is represented by a right-hand or left-hand polarized component propagating in the z direction [9, 10]:

$$\vec{E}_{\pm}=\left(\vec{e}_x\pm j\vec{e}_y\right)\Psi_{\pm}\left(\vec{r},t\right)e^{-j\left(k_{\pm}z-\omega_0 t\right)} \qquad (11)$$

The two modes of propagation: right circular polarized wave (RCP) and left-circular polarized wave (LCP) propagating respectively with the wave numbers k_+ and k_- defined by:

$$k_{\pm}=\pm\kappa\sqrt{\mu_0\varepsilon_0}+\sqrt{\mu\varepsilon-\delta^2\mu_0\varepsilon_0}$$

Slowly varying envelope conditions in the weak guidance approximation are cited by the author [9, 10]:

$$\left|\frac{\partial^2}{\partial z}\vec{\Psi}_{\pm}\right|<<\left|j2k_{\pm}\frac{\partial}{\partial z}\vec{\Psi}_{\pm}\right|,\left|\frac{\partial}{\partial t}\vec{\Psi}_{\pm}\right|<<\left|j\omega_0\vec{\Psi}_{\pm}\right|$$

$$,\left|\frac{\partial^2}{\partial t}\left|\vec{\Psi}_{\pm}\right|^2\vec{\Psi}_{\pm}\right|<<\left|j\omega_0\frac{\partial}{\partial t}\left|\vec{\Psi}_{\pm}\right|^2\vec{\Psi}_{\pm}\right|<<\left|j\omega_0\left|\vec{\Psi}_{\pm}\right|^2\vec{\Psi}_{\pm}\right| \qquad (12)$$

$$\frac{A_{\pm}(z,t)}{2k_{\pm}}.\vec{e}_z=\vec{\Psi}_{\pm} \qquad (13)$$

Where $\vec{A}_{\pm}$ is the complex envelope for both RCP and LCP waves.

These conditions of high frequency approximations were used; and after algebraic manipulations we obtain the Chiroptical fiber propagation equation:

$$\left(\frac{\partial}{\partial z}A_{\pm}(z,t)+\frac{1}{v}\frac{\partial}{\partial t}\left(1\mp\frac{\vartheta}{k}\right)A_{\pm}(z,t)\right)=$$

$$-j\frac{\left(\omega_0^2\mu\varepsilon_{Kerr}+k\vartheta^{Kerr}\right)}{\left(2k_{\pm}\right)^3}\left|A_{\pm}(z,t)\right|^2A_{\pm}(z,t) \qquad (14)$$

$$-\frac{\mu\sigma\omega_0}{2k_{\pm}}A_{\pm}(z,t)$$

$$\frac{k}{\omega_0}=\frac{1}{v}\ \text{and}\ \vartheta^{Kerr}=\omega_0\sqrt{\mu_0\varepsilon_0}\kappa^{Kerr}$$

Using Fourier transform of $\Delta k=\frac{1}{v}\frac{\partial}{\partial t}$ and $\Delta\omega$ for approximating $1/v\cong\Delta k/\Delta\omega$, and according to a development in Taylor series, which gives [9, 10]:

$$\Delta k=\frac{1}{v}\frac{\partial}{\partial t}=\frac{\partial k}{\partial\omega_0}\frac{\partial}{\partial t}+j\frac{1}{2}\frac{\partial^2k}{\partial\omega_0^2}\frac{\partial^2}{\partial t^2}-\frac{1}{6}\frac{\partial^3k}{\partial\omega_0^3}\frac{\partial^3}{\partial t^3} \qquad (15)$$

This leads to the nonlinear Schrödinger equation on the field strength along the Chiroptical fiber:

$$\left(\frac{\partial}{\partial z}A_{\pm}(z,t)+\frac{1}{v_g}\left(1\mp\frac{\vartheta}{k}\right)\frac{\partial}{\partial t}A_{\pm}(z,t)\right.$$

$$+j\frac{1}{2}k^{''}\left(1\mp\frac{\vartheta}{k}\right)\frac{\partial^2}{\partial t^2}A_{\pm}(z,t)$$

$$\left.-\frac{1}{6}k^{'''}\left(1\mp\frac{\vartheta}{k}\right)\frac{\partial^3}{\partial t^3}A_{\pm}(z,t)\right)$$

$$=-j\frac{\left(\omega_0^2\mu\varepsilon_{Kerr}+k\vartheta^{Kerr}\right)}{\left(2k_{\pm}\right)^3}\left|A_{\pm}(z,t)\right|^2A_{\pm}(z,t) \qquad (16)$$

$$-\frac{\mu\sigma\omega_0}{2k_{\pm}}A_{\pm}(z,t)$$

$k^{'}=\frac{\partial k}{\partial\omega}=\frac{1}{v_g}$: indicates that the pulses are moving with the group velocity, v_g ,while the dispersion of the group velocity is represented by $k^{''}=\frac{\partial^2k}{\partial\omega_0^2}$. $k^{'''}=\frac{\partial^3k}{\partial\omega_0^3}$ represents the slope of the group velocity dispersion also called cubic dispersion and corresponds to a higher order dispersion; important in ultra-short pulses [10].

We define the following parameters:

$$\beta_1=\frac{1}{v_g}\left(1\mp\frac{\vartheta}{k}\right)\ \text{and}\ \beta_2=k^{''}\left(1\mp\frac{\vartheta}{k}\right),\ \beta_3=k^{'''}\left(1\mp\frac{\vartheta}{k}\right)$$

and $\alpha=\frac{\omega_0\mu\sigma}{k_{\pm}}$

The nonlinear coefficient is:

$$\gamma=\frac{\left(\omega_0^2\mu\varepsilon_{Kerr}+k\vartheta^{Kerr}\right)}{\left(2k_{\pm}\right)^3}\quad\text{Where: }\gamma\in\left]0,1\right]$$

We note that, by setting the variable $\tilde{t}=t-\beta_1z$, we obtain the nonlinear Schrödinger equation as follows:

$$j\frac{\partial A_{\pm}(z,\tilde{t})}{\partial z}+\frac{1}{2}\beta_2\frac{\partial^2}{\partial\tilde{t}^2}A_{\pm}(z,\tilde{t})-j\frac{1}{6}\beta_3\frac{\partial^3}{\partial\tilde{t}^3}A_{\pm}(z,\tilde{t})= \qquad (17)$$

$$\gamma\left|A_{\pm}\right|^2A_{\pm}(z,\tilde{t})-j\frac{\alpha}{2}A_{\pm}(z,\tilde{t})$$

From the wording of this equation, two effects are apparent: the dispersion and nonlinearity. We can introduce two lengths [10] that quantify them.

IV. CONCLUSION

This research work is concerned with a new formulation of constitutive relation linking to the magnetic effect, to understand rigorously the physical nature of chiral effects and to generalize the main macroscopic models of chirality to nonlinear ones. We inferred the nonlinear Schrodinger equation for a chiral medium term with a nonlinear term of magnetizing.

REFERENCES

[1] D. L. Jaggard, A. R. Mickelson and C. H. Papas, "On electromagnetic waves in chiral media, "Applied physics, Vol. 28, pp 211 - 216, 1979

[2] Mezache, Z., and Benabdelaziz, F. Rigorous Approach of the Constitutive Relations for Nonlinear Chiral Media. Progress in Electromagnetics Research Letters. **52** 57-62 (2015).

[3] Mezache, Z., Aib, S., Benabdelaziz, F., Zebiri, C. Modeling of a light pulse in bi-isotropic optical fiber with Kerr effect: case of Tellegen media. Nonlinear Dynamics, **86**(2), 789-794 (2016).

[4] Mezache, Z., and Benabdelaziz, F. Study of chiroptical fiber nonlinearities with new formulation of constitutive equations. Journal of Electromagnetic Waves and Applications. **29** 2257-2268 (2015).

[5] Mezache, Z., and Benabdelaziz F. Effect of the Nonlinear Parameters on the Propagation in Bi-isotropic Media. International Journal of Nonlinear Sciences and Numerical Simulation **18**(6), 541-547 (2017).

[6] Mezache, Z., and Benabdelaziz, F. Nonlinear effects in chiral nihility metamaterial. Optical and Quantum Electronics, **50** (8), 328 (2018).

[7] A. H.Shivola and I.V.Lindell, "Chiral Maxwell Garnett mixing formula, "Electronics Letters, Vol. 26, no. 2, pp. 118-119, 1990.

[8] A.H.Sihvola and I.V.Lindell, "Bi-isotropic constitutive relations, "Micro.Opt.Tech.Lett, Vol.4, no.3, 391-396, 1991.

[9] M. Zamorano and H. Torres Silva, "Schrödinger equation for a Fiber chiral", Journal Mexicana Physics, Vol. 46, Nº1, pp 62-66, Feb. 2000.

[10] Torres-Silva, H., and M. Zamorano Lucero. "Non-linear polarization and chiral effects in birefringent solitons." Pramana 62.1 (2004): 37-52.

Inverse Problems using Genetic Algorithm for Cracks Characterization in Materials

O. S . Benmoussa[1]
[1] Electrical Engineering Department, Kasdi Merbah university ,ouargla.
Ouargla Algeria
b.selma1992@gmail.com

T. Bouchala[2], A. N. A. I. Ayad[2]
[2] Electrical Engineering Department, Kasdi Merbah University, Ouargla.
Ouargla Algeria
buizra@yahoo.fr, ayadnourislam@yahoo.fr

***Abstract*—**In this paper, we will be interested in The study of eddy current nondestructive testing systems for cracks characterization using finite element method requires a high cost in view of calculation time and memory space. Therefore, the optimization of the inversion technique associated to this method permits to reduce the time of defect characterization .In this work we will be interested in the identification and estimation of the physical and geometrical parameters of an aeronautical construction metal sheet made of Al, Ti and stainless steel 304L by using the inverse approach associated with the genetic algorithm. We identifying those parameters that have been changed, such as electrical conductivity, permeability and thickness.

Keywords: Eddy Current; Inverse Problem; Aeronautic Materials; genetic algorithm.

I. INTRODUCTION

Eddy currents nondestructive testing is a well-known method for material characterization, which is sensitive to conductive materials properties such as: electrical conductivity and thickness, [1].

Eddy current testing is one of the non destructive techniques (NDT) often used to detect defects and ensure total integrity of conducting materials. It is one of the most applied methods in aeronautical field. [2]

In this paper, our aim is to associate finite element method and the optimization methods to estimate thickness and electric conductivity and the magnetic permeability of Al, Ti and stainless steel 304L metal sheet largely used in aeronautic construction. the joint use of optimization methods and the finite element method in order to solve some inverse problems related to non-destructive testing, such as the characterization of materials

II. AERONAUTIC CONSTRUCTION MATERIALS

The alloys that form the hull of an aircraft are mostly aluminum alloys and belong to two series of alloys, the 2000 series and the 7000 series, which are respectively aluminum alloys with copper and zinc. Aluminum is widely used in general because its density is very low, which is of great interest in aeronautics. In fact, the lighter the airplane, the less fuel it will consume. Aluminum is also highly valued for its good resistance to corrosion.

In aeronautics, several types of composites are used for the structure of an airplane. In general, composite materials have certain advantages over other materials. They have higher rigidity, excellent mechanical properties, and excellent resistance to fatigue and corrosion. Another advantage of composite materials is that they do not promote the propagation of damage during impact for example. This type of material also brings great flexibility in the design.

• The Titan is today one of the key elements of aerospace construction since its use is justified by its characteristics: incomparable resistance to corrosion and oxidation, non-magnetic tendency, high thermal and mechanical resistance, ductility, biocompatibility, low density.

• Inox is an alloy that is not very sensitive to corrosion. This alloy is the ideal material for work piece machining in applications in very demanding environments, such as Stainless Steel 304L

• Stainless steel 304L Correct corrosion resistance. It is weldable in aeronautics.

III. DESCRIPTION OF THE PROBLEM

A. FINITE ELEMENT MODELLING

The eddy current problem can be described mathematically by the following partial differential equation
in terms of the magnetic vector potential [3] [4].

$$rot\ (\ 1/\mu\ rot(A)) = -\ j\ \sigma\ \omega A + J_s \qquad (1)$$

Where, **A** represents the magnetic vector potential, j is the imaginary unit, ω is the angular frequency of the excitation current (rad/s), μ is the magnetic permeability of the media involved (H/m), σ is the electrical conductivity (S/m), and J current density (A/m2).
The finite element formulation for the 2D axisymmetric eddy current phenomena was developed in many works. For axisymmetric geometries equation (1) reduces to the 2D form [2][4].

$$\frac{1}{\mu}\left(\frac{\partial^2 A}{\partial r^2}+\frac{1}{r}\frac{\partial A}{\partial r}+\frac{\partial^2 A}{\partial z^2}-\frac{A}{r^2}\right)=j\sigma\omega A-J_s \qquad (2)$$

This equation describes the problem shown in Fig. 2.

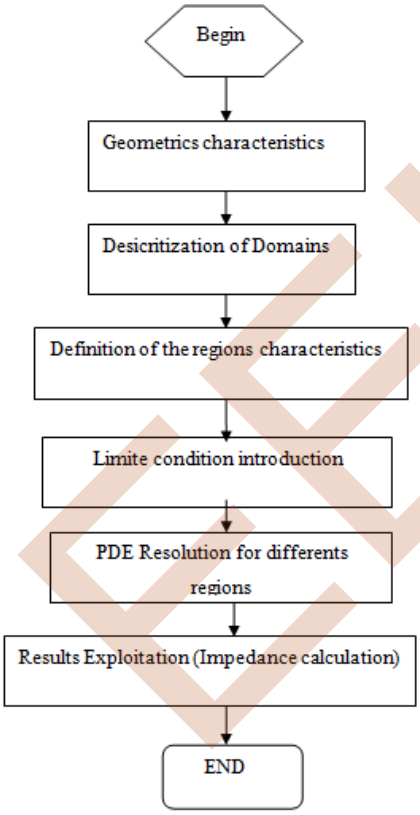

Fig. 1 Finite element modelization steps

B. *Studied device*

The geometry of the problems considered is illustrated schematically in Fig.2. In this study, the metal sheet presents a flat surface with a thin nonconductive coating. In actual situation, when using eddy current to measure thickness and electric conductivity, it is important to ensure that the other factors (geometry, the specimen temperature and lift-off) are kept under control. A pancake-type, probe formed of coil is perpendicular to the tested metal sheet surface .

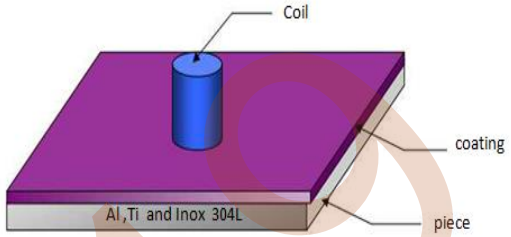

Figure 2. Studied device configuration

The geometrical and physical characteristics are reported on Table 1.

Table 1. Characteristics of the Modeled System

coil	
Current intensity	0.04 A
Frequency	10 kHz
Inner radius	5.35 [mm].
Length	2.35 [mm].
High	2.3 [mm].
Metal Sheet	
Thickness	2 [mm].
Electric conductivity	That of Al, Inox 304L, Ti
Magnetic permeability	1

IV. OPTIMIZATION MODEL

In order to solve the problem in reverse, which is the search for the physical and geometric characteristics of the materials (Al, Ti and stainless steel 304L), we need a direct model based on the finite element method associated with an optimization method. Indeed, once the coupling is achieved and the optimization algorithm is implemented under Matlab we exploit it for the simultaneous measurement of the thickness and the conductivity and permeability of hull construction plates of an aircraft.

A. PROPERTIES EVALUATION BY INVERSION

An iterative algorithm of inverse technique is elaborated in order to evaluate the physical properties of the conducting

piece (i.e., electric conductivity σ and magnetic permeability μ). The inversion is achieved by stochastic method (genetic algorithm (GA), [6] associated to direct model (finite element). It uses selected evaluation parameters and gives the evaluated properties.

A. Genetic Algorithm

At first, individual populations are created according to a random process. Each individual takes a set of the evaluation parameters. Then, in an iterative way, the fitness (objective function) is computed for all individuals, and couples of individuals are mixed together and someone's are probably muted so as to obtain a better population, using genetic operators in a way inspired by natural evolution of living organisms [6].

V. THICKNESS AND ELECTRIC CONDUCTIVITY AND PERMEABILITY CALCULATION BY METHODS OF OPTIMIZATION

Thickness and electric conductivity of the inspected metal sheet largely used in aeronautic construction are calculated by genetic method. The previous parameters and the fitness function according to iteration number are given in the following figures. We recall that these results are obtained for a metal sheets of 2 mm of thickness and made of Al , stainless steel 304L and Ti of electric conductivity 37.7MS/m, 1.36 MS/m and 2.52 MS/m, Respectively, [7, 8].

VI. . RESULTS AND DISCUSION

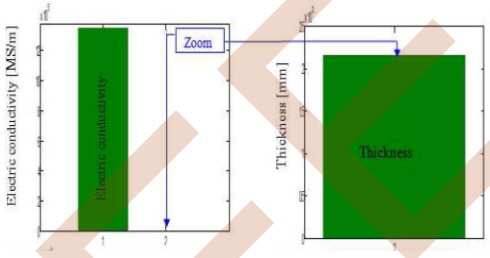

Fig 3. Thickness and electric conductivity obtained by GA of Inox

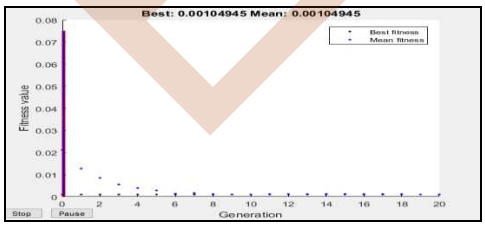

Fig 4. The objective function of the conductivity with the iterations of Inox

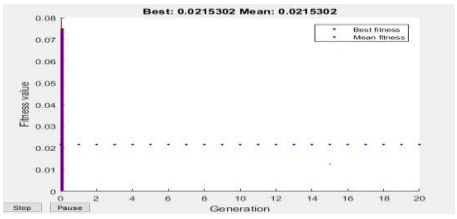

Fig 5. The objective function of the permeability with the iterations of Inox

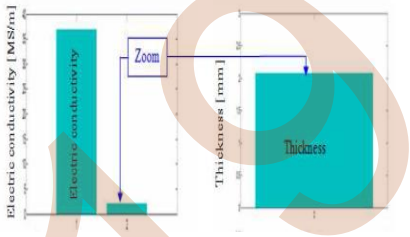

Fig 6. Thickness and electric conductivity obtained by GA of Aluminum

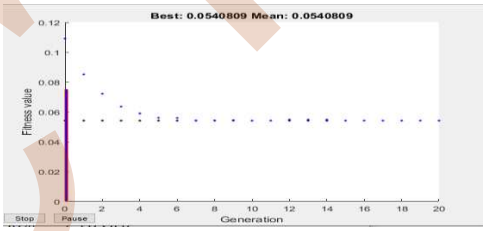

Fig 7. The objective function of the conductivity with the iterations of Aluminum

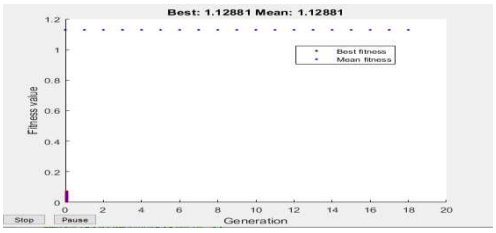

Fig 8 .The objective function of the permeability with the iterations of Aluminum

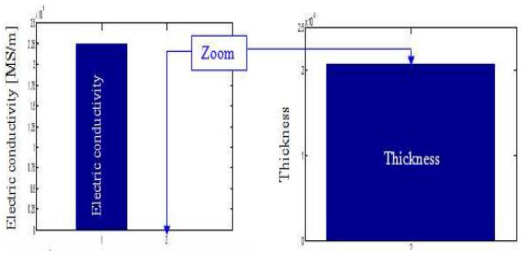

Fig.9. Thickness and electric conductivity obtained by GA of Titanium

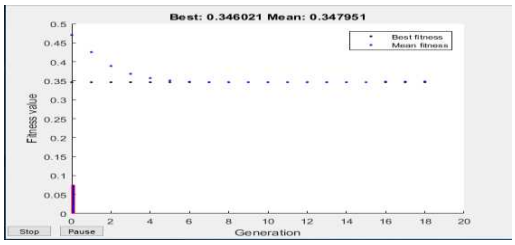

Fig 10. The objective function of the conductivity with the iterations of Titanum

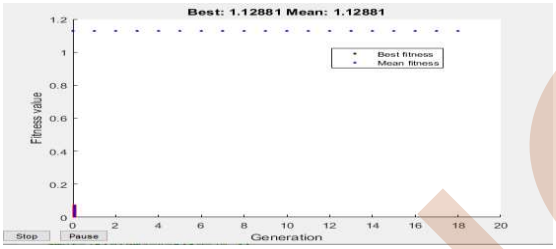

Fig 11. The objective function of the bermeability with the iterations of Titanum

During this application we have seen that the values obtained by the method of genetic algorithm, are very accurate and closer to optimal values; this which shows the robustness of this method.
but we have seen also, that the method of the genetic algorithm is very expensive in time of calculation because of the high number of objective function evaluations at each iteration of the algorithm. On the other hand, to achieve an acceptable accuracy the size of the population must be increased, which causes a significant calculation time.

CONCLUSION

It is very important to make sure that application of artificial intelligence will be good substitute or help of the NDT operators' [9]
Absolutely, when using inverse algorithms involving artificial intelligence, the measurement can be made simultaneously and rapidly, [1] we have found that the genetic algorithm is a method that takes a *very long time* and falls into a local minimum, for this reason in the next work we will look for other optimization methods and we will use GA as a reference tool.

REFERENCES

[1] T. Bouchala, B. Abdelhadi and A. Benoudjit, ''New Contactless Eddy Current Non-destructive Methodology of Electric Conductivity Measurement'' Journal of non-Destructive Testing and Evaluation. Francis and Taylor. Vol. 30, Issue 1, pp. 63-73. 2015.

[2] Bouchala T., Abdelhadi B. and Benoudjit A., ''Novel Coupled Electric Field Method for Defect Characterization in Eddy Current non Destructive Testing''. Journal of Non-Destructive Evaluation, Springer, Vol. 32, Issue 4, pp., 2013.

[3] A. Ayad, A. Semmah, Y.Ramdani, H. Hamdaoui, K. M. Faraoun " Design of an Optimal Neural Network for Evaluating the Thickness and Conductivity of the Metal Sheet " Journal of Computer Science INFOCOMP, Vol 07,N°02,pp52-57, June 2008.

[4] N. Ida "Alternative approaches to the numerical calculation of impedance". NDT International v 21, February 1988.

[5] S-J Song, Y-K Shin "Eddy current flaw characterization in tubes by neural networks and finite element modeling". NDT&E International Vol 33,pp 233-243, 2000.

[6] Bouzidi A., Maouche B. and Feliachi M., ''Pulsed Eddy Current NDE of Groove Dimensions by Inversion with Simplex Method Associated with Coupled Electric Circuits Method''.IEEE Transactions on Magnetics, Vol.51, No. 3, pp. , March 2015.

[7] Maa X., Peytona A. J. and Zhaob Y .Y., ''Measurement of the Electrical Conductivity of Open- Celled Aluminium Foam using non-Contact Eddy Current Techniques''. NDT&E Int., 38, 359–367, 2005.

[8] Lunin V. P., ''Phenomenological and Algorithmic Method for the Solution of Inverse Problem of Electromagnetic Testing''. Russ J. Non-Destr Test. 42(6), pp. 353–362, 2006.

[9]

Numerical Simulation of Streamer Propagation in Point-Plane Air Gaps using COMSOL Multiphysics

M.A.Benziada, A.Boubakeur, A.Mekhaldi
Laboratoire de Recherche en Electrotechnique, Ecole Nationale Polytechnique
B.P 182 El-Harrach 16200 Algiers, Algeria
mohamed_abdelghani.benziada@g.enp.edu.dz, ahmed.boubakeur@g.enp.edu.dz and abdelouahab.mekhaldi@g.enp.edu.dz
www.enp.edu.dz

***Abstract*— In this paper, the formation and propagation of streamers in point-plane geometry under DC voltage is studied. The electrical streamer discharge in the air is presented using a two-dimensional hydrodynamic model, which introduces the photo-ionization effect. This model of non-thermal streamer discharges has been successfully implemented in the commercial software COMSOL Multiphysics® using finite element method and has been developed for a point-plane system with a distance between electrodes equal to 5 cm. Results of simulations demonstrating propagation of streamer in air under normal conditions in a point-plane electrode system are analyzed. The numerical simulation makes it possible to predict the behavior of the system studied without having to go through the realization of real tests expensive and difficult to put in place.**

Keywords – streamer discharge, hydrodynamic model, finite element method, point-plane air gap, numerical method.

I. INTRODUCTION

The phenomena of electric discharge, which have been studied for nearly two centuries, are always the object of active research with scientists. We might be surprised at this fact but we quickly understand that it is only due to the great complexity of the phenomenon and the mechanisms that constitute it.

However, great advances have been made in recent decades in the improvement of the means of diagnosis of the first instants of discharge and hence in the study of the mechanisms of initiation. This has led to an increase in knowledge about the phenomenon and progress in applications that have experienced much wider expansions [1].

The theory of the streamers was developed following the work of Loeb, Meek, and Raether in 1940 [2,3,4]. In their model, the advance of the discharge is explained by that of an ionization front, which propagates within the inter-electrode space. Once the initialized discharge is observed, its propagation is ensured without the aid of any external agent.

Several investigations by a number of authors have been carried out to study the streamer discharge and many papers have been published on this effect [5,6].

The recent work of Y. Serdyuk and al [7,8] studied various geometries of electrodes, for the study of a streamer in the air at atmospheric pressure. They have considered that the streamer has the shape of a cylindrical channel of a fixed radius and that the charge is uniformly distributed over the entire cross-section of the channel. A hydrodynamic model has been used in their work to calculate particle densities. The electric field is calculated by solving the Poisson equation by applying the cylindrical coordinates.

The formation of a streamer is explained by the phenomena of photo-ionization in primary avalanches. The electrons accelerated by the electric field excited by collision atoms of the surrounding gas, which return to their fundamental state with emission of the photons.

If these photons have an energy less than the ionization energy of the atoms of the gas, these atoms can absorb them before being emitted again. If their energy is higher than the ionization energy of the atoms of the gas, new electrons can be released. If the electrons thus produced are located near the primary avalanche, they will create new avalanches called secondary avalanches [9,10]. The formation and propagation of secondary avalanches through the anode leave in their wake positive ions and fewer electrons, which form a zone of space charges, called "streamer".

For the transition of the avalanche to a streamer, the local electric field needs to become comparable with the initial background field that happens when the number of charge carriers (electrons) in the avalanche head becomes larger than $\sim 10^8$. This corresponds to the density $\sim 10^{20}$ m^{-3} and degree of ionization of the gas $\sim 10^{-5}$ [11].

Simulation of an electrical discharge is not a new problem. Indeed, for many years the authors have proposed simulations first in one dimension by considering only on the axis. These one-dimensional models remain limited and do not fully account for the physics of discharges. This is why many authors have studied two-dimensional modelling. Thus, simulations with a uniform field (plane-plane) and then a non-uniform field have appeared successively [12,13].

In this study, we model the streamer discharge in a point-plane air gap with positive applied voltage. A two-dimensional simulation was performed using COMSOL Multiphysics based on finite element method.

II. SIMULATION MODEL

The hydrodynamic approach is one of the most widely approaches used for modelling the streamer discharge and it is therefore presented in detail below.

A. Governing Equations

To simulate the electric field in the air, a hydrodynamic model is used. This model describes the generation, the annihilation and the movement of three species (electrons, positive ions, and negative ions) [7]. It includes a set of mass conservation equations for the charge carriers in the gas coupled with the Poisson's equation for the calculation of the electric field and is described by the equations (1) to (4) [7]:

$$\frac{\partial N_e}{\partial t} + \nabla.(-N_e W_e - D_e \nabla N_e) = R_e \quad (1)$$

$$\frac{\partial N_p}{\partial t} + \nabla.(-N_p W_p - D_p \nabla N_p) = R_p \quad (2)$$

$$\frac{\partial N_n}{\partial t} + \nabla.(-N_n W_n - D_n \nabla N_n) = R_n \quad (3)$$

$$(-\varepsilon_0 \varepsilon_r \nabla V) = q(N_p - N_e - N_n),\ E = -\nabla V \quad (4)$$

Here, subscripts *e, p,* and *n* indicate the quantities related to electrons, positive ions, and negative ions, respectively. *N* stands for the charge carrier density, [m^{-3}]; *D* is the diffusion coefficient, [$m^2\ s^{-1}$]; μ is the mobility, [$m^2V^{-1}s^{-1}$]; ***E*** is the vector of electric field, [Vm^{-1}]; V is the electric potential, [V]. *t* stands for time, [s]; and *R* specifies source terms (rates of the processes in discharge plasma), [$m^{-3}\ s^{-1}$]; $q = 1.6 \cdot 10^{-19}$ [C] is the elementary charge, and $\varepsilon_o = 8.854 \cdot 10^{-12}$ [Fm^{-1}] is the permittivity of vacuum.

The mobility of ions is much lower than that of electrons; hence, the ions are assumed immobile.

The so-called source terms on the right-hand side of (1)-(3) include rates of processes taking place in the discharge volume. Thus, background ionization, electron impact ionization, electron attachment, electron-ion recombination and ion–ion recombination are the main phenomena to be considered when (1)-(3) are used to describe the development of electron avalanches in air.

Note that the shown source terms are dependent on the local electric field strength, which is obtained by solving equation (4) taking into account the density of the space charge (right-hand side of the equation).

The resulting process rates for the different charged particles can be expressed as follows [7]:

$$\begin{aligned} R_e &= R_{ion} + R_{det} + R_0 - R_{att} - R_{ep} + R_{ph} \\ R_p &= R_{ion} + R_0 - R_{pn} - R_{ep} + R_{ph} \\ R_n &= R_{att} - R_{det} - R_{pn} \end{aligned} \quad (5)$$

Where R_0 represents the rate of background ionization in zero field limit; $R_{ion} = \alpha N_e W_e$ is the rate of electron impact ionization (α stands for Townsend's ionization coefficient, m^{-1}); $R_{att} = \eta N_e W_e$ is the rate of electron attachment to electronegative molecules (η is attachment coefficient, m^{-1}); $R_{det} = k_{det} N_e N_n$ is the rate of detachment of electron from negative ions (k_{det} is detachment coefficient, m^3/s).

R_{ph} describe the rate of generation of ions and electrons due to photo ionization. More details about this rate can be found in section B.

Two types of recombination are considered, electron-ion and ion-ion, with the rates $R_{ep} = \beta_{ep} N_e N_p$ and $R_{pn} = \beta_{pn} N_p N_n$, respectively ($\beta$ stands for corresponding recombination coefficient, m^3/s).

The model parameters used in the present study are adopted from [7] and are:

$$\begin{aligned} \mu_p &= 2.10^{-4} && [m^2/V\,s] \\ \mu_n &= 2.2.10^{-4} && [m^2/V\,s] \\ D_p &= 5.05.10^{-6} && [m^2/s] \\ D_n &= 5.56.10^{-6} && [m^2/s] \\ \beta_{ep} &= 5.10^{-14} && [m^3/s] \\ \beta_{pn} &= 2.07.10^{-12} && [m^3/s] \\ k_{det} &= 10^{-18} && [m^3/s] \\ R_0 &= 1.7.10^9 && [1/m^3\,s] \end{aligned} \quad (6)$$

Drift velocity and diffusion coefficient of electrons as a function of the electric field are approximated as [7]:

$$W_e = 3200 \left(\frac{E}{N}\right)^{0.8} \quad (7)$$

$$D_e = 0.07 + 8 \left(\frac{E}{N}\right)^{0.8} \quad (8)$$

With $N = 2{,}5.10^{25}$ [$1/m^3$] is the gas density.

The equations of the model have been complemented with boundary conditions and initial conditions given in [7] and are implemented in the COMSOL Multiphysics software.

B. Modeling of the photoionization

The additional source included in the drift-diffusion equation is photo-ionization, which is a non-local source of seed electrons in front of streamer head during streamer propagation.

There are several methods and numerical solutions to obtain the rate of photoionization [14,15]. Among these methods, we use the differential approach proposed in [14] where it is found as a sum of solutions of Helmholtz equations, which are used to represent the real problem of radiation transport in a gas:

$$\nabla^2 R_{ph}^j(r) - \left(\lambda_j p_{o_2}\right)^2 R_{ph}^j(r) = -A_j {p^2}_{o_2} I(r) \quad (9)$$

$$R_{ph} = \sum_j R_{ph}^j \quad (10)$$

Where $R_{ph}^j(r)$ is the intensity of photoionization per unit volume; p_{o_2} is partial pressure of oxygen (=150 Torr at atmospheric pressure); λ_j and A_j are fitting parameters and $I(r)$ is the photon production rate proportional to the ionization rate.

In the present study, two exponential fit is used with the parameters λ_j and A_j from [15] presented in table 1.

The local intensity of generation of photons is a function of electron impact ionization rate $I(r) = P_q \varepsilon R_{ion}/(P_{O_2} + P_q)$, where P_q is the quenching pressure (60 Torr) and ε is the efficiency of generation of photons.

j	Aj (cm^{-2} $Torr^{-2}$)	λ_j (cm^{-1} $Torr^{-1}$)
1	0.0021	0.0974
2	0.1775	0.5877

Table 1. Parameters of the two-exponential fit.

C. Implementation

The geometry of the used point-plane electrode system is presented in figure 1.

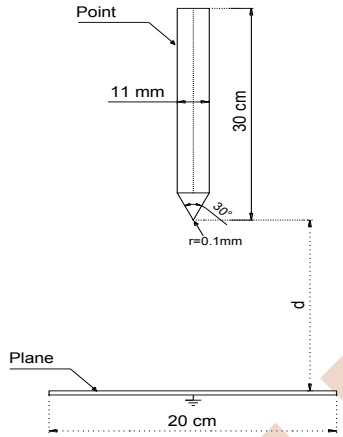

Fig.1 Point-plane configuration.

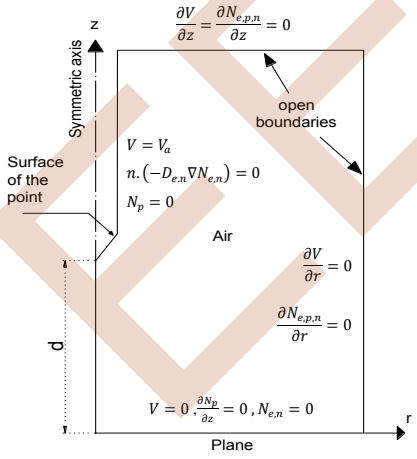

Fig.2 Computational domain, **n** is the unit vector normal to the boundary.

The point-plane arrangement consists of two electrodes. The high voltage electrode (point) consists of a cylindrical tube with a diameter of 11 mm, terminated by a conical tip, having an angle of 30°, which terminates in a hemispherical surface with a radius of curvature 0.1 mm [16].

The grounded electrode consists of a 20 cm wide plane, and the separation between the electrodes equal to 5 cm [16].

In our investigations, a positive DC voltage has been applied to the high-voltage electrode (point) and the plane is grounded. The atmospheric conditions are considered normal.

The model is implemented in COMSOL Multiphysics package. The package's "Convection and diffusion, transient analyzes", "Helmholtz Equation" and "Electrostatics" application modes are used to implement the system of Equations (1)-(10) together with boundary conditions shown in figure 2.

To accelerate the convergence, a few initial conditions and simplifying appropriate assumptions are used. A user-controlled mesh is applied; the meshes dimension varies by adapting to the geometry of the arrangement.

III. RESULTS AND DISCUSSIONS

Figure 3 shows the distribution of the electron density in the case of a positive streamer for the times 0.5, 4, 20, 34 and 40 ns after voltage application.

The first figure shows the system in the initial state when the voltage is applied. We note that the position of the Gaussian density representing the seed electron.

At 4ns, we see the effect of the ionizing avalanches. The seed electron moving towards the anode caused the ionization of the species, leading to an increase in the electronic density whose maximum value is on the point.

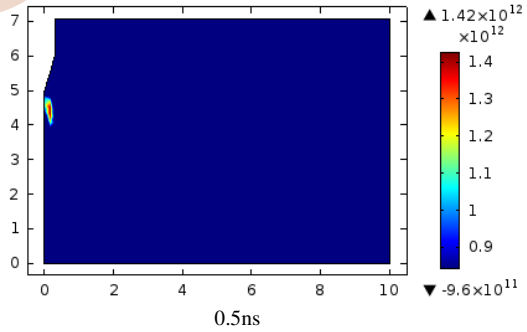

0.5ns

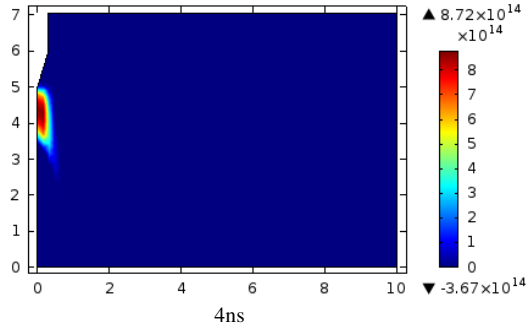

4ns

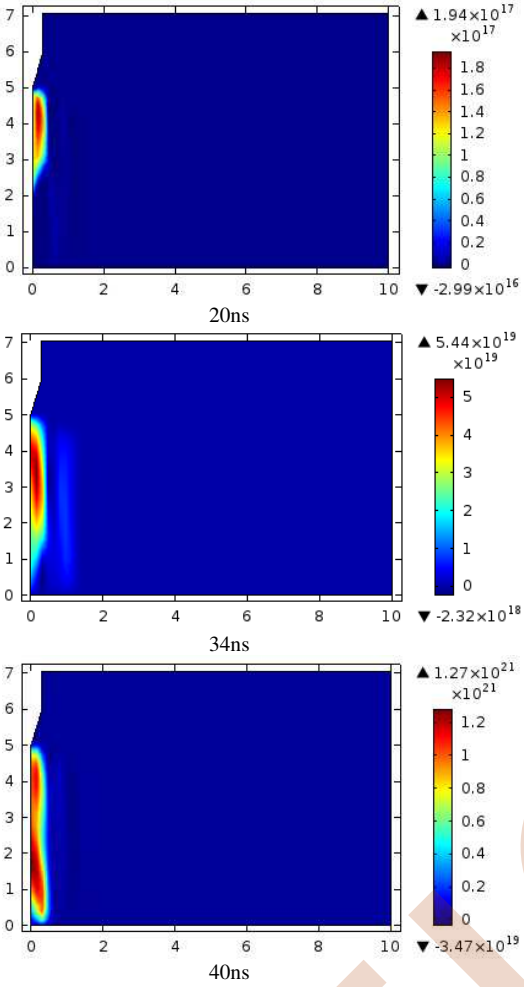

Fig.3 Distributions of electron density at different instants after voltage application.

In the following figures, we follow the progression of the ionization wave through the creation of electronic avalanches. At time 40ns, the streamer reaches the cathode, and we observe an increase in the maximum density of the electrons at the cathode.

We finish our work by representing the electric field distribution and equipotential lines at time 0.5ns (figure 4).

From the first figure (figure 4a), we observe that the electric field has a maximum value under the point equal to 34.2 kV/cm induced by the potential applied to the high-voltage electrode and decreases as one moves away from the axis of the point. There is not yet a discharge and the shape of the point, equipotential, is clearly visible (figure 4b).

The value of the electric field obtained is greater than 30 kV/cm defined as the value of the electric field from which the probability of ionization of a molecule by a free electron is greater than that of the attachment in the air and in the reference conditions.

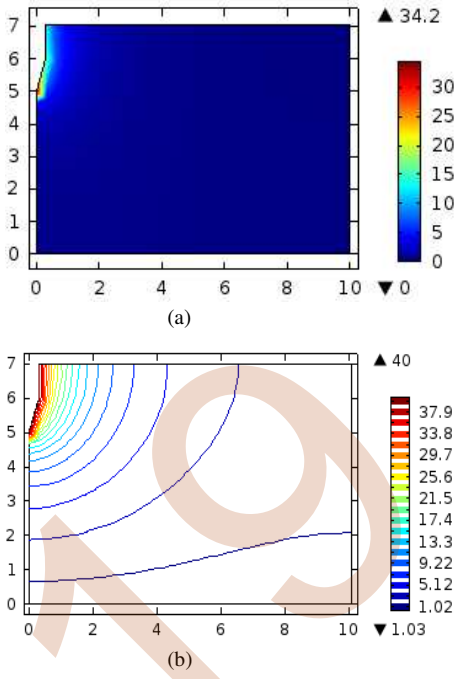

Fig.4 Point-plane system at 0.5ns.
(a) Eectric field distribution (kV/cm)
(b) Equipotential lines (kV)

IV. CONCLUSION

Based on a two-dimensional hydrodynamic model, the formation and propagation of streamer in a point-plane configuration have been investigated which introduces the photoionization effect. This model includes a set of nonlinear partial differential equations represents the motion and the diffusion of charge carriers associated with the reactions between them. The simulation results show that the process of the discharge starts from the high voltage electrode to the grounded plane, the streamers tend to spread vertically. The results obtained are consistent with those given by different authors regarding the development of the streamer discharge in the point-plane air gaps. The advantage of the numerical approach is the reduction of time, cost, and get results close to reality.

REFERENCES

[1] S. Y. Li, K. D. Srivastava and G. D. Theophilus, "Nanosecond Streak Photography of Discharges on Spacer Surface in Gases", IEEE Transactions on Electrical Insulations Magazine, 2(1), pp. 114- 120, 1995.

[2] J.M. Meek, J.D. Graggs, "Electrical breakdown of gases", Clarendon, Oxford, 1953.

[3] L. B. Loeb, "Electrical Coronas, Their Basic Physical Mechanisms", University of California Press, United States, 1965.

[4] H. Raether, "Electron avalanches and breakdown in gases" Butterworths, London, 1964.

[5] N. L. Aleksandrov and E. M. Bazelyan, "Simulation of long-streamer propagation in air at atmospheric pressure," Journal of Physics D: Applied Physics, vol. 29, pp. 740- 752, 1996.

[6] R. Morrow and J. J. Lowke, "Streamer propagation in air," Journal of Physics D: Applied Physics, vol. 30, 1997.

[7] Y. V. Serdyuk, "Numerical simulations of non-thermal electrical discharges in air: Lightning electromagnetics", IET power and energy series, pp. 87-138, 2012.

[8] S. Singh, Y. V. Serdyuk and R. Summer, "Adaptive Numerical Simulation of Streamer Propagation in Atmospheric Air" COMSOL Conf., Rotterdam, Netherlands, 2013.

[9] G. Le Roy, C. Gary, B. Hutzler, J. Lalot, Ch. Dubanton, "Les propriétés diélectriques de l'air et les très hautes tensions", Edition Eyrolles, Paris 1984.

[10] E. Kuffel, W.S. Zaengl, J. Kuffel, "High Voltage Engineering - Fundamentals-",Second edition, published by Butterworth-Heinemann, British, 2000.

[11] S. Singh, "Computational framework for studying charge transport in high-voltage gas-insulated systems", Chalmers University of Technology, Sweden, 2015.

[12] Yu .N, Babaeva, Nadis G.N. "Two dimensional modelling of positive streamer dynamics in non uniform electric field in air" in J. Phys D 29, pp.2423-2431, 1996.

[13] A.A Kulikovsky "The role of photoionization in positive streamer dynamics" in J. Phys. D: Appl Phys 33, Num 12, pp.1514-1524, 2000.

[14] P. Ségur, A. Bourdon, E. Marode, D. Bessieres, and J. H. Paillol, "The use of an improved Eddington approximation to facilitate the calculation of photoionization in streamer discharges," Plasma Sources Science and Technology, vol. 15, pp. 648-660, 2006.

[15] A. Bourdon, V. P. Pasko, N. Y. Liu, S. Célestin, P. Ségur, and E. Marode, "Efficient models for photoionization produced by non-thermal gas discharges in air based on radiative transfer and the Helmholtz equations," Plasma Sources Science and Technology, vol. 16, pp. 656-678, 2007.

[16] S. Mouhoubi, A. Boubakeur, "Partial discharges behaviour in a rod-plane arrangement with an insulating barrier", Archives of Elect Eng. Vol. I.VI. N° 3-4, pp. 187-196, 2007.

Experimental study of the active and controlled neutralization of polypropylene nonwoven media

Akila Messaoudène
Laboratoire de Génie Electrique, Faculté de Technologie, Universié de Bejaia, Bejaia, Algeria
akimessa@yahoo.fr

Lucian Dascalescu
PPRIME Institute, UPR 3346 CNRS - University of Poitiers – ENSMA, IUT
Angoulême, France
lucian.dascalescu@univ-poitiers.fr

Boukhalfa Bendahmane
Laboratoire de Génie Electrique, Faculté de Technologie,Universié de Bejaia, Bejaia, Algeria
boukhabend@yahoo.fr

Belkacem Yahiaoui
Laboratoire de Génie Electrique, Faculté de Technologie,Universié de Bejaia, Bejaia, Algeria
bel.yahiaoui@gmail.com

Mohamed Rachid Mekidèche
Laboratoire L2E
Faculté FST, Université de Jijel,
Jijel, Algeria
mek_moh@yahoo.fr

***Abstract*— Faced to the many problems due to the presence of electrical charges on the surface of dielectric materials, it is necessary to find adequate solutions to neutralize them, and this on an industrial scale. In this context, we were interested in the active neutralization of polypropylene nonwoven media based on the principle of ambient air ionization by alternating corona discharge at industrial frequency (50 Hz) in a configuration system of the "triode" type. The purpose of this work is to evaluate the possibility of using such an electrode configuration to impose a zero electric potential on the surface of materials exposed to corona discharge. The effectiveness of the neutralization is evaluated by comparing the profiles of the surface potential before and after neutralization, performed in static or scanning modes. In the first mode, the charged sample remains stationary under the corona discharge for a defined time to ensure neutralization. In the second, the sample scrolls under the corona electrode at a well controlled speed. Several parameters contribute to a better neutralization efficiency: the neutralization intensity, the scanning speed, the grid potential, and the duration of exposure to the corona discharge.**

I. INTRODUCTION

Corona discharge is widely employed in variety of electrostatic applications, such as separation of granular mixtures [1, 2], charging of fibrous nonwoven media for air filters, cable insulation evaluation [3-5], dust precipitation [6, 7], xerographic processes [8], electrostatic painting [9].

Many industrial sectors are affected by problems related to electrostatic phenomena. The static electricity is often perceived as a source of nuisance [10, 11], the most serious consequences of which are undoubtedly, fires and explosions. Faced with these many problems, the neutrality of dielectrics is sought. Thus, we are interested in the active neutralization of dielectrics based on the principle of ionization of the ambient air by corona effect.

Indeed, by ionizing the air near charged materials, the charges accumulated on the surface are partially or totally neutralized. Several studies have been carried out to evaluate the efficiency of the neutralization of the electric charges by appealing either to a commercial generator of bipolar ions, or to a dual electrode producing an alternating corona discharge [12 -19]

The aim of this paper is the experimental characterization of the active neutralization of polypropylene nonwoven media in a triode-type corona electrode configuration.

The use of standard configurations of corona discharge electrodes does not guarantee the effectiveness of neutralization, as it is accompanied by the manifestation of new charges.

In order to impose the surface and volume neutrality of the materials, the use of a triode type discharge electrode configuration [20] is a wise choice. The presence of the grid connected to the mass avoids the appearance of an opposite potential.

The characterization of the neutralization process consists of an identification of the different parameters that contribute to better neutralization efficiency, evaluated by comparing the surface potential profiles before and after neutralization. The profile is obtained by non-contact measurements of the surface potential using the capacitive probe of an electrostatic voltmeter [21, 22].

We have analyzed the influence of several parameters on the efficiency of polypropylene films neutralization by a

sinusoidal discharge generated at industrial frequency. These parameters are: the neutralization intensity, the scanning speed, the grid potential, and the duration of exposure to the corona discharge.

II. MATERIALS AND METHODS

The experiments were conducted with two triode type electrodes systems. The triode-type electrode configuration used in the study was consists in a high-voltage wire-type dual electrode, a grid electrode connected to ground through a resistor during sample electric charging, and a grounded plate electrode (Fig. 1). On the other hand, during the neutralization process, the grid electrode was connected directly to the ground [23] (Fig. 1).

The dual electrode consisted of a tungsten wire (diameter: 0.2 mm) supported by a metallic cylinder (diameter of 26 mm) and distanced at 34 mm from its axis.

To perform the corona charging of the samples, the wire and the cylinder were energized from the same adjustable DC high- -voltage supply 100kV,3mA (model SL300 Spellman, Hauppauge ,NY,USA), as shown in Fig. 1.

The grid electrode was connected to the ground through a resistor R_g = 100 MΩ in series with a micro-ammeter measuring a current of intensity I_g.

The role of the grid is to control the level of charge at the surface of the samples, by means of its electric potential $V_g = R_g \times I_g$ with respect to the grounded plate. Part of the ions produced by the corona discharge pass through the mesh of the grid and are driven by this potential to the surface of the film. V_g limits the potential at the surface of the sample.

The surface potential was measured with an electrostatic voltmeter (Trek Model 341B, equipped with a static probe model 3450). The electrical potential measurements were captured by an electrometer (Keithley, model 6514) connected to a personal computer. The acquisition of experimental data was carried out by an ad-hoc virtual instrument, developed in LabView environment (Fig.1).

The active neutralization was performed by connecting the dual electrode to a high-voltage amplifier 30 kV, 20 mA (model 30/20A, Trek Inc., Medina, NY). The waveform and the frequency f of the high-voltage were adjusted using a synthesized function generator (model FG300, Yokogawa, Japan). During the neutralization, the charged sample was exposed to the AC corona discharge generated at the industrial frequency (50 Hz) in the triode type configuration system (Fig. 1), with the grid connected to the ground (V_g = 0 V).

The experiments were performed on 110 mm x 100 mm samples cut from the same polypropylene nonwoven media, in climatic conditions : temperature : 25 °C to 28 °C; relative humidity: 40 % to 48 %. .The samples were placed on an aluminum plate (165 mm x 115 mm) connected to the ground.

The neutralization can be performed in static or scanning modes. In the first mode, the charged sample remains stationary under the corona discharge for a definite time to ensure neutralization. In the second, the sample moves under the corona electrode at a well-controlled speed.

In the following sections, the charging and neutralization profiles respectively designate the profiles before and after neutralization.

The efficiency of the process was evaluated by calculating the neutralization rate N, expressed as a function of V_1 and V_2, which are respectively the potentials before and after neutralization in a given point at the surface of the sample [17]:

$$N[\%] = [1 - V_2/V_1\ ] \times 100 \qquad (1)$$

III. RESULTS AND DISCUSSION

The profiles obtained, before and after neutralization, are presented as a function of the position on the central axis (OX) of the sample. The corona electrode is positioned above the middle (5 cm) of the sample, the positions 0 cm and 10 cm of the sample. The charge deposition is characterized by the distance d (grid sample) =15 mm. The electric charging of all samples was performed in static mode (the sample have a fixed position under the corona electrode) during 10 s.

A. Successives neutralizations

Fig.2 shows surface potential profiles before and after two successive neutralizations in scanning mode of same sample where the deposition was carried out with a grid potential V_g = - 1.5 kV. The first neutralization intensity is (I_N = 10 µA), and the second neutralization is characterized by I_N = 50 µA. The scanning speed Vb = 3 cm/s.

The neutralization efficiency is obtained after the second neutralization where the surface potential profile obtained is flattened.

Similar tests were considered in static mode (Fig. 3).A new sample charged under the same conditions. The neutralization duration tn = 10s. The first neutralization is performed with neutralization intensity (I_N = 50 µA) and followed with second neutralization characterized by an intensity I_N = 50 µA. We note that the second naturalization is more efficient. Indeed the successive neutralizations increase the duration of exposure to the flux of bipolar ions.

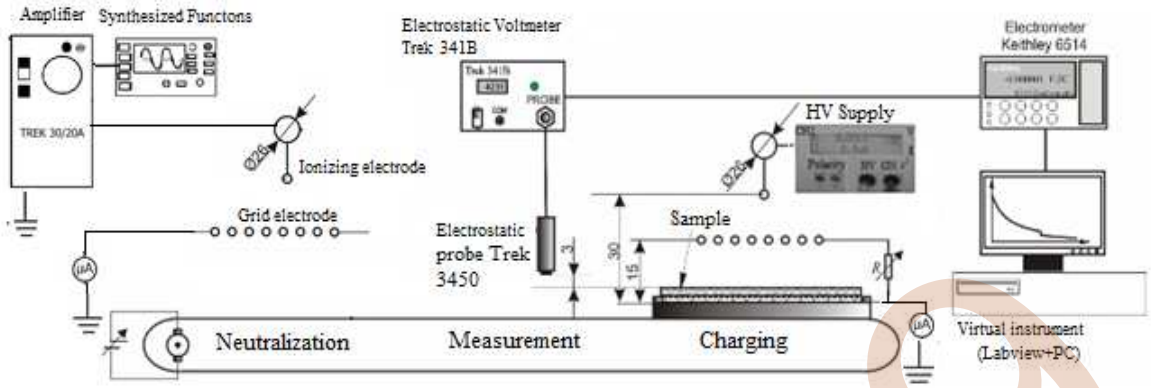

Figure. 1. Experimental set-up for the measurement of the surface potential before and after neutralization (all dimensions are in millimeters)

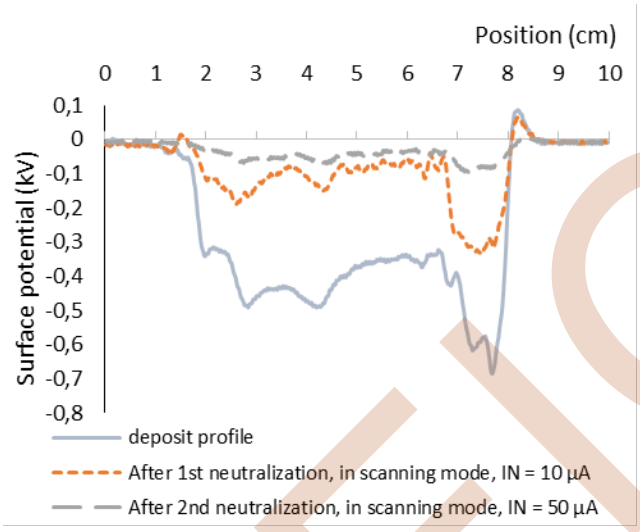

Figure. 2. Surface potential profiles before and after 2 successive neutralizations of the same sample in scanning mode.

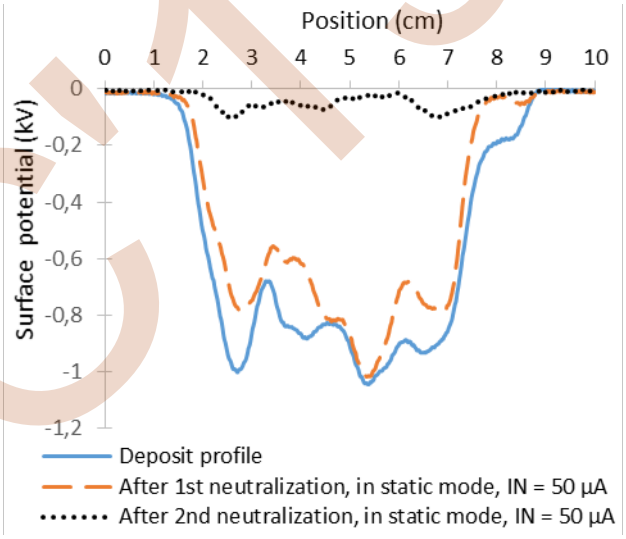

Figure. 3. Surface potential profiles before and after 2 successive neutralizations of the same sample in static mode.

B. *Scanning speed V_b*

Fig.4 present typical surface potential repartition profiles obtained under various AC corona neutralization in scanning mode.

The nonuniformity of these profiles before neutralization is due to the nonhomogeneous structure of the media. Three new samples charged with grid potential V_g = - 1 kV were exposed to the same neutralization intensity in scanning mode (I_N = 20 µA), but each sample passes under the AC neutralizer at a different speed. We note that for high scanning speeds, the neutralization is less effective. Indeed the increase in speed means that the sample is exposed for a shorter time to the alternative corona discharge.

C. *Neutralization intensity*

In Fig. 5 are presented the profiles of the surface potential after neutralization in static mode. Three samples were charged under the same conditions (V_g = -1 kV and the neutralization duration equal to 10 s). The media were exposed to different values of neutralization intensity: 10 µA, 15 µA and 20 µA. From the results obtained (Fig.5), we find that the neutralization rate increases with the neutralization intensity. Figure 5.a shows that for a low neutralization intensity the surface potential profile after neutralization is the same as the profile before neutralization. On the other hand, the neutralization profile almost completely flattened for the maximum neutralization

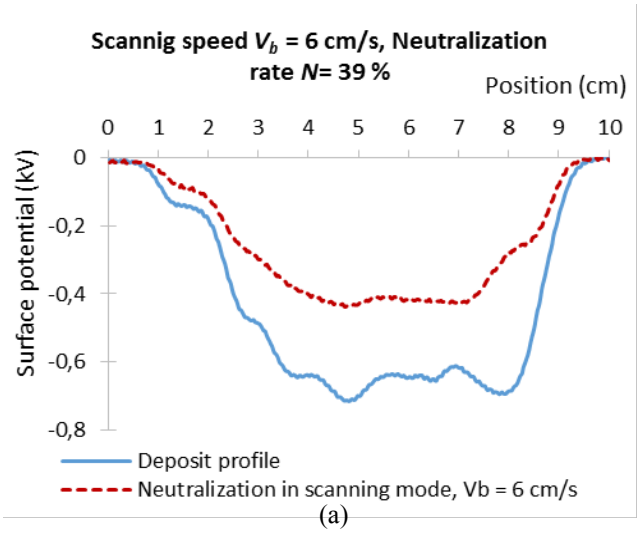

(a)

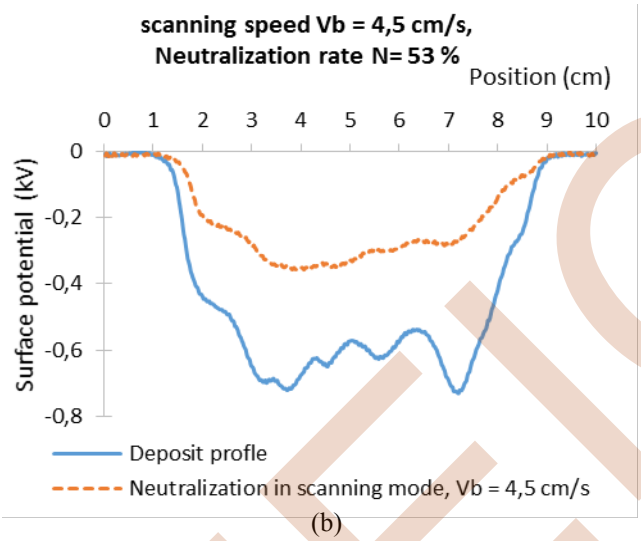

(b)

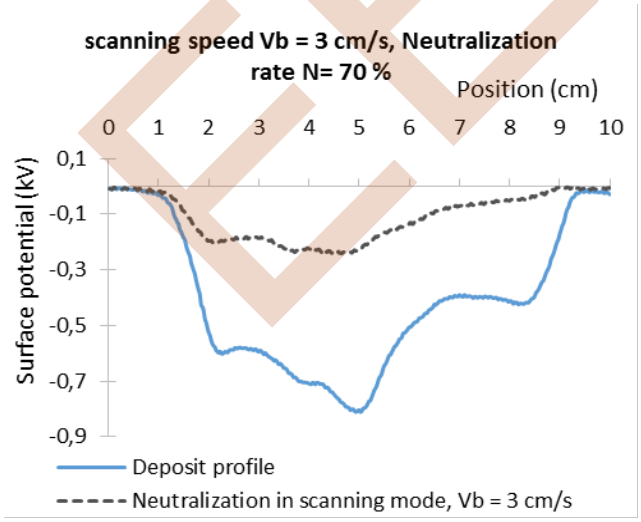

(c)

Figure. 4. Surface potential profiles before and after neutralization for different scanning speeds

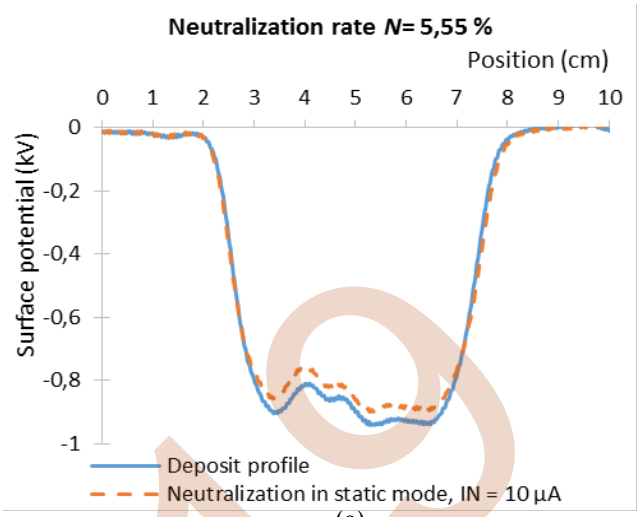

(a)

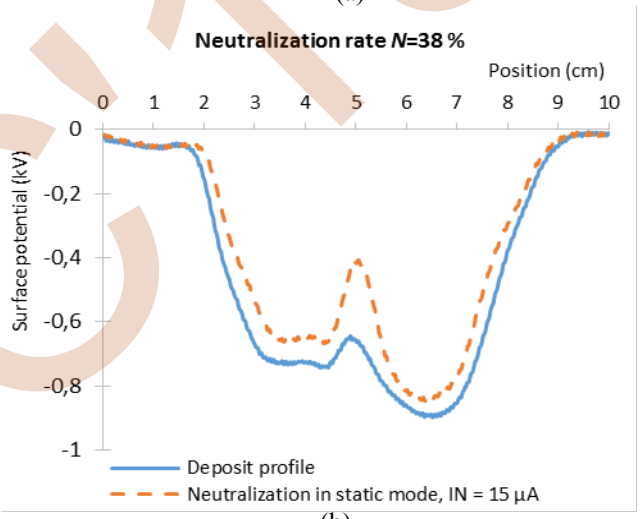

(b)

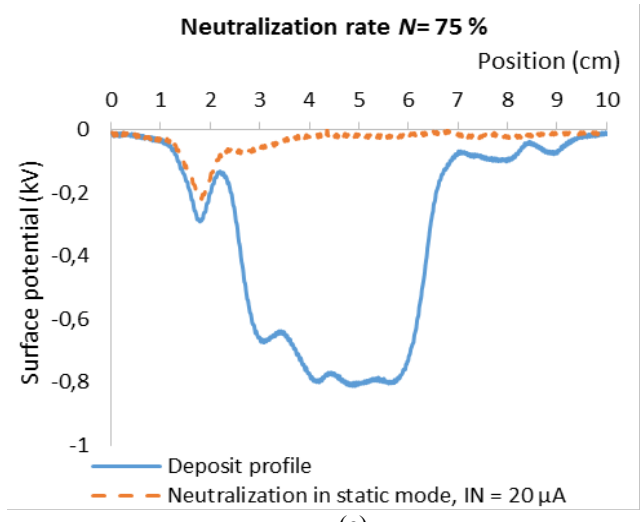

(c)

Figure.. 5. Surface potential profiles before and after neutralization for different intensities, in static mode.

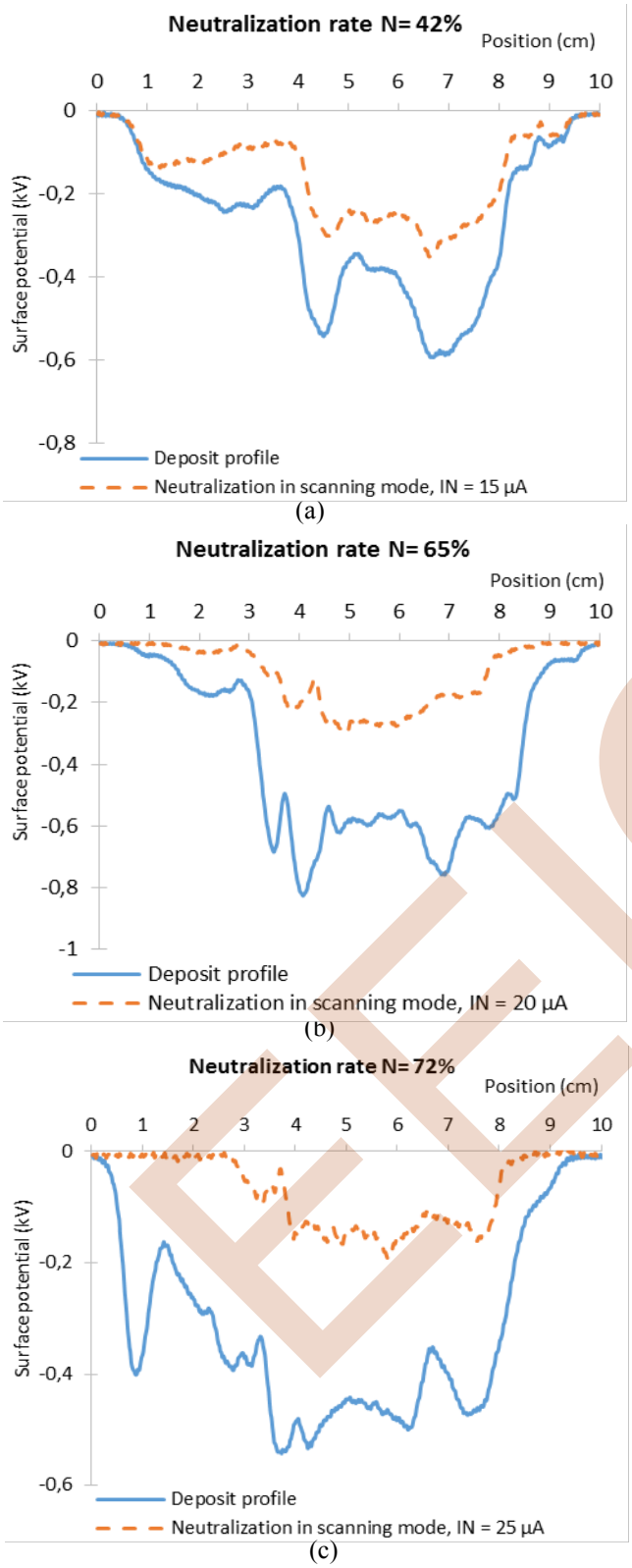

Figure. 6. Surface potential profiles before and after neutralization for different intensities, in scanning mode.

intensity, as shown in Figs. 5 (c). Further neutralization tests were applied on 3 new media in scanning mode where the samples pass through the corona discharge zone at a scanning speed V_b = 3 cm/s, for different amplitudes of the neutralization intensities I_N: 15 µA, 20 µA and 25 µA (Fig. 6). Fig. 6 shows that the neutralization rate increases with the neutralization intensity in scanning mode. These results are in agreement with those obtained for the static case, as shown in Fig.5.
Indeed, as AC voltage increases, more ions are produced.

IV. CONCLUSIONS

The measurement of the surface potential of the nonwoven media samples after charging and neutralization is an effective means of evaluating the degree of neutralization achieved. The neutralization system considered in this study is based on a triode configuration, where the active electrode is subjected to a sinusoidal waveform alternating discharge of industrial frequency (50 Hz). This method allows achieve very high neutralization rates correlated with the amplitude of the applied high voltage and the sample passage speed under the corona discharge in the case of the scanning mode. Complete sample neutralizations are obtained from repetitive neutralizations.

REFERENCES

[1] L. Dascalescu, R. Morar, A. Iuga, A. Samuila and V. Neamtu, "Electrostatic separation of insulation and conductive particles from granular mixes," Particulate Science and Technology, vol. 23, pp. 25-42, 1998.
[2] A. Iuga, R. Morar, A. Samuila, and L. Dascalescu, "Electrostatic separation of metals and plastics from granular industrial wastes," Proc. IEE—Sci. Meas. Technol., vol. 148, pp. 47–54, 2001.
[3] B. Tabti, M. Mekideche, M. Plopeanu, L. M. Dumitran, L. Herous, and L. Dascalescu," Corona charging and charge decay characteristics of non-woven filter media," IEEE Trans. Ind. Appl, vol. 46, pp.634 – 640, 2010.
[4] B. Tabti, L. Dascalescu, M. Plopeanu, A. Antoniu, B. Yahiaoui, and A. Melahi, "Factors that influence the negative corona charging of nonwoven filter media," Proc. 2012 Joint Electrostat Conf, 2012, Cambridge, ON, Canada
[5] M. Nifuku, Y. Zhou, A. Kisiel, T. Kobayashi, and H. Katoh, "Charging characteristics for electret filter materials," J. Electrostat, vol. 51/52, pp. 200–205, May 2001.
[6] A. Jaworek, A. Krupa, and T.Czech, "Modern electrostatic devices and methods for exhaust gas cleaning," J. Electrostat., vol. 65, pp. 133–155, 2007.
[7] Z. Long, Q. Yao,"Evaluation of various particules charging modele for simulting particule dynamics in electrostatics precipitators," Journal of Aerosol Science, Vol 41, 702-718, 2010
[8] A. Reguig, L. Dascalescu, P. Dordizadeh, and A. Bendaoud, "Corona discharge generated by dual-type electrode fixed between parallel grounded strips," IEEE Trans. Ind. Appl, vol. 53, no. 2, march/april 2017

[9] G.S.P. Castel, Industrial application of electrostatics: the past, present and future," J. Electrostat., vol. 51-52, pp. 1-7, 2001.
[10] S. H. Voldman," The state of the art of electrostatic discharge protection: physics, technology, circuits, design, simulation, and scaling," IEEE, J. Solid –state Circuits, vol.34, No.9, pp.1272-1282, 1999.
[11] C. Duvvury and E. A. Amerasekera, ESD in Silicon Integrated Circuits.New York, NY, USA: Wiley, 2002.
[12] M. Kachi, and L. Dascalescu, ''Corona-discharge-based neutralization of charged granular insulating materials in contact with an electrode of opposite polarity," Journal of Electrostatics, Volume 76, August 2015, pp. 246 – 253
[13] J. S. Chang, "Neutralization theory of static surface charge by an ionizer under wide gas pressure environments," IEEE Trans. Ind. Appl., vol. 37, no. 6, pp. 1641–1645, Nov./Dec. 2001.
[14] Y. Tabata, T. Kodama, W. L. Cheung, and N. Nomura, "General characteristics of a newly developed bipolar static charge eliminator," J. Electrostat., vol. 42, no. 1/2, pp. 193–202, Oct. 1997.
[15] A. Antoniu, B. Tabti, M. C. Plopeanu, and L. Dascalescu, "Accelerated discharge of corona-charged non-woven fabrics," IEEE Trans. Ind. Appl., vol. 46, no. 3, pp. 1188–1193, May/Jun. 2010.
[16] A. Antoniu, A. Smaili, I-V.Vacar, M. C. Plopeanu and L. Dascalescu,"Sinusoidal and triangular AC high-voltage neutralizers for accelerated discharge of non-woven fibrous dielectrics," IEEE Trans. Ind. Appl.,Vol. 48, No. 3., pp. 857-863, 2012.
[17] B. Yahiaoui, B. Tabti, M. Megherbi, A. Antoniu, M. C. Plopeanu, and L. Dascalescu, "AC corona neutralization of positively and negatively charged polypropylene non-woven fabrics,"IEEE Trans.Diel.Elect.Insul., vol. 20, pp. 1516-1522, 2013
[18] M. Kachi, M. Nemamcha, L. Herous, and L. Dascalescu, "Neutralization of charged insulating granular materials using corona discharge," J.Electrostat, vol. 69, pp. 296-301, 2011.
[19] M. Kachi, L. Dascalescu, L. Herous, and M. Nemamcha, "Experimental study of charge neutralization at the surface of granular layers of insulating material," IEEE Trans. Ind. Appl., vol. 48, pp. 691-698, 2013.
[20] L. Dascalescu, A. Iuga, R. Morar, V. Neamtu, I. Suarasan, A. Samuila, and D. Rafiroiu, "Corona and electrostatic electrodes for high-tension separators," J. Electrostat., vol. 29, no. 3, pp. 211–225, Jun. 1993.
[21] M. A. Noras, "Non-contact surface charge/voltage measurements. Capacitive probe–principle of operation," Trek Appl. Note 3001(2002) 1-8.
[22] P. Molinié, P.Uovera, "Surface potential measurements: implementation and interpretation, dielectric materials, measurements and application," in: IEE Conference Publication No 473, 2000, pp. 253-258.
[23] X. Deng and K. Adamiak, "The Electric Corona Discharge in the Triode System," IEEE Industry Application Society Annual Meeting New Orlean, Louisiana, October 5-9, 1997.

Corona Charging and Charge Decay on Polyethylene Terephthalate Films (PET)

Karima SMILI [1,2]
1: Laboratory of Electromechanical Engineering, UBMA.
2: Higher School of Industrial Technologies,
Annaba, Algeria
k.smili@esti-annaba.dz

Allaoua RAHMANI[1,2]
1 : Laboratory of Electrical Engineering,
2: University of Bejaia, Algeria
rahmani_ht@yahoo.fr

Ouarda CHIBANE[1,2]
1 : Laboratory of Electrical Engineering,
2: University of Bejaia, Algeria
O_rahmani@yahoo.fr

Lazhar HEROUS [1,2]
1: Laboratory of Electrical Engineering, Guelma
2: University of Badji Mokhtar
Annaba, Algeria
lherous@yahoo.fr

***Abstract*-- Surface potential decay (SPD) measurements have been considered as the most appropriate technique to investigate the electrical properties of insulating materials. Its main interest is to avoid any contact with the surface; providing that charge is deposited by means of a DC corona discharge. Besides, the interpretation of the surface potential evolution remains a major problem. For this reason, this study aims at considering surface potential measurements and the mechanisms of the potential decay and transport processes that might be involved in the decay. To reach a conclusion, samples that were used took the form of polyethylene terephthalate films (thickness: 0.5 mm; surface: 50 mm x50 mm). A negative corona discharge produced in a needle–grid–plate electrode system was employed to charge the surface of the film samples. All surface potential decay measurements were carried out in a commercial climatic chamber, where relative humidity *RH* and temperature *T* were rigorously controlled. Initially, we have shown an injection process of the charge deposited on the surface of the material. The investigation on the kinetics of charge carriers (charge carrier mobility), allowed us to determine the mobility of the charge derived in the material. We noted a strong dependence of the charge density put on the evolution of SPD.**

Index Terms-- Charge injection, corona discharge, mobility, polymer, surface potential decay.

I. INTRODUCTION

Since several years, synthetic polymers have been applied in electrical industry due to their excellent electrical, thermal, and mechanical properties. 1

Meanwhile, solid insulating polymers are used in hostile environments where they may be subjected to water attack, high static non-ionizing radiation and other corrosive materials or reactions. Therefore, the insulation properties are deteriorated and involve a premature ageing of electrical insulation. Electrostatic charges can play an undesired role in diverse industrial applications, particularly, in plastic industry and in high impedance circuitry.

If these charges are injected into the volume of material either by strengthening the local electric field, or by interaction with the material, they will induce local heating and degradation of physico-chemical properties. The latter will impair the insulating properties of the material and thus lead to the breakdown of the dielectric.

To understand the origin of electrostatic nuisance and optimize the performance of polymers, it is important to have appropriate knowledge on generation and charge transport processes. In this respect, a great effort has been devoted to the characterization and understanding of charges transport in insulation polymer [2,3,4,5,6,7]. Despite recent progress achieved with measuring instruments, identifying the predominant mechanism remained obscure. The process of conduction, polarization or charge injection, trapping process / detrapping is complex phenomena and difficult to explain. The interpretation of the results is still quite delicate.

The recent literature on potential decay measurements is dominated by the hypothesis of injection and polarization phenomenon of the charge deposited on the surface. The "Cross-over" of the curves which were reported initially by Ieda and co-Workers [7] on polyethylene and, also, has been observed by other research works [3]-[5]-[8], has been widely admitted as an experimental evidence of a partial injection into the bulk of the charge deposited on the surface.

II. THE EXPERIMENTAL TECHNIQUES

The surface potential decay experiment is described in figure 1. The samples were charged on their free surface by exposure to a corona discharge generated by a needle

electrode situated above the grounded metallic plate and connected to a negative DC high-voltage supply *Vp*. A grid electrode, connected at a different negative DC potential *Vg*, was interposed between the needle electrode and the grounded plate. In this way, a reasonably uniform field could be generated in the gap between the grid and the surface of the PET samples. By selecting appropriate corona point and grid potential, *Vp* and *Vg* respectively, it was possible to charge the polymer surface with ions of either sign. The surface potential was limited by the grid potential *Vg*.

After charging, the grounded metal plate was rotated, so that to transfer the sample under the probe of an electrostatic voltmeter (Monroe Electronics), connected to the computer that controlled the measuring procedure. The surface potential was thus continuously measured and recorded. All surface potential decay measurements were carried out in a commercial climatic chamber, where relative humidity (RH) and temperature (T) were rigorously controlled. The duration of sample exposure to the corona discharge was 1 s. prior to corona exposure, the samples were maintained for one hour in the conditions prescribed for each experiment.

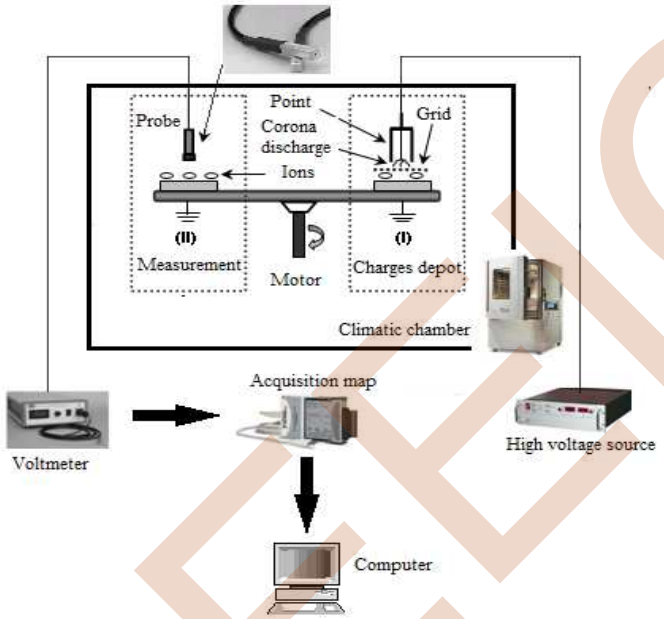

Figure1. Experimental setup for the study of the surface potential decay of PET samples

III. DESCRIPTION OF THE SAMPLES

The polyethylene terephthalate "PET" is a thermoplastic that belongs to the family of polyesters. It is widely known under the trade name Myler, Melinex or hostaplan. PET is often used as dielectric in high-performance foil capacitor, or as an insulator for electric cables and electric motors coils. The PET samples used in the experiment were square sheets of 5 cm side-length and 0.5 mm thickness. One face of the samples was coated by silver paint so that to ensure a good contact with the mirror-polished metal plate on which they were laid.

IV. RESULTS AND DISCUSSION

A. *Initial potential effect V_0:*

Figure 2, shows the surface potential decay for different values of initial potential, fixing temperature and relative humidity at 55°C and 50% respectively.

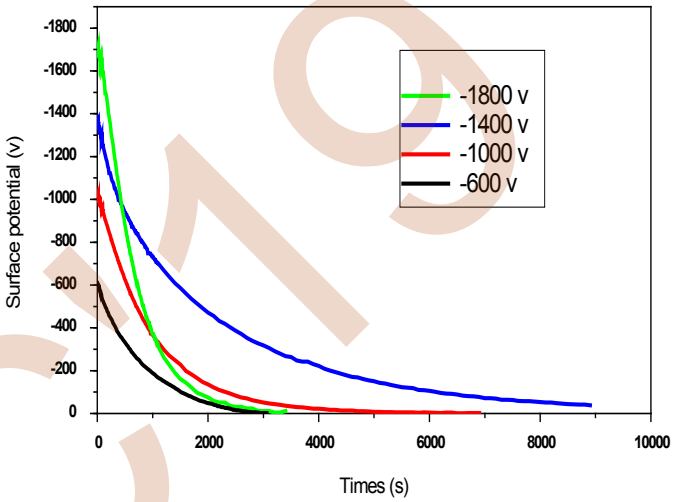

Figure 2. Surface potential decay as function initial potential V_0

We noted a strong dependence of the deposited charge density on the SPD evolution. Moreover, after some time, none of the charges remained on the sample surface. To show the potential deposited effect on the sample surface, we represented the curves normalized to the initial potential V_0 (Fig. 3).

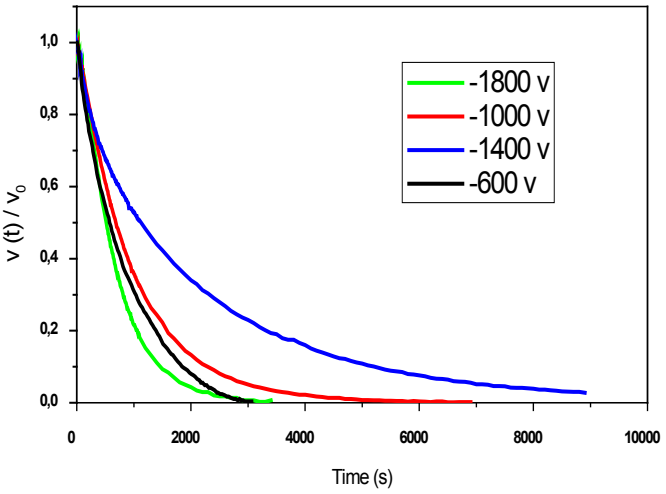

Figure 3. Characteristic $V(t)/V_0$

The results presented indicate that the curves are not superimposed. Two hypotheses may explain this result. When measurements were made on a single sample, then we can assume that the sample surface would progressively degrade by the corona discharges undergone on each deposit. This degradation implies a variation of the conductivity and therefore a change potential decay speed.

The second case, when virgin samples are used for each test (our case), then we can think about the existence of field effect on the material. We may think that the phenomenon related to the electron mobility (trapping -acceleration -trapping) will be more dependent on the field. An electron hops from a level of surface trap into the bulk is a charge injection dependent on the field and can assist the hop and then accelerate it in material. The charges then move under their own electrical field towards the grounded electrode.

Based on our interpretation, we found that the injection process can be observed for moderate voltages. It leads to explaining this phenomenon by the extremely pointed tip of the electrode that might be the cause of the high electric field generation and easily inject a charge into the dielectric. This result goes hand in hand with the Baum work [8]which noted in his work on PET, a charge injection at low voltage values.

This study also revealed the existence of the "Cross-Over" phenomenon (fig. 2). In fact, after the same time of measurement, the potential decay of the sample charged with -1800V is more significant than -1400V,-1000V and -600V. This cross-over phenomenon has been already observed by several authors [3]-[5]-[9]-[10]. It indicates a charge injection into the bulk of the material.

We also observed a high initial growth rate followed by a slower value. The strong initial decrease may be due to the injection of charges deposited under the field effect created by their own charges.

Cross-over phenomenon can be attributed to the fact that the injected charge is dependent on the deposited charge quantity. This decay may be explained by a total injection of the deposited charges on the dielectric surface under the electrical field generated by the charges themselves. When the injected charges are subject to local field this will lead them to the sample back face.

This hypothesis may be explained by the existence of two linear phases of the surface potential decay curve; a linear phase which corresponds to the movement of charges through the material and a second phase corresponding to the charges leaving the material.

Molinié [11] pointed out the existence of a link between the potential decay and the absorption current. Knowing that in the case where the volume polarization phenomenon is the only mechanism or the predominant mechanism responsible for the charges evolution deposited on the insulator surface by corona discharge; the absorption current should decrease following a power law according to form:

$$I_{abs} = At^{-n} \quad (1)$$

And the potential derivative follows a law of the type:

$$\frac{dV}{dt} \alpha (t)^{-n} \quad (2)$$

Which causes proportionality between the absorption current and dV /dt. The decay rate dV/ dt is a convenient means to show the conduction intervening nature at charges deposition.

dV / dt characteristics relating to the curves of figure 2 are displayed in figure 4.

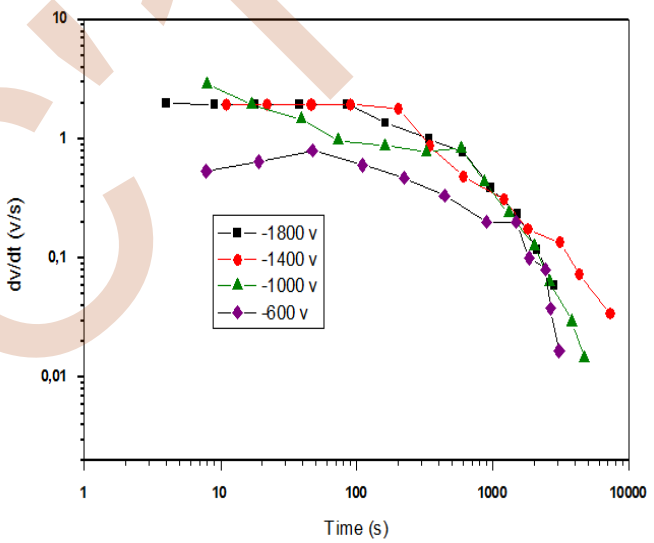

Figure 4. Log (dV/dt)-vs-Log(t) for various initial potential

We note a cross of two straight lines with different slopes. This, therefore, confirms the absence of a prevalent dipolar polarization and corresponds rather to the existence of two modes of surface potential decay regimes separated by a transit time τ.

This time corresponds to a slope change on the rate decay evolution as function of time.

Transit time:

τ (-1800V) = 85 s

τ (-1400V) = 202 s

τ (-1000V) = 582 s

τ (- 600 V) = 1480 s

Von Berlepsch [4] observed this representation in studies on polyethylene a slope change which is attributed to the existence of two regimes of surface potential decay separated by a transit time which represents the transition charge to the back face. We can see on the curves derivative dV/dt a shape quite conforming to injection models [12]-[13].

Particularly, a charge injection [13]-[14] based on the charges geometric motion in the material with density and mobility of constant charge.

Therefore, it is possible to determine the charge carriers mobility in the material after having been deposited on the surface for
T < τ [15].

This mobility is expressed:

$$\mu = L^2 / V_0 \tau \qquad (3)$$

L: the insulating material thickness.
V_0 : the initial potential.
τ : the transit time.

Extrinsic electron mobility:

V_0 = -1800 V

$$\mu = \frac{(0{,}5X10^{-3})^2}{1800X85} = 1{,}633986.10^{-12} m^2/V.s$$

V_0 = -1400 V

$$\mu = \frac{(0{,}5X10^{-3})^2}{1400X202} = 8{,}840169.10^{-13} m^2/V.s$$

V_0 = -1000 V

$$\mu = \frac{(0{,}5X10^{-3})^2}{1000X582} = 4{,}295532.10^{-13} m^2/V.s$$

V_0 = -600 V

$$\mu = \frac{(0{,}5X10^{-3})^2}{600X1480} = 2{,}815315.10^{-13} m^2/V.s$$

Figure 5, shows the mobility evolution for different values of V_0 relating to the curves in figure 2.

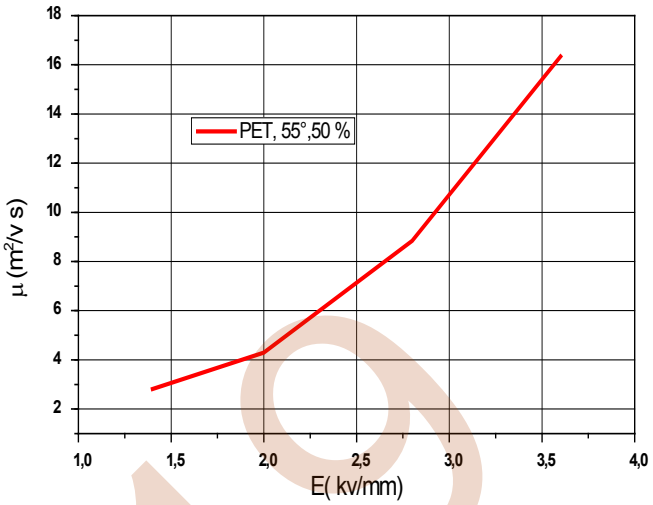

Figure 5. Mobility depending on the field applied during the transit time.

The mobility increases with the electric field. This seems quite relating to the field dependence. Moreover, we plotted in figure 6 the inverse of the transit time evolution (1 / τ) as a function of E/L in log-log coordinates.

We note a slope around 2,7. According to [12, 16], this shows a rather dispersive transport governed by a hopping process between distributed energy sites. This calculation allows us to confirm the initial hypothesis on the mechanism dominating the charge flow in the insulating material.

Inverse of the transit time as a function of E/L:

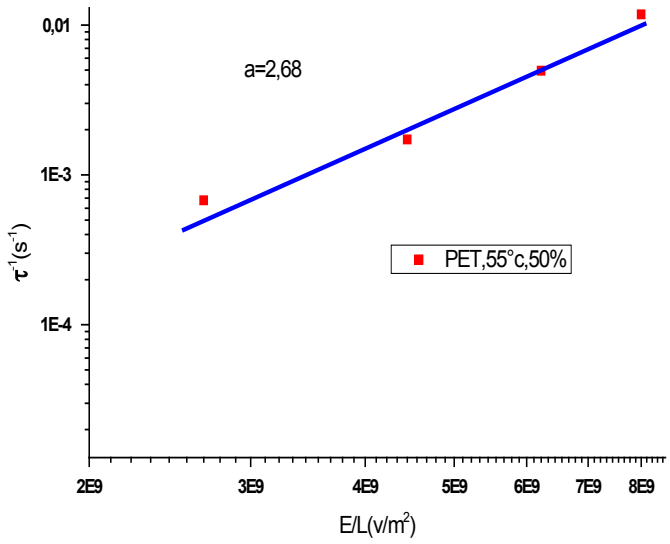

Figure 6. Log-log inverse curve of the transit time as a function of E/ L

V. CONCLUSION

The surface potential decay characteristic of corona charged PET has been analyzed in terms of a theory that assumes injection into the bulk of the charge deposited on the surface and that would account well for the curves in representation dV /dt. The amount of charge injected depends on the initial potential value.

Charge plane model based on the geometric movement charges in the material with the assumption of constant charge mobility can be applied to our experimental results of Surface Potential Decay.

This interpretation lends particular interest to mobility and how it depends on the field. The graphical representation of the mobility suggests a rather dispersive transport governed by a process of hop in sites distributed in energy.

Finally, this study has demonstrated the importance of the experimental methodology for evaluating the physical phenomenon that governs the potential decay. We suggest that this technique of Surface Potential Decay may open multiple way for the evaluation of the state aging of the insulating materials.

VI. ACKNOWLEDGMENTS

Part of the work reported in this paper was carried out within the framework of the programme CMEP01MDU523 financed by the French and Algerian governments. Another part of the work was financially supported by the Laboratory of Electromechanical Engineering of Badji Mokhtar Annaba University, Algeria.

VII. REFERENCES

[1] G.S.P Castle, "Industrial applications of electrostatics: the past, present and future, " J. Electrostatic, vol.51-52, pp.1-7, 2001.

[2] N. Liu, M. He, H. Alghamdi, G. Chen, M. Fu, R. Li, S. Hou, "An improved model to estimate trapping parameters in polymeric materials and its application on normal and aged low-density polyethylenes", J. Appl. Phys., Vol. 118, pp.064102–064112, 2015.

[3] S. Sahli, A. Ziari, A. Kahlouche, Y. Segui, "Measure and analysis of potential decay in polypropylene film after negative corona charge deposition," Journal of Electrostatics, vol.57, pp.169-181, 2003.

[4] P. Lovera, P. Molinie, "New methodology for surface potential decay measurements-application to study charge injection dynamics on polypropylene films," IEEE Trans. Dielec. Elect. Insul. vol.11, pp.1049-1056, 2004.

[5] L. Herous, M. Nemamcha, M. Remadnia, L. Dascalescu, "Factors that influence the surface potential decay on a thin film of polyethylene terephthalate (PET)," Journal of Electrostatics, vol.67, pp.198-202, 2009.

[6] K. Rouagdia, L. Herous, M. Nemamcha, L. Dascalescu, A. Fatihou, B. Tabti, "Experimental modeling of the electric potential decay at the surface of polypropylene films (PP)," Journal of Electrostatics, vol.76, pp. 262-267, 2015.

[7] J. Kindersberger, and C. Lederle, "Surface Charge Decay on Insulators in Air and Sulfurhexafluorid: Par II-Measurements," IEEE Trans. Dielec. Elect. Insul. vol.15, pp.948-957, 2008.

[8] E. A. Baum, T.J. Lewis, R. Toomer, "The lateral motion of charge on thin of film of polyethylene terephtalate, " J. Phys. D: Appl. Phys, vol. 11, pp.963-977, 1978

[9] .M. Ieda, G. Sawa, U. Schinohara, "A decay process of surface electric charges across polyethylene film, " Japan. J.Appl .Phys, vol.6, pp.793-794, 1967.

[10] M. Remadnia, M. Nemamcha, L. Herous, and L. Dascalescu, "Decay of the electric potential at the surface of corona-charged uniform layers of HIPS granules," IEEE Trans. Dielec. Elect. Insul., vol. 18, pp.579-587, 2011.

[11] P. Molinie, M. Goldman, J. Gattelat, "Surface Potential decay on corona-charged epoxy samples due to polarization process, " J. phys. D, vol.28, pp.1601-1610, 1995.

[12] J. Bigarré, P. Hourquobie, L. doucet, J. Matallana, "New setup of surface potential decay " 3 rd Conf. French Society of Electrostatics, Toulouse, France, 2002.

[13] R. Coelho, P. Jestin, L. levy, D. serial, "On the return – voltage build up in insulating materials, " IEEE. Trans. Elect. Insul. vol.22, pp.683-690, 1987.

[14] N. Liu, C. Zhou, G. Chen, and L. Zhong, "Determination of threshold electric field for charge injection in polymeric materials," Applied Physics Letters, 106, pp.192901-192905, 2015.

[15] H. Scher, E.W. Montroll, "Anomalous transit time dispersion in amorphous solids, " Phys. Rev. B. vol.1L, pp.2455-2477, 1975.

[16] S. Agnel, J. Castellon, P. Notingherjr, A. Toureille, J. Franceschi, C. Laurent, D. Marty Dessus, D. Mary, A. Petre, G. Teyssedre, "Comportement diélectrique du polyéthylène téréphthalate (PET). Mesures de charges d'espace," RIGE. vol. 8, pp.20, 2005

Optimization of a superhydrophobic insulation's performance by ejection of water drops deposit under an alternating electrical field

K. Hamour[1], F. Bouchelga[1,2], R. Boudissa[1],
[1]Laboratory of Electrical Engineering
Department of Electrical Engineering,
University A. Mira de Bejaia, 06000 Bejaia, Algeria
[2]University of Ghardaia, Algeria

S. Kornhuber[3] and K.D. Haim[3]
[3]University of Applied Sciences,
Theodor - Koerner - Allee 16 Zittau 8800, Germany

Abstract— **In this study, a superhydrophobic surface insulation and a very suitable electrode profile were manufactured to eject from its surface any water drops deposit in order to inhibit any partial electrical discharges formation and/or its flashover under AC voltage. The expulsion mode of the water drops was visualized using a camera. Some water drops' electro-geometric parameters effect on the insulation performance has been quantified. The obtained results show that the chosen device allows a groupo-individual and bidirectional evacuation of the water drops, without creating any electrical discharges on any surface. The maximum ejection voltage of the water drops is slightly greater than half of its flashover in dry case. Therefore, the superhydrophobicity of the material is conserved and its longevity is optimized regardless of the factors' influence. These results militate well in the use of the electrical insulation of energy equipment.**

Keywords – Superhydrophobic surface, water drops, groupo-individual and bidirectional evacuation, AC performance.

I. INTRODUCTION

In order to alleviate the world wide power transmission networks disturbances, due to wet pollution affecting the insulators performance, insulating surface scientists have developed hydrophilic and hydrophobic insulations [1- 2].

Hydrophilic insulation is frequently short-circuited by electrical arcs under wet pollution, because of the facility and wetting speed of its surface. The hydrophobic insulation is not only lightweight but also has a high waterproofing power at long-term. Any kind of moisture coming into contact with its surface, beads on its surface as discrete water drops [3]. This result in a minimization of short-circuits currents and an inhibition of the spatio-temporal evolution of flashover discharges, even if the surface is heavily contaminated, because the silicone transfers its hydrophobicity to the polluting deposits [4]. Although their electrical performance is significantly higher than that of ceramics; in-service these insulations alterates under high humidity, since the occurrence of a drops' deposit cause the elevation of the electrical field prevailing between their ends. This results a taper which leads to a short-circuit of their dry creepage distance and consequently to the surface flashover. The recurring heating of the surface by the formed electrical arcs can generate their irreversible failure resulting in cracks and surface erosions [5 - 6].

As new solutions to the mentioned problem, we can mention among others the addition of some adjuvants to the composition of this kind of polymer [7 - 8].

By virtue of a lotus, some researchers have developed, at the same time, artificial materials with superhydrophobic surfaces already exploited in some industrial fields [9-11]. Their design is based on the non-adhesion of any kind of moistur;e coming in contact with their surface, which allows the conservation of their drought. Therefore, in the case of their use as electrical insulators, their isolation power will remain invariably constant regardless of their use environment humidity degree.

Up to now, there are few published results on the electrical discharges inhibition on their surface by evacuation of any surrounding moisture under the AC effect [12 - 20].

The purpose of this paper is to quantify the electrical performance of a silicon-based superhydrophobic insulation with suspended electrodes system above the material. This, in order to allow the evacuation of any water drops deposit coming into contact with its surface, under the alternating electrical field effect and by varying some of their electro-geometric parameters.

II. EXPERIMENTAL MODEL AND MEASURING TECHNIQUES

The experimental setup consists on a glass plate with a superhydrophobic surface and edges, and two parallelepiped

stainless steel electrodes with rounded ends and (120 x 30 x 8) mm^3 in dimensions. The electrodes are raised 10 mm above the insulation's surface through two insulating supports (Fig. 1a3). The distances between the insulation and the electrodes, as well as the tank are chosen so to have easy evacuation of the water drops outside the insulation and their recovery by the tank (Fig. 1a4) regardless of their volume [17].

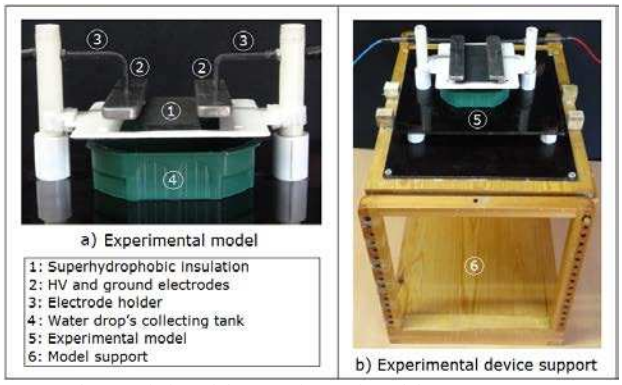

Fig. **1**. Characteristics of the experimental model

The insulation, the device and the wooden support are fastened to each other by plastic screws (Figs 1a1 and 1b5). The wooden parallelepiped support has for dimensions: 500 mm x 500 mm x 400 mm.

Its upper face is connected to a ball joint by which the inclination angle α of the insulation with respect to the horizontal is varied. Its arbitrary positioning is established using two varnished wooden rods. These pass through appropriate holes and made especially on its two opposite vertical faces in order to fix it at a position corresponding to the chosen angle. Thus, the sliding angle of a water drop without voltage on a superhydrophobic insulation by this support is obtained [1]. Figure 1b reflects the image of the insulation in horizontal position (α = 0 °). Its choice is motivated by the simulation of a real flat insulator's profile. The low mobility of the water drops on its horizontal surface and their elongation under the effect of an alternating electrical field can reduce its electrical performance [1].

The insulation to be coated with a superhydrophobic layer is a glass plate, of dimensions 120 mm x 50 mm x 5 mm. Its upper surface and its four edges are manually coated with two layers which are composed of different materials. The first layer of silicone gel is from a commercial product (Fig.1a). The second layer is composed mainly of soot. This one is obtained by carbonization of some amount of silicone gel from the same product and watered with isopropanol alcohol (Fig.1b). Its provision on the first fresh layer of silicone gel covering the glass (Fig.1c) is possible by bringing it momentarily close to the flame (Fig.1b). The soot is added to the fresh layer of silicone gel so that the carbon produced can adhere well to the silicone coating. Figure 1d reflects the image of the upper surface of the glass, blackened with soot and washed with tap water.

Measurement of the water drops' volume of a polluting solution is carried out using a micropipette, graduated from 5 to 100 µl (Fig. 3). A given quantity of water is adjusted by its meter and aspiration of a beaker is carried out using the pipette (Figs 3a and 3b). This water's volume is then deposited with the same pipette in the form of a water drop on the superhydrophobic insulation's surface (Fig. 3b). The positioning of the water drops on its surface is done using a nylon thread (Fig 3c). The contact angle of a water drop on it is measured using of a goniometer. Its value is about 161 °, corresponding to a volume of 20 µl. Its sliding angle on this inclined surface is less than 2° (Fig. 3d). These values are consistent with those obtained by other researchers [12 - 13].

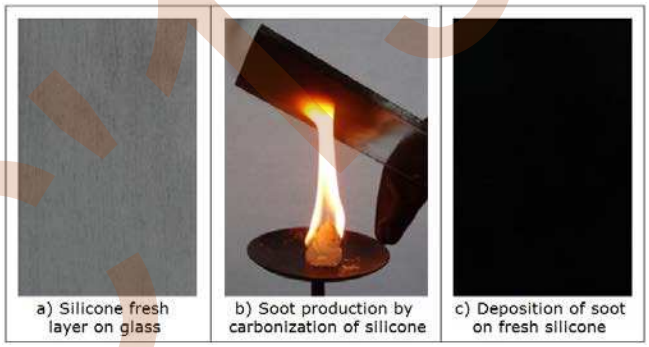

Fig. **2**. Main phases of a superhydrophobic glass surface's preparation

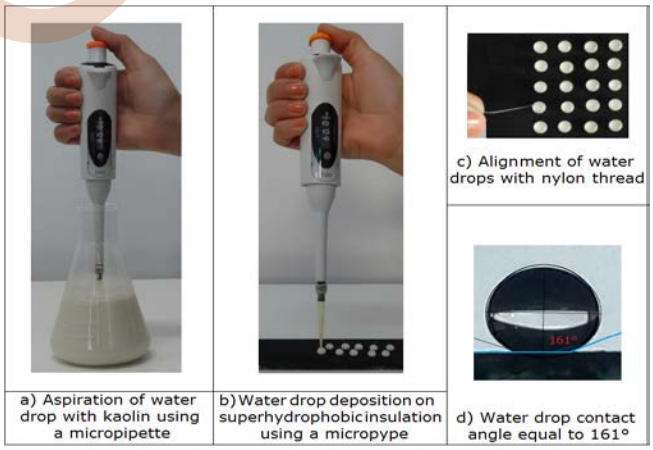

Fig. **3**. Micropipette for measuring the water drops' volume between 10 and 100 µl

For qualitative reproduction's reasons of the very random distribution of the number and the size of condensation or natural rain's water drops, our choice is focused on two types of arrangements either in zigzag A_z (Fig. 4a) or straight lines A_s (Fig. 4b). Each of these modes of arrangement consists of a maximum of 20 water drops of deposited in five rows of 4 water drops in each row. These water drops can be aerated (Figs 4a and 4b) or sandwiched between the superhydrophobic insulation on which they rest and a glass insulation as cover simply resting on the two

suspended electrodes (Fig.4c). There are two possibilities for the supply of water drops' rows on the surface of the insulation, either they are deposited in parallel (Fig. 5) or perpendicular to the electrodes (Fig. 6), whatever the mode of their arrangement.

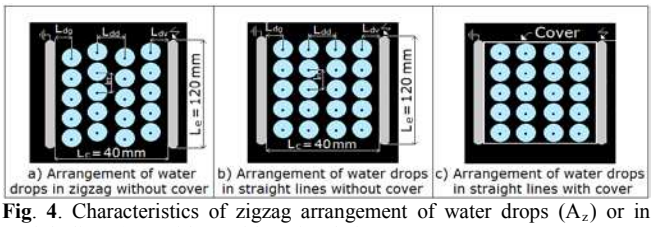

Fig. 4. Characteristics of zigzag arrangement of water drops (A_z) or in straight lines (A_s) with or without insulation cover

The covering of the material's surface in rows of water drops parallel to the electrodes can begin from the HV electrode towards the grounded one (Fig. 5a) or vice versa (Fig. 5b). The covering of the insulation's surface in rows of water drops perpendicular to the electrodes is affected by going from their ends (left or right) towards their middle whatever the mode of their arrangement considered in this study (Fig. 6). The distances between the centers of the drops and the electrodes HV (L_{dv}) or G (L_{dg}) as well as that separating the centers of two adjacent drops along the leakage distance of the insulation (L_{dd}) or perpendicular to it (l_{rr}), are held constant throughout this investigation (Fig. 4).

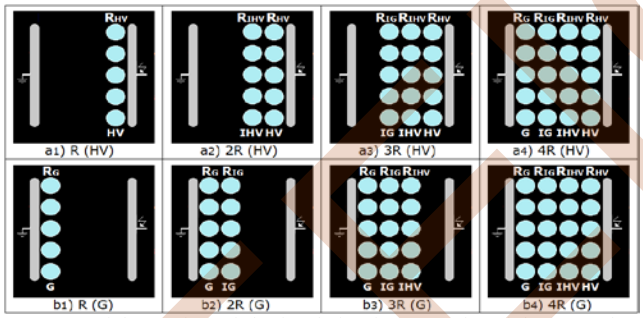

Fig. 5. Partial covering of the insulation in rows of straight water drops parallel to the electrodes (R_G: Ground row, R_{IG}: Intermediate ground line, R_{IHV}: High voltage intermediate row, R_{HV}: High voltage row, $V_d = V_{30}$ = 30 µl)

For reproduction reasons of the size's different values of the water drops of condensation and / or natural rain, as well as the various degrees of their pollution, the volume of a single row of five water drops (V_i) is taken as equal to (10, 30, 40, 60 and 80) µl. Their electrical conductivity (σ_i) is varied between 10 µS / cm and 20 mS / cm. During the variation of the volume and the electrical conductivity of the water drops, the position of their row (HV, M and G) as well as the mode of their arrangement (Straight line, zigzag) have been varied (Figs.7 and 8).

The measurement of the expulsion voltage of each of the water drops outside the insulation and its flashover in the dry case is carried out with using the test station illustrated in figure 9.

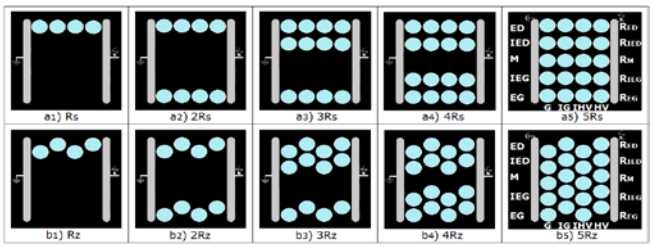

Fig. 6. Insulation covering in water drops' rows of straight line (A_s) or zigzag (A_z) perpendicular to the electrodes (R_{ED}: Row of the right end of the electrode, R_{IED}: Intermediate row at the right end of the electrode electrode, R_M: Row in the middle of the electrode, R_{IEG}: Intermediate row at the left end of the electrode, R_{EG}: Row at the left end of the electrode, $V_d = V_{30}$ = 30 µl)

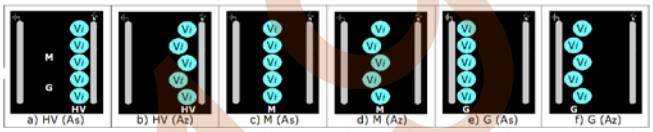

Fig. 7. Variation of the water drops' volume of a row on the surface of the insulation with variable position (P_r) and arrangement (A_r) (σ_v = 50 µS / cm, V_i variable)

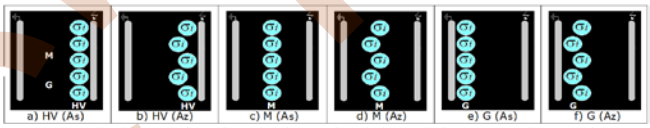

Fig. 8. Variation of the electrical conductivity of the water drops of a row on the insulation's surface with variable position and arrangement (V_d = 30 µl, variable σ_i)

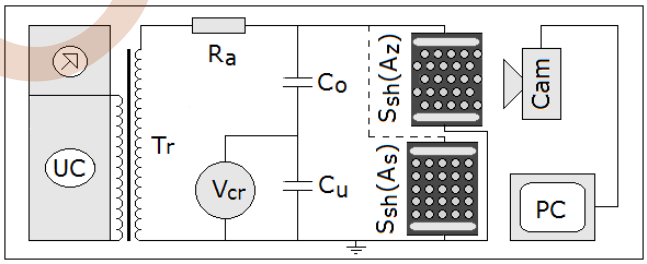

Fig. 9. Diagram for measuring the ejection voltage of water drops and visualizing their expulsion

The test station consists of a high voltage transformer (0.08A / 135kV), a capacitive voltage divider (C_o/C_u), a digital display peak voltmeter (V_{cr}) and a superhydrophobic insulating surface (S_{sh}). The visualization circuit comprises a fast camera (Cam) for recording the evacuation mode of water drops outside the insulation and a PC for processing images using a software Free Video. The value of the insulation's leakage distance (L_c) considered in this study is equal to 4 cm. The test voltage applied to the superhydrophobic insulation covered with water drops is manually increased in steps of 0.5 kV until the expulsion of the last water drop outside the insulation. The test voltages corresponding to the ejection of each of the water drops and their destination were noted. For each of the influence parameters aforementioned, a series of 20 tests was carried out and the value retained for the expulsion voltage of each

of the drops is the arithmetic average of all those obtained on the same series of measurements. Given the very good repeatability of the measurement techniques used in this study, the relative maximum error obtained is equal to 5% of this average value.

III. RESULTS AND DISCUSSIONS

III.1. Evacuation Mode of the water drops

The analysis of the hydrodynamic and electrical forces, governing the expulsion of water drops outside the insulation's surface is supported by the Navier-Stockes equation, based on the conservation of motion forces and modeling the motion of an incompressible water drop according to relation 1:

$$-\nabla P_{\Delta} + \mu \nabla^2 \vec{V} + \vec{F} = d\left(\frac{\partial \vec{V}}{\partial t} + \vec{V}.\nabla \vec{V}\right) \quad (1)$$

Where:

- d, V and μ respectively represent the density of the fluid, its velocity and its viscosity;

The three terms: ∇P_{Δ}, $\mu \nabla^2 \vec{V}$ and $\vec{F}$ respectively represent the effects of forces due to the pressure, the viscosity and the electrostatic force exerted on the drop of water;

- The right member of equality 1 refers to the acceleration of drop under the effect of the three mentioned forces.

Assuming that the drop retains its spherical shape during its motion and that the surface is superhydrophobic (θ = 161 °), the electrostatic force $\vec{F}$ plays a predominant role in the motion of the drop on the superhydrophobic surface of the insulation [15, 21].

For an individual water drop, placed on this surface and put under the effect of an electric field, the expression of this electrical force is of the form [22]:

$$F = \rho_t E - \frac{1}{2}|E|^2 \nabla \varepsilon + \frac{1}{2}\nabla\left(|E|^2 \frac{d\varepsilon}{d\rho_m}\rho_m\right) \quad (2)$$

Where:

E, ρ_t, ε and ρ_m respectively represent the electrical field, the total charge, the absolute permittivity of the water and the voluminal density.

The three terms of the right member of equation 2 represent the Coulomb force, the dielectrophoretic force, and the electrostriction pressure, respectively. In this study, the last two terms are neglected because of the uniformity of the electrical field prevailing in the planar electrode system and the maintenance of the spherical shape of the water drop during its expulsion from the insulation. Therefore, the ejection of an individual water drop of outside the insulation is practically caused by the Coulomb force.

In the case of several water drops, the expulsion of a water drop from a row parallel to the electrodes and very close to them is governed by the resultant Coulomb forces and mutual forces of attraction along the creepage distance of the insulation and repulsion, perpendicular to the creepage distance in the plane of the insulation [23]. As the water drops in a row move parallel to the direction of the applied field, so the repulsive forces are considered negligible in this case. In summary, the ejection outside the isolation of the water drops of each row is governed mainly by the resultant Coulomb force directed to the nearest electrode (HV or G) and the mutual force of attraction directed towards the row of adjacent drops and the force of Coulomb is the most dominant in this case.

In this study, the water drops are deposited on the superhydrophobic surface of the insulation in the absence of voltage. Then, the voltage, applied to the material with drops is increased in steps of 0.5 kV until the expulsion of the last drop outside the insulation. Figures 10 and 11 respectively give the histograms of the ejection voltages of the insulation without cover, 4 rows x 5 water drops, under arrangement in straight lines A_s or zigzag A_z, according to their rank and the place of their transit (HV or G electrode) before landing in the recovery tank.

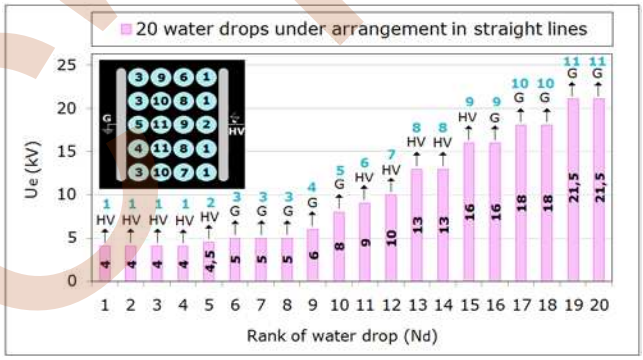

Fig. 10. Histogram of expulsion voltages of 5 rows x 4 water drops in straight lines outside superhydrophobic insulation without cover (V_d = 30 µl, σ_v = 50 µS/cm)

This results in a groupo-individual and bidirectional evacuation mode of water drops. This expulsion is carried out either in complete or partial rows; it means the evacuation of water drops of the same row can be established at most in three stages. The first concerns the evacuation of the extreme drops, the second, the intermediate ones finally the third, the middle one. Regarding the direction of their evacuation, those in the vicinity of the HV electrode pass through it and those deposited in the area around the ground electrode pass through the latter.

The water drops expelled in the first place belong to the rows very close to the HV and ground electrodes. Next comes those in the intermediate rows at the HV and G electrodes. Finally the drops of the middle row come out last. It should be noted that the number of drops expelled via the under high voltage electrode is greater than or equal to that of the drops passing through the ground electrode. The ejection mode of the water drops is similar in the two figures 10 and 11, the only difference resides in the value of

the expulsion voltage which is lower under a zigzag arrangement of water drops than in straight lines because of the important effect of the forces of mutual attraction in the latter case.

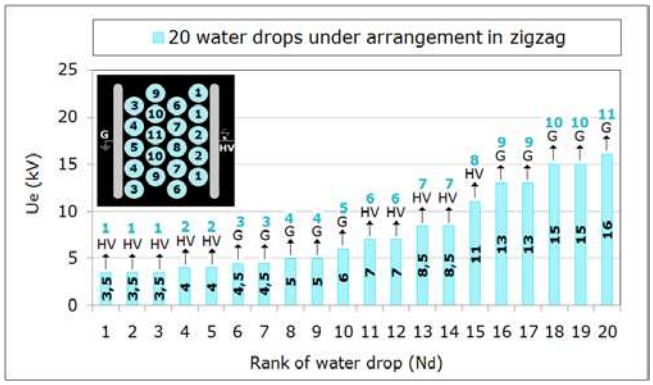

Fig. 11. Histogram of ejection voltages of 5 rows x 4 water drops in zigzag outside the superhydrophobic insulation without cover (V_d = 30 µl, σ_v = 50 µS/cm)

Figure 12 shows the evolution of the evacuation voltage of the last drop according to the number of rows parallel or perpendicular to the electrodes under their arrangement in straight lines or in zigzag. It results its growth with the displacement of the last drop's position of the insulation's ends parallel to its leakage distance towards its middle, until a limit value of the number of rows equal to 2. Beyond this number, it becomes constant and it depends on the arrangement mode of the water drops. Its value is weaker in zigzag arrangement than in straight lines because of the importance of the effect of the mutual attraction forces of the drops in the latter case. Knowing that the flashover voltage of the insulation without drops is 39 kV, expulsion voltage of the last drop is about 56 % of the value of that of the insulation's flashover in the dry case.

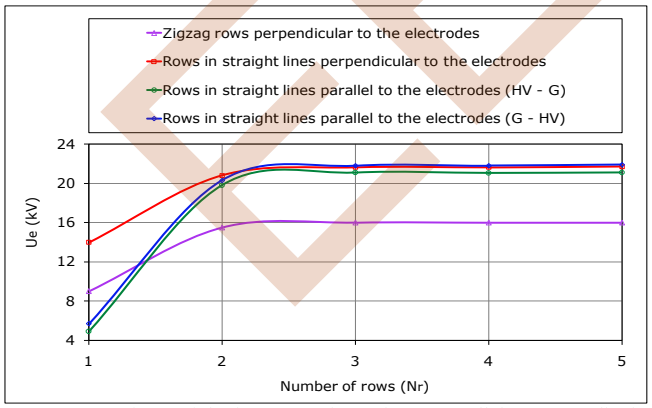

Fig. 12. U_e = f(Nr) of the last water drop of rows parallel or perpendicular to the electrodes defining the insulation without cover (V_d = 30 µl, σ_v = 50 µS/cm)

Figure 13 shows the images of some essential phases of a groupo-individual and bidirectional expulsion mode of 5 rows x 4 water drops covering insulation without coverage depending on the mode of their arrangement. Each image reflects the number of persistent drops at a corresponding voltage level applied to the insulation. It should be noted that this expulsion process is not accompanied by the formation of any partial electrical discharge or flashover that can cause the alteration of the material used. This justifies the conservation of the superhydrophobicity of its surface.

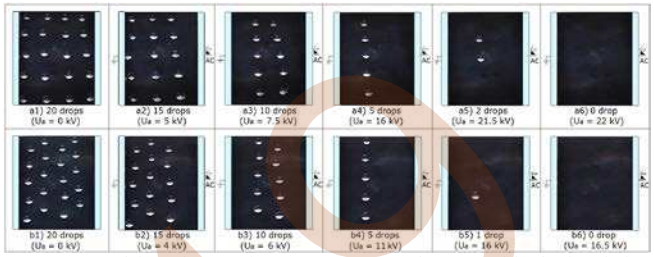

Fig. 13. Expulsion phases of 5 rows x 4 water drops outside the insulation according to the mode of their arrangement a: Arrangement in straight lines A_s, b: Arrangement in zigzag A_z (V_d = 30 µl, σ_v = 50 µS/cm)

III.2. Volume and Electrical Conductivity of Drops Water

In this section, we were particularly interested in the effect of volume and electrical conductivity of the last water drop in a five-drop row for three different positions (HV, M and G) on its insulation's ejection voltage. Figure 14 shows a decline in its evacuation voltage as a function of its volume [21], regardless of the row's position on the surface of the insulation and the arrangement mode of the water drops (Fig. 7).

The expulsion voltage of the last water drop in a row, very close to the HV or G electrode, is higher in zigzag arrangement than in straight line. On the other hand, the opposite has been noticed when the water drops' row is placed in the middle of the insulation. This is justified by the fact that in the case of a row very close to the HV or G electrode, the evacuation of the last water drop under zigzag arrangement requires a higher voltage because of its shift of its pairs towards the middle of the insulation. On the other hand, when the row is placed in the middle of the insulation, the zigzag water drops are shifted from the middle towards the HV and G electrodes so that the ejection voltage of the last drop is lower in this case. Finally, the expulsion voltage of the drops of the row increases from the HV and G electrodes to the middle of the insulation whatever the mode of its arrangement.

The expulsion voltage of the last water drop outside the uncovered insulation (Fig. 15a) is 14 % higher than that with cover (Fig. 15b). The ejection mode of water drops is similar for both cases; the only difference resides in the value of the expulsion voltage which is lower when the superhydrophobic surface is covered by glass insulation. This can be explained by the fact that the insulating cover acts as a screen and condenses the field lines prevailing in the interelectrode air gap at the top of the drops (Fig. 15b), which leads to decrease of the voltage of their evacuation and the elevation of its electrical performance.

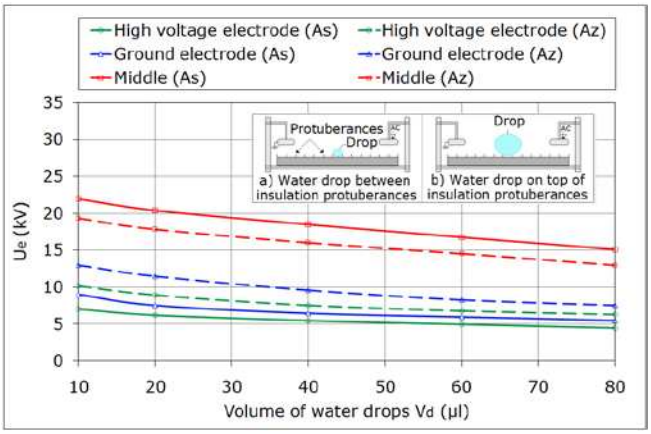

Fig. 14. $U_e = f(V_d, P_r, A_r)$ of the last of the five water drops in a row outside the uncovered insulation (σ_v = 50 µS/cm)

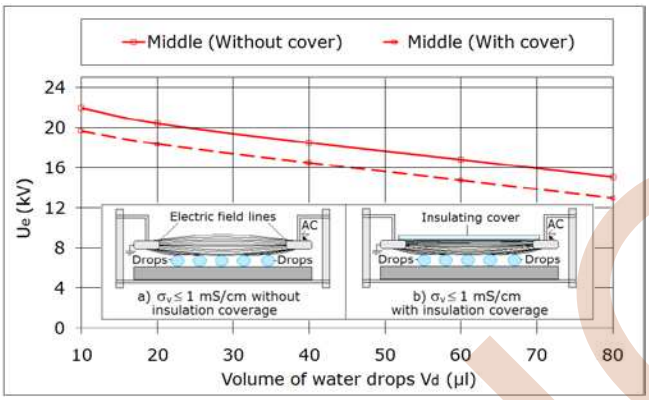

Fig. 15. $U_e = f(V_d)$ for a straight row of 5 water drops in the middle of the creepage distance of the insulation with or without cover (σ_v = 50 µS/cm)

It also results from figure 15 that a drop of small volume requires a greater expulsion voltage than when this one is higher but does not exceed 56 % of that of the insulation's flashover in the dry case. This can be explained by the sticking of water drops between the asperities of the material's surface (Fig. 15a). Their deep penetration on the interstices, formed by these asperities, is easier as their volume is small. On the other hand, when their size is large, they rest almost on the top of the asperities (Fig.15b), which triggers their movement under lower test voltages.

The characteristic $U_e = f(\sigma_v)$, shown in figure 16, shows a slight decline in the evacuation voltage of the last water drop in a row with the rise in the value of the electrical conductivity [22] up to 1 mS/cm and above which it remains virtually constant regardless of the arrangement mode (zigzag or straight line) and the position of the row (HV, G or M). For the same reasons given for the volume of water drops, figure 16 shows that the evacuation voltage of the last water drop of a row located in the middle of the insulation is smaller under zigzag arrangement than that in a straight line. On the other hand, the opposite has been observed when the row of water drops is placed in the vicinity of the two electrodes. Likewise, the expulsion voltage of the drops of the row increases from the HV and G electrodes towards the middle of the insulation whatever the mode of its arrangement.

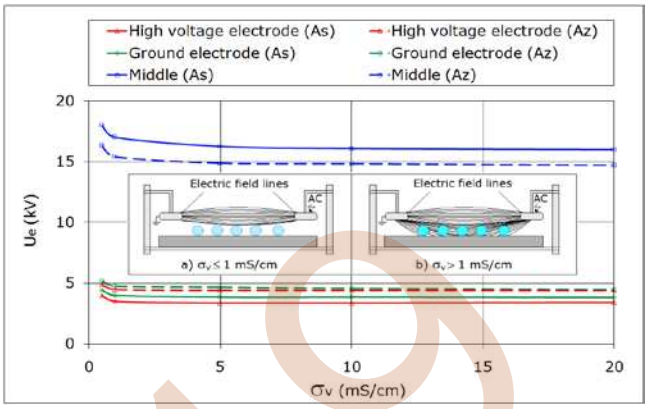

Fig. 16. $U_e = f(\sigma_v, P_r, A_r)$ of the last of the five water drops of a row outside the insulation without cover (V_d = 30 µl)

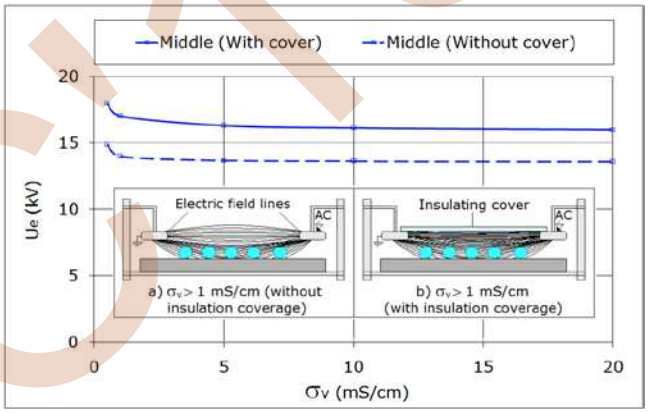

Fig. 17. $U_e = f(\sigma_v)$ for a straight row of 5 water drops in the middle of the creepage distance of the insulation with or without cover (V_d = 30 µl)

It results from figure 17 that the output voltage of the last water drop of insulation with cover is 15 % lower than that without it regardless of the value of its electrical conductivity. The image of figure 17a shows that for a very low electrical conductivity of the water drops, the lines of the field move away from them, which requires a slightly higher ejection voltage in this case. On the other hand, with the elevation of their conductivity, the free charges are numerous and distributed uniformly within their volume and drops are crossed by the field lines, which causes their expulsion for lower test voltages (Fig. 17b). This reaches a minimum when the drops become conductive. This result is consistent with those obtained by other researchers on AC superhydrophobic isolation [17 and 19].

IV. CONCLUSION

The main results emanating from this study can be summarized as follows:

- Water drops manually deposited on the surface of a superhydrophobic insulation are expelled to the outside in a groupo-individual and bidirectional evacuation mode. When

they exit, the number of water drops passing through the high voltage electrode is slightly greater than that passing through the ground electrode.

- The ejection voltage of the water drops outside the insulation increases by going from the edges of the insulation parallel to its creepage distance or HV and G electrodes towards its middle whatever the volume, the electrical conductivity of water drops and their arrangement.
- The evacuation voltage of a deposit of water drops is lower in zigzag arrangement than in straight lines, regardless of their volume and electrical conductivity. It is even more reduced when the surface of the material is covered with glass insulation, whatever the influence parameters aforementioned.
- The expulsion voltage of insulating water drops increases with the decrease of its volume, but without exceeding 56% of that of the material surface's flashover in the dry case.
- The electrical conductivity of the water drops has little influence on the voltage of their expulsion.
- In all cases, the process of groupo-individual and bidirectional expulsion of the water drops of the material does not generate partial electrical discharges or the insulation's flashover that can generate any trace of its degradation. The retention of its superhydrophobicity under the aforementioned conditions militates well for its use for the isolation of electrical energy equipment.

REFERENCES

[1] S. Ilhan S, A. Ozdemir A, S.H. Jayaram, E.A. Cherney, "Numerical and experimental investigation of the effects of pollution on glass suspension-type insulators", IEEE Transactions on Dielectrics and Electrical Insulation, Vol. 22, n° 5, pp. 2987 - 2994, 2015.

[2] R. Boudissa, F. Bouchelga, S. Kornhuber and K. D. Haim," Constellation of Condensation and Raindrops and Its Effect on the DC Flashover Voltage of Inclined Silicone Insulation", Energies 2019, 12, 3549, pp. 1-17.

[3] C. Baer, R. Baersch, A. Hergert, J. Kindersberger, "Evaluation of the Retention and Recovery of the hydrophobicity of Insulating Materials in High Voltage Outdoor Applications under AC and DC Stresses With the Dynamic Drop Test", IEEE Transactions on Dielectrics and Electrical Insulation,Vol. 23, Issue n° 1, pp. 294-303, 2015.

[4] D. A. Swift, C. Spellman and A. Haddad, "Hydrophobicity Transfer from Silicone Rubber to Adhering Pollutants and its Effect on Insulator Performance", IEEE Transaction on Dielectrics and Electrical Insulation, Vol. 13, No. 4, pp. 820-829, 2006.

[5] Arshad, A. Nekahi, S. G. McMeekin, M. Farzaneh, "Measurement of surface resistance of silicone rubber sheets under polluted and dry band conditions", Electr. Eng. 100, pp. 1729 -1738, 2018.

[6] A. Ren, H. Liu, J. Wei and Q. Li, "Natural Contamination and Surface Flashover on Silicone Rubber Surface under Haze–Fog Environment", Energies, 10, 1580, pp. 1-18, 2017.

[7] B. X. Du and M. Xiao, "Effects of thermally conducting particles on resistance to tracking failure of polyimide/BN composites", IEEE Transaction on Dielectrics and Electrical Insulation Vol. 21, Issue 4, pp. 1565 – 1572, 2014.

[8] R. F. da Silva and V. S. Filho, "Analysis of electrical tracking by energy absorption during surface discharge in polymeric materials", IEEE Transaction on Dielectrics and Electrical Insulation, Vol. 23, Issue 1, pp. 501-506, 2016.

[9] N. Wang, D.S. Xiong, M.T. Li, Y.L. Deng, Y. Shi, K. Wang, "Superhydrophobic surface on steel substrate and its anti-icing property in condensing conditions", Appl. Surf. Sci. 355, pp. 226–232, 2015.

[10] Y. Liu, Y. Bai, J.F. Jin, L.M. Tian, Z.W. Han, L.Q. Ren, Facile fabrication of biomimetic superhydrophobic surface with anti-frosting on stainless steel substrate, Appl. Surf. Sci. 355, pp. 1238–1244, 2015.

[11] J. Li, Y. Wie, Z. Huang, F. Wang, X. Yan, Z. Wu, "Electrohydrodynamic behavior of water droplets on a horizontal super hydrophobic surface and its self-cleaning application", Applied Surface Science 403, pp. 133 – 140, 2017.

[12] Y. Li, H. Jin, S. Nie, P. Zhang, N. Gao, "Dynamic behavior of water droplets and flashover characteristics on a superhydrophobic silicone rubber surface", Applied Physics Letters 110, 201602, 2017.

[13] Y. Li, H. Jin, S. Nie, C. Tong, N. Gao, "Effect of superhydrophobicity on flashover characteristics of silicone rubber under wet conditions", AIP Advances 8, 015313, pp. 1 – 11, 2018.

[14] S. Vallabhuneni, S. Movafaghi, W. Wang, A. K. Kota, "Superhydrophobic Coatings for Improved Performance of Electrical Insulators", Macromolecular Materials & Engineering, 2018.

[15] J. Li, Y. Wei, Z. Huang, F. Wang, X. Yan, "Investigation of the Electric Field Driven Self-propelled Motion of Water Droplets on a Super-hydrophobic Surface", IEEE Transactions on Dielectrics and Electrical Insulation Vol. 23, No. 5, pp. 3007 – 3015, 2016.

[16] S. Wei , H. Jin , H. Zhou, K. Yang, N. Gao, and W. Li, "Dynamic behavior of water droplets on wetted superhydrophobic surfaces under a high AC electric field", AIP Advances **9**, 065307, pp. 1-5, 2019.

[17] K. Hamour, B. Smati, S. Soudani, F. Bouchelga, R. Boudissa, S. Kornhuber, K. D. Haim, "Effet du profil des électrodes sur la performance électrique d'une isolation superhydrophobe recouverte de gouttes d'eau sous tension continue", 11ème Conférence nationale sur la haute tension (CNHT19), pp. 200-206, Oran (Algérie) 2019.

[18] N.E.H. Tadrent, A. Benamsili, K. Hamour, F. Bouchelga, R. Boudissa, S. Kornhuber and K.D. Haim, "Electrical performance of superhydrophobic insulation covered with water drops under alternating voltage", 4th ISNPEDADM 2019 (New electrical technologies for environment), Bonifacio Corsica Island, France, 2019.

[19] K. Hamour, F. Bouchelga, R. Boudissa, S. Kornhuber, and K. D. Haim, "Inhibition of superhydrophobic insulating surface's flashover by expulsion of water drops covering its surface under DC voltage", 4th ISNPEDADM 2019 (New electrical technologies for environment), Bonifacio Corsica Island, France, 2019.

[20] K. Hamour , S. Soudani , B. Smati, F. Bouchelga, R. Boudissa, St. Kornhuber, K. D. Haim, "Contribution to the optimization of the electrical performance of a superhydrophobic insulation covered with water drops under DC voltage", Journal of Electrostatics 102 (2019) 103375, pp. 1-9.

[21] K. Takeda, A. Nakajima, Y. Murata, k. Hashimoto and T. Watanabe, "Control of water droplets on super-hydrophobic surfaces by static electric field", Jpn. J. Appl. Phys., Vol. 41 (2002), Part. 1, No. 1, pp. 287-291.

[22] H. Morgan *and* N. G. Green, "AC Electrokinetics: colloids and nanoparticles", Research Studies Press LTD, Baldock, Hertfordshire, England, 2003.

[23] J. Ndoumbe, "Behavioral study of water droplets deposited on the surface of a high-voltage composite insulator in the presence of the electric field", Doctoral Thesis 2014, Doctoral School Electronics, Electrotechnics, Automation, Central School of Lyon, France.

Characterisation of a two-wire corona electrode

A. Rahmani[1], O. Chibane[1], K. Smili[2,3]
B. Bendahmane[1], A. Kasdi[1]
(1) Laboratoire de Genie Electrique de Bejaia
University of Bejaia 06000, Algeria
rahmani_ht@yahoo.fr
(2) Higher School of Industrial Technologies, Safsaf city,
B.P. 218, Annaba 23000, Algeria
(3) Laboratory of Electromechanical Engineering, B.P.12,
Sidi Amar Annaba 23220 Algeria

L. Dascalescu[4]
(4) PPRIME Institute, UPR 3346 CNRS, University of
Poitiers IUT d'Angoulême 16021, France.
lucian.dascalescu@university-poitiers.fr

Abstract— The static electricity phenomenon is used in various industrial applications such as electrostatic painting, precipitation of dust and separation of granular materials. The objective of the present experimental study carried out with various models of two-wire corona electrodes is to enhance the efficiency of insulating materials charging. The experimental set-up enabled the measurement of corona current-voltage characteristics and potential surface distributions. The results obtained show that the corona discharge intensity increases with the spacing between the two wires. As expected, the current collected at the grounded electrode increases with the number of wires, for the same voltage. By measuring the electric potential at the surface of a Polyethylene film exposed to the corona discharge generated by the two-wire electrode it was possible to evaluate the corona charging conditions of granular materials in electrostatic separators.

I. INTRODUCTION

Corona discharge is a common method used for electrical charging of fibrous media, powders or granular materials in various electrostatic processes [1, 2]. It is produced between two highly asymmetrical electrodes, an active electrode (in the form of metal needles, blades or wires) connected to a DC high voltage supply, and a grounded electrode (metal cylinder or plate). Though dual-type corona electrodes [3] are widely used to generate corona discharges, but fine-wire-type electrodes still have bright days ahead of them, for their simplicity and low cost. The aim of this study we is to assess a new two-wire corona electrode current-voltage characteristics and distribution of the electric potential the surface potential of an insulating film exposed to the corona discharge in this specific configuration [4].

II. EXPERIMENTAL ARRANGEMENT

The measuring bench includes a corona discharge station, and an electric potential measuring station. A conveyor belt supported the sample carrier and transferred it from the charging position to the surface potential measurement (Fig. 1). The corona discharge station consists of two thin tungsten wires, 0.25 mm diameter and 300 mm length, attached to the ends two Plexiglas plates. The ionizing wires are powered by a high voltage power supply (ISEG, High Voltage Power Supply) model T1 CP300n 30 kV/0.3 mA. The two wires are parallel with respect to the grounded plane. The sample (Polyethylene film) is in contact with a flat electrode connected to that plane. Once it is subjected to a corona discharge, the conveyor moves the sample to the measuring station (Fig. 1).

The surface potential is measured with an electrostatic probe (Trek, Model 3450), placed at 3 mm above the sample. The probe is connected to an electrostatic voltmeter, Model 341B of Trek, which has the ability to measure potentials ranging from 0 to 20 kV with a response time less than 200 µs. The analogue signal given by the electrostatic voltmeter represents the image of the electrical potential measured by the electrostatic probe. The data is transmitted to the computer via the National Instruments NI USB 6009 acquisition card.

III. RESULTS AND DISCUSSIONS

A. Current-Voltage characteristics

1) Influence of the number of discharge wires

Figure 2 shows that, as expected, for a given value of the applied voltage the collected current at the measuring plate increases with the number of wires [4, 6, 7].

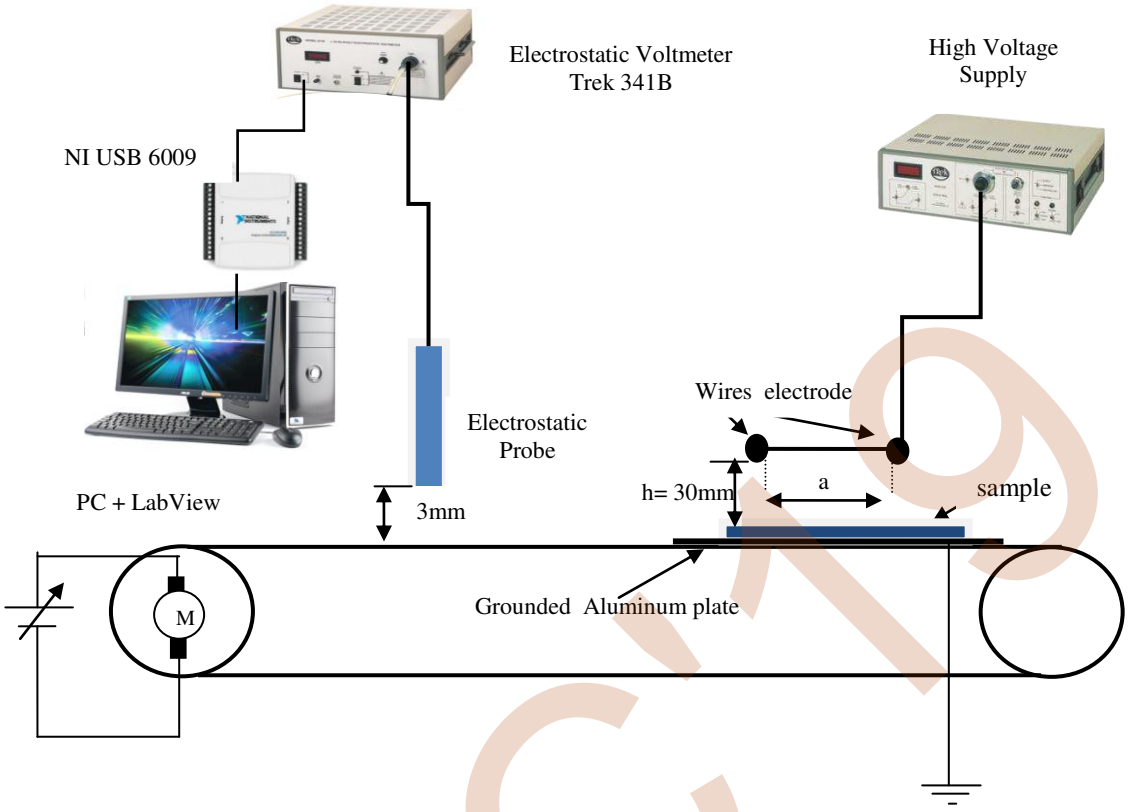

Figure 1. Schematic representation of the experimental set-up.

2) Influence of wire- to- wire spacing

The experimental results on Fig. 3 show that the corona discharge current increases with increasing the distance "*a*" between the two wires, for a fixed voltage. This is due to the shielding effect exerted by the wires on each other. This effect increases with the decrease of the wires spacing reducing the discharge current of each wire; then, as consequence, the total current at the plate is lower [4, 8, 9].

B. Corona Charging Efficiency

1) Static charging of the polyetylene film

In this experiment, the sample are charged for one second with the same high-voltage (V=15 kV). As soon as the high-voltage supply of the corona charger was turned off, the conveyor belt that supports the sample carrier and transferred it from the charging position to the surface potential measurement station, at a constant speed of 5 m/min. Figure 4 illustrates the electric potential distributions in static charging for the Polyethylene film for one second, using one and two wires electrode configurations.

The potential surface is maximal under the coronating wire and then decreases gradually away from it. For the studied two wires-to-plane configuration, the profile of the potential surface distribution along the collecting plate presents a "wave shape" with higher potential values under each wire and lower values midway between the two wires. This observation is consistent with what related by other authors about the current density [4, 9, 10].

2) Dynamic charging of the polyetylene film

In this experiment (Fig. 5), the Polyethylene film sample is placed on the conveyor and passed under corona charge with the same high-voltage (15 kV), using one then two wires electrode with 5 m/min speed. The surface potential is measured once the film reaches the probe. However, the electric potential distributions in dynamic charging at the surface of the polyethylene film sample corona charge, the electric potential values are higher in two wires than in one wire.

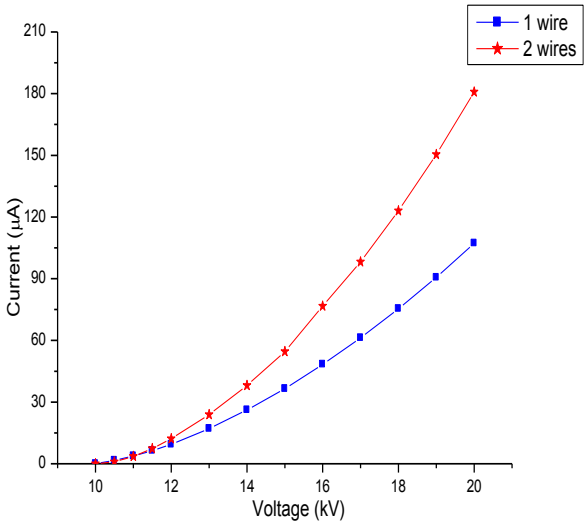

Figure 2. Current-Voltage characteristics for one and two wires spacing " (*a=80 mm, h=30 mm*)

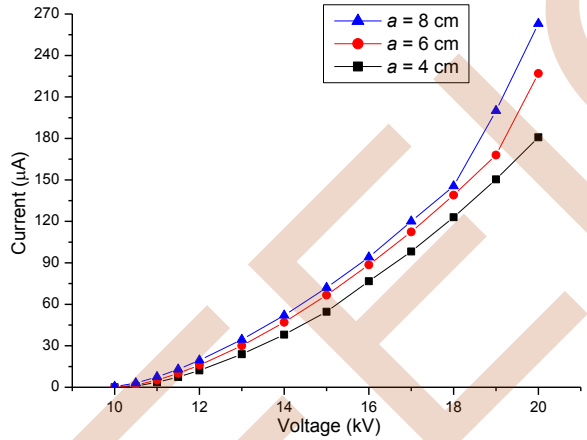

Figure 3. Current-Voltage characteristics for different values of the wires spacing "*a*" (h=30 mm)

3) Dynamic charging of the polyetylene film

In this experiment (Fig. 5), the Polyethylene film sample is placed on the conveyor and passed under corona charge with the same high-voltage (15 kV), using one then two wires electrode with 5 m/min speed. The surface potential is measured once the film reaches the probe. However, the electric potential distributions in dynamic charging at the surface of the polyethylene film sample corona charge, the electric potential values are higher in two wires than in one wire.

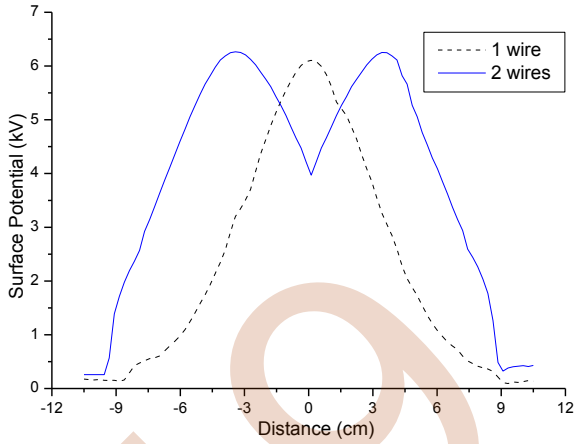

Figure 4. Repartition of the surface potential along the x axis for Polyethylene film in static charging for one and two-wire *(15kV, a=80 mm, h=30 mm)*

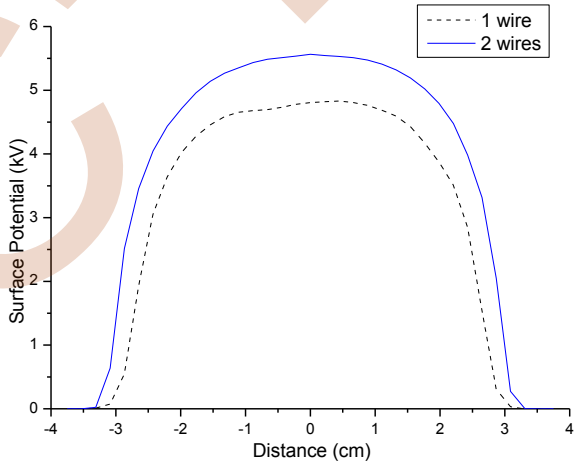

Figure 5. Repartition of the surface potentiel along the x axis for Polyethylene film in dynamic charging for one and two-wire (15kV, a=80mm, h=30mm, speed is 5m/min)

4) Electric amplitude voltage in dynamic charging

In this experiment (Fig. 6), the polyethylene film samples are placed on the conveyor and passed under corona charge with the same high-voltage (15 kV), using one then two wires electrodes with 5 m/min speed. The surface potential is measured once the film reaches the probe. The magnitude of the potential surface distribution increases with the increase of the magnitude of the applied voltage (Fig. 6) [11].

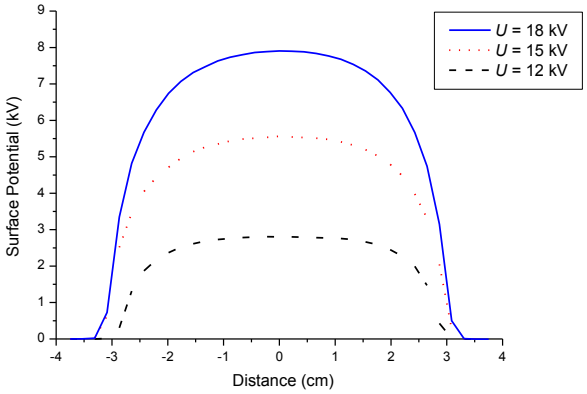

Figure 6. Effect of the amplitude of applied voltage V on the repartition of the surface potentiel along the x axis

IV. CONCLUSION

The results of experiments described in this work are the current-voltage characteristics and the surface potential distributions of a laboratory-scale model of a two wire corona electrode. These characteristics are largely influenced by the applied voltage. However, the corona discharge increases with increasing the spacing between the two wires and the reduction in the wires spacing leads to decrease the collected current at the grounded plane. Moreover, the magnitude of the surface potential increases with the increase of the magnitude of the applied voltage.

When using two discharging wires, the charging performance of the insulating materials is improved. It has been found that the surface potential profile along the collecting plate presents a wave shape with higher values under each wire and lower values in the midway of wires.

REFERENCES

[1] G. S. P. Castle, "Industrial applications of electrostatics: the past, present and future", J. Electrost., vol. 51-52, pp. 1-7, 2001.

[2] T. Oda and J. Ochiai, "Charging characteristics of a non-woven sheet air filter" in Proc. 6th International Symposium on Electrets, pp. 515–519, 1-3 September 1988.

[3] A. Bendaoud, A. Tilmatine, K. Medles, M. Rahli, M. Huzau, and L. Dascalescu, "Characterization of dual corona-electrostatic electrodes for electrostatic processes applications," IEEE Trans. Ind. Appl., vol. 44, pp. 692-698, 2008.

[4] A. Kasdi, "Computation and measurement of corona current density and V-I characteristics in wires-to-plates electrostatic precipitator" J. Electrost., vol. 81, pp. 1-8, 2016.

[5] B. Tabti, "contribution à la caracterisation des filtres à électret par la mesure du declin de potentiel de surface'' Thèse de doctoat, université de poitiers, Decembre 2011.

[6] H. Ait Said, H. Nouri and Y. Zebboudj, "Analysis of currente voltage characteristics in the wires-to-planes geometry during orona discharge" Eur. Phys. J. Appl. Phys., vol. 67, pp. 1-8, 2014.

[7] K. Parker," Electrical Operation of Electrostatic Precipitators". London, United Kingdom, in: IET Power and Energy Series 41, 2007.

[8] U. Khaled, A.Z. Eldein, "Experimental study of V-I characteristics of wiree plate electrostatic precipitators under clean air conditions", J. Electrost., vol. 71, pp. 228-234, 2013.

[9] M. Abdel-Salam, A. Eid, "Finite Element Simulation of Corona in Wire-Duct Precipitators", IEEE 37th IAS Annual Meeting Conf 2, 2002, pp. 1383-1389

[10] Z.M. Al-Hamouz, A. El-Hamouz, N. Abuzaid, "Simulation and experimental studies of corona power loss in a dust loaded wire-duct electrostatic precipitator", Adv. Powder Technol., vol. 22, pp. 706-714, 2011.

[11] B. Yahiaoui, B. Tabti, M. Megherbi, A. Antoniu, M.C. Plopeanu, and L. Dascalescu, "AC corona neutralisation of positively and negatively charged polypropylene non-woven fabrics" IEEE Trans. Diel. Elect. Insul., vol. 20, pp. 1516-1522, 2013.

Optimization of the inter electrode spacing to improve the efficiency of a Multi-wires-to-plates type electrostatic precipitator

Ahmed KASDI
Electrical Engineering Department
Electrical Engineering Laboratory, Faculty of Technology
University A. MIRA of Bejaia, Algeria
dkasdi@yahoo.fr

***Abstract*—The analysis of corona-ionized fields in different geometrical electrode arrangements has an important area of research. One of the most applications of corona discharge is its use in the electrostatic precipitation. This paper aims to improve the efficiency of a multi-wires-to-plates type electrostatic precipitator (WP-ESP) by optimizing the inter electrode spacing, namely the distance between wires and the wires-to-plates spacing. The corona current-voltage characteristics and current density curves are measured for a laboratory-scale model of precipitator. A numerical model was also used to simulate the ESP and to predict the effect of the geometric parameters. The numerical predictions are in good agreement with those measured experimentally. Moreover, it has been found that increasing the distance between wires and plates leads to reduce the corona discharge current, and the increase in wires spacing tends to increase the corona current. This last is due to the shielding effect exerted by each wire on the other.**

Keywords – Electrostatic Precipitator; Corona Discharge; Space Charge; Ionized Fields; Current Density;

I. INTRODUCTION

CORONA discharge is used in various ways in an increasing number of engineering applications with different geometrical electrode arrangements. One of the configuration mostly used for theoretical and experimental studies is the Multi-wires-to-plates geometry, largely used in the design of the electrostatic precipitator (ESP). An ESP is a cleaner device that removes particles from a flowing gas using electrostatic forces, and consists of discharge electrode and collecting plan. Corona discharge occurs when a high voltage is applied between a high tip curvature corona wire and a low tip curvature collecting electrode. Consequently, the inter-electrode space is divided into two different regions; a high-field ionization region surrounded the active electrode where free charges are produced, and a low-field drift region occupying the remainder of the interval [1]. The ions created in the ionization region drift to the passive collector electrode and forms a space charge. When gas (such as air) that contains an aerosol flows between the corona wire and the collecting electrode, the pollutants in the gas are electrostatically charged by the ions. The passive collector electrode attracts the charged particles, which are then neutralized and removed [2].

II. EXPERIMENTAL SET-UP

The multi wires-to-plates type ESP consists of a set of conducting wires (1) carried at DC high voltage (V_a) and rising halfway between two parallel collecting plates (2 and 3), which are separated by a width of $2\times D_P$ (Fig. 1). The wires of radius R_w are set at equidistant intervals d_w by two insulating supports (4). The lower plate electrode is composed of a measuring plane 2a surrounded by two grounded guard plates 2b. The three plates are separated by very small air gaps to ensure the continuity of the electric field and based on a set of supports (5). A current collector (S), incorporated in the centre of the measuring plane 2a, is connected to a current measuring device (7) via a coaxial cable (6). The upper plane electrode (3) is grounded and rests on the two wires insulating supports (4).

III. NUMERICAL PROCEDURE

The second part of our work is devoted to modelling and simulation of the corona discharge in the studied configuration. In the present study, the corona electrodes are supposed to be of infinite length (in z-direction) and consequently the geometry is reduced to a two-dimensional system, Fig. 2.

The DC corona electric field-space charge problem can be described in the air by a set of the following equations [3]:

$$\Delta\phi = -\rho/\varepsilon_0 \text{ (The Poisson's equation)} \quad (1)$$

$$\vec{J} = \mu\rho\vec{E} \quad \text{(Equation for current density)} \quad (2)$$

$$\nabla \cdot \vec{J} = 0 \quad \text{(Current continuity condition)} \quad (3)$$

$$\vec{E} = -\nabla\phi \quad \text{(Equation relating the potential to the field)} \quad (4)$$

Where ϕ [V] is the electric potential, E [V/m] is the electric field, J [A/m^2] is the current density, ρ [C/m^3] is the ionic charge density, ε_0 [F/m] is the air permittivity and μ [m^2/V.s] is the ionic mobility.

These corona governing equations clearly show the physical interactions between the electric field and the space charge density.

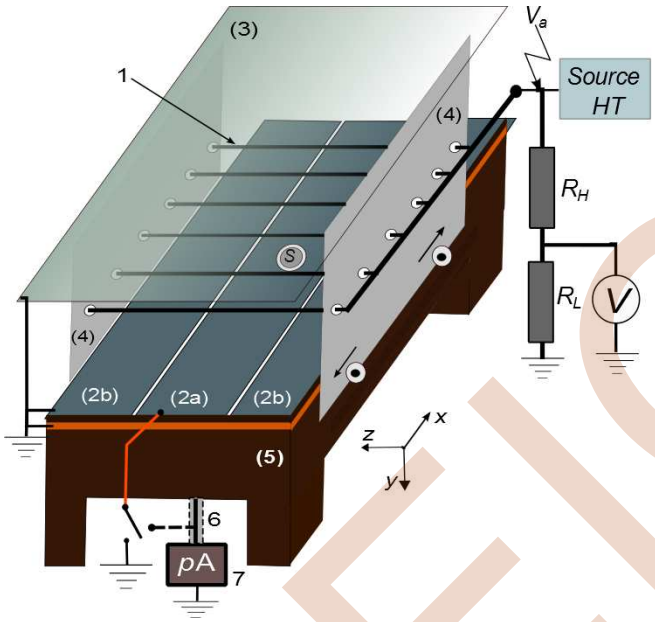

Figure 1. General view of the experimental arrangement

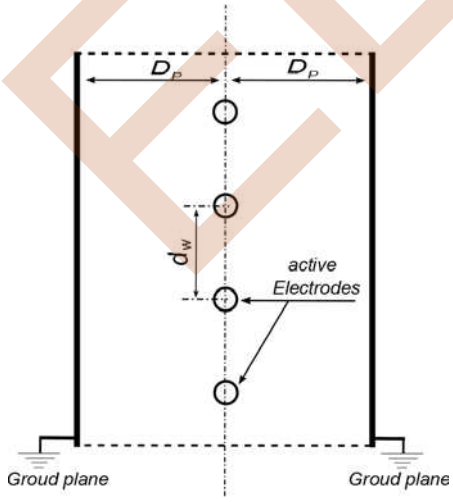

Figure 2. 2D cross-sectional geometry of the Multi-wire ESP

The process of numerical calculations is therefore iterative. Indeed, after straightforward substitutions the above set (1)-(4) is reduced to two coupled partial differential equations (PDE):

$$\nabla^2\phi = -\rho/\varepsilon_0 \quad (5)$$

$$\vec{E}\nabla\rho = -\rho^2/\varepsilon_0 \quad (6)$$

It should be noted that, despite advances in numerical and computational techniques, obtaining accurate solutions of the corona governing equations is very difficult because of the distortion of the electric field due to the presence of the space charge. Several numerical techniques have therefore been employed to solve the problem using the charge simulation method [4], the finite difference method [5] and the finite element method [6-7], often combined with the method of characteristics [8] to evaluate the space charge density.

All these methods are based on some simplifying assumptions [4–11], where the most common ones are:

- The thickness of the ionisation layer around the ionizing wire is so small as to be neglected with respect to the inter electrode spacing.
- The average mobility μ of ions is often assumed constant during the transit time from the ionisation region to the collecting electrode. It is also considered independent of electric field intensity.
- Diffusion of ions D_i is neglected.
- The surface field of the wire remains constant at the onset values E_p, given by the well-known empirical Peek's law (Kaptzov's assumption).

A two-dimensional axisymmetric simulation of the coupled space charge-electric field problem is performed using COMSOL Multiphysics software. Two application modes are used to solve the corona governing equations. The Poisson's equation (5) is solved using PDE (General Form) mode to find the electric potential distribution, and the current continuity equation (6) is solved using Convection and Diffusion mode [12].

Moreover, the solution of equations (5) and (6) subject to the following boundary conditions;

– The potential of the ionizing wires is equal to the applied voltage: $\phi_w = V_a$,
– The potential of the plates is set to zero (ground): $\phi_p = 0$,
– Zero diffusive flux condition, $\partial\rho/\partial n = 0$, is imposed on all boundaries except at wire' surfaces where the charge density is fixed to an initial value ρ_0, which is adjusted iteratively until an auxiliary condition is satisfied [12]. This auxiliary condition requires that the electric field strength at the surface of each wire (E_w) agrees with the threshold field value E_p.

IV. Results and Discussion

The described method was tested through its application to a 25 kV ESP laboratory model of three and four active wires of radius R_W=0.2 mm. The effect of two parameters have been studied; the wire-to-wire spacing (d_w) and the plate-to-plate distance ($2\times D_p$). The measured data obtained from the experiment has been therefore used to validate the Comsol numerical model.

Fig. 3 shows the measured and calculated current density distributions $J_p(x)$ along the collecting plane of the 04 wires-to-plates ESP (4WP-ESP) under two applied voltage levels; 20 and 15 kV. It is clear from the figure that the plane current density distributions predicted by the Comsol program agree well with the measured curves.

The drawn curve shows peak values of plane current density at the foot of each active wire and minimum ones measured at positions located in the front of the midpoints of adjacent wires. This is due, in fact, to the smallest distance between the plates and the discharge wires, where space charge is more concentrated. Moreover, it is visible from figure 3 that the plane current density measured under the two outer discharge wires (wires #1 and #4) exhibit the highest values compared to those measured under inner wires (#2, #3). This is due to the shielding effect mutually exerted between wires resulting in the reduction of the emitting discharge current, except for the two wires at the ends of the sheet, which are influenced by only a neighboring wire [11-13].

To study the effect of variation of inter electrode distances (d_w and D_p) on the shielding effect, we propose first to define the shielding ratio R_{SH} as the relative difference between the peak current densities obtained at the plane under an outer wire and a neighboring inner wire.

For the configuration of 4 wires-to-plates ESP of Fig. 3:

$$R_{SH} = \frac{J_{p(w_1)} - J_{p(w_2)}}{J_{p(w_1)}} \quad (7)$$

Where:

- $J_{p(w1)}$ is the plane current density measured (or calculated) under the wire number 1.
- $J_{p(w2)}$ is the plane current density measured (or calculated) under the wire number 2.

Fig. 4 shows the variation of total corona current measured and calculated along the collecting plane as a function of wires spacing d_w. By increasing the wires spacing, the total current increases and then tends to become constant for the high values of d_w. As explained previously, this is due to the shielding effect arising between adjacent discharge wires. As a result, currents deriving from opposite sides of two adjacent wires are reduced with decreasing the spacing d_w, involving the reduction of the total collected current [11-13]. On the other hand, the spacing of the wires contributes to the reduction of this effect and to the increase of the discharge current. When wires are widely separated (d_w>200mm), they behave very nearly as independent conductors and the discharge current stops growing.

The variation of calculated corona current along the collecting plane as a function of wires-to-plates distance D_p is shown in Fig. 5. By increasing the distance between wires and plates, the total current decreases considerably. Obviously, this is due to the fact that, in any corona discharge configuration, increasing the distance between the active and passive electrodes yields to increasing the corona discharge threshold voltage [6,10], and consequently the decrease of the corona current.

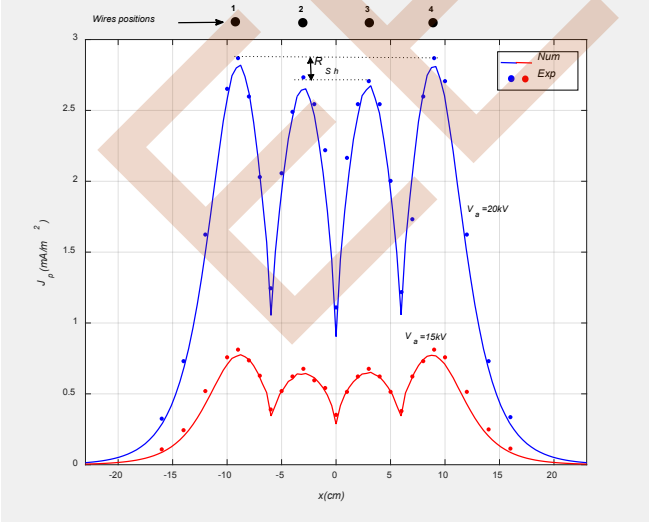

Figure 3. Profile of the plane current density distribution (4WP-ESP, d_w=60mm, D_p=50mm)

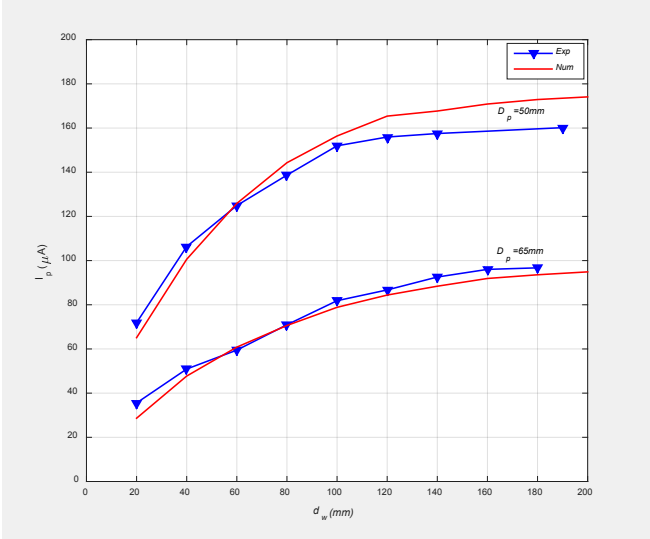

Figure 4. Effect of variation of the wires spacing d_w on the total corona discharge current (3WP-ESP, V_a= 25kV)

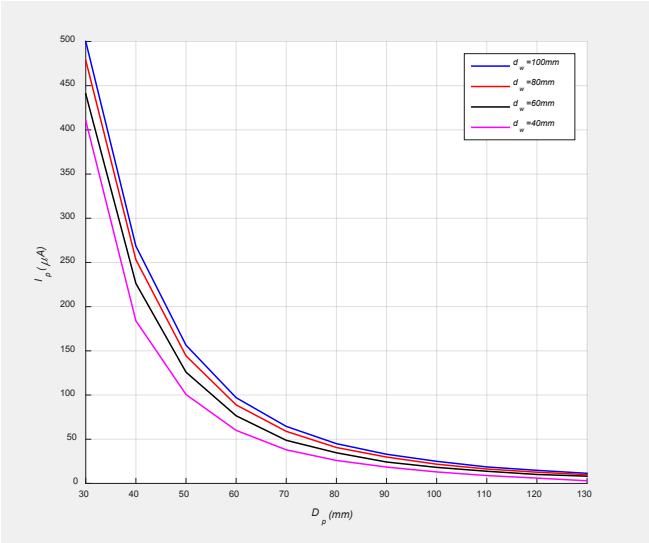

Figure 5. Effect of variation of wires-to-plates spacing D_p on the corona discharge current (3WP-ESP, V_a= 25kV)

The shielding effect is also visible on the space charge density distribution around the discharge wires. From Fig. 6, we can see that the space charge density due to the corona discharge of the central active electrode has been significantly compressed. By increasing the wires spacing d_w from 60 mm (Fig. 6-a) to 80 mm (Fig. 6-b), the shielding effect decreases. However, by increasing the distance plates-wires D_p from 50 mm (Fig. 6-b) to 100 mm (Fig. 6-c), the effect of shielding is accentuated.

To improve the efficiency of the precipitator, it is then necessary to optimize the inter electrode spacing yielding the lowest shielding rate. For this, we simulated with Comsol Multiphysics the variation of the two parameters (D_p and d_w) for a 03 wires-to-plates ESP (3WP-ESP).

Fig. 7 shows the effect of variation of the two parameters upon the shielding ratio calculated by the expression of equation 7. The obtained curves confirm the results of figures 4-6. The shielding ratio varies according to the wires-plan distance, on the other hand, the shielding effect is attenuated when the wires spacing increases.

Furthermore, from the figure, it can be seen that the minimum shielding ratio, for a given wires spacing d_w and a wires-plate distance D_p, is obtained when the two parameters are equal to each other.

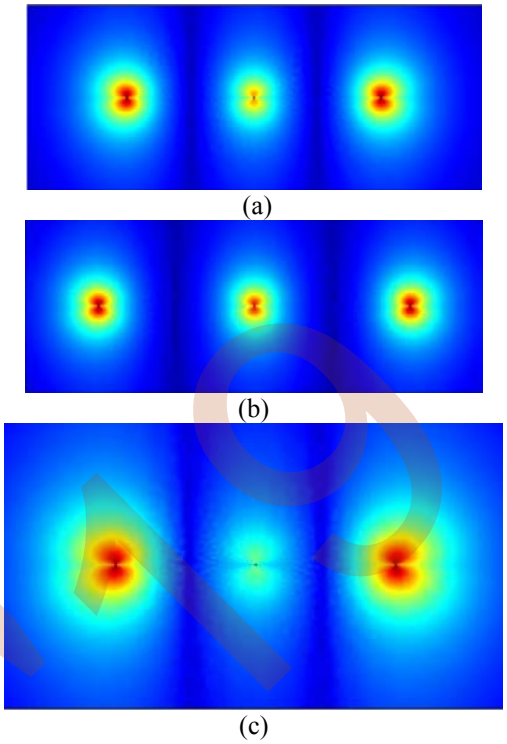

Figure 6. 2D Space charge density distribution in the computed domain (3WP-ESP, V_a= 25kV)
(a) D_p =50mm, d_w =60mm
(b) D_p =50mm, d_w =80mm
(c) D_p =100mm, d_w =80mm

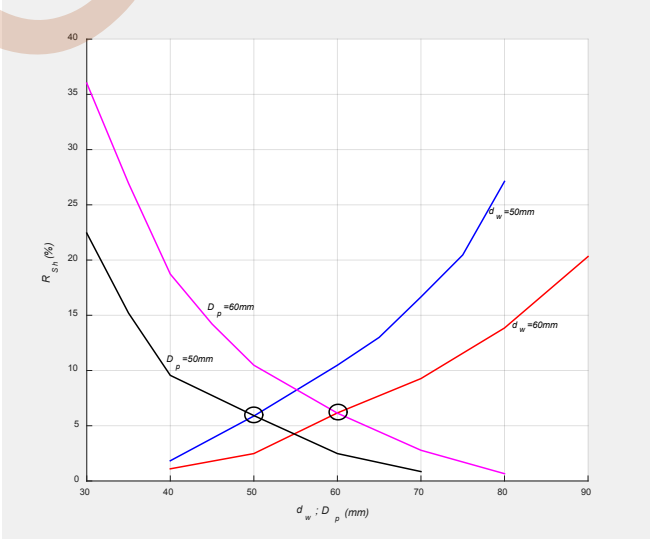

Figure 7. Shielding rate variation according to wires spacing d_w and wires-to-plates distnace D_w (3WP-ESP, V_a= 25kV).

V. CONCLUSIONS

This paper describes the results of optimization of the inter electrodes spacing to improve the efficiency of a multi-wires-to-plates type electrostatic precipitator. The experimental results obtained from a laboratory-scale model of precipitator were used to validate the numerical simulation performed using Comsol Multiphysics software.

Results show good agreement between numerical and experimental values. It has been found that the wires spacing and wires-to-plate distance have an appreciable effect on the degree of shielding. The increasing in the wires-to-plane spacing, as well as the reduction in the wires spacing, leads to decrease the total collected corona current. The study showed that the degree of shielding is minimized for equal values of the two distances.

REFERENCES

[1] Y. Zebboudj, G. Hartmann, "Current and electric field measurements in coaxial system during the positive DC corona in humid air," EPJ-Applied Physics 7, 1999, 167–176.

[2] M. Abdel-Salam, M. Nakano, A. Mizuno, "Corona-induced pressures, potentials, fields and currents in electrostatic precipitator configurations". J. Phys. D: Appl. Phys. 40, pp. 1919–1926, 2007.

[3] J. Lobry, "A new numerical scheme for the simulation of corona fields". IEEE Trans. Magn. , vol. 50, No. 2, 7013304, 2014.

[4] A.A. Elmoursi, G.S. Peter Castle: "The analysis of corona quenching in cylindrical precipitators using charge simulation", IEEE Trans. Ind. Appl. 22, 80-85, 1986.

[5] C. Budd: "Coronas and the space charge problem", Euro. J. Appl. Math. 2, 43-81, 1991.

[6] Z. M. Al-Hamouz, A. El-Hamouz, N. Abuzaid, "Simulation and experimental studies of corona power loss in a dust loaded wire-duct electrostatic precipitator". Advanced Powder Technology 22, pp. 706-714, 2011.

[7] S. Cristina, G. Dineli, M. Feliziani: "Numerical computation of corona space charge and V-I characteristic in DC electrostatic precipitators", IEEE Trans. Ind. Appl. 27, 147-153, 1991.

[8] J. Anagnostopoulos, G. Bergeles: "Corona discharge simulation in wire-duct electrostatic precipitator", Journal of Electrostatics 54, 129–147, 2002.

[9] A. Kasdi, Y. Zebboudj, H. Yala, "Simulation of Corona Discharge in DC Electrostatic Precipitator", J. Electrical Systems 11-4, pp.384-396, 2015.

[10] M. Abdel-Salam, A. Eid, "Finite Element Simulation of Corona in Wire-Duct Precipitators". IEEE 37th IAS Annual Meeting Conf., vol.2, pp. 1383-1389, 2002.

[11] U. Khaled, A.Z. Eldein, "Experimental study of V-I characteristics of wire-plate electrostatic precipitators under clean air conditions". J. Electrost. 71, pp. 228-234, 2013.

[12] A. Kasdi, "Computation and measurement of corona current density and V-I characteristics in wires-to-plates electrostatic precipitator". J. Electrost. 81, pp. 1-8, 2016.

[13] S. Arif, D.J. Branken, R.C. Everson, H.W.J.P. Neomagus, A. Arif, "The influence of design parameters on the occurrence of shielding in multi-electrode ESPs and its effect on performance", Journal of Electrostatics 93, pp. 17–30, 2018.

FTIR and DSC Study of XLPE Exposed to Thermal and Electrical Constraints

Abdallah Hedir, Mustapaha Moudoud, Ferhat Slimani
Laboratoire des Technologies Avancées en Génie Electrique (LATAGE)
Université Mouloud MAMMERI
Tizi Ouzou, Algeria
abdallahhedir@yahoo.fr

Ungarala Muhan Rao, Issouf Fofana
Canada Research Chair, tier 2, on Insulating Liquids and Mixed Dielectrics for Electrotechnology, University of Quebec in Chicoutimi, 555, Boulevard de l'Université, G7H 2B1, Chicoutimi, Qc, Canada
mohan13.nith@gmail.com
Issouf_fofana@uqac.ca

***Abstract* – Medium and high voltage power cables are presently subjected to thermal and electrical constraints, leading to the acceleration of their failure rate. In this paper, the aging of Cross-linked Polyethylene (XLPE) power cables insulating material when exposed to service conditions (temperature and electric field), was studied. The induced degradation was determined by evaluating the physico-chemical changes in XLPE. For this purpose, FTIR and DSC techniques were monitored. Obtained results show that both temperature and electric field induce structural changes in the insulating material.**

***Keywords:* -** Cables, failure, aging, Crosslinked Polyethylene, Insulating Material.

I. INTRODUCTION

Cross-linked polyethylene (XLPE) cable is widely used in medium and high voltage power cables because of its low density, simple manufacturing requirements, easy installation, good electrical specifications, heat resistance, and convenient maintenance [1]. Like all other insulating materials, XLPE properties deteriorate over the time when it is subjected to service conditions [2]. The stressing factors lead to the insulation properties degradation and a significant reduction in the effective operation life of the cables [3],[4] Temperature and electric field are assumed as the most dangerous constraints.

Under temperature stress and over a period of time, chemical composition and physical morphology, of XLPE may change [5]. The induced structural changes will likely induce the insulating material aging [6], which may strongly reduce the properties of XLPE and lead to the insulation degradation.

According to the literature, electrical stress is one of the most destructive constraints which affect the XLPE insulating material performances. Stancu *et al.* [7] have shown that electrical stress along with the presence of water leads to the appearance and growth of water trees. Wang *et al.* [8] have noticed that under a high-voltage DC field, space charges can accumulate in polyethylene, and cause partial discharge.

The literature includes research about the impact of electrical aging or thermal aging on the electrical and mechanical properties of XLPE, but few works are devoted to study the effect of the aforementioned constraints on the structural characteristics of the insulating material.

Our present study is devoted to analyze the impact of thermal and electrical constraints on the physico-chemical behavior of XLPE power cable insulation. For this purpose, two techniques were monitored namely ATR-FTIR and DSC. Obtained results show that both temperature and electric field induce structural changes in XLPE.

This paper is organized as follows: Section II presents the experimental setup. In Section III, the obtained experimental results are illustrated and discussed. Section IV concludes this paper.

II. EXPERIMENTAL SETUP

A. Material

Square plates of 130 mm x 130 mm with 2±0.2 mm have been obtained from granules containing dicumyl peroxide with concentration of 2% to generate cross-links. The granules were preheated for 5 min to a temperature of 130 °C, at different pressures and for different time durations. After that they were crosslinked at a high pressure of 300 bars and temperature of 180 °C. The preheating/crosslinking process was followed by cooling at 45°C.

B. Thermal Aging

Aging under thermal constraint experiments were carried out in a thermo-ventilated oven that could maintain the average ±2 °C. The temperature of aging was 100°C. The total duration of aging was 2000 hours.

C. Electrical Aging

The electrical aging was carried out by placing XLPE samples in sandwich between two plane electrodes (with Rogowski profile) of 50 mm diameter, under AC electrical field of 5 kV/mm. The upper electrode is connected to the high voltage and the lower one to the ground.

The applied voltage is delivered by a test transformer whose characteristics are: U=100 kV, f=50 Hz, P=10 kVA. The applied voltage is controlled by means of an autotransformer.

D. FTIR Spectroscopy

FTIR analysis was carried out using a Shimadzu FTIR-8400s spectrometer. Unaged and aged samples were performed at 50 scans in the range of 650-4000 cm^{-1} with a resolution of 4 cm^{-1}.

E. DSC Analysis

DSC studies were carried out using DSC 204-F1 Phoenix, Netzsch Co with computer data system under a constant nitrogen gas flow. The measurement was performed by heating and cooling the samples from 20 to 160 °C in order to follow the changes in the melting temperature, the crystallization temperature, the crystallinity, the enthalpy of fusion and the enthalpy of crystallization.

III. Results and Discussion

A. Thermal aging

a) FTIR analysis

Virgin XLPE has characteristic bands corresponding to the wavelengths 720 cm^{-1}, 1078 cm^{-1}, 1377 cm^{-1}, 1471 cm^{-1}, 1740 cm^{-1}, 2150 cm^{-1}, 2856 cm^{-1}, 2937 cm^{-1}, 3300 cm^{-1}, and 3500 cm^{-1}.

As shown in Figure.1, the main changes after aging at 100 ° C are:

a) Decrease in the absorption intensity of the bands characterizing the antioxidant (1078 cm^{-1}) which means that the antioxidant is consumed with the thermo-oxidation extent.
b) Appearance of absorption peaks at 1120 cm^{-1} and 1170 cm^{-1} attributed to silicon monoxide Si-O [9].
c) Manifestation of a peak at 1316 cm^{-1}, assigned to acetophenone absorption.
d) Formation of carboxyl groups at 1718 cm^{-1} due to the thermo-oxidation phenomenon [10].
e) Manifestation of a peak at 2361 cm^{-1} which can describe the appearance of CO_2.

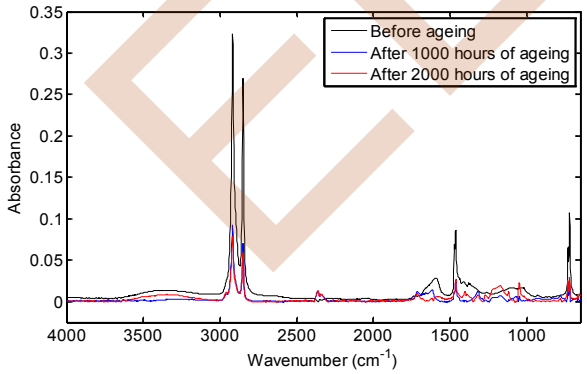

Figure.1. ATR-FTIR analysis of XLPE samples at different thermal aging time

b) DSC analysis

As shown in Figure.2 corresponding to the DSC thermograms of the studied samples, the shape of the peaks indicates that the material is semi-crystalline [11], [12]. The DSC analysis shows, from a general way that the main endothermic peak corresponding to the melting of the crystalline part of the XLPE, is sharp after aging. This shape confirms the existence of crystalline chains of uniform sizes and well aligned. This phenomenon results in an increase in the crystallinity rate and a slight shift in peak of the crystalline melting temperature towards higher temperatures [13]. Thermograms of the heating run show that the melting temperature value T_m of the unaged sample is 107.1 °C. For aged samples, T_m increases with aging time and reaches the value of 114.5°C. From the cooling thermograms, it can be seen that the crystallization temperature T_c decreases from 89.5 °C (unaged sample) and reaches the value of 87.03°C after aging. The decrease in crystallization temperature with aging time suggests that material has undergone severe degradation. Changes in melting and crystallization temperatures are presented in Table.1.

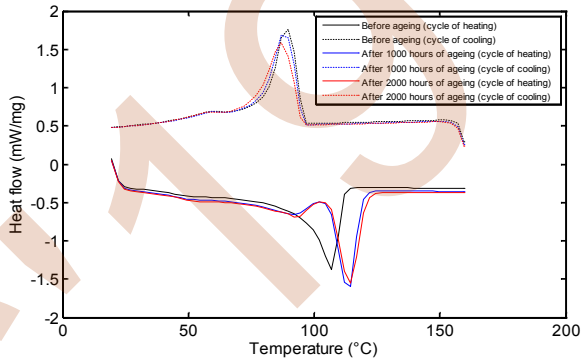

Figure. 2. DSC heating and cooling thermograms of unaged and thermally aged XLPE samples.

TABLE.1. Changes in melting and crystallization temperatures with thermal aging

Sample	T_m(°C)	T_c(°C)
Before ageing	107.1	89.55
After 1000 hours of ageing	114.5	87.03
After 2000 hours of ageing	114.5	87.03

B. Electrical aging

a) FTIR analysis

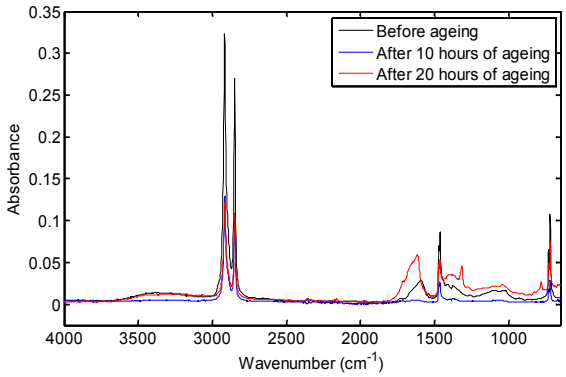

Figure.3. ATR-FTIR analysis of XLPE samples at different electrical aging time

After aging, the changes to note are as follows:

a) Appearance of an absorption band at 3500 cm^{-1} which corresponds to the amorphous phase absorption.

b) Increase in the absorbance in the region 800 cm^{-1}-1100 cm^{-1} attributed to the unsaturated C = C groups.
c) Manifestation of a peak at 2361 cm^{-1} that can describe CO_2 appearance.
d) Absorption of acetophenone supported by the appearance of a peak at 1316 cm^{-1}.

b) DSC analysis

As can be seen in DSC curves (Figure.4), the electrical aging appears did not affect the melting temperature of XLPE. Nevertheless, it was observed that this constraint causes a slight decrease in intensity and broadening of the endothermic peak. This broadening indicates the presence of smaller chains segments resultant from the bond scission of XLPE associated to the oxidative process [14]. From Table.2 it can be seen that the melting temperature T_m has increased from 107.1 °C to 109.5 °C; while the crystallization temperature T_c decreased from 89.5 °C to 87.03 °C.

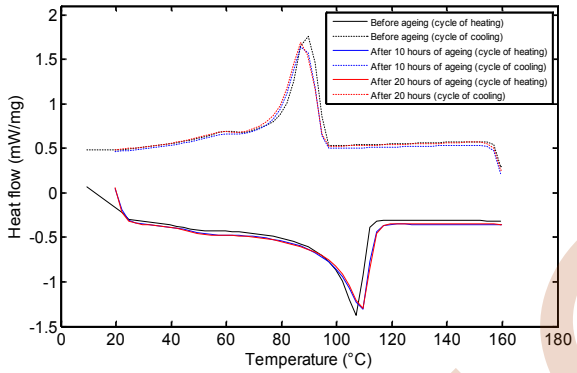

Figure 4. DSC heating and cooling thermograms of unaged and electrically aged XLPE samples.

TABLE.2. Changes in melting and crystallization temperatures with electrical aging

Sample	T_m(°C)	T_c(°C)
Before ageing	107.1	89.5
After 10 hours of ageing	109.5	87.03
After 20 hours of ageing	109.5	87.03

IV. CONCLUSION

The work presented in this paper concerns with the impact of thermal and electrical aging on the structural properties of XLPE used as high voltage power cable insulation. Based on the information obtained from the ATR-FTIR and DSC techniques, the results can be summarized as follows:

-Changes in the intensities of several peaks in ATR analysis are noticed. This behavior indicates that electrical and thermal aging reduce the cohesive forces between the chains.

-DSC analysis shows that electrical and thermal constraints induce slight changes in melting and crystallization temperatures. These changes indicate that XLPE undergo degradation.

REFERENCES

[1] D. He, J. Gu, W. Wang, S. Liu, S. Song and D. Yi "Research on mechanical and dielectric properties of XLPE cable under accelerated electrical-thermal aging, '', Polym. Adv. Technol. 2017, 28 1020–1029.

[2] G. Chen and C.H. Tham, "Electrical Treeing Characteristics in XLPE Power Cable Insulation in Frequency Range between 20 and 500 Hz", IEEE Trans. Dielectr. Electr. Insul., vol. 16, no. 1, pp. 179-188, February 2009.

[3] Ďurman, V.; Lelák, J. "Influence of Radiation on the Dielectric Properties of XLPE Based Insulation systeme, J. Electr. Eng. 2010, 61, 229.

[4] A. Hedir, M. Moudoud, O. Lamrous, S. Rondot, O. Jbara, Ph. Dony, ''Ultraviolet radiation aging impact on physicochemical properties of crosslinked polyethylene cable insulation'' Journal of applied polymer science, Vol. 137, No. 4, January 2020.

[5] L. Boukezzi, A. Boubakeur, ''Prediction of Mechanical Properties of XLPE Cable Insulation Under Thermal Aging: Neural Network Approach'', IEEE Transactions on Dielectrics and Electrical Insulation Vol. 20, No. 6; December 2013.

[6] A. Hedir, M. Moudoud, O. Jbara, S. Rondot and F. Slimani,''Degradation Mechanisms of Cross-linked Polyethylene Insulation by Thermal and Electrical Aging'' 11éme conférence de la Société Française d'Electrostatique, 29-31 Aout 2018, Grenoble, France

[7] C. Stancu, P. V. Notingher, F. Ciuprina, P. Notingher, S. Agnel, J. Castellon, A. Toureille, "Computation of the electric field in cable insulation in the presence of water trees and space charge", IEEE Trans. Ind. Appl., vol. 45, no. 1, pp. 30-43, 2009.

[8] Y. Wang, C. Wang, K. Xiao, "Investigation of the electrical properties of XLPE/SiC nanocomposites", Polym. Test., vol. 50, pp. 145-151, 2016.

[9] Z. Ma, X. Huang, J. Yang, P. Jiang, "Synergetic effects of Silane-grafting and Eva on water tree resistance of LDPE", Chin. J. Polym Sci., vol. 28, no. 1, pp. 1-11, 2010.

[10] A. Shimada, M. Sugimoto, H. Kudoh, K. Tamura, T. Segushi, "Degradation distribution in insulation materials of cables by accelerated thermal and radiation ageing", IEEE Trans. Dielectr. Electr. Insul., vol. 20, no. 6, pp. 2107-2116, December 2013..

[11] D. Bouguedad, A. Mekhaldi, O. Jbara, S. Rondot, A. Hadjadj, J. Douglade and Ph. Dony, "Physico-chemical study of thermally aged EPDM used in power cables insulation" IEEE Trans. Electr. Insul., vol. 22, no.6, pp. 3207-23215, 2015.

[12] Y.A. Bencherif, A. Mekhaldi, J. Lobry, M. Olivier, M. Poorteman, L. Bonnaud, Multiscale Analysis of the polymeric Insulators Degradation in Simulated Arid Environment Conditions: Cross-Correlation Assessment'' Journal of Electrical Engineering and Technology, June 2019.

[13] L. Boukezzi, A. Boubakeur, S. Rondot, O. Jbara, C. Laurent, ''Characterization Tests and analysis of cross-linked polyethylene (XLPE) used in high voltage cables insulation under thermal constraint'' 2014.

[14] A. M. Nóbrega, M. L. Barreira-Martinez, A. A. Alencar de Queiroz, "Analysis of the XLPE insulation of distribution covered conductors in Brazil", IEEE Trans. Dielectr. Electric. Insul., vol. 23, No. 3, pp 723-735, March 2014.

Effect of natural rain on the electrical performance of inclined silicone insulation putting out of voltage

Samia Slimani et Rabah Boudissa
Laboratory of Electrical Engineering, Department of Electrical Engineering
University A. Mira of Bejaia
Bejaia 06000, Algeria
samou8455@yahoo.com, raboudissa@yahoo.fr,

Stefan Kornhuber and Klaus Dieter Haim
Faculty of Electrical Engineering and Computer Science
University of Applied Sciences
Theodor-Koerner-Allee 16, 8800 Zittau, Germany
s.kornhuber@hszg.de,kd.haim@hszg.de,

***Abstract*— The present work deals with the study of the phenomenon of natural rain on the electrical performance of a hydrophobic silicone surface during three distinct periods of the fall of this one (January 2018 and January 2019) when the insulation is putting out of voltage. Our investigation focuses on the characterization of the amount of rainwater collected and the evolution of the volume of drops of impact water on a hydrophobic silicone insulating surface at an angle of inclination in comparaison to the horizontal varying between 0 ° to 90 ° and putting out of voltage. An experimental device was made to allow the variation of the angle of its inclination compared to the horizontal, the insulation is inclined at an arbitrary angle then it is exposed to rain immediately after the beginning of the latter. The tests were supported by a visualization using a camera. The measurement results during the three periods show that when the angle of inclination increases, the size of the drops of water decreases, however the volume of the residual drops reaches its maximum value when the insulation is in horizontal position and it can go up to 140 µl for a drop.**

I. INTRODUCTION

Insulators of power transmission lines play a very important role in the transport quality of the latter. The reliability of the service depends on the selection and sizing of these insulators which are based on a reliable design and take into account external environmental constraints and in particular those of pollution [1, 2]. In recent decades, the use of silicone insulation has been favored over ceramics in power lines [13, 14]. This is justified by their multiple advantages such as strong resistance to pollution, lightness and good hydrophobicity [1-8].

The most cited disadvantage of such isolations is the reduction or loss of hydrophobicity of their surface and their long-term deterioration, due to the partial electrical discharges generated by the voltage recovery of the surface of these insulations by drops of water, rain, condensation or fog [9-12]. Influence of various arrangements of these manually applied water drops on silicone insulations on horizontal position and under different voltage constraint on their electrical performance has been investigated several times [3-12].On the other hand, the effect of the various angles of inclination of the upper and lower surfaces of the fins and stems of several types of insulators made of ceramics covered with a polymer coating or polymer insulators under the action of water drops of Natural rain on their electrical performance in AC has not been sufficiently investigated by researchers [6].

These multiple reasons justify our interest, initially focused on the determination in a first place of the degree of wetting of the creepage of hydrophobic silicone insulation by natural rainwater depending on the angle of inclination of its surface in relation to the horizontal when the latter is putting out of voltage. Then the constellation of natural raindrops and their resulting volume will be reproduced in the laboratory.

II. TECHNIQUE OF MEASUREMENT AND MODEL EXPERIMENTAL

A. Measurement technique

The water volume measurements, of which the results will be presented later, were carried out on one semicircular silicone surface of diameter ϕ equal to 12 cm.

Eight samples were used for each inclination angle α (0 °, 30 °, 45 °, 60 ° and 90 °). The retained value of the volume of drops of water is the average of all those obtained on 4 sectors of 1 cm^2 of area distributed over the insulation in accordance with figue 1. The choice of the location of the four sectors has been made so that two sectors are placed on the creepage of the insulation from the center to the periphery of the half-fin. After every half an hour a sample of the silicone insulation is removed to make the necessary

measurements. So the first sample is exposed to rain for half an hour, the last one is removed after four hours of rain. The volume of all the drops of water recorded on each sector of the insulation is measured by means of a syringe graduated in microliter "Fig. 2 ",. The average volume is the average of the volumes of the drops of water found in the four sectors.

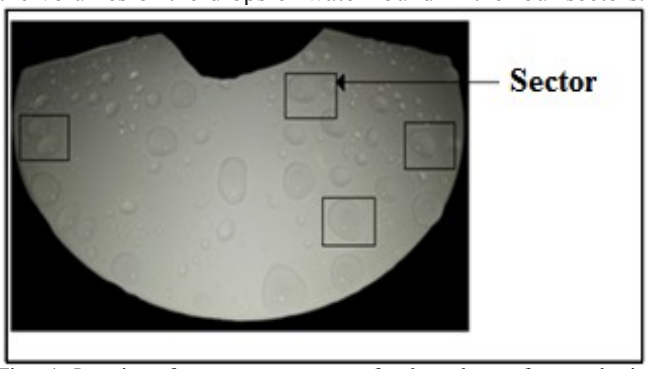

Fig. 1. Location of measurement sectors for the volume of natural rain drops

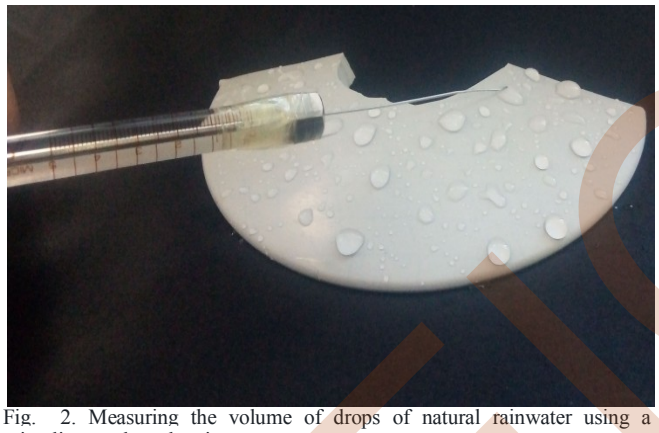

Fig. 2. Measuring the volume of drops of natural rainwater using a microliter graduated syringe

The interval of the break time between two successive tests on the same test specimen is greater than 12 hours. This was chosen to allow the sample to completely recover the hydrophobicity of its surface before the next test. To accelerate this return of hydrophobicity, all samples are deposited after their cleaning in a desiccator at the end of each measurement series.

B. Experimental model

The variation of the angle of inclination of the insulating surface with respect to the horizontal is obtained by means of a device illustrated in "Fig. 3",. A wooden support, 1m x 1m x 80cm in size, is painted with several layers of varnish so as not to absorb drops of rainwater landing on it after the tests carried out under it. Its upper base is equipped with 5 stems of 1 m and 80 cm on which are placed wooden plates of 13 cm x 13 cm spaced 15 cm. Above these are fixed the hydrophobic silicone samples.

Fixing any angle of inclination can be obtained by turning the rod to a position corresponding to the angle then aroused block at this selected inclination angle.

Fig. 3. Stem's device ensuring the variation of inclination of the angle α of the silicone insulation in compararaison to the horizontal

III. RESULT AND DISCUSSION

The evolution of the volume of drops of water per cm^2 on a hydrophobic silicone insulating surface, as a function of the time of exposure to natural rain for three distinct periods and different angles of inclination α (0°, 30°, 45°, 60°, 90°) is illustrated by the following figures: "Fig. 4", gives the shape of the maximum volume (V_{1max}, V_{2max} and V_{3max}) of the drops of water measured on sectors of 1 cm^2 as a function of the exposure time (t_e) to the natural rain respectively for the three periods (α = 0 °).

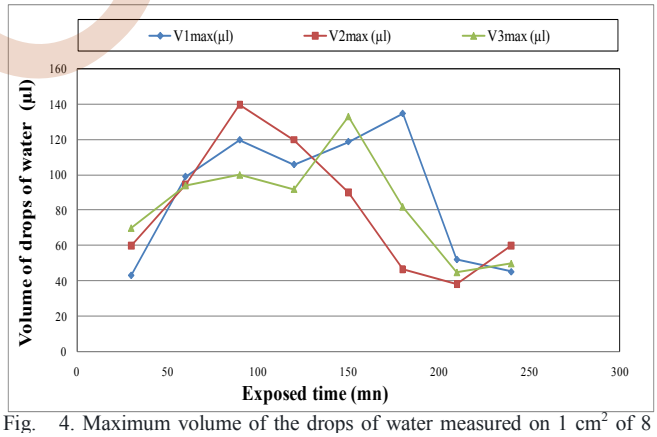

Fig. 4. Maximum volume of the drops of water measured on 1 cm^2 of 8 silicone samples according to their time of exposure to rain during three periods (α = 0 °)

It is to be noticed two peak values of the volumes of drops of water measured on samples 3 and 6, for the first period (120 µl and 135 µl), 3 and 5 for the third (100 µl and 133 µl) and only one peak value of the maximum volume of drops of water measured on the third sample during the second period (V_{2max} = 140µl), this explains the tendency of raindrops to gain volume by combining together to a limit value, then they fall under the effect of gravity forces when no voltage is applied to the insulation.

The curves shown in "Fig. 4", make it possible to compare the maximum volumes of the drops of water measured over the three periods, with the result that all the curves are practically identical with a slight difference due to the constant of the climatic conditions such as the wind and temperature during these 3 periods (board, 1).

Périods	10 /02/2018	11/01/2019	21/01/2019
Temperature (°C)	8 to 9	6 to 7	11
Wind (Km /h)	25	27	25
Humidity (%)	90 to 85	86 to 92	92 to 87
Total volume of rain (ml)	420	350	380

Fig. 5. Climatic conditions during periods the natural rain measurement

The pace of the average volumes (V_{avr}) of the drops of water measured during these three periods "Fig. 6", similar to that found in "Fig. 4", except that the volume of drops of water measured is smaller. The ascents and descents of the volumes are explained by the nature of the rain or by its intensity. For example, during the first period, the cessation of the rain from the 180th to the 210th minute results in a sharp drop in the maximum and average volumes of the drops of water ("Fig.4", and "Fig.6",).

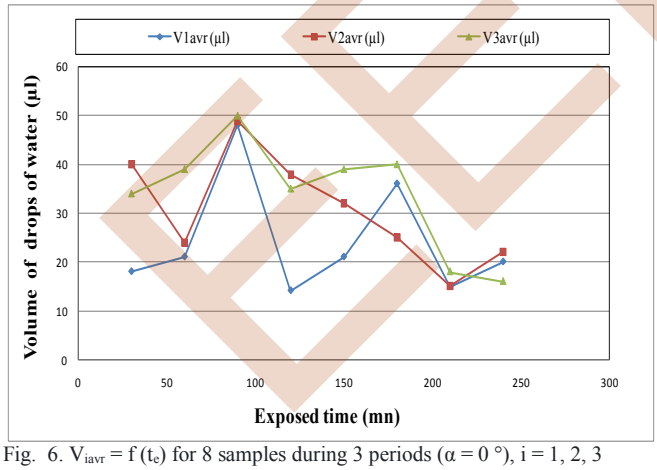

Fig. 6. $V_{iavr} = f(t_e)$ for 8 samples during 3 periods ($\alpha = 0$ °), i = 1, 2, 3

As a result in summary, the maximum volume of drops of water that can be collected on a hydrophobic silicone surface in a horizontal position varies between 133 µl and 140 µl, while the minimum volume of drops of water is of the order 0.1µl to 0.2µl "Fig. 7",.

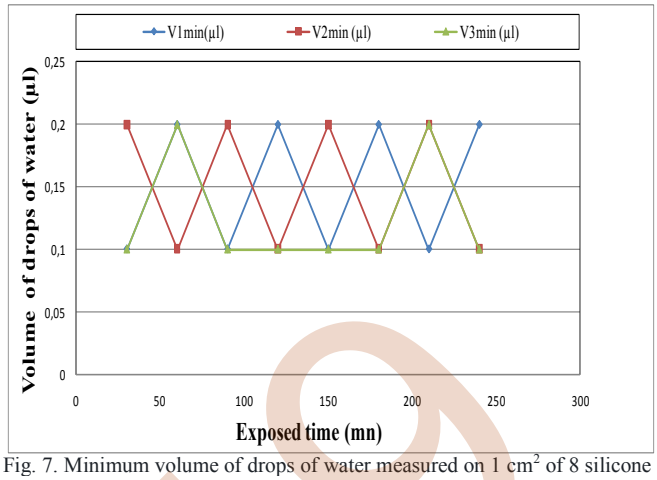

Fig. 7. Minimum volume of drops of water measured on 1 cm^2 of 8 silicone samples according to their time of exposure to rain during three periods ($\alpha = 0$ °)

Figures 8 and 9 show the pace of the maximum and average volume of the drops of water measured on the silicone samples as a function of their time of exposure to rain during the three periods for an angle of inclination $\alpha = 30$ °. It emerges that the quantity of water collected by sectors increases up to $t_e = 120$ nm of exposure to reach a maximum volume corresponding to the peaks illustrated by these figures.

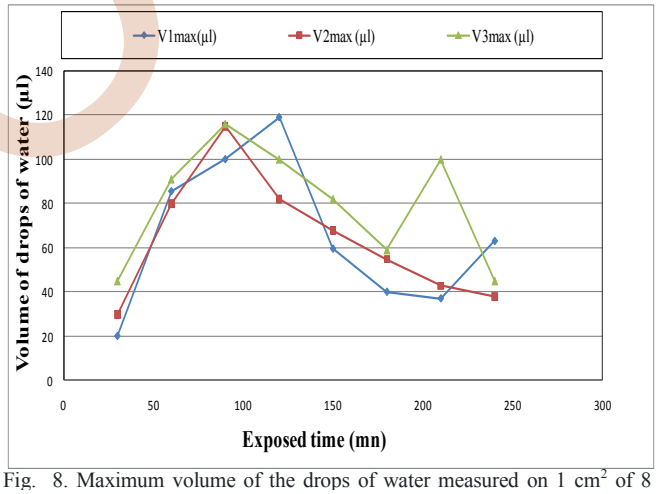

Fig. 8. Maximum volume of the drops of water measured on 1 cm^2 of 8 silicone samples according to their time of exposure to rain during three periods ($\alpha = 30$ °)

This is due to intense rain during this period, the largest recorded volume is 119 µl. From the 120th minute, a rain stop is recorded leaving behind fine droplets. Which explains the decrease in volumes during this trial periode. The volumes of the drops as a function of the exposure time leaves to say that even after the rain stops the drops do not fall all, but a part evaporates according to the time and the temperature of the material and another part of drops falls under the effect of the wind or their weight as a function of the angle of inclination of the hydrophobic insulating surface.

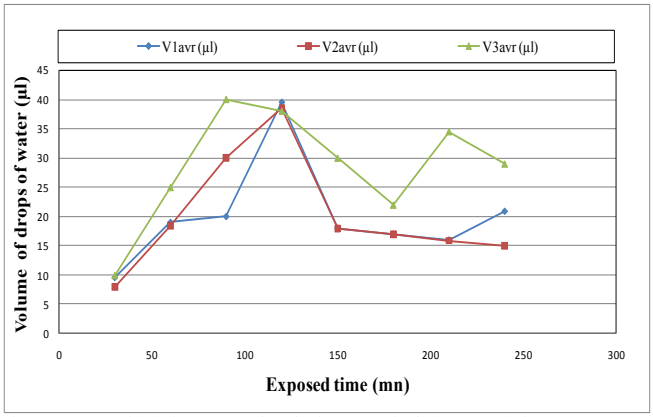

Fig. 9. $V_{iavr} = f(t_e)$ for 8 samples during 3 periods (α =30 °), i = 1, 2, 3

From the 180th and the 210th minute of exposure, it is to note an increase of the volumes of drops of water and this is due to the return of the rain during respectively the third and the first period. The minimum volume of drops of water is of the order of 0.1µl to 0.2µl whatever the period of exposure time considered "Fig. 10",.

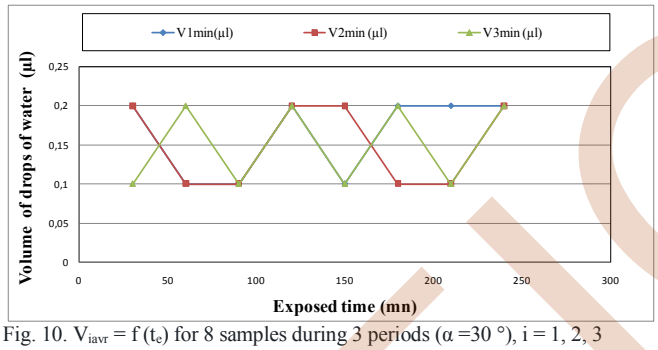

Fig. 10. $V_{iavr} = f(t_e)$ for 8 samples during 3 periods (α =30 °), i = 1, 2, 3

Figures 11, 12, 13, 14, 15 and 16 for α = 45 ° and α = 60 ° are similar to those found when the insulating surfaces are inclined compared to the horizontal of α = 0 ° and α = 30 °. The slight difference is recorded in the volume values of the drops of water (V_{max} = 78µl, V_{avr} = 30 µl for α = 45 °) and (V_{max} = 40µl, V_{avr} = 20µl for α = 60 °). The minimum volume of drops of water is always of the order of 0.1 to 0.2 µl.

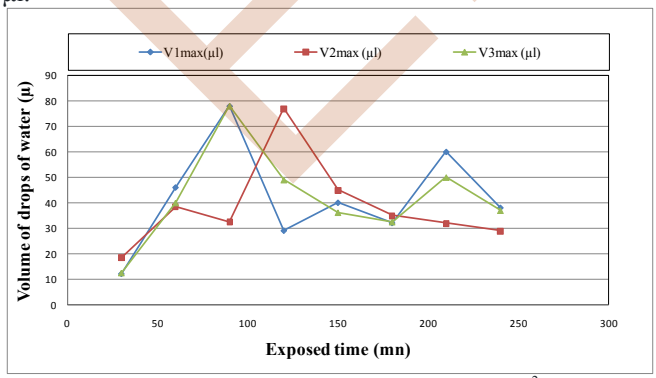

Fig. 11. Maximum volume of water drops measured on 1 cm^2 of 8 silicone samples according to their time of exposure to rain during three periods (α = 45 °)

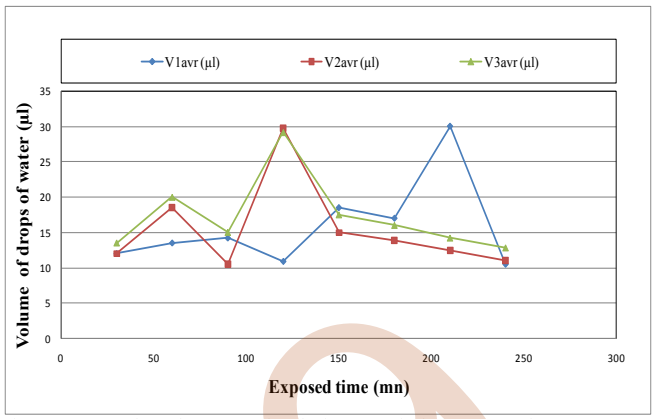

Fig. 12.$V_{iavr} = f(t_e)$ for 8 samples during 3 periods (α =45 °), i = 1, 2, 3

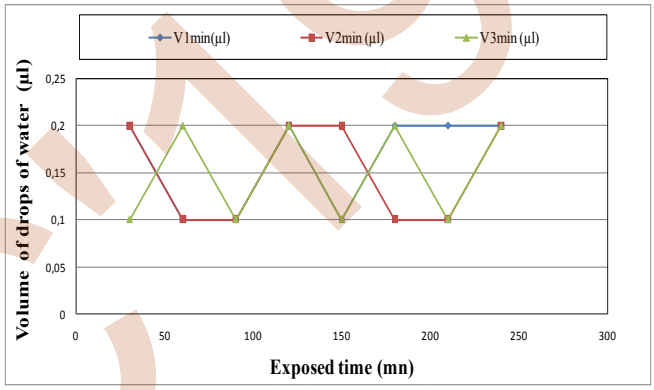

Fig. 13. $V_{imin} = f(t_e)$ for 8 samples during 3 periods (α =45 °), i = 1, 2, 3

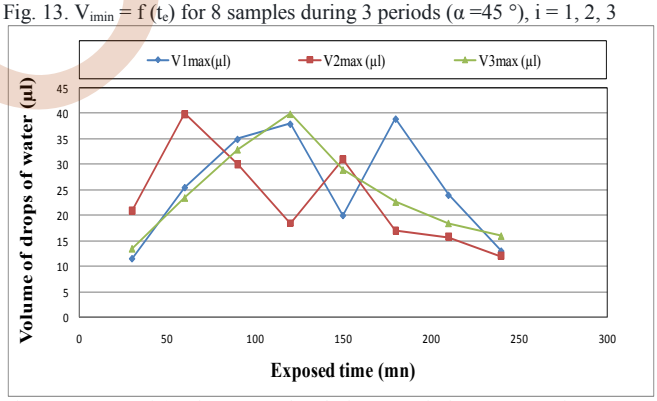

Fig. 14. $V_{imax} = f(t_e)$ for 8 samples during 3 periods (α =60 °), i = 1, 2, 3

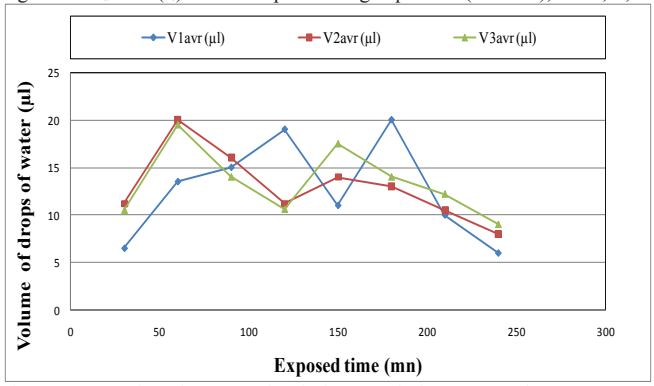

Fig. 15. $V_{iavr} = f(t_e)$ for 8 samples during 3 periods (α =60 °), i = 1, 2, 3

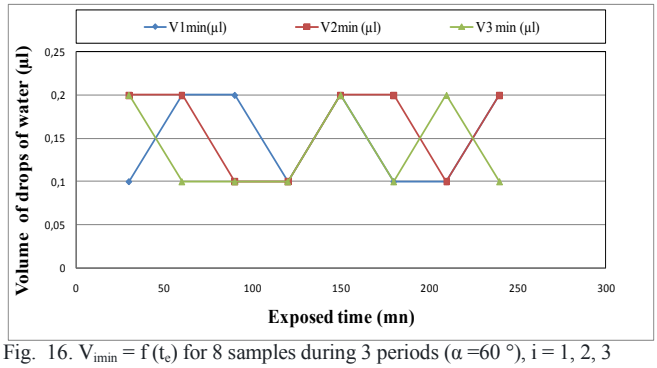

Fig. 16. $V_{imin} = f(t_e)$ for 8 samples during 3 periods (α =60 °), i = 1, 2, 3

Figures 17, 18 and 19 show the curves of the maximum, average and minimum volumes of drops of water on silicone insulating surfaces inclined at 90 ° to the horizontal, the rain during the first period was unstable or in other words the existence of these vertices separated by minimums results in the fall of several successive rains which explains the growth and the sudden decrease of the volume of the drops of water.

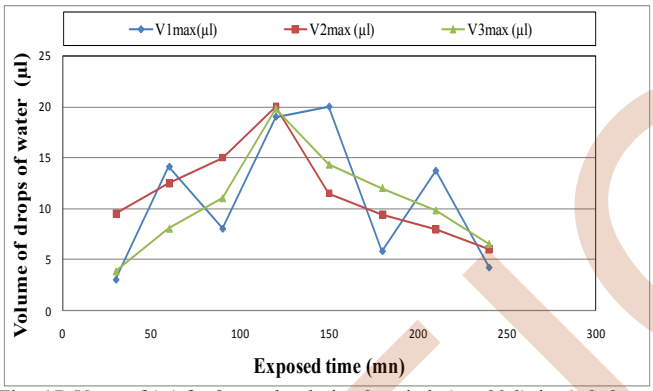

Fig. 17. $V_{imax} = f(te)$ for 8 samples during 3 periods (α = 90 °), i = 1, 2, 3

The presence of a single peak during the second and third periods corresponds to the fall of a single natural rain. It should also be noted that the maximum volume of drops of water retained by the insulating surface does not exceed 20µl from one rain to another during the same period and from one measurement period to another. Beyond this volume drops of water fall according to their weight. The minimum volume is 0.1 to 0.2 µl "Fig. 19",.

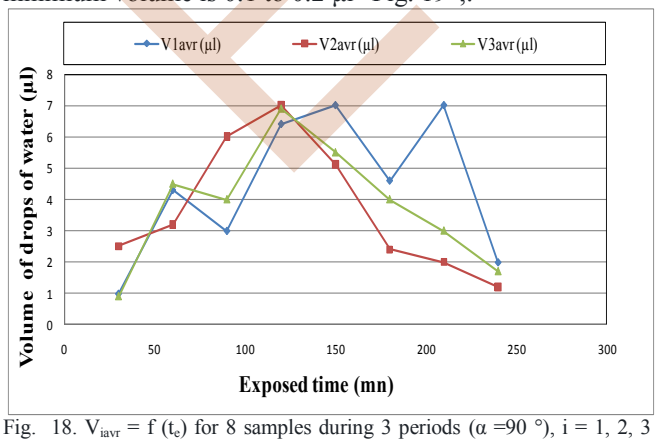

Fig. 18. $V_{iavr} = f(t_e)$ for 8 samples during 3 periods (α =90 °), i = 1, 2, 3

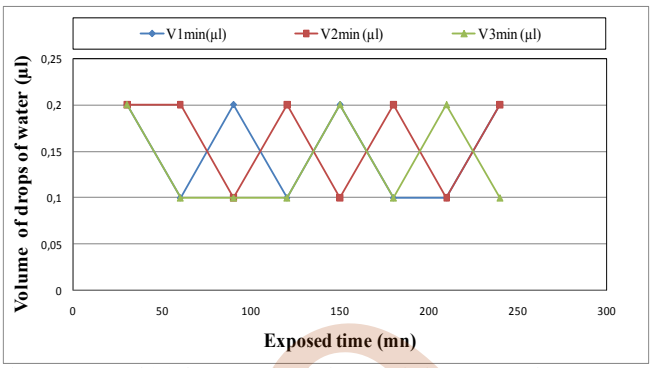

Fig. 19. $V_{imin} = f(te)$ for 8 samples during 3 periods (α = 90 °), i = 1, 2, 3

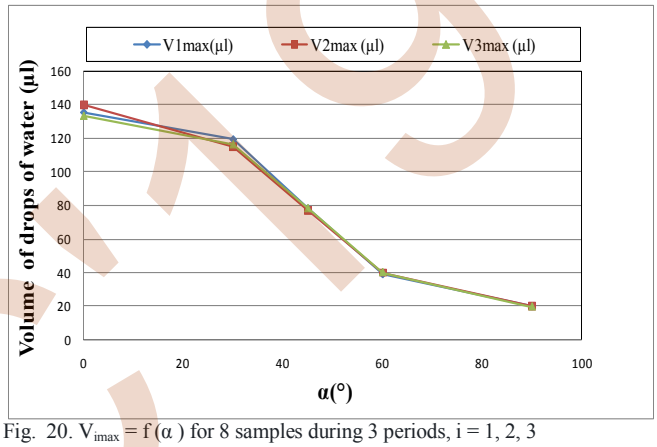

Fig. 20. $V_{imax} = f(\alpha)$ for 8 samples during 3 periods, i = 1, 2, 3

Figure 20 illustrates the evolution of the maximum volume of drops of rainwater collected on the hydrophobic silicone insulating surface in variable inclination. As a result, a decline in the maximum volume with tilt regardless of the period of exposure time considered.

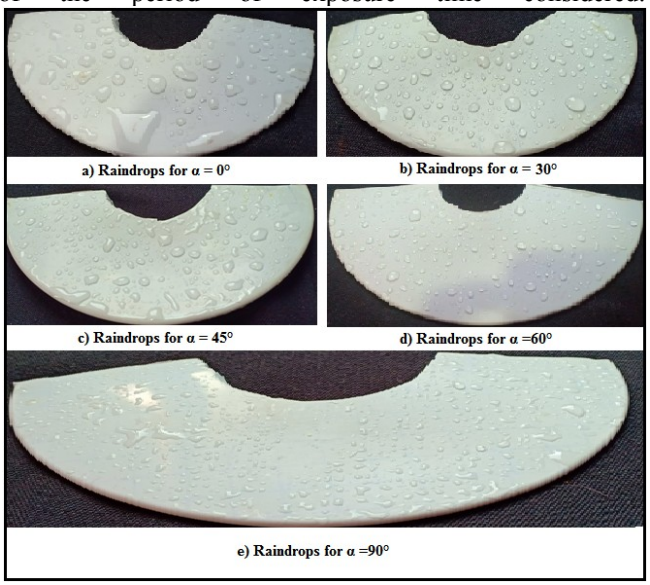

Fig. 21. Drops of rainwater collected on silicone samples with variable inclination in comparaison to the horizontal

The maximum volume is recorded when the sample is in horizontal position (α = 0°), while the minimum is obtained for α = 90° "Fig.21",. It also appears that the ratio of the

volume between α = 0° and α = 90° is 7, which means that the dry leakage line of the insulation for α = 0° is 7 times lower than that found for α = 90°. Therefore, its electrical performance is 7 times greater in vertical position than in horizontal position.

IV. CONCLUSION

The study of natural rain on inclined silicone insulation putting out of voltage leads to the following key results:

• Rain is a random phenomenon;

• The results found are verified over three periods of measurement of natural rain;

• Under the natural fall of rain, the volume of the drop reaches a maximum value equal to 140 µl in the case where the insulating surface is in horizontal position (α = 0 °). This case is very unfavorable for the hydrophobic silicone insulation because the wet leakage path is very large compared to that of its dry zone. As a result, the risk of flashover and altering insulation by landfills is enormous;

• The volume of drops of rainwater collected in several sectors of the same silicone sample decreases with the growth of the angle of inclination of the insulating surface relative to the horizontal;

• The maximum volume of water drops found in the case of the insulating surface in the vertical position is 20µl. Beyond this volume the drop falls, under the effect of the speed of its fall and its weight. In this case, the size of the leakage line is the smallest and that of the dry zone is larger.

REFERENCES

[1] R. Hackam, "Outdoor HV Composite polymeric Insulators", IEEE Trans. on Dielectr. and Electr. Insul. Vol. 6, No. 5, pp. 557-5585, 1999.

[2] E. A. Cherney and R.S. Gorur, "RTV Silicone Rubber Coatings for outdoor Insulators", IEEE Trans. on Dielectr. and Electr. Insul. Vol. 6, No. 5, pp. 605-611, 1999.

[3] D. A. Swift, "Flashover of an Insulator Surface in Air Due to polluted Water Droplets", Proceedings of the 4th International Conference on Properties and Applications on Dielectric Materials, July 3-8, 1994, Brisbane Australia.

[4] C. Yuan, G. Zhichang, L. Xidong, "Analysis of Flashover on the contaminated Silicone Rubber Composite Insulator", Proceedings of the 5th International Conference on Properties and Applications on Dielectric Materials, May 25-30, 1997, Seoul Korea.

[5] G. G. Karady, "Flashover mechanism of Non-ceramic Insulators", IEEE Trans. on Dielectr. and Electr. Insul., Vol. 6, No. 5, pp.718-723, 1999.

[6] M. G. Danikas, R. Sarathi, P. Ramnalis, S. L. Nalmpantis, "Analysis of Polymer Surface Modifications due to Discharges Initiated by water Droplets under High Electric Fields", International Journal of Electrical and Electronics Engineering 4-5 2010, pp.329-334.

[7] W. Shaowu, L. Xidong, H. Lengceng,"Experimental Study on the Pollution Flashover Mechanism of Polymer Insulators" Proceedings of the IEEE; 2000, pp. 2830-2833.

[8] I. J. S. Lopes, S.H. Jayaram, E. A. Cherney, "A Study of Partial Discharges from Water", IEEE Transactions on Dielectrics and Electrical Insulation, Vol. 6 No. 2, pp. 262-267, 2001.

[9] Y. Zhu, K. Haji, M. Otsubo, C. Honda and N. Hayashi, "Electrohydrodynamic behaviour of water droplet on an electrically stressed hydrophobic surface", Journal of Applied Physics 39 (2006) 1970-75.

[10] A. J. Phillips, D. J. Childs and H. M. Schneider, "Aging of non–ceramic Insulator due to corona from water drops", IEEE Trans. on Power Delivery, vol.14, no. 3, pp. 258-263, 1999.

[11] S. M. Rowland and F. C. Lin, "Stability of alternating current discharges between water drops on insulation surfaces", Journal of Applied Physics 39 (2006) 3067-76.

[12] D. A. Swift, C. Spellman and A. Haddad, "Hydrophobicity Transfer from Silicone Rubber to Adhering Polluants and its Effect on Insulator Performance", IEEE Trans.Dielectr.Electr. Insul. Vol. 13, No. 4, pp.820-829,2006

[13] Baer, C.; Baersch, R.; Hergert, A.; Kindersberger, J. Evaluation of the Retention and Recovery of the hydrophobicity of Insulating Materials in High Voltage Outdoor Applications under AC and DC Stresses With the Dynamic Drop Test. *IEEE Trans. Dielectr. Electr. Insul.* **2015**, *23*, 294–303.

[14] Ghunem, R.; Ghunem, A. Using the Inclined-Plane Test to Evaluate the Resistance of Outdoor Polymer Insulating Materials to Electrical Tracking and Erosion. *IEEE Electr. Insul. Mater.* **2015**, *31*, 16–22.

Effect of the High Voltage Electrode Geometric Parameters on the Characteristics of Negative Corona Discharge

E. Ouatah, S. Megherfi, Y. Zebboudj

Laboratoire de Génie Electrique, Université de Bejaia
Bejaia, Algeria
ouatah_hanafi@hotmail.com

M. Aissou

Electrical Engineering Department
University Center of Ain Temouchent
Ain Temouchent, Algeria

***Abstract*— The negative corona current pulses observed in electronegative gases have a highly regular form, they are called Trichel pulses. Many parameters can affect the repetition frequency, the current amplitude and the mean current of Trichel pulses. Such as, the high voltage applied to the active electrode, the space between electrodes and the radius curvature of the active electrode. In the present work, we realized an experimental study of corona discharge in point-plane electrode system under different conditions to illustrate the influence of each parameter. The experimental results show that the frequency repetition and the average current increase with applied voltage and they decrease with the gap space and the radius curvature. Our results were performed with numerical fitting to derive a numerical model and compare it with theoretical models.**

I. INTRODUCTION

In negative corona discharge, when we increase the voltage applied to the corona electrode in electronegative gases, the different regimes of discharge appear. Goldman and *all* [1] have classified the currents discharge of these regimes to (a) auto-stabilization, (b) regular pulses and (c) continuous current discharge. The pulses observed in the regime (b) were later called Trichel pulses [2] and are regular with very short rise times and very durations separated by longer inter-pulse periods. These pulses occur in electronegative gases only and they are very regular in oxygen and air, but they are more irregular in some other gases, like SF_6 [3].

Several investigations have carried out to express the mean current of the Trichel pulses as a function of the applied voltage. In 1986, Ferreira and *all* [4] say that it is better to express the current-voltage characteristic of point-plane negative corona current by $K(V-V_0)^2$. Later, in 2008, Meng and *all* [5] developed a general empirical formula of this characteristic in the form of $K(V-V_0)^n$.

In his investigation on the negative corona discharge in a point-grid electrode geometry, Yamada [6] introduced the influence of ambient temperature and inter-electrode distance on the mean current and described the current-voltage characteristic of Trichel pulses by an empirical formula:

$$I = C_1(T-132)h^{-2.8}V(V-C_2T^{-1}h^{0.39}) \qquad (1)$$

Where: I (μA) is the mean current, V (kV) is the applied voltage, C_1 and C_2 are coefficients which depend on the electrode geometry, T (°K) is the ambient temperature, h (cm) is the inter-electrode space.

The researchers cited above were interested only on the current-voltage characteristic of Trichel pulses without discuss their specific characteristics like repetition frequency, amplitude, rise time, and the duration of the pulses.

In 1974, Lama and *all* investigated the electrical characteristic of Trichel pulses [7]. They expressed the frequency of repetition as a function of the applied voltage and the inception voltage (Eq 2).

$$f = KV(V-V_0) \qquad (2)$$

Recently, in 2013, Zhen and *all* studied the negative corona pulses in a point-to-plane discharge gap and they developed new empirical formulas to express the detailed characteristics of the pulses under given discharge conditions [8]. In their paper, authors have derived formulas in a more universal form, by using the electrical field intensity as the variable, which contains the information about all the experimental parameters (Applied voltage, electrode radius and gap spacing). They found that the repetition frequency of the pulses is proportional to $(E-E_0)^2$, the amplitude of pulses is proportional to

$(E - E_0)^{-0.4}$, the mean current of pulses is proportional to $(E - E_0)^{1.6}$ and rise time and the duration of the pulses are almost independent of the experimental parameters. Where E is the average electric field intensity of the discharge zone and E_0 is the inception field intensity of the negative corona.

In this paper, we present an experimental study of the negative corona discharge. The effect of some parameters on the characteristics of the discharge current will be treated.

II. EXPERIMENTAL SETUP

The negative corona discharge reactor used in the experiments consisted of a point-to-plane electrode system, as shown schematically in Figure 1.

A. Experimental apparatus

The negative direct voltage supplied by the high voltage (HV) source (1) (±140 kV, 80 mA) was applied to the point corona (cathode) electrode (2). The HV source is equipped with voltmeter of crest making it possible to measure the output high voltage. The point electrode of a variable curvature radius is fixed with the insulating support (3). The circular plane (4) of radius 360 mm forms the ground electrode (anode) and it is set to earth via the variable resistance (6) which forms a shaping circuit (RC) with the capacitance of the coaxial cable (7). The point-to-plane space (d) is variable. To protect the system from external electromagnetic field, we used a cylindrical guard electrode (5). The potential difference at the terminals of the resistance (6) is displayed on the oscilloscope TD1012 (8) with interface TDS 2CMAX. The computer (10) is connected to the oscilloscope with the RS232 bus (9) for data processing.

It should be noted that the three electrodes (the point, the plane and the guard cylinder) are machined with stainless-steel.

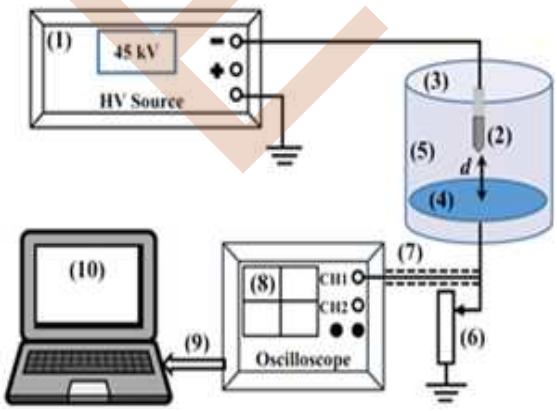

Figure 1. Experimental setup for point-plane negative DC

B. Active electrode configuration

The high voltage electrode is a point of variable radius of curvature. The scheme of the point electrode is illustrated in figure 2. In order to vary the curvature radius of the high voltage electrode, we act on the length h, while the diameter D is constant.

Then, the angle α is variable, knowing that:

$$\alpha = tang^{-1}\left(\frac{D/2}{h}\right) \quad (3)$$

We note that more the angle (α) is small, more the radius of curvature (r) is weak. In this work, we have used 3 electrodes of curvature radius 21, 40, 90 µm.

III. RESULTS AND DISCUSSIONS

A. Current-Voltage characteristic

Fig. 3 shows the variation of the discharge current in function of applied voltage to the point electrode.

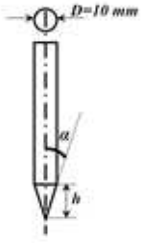

Figure 2. Scheme of the corona electrode

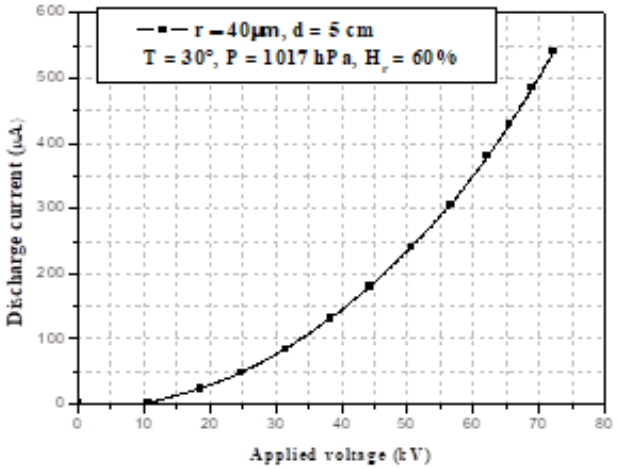

Figure 3. Current-voltage characteristic on point-plane system

These results are obtained with active electrode of curvature radius $r = 40\mu m$, the inter-electrodes spacing $d = 5cm$ and the atmospheric conditions: temperature $T = 30°C$, pressure $P = 1017\ hPa$ and relative humidity $H_r = 60\%$.

According to this figure, the discharge current increases in a non-linear manner with the voltage.

In general, the Current-Voltage characteristic of corona discharge described by the empirical Townsend relationship is usually written in the form of I/V ∝ V. This relation has originally been found in coaxial wire-cylinder geometry [9]. Later, it was proven that this relationship can be generalized for other geometry like: point-to-plan [10], point-to-grid [6] and point-to-ring [11].

$$I = A.V.(V - V_0) \quad (4)$$

Where I is the corona discharge current, V the applied voltage, V_0 the inception voltage for corona and A is a constant depending on electrode geometry and ion mobility.

According to Ferreira's paper, $K(V - V_0)^2$ better represents the *(I-V)* characteristic of negative corona discharge. Later (2008), Meng and all have generalized this relationship in the form of $K'(V - V_0)^n$.

After analyzing the results by the different models mentioned above, we noticed that the most suitable model is governed by equation 4.

To determine the parameters of this equation (A and V_0), we plotted in figure 4 the ratio (I/V) as a function of V, such as:

$$I/_V = A.(V - V_0) \quad (5)$$

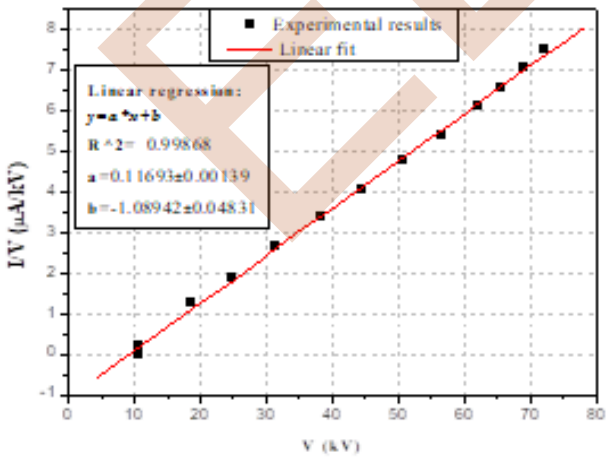

Figure 4. Linear fit of (I/V) current in function of V

The fit of the curve (I / V) as a function of V gave a line of equation $y = a.x + b$, such that:

- the slope of the curve $a = 0.11693$;
- the initial value $b = -1.08942$.

The parameters a and b of the curve respectively represent the parameters A and ($-A.V_0$) of the equation 4.
So: the constant depending on electrode geometry and ion mobility $A = 0.11693\ \mu A/(kV)^2$ and the inception voltage $V_0 = 9.31\ kV$.

Finally, under the experimental conditions described in figure 3, the discharge current as a function of the applied voltage can be written:

$$I(\mu A) = 0.11693 * \mathrm{V} * (\mathrm{V} - 9.31), V(kV) \quad (6)$$

B. Effect of gap spacing

The gap spacing (d) of the point-to-plane electrodes system significantly affects the behavior of the corona discharges.

Then, the (I-V) characteristic of the discharge strongly depends on the distance "d". Figure 5 shows the (I-V) characteristic of negative corona discharge for the gap distances of 10, 20, 25, 30, 35, 40 and 50 mm.

As shown in this figure, for the same voltage level applied to the active electrode, the discharge current decreases with increasing of inter-electrodes spacing.

The increase of the inter-electrode distance causes the reduction of the electric field between the electrodes, which will induce a decrease in the discharge current. We also notice that the inception voltage V_0 increases with the inter-electrodes spacing.

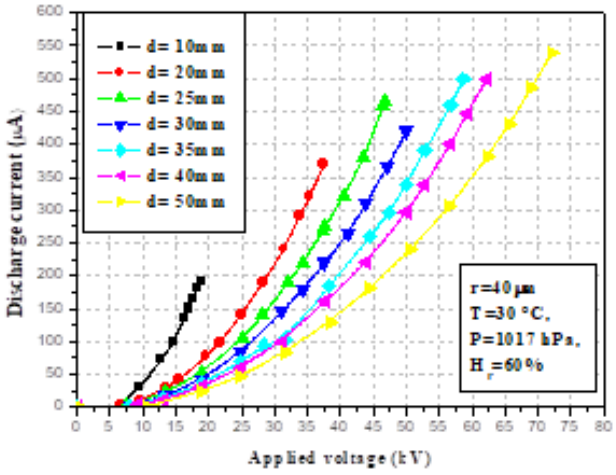

Figure 5. Effect of gap spacing on negative (I-V) characteristic

To study the effect of the space between electrodes on the parameters of equation 4, we traced on the figure 6 the linear fits of the characteristics (*I/V, V*).

The fits obtained results are summarized in figure 7 and 8.

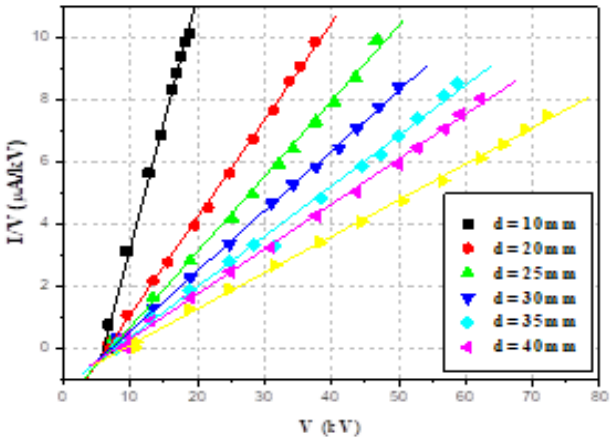

Figure 6. Linear fits of the characteristic (I/V, V) with different space between electrodes

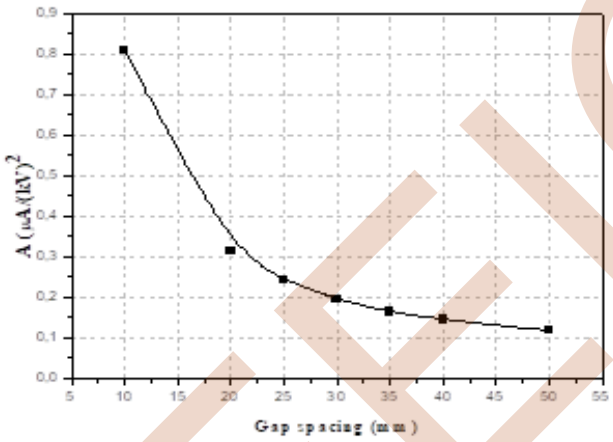

Figure 7. Variation of the parameter A with gap spacing

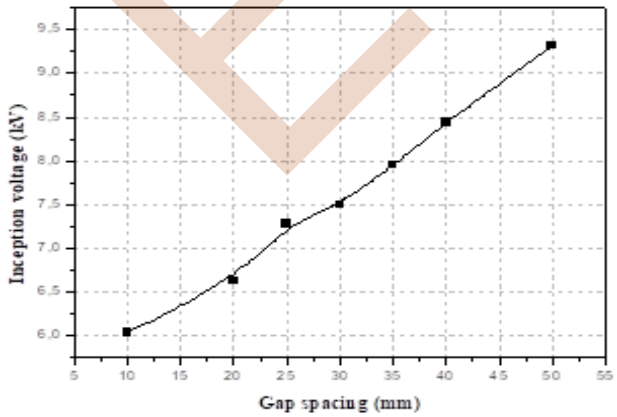

Figure 8. Effect of gap spacing on inception voltage

According to these figures, it appears very clearly that the parameter A of the equation 4 reduces with the increase of the gap spacing, while the corona inception voltage V_0 increases.

C. Effect of the high voltage electrode radius

Fig. 9 shows the (*I-V*) characteristic of a point-plane negative corona discharge with different curvature radius ($r = 21, 40, 90\ \mu m$).

The curvature radius of the high voltage electrode acts exactly like the gap spacing. Such as, the increase of the curvature radius causes the reduction of the electric field between electrodes and the current measured on the ground electrode. Then, we can deduce that parameter A decreases with the curvature radius whereas the inception voltage V_0 increases.

D. Discharge current waveform

The essential characteristic of the DC corona discharges is the existence of a drift zone of the ions. This zone gives to the corona discharges their stability [12].

When a negative voltage is applied to the active electrode (negative discharge), the negative ions are created by attachment of electrons and the positive ions are created by ionization. The negative ions migrate in the drift zone where the field is weaker, whereas the positive ions return to cathode enough quickly. The discharge current creates through the RC circuit a voltage *u(t)* with a continuous and pulse component.

The waveform of the voltage *u(t)* which the image of the discharge current is clearly observed on the oscilloscope when the applied voltage is higher than the inception voltage V_0 like shown in figure 10.

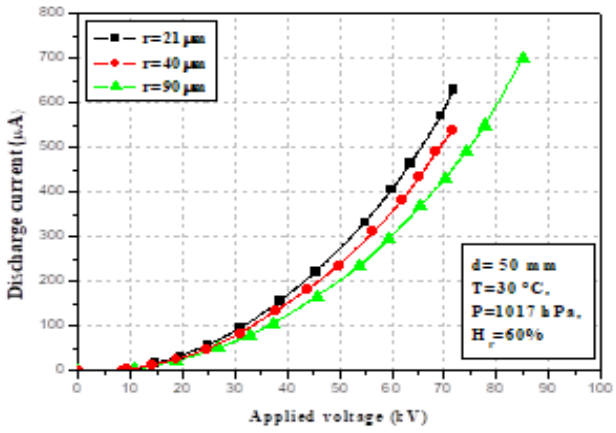

Figure 9. Effect of the active electrode curvature radius on negative *I-V* characteristic

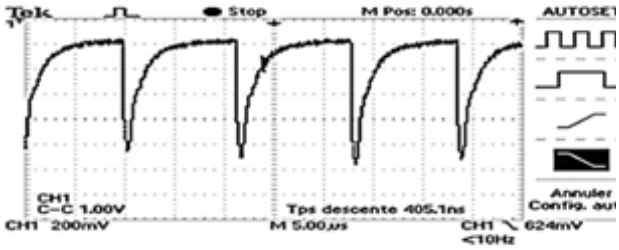

Figure 10. Discharge current waveform

The pulses train observed is regular with a frequency in order of a few hundred kHz to a few MHz. The form of pulses is asymmetric with a time rise in order of 10 ns and time decay depending on the values of the capacitance C and the resistance R. These pulses are called Trichel pulses [13].

E. Effect of the applied voltage on the repetition frequency of pulses

Several experimental parameters can modify the electric field between electrodes and the discharge current, like the applied voltage, the gap spacing and the curvature radius of the active electrode. So, the pulses repetition frequency of discharge current can be modified by these parameters.

Fig. 11 illustrates the variation of pulses repetition frequency with the applied voltage.

According to this figure, the variation of the Trichel pulse repetition frequency with the applied voltage is governed by a non-linear relation-ship. As the applied voltage increases, the repetition frequency increases which agrees with the results presented by Trinh [14–16].

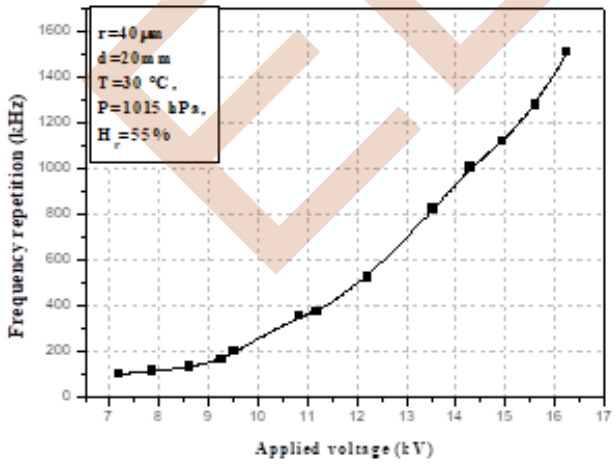

Figure 11. Pulses frequency repetition of discharge current variation with applied voltage

Lama and *all* [7] expressed the variation of Trichel pulses repetition frequency with the applied voltage by the equation 2, which has as parameters the constant K and the inception voltage V_0.

F. Effect of the gap spacing on the repetition frequency of pulses

The effect of the distance between the active electrode and grounded electrode on repetition frequency of Trichel pulses for 3 voltage levels is illustrated in the figure 12.

Contrarily to the effect of applied voltage, the increase of the distance between the electrodes induces the decrease of the repetition frequency. Such as, the increase of gap spacing causes the decrease of the electric field between electrodes, which leads the decrease of repetition frequency [14-16].

G. Effect of the curvature radius on the repetition frequency of pulses

In the figure 13, we have plotted the repetition frequency according to the curvature radius of the active electrode for 3 voltage levels.

As shown in this figure, the curvature radius of the active electrode has the same effect as the gap spacing. Such as, the repetition frequency of Trichel pulses decreases with the curvature radius of the high voltage electrode [14-16].

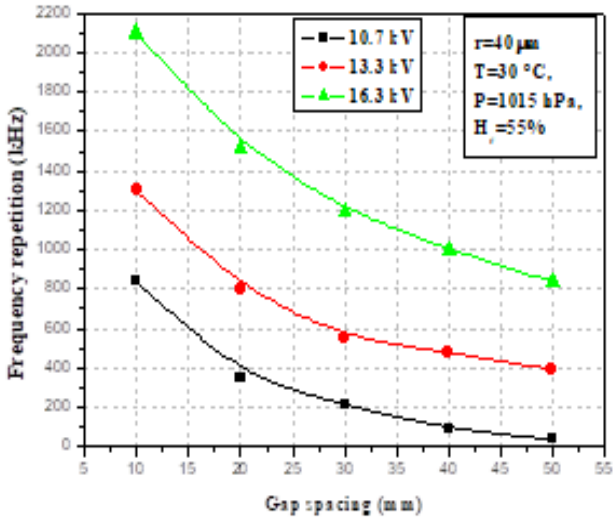

Figure 12. Trichel pulses frequency repetition of discharge current variation with gap spacing

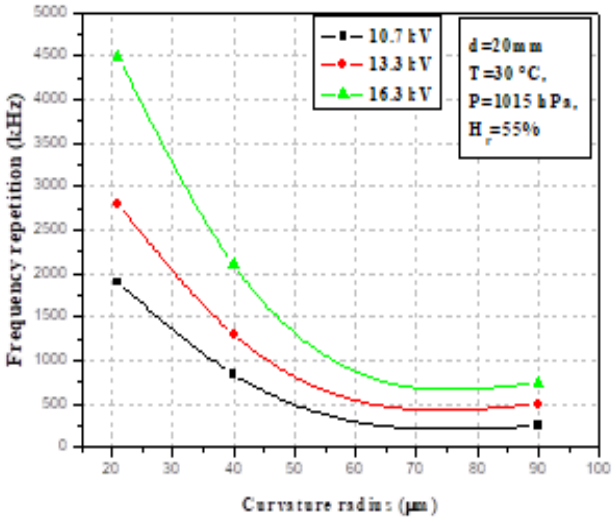

Figure 13. Pulses frequency repetition of discharge current variation with curvature radius of the active electrode

VI. CONCLUSION

In this work, an experimental study of the negative corona discharge in point-plane geometry was exposed. The effect of the applied voltage, the gap spacing and the curvature radius of high voltage electrode on the discharge current has been discussed. So, we can conclude:

- The current-voltage characteristic is governed by the Lama model with which we can deduce the constant A (depending on the geometry of the electrodes and the ions mobility) and the inception voltage of the corona effect.
- The experimental results showed the decrease of the parameters A and the increase of V_0 of Lama's model with the gap spacing and the radius of curvature.
- The discharge current decreases with the gap spacing and the curvature radius of the active electrode.
- The discharge current contains a continuous component and a pulse component. The last one is characterized by its amplitude and repetition frequency.
- The repetition frequency of Trichel pulses increase with the applied voltage and the Lama's model can be attributed to this variation.
- The pulse component of the discharge current decreases with the applied voltage. This component disappears at a certain voltage level applied to the high voltage electrode and the current contains only a continuous component.
- The repetition frequency of Trichel pulses decreases with the distance between electrodes and the curvature radius of the active electrode

REFERENCES

[1] M. Goldman and A. Goldman, "Gaseous Electronics", M.N. Hirsh and H.J. Oskam, Eds., vol. I, New York: Academic Press, 1978, pp. 219-290.

[2] G. W. Trichel, "The mechanism of the negative point to plane corona near onset," Phys. Rev. 54, 1938, pp. 1078–1084.

[3] L. B. Loeb, "Electrical Coronas: Their Basic Physical Mechanisms", Berkeley: University of California Press, 1965.

[4] G. F. L. Ferreira, O. N. Oliveira, and J. A. Giacometti, "Point-to-plane corona: Current-voltage characteristics for positive and negative polarity with evidence of an electronic component," J. Appl. Phys. 59, 1986, pp. 3045–3049.

[5] X. Meng, H. Zhang, and J. J. Zhu, "A general empirical formula of current voltage characteristics for point-to-plane geometry corona discharges", J. Phys. D 41, 065209, 2008.

[6] K. Yamada, "An empirical formula for negative corona discharge current in point-grid electrode geometry," J. Appl. Phys. 96, 2004, pp. 2472–2475.

[7] W. L. Lama and C. F. Gallo, "Systematic study of the electrical characteristics of the "Trichel" current pulses from negative needle-to-plane coronas," J. Appl. Phys. 45, 1974, pp. 103–113.

[8] L. Zhen, Bo Zhang, and Jinliang He, "Specific characteristics of negative corona currents generated in short point-plane gap", Phys. Plasmas 20, 2013, 093507.

[9] J. S. E. Townsend, "Electricity in Gases", Clarendon Press, 1915.

[10] B. L. Henson, "A space-charge region model for micro-scopic steady coronas from points", J. Appl. Phys., Vol. 52, 1981, pp. 709-715.

[11] P. Giubbilini, "The current-voltage characteristics of point-to-plane corona", J. Appl. Phys., Vol. 64, No. 7, 1988, pp. 3730-3732.

[12] Y. Zebboudj, R. Iken, "Positive corona inception in HVDC under variable air density and humidity conditions", European Physical Journal: Applied Physics 10, 2000, 211.

[13] E. Ouatah, S. Megherfi, Y. Zebboudj, "Characteristics of partial discharge pulses propagation in shielded power cable", Electric Power Systems Research 99, 2013, pp. 38– 44.

[14] 0. G. Trinh and J. B. Jordan, "Modes of corona discharges in air," IEEE Trans. Power Apparatus Syst. PAS-87,1968, pp. 1207–1215.

[15] N. G. Trinh and J. B. Jordan, "Trichel streamers and their transition to pulseless glow discharge," J. Appl. Phys. 41, 1970, pp. 3991–3999.

[16] N. G. Trinh, "Partial discharges XIX: Discharges in air – Part I: hysical mechanisms," IEEE Electr. Insul. Mag. 11, 1995 pp. 23–29.

Electrical performance of rod-plane system with superhydrophobic flat barrier under AC voltage and any atmosphere

S. Messad /R. Boudissa
Laboratory of Electrical Engineering, Department of Electrical Engineering,
University A. Mira of Bejaia, Targa Ouzemmour,
06000 Bejaia, Algeria

S. Kornhube
University of Applied Sciences
Theodor – Koerner - Allee 16 Zittau
8800, Germany

***Abstract*:** *The aim of this work is an experimental study of the electrical performance of a rod-plane system protected by a super-hydrophobic plane barrier under AC voltage and any conditions of atmosphere. For this effect, we proceeded to manufacture a superhydrophobic surface, similar to that of the lotus leaf, having a contact angle equal to 160°. Two experimental U-shaped devices were made to ensure this study; one of them is to maintain the two used electrodes which are screwed with bolts into its two wooden arms. The other is only a support that maintains the flat barrier perpendicular to the electrodes. This study is supported by the visualization of the electrical phenomenon using a camera.*

The results of this investigation put in profile the improvement of the electrical performance of the studied system with using superhydrophobic barrier. This increases with the barrier's size and the air gap. If we compare the electrical performance of the system without barrier with that realize by intercalating the superhydrophobic barrier, we remark that the performance with the 10 cm barrier is 49% greater and for the 20 cm barrier is greater about 90% compared to the system without barrier. Even in very severe pollution conditions the superhydrophobic barrier keeps the same electrical performance unlike its counterpart, the hydrophilic barrier which see its performance fall by 92% compared to the case when the hydrophilic barrier are clean and dry, its performance coincides that of the system without barrier.

Keywords: *Superhydrophobic; contact angle; hydrophilic; electrical performance.*

I. *INTRODUCTION*

In high voltage systems in particular, it is more advantageous to use materials with a low permittivity, a high rigidity and impermeability in order to avoid any development of superficial electric discharge and to remedy the problem of circumvention isolations. Unlike traditional insulating materials, such as porcelain and glass, silicone has been widely used in high-voltage equipment. One of its main advantages is its hydrophobic character, in contrary for hydrophilic materials, water droplets, instead of continuous water films; appear on their surface in humid conditions [1-3]. Despite the fact that this type of hydrophobic barrier offers a better insulating power with regard to the hydrophilic barriers, this material can be short circuits by flashover discharges owing to taper of water drops deposit on its surface, under the action of an electric field [4]. On the other hand the interest of the researchers leaned towards superhydrophobic surfaces because of the weak adhesion between the water and this surface, this type of surfaces are called self-cleaning and it is similar to that of the lotus leaf. Several studies have been carried out to develop this surface, and several have achieved good results by showing that the flashover voltage could be greatly improved by using this type of barrier [5], but these results have not been oriented in order to study the electrical performance of such a material used as an insulating barrier.

Nowadays many experimental works have been carried out in order to study the influence of different experimental factors such as the geometries of barriers and electrodes on the electrical performance of electrical systems [6]. Contrary to previous work, our work consists in the study of the electrical performance of a rod-plane system with a superhydrophobic flat barrier under AC voltage and any atmosphere.

II. EXPERIMENTAL MODEL AND MEASUREMENT TECHNIQUE

The rod-plane electrode system adopted during this investigation is illustrated in figure. 1a. The two electrodes used in this study are screwed with bolts into two wooden arms. The latter are recessed on the two opposite sides of U shaped wooden support (Fig. 1a).
The high voltage and ground electrodes are constituted by a steel cylindrical rod with 14 mm in diameter and 180 mm in length. The rod on the high voltage side is finished by a conical bronze rod having an angle of 60 ° and 0.2 mm of

curvature radius, the other one on the ground side, it is a circular steel disk, with 400 mm in diameter and 5 mm of thickness. The size of the air gap between these two electrodes (d) varies between 0 and 140 mm.

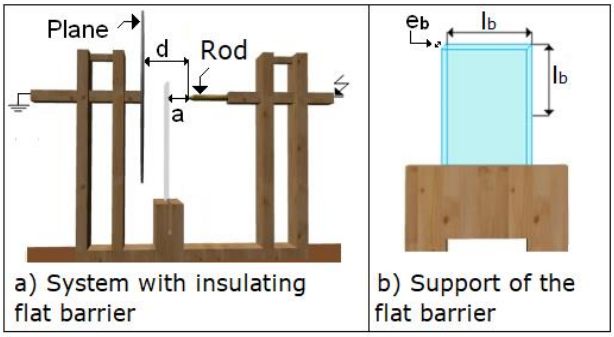

Figure 1: *characteristic of the rod-plane system with flat superhydrophilic barrier*

The insulating flat barriers used in this study are square and in glass, with sides equal to 100 or 200 mm and 6 mm thickness. The surface of the planar barrier is held perpendicular to the axis of the two electrodes of the system by means of a U-shaped wooden support (Fig. 1b), which slides on the base of the U-shaped wooden support supporting the two electrodes (Fig. 1a). With this device, the relative position (a / d) of the barrier relative to the HT electrode can be easily varied.

We applied a coating on a part of the barrier, on a limited area per lb*lb. This coating constitutes the superhydrophobic surface. The essential steps in the manufacture of this superhydrophobic insulating surface are summarized in figure 2. The first step is to manually apply a thin layer of the silicone product (Fig. 2a) on both the large faces and the three edges of the glass barrier. Once this layer is well spread, we then go to carbonization. We burn a small amount of silicone; it's from the same tube, which is deposit on an iron support (Fig. 2b). The flat glass barrier with the first layer of fresh silicone is then approached by the flame to cover it with a layer of soot (Fig. 2b). Finally the figure 2c shows the flat barrier blackened superficially and washed with tap water.

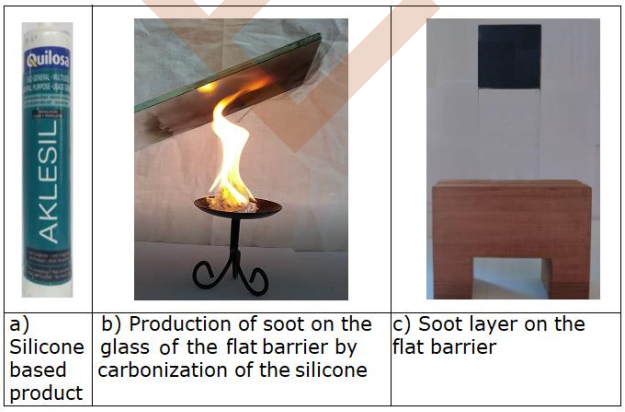

Figure 2: *Main steps in the manufacture of a silicone superhydrophobic insulating layer*

The technique of applying the pollution layer on the flat barriers is shown in the figure 3. This method consists of immersing the flat barrier in a container containing the polluting solution for a few seconds, making it drip and finally testing it.

The polluting solution used contains mainly tap water, 40 g of kaolin per liter of water for the thickening of the polluting layer and sodium chloride, the proportion of which is determined according to the desired volume conductivity of the solution. This is measured using a moving probe conductivity meter. The value of the voluminal conductivity (σ_v) of the solution used in this study is 25 mS/cm. the value of the equivalent superficial conductivity (σ_s) is of the order of 14 µS [7]. This one corresponds to a very high level of pollution of an indoor site [8].

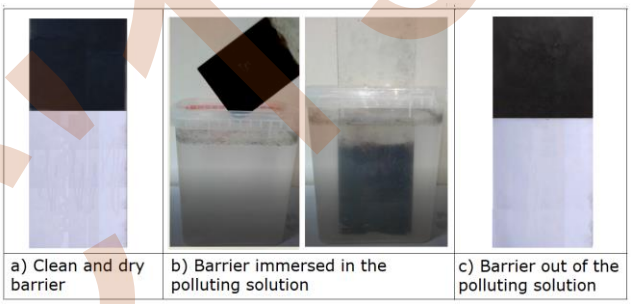

Figure 3: *Steps followed to immerse the barrier in the pollution solution*

The measurement of the electric performance of the rod-plane system with clean or polluted flat superhydrophobe barrier as well as the visualization of the electric discharge evolving in the space between electrodes can be achieved using the electric diagram illustrated by the figure 4.

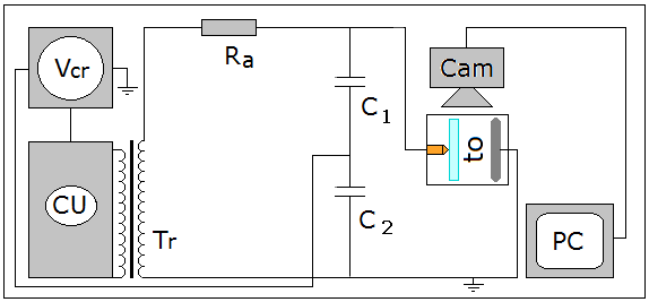

Figure 4*: Electrical circuit for measuring the disturbing voltage of the system and visualizing the electrical discharge*

The initiating voltage measuring circuit consists of a transformer (Tr) which can deliver at its secondary a maximum AC voltage of 135 kV and whose time variation of its ramp can be obtained automatically or manually using the control unit (CU) (Fig. 4). The test voltage is read directly from the digital display peak voltmeter (Vcr). The test object (to) is connected across to the limits of the

protection resistance Ra and the capacitive voltage divider (C1, C2).

The display circuit comprises a camera, for recording the different phases of the development of the electric discharge, in the air gap between electrodes of the studied system as well as a PC for a better analysis and treatment of this one.

For each of the influence's parameters investigated in this paper, a series of 20 tests were performed and the value retained for the disruptive voltage of the air gap of the system is the arithmetic mean of the set of those obtained on the same series of measurement techniques used in this study, the relative maximum error obtained is equal to 5% of this average value. All the values of the disruptive voltage of the air gap of the considered system are measured under different meteorological conditions and they have been brought back to the normal conditions of temperature θ_0, pressure P_0 and humidity H_0 ($\theta_0 = 20$ ° C, $P_0 = 100$ kPa and $H_0 = 11$ g / m3), by means of to empirical relationships [9].

III. RESULTS AND DISCUSSIONS

A. *Clean and dry atmosphere*

Before evaluating the effect of a flat barrier inserted in the studied system, on its electrical performance, we must first determine its optimal position which offers a greater power of isolation. Precisely, Figure 5 illustrates the appearance of the breakdown voltage of the rod-plane system with the four flat barriers used in this work, depending on the relative position (a / d) with respect to the electrode under voltage.

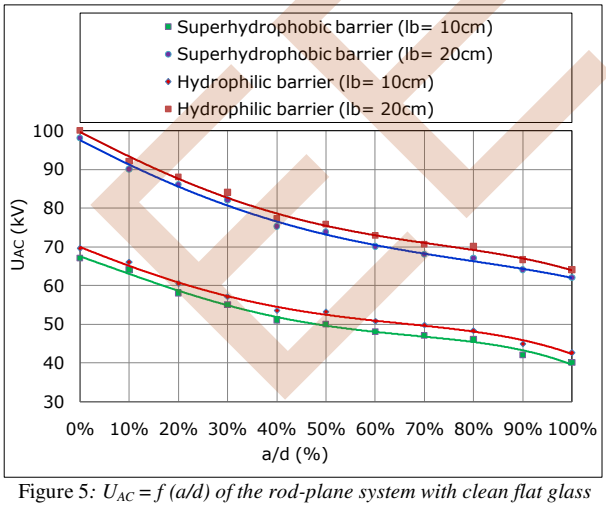

Figure 5: $U_{AC} = f\,(a/d)$ *of the rod-plane system with clean flat glass barrier*

It results, the maximum value of the rigidity of the system is obtained when the four barriers are in contact with the rod under voltage (a / d = 0%), and it is exactly this position of the barriers that we adopted for the following work.

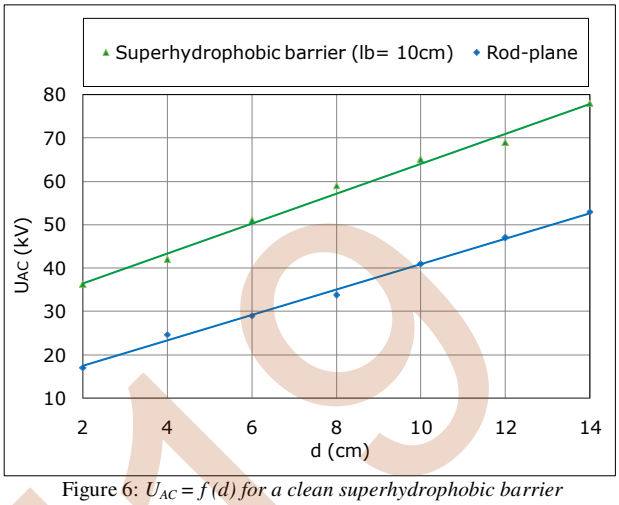

Figure 6: $U_{AC} = f\,(d)$ *for a clean superhydrophobic barrier*

This figure shows that the introduction of vertical solid insulation between the HV rod and the plane increases its breakdown voltage compared to the system without it. This improvement in the electrical performance of the system is explained by a deformation of the initial electric field. Thus a redistribution of the electric field which results in the increase of the disruptive voltage of the system in question, because of the borrowing of the electric discharge of a path different from that in the system without barrier.

These two paths connection between the two electrodes require a very high breakdown voltage compared to that resulting in the disruption of the same air gap without the insulating barrier.

We wanted to further improve the performance of our system by acting on the length of the superhydrophobic barrier. Figure 8 gives us the characteristics UAC = f (lb, d).

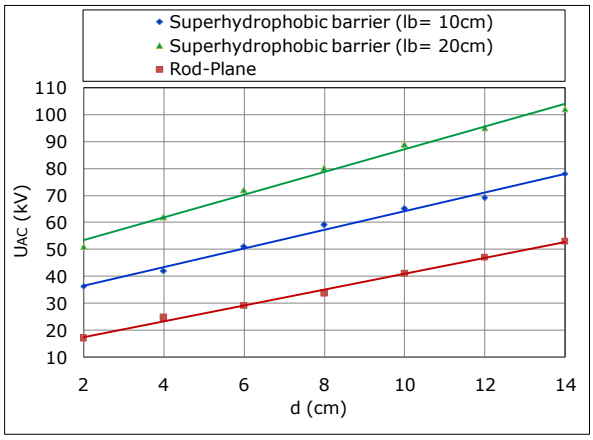

Figure 7: $U_{AC} = f\,(l_b, d)$ *for clean superhydrophobic barriers*

This figure shows that the breakdown voltage increases with the size of the air gap. The rigidity of the system is more significant for a length lb = 20 cm. The observed

phenomenon is explained by the increase of the flashover voltage which is the path taken by the electric discharge on the increasing barrier surface (Fig. 8). This implies that the flashover path of the 20 cm barrier is twice that of the 10 cm barrier (Fig 9).

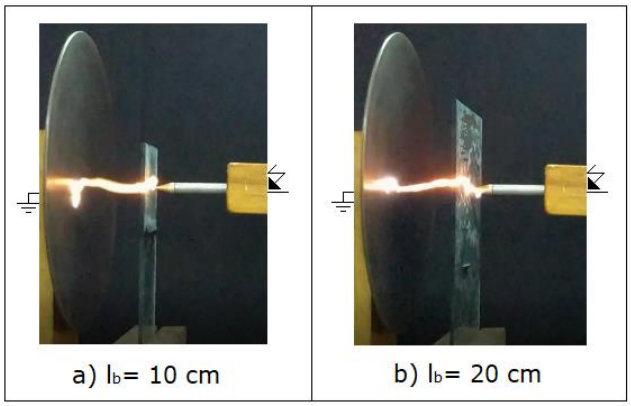

Figure 8*: Length of the flashover path of the clean superhydrophilic barriers and the breakdown path of the air gap (d = 10 cm)*

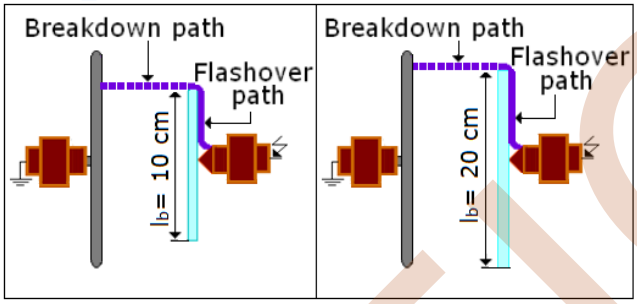

Figure 9: *Explanatory diagram showing the path taken by the electrical discharge*

In this part we compared the superhydrophobic barriers to the hydrophile barriers; to make this we took barriers with the same dimensions. Figure 10 gives the characteristics UAC = f (lb, d) for the studied system by changing each time the insulating barrier.

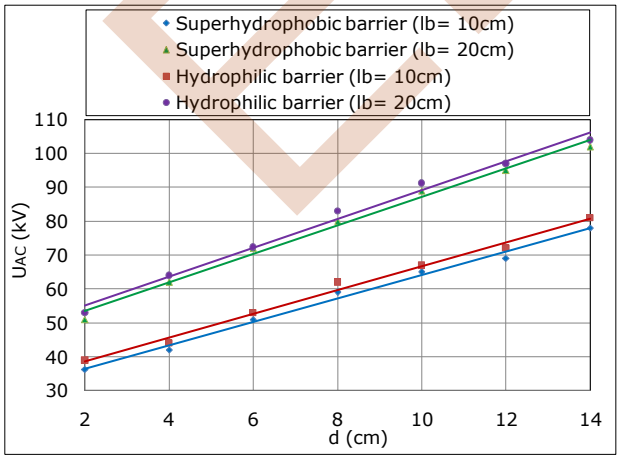

Figure 10*: $U_{AC} = f(l_b, d)$ for clean superhydrophobic barriers*

It follows that the characteristics corresponding to the system studied with barriers of the same size, are very close to each other. The difference between the two is negligible compared to the maximum permissible error.

This similarity is explained by the disruption path of the system, which is practically identical for the case of barrier of the same dimension. This path is composed of the flashover path of half surface of the barrier both the hydrophobic or superhydrophobic barrier and the breakdown path of the air gap between the edge of the barrier and the ground electrode (Figs 8, 11).

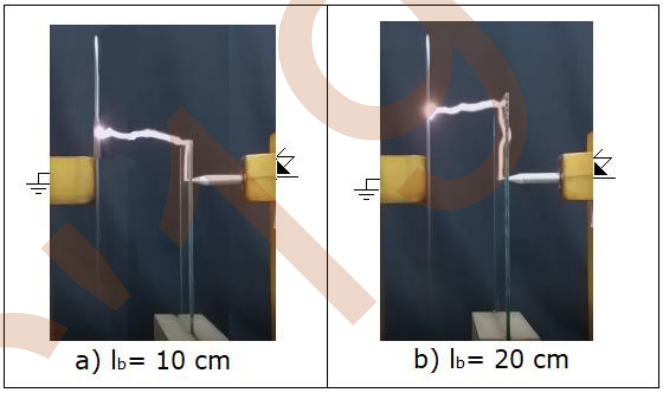

Figure 11: *Length of the flashover path of both clean barriers used and the breakdown path of the air gap (d = 12 cm)*

B. *Polluted and humidified atmosphere*

We preceded to the pollution of the superhydrophophic barriers before each test. The mode of pollution applied is chosen in such a way as to have an effect on the insulating barriers similar to that produced by humidification in closed sites. Figure 12 gives the characteristics U_{AC} = f (lb, d) of the hypohydrophobic barriers for the two different atmospheric cases.

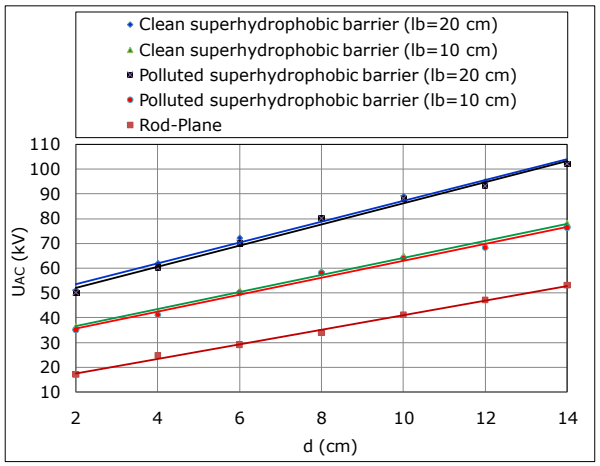

Figure 12: *$U_{AC} = f(l_b, d)$ for superhydrophobic flat barriers in any atmosphere*

As a result, the performance of the system with the superhydrophobic barrier (lb = 10cm) is practically the same whether for the case of a polluted or clean and dry atmosphere, the same applies for the case of the 20cm barrier. This proves that the water does not adhere to the surface of these barriers. However with this superhydrophobe character, the barriers keep their dry surface which allows to maintain the flashover discharge on their surface. Figure 13 shows the path taken by the electrical discharge of the system with polluted superhydrophobic barriers.

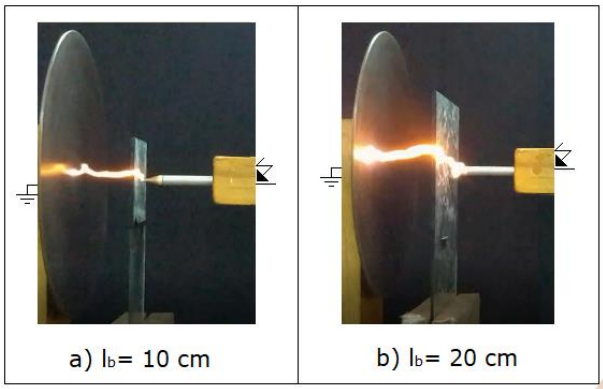

Figure 13: *The path taken by the electrical discharge for the superhydrophobe barrier (l_b = 10cm)*

For a better comparison between the two types of material, figure 14 gives the characteristics UAC = f (lb, d) of the superhydrophobic and hydrophilic barriers for the two different cases of atmosphere.

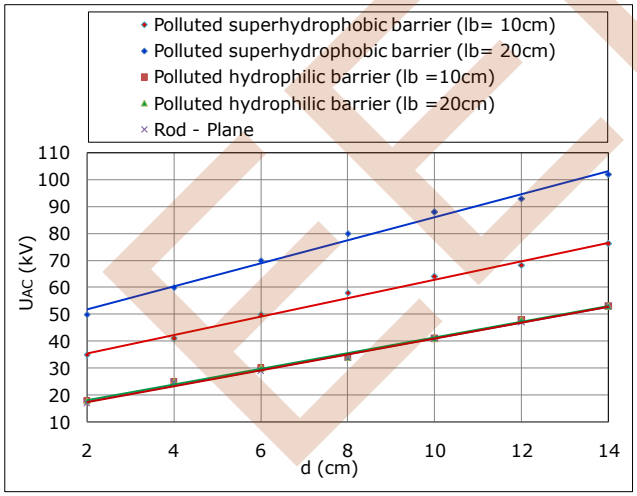

Figure 14: *U_{AC} = f (d) for polluted flat barriers (σ_v = 25 mS/cm)*

It result of Figure 14, the characteristics of the disruptive voltages with the two hydrophilic barriers (lb = 10cm and lb = 20cm) are confused with the system without barrier. That said, the barriers once polluted have absolutely no impact, and do not allow any protection of the system. Such behavior can even be very unfavorable for a real system in industry, because with low voltages an electric discharge can easily appear.

The figures 15 explain the path taken by the electrical discharge in the air gap of the system with clean barrier as well as polluted.

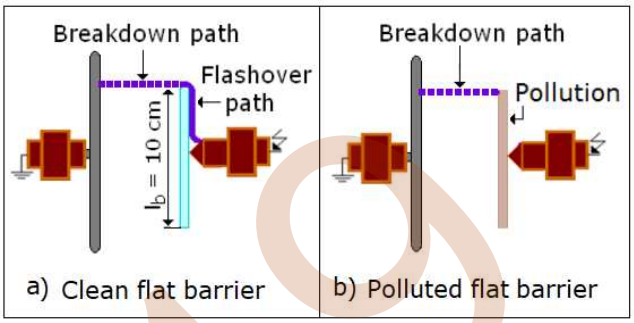

Figure 15: *Explanatory diagram showing the path taken by the electrical discharge*

Under very severe pollution conditions, we note the absence of the flashover discharge on the surface of the hydrophilic barriers, which explains its weak dielectric strength; the discharges is manifested on the surface of the barrier by an electric current to the edges of it and then join the plane by a breakdown discharge (Figs 16c and d).

While the sperhydrophobic barrier with its high power of impermeability succeed to keep its surface dry, so the electrical discharge of the system is always done with a flashover path and breakdown of the air (Figs 16a and d).

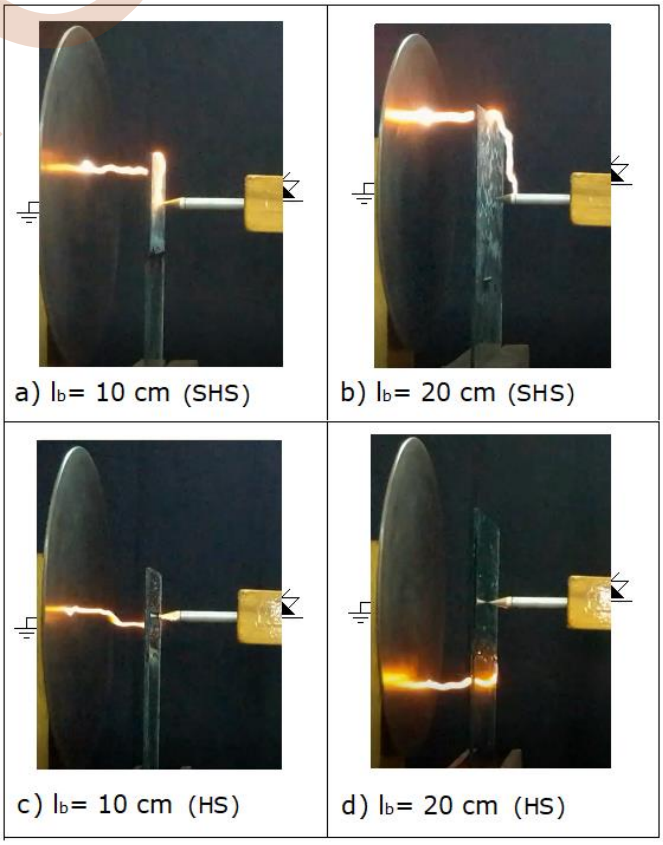

Figure 16: *The path taken by the electrical discharge for the polluted flat barrier (SHS: Superhydrophobic surface, HS: Hydrophilic surface, l_b = 12cm, σ_v = 25 mS/cm)*

IV. CONCLUSION

The results from this experimental study can be summarized as follows:

- The electrical performance of the system increases with the size of the barrier (lb) and the interelectrode air gap (d);

- The technique adopted for the manufacture of the superhydrophobic layer was successful because it allowed us to obtain a surface that has a contact angle of 160 °, where the water hardly ever adheres;

- The use of a superhydrophobic barrier as an insulator in high voltage systems offers better advantages over hydrophilic materials;

- The electrical performance of the 10 cm barrier is 49% greater than the system without barrier, regardless of the nature of the chosen atmosphere;

- The electrical performance of the 20 cm barrier is 92% larger than the system without barrier, regardless of the nature of the chosen atmosphere;

- The disruption path of the rod-plane electrode system with the superhydrophobic plane barrier in the two atmosphere cases is composed of the flashover path of its half surface's and the breakdown path of the air gap separating the barrier edge and the ground electrode.

REFERENCES

[1] R. A. Ghunem, L. L. Tay, H. Terrab, and A. H. El-Hag, "Analysis of service-aged 200 kV and 400 kV silicone rubber insulation in the Gulf region", IEEE Trans. Dielectr. Electr. Insul. 23, 3539 (2016).

[2] S. F. Kaaiye and C. Nyamupangedengu, "Comparative study of AC and DC inclined plane tests on silicone rubber (SiR) insulation" High Volt. 2, 119 (2017).

[3] I. J. S. Lopes, S. H. Jayaram, and E. A. Cherney, "A study of partial discharges from water droplets on a silicone rubber insulating surface", IEEE Trans. Dielectr. Electr. Insul. 8, 262 (2001).

[4] S. Messad, F. Bouchelga, R. Boudissa, S. Kornhuber, and K. D. Haim , "Electrical performance of rod-plane system with silicone tubular barrier under DC voltage and atmosphere conditions" , Conference on silicone insulation , July2 – 3, Muenchen, Germany, 2019.

[5] Yufeng Li, Haiyun Jin, Shichao Nie, Cheng Tong, and Naikui Gao "Effect of superhydrophobicity on flashover characteristics of silicone rubber under wet conditions" State Key Laboratory of Electrical Insulation and Power Equipment, Xi'an Jiaotong University, Xi'an 710049, China (2018)

[6] S. M. Lebedev, O. S. Gefle and Y. P. Pokholkov "The Barrier Effect in Dielectrics: The Role of Interfaces in the Breakdown of Inhomogeneous Dielectrics", IEEE Transactions on Dielectrics and Electrical Insulation Vol. 12, No. 3; June 2005.

[7] H. Madi, R. Boudissa, "Effet du mode de distribution de pollution sur l'efficacité d'une barrière isolante contaminée sous tension alternative", 2ème Journée Internationale d'Electrotechnique de Maintenance et de Compatibilité Electromagnétique, Paper No. HT-12, Oran, Algeria, 2010.

[8] G. Päsold, R. Baersch, J. C. Mauroux and T. Schoenemann, "Elektrisches Verhalten von polymeren Isolierstoffoberflächen unter erschwerten klimatischen Innenraumbedingungen", ETG - Fachbericht No. 112, pp. 27-34, VDE-Verlag 2008.

[9] W. Mosch, E. Lemke, M. Eberhardt, "Einführung in die Hochspannungstechnik: Luftisolierung". VEB Kongress- und Werbedruck, Oberlungwitz, mars 1984, Dresden, RFA.

Experimental study of the short-term aging of thepaper pressboard impregnated with Borak22 oil

A. Laifaoui, M. S. Herzine, H. Ait Said and Y. Zebboudj
Laboratoire de Génie Electrique de Bejaia – LGEB
Université de Bejaia
Bejaia, Algérie
abdelkrim2002@yahoo.fr

J. M. Reboul
Laboratoire Universitaire des Sciences Appliquées de Cherbourg – LUSAC
Universitaire de Caen
Cherbourg-en-Cotentin, France
jean-michel.reboul@unicaen.fr

***Abstract*—This work deals with the effect of the applied form of tensionas well as its speed of rise on the breakdown voltage of pressboard paper impregnated in Borak22 insulating oil. First, we present the statistical model of Weibull used for the treatment of the obtained results, in all 840 results will be treated.The latter will be sowing a Kolmogorov-Smirnov adequacy test to validate this model, then we present the experimental devices used. Finally, we give the evolution of the nominal breakdown voltage as a function of the voltage ramp and this, for the three forms of applied voltage: AC-50Hz, DC + and DC-,**

Keywords—Impregnated paper, Pressboard paper, Borak22 mineral oil,Dielectric strength, Electric Aging, Weibull model, Breakdown, Kolmogorov-Smirnov adequacy test.

I. INTRODUCTION

The pressboard has many possibilities of applications in the manufacture of transformers, but also that of electric motors under low thermal stresses. Although, when this paper is impregnated, its resistance to electrical voltage and its dielectric properties are greatly improved [1].

However, even if this insulation pressboard paper impregnated has serious advantages and not negligible both technically and economically, the fact remains that this material has some disadvantages, among which we can quote significant dielectric losses from a certain value of the operating voltage. Thus, the knowledge of the dielectric strength of this material is essential to size and use this dielectric material in a medium or high voltage device. [1].

This work deals with the effect of the applied voltage form and its rise rate on the breakdown voltage of paper pressboard plates impregnated in Borak insulating oil.

Nevertheless, the dielectric breakdown is a random phenomenon, therefore it is necessary to make the experiments on a large number of samples. The most widely used statistical model for the fracture characterization of solid insulators is the Weibull model [2].

II. EXPERIMENTAL TECHNIQUES

A. Material studied

The pressboard paper, which was the subject of our study was provided by the Electro-Industrial Company (Algeria). Its thickness is of the order of 500 µm. Before the tests, the samples were conditioned in a desiccator with silicone gel, for at least 24 hours in order to eliminate any presence of moisture. Then these samples were impregnated in Borak22 oil for at least a week.

B. Experimental devices

For the measurement of the AC voltage breakdown voltage, we used the device shown in the figureFig. 1, comprising the following elements:

- A voltage source consisting of a transformer HT (T100) 0,8/135 kV; capable of delivering a voltage from 0 to 100 kV for AC testing and from 0 to 135 kV DC and an automatic and manual control unit with multiple ramp up rates,
- A capacitive voltage divider (C_0=0,1µF and C_u=41,4µF) for AC voltage measurements. For DC voltage measurements, we will use a resistive voltage divider (R_0=0,1 MΩ and R_u=250 MΩ),
- An AC/DC peak voltmeter (V) of type MU11, with digital display for measuring, according to the electrical installation, high AC or DC voltages.
- A protective resistor R_a=106kΩ current limiting,
- A support for the test tube and electrodes,
- A cylindrical plane electrode in bronze,
- The cylindrical flat earth electrode made of bronze,
- Finally, the device-sample assembly is surrounded by a protective cage.

For the measurement of the DC voltage breakdown voltage, we have used the device shown in Fig. 2, comprising the same elements as the previous device, except that in place of the capacitive divider, a resistive divider associated with a smoothing capacitor and a high voltage diode type G270

(HVD) is used. The mounting direction of this diode will determine the type of polarity of the voltage.

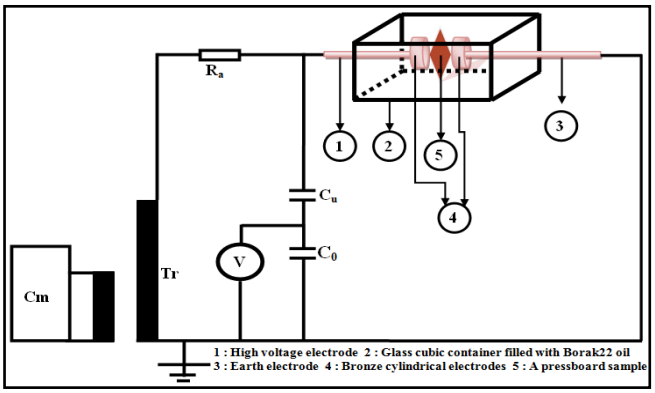

Fig. 1. Device diagram of breakdown tests under sinusoidal alternating voltage

We would like to point out that these two devices are in the High Voltage Laboratory of the University of Bejaia.

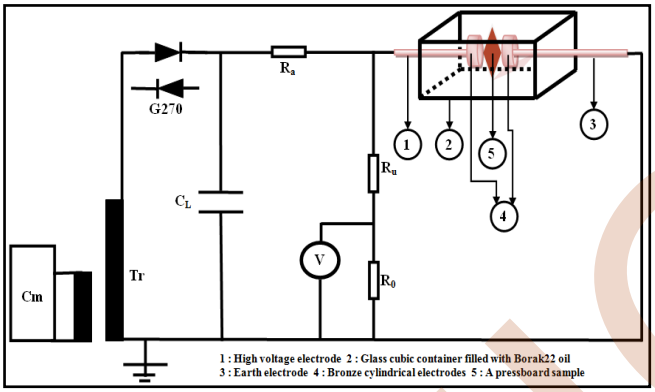

Fig. 2. Device diagram of breakdown tests under *DC voltage*

C. *Test procedure*

The tests consist of placing the sample considered between two flat electrodes in bronze and apply a constant speed voltage ramp to the breakdown. After breaking, we read the value of the breakdown voltage.

The tests were carried out at different voltage ramp rates: 0.69; 1.07; 1.4; 1.89; 2.38; 2.94; 3.28 and 4.17 kV / s.

The tests are held in the open air and the ambient temperature of the laboratory, however, attempts have been made to reproduce the same conditions for all tests (normal conditions of temperature, humidity and pressure).

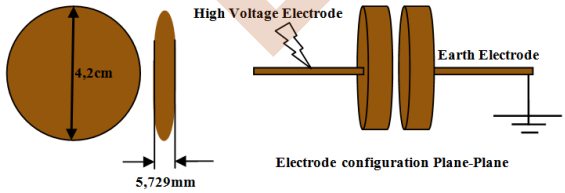

Fig. 3. *Configuration and dimensions of the electrodes useds*

The tests are carried out under three forms of voltage: sinusoidal alternative, continuous of positive polarity and continuous of negative polarity. And for each voltage form, eight voltage ramp rates are used and for each ramp rate of each voltage form; 35 samples pressboard paper are used and tested, giving a number of 840 measuring points obtained.

III. RESULTS

A. *Statistical treatment*

For the treatment of the measurement results obtained during the breakdown tests, we have chosen: The Weibull statistical model [2-7]. The equation of this two-parameter model, suitable for the study of rupture voltages, is written in the following form:

$$P(U) = 1 - \exp\left[-\left(\frac{U}{U_b}\right)^{\beta}\right] \quad (1)$$

With:

P (U): probability of failure,
U: measured breakdown voltage,
β:shape parameter,
Ub:nominal breakdown voltage which represents the scale parameter and which corresponds to a probability of 63.2%.
This probability of rupture is calculated by the formula of the median ranks given by the following equation [8,9]:

$$P(i, N) = \frac{i-0.3}{N+0.4}\ 100\% \quad (2)$$

With:

i: Rank of breakdown values,
N: Number of samples tested.

For the estimation of Weibull parameters and the smoothing of experimental points, the maximum likelihood method [2,4,10] was chosen, and confidence intervals [2-4,11-14] were considered. at 95%.

Finally, the Kolmogorov-Smirnov adequacy test [2,4,15-17] was used to validate and adjust the statistical processing results obtained.

B. *The two parameter Weibull diagram*

The results are presented in a system of axes, giving $Y_i = \log\mathrm{Ln}(\frac{1}{1-P_i})$ as a function of $X_i = \log U_i$. Where: U_i is the breakdown voltage and P_i is the cumulative probability of failure.

Thus, of Fig. 4 to Fig. 11, the two-parameter Weibull graphs are represented by the rupture values of our samples.

In the figures below (Fig. 4 to Fig. 11):

AC-50Hz:sinusoidal alternating voltage,
DC+:positive polarity of continuous voltage,
DC-: negative polarity of continuous voltage,
Si:applied voltage ramp speed.

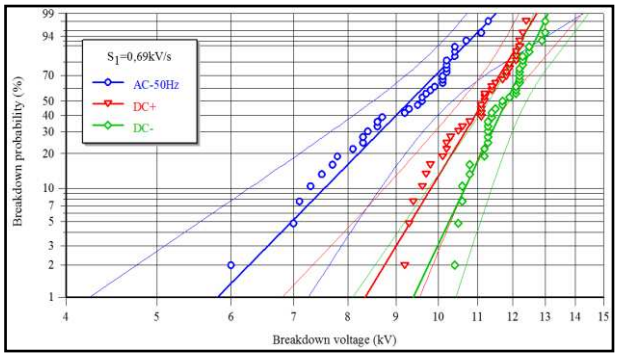

Fig. 4. *Weibull diagram for a speed ramp of 0,69 kV/s*

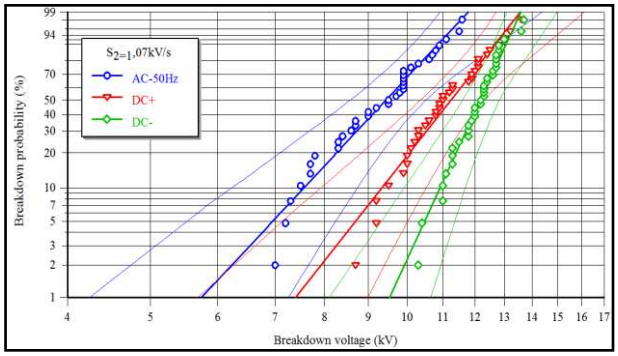

Fig. 5. *Weibull diagram for a speed ramp of 1,07 kV/s*

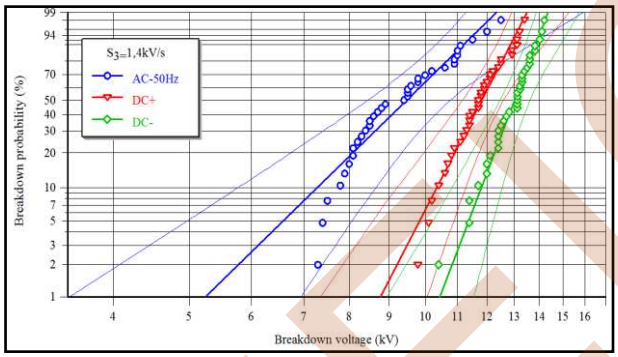

Fig. 6. *Weibull diagram for a speed ramp of 1,4 kV/s*

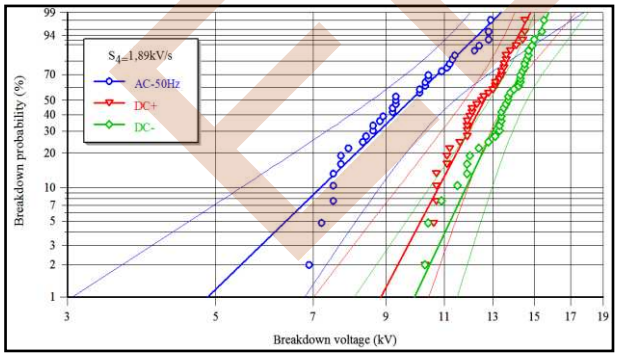

Fig. 7. *Weibull diagram for a speed ramp of 1,89 kV/s*

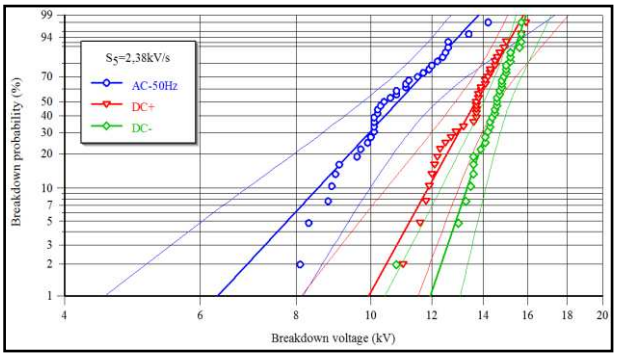

Fig. 8. *Weibull diagram for a speed ramp of 2,38 kV/s*

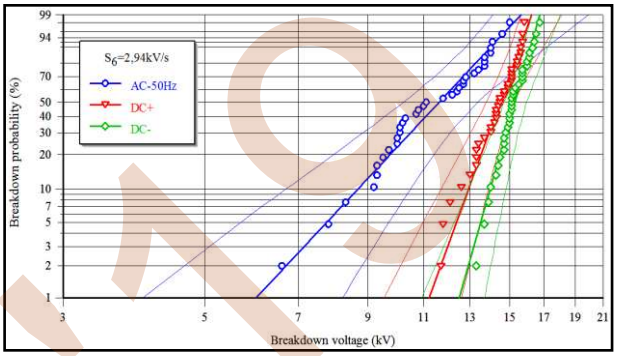

Fig. 9. *Diagramme Weibull diagram for a speed ramp of 2,94 kV/s*

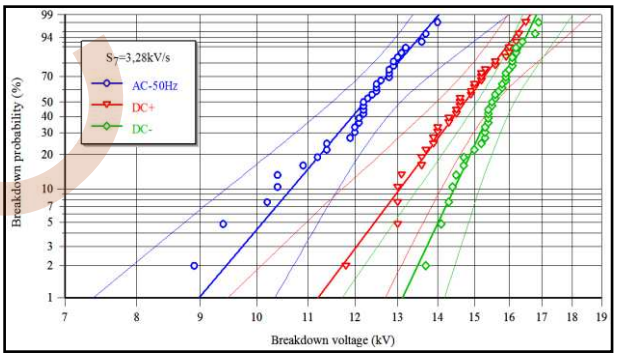

Fig. 10. *Weibull diagram for a speed ramp of 3,28 kV/s*

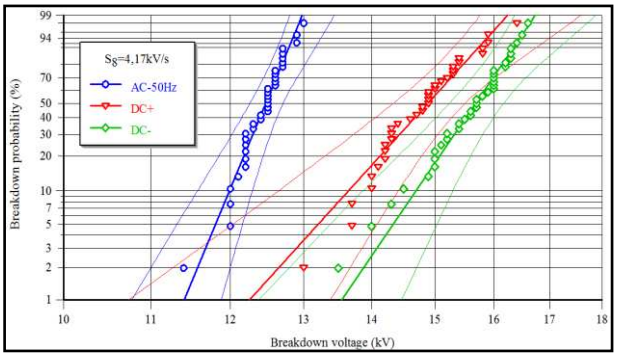

Fig. 11. *Weibull diagram for a speed ramp of 4,17 kV/s*

We find that for all these Weibull diagrams are partially or totally within the confidence intervals indicated by fine lines.

The width of these intervals is greater for lower failure probabilities.

For all voltage levels, there is no low probability point on the left of the confidence interval, so the search for a threshold of breakdown is not justified. It would therefore be logical to be satisfied with two-parameter Weibull plots rather than three parameters.

C. Statistical treatment results

In the tables below, are worn all treatment results of statistical breakdown tests.

TABLE 1. PROCESSING UNDER RAMP OF SINUSOIDAL ALTERNATIVE VOLTAGE

AC-50Hz			
Voltage ramp (kV/s)	**Shape parameterβ**	**Breakdown voltageU_b(kV)**	**Kolmogorov-Smirnov test $P_{K\text{-}S}$**
0,69	8,93	9,72	0,056
1,07	8,53	9,86	1
1,4	7,16	9,97	1
1,89	6,05	10,40	0,119
2,38	7,85	11,36	1
2,94	6,42	12,31	1
3,28	13,72	12,56	0,058
4,17	47,61	12,57	0,21

TABLE 2. PROCESSING UNDER RAMP OF CONTINUOUS VOLTAGE ONPOSITIVE POLARITY

DC+			
Voltage ramp (kV/s)	**Shape parameter β**	**Breakdown voltage U_b (kV)**	**Kolmogorov-Smirnov test $P_{K\text{-}S}$**
0,69	14,49	11,46	1
1,07	10,12	11,66	1
1,4	14,21	12,13	1
1,89	11,87	13,02	1
2,38	13,24	14,08	0,055
2,94	16,64	14,80	1
3,28	15,52	15,09	1
4,17	21,79	15,13	1

TABLE 3. RESULTS OF STATISTICAL PROCESSING UNDER RAMP OF CONTINUOUS VOLTAGE ON NEGATIVE POLARITY

DC-			
Voltage ramp (kV/s)	**Shape parameter β**	**Breakdown voltage U_b (kV)**	**Kolmogorov-Smirnov test $P_{K\text{-}S}$**
0,69	18,49	12,05	0,128
1,07	17,29	12,44	1
1,4	19,30	13,25	0,052
1,89	13,21	14,04	1
2,38	21,33	14,82	1
2,94	21,05	15,56	0,149
3,28	24,63	15,82	1
4,17	28,94	15,88	0,139

In the study of short-term electrical aging of polyethylene material, Chauvet has shown that the results are less dispersed when the form factor is large [18]. As a result, the distribution is more dispersed for the 0.69 kV / s speed under sinusoidal alternating voltage and less dispersed for the speed of 4.17 kV / s under negative polarity DC voltage.

The principle of adequacy tests is to compare the observed or derived distribution of the adopted model with the theoretical distribution of the test [14-17]. From the three tables (I, II and III), we note that the values of the Kolmogorov-Smirnov PK-S test are all without exception greater than 0,05. It is deduced that these tests are very favorable and confirm the results obtained with the two-parameter Weibull model.

D. Influence of the applied voltage ramp on the breakdown voltage of thepressboard paper impregnated in oil Borak22

From the three previous tables, we have drawn the characteristics giving the variation of breakdown voltage as a function of the speeds of the applied voltage for a sinusoidal alternating voltage (AC-50Hz) and a DC voltage with two polarities (DC + and DC-).

We obtain the curves in Fig.12:

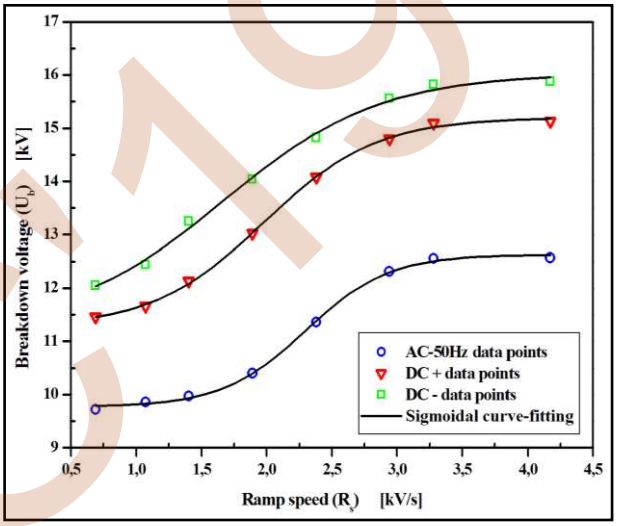

Fig. 12. *Breakdown voltage according to the ramp rates of the applied voltagefor a sinusoidal AC voltage and a DC voltage with two polarities*

Fig.12, shows the evolution of the nominal voltage breakdown depending on type and speed ofthe voltage ramp applied to the pressboard material impregnated in oil Borak 22.

IV. DISCUSSION

The three characteristics of Fig. 12, have the same shape and looks like the letter "S".This leads us to make the adjustment of the measuring points by the sigmoidal function, also known as the S-curve.

This function is written as follows:

$$f(x) = d + \frac{a-d}{1+(\frac{x}{c})^b} \quad (3)$$

With: a, b, c et d are constants to be determined experimentally.

Then, for the three types of applied voltage, we will have the following empirical equations:

$$\text{AC-50Hz} : U_b = 12{,}686 + \frac{9{,}823-12{,}686}{1+(\frac{S_i}{2{,}304})^{7{,}277}} \quad (4)$$

$$\text{DC+} : U_b = 15{,}347 + \frac{11{,}481 - 15{,}347}{1+(\frac{S_i}{2{,}304})^{4{,}738}} \quad (5)$$

$$\text{DC-} : U_b = 16{,}291 + \frac{11{,}891 - 16{,}291}{1+(\frac{S_i}{1{,}872})^{3{,}276}} \quad (6)$$

Under sinusoidal alternating voltage and positive voltage of positive polarity, we find that the breakdown voltage increases first linearly for low speeds. Beyond a speed of 1,75 kV/s, the breakdown voltage increases and takes an exponential formand then as one might expect,tends to a certain saturation from the rate of 3,2 kV/s.

Under continuous negative polarity, the characteristic U_b=f(S) is different from the other two characteristics. It increases linearly from 0,6 kV/s to 3 kV/s. Then, beyond this value, there is some saturation.

Note also that for the three forms of applied voltage, the highest breakdown voltage corresponds to the highest ramp rate. These voltages are greater in the case of a negative polarity DC voltage than in the case of a positive polarity voltage. So what are less important when applying a sinusoidal alternating voltage.

During the conditioning time which occurs the accumulation of defects and loads causing breakage,the ramp speed of the voltage applied to the insulation plays an important role on its breakdown voltage.

The increase of the breakdown voltage with the ramp speed of the applied voltage, can be explained by the time required for the accumulation of defects and / or charges leading to a breakdown of the insulation.This phenomenon was reported by Jonscher and Lacoste [19] and confirmed by Fanggao Cheng [20], who indicated that the breakdown voltage tends to be higher for the higher speeds of the ramp.Indeed, the insulation is subjected to the cumulative action of the electric field and time [2,4,21].It can be said, simplifying, that it is an illustration of the combined action of field and time, that is to say of the amplitude and duration of the stress.Thus, the increase in the stiffness of the ramp decreases in some way the time allowed for incubation and increases the amplitude of the breaking field at least as long as it does not reach the so-called intrinsic breakdown of the material that occurs. a progressive way [2,4,20,21].

We can see that the breakdown voltage under DC voltage ramp is higher than those obtained for the AC voltage ramp, and are higher under negative polarity than those under positive polarity voltage.These results are consistent with what is found in the literature; the work done on solid insulators has shown that the breakdown voltage under DC ramp is higher than that obtained under AC voltage ramp [22-26].Undoubtedly,the phenomenon is attributed to some extent to energy dissipation due to fatigue caused by alternating stress [23,27].

The breakdown voltage under continuous voltage ramp, depends on the polarity [2,4,21,23,27-33].This phenomenon can be explained by the fact that the amplitude and the space charge distribution between the electrodes depends on the polarity of the applied voltage [2,4,19,21].The same thing has been found in work on liquid-solid compounds.Narasaki et al [31-33], reported that under positive polarity, the breakdown of the composite insulation is caused by the degradation initiated in the oil.On the other hand, in negative polarity the cause of the rupture is due to the presence of space charge in the solid insulator.The same phenomenon was observed during breakdown voltage measurement on polyvinyl chloride sheaths [2,4,21].

It is noted that the breakdown voltage tends towards a certain saturation which corresponds to substantially higher speeds.This phenomenon is probably obtained because of the existence of the greatest number of defects in the material as well as their nature.It may be thought that the breakdown voltage is very much related to the structure of the material and to one of its intrinsic defects [2,4,21].

V. CONCLUSION

The purpose of this study,was to verify and study experimentallythe influence of the voltage rise and the voltage waveform applied to the breakdown voltage of paper pressboard impregnated into the Borak 22 oil used in power transformers.

After completing the breakdown tests, a total of 840 measurement points were obtained. These have been the subject of a statistical analysis.

Weibull model chosen for treatment of breakdown resultssince it is the best and most used in the field of dielectric breakdown of solid insulators.On the other hand,the maximum likelihood method,because they exist within the same series of breakdown measurements, values that are repeated.

For all tests on the dielectric breakdown of the material studied,no low-probability point goes out to the left ofthe confidence bands,so researcha rupture thresholdis not justified. The two-parameter representation of the Weibull model proved to be the most adequate than the three parameter one. As a result, the rupture threshold is zero during these tests.

The dispersion of rupture values can probably be explained by the presence of large defects within the insulation studied.As a result, this dispersion imposed 95% confidence intervalsto identify the points with low probabilities whose dispersion is large.Moreover, this statistical character could be explained by the existence of heterogeneities and / or local microscopic defects in the dielectric material.

The results of theadequacy testwere favorable, and the choice of the Kolmogorov-Smirnov test is justified by the average number (≤ 35) of specimens of the tested paper during the same series of measurements.

The median rank method is used for plotting Weibull diagrams, and for estimating the various parameters of this law,the maximum likelihood method has been used.

We have shown in this work that dielectric breakdown is a random phenomenon that always results in the formation of preferential paths with high conductivity. The conditions in which it develops depend on the configuration of the electric field, the level of the ramp speed and the form of applied voltage.

The results show that the rise speed of the voltage ramp has a considerable influence on the breakdown voltage. Indeed, for the low speeds of the ramp, the breakdown voltage increases linearly. For higher speeds, there is an exponential shape variation. Finally, a saturation plateau was found beyond a speed of 3,5 kV/s.

The breakdown voltage of the studied material is greater in the case where a DC voltage is applied than that obtained in alternative, even greater if the polarity of the DC voltage is negative.

REFERENCES

[1] C. Bouvier, l'histoire du papier, édition Brepols, Paris, 1994.

[2] A. Laifaoui, J.M. Reboul, M.S. Herzine and al: "Breakdown strength measurements on cylindrical polyvinyl chloride sheaths under AC and DC voltages" Dielectrics and Electrical Insulation, IEEE Transactions on, 2014, vol. 21, no 5, pp. 2267-2273.

[3] M. Nedjar, "Evaluation de la tenue diélectrique à court et à long termes des polymères utilisés dans les dispositifs haute tension", Thèse doctorat, Université de Tizi Ouzou, Algérie, 2003.

[4] A. Laifaoui, "Etude de la tenue diélectrique des gaines en polychlorure de vinyle sous tension alternative et continue", Thèse doctorat, Université de Bejaia, Algérie, 2016.

[5] W. Weibull, "A statistical distribution function of wide applicability", J. Appl. Mechanics, Vol. 18, pp. 293-297, 1951.

[6] V. Englund, R. Huuva, S.M. Gubanski and T. Hjertberg, "High efficiency voltage stabilizers for XLPE cable insulation", Science Direct: Polymer Degradation and Stability No. 94, pp. 823–833, 2009.

[7] K. Wu, Y. Wang, Y. Cheng, L.A. Dissado and X. Liu, "Statistical behavior of electrical breakdown in insulating polymers", J. Appl. Phys., Vol. 107, 064107, pp. 064107-1-064107-6, 2010.

[8] Enis Tuncer, D Randy James, Isidor Sauers, Alvin R Ellis and Marshall O Pace, "On dielectric breakdown statistics", J. Phys. D: Appl. Phys. N°39, 2006, pp 4257–4268.

[9] L.A. Dissado and J.C. Fothergill, Electrical Degradation and Breakdown in Polymers, Collection: IEE materials and devices series, 9. Editor: G.S. Stevens, Peter Peregrinus Ltd, London, 1992.

[10] A.C. Cohen, "Maximum likelihood estimation in the Weibull distribution based on complete and on censored samples", Thechnometrics, Vol. 7, No. 4, pp. 579-588, 1965.

[11] J.F. Lawless, "Confidence interval estimation for the Weibull and extreme-value distribution", Thechnometrics, Vol. 20, No. 4, pp. 355-363, 1978.

[12] J.F. Lawless, "Construction of tolerance bounds for the extreme-value and Weibull distributions", Thechnometrics, Vol. 17, No. 2, pp. 255-261, 1975.

[13] G.C. Stone and R.G. Van Heeswijk, "Parameter estimation for Weibull distribution", IEEE Trans. Electr. Insul., Vol. 12, No. 4, pp. 253-261, 1977.

[14] P. Chapouille, R. de Paizzis, "Fiabilité des systèmes", Édition Masson, 1965.

[15] R. Lacoste, E. Loudghiri, J. Meric, "Sur la notion du gradient de seuil dans le phénomène de rupture diélectrique des isolants solides soumis à des rampes de tension", REG, 10/85, Octobre 1985, pp. 769-775.

[16] C. Chauvet, C. Laurent, "Weibull statistics in short-term dielectric breakdown of thin polyethylene films", IEEE Trans. On Elect. Insul., Vol. 28, N°1, February 1993,pp. 18-29.

[17] L. Simoni, "Dielecttrici proprieta e comportamento nel tempo", Universitaria Editrice, Bologna, 1974.

[18] C. Chauvet, "Mise au point d'une méthodologie pour les essais de rupture à court terme en vue de la caractérisation des isolants synthétiques", thèse de doctorat, Université Paul Sabatier, Toulouse, 1992

[19] A.K. Jonscher and R. Lacoste, "On a cumulative model of dielectric breakdown in solids", Electrical Insulation, IEEE Transactions on, no 6, 1984, pp. 567-577.

[20] F. Chang, "Electrical properties of flexible polypropylene based cable insulation materials", J MATER SCI 41, 2006, pp. 2037–2043.

[21] A. Laifaoui, J.M. Reboul, M. Aissou and al, "Study of the dielectric failure of polyvinyl chloride sheaths under AC and DC high voltages", International Conference on Electrical Engineering and Automatic Control, ICEEAC'2013, Setif, Algeria, 24-26 November 2013.

[22] W. Li, J. Li, F. Zhou, S. Wang, H. Li, S. Li, "The Effect of Frequency on the Breakdown of XLPE Cable Insulation with Artificial Defects", Electrical Insulation and Dielectric Phenomena (CEIDP), 2012 Annual Report Conference on. IEEE, 2012, pp. 375-378.

[23] M. Nedjar, Y. Mecheri, A. Lamure, M. Aufray, C. Drouet, "Effect of moisture on breakdown voltage of Polyesterimide used in electrical machines", Electrical Insulation and Dielectric Phenomena (CEIDP), 2010 Annual Report Conference on. IEEE, 2010. pp. 1-4

[24] S. Grzybowski, E.A. Feilat, P. Knight, L. Doriott, "Breakdown voltage behavior of pet thermoplastics at DC and AC voltages", Southeastcon'99. Proceedings IEEE. IEEE, 1999. pp. 284-287.

[25] E. Gockenbach, G. Schiller, "The breakdown behavior of XLPE samples at voltages of different shapes, ninth international symposium of high voltage engineering", august 28-septembre 1, 1995, pp 1493-1-1493-4.

[26] K. Katsutsa, A. Toya, S. Katakai, M. Kanoaka, Y. Sekkii, "Influence of defects on insulating properties on XLPE cable", 3rd international conference on properties and applications of dielelectric materials, july 8-12, 1991, pp. 485-489.

[27] J.P. Crine, "AC and DC electrical aging of polyethylene", Conference on Electrical Insulation and Dielectric Phenomena, 26 - 29 October 2008, pp. 60-62.

[28] J.P. Crine, "On the interpretation of some electrical aging and relaxation in solid dielectrics", IEEE Trans. DEI, vol. 12, 2005 pp. 1089-1107.

[29] J.P. Crine, "A molecular model for the electrical aging of PE", Proc. CEIDP, 2007.

[30] M. Nedjar, "Évaluation de la tenue diélectrique à court et à long termes des polymères utilisés dans les dispositifs haute tension", Thèse doctorat, Université de Tizi Ouzou, Algérie, 2003.

[31] N. Narasaki, K. Kudo, Y. Nitta, "Direct voltage breakdown of silicone oil/polymer film composite with needle/plane electrode system", IEEE Trans. on Elec. Insul. Vol. EI-19, 1984, pp. 354-358.

[32] I. Kitani, K. Arii, "Prebreakdown phenomena in silicone oil/PET film composite with point-plane electrode system", Trans. IEE of Japan, Vol. 108, 1989, pp. 1-5.

[33] M. Nagao, S. Jayaram, M. Sugio, M. Kosaki, "Breakdown Characteristics of Oil-polymer Composite Insulation under AC and DC Voltages", Proceedings of 13Ih International Conference on Dielectric Liquids (ICDL '99), Nm , Japan, July 20-25, 1999, pp. 140-143.

Chemical and Electrical Characterization of Polyvinyl Chloride (PVC) Under Electrical Aging

E. Belhiteche[1,2*], M. Moudoud[2]
1- Département de Génie Electrique, université Med Boudiaf, M'sila, Algérie
2- Laboratoire des Techniques Avancées en Génie Electrique (LATAGE), université Mouloud Mammeri, Tizi-Ouzou, Algérie.
h.belhiteche@yahoo.fr

S. Rondot[3], O. Jbara[3]
3- Laboratoire d'Ingénerie et Sciences des Materiaux (LISM), Université Champagne-Ardennes, Reims, France

Abstract **– Polyvinyl chloride is one of the most polymers used in electrical cable insulation. It has a greater resistance to moisture and abrasion and an excellent resistance to high temperature and good mechanical properties.**
However under the action of electric field, the surface of the polymer is degraded. This degradation caused by irreversible changes in the material can rapidly shorten lifetime. The chemical reactions occurring in the process are: cross-linking reactions between the chains, oxidation, hydrolyses...etc. The kinetics of degradation depends on the concentration of the different constituents of the polymer. This paper presents an experimental study the effect of electrical aging on surface degradation of the polyvinyl chloride. We have subjected the samples (PVC) to AC voltage in plane-plane electrodes geometry during 10 hours. The PVC material used in the present investigation is employed as insulation for medium voltage (MV) cables (18/30 kV). The goal of this paper was to investigate the degradation of PVC insulation under electrical aging effect by characterization techniques. For this purpose, measurements of dielectric losses factor, relative permittivity, and volume resistivity were performed for each applied voltage as a function of aging time and frequency (1 Hz – 10^7 Hz). Based on the obtained results, the electrical aging influences slightly the dielectric constant. However, we observed a significant degradation of the used material (PVC) under the aging conditions abovementioned. This degradation is characterized by the dissipation factor increase and the decrease of volume resistivity. Morphology and surface chemistry of the PVC before and after aging were also investigated through scanning electron microscopy (SEM) and Fourier transform infrared (FTIR) spectroscopy, respectively. Aging had a significant impact on the surface of specimens. The un-aged sample had a smooth and homogenous surface. However, after the ageing test, it was found that damages caused by electrical stress occurred at the surface and craters were exhibited.

Keywords — Aging, electrical properties, FTIR, PVC, SEM.

I. INTRODUCTION

The insulating polymers have important assets then the classical ones, as the glass, porcelain and the impregnated paper, they have the best mechanical properties, a weaker wet ability, to be more easily lighter and set in work [1]. However, they present the inconvenience to be more vulnerable to the surface discharges that cause their deterioration [2]. A discharge that appears in the surface of the polymer constitutes a factor of ageing responsible for the destruction of the insulation[3], where, the physical and chemical processes are not very known again [4,5].
In the present work, we will put in evidence the effects of electric ageing on the deterioration of PVC surface using different methods of characterization.

II. EXPERIMENTAL SETUP

Fig.1. shows the experimental setup used in our study. The electric discharges have been gotten by nourishing the two electrodes with an alternating voltage delivered by a transformer whose features are :
U = 100 kV, f = 50 Hz, P = 10 kVA.
The voltage variation was obtained with an auto-transformer placed in the control desk.

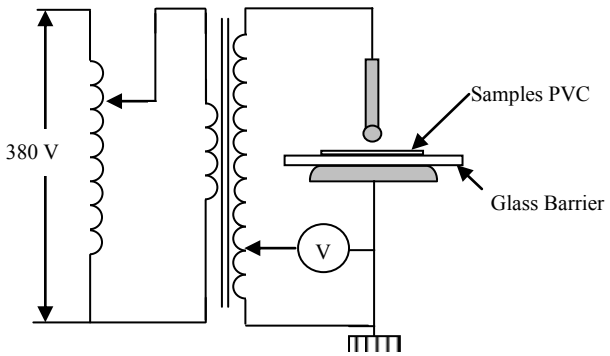

Fig.1. experimental setup

III. RESULTS AND DISCUSSION

In our analysis, we have used two kinds of polymer samples: plates of 3 mm thick and PVC's films of a few microns thick, for FTIR analysis.
We studied the effect of electric ageing on the permittivityε_r, the loss factor tgδ and the resistivity of PVC according to the frequency in the range of 500 Hz to 10 Hz.
The permittivity is deduced from the measurement of the capacity using the following relation:

$$\varepsilon_r = \frac{e.C}{S.\varepsilon_0} \qquad (1)$$

with
e : sample thickness (m)
C : capacity between two electrodes (C)
ε_0 : the permittivity of vacuum, ε_0= 8,85 10^{-12} F/m
S : the sample surface (m^2)

The resistivity is deduced from the measurement of the capacity using the following relation:

$$\rho = R.\frac{S}{e} \qquad (2)$$

with :
e : sample thickness[m]
S : the sample surface [m^2]
R : resistance between the two electrodes[Ω].

A. dielectric spectroscopy

Figures 2, 3 and 4 show the influence of the frequency and duration of aging on the dielectric properties of PVC. The samples were aged under an electric field of 5 kV / mm. The increase in frequency and duration of application of the electrical stress induces a significant decrease of relative permittivity, and the resistivity, but the increase of the dielectric loss factor in time.

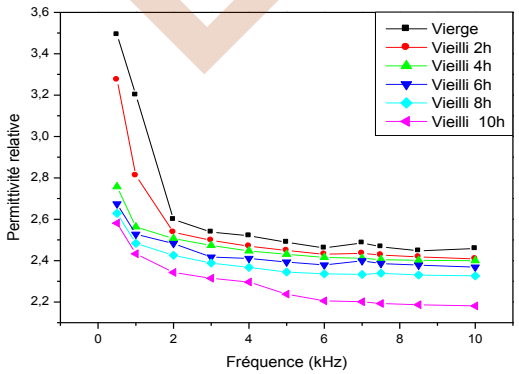

Fig.2. Variation of the relative permittivity as a function of the frequency and time of aging

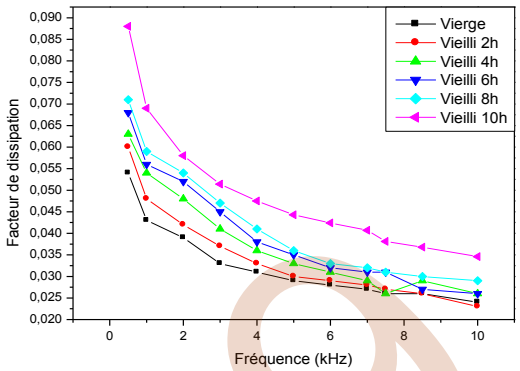

Fig.3. Variation of the dielectric loss factor as a function of the frequency and time of aging

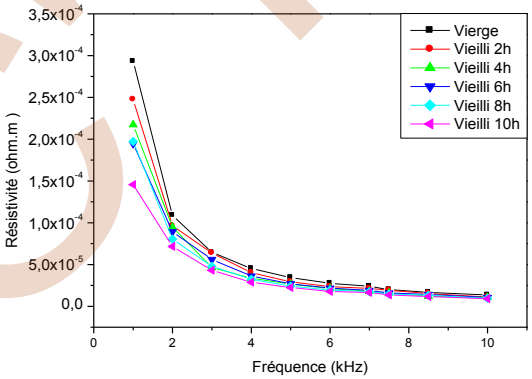

Fig.4. Variation of the resistivity as a function of the frequency and time of aging

We note that the dielectric constant decreases with increasing frequency, the curves have the same hape . The increase in aging time is accompanied by a reduction of the permittivity. This can be explained by the rearrangement of the molecular structure and the reticulation phenomenon.
We find that tgδ decreases with increasing frequency and it increases with the application of stress duration (electric field) .
The elevation of the dielectric depertes factor can be explained by the decrease in the viscosity of the polymer, thus high mobility of the charge carriers on the one hand , [6] and the oxidation phenomenon that leads to the formation of compounds carbonyl [7] .
We note that the resistivity decreases with increasing frequency. We observe that increasing the aging time is accompanied by a decrease in resistivity. This can be explained by the injection of charge carriers from the electrodes.

B. FTIR Analysis

Analysis by infrared spectroscopy Fourier transform were made using a Shimadzu type apparatus 8400. They give us the chemical transformations undergone by the sample: appearance or disappearance of functional groups under the effect of electrical discharges.
The results are shown in Figure 5.

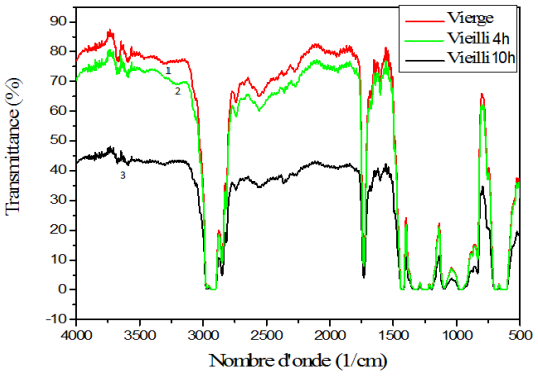

Fig.5 FTIR spectrum of PVC

Figure 5 shows that after 4 hours of aging, there is the disappearance of the peak 1 (3300 cm^{-1}) corresponding to intermolecular OH group and appearance of peak 2 (3150 cm^{-1}) corresponding to intermolecular CH group, thus there is rupture of the OH bond and the birth of the CH bond. After 10 hours, the chemical structure of PVC has changed disappearance of the peak 2 and decrease in the intensity of the peaks 3 due electrical discharges.

C. Observation with a scanning electron microscope (SEM)

Visual observation of the samples showed a change in color of the regions subjected to discharge.
The topography of these regions was observed with a scanning electron microscope (SEM) brand Philips XL30 JOEL tungsten filament.
For the analysis of insulating samples we used it in environmental mode to not metalize the observed surfaces as required in conventional SEM. The electron beam acceleration voltages can vary from 0.2 to 30kV according to the desired depth of analysis. Voltage 20kV corresponds to a depth of about 1à10µm.

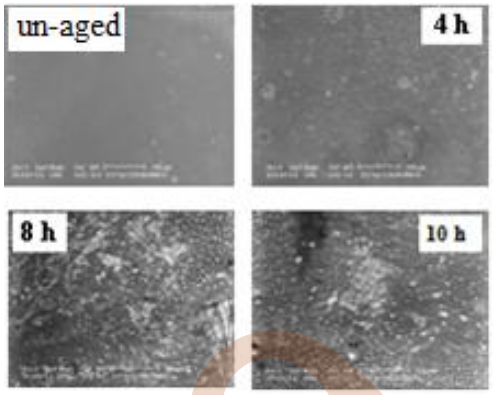

Fig. 6. SEM micrographs of PVC

Figure 6 shows micrographs of samples of PVC. The blank sample has as mooth, homogeneous surface free from any degradation, while samples submitted to the electric field show areas that have been adversely affected. Craters are born and grow to the sample surface. We also note the presence of white dots indicating the degradation of the material.

IV. CONCLUSION

The duration of the applied stress (electric field) and the high frequencies affect the dielectric properties of the material studied. FTIR analysis showed the existence of water molecules attached to the surface of PVC under the effect of molecular forces of attraction, as we observed the hydroxyl OH formation and disappearance of the CH group. The physicochemical transformations cause a decrease of the dielectric insulating properties of the surface, which can promote the development of the craters.

V. REFERENCES

[l] R. Hackam, "Outdoor HV Composite Polymer Insulators", IEEE Transactions on Dielectrics and Electrical Insulation, Vol.6, N°5, pp. 557-585, 1999.

[2] R. Bartnikas, "EngineeringDielectrics – Vol. I: Corona Measurement and Interpretation", ASTM Press, Philadelphia PA, 1979.

[3] A.J. Philips, D.J. Childs and H.M. Schneider, "Water drop corona effects on full-scale 50kV non-ceramic insulators" IEEE Transactions on Power Delivery, Vol.14, pp. 258-265, 1999.

[4] G. Zhang, W. Zhao, Y. Sun and Z. Yan, "Surface discharge phenomena of silicon in atmospheric air" Annual Report Conference on Electrical Insulation and Dielectric Phenomena, 2003.

[5] M.A. Handala and O. Lamrous, "Surface degradation of styrene acrylonitrile exposed to corona discharge", European Transactions on Electrical Power, pp. 494-505, 2008.

[6] A. Schmitz, "Measuring the Distribution of Oxydative Damages (OH-groups) by the method of Fourier Transform Infrared Spectroscopy (FTIR) Attenuated Total Reflction (ATR) in Thin Polypropylene Films", IEEE International Symposium on Electrical Insulation, pp.36-39. Anaheim, USA, 2000.

[7] G. C. Montanari, "Chemical, physical and microstructural properties of thermally aged cables models", IEEE International Symposium on Electrical Insulation, pp. 764-768, 1988.

Modeling and Control of a Knee Orthosis for Gait Assistance

Bentounes Salima[a], Aitghezala Amel[a], Guiatni Mohamed[b], Achour Noura[a]

[a]FEI,Université des Sciences et de la Technologie Houari Boumedienne, Algiers ,salima-bent@hotmail.com
[a]FEI, Université des Sciences et de la Technologie Houari Boumedienne, Algiers,amelaitghezala@gmail.com
[b] Ecole Militaire Polytechnique, Algiers, mohamedguiatni@gmail.com
[a]FEI, Université des Sciences et de la Technologie Houari Boumedienne, Algiers, noura.achour@gmail.com

***Abstract*— This paper presents a solution to increase the autonomy of people with a motor deficiency affecting the mobility of the human knee. To do this we propose a motorized exoskeleton with one degree of freedom that can assist and reproduce the movement of the knee joint. The work is limited to the realization, modelling, identification and control of the exoskeleton. The system used is essentially composed of an elastic actuator, a gear chain and an electronic part. This latter includes a DSPACE 1103 card, a motor shield card and two position sensors. Two control strategies have been implemented PID for low level control and sliding mode for high level control.**

Keywords: Lower limb exoskeleton; elastic actuator; PID control; sliding mode control.

I. INTRODUCTION

Nowadays, assistive robotics has become a current topic for many researchers in order to find a solution for people with a motor deficit. Japan is the most mobilized on research in this field after having noted that since 2006 the population over 65 years old exceeds 20% and that by 2060 this category will reach up to 40% [1]. The METI (Ministry of Economy, Trade and Industry, Japan) has also given great importance to this subject, it has launched several projects such as: "Humanoid Robot Project" in 1998 and the "21st Century Robot Challenge" in January 2001[2].

For this work we are particularly interested in exoskeletons for the assistance of the knee joint where several works have been carried out on this subject. We have the "Roboknee exoskeleton" made by the Institute of Human and Machine Cognition in the United States. It consists of a mechanical structure and a series elastic actuator controlled by a PD controller, the intent of the operation is identified with force sensors and measurement of the knee angle [3].
There is also the exoskeleton" ELEGS" developed by a team from the University of Berkeley, this one is made with elastic actuators arranged at the hips and knees limited by stops. The reference signal is identified using an IMU sensor and executed with a PID controller [4].

The aim of this work is to model and control a knee orthosis device that can assist and reproduce the movement of a human knee by using an elastic actuator. The controlled device must be usable for the mobility assistance for people suffering from a motor disability affecting the knee joint. In this paper, the device is modeled and controlled using both the traditional PID controller and sliding mode controller.

II. EXOSKELETON DESIGN

The exoskeleton (orthosis) imitate the shape of the human knee (Figure 1). It consists of two parts, a structure that covers the elastic actuator and a long segment that will hold the user's leg.The realization is done under certain conditions so that the device is light, not cumbersome and easy to use.

Figure 1: Realized Knee exoskeleton.

A. *Rotary Elastic actuator*

The design of our exoskeleton is actuated using a designed elastic actuator (Figure2). This later is a combination of a conventional actuator and a torsion spring. It offers a low impedance and very low friction which allows to get a high quality force control. A gear chain is integrated (Figure 3) to amplify the the motor resulting torque and allow the exoskeleton to lift the weight of a leg.

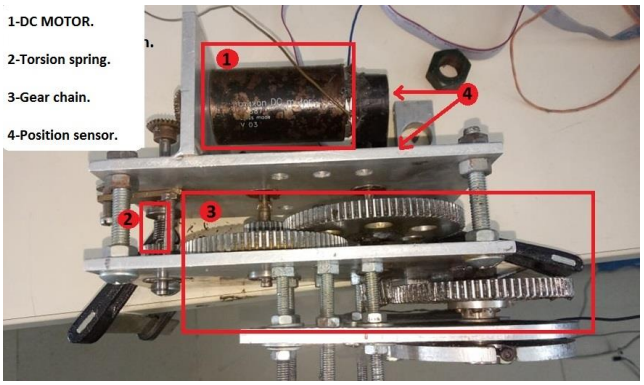

Figure 2: Real picture of the actuator used.

The motor chosen is a DC electric actuator from Maxon RE40 with a power of 150w [5].

A spring is integrated between the actuator and the gear chain, it reproduces the movements of the human body by reducing the rigidity of the system, it offers a high tolerance to shocks, a lower reflected inertia, a more precise stable force control and an energy storage capacity.

B. *Gear chain:*

A gear system is installed to amplify the torque at the spring output. The power transmission kinematics is shown in Figure 3

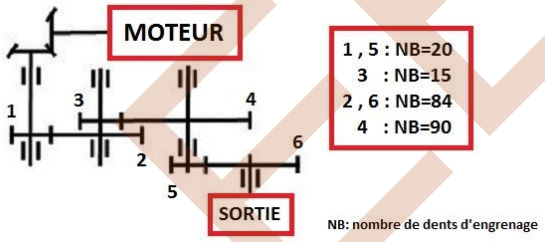

Figure 3: Gear chain.[6]

Starting from the motor, the reduction ratios are:

$$\frac{NB(2)}{NB(1)} = 4.2 \;|\; \frac{NB(4)}{NB(3)} = 4.5 \;|\; \frac{NB(6)}{NB(5)} = 5.6 \qquad (1)$$

This brings us back to a total reduction ratio of 105.84 which allows to reach a torque of around 18 N.m:

C. *Architecture of the devise*

In order to use the exoskeleton in real time, a system is set up as shown in Figure 4.

Dspace real time toolbox under Simulink from the Matlab software are used to implement the controllers. A DSPACE1103 control board is used as hardware for acquisition and control, which receives all the necessary information on the state of the exoskeleton using the position and current sensors. The board will execute the program and send the instructions to the shield motor board that the motor will have to follow in order to execute the desired trajectory.

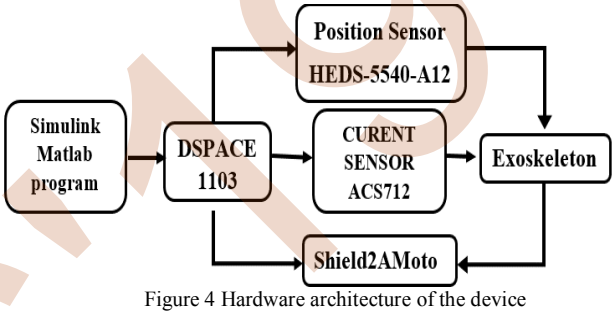

Figure 4 Hardware architecture of the device

III. EXOSKELETON MODELING AND IDENTIFICATION

A. *Geometric model*

1) *Direct geometric model*

The direct geometric model is the relationship between the operational coordinates of the terminal organ and the joint coordinates, the calculation of this model is done with the modified denavith-hardenberg method.

The figure 5 shows the gometric description of the exoskeleton we used for the modelling.

The generalized coordination vector will be p[x,y]

$$\begin{cases} x = l\cos\theta \\ y = l\sin\theta \end{cases} \qquad (2)$$

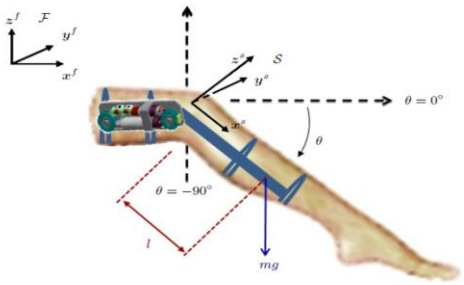

Figure 5: Geométric description of the exoskeleton.

2) Inverse geometric model:

The inverse geometric model determines the configuration of the links (rotation, translation) according to the configuration (position and orientation) of the terminal element. The calculation of this model is done using a system of trigonometric equations.

$$\theta = \tan^{-1}\left(\frac{X}{Y}\right) \quad (3)$$

B. Kinematics model

1) Direct kinematics model

The direct kinematic model describes the speeds of the operational coordinates of the terminal organ according to the joint speeds, with $\dot{x} = J(q)\,\dot{q}$ where J (q) designates the Jacobean matrix. By applying the latest law we find:

$$\begin{cases} \dot{x} = -L\dot{\theta}\sin\theta \\ \dot{y} = L\dot{\theta}\cos\theta \end{cases} \quad (4)$$

2) Inverse kinematics model

The inverse kinematic model makes it possible to calculate the generalized velocity vector corresponding to a given translation and rotation speed of the terminal member.

The inverse of the direct kinematic model is used for model calculation:

$$\dot{\theta} = \frac{\sqrt{x^2+y^2}}{L} \quad (5)$$

C. Dynamic model

The dynamic model is a system of equations that make the relationships between the vector of generalized forces applied to the joints and kinematic parameters (Cartesian coordinates, velocities and accelerations)

$$\Gamma = f(q, \dot{q}, \ddot{q}, f_{ext}) \quad (6)$$

Γ: torque vector, Fext : external force and torque.

After calculating the Lagrange equation and defining the torques applied by the actuator, we find:

$$J\ddot{\theta} + mgl\cos\theta = \Gamma c + \Gamma f + \Gamma r + \Gamma z + \Gamma h \quad (7)$$

- $\Gamma f = -A sign\dot{\theta} - B\dot{\theta}$ Friction torque
- A : solidity coefficient. B : viscosity coefficient.
- $\Gamma r = C(\theta - \theta r)$ stiffness Torque (human knee)
- C: stiffness coefficient, θr : Knee rest position.
- Γz=K(θm-θsr) Torque amplified by the spring
- K: spring stiffness constant, θm : motor angle, θsr spring output angle.
- Γc : Control torque
- L: gear reduction ratio
- Γh Human couple considered as disturbance
- J: moment of inertia (knee + orthosis)
- m : mass (knee + orthosis), g: gravity, T=mgl

IV. IDENTIFICATION OF THE DYNAMIC MODEL

In order to facilitate the identification of the model we will divide it into two sub- models, one representing the human knee and the other the exoskeleton (orthosis) [7].

A. Knee model

$$Jg\ddot{\theta} + Tg\cos\theta + Ag\,sign(\dot{\theta}) + Bg\dot{\theta} + C(\theta - \theta r) = 0 \quad (8)$$

To identify the anthropometric parameters of the human body such as: mass (M), length (l), positions of center of gravity (CoG) and inertial propertie (J) of the body segment, we use winter's regression equations.

The rest of the parameters are identified with the free pendulum experiment (figure 6) and the least squares method. [8]

The knee angle is measured thanks to a potentiometer. The output value is then converted to degrees. The angle output is depicted in figure 7.

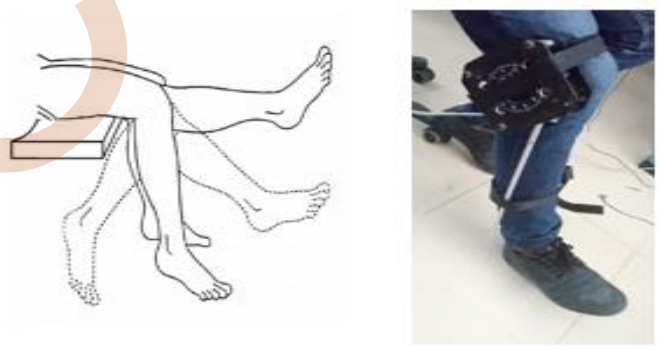

Figure 6: Free pendulum experiment.

After application of the least squares method on a male subject with: age=24, weight=1.74m, weight=68kg.

Table 1: Identified parameters of the knee model

Parameters	values
Tg	12.2285 N.m
Ag	0.2296 N.m
Bg	0.013 N.m.s/rad
Jg	0.5511 kg.m2
C	0.6834 N.m/rad

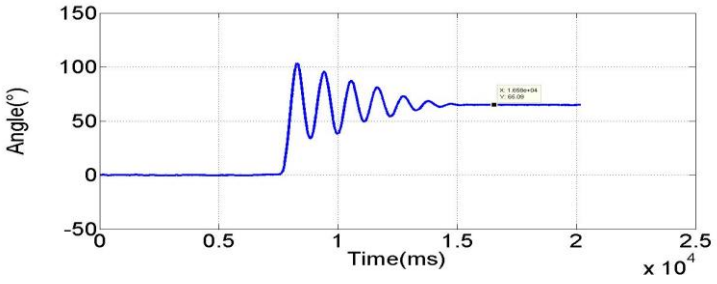

Figure 7: Angular response of the free pendulum experiment applied to the knee

B. *Exoskeleton model*

$$Jo\ddot{\theta} + To\cos\theta + Ao\,sign(\dot{\theta}) + Bo\dot{\theta} + K(\theta m - \theta s) = \Gamma c \quad (9)$$

For the identification of the exoskeleton we excite the system by a signal SBPA (pseudo-random binary sequence), rich in frequencies and amplitude which allows to test the dynamics of the system.
The angular position and the resulting torque of the actuator are used as data to apply the least squares method.

parameters	values
To=mglo	0.1528 N.m
Ao	0.2293 N.m
Bo	0.0989 N.m.s/°
Jo	0.006 kg.m2
K	0.00193 N.m/°

Table 2: Identified parameters of the exoskeleton model.

C. *Model validation*

In order to continue the work and move to the control step, we must first validate the model found. To do this, we compare an angular response taken from the real system with that compute with the model using the same input figure (8).
The model is validated with an average error of 0.1 °

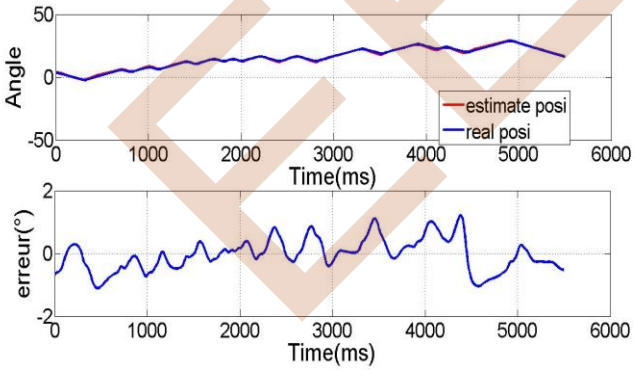

Figure 8: Comparison between the real response of the exoskeleton and that estimated with the model.

V. EXOSKELETON CONTROL

For the control of the exoskeleton we add a charge of 3kg which is the average weight of a human leg.

A. *PID control*

Often used in industry, the PID controller is a control element that allows the closed-loop system to follow a desired reference value with the objective of being robust, fast and precise.
The working principle of a PID is based on the calculation of the error between the reference and the measurement, the Control is based on the following actions:
- Proportional: a gain G is calculated and multiplied by the error.
- Derivative: the error is derived and then multiplied by a gain Td.
- Integral: the error is integrated and divided by an IT gain.

The controller used is based only on the proportional action with G=0.6, the integral action is already integrated in the system since the control is in position. The derivative action is not used because of the inconvenience of amplifying the disturbances it can cause.
Figures 9 and 10 represent the system response for a trajectory of a flexion extension cycle with no load and under load, the average error is calculated Enc=1.39°, Ewc=1.17°
The exoskeleton has followed the trajectory well with the presence of some disturbances due to the mechanical system that affected the output signal, this also comes back to the sensitivity of the PID control to disturbances.

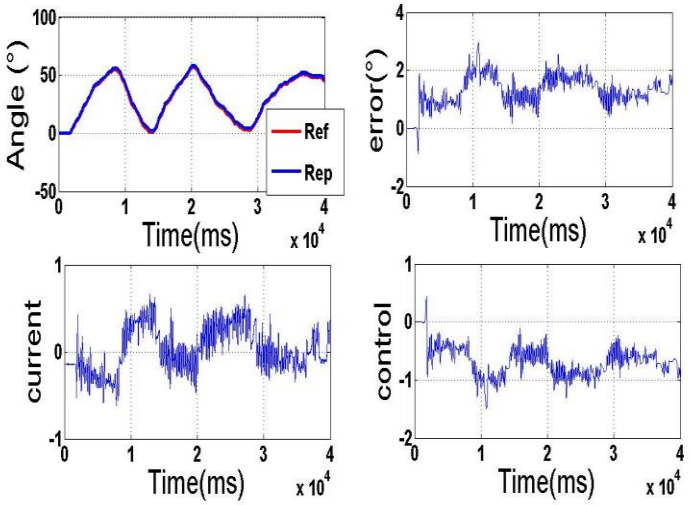

Figure 9: System response to a reference of a knee extension flexion signal with proportional correction.

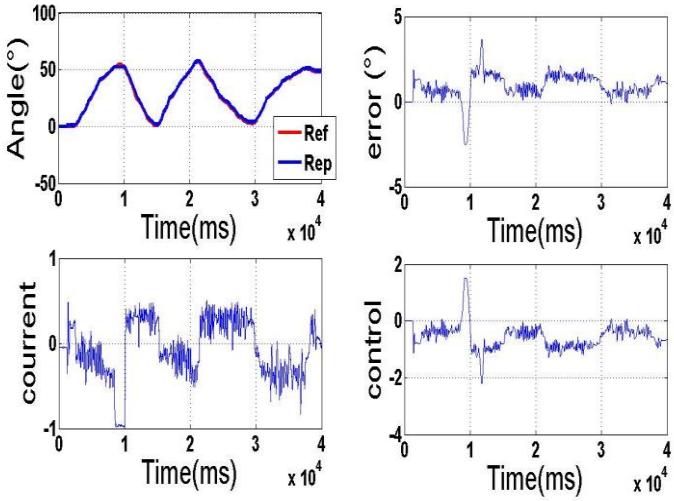

Figure 10: System response to a reference of a knee extension /flexion signal with proportional correction (with a 3Kg load).

B. Sliding mode control

Sliding mode control is a non-linear control used for systems exposed to disturbances; it consists in bringing the state path from a system to the sliding surface and switching it using an appropriate switching logic.

The sliding mode exists when the switching takes place continuously between the two parameters Umax and Umin[9]. The control law injected into our system is:

$$U = -k1\ tanh(s) + T0\cos\theta + Ao\ sign(\dot{\theta}) + Bo\dot{\theta} + K(\theta m - L\theta s) - (\ddot{\theta}d - \lambda\dot{e})J \quad (10)$$

With k1=40, $\lambda = 20$

Figures 11 and 12 represent the system's response to a reference of knee flexion extension signal with no load and under load.

The system responds to the control law and perfectly executes the desired reference with no sensitivity to disturbances.

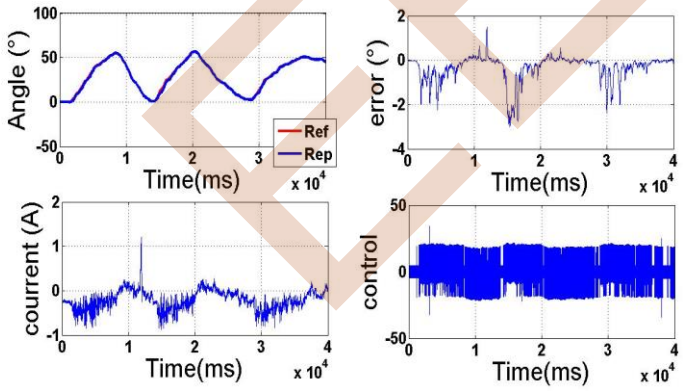

Figure 11: Response of the system to a reference of a knee flexion extension signal with a sliding mode control (no load).

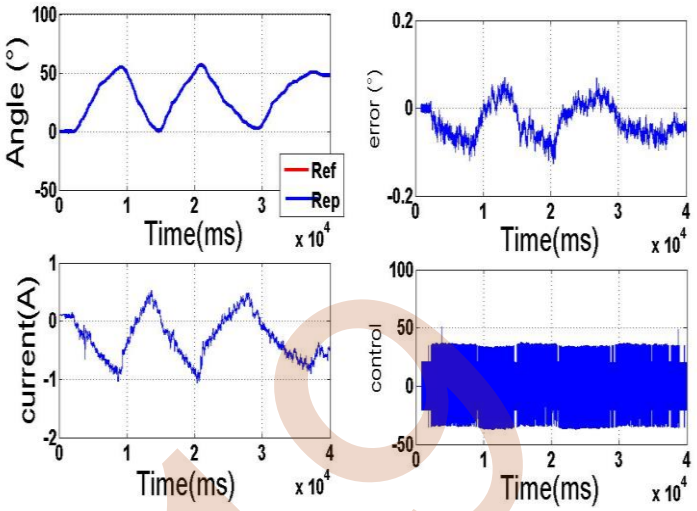

Figure 12: Response of the system to a reference of a knee flexion extension signal with a sliding mode control (charge of 3Kg).

The two controls used proportional and sliding mode, have responded well to the trajectory of the intention of walking, however they are comparable according to a number of characteristics. Table 3 shows a comparison of the two controls.

Proportional control	Sliding mode
Good precision	Very good precision
Sensitive to disturbances	insensitive to disturbances
Doesn't requires a model	Requires a model
Simple to apply	Difficult to apply
No chattering	Presence of chattering

Table 3: Comparison of the two proportional and sliding mode controls

I. CONCLUSION

In this paper, the presented work aims to improve the autonomy of impaired people with a motor knee joint deficiency. Our proposal is an exoskeleton in the shape of a human leg that is worn like an orthosis. This one will support the weight of the knee and produce a sufficient torque to perform the function of walking.

The work consisted in the realizing, modeling the system (exoskeleton + knee) and identifying its parameters. Two controllers were applied in real time using the DSPACE1103 control board, a low level proportional and a high level sliding

mode control. The superiority of the sliding mode controller has been remarked.
The initial objective has been achieved, the modelling and identification are valid, the exoskeleton perfectly responds to the desired requirements.

References

[1]. Dana Neumann, « Human Assistant Robotics in Japan - Challenges and Opportunities for European Companies », EU-Japan Centre for industrial Cooperation, 2016.

[2]. Asma Chaudri, Natalia Henao, Zahra Maqsood, « "Future Assistive Robots », Worcester Polytechnic Institute • Interactive Qualifying Project Report. 2016.

[3]. J. E. Pratt, B. T. Krupp, C. J. Morse, and S. H. Collins, The roboknee : an exoskeleton for enhancing strength and endurance during walking," in IEEE International Conference on Robotics and Automation, Proceedings. ICRA'04. 2004.

[4]. Evan Ackerman, Berkeley Bionics Introduces eLEGS Robotic Exoskeleton, IEEE Spectrum, 2018.

[5]. Maxon groupe, « Maxon DC Motor », P82,May 2012 edition.

[6]. Ghezal, M., Guiatni, M., Boussioud, I., & Renane, C. S. (2018, December). Design and Robust Control of a 2 DOFs Lower Limb Exoskeleton. In 2018 International Conference on Communications and Electrical Engineering (ICCEE), 2018.

[7]. Samer Mohammed, Weiguang Huo, Hala Rifaï,Walid Hassani, and Yacine Amirat «Robust Control of an Actuated Orthosis for Lower Limb Movement Restoration" , Intelligent Assistive Robots, Springer Tracts in Advanced Robotics 106, D, 2015.

[8]. Casabona, Antonino et al. "Functional assessments of the knee joint biomechanics by using pendulum test in adults with Down syndrome." Journal of applied physiology (Bethesda, Md. : 1985) vol. 113,11, pp 1747-55. 2012.

[9]. Vadim Utkin, Juergen Guldner, Jingxin Shi, Sliding Mode Control in Electro-Mechanical Systems, CRC Press, Published May 1, 2009.